



**IOP Conference Series:
Environment Science and Engineering**

**2018 2nd International Conference on
Power and Energy Engineering
(ICPEE 2018)**

**September 3-5, 2018
Xiamen, China**

**ISSN: 17551307
E-ISSN: 17551315**

PREFACE

It is our great pleasure to welcome you to 2018 2nd International Conference on Power and Energy Engineering (ICPEE 2018) which will be held in Xiamen University of Technology, China during Sept 3-5, 2018. ICPEE 2018 is dedicated to issues related to Power and Energy Engineering.

The major goal and feature of the conference is to bring academic scientists, engineers, industry researchers together to exchange and share their experiences and research results, and discuss the practical challenges encountered and the solutions adopted. Professors from China are invited to deliver keynote speeches regarding the latest information in their respective expertise areas. It will be a golden opportunity for the students, researchers and engineers to interact with the experts and specialists to get their advice or consultation on technical matters, sales and marketing strategies.

These proceedings present a selection from papers submitted to the conference from universities, research institutes and industries. All of the papers were subjected to peer-review by conference committee members and international reviewers. The papers selected depended on their quality and their relevancy to the conference. The volume tends to present to the readers the recent advances in the field of power and energy engineering and various related areas, such as power distribution, power quality, energy conversion, renewable energy sources, energy policies and regulation, computational electromagnetics and power system planning, etc..

We would like to thank all the authors who have contributed to this volume and also to the organizing committee, reviewers, speakers, chairpersons, sponsors and all the conference participants for their support to ICPEE 2018.

Prof. Gordon Huang

Faculty of Engineering and Applied Science, University of Regina, Canada

Sept. 10, 2018



Conference Committee

Conference Chair

Prof. Gordon Huang, International Society for Environmental Information Sciences

Prof. Yongping Li, Beijing Normal University; Xiamen University of Technology, China

Program Chair

Prof. Satya Harpalani, Southern Illinois University Carbondale, USA

Local Organizational Committee

Co-Chair: Changping Chen, Xiamen Ocean Vocational College, China

Co-Chair: Haiyan Fu, Xiamen University of Technology, China

Tian Chai, Xiamen University of Technology, China

Xiaoqing Chen, Xiamen University of Technology, China

Huajing Cheng, Xiamen University of Technology, China

Huiyan Cheng, Xiamen University of Technology, China

Qian Cheng, Xiamen University of Technology, China

Zineng Dai, Xiamen University of Technology, China

Panfeng Gao, Xiamen University of Technology, China

Yanhong Jiang, Xiamen University of Technology, China

Bangbang Jiu, Xiamen University of Technology, China

Wenchao Liao, Xiamen University of Technology, China

Guangsheng Liu, Xiamen University of Technology, China

Jing Liu, Xiamen University of Technology, China

Jiangxue Long, Xiamen University of Technology, China

Yicheng Wu, Xiamen University of Technology, China

Aili Yang, Xiamen University of Technology, China

Mengxiang Zeng, Xiamen University of Technology, China

Qiwei Zhang, Xiamen University of Technology, China

Mulan Zhu, Xiamen University of Technology, China

International Program Committee

Co-Chair: Shuguang Wang, Shandong University, China

Co-Chair: Mohamed El-Din, University of Alberta, Canada

Yanfeng Li, South-South Cooperation Center for Sustainable Development, China

Yongtae Ahn, Gyeongnam National University of Science and Technology, Korea

Bandar Alqahtani, Duke University, USA

Hasan Aydogan, Mechanical Engineering Department, Selcuklu, Konya, TURKEY

Ipek Barut, Istanbul University, Turkey

Serdar Celik, Southern Illinois University Edwardsville, USA

Ali Cheshmehzangi, University of Nottingham Ningbo, China

Bal Deshwal, A. I. Jat H. M. College, India

Saad El-Syaed, Mechanical power engineering-Zagazig university, Egypt

Ahmed Hossam-Eldin, Alexandria University, Alexandria, Egypt



Jinliang Liu, Ontario Ministry of Environment and Climate Change
Lei Liu, Dalhousie University, Canada
Rodrigo Muñoz, Bataan Peninsula State University, Philippines
Hui Kwun Nam, University of Macau, China
Hedayat Omidvar, National Iranian Gas Company, Iran
Nugroho Pambudi, Sebelas Maret University, Indonesia
Wei Peng, University of Regina, Canada
Xiaosheng Qin, Nanyang Technological University, Singapore
Jagdish Sharma, JK Lakshmi Pat University, India
Sunil Singal, Indian Institute of Technology, India
Eric Strauss, Michigan State University, USA
Wei Sun, Zhongshan University, China
Qian Tan, China Agricultural University, China
Mohd Teridi, National University of Malaysia, Malaysia
Tsung-Mou Huang, Taiwan Power Company, Taiwan
Dimitar Velev, University of National and World Economy, Bulgaria
Shuo Wang, Hongkong Polytechnic University, Hong Kong
Xiuquan Wang, University of Louisiana, USA
Jia Wei, Beijing Polytechnic University, China
Bin Yan, Xiamen University of Technology, China
Shin-Cheng Yeh, National Taiwan Normal University, ROC
Hui Yu, Temple University, USA
Baiyu Zhang, Memorial University, Canada
Hua Zhang, Texas A&M University, USA
Xiaodong Zhang, Los Alamos National Laboratory, Los Alamos, USA
Yimei Zhang, North China Electric Power University, China
Jiancheng Zheng, University of Ottawa, Canada
Eric James Strauss, Michigan State University, USA
Yongtae Ahn, Gyeongnam National University of Science and Technology, Korea
Saad Abdel-Hamid El-Syaed, Mechanical power engineering-Zagazig university, Egypt
Ahmed A. Hossam-Eldin, Alexandria University, Alexandria, Egypt
RODRIGO C. MUÑOZ, BATAAN PENINSULA STATE UNIVERSITY, Philippines
Mohd Asri Mat Teridi, The National University of Malaysia
Jiancheng (James) Zheng, University of Ottawa, Canada
Dimitar Velev, University of National and World Economy, Bulgaria
Hartmut Hinz, Frankfurt University of Applied Sciences, Germany
Hamidah Ibrahim, Universiti Putra Malaysia, Malaysia
Zuriati Ahmad Zukarnain, Universiti Putra Malaysia, Malaysia
Shengying Yang, Hangzhou Dianzi University, China
Serdar Celik, Southern Illinois University Edwardsville, USA
Hasan AYDOGAN, Mechanical Engineering Department, Selcuklu, Konya, TURKEY
Bal Raj Deshwal, Dept. of Chemistry, A. I. Jat H. M. College, Rohtak, India
Sunil Kumar Singal, Alternate Hydro Energy Centre, Indian Institute of Technology, India
Ali Cheshmehzangi, The University of Nottingham Ningbo, China

Bandar Jubran Alqahtani, Duke University, USA

Hedayat Omidvar, Research & Technology Dept., National Iranian Gas Company, Iran

Jagdish Prasad Sharma, JK Lakshmi Pat University, Jaipur, Rajasthan, India

Hui Kwun Nam, University of Macau, China

Nugroho Agung Pambudi, Sebelas Maret University, Indonesia

Wei Peng, University of Regina, Canada

RAJA SEKHAR DONDAPATI, Lovely Professional University, India

Ipek F. Barut, Istanbul University, Turkey

Tsung-Mou Huang, Taiwan Power Company, Taiwan

Eduardo M. G. Rodrigues, The School of Design, Management and Production Technologies of

Northern Aveiro, Portugal

OOI CHIA AI, Power Electronics Converter and System Control, Malaysia

PATRICK GOH KUAN LYE, Universiti Sains Malaysia, Malaysia

Peer review statement

All papers published in this volume of *IOP Conference Series: Earth and Environmental Science* have been peer reviewed through processes administered by the proceedings Editors. Reviews were conducted by expert referees to the professional and scientific standards expected of a proceedings journal published by IOP Publishing.



Table of Contents

Chapter 1: Electrical theory and new technology

Study on the Subsynchronous Resonance Control Method Based on the DFIG Grid-Side Converter.....3

M X Yin, H Liu, Y H Li and W Song

Coordination of Multistage Scheduling Strategy in Cogeneration System.....11

Zhenyu Li, Dong Zhao, Qing Ye and Guibo Ma

Development of a Comprehensive Transformer Material System Analyzer.....18

Yuan Gao, Zhiwei Zhao, Xinyu Wang and Xin Hu

Hierarchical Topology Analysis Method for Substations Based on Electrical Bays.....27

X Zhang, Z F Xu, B Zhou, H F Wang and H X Pan

Study on Thermal Performance of a Phase Change Thermal Storage Device by Utilizing Off-peak Power.....33

B Tang, Q H Shangguan and Y Lu

Improvement of Performance Calculation Methods for Pulverized Coal and Blast-furnace Gas Co-fired Boilers.....40

Yalan Ye, Hongming Wang, Xiang An and Wenhao Jiang

Effect of Different Reductants on Leaching Lithium and Cobalt from Lithium Ion Batteries in Tartaric Acid Solution.....49

Qian Cheng

Chapter 2: Motor and electrical control technology

The Numerical Simulation of a High Power Hall Effect Thruster.....59

Lai Li, Xi Lu, Hulin Huang, Xidong Zhang and Guiping Zhu

A New Software Phase-locked Loops.....66

Cunbing Gui, Zhangbao Chen and Xuehui Luo

Space Vector Flux Weakening Control of PMSM Driver.....72

Gentao Dong, Jianfei Yang, Xin Qiu, Xun Liu and Cao Wei

Research and Verification of Setting Value Coordination Method Considering the Responding Deviation of under Excitation Limit and Loss of Excitation Protection for Generator.....	79
<i>Quan Hong, Li Li, Haifeng Liu, Wenqi Mao and Wenjun Lu</i>	
Impact of Wind Generators Number and Location on the Resonance Risk of Wind Farm Integration through Flexible HVDC System.....	88
<i>Xiao Wang, Xiaobao Hu, Hui Liu, Linlin Wu and Siqing Sheng</i>	
Small-Signal Modelling and Stability Analysis of Current-Controlled Virtual Synchronous Generators.....	96
<i>D W Sun, H Liu, P Song, S Zhu and Z Wei</i>	
Rotation Speed Recovery Strategy Based On Variable Power Curve of Inertia Control from DFIG Wind Turbine.....	105
<i>R Liu, P Song, X S Wang and Z W Lin</i>	
Chapter 3: Electrical equipment failure detection	
Fault Diagnosis of Gas Turbine Based on Improved BP Neural Network with the Combination of N-W and L-M Algorithm.....	117
<i>Yun Zhang, Yu-liang Qian, Zheng Qiu and Xiao Zhang</i>	
Research on Short-term Prediction Method of Substation Bus-bar's Voltage Trend Based on Multidimensional Time Series Data Mining.....	128
<i>Fei Xiao, Xiwu Leng, Kang Ye, Youlin Hu, Xiongli Li and Licheng Zhu</i>	
Grounding Fault Analysis and Protection Measures Study of Composite Grounding Arc-suppression Model.....	135
<i>B Yu, H Li, W J Zhu, H F Liu, W W Liang, Z D Zhang and S Y Guo</i>	
Research on Intelligent Diagnosis Strategy of Secondary Device Abnormity in Smart Substation.....	145
<i>Meizi Hong, Peng Li, Di Wu, Bo Wen and Hengxuan Li</i>	
Research on Logic Optimization and Reliable Calculation Model of Satellite Based Wildfire Monitoring for Power Transmission Line.....	157
<i>Zhenzhen Zhou and Gang Chen</i>	
The Research of Anomaly Detection Method for Transformer Oil Temperature Based on Hybrid Model of Non-Supervised Learning and Decision Forests....	164

Fei Xiao, Xiwu Leng, Kang Ye, Youlin Hu, Xiongli Li and Licheng Zhu

Fault Ride through Strategy for Virtual Synchronous Control based Doubly-Fed Induction Generators.....	171
<i>Xuekun Cheng, Hui Liu, Peng Song and Hao Jiang</i>	

Chapter 4: High voltage and insulation technology

Improved Control Strategy for AC-Filters Switching in UHVDC Converter Station.....	181
<i>Hui Li, Xiaofei Wang, Bin Yu, Haifeng Liu, Hao Xu and Siyuan Guo</i>	

Researches on Two Kinds of Fault Restart Logic of Qishao \pm 800 kV UHVDC Project.....	191
<i>Hao Xu, Lei Zhang, Haifeng Liu, Wenwu Liang and Hui Li</i>	

Study on the Electrochromic Label for High-voltage Equipment with $W\text{O}_3$	199
<i>Linong Wang, Enwen Li, Bin Song and Yaqi Fang</i>	

Study on Influence Factors of Lightning Impulse Test Waveform of UHV GIS Equipment.....	204
<i>Jiadong Meng, Tianxiang Chen, Dajin Chen, Rongquan Wang and Lei Wang</i>	

Electric Field Analysis on Buffer Layer of HV XLPE Power Cable by Finite Element Method.....	210
<i>Weiwei Zhang, Youxiang Yan, Weiling Lin, Shanshan Li and Lei Wang</i>	

Chapter 5: Smart Grid Analysis and Optimization

Preferably Receiving <i>End's Infeed</i> Modes for UHVDC Power Transmission...	219
<i>Bi Zhen, Guo Qiang, Zhou Qinyong, Jiang Yilang and Qin Xiaohui</i>	

Droop control Based Seamless Transfer Strategy for Three-phase Converter in Microgrid.....	227
<i>Guopeng Zhao, Xinwei Zhou, Hongwei Yang, Feng Xu and Yanjie Wang</i>	

Study on Coordinated Optimization of the Grid Voltage Control Strategy Considering Comprehensive Cost.....	235
<i>Jingbo Wu, Jianling Zhang, Weijun Zhu, Dijun Hu, Xinfan Jiang and Wei Zhong</i>	

Research on Improved Droop Control Strategy Based on Virtual Impedance...244
X M Liu, B C Lu, Z P Ren and R X Zhang

Analysis of Hierarchical and Time-phased Model of Large-scale Power Grid
Based on Fp-growth Algorithm.....252
Tianyue Wang, Jinxiu Hou and Zhihong Yu

Deep Learning Algorithm for Preliminary Siting of Substations Considering
Various Features in Distribution Network Planning.....260
*Liang Feng, Can Cui, Runze Ma, Jian Wu, Yang Yang, Xiaolei Zhang and
Shengyuan Liu*

Study on Power Quality Impacts of Rural Distribution Network with Large-scale
Heat Pumps.....268
*Zhenwei Li, Wenliang Zhu, Pengfei Sun, Siyao Hu, Kaiyuan Jin and
Jianhua Yang*

Power Grid Partition Method for Black Start Based On Complex Network
Theory.....275
Fubin Xu, He Zhang, Run Li and Jian Cai

The Power Grid Development with Distributed Wind Plant Growth Based on
Coordination Analysis.....282
Yudong Tan, Xianghua Li, Pengfei Zhang, Yong Li and Dong Peng

Power Quality Monitoring and Energy Efficiency Management of Microgrid
based on wind-PV-ES Hybrid System.....290
Guanlu Yang, Minxu Wu, Yang Wang and Zehong Huang

The Research on P2G Gas-Electric Hybrid Optimal Economic Dispatch
Strategy.....297
Zheng Zhang, Tianran Li, Quan Liu and Chao Yuan

Chapter 6: Power system and automation

Study on Data Selection Method of Historical Operation Data for Large Scale
Power System.....307
*Hongyang Dai, Ying Lv, Zhihong Yu, Guangming Lu, Chang Xie and Jinxiu
Hou*

Tuning Approach for Power System Stabilizer PSS4B using Hybrid PSO.....	315
<i>Siyuan Guo, Shoushou Zhang, Junying Song, Yongsheng Zhao and Weijun Zhu</i>	
Short-term Electricity Load Forecasting in Thailand: an Analysis on Different Input Variables.....	322
<i>Wutyi Hnin Su and Jeenanunta Chawalit</i>	
Design of Rated Power Control Strategy of Wind Turbine Based on Particle Swarm Optimization.....	330
<i>YC Yang, Y Liu, P Song, Y Cui and Y Bai</i>	
The Profit Influence of Additional Heat Sources on Combined Heat and Power System in Existing Peak Shaving Compensation Mechanism.....	337
<i>Yang Bai, Jianxing Qin, Qi Guo and Zhongkai Yi</i>	
Suppression Methods for Low Frequency Oscillation of Wind Farm Considering SVG Minimum Output Dead Zone.....	345
<i>Yangfan Zhang, Xu Xie, Peng Song, Hui Liu and Tao He</i>	
RPT Runner Flow Structures Dependence on Guide Vane Opening Angle: A CFD Numerical Simulation.....	351
<i>Maxime Binama, Wei-Hua Cai, Wen-Tao Su, Feng-Chen Li, Xian-Zhu Wei and Alexis Muhirwa</i>	
Research on Reduced Scene Sets Based on ARMA Model of Wind Farms Day-ahead Total Output Forecasting.....	358
<i>Hui chao Wang, Lei Liu, Jin hui Ma, Jie Ding and Chang Zhou</i>	
Design and Energy Efficiency Management of Cascade Hydropower System.....	367
<i>Guanlu Yang, Zehong Huang, Shuyang Wang and Minxu Wu</i>	
The Solar Power Plant Prediction A case Study in Phitsanulok, Thailand.....	373
<i>W Srisuriyajan and C Thongchaisuratkrul</i>	
Research on steady-state power distribution calculation technology of electrothermal coupled regional energy system.....	381
<i>Jinning Shan, Zhenyu Li, Gang Chen and Xin Wang</i>	

Chapter 7: Energy development and utilization

- Optimal design of distributed energy systems in rural area of developing country: a case study of Guanzhong area, China.....391
Y Zhu, X X Yan and Q L Tong
- The Unit Commitment Model and Analysis for Promoting Clean Energy Consumption with Considering of Tie Line Plan Adjustment.....398
Zhang Xu, Shi Xinhong, Zhu Bingquan, Sun Ke and Xiao Yanwei
- Performance Analysis of the BIPV of an Industrial Park in Wuhan.....406
Jingkang Ba, Xiaoli Huang, Guogang Yan and Xiaojing Wang
- The Capacity Optimization of the Energy Storage System used for Peak Load Shaving.....411
Kai Deng, Xiaobo Tang, Jie Lei, Zhenyao Qian and Bangcheng Wei
- Review on Target Tracking of Wind Power and Energy Storage Combined Generation System.....418
Xuwei Guo, Man Xu, Linlin Wu, Hui Liu and Siqing Sheng
- Survey on the Operation of the District Energy Supply System in Japan According to Secular Change.....426
Anna Won
- Study on Modification of Phase Change Energy Storage Materials Suitable for Biogas Fermentation.....431
Zhipeng Yang, Jinheng Li, Anxing Lai, Gang Li and Lei Wang
- The Study of Banana Leaf Fiber Based Biomass Pellets Fuel.....437
Xinwen Wang, Shimin Wu, Xin Rao, Jie Chi and Su Xu
- Research on the Cellulase Hydrolysis of Colocasia Antiquorum in Producing Ethyl Alcohol.....442
H Z Yan, H Y Fu, G X Su, D Zhao, Y C Wu, J F Liu, P F Gao and Y T Huang
- Oil Price Factors: Forecasting on the Base of Modified ARIMA Model.....447
Anthony Msafiri Nyangarika and Bao-jun Tang
- DSGE Model of the Russian Economy: Economic Impact of Oil Price..... 457

Anthony Msafiri Nyangarika and Bao Jun Tang

Chapter 8: Environment and economy

Study on Performance Optimization of SCR Denitrification of an Ultra-low Emission Coal-fired Power Unit.....469

Bing Li, Yongqiang Song, Qilong Zhang, Can Zhou and Haoran Duan

Aquaculture Wastewater Treatment with Immobilized Microorganisms-aquatic Plants Strengthened Purification System.....475

HY Cheng, JX Long and Z Liu

Treatment of Candied Fruit Wastewater by Adsorption Oxidation Combined Process.....480

Mengxiang Zeng

Application of Deodorant in Odor Control of Municipal Solid Waste.....488

Z N Dai, F S Zeng, J Liu, A L Yang and H Y Fu

Micro-weather Station System for Small Geographical Coverage in the Philippines.....495

R C Muñoz Jr., X S Yumang, S J A Japitana, K R C Medina and J E T Tibayan

The Effect of Silicon Fertilizer on The Growth of Chives.....506

Jiang-xue Long, Hui-yan Cheng, Zhi-neng Dai and Jian-fu Liu

Influence Oil Price towards Economic Indicators in Russia.....512

Anthony Msafiri Nyangarika and Bao-jun Tang

Chapter 9: Modern information science and technology

Routing Architecture of Software Defined Energy Internet.....523

Dilin Mao, Xiu Cao, Xinyang Han, Chengzhi Zhu and Wei Geng

Optimizing Thermal Performance of Data Centers with Novel Local Partition Configurations.....531

Hongjie Lu and Zhongbin Zhang

Interpolation Estimation Method of Tropospheric Delay for Long Baseline Network RTK Based on Support Vector Machine.....	536
<i>Jian Deng, Miaoqiang Xu, Xuexiang Yu and Aiguo Zhang</i>	
Application of Point Cloud Data in the Construction and Management of Interior Design.....	544
<i>Minyong Li and Jianwen Liu</i>	
The Application Research of Oblique Photogrammetry Technology in Road Planning.....	552
<i>Zhihuang Zheng</i>	
Research on LED Advertising Display Wireless Control System Based on MT6589.....	563
<i>Yizhou Mao, Yingchao Xu, Subin Wang and Wenwei Zhu</i>	
Author Index.....	571

Chapter 1:
Electrical Theory and New Technology

Study on the Subsynchronous Resonance Control Method Based on the DFIG Grid-Side Converter

M X Yin^{1,2}, H Liu^{1,3}, Y H Li^{1,3} and W Song²

¹State Grid Jibei Electric Power Research Institute, North China Electric Power Research Institute Co. Ltd., Beijing, 100045, China

²Department of Electrical and Electronic Engineering, North China Electric Power University, Baoding, China

³Grid-connected Operation Technology for Wind-Solar-Storage Hybrid System State Grid Corporation Key Laboratory, Beijing, 100045, China

Abstract. DFIG-based series-compensated can increase the capacity of wind power transmission, but it can also cause the sub-synchronous resonance (SSR) problem. Based on the mechanism of subsynchronous resonance in DFIG, the electromagnetic torque variation under the variation of rotor speed can be divided into two parts, i.e. rotor torque variation and stator torque variation. Supplementary controller is added to the stator side converter, which is generated to provide positive damping. MATLAB simulation is carried out to compare the result of supplementary damping. Results show that supplementary damping controller makes DFIG keep stable under various rotor speeds and RSC inner-loop gain.

1. Introduction

Wind energy has been widely used and developed worldwide as a clean and environmentally friendly renewable energy source in recent years. China has now become the country with the largest installed capacity of wind power in the world. However, wind power is mainly concentrated in remote areas and is far from the center load. Therefore, the long-distance large-scale delivery of wind power is imperative¹. Series-compensated technology is often used to increase the transmission capacity and perform long-distance power transmission, but it also leads to SSR problems. There have been many subsynchronous resonance accidents caused by series-compensated at home and abroad [1]-[3].

At present, subsynchronous resonance suppression methods for wind power series-compensated systems are mainly divided into two types: one is controlled by adding FACTS devices, and the other one is controlled by additional damping control in the wind turbine itself. The addition of FACTS to control SSR will not only increase investment, but also will be underutilized [4]. In terms of the additional damping control of the wind turbine, [5], [6] mainly control on the GSC side which analyze the results using the eigenvalue analysis method by adding a damping control strategy to the GSC DC voltage control loop (active power control loop) or the terminal voltage control loop (reactive power control loop) and verify its accuracy and effectiveness by time domain simulation. [7] adds damping control to the RSC to achieve SSR control. [12] separately uses the rotor speed, transmission line active power, and series capacitor voltage as input control signals. After the high-pass filter and the proportional limiting section with additional damping control, SSR control is implemented in the GSC and RSC, respectively [9]. Because of the lack of research on the SSR mechanism, the physical

This work is supported by the Operation Characteristics and Control of Large Scale Renewable Energy with Series Compensated Transmission System Project of State Grid Corporation of China (52010116000S).



Content from this work may be used under the terms of the [Creative Commons Attribution 3.0 licence](https://creativecommons.org/licenses/by/3.0/). Any further distribution of this work must maintain attribution to the author(s) and the title of the work, journal citation and DOI.

Published under licence by IOP Publishing Ltd

significance of the control method is not clear enough, and the design of the parameters is not specific enough [10].

In this paper, starting from the GSC, the additional damping suppression increases the positive damping of the torque to the system and realizes the control of SSR. The complex torque analysis method is used to explain the mechanism of subsynchronous resonance and the design of the controller. Detailed controller design parameters and procedures are given. The system can run safely and stably with low wind speed and high inner loop proportional coefficient. And verified with time domain simulation.

2. DFIG-series-compensated system modeling

This paper takes the equivalent modeling of a certain wind farm in North China. The wind farm is boosted by the transformer and then connected to the series-compensated transmission system, taking account of the impedance of the low-voltage transmission line, from the perspective of the wind farm, the equivalent series compensation degree of the grid is 6.67% [1]-[3]. When the operating conditions of each wind turbine in the wind farm are not much different, the entire wind farm can be equivalent to a DFIG [11], [12]. The equivalent system is shown in figure.1.

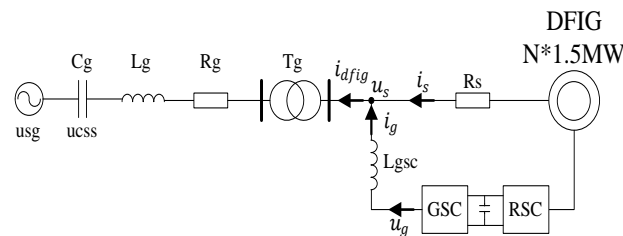


Figure 1. The equivalent model of wind farm series-compensated system

In figure.1, R_s , resistance of the stator windings; L_{gsc} , connection inductance of the GSC side; R_g , L_g , C_g , the equivalent resistances, inductances, and capacitances of the series-compensated transmission lines, respectively; i_g represents the GSC output current, i_s represents the stator current, i_{dfig} represents the DFIG current, u_g represents the GSC output voltage, u_s represents the stator voltage, u_{cgs} represents the series-compensated capacitor voltage, and u_{sg} represents the grid voltage. DFIG and transmission line parameters are shown in Table 1.

Table 1. DFIG and transmission line parameters

Parameters	Value	Parameters	Value
Capacity base value S_B /MVA	100	Line equivalent resistance R_g /pu	1.8948
Stator resistance R_s /pu	0.023	Line equivalent inductance L_g /pu	0.05314
Stator leakage reactance L_{ls} /pu	0.18	Series compensated capacitor C_g /pu	0.003290
Rotor resistance R_r /pu	0.016	Excitation reactance L_m /pu	2.9
Rotor leakage reactance L_{lr} /pu	0.16		

3. SSR mechanism interpretation based on complex torque analysis

3.1 DFIG torque analysis

Electromagnetic torque relationship of asynchronous motor in DFIG:

$$T_{e*} = -n_p L_{m*} (i_{sq*} i_{rd*} - i_{sd*} i_{rq*}) \quad (1)$$

n_p is the number of pole pairs, i_{sd*} , i_{sq*} , i_{rd*} , i_{rq*} are the currents of the dq axis of the stator and the rotor, and L_{m*} is the mutual inductance between the stator and the rotor.

Linearize (1) to get

$$\begin{aligned}
\Delta T_{e^*} &= -n_p L_m^* (i_{sq0^*} \Delta i_{rd^*} - i_{sd0^*} \Delta i_{rq^*}) \\
&\quad - n_p L_m^* (i_{rd0^*} \Delta i_{sq^*} - i_{rq0^*} \Delta i_{sd^*}) \\
&= \Delta T_{er^*} + \Delta T_{es^*}
\end{aligned} \tag{2}$$

From the formula (2), it can be seen that the amount of change in the electromagnetic torque when the rotational speed changes is divided into two parts: the rotor variation ΔT_{er^*} and the stator variation ΔT_{es^*} .

This article mainly analyzes the relationship between the variation of the stator torque and the variation of the speed. There is the following internal relationship between the variation of the stator torque and the variation of the speed:

Speed increment \rightarrow Stator flux increment \rightarrow Stator induced EMF increment \rightarrow Stator current increment \rightarrow Stator torque increment

In order to simplify the derivation process, this paper makes the following assumptions: ignore the ratio and integral coefficient of RSC control strategy, and the integral coefficient of inner loop. For details, see the next section.

3.2 The relationship of stator torque variation and speed variation

The steady-state value of the rotor speed of DFIG is ω_{r0^*} . At the same time, there is perturbation $\Delta\omega_{r^*}$ with an amplitude ε , and the angular frequency Ω , ie $\Delta\omega_{r^*} = \varepsilon \sin(\Omega t + \varphi)$. The flux linkage equation, Lenz's law and Laplace transformation of an induction motor can get the variation of the induced electromotive force of the stator dq axis.

$$\begin{bmatrix} \Delta E_{sd^*}(s) \\ \Delta E_{sq^*}(s) \end{bmatrix} = \begin{bmatrix} -L_m^* i_{rq0^*} - \frac{\omega_{Base} \omega_{s^*} L_m^* i_{rd0^*}}{s} \\ -L_m^* i_{rd0^*} - \frac{\omega_{Base} \omega_{s^*} L_m^* i_{sq0^*}}{s} \end{bmatrix} \Delta\omega_{r^*}(s) \tag{3}$$

ω_{Base} is the reference angular frequency, and ω_{s^*} is the standard value of the stator angular frequency.

From the circuit of the stator part and the stator-side converter part in figure. 1, we can get the equations in abc coordinates and then dq transformation, divided by the reference value, and after the Laplace transformation, the circuit equations of these two parts are:

$$\begin{bmatrix} \Delta U_{sd^*}(s) \\ \Delta U_{sq^*}(s) \end{bmatrix} = \begin{bmatrix} \Delta E_{sd^*}(s) \\ \Delta E_{sq^*}(s) \end{bmatrix} + \begin{bmatrix} R_{s^*} & 0 \\ 0 & R_{s^*} \end{bmatrix} \begin{bmatrix} \Delta I_{sd^*}(s) \\ \Delta I_{sq^*}(s) \end{bmatrix} \tag{4}$$

The GSC control strategy is shown in figure. 2. The dq axis adopt a double closed-loop control strategy. The d -axis control target is to maintain the converter DC bus voltage constant and the q -axis control target is to maintain the input current sine. Assuming that the output voltage of the converter is equal to the reference voltage, the variation of the output voltage at the GSC side can be

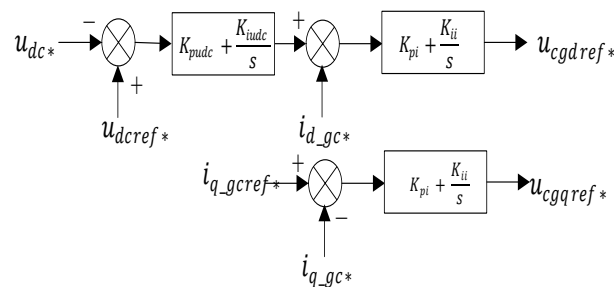


Figure 2. GSC side control figure

$$\begin{cases} \Delta U_{cgd^*}(s) = (K_{pudc} + \frac{K_{iudc}}{s})(K_{pi} + \frac{K_{ii}}{s})\Delta U_{dc^*}(s) \\ \quad - (K_{pi} + \frac{K_{ii}}{s})\Delta I_{d-gc^*}(s) \\ \Delta U_{cgd^*}(s) = - (K_{pi} + \frac{K_{ii}}{s})\Delta I_{q-gc^*}(s) \end{cases} \quad (5)$$

$$\begin{bmatrix} s - \frac{\omega_{Base} K_{Pi}}{L_{gsc^*}} & -\omega_{Base} \omega_{s^*} \\ -\omega_{Base} \omega_{s^*} & s - \frac{\omega_{Base} K_{Pi}}{L_{gsc^*}} \end{bmatrix} \begin{bmatrix} \Delta I_{gd^*}(s) \\ \Delta I_{gq^*}(s) \end{bmatrix} = \frac{\omega_{Base}}{L_{gsc^*}} \begin{bmatrix} \Delta U_{sd^*}(s) \\ \Delta U_{sq^*}(s) \end{bmatrix} \quad (6)$$

The current relationship is available in figure. 1.

$$\begin{cases} \Delta I_{dfigd^*}(s) = \Delta I_{sd^*}(s) + \Delta I_{gd^*}(s) \\ \Delta I_{dfiqq^*}(s) = \Delta I_{sq^*}(s) + \Delta I_{gq^*}(s) \end{cases} \quad (7)$$

According to the line-side voltage relationship, the dq transform is performed, divided by the reference value, and is obtained after Laplace transformation:

$$\begin{bmatrix} s + \frac{\omega_{Base} R_{g^*}}{L_{g^*}} & -\omega_{Base} \omega_{s^*} \\ \omega_{Base} \omega_{s^*} & s + \frac{\omega_{Base} R_{g^*}}{L_{g^*}} \end{bmatrix} \begin{bmatrix} \Delta I_{dfigd^*}(s) \\ \Delta I_{dfiqq^*}(s) \end{bmatrix} = \frac{\omega_{Base}}{L_{g^*}} \begin{bmatrix} \Delta U_{sd^*}(s) \\ \Delta U_{sq^*}(s) \end{bmatrix} - \frac{\omega_{Base}}{L_{g^*}} \begin{bmatrix} \Delta U_{cssd^*}(s) \\ \Delta U_{cssq^*}(s) \end{bmatrix} \quad (8)$$

$$\begin{bmatrix} s & -\omega_{Base} \omega_{s^*} \\ \omega_{Base} \omega_{s^*} & s \end{bmatrix} \begin{bmatrix} \Delta U_{cssd^*}(s) \\ \Delta U_{cssq^*}(s) \end{bmatrix} = \frac{\omega_{Base}}{C_{g^*}} \begin{bmatrix} \Delta I_{dfigd^*}(s) \\ \Delta I_{dfiqq^*}(s) \end{bmatrix} \quad (9)$$

Eliminating the intermediate variables, (3)-(5) can obtain the stator current variation as

$$\begin{cases} \Delta I_{sd^*}(s) = G_{isd^*}(s)\Delta \omega_{r^*}(s) \\ \Delta I_{sq^*}(s) = G_{isq^*}(s)\Delta \omega_{r^*}(s) \end{cases} \quad (10)$$

Substituting (10) into (2) gives the relationship between ΔT_{es^*} and $\Delta \omega_{r^*}$, which can be expressed as

$$\frac{\Delta T_{es^*}(j\Omega)}{\Delta \omega_{r^*}(j\Omega)} = G_{Tes}(j\Omega) = |G_{Tes}(j\Omega)| \angle \varphi_{Tes} = G_{Tessx} + jG_{Tesy} \quad (11)$$

3.3 Mechanism Explanation

Without loss of generality, it can be assumed that the initial phase of the rotational speed $\Delta \omega_{r^*}$ is 0, and the position of $\Delta \omega_{r^*}$ on the vector diagram coincides with the positive direction of the x -axis, as shown in Figure 3. For a rotational speed variation with an angular frequency of Ω , if the projection of ΔT_{es^*} on the x -axis is in the same direction as $\Delta \omega_{r^*}$, that is, when G_{Tes} is in the first or fourth quadrant, $\varphi_{Tes} \in [90^\circ, -90^\circ]$, when the real part of G_{Tes} is $G_{Tessx} > 0$, then the effect of ΔT_{es^*} will cause the amplitude of $\Delta \omega_{r^*}$ to increase, and thus it will act as a negative damping, and the larger the G_{Tes} , the greater the negative damping.

On the other hand, if the projection of ΔT_{es^*} on the x -axis is opposite to that of $\Delta \omega_{r^*}$, when the vector G_{Tes} is located in the second or third quadrant, $\varphi_{Tes} \in [90^\circ, 270^\circ]$, when $G_{Tessx} < 0$, the effect

of ΔT_{es}^* is to reduce the amplitude of $\Delta\omega_{r^*}$, and therefore it acts as a positive damping, and the larger the projection, the greater the positive damping.

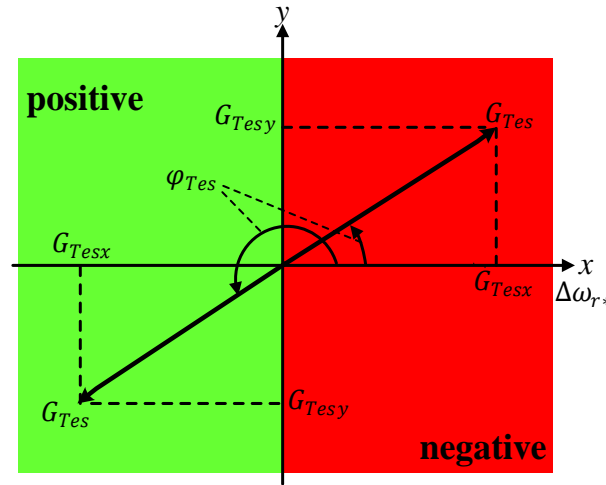


Figure 3. The relationship between stator torque variation vector and angular velocity variation vector

4. Design of GSC damping controller

According to the analysis in the previous section, the purpose of the rotor-side additional damping control strategy is to generate an electromagnetic torque that is in anti-phase with the rotational speed variation, thereby acting as a positive damping. Therefore, the rotational speed of the rotor is selected as feedback, and the d-axis of the GSC introduces feedback. The block diagram of the additional damping control strategy is shown in figure. 4, where $G_{SEDC}(s)$ is the additional damping control. At this point, the GSC reference voltage can be expressed as:

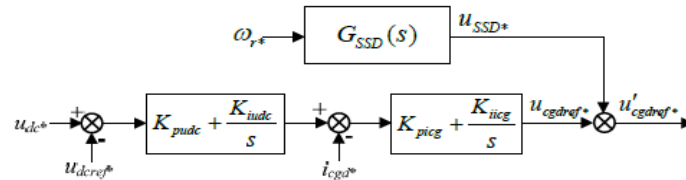


Figure 4. The d -axis control strategy of GSC after adding additional damping control

$$u'_{cgdref} = u_{cgdref} + u_{cgdsedc} = u_{cgdref} + G_{SEDC}(s)\omega_{r^*} \quad (12)$$

u_{cgdref}^* , output reference voltage without GSC additionally controlled; $\Delta u_{cgdsedc}^*$, output voltage generated by additional torque control.

Therefore, when the rotor speed includes the variation of $\Delta\omega_{r^*}$, the variation of GSC reference voltage can be expressed as:

$$\Delta u'_{cgdref} = \Delta u_{cgdref} + \Delta u_{cgdsedc} = \Delta u_{cgdref} + G_{SEDC}(s)\Delta\omega_{r^*} \quad (13)$$

According to the superposition theorem, the GSC output voltage change $\Delta u_{cgdsedc}^*$ generated by the additional torque control will generate additional currents Δi_{sdsedc} and Δi_{sqsedc} in the rotor. These two currents will generate additional torque ΔT_{essedc} , which affects the damping of subsynchronous oscillations. Note

$$\Delta T_{essedc} = G_{essedc}(s)\Delta\omega_{r^*} \quad (14)$$

Among them, $G_{essedc}(s)$ is the relationship between torque and speed. According to the analysis in the previous section, as long as the phase of $G_{essedc}(s)$ at the system's subsynchronous oscillation

frequency is placed in the second or third quadrant, the maximum positive damping of the additional torque can be achieved.

4.1 The design of high-pass filter

The high-pass filter is used to block straight and avoid the influence of additional damping control on the system in the steady state. The high-pass filter $G_{HP}(s)$ can be expressed as:

$$G_{HP}(s) = \frac{Ts}{Ts+1} \quad (15)$$

T generally takes 5~10.

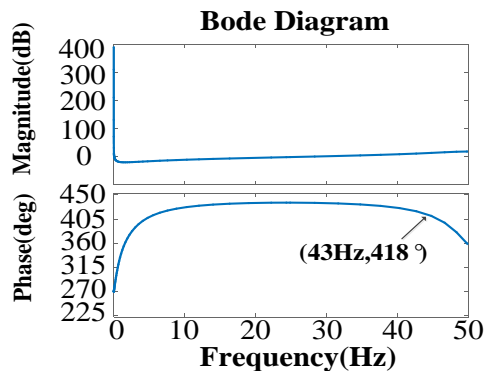


Figure 5. Magnitude and phase of $G_{essdc}(s)$ after high-pass filter

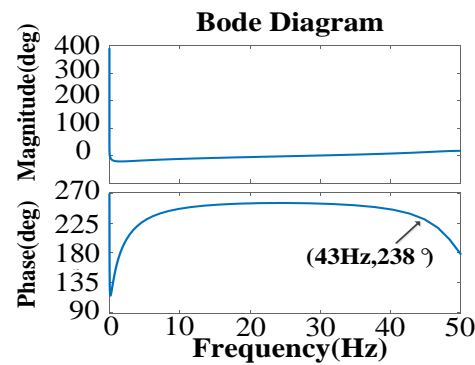


Figure 6. Magnitude and phase of $G_{essdc}(s)$ after high-pass filter and proportional phase-shifting

4.2 The design of proportional phase-shifting

In order to make the phase of the additional torque at the sub-synchronous frequency in the second or third quadrant, the $G_{SEDC}(s)$ must be added with a proportional phase shift $G_{BP}(s)$ with a time constant of $T_{PS}(s)$ and a gain of K :

$$G_{PS}(s) = K \frac{1 - T_{ps}s}{1 + T_{ps}s} \quad (16)$$

5. Simulation verification

5.1 Under different wind speed

The simulation results under various wind speed conditions are shown in the Figure 7. From the Figure 7, we can see that when there is no additional damping control when the wind speed is 5m/s or 6m/s, the system will oscillate. After adding additional damping control, the oscillation is controlled.

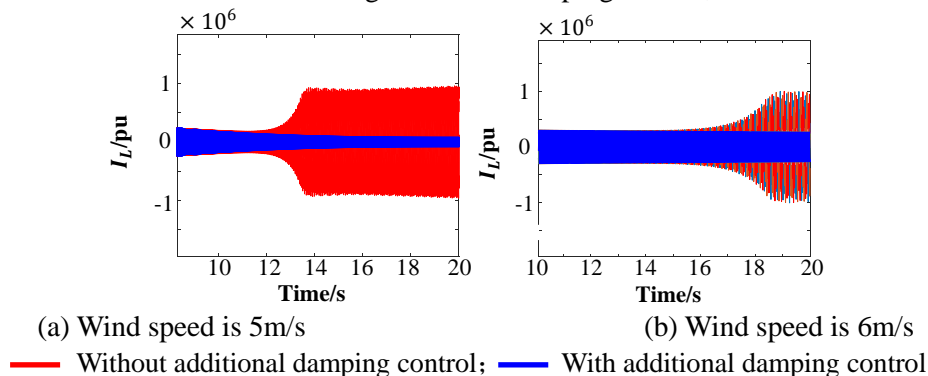


Figure 7. Output current with or without additional damping at different wind speeds

5.2 Different RSC inner-loop gain

In the case of different RSC inner-loop gains, compare whether there is an additional damping control strategy to control the SSR, as shown in the

Figure 8. When K_{pir} is 0.5 and 0.6, the system oscillates when there is no damping controller, and the system converges quickly when there is a damping controller.

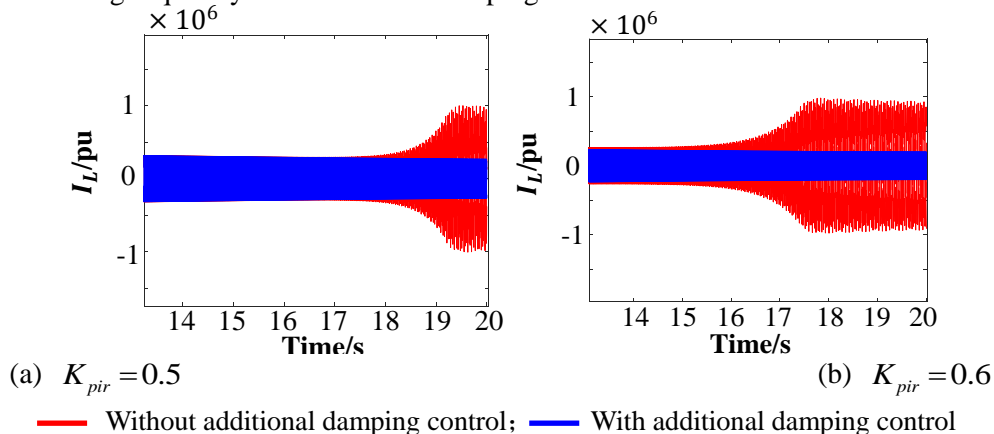


Figure 8. Simulation results with and without additional damping controller under different values of RSC inner-loop gain

6. Conclusion

1) Based on the study of the subsynchronous resonance mechanism of the DFIG series-compensated system, a control strategy for damping control on the stator side is proposed, which mainly contains the high-pass filter and the proportion of phase shift two parts. The high-pass filter is used to block straight and avoid the influence of additional damping control on the system in the steady state. The phase-shifting link makes the phase of the additional torque at the subsynchronous frequency lie in the second or third quadrant, and acts as a positive damping role.

2) Supplementary damping controller on GSC makes DFIG keep stable under various rotor speeds and inner-loop gain.

7. References

- [1] X L Dong, X R Xie, H Liu, et al. SSR Characteristics of a Wind Farm Connected to Series-Compensated Transmission System under All Operation Region of DFIG [J]. *Power System Technology*, 2014, 38(9):2429-2433.
- [2] Liang W, X R Xie, Q R Jiang, et al. Analysis and Mitigation of SSR Problems in Large-scale Wind Farms with Doubly-fed Wind Turbines [J]. *Automation of Electric Power Systems*, 2014, 38(22):26-31
- [3] X L Dong, X R Xie, Y Yang, et al. Impacting factors and stable area analysis of subsynchronous resonance in DFIG based wind farms connected to series-compensated power system [J]. *Power System Technology*, 2015, 39(1):189-193(in Chinese).
- [4] W S Wang, C Zhang, G Q He, et al. A Survey of Subsynchronous Oscillations in Large Scale Wind Farms [J]. *Power System Technology* 2017, 41(4):1050-1060.
- [5] L Fan, Z X Miao. Mitigating SSR using DFIG-based wind generation [J]. *IEEE Transactions on Sustainable Energy*, 2012, 3(3):349-358.
- [6] L Fan, C Zhu, Z Miao, et al. Modal analysis of a DFIG-based wind farm interfaced with a series compensated network [J]. *IEEE Transactions on Energy Conversion*, 2011, 26(4):1010-1020.
- [7] Wang Bo, Lu Jiping, Gong Jianyuan, et al. A Method to Suppress Sub-Synchronous Oscillation of Wind Farm Composed of Doubly Fed Induction Generators With Additional Rotor Side Control [J]. *Power System Technology*, 2013, 37(9):2580-2584.
- [8] E. Muljadi and B. Parsons, Comparing single and multiple turbine representations in a wind farm simulation, in Proc. *Eur. Wind Energy Conf.*, Athens, Greece, 2006.

- [9] X. L. Dong, X. R. Xie, Y. D. Han, et al. Mechanism Study of DFIG-Related SSR Based on Separate Stator and Rotor Torque Analysis [J]. *Proceedings of the CSEE*, 2015, 35(19):4861-4869.
- [10] B. F. Gao, R Li, D Y Yang, et al. Damping characteristics and countermeasures of DFIG subsynchronous oscillation [J]. *Electric Power Automation Equipment*, 2015, 35(12):11-21(in Chinese).
- [11] Vieto I, Sun J. Sequence Impedance Modeling and Analysis of Type-III Wind Turbines [J]. *IEEE Transactions on Energy Conversion*, 2016, PP(99):1-1.
- [12] Mohammadpour H A, Santi E. SSR Damping Controller Design and Optimal Placement in Rotor-Side and Grid-Side Converters of Series-Compensated DFIG-Based Wind Farm [J]. *IEEE Transactions on Sustainable Energy*, 2015, 6(2):388-399.

Coordination of Multistage Scheduling Strategy in Cogeneration System

Zhenyu Li¹, Dong Zhao¹, Qing Ye¹ and Guibo Ma¹

¹ State Grid Liaoning Electric Power Supply Co. Ltd, Fuxin Power Supply Company
Fuxin, China

E-mail: 13941840787@139.com

Thesis was funded by State Grid Liaoning Electric Power Co., Ltd.

Project number: 2018YF-24

Abstract. Due to the characteristics of wind intermittent, fluctuating, anti peak, and large prediction error, large-scale wind power access to the grid has brought negative impact on the planning and operation of the power grid. The contradiction between the power load and the peak and valley of the heating load expands the difficulty of the power grid to reduce the wind power. In addition, the thermoelectric coupling characteristic of the cogeneration unit determines the limit of the electric output regulating range of the thermoelectric unit, and the planning and operation policy of the thermoelectric co production unit with thermal power intensifies the problem of the high incidence of the discarded wind in the heating season. According to the analysis of the energy flow model of the electric heating combined system, the energy flow method is used to optimize the dispatching model and improve the capacity of wind power consumption during the heating period. The results show that the use of the electric heating station can increase the low valley electric load, reduce the thermal power output of the unit and leave the space for the wind power network. The indoor temperature of the user affects the heat load, and then affects the total amount of the wind power consumption, and the optimal scheduling results calculated by the optimized scheduling model considering the constraints of the heat transfer link are more accurate and feasible.

1. Introduction

At present, the major trend of the energy revolution has no doubt been the development and reuse of wind energy and other renewable energy sources. At this stage, the issue of wind erosion is significant, especially in the Three North region of China, while meeting the heating needs of users. It is also necessary to satisfy the “heat-set” operation mode of the cogeneration unit, which undoubtedly limits the peak-shaving capacity of the power grid, and in turn enables the unit to significantly reduce its capacity for absorbing wind power.

Considering the power and thermal systems as a whole and considering them in a unified manner, and then adopting the dispatching measures of the power grid, this method has become the main idea for solving the problem of serious wind curtailment during the winter valley period. To this end, scholars at home and abroad have been working on this idea. A lot of research has been done: The literature [1] concluded that when wind power is connected to large-scale grids, the grid is peaked. FM capabilities have been reduced. The literature [2] analyzes large-scale wind power grid connection, which has a great impact on grid dispatch and economy in the United States. Literature [3] pointed out that in order to ensure the stable operation of the power system, a reasonable amount of wind rejection is desirable and can improve the capacity of wind power absorption. The literature [4]-[5] proposes to quantify the



quantity of electricity that has been discarded at different time scales, and to find out the reasons for the frequent occurrence of wind abandonment during the heating season.

Danish scholars detailed in [6], [7] the method of configuring electric boilers and heat pumps for cogeneration units to increase the capacity of wind power absorption and compare the economics. The literature [8] describes that in Finland, the heat storage unit is equipped with a cogeneration unit to achieve the power balance of the power generation and consumption of the power system at the national level. In addition, studies have also shown that the provision of heat storage devices next to a suction-type cogeneration unit can also improve the peak-shaving capability of the power grid and the absorption of wind power, which was analyzed in [9]. In summary, all the mentioned research methods need to transform existing electric or thermal power systems. This undoubtedly poses a huge challenge to the investment and construction cycle. The literature [10] pointed out that the heating pipe network can be regarded as a dynamic heat storage system to store excess thermal energy to solve the thermo-electric coupling due to its heat storage capacity and thermal inertia. Therefore, the centralized heating pipe network is regarded as a heat storage system. Helps the power system improve its ability to absorb new energy. The literature [11] is similar to [10], considering that the heating network can act as an energy storage system, taking into account the differences in the transfer of electricity and heat energy and use, and formulating a coordinated scheduling strategy.

In this paper, by studying the thermal system, using the thermal system, the response time is slow, the inertia is large, and the human temperature sensing interval. In the heating season, we use the characteristics of multiple electrothermal and thermal coupling elements and the thermal system characteristics of the combined thermal and electric system to develop an electric thermal joint. The energy flow model of the system realizes multi-level coordination and coordination of provincial and local coordination and electric and thermal coordination, promotes the consumption of renewable electricity, and consumes as much wind energy as possible.

2. Energy flow model of combined heat and power system without additional heat source

2.1. Energy flow model of cogeneration units

The heating heat load of the heat source depends on the heat source outlet circulation, the outlet water supply temperature, and the inlet return water temperature:

$$Q_h = G_h \cdot c \cdot (t_{hc} - t_{hr}) \quad (1)$$

2.2. Heating network model

The heating pipeline and its internal thermal medium together form a heating pipe network. During the conduction process, the temperature of the heating medium is directly changed by the thermal characteristics of the pipeline, and because of the high internal energy, a large amount of high-temperature heating medium exists in the first-level heating network. In the heating pipeline, usually, under the condition of ensuring the heat transfer of the first and second heat networks is stable, a method of reducing its internal energy is adopted to soften the hard connection between the heat load and the heat source tip, so as to reduce the heating demand of the heat network. This breaks the "heat-set" limit, decouples the thermo-mechanical coupling of the thermal motor, and ultimately increases the capacity of the unit to absorb wind power. Compared with adding additional heat sources, this method can make better use of the heat storage characteristics of its own pipe network, and does not require initial investment and has a short construction period. This way of improving wind power absorption capacity has better economic and timeliness.

Since the heat medium present in the primary heating pipe has a high temperature, these heating pipes all have pressure bearing characteristics. In order to improve its pressure bearing capacity, generally higher strength steel pipes are used in the inner layer of the heating pipe, and a certain thickness of insulation material is used as the insulation layer on the outer layer of the steel pipe to reduce the heat loss generated by the heat medium during the transmission process. The outermost protective layer of the heating pipe is used to prevent corrosion and damage.

The heat source emits heat to the heat medium. After the heat medium absorbs heat, the temperature rises, and the heat network then enters the water supply pipeline of the primary heat network. The

operation of the circulating water pump provides kinetic energy to continue to move toward the heat load at a certain speed. Therefore, the temperature of the heat medium when it is output from the heat source is closely related to the temperature at the heat load, and there is a certain delay effect of the temperature change of the heat medium at both places (and the heat load and the heat source). The definition of the thermal delay time for the heating pipeline is defined as the time required for the temperature to change during the transition from the heat medium temperature at the heat source outlet to the end of the corresponding heat load inlet.

Neglecting the frictional heat of the heat medium and the inner wall of the pipe, the heat medium exchanges heat with the pipe during the process of passing through the pipe. Therefore, the unit volume of the heat medium at the outlet of the pipe can be lower than the inlet, and the main performance is that the temperature drops.

The temperature relationship at both ends of the heating pipeline is:

$$T_{end} = (T_{start} - T_e)e^{-\frac{\lambda L}{C_p M}} + T_e \quad (2)$$

According to equation (1-2), the temperature difference at the beginning and end of the heating pipeline can be determined.

$$\Delta T = T_{start} - T_{end} = (T_{start} - T_e)(1 - e^{-\frac{\lambda L}{C_p M}}) \quad (3)$$

As can be seen from the above equation, the distance between the pipeline and the temperature difference between the beginning and the end is proportional to. Therefore, due to the short distance of the secondary pipeline, the distance from the thermal load is also very close, and the temperature change of the working fluid in the pipeline during the transfer process can be ignored, and only the temperature change of the pipeline is considered.

2.3. Heat load model

Contains the thermal load of a person's psychological reaction to the temperature-sensing behavior (humans are subjected to high and low temperature intervals and reaction times, that is to say, people do not have to maintain a comfortable constant temperature, appropriately higher or lower, from the human behavioral psychology Academic considerations can be tolerated, or given appropriate compensation), the building's thermal characteristics.

Take a counterflow heat exchanger as an example, as shown in Figure 1.

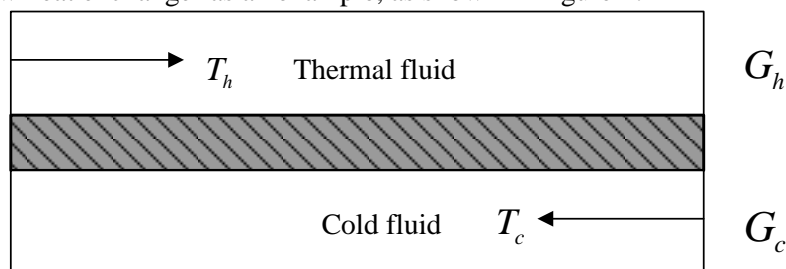


Figure 1. Countercurrent heat exchanger model.

The dissipation rate of the countercurrent heat exchanger can be expressed as

$$\phi_H = \frac{1}{2} G_h (T_{h,i}^2 - T_{h,o}^2) - \frac{1}{2} G_c (T_{c,i}^2 - T_{c,o}^2) \quad (4)$$

3. Provincial coordination and coordination strategy

The research on the power load shows that during the peak hours and waist-load period, the power demand is higher, and the heat-powered cogeneration units are less affected by the “heat-set” model, and the power system can consume wind power more than normal. However, during the load phase of

the power load, the load is greatly reduced, so the required power output is relatively reduced. At this time, due to the influence of the outdoor temperature, a relatively high thermal load is required. Contradiction arises. At the same time, the thermal power unit The “heat-set” model and thermo-electric coupling restriction result in the inability of the electric output to be reduced. In order to ensure the power balance of the power grid, the wind is the only choice, which is the reason why the amount of wind curtailment in the valley was significantly higher than in other periods. In addition, during the daily actual operation of the power grid, the technology of load forecasting is not yet very mature. Coupled with the influence of wind speed, the actual net load of the system is far from the predicted load. This large net load error worsens the grid seriously. With regard to the capacity of wind power consumption, the occurrence of the wind abandonment phenomenon has been exacerbated in the period of Guru. Therefore, in order to better realize the acceptance of wind power, it has become a key issue to consider the coordination and scheduling strategies of provincial-territorial coordination, combined heat and power systems, ie, primary heat networks, cogeneration units, and additional heat sources.

First of all, the provincial regulation will conduct safety check and check on the transmission channel to ensure that the channel can fully absorb wind power. Secondly, considering the size of power grids in each region from the provincial grid, the size of the power supply will be determined by the type and capacity of each region. Finally, the minimum cost of coordinated scheduling is used as an objective function to develop a rolling plan for combined heat and power systems. The specific method is: based on the well-established daily power generation and heating plan, adjust the intraday rolling power generation plan based on the power grid load forecasting information and the ultra-short time wind power. Among them, it is necessary to pay attention to the recent prediction that the wind power output, electricity, and heat load should all be taken into consideration, and the heat load should be specifically reflected in the air temperature.

The cost of coordinating and dispatching mainly consists of two parts: the dispatching cost of the cogeneration unit and the operating cost of the additional heat source system. Additional heat sources include electric boilers and thermal storage devices. Because the primary heat network is an inherent device of the heat network itself, the use of its heat storage characteristics to dissipate the scheduling costs incurred by the wind power is negligible. Therefore, the objective function can be expressed as:

$$\min C_{dis} = C_{CHP} + C_{EB} + C_{HS} \quad (5)$$

In the combined heat and power system, the electric heating load needs to maintain the balance between supply and demand at all times. Arranging a reasonable dispatching plan is the primary task of the dispatching department, and secondly meeting the user's electricity consumption and heat demand on the premise of satisfying the system constraints. The goal of optimal scheduling is to reduce the power supply and heating costs to a minimum on this basis. The day before the optimization of the scheduling is the need to schedule the schedule of the second day before the operation day by the load and wind power forecast data. Prior to scheduling, an optimization scheduling model was established, including objective functions and constraints for each aspect. Then the model was solved according to a suitable algorithm to obtain the output of various units and thermal network equipment at various time periods.

In this combined heat and power system, it is assumed that each of the blocks in the thermal power plant R contains R_i cogeneration unit and i represents the number of each thermal power plant. Each thermal power plant supplies heat to its corresponding area and is responsible for its heat load; each secondary heat network is heated by its corresponding heat exchange station, and there are L_i heat exchange station equipped with a suitable capacity peaking electric boiler. The system also contains S -station thermal power units. The R_i thermal power units on the same station supply power to the entire power grid. Therefore, thermal power units are not divided by thermal power plants. All wind turbines can also be grouped into a wind park to act approximately as an equivalent generator.

With the aim of energy conservation and emission reduction, the minimum total coal consumption of the system is the goal. In response to the country's call for energy conservation and emission reductions, wind energy costs are encouraged, and clean energy wind power is encouraged to go

online. The day-to-day optimization scheduling objective function of the combined heat and power system can be expressed as follows:

$$\min F = \sum_{t=1}^T \left(\sum_{i=1}^R \sum_{n=1}^{N_i} F_{CHP}^{t,i,n} + \sum_{j=1}^s F_{CON}^{t,j} \right) \Delta t \quad (6)$$

In addition, it is necessary to pay attention to adjusting the outlet temperature of the heating pipe network, the user's feelings about the temperature change, and the withstand time.

4. Analysis of examples

This example uses the provincial grid as the main research object, and the specific research is mainly between the provincial network and the city network. The dispatching departments corresponding to the two grids are provincially adjusted. The types of power in the network include firepower, hydraulic power, wind power, and thermal power.

The system used in this example is a six-node system. As shown in the following figure, the grid structure includes three units and one wind farm. The installed capacity of the wind farm is 220MW, and the three units are a thermal power plant and two thermal power plants. There are three secondary pipelines connected to the thermal power plant and each station is equipped with an electric heating station. Each heating station has a conversion efficiency of 1 and the enthalpy drop is 2 327.53 kJ/kg. All the units in the system are in the starting state. In the example, a mass-adjusted heat network dispatching method is adopted. This method changes the heat source on the basis that the circulating water volume of the network is constant and the heat resistance of the heat exchanger is constant. The system water supply temperature. In addition, the hot user room temperature was set to 25° C.

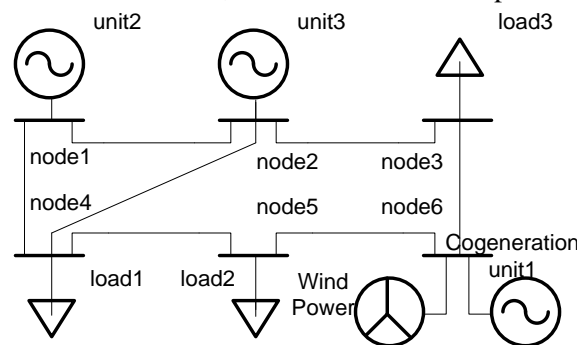


Figure 2. Example system.

Matlab optimization toolbox can be used to solve the optimal scheduling results. The following figure shows how to optimize the distribution unit's power output and pumping capacity during dispatching.

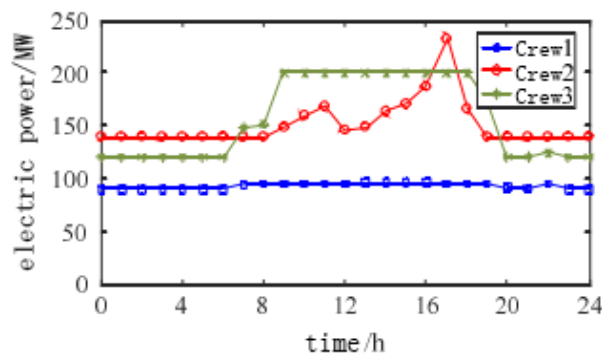


Figure 3. Optimal distribution of power output of each unit.

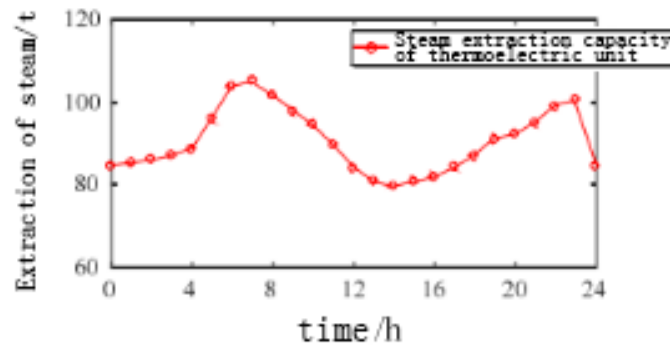


Figure 4. Optimal distribution of exhaust gas in a thermoelectric unit.

Excluding the heat transfer constraint and other constraints unchanged, the total wind volume of the system is not 1793.73 MW·h, which is 1073.11 MW·h, and there is a large error. The following figure shows the wind power output under different conditions.

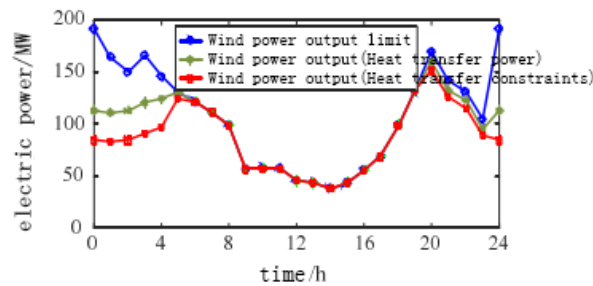


Figure 5. Wind power output under different circumstances.

As can be seen in the above figure, wind power output results are not the same in different situations. Because heat transfer between the heat exchange between the working fluids and the flow of the working fluid itself does not consider the irreversibility of the transport process once the heat exchange process is not considered, most of the thermal energy required by the hot users is required. Scheduled to achieve delivery, the equivalent heat load also increases. In order to realize the supply of thermal energy to thermal consumers, wind power heating can be used to dissipate more wind power. Therefore, there is a certain degree of error in the application of scheduling in an electrothermal integrated energy system. That means that not considering the heat exchange process does not mean that it can include All the constraints have caused the incompleteness of the research, so the heat exchange process can not be ignored.

5. Summary

In this paper, the unified heat and power system is realized by studying the established electro-thermal compatible energy flow model, and the two are unified into the power grid dispatch. Then the optimal dispatch model is proposed to improve the capacity of the combined heat and power system to eliminate and wind the wind, effectively The problem of severe wind abandonment during the winter grain load was solved and the power grid's capacity for dissipating the wind was also improved. According to the results of the study example, it can be concluded that the heating of the electric heating station can be used to increase the electric load during the period of the Dutch dynasty. This can reduce the electricity output of the unit and also allow room for wind power to be connected to the grid. Therefore, the grid is improved to consume wind power. Ability. In addition, from the point of view of behavioral psychology, people's adaptation to comfortable temperature is not limited to a constant temperature, and a reasonable high or low temperature at this temperature is acceptable, so the consumption of wind power can be controlled by Hot user room temperature to judge. At the same

time, in the establishment of the optimization scheduling model, the heat exchange link should be taken into account, which will increase the accuracy and credibility of the results to some extent.

6. References

- [1] Chi Yongning, Liu Yanhua, Wang Shengwei, et al. *Influence of wind power access on power system* [J]. Power grid technology, 2007, 31(3):77-81.
- [2] Parsons B, Milligan M, Zavadil B, et al. *Grid impacts of wind power: a summary of recent studies in the United States* [J]. Wind Energy, 2004, 7 (7) : 87-108.
- [3] Liu Xindong, Fang Ke, Chen Huanyuan, et al. *Theoretical study on large-scale wind power utilization to improve the rational use of abandoned wind* [J]. Power system protection and control, 2012, 40(6):35-39.
- [4] Liu D, Zhang G, Huang B, Liu W. *Optimum Electric Boiler Capacity Configuration in a Regional Power Grid for a Wind Power Accommodation Scenario* [J]. Energies, 2016, 9(3):144-153.
- [5] Hiibner S, Eck M, Stiller C, et al. *Techno-economic heat transfer optimization of large scale latent heat energy storage systems in solar thermal power plants* [J]. Applied Thermal Engineering, 201, 98(4): 483-491.
- [6] Lund H. *Large-scale integration of wind power into different energy systems* [J]. Energy, 2005, 30(13): 2402-2412.
- [7] Nielsen M G, Morales J M, Zugno M, et al. *Economic valuation of heat pumps and electric boilers in the Danish energy system* [J]. Applied Energy, 2016, 167: 189-200.
- [8] Rinne S, Syri S. *The possibilities of combined heat and power production balancing large amounts of wind power in Finland* [J]. Energy, 2015, 82: 1034-1046.
- [9] Lv Quan, Chen Tianyou, Wang Haixia, et al. *Analysis of peak regulating ability of thermoelectric unit after heat storage* [J]. Power system automation, 2014, 38(11): 34-41.
- [10] Balic D, Maljkovic D. District h ZHANG Ming, WANG Wu, ZHAO Lili, et al. *The simulation analysis of power loss prediction model based on large data analysis* [J]. Shaanxi Electric Power, 2016, 44(6): 31-35.
- [11] Long Hongshu, Fu Lin, Xu Ruilin, et al. *Power grid dispatching using gas turbine and heat pump to reduce uncertainties*[J]. Transactions of China Electrotechnical Society, 2015, 30(20): 219-226.
- [12] Yang Shuai, Chen Lei, Xu Fei, et al. *The energy flow of electric integrated energy system optimization model based on the disposal of abandoned wind* [J]. Power grid technology, 2018, 2:417.
- [13] Rong Shuang. *Multi-heat source capacity planning and coordinative dispatching strategy for promoting wind power consumption in heating period* [D]. Harbin Institute of Technology, 2016.

Acknowledgments

First of all, I would like to thank everyone who helped me during the writing of this article. I am very grateful for the help of the remaining authors who provided me with valuable advice in academic research. In preparing this paper, everyone spent a lot of time reading each draft and provided me with inspiring suggestions. Without their patient guidance, profound criticism and expert guidance, the completion of this paper will not be possible.

Secondly, I am particularly grateful to professors in the field of electricity. They provided many useful teaching and inspirational lectures for my dissertation and made a lot of preparations for my study.

Finally, I finally want to thank my dear parents, who have been helping me out of difficulties and support without complaint.

Development of a Comprehensive Transformer Material System Analyzer

Yuan Gao¹², Zhiwei Zhao¹³, Xinyu Wang¹⁴ and Xin Hu¹⁵

¹ State Grid Tieling Power Supply Company, Tieling, China

E-mail: 635218776@qq.com; 815343321@qq.com; 2631995464@qq.com;
245954159@qq.com

Abstract. In view of the phenomenon that the existing dry-type distribution transformers are replaced by aluminum and copper, there is no aluminum wire or aluminum wire-wrapped dry-type transformer standard for distribution in China, and it is impossible to accurately detect whether the dry-type transformer exists in aluminum-based copper. Based on this situation, a high-precision distribution network dry-type transformer comprehensive test system is developed. This system is a combination of transformer property testing, material testing, capacity testing, direct resistance testing, and ratio-ratio testing. It is for dry-type transformers. A high-precision comprehensive test system specially developed. The data conversion method of DC resistance and transformer capacity is mainly used. The method of accurately measuring the transformer ratio and the method of determining the material based on the transformer current density are used to detect whether the dry transformer is replaced with aluminum and copper. Accurately testing the transformer capacity can accurately detect whether the user changed or replaced the transformer nameplate. It can also accurately measure power frequency parameters such as capacity, load loss, no-load loss, impedance voltage, and no-load current of various transformers, thereby improving the ability to detect the quality of power equipment.

1. Introduction

In view of the existing phenomenon that distribution transformers are sub-assembled with aluminum-based copper, and there is no aluminum foil or aluminum wire-wrapped distribution dry-type transformer standard in China, it is impossible to accurately detect the existence of dry-type transformers in aluminum-based copper. The problem [1]-[3], through the implementation of this project, develops a high-precision distribution network dry-type transformer comprehensive testing system to accurately measure the transformer capacity and accurately measure the power frequency parameters such as load loss, no-load loss, impedance voltage, and no-load current. And can accurately detect whether the user to change, change the transformer nameplate, improve the ability to detect the quality of electrical equipment [4], [5].

In the current production of distribution transformers, using aluminum wire instead of copper wire as a Fund Project number: 2018YF — 48 conductor material has become an unspoken rule in the industry. The main reason [6] for this is that aluminum wire transformers can reduce costs compared to copper wire transformers and have strong Economical. Transformer is a kind of static electrical equipment made according to the principle of electromagnetic induction. It has the functions of transforming voltage, converting current, and transforming impedance. It is widely used in various fields of engineering [7]. If the transformer uses aluminum wire instead of copper wire, it will cause large power consumption and poor quality of power.



First of all, in principle [8], the two are used as conductive materials. The difference lies in the difference in conductivity. The copper wire has higher conductivity than aluminum wire, and the copper wire has lower power loss, which ultimately leads to the quality of the user's electricity. The difference. From the cost point of view, the difference between copper and aluminum wire is also the price, the same unit of copper wire is about twice the price of aluminum wire. Transformer companies use dry-type transformers to make them bulky and take up a lot of space. In addition, copper wires have higher thermal conductivity than aluminum wires. In terms of safety, long-term use of copper wires has advantages over aluminum wires [9]

If there are aluminum wires instead of copper wires in the tendering project, there will be serious infidelity. The development of a comprehensive analysis and detection system for the characteristics and materials of dry-type transformers in distribution networks is a combination of characteristics testing, material testing, capacity testing, direct resistance testing and ratio-ratio testing of transformers [10]. It is a high-precision developed specifically for dry-type transformers. The comprehensive test system can easily detect whether the dry-type transformer is filled with aluminum and copper, and can accurately test the transformer capacity, and can accurately detect whether the user changes or replaces the transformer nameplate. It can also accurately measure power frequency parameters of various transformers such as capacity, load loss, no-load loss, impedance voltage, and no-load current [11].

1.1 Project significance

In China, dry-type transformers with only copper or copper wire for dry-type transformers have no standard for dry-type transformers with aluminum foil or aluminum wire, and the aluminum dry-type transformers produced must have copper or copper foil wound around the nameplate. The nameplate of the transformer is actually inconsistent with the nameplate, and the enterprise is falsified [12]. Nowadays, transformers made of dry aluminum in the country can be seen everywhere. Therefore, it is an urgent requirement of the law enforcement agencies to investigate and deal with irregularities and illegally produce dry aluminum transformers. The development of a comprehensive analysis and detection system for the characteristics and materials of dry-type transformers in distribution networks is the first in China and will fill the gaps in the country [13].

1.2 Application prospect

The results of the project research on the identification of dry-type transformers have been adapted to the current requirements for improving the safety and reliability of power systems. They can reduce the maintenance costs of dry-type transformers and reduce the number of maintenance. Therefore, they have a very good application prospect. Based on the research results of the project, it is possible to discover the potential hazards of aluminum-wound dry-type transformers in a timely manner, avoid sudden accidents, and improve the safety and reliability of operations. It is of great significance to apply them in practice.

2. Analysis of dry transformer material synthesis system

2.1. Dry-type transformer test system principle analysis

The related theories of transformers and conductor materials have been studied in depth, and certain researches and researches have been carried out on the production process of transformers and the manufacturing processes of various components. Among them, there are several key points that affect the data:

- Transformer line package design: including high and low voltage turns number design, high and low voltage wire diameter (cross-sectional area) design, different conductive materials, different turns and cross-sectional area requirements;
- Transformer insulation: including internal and external Insulation, wire insulation, etc.

There are many parameters in the transformer design calculation, including core-related dimensions, magnetic flux, package size, wire diameter, winding method, and insulation method. There are also DC resistance, loss, and short-circuit impedance of the wire package. A careful analysis of these parameters reveals that none of the parameters are unique characteristics of copper or aluminum

materials. For example: DC resistance, the direct current resistivity of aluminum material is larger than copper, but can reduce the DC resistance of aluminum winding by increasing the cross-sectional area. In our study of transformer manufacturing related processes, we found a parameter - "current density." This parameter has its own range of values for copper and aluminum in design data and does not overlap.

Therefore, after a long period of analysis and discussion, it was decided to try to determine the material of the transformer winding through the current density parameter.

Determined by the use of current density parameters to determine the transformer winding conductor material. Next, we need to follow this direction and study the relevant data and processes in detail to obtain a solution: from the transformer's external geometry and measured parameters such as winding currents, calculate and analyze the current density data.

The current density, whether it is from the design and calculation link or the test and verification link of the finished transformer, is a calculation parameter and should not be directly tested under the current technical conditions. In order to obtain the current density data, we need to obtain a series of parameters before we can calculate the current density. Known data:

- Transformer winding size, including package height, high and low pressure package thickness;
- The nameplate parameters of the transformer, including capacity, voltage and so on.

Current density, in the design and calculation of dry-type transformers, there are some guiding suggestions. The choice of current density for dry power transformers will directly affect load loss, temperature rise, short circuit mechanical force and material consumption. Normally when dry-type transformers are wound with copper wire, the current density can be selected with a higher initial value of 2-2.6A/mm², while the aluminum wire can be taken with 1.2-1.4A/mm². When the foil-type winding is used, foil is taken into consideration. Due to the skin effect, the current distribution is uneven, so that the current density can be selected to be 2% to 5% lower than the wire winding. Comprehensive calculation data and transformer manufacturer's actual production plan, usually transformer windings using copper material, the current density of about 2A/mm² or more, usually transformer windings using aluminum material, the current density is about 1A/mm² or so, sometimes low In 1A. There is a significant difference in the current densities of the two materials, and the maximum current density of the aluminum material does not coincide with the minimum current density of the copper material. When the transformer is a qualified transformer, the current density of copper and aluminum can be distinguished.

From the above studies, we can find that in this project, if we can accurately obtain a transformer's rated current and conductor cross-sectional area, we can calculate and analyze the transformer's conductor current density, and then analyze the conductor material.

After analysis, to achieve material judgment, it is necessary to accurately obtain the cross-sectional area of the transformer and the true rated current. The rated current is a parameter closely related to the true capacity. All parameters need to be obtained through analysis and calculation of external signal test data. This project is to conduct a comprehensive test of a dry-type transformer. The key issues to be solved in the project research process are as follows:

- Accurate judgment of dry-type transformer capacity

In the country, the equipment for testing the capacity of dry-type transformers generally has a lot of defects. Accurately determine the capacity of the transformer and obtain accurate and real rated current. This is the key to solving the problem of dry-type transformer material judgment accuracy.

- Accurately test the current density of high and low voltage packages of dry-type transformers

The ability to accurately test the current density of high and low voltage packages is the key to determining whether the transformer is a copper or aluminum package. The key point ahead is to obtain the true transformer capacity, which is the rated current. The key point is to obtain the true conductor cross-sectional area. The key to the successful development of the project must be a lot of practice to arrive at a correct conclusion.

2.2. Acquisition of conductor cross-sectional area

Current density calculation formula: $J=I/S$. Among them: J: current density; I: transformer winding phase current; S: conductor cross-sectional area.

According to the above formula, if we need to obtain the current density of the finished transformer, we must obtain a series of accurate parameters: conductor cross-sectional area, phase current.

When we face a finished transformer, we can only directly obtain the external dimensions of the transformer's high and low voltage packages. The conductor cross-sectional area can neither be directly obtained nor measured from electrical parameters. Without the cross-sectional area of the conductor, the calculation of the current density cannot be achieved at all.

Through the outer dimensions of the package, we can get the cross-sectional area of the entire package. This cross-sectional area is composed of the following parameters: cross-sectional area of the conductor * number of turns, cross-sectional area of the insulating layer, and cross-sectional area of the winding material. If we can determine the area occupied by these structures such as insulating materials, then the cross-sectional area of the conductor can be obtained.

In order to accurately obtain the parameters of the conductor cross-sectional area, we have carried out in-depth field analysis of the transformer winding manufacturing process and accumulated a large amount of data. First of all, we can get the height and thickness of the package, and we can get the cross-sectional area of the package. The composition of the cross-sectional area of the wire package is composed of the cross-sectional area of the conductor wire and the cross-sectional area of the insulation layer. The insulating layer includes outer conductor insulation, adhesive layer, and outer insulation of the wire package.

The thickness of the conductor insulation layer is different according to the conductor thickness of different models, and the insulation of different types of wire insulation is different. One thing that can be determined is that any manufacturer of transformers will not arbitrarily thicken the insulation. Insulation layer thickening, will lead to poor heat dissipation, increased material costs, increased stress causes easy cracking and other issues, therefore, the external insulation of the transformer will have a reasonable size in accordance with the insulation requirements. This parameter, which is not specified in the document, is a millimeter. However, the formed transformer is a basically determined data. Therefore, the size of the external insulation, we collected a large number of transformer insulation layer data of various transformer manufacturers, made a database for calculation and processing, and at the same time according to the dry transformer design process and calculation program comprehensive comparison, can be to a certain extent Analyze the insulation thickness of each type of transformer winding.

Second, the question of winding turns. This involves parameters such as transformer ratio and short-circuit impedance of the transformer. For a qualified transformer, if you want to achieve the correct transformer ratio and correct short circuit impedance, the number of turns in the same model should be basically the same. Because most of the current transformer design uses computer-aided design, different parameter combinations such as different number of turns, different heights, and winding thickness can produce different impedances and different material consumption. All manufacturers will select the qualified impedance data set and choose the data set option with the least material consumption. Therefore, qualified transformers have a certain number of parameters. According to this feature, a large amount of related data is also collected to form a database, and comprehensive calculation and analysis are performed to obtain basic data of the number of transformers of each model.

By collecting various data summation transformer winding turns, the final goal is to compare it as a back-end database. For the transformer under test, it must also be measured.

The program of measuring the number of turns actually has practical application, which is the conventional transformer ratio test. However, in the current market related instruments and test programs, as well as the requirements of various test procedures for transformers, the required parameters are the ratio or turns ratio, which is a ratio of high voltage to low voltage. This parameter is very effective in routine tests, but it is useless for our project. No one of us can clearly know the number of turns of high and low voltage windings from a variable ratio parameter. The exact number is what we must get. Also, the winding ratios of different connection groups do not equal the turns ratio. So, getting the exact number of transformer turns is also a key point.

Usually we measure the turns ratio by using the voltage method. We also use this method to measure the turns ratio. According to the formula: $U_1/U_2/U_3=N_1/N_2/N_3$, the voltage $U_1U_2U_3$ is obtained by

our instrument output or test, which we count as a known quantity. With the additional number of turns N , we can see that as long as there is a known N value, we can accurately calculate the other N data.

Therefore, a scheme of a known coil is adopted. That is, a special measurement winding is used. It consists of a bundle of soft wires, which has a known number of turns and cooperates with the measurement output of the instrument as part of the active excitation signal. The coil is placed on the iron core concentric to the transformer and an excitation signal is applied. Then, on the transformer high and low voltage windings, a voltage signal with the same ratio as the known coil is generated. At the same time, the output voltage, the voltage of the high and low voltage windings are measured, and then we know the number of turns of the coil. In this way, we accurately obtain the number of turns of the high and low voltage windings.

Finally, use the data obtained (cross-sectional area of the package - area of the insulation portion)/number of turns = cross-sectional area of the conductor. In this way, one of the key problems is solved, and the conductor cross-sectional area of the transformer winding is accurately obtained. In order to obtain the accurate winding current, the current density can be calculated.

2.3. Obtaining winding current parameters

The size of the winding current is designed according to the transformer capacity. The conductor cross-sectional area determines whether the winding can withstand the design current.

In the calculation parameters of the transformer winding, parameters such as the number of turns, cross-sectional area, and height of the wire package will eventually affect the capacity and impedance of the transformer. The rated current of the winding operation can be calculated by the formula based on the transformer capacity and rated voltage. However, the transformer's rated capacity also has the potential to be ambiguous. It may have an elevation or may be low. Therefore, we cannot use the nameplate standard capacity or current data to participate in the calculation. In this way, the ability to accurately measure the capacity of the transformer is also a key issue.

In the nameplate parameters of the transformer, the only parameter that will not be virtually falsified is the rated voltage. Other parameters, such as capacity, impedance voltage, etc. may not be real data.

Transformer rated current calculation formula, $I = S / (U \sqrt{3})$, where, I : transformer rated current; S : transformer rated capacity; U : transformer rated tap bit voltage. When the transformer high voltage winding is Y type, the current calculated by the formula is the rated current of the winding, that is, the phase current is the same as the line current. When the high voltage winding is Δ type, the result of the formula calculation is the line current, and the phase current is also the winding current, and it needs to be divided by $\sqrt{3}$. From the above formula, it can be concluded that the rated current of the transformer winding has a direct and decisive relationship with the transformer capacity (in the case of known voltage and certain conditions, a transformer is generally not suitable for multiple voltage levels).

From the above conditions, it can be found that the rated voltage can obtain accurate data. Next, accurate transformer capacity data must be obtained to obtain the accurate data of the rated current of the winding to calculate the current density.

The capacity of the transformer is calculated by theoretical calculations, combined with parameters such as rated voltage and rated current. The transformer capacity parameters cannot be directly tested unless a full type temperature rise method is used for type testing. Without accurate capacity data, accurate winding current data cannot be obtained. However, it is not possible to use the full load temperature rise method to test the transformer capacity. Moreover, using the temperature rise method can not test the exact capacity of the transformer, only to verify whether the rated capacity marked on the transformer nameplate is satisfied. Therefore, it is very necessary to find and design a scheme or equipment that can accurately measure the transformer capacity.

There are some instruments on the market that specifically measure the capacity of transformers. The principle is to use a calculation relationship between the capacity and the short-circuit impedance of the transformer. Its formula is $(S = (\sqrt{3} * U^2 * U_K) / Z)$. Among them: U is the transformer rated line voltage, U_K is the impedance voltage, Z is the linear impedance in the test. From the formula, we can

see that in this formula, only the voltage is an accurate known quantity. In addition, the linear impedance value can also be said to be accurate. It is the ratio of the applied voltage to the formed current. There is also one parameter: the percentage of impedance voltage. This parameter is theoretically accurate, but in reality, this parameter has the potential to be falsified. It can be seen from the formula that the percentage of impedance voltage is high, the transformer capacity is large, and the transformer capacity is low. It can be said that the size of the impedance voltage percentage parameter determines the size of the measured transformer capacity. Some of the results obtained by this test are correct, but for transformers with imaginary parameters, his test results are erroneous. Even deviations from the correct data are very large, and the test results are not objective. Therefore, we must find an algorithm and scheme that can objectively determine the transformer capacity.

Through the calculation and analysis of a large number of transformers, the final capacity analysis program is an impedance method combined with a load loss lookup table analysis program.

First, through the test, the measured loss is obtained. According to the measured actual data, the short-circuit loss value at the rated condition is corrected as required, and the actual capacity of the transformer under test is obtained by looking up the table.

Transformer short-circuit test (measurement of short-circuit loss) when the test power test results are calibrated to the temperature scale (the rated condition of the short-circuit test is the temperature scale), (correction formula is: $P = K \times PK$, where K represents the temperature coefficient of resistance, the algorithm is $K = (235 + \text{temperature scale}) / (235 + t)$, where it is the actual temperature at the time of the test. For the correction of the impedance voltage, it is also automatically corrected according to the formula using the measured value.

Where UKT represents the actual measured impedance voltage percentage, PKT represents the measured short-circuit loss at the current temperature, and SN represents the rated capacity of the transformer under test.

At the same time, based on the obtained capacity data and the input transformer rated voltage data, the rated currents on the high and low voltage sides are calculated. Then, based on the measured DC resistance, the rated load loss of the transformer can be calculated. Also check the table to get the actual capacity of the transformer. Comprehensive analysis and judgment in two ways make the analysis and judgment accuracy of the transformer capacity greatly improved.

3. Dry-type transformer test system hardware and software

Accurate capacity testing of dry-type transformers: hardware theory and software block diagram design:

3.1 The hardware structure design of the system

The following figure shows the system's hardware design schematic. The system can be divided into five major modules: Dry-type transformer interface, standard source output, data acquisition and operation control unit, 7-inch high-brightness color touch LCD screen and upload USB and print interface.

- Capacity standard source output

The module consists of a transformer, rectifier bridge and adjustable resistor. Adjusting the resistance of the adjustable resistor can change the voltage and current value of the primary side of the transformer, complete the voltage and current characteristics of the transformer, thereby realizing the adjustment of the transformer capacity; ensuring the accuracy of the test data of the test items under non-rated conditions) The power amplifier can provide three-phase precision AC test source.

- Data Acquisition Module

As shown in the figure below, the module uses high-precision AD to sample the voltage and current. The current signal is converted into a voltage signal through the current transformer. The six sampling synchronization signals are composed of a programmable timing force counter and a phase-locked loop. The D converter collects 256 points, and the sampled data is packaged by the CPLD and transmitted to a high-performance CPU. After processing by the CPU, an accurate voltage, current value, and phase between the voltage and the current are obtained, and the formula is used to implement the pairing. Transformer capacity calculation.

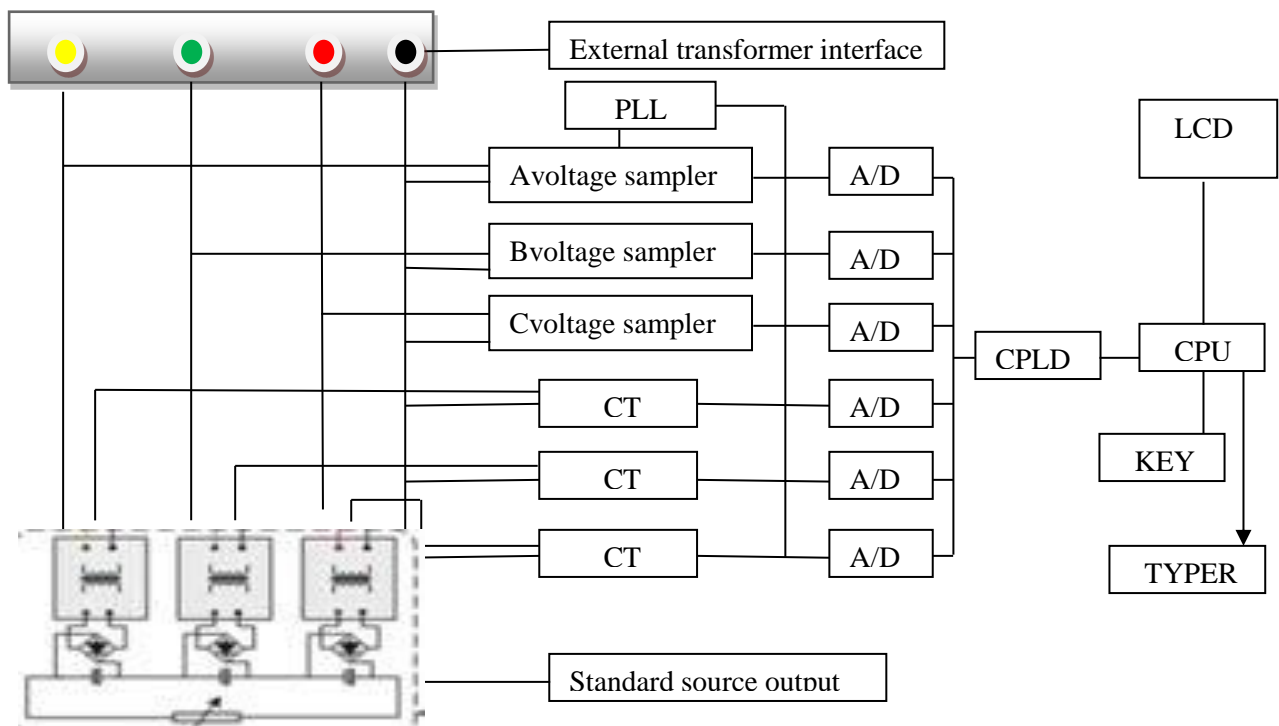


Figure. 1 Transformer capacity characteristics test system hardware design schematic

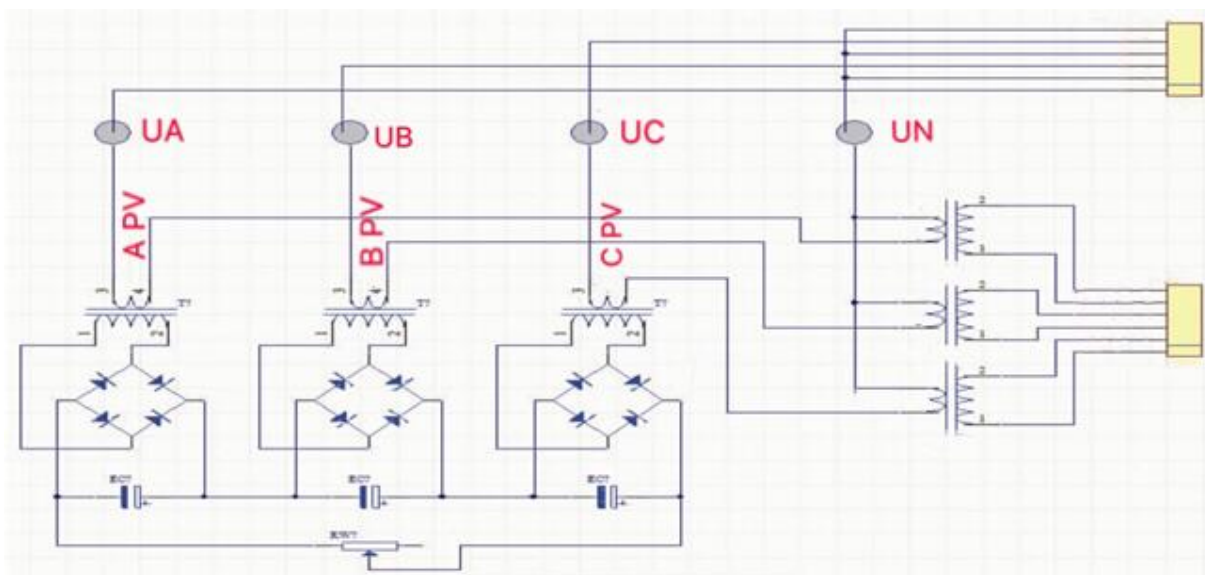


Figure. 2 Data Acquisition Module

- Operation control module

The module consists of an ARM chip, peripheral circuits, and a keyboard. It mainly performs functions such as data conversion, hardware control, display control, system, and key operation.

- Display module

The interface can display the corresponding voltage, current, impedance and capacity values according to measurement and calculation, and can manually set the temperature and transformer parameters, increasing the testable range.

3.2 The software structure design of the system

The system software generally includes: a data acquisition module that receives 6 A/D data transmitted from the CPLD, the conversion module converts the 16-bit A/D sampling data into an actual physical quantity under the international system of units; a capacity calculation module according to the transformer parameters and sampling Data, calculated transformer capacity value; temperature parameter conversion module, the current temperature capacity is converted to 75 °C capacity; press the button to resolve the module, according to the prompts to enter the transformer parameters, the current temperature, to achieve the transformer capacity characteristics of the tester to set the analog transformer parameters Display module provides humane LCD display interface. The software design principle flow chart is shown in the figure below.

3.3 The principle of material analysis

Through the above detailed description, the current density of the high and low pressure packages is comprehensively calculated and the dry transformer material is determined.

Using a transformer DC resistance tester to test the line-to-line DC resistance R_{ab}, R_{ac}, R_{bc} and r_{ab}, r_{ac}, r_{bc} of the high and low voltage coils to verify whether the capacity of the dry transformer is accurate, so that the true transformer current can be obtained; by using a specific test Coil test transformer ratio, test the number of turns of the dry-type transformer package, and then test the height and thickness of the high-low pressure package through the electronic ruler to calculate the area of the high-low pressure package. After comprehensive calculation and analysis, the cross-sectional area of the conductor can be obtained. Therefore, after comprehensive analysis, we can test the current density of high and low voltage packages.

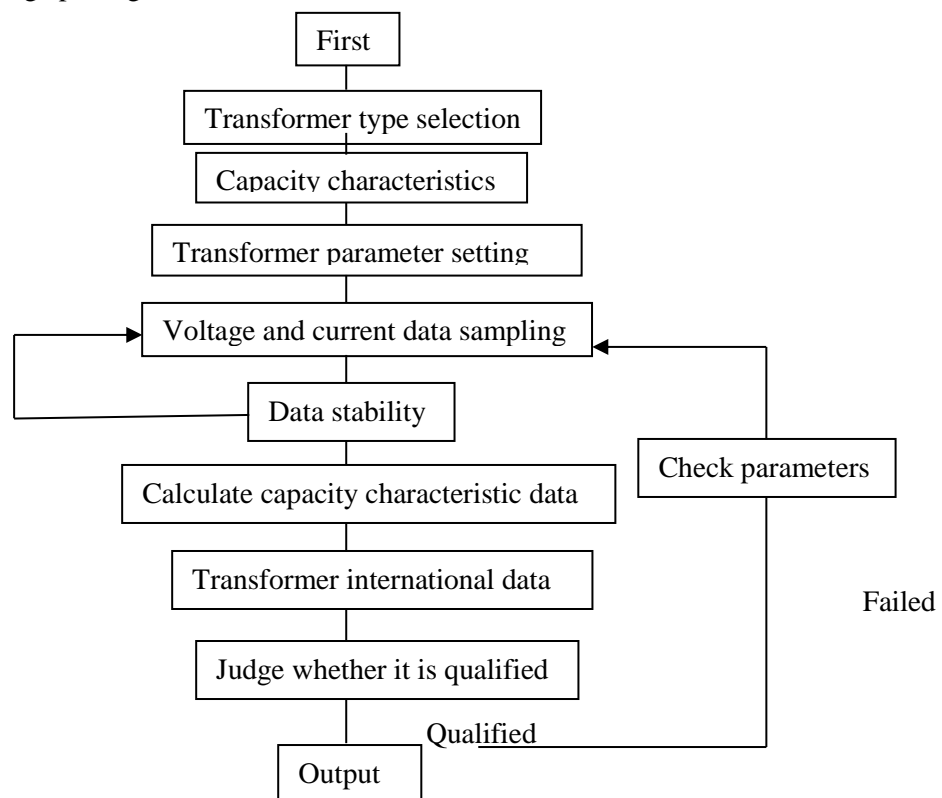


Figure. 3 Test System Software Flow Chart

4. Conclusion

This article analyzes and develops a new type of technical theory—the technical characteristics of current density to analyze the material of the transformer under test. This technology makes the material identification of the transformer easy to operate, low in cost, and can be universally realized. Completely lossless. At the same time, through a direct impedance transformer capacity test program, the test accuracy of the dry-type transformer capacity is greatly improved. Furthermore, a method of measuring the transformer turns ratio using a flexible coil with known parameters was studied.

According to the coil of our known parameters, the exact number of transformer turns can be obtained. Finally, combined with the above, the developed equipment integrates multiple functions, including transformer capacity testing, direct resistance testing, transformer loss testing, transformer ratio, turn ratio, and number of turns testing. The instrument not only realizes these conventional transformer test functions, but also calculates and analyzes the material of dry-type transformer windings through a series of parameter tests and statistical analysis calculations.

5. Reference

- [1] Xinxu Yu. Research on detection method of winding material of distribution transformer based on thermoelectric effect. Chongqing: Chongqing University, 2016.
- [2] Jinliang Ju. Skills for investigating and handling aluminum transformers for copper transformers [J]. China Quality & Technical Supervision, 2014. 01:30-31.
- [3] Jinqiang Chen, Bin Pan, Zhixin Li, Present situation and prospect of material identification for distribution transformer windings. Beijing, Transformer, 2013, (1)
- [4] Jia Deng, Shuqin Sun. Characteristic test and operational status analysis of substation transformer equipment. Changchun, Jilin University, 2014.
- [5] Fengxian Bai, Weijie Dong, Yuan Pengchao. Simulation measurement and analysis of parameters of Rosen piezoelectric transformer based on frequency characteristics. Journal of Power Supply, 2016(5), 3.
- [6] Taijin Wang, Qiuzhu Yang, Min Zhang. A new method for material diagnosis of distribution transformer windings. Communication Power Technology, 2018 (1), Vol. 55, No.1.
- [7] Jiarui Hu, Wei Chen, Hongdong Chen. Non-destructive testing of material for differential transformer windings. Transformer, 2018, (2): 55 volumes.
- [8] Yundong Sun, Junguo Dong, Mingbo Zhang. Non-destructive testing method of transformer winding material based on improved natural cooling method. Journal of Electric Power Systems and Automation. 2016(12), vol.28.
- [9] Danju Song. Analysis of development trend of dry-type transformers. China New Technology and New Products 2017 NO.03 (2)
- [10] Susa D, Lehtonen M. Dynamic thermal modeling of power transformers: Further development- Part I. IEEE Transactions on Power Delivery .2016:1961 — 1970.
- [11] Crompton, A. B. & Rowe, K. S. Principles of Transformer Design [M].
- [12] Green, H. E. The economics of aluminum for power transformer wdgs [J]. Electrical Review, 2016, 192(18): 631.
- [13] W. W. ORR. Aluminum and its future in power transformers [J].Power Appar. Syst. Part III:Trans. Am. Inst. Electr. Engnr, 2013, 77(3): 978-979.

Hierarchical Topology Analysis Method for Substations Based on Electrical Bays

X Zhang^{1,2}, Z F Xu^{1,2}, B Zhou^{1,2}, H F Wang^{1,2} and H X Pan^{1,2}

¹ NARI Group Co.,(State Grid Electric Power Research Institute), Nanjing, China

² NARI Technology Co., Ltd., Nanjing, China

E-mail: zhangxie@sgepri.sgcc.com.cn

Abstract. According to the requirements of the advanced applications in smart substations, hierarchical topology analysis method based on electrical bays is proposed in this paper. Based on the node connection relationships of each device in the substation, all primary devices can be organized into the hierarchical structure as “transformer (winding) - bus - electrical bay”. The typical 3/2 circuit breaker connection and the inner bridge connection are also recognized. On this basis, the identification of the static topology and the judgment of the dynamic connectivity in the main wiring diagram of the substations are realized, which is helpful in the quick search of the devices. The topology analysis method introduced in this paper will effectively support the advanced applications for substations such as fault diagnosis, state estimation, the status analysis of electrical bays and so on.

1. Introduction

In the control and analysis of power grid operation, network topology analysis plays an important role as the premise of various advanced applications, including the state estimation [1]-[3], fault diagnosis [4] and the status analysis of electrical bays [5], etc.

The traditional network topology algorithm [6]-[9] usually uses the adjacency matrix method or the tree search method to store the connection relationship among nodes in the stack manner or the queue manner. In this case, there is no hierarchy among the connected devices. Also there is no detailed information about the electrical bay of the device and other devices in the same electrical bay. In the practical application, the topology search needs to be repeated by the repeated search of the connection relationship, resulting in the repeatability and cumbersomeness of the topology search. It is not conducive to the intuitive and convenient access to power grid structure information. Meanwhile, there is basically no corresponding method in the traditional network topology analysis to recognize the typical 3/2 circuit breaker connection and inner bridge connection.

In this paper, a hierarchical topology analysis method for substation based on electrical bays is proposed, which makes the connection relationship between devices more organized, and more convenient to meet the topology requirements in advanced applications such as fault diagnosis and the status analysis of electrical bays. At the same time, the identification and processing of the 3/2 circuit breaker connection and the inner bridge connection which involve multiple bays are proposed. It helps to expand the application range of network topology analysis method, and simplify the engineering configuration of substation automation system.

2. Hierarchical topology analysis based on electrical bays

The key of the electrical bay-based hierarchical network topology is to organize the primary devices of the substation in a hierarchical structure as “transformer (winding) - bus - electrical bay”.



Firstly, according to the connection relationship in the main wiring diagram of the substation, the node numbers of the two ends of the device are obtained. Starting from the transformer, the windings of each side of the transformer are traversed according to the connection relationship of the nodes, thereby the transformer winding structure can also be obtained.

Secondly, the bus group (single-bus, double-bus or bypass-bus) connected to the end of the winding can also be obtained according to the device node number, and then the transformer (winding) - bus structure is identified. If the transformer does not exist, the corresponding transformer (winding) structure will not exist. So the topology analysis will start from the bus to get the associated bus group. Thirdly, on the basis of the above connection relationship, each device group that belongs to the electrical bay can be obtained, which is connected to the same bus group. The device group of the electrical bay is a set of related devices, including the circuit breaker, the disconnector, the ground disconnector and so on.

Finally, the relevant primary devices in the diagram of the substation have been organized according to the hierarchical structure of “transformer (winding) - bus - electrical bay”, as shown in Figure 1.

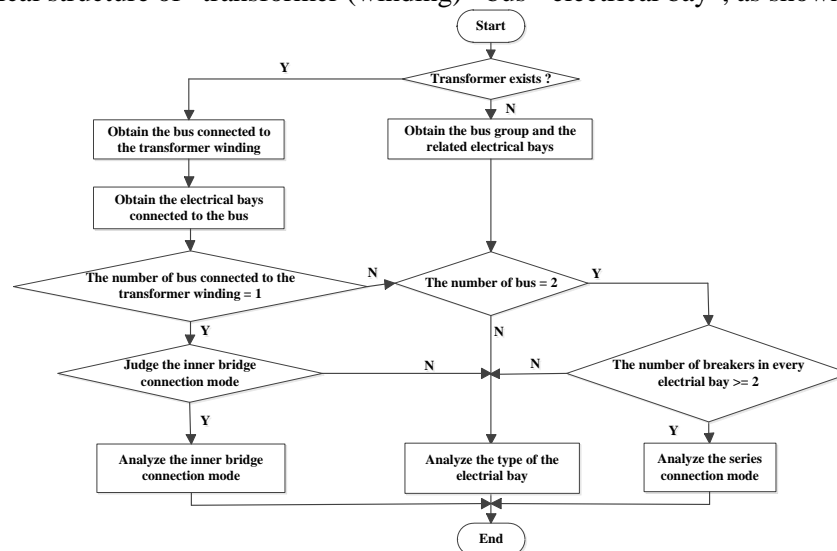


Figure 1. Flow chart of hierarchical topology analysis method based on bay.

The structure of the transformer is defined as shown in Figure 2.

The structure of transformer

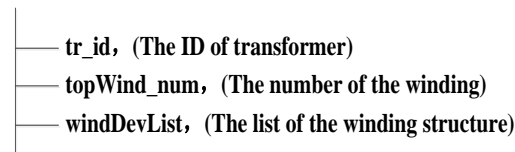


Figure 2. The structure of the transformer.

Furthermore, the structure of the windings under the transformer is defined as shown in Figure 3.

The structure of winding

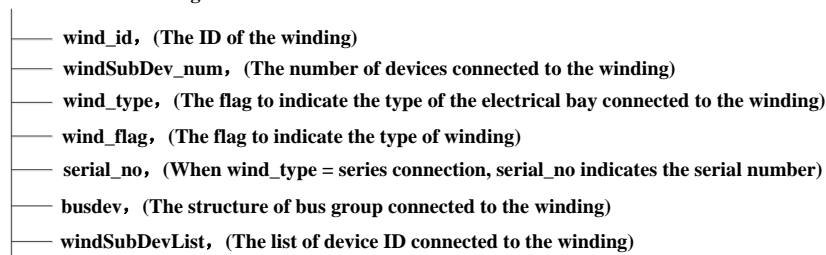


Figure 3. The structure of the winding.

The structure of the bus connected to the windings is defined in Figure 4.

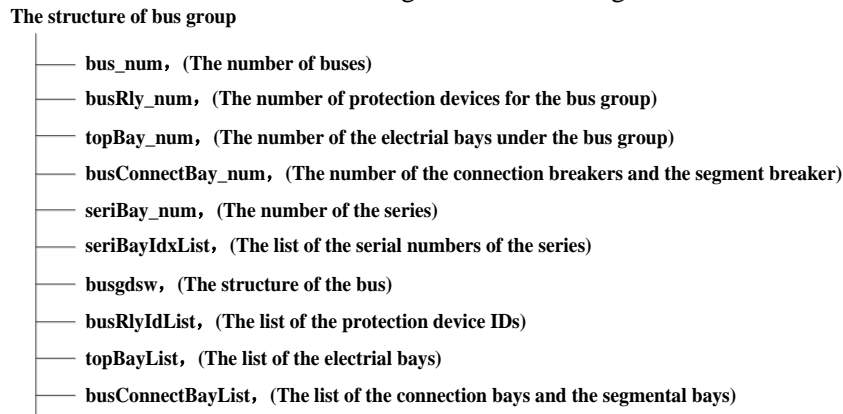


Figure 4. The structure of the bus.

According to the structure characteristics of the typical electrical bay, all the bays are divided and stored with different data structures, usually including the line bay, the connection bay and the segmental bay. In addition to the common single-bus structure and double-bus structure, the typical structures of the line bay also include the complex 3/2 circuit breaker connection and the inner bridge connection.

3. Identification of complex connection

3.1. Identification of 3/2 circuit breaker connection

The 3/2 structure connection is formed by three circuit breakers connected to two sets of busbars with two devices (line or transformer unit). Each circuit is connected to the bus by a circuit breaker. The two circuits make up a series connection together, so it is called the 3/2 circuit breaker connection mode, also known as a series connection mode, as shown in Figure 5(a). In view of the small scale of 500kV substations, there is an incomplete series connection structure compared to the complete series connection mode formed by three circuit breakers. In this structure, there are only two bus breakers connected to the same line, as shown in Figure 5(b). No matter what kind of the series connection structure is, it has the advantages of high reliability, good running flexibility, convenient operation and maintenance.

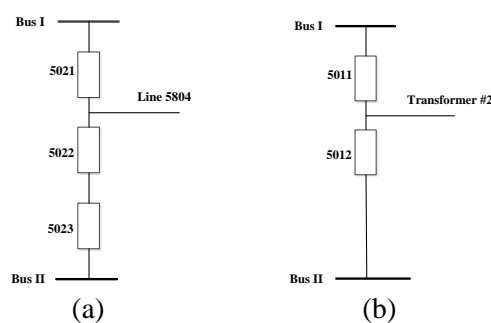


Figure 5. The series connection mode.

According to the connection mode of the series structure, when the bus layer is recognized as the double-bus, the connection mode is further identified by the constraints of the number of breakers in every electrical bay which connects to the bus, that is, if there are two or more breakers, it is identified as a series connection structure. Combined with the topology connection mode, the breaker which connects directly to the bus is recognized as the side breaker. And the middle breaker can also be recognized as its two ends respectively connect to the other breaker. So far, the identification of the series connection structure has been completed. Furthermore, according to the topological connection

between the side breaker and the line equipment, the corresponding series-line structure can also be identified.

The definition of the 3/2 circuit breaker connection structure is shown in Figure 6.

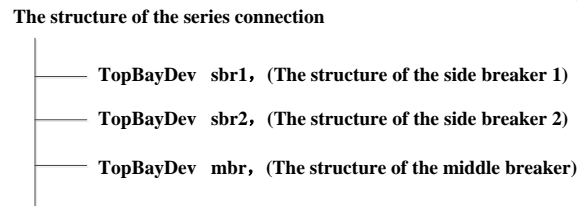


Figure 6. The structure of the series connection.

The TopBayDev represents the detailed structure of the breaker in the 3/2 connection, as shown in Figure 7.

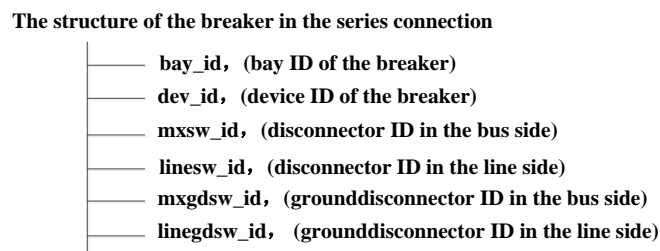


Figure 7. The structure of the series breaker.

Through the series structure and the series-line structure obtained above, the other devices in the structure can be obtained directly and conveniently by any of the devices, which greatly improves the topology efficiency.

3.2. Identification of inner bridge connection

The bridge connection is formed by a circuit breaker and two disconnectors, which connect two transformer-line groups horizontally. The bridge breaker of the inner bridge connection is located at the outlet of the transformer (close to the transformer), as shown in Figure 8. This connection mode is often used in the 110kV substation system, which decreases the number of devices compared to the ordinary bridge connection. Moreover, one line failure will not affect the operation of another line and the transformer.

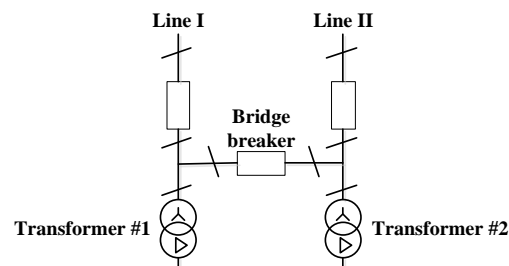
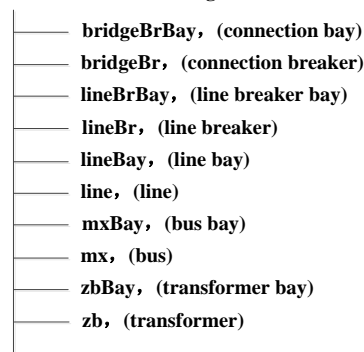


Figure 8. The inner bridge connection.

According to the connection mode of the inner bridge structure, when the bus layer is recognized as the single-bus, the connection mode is further identified by the constraints of the connection breaker and the line breaker in every electrical bay which connect to the bus, that is, if the bus is only connected to two electrical bays which are the connection bay and the line bay respectively, the inner bridge structure, together with the corresponding bridge breaker and the line breaker can be identified. The definition of the inner bridge connection structure is shown in Figure 9.

The structure of the inner bridge connection

**Figure 9.** The structure of the inner bridge connection.

According to the inner bridge structure obtained above, the transformer, the bus, the bridge breaker and the line are obtained in the basic structure of the inner bridge, which avoids the repeated search of the topology structure in the advanced application.

4. Identification of the static topology and judgment of the dynamic connectivity

Based on the hierarchical structure of “transformer (winding) - bus - electrical bay”, the following static topology identification functions are available:

- 1) Judgement of the breaker type: such as the ordinary line breaker, the side breaker, the middle breaker, the connection breaker, the segment breaker, etc.
- 2) Judgement of the disconnector type: such as the disconnector of the main busbar, the disconnector of the secondary bus, the line disconnector, etc.
- 3) Judgement of the grounddisconnector type: such as the line grounddisconnector, the grounddisconnector in the bus side of the breaker, the grounddisconnector in the line side of the breaker, etc.
- 4) In one electrical bay structure, the other types of devices can be obtained from one device.

Based on the static topological relationship of the primary devices and the actual state of breakers and disconnectors, the following query functions of the dynamic connection can be provided:

- 1) Determine whether the two primary devices are connected.
- 2) Get another type of device that is connected to a specified device.

5. Applications of bay-based hierarchical topology

5.1. Fault diagnosis

In the traditional substation monitoring system, network topology analysis is often used in the topological coloring application and the logic blocking application. Fault diagnosis has put forward higher requirements for the network topology, which not only needs regular functions, but also can automatically identify the connection mode of power devices (such as the series connection, the single-bus connection, the double-bus connection) and subtypes of power devices (such as the bus disconnector, the line disconnector). In addition, network topology analysis is also required to obtain electrical connections between fault bays, including retrieving and providing all electrical bays connected to the designated bus to confirm the fault.

5.2. The status analysis of electrical bays

The status analysis of the bay is mainly used to analyze the bay status such as the operation, hot standby, cold standby and maintenance status, so as to improve the control capability of the devices. This function depends greatly on the status of the breaker and the disconnector in the same electrical bay. When it comes to the analysis of the operating status of each device in the series connection, the network topology function is required to provide the state of the side breaker or the middle breaker in the same series.

6. Conclusion

The hierarchical topology analysis method based on electrical bays is presented in this paper. And the primary devices of the substation is organized according to the hierarchical structure as “transformer (winding) - bus - electrical bay”. On this basis, the identification and processing of the 3/2 circuit breaker connection and the inner bridge connection have been proposed, which are helpful for the advanced applications such as fault diagnosis and the status analysis of electrical bays.

In the follow-up work, based on the hierarchical topology introduced in this paper, the identification of the static topology and the judgment of the dynamic connectivity will be improved gradually, combined with engineering application experience. It will help to promote the advanced applications in smart substations.

7. References

- [1] Costa A S, Lourenco E M and Colzani L 2008 Reduced Anomaly Zone Determination for Topology Error Processing in Generalized State Estimation *J. Power Tech, 2007 IEEE Laus.* **24** 137-42
- [2] Lourenco E M, Costa A S and Clements K A 2004 Bayesian-based hypothesis testing for topology error identification in generalized state estimation *Power Systems IEEE Transactions on* **19** 1206-15
- [3] Coelho T C, Lourenço E M and Costa A S 2013 Anomaly zone determination for topology error processing in power system state estimation *Journal of Control Automation & Electrical Systems* **24** 312-23
- [4] Gong J W, Sun H B, Tang L and Zhang B M 2006 Dispatching Order Generating Expert System Based on Network Analysis and Intelligent Reasoning *Power System Technology* **30** 19-24
- [5] Lin X Q, Ren J W, Zhang B H, Zhou X H and Zhou Q J 2012 An intelligent dispatching operation-tickets system in electric power system based on network reconfiguration *Power System Protection & Control* **40** 143-7
- [6] Chai B, Qiu H, Liu S, Zhang B, Gao K and Zhou A 2017 A study of topology analysis engine based on graph databases in electric utilities *IEEE, Information Technology, Networking, Electronic and Automation Control Conference* **1** 585-8
- [7] Ravikumar G and Khaparde S A 2015 CIM oriented graph database for network topology processing and applications integration *Power Engineering Conference* **1** 1-7
- [8] Zhang W, Zhang G, Gou L, Kong B and Bian D 2015 A hierarchical autonomous system based topology control algorithm in space information network *Ksii Transactions on Internet & Information Systems* **9** 3572-93
- [9] Long Q F, Chen G, Ding X Q, Ding Y, Chun M A and Huang W Y 2005 New method of power network topology analysis based on object-oriented technology *Proceedings of Electric Power System & Automation* **3** 172-5

Acknowledgments

This article is supported by the State Grid Corporation science and technology project, "The application standardization and evaluation technology research of substation integrated monitoring and control system" (SGTJDK00DWJS1700032).

Study on Thermal Performance of a Phase Change Thermal Storage Device by Utilizing Off-peak Power

B Tang¹, Q H Shangguan¹ and Y Lu^{1,2}

¹School of Energy and Environment, Southeast University, Nanjing 210096, China

²Address for correspondence: School of Energy and Environment, Southeast University, Nanjing 210096, China

E-mail: luyong@seu.edu.cn

Abstract. Based on the background of peak load shifting, this paper proposes a phase change thermal storage device by utilizing off-peak power. Experimental investigations on its thermal performance is conducted, it shows that the regenerator has high density of thermal storage and good thermal storage efficiency of 91.3%. At the same time, numerical simulations of the heat transfer enhancement by using fins are performed on the exothermic process, the results show that the addition of fins can effectively improve the exothermic efficiency to 80%. The experimental and simulation results have some reference value for exploring the application of latent heat thermal storage in real life.

1. Introduction

With the continuous development of China in recent years, the peak-valley difference of the power grid has been increasing year by year, and the problem of grid peak regulation has become increasingly prominent. The solution, evaluating the domestic power supply and demand situation and adopting the method of peak load shifting to ease the pressure on the power grid, is widely promoted by energy management department in various countries [1]. Peak load shifting [2] refers to the storage of surplus electric energy during low period of electricity consumption, it is released during the peak period of electricity consumption and used in daily life. The energy storage technology as an effective means can solve the problem that energy supply and energy using cannot be matched in time and space [3].

Latent heat thermal storage [4] is an advanced thermal storage technology that uses PCM (phase change materials) which can absorb or release heat during phase change to achieve energy storage. The Combination of off-peak power and phase change energy storage is valuable for peak load shifting and reduce heating costs. It means that Latent heat thermal storage technology would be used for energy storage during valley period, then energy is released for building heating during peak period. Liu et al. [5] prepared a high-temperature phase change thermal storage heater, and the experimental research on the charging and discharging thermal performance was addressed. The results show that the rate of heat release could meet the general heating requirements, but the heat storage efficiency is not high. Zhu et al. [6] studied the latent thermal storage equipment using valley electricity, and the device is in the ground source heat pump system. The results show that the use of phase change material for heat storage can make full use of valley electricity, saving operating costs and having good economic returns.

It can be seen that in the background of peak load shifting and valley utilization, PCM storage applications which are suitable for actual production are still not much. So this paper proposes a PCM



storage device by utilizing off-peak power that is suitable for building heating. The device has compact size and high heat storage density. Especially, it is easy to install them modularly.

2. PCM storage device

2.1. Phase change material

The goal of the thermal storage system designed in this paper is building heating, which is mainly to provide domestic water. In the general building heating, the common temperature of domestic water is 30~50 °C. Therefore, the material should not have a high phase change temperature. By comparing the properties of various types of phase change materials, $\text{NH}_4\text{Al}(\text{SO}_4)_2 \cdot 12\text{H}_2\text{O}$ is used in this paper. Its phase transition temperature is about 95 °C, the latent heat value is about 254 kJ/kg. It has a high thermal conductivity (0.53 W/m·k) and low rate of volume change, also the material has a relatively stable performance as inorganic salts. Certainly, it is low-cost and recyclable.

2.2. Device design

The comparative study [7] found that the square PCM storage device has the advantages of simple packaging and high density per unit volume of heat storage. Therefore, a square plate type phase change heat storage structure is adopted in this paper, as shown in figure 1.

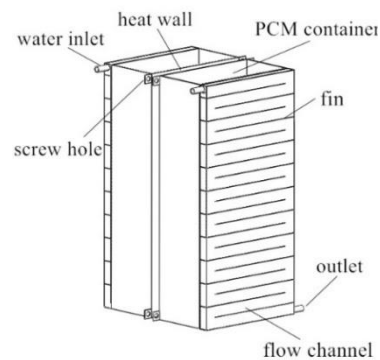


Figure 1. PCM storage device

The flexible double-sided electric heating plate is adopted, and the internal heating resistance wire of the heating plate is evenly distributed, which has the characteristics of high electrothermal conversion efficiency and long service life, also a temperature control device can be used to adjust the heating temperature in real time. In order to avoid the corrosion of the PCM to the electric heating plate, the heating plate is bolted between two symmetrically arranged body surfaces of the thermal storage unit and the PCM is heated by heating the wall surface of the thermal storage unit. Certainly, the size of the electric heating plate is equivalent to the wall surface of the unit. And the polyurethane insulation material is wrapped outside the entire heat accumulator to prevent heat loss.

3. Experimental study

In order to search the thermal performance of the designed PCM storage device, it is necessary to test the charge and discharge efficiency and the best operating conditions through experiments. Since the two sides of the thermal storage unit are symmetrically arranged, the experimental conditions and working conditions are completely same, this experiment and the subsequent numerical simulations would only test the single sided unit.

3.1. Test system

The test device is mainly composed of four parts: an electric heating system, a phase change thermal storage unit, a heat release system that mainly includes water tanks, pumps, pipeline valves, a data acquisition system which consists of flowmeter, temperature sensor, signal transmission module, and computer.

During the charge experiment, the electric heating plate was energized and heated while the flow channel was closed. The temperature at each measuring point during the phase change process and the

amount of electricity consumed during the entire process were recorded.

The electric heating was turned off and the valves on the pipeline were opened in the discharge experiment. HTF (heat transfer fluid) was drawn from the water tank and exchanged with the thermal storage unit through the heat exchange flow path and then transferred to the hot water tank for storage. The temperature of the inlet and outlet was recorded in real time. Also, the experiment was repeated with changing the test conditions (Table 1) in the exothermic process.

Table 1. Test conditions

Variable flow rate			
6.5L/h	9.5L/h	12L/h	15.5L/h
Variable flow direction			
top injection		bottom injection	

3.2 Experimental results and analysis

3.2.1 Thermal storage process. Since the PCM selected in this paper starts to dehydrate the crystal when the temperature is higher than 120 °C, the target temperature of the heating wall is set below 120 °C. Also, after the initial heat storage experimental observation, the upper surface of the phase change unit would be encapsulated.

The figure 2 shows the temperature change of three points in the vertical direction (P1 is highest, P3 is lowest) on the same section during the thermal storage process. It could be seen that the temperature changes at three points generally go through three processes: at the beginning, it is the solid sensible thermal storage stage, where the temperature rises quickly; when the temperature reaches the melting point, the PCM enters the latent thermal storage stage and the temperature rise is gentler; then the molten liquid PCM continues to start sensible thermal storage and gradually reaches the heat temperature. Meanwhile, it can be seen that the temperature of the upper PCM is always higher than the lower part during the whole process. This is similar to the experimental result of Martin et al. [8], although this trend is less obvious. The main reason for this is as follows: after heating starts, the PCM increases rapidly. At this time, heat conduction occupies a major position, and then the PCM near the heating surface firstly melts into liquid, and then the liquid with a higher temperature at the bottom will rise upward which causes natural convection, so that the upper temperature will be higher than the lower part. At this time, the convective heat exchange occupies a dominant position, the entire phase change interface presents a trend of moving from the top to bottom and from the heating surface to the outer wall surface.

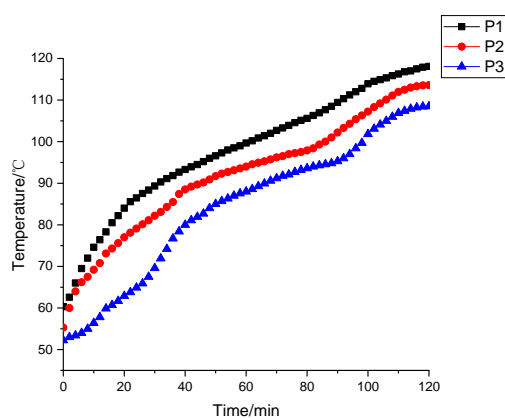


Figure 2. The temperature of three points inside the PCM

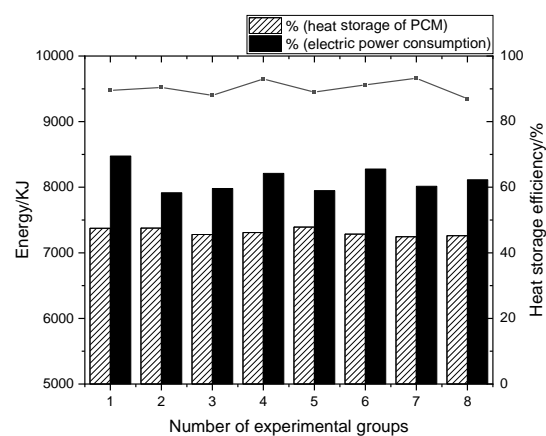


Figure 3. Energy consumption and the thermal storage of the PCM

Of course, the most important thing is that we need an indicator to measure the performance of the thermal storage process of this device. As a ratio of PCM thermal storage and power consumption, the thermal storage efficiency is of great significance to evaluate the efficiency and economy of electro-thermal conversion, the formula is as follows:

$$\eta_{st} = \frac{Q_{st}}{Q_E} \quad (1)$$

$$Q_{st} = m_{pcm}[C_{p,s}(T_{pcm} - T_{pcm,ini}) + L + C_{p,l}(T_{pcm,end} - T_{pcm})] \quad (2)$$

A number of thermal storage tests were performed to calculate the energy consumption and the thermal storage of the PCM in the phase change unit, the result is shown in the figure 3. Since the thermal storage experiment and the thermal release experiment are alternately performed, the amount of thermal release each time is not the same, so the time required for the material to reach the same initial state (the average temperature of PCM reaches to 105 °C) during each thermal storage experiment is different, resulting in different power consumption.

By calculating the efficiency of multiple thermal storage processes, shown in figure 3, the average thermal storage efficiency of the thermal accumulator is calculated to 91.3%, it shows that the consumed electrical energy cannot be fully converted to the energy stored in the PCM.

3.2.2. Thermal release process. Similar to the above mentioned thermal storage efficiency, the effective thermal release efficiency (equation (3)) based on the first law of thermodynamics is used to evaluate the performance of the phase change unit, and the effective thermal release performance of the phase change unit with different flow rates and different flow directions is mainly discussed. The effective thermal release efficiency is the ratio of the energy contained in the cumulative water during the thermal release (outlet water temperature $T_{out} \geq 30^\circ\text{C}$) to the energy contained in the unit at the beginning of the thermal release process. Taking into account the actual operation of the storage and release process is a cycle, with 70 °C as a reference temperature when calculating the storage heat. While focusing on effective heat extraction, the thermal release rate which measured by the instantaneous exothermic power (equation (5)) and the average exothermic power (equation (6)) should not be ignored.

$$\eta_{dis} = \frac{Q_{dis}(t_u)}{Q_{st}} \quad (3)$$

$$Q_{dis}(t_u) = q_v \rho_w V_w C_{p,w} \Delta t \sum_{n=1}^k (T_{out}(t) - T_{in}) \quad (4)$$

$$P_{dis} = q_w \rho_w C_{p,w} (T_{out}(t) - T_{in}) \quad (5)$$

$$\overline{P}_{dis} = \frac{Q_{dis}(t_u)}{t_u} = \frac{q_v \rho_w C_{p,w} \Delta t \sum_{n=1}^k (T_{out}(t) - T_{in})}{t_u} \quad (6)$$

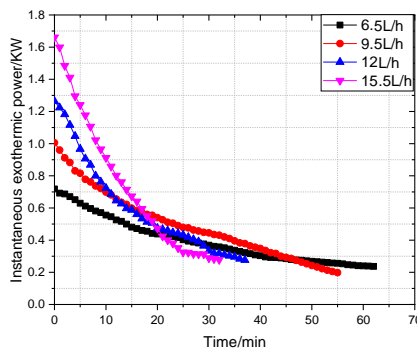


Figure 4. The variation curve of the exothermic power of top injection

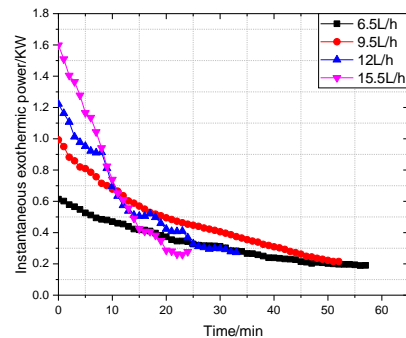


Figure 5. The variation curve of the exothermic power of bottom injection

Figure 4 and figure 5 show the variation curve of the exothermic power with different flow directions and rates, the phenomenon of varying lengths of the curve is due to the difference in effective thermal release time. The overall trend of power changes in the two figures is the same. Initially, the

exothermic power is basically related to the flow rate, but it quickly decreases to a lower level as the heat exchange progresses, mainly because of the decrease of the outlet water temperature. After 20 minutes, the instantaneous exothermic power at the 9.5 L/h flow rate is greater than another three conditions, and has remained at the leading level since then. At the same time, it can be seen that the greater the flow rate, the shorter the effective thermal release time, which may be caused by insufficient heat exchange between the fluid and the PCM when the flow rate is too fast. From the perspective of thermal release efficiency and release time, the thermal release quality is higher when the flow rate is 9.5 L/h.

By calculating the effective thermal release efficiency and average thermal release power for different flow directions and flow rates, shown in figure 6, the thermal release performance when the flow direction is from bottom to top is relatively good. This is mainly due to the fact that the temperature of PCM inside the regenerator increases with the depth decreasing in the height direction, following the principle of energy cascaded utilization, the method of using the fluid from bottom to top through the heat exchange channel can extract more effective heat. The results indicate that the exothermic efficiency is only 50%-60%, and there is still a lot of heat that cannot be used effectively.

4. Numerical Simulation

4.1. Numerical model

As the PCM near the side of the heat exchange wall gradually solidifies in the heat transfer process, the thermal resistance of heat transfer is increased, so that the heat stored in the internal high temperature PCM cannot be transmitted to the external heat exchange fluid. The addition of fins to the heat transfer surface is a more economical enhancement of heat transfer [9]-[12]. So we have tried to increase the heat transfer capacity by adding horizontal fins inside the phase change unit.

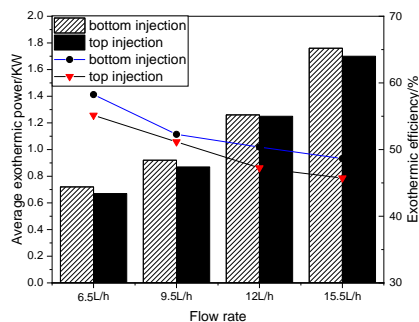


Figure 6. Effective thermal release efficiency and average thermal release power

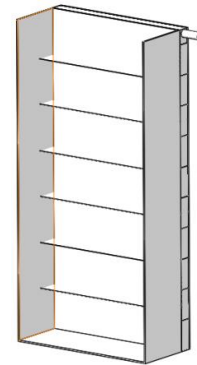


Figure 7. Numerical model with fins

A numerical simulation model is established based on the single phase change unit used in the experiment. As shown in the figure 7, the model size is the same as the actual unit size, and the fin lengths are 2, 4, 6, and 8 cm, respectively. The simulated exothermic condition is preferably flow direction from bottom to top with a flow rate of 9.5 L/h. Transient simulations of the heat exchange were conducted using the commercial CFD software Fluent, three zones were modeled: PCM, heat transfer flow channel and fins, using the melt/solidification model provided by Fluent, while simplifying and assuming the calculation process accordingly.

4.2. Numerical results

Due to the limited space, this paper has selected internal temperature changes of the PCM with a typical internal fin length of 4cm and 8cm compared with the operating conditions without fins (figure 8), the intermediate section perpendicular to the fins and the flow channels was selected.

With the progress of the thermal release, the phenomenon of temperature delamination in the lateral direction can be clearly observed, the temperature of the PCM near the flow channel decreases rapidly, while in the vertical direction, the bottom PCM is first cooled and the upper temperature is still high. When the entire device loses its ability to further thermal release due to the small temperature

difference between the PCM layer near the external wall and the fluid, the inner wall and the upper PCM remain at a higher temperature. The solid PCM with a relatively low temperature near the external wall has a large thermal resistance, so that a large amount of heat is still not released in the unit. this is also the main cause of the low exothermic efficiency in the previous experimental results.

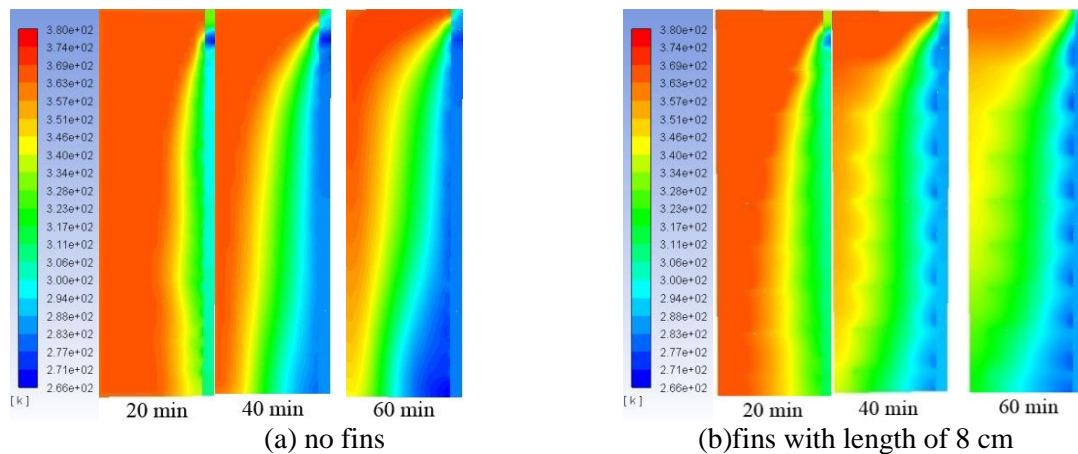


Figure 8. Comparison of temperature contour

With the addition of horizontal fins (figure 8), the overall temperature gradient of the phase change unit is smaller than before. It cuts off the continuity of the external low-temperature PCM to a certain extent, reduces the thermal resistance of heat transfer, thereby improves the heat exchange efficiency. But there is still a high temperature zone on the top.

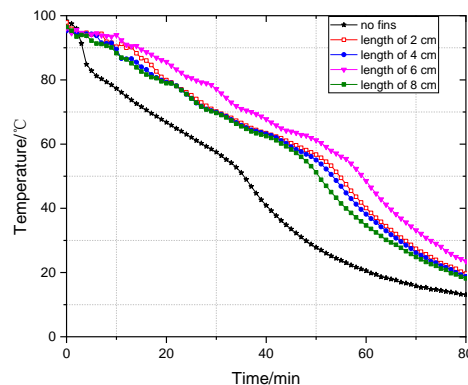


Figure 9. The temperature of outlet water

From the simulation result, it can be seen that the outlet temperature after adding fins is significantly increased, indicating that the overall thermal release performance is enhanced. But the outlet temperature and exothermic power do not increase with the length of the fins. The fin lengths of 2 cm and 4 cm have similar strengthening effects. When the length is 6 cm, the strengthening effect is further enhanced. But the result is not as expected when the length is increased to 8 cm, maybe too long fins hinder natural convection heat transfer at vertical direction. The exothermic efficiency is calculated to be 80% when the length of fin is 6cm, compared with no fins, the efficiency is much improved.

5. Conclusion

This paper proposes a phase change thermal storage device by utilizing off-peak power, experimental investigations and numerical simulation on its thermal performance are conducted.

Through experimental research, it was found that the device can complete the thermal storage within two hours and its thermal storage efficiency reached to 91.3%. When the HTF flows from bottom to

top, it is preferable to thermal release, but the overall thermal release efficiency is not high.

According to the results of numerical simulation, the addition of fins inside the unit can effectively increase the thermal release efficiency to 80% when the length of fin is 6 cm.

Further study will focus on the improvement of heating method, in order to create a more uniform temperature distribution. Additionally, more methods for heat transfer enhancement will also be explored in this device.

6. Reference

- [1] Khan A S M, Verzijlbergh R A, Sakinci O C, and Vries L J D 2018 How do Demand Response and Electrical Energy Storage Affect (the Need for) a Capacity Market? *Appl. Energy.* **214** 39-62
- [2] Barzin R, Chen J J J, Young B R, and Farid M M 2015 Peak Load Shifting with Energy Storage and Price-based Control System *Energy.* **92** 505-514
- [3] Li G, Qian S, Lee H, Hwang Y and Radermacher R 2014 Experimental Investigation of Energy and Exergy Performance of Short Term Adsorption Heat Storage for Residential Application *Energy.* **65** 675-691
- [4] Pirasaci T, Wickramaratne C, Moloney F, Goswami D Y, Stefanakos E, and Yan J 2018 Influence of Design on Performance of a Latent Heat Storage System at High Temperatures *Appl. Energy.* **224** 220-229
- [5] Liu G, Wang X, Zhang Y, Di H and Jiang Y 2004 Experimental Research on High-temperature Phase Change Thermal Energy Storage Heater *J. Eng. Thermophys.* **36** 62-65
- [6] Zhu J L, Li H and Zhang W 2012 Numerical Simulation and Optimization of Phase Change Heat Storage Process with Spiral Pipe *J. Tianjin Univ.* **45** 875-880
- [7] Abdulateef A M, Mat S, Abdulateef J, Sopian K, and Al-Abidi A A 2017 Geometric and Design Parameters of Fins Employed for Enhancing Thermal Energy Storage Systems: a Review *Renew. Sust. Energ. Rev.* **82** 1620-35
- [8] Longeon M, Soupart A, Fourmigué J F, Bruch A, and Marty P 2013 Experimental and Numerical Study of Annular PCM Storage in the Presence of Natural Convection *Appl. Energy.* **112** 175- 184
- [9] Wang P, Yao H, Lan Z, Peng Z, Huang Y, and Ding Y 2016 Numerical Investigation of PCM Melting Process in Sleeve Tube with Internal Fins *Energy Conv. Manag.* **110** 428-435
- [10] Kazemi M, Hosseini M J, Ranjbar A A, and Bahrapoury R 2017 Improvement of Longitudinal Fins Configuration in Latent Heat Storage Systems *Renew. Energy.* **116** 447-457
- [11] Joybari M M, Haghghat F, Seddegh S, and Al-Abidi A A 2017 Heat Transfer Enhancement of Phase Change Materials by Fins under Simultaneous Charging and Discharging *Energy Conv. Manag.* **152** 136-156.
- [12] Zhao D and Tan G 2015 Numerical Analysis of a Shell-and-tube Latent Heat Storage Unit with Fins for Air-conditioning Application *Appl. Energy.* **138** 381-392

Acknowledgments

This paper is a part of the research that is sponsored by The National Natural Science Foundation of China (51376048).

Improvement of Performance Calculation Methods for Pulverized Coal and Blast-furnace Gas Co-fired Boilers

Yalan Ye^{1*}, Hongming Wang¹, Xiang An¹, Wenhao Jiang²

¹ Jiangsu Maritime Institute, Nanjing, Jiangsu, 211170, China

² MCC Huatian Engineering & Technology Corporation, Nanjing, Jiangsu, 210000, China

* Corresponding author's e-mail: yyl_jessica@sina.com

Abstract. In power plants of steel mills, the performance of pulverized coal and blast-furnace gas co-fired boilers was tested according to GB/T10184-2015 "Performance test code of utility boiler". However, the calculation and analysis models in this code are mainly based on conventional fuels. Besides, the special properties of blast furnace gas were not taken into account. Therefore, the code GB/T10184-2015 is not suitable to be directly used for pulverized coal and blast furnace gas co-fired boilers. According to the differences between co-fired boilers and conventional boilers, the key points for calculating the performance of co-fired boilers were analyzed on the basis of GB/T10184-2015, and the corresponding improved methods were proposed, in view of fuel composition conversion, combustion calculation, coal feed rate, exhaust gas temperature value, and pollutant emission concentration conversion. The results can provide reference for the performance test of such boilers, with certain practical significance.

1. Introduction

With the development of combustion technology, pulverized coal and blast-furnace gas co-fired boilers have been successfully applied in many steel plants (especially in steel plants of China). In this way, many problems existing in the separate combustion of blast-furnace gas can be solved effectively. Therefore, pulverized coal and blast-furnace gas co-fired boilers have been rapidly promoted in various steel enterprises.

In recent years, many scholars have carried out relevant research on pulverized coal and blast-furnace gas co-fired boilers. However, the research scope is mainly focused on the combustion, heat transfer, and emission characteristics [1]-[8]. There are few studies on the performance calculation of pulverized coal and blast-furnace gas co-fired boilers. At present, the main basis for the performance of boilers in steel plant is based on the Chinese standard GB/T10184-2015 "Performance test code of utility boiler" [9], which provides a method for analyzing the performance of co-fired boilers. However, this method is not suitable for pulverized and blast-furnace gas co-fired boilers directly. First, blast-furnace gas has high nitrogen content, its combustion calculation method is different from the traditional simplified method. Second, in converting the composition, only the moisture in the form of gaseous water vapor is considered, but the blast-furnace gas may contain moisture in the form of liquid droplets, neglecting liquid moisture or regard it as water vapor will inevitably cause errors in calculation results. Third, there are several layouts for the tail heating surface of pulverized coal and blast-furnace gas co-fired boilers, so the exhaust gas temperature should also be selected according to the heating surface layout. Therefore, for the pulverized coal and blast-furnace gas co-fired boilers, its performance calculation cannot directly apply GB/T10184-2015.



In addition, it is difficult to accurately measure the mass flow of pulverized coal entering the furnace, leading to the difficulty in the boiler combustion calculation, and the concentration of atmospheric pollutants should not be converted directly according to the current method.

Thus, starting from fuel composition conversion, combustion calculation, coal feed rate, exhaust gas temperature value, and pollutant emission concentration conversion, we analyzed the performance calculation points of the pulverized coal and blast-furnace gas co-fired boilers that are different from conventional boilers, based on GB/T10184-2015. And we proposed corresponding improvement methods, which can provide reference for the performance test of the co-fired boilers.

2. Problems exit in current performance calculation methods

2.1. Combustion calculation model

The fuel combustion calculation is the primary task for boiler performance calculation. It mainly include calculating the amount of air required for combustion, excess air coefficient, and combustion products (flue gas). Among them, excess air coefficient is the key solution object. Based on the actual combustion conditions in GB/T10184, a correctional excess air coefficient calculation formula is given as follows:

$$\alpha = \frac{21 \varphi_{N_2,fg,d}}{21 \varphi_{N_2,fg,d} - 79 \varphi_{O_2,fg,d}} \quad (1)$$

Where, α is the correctional excess air coefficient, $\varphi_{O_2,fg,d}$ and $\varphi_{N_2,fg,d}$ are respectively the volume fractions of O_2 and N_2 in dry fuel gas.

GB/T 10184 also states that after ignoring the presence of combustible gases such as residual CO in the flue gas, the excess air coefficient can be calculated according to the simplified formula (2):

$$\alpha = \frac{21}{21 - \varphi_{O_2,fg,d}} \quad (2)$$

The formula (2) is commonly used in engineering to calculate the excess air coefficient.

It can be seen that, in the calculation formula provided by GB/T10184, both the simplified formula (2) and formula (1) do not consider the effect of fuel nitrogen content on the excess air coefficient. This simplification is suitable for most fuels boilers, but not suitable for boilers burning blast-furnace gas. Blast-furnace gas is rich in nitrogen, resulting in a high nitrogen content in the mixed fuel. If the formula (1) or (2) is used to solve the excess air coefficient of pulverized coal and blast-furnace gas co-fired boilers, it will inevitably bring about error.

2.2. Conversion of fuel composition

Before combustion calculation is performed in a co-fired boiler, the characteristics of the mixed fuel should be converted through mass flow of the two fuels. Mixed fuel properties are generally calculated according to equation (3):

$$y_i = w_{coal} x_{coal,i} + w_{gas} x_{gas,i} \quad (3)$$

Where, y_i is a certain characteristic data for the mixed fuel; $x_{coal,i}$ 、 $x_{gas,i}$ are the corresponding characteristic data of coal and blast-furnace gas respectively; w_{coal} 、 w_{gas} are the ratio of coal consumption and blast furnace gas consumption in total fuel consumption respectively.

When performing the above calculations, since the characteristics of the blast-furnace gas and the coal differ in the expression, it is necessary to convert the parameters of the blast-furnace gas in advance. Taking the fuel composition as an example, the gas volume components of the blast-furnace gas should be converted into elemental components expressed by mass fraction before they can be synthesized with the elemental components of the coal. Similarly, the ash and moisture should also be converted. Regarding composition conversion, GB/T 10184 gives the following calculation model:

$$w_{C,g} = \frac{0.54}{\rho_{g,st}} (\varphi_{CO,g} + \varphi_{CO_2,g} + \sum m \varphi_{C_m H_n,g}) \quad (4)$$

$$w_{H,g} = \frac{0.045}{\rho_{g,st}} (2\varphi_{H_2,g} + 2\varphi_{H_2S,g} + \sum n \varphi_{C_m H_n,g}) \quad (5)$$

$$w_{O,g} = \frac{0.715}{\rho_{g,st}} (\varphi_{CO,g} + 2\varphi_{CO_2,g} + 2\varphi_{O_2,g}) \quad (6)$$

$$w_{N,g} = \frac{1.25}{\rho_{g,st}} \varphi_{N_2,g} \quad (7)$$

$$w_{S,g} = \frac{1.43}{\rho_{g,st}} \varphi_{H_2S,g} \quad (8)$$

$$w_{m,g} = \frac{0.8}{\rho_{g,st}} \varphi_{wv,g} \quad (9)$$

$$w_{as,g} = \frac{0.1}{\rho_{g,st}} \rho_{as,g} \quad (10)$$

Where, $w_{C,g}$ 、 $w_{H,g}$ 、 $w_{O,g}$ 、 $w_{N,g}$ 、 $w_{S,g}$ 、 $w_{m,g}$ 、 $w_{as,g}$ are the mass fraction of the element carbon, hydrogen, oxygen, nitrogen, sulfur, steam, and ash in blast-furnace gas respectively; $\rho_{g,st}$ is the density of blast-furnace gas under standard conditions, and is calculated as follow:

$$\rho_{g,st} = 0.0125\varphi_{CO,g} + 0.0009\varphi_{H_2,g} + 0.01 \sum (0.54m + 0.045n)\varphi_{C_mH_n,g} + 0.0152\varphi_{H_2S,g} + 0.0196\varphi_{CO_2,g} + 0.0125\varphi_{N_2,g} + 0.0143\varphi_{O_2,g} + 0.008\varphi_{wv,g} + 0.001\rho_{as,g} \quad (11)$$

Where, $\varphi_{CO,g}$ 、 $\varphi_{H_2,g}$ 、 $\varphi_{C_mH_n,g}$ 、 $\varphi_{H_2S,g}$ 、 $\varphi_{CO_2,g}$ 、 $\varphi_{N_2,g}$ 、 $\varphi_{O_2,g}$ 、 $\varphi_{wv,g}$ are volume fraction (%) of CO, C_mH_n , H_2S , CO_2 , N_2 , O_2 and water vapor in blast-furnace gas respectively; $\rho_{as,g}$ is the mass concentration of ash in blast-furnace gas.

It can be seen that the national standard GB/T10184 only considers the moisture in gaseous fuels in the form of gaseous water vapor. This can be applied to most gaseous fuels, but should not be applied directly to metallurgical blast-furnace gas. Because the blast-furnace gas may contain moisture in the form of mechanical water, which is related to the upstream blast-furnace gas dust removal process: If the wet dust removal process is used, the blast-furnace gas after dust removal treatment will contain not only saturated water vapor but also mechanical water in the form of liquid droplets; If a dry dust removal process is used, since the blast-furnace gas does not touch water in the dust removal process, the gas contains only a small amount of water vapor, so it will not carry mechanical water.

Obviously, for the blast-furnace gas after wet dust collection, the water content in the form of mechanical water should be taken into account in the composition conversion. Therefore, it is necessary to improve the relevant formula in GB/T10184.

2.3. Measurement of pulverized coal entering into the boiler furnace

For pulverized coal and blast-furnace gas co-fired boilers, the coal mass flow fed into the boiler furnace is the basic input parameter for solving the mixed fuel composition, and it is an indispensable basic data for calculating the performance of the co-fired boiler. However, until now, the accurate measurement for the mass flow of coal entering the furnace is still an unsolved technical problem, especially for the middle storage pulverizing system, the mass flow measured by the coal feeder cannot represent the pulverized coal mass flow fed into the furnace. The relevant technicians have not yet found a recognized reliable solution for this problem.

The measurement of the fed mass flow of pulverized coal will not affect the performance calculation for conventional coal-fired boilers, because the performance of the boiler fired single fuel is calculated based on the per-mass fuel. But for the pulverized coal and blast-furnace gas co-fired boilers, if the mass flow of pulverized coal cannot be accurately measured, it will directly affect the solution of the mixed fuel characteristics, and so will affect other subsequent calculations. Therefore, constructing a practical and reliable method to obtain the pulverized coal flow, must be solved to enable the performance calculation of the co-fired boiler can be carried out smoothly.

2.4. Selection of flue gas exhaust temperature

The temperature of the flue gas is an important parameter to characterize the operation economy for the boiler, and it can affect the heat loss of the flue gas and affect the boiler efficiency. GB/T10184 takes the air preheater as the last stage heating surface in the boiler tail, so the outlet flue gas

temperature of the air preheater is used as the exhaust temperature. This is suitable for conventional boilers, but for pulverized coal and blast-furnace gas co-fired boilers, it may not be suitable. The co-fired boilers is different from the conventional boiler in the design for tail heating surface. Therefore, the temperature value of the exhaust gas must be differentiated according to the characteristics of the heating surface.

2.5. Conversion of air pollutants emission concentration

GB/T10184 provides the method for measuring the emission concentration of boiler air pollutants (including NO_x, SO₂ and so on). Taking SO₂ emission concentration as an example, GB/T10184 points out that the emission concentrations of SO₂ and O₂ in flue gas should be measured at the same time, and then the measured SO₂ concentration should be converted to the standard concentration with excess air coefficient as 1.4, according to GB13223. The conversion formula is as follows:

$$\rho_{\text{SO}_2, \text{re}} = \rho_{\text{SO}_2, \text{m}} \frac{\alpha}{1.4} \quad (12)$$

Where, $\rho_{\text{SO}_2, \text{re}}$ is the mass concentration of SO₂ converted to the excess air coefficient as 1.4, mg/m³; $\rho_{\text{SO}_2, \text{m}}$ is the measured SO₂ mass concentration in the flue gas, mg/m³.

According to the GB/T10184, we consulted GB13223 "Emission Standard of Air pollutants for Thermal Power Plants", in which the 2003 version (GB13223-2003[10]) stipulated that the emission concentration should be converted by the excess air coefficient α , and the coefficient of coal-fired boiler was given as $\alpha=1.4$. The 2011 version (GB13223-2011[11]) replaced it with the oxygen content and specifies the reference oxygen content for various types of thermal energy conversion facilities, as showed in Table1.

Table1. Reference oxygen content

No	Thermal energy conversion facility type	Reference oxygen content /%
1	Coal-fired boiler	6
2	Oil or gas boiler	3
3	Gas turbine unit	15

It can be seen that, according to GB13223-2011, the conversion factor 1.4 in equation (12) corresponds to the reference oxygen content of 6%. However, for the pulverized coal and blast-furnace gas co-fired boiler, this conversion method has the following two problems:

1) Due to the high nitrogen content in the fuel, the excess air coefficient should not be calculated through the simplified formula shown in equation (2), but should be calculated through the exact formula considering nitrogen content in the fuel. The results from the two formulas are different, so simplifying the excess air coefficient value as 1.4 will inevitably cause large errors.

2) Pulverized coal and blast-furnace gas co-fired boilers are divided into two types: one is based on the structure of pulverized coal boiler, and the other is based on structure of gas boiler. Since current standards only stipulate the reference oxygen content in a single fuel boiler, and no special provisions have been made for the co-fired boiler. Thus, the pulverized coal and blast-furnace gas co-fired boilers can only be classified as coal-fired boilers or gas-fired boilers. For the first type co-fired boiler, the reference oxygen content should be selected as pulverized coal boiler. And for the second co-fired boiler, the reference oxygen content should be selected as gas boiler. Obviously, with different oxygen content, the corresponding conversion coefficient is also different.

Therefore, when measuring the concentration of pollutants discharged from pulverized coal and blast-furnace gas co-fired boilers, the method in GB/T10184 should not be directly applied. Otherwise, the results may be seriously distorted.

3. Improvements of the performance calculation methods

3.1. Improvement of combustion calculation model

For pulverized coal and blast-furnace gas co-fired boilers, the excess air coefficient should be solved according to the complete calculation formula, as follows:

$$\alpha = \frac{21}{21 - 79 \frac{\varphi_{O_2,fg,d}}{\varphi_{N_2,fg,d} - \frac{0.8w_{N,ar}}{V_{fg,d}}}} \quad (13)$$

Where, $w_{N,ar}$ is the mass fraction of nitrogen elemental in the mixed fuel; $V_{fg,d}$ is the volume of dry flue gas generated from the mixed fuel combustion, m^3/kg , and the formula is as follows:

$$V_{fg,d} = V_{fg,d,th} + (\alpha - 1)V_{a,d,th} \quad (14)$$

Where, $V_{fg,d,th}$ is the theoretical dry flue gas volume generated by per kilogram of mixed fuel combustion; $V_{a,d,th}$ is the theoretical dry air volume required by per kilogram of mixed fuel combustion.

Formula (13) can be derived from the definition of the excess air coefficient and the air component. Due to limited space, the derivation process is omitted here. By comparing equations (1) and (2) with the modified formula (13), it can be found that formula (1) is a simplified formula that ignores the effect of containing N in the fuel, and formula (2) is based on formula (1) and is simplified with the further assumption that N_2 in dry flue gas is close to 79%. Obviously, the above simplified conditions are not applicable to the burning blast-furnace gas with rich N element.

3.2. Improvement of fuel composition conversion model

For the blast-furnace gas carrying mechanical water, the mechanical water should be taken into account, and the water mass should be calculated according to formula (15):

$$w_{m,g} = \frac{0.8}{\rho_{g,st}} \varphi_{wv,g} + d_{jx} \quad (15)$$

Where, $w_{m,g}$ is the mass fraction of water in blast-furnace gas, %; d_{jx} is the mechanical water mass in unit volume of blast-furnace gas, kg/m^3 .

Correspondingly, the calculation formula for the blast-furnace gas density shown in equation (11) also needs to be adjusted. The improved formula is as follows:

$$\rho_{g,st} = 0.0125\varphi_{CO_2,g} + 0.0009\varphi_{H_2,g} + 0.01 \sum (0.54m + 0.045n)\varphi_{C_mH_n,g} + 0.0152\varphi_{H_2S,g} + 0.0196\varphi_{CO_2,g} + 0.0125\varphi_{N_2,g} + 0.0143\varphi_{O_2,g} + 0.008\varphi_{wv,g}w_{m,g} + 0.001\rho_{as,g} + d_{jx} \quad (16)$$

Obviously, using formula (15) instead of formula (9) to characterize the moisture content in blast-furnace gas appears more reasonable. The formula (15) has better applicability and it can be used not only for wet gas with gaseous water vapor, but also for wet gas that contains liquid mechanical water. For wet gas carrying mechanical water, $\varphi_{wv,g}$ in equation (15) is the volume fraction of saturated steam in the wet gas, which can be obtained from the gas temperature.

3.3. Solving model of coal mass flow injected into the boiler furnace

In order to solve the problem of measuring the mass flow of pulverized coal injected into the boiler furnace, this paper proposes a soft measurement method based on the content of triatomic gas in the flue gas. The specific steps are as follows:

- 1) Assume that the mass flow of pulverized coal entering the furnace is B_c ;
- 2) Convert the coal composition and the blast-furnace gas composition to the mixed fuel composition data by formulas (3) to (11), based on the presumed coal mass flow B_c and the measured gas volume B_g . The result includes mass fraction of elemental carbon, hydrogen, oxygen, nitrogen, sulfur, and ash.
- 3) Calculate the mass fraction of carbon actually burned in boiler furnace:

$$w_{C,b} = w_{C,ar} \left(\frac{w_{s,ar}}{1 - w_{c,ar}} + \frac{w_{pd,ar}}{1 - w_{c,ar}} + \frac{w_{as,ar}}{1 - w_{c,ar}} \right) \quad (17)$$

Where, $w_{C,b}$ is the mass fraction of carbon actually burned in boiler furnace, %; $w_{C,ar}$, $w_{as,ar}$ are the mass fraction of carbon and ash in the mixed fuel, %; w_s , w_{pd} , w_{as} are respectively the percentage of slag,

sedimentation ash and fly ash in the total ash content, %; $w_{c,s}$, $w_{c,pd}$, $w_{c,as}$ are respectively the mass fraction of slag in slag, settlement ash and fly ash, %;

4) Calculate the fuel characteristic coefficient:

$$\beta = 2.35 \frac{w_{H,ar} - 0.126w_{O,ar} + 0.038w_{N,ar}}{w_{c,b} + 0.375w_{S,ar}} \quad (18)$$

Where, β is the fuel characteristic coefficient; $w_{H,ar}$, $w_{O,ar}$, $w_{N,ar}$, $w_{S,ar}$ are respectively the mass fraction of elemental hydrogen, oxygen, nitrogen, and sulfur in the mixed fuel;

5) Solve the theoretical content of triatomic gas RO_2 in dry flue gas based on the oxygen content of the flue gas and the fuel characteristic coefficient:

$$\varphi_{RO_2,fg,th,d} = \frac{21 - \varphi_{O_2,fg,d}}{1 + \beta} \quad (19)$$

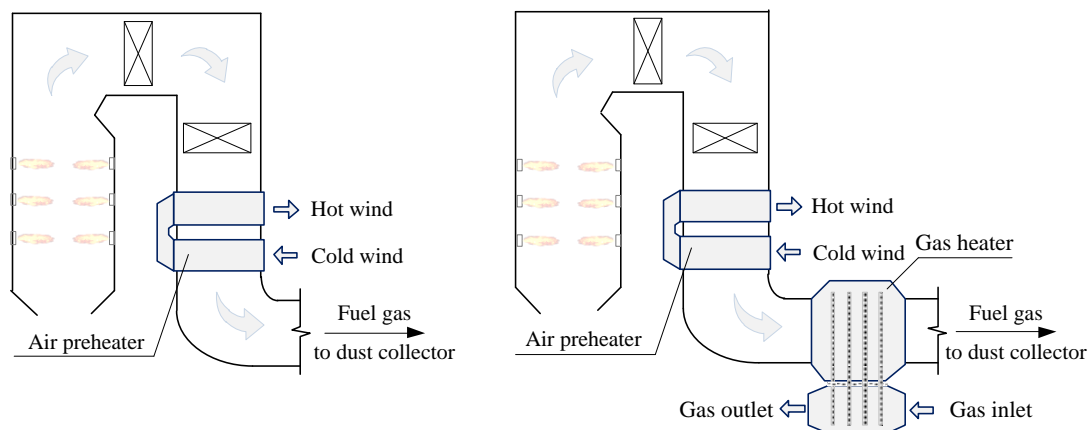
Where, $\varphi_{RO_2,fg,th,d}$ is the theoretical volume fraction of triatomic gas RO_2 in dry fuel gas, %;

6) Compare the theoretical volume fraction of triatomic gas RO_2 in the dry flue gas with the measured value, and determine whether the difference between the two is within the set error range. If it is not satisfied, then re-assumed the coal amount B_c , and perform step 2) ~ step 6) again;

7) Output B_c as the final pulverized coal mass flow.

3.4. Improvement of the exhaust temperature value selection

The exhaust fuel gas temperature of the pulverized coal and blast-furnace gas co-fired boilers shall be differentiated, according to setting characteristics of the boiler tail heating surface. Figure 1 shows the most common two heating surface layouts:



a) Conventional pulverized coal and blast-furnace gas co-fired boilers

b) Pulverized coal and blast-furnace gas co-fired boiler with gas heater

Figure 1. The tail heating surface layout of the pulverized coal and blast-furnace gas co-fired boiler

1) Figure 1-a shows the conventional pulverized coal and blast-furnace gas co-fired boiler whose tail heating surface is set in the same way as the conventional boiler. The last stage of the boiler tail heating surface is the air preheater. For this type of boiler, the outlet gas temperature of the air preheater should be taken as the boiler exhaust temperature.

2) Figure 1-b shows the new type of pulverized coal and blast-furnace gas co-fired boiler that has been used in some steel plants in recent years. A gas heater has been added in the boiler tail, in order to recover the residual heat of the flue gas and improve the combustion of blast furnace gas. For such boilers, the outlet gas temperature of the gas heater should be taken as the boiler exhaust temperature.

3.5. Improvement of the air pollutants emission concentration conversion method

The analysis showed that the origin of the air pollutants emission concentration through excess air coefficient is as follows: For conventional fuel boilers (especially coal-fired boilers), theoretical dry air volume $V_{a,d,th}$ and theoretical dry flue gas volume $V_{fg,d,th}$ are very close, so the formula (14) can be simplified to $V_{fg,d} = \alpha V_{a,d,th}$, and then the conversion method based on the excess air coefficient was obtained. However, for the pulverized coal and blast-furnace gas co-fired boiler, the theoretical dry air volume and the theoretical dry flue gas volume differ greatly, and the greater the mixing ratio of blast-furnace gas, the greater the difference between the theoretical dry air volume and the theoretical dry flue gas volume. Therefore, the dry fuel gas volume of the co-fired boiler cannot be simplified, and the concentration of air pollutants emissions should not be converted according to the excess air coefficient. Effectively, the emission concentration should be converted by the oxygen content in the flue gas as follows:

$$\rho_{re} = \frac{21 - \varphi_{O_2,fg,d,m}}{21 - \varphi_{O_2,fg,d,re}} \rho_m \quad (20)$$

Where, ρ_{re} , ρ_m are the emission concentration of air pollutants converted to the reference oxygen content and the measured emission concentration, respectively, mg/m^3 ; $\varphi_{O_2,fg,d,re}$, $\varphi_{O_2,fg,d,m}$ are the reference oxygen content and the measured oxygen content, respectively.

Formula (20) can be derived through the calculated relationship between the concentration of gaseous pollutants and the dry flue gas volume. It is applicable to various combustion conditions and is currently used by most environmental protection standards.

For the pulverized coal and blast-furnace gas co-fired boilers, it can be seen from the analysis in Part 1.5 that the reference oxygen content should be distinguished by the boiler type. In addition, in the standards for pollutant emissions in China, according to the size of boiler capacity, the boiler with an output above 65t/h should comply with the standard GB13223-2011 "Emission Standard of Air pollutants for Thermal Power Plants", and the boiler with output of 65t/h and below 65t/h should comply with the standard GB13271-2014 "Emission Standard of Air pollutants for Boilers" [12], while the requirements for reference oxygen content in GB13223 and GB13271 also have some differences. In summary, the selection of reference oxygen content for the pulverized coal and blast-furnace gas co-fired boilers should be combined with the furnace type and the boiler capacity, as shown in Table 2.

Table2. Reference oxygen content of pulverized coal and blast-furnace gas co-fired boilers

Boiler type	Boiler capacity / t h^{-1}	Reference oxygen content / %
Pulverized coal boiler (co-fired gas)	>65	6
	≤ 65	9
Gas boiler (co-fired pulverized coal)	>65	3
	≤ 65	3.5

4. Conclusion

In engineering, the performance of pulverized coal and blast-furnace gas co-fired boilers are tested mainly according to Chinese GB/T10184-2015 "Performance test code for utility boiler". However, the calculation model in this regulation is mainly based on conventional fuels such as coal, oil or natural gas, it does not take the special properties of blast-furnace gas and the characteristics of the

boiler tail heating surface into account. Thus, GB/T10184-2015 cannot be directly used in pulverized coal and blast-furnace gas co-fired boilers.

In this paper, several characteristics of pulverized coal and blast-furnace gas co-fired boilers different from conventional boilers were analyzed, and the problems of GB/T10184 has been pointed out and the corresponding improved methods were proposed. Eventually, the following conclusions were obtained:

- 1) Because of the high nitrogen content in blast-furnace gas, the combustion calculation (especially the solving of excess air coefficient) for the pulverized coal and blast-furnace gas co-fired boiler should not adopt the conventional simplified formula, but should adopt the complete calculation method considering the fuel composition.
- 2) When solving the characteristics of the mixed fuel, the blast-furnace gas components should be generally converted into elemental components expressed in terms of the received mass fraction, and then combine with the coal components. In moisture conversion, since the blast-furnace gas may contain moisture in the form of mechanical water, the conversion model should also take it into account, in order to avoid the fact that traditional method ignoring mechanical water will cause the calculation error.
- 3) The mass flow of pulverized coal entering the boiler furnace is essential data for calculating the performance of the pulverized coal and blast-furnace gas co-fired boiler. However, it is difficult to accurately measure the mass flow of pulverized coal, especially for the boiler with intermediate storage pulverizing system. It will undoubtedly hinder the smooth implementation of the related calculations. For this reason, this paper proposed a soft measurement method based on the content of triatomic gas in the flue gas, which skillfully solves the problem.
- 4) There are two layouts for the tail heating surface of pulverized coal and blast-furnace gas co-fired boiler. One is to adopt the air preheater as the final heating surface. For this type of boilers, the outlet flue gas temperature of the air preheater should be taken as the boiler exhaust temperature. The other is to adopt the gas heater as the last heating surface. For this type of boilers, the outlet gas temperature of the gas heater should be taken as the boiler exhaust temperature.
- 5) The pollutants emission concentration from pulverized coal and blast-furnace gas co-fired boilers shall not be converted through the excess air coefficient, it shall be converted through the oxygen content in flue gas, and the reference oxygen content shall be selected according to the boiler type and output capacity.

5. References

- [1] Wang C B, Wei J G, Sheng J G. 2012 Numerical simulation of combustion characteristics of a 300 MW blast furnace gas/pulverized coal combined combustion boiler, *Proceedings of the CSEE*, 32(14) 14-19.
- [2] Fang L J, Wu S, Hu Y L. 2013 Study on blended BFG boiler's combustion characteristics, *Journal of North China Electric Power University*, 40(1) 66-70.
- [3] Liang Z W, Chen H W, Yang X. 2017 Characteristic of NO_x emissions in co-firing gases and modeling prediction, *Chemical Industry and Engineering Progress*, 36(11) 4265-4271.
- [4] Wu S, Fu X F, Yin R R. 2015 Study on characteristics of oxygen-rich combustion and nitrogen emissions of blast furnace gas and pulverized coal blended combustion boiler, *Boiler Technology*, 46(3) 43-47+69.
- [5] Wang C B, Li W. 2013 Numerical simulation on combustion characteristics of a 300MW

- bituminous coal/BFG co-firing boiler mixed with lignite and the economic analysis, *Journal of Chinese Society of Power Engineering*, 33(6) 413-418.
- [6] Li W, Wang J X, Huang J C. 2012 Numerical simulation of 300MW blast furnace gas and pulverized coal blended combustion boiler on the optimizing of NO_x, *Electric Power Science and Engineering*, 28(7) 55-60.
- [7] Li L L, Xie A G, Li X C. 2008 Numerical simulation on the combustion process in a pulverized coal and BGF mixture fired boiler, *Energy for Metallurgical Industry*, 2 29-31+40.
- [8] Zhao L F, Wang W H, Zong Y W. 2007 Study on heat transfer characteristics of the convection heating surfaces of boiler burning pulverized coal blending blast furnace gas, *Journal of Shanghai University of Electric Power*, 4 341-344.
- [9] General Administration of Quality Supervision, Inspection and Quarantine of the People's Republic of China. 2016 GB/T 10184-2015 Performance test code for utility boiler, *China Standards Press*.
- [10] State Environmental Protection Administration of the People's Republic of China. 2004 GB13223-2003 Emission standard of air pollutants for thermal power plants, *China Environmental Science Press*.
- [11] Ministry of Environmental Protection of the People's Republic of China. 2012 GB13223-2011 Emission standard of air pollutants for thermal power plants. *China Environmental Science Press*.
- [12] Ministry of Environmental Protection of the People's Republic of China. 2014 GB13271-2014 Emission standard of air pollutants for boiler, *China Environmental Science Press*.

Acknowledgements

This work was supported by the Natural Science Foundation of the Jiangsu Higher Education Institutions of China (Grant No. 17KJD470001) and sponsored by Qing Lan Project of the Jiangsu Higher Education Institutions of China.

Effect of Different Reductants on Leaching Lithium and Cobalt from Lithium Ion Batteries in Tartaric Acid Solution

Qian Cheng ¹

¹ Fujian Engineering and Research Center of Rural Sewage Treatment and Water Safety, School of Environmental Science and Engineering, Xiamen University of Technology, Xiamen, China
E-mail: chengq@xmut.edu.cn

Abstract. The cathode active materials of spent lithium ion batteries contain significant amounts of lithium and cobalt, which is worthy of recycling. The cathode active materials were employed as raw materials. The effect of reduction on the leaching efficiency of Li^+ and Co^{2+} was compared among glucose, ascorbic acid and hydrogen peroxide with tartaric acid as the acid leaching solution. The results show all three reducing agents can convert the Co^{3+} of the cathode active materials to soluble Co^{2+} . The complex of Co(III) can also be found during the reduction process. All three reductants can promote the leaching efficiency of Co^{2+} , while having a marginal effect on the leaching efficiency of Li^+ . The maximum leaching efficiency of Co^{2+} is 36.94% for 20 g/L glucose, 47.22% for ascorbic acid, and 69.66% for 15% hydrogen peroxide, respectively. Among the three, hydrogen peroxide exhibits the best reduction effect.

1. Introduction

Presently, the production of lithium-ion batteries (LIBs) continues to increase with the rising popularity of new energy vehicles and portable electronic devices [1]. Therefore, it is predicted that a large number of spent LIBs will be produced in the coming years, as their service life is only three years [2]. These spent LIBs contain large amounts of heavy metals and organic compounds which could pose a serious threat to biological health and are hazardous to the environment [3]. However, these spent LIBs are important secondary sources of metals, such as cobalt and lithium. It is reported that the amount of cobalt found in the spent LIBs is 15%, which is higher than that found in some ores from which it is extracted [4]. Thus, the recycling of spent LIBs is crucial, not only from an environmental point of view, but also from an economic standpoint as they are quite valuable.

Hydrometallurgical processes can be used as a recycling technique to recover the metal with high efficiency. Acidic leaching has been proposed as the main method for the leaching process. Inorganic acids can efficiently leach metal ions, however, they often result in the emission of toxic gas [5, 6]. Recent studies have been focusing on organic acids as they are more environmentally-friendly. Pure organic acids, such as citric acid, oxalic acid, malic acid, aspartic acid, and tartaric acid can be used as the leaching agent, but they do not provide efficient leaching [7-9]. To improve the leaching efficiency, reductants (e.g., glucose [10], hydrogen peroxide [9], NaHSO_3 [11]) are typically introduced to the leaching solutions to convert the metals of higher valency, from the cathode active material (e.g. Co^{3+}), to lower valence metals (e.g. Co^{2+}). The reduction process and the effect of the reduced products on the environment depend considerably on the chosen reducing agent. Therefore, this paper presents the tartaric acid leaching process of cathode active materials with a series of reducing agents (i.e., glucose, aspartic acid, and hydrogen peroxide) with the objective of comparing the three reductants and their



effect on the leaching efficiency. The results can provide further insight towards developing a more efficient leaching process.

2. Materials and methods

2.1. Materials

The spent LIBs were collected from a recycling factory. N-methyl-2-pyrrolidone (NMP) was used as the solvent to extract the cathode materials from aluminum foil. The leaching reagents used in the following studies consisted of HCl for characterization of the total lithium and cobalt content in the cathode material, while a mixture of tartaric acid and reducing agent (glucose, aspartic acid and hydrogen peroxide) was used for the battery leaching experiments. All solutions were prepared using distilled water and all reagents were analytical grade.

2.2. Pretreatment process

The cathode active materials were obtained using a series of techniques including crushing, sieving, magnetic separation and fine crushing. The initial dismantling procedure was accomplished using a 100 mL beaker in a magnetic heating agitator in a fume hood. The scraps and the NMP solution were added to the reactor with a solid-to-liquid ratio in the range of 30 - 60 g/L. After stirring for 60 min, the cathode active materials were completely separated from the aluminum foil, leaving the aluminum foil essentially 100% pure which makes for effortless recycling. The suspension was then filtered and the separated cathode active material was calcined at 700 °C for 6 h to remove the carbon and other organic compounds [8]. After cooling, the resulting cathode active materials were ground to a fine powder to facilitate leaching [12]. The leaching solution is obtained under the following optimal experimental conditions: 1 mol/L tartaric acid, solid-to-liquid ratio 10 g/L, reaction time 90 min, and a temperature of 80 °C, respectively [13].

2.3. Experimental procedure

The leaching experiments were conducted in a 100 mL three-necked round-bottomed flask on a heated, magnetic heating agitator. The flask was fitted with a thermometer, piston, and condenser to minimize the loss of water by evaporation. The crude LiCoO₂ powder from the spent LIBs was added to the flask and stirred at a rate of 300 rpm. The reported concentrations of tartaric acid solutions and reducing agent were then added to the flask. The reaction time for all leaching experiments was 90 min, since preliminary results have shown there is no significant leaching after 90 min. The reaction mixture was then filtered and washed with solvent three times to provide the resulting residue and the leachate solution. The leaching efficiencies were investigated by varying the reductants and reductant concentrations.

2.4. Analytical method.

The UV-vis spectra of the leaching solutions were recorded using a UV-visible spectrophotometer (UV-2540A, SHIMADZU Corporation, Japan) with distilled water as the reference solution. The concentration of Li and Co in the leachate was determined using an inductively coupled plasma optical emission spectrometer (ICP-OES Optima 7000, Perkin Elmer Instruments, U.S.A.). The fraction of Li and Co in the original cathode material was obtained by dissolving the cathode completely in concentrated hydrochloric acid, which yielded 6.23% and 68.43% (wt.%), respectively. The leaching efficiency of M (M = Li and Co) was calculated as follows:

$$\text{Leaching Efficiency\%} = \frac{\text{Content of M in the leachate}}{\text{Total content of M in the cathode}} \times 100\% \quad (1)$$

3. Results and discussion

3.1. UV-visible spectra characteristics of tartaric acid, glucose, aspartic acid and hydrogen peroxide

UV-visible spectra of tartaric acid, glucose, aspartic acid (H₂A) and hydrogen peroxide were collected in the range of 200-800 nm, as shown in Figure 1A. The spectra (a), (b), (c), and (d) correspond to 1

mol/L tartaric acid, 10 g/L glucose, 0.5 g/L aspartic acid and 0.24% hydrogen peroxide, respectively. Spectrum (a) shows a strong UV absorption occurring at a wavelength of 230 nm, which is potentially induced by the tartrate. No peaks can be observed in spectrum (b), as glucose has no absorbance in the 200-800 nm range. Spectrum (c) shows the presence of two shoulders at the wavelengths of the 230 and 290 nm, which can be ascribed to the H_2A and HA^- forms of aspartic acid, respectively [14]. The spectrum (d) of hydrogen peroxide exhibits a strong UV absorption at approximately 230 nm. The spectra (a), (b), (c), and (d) in Figure 1B correspond to 1 mol/L tartaric acid, a mixture of 1 mol/L tartaric acid and 10 g/L glucose, a mixture of 1 mol/L tartaric acid and 0.5 g/L aspartic acid, and a mixture of 1 mol/L tartaric acid and 0.24% hydrogen peroxide, respectively. The maximum absorption peaks of the solution are exhibited in the Table 1. Spectrum (b) exhibits no new peaks compared with the spectra (a) and (b) in Figure 1A, which suggests that there are no by-products formed. The same phenomenon can be observed in the spectra (c) and (d), which is indicative that the mixture will not generate any by-products.

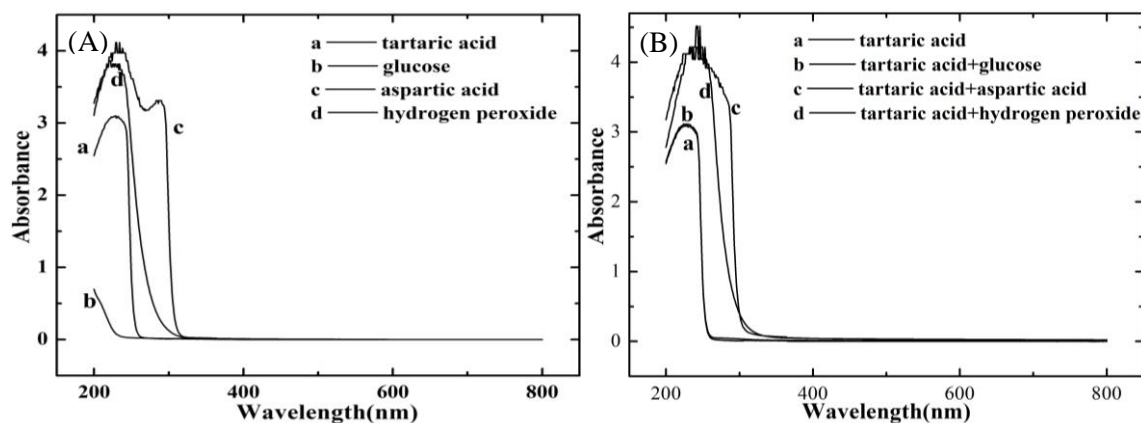


Figure 1. UV–visible spectra of (A): tartaric acid(a), glucose(b), ascorbic acid(c), and hydrogen peroxide(d); (B): tartaric acid(a), mixture of tartaric acid + glucose(b), tartaric acid + ascorbic acid(c), and tartaric acid + hydrogen peroxide(d).

Table 1. The maximum absorption peaks of the UV-vis spectra of the solution before leaching

Solution	Maximum absorption peaks(nm)
tartaric acid	230
glucose	none
ascorbic acid	230, 290
hydrogen peroxide	230
tartaric acid + glucose	230
tartaric acid + ascorbic acid	230, 290
tartaric acid + hydrogen peroxide	230

3.2. Comparison of varying reductants in the tartaric acid leaching solution

Figure 2 shows the UV–visible spectra of the leaching solution. The spectrum (a) corresponds to the leaching solution with 1 mol/L tartaric acid, and the spectra (b), (c), and (d) contain the same concentration of tartaric acid along with varying reducing agents with concentrations of 10 g/L

glucose, 0.2 g/L H_2A , and 2.5% hydrogen peroxide, respectively. The inset in Figure 2 is the enhancement of spectrum (c) in the range of 400-800 nm. The maximum absorption peaks of the leaching solution are exhibited in the Table II. A significant UV-visible absorption occurred at around 514 nm in all spectra (a), (b), (c), and (d), which appears to be due to the production of Co(II) [15]. This demonstrates that the Co(III) of $LiCoO_2$ is successfully reduced to the Co(II) in the solution. Comparing the spectrum (b) with (a), a weak shoulder can be observed and occurs in the range of 270-320 nm, which may be ascribed to the UV absorbance of a complex of Co(III) [15]. The same phenomenon can be observed in the spectrum (d). As for the spectrum (c), there are three peaks that can be observed in the 200 - 400 nm range, located at approximately 210, 240, and 290 nm, respectively. The peaks at 210 and 240 nm may be ascribed to the UV absorbance of H_2A and HA^- . Compared to spectrum (c) in the Figure 1A, the peaks are blue shifted which may be due to the decrease in the concentration of H_2A and HA^- [14]. The shoulder which occurs at 290 nm may be due to Co(III) complexation with HA^- .

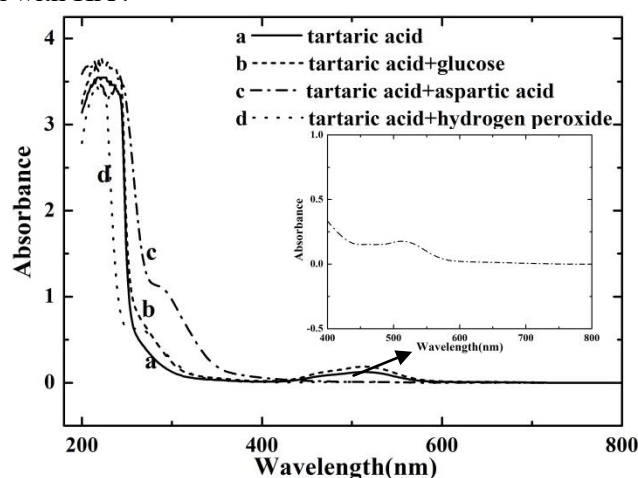


Figure 2. UV-visible spectra of leaching solution: tartaric acid(a), tartaric acid + glucose(b), tartaric acid + ascorbic acid(c), and tartaric acid + hydrogen peroxide(d).

Table 2. The maximum absorption peaks of the UV-vis spectra of the leaching solution

Leaching solution	Maximum absorption peaks(nm)
tartaric acid	230, 514
tartaric acid + glucose	230, 270-320, 514
tartaric acid + ascorbic acid	210, 240, 290, 514
tartaric acid + hydrogen peroxide	230, 270-320, 514

Figure 3 shows the UV-visible spectra of the leaching solution of different reductant at different concentrations with 1 mol/L tartaric acid, 10 g/L of the cathode active material in suspension, and a reaction temperature of 80 °C. Figure 3A demonstrates the five different glucose concentrations that were examined (5, 10, 20, 30, and 40 g/L) to investigate the effect on the absorbance and the change of peaks. It can be observed that the peaks at 200 - 400 nm and 514 nm did not shift but the intensity of the peak firstly increased and then decreased as the glucose concentration increased. This is because glucose can promote the Co(III) of $LiCoO_2$ reduced to the Co(II) in the solution. But the high concentration of glucose does not favor the conversion of high valence metal ions to their low valence state [16, 17]. Figure 3B demonstrates the four different H_2A concentrations that were examined (0.5, 1, 3 and 4 g/L) to investigate the effect on the absorbance and the change of peaks. As the absorbance

will exceed the detection line, the concentrations were all diluted 10 times. The inset is the absorption spectrum at 400 - 800 nm of different H₂A concentrations (5, 10, 30 and 40 g/L). The intensity and the spectrum peak do not change as the H₂A concentration increased, while the peak at 514 nm firstly increased and then decreased. The same phenomenon can be observed in the Figure 3C. The H₂O₂ concentrations were set as 0.25, 0.5, 0.75, and 1% for the UV experiment. They were all diluted 20 times as the absorbance of the primary concentration will exceed the detection line in the wavenumber of 400 - 800 nm.

3.3. The leaching efficiency of Li⁺ and Co²⁺ of different reductants with tartaric acid

The extractions were carried out at different reductant concentrations while the other variables were fixed at 1 mol/L tartaric acid in the leaching solution, 10 g/L of the cathode active material in suspension, and a reaction temperature of 80 °C. Figure 4A demonstrates the six different glucose concentrations that were examined (0, 5, 10, 20, 30, and 40 g/L) to investigate its effect on the leaching efficiencies of Li⁺ and Co²⁺. Figure 4B shows the effect of H₂A concentrations (0, 2.5, 5, 10, 20, and 30 g/L) on the leaching efficiencies of Li⁺ and Co²⁺. Figure 3C shows the effect of hydrogen peroxide concentrations (0, 5, 10, 15, and 20%) on the leaching efficiencies of Li⁺ and Co²⁺. From the experimental data, it can be observed that the leaching efficiencies of Li⁺ only changed slightly as the reductant concentrations increased in the Figure 4A, 4B, and 4C. Meanwhile, the leaching efficiencies of Co²⁺ increase initially and then decrease as the concentration continues to increase. This is due to the presence of Li ions which exist in a free state in the LiCoO₂ layered structures and are readily available for leaching. The stronger chemical bonds of Co-O in the layered structure make the leaching of Co difficult. However, the reaction can be promoted through addition of a reducing agent for converting Co(III) to Co(II) [10, 17]. Increasing the reductant concentration promote the formation of the metal-ion products which diffuse through the diffusion layer to the liquid-liquid interface. Thus, enhancing the ion transfer to the solution which leads to an increase in leaching efficiency [17]. However, the rate of formation of the metal-ion product is too rapid to prevent the reaction from further progress, leading to an excess of metal-ion products attaching to the solid-liquid interface. Therefore, the leaching efficiencies of Co²⁺ decrease when increasing reductant concentrations. The maximum leaching efficiencies of Li⁺ and Co²⁺ are 82.7% and 46.6%, respectively, for a glucose concentration of 20 g/L; 84.3% and 47.3%, respectively, for a H₂A concentration of 30 g/L; and 82.4% and 53.2%, respectively, for a hydrogen peroxide concentration of 10%. Hydrogen peroxide shows stronger reducibility as it can provide more activation energy under the same reaction conditions [18].

4. Conclusion

The leaching process and the effect of a reductant on the leaching efficiency of Li⁺ and Co²⁺ was investigated using glucose, ascorbic acid and hydrogen peroxide with tartaric acid as the acid leaching solution. The analysis of the UV-visible spectra shows that there are no undesired by-products generated when mixing the reactants with tartaric acid. All three reducing agents can convert Co³⁺ of the cathode active materials to soluble Co²⁺. The complex of Co(III) can also be observed during the reduction process. The leaching efficiencies of Co²⁺ exhibits a trend of increasing initially and decreasing at higher concentrations, while the leaching efficiencies of Li⁺ changed only slightly as the reductant concentrations increased. Hydrogen peroxide shows the strongest reducing ability among the three reductants.

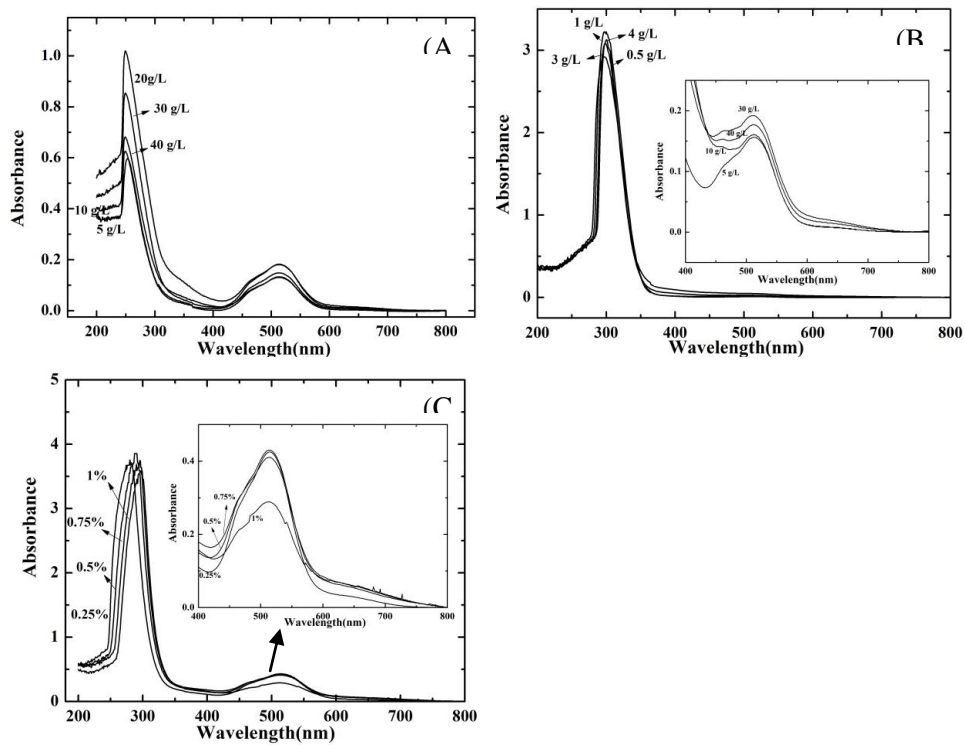


Figure 3. UV-visible spectra of leaching solution of different reductant at different concentrations with 1 mol/L tartaric acid, 10 g/L of the cathode active material in suspension, and a reaction temperature of 80 °C. (A) glucose; (B) ascorbic acid; (C) hydrogen peroxide.

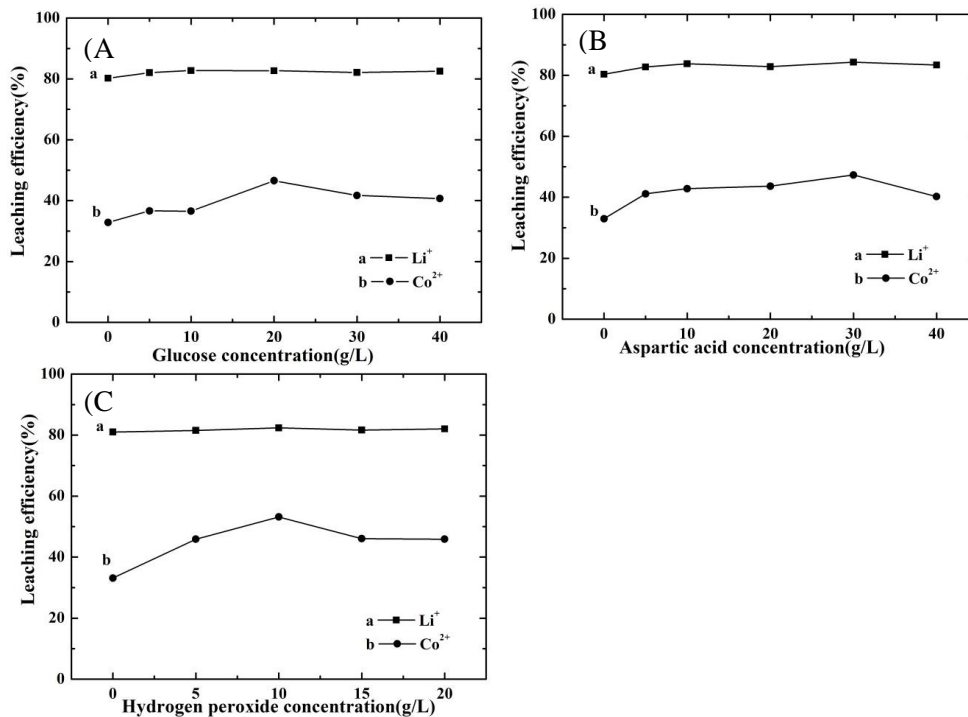


Figure 4. The relationship between the leaching efficiency of Li^+ and Co^{2+} and glucose concentration(A), ascorbic acid concentration(B), and hydrogen peroxide concentration(C) in a 1 mol/L tartaric acid solution

5. References

- [1] W. G. Lv, Z. H. Wang, H. B. Cao, Y. Sun, Y. Zhang, and Z. Sun, "A critical review and analysis on the recycling of spent lithium-ion batteries," *ACS Sustainable Chemistry & Engineering*, vol. 6, no. 2, pp. 1504-1521, Dec. 2017.
- [2] J. Li, G. Wang, and Z. Xu, "Environmentally-friendly oxygen-free roasting wet magnetic separation technology for in situ recycling cobalt, lithium carbonate and graphite from spent LiCoO_2 graphite lithium batteries," *Journal of Hazardous Materials*, vol. 302, pp. 97-104, Sep. 2015.
- [3] X. H. Zhang, Y. B. Xie, H. B. Cao, F. Nawaz, and Y. Zhang, "A novel process for recycling and resynthesizing $\text{LiNi}_{1/3}\text{Co}_{1/3}\text{Mn}_{1/3}\text{O}_2$ from the cathode scraps intended for lithium-ion batteries," *Waste Management*, vol. 34, pp. 1715-1724, June 2014.
- [4] Dorella G, and M. M. B, "A study of the separation of cobalt from spent Li-ion battery residues," *Journal of Power Sources*, vol. 170, no. 1, pp. 210-215, March 2007.
- [5] S. P. Barik, G. Prabakaran, and L. Kumar, "Leaching and separation of Co and Mn from electrode materials of spent lithium-ion batteries using hydrochloric acid: Laboratory and pilot scale study," *Journal of Cleaner Production*, vol. 147, pp. 37-43, Jan. 2017.
- [6] S.-H. Joo, D. j. Shin, C. Oh, J.-P. Wang, G. Senanayake, and S. Shin, "Selective extraction and separation of nickel from cobalt, manganese and lithium in pre-treated leach liquors of ternary cathode material of spent lithium-ion batteries using synergism caused by Versatic 10 acid and LIX 84-I," *Hydrometallurgy*, vol. 159, pp. 65-74, Oct. 2015.
- [7] G. P. Nayaka, K.V.Pai, G.Santhosh, and J.Manjanna, "Dissolution of cathode active material of spent Li-ion batteries using tartaric acid and ascorbic acid mixture to recover Co," *Hydrometallurgy*, vol. 161, pp. 54-57, Jan. 2016.
- [8] L. Li, J. Ge, F. Wu, R. J. Chen, S. Chen, and B. R. Wu, "Recovery of cobalt and lithium from spent lithium ion batteries using organic citric acid as leachant," *Journal of Hazardous Materials*, vol. 176, pp. 288-293, Nov. 2009.
- [9] C. H. Sun, L. P. Xu, X. P. Chen, T. Y. Qiu, and T. Zhou, "Sustainable recovery of valuable metals from spent lithium-ion batteries using DL-malic acid: Leaching and kinetics aspect," *Waste Management & Research*, vol. 36, no. 2, pp. 113-120, Nov. 2017.
- [10] Q. Meng, Y. Zhang, and P. Dong, "Use of glucose as reductant to recover Co from spent lithium ions batteries," *Waste Management*, vol. 64, pp. 214-218, March 2017.
- [11] P. Meshram, B. D. Pandey, and T. R. Mankhand, "Hydrometallurgical processing of spent lithium ion batteries (LIBs) in the presence of a reducing agent with emphasis on kinetics of leaching," *Chemical Engineering Journal*, vol. 281, pp. 418-427, June 2015.
- [12] R. C. Wang, Y. C. Lin, and S. H. Wu, "A novel recovery process of metal values from the cathode active materials of the lithium-ion secondary batteries," *Hydrometallurgy*, vol. 99, pp. 194-201, Aug. 2009.
- [13] Q. Cheng, X. Luo, and H. Zhuang, "Leaching of cobalt and lithium from spent lithium ion batteries in tartaric acid solution.," *Journal of Xiamen University of Technology*, Sep. 2018, to be published.
- [14] T. Lei, L. Gao, M. Dang, H. Li, P. Xu, and S. Wang, "L- ascorbic acid (vitamin C) ultraviolet spectra study " *Spectroscopy and Spectral Analysis*, vol. 18, no. 4, pp. 149-150, Aug. 1998.
- [15] G. P. Nayaka, K. V. Pai, J. Manjanna, and S. J. Keny, "Use of mild organic acid reagents to recover the Co and Li from spent Li-ion batteries," *Waste Manag*, vol. 51, pp. 234-238, Dec. 2015.
- [16] X. H. Zhang, H. B. Cao, Y. B. Xie, P. G. Ning, H. J. An, H. X. You, and F. Nawaz, "A closed-loop process for recycling $\text{LiNi}_{1/3}\text{Co}_{1/3}\text{Mn}_{1/3}\text{O}_2$ from the cathode scraps of lithium-ion batteries: Process optimization and kinetics analysis," *Separation and Purification Technology*, vol. 150, pp. 186-195, June 2015.
- [17] L. Li, Y. F. Bian, X. X. Zhang, Y. B. Guan, E. S. Fan, F. Wu, and R. J. Chen, "Process for recycling mixed-cathode materials from spent lithium-ion batteries and kinetics of leaching," *Waste Management*, vol. 71, pp. 362-371, Oct. 2017.

- [18] P. Meshram, Abhilash, B. D. Pandey, T. R. Mankhand, and H. Deveci, "Comparision of Different Reductants in Leaching of Spent Lithium Ion Batteries," *Jom*, vol. 68, no. 10, pp. 2613-2623, July 2016..

Acknowledgments

This work was supported by the Foreign Scientific and Technological Cooperation Project of Xiamen University of Technology (No. E201401700), Education and Scientific Research Youth Foundation of Fujian Province (No. JAT170431), and Open Research Fund Program from Fujian Engineering and Research Center of Rural Sewage Treatment and Water Safety (No. RST201802).

Chapter 2:
Motor and Electrical Control Technology

The Numerical Simulation of a High Power Hall Effect Thruster

Lai Li¹, Xi Lu², Hulin Huang¹, Xidong Zhang³, Guiping Zhu^{1*}

¹ College of Astronautics, Nanjing University of Aeronautics and Astronautics, Nanjing 210016, China

² Shanghai Key Laboratory of Deep Space Exploration Technology, Shanghai 201109, China

³ College of Energy and Power Engineering, Nanjing Institute of Technology, Nanjing 211167, China

Corresponding author's E-mail: zhuguiping@nuaa.edu.cn

Abstract: This work studied and presented a high-power Hall-effect electric propulsion thruster. The working Xenon gas is heated and ionized by nuclear energy to generate plasma which is injected into the channel. The plasma in the channel is described by two-temperature model consists of ions, electrons and atoms with the electron density of plasma above 10^{20} m^{-3} . The Lorentz force acting on the plasma makes the flow velocity increase obviously. The operating power of the thruster is about 20 kW. The mass flow rate of xenon is set at 1.56 g/s.

1. Introduction

The concept of electric propulsion was brought up by Tsiolkovsky since 1903 and Goddard since 1906 [1], respectively. So far the electric propulsion technology has been developed for more than a century. There are four main types of electric propulsion technology: electrothermal, electromagnetic, electrostatic and the mixed type. Electrothermal propulsion, which was not strictly an electric propulsion technology because there was no obvious plasma ionization and electromagnetic field to accelerate plasma, is not the mainstream of future development. The study of electromagnetic, electrostatic, mixed type propulsion technology [2]-[12] mainly includes two points. The main concern is the way to realize the ionization of the working fluid. The other critical issue is the approach to make the ionized plasma to be ejected from the electrical power. The current thrust of electric propulsion technology is very small, only dozens to hundreds of mN orders. The chemical propulsion can dive the satellite transfer to the requirements orbit with only short-term thrust because of its large magnitude of the thrust. However, the same orbit transferring may take a number of circle orbits by the electric propulsion, which means it needs more time to complete the task.

With the continuous developing of manned deep space exploration technology, propulsion technology is one of the most critical technologies. A manned deep space exploration task with large load quality requires large actual load and stability of spacecraft operation, which causes the complex and cumbersome of spacecraft. Therefore, it is necessary to save the propellant for the thruster and ensure the smooth work. The time of voyage is required to be as short as possible for the life needs, the safety and endurance of the astronauts. Hence, larger thrust propulsion technology is needed to shorten the transit time than a small thrust. Larger thrust can be achieved by chemical propulsion, but the specific impulse of chemical propulsion is lower and the improving space of the chemical propulsion is also small. The specific impulse of the nuclear thermal propulsion is about 2-3 times that of the chemical



propulsion [13], [14]. However, the demand for propellant is too much during the deep space exploration tasks for the high speed increment. Electric propulsion has a remarkable characteristic of high specific impulse whose thrust is proportional to the power \times efficiency/specific impulse. Large power electric propulsion can achieve the needed thrust to shorten the time of orbit transfer or the space traveling.

For further optimize the configuration and performance, the Hall electric propulsion is studied in this paper. Different from the general Hall effect thruster, the magnetic flux in this study is uniform and only applied on the z-direction. Xenon is used as the working gas and assumed to be heated and pre-ionized by the nuclear energy before inflowing into the channel. The conducting flow is accelerated by the Lorentz force through the applied electric field and a magnetic field. The working flow is also heated by the Joule heating when flowing through the channel.

2. Numerical model

2.1 Numerical simulation domain

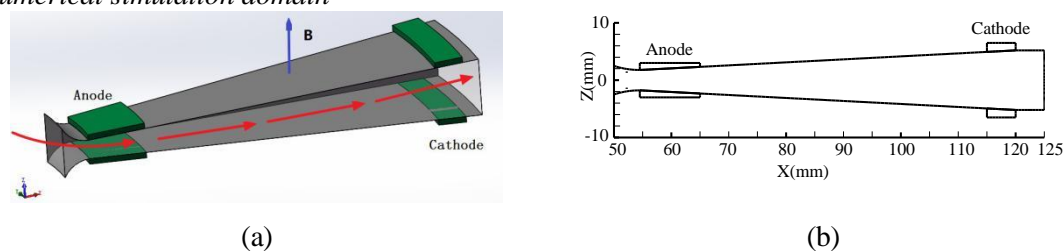


Figure 1. The model and computational domain of the calculation: (a) The structure of the simulation domain; (b) Channel cross-section.

Figure 1 illustrates the structure of the simulation domain. The thruster is an broad-leaved structure. The electrodes are placed in the front and rear ends, respectively. The throat height and the cathode inlet height are 3.55 mm ($x=54.5$ mm) and 9.87 mm ($x=115$ mm), respectively.

2.2. Mathematical model and working conditions

In our work, the working gas is assumed to be pure noble gas. The governing equations of state equations and Maxwell equations are in combination to describe the non-equilibrium plasma. The non-equilibrium plasma in the channel consists of ions, electrons and atoms under two-temperature model [15], [16]. The Navier-Stokes equations and the energy equation include Lorentz force and Joule heating terms, respectively. Large Eddy simulation (LES) is used to describe the flow.

This work adopted high-temperature seed-free xenon plasma. Table 1 shows the working conditions in the simulation processes. A non-slip wall condition is applied as the boundary condition for the flow. The wall of the partial channel is electrically insulated and its temperature is set to be 300K. The boundary condition for the electrical equation is set to be on the anode and on the cathode.

Table 1. Conditions used in calculation.

Working gas	Xenon
Total inflow pressure	0.16 MPa
Total inflow temperature	9000 K
Inlet electron temperature	11603K
Magnetic flux density	4T

2.2.1 Governing equations for MHD plasma flows.

The time dependent compressible Navier-Stokes equations coupled with Lorentz force and Joule heating terms are shown following:

Continuity equation:

$$\frac{\partial \rho}{\partial t} + \nabla \cdot (\rho \mathbf{u}) = 0 \quad (1)$$

Momentum equation:

$$\frac{\partial \rho \mathbf{u}}{\partial t} + \nabla \cdot (\rho \mathbf{u} \mathbf{u}) = \mathbf{j} \times \mathbf{B} - \nabla p + \nabla \cdot \boldsymbol{\tau} \quad (2)$$

Energy equation:

$$\frac{\partial E_s}{\partial t} + \nabla \cdot (E_s + p) \mathbf{u} = \mathbf{j} \cdot \mathbf{E} - \nabla \cdot \mathbf{q} + \nabla \cdot (\boldsymbol{\tau} \mathbf{u}) \quad (3)$$

$$E_s = \rho \left(c_v T + \frac{1}{2} \mathbf{u}^2 \right) \quad (4)$$

where ρ is mass density, \mathbf{B} is the magnetic flux density vector, \mathbf{u} is the velocity vector of flow, c_v is the constant volume specific heat, T is the static temperature, \mathbf{j} is the current density vector, E_s is the total energy, p is the static pressure, σ is the electrical conductivity, \mathbf{q} is the conductive heat flux vector, $\boldsymbol{\tau}$ is the viscous stress.

2.2.2. *Governing equations for ionization.* conservation of ion number density:

$$\frac{\partial n_i^+}{\partial t} + \nabla \cdot n_i^+ \mathbf{u} = n_i^{g^+} = k_{fi} n_e n_i - k_{ri} n_e^2 n_i^+ \quad (5)$$

$$n_e = \sum_i^{ion} n_i^+ \quad (6)$$

Energy equation for electron:

$$\frac{\partial U_e}{\partial t} + \nabla \cdot (U_e \mathbf{u}_e) = \frac{|\mathbf{j}|^2}{\sigma} - p_e \nabla \cdot \mathbf{u}_e - 3n_e k (T_e - T) \sum_h^{heavy} \frac{m_e^-}{m_h} \bar{v}_{eh} \quad (7)$$

$$p_e = n_e k T_e, \quad U_e = \frac{3}{2} n_e k T_e + n_i^+ \varepsilon_i \quad (8)$$

In equation (5), n_i^+ is the number density of xenon ions, n_e is the number density of electron, n_i is the number density of xenon atom, the three-body recombination rate coefficient k_r is determined by the following relations[13]: $k_r = k_{rh} k_{ro} / (k_{rh} + k_{ro})$, $k_{rh} = 1.09 \times 10^{-20} T_e^{-9/2}$,

$k_{ro} = \frac{1.21 \times 10^{-35}}{T_e^2} \exp\left(\frac{55300}{T_e}\right)$, the ionization rate coefficient k_f is derived on the basis of the principle

of detailed balance with the Saha equilibrium: $k_f n_i n_e = k_r n_i^2$, $k_f = k_r \times \frac{g_i}{g_0} \left(\frac{2\pi m_e k T_e}{h^2}\right)^{3/2} \exp\left(-\frac{\varepsilon_i}{k T_e}\right)$,

where g_i is the statistical weight of the ground state of the ion, g_0 is the statistical weight of the ground state of the neutral xenon atom, ε_i is ionization potential of xenon atom[14], the subscripts e, i and the

superscript + denote the electrons, neutral atoms and ionized particles, respectively. In equation (7), U_e is the electron energy, \mathbf{u}_e is the velocity vector of electrons, m_h is the mass of heavy particle, m_e is the mass of electron, p_e is the electron pressure. In equation (8), k is Boltzmann constant, T_e is electron temperature, ε_i is the ionization energy.

2.2.3. *Governing equations for electrical-magnetic. generalized ohm's law:*

$$\mathbf{j} + \frac{\beta}{|\mathbf{B}|} \mathbf{j} \times \mathbf{B} = \sigma (\mathbf{E} + \mathbf{u} \times \mathbf{B}) \quad (9)$$

$$\sigma = \frac{e^2 n_e}{m_e \nu_{eh}}, \quad \beta = \frac{e |\mathbf{B}|}{m_e \nu_{eh}} \quad (10)$$

Maxwell equations:

$$\nabla \times \mathbf{H} = \mathbf{j} + \frac{\partial \mathbf{D}}{\partial t}, \quad \nabla \cdot \mathbf{B} = 0 \quad (11)$$

$$\nabla \times \mathbf{E} = -\frac{\partial \mathbf{B}}{\partial t}, \quad \nabla \cdot \mathbf{D} = \rho_e \quad (12)$$

Since the charge neutrality is assumed and magnetic Reynolds number is quite small, the Maxwell equations are simplified as follows:

$$\nabla \times \mathbf{E} = 0, \quad \nabla \cdot \mathbf{j} = 0 \quad (13)$$

Equation (9) is the general Ohm's law, In equation (10), $\bar{\nu}_{eh} = \sum_h^{heavy} n_h Q_{eh} C_e$ is the average momentum transfer collision frequency for an electron e with a heavy particle h , where Q_{eh} is the energy-averaged momentum transfer cross section, $C_e = \sqrt{8kT_e/\pi m_e}$ is the mean electron velocity for a Maxwellian distribution, β is Hall parameter. In equation (12), $\mathbf{E} = -\nabla \Phi$ is the electric field vector, where Φ is the electrical potential.

3. Results and Discussions

3.1 The characteristics of the plasma

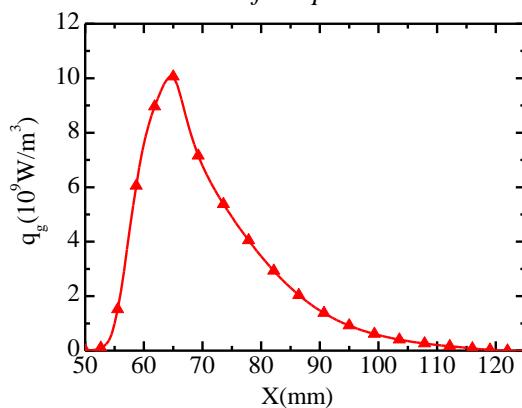


Figure 2. The distribution of the electric power

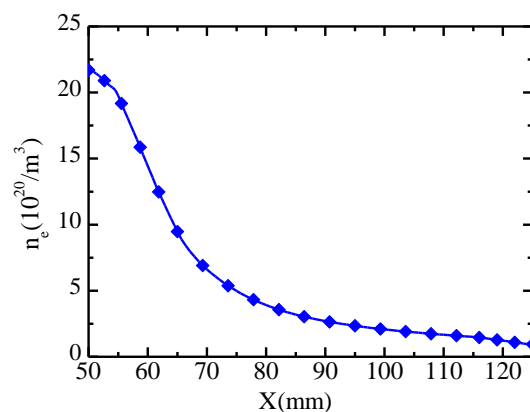


Figure 3. The distribution of the electric conductivity

The energy exchange between the external system and the fluid $\mathbf{j} \cdot \mathbf{E}$ is denoted by q_g . Fig 2 shows the distribution of q_g indicating the electric power injected into the fluid, which is about 20 kW.

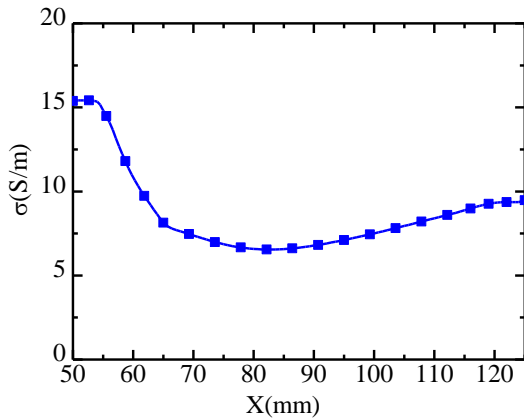


Figure 4. The distribution of the electrical conductivity

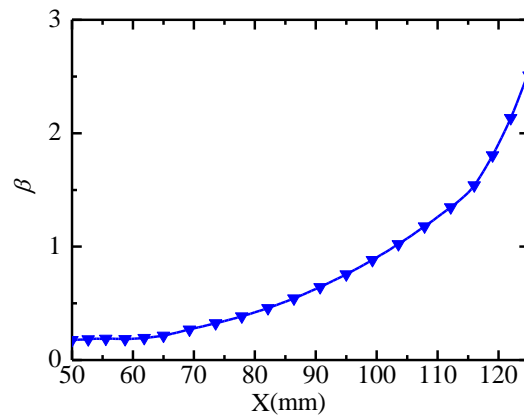


Figure 5. The distribution of Hall parameter

The electron number density under pre-ionization of inlet is about $2.17 \times 10^{21}/\text{m}^3$, as the velocity increases, the electron number density decreases rapidly as shown in Fig 3. The channel's broad-leaved structure also has an influence on the distribution of electron number density. Fig 4 shows the distribution of electrical conductivity, which changes within the 6-15 range, because of inhomogeneous distribution of electrons. The Hall parameter changes at the range of 0.2-2.5, which can be seen from Figure 5.

3.2 The characteristics of the flow

There are three kinds of current in the channel, one is in the radial direction:

$$j_r = \frac{\sigma}{1 + \beta^2} (E_r - \beta E_\theta + \beta u_r B + u_\theta B) \tag{14}$$

The second is in the tangential direction:

$$j_\theta = \frac{\sigma}{1 + \beta^2} (\beta E_r + E_\theta - u_r B + \beta u_\theta B) \tag{15}$$

The third is in the z direction:

$$j_z = \sigma E_z \tag{16}$$

Where E_r, E_θ are the component of electric field in r, θ directions, respectively; j_r, j_θ, j_z are the component of current density in radial, tangential, z directions, respectively; u_r, u_θ are the component of flow velocity in the radial, tangential directions, respectively.

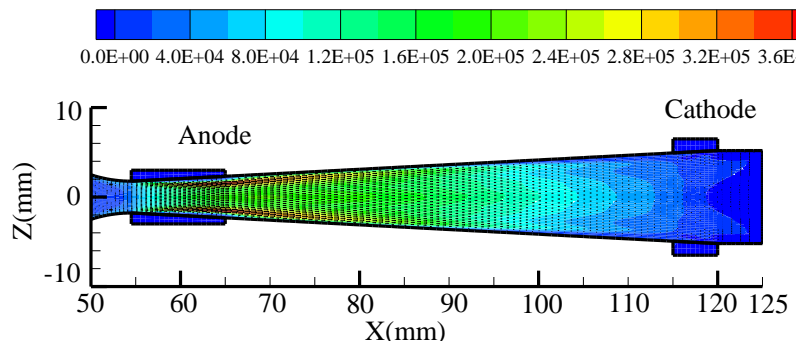


Figure 6. The contours of Lorentz force in the radial direction: F_x

The Lorentz force $F_x = j_\theta B$ is with the same direction of the radial velocity. From Figure 6, we can find the distribution and direction of Lorentz force. The Lorentz force near the anode is the strongest

because of the relative low flow velocity and strong electric field strength. From the equation (15), the radial velocity increases because of the Lorentz force and meanwhile the electric field E_r decreases, therefore, j_θ decreases along the flow direction downstream (Figure 7). As a result, based on the constant assumption of the magnetic flux density, the Lorentz force is also reduced even in the reverse direction (Figure 8) at the end of the channel.

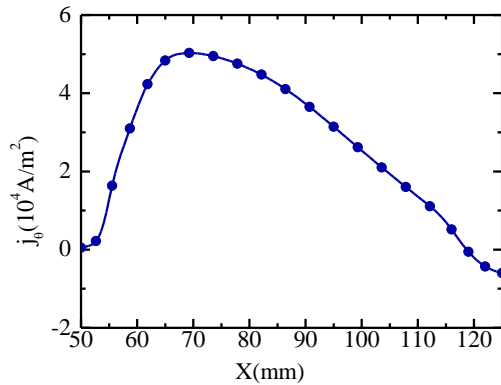


Figure 7. The distribution of the tangential current

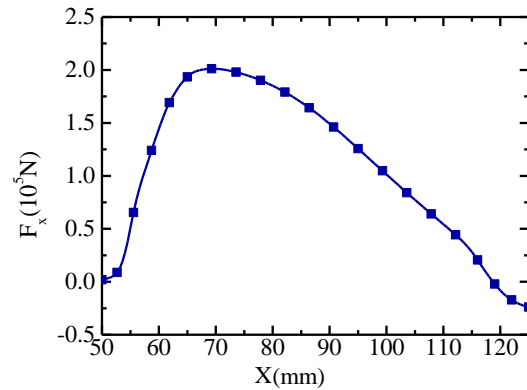


Figure 8. The distribution of the Lorentz force

For contrast, the radial velocity of no magnetic flow is shown in Figure 9(a). The radial velocity is accelerated by the Lorentz force obviously when the 4T external magnetic is applied from Fig 9(b). From the comparison, the radial velocity from the outlet is about 1800 m/s, which is almost two times that of no magnetic flow. The mass flow rate of the outlet in the acceleration channel is 1.56 g/s at the moment.

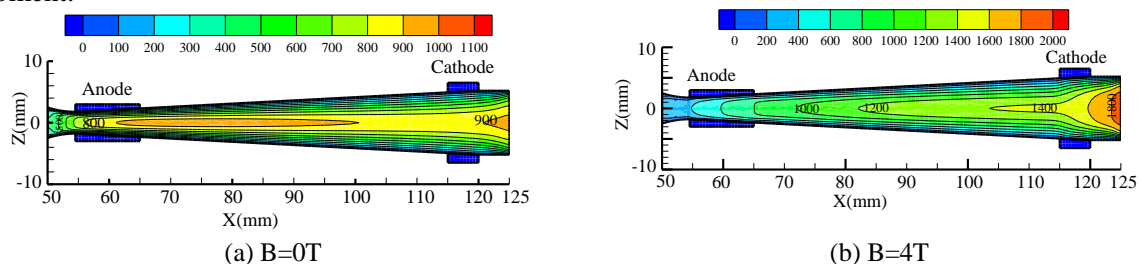


Figure 9. The contours of radial velocity

4. Summary

The numerical simulation of the Hall effect electric propulsion thruster was carried out by using the high temperature xenon gas. The high density plasma from the inlet is produced by the nuclear power and maintained at an appropriate level by the input electric power, the number density of electrons is kept to the level of $10^{21}/\text{m}^3$, which help to keep an adequate electrical conductivity about 5-15 S/m. In this model, the Hall parameter was about 0.2-2.5, which is high enough to maintain the Hall effect. The Lorentz force is the strongest because of the lower flow velocity and stronger electric field strength near the anode. For the xenon gas is too heavy, the acceleration is not as well as the light gas, such as krypton and argon gas. Thus, the different gas, the combination of the electric power input and magnetic flux density, thrust assessment, the internal ionization structure of the plasma still requires further research.

5. Acknowledgments

This research was supported by the Shanghai space science and Technology Innovation Fund (Grant No. SAST2016030), Scientific Research Project of Shanghai Science and Technology Commission (Grant No. 16DZ1120300), Project of Nanjing Institute of Technology (Grant No. YKJ201524), and the Natural Science Foundation of Jiangsu Province (Grant No. BK20160775).

6. References

- [1] Choueiri E Y 2004 *J. Journal of Propulsion & Power* **20** 193.

- [2] Cassady R J, Frisbee R H, Gilland J H and et al 2008 *Energy Conversion & Management* **49** 412.
- [3] Lafleur T, Baalrud S, Chabert P 2016 APS Meeting APS Meeting Abstracts.
- [4] Ekholm J, Hargus W 2013 Exb Measurements of A W Xenon Hall Thruster.
- [5] Rayburn C D, Campbell M E and Mattick A T 2005 J. Journal of Spacecraft & Rockets 42 161.
- [6] Chang Diaz FR 2000 Scientific American 283 90.
- [7] Choueiri E Y and Ziemer J K 2001 J. Journal of Propulsion & Power 17 967.
- [8] Hofer R R and Randolph T M 2012 J. Journal of Propulsion and Power 29 166.
- [9] Jacobson D T, Manzella D H, Hofer R R and et al 2004 40th Joint Propulsion Conference and Exhibit cosponsored by the AIAA, ASAE, and ASEE, AIAA 3600.
- [10] Hopkins M A, Jason M, Makela J M and et al 2010 AIAA 6681.
- [11] Wei L, Wang C, Zhang C, et al 2013 Applied Physics Letters, 102 2009.
- [12] Ortega A L, Mikellides I G 2016 Physics of Plasmas, 23 295.
- [13] Joyner C R, Levack D and Borowski S K 2012 *48th AIAA, ASME, SAE, ASEE, Joint Propulsion Conference & Exhibit* **4207**.
- [14] Frisbee R H, Mikellides IG 2005 *Joint Propulsion Conference & Exhibit*
- [15] Tanaka M, Murakami T, and Okuno Y 2014 *IEEE Transactions on Plasma Science*. **42** 4020.
- [16] M Mitchner and C H Kruger 1973 *Partially Ionized Gases* (New York: Wiley).

A New Software Phase-locked Loops

Cunbing Gui¹, Zhangbao Chen² and Xuehui Luo¹

¹Guangzhou Institute of Technology, Guangdong, China

²The Education Training and Evaluation Center of Guangdong Power Grid Co., Guangdong, China

E-mail: ahui200491@126.com

Abstract. A new type software phase-locked loops is proposed. The amplitude integral and selective characteristic of frequency are used to form the positive frequency fundamental filter. The K is derived, the principle of the variable sampling period phase-locked loops is further analyzed, it's mathematical is established, and the regulators parameters is optimize designed. Simulation and experiment show that the proposed phase-locked loops can lock the phase and frequency of the positive sequence fundamental voltage quickly and accurately, So it can provides a reliable base for grid-connected system.

1. Introduction

Phase-locked loop is a way to stabilize the frequency, it is mainly composed of a voltage-controlled oscillator and a phase-locked loop integrated circuit, the voltage-controlled oscillator gives a signal, part of this signal is output, and part of this signal is compared in phase with the local oscillator signal, the local oscillator signal is produced by the frequency division and phase-locked integrated circuit, in order to maintain the consistency of their frequencies, the phase difference between them should not change, if there is change of the phase difference, the phase-locked loop integrated circuit voltage output voltage will change to make the phase difference recovery. With the rapid development of new energy power generation, the quality of phase-locked loop directly affects the performance of various grid control performance of the inverter, the detect accuracy of the grid voltage synchronizing signal will affect the normal operation and control of the converter [1]. The influence of 100 hz signal can be eliminated, but the filtering effect of the traps will be affected when the frequency changes. A decoupled double synchronous reference frame phase-locked loop (DDSRF-PLL) is proposed, it can efficiently reduce the influence of negative sequence component to the synchronous signal, but the structure is complicated. Adaptive notch filter (ANF) and double second-order generalized integrator (DSOGI) were also proposed to detect the fundamental positive and negative sequence components [2], but it cannot distinguish positive sequence and negative sequence components from the fundamental component, it is need to use the instantaneous symmetrical component method for the separation of positive and negative sequence component, the algorithm is complicated. Multiple second order generalized phase-closed loops (MSOGI-PLL) was proposed, multiple complex coefficient filter based phase-locked loops (MCCF-PLL) was also proposed in reference, but all these two methods need to set the specific harmonic frequency in advance, multiple basic computing units should be designed, thus make the system structure complicated, a three-phase phase-locked loops method was also proposed, which is based on four extended phase-locked loops (EPLL), but the parameter design process is more complicated, a phase locked loops based on double synchronous reference frame (DSRFPLL) was also proposed, in which the orthogonal signal generator, the positive and negative sequence component calculator were included to extract the positive sequence component and



eliminate the influence of voltage unbalance. An adaptive complex filtering phase locking method based on the crossover decoupling frequency was also proposed, but these two kinds of methods are also more complex.

According to the research on above, a new phase-locked loops is proposed in this paper, this new phase-locked loops, without more software resources, it can fast and precisely track the changing frequency and phase of power grid, it has adaptability to the frequency and distortion of power grid.

2. The positive sequence fundamental filter

2.1. The positive sequence fundamental filter

If the sine signal is $u_1 = U \sin(\omega_0 t + \varphi)$, the corresponding auxiliary signal is $u_2 = U \cos(\omega_0 t + \varphi)$ when u_1 is shifted 90° phase, then it can be derived:

$$u(s) = \frac{s}{s^2 + \omega_0^2} u_1(s) + \frac{\omega_0}{s^2 + \omega_0^2} u_2(s) \quad (1)$$

It also can be derived that when the integral process accumulated to per unit time, $u(s) = u_1(s)$, $u(s) = u_2(s)$, in order to improve the speed of tracking, the negative feedback is introduced respectively to the input, proportional control is used, the proportion coefficient is selected as K, the corresponding closed-loop transfer function is shown as follows:

$$G(s) = \frac{2Ks}{s^2 + 2Ks + \omega_0^2} \quad (2)$$

When the the distorted power grid voltage is used as the input, then the $u(s)$ is the corresponding positive sequence fundamental voltage filter. The schematic diagram of positive sequence fundamental voltage filter in time field is shown in Figure 1

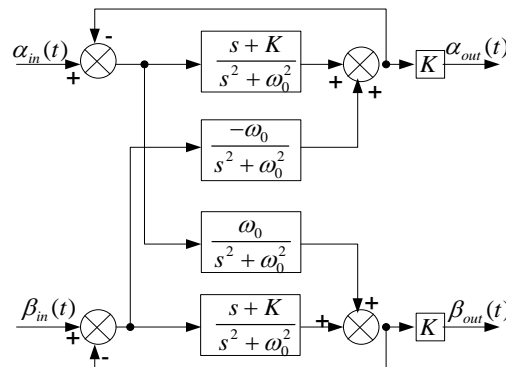


Figure 1. Schematic diagram of positive sequence fundamental voltage filter in time field

Where $\alpha_{in}(t)$ and $\beta_{in}(t)$ is the input power grid voltage in two-phase static coordinate, $\alpha_{out}(t)$ and $\beta_{out}(t)$ is the positive sequence fundamental voltage in two-phase static coordinate.

When the input voltage signal is the positive sequence signal, it can be derived:

$$\alpha_{out}(s) = \left(K \frac{s+K}{(s+K)^2 + \omega^2} \right) \left(A \frac{s \cos \varphi - \omega \sin \varphi}{s^2 + \omega^2} \right) - \left(K \frac{\omega}{(s+K)^2 + \omega^2} \right) \left(A \frac{s \sin \varphi + \omega \cos \varphi}{s^2 + \omega^2} \right) \quad (3)$$

When the input voltage signal is the negative sequence signal, the expression of $\alpha_{out}(s)$ can be derived similarly.

2.2. The choice of K

The relation between K and the frequency deviation and phase deviation can be derived as following:

$$\tan(90^\circ - \Delta\varphi) \approx \frac{K}{2\pi\Delta f} \tag{4}$$

Where Δf is the frequency deviation of the power frequency, $\Delta\varphi$ is the phase deviation of power voltage, so take the K value as 60 [3].

3. The adaptive sampling period technique

Sampling points is kept as constant in a fundamental period, sampling period is defined as follows:

$$T_s = \frac{T_0}{N} \tag{5}$$

Where: N is the sampling points in one fundamental period, T_0 is the fundamental period of power grid.

The voltage-controlled oscillator transfer function in z domain of three-phase phase-locked loops , which is controlled base on adjustable control period, can be derived as follows[1]:

$$V_{co}'(z) = \frac{\hat{\theta}(z)}{T_s(z)} = -\frac{\omega_0}{z^2 - z} \tag{6}$$

It can be seen from equation (6) that the Phase-locked loops voltage controlled oscillator is a second order system, when the non-dominant pole z=0 is ignored, $V_{co}'(z)$ can be simplified as follows:

$$V_{co}'(z) = -\frac{\omega_0}{z - 1} \tag{7}$$

When the sampling time is $t_s = 0.0001s$, the corresponding closed-loop transfer function can be derived as following: ξ is set to 0.707, t_s is set to 5ms. Considering response speed and steady accuracy, K_p is set to 20, K_I is set to 1.

$$\Phi_c(s) = \frac{\hat{\theta}(s)}{\theta(s)} = \frac{K_p(s) + K_I}{s^2 + K_p s + K_I} \tag{8}$$

New software phase-locked loops block diagram base on variable sampling period and the positive sequence fundamental voltage filter is shown in Figure 2.

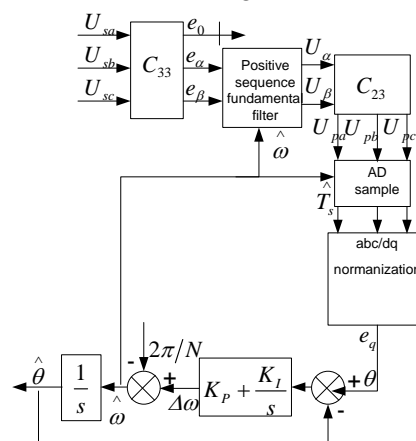


Figure 2. The block diagram of new software phase-locked loop

4. Simulation

At the time of $t=0.5s$, the dc bias component of $d_a=5V$, $d_b=10V$, $d_c=-10V$ is separately added the symmetric three-phase voltage system, in this case, the frequency information extracted by the method

proposed in this paper, the method of SRF-PLL, the method proposed in reference [4], is respectively shown in Figure 3.

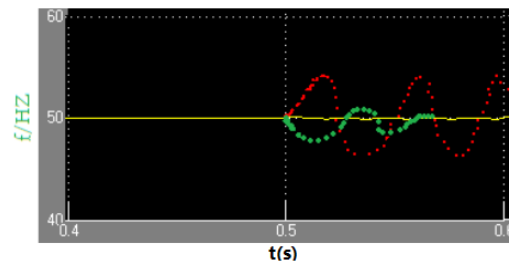


Figure 3. The extracted synchronization signals of frequency

As shown in Figure 3, the yellow line parts is corresponding to the extracted synchronization signals of frequency used with the method proposed in this paper, orange color line parts is corresponding to the extracted synchronization signals of frequency used with the method of SRF-PLL, green color line parts is corresponding to the extracted synchronization signals of frequency used with the method proposed in reference [4], it can be easily deduced that When there are dc bias component contained in the input three-phase voltage, the extracted synchronization signals of frequency is ac component fluctuating around 50hz when it is extracted by the SRF-PLL or by the method proposed in reference [4], so the synchronization performance is greatly affected, when the method proposed in this paper is used the affection of the dc bias component can be eliminated, so the synchronization performance is good.

At the time of 0.10s, third harmonic voltage which it's amplitude is 15% of the positive sequence fundamental voltage amplitude is added to the three-phase voltage, the waveform of positive sequence fundamental voltage and the synchronous phase angle is shown in Figure 4.

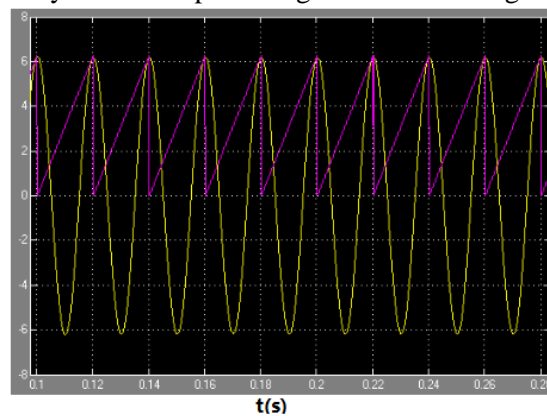


Figure 4. The waveform of positive sequence fundamental voltage and the synchronous phase angle when third harmonic voltage is added

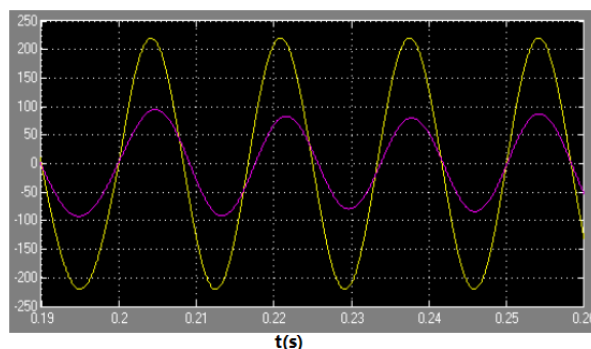


Figure 5. The power grid voltage of A phase and positive sequence fundamental voltage waveform when the power grid frequency changes

In this case, the peak synchronous phase difference is less than 1 degree.

At the time of 20ms, the power grid frequency changes from 50Hz to 60Hz, the frequency and phase of power grid is locked after about two cycles by the new software phase-lock loop, the power grid voltage of A phase and positive sequence fundamental voltage output from the new software phase-locked loops are shown in Figure 5.

It can find that the rapidity and accuracy of locking frequency and phase is demonstrably superior.

5. Experiments

When the dc bias component of $d_a=5V$, $d_b=10V$, $d_c=-10V$ is separately added the symmetric three-phase voltage system, the extracted synchronization signals of frequency is shown in Figure 6.

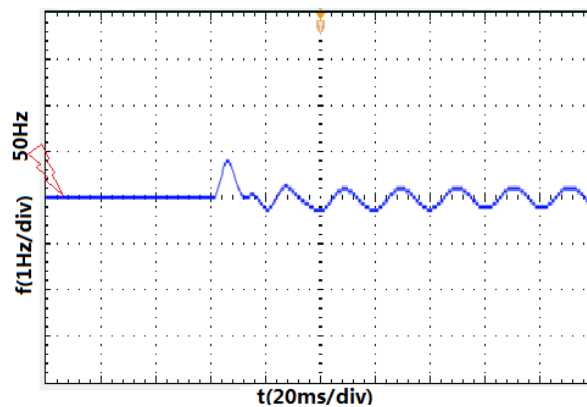


Figure 6. The experimental extracted synchronization signals of frequency

As shown in Figure 6, the existence of dc bias component have little effect on the extraction of synchronization signals of frequency.

When the third harmonic voltage which it's amplitude is 15% of the positive sequence fundamental voltage amplitude is added to the three-phase voltage, the experimental waveform of three-phase voltage is shown in Figure 7

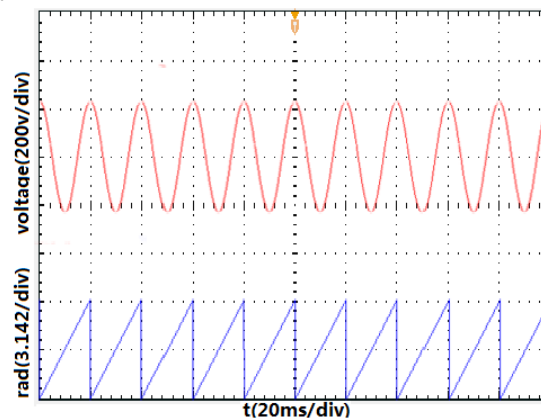


Figure 7. The experimental waveform of positive sequence fundamental voltage and the synchronous phase angle when third harmonic voltage is added

As shown in Figure 7, the peak synchronous phase difference is very small.

When the power grid frequency changes from 50Hz to 60Hz, the power grid voltage of A phase and positive sequence fundamental voltage output from the new software phase-locked loops are shown in Figure 8.

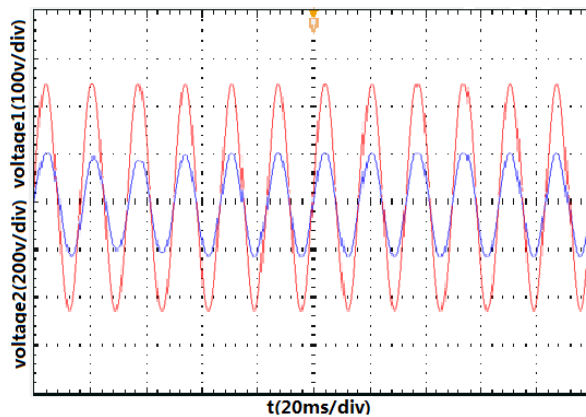


Figure 8. The experimental power grid voltage of A phase and positive sequence fundamental voltage waveform when the power grid frequency changes

As shown in Figure 8, the frequency and phase of power grid can be locked in about two periods by the new software phase-locked loop.

6. Conclusion

The theory of positive sequence fundamental filter and function model of variable sampling period phase-locked loops are first analyzed in this paper, the relatively design parameters were given, on this basis, a kind of frequency adaptive software phase-locked loops is proposed which combine the advantages of the above filter and variable sampling period phase-locked loops. The results of simulation and experiment indicate that the effects of some disturbances can be eliminated effectively, synchronous fundamental frequency voltage sign can be got quickly, so the new software phase-locked loops proposed in this paper has strong advantage.

The application research of software phase-locked loop in the new energy field should be intensified in the future.

7. Acknowledgments

This work is supported in part by the science and technology planning project of education department of Guangdong province, China. Grant 2017GKTSCX052.

8. References

- [1] ZENG Zheng and YANG Jia-qian A Grid Synchronization Method Using Frequency Adaptive Moving Average Filter 2014 *Journal of Zhejiang University (Engineering Science)* **48(9)**.1696-1703
- [2] ZHAO Gui long, CAO Ling ling and ZHU Long ji Improved PLL Design of PV Grid Inverter System 2015 *Power System Protection and Control* **432(2)** 108-112
- [3] WANG Baocheng, SAN Guocheng and GUO Xiaoqiang Grid Synchronization And PLL For Distributed Power Generation Systems 2013 *Proc of the CSEE* **33(1)** 50-56
- [4] Du Xiong, Liu Yandong, Sun Pengju and Zhou Luowei SRF-PLL Method of Grid-Tied Converter for Eliminating The Influence Of DC Components 2013 *Transactions of China Electrotechnical Society* **28(12)** 24-31

Space Vector Flux Weakening Control of PMSM Drivers

Gentao Dong, Jianfei Yang, Xin Qiu , Xun Liu and Cao Wei

Nanjing Normal University, Nanjing, China

E-mail: d1517245733@163.com

Abstract. Permanent Magnet Synchronous Motor is widely used in industry, medicine and other fields. Based on the mathematical model of permanent magnet synchronous motor (PMSM), a system of modeling and simulation of PMSM was constructed by MATLAB/Simulink, and two PI controllers were used in the speed loop and current loop. This paper presents the principle of pulse width modulation based on voltage space vector, and the simulation model of PMSM control system based on SVPWM is built in MATLAB/Simulink. In the end, some experiments are carried out to the whole system, and it proves that the system is of good performance both in steady and dynamic state.

1. Introduction

Permanent magnet synchronous motor (PMSM) has a wide range of applications thanks to its simple structure, high power factor and high efficiency. Due to the permanent magnet excitation, the excitation magnetic field cannot be adjusted by the excitation winding. The permanent magnet synchronous motor must adopt the flux weakening control technology to meet the speed regulation requirement of the wide speed range. According to the operating principle of the motor, the back electromotive force will gradually increase as the rotor speed increases. The permanent magnet synchronous motor drive control is realized by the inverter, so the inverter output voltage also increases with the increase of the rotational speed. Since the maximum output voltage of the inverter is limited by the DC side bus voltage value, when the motor speed is higher than the maximum speed corresponding to the maximum voltage, the inverter will not be able to continue to provide a higher voltage to achieve an increase in the motor speed. If it is necessary to further increase the rotational speed, it can be achieved by reducing the excitation magnetic field and reducing the back electromotive force without changing the hardware. Since the excitation field of the permanent magnet synchronous motor is generated by the permanent magnet and cannot be directly changed, it is necessary to control the stator direct-axis current, and the weakening of the air gap magnetic field by the direct-axis armature reaction is equivalent to weakening the excitation magnetic field [1]-[2]. Therefore, the implementation of flux weakening control is based on this principle.

Since the mid-1980s, the mechanism of flux weakening operation has been deeply studied by scholars. In 1985, Brigitte et al. analyzed the variation of motor power and torque during the field weakening process, and discussed the influence of the cross-coincidence term on the flux weakening control performance in the AC motor model. Thomas et al. obtained the maximum torque-to-current ratio (Maximum Torque Per Ampere, MTPA) curve. A method based on the direct-axis current tracking error to adjust the target value of the AC current is proposed. This achieves a smooth switching from the constant torque speed regulation phase to the constant power flux weakening speed regulation phase [3]. In the early 1990s, Japanese scholar Morimoto divided the motor operation into three areas. The research results cover both surface-mount and in-line motors and take into account the



demagnetization that may be caused by flux weakening currents, which promotes the in-depth development of flux weakening speed regulation research [4].

With the in-depth development of modern motor design and control technology, scholars and engineers have proposed effective solutions from the body design and control algorithms of the motor, which greatly improved the dynamic response performance and steady state accuracy of the permanent magnet synchronous motor in the high-speed region [5]. In summary, the flux weakening control is a key problem that hinders the wide application of high-speed permanent magnet synchronous motors.

This paper introduces the basic principles of SVPWM and flux weakening, and details in the MATLAB/Simulink environment. The implementation method of SVPWM is finally combined with the permanent magnet synchronous motor control system to give the simulation experiment results.

2. Mathematical model of permanent magnet synchronous motor

The vector control is a control method based on the coordinate transformation theory. After the coordinate transformation, the permanent magnet synchronous motor has the same speed regulation performance as the DC motor. The literatures 6 and 7 first derive the vector equation of the ABC axis system, and then pass the vector transformation transform these equations into any coordinate system [6], [7]. Here, only the mathematical model of the permanent magnet synchronous motor in the d, q coordinate system is given. The circuit and torque equation are expressed as:

$$\frac{di_d}{dx} = \frac{1}{L_d} v_d - \frac{R}{L_d} i_d + \frac{L_q}{L_d} \omega_r i_q \quad (1)$$

$$\frac{di_q}{dx} = \frac{1}{L_q} v_q - \frac{R}{L_q} i_q + \frac{L_d}{L_q} \omega_r i_d - \frac{\lambda \omega_d}{L_q} \quad (2)$$

$$T_e = 1.5p[\lambda i_q + (L_d - L_q)i_d i_q] \quad (3)$$

Where L_q , L_d are the inductance of the q-axis and d-axis; ω_r is the angular velocity of the rotor; R is stator internal resistance; i_q , i_d are the current components of q-axis and d-axis; v_q , v_d are the voltage components of q-axis and d-axis; λ is electromagnetic torque coefficient; p is the stator pole pair; T_e is the electromagnetic torque.

Based on the above mathematical model of d q axis, the flux weakening control chart of permanent magnet synchronous motor is given, as shown in Figure 1. PMSM flux weakening control simulation system adopts double closed loop control scheme. The speed loop is the control outer loop, which keeps the actual speed of the motor consistent with the given speed value, and eliminates the influence of load torque disturbance and other factors on the motor speed in time. The current loop is the control inner loop. Its function is to control the inverter to generate accurate current on the stator winding.

3. SVPWM

3.1 Basic principle of SVPWM

For the three-phase voltage inverter shown in Figure 2, the phase voltage of the motor depends on its corresponding state of inverter arm. The three-phase bridge voltage inverter has eight operating states. V1 to V6 are six power switching tubes, and the switching functions (Sa, Sb, Sc) represent the switching states of the three bridge arms. There are 8 basic working states, namely: 100, 110, 010, 011, 001, 101, 111, 000. The first six working states are valid, called non-zero vectors; the latter two working states are called zero vectors. If these eight spatial states are represented by vectors, the space voltage vector of the permanent magnet synchronous motor (PMSM) is obtained as shown in Figure 3. In order to make the voltage vector of the inverter output close to a circle and finally obtain a circular rotating magnetic flux, it is necessary to use the inverter to combine the output voltages of the devices forms a polygonal voltage vector trajectory that is closer to a circle [8]. This is the basic starting point of the SVPWM principle.

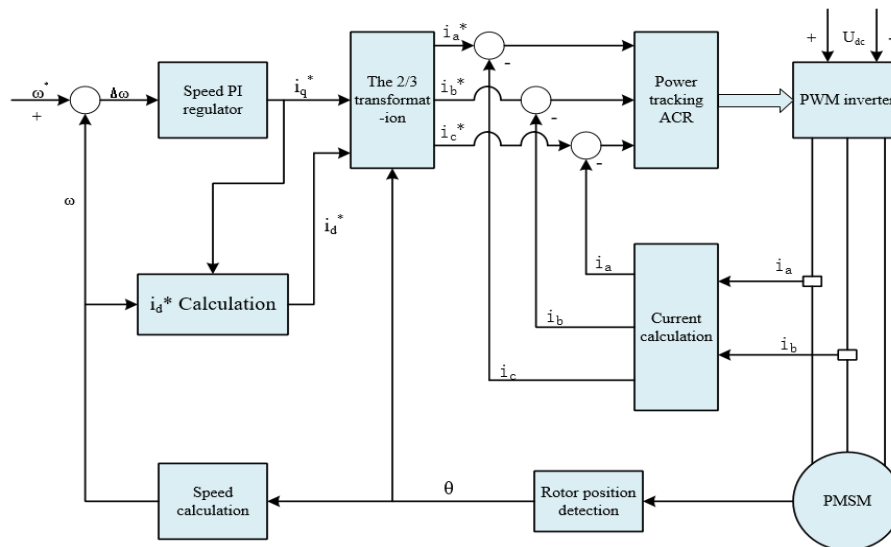


Figure 1. PMSM flux-weakening control Chart

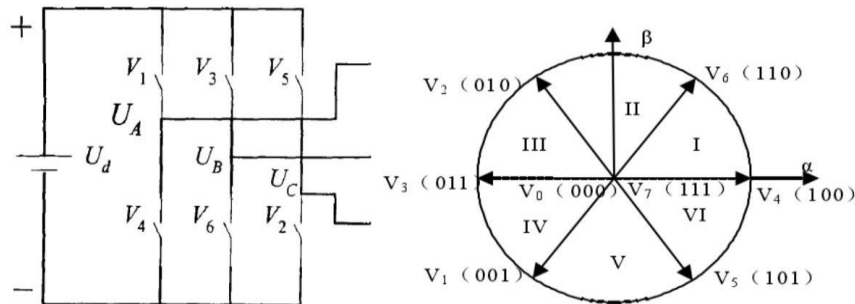


Figure 2. Inverter & Figure 3. Basic voltage space vector

3.2 Implementation of SVPWM Control Algorithm

The control scheme of SVPWM is divided into three parts, namely the interval allocation of three-phase voltage and the optimal sequence selection of vector synthesis selection and control algorithm. So the basic steps of the SVPWM algorithm are as follows:

(1) determining the sector in which the reference voltage vector U is located

For the case where U is given in the form of $[u_\alpha, u_\beta]^T$, set 3 auxiliary variables u_{ref1} , u_{ref2} , u_{ref3} , The sector in which it is located can be obtained by the following algorithm.

$$u_{ref1} = u_\beta \tag{4}$$

$$u_{ref2} = \sin 60^\circ u_\alpha - \sin 30^\circ u_\beta \tag{5}$$

$$u_{ref3} = -\sin 60^\circ u_\alpha - \sin 30^\circ u_\beta \tag{6}$$

$$N = \text{sign}(u_{ref1}) + 2\text{sign}(u_{ref2}) + 4\text{sign}(u_{ref3}) \tag{7}$$

Then look at Figure 4 according to the value of N to get the sector, Figure 5 shows the simulation graph for judging the sector.

N ^o	Sector ^o
1 ^o	II ^o
2 ^o	VI ^o
3 ^o	I ^o
4 ^o	IV ^o
5 ^o	III ^o
6 ^o	V ^o

Figure 4. Relationship of N and the sectors

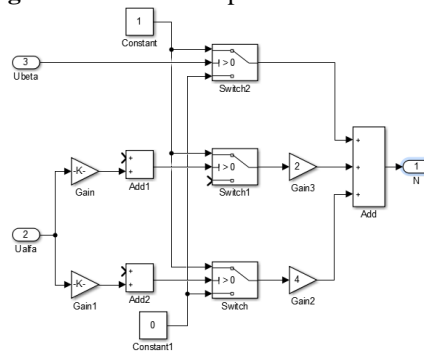


Figure 5. Judge the sectors

(2) Calculate the time of the action of the adjacent two switching voltage vectors

It should calculate the time of the switching voltage vector, and then determine if the sum of the two action times is greater than the PWM period. If it is larger than the PWM period, it will be corrected [9]. Literature 9 gives a detailed derivation and calculation of the vector action time. Figure 6 and Figure 7 below show the simulation of this step.

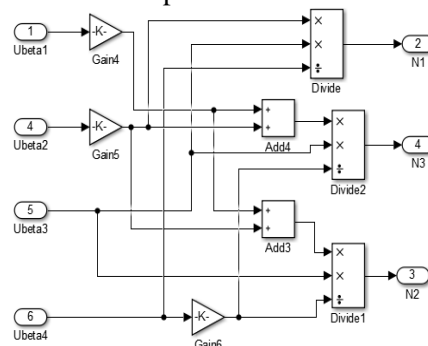


Figure 6. Neighboring motion vectors' acting time

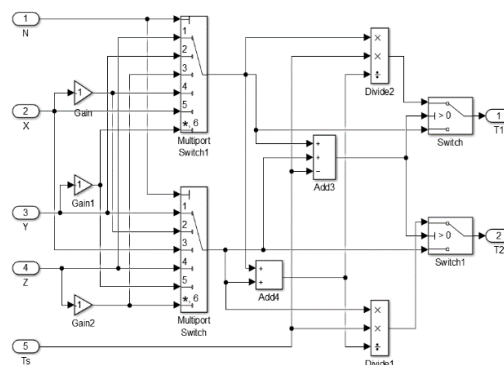


Figure 7. Neighboring motion vectors' acting time

(3) Synthesized into three-phase PWM signals according to the switching voltage vector action time

The simulation graph for this step is shown in Figures 8, 9 and 10.

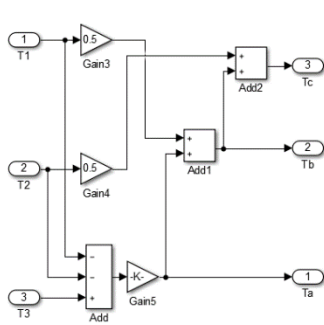


Figure 8. SVPWM wave form

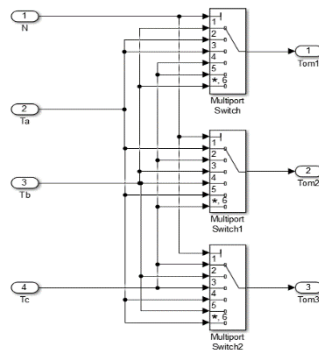


Figure 9. SVPWM wave form

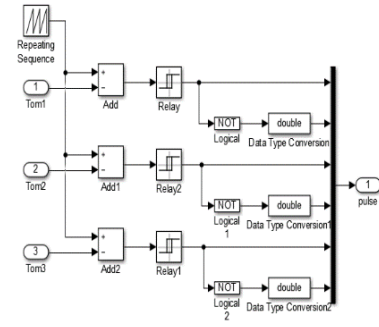


Figure 10. SVPWM wave form

4. Flux-weakening control

In a permanent magnet synchronous motor, the induced potential increases with the increase of the rotational speed. When the terminal voltage of the motor reaches the DC side voltage of the controller, the PWM controller loses the ability to track the current. Therefore, the stator terminal voltage U_s and the phase current I_s are limited by the inverter output voltage and the output current limit ($U_{s\max}$ and $I_{s\max}$) [10], [11]. Current limit circle and voltage limit circle is expressed as:

$$I_d^2 + I_q^2 \leq I_{s\max}^2 \tag{8}$$

$$(E_0 + I_d x_d)^2 + (I_q x_q)^2 \leq U_{s\max}^2 \tag{9}$$

Because $E_0 = \omega\psi_f$, $x_d = \omega L_d$, $x_q = \omega L_q$, so the voltage limit elliptic equation can be rewritten as:

$$(\psi_f + I_d L_d)^2 + (I_q L_q)^2 \leq (U_{s\max} / \omega)^2 \tag{10}$$

The operating range of a permanent magnet synchronous motor is limited by the conditions of the current limit circle and the voltage limit ellipse. The motor's current vector I_s should be within the area enclosed by the two curves, as shown in Figure 11[12]. It can be seen from Figure 11 that the motor speed ω increases, the I_d component tends to increase, and the corresponding I_q component must decrease. Therefore, the electromagnetic torque of the motor also decreases with the increase of the rotational speed, showing the characteristic of constant power.

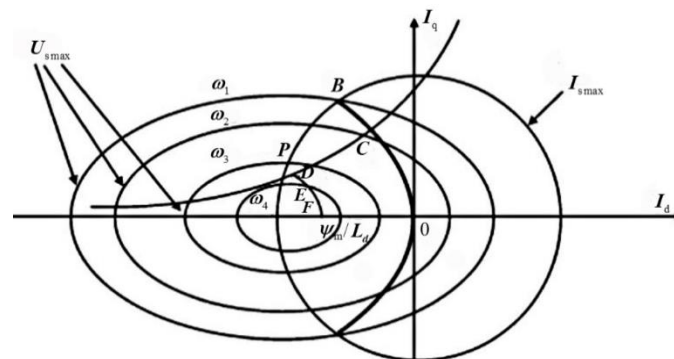


Figure 11. MAX circle

For the plug-in permanent magnet synchronous motor, the permanent magnet synchronous motor has two parts of torque due to the unequal parallel shaft inductance. They are permanent magnet torque and reluctance torque. In order to find the best match between current and torque, and use the minimum current to generate the maximum torque. Using the Lagrangian extreme value theorem in mathematics, The derivative of the current of the quadrature axis and the straight axis is obtained for

the torque equation to find the optimal current and torque matching. The maximum torque/current ratio control speed trajectory of the built-in permanent magnet synchronous motor is directly given, as shown in Figure 11 above. When the motor speed exceeds the rated speed or the DC bus voltage of the voltage source inverter decreases, the voltage constraint curve retracts. The system cannot continue to run at point B. The motor torque is reduced and the current vector runs along the BP curve. The current at this time is constrained by both voltage and current constraints, and the current vector remains at the maximum effective value $I_{s,max}$. To continue to increase the speed, it is only by adjusting I_d and I_q . This is the weak magnetic speed regulation of permanent magnet synchronous motor.

If the motor initially runs at point C with a constant torque and the speed reference is increased to ω_3 , the current regulator can be guaranteed to run from point C to point D with constant torque. In this case, the current increases as the speed is given increasing. The current does not reach the maximum constraint value, and the air gap flux linkage of the motor decreases as the direct axis component of the current increases. As the given speed increases further, the motor torque is limited by the maximum voltage value. To achieve the maximum torque/current ratio, the current vector will travel along curve D-E-F. If the motor speed is given as ω_3 , the motor will travel along the field weakening curve BP to ω_3 after running to the point B at the maximum torque/current ratio.

5. SIMULINK simulation

5.1 Simulated motor parameters and waveform

The phase winding resistance R is 2.87Ω , the limit voltage value $U_{s,max}$ is 240 V, and the d-axis inductance component L_d is 388.5 mH. The current value $I_{s,max}$ is 1.6 A, the q-axis inductance component L_q is 475.5 mH, permanent magnet flux linkage ψ_m is 0.3 Wb and the initial mechanical torque T_i is 4 Nm. the mechanical torque change time t is 0.015 s, the pole log p is 4, and the final mechanical torque T is 2 Nm. The simulated waveform is shown below.

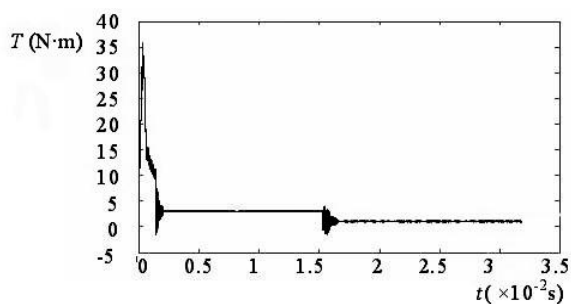


Figure 12. Torque curve

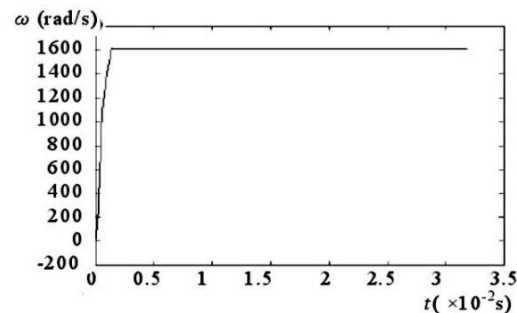


Figure 13. Speed curve

5.2 Simulation results

In the simulation, the minimum speed of the motor is set to 400 rad/s. After the flux weakening speed regulation based on SVPWM, the speed ratio of the constant power running area reaches 4:1. It can be seen from the simulation waveform that the system torque response is fast and stable at a speed of 1600 rad/s. The waveform is ideal, and there is no static difference in steady state operation. The simulation results demonstrate the effectiveness of the SVPWM-based flux weakening method used in this paper.

6. Conclusions

According to the principle of SVPWM, MATLAB/Simulink is used as the simulation software to build a SVPWM-based simulation model of flux weakening control of permanent magnet synchronous motor, the simulation results show that the designed simulation model is correct, the system has good

robustness and rapidity, and effectively improves the control effect of the system. At the same time, in the simulation different control strategies can be tried to optimize the design, which provides an effective way for the analysis and design of the permanent magnet synchronous motor control system.

7. Acknowledgements

This work was supported by Postgraduate Research & Practice Innovation Program of Jiangsu Province , Project KYCX18_1223 , KYCX18_1225 and by National Natural Science Foundation of China, Project 51607094.

8. References

- [1] Jang Mok K, Seung Ki S. Speed Control of Interior Permanent Magnet Synchronous Motor Driver for the Flux Weakening Operation[J]. IEEE Transactions on Industry Application, 1997, 33(1):43-48.
- [2] De Carvalho F V, Pinto J O P, Da Silva L E B. A DSP based torque meter for induction motors[C]. Proceedings of Annual conference of IEEE Industrial Electronics Society, Acapulco, Mexico, 2003: 414-418.
- [3] Y. Guo, J. Yang, Y. Dou, X. Qiu, J. Liu, Y. Zhang and M. Wang, "New zero voltage vectors in direct torque control of brushless DC motor," Proc. of 19th Int. Conf. on Electrical Machines and Systems, Chiba (Japan), pp. 1-5, Nov., 2016.
- [4] Gilbert Foo, Saad Sayeef, M F Rahman. Low-speed and standstill operation of a sensorless direct torque and flux controlled IPM synchronous motor drive[J]. IEEE Transactions on Energy Conversion, 2010, 25(1): 25-33.
- [5] Ching-Tsai P, Sue S M. A Linear Maximum Torque Per Ampere Control for Ipmsm Drivers Over Full-speed Range[J]. IEEE Transactions on Energy Conversion, 2005, 20(2):359-366.
- [6] Xueqing Wang, Zheng Wang, Ming Cheng, Yihua Hu. Remedial Strategies of T-NPC Three-Level Asymmetric Six-Phase PMSM Drive Based on SVM-DTC[J]. IEEE Transactions on Industrial Electronics, 2017, 64(9): 6841-6853.
- [7] Hinkkanen M, Luomi J. Modified integrator for voltage model flux estimation of induction moters[J]. IEEE Transactions on Industrial Electronics, 2003, 50(4): 818-820.
- [8] Hu J, Wu B. New integration algorithms for estimating motor flux over a wide speed range[J]. IEEE Transactions on Power Electronics, 1998, 13(5): 969-977.
- [9] Anfei Xu. Simulation Analysis of Permanent Magnet Synchronous Motor Vector Control System [J]. Micromotors Servo Technique, 2009, 41(9):30-33.
- [10] Lascu C, Boldea I, Blaabjerg F. A modified direct torque control for induction motor sensorless drive [J]. IEEE Transactions on Industry Applications, 2000, 36(1): 122-130.
- [11] Xu W, Lorenz R D. Reduced Parament Sensitivity Stator Flux Linkage Observer in Deadbeat-Direct Torque and Flux Control for IPMSMs [J]. IEEE Transactions on Industry Applications, 2014, 50(4): 2626-2636.
- [12] Zhuang Xu, M.F. Rahman. Comparison of Sliding Observer and a Kalman for Direct-Torque-Controlled IPM Synchronous Motor Drives [J]. IEEE Transactions on Industry Electronics, 2012, 59(11): 4179-4188.

Research and Verification of Setting Value Coordination Method Considering the Responding Deviation of under Excitation Limit and Loss of Excitation Protection for Generator

Quan HONG¹, Li LI¹, Haifeng LIU¹, Wenqi MAO², Wenjun LU³

¹ State Grid Hunan Electric Power Co. Ltd. Power Research Institute, Changsha 410007, Hunan Province, China;

² State Grid Hunan Electric Power Co. Ltd., Changsha 410004, Hunan Province, China.;

³ School of electrical and information engineering, Hunan University, Changsha 410082, China)

Email: 78851329@qq.com

Abstract: The general principle of the matching between the under excitation limit and the loss of excitation protection has been extensively described, which mostly concentrated on the theory and method of converting them to the same power plane or impedance plane for verifying, but there is little literature of considering the influence of the action characteristics of the field device to the matching results for the setting value. In theory, the influence of parameter variation to the matching result is analyzed in detail. This paper proposed the matching testify principle based on the application operation deviation and expounds the adjustment method of setting value mismatch, which provides an effective guidance principle for power plants with verification and cooperation of under excitation limit and loss of excitation protection.

1. Introduction

Excitation system grid-related and related protection parameter coordination is an important content of grid-source coordination. At present, there are many papers on the cooperation of the excitation system parameters and related protection, which are mainly concentrated on cooperation between under excitation limit and loss of excitation protection [1]-[5]. The general principle of the matching of under excitation limit and loss of excitation protection has been extensively discussed, mostly concentrated in the principles and methods of transfer the loss of excitation protection and under excitation limit parameter to the same impedance plane or a power plane for checking. However, there is no in-depth analysis of the influence of protection and limit parameter variation to the coordination relationship. There is no research on how to choose the coordination difference between under excitation limit and loss of excitation protection and no verification method for whether the match relationship is reasonable is given. In particular, there is a lack of consideration of the influence of the actual device action error on the setting value matching result.

This paper theoretically analyzes the influence of various parameter changes on the loss of excitation protection and the under excitation limit, and proposes to use the measured limit curve of the generator as the setting and coordination basis, and proposed the matching and check principle of under excitation limit and the loss of excitation protection based on the device operation error. And the method of setting value adjustment when the value is mismatched is discussed, which provides



effective guiding principles for current power plants to carry out the calibration and setting of under excitation limit and loss of excitation protection.

2. The cooperation of under excitation limit and loss of excitation protection.

2.1. The cooperation principle

According to relevant regulations and standards, the operation relationship between the loss of excitation protection of the generator and the under excitation limit should be that the under excitation limit works precedes to the loss of excitation protection operation. Under excitation limit setting in excitation system mainly based on the static stability, as well as the stator end heat, plant power voltage constraints. The under excitation limit is generally calculated on the P-Q plane. The main consideration of generator loss excitation protection is the damage of the generator after the loss of excitation [6], [7]. For example: the stator end heating, voltage collapse, rotor overheating, unit vibration, stator winding overheating [8]. The setting parameter of the loss of excitation protection is calculated on the R-X impedance plane. Therefore, the basic theory of the Under excitation limit and the loss of excitation protection is a little bit different, which makes the research point focusing on the method of transformation of coordinates. The loss of excitation protection impedance circle is transformed into the P-Q plane through the coordinate transformation, and its cooperation with the static stability circle is shown in Figure 1.

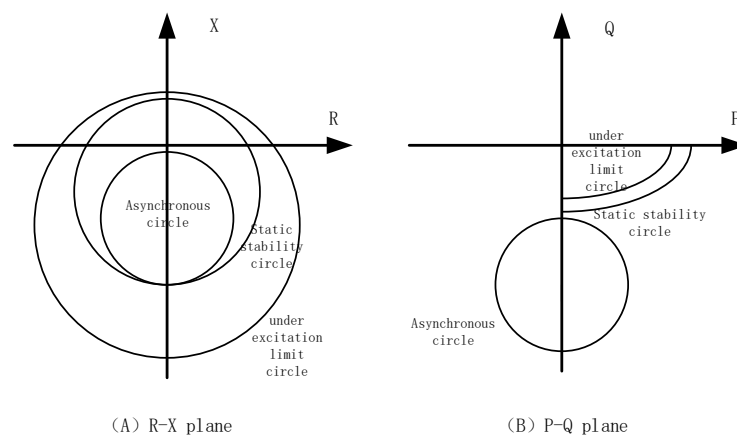


Figure 1 Matching of under excitation limit and loss of excitation protection

In the R-X plane, the under excitation limit circle contains a static stability circle for loss of excitation, and the static stability circle for loss of excitation contains an asynchronous impedance circle. The matching relationship to the P-Q plane is shown in Figure 1(B). The under excitation limit precedes the loss of excitation protection. Studies have shown that as long as the under excitation limit can be matched with the static stability of the loss of excitation protection, it can certainly cooperate with the asynchronous impedance circle protection of the loss of excitation protection [2]. The salient pole static stability circle and the hidden pole static stability circle characteristics are very different and will be discussed in another article. Therefore, in this paper, we only study the relationship between the loss of excitation protection and the under excitation limit in the use of the static stable circle as the criterion for the non-salient pole generator.

2.2. Analysis of influence of parameters on coordination

2.2.1 Influence of the loss of excitation protection parameters on coordination relationship

The loss of excitation protection is set in the R-X impedance plane, and the under excitation limit is set in the P-Q plane. Therefore, in order to study the cooperation relationship between the two function, these two must be reduced to a same plane, and the loss of excitation protection action equation is:

$$R^2 + (X - X_0)^2 < R_0^2 \quad (1)$$

The loss of excitation protection action equation is a circle whose center point coordinates are $(0, X_0)$ and radius is R_0 . The action equation after converting it to the P-Q plane is:

$$P^2 + \left(Q - \frac{X_0 U_g^2}{X_0^2 - R_0^2}\right)^2 > \left(\frac{R_0 U_g^2}{R_0^2 - X_0^2}\right)^2 \quad (2)$$

Where U_g is the actual voltage of the generator stator. The under excitation limit criterion for the static stability circle equation is:

$$P^2 + \left(Q - \frac{U_g^2}{2} \left(\frac{1}{X_s} - \frac{1}{X_d}\right)\right)^2 > \left(\frac{U_g^2}{2} \left(\frac{1}{X_s} + \frac{1}{X_d}\right)\right)^2 \quad (3)$$

Where X_s is the contact resistance of the generator to the system and X_d is the synchronous reactance of the turbine generator.

The setting parameters for the static stability criteria of the loss of excitation protection are generally the upper boundary impedance X_c and the lower boundary impedance X_b . Its relationship with the impedance circle is as follows:

$$X_0 = -\frac{X_b - X_c}{2} \quad (4)$$

$$R_0 = \frac{X_b + X_c}{2} \quad (5)$$

From the above formula, it can be seen that the main parameters affecting the loss of excitation protection action are the upper boundary impedance X_c and the lower boundary impedance X_b and the generator terminal voltage U_g . Therefore, it is important to study how the changes of the three parameters of the loss of excitation protection affect its cooperation with the under excitation limit curve.

When the generator is in leading phase operation, its curve in the P-Q plane is in the fourth quadrant. From the formula (2), it can be seen that the allowable leading power factor depth is determined by the radius size and the center of the circle.

Substitute (4), (5) into (2) to get the center coordinates and radius:

Center ordinate:

$$\frac{1 - \frac{X_c}{X_b} U_g^2}{2X_c} \text{ 或 } \frac{\frac{X_b}{X_c} - 1}{2X_b} U_g^2 \quad (6)$$

Radius:

$$\frac{1 + \frac{X_c}{X_b} U_g^2}{2X_c} \text{ 或 } \frac{\frac{X_b}{X_c} + 1}{2X_b} U_g^2 \quad (7)$$

When $P=0$, the maximum allowable leading power factor depth is:

$$Q = \frac{R_0 U_g^2}{R_0^2 - X_0^2} - \frac{X_0 U_g^2}{X_0^2 - R_0^2} = -\frac{U_g^2}{R_0 - X_0} \quad (8)$$

Substitute (4) and (5) into and simplify to:

$$Q = -\frac{U_g^2}{X_b} \quad (9)$$

Keep X_c, U_g unchanged, X_b increases, From equation (6), it can be seen that the ordinate of the center of the circle increases. From equation (7) it can be seen that the radius decreases. The loss of excitation protection allows the leading power factor depth to become smaller, and it appears in the P-Q plane that the fourth quadrant circle translates in the positive direction of the Q axis. On the contrary, X_b decreases, and the loss of excitation protection allows the leading power factor depth to

become larger. In the P-Q plane, the circle of the fourth quadrant moves in the negative direction of the Q axis.

Keep X_b, U_g unchanged, X_c increases, From equation (6), it can be seen that the ordinate of the center of the circle decreases. From equation (7) it can be seen that the radius decreases. From equation (9), it can be seen that the maximum allowable reactive power at $P=0$ remains unchanged, but because of the radius decreasing, the loss of excitation protection allows the leading power factor depth smaller when $P>0$. In the P-Q plane, the circular arc rotates in the positive direction of the Q axis, except for the position of the intersection of the fourth quadrant and the ordinate. In contrast, X_c decreases, the maximum allowable leading power factor depth at $P=0$ remains unchanged, and increase when $P>0$. In summary, as the X_b increases, X_c decreases, the allowable leading power factor depth decreases, As the X_b decreases, X_c increases, the allowable reactive power increases. In addition, as can be seen from equations (6) and (7), The actual voltage of the generator U_g affects the actual allowance of leading power factor depth.

2.2.2 The influence of under excitation limit parameters on the coordination relationship.

At present, the principle of under excitation limit is to connect the multi-point allowable leading power factor depth coordinates (P, -Q) into a poly-line. Below the poly-line is the action area. Considering the influence of the actual voltage U_g , the coordinate value are multiplied by coefficients $(U_g / U_N)^2$ for correction. The influence of U_g to the under excitation limit action is exactly the same as the effect to the loss of excitation protection. Therefore, the effect of U_g on cooperation setting can be neglected. The under excitation limit setting value is determined by the (P, -Q) coordinate value. Increasing the Q value allows the leading power factor depth to increase, but it is easier to mismatch with the loss of excitation protection. Decreasing the Q value allows leading power factor depth to be reduced, which is easier to match with the loss of excitation protection.

2.2.3 The influence of the phase-in test curve of generator on the coordination relationship.

Both of the under excitation limit and the loss of excitation protection use the generator static stability circle as the boundary for action. However, the generator is restrained by factors such as the heating of the stator terminal and the factory electrical voltage. The actual allowance of leading power factor depth is less than the amount by the static stability circle. Different generator parameters and operating environments may not be the same, and it is difficult to describe the allowable leading power factor depth range of the generator with several simple system parameters. Stator end heating, factory electrical voltage and other conditions may be more restrictive than the static stability criterion of the generator. It is generally inconvenient to express the amount of leading power factor depth of the actual generator determined by the three constraints expressed above in an exact mathematic model, which is not necessary in engineering as well. In practical applications, the under excitation limit curve is generally formulated according to the leading power factor test. In the actual measurement process, several conditions such as static stability, stator heating, and factory power voltage have been comprehensively considered. Therefore, it is recommended that taking the allowable leading power factor depth limit curve measured by the generator as an important reference for the under excitation limit and the loss of excitation protection. In principle, the under excitation limit works precede to the generator limit curve action, the generator limit curve works precede to the loss of excitation protection action, and the loss of excitation protection works precede to the standard static stability circle. The ideal matching relationship between the four groups of curves in the P-Q plane is shown in Figure 2.

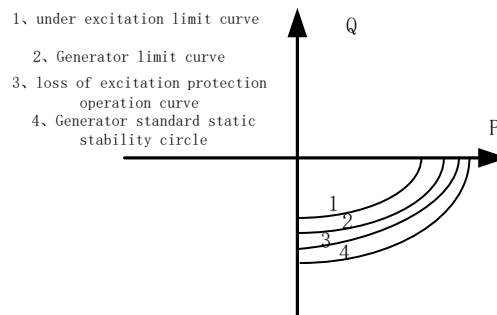


Figure 2 Ideal matching relation of curves

2.3 the principle of the matching and checking of the under excitation limit and the loss of excitation protection in consideration of the device action error

There is no regulation or standard to quantify the matching differential levels of the under excitation limit and the loss of excitation protection, which only qualitatively stipulates that the under excitation limit works precede to the loss of excitation protection action. The under excitation limit must meet the three constraints of the excitation system at first, followed by the cooperation with the loss of excitation protection. How to ensure adequate safety margin and maximize the depth of the generator's leading power capability is worth of studying. The maximum allowable protection operating value error is $\pm 5\%$ according to the relay protection regulations and $\pm 0.2\%$ of the excitation systems according to national standards. The error of excitation limiter can be ignored during calibration. Considering various errors in a comprehensive manner, it is feasible to set the differential level of each curve as 5%. With reference to the matching relationship shown in Figure 2, the under excitation limit action value is 5% less than the measured value of the generator leading power factor depth curve, and the loss of excitation protection action value is 5% greater than the limit curve action value. The loss of excitation protection operation value is 5% less than the standard static circle operation value.

The generator terminal voltage U_g affects the leading power factor depth, but the influence of this parameter is already included in the under excitation limit action curve and the loss of excitation protection action equation, and its effect on the two curve operation ranges is the same, so U_g does not affect the coordination relationship between the under excitation limit and the loss of excitation protection. But when U_g decreases, the under excitation limit and the loss of excitation protection allowable generator leading power factor depth becomes smaller, and the under excitation limit more easily matches the leading power factor ability curve, but the loss of excitation protection may be mismatched. Considering that the actual voltage of the generator during the leading power factor test is generally lower than the rated voltage, it should be checked whether the loss of excitation protection and the limit curve are mismatched under the condition of decreasing U_g .

The standard static stability circle of the generator is determined by X_s and X_d , When X_s becomes larger, the standard static stability circle allowable leading power factor depth becomes smaller, and it is easily mismatched with the loss of excitation protection. Therefore, whether the loss of excitation protection and the standard static stability circle is mismatched should be checked in the minimum operating mode of the system.

2.4 Parameter adjustment method in case of mismatch

In total, when the generator is in leading power factor operation, the correct matching relationship must be ensured between the excitation system's under excitation limit curve, the loss of excitation protection operation curve, the generator leading power factor depth limit curve, and the standard static stability circle. The generator leading power factor depth curve is determined by the leading

power factor test. The standard static circle is determined by the system parameters. There is no parameter adjustment problem for the two curves. Generator under excitation limit is a polyline forming action area composed of multi point (P, -Q) coordinates. Adjusting the coordinate value can modify the action range of the curve. The leading power factor depth of the loss of excitation protection is mainly determined by the upper boundary impedance X_c and the lower boundary resistance X_b . When X_b becomes larger or X_c becomes smaller, the leading power factor depth becomes smaller, and when X_b becomes smaller or X_c becomes larger, the leading power factor depth becomes greater.

If the under excitation limit and the loss of excitation protection or leading power factor depth curve gets unmatched, the following method can be used to adjust the parameters:

The first step is to adjust the parameters of the under excitation limit (P, -Q) coordinate values so that the under excitation limit curve matches the leading power factor depth limit curve and meet the 5% differential. Considering the maximum +5% error in the loss of excitation protection and the decrease in U_g at the same time, the allowed leading power factor depth reduced. If the loss of excitation protection works precedes to the leading power factor depth limit curve, it is recommend to decrease X_b or increase X_c setting value and keep a 5% difference from the limit curve.

The second step: considering the maximum -5% error in the loss of excitation protection. At the same time, the system is in the minimum operating mode, which makes the leading power factor depth to be larger, and the action curve may be unmatched with the standard static stability circle. At this time, X_b can be increased or X_c can be decreased to reduce the leading power factor depth determined by the loss of excitation protection. After adjusting X_b and X_c , it is necessary to check whether the matching meets the 5% differential requirement, between the loss of excitation protection and the leading power factor depth ability curve, if it does not meet the requirements, it needs to further adjust X_b , until it meets the requirements.

By adjusting the above parameters, the correct matching relationship can be guaranteed among the four, under excitation limit, generator leading power factor depth ability curve, loss of excitation protection curve and the standard static stability circle.

3. Coordination examples

The parameters of a 300MW unit in a power plant are as follows: $S_N=353\text{MVA}$, $P_N=300\text{MW}$, $U_N=20\text{KV}$, $X_d=204.7\%$, $X_d'=0.2957$, $X_s^*=0.2063$ (the system minimum operation mode), $n_{TA}=15000/3$, $n_{TV}=20/0.1$, the action field of the loss of excitation protection uses the static stability circle criterion, Setting value: upper boundary resistance $X_c=8.55\Omega$, Lower boundary impedance $X_b=85.49\Omega$, (General setting $X_c=X_s$, $X_b=X_d+0.5X_d'$. Because X_c , X_b generally use the nominal value, In the calculation process, X_s and X_d must be first converted to a nominal value, After getting the X_c , X_b nominal values, convert X_c , and X_b into standard values.)

The under excitation limit curve coordinates are:

$$\{0, -105\}, \{70, -95\}, \{140, -70\}, \{210, -50\}, \{300, 0\}.$$

Generator leading power factor ability curve coordinates are:

$$\{0, -130\}, \{80, -120\}, \{160, -110\}, \{200, -100\}, \{300, -60\}$$

The calculation process is as follow:

Both X_d^* and X_s^* use the generator's rated voltage and apparent power as benchmarks, and their standard values do not need to be converted. Loss of excitation protection impedance needs to be converted. Each impedance calculation formula is as follow:

$$Z_B = \frac{U_N^2}{S_N}, \quad X_c^* = \frac{X_c n_{TV}}{Z_B n_{TA}},$$

$$X_b^* = \frac{X_b n_{TV}}{Z_B n_{TA}}, \quad X_0^* = -\frac{X_b^* - X_c^*}{2},$$

$$R_0^* = \frac{X_b^* + X_c^*}{2}$$

The impedance plane is converted to the P-Q plane center coordinates

$$\left\{0, \frac{X_0^* U_g^{*2}}{X_0^{*2} - R_0^{*2}}\right\},$$

Radius is:

$$\frac{R_0^* U_g^{*2}}{R_0^{*2} - X_0^{*2}} \circ$$

The calculation results are shown in Figure 3~Figure 6.

As shown in Figure 3 that regardless of the operating error of the protection device, when system X_s operates in the minimum operating mode, generator U_g maintains the rated voltage, the curves maintain the correct matching relationship.

As shown in Figure 4, considering the protection parameter a +5% error, and U_g maintains the rated voltage, the loss of excitation protection curve is almost unmatched with the generator leading power factor ability curve.

As shown in Figure 5, when the other parameters remain unchanged and U_g decreases to 19KV, the loss of excitation protection curve actions precedes to the generator leading power factor ability curve, which is unmatched with the generator ability. Therefore, the verification should be performed when U_g is lower than the rated voltage. At this time, the setting impedance value of the loss of excitation protection setting should be reduced.

From the data of Figure 6, it can be seen that considering the -5% error of protection parameters, the radius of the impedance circle is smaller, the radius of the action circle in the P-Q plane becomes larger, the allowable leading power factor depth gets larger, and it is easier to match with the under excitation limit curve. Comparing with the data of Figure 3, the loss of excitation protection curve will be easier to get unmatched with the generator leading power factor ability curve at this time. Therefore, it is necessary to consider whether the protection curve is matched with the standard static stability circle when there is a negative error for the protection.

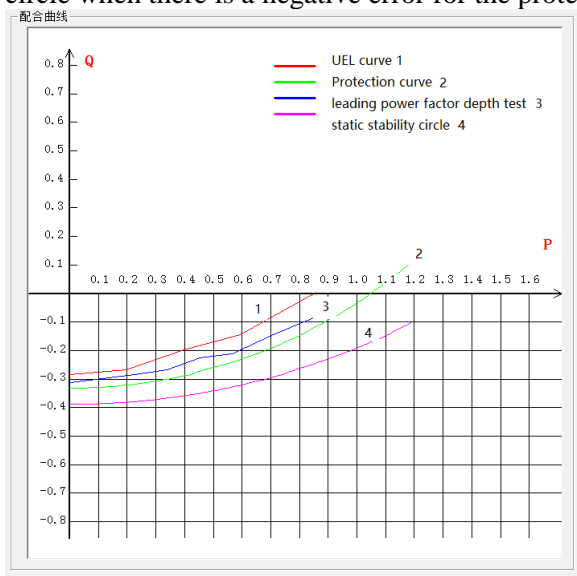


Figure 3 protection without deviation($X_c=8.55$, $X_b=85.49, U_g=20KV$)

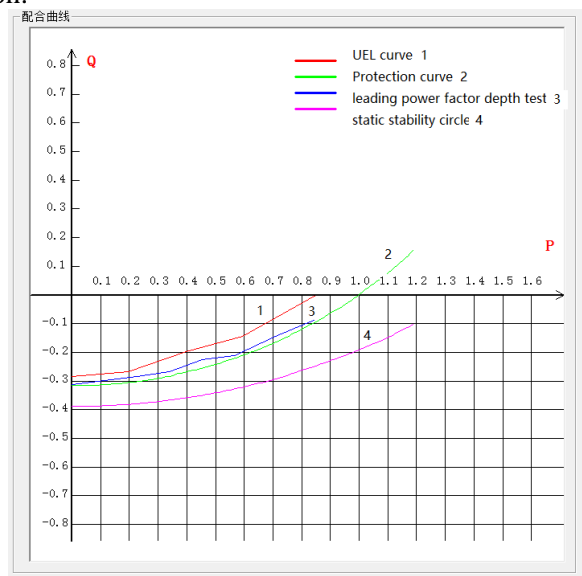


Figure 4 protection of +5% deviation($X_c=8.98$, $X_b=89.76, U_g=20KV$)

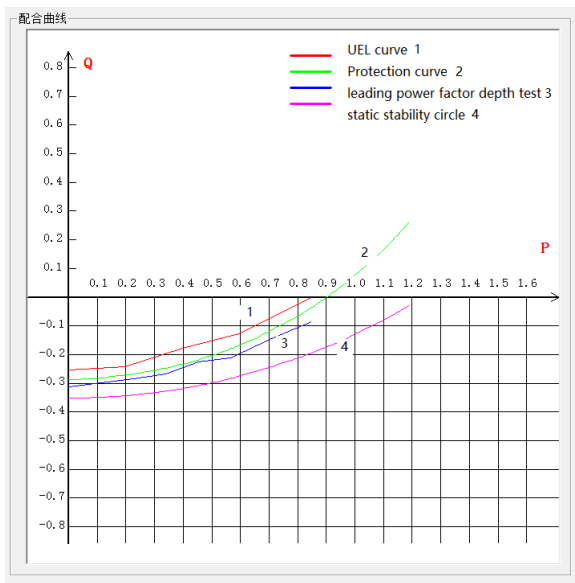


Figure 5 protection of +5% deviation($X_c=8.98$,
 $X_b=89.76$, $U_g=19KV$)

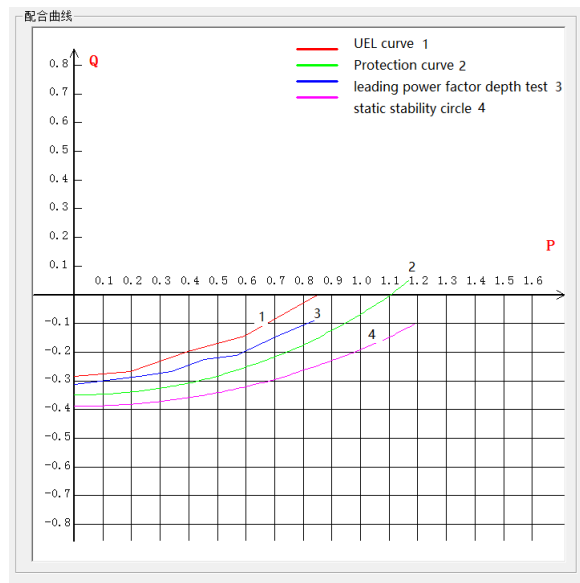


Figure 6 Protection of -5% deviation($X_c=8.12$,
 $X_b=81.22$, $U_g=20KV$)

4. Conclusion

This paper theoretically analyzes the influence of various parameter changes on the loss of excitation protection and the under excitation limit, and proposes to use the measured limit curve of the generator as the setting and coordination basis, and proposed the matching and check principle of under excitation limit and the loss of excitation protection based on the device operation error. The method of adjusting parameter when mismatching occurs is discussed. With a calculation of an engineering example, the influence of various parameter changes on the matching relationship is verified, and the effectiveness of the adjustment method is verified. The combination of the under excitation limit and the setting value of the loss of excitation protection and the checking method proposed in this paper provide a effective guiding principle for the current power plants to check and adjust the setting value of the under excitation limit and the loss of excitation protection. But the equations of salient pole synchronous generator for transformation of coordinate is much more complex and needs for further discussion.

5. References:

- [1] SONG Wei, LIU Guilin, WU Guoyang, SONG Xinli, LIU Yanjia. *Electric Power Automation Equipment* [J]. 2015, 35 (9):163-166.
- [2] XIAO Ming, SUN Chenghai, LUO Min, WANG Fengyue, LI Xuanxuan. Research on Coordination of Field Loss Protection and Low Excitation Limitation for Generators [J]. *Shandong Electric Power*, 2018, 2:49-51.
- [3] GUO Siyuan, LI Li, HONG Quan, LI Hui, LIU Haifeng, CAI Yuhua, ZHANG Mingqiang. Impedance Characteristics Analysis of Excitation-loss Protection for Hydro-generator [J]. *Hunan Electric Power*, 2017, 4:4-7
- [4] LI Xiquan, XIE Yanjun, CHEN Xiaoming, BI Xinying, FENG Xiaosong. Research and Practice in Matching Setting of Low Excitation Limit and Loss -of-Excitation Protection for Hydro Generator [J]. *Large Electric Machine and Hydraulic Turbine*, 2016, 1:59-61.
- [5] XU Yerong, BAO Minglei, LI Yuping, SANG Jianbin, LI Ming. Discussion on setting calculation of large steam turbine generator loss-of-excitation protection [J]. *Relay*, 2016, 20: 154-159.
- [6] LI Hui, LU Gong-qiang, WANG Yu-xue, HONG Xin, ZOU Jian, FENG Xiao-song. Discussion on coordination between loss of excitation protection and under excitation limit control for large hydro-generator [J]. *Relay*, 2014, 5:68-72.
- [7] Jia Wen-shuang, Yue Lei, Cuo Mu, Yang Yong-jun, Gao Jun. Matching Method of Loss-of-excitation Protection and Low Excitation Limitation for Generator [J]. *North China*

Electric Power, 2013, 1:11-14.

- [8] GUO Chunping, YU Zhen, YIN Xiutao. Coordinative Setting Calculation of Minimum-excitation Limit and Loss-of-excitation Protection for Generator [J]. *Proceedings of the CSEE*, 2012, 28:129-132.

Acknowledgments

This work was supported by Science & Technology Project of State Grid Electric Power Corporation in China (Project name: Research on Synchronous condenser and HVDC converter station reactive power compensation device coordinate control strategy).

Impact of Wind Generators Number and Location on the Resonance Risk of Wind Farm Integration through Flexible HVDC System

Xiao Wang^{1,3}, Xiaobao Hu^{1,2}, Hui Liu^{1,3}, Linlin Wu^{1,3} and Siqing Sheng²

¹ State Grid Jibei Electric Power Co. Ltd. Research Institute, North China Electric Power Research Institute Co. Ltd., Beijing, China

² Department of Electrical and Electronic Engineering, North China Electric Power University, Baoding, China

³ Grid-connected Operation Technology for Wind-Solar-Storage Hybrid System State Grid Corporation Key Laboratory, Beijing, China
E-mail: 1465951274@qq.com

Abstract. Resonances or instability phenomena may occur in wind farms integration through a flexible HVDC transmission system. The relationship between the resonance risk and wind turbines number under different lengths of the line from wind farms to the flexible HVDC converter station is studied in this paper. First, the effect of the line length on the impedance characteristics of interconnected system is analyzed, and the aggregated RLC circuit approach is applied for the quantitative assessment of potential resonance risk. Then, the variation trend of system impedance characteristics caused by different wind turbines number is revealed, and resonance risk affected by the number of wind turbines integrated from the different location is evaluated by calculating system resonance damping around the resonant frequency. Finally, the simulation results on the RT-LAB platform validate the theoretical analysis.

1. Introduction

In recent years, the renewable energy represented by wind power has been developed rapidly, and the regional power system with a high proportion of renewable energy is gradually formed. However, the renewable energy generators are connected to the power grid directly or indirectly by the power electronic converter, while the interaction between converters and power grid may cause resonances or instability problems. The interaction between the wind turbines and the series-compensated system caused sub-synchronous resonances of 3~10Hz in the Hebei Guyuan district of China in 2011. The sub-synchronous resonances of 20~40Hz involving wind turbines occurred in Xinjiang Hami district of China in 2015. The resonance phenomena at hundreds of Hertz appeared in the German North Sea wind farms connected to the onshore ac grid through flexible HVDC transmission system, when the filter capacitors of converter station was damaged in 2014.

Many scholars have conducted extensive research on the resonance mechanism caused by the interaction between wind farms and weak ac power grid or series-compensated system. The reason for the resonance of wind farms connected by weak ac system is wind turbines behave as a “capacitive reactance with a negative resistance” at the resonant frequency, whose interaction with the AC grid (considered as inductance) constitutes the L-C-R resonance circuit and negative resistance effect will lead to risky resonance phenomenon [1]-[3]. Similarly, the resonance phenomenon of the doubly-fed wind power plants connected by series-compensated lines is induced by negative damping



characteristics, which is an induction generator effect involving the controller of wind turbine [4], [5]. Literatures [1], [6]-[7] established the model of type-III and type-IV wind turbines respectively connected to the ac power grid, and pointed out that the weaker the strength of ac system (the longer the connection line), the more unstable the system is. Further, the influence of the grid-connected wind turbines number on the system stability was studied in [4]-[5], [8]-[9], and it was pointed out that the risk of system resonance increases with the increase of the wind turbines number.

At present, the complicated resonance mechanism caused by the interaction of multiple power electronic equipment in the system of wind farms integration via flexible HVDC transmission system is a research hot spot. Literature [10] reported a sub-synchronous oscillation phenomenon of doubly-fed induction generator (DFIG) integration via an MMC-based HVDC system, analyzed the distribution and transmission mechanism of subsynchronous oscillation current in HVDC system. The effect of control parameters of flexible HVDC control loop, wind turbine converter current loop and phase lock loop (PLL) on the system stability was studied in [11], where it is pointed that accelerating the control speed of flexible HVDC or slowing down the control speed of the PLL can improve the system stability. It was further proposed that system resonance is aroused when the control bandwidth of VSC-HVDC converter is less than the wind turbine converter [12]. Moreover, the stability margin of the interconnection system is influenced by circulation control of flexible HVDC consisting of modular multilevel converter [13]. However, there is little research on the comprehensive influence of connected line length and integrated wind turbines number on the stability of HVDC-connected wind farms.

It is studied that the impact of wind generators number and location on the resonance risk of wind farm integration through flexible HVDC system in this paper. First, the system model consisting of doubly-fed induction generators integration via two-terminal MMC-HVDC is built. Using the equivalent circuit damping stability criterion, the change of the impedance characteristics of interconnected systems under the condition of different line lengths is analyzed. Further, the potential resonance risk is evaluated by introducing resonance damping parameter based on the aggregated RLC fitting method. Taking the wind turbines number and location into account, the equivalent RLC circuit parameters under a variety of conditions are calculated, then the variation trend system resonance frequency is analyzed and the resonances risk is evaluated quantitatively. Finally, the same simulation model is built on the RT-LAB platform and the simulation results validate the theoretical analysis.

2. Interconnection system model

The typical topology of wind power integration via flexible HVDC is shown in figure 1. The flexible dc transmission system is two-terminal MMC-HVDC structure including MMC converter, converter transformer and dc line. Wind farm is made up of doubly-fed induction generators and box-type transformers, which can be modelled by single machine polymerization. The wind farm connect to Point of Common Coupling (PCC) by step-up transformer and ac line. The terminal ac power grid can be realized by using Thevenin equivalent modelling.

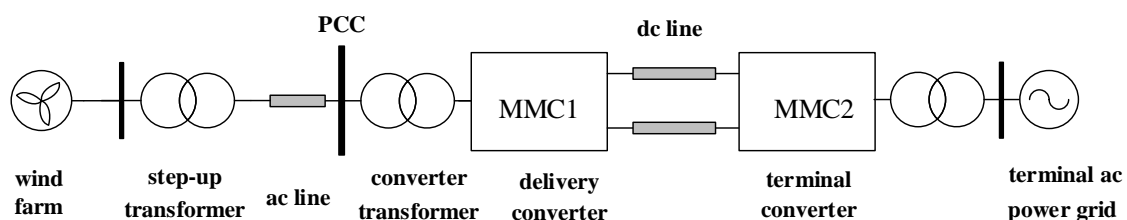


Figure 1. Topology structure of wind farms integration via an MMC-based HVDC system

3. Influence analysis on the length of line

3.1. Impedance characteristics analyses

Taking PCC as a demarcation point, the interconnection system can be divided into the wind turbine subsystem and MMC-HVDC subsystem. Impedance analysis is used to analysis the impedance

characteristics of interconnected systems. The different lengths of line may have impact on the impedance characteristics of interconnected system. With the number of wind turbines set to 700, we change the length of the line gradually and observe its effect on the impedance characteristics of system. The equivalent impedance characteristics of interconnected systems in the range of 250 to 450Hz is shown in figure 2. The dashed line indicates the equivalent impedance amplitude of the MMC-HVDC subsystem $|Z_W|$, and the dash-dotted line indicates the equivalent impedance amplitude of the wind turbine subsystem $|Z_M|$, the solid line represents the equivalent resistance of the interconnection system R_Σ . According to the equivalent circuit damping stability criterion [14], the equivalent resistance R_Σ of the interconnection system is negative at two resonance points, at this point, the system is in an unstable state.

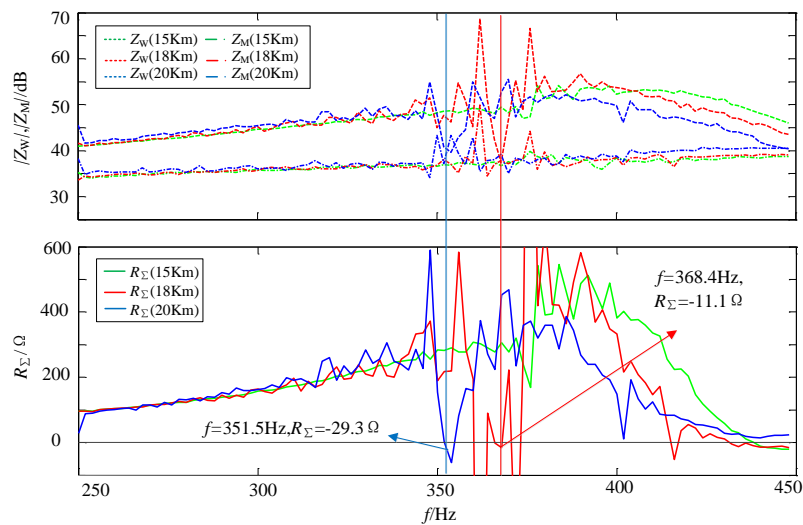


Figure 2. The impedance characteristics of system with different line lengths

As shown in figure 2, the variation of line length can change the impedance characteristics of the system, and the interconnected system become negative damping resonance condition when the length increased to 18 km. With the length of line further increased, the resonance frequency continues to decrease.

3.2. Resonance risk evaluation

In order to evaluate the resonance risk of the system quantitatively, the method in literature [9] is used. According to literature [9], impedance-versus-frequency curves can be approximated with a second-order series RLC circuit model in a very small frequency range. The characteristics of resonance can be effectively determined by the circuit parameters, i.e. R , L and C . The damping σ and resonance frequency ω of the circuit, or of the resonance, can be computed by:

$$\sigma = \frac{R}{2L} \quad \omega = \left(\frac{1}{LC} - \left(\frac{R}{2L} \right)^2 \right)^{1/2}$$

Obviously, if $R > 0$, σ is positive, indicating the system has positive damping and resonance is stabilized; otherwise, unstable resonance will occur.

With the wind turbines number set to 700, we change the length of the line gradually and observe its effect on the characteristics of resonance and evaluate the resonance risk. Table 1 shows the RLC second-order circuit parameters of the fitted impedance frequency curve when the length of the line changes.

As shown in table 1, if line length is increased to 18 km, the interconnected system began to oscillate. With the line length further increased, the resonance frequency continues to decrease, then the resonance risk increases.

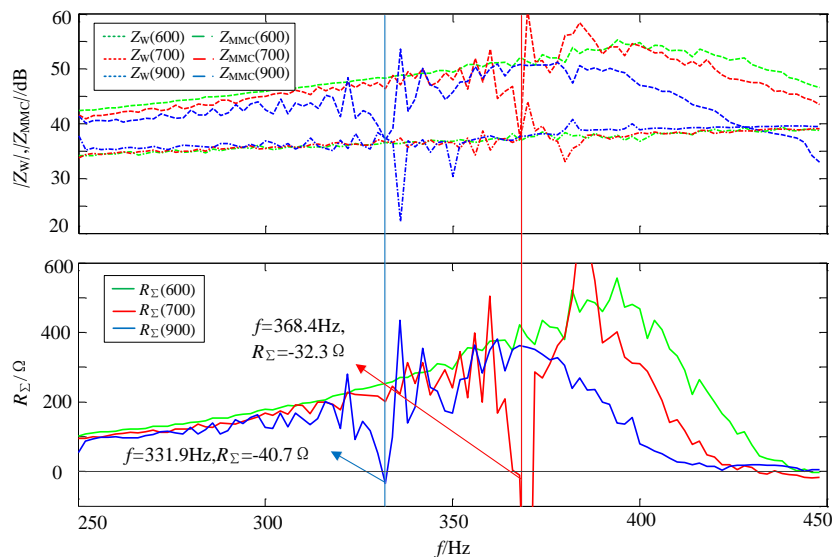
Table 1 Parameters of the aggregated RLC circuit model and resonance

Length of line	Circuit parameters			Resonance parameters	
	R	L	C	σ	ω
15	+	NaN	NaN	NaN	NaN
16	+	NaN	NaN	NaN	NaN
17	+	NaN	NaN	NaN	NaN
18	-11.1059	67.2727	1.09E-07	-0.0825	368.4791
19	-17.5231	39.1840	1.78E-07	-0.2236	360.5519
20	-29.3844	43.0225	2.06E-07	-0.3415	351.5429

4. Influence analysis on the number of wind turbines

4.1. Impedance characteristics analyses

With the length of the line set to 18 km, we change the wind turbines number gradually and observe its effect on impedance characteristics of system. The impedance characteristics of interconnected systems with different wind turbines number in the range of 250 to 450Hz is shown in figure 3. The variation of wind turbines number can change the impedance characteristics of the system. If the line length is 18 km and wind turbines number increased to 700, the interconnected system becomes negative damping resonance condition around the resonance frequency. With the wind turbines number further increased, the resonance frequency continues to decrease.

**Figure 3** The impedance characteristics of system with different wind turbines number

4.2. Comprehensive resonance risk evaluation considering location factors

To evaluate the influence of wind turbines number and line length on the resonance risk of interconnected system, aggregated RLC circuit parameters are fitted by the impedance frequency curve of the system under different wind turbines number and line length. The resonance frequency ω and resonance damping σ are shown in table 2 and table 3.

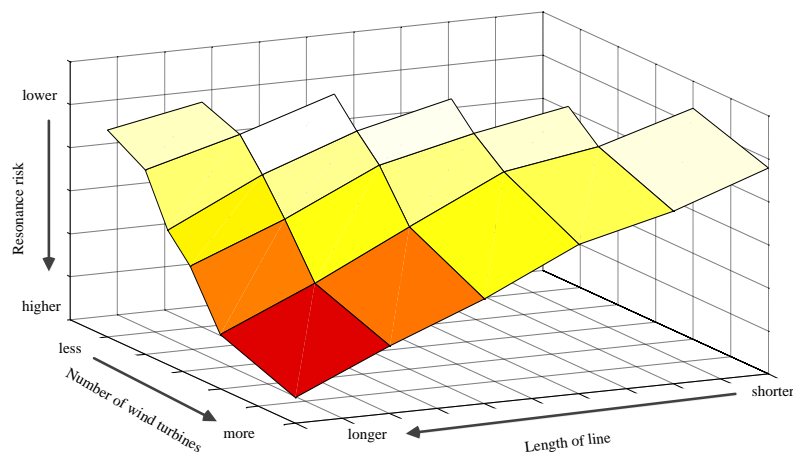
As shown in table 2 and table 3, resonance phenomenon will occur when wind turbine number or line length is increased and the resonance frequency is near 350Hz in unstable region. In the stable area with fewer wind turbines number and shorter line length, there is no such resonance mode in the interconnection system. In the resonance region, the resonant frequency and the resonant damping decrease with the increase of wind turbine number and the line length. The influence trend of wind turbines number and line length on system resonance risk is shown in figure 4, which are positively correlated.

Table 2 The resonance frequency ω with different wind turbines number and line lengths

Wind turbines number	Length of line (Km)					
	15	16	17	18	19	20
500	NaN	NaN	NaN	NaN	NaN	NaN
600	NaN	NaN	NaN	NaN	NaN	371.3421
650	NaN	NaN	NaN	NaN	370.9327	360.0527
700	NaN	NaN	NaN	368.44	360.5519	351.5249
730	NaN	NaN	364.8341	360.3511	356.6492	348.4553
760	NaN	365.003	361.1206	351.3871	351.3871	345.096
800	358.5092	353.6716	348.4375	346.6751	342.095	338.4791
900	341.3561	336.9012	334.6977	331.9766	330.6015	327.1952

Table 3 The resonance damping σ with different wind turbines number and line length

Wind turbines number	Length of line (Km)					
	15	16	17	18	19	20
500	NaN	NaN	NaN	NaN	NaN	NaN
600	NaN	NaN	NaN	NaN	NaN	-0.104
650	NaN	NaN	NaN	NaN	-0.1526	-0.2374
700	NaN	NaN	NaN	-0.0825	-0.2236	-0.3415
730	NaN	NaN	-0.1025	-0.2051	-0.363	-0.5753
760	NaN	-0.1349	-0.214	-0.3165	-0.5207	-0.693
800	-0.126	-0.2579	-0.328	-0.583	-0.7554	-0.947
900	-0.2436	-0.3947	-0.5048	-0.7139	-0.8852	-1.08

**Figure 4** The influence trend of wind turbines number and line length on system resonance risk

5. Simulation verification

To verify the correctness of the above analysis, the interconnection system model shown in Fig 1 is built on the real-time simulation platform of RT-Lab, whose parameters refer to literature [14]. The waveforms of simulation adjusting the wind turbines number and the line length are shown in Figure 5, which are consistent with impedance analysis and circuit fitting analysis.

The system is stable with 700 DFIGs and 15 km line as shown in figure 5 (a). The resonance phenomenon occur with the length of line increased to 18 km, and the current of phase a through the interconnection system PCC point contains 2.3% of the 368Hz harmonic components, as shown in figure 5 (b). On the basis of 18 km line, with wind turbines number increased to 900, the current of phase a through the interconnection system PCC point contains 2.8% of the 332Hz harmonic

components as shown in figure 5 (c), where the resonance is more serious and the resonance frequency is lower in contrast to figure 5 (b). Under the condition of interconnection system with 900 DFIGs and 20 km line as shown in figure 5 (d), the current of phase a through PCC point contains 3.2% of the 328Hz harmonic components, where resonance phenomenon is the most serious and the resonance frequency is lowest.

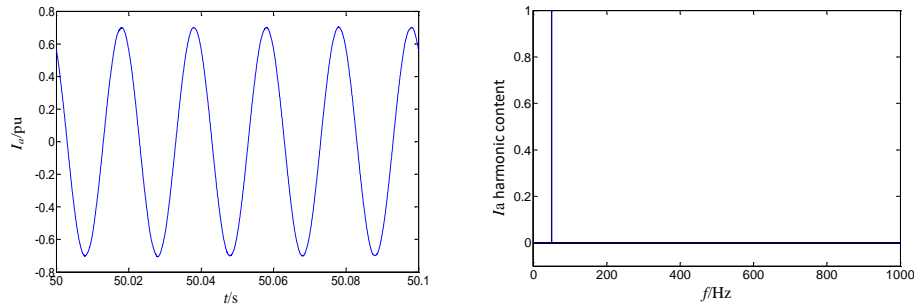


Figure 5 (a) The current waveform and spectrum characteristic of phase a at the PCC point for the interconnection system with 700 DFIGs and 15 km line.

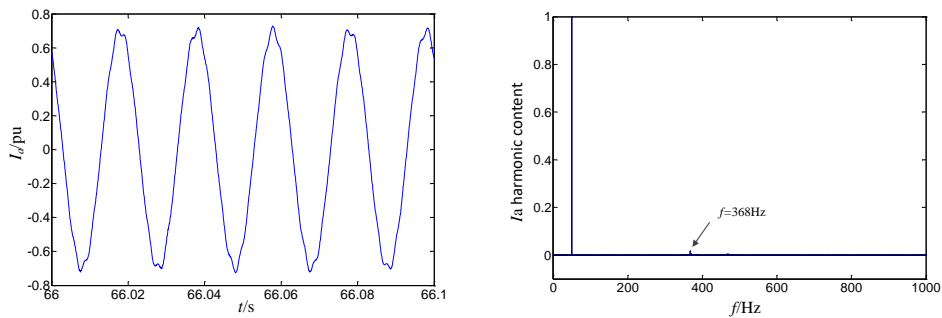


Figure 5 (b) The current waveform and spectrum characteristic of phase a at the PCC point for the interconnection system with 700 DFIGs and 18 km line.

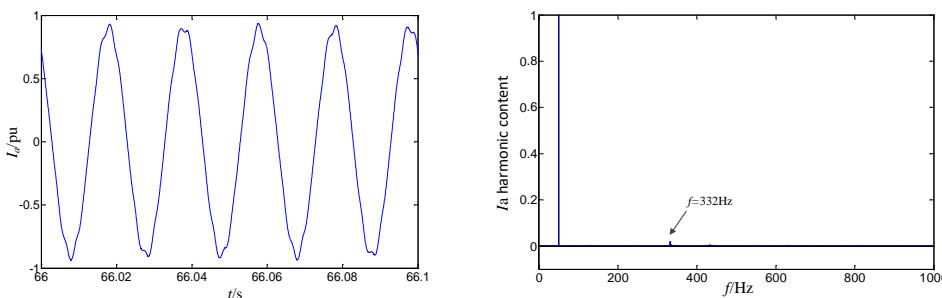


Figure 5 (c) The current waveform and spectrum characteristic of phase a at the PCC point for the interconnection system with 900 DFIGs and 18 km line.

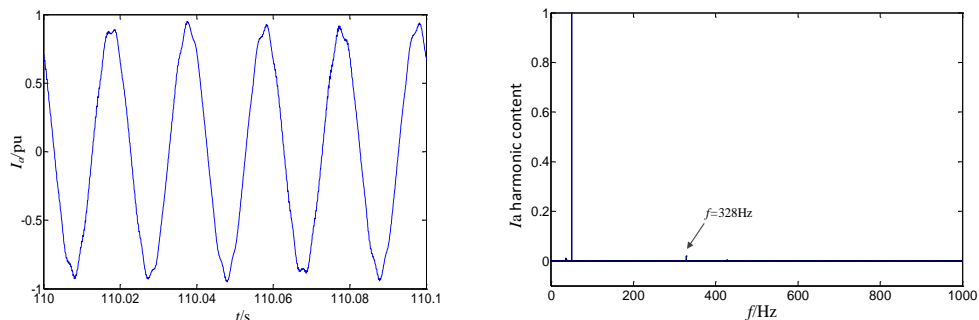


Figure 5 (d) The current waveform and spectrum characteristic of phase a at the PCC point for the interconnection system with 900 DFIGs and 20 km line.

6. Conclusion

As the research background based on doubly-fed induction generators integration via a two-terminal MMC-HVDC system, the influence of wind turbines number and connected line length on the resonance risk is studied. By the impedance analysis and time domain simulation, the resonance frequency decreases with the line length increased, while the resonance damping becomes small. In the case of fixed wind farm location, the more wind turbines number is, the less stability margin of the system is. If the wind turbines are too many and far away from the HVDC converter station, the system is difficult to operate stably. Therefore, large wind farms with more wind turbines should be planned and constructed closer to the flexible HVDC converter station for the stability requirement of the interconnection system. The influence of wind speed and multiple wind farms on the resonance characteristics of the system will be considered more comprehensively in subsequent studies.

7. References

- [1] Xie Xiaorong, Liu Huakun, He Jingbo, et al. 2016 Mechanism and Characteristics of Subsynchronous Oscillation Caused by The Interaction Between Full-Converter Wind Turbines and AC Systems *J Proc of the CSEE* **36(9)**: 2366-72
- [2] Xie Xiaorong, Wang Luping, He Jingbo, et al. 2017 Analysis of Subsynchronous Resonance Oscillation Types in Power Systems *J Power system Technology* **41(4)**: 1043-49
- [3] Li Mingjie, Yu Zhao, Xu Tao, et al. 2017 Study of Complex Oscillation Caused by Renewable Energy Integration and Its Solution *J Power System Technology* **41(4)**: 1035-42.
- [4] Wang Liang, Xie Xiaorong, Jiang Qirong, et al. 2014 Analysis and Mitigation of SSR Problems in Large-Scale Wind Farms with Doubly-Fed Wind Turbines *J Automation of Electric Power Systems* **38(22)**: 26-31
- [5] Dong Xiaoliang, Xie Xiaorong, Yang Yu, et al. 2015 Impacting Factors and Stable Area Analysis of Subsynchronous Resonance in DFIG Based Wind Farms Connected to Series-compensated Power System *J Power System Technology* **39(1)**: 189-193
- [6] Esmaeil Ebrahimzadeh, Frede Blaabjerg, Wang Xiongfei, et al. 2016 Modeling and Identification of Harmonic Instability Problems in Wind Farms *C IEEE Energy Conversion Congress and Exposition* pp 1-6
- [7] Jiabing Hu, Yunhui Huang, Dong Wang, et al. 2015 Modeling of Grid-Connected DFIG-based Wind Turbines for DC-Link Voltage Stability Analysis *J IEEE Transactions on Sustainable Energy* **6(4)**: 1325-36
- [8] Dong Xiaoliang, Tian Xu, Zhang Yong, et al. 2017 Practical SSR Incidence and Influencing Factor Analysis of DFIG-based Series-compensated Transmission System in Guyuan Farms *J High Voltage Engineering* **43(1)**: 321-328
- [9] Liu Huakun, Xie Xiaorong, Zhang Chuanyu, et al. 2017 Quantitative SSR Analysis of Series-compensated DFIG-based Wind Farms Using Aggregated RLC Circuit Model *J IEEE Transactions on Power Systems* **32(1)**: 474-483
- [10] LüJing, Dong Peng, Shi Gang, et al. 2015 Subsynchronous Oscillation and Its Mitigation of MMC-based HVDC with Large Doubly-fed Induction Generator Based Wind Farm Integration *J Proc of the CSEE* **35(19)**: 4852-60
- [11] Liu H, Sun J. 2014 Voltage Stability and Control of Offshore Wind Farms with AC Collection and HVDC Transmission *J IEEE Journal of Emerging & Selected Topics in Power Electronics* **2(4)**: 1181-89.
- [12] Amin M, Molinas M. 2017 Understanding The Origin of Oscillatory Phenomena Observed between Wind Farms and HVDC Systems *J IEEE Journal of Emerging & Selected Topics in Power Electronics* **5(1)**: 378-392.
- [13] Lyu J, Cai X, Molinas M. 2016 Frequency Domain Stability Analysis of MMC-based HVDC for Wind Farm Integration *J IEEE Journal of Emerging & Selected Topics in Power Electronics* **4(1)**: 141-151.

- [14] WANG Xiao, LIU Hui, HU Xiao-bao, et al. 2018 Analysis of Risk and Impacting Factors of Oscillation in Wind Farms Integration via A Flexible HVDC System Based on Equivalent Circuit Damping Stability Criterion J *Global Energy Interconnection* (**1**):48-55.

Acknowledgments

This paper is partly supported by the national R&D project (A comprehensive demonstration project for smart grid supporting low-carbon winter Olympics, 2016YFB0900500) and State Grid Corporation of China Headquarter technology project (52010118000L)

Small-Signal Modelling and Stability Analysis of Current-Controlled Virtual Synchronous Generators

D W SUN^{1,2}, H LIU^{1,2}, P SONG^{1,2}, S ZHU³ and Z WEI⁴

¹State Grid Jibei Electric Power Co. Ltd. Research Institute, Beijing, China

²Grid-connected Operation Technology for Wind-Solar-Storage Hybrid System State Grid Corporation Key Laboratory, Beijing, China.

³Zhangjiakou Wind and Solar Power Energy Demonstration Station Co. Ltd. Zhangjiakou, China

⁴Nari Solar Energy Technology Co. Ltd., Nanjing, China

E-mail: dddd129216713@126.com

Abstract. Virtual Synchronous Generators (VSG), as an effective mean to improve the frequency and voltage regulation ability of the renewable power, had aroused wide concern. Researchers have proposed several VSG implementations, which can be classified into two categories: voltage-controlled VSG and current-controlled VSG. Voltage-controlled VSG have been extensively studied. However, few researches focused on current-controlled VSG. In this paper, we concentrated on the current-controlled VSG and its stability problem. Firstly, a small-signal model of current-controlled VSG was established to identify the oscillation modes of grid-connected VSG system. Moreover, the developed model was used to investigate damping characteristics of the system under various scenarios and with different control parameters. The results revealed that stability of VSG system was sufficiently impacted by virtual inertia and phase lock loop in VSG. Under some unfavourable conditions, current-controlled VSG would contribute to high-frequency or subsynchronous oscillation.

1. Introduction

Renewable power generators (RPG) based on wind and photovoltaic are developing rapidly in recent years and the percentage of RPG connected to the grid is in growing [1]. As the interface between RPG and the grid, the grid-connected inverter is not able to provide inertia and damping for the power system [2]. The increasing of RPG and grid-connected inverters will cause stability problems in power grid because of the lack of inertia and damping [3]. To solve this problem, virtual synchronous generator (VSG) technology was proposed to control the grid-connected inverter to emulate the essential behaviour of synchronous generators [4], including the droop mechanism and inertial characteristic [5].

Recently, some researches have been conducted on VSG technology. Technical route and stability problem of VSG are two important research directions. For the first direction, existing studies proposed two different technical routes, which are voltage-controlled and current-controlled VSG [6]-[9]. Refer to the stability of VSG, researches concentrated on the risk of oscillation caused by voltage-controlled VSG [10]-[12] discussed the small-signal stability of current-controlled VSG, which was applied in photovoltaic power generator in microgrid. A method was proposed in [13] to improve the oscillation damping by optimizing the control parameters of VSG. This method was designed for voltage-controlled VSG in microgrid. The oscillation mechanism in parallel operations of voltage-controlled VSGs was clarified in [14], which also analysed the influence from parameters of VSG to



oscillation mode. The existing studies mainly concentrated on the stability problem of voltage-controlled VSG. However, the same problem for current-controlled VSG has not been researched.

The analysis of current-controlled VSG stability faced the difficulty of modelling phase lock loop (PLL). The difficulty can be summarized as the following two aspects:

1. There is a big difference between the small-signal model of current-controlled VSG and the model of voltage-controlled VSG. Because voltage-controlled VSG has no PLL, it is not necessary to model PLL [10]-[12]. However, PLL performs an important role in current-controlled VSG. Because PLL has a significant influence on stability of grid-connected current-controlled VSG, it is essential to model the PLL in detail.

2. The model of current-controlled VSG is significantly different from the model of traditional inverter or inverter equipped with droop control [13]. In traditional inverter, PLL provides phase angle to Park transformation [14]. In the inverter equipped with droop control, PLL also sends frequency signal to droop control. However, in current-controlled VSG, PLL not only offers the signal of phase angle and frequency to Park transformation and droop control, but also gives the rate of change of frequency (ROCOF) to the virtual inertia control in VSG. Therefore, the PLL in current-controlled VSG should be modeled accurately.

Besides the above observations, it is worth noting that no prior research on the oscillation problem of current-controlled VSG, which has been adopted in the widely employed grid-connected RPG. To address these issues, this paper investigates the small-signal stability of current-controlled VSG.

The rest of this paper is organized as follows: In Section II, the small-signal model is established for a grid-connected current-controlled VSG system. The damping characteristics of VSG system are analysed in Section III. The developed model is used in Section IV to investigate characteristics of all oscillation modes with control parameters. In Section V, the stability of VSG system is identified under various system scenarios. Finally, brief conclusions are drawn in Section VI.

2. Small-signal model of the VSG

An overview of the studied grid-connected current-controlled VSG system is shown in figure 1, where an inverter is connected to a grid at the point of common coupling (PCC) through an LC filter. R_1, L_1 denote the grid impedance at the PCC. The VSG-based inverter control has five functional modules, namely filter processing, PLL, power control, reactive power control and current control.

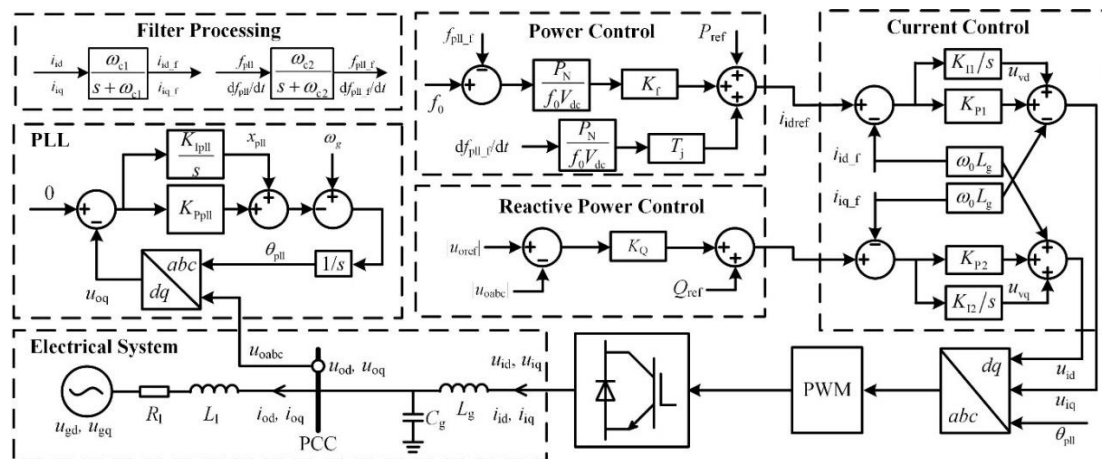


Figure 1. The studied grid-connected current-controlled VSG system

In figure 1, all three phase variables have been transformed into Synchronous Reference Frames (SRFs) based on the amplitude-invariant Park transformation [9]. It is clarified that the entire system is implemented in a SRF defined by the angular position θ_{pll} , which is the phase angle locked by PLL.

2.1. Electrical system

The linearized small-signal model of VSG system can be presented by (1).

A steady-state point with an active power reference of 1 pu, resulting in i_{id} and f_{pll} equal to 1 pu and 50 Hz respectively, is used for the validation. At time $t=0s$, the power reference is stepped up to the value of 1.1 pu in both of the small-signal and simulation models. Comparisons of the response obtained with both models are shown in figure 2.

The results of figure 2 clearly show that the i_{id} and f_{pll} of the VSM, which can be calculated from the state variables of the small-signal model, are coinciding with the results from the nonlinear simulation model. Thus, the presented results sufficiently demonstrate that the small-signal model is able to accurately capture the dynamic response of the system.

3. System eigenvalue analysis

Based on the proven small-signal model of VSG, the eigenvalues of the A matrix can be calculated to systematically identify the oscillation modes and accurately evaluate the stability of VSG system.

Table 2 lists all the system eigenvalues for the steady-state operating point, where the reference values of active and reactive power are set as 1.0 pu and 0. The state variables of highly sensitive to the relevant eigenvalue are also presented in table 2.

Table 2. System eigenvalues

No.	Real part of eigenvalues	Oscillation frequency/Hz	Damping	State variables of highly sensitive
λ_{1-2}	-69.7	2873	1.7×10^{-4}	$u_{od}, u_{oq}, i_{od}, i_{oq}$
λ_{3-4}	-157.9	2862	3.2×10^{-4}	$u_{od}, u_{oq}, i_{od}, i_{oq}$
λ_{5-6}	-1711.6	400	0.56	$i_{id}, i_{iq}, i_{id_f}, i_{iq_f}$
λ_{7-8}	-1424.1	350	0.54	$i_{id}, i_{iq}, i_{id_f}, i_{iq_f}$
λ_{9-10}	-6.01	0.022	0.99	u_{vd}, u_{vq}
λ_{11-12}	-5.01	6.95	0.22	x_{pll}, θ_{pll}
λ_{13-14}	-62.84, -62.83	0	1	$f_{pll_f}, df_{pll_f}/dt$

As shown in table 2, eight oscillation modes were identified corresponding to 14 eigenvalues. All the real parts of eigenvalues are negative, which clarifies that the system is stable with the parameters and operating conditions specified in Table 1. For a further discussion in the oscillation characteristics of VSG system, the poorly damped eigenvalue will be of most interest. From table 2, it can be noticed that λ_{1-2} are the complex conjugate poles of most poorly damp. We placed emphasis on the eigenvalue trajectory of λ_{1-2} in the following sections.

4. Impact of VSG control parameters on stability

For systematically analyzing the impact of VSG control parameters on stability, the parameters are classified into 3 groups: (1) control parameters relevant to VSG function and (2) parameters of PLL. The influence from these three catalogs of parameters are introduced successively in the next subsections.

4.1. Control parameters relevant to VSG function

4.1.1. Virtual mechanical time constant T_j .

The eigenvalue trajectory of the system when sweeping the virtual mechanical time constant T_j from 0.01 to 10 is shown in figure 3.

From figure 3(a), it is observed that λ_{1-2} monotonously move toward the right when T_j increases. The opposite trend appears for λ_{3-4} . No such obvious relationship can be found for the other eigenvalues. This observation proves that the oscillatory eigenvalues (λ_{1-4}) associated with the LC filter of inverter are strongly influenced by T_j , which directly impacts the damping of high-frequency oscillation mode in the system.

The results from figure 3(b) demonstrates that the damping of oscillation mode corresponding to λ_{1-2} decreases rapidly when T_j increases. When T_j exceeds 0.27s, VSG will produce negative damping that is sufficient to cause unstable high-frequency oscillation.

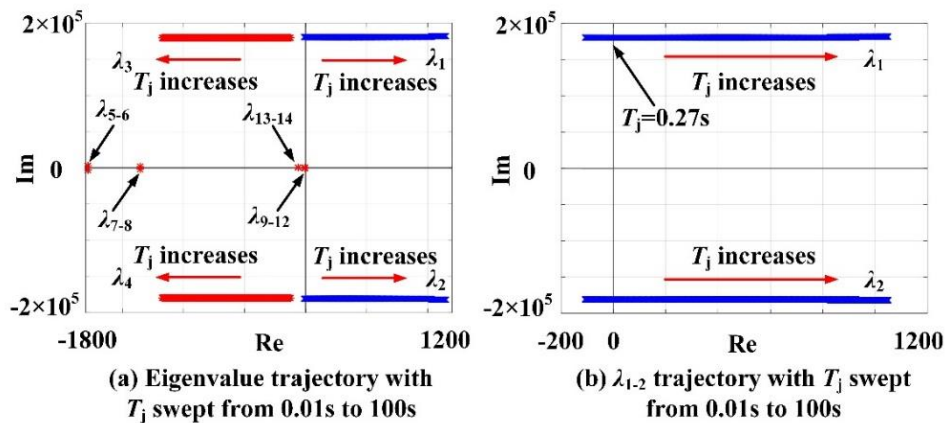


Figure 3. Influence from T_j to eigenvalues

4.1.2. The droop coefficient of power control K_f

The eigenvalue trajectory with K_f swept from 5 to 20 is given by figure 4.

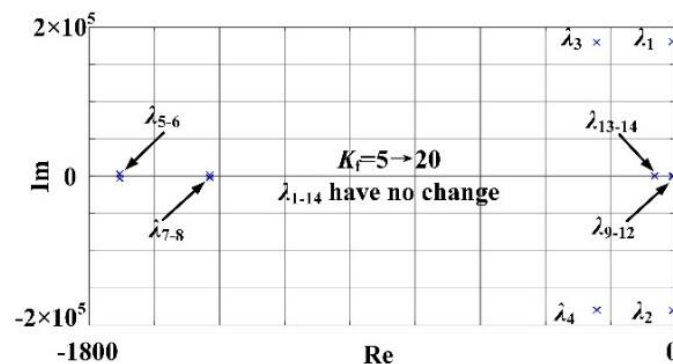


Figure 4. Influence from K_f to eigenvalues

It is obvious that the system eigenvalues have no change in figure 4, which indicates that the change of K_f has little impact on the damping characteristic of VSG system.

From figure 3 and 4, it can be noticed that, T_j has a stronger influence than K_f on VSG system stability. This observation is opposite to that of the voltage-controlled VSG [10]. The diverse impact from T_j and K_f can be explained through the different roles T_j and K_f plays in VSG control. Because ROCOF is considerably larger than frequency difference under small-signal deviation around the point of linearization, T_j , which is corresponding to ROCOF, is more influential than K_f , which is relevant to frequency difference.

4.2. Parameters of PLL

4.2.1. Proportion coefficients of PLL K_{Ppll}

The eigenvalue trajectory of the system when sweeping the proportion coefficients of PLL K_{Ppll} from 1 to 100 is shown in figure 5.

From figure 5(a), it can be seen that λ_{1-2} move toward the right as K_{Ppll} increases. In contrast, λ_{3-4} and λ_{13-14} move to the left. The other eigenvalues are insensitive to the change of K_{Ppll} .

Figure 5(b) indicates that the damping of oscillation mode corresponding to λ_{1-2} declines when K_{Ppll} increases. Unstable high-frequency oscillation will appear in VSG system when K_{Ppll} exceeds 26.

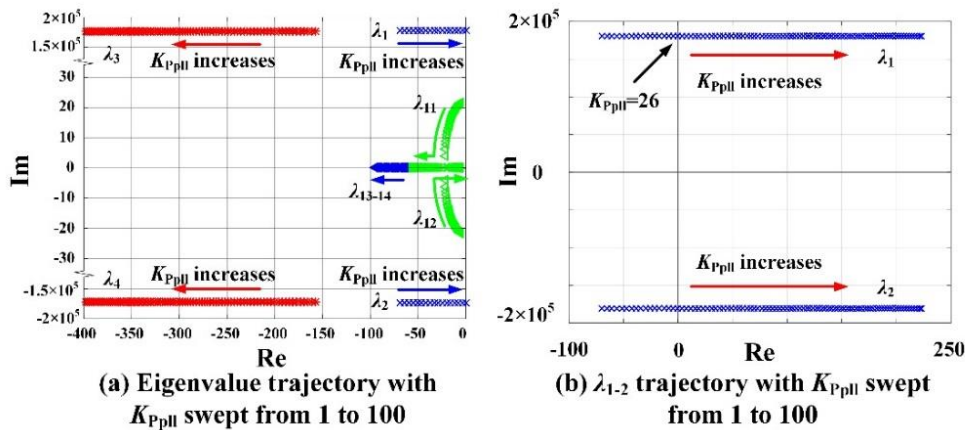


Figure 5. Influence from K_{Ppll} to eigenvalues

4.2.2. Integral coefficients of PLL K_{Ipll} .

The eigenvalue trajectory of the system when sweeping the proportion coefficients of PLL K_{Ipll} from 500 to 1 is shown in figure 6.

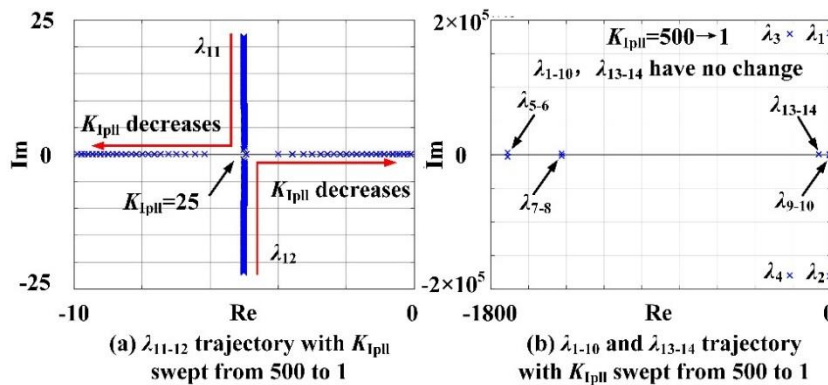


Figure 6. Influence from K_{Ipll} to eigenvalues

From figure 7(a), it can be noted that λ_{11-12} move toward the x-axis as K_{Ipll} grows initially. When K_{Ipll} is above 25, λ_{12} begins to move toward the origin, but will not go over y-axis.

Figure 7(b) illustrates that, except for λ_{11-12} , the system eigenvalues have no change, which indicates that the change of K_{Ipll} has rare influence on the stability of VSG system.

5. Adaptation of VSG to various grid conditions

For systematically analyzing the adaptation of current-controlled VSG, the damping characteristics of VSG system are investigated under various conditions, for instance, different voltage levels and grid impedances.

5.1. Impact of voltage level on stability

As the ratio of ac grid resistance (R_1) and reactance (X_1) in figure 1, $r_{R/X}$ is defined by (2).

$$r_{R/X} = R_1 / X_1 = R_1 / (L_1 \times 100 \times \pi) \tag{2}$$

Where L_1 denote grid inductance.

The value of $r_{R/X}$ can reflect the voltage level of ac system because a smaller $r_{R/X}$ will accordingly appear in a higher voltage power grid. Corresponding to voltage levels of 10kV and 500kV, the typical values of $r_{R/X}$ are 6 and 0.1 respectively. For studying the system stability under most kinds of voltage levels, the eigenvalue trajectory when sweeping $r_{R/X}$ from 0.1 to 6 is shown in figure 8.

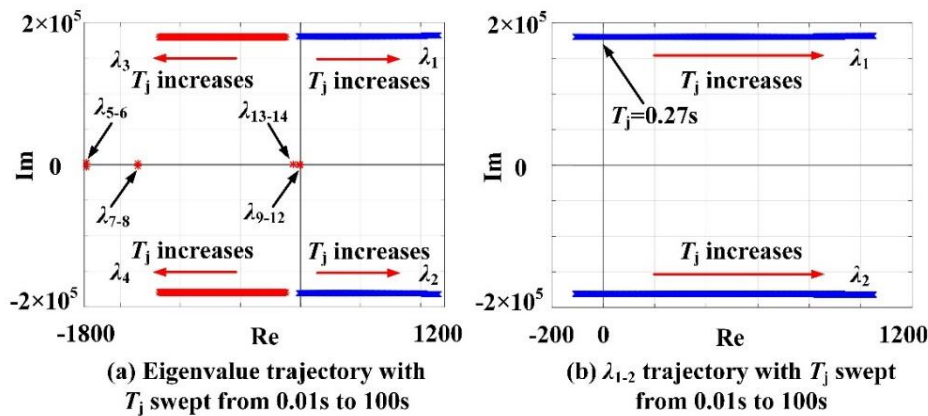


Figure 7. Influence from T_j to eigenvalues

From figure 7, it is observed that λ_{1-4} monotonously move toward the right when $r_{R/X}$ decreases. The other eigenvalues are insensitive to the change of $r_{R/X}$. This observation can be explained by that the real parts of λ_{1-4} are closely relevant to damping characteristic of the connected ac system. The reducing of $r_{R/X}$ will diminish the grid resistance, which develops a negative effect on the damping characteristic.

Therefore, the stability margin will be negatively affected when current-controlled VSG is connected to a high voltage power grid whose $r_{R/X}$ is relatively small. However, it should be noticed that RPG equipped with VSG control will not operate in parallel with the high voltage power grid in most cases. Hence, the instability caused by $r_{R/X}$ is not an important problem for applying current-controlled VSG.

5.2. Impact of grid impedance on stability

The grid impedance Z_L is defined by (3).

$$Z_L = S_b \sqrt{R_1^2 + X_1^2} / (V_b)^2 \quad (3)$$

Where $S_b=500\text{kVA}$ and $V_b=315\text{V}$ respectively represent the rated power and voltage of VSG.

The eigenvalue trajectory of VSG system when sweeping Z_L from 0.01pu to 6pu is shown in figure 8.

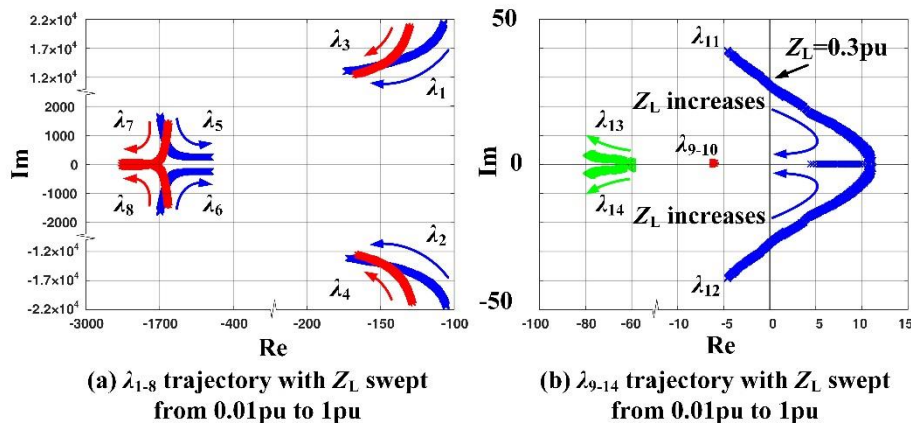


Figure 8. Influence from Z_L to eigenvalues

From figure 8(a), it can be seen that eigenvalues associated with high-frequency oscillation modes stay in the left half plane as Z_L swept from 0.01pu to 1pu, which indicates that the damping of the high-frequency mode is positive. Figure 8(b) indicates that the damping of oscillation mode corresponding to λ_{11-12} declines when Z_L increases. Unstable subsynchronous oscillation will appear in VSG system when Z_L exceeds 0.3pu, which indicates that it may destabilize the whole system by connecting current-controlled VSG to weak power grid.

6. Conclusion

This paper investigates the stability of grid-connected current-controlled VSG system. A small-signal model of the VSG system is developed to quantify the modal damping and it is affected by VSG control parameters. The adaptation of VSG to various grid conditions has also been identified. The following conclusions can be drawn:

1. Oscillation mode of current-controlled VSG system: No oscillation mode will be brought in by introduction of VSG function into traditional inverters, which, however, will have a negative effect on the damping of high-frequency oscillation mode associated with the LC filter of inverter.
2. Impact of VSG control parameters on stability: VSG would contribute to negative damping under some unfavourable conditions, for instance, improper selection of VSG control parameters such as virtual mechanical time constant and proportion coefficients of PLL. In the worst cases of lower electrical and mechanical damping, the high-frequency oscillation mode of VSG system would be marginally stable or even cause sustained oscillation.
3. Adaptation of VSG to various grid conditions: The subsynchronous oscillation will be excited when current-control VSG is connected to a weak power grid, which may result in instability of the system. This paper focus on the stability of current-controlled VSG when VSG is connected to infinite bus. However, it is also significant to research on the stability of grid-connected current-controlled VSG system under the scenarios of high permeability of renewable power generation, which is the future work and beyond the scope of this paper.

7. References

- [1] Sun D, Xie X, Liu Y, et al. Investigation of SSTI Between Practical MMC-based VSC-HVDC and Adjacent Turbogenerators through Modal Signal Injection Test[J]. IEEE Transactions on Power Delivery, 2016, PP (99):1-1.
- [2] Sun D, Xie X, Wang J, et al. Integrated generation-transmission expansion planning for offshore oilfield power systems based on genetic Tabu hybrid algorithm [J]. Journal of Modern Power Systems & Clean Energy, 2017, 5(1):117-125.
- [3] Sakimoto K, Miura Y, Ise T. Stabilization of a power system including inverter-type distributed generators by a virtual synchronous generator [J]. Electrical Engineering in Japan, 2014, 187 (3): 7-17.
- [4] Zhong Q C, Hornik T. Control of Power inverters in renewable energy and smart grid integration [M]. New York: Wiley-IEEE Press, 2013.
- [5] Li Heming, Zhang Xiangyu, Wang Yi, Zhu Xiaorong. Virtual inertia control of DFIG-based wind turbines based on the optimal power tracking [J]. Proceedings of the CSEE, 2012, 32(7):32-39.
- [6] Lv Zhipeng, Sheng Wanxing, Zhong Qingchang, et al. Virtual synchronous generator and its applications in micro-grid [J]. Proceedings of the CSEE, 2014, 34(16): 2591-2603.
- [7] D'Arco S, Suul J A. Virtual synchronous machines-Classification of implementations and analysis of equivalence to droop controllers for microgrids [C]. IEEE PowerTech Grenoble, Grenoble, France: IEEE, 2013:1-7.
- [8] He J, Li Y W, Guerrero J M, et al. An Islanding Microgrid Power Sharing Approach Using Enhanced Virtual Impedance Control Scheme [J]. IEEE Transactions on Power Electronics, 2013, 28(11):5272-5282.
- [9] Z Tianwen, C Laijun, C Tianyi, et al. Review and Prospect of Virtual Synchronous Generator Technologies [J]. Automation of Electric Power Systems, 2015, (21): 165-175.
- [10] Yan Xiangwu, Liu Zhengnan, Xu Hengbo, et al. Small-signal modeling and analysis of three-phase characteristics of virtual synchronous generator [J]. Journal of North China Electric Power University, 2016, 43(3): 1-8.
- [11] Xie Lingling Shi Bin, Hua Guoyu, et al. Parallel Operation Technology of Distributed Generations Based on Improved Droop Control [J]. Power System Technology, 2013, 4: 992-998.

- [12] Zhong Q C. Robust Droop Controller for Accurate Proportional Load Sharing Among Inverters Operated in Parallel [J]. IEEE Transactions on Industrial Electronics, 2012, 60(4):1281-1290.
- [13] Soni N, Doolla S, Chandorkar M C. Improvement of Transient Response in Microgrids Using Virtual Inertia [J]. IEEE Transactions on Power Delivery, 2013, 28(3):1830-1838.
- [14] Bevrani H, Ise T, Miura Y. Virtual synchronous generators: a survey and new perspective [J], International Journal of Electrical Power and Energy Systems, 2014(54): 244-254.

Acknowledgments

The work of this paper was supported by the projects “research on application technology and grid connection adaptability of renewable power generators equipped with actively supporting ability (52010118000N)” and “research on transmission network planning of renewable power generation convergence area by considering large-scale wind power virtual synchronous generator (52018K180002)”.

Rotation Speed Recovery Strategy Based On Variable Power Curve of Inertia Control from DFIG Wind Turbine

R LIU^{1,2,3}, P SONG^{2,3}, X S WANG^{2,3} and Z W LIN¹

¹ State Key Laboratory of Alternate Electrical Power System with Renewable Energy Sources, School of Control and Computer Engineering, North China Electric Power University, Beijing, 102206, PR China

² State Grid Jibei Electric Power Research Institute, North China Electric Power Research Institute Co. Ltd., Beijing, 100045, China

³ Grid-connected Operation Technology for Wind-Solar Storage Hybrid System State Grid Corporation Key Laboratory, Beijing, 100045, China

E-mail: 18810803027@163.com

Abstract. With the increase of wind power capacity incorporated into the grid, the permeability of wind power increases continuously, which leads to the reduction of the equivalent inertia of the system. A new strategy of recovering rotor speed that increases the output power by modifying the variable power curve is proposed in this paper, which decreases the drop of the active power. So as to reduce the secondary frequency dips caused by the sudden drop of the active power when the speed restores. The paper optimizes the secondary frequency dips by modifying the variable power curve continuously. This article simulates this strategy through setting up a system by Simulink. Compared with the traditional recovery strategy, validity of the proposed strategy is demonstrated through simulation and analysis.

1. Introduction

In recent years, the total installed capacity of wind power has increased rapidly in China, and the penetration of wind power has been increasing. The instability of wind power has had an impact on the power system security. At present, the mainstream doubly fed induction generator connects to the power grid through the power electronic converter. The output electromagnetic power decouples from the frequency of the system. It can't respond to the frequency change of the system. The wind turbine loses the inertia response of the traditional synchronous generator, resulting in reducing a dramatic reduce in the inertia of the system. It also has a threat to the system.

Domestic and overseas scholars have made a large number of researches on frequency regulation of wind turbines in the power system. There are two ways for wind turbines to participate in the system frequency regulation, the first is standby mode and the second is non-standby mode. The purpose of the standby is to reduce the steady state output power of the wind turbine through changing the pitch angle or rotor steady speed, which makes the wind turbine run in the load-shedding state in order to obtain a part of the reserve capacity. We can increase the value of the output electromagnetic power, while the system frequency is lower than the normal value. Then we can use the spare capacity to participate in the frequency regulation. Although the standby mode has the similar frequency regulation performance as that of the thermal power unit, it can't be popularized in the project because it is involved in the system frequency regulation to reduce the load of the wind turbine for a long time and reduce the economic benefit of the wind power generation. The non-standby mode is to change the output power of the turbine through the inertia control of the virtual rotor, and promote the turbine



to release the kinetic energy that stores in the rotor, simulate the inertia characteristics of the synchronizer, reduce the adverse effects of the wind power grid connected to the system, and help to improve the frequency response of the system [1]. The rotor inertia control makes use of the kinetic energy stored in the rotor of the turbine. When the frequency of the system reduces, the kinetic energy released by the motor will carry out the frequency support, so the rotor speed is constantly decreasing. When the rotor speed reaches the lower speed limit, the wind turbine must withdraw from the frequency regulation. The inertial control of rotor is introduced in the paper [2]-[6]. The exit frequency regulation of the rotor caused by the inertia control of the rotor causes the sudden drop of its output power, which causes the secondary dips of the system frequency.

With regard to the optimization of the secondary frequency dips, a great number of domestic and overseas scholars have done a lot of researches. One is model the frequency regulation process of wind power, and to find variables that causes the frequency change of the system. In literature [6], the frequency regulation process of wind turbine is modelled. The relationship between frequency regulation time and frequency second frequency dips is studied. The optimal exit equation group is found. This method improves the secondary frequency dips problem well, but it is too complex for calculation to operate in engineering. The other is to avoid the frequency tumble caused by the recovery of the speed out of the frequency regulation by changing the model of the wind power frequency regulation. For this method, reference [7], [8] have changed the coefficient of the power tracking curve by constantly changing the coefficient of the power tracking curve. In order to avoid switching directly to MPPT when the wind turbine exits frequency regulation, the secondary dips of frequency is reduced. Because of revising the coefficient of power tracking curve constantly in this method, there is usually no way to apply it in engineering. According to [9], when the wind turbine exits frequency regulation, the relationship between electromagnetic power and time is linear and the frequency is reduced greatly. The reference value of literature [10] is stepped back to avoid the falling of speed recovery by controlling the reference value of speed. The rotor speed decreases continuously during the frequency regulation. In paper [11], [12], which use fixed acceleration torque and PI controller to recovery the rotor speed respectively and improve the smoothness of the mode switching. The above method can improve the secondary frequency dips problem, but it needs to change the parameters in real time, the operation is complex, and it is not easy to realize in project. In article [13], an extended state observer is used to estimate the input mechanical power of the wind turbine in real time. On this basis, a given curve of electromagnetic power is designed to improve the secondary frequency dips. However, the design criterion of the power given curve is not given, which is not easy to achieve in engineering. Based on this, a new speed recovery strategy is proposed in this paper to design a given curve of electromagnetic power in the recovery phase, thus slowing down the dips speed of the electromagnetic power of the exit of the frequency regulation moment and reducing the frequency of the secondary frequency dips caused by the sudden landing of the active power output when the speed restores.

2. The Inertia Control

2.1. The models of wind turbine and drive train

The variable speed wind turbine consists of wind turbine, drive train, double fed induction generator (DFIG), back to back converter and control system, and its structure is shown in Figure 1.

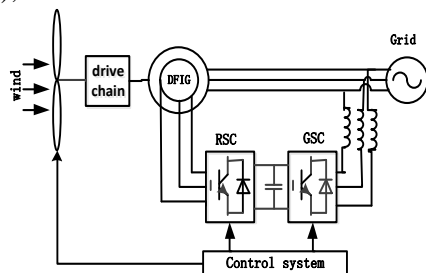


Figure 1. The structure of the variable speed wind turbine.

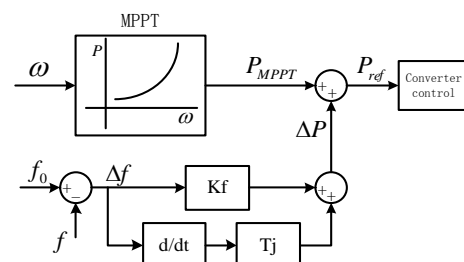


Figure 2. Principle diagram of wind turbine rotor inertia control.

The wind turbine plays the great role of converting wind energy into mechanical energy. The expression of the mechanical power captured by the wind turbine is then given by:

$$P_m = \frac{1}{2} C_p \rho v^3 s \quad (1)$$

Where P_m is the mechanical power captured by wind turbine, v is the wind speed in m/s, s is the area swept by the rotor blades in m^2 , ρ is the air density in kg/m^3 , β is pitch angle and $\lambda = R \frac{\omega}{v}$

stands for the tip speed ratio and C_p stands for coefficient of utilization of wind energy. Different wind speeds have different optimal tip speed ratios. In order to capture the maximum wind energy and realize the control of MPPT. It is important to maintain the optimal tip speed ratio through adjusting the speed of the wind turbine.

2.2. The method and process of the rotor inertial control

The method of the rotor inertial control. Rotor inertial control is a common frequency-modulation technique engineering, which is usually used at present. Rotor inertial control is the ability to simulate the inertia response and primary frequency regulation of traditional wind turbine. The active power reference value (P_{ref}) is transmitted to the converter control system by superimposing the frequency regulation power increment ΔP on the power reference value P_{MPPT} given by the original MPPT curve of the wind turbine. The rotor inertial control schematic diagram is shown in Figure 2. Where ΔP is expressed by formula (3), in which f is the system frequency K_f is the primary frequency regulation coefficient, and in the second term, the inertial frequency regulation factor T_j is the inertial response coefficient of the synchronous generator.

$$\Delta P = K_f (f_0 - f) + T_j \frac{\Delta f}{\Delta t} \quad (2)$$

The process of the rotor inertial control. There are two stages of the frequency regulation process of DFIG during the speed recovery in the rotor inertia control strategy, which are inertia support and the speed recovery. As shown in Figure 3, the frequency-modulation process begins to frequency-modulation when the frequency reduces, and enters the inertial support stage. The wind turbine releases part of the rotor kinetic energy in order to increase the electromagnetic power output for the power support, and the speed continues declining at this time. When the speed of the wind turbine is reduced to the lower speed limit, the wind turbine exits frequency regulation, the wind turbine enters the speed recovery stage, the traditional speed recovery way is MPPT curve, and the electromagnetic power falls to the current speed corresponding to the current speed on the MPPT curve, and the subsequent speed and the electromagnetic power are gradually restored.

As shown in Figure 4, compared wind power participating in frequency regulation by MPPT curve recover with that are not involved in frequency regulation, the former reduces the depth of the first dips, but causes the secondary dips of power grid frequency seriously, so it is necessary to adopt an appropriate speed recovery strategy of the wind turbine.

According to the wind speed, the working status of wind turbine can be divided into three typical phases: MPPT phase, constant speed interval and constant power phase. In condition of participating in the system frequency regulation while the wind turbine works in constant power status, it does not need to release rotor kinetic energy so that it will not cause the second frequency dip. Therefore, this article will focus on the analysis of the other two operating phases. The principle of the speed recovering method when the wind turbine runs in the MPPT phase is shown in Figure 5.

In Figure 5, the solid line shows the MPPT power curve of wind turbine while the dashed line is the mechanical power curve at some wind speed. Assuming the wind turbine operates at point A at the first time, as power grid frequency drops, the electromagnetic power will rise to point B while the rotor speed will decrease to point C gradually during the frequency regulation. Once the rotor speed reaches the low speed limit (point C), the wind turbine will withdraw from the frequency regulation. If

the traditional MPPT curve recovery method is adopted, the output electromagnetic power of the wind turbine will drop to point E instantly, then resume gradually along the MPPT power curve. It can be seen that the output power of the wind turbine is moving along the path as the A-B-C-E-A using the traditional MPPT curve. And at the moment of exiting frequency regulation, the drop of electromagnetic power with the amplitude $\Delta P_{e1} + \Delta P_{e2}$ occurred, causing serious second frequency dropping. In order to reduce the drop depth of the electromagnetic power, a new method has been designed which makes the electromagnetic power slowly drops along the red curve until it intersects the MPPT power curve (point G) before the electromagnetic power gradually recovered along the path of G-A. It can be seen that the output power of the wind turbine is moving along the path of A-B-C-G-A using new recovering method. And the drop amplitude of the electromagnetic power is $P_{e1} + P_{e3}$, which could reduce second frequency dropping greatly.

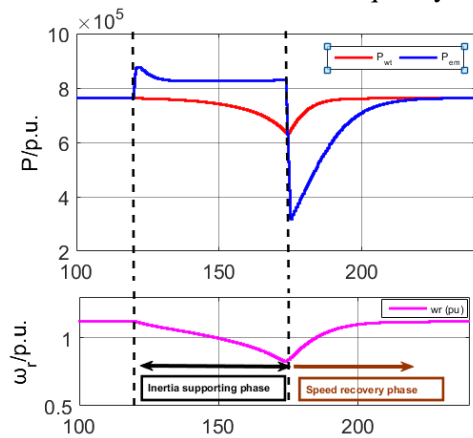


Figure 3. Diagram of frequency regulation with rotor inertia control.

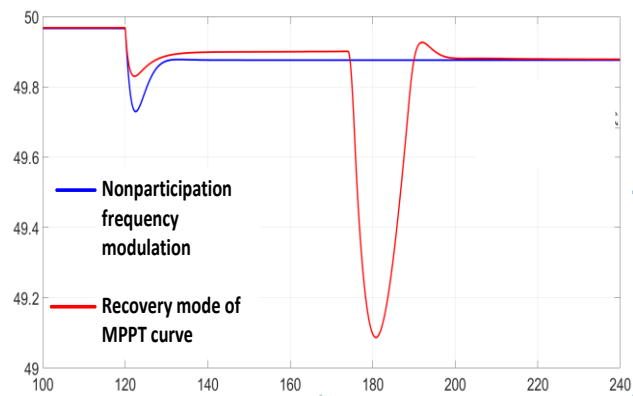


Figure 4. The contrast diagram of the frequency variation.

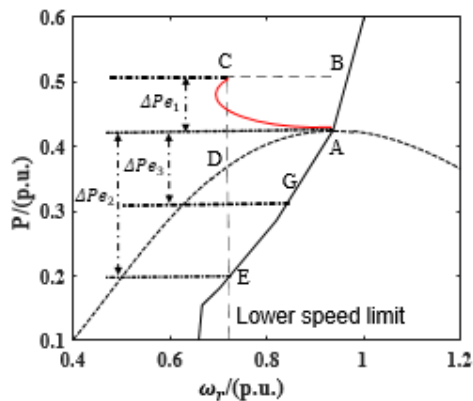


Figure 5. The contrast diagram of the principle of speed recovery.

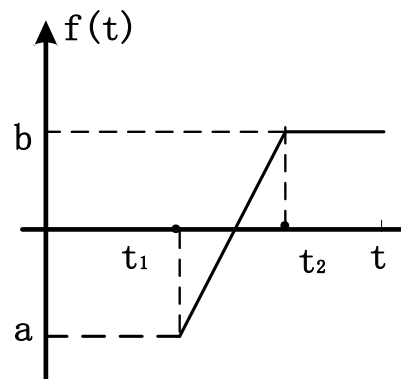


Figure 6. The image of the variable power function $f(t)$.

3. Speed recovery strategy based on variable power curve for rotor inertia control of DFIG

3.1. The working principle of the proposed speed recovery strategy

Using MPPT strategy to recover the rotor speed, the sudden drop of the active power of the wind turbine will cause the second frequency dropping. For this consequence, a new speed recovery strategy based on the variable power curve has been proposed in this paper. This strategy aims at reducing the

active power output gradually by changing the parameters of the variable power curve, so as to optimize the secondary dips of frequency. The structure of the proposed strategy is shown in Figure 6.

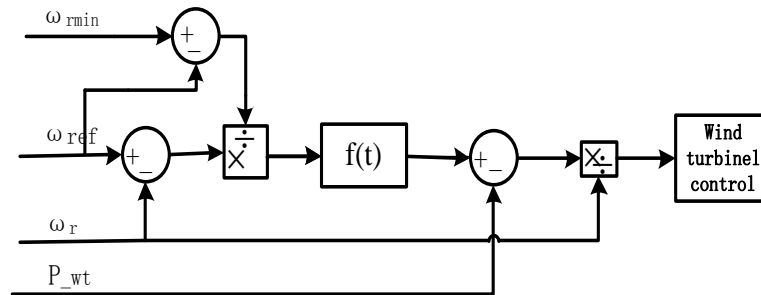


Figure 7. The structure of the proposed speed recovery strategy.

In Figure 7, ω_{ref} presents the reference value of the rotor speed, and ω_{rmin} is the lower limit of the speed drop of the DFIG when it participates in frequency-modulation. $f(t)$ is a variable power function, it is a human set function, and the expression of the variable power curve P_{ac} of the strategy is:

$$P_{ac} = f(t) \cdot \frac{\omega_{ref} - \omega_r}{\omega_{ref} - \omega_{rmin}} \quad [13] \quad (3)$$

The wind turbine would withdraw from the frequency regulation once the rotor speed ω_r drops to the lower speed limit ω_{rmin} . Set the coefficient of the variable power curve $\frac{\omega_{ref} - \omega_r}{\omega_{ref} - \omega_{rmin}}$ to avoid the output electromagnetic power of wind turbine dropping too much at the beginning of the exiting of frequency regulation during which the rotor speed ω_r restores to ω_{ref} and the variable power curve coefficient reduces from 1 to 0 gradually.

3.2. The design of variable power curve

The image of the variable power function $f(t)$ is shown in the figure 7, where t_1 is the time of exiting the frequency regulation, and t_2 is the time when the variable power function reaches the maximum value. After t_2 , $f(t)$ remains unchanged.

4. Simulation analysis

4.1. Construction of simulation system

A wind power system simulation model has been built which includes both of virtual and conventional synchronous units to simulate the secondary dips of wind power virtual synchronous machine based on rotor inertial control strategy. The proposed variable power curve recovery method has been studied and verified comparing with the classic MPPT recovery method.

Firstly, building a wind power system simulation model first which includes both of virtual synchronous generator (2MW/690V x 31) and conventional synchronous generator (250MVA/13.8kV). The structure of the system is shown in Figure 8 of which main parameters are given in Tables 1 and 2 [15].

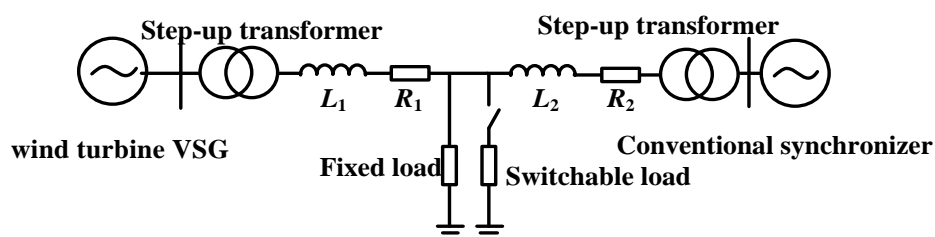


Figure 8. Topology diagram of simulation system.

Table 1. Main parameters of normal synchronous generator

Inertia constant /s	5	drum heat storage volume time constant /s	300
frequency regulation coefficient	15	Super heater volume time constant /s	10
Load frequency modulation coefficient	2	boiler fuel release time constant /s	10
One frequency regulation limited amplitude	3.5%	combustion release delay /s	20
Main steam pressure pipe flow coefficient	3	drum heat storage volume time constant /s	300

Table 2. Main parameters of wind turbine VSG

Inertia constant /s	5.005	inertial frequency regulation coefficient	5
Primary frequency regulation coefficient	20	frequency regulation speed lower limit /pu	0.83

By the end of 2016, the proportion of new energy machine assembly capacity in the regional power grids such as the Northwest Power Grid and North China Power Grid has reached about 20% [14]. In the event of grid frequency disturbances that have occurred in recent years, the maximum power shortage is about 4% [15]-[16]. Therefore, in the simulation, wind power accounts for about 20% of the installed capacity of the system and power shortage of 4% of the system capacity occurs in the power grid.

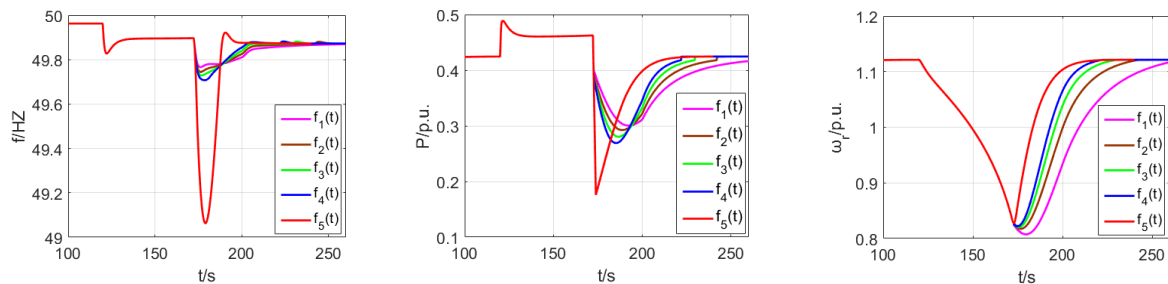
4.2. The selection of variable power function $f(t)$ and Simulation Analysis under the different variable power functions

In order to apply this method better in engineering, the variable power function $f(t)$ should be as simple as possible. By changing the four parameters a , b , t_1 , and t_2 , a simple primary function $f(t)$ has been constructed as a variable power function in this paper. And a variable power function with different parameters has been selected for simulation and comparison. At 172s, the rotor speed of the wind turbine constructed in this paper reaches the lower speed limit (0.83p.u.) while the wind turbine exits the frequency regulation. So t_1 is equal to 172.

Influence of the Change of b in $f(t)$ on system. Keeping a , t_1 , and t_2 constant ($a=-0.00428$, $t_1=172$, and $t_2=200$). Take a different value for parameter b in $f(t)$. $f_5(t)$ stands for speed recovery strategy based on MPPT curve. Then perform simulation analysis and compare the changes in frequency, power, and speed as shown in Figures 9(a), (b) and (c) respectively:

From the simulation results shown in Figures 9(a), (b) and (c), it can be seen that the proposed strategy for changing the power curve reduces the depth of the second drop significantly. Keep a , t_1 , and t_2 constant. With the increase of b , the depth of the second drop is getting smaller and smaller, which leads to that the effect is getting better and better. But the speed of speed recovery becomes slower. In other words, the decrease of the second drop depth is at the expense of the speed of speed recovery. Therefore, when ensuring the speed of speed recovery properly, the value of b cannot exceed the value of b in $f_4(t)$, in that, b is equal to 0.3772. In addition, the proposed strategy improves the smoothness of the output electromagnetic power significantly. At the moment of exiting the frequency regulation, the output electromagnetic power does not fall to the minimum immediately in order to reduce the

depth of the second drop. It will cause the active power to drop to the lowest value when using the classic MPPT strategy to recover the speed, which will lead to the second drop.



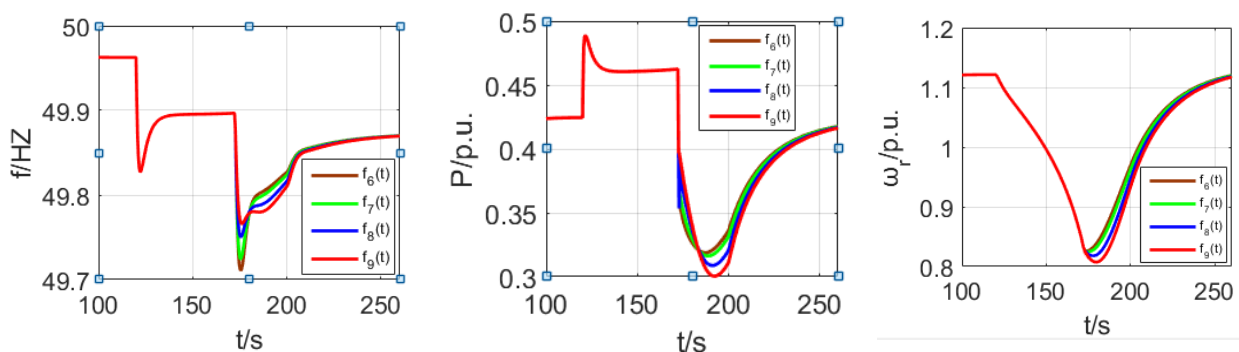
(a). Frequency simulation contrast diagram at different b.

(b). Power simulation contrast diagram at different b.

(c). Speed simulation contrast diagram at different b.

Figure 9. Simulation contrast diagram at different b.

Influence of the Change of a in f(t) on system. Keeping b, t₁, and t₂ constant (b=0.13, t₁=172, and t₂=200). Take a different value for parameter a in f(t). Then perform simulation analysis and compare the changes in frequency, power, and speed as shown in Figures 10(a),(b) and (c), respectively:



(a). Frequency simulation contrast diagram at different a.

(b). Power simulation contrast diagram at different a.

(c). Speed simulation contrast diagram at different a.

Figure 10. Simulation contrast diagram at different a.

The simulation results shown in Figure 10(a), (b) and (c) show that the depth of the second drop will get smaller and smaller when keeps b, t₁, and t₂ constant and with the decrease of a. So the effect will get better. The active output drops of using the strategy mentioned in the article is shallower than using the MPPT curve strategy at the moment of exiting the frequency regulation. But the speed recovery of the former is slower than the latter. In other words, the decrease of the second drop depth is at the expense of the speed of speed recovery.

Influence of the Change of t₁ in f(t) on system. Keeping b, a, and t₂ constant (a=-0.00428, b=0.3772, and t₂=200). Take a different value for parameter t₁ in f(t). Then perform simulation analysis and compare the changes in frequency, power, and speed as shown in Figures 11(a), (b) and (c) respectively:

The simulation results show that the decrease of the second drop depth is at the expense of the speed of speed recovery. With the increase of t₂ (keep a, b, and t₁ constant), the depth of the second drop becomes smaller, the effect becomes better, but the speed of speed recovery becomes slower.

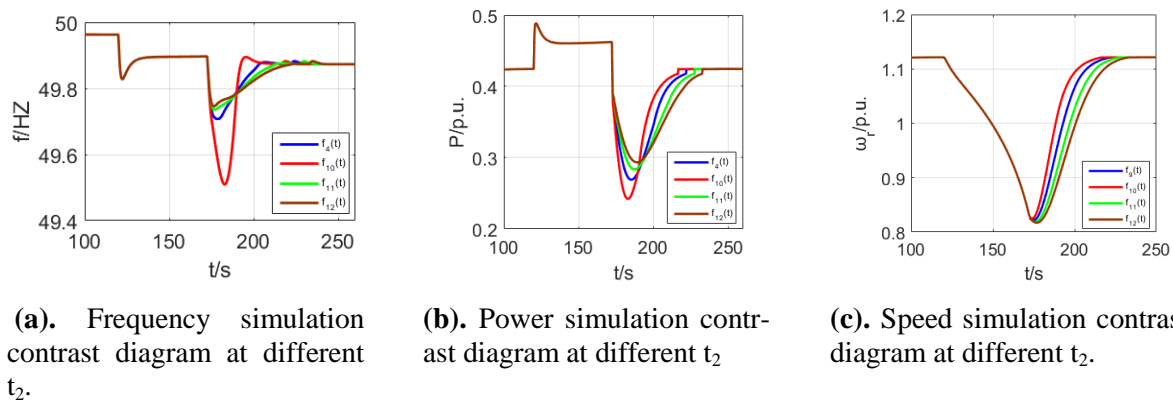


Figure 11. Simulation contrast diagram at different t_2 .

5. Conclusion

In recent years, the cumulative installed capacity of wind power in China has increased rapidly, and the penetration rate of wind power continues to increase. The instability of wind power has had threaten to the safety of power systems. DFIG cause the secondary dips of frequency when rotor inertia control is used to participate in frequency regulation. This paper proposes a new speed recovery strategy. By changing the power curve to increase the value of the output power and reduce the drop of the active output, the second drop of the frequency caused by the sudden drop of active power output reduces at the moment of the speed recover. Power changes smoothly. The secondary dips is optimized by continuously designing a modified variable power curve. The simulation verified its effectiveness. This strategy optimizes the secondary dips of the system frequency on the premise of ensuring the recovery speed of the wind turbine speed. Effectively improve the secondary dips of frequency after adopting the rotor inertial control. There are still some deficiencies in this article. It needs to continue to be optimized. For the improvement of the secondary dips problem, we can use the combination of energy storage system and wind power. We can adopt a multi-machine coordinated control strategy as well. In addition, the model predictive control theory can be applied to wind power frequency regulation. The model predictive control can achieve accurate tracking of frequency, power and speed, which achieves the purpose of reducing secondary dip.

6. References

- [1] T Fei, G Strbac. Assessment of the role and value of frequency response support from wind plants. 2017,7(2):586-595
- [2] Gautam D, Goel L, Ayyanar R, et al. Control strategy to mitigate the impact of reduced inertia due to doubly fed induction generators on large power systems[C]// Power and Energy Society General Meeting. IEEE, 2011:1-1
- [3] TANG Xisheng, MIAO Fufeng, QI Zhiping, et al. Survey on frequency control of wind power [J]. Proceedings of the CSEE, 2014, 34(25): 4304-4314
- [4] LIU Ju, YAO Wei, WEN Jingyu, et al. Prospect of technology for large-scale wind farm participating into power grid frequency regulation [J]. Power System Technology, 2014, 38(3): 638-646
- [5] TIAN Rubing, YANG Yupeng, LIU Zhiwu, et al. Research on primary frequency control for power system with participation of wind turbines [J]. Heilongjiang Electric Power, 2015, 37(1): 42-53
- [6] X.Wang, W.Du. Virtual inertia control of grid-connected wind farms [J]
- [7] Liu Zhiwind turbine, Optimal termination time of inertia control from DFIG wind turbine. [D]. Master's thesis of Shandong University. 2017
- [8] Li Licheng, Ye Lin.Coordinated Control of Frequency and Rotational Speed for Direct Drive Permanent Magnet Synchronous Generator Wind Turbine at Variable Wind Speeds. [J]. Automation of Electric Power Systems, 2011, 35(17): 26-31

- [9] LIU Zhangwei, LIU Feng, MEI Shengwei, et al. Application of extended observer in wind turbines speed recovery after inertia response control[J]. Proceedings of the CSEE, 2016, 36(5): 1207-1217
- [10] Wu Ziping, Gao Wenzhong, Wang Jianhui, et al. A coordinated Primary Frequency Regulation from Permanent Magnet Synchronous Wind Turbine Generation [C]//IEEE in Power Electronics and Machines in Wind Applications (PEM-WA). Denver, Co, USA: IEEE Press, 2012:1-6
- [11] Erlich I, Wilch M. Primary frequency control by wind turbines [C]// Power and Energy Society General Meeting. IEEE, 2010:1-8
- [12] Yuan G Y, Lei Z, Wang M J, et al. Synthesis and characterization of a cadmium(II)-organic supramolecular coordination compound based on the multifunctional 2-amino-5-sulfobenzoic acid ligand [J]. Acta Crystallogr C Struct Chem, 2016, 72(12):939-946
- [13] Liu Z, Feng L, Mei S, et al. Application of Extended State Observer in Wind Turbines Speed Recovery After Inertia Response Control [J]. Proceedings of the Csee, 2016
- [14] SHU Yinbiao, ZHANG Zhigang, GUO Jianbo, et al. Study on key factors and solution of renewable energy accommodation [J]. Proceedings of the CSEE, 2017, 37(1): 1-8
- [15] LI Zhaowei, WU Xuelian, ZHUANG Kanqin, et al. Analysis and reflection on frequency characteristics of east China grid after bipolar locking of "9.19" jinping-sunan DC transmission line [J]. Automation of Electric Power Systems, 2017, 41(7): 149-155
- [16] MA Jin, ZHAO Dawei, QIAN Minhui, et al. Reviews of control technologies of large-scale renewable energy connected to weakly-synchronized sending-end dc power grid [J]. Power System Technology, 2017, 41(10): 3112-3120

Acknowledgments

This paper is partly supported by 52010118000N.

Chapter 3:

Electrical Equipment Failure Detection

Fault Diagnosis of Gas Turbine Based on Improved BP Neural Network with the Combination of N-W and L-M Algorithm

Zhang Yun¹, Qian Yu-liang¹, Qiu Zheng¹ and Zhang Xiao¹

¹ Department of automation, Shanghai University of Electric Power, Shanghai, China.
E-mail: ZhangYun0911@126.com

Abstract. In order to solve the problem that the training speed of traditional BP neural network is slow in the process of gas turbine fault diagnosis, a new fault diagnosis method based on a combination of Nguyen-Widrow method and L-M optimized BP algorithm was proposed. The Nguyen-Widrow method is used to initialize the weights and thresholds of neurons in the BP neural network, and the L-M algorithm is used to improve the search space of the BP neural network, which reduces the times of network training and accelerates the learning speed of the network. The gradient descent method, the conjugate gradient method and the N-W and L-M combination optimization methods are respectively applied to the fault diagnosis of gas turbine. The results show that the BP neural network model optimized by combining N-W and L-M has faster learning speed and higher diagnostic efficiency for gas turbine fault diagnosis.

1. Introduction

In recent years, under the guidance of the national energy conservation and emission reduction policies, gas-fired power generation technologies with green pollution-free, small size, rapid start-stop, and other outstanding advantages have been vigorously promoted. The installed capacity of domestic gas turbine unit has been continuously improved. As the core component of the gas turbine unit, the gas turbine is operated under high temperature and high pressure conditions for a long time. It is prone to failure, resulting in production accidents. Therefore, the condition monitoring and fault diagnosis of the gas turbine is of great significance for ensuring safe and reliable operation of the gas turbine unit [1]-[3].

At present, various intelligent algorithms such as neural networks, expert systems, and knowledge systems are widely used for gas turbine fault diagnosis. The neural network is widely used in fault diagnosis due to its simple structure, strong self-learning ability, and the ability to approximate any nonlinear function. For example, in 2000, Huang et al. [4] studied the application of the standard BP algorithm in fault diagnosis of gas turbines in power stations. However, there is a slow convergence rate and it is easy to fall into the local minimum. In 2006, Xie and Shi [5] proposed a dynamic gas turbine fault diagnosis based on RBF neural network. It can effectively identify fault types. In 2012, Jiang and Zhu [6] proposed to apply PNN neural network to gas turbine fault diagnosis system, which has advantages of fast training speed and high diagnostic efficiency. In 2017, Zhu et al. [7] proposed a fault diagnosis method combining fuzzy logic and neural networks. Firstly, the continuous variable membership function is used to represent the fuzzy subset of symptoms. Then the BP neural network is used for training after fuzzification. This method has better training results.

Aiming at the deficiency of BP neural network, a BP neural network method based on combination optimization of N-W and L-M is proposed in this paper. The N-W algorithm is mainly used to



initialize the weights and thresholds of neurons in the hidden layer ,so as to reduce the adjustment of the weights and thresholds during the network training process [8]. The L-W algorithm combines the locality of the Gauss-Newton method with the globality of the gradient method to quickly search optimal solutions of the weights and threshold of the BP neural network, thereby accelerating the network convergence speed. This paper establishes a fault diagnosis model based on this method to diagnose gas turbine faults. The diagnosis results show that the BP neural network constructed by this method has fast learning speed and good diagnosis result. The method proposed in this paper provides a new approach for gas turbine fault diagnosis.

2. BP neural network [9]-[10]

BP neural network is a kind of error backpropagation neural network. The BP network is trained by minimizing the value of the objective function through error back propagation. The objective function is Eq. (1):

$$E = \frac{1}{2} \sum_{k=1}^n (y_k - o_k)^2 \quad (1)$$

Where,

E Systematic average error

n Number of system learning samples

y_k The target output of the k-th sample

o_k The actual number of the k-th samples

Traditional BP algorithm uses gradient descent method to adjust weights and thresholds of individual neurons during training of learning samples:

$$\Delta\omega_{ji} = -\alpha \frac{\partial E}{\partial \omega_{ji}} \quad (2)$$

Where,

α Learning rate

Specific algorithm derivation refer to literature[9]. The traditional BP neural network mainly has the following two defects. The first is that the learning speed is slow, especially when the learning rate and initialization weights are not selected properly. Second, it is easy to fall into the local minimum during the training process and cannot guarantee convergence to the global minimum point. To solve the above problems, the L-M algorithm can be used to improve the traditional BP algorithm.

3. L-M algorithm [11]-[13]

The L-M algorithm is a combination of the advantages of the Gauss-Newton method and the gradient descent method. It has the global characteristics of gradient descent method, that is, the descent of initial several steps is faster. It also has the local characteristics of Gaussian Newton method, that is, it can produce an ideal search direction near the optimal value. Therefore, the L-M algorithm can effectively overcome the problems that the BP algorithm has a slow convergence rate and is easy to fall into local minimum. It is assumed that the vector composed of each neuron weight and threshold is x . $x^{(k)}$ denotes the vector x of the k-th iteration, then the iterative expression of the L-M algorithm is as follows:

$$x^{(k+1)} = x^{(k)} + \Delta x \quad (3)$$

Where, we have

$$\Delta x = -\left(J^T(x)J(x) + uI\right)^{-1} J(x)e(x),$$

$$J(x) = \begin{bmatrix} \frac{\partial e_1(x)}{\partial x_1} & \frac{\partial e_1(x)}{\partial x_2} & \dots & \frac{\partial e_1(x)}{\partial x_j} \\ \frac{\partial e_2(x)}{\partial x_1} & \frac{\partial e_2(x)}{\partial x_2} & \dots & \frac{\partial e_2(x)}{\partial x_j} \\ \dots & \dots & \dots & \dots \\ \frac{\partial e_n(x)}{\partial x_1} & \frac{\partial e_n(x)}{\partial x_2} & \dots & \frac{\partial e_n(x)}{\partial x_j} \end{bmatrix}$$

In the formula, u is the scale coefficient and $u > 0$. $e_i(x)$ is the error of the i -th network node. I is the identity matrix. $J(x)$ is a Jacobian matrix.

Set the error evaluation function for Eq.(4):

$$E(x) = \frac{1}{2} \sum_{i=1}^N e_i(x) \quad (4)$$

When the scale coefficient $u \rightarrow 0$, then $uI \rightarrow 0$, $\Delta x = -(J^T(x)J(x))^{-1} J(x)e(x)$. This formula is Gauss Newton method.

When the scale coefficient $u \rightarrow 1$, then $uI \rightarrow I$, $\Delta x = -(J^T(x)J(x)+I)^{-1} J(x)e(x)$. The L-M algorithm is transformed into a gradient descent method. As the number of successful iterations increases, the value of u gradually decreases. When the approximation error is at a minimum, the L-M algorithm gradually evolves to a Gauss-Newton method.

3.1. L-M algorithm implementation steps

(1) Set training error allowable values ε , coefficients β , and initialize the vector of weights and thresholds $x^{(0)}$. Let $k = 0$, $u = u_0$.

(2) Calculate network output and systematic average error $E(x^{(k)})$.

(3) If $E(x^{(k)}) < \varepsilon$, go to step (7), otherwise continue.

(4) Calculate the Jacobian matrix $J(x)$.

(5) Calculate Δx . Calculate the error function $E(x^{(k+1)})$ with $x^{(k+1)} = x^{(k)} + \Delta x$ as the weight and the threshold.

(6) If $E(x^{(k+1)}) < E(x^{(k)})$, then $k = k + 1$, $u = u/\beta$, and go to step (2). Otherwise, do not update x (weights and thresholds) this time. Let $\omega^{(k+1)} = \omega^{(k)}$, $\mu = \mu\beta$ and go to step (5).

(7) End.

4. N-W variable parameter initialization method [14]

L-M algorithm has the advantage of fast convergence rate. It is also not easy to fall into local minimum. So it is an algorithm suitable for training neural networks. However, when the algorithm is determined, the training process of the network will have a great relationship with the initial weights and thresholds of the network. After Nguyen-Widrow's analysis of the neurons in the hidden layer, an initialization method for N-W variable parameters was obtained. For the three-layer BP neural network whose structure is n - m - k , the hidden layer neurons use the sigmoid function as the activation function, the output layer neurons use the linear function. The BP neural network handles the input data as follows.

$$\text{Hidden layer: } y_j = f \left[\sum_{i=1}^n \omega_{ji} x_i + b_j \right], \quad (j = 1, 2, \dots, m) \quad (5)$$

$$\text{Output layer: } o_i = \sum_{j=1}^m \omega_{ij} y_j + b_i, \quad (i = 1, 2, \dots, k) \quad (6)$$

Where, y_j is the output of the j -th neuron of the hidden layer. ω_{ji} is the weight from the i -th neuron in the input layer to the j -th neuron in the hidden layer. $f(x)$ is the sigmoid function. b_j is the threshold of the j -th neuron of the hidden layer; o_i is the output of the i -th neuron in the output layer; ω_{ij} is the weight from the j -th neuron in the hidden layer to the i -th neuron in the output layer. b_i is the threshold of the i -th neuron in the output layer.

Since the sigmoid function is close to a linear function within a range $[-0.7, 0.7]$ centered on 0. It can be seen from Eq.(5) and Eq.(6) that the output of neurons in the hidden layer is close to a linear function in a certain interval. The length of the interval is related to ω_{ji} , and the center position is related to b_j . Hidden layer neuron linear interval can average sample input interval by adjusting the initial values of the weights ω_{ji} and the threshold b_j with the N-W method, so as to reduce the adjustment times of the weights and thresholds in the network training process. The adjustment formula is:

$$\omega_{ji} = \omega_{ji} / |r_i - l_i| \quad (7)$$

$$|\omega_j| = 1.4H^{1/n} \quad (8)$$

$$b_j = \text{rand}(-|\omega_j|, |\omega_j|) - \omega_j M \quad (9)$$

Where, ω_{ji} is the weight from the j -th neuron in the hidden layer to the i -th neuron in the input layer. r_i is the maximum value of the i -th dimension in the input sample matrix. l_i is the minimum value of the i -th dimension in the input sample matrix. H is the number of neurons in the hidden layer. n is the number of input layer neurons. ω_j is the weight vector from the input layer neuron to j -th neuron in the hidden layer, and $M = [v_1, v_2, \dots, v_m]^T$, where $v_i = (l_i + r_i)/2$.

The output layer neurons use a linear function as an activation function, which has nothing to do with the linear interval of the hidden layer neurons. Therefore, the initial value of the weight and threshold which is from the hidden layer to the output layer can be any value within the range of $[-1, 1]$.

When the multi-layer neural network adopts random number to initialize the weights and thresholds of neurons, if the input range of the network is large, the activation function of neurons in the hidden layer is easily saturated, which affects the learning speed of the network. Through the Nguyen-Widrow method, initializing the weights and thresholds of the hidden layer can effectively accelerate the learning speed of the BP network.

5. The process of optimizing BP algorithm based on combination of N-W and L-M

The algorithm proposed in this paper mainly consists of two parts:

1. Firstly, the N-W method is used to initialize the weights and thresholds of the hidden layers in the determined BP neural network.
2. L-M algorithm is used to train learning samples in BP neural network. Then we can test the samples with the trained BP network.

The specific flow of optimizing BP algorithm based on combination of N-W and L-M is shown in Figure 1:

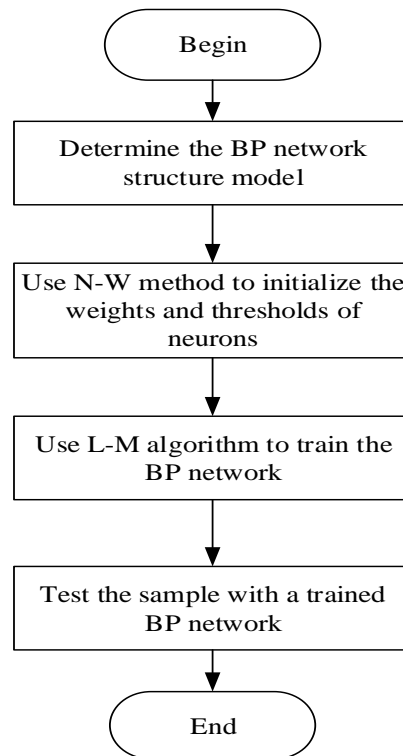


Figure 1. Flow of optimizing BP algorithm based on combination of N-W and L-M.

6. Experimental simulation and result analysis

In the paper, it adopts the BP neural network structure in the form of 5-11-10. (that is, the number of input, hidden and output neurons is 5, 11, and 10 respectively.) The network error is in the form of a square sum, and the target error is 10⁻³. The maximum number of training is 10000. The gas turbine fault samples were trained respectively by gradient descent method, conjugate gradient method and combination algorithm of N-W Method and L-M algorithm. The five neurons in the input layer of the BP network are expressed as: the speed change of low pressure compressor ($\delta n_1\%$), the speed change of high pressure compressor ($\delta n_2\%$), compression ratio variation of low pressure compressor ($\delta\pi_{LC}\%$), compression ratio variation of high pressure compressor ($\delta\pi_{HC}\%$) and the change in fuel flow ($\delta wf\%$). The input of the sample data needs to be normalized and the normalized formula is as follows:

$$x^* = \frac{x - x_{\min}}{x_{\max} - x_{\min}} \quad (10)$$

The number of input layer neurons is m and the number of hidden layer neurons is n . They have the following approximate relationship [15]:

$$n = 2m + 1 \quad (11)$$

Since the number of input layer neurons of the BP neural network is 5, the number of hidden layers is 11. Experiments have shown that the training results using 11 hidden layer neurons are more effective than those of other hidden layers. The combined vectors of the 10 neurons in the output layer represent 10 types of gas path faults common in gas turbines, respectively. Learning sample data based on an improved BP neural network which is constructed in this paper is shown in Table 1. It can be seen from the table that there are 10 gas fault types (9 fault types and 1 fault-free type) for gas turbine, and there are totally 30 groups of training samples. Among them, data from the first group to the third group represents the data of fault-free system, and the output of the sample target is (0000000000).

Data from the fourth group to the sixth group represents the data of compressor blade fouling fault system. The three groups of data are respectively the fault data of running samples under the condition of 70%, 80%, and 90% of the gas turbine system. The output of the sample target is (0100000000) . Similarly, the data from the seventh group to the ninth group indicates the sample data in the event of compressor tip clearance failure. The data of the tenth group to the twelfth group indicates the sample data of the compressor blade corrosion failure in the system, etc. Each type of failure has three groups of learning sample data which corresponds to the data when the gas turbine system is running at 70%, 80%, and 90% operating conditions[16], [17].

Table 1. BP neural network training samples.

Fault type	δn_1 %	δn_2 %	$\delta \pi_{LC}$ %	$\delta \pi_{HC}$ %	δwf %	Target output of the sample
Fault-free	-0.050	-0.050	-0.050	-0.050	-0.050	0000000000
	0.000	0.000	0.000	0.000	0.000	0000000000
	0.050	0.050	0.050	0.050	0.050	0000000000
Compressor blade fouling	3.781	1.732	-2.083	-0.592	1.438	0100000000
	4.312	1.824	-2.127	-0.732	1.773	0100000000
	4.823	1.738	-2.462	-0.672	1.896	0100000000
Compressor tip clearance	1.354	0.942	-1.731	-0.100	0.286	0010000000
	1.654	1.042	-1.891	-0.121	0.364	0010000000
	1.983	1.254	-2.280	-0.139	0.438	0010000000
Compressor blade wear	1.132	-0.013	0.961	-0.421	0.915	0001000000
	1.412	-0.011	1.182	-0.531	1.143	0001000000
	1.693	-0.014	1.422	-0.643	1.371	0001000000
Compressor blade mechanical damage	2.971	-0.023	2.491	-1.117	2.412	0000100000
	3.593	-0.026	2.957	-1.328	2.861	0000100000
	4.088	-0.031	3.432	-1.539	3.315	0000100000
Turbine blade hot corrosion	1.012	-0.319	0.872	-0.037	0.123	0000010000
	1.149	-0.359	1.008	-0.038	0.137	0000010000
	1.311	-0.402	1.147	-0.041	0.163	0000010000
Turbine blade fouling	0.073	-0.191	-0.282	-0.663	0.051	0000001000
	0.161	-0.252	-0.271	-0.787	0.063	0000001000
	0.251	-0.303	-0.262	-0.928	0.082	0000001000
Turbine blade wear	1.963	-0.729	1.451	-0.573	0.262	0000000100
	2.351	-0.882	1.735	-0.710	0.319	0000000100
	2.740	-1.039	2.011	-0.842	0.373	0000000100
Turbine blade mechanical damage	2.521	-1.113	1.521	-1.403	0.382	0000000010
	3.001	-1.324	1.813	-1.672	0.451	0000000010
	3.482	-1.531	2.101	-1.933	0.519	0000000010
Combustion chamber failure	-2.121	-0.242	-0.783	1.373	1.872	0000000001
	-2.523	-0.292	-0.934	1.632	2.781	0000000001
	-3.212	-0.349	-1.113	1.962	2.661	0000000001

6.1 Result analysis

The experimental results are shown in Figure 2, Figure 3, and Figure 4 respectively. They represent the error curve simulation diagram of gas turbine fault learning samples training which respectively use gradient descent method, conjugate gradient method, and L-M optimization algorithm combined with N-W method. From these three graphs, it can be seen that the training times of BP network using the N-W and L-M combined optimization algorithm are much smaller than those of the BP network using the gradient descent algorithm and the conjugate gradient algorithm. It takes only 13 steps to complete the training of BP neural network. Error accuracy reaches 10^{-7} , and no training trapped in local minima. The conjugate gradient method requires about 170 iterations to make the error accuracy reach 10^{-2} . Gradient descent method will fall into the local minimum during training of BP neural network, and the error accuracy has not yet reached 10^{-1} . Therefore, compared with the gradient descent method and the conjugate gradient method to optimize BP algorithm, the BP algorithm based on the combination of N-W and L-M has the advantage of fast training, and it is not easy to fall into the local minimum. It effectively improves the traditional BP neural network.

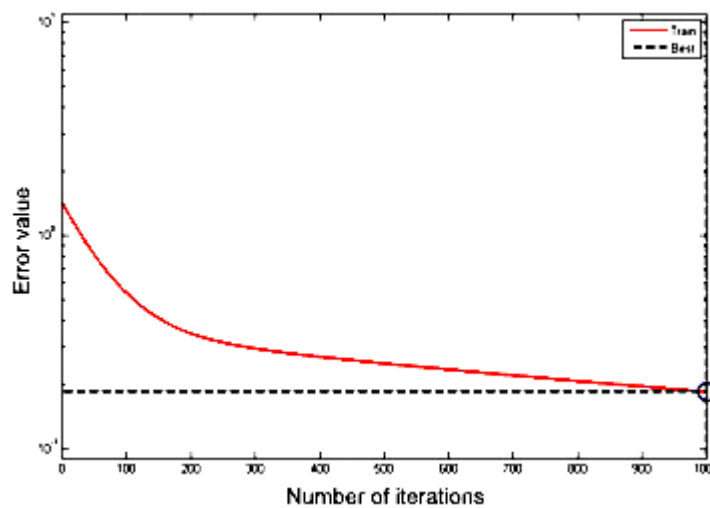


Figure 2. Error curve trained by gradient descent method.

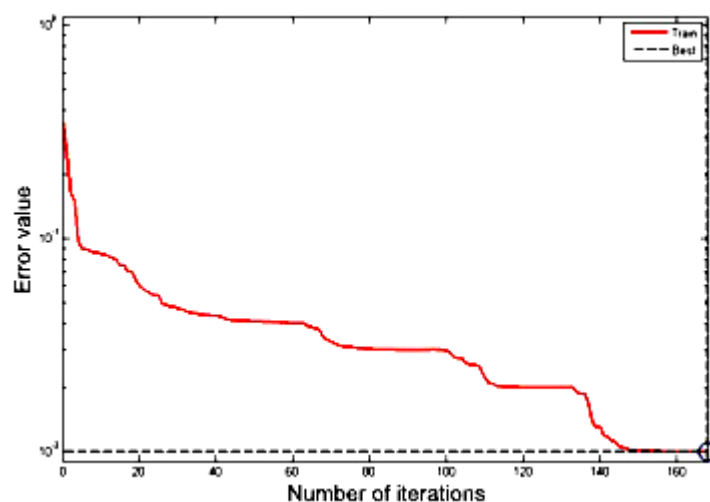


Figure 3. Error curve trained by conjugate gradient method.

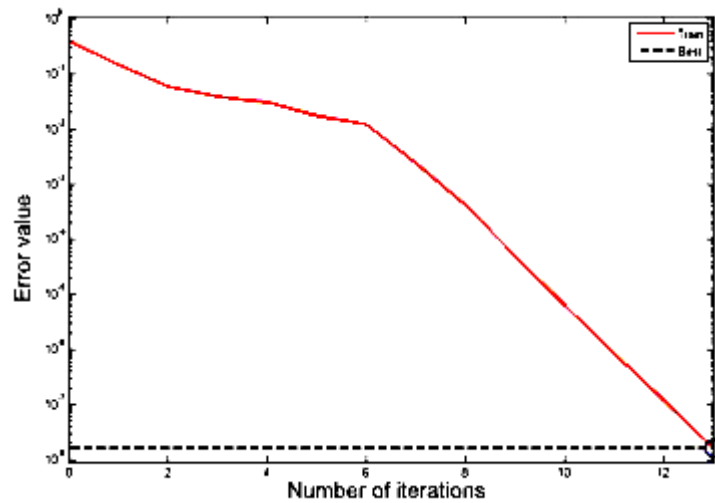


Figure 4. Error curve trained by the combination of N-W and L-M.

The training samples are tested by the BP network based on N-W and L-M combinatorial optimization algorithms. The test results are shown in Table 2. It can be seen from Table 2 that the output of the training sample is very close to the target output of the actual sample, which shows that the trained BP algorithm model has a good learning ability.

Table 2. Verification results of training samples.

Training sample number	Network output									
	1	2	3	4	5	6	7	8	9	10
1	0.0000	0.0000	0.0000	0.0000	0.0000	0.0000	0.0001	0.0000	0.0002	0.0000
2	0.0000	0.0000	0.0000	0.0000	0.0000	0.0000	0.0000	0.0000	0.0001	0.0000
3	0.0000	0.0000	0.0000	0.0000	0.0000	0.0000	0.0000	0.0000	0.0000	0.0000
4	0.0000	1.0000	0.0000	0.0000	0.0000	0.0000	0.0000	0.0000	0.0000	0.0000
5	0.0000	1.0000	0.0000	0.0000	0.0000	0.0000	0.0000	0.0000	0.0000	0.0000
6	0.0000	1.0000	0.0000	0.0000	0.0000	0.0000	0.0000	0.0000	0.0000	0.0000
7	0.0000	0.0000	0.9999	0.0000	0.0000	0.0000	0.0000	0.0000	0.0000	0.0000
8	0.0000	0.0000	0.9999	0.0000	0.0000	0.0000	0.0000	0.0000	0.0000	0.0000
9	0.0000	0.0000	0.9999	0.0000	0.0000	0.0000	0.0000	0.0000	0.0000	0.0000
10	0.0000	0.0000	0.0000	0.9998	0.0000	0.0001	0.0000	0.0000	0.0000	0.0000
11	0.0000	0.0000	0.0000	0.9999	0.0000	0.0000	0.0000	0.0000	0.0000	0.0000
12	0.0000	0.0000	0.0000	0.9998	0.0001	0.0000	0.0000	0.0000	0.0000	0.0000
13	0.0000	0.0000	0.0000	0.0001	0.9995	0.0000	0.0000	0.0000	0.0000	0.0000

14	0.0000	0.0000	0.0000	0.0000	0.9996	0.0000	0.0000	0.0000	0.0000	0.0000
15	0.0000	0.0000	0.0000	0.0000	0.9996	0.0000	0.0000	0.0000	0.0000	0.0000
16	0.0000	0.0000	0.0000	0.0001	0.0000	0.9992	0.0000	0.0000	0.0000	0.0000
17	0.0000	0.0000	0.0000	0.0000	0.0000	0.9996	0.0000	0.0000	0.0000	0.0000
18	0.0000	0.0000	0.0000	0.0000	0.0000	0.9994	0.0000	0.0001	0.0000	0.0000
19	0.0000	0.0000	0.0000	0.0000	0.0000	0.0000	0.9997	0.0000	0.0000	0.0000
20	0.0000	0.0000	0.0000	0.0000	0.0000	0.0000	0.9997	0.0000	0.0000	0.0000
21	0.0000	0.0000	0.0000	0.0001	0.0000	0.0000	0.9996	0.0000	0.0001	0.0000
22	0.0000	0.0000	0.0000	0.0000	0.0000	0.0001	0.0000	0.9987	0.0000	0.0000
23	0.0000	0.0000	0.0000	0.0000	0.0000	0.0001	0.0000	0.9994	0.0001	0.0000
24	0.0000	0.0000	0.0000	0.0000	0.0000	0.0001	0.0000	0.9995	0.0001	0.0000
25	0.0000	0.0000	0.0000	0.0001	0.0000	0.0000	0.0000	0.0001	0.9997	0.0000
26	0.0000	0.0000	0.0000	0.0001	0.0000	0.0000	0.0000	0.0000	0.9998	0.0000
27	0.0000	0.0000	0.0000	0.0001	0.0000	0.0000	0.0000	0.0000	0.9998	0.0000
28	0.0000	0.0000	0.0000	0.0000	0.0000	0.0000	0.0000	0.0000	0.0000	0.9999
29	0.0000	0.0000	0.0000	0.0000	0.0000	0.0000	0.0000	0.0000	0.0000	1.0000
30	0.0000	0.0000	0.0000	0.0000	0.0000	0.0000	0.0000	0.0000	0.0000	1.0000

In the test of the test samples, there are totally 150 test samples, and the number of samples for each gas circuit fault type is 15. The test results are shown in Table 3. It can be seen from the table that for the 150 groups of test samples, only three sets of sample data were diagnosed incorrectly, and 147 sets of sample data were correctly diagnosed. The accuracy rate reached 98%, which can meet the requirements of the actual gas turbine fault diagnosis. Therefore, this algorithm has a good practical application value for gas turbine fault diagnosis.

Table 3. The results of test samples.

Fault types of test samples	The number of test samples	The number of correct diagnoses	The number of incorrect diagnoses
Fault-free	15	15	0
Compressor blade fouling	15	15	0
Compressor tip clearance	15	14	1
Compressor blade wear	15	15	0
Compressor blade	15	15	0

mechanical damage			
Turbine blade hot corrosion	15	15	0
Turbine blade fouling	15	14	1
Turbine blade wear	15	14	1
Turbine blade mechanical damage	15	15	0
Combustion chamber failure	15	15	0
Total number	150	147	3

It can be seen from the above experimental results that the optimized BP algorithm based on the combination of N-W and L-M algorithm has good effects on the training results, the training speed, the test of the training samples, and the results of the test samples. It can make accurate and efficient intelligent fault diagnosis for gas turbine.

6.2. Comparison with a PNN fault diagnosis method

For the complex fault diagnosis problem of gas turbine, Jiang and Zhu[6] proposed a probabilistic neural network (PNN) fault diagnosis method. Probabilistic Neural Networks (PNN) is a radial basis network suitable for classification problems. It is a parallel algorithm developed from Bayesian classification rules and Parzen window probability density function. It has the advantages of being fast, accurate, and easy to modify. Here, we use the two methods which are PNN algorithm and the method we proposed in this paper to diagnose the original fault samples respectively. The contrast result is shown in Table 4.

Table 4. Comparison of N/W - L/M Algorithm and PNN network diagnosis results.

Diagnostic method	Number of iterations	Diagnostic time /s	Accuracy rate
PNN network	20	6.162482	95%
N/W - L/M Algorithm	13	4.352974	98%

It can be seen from Table 4 that the fault diagnosis of gas turbine based on N/W - L/M Algorithm is superior to PNN network in diagnostic speed and diagnostic accuracy. The combination of N-W and L-M Algorithm has faster network convergence rate than PNN network, and smaller network can fall into the local minima. This algorithm can effectively train the fault diagnosis model of gas turbine. Therefore, the algorithm proposed in this paper has higher diagnostic accuracy than PNN network, It can meet the requirements of gas turbine fault diagnosis.

7. Conclusion

In order to solve the problem that BP algorithm has slow convergence rate and is easy to fall into local minimum problem, this paper presents the combination of N-W algorithm and L-M algorithm to optimize BP algorithm and builds a fault diagnosis model to diagnose gas turbine faults based on this method. Comparing this algorithm with BP algorithm based on gradient descent method and BP algorithm based on conjugate gradient method, the experimental results show that the optimized BP algorithm model based on combination of N-W and L-M has better training speed and can effectively avoid falling into local minimum. It meets the real-time requirements for fault diagnosis of gas turbine. When the trained model tests the training samples and the test samples, it can be found that the output value of the training sample is almost consistent with the expected result, and the the diagnosis of the test samples has a good accuracy, which can meet the needs of gas turbine fault diagnosis. Therefore,

this method provides a new approach for fault diagnosis of gas turbines. It is especially suitable for application in diagnostic environments with high real-time requirements and accurate diagnostic results. The method has broad application prospects.

8. References

- [1] Xie C L and Dai J M 2010 Review and prospect of gas turbine fault diagnosis technology *J. Steam Turbine Technol.* **52** 1-3
- [2] Sina T B 2014 Dynamic neural network based fault diagnosis of gas turbine engines *J. Neuro Computing* **125** 153-165
- [3] Jiang K 2016 Research on gas turbine fault diagnosis technology *J. Petrochemical Technol.* **23** 105
- [4] Huang X G, Wang Y H and Weng S L 2000 Gas turbine fault diagnosis based on BP algorithm *J. Chinese Journal of Electrical Engineer* **20** 72-74
- [5] Xie C L and Shi X C 2006 Gas turbine fault diagnosis based on neural network *J. Gas Turbine Technol.* **19** 58-60
- [6] Jiang R, Zhu W 2012 A PNN fault diagnosis method for gas turbine *C. World Automation Congress* 1-4
- [7] Zhu Y J, Ding C and Fan Z J 2017 Research on fault diagnosis of thermal component of gas turbine based on fuzzy neural network *J. Electric Automation* 110-112
- [8] Xu Z N and Lv F C 2006 Nguyen-Widrow method for fault diagnosis of transformer oil and gas analysis *J. High Voltage Technol.* **32** 46-48
- [9] Yu J L and Bian S 2014 Transformer fault diagnosis model based on BP neural network *J. Journal of System Simulation* **26** 1343-49
- [10] Wu L Y and Wang H 2003 Application of BP neural network expert system in fault diagnosis. *Info. Technol.* **2** 66-68
- [11] Xiang W Q, Zhang H and Wang H 2011 *J. Power System Protection and Control* 100-103
- [12] Liu J H and Ren X H 2015 Fault diagnosis of spindle system of CNC machine tool based on BP neural network *J. Machine Tools & Hydraulics* **43** 193-196
- [13] Zhu B H, Zhou D, and Chen S X 2011 Using BP neural network improved by L-M method to evaluate slope stability *J. Western Exploration Project* **23** 21-24
- [14] Xu Z N, Lv F C and Liu Y P 2015 *J. Journal of North China Electric Power University* **32** 1-4
- [15] Yang S, Yao S G, Liu H W and Jiang L 2007 Research and application of BP neural network in expert system development *J. Sc.i Tech.Engng.* **7**
- [16] Yao J, Li H W and Ma X 2012 Fault diagnosis of hot and cold gas turbine components based on BP neural network *J. Gas Turbine Technol.* **25** 39-43
- [17] Peng T 2007 An improved neural network expert system for mechanical fault diagnosis *J. Computer Engineering and Appl.* **43** 232-234

Acknowledgments

This work was sponsored by Shanghai Sailing Program(16YF1404700).

Research on Short-term Prediction Method of Substation Bus-bar's Voltage Trend Based on Multidimensional Time Series Data Mining

Fei Xiao¹, Xiwu Leng², Kang Ye¹, Youlin Hu¹, Xiongli Li³, Licheng Zhu³

¹ State Grid Shanghai Electric Power Company Power Dispatch Control Centre, Shanghai, P.R. China

² National Power Dispatch Communication Centre, Beijing, P.R. China

³ Tellhow Software Co. Ltd., Nanchang, P.R. China

E-mail: xiaofei@sh.sgcc.com.cn; xiwu-leng@sgcc.com.cn;
yekang_yk@sh.sgcc.com.cn; 3311481@qq.com; 66653752@qq.com;
zhulc@tellhow.com

Abstract. The short-term prediction of voltage trend is the important technical foundation of the voltage exceeding intelligent alarm system in power substation. According to correlation between the adjacent lines in the same substation, the time series data of different bus-bars in same section, was constructed into a multi-dimensional time series data matrix model for prediction of voltage trend. Moreover, based on above matrix model, a novel prediction method based on multidimensional time series data was proposed, which transformed the multidimensional time series data matrix into a classical two-dimensional decision information system in the first stage via preprocessing and clustering. In the second stage, various classical machine learning algorithms are ensembled to forecast the short-term future trend of the specific bus-bars' voltages. The efficiency of the prediction method based on multi-dimensional time series data mining was validated by the implement in a 500 KV bus-bar's prediction in a Substation of the State Grid Shanghai Company. The results represented that the prediction method in this paper had sound precision in practice and can improve the functionality of voltage exceeding intelligent alarm system via assistance to filter plenty of fake alarms.

1. Introduction

The short-term prediction of bus-bars' voltage trend in substation is basic technology of the voltage exceeding intelligent alarm system in power substation. At present, the voltage exceeding intelligent alarm system in our country mainly depended on the real-time alarm data from the SCADA system of power grid D5000 and the operation state data of voltage control system from AVC system. However, in practice, the voltage value of bus-bars' voltage exceeding alarm preset in D5000 system and the busbars' voltage automatic regulating preset in AVC system are always inconsistent. D5000 system can deliver a large number of alarms in a short time, which is mixed with the true and fake alarms. Thus, the monitor in control centre almost cannot identify the effective alarm information quickly, and the plenty of fake alarms are seriously affecting the efficiency and functionality of the voltage exceeding alarm system.

Based on the traditional voltage exceeding alarm technology, this paper proposed an effective intelligent alarm method for busbars' voltage exceeding alarm with busbars' voltage short-time prediction technology. Furthermore, the principle of this method is to forecast the busbar's voltage



trend in short-term future when the D5000 system delivered alarms and the AVC reactive power regulation capacity has been exhausted. If the trend is upward in short-term future, the alarm is a real alarm, otherwise it is a false alarm. The practical results in a substation in Shanghai showed that this method can effectively remove a large number of fake alarms and improve the efficiency of busbars' voltage exceeding alarm system.

The traditional methods of voltage prediction include least squares estimation [1], power flow estimation [2], sensitivity matrix estimation, and public coupled point voltage estimation [3], which is suitable for small and medium-sized electricity grid with only partial information of grid. In the era of big data, the data acquisition of the power grid is increasing rapidly, and the information has been improved. However, these information with multi-source, time series, heterogeneous structure and diverse characteristics are difficult to be implemented into the existing traditional method of voltage prediction at present. Y. Wei proposed a voltage prediction algorithm based on the dynamic pattern matching of voltage time-series data [4]. B. Wei proposed a method to predict the average output voltage of the system based on BP Neural Network [5]. the methods based on non-parametric estimation and adaptive neural network is proposed to realize the voltage rapid estimation [6], [7]. However, in practice, the voltage prediction methods, which based on a single algorithm or one-dimensional data of grid, cannot figure out the dynamic characteristics of the data from large power grid. The stability and accuracy of their prediction are seriously limited.

Given the defects of traditional voltage prediction, this paper constructed a multi-dimensional time series data model and utilized ensemble learning strategy with various classical data mining algorithms to establish a new framework of busbars' voltage prediction. The research results have been successfully implemented in busbars' voltage exceeding intelligent alarm system of a substation in Shanghai.

2. The features of voltage trend prediction data

The data of voltage trend prediction involving working conditions of related power lines in substation were shown in Fig. 1, which included the historical voltage time series data of busbar, the history voltage time series data of relevant power lines, history remote signal displacement data of related switch, the operation records of relevant AVC system, the historical data of environmental temperature and so on. Firstly, all multiple historical time series data of working conditions were segmented by sliding windows with certain time span in the paper. Moreover, the voltage trend in short-term future was taken as a predictive attribute, which have 3 decision values as upward trend (recorded as P), downward trend (recorded as N) and stable trend (recorded as B).

After data preprocessing, a data model was established as following. A specified relevant L data set were represented to $D = \{D_1, D_2, L, D_L\}$, $D_i \in D$, Among them, D was the time series

information system shown in Fig.1, and can be describe as $D_i = (A_i, V_i, N, f, g)$.

$A_i = \{a_{i1}, a_{i2}, L, a_{im}\}$ means the attribute i time series dataset of busbar working condition with m segments. $V_i = \{TS_{i1}, TS_{i2}, TS_{i3}, \dots, TS_{im}\}$ stands for the attribute i time series dataset of

transformer working condition with m segments. f is a mapping relationship: $f: a_{ij} \rightarrow TS_{ij}$.

$N_i = \{N_1^k, N_2^k, L, N_m^k\}$ represents the dataset of busbar voltage trend values for a continuous K -minute after each historical working condition V_i . Its value is determined by the mapping $g: TS_{ij} \rightarrow N_j^k$, where $j \in \{1, 2, L, m\}$. In this paper, finally, the future k -minute voltage trend

predictive value $N = \{N_1, N_2, K, N_m\}$ synthesize into the corresponding time period, and the voltage trend data matrix model DB as shown in following equation is the training dataset of predictive model.

$$DB = \begin{bmatrix} TS_{11} & TS_{21} & L & TS_{L1} & N_1^k \\ TS_{12} & TS_{22} & L & TS_{L2} & N_2^k \\ M & M & M & M & \\ TS_{1m} & TS_{2m} & L & TS_{Lm} & N_m^k \end{bmatrix}, j \in \{1, 2, L, m\}, i \in \{1, 2, L, L\}$$

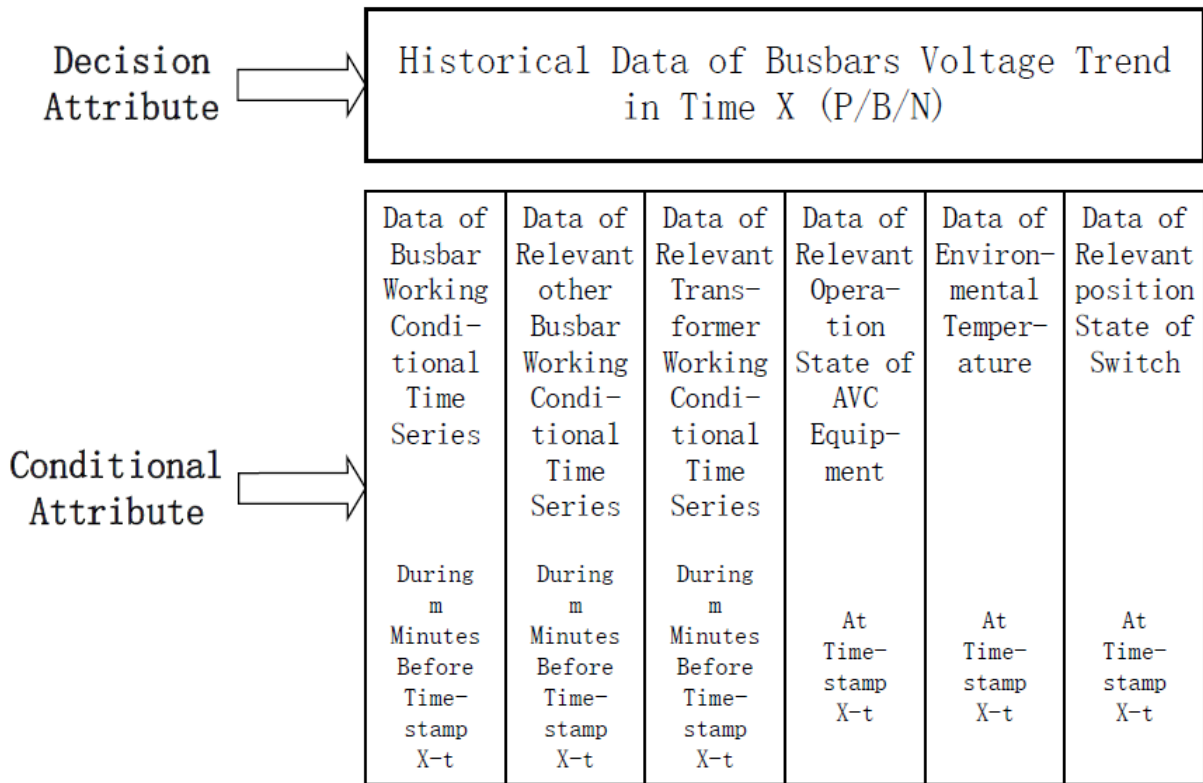


Figure 1. Diagram of data model of relevant busbar's voltage prediction

3. The method for short-term prediction of busbars' voltage trend based on multi-dimensional time series data mining

The short-term prediction method of busbars' voltage trend based on multidimensional time series data mining is shown in Figure 2 as following. Firstly, the multi-dimensional time series dataset of all relevant historical dataset for busbars' voltage trend prediction were modelled and transformed into multi-dimensional time series matrix model. After that, the time series clustering method was used to transform and reduce the multi-dimensional time series matrix model into the classical two-dimensional information table. Then, the classical two-dimensional information system was imported into multi-machine learning group. Finally, an optimal classifier was generated via competition of the multiple algorithm models (ANN, C4.5, SVM, etc.) based on test dataset.

As shown in Fig. 2 and Fig. 3, the short-term prediction model for the busbar voltage trend prediction in this paper was based on 2 critical algorithms, dimensional reduction algorithm based on DTW [6]-[9] (Dynamic Time Wrapping), and ensemble learning [10]-[14] algorithm.

The steps of short-term prediction model of busbar voltage trend are described as follows:

Input: a set D of historical data of L -Lines related to a given busbar,

Output: optimal classifier.

Step 1: The Set D of historical data was preprocessed and transformed into relevant time series dataset of decision information system for busbar voltage trend prediction.

Step 2: The time series dataset was clustered for each column of time series data (except the decision column) in the DB matrix.

Step 3: Based on the clusters of Step 2, DB matrix was transformed into a two-dimensional decision information table IS_{DB} , in which any C_{xy} is a TS_{xy} cluster type.

Step 4: Based on the two-dimensional decision information table IS_{DB} of step 3, the classical machine learning classification algorithm (SVM, RNN, C4.5 decision tree, etc.) was training to model classifier.

Step 5: Based on the decision knowledge and classifier models of step 4, the bagging strategy of ensemble learning [12]-[17] algorithm was utilized to choose the optimal classifier model

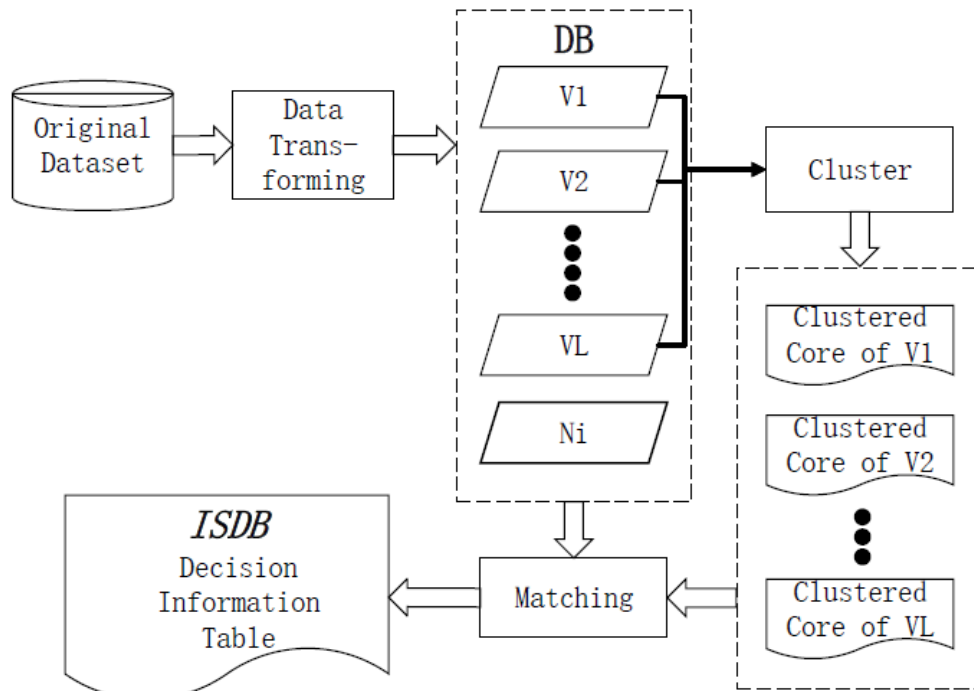


Figure 2. Flowchart of DTW dimensional reduction algorithm

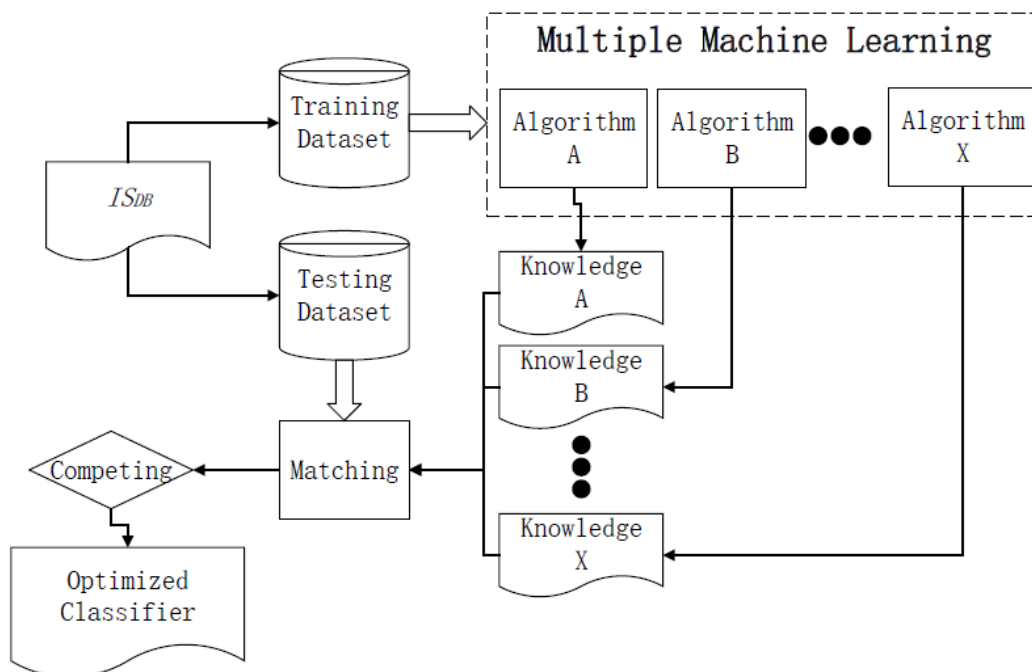


Figure 3. Flowchart of ensemble learning algorithm

$$DB = \begin{bmatrix} TS_{11} & TS_{21} & L & TS_{L1} & N_1^k \\ TS_{12} & TS_{22} & L & TS_{L2} & N_2^k \\ M & M & M & M & \\ TS_{1m} & TS_{2m} & L & TS_{Lm} & N_m^k \end{bmatrix} \xrightarrow{\text{Cluster}} IS_{DB} = \begin{bmatrix} C_{11} & C_{21} & L & C_{L1} & N_1^k \\ C_{12} & C_{22} & L & C_{L2} & N_2^k \\ M & M & M & M & \\ C_{1m} & C_{2m} & L & C_{Lm} & N_m^k \end{bmatrix}$$

4. Experiments and analysis

The data of experiment was abstracted from D5000 system in a substation of the State Grid Shanghai company. The goal of busbar voltage trend prediction was to forecast No. I 500kV busbar historical Uac line voltage sequence from 2015 to 2017, and the relevant data included 4 related historical 220kV busbar line Uac line voltage sequence, the relevant transformer time sequence, switching log records and status records of related AVC equipment, related historical remote signal of switch, and environmental temperature sequence. Support Vector Machines, BP Artificial Neural Network, C4.5 Decision Tree were chosen as the algorithms of multiple machine learning for ensemble learning.

Figure 4-6 demonstrated three algorithms (C4.5 decision tree, BP neural network, SVM) with different h values, which represent the time window granularity of predictive model, with the dataset of year 2015-2017. The results of experiment validated that the efficiency of predictive model was depended on the granularity of time windows and the feature of algorithms. The predictive accuracy of the optimal classifier from ensemble learning was the highest, which also indicated that ensemble learning method can effectively resist the conceptual drift of the short-term predictive data of voltage trend.

In addition, three experiments showed that the effect of bus voltage trend prediction with optimal classifier model window granularity $h = 8$ was better than the others with granularity $h = 4$ or $h = 12$. The predictive accuracy of model in year 2015 was 91.3% when the granularity was $h=8$. The accuracy was 92.5% when the granularity was $h=4$, and the accuracy was only 88.5% when the granularity was $h=12$. Furthermore, in 2016 and 2017, the predictive accuracy of model was also highest when granularity was $h=8$. The experimental results discovered that the potential knowledge in the experiment cannot be completely extracted if the timing window granularity of model was too small. On the other side, if the timing window granularity of model was too large, it was possible to overfit the real pattern of knowledge. Therefore, in the short-term prediction method of busbars' voltage trend, it is an important factor to choose the appropriate timing window granularity of model.

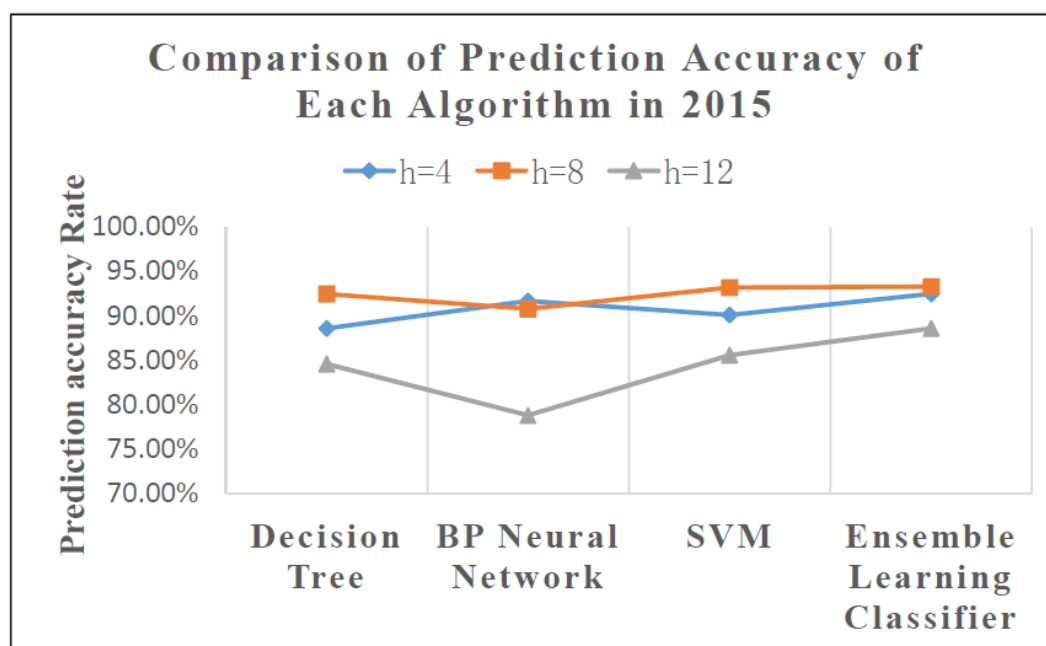


Figure 4. Comparison of predictive accuracy between each predictive models in year 2015.

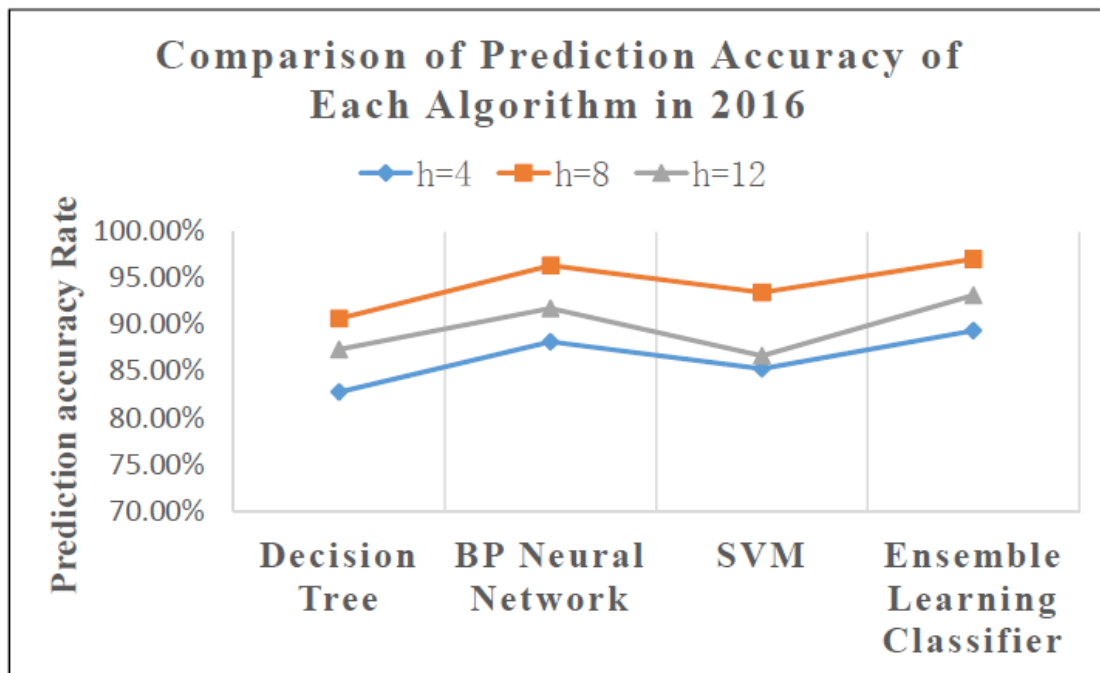


Figure 5. Comparison of predictive accuracy between each predictive models in year 2016.

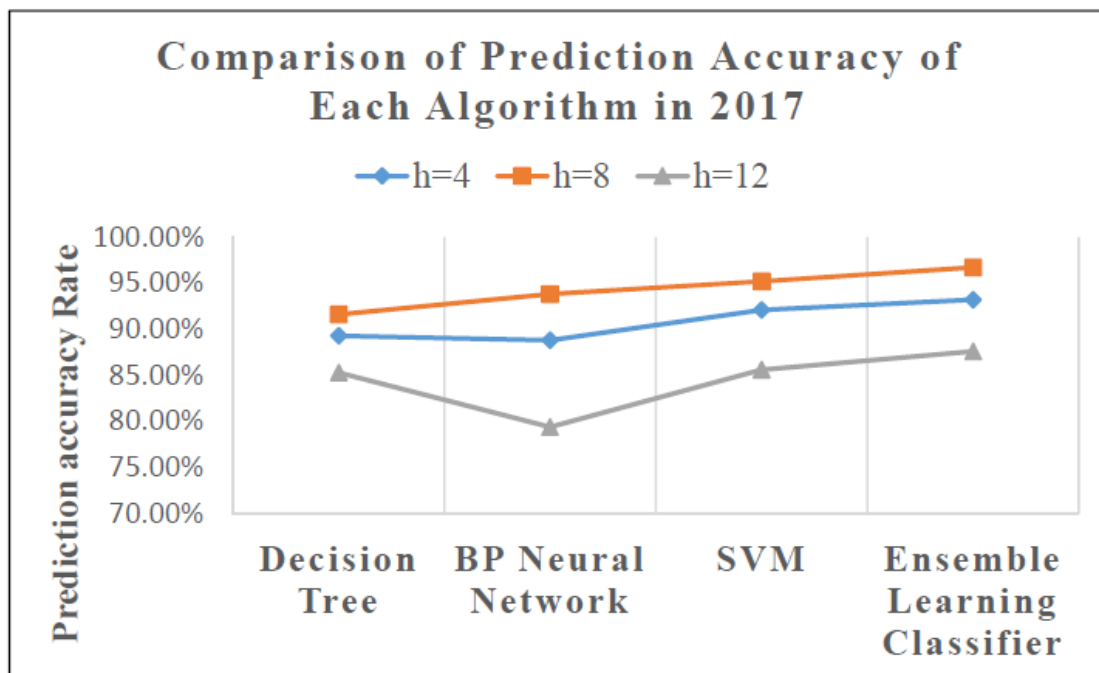


Figure 6. Comparison of predictive accuracy between each predictive models in year 2017.

5. Conclusion

This paper proposed a short-term prediction method based on multi-dimensional time series data mining and had been succeeded to implement in practical scenarios of State Grid Shanghai Company. Compared with the traditional voltage prediction algorithm based on one dimensional data, the ensemble learning strategy with various classic machine learning algorithm was proposed in this paper and validated its efficiency for short-term prediction of voltage trend. The results of prediction can support the function of fake alarms filtering in the voltage exceeding intelligent alarm system, and

improve the efficiency of whole alarm system. However, the prediction method was still possible to improve, for example, via Dynamic Time Wrapping (DTW) clustering algorithm used in the decision table. On account of the high computational complexity of classical DTW algorithm, efficiency of clustering is the critical tasks in the next stage. In addition, the strategy of ensemble learning classifier in this paper is Bagging strategy based on voting mechanism, and whether Boosting strategy [14] is more efficient than Bagging strategy or not in short-term prediction for busbar's voltage trend, also need further research.

6. Acknowledgments

I really appreciate the support and assistant of every expert and colleague from State Grid Shanghai Company for this project. Their advices and knowledge made this method discussed in the paper to be feasible and implement. However, I also thank for the help of Dr. Yu, Dr. Xu and Dr. Zhao from Nanchang University and Tellhow Company.

7. References

- [1] Wang Chen, Dong Xiaoyang, Wang Ruihan. 2015. Wide area back-up protection algorithm for least squares estimation under finite phasor measurement unit. *Power system automation*, 39 (20), p124-129.
- [2] Shao Li, Xie Kaigui, Wang Jin et al. 2008. Distribution network Reliability evaluation algorithm based on power flow estimation and block load reduction. *Power grid Technology*, 32 (24), p34-37.
- [3] Zhang Jihong, He Zhiyong, Xing Jun. 2015. Droop control strategy of micro-power grid inverter using public coupled point voltage estimation. *Large motor Technology*, 1 (1) p57-61.
- [4] Zeng Yi, Zhu Zhenmin, Liu Jinla, Chen Yuanfei. 2010. Dynamic voltage regulation prediction algorithm based on periodic pattern matching. *Computer Engineering*, 36 (13) p265-268
- [5] Li Xiaomin, Yin Ming. 2016. Research on the state prediction method of BP neural network Electronic system based on genetic algorithm. *Electronic measurement technology*, 39 (9) p182-186
- [6] You Jin, Liu Junyong, Qiu Gao. 2017. Voltage fast estimation based on adaptive neural network. *Power Exploration Design*, 02 (1) p44-49
- [7] You Jin. 2017. On-line voltage prediction on the basis of nonparametric estimation. *Sichuan Electric Power Technology*, 40 (5) p1-5
- [8] Phan, T., Caillaud, E. 2017. Dynamic time warping-based imputation for univariate time series data. *Pattern Recognition Letters*.
- [9] Górecki, Tomasz, Łuczak, Maciej. 2014. Non-isometric transforms in time series classification using DTW. *Knowledge-Based Systems*, 61 p98-108.
- [10] Łuczak, Maciej. 2016. Hierarchical clustering of time series data with parametric derivative dynamic time warping. *Expert Systems with Applications*, 62 p116-130.
- [11] Yang Yanlin, Ye Feng. 2016. a method for mining hydrological time series similarity based on DTW clustering. *Computer science*, 42 (2) p245-249
- [12] Krawczyk, B. Minku, L. 2017. Ensemble learning for data stream analysis: A survey. *Information Fusion*
- [13] Li, S. Goel, L. 2016. An ensemble approach for short-term load forecasting by extreme learning machine. *Applied Energy*, p22-29
- [14] Chen, K., Jiang, J. 2018. A novel data-driven approach for residential electricity consumption prediction based on ensemble learning. *Energy*, 150 p49-60.
- [15] Heinermann, J., Kramer, O. 2016. Machine learning ensembles for wind power prediction. *Renewable Energy*, 89 p671-679.
- [16] Peimankar, A., Weddell, S. J. 2018. Multi-Objective Ensemble Forecasting with an Application to Power Transformers. *Applied Soft Computing*
- [17] Collell, G., Prelec, D. 2018. A simple plug-in bagging ensemble based on threshold-moving for classifying binary and multiclass imbalanced data. *Neurocomputing*, 275 p330-340

Grounding Fault Analysis and Protection Measures Study of Composite Grounding Arc-suppression Modes

B Yu¹, H Li², W J Zhu², H F Liu², W W Liang², Z D Zhang², S Y Guo²

¹ Junior Engineer, State Grid Hunan Electric Power Company Limited Research Institute, Hunan, China

² Senior Engineer, State Grid Hunan Electric Power Company Limited Research Institute, Hunan, China

E-mail: bindongsanchi@163.com

Abstract. Centering on analysis of single-phase ground fault, and based on a wide-range survey of typical structure and accessing equipment of 10kV distribution network, accurate simulation model reflecting engineering practice is established according to the existing power design standards. For composite grounding arc-suppression modes, this paper describes both the principle and fault treatment process of grounding fault transfer mode and intelligent multimode grounding mode. According to the fault treatment process, a line selection method based on the first transient half wave of fault grounding and operation grounding of the own line is put forward for grounding fault transfer mode, and the effect of transition resistance on zero-sequence current protection for intelligent multimode grounding mode is analyzed. All of this is verified by our simulation model in PSCAD. This research lays a solid theoretical foundation for the engineering application of composite grounding arc-suppression mode.

1. Introduction

Widely distributed distribution network always operates in complex environment. Power outages caused by frequent random failures have resulted in significant economic losses. Building a strong and safe distribution network is an important part of the national development strategy named “developing smart grid and distributed energy” [1]. Neutral grounding mode of distribution network which is closely related to its safe and reliable operation. System with different grounding modes has different fault characteristics under single phase grounding fault [2]. The grounding mode relates to ground fault current, the insulation level of equipment, communication interference, dynamic stability, the reliability of relay protection and power supply, safety and so on[3], which has attracted much attention in the network construction of city and rural. The increasingly complex network structure, the gradually increasing cable proportion, the rising automation degree of system and the increment of new energy permeability [4]-[5] contributed to the complicated situation that a variety of grounding modes coexist and safety control strategies diversify.

The typical neutral grounding mode including unground, resonant ground and low resistance ground. With the reconstruction of city network, the capacitive current is more and more big. There is insufficient capacity for arc suppression coil to compensate power component and harmonic components. And the low resistance ground mode trips frequently. Therefore, relevant experts and scholars began to get involved in the research for composite grounding arc-suppression modes, such as grounding fault transfer mode [6], intelligent multimode grounding mode [7] and flexible grounding mode [8]. For neutral non-grounded mode, literature [6] elaborated a grounding fault transfer mode that makes the bus phase with fault grounding. This mode switches arc grounding fault of lines to



metallic grounding fault on bus. For resonant grounding mode, in addition to the way cooperating with grounding fault transfer mode in [9], intelligent multimode grounding mode that consists of arc suppression coil and parallel resistance was put forward by [7], which not only can eliminate transient grounding fault automatically, but also can isolate permanent grounding fault quickly. In the background of rapid development of power electronics technology, the authors of [8] proposed flexible grounding arc suppression method. This method can realize the total compensation of fundamental reactive component, fundamental active component and harmonic components by using the active inverter to inject current. At present, there is few literature on the action mechanism and protection countermeasures of composite grounding arc-suppression modes.

All things considered, the wiring form of typical neutral grounding modes and composite grounding arc-suppression modes are introduced. The system simulation model reflecting the actual distribution network is established for the analysis of single-phase grounding fault. Based on this, grounding fault analysis and fault protection measures study for grounding fault transfer mode and intelligent multimode grounding mode are respectively well done.

2. Grounding mode and simulation modeling for distribution network

As shown in figure 1, the wiring form of unground, resonant ground and low resistance ground, grounding fault transfer and intelligent multimode grounding are depicted. When the switch K is switched off, the neutral point are not grounding. When K is closed to L_C , it is resonant ground mode. When K is closed to R_d , the neutral point grounds through low resistance. QK is fault phase grounding switch used to transfer the earthing fault quickly. When K is closed to L_C and K1 is closed, it is intelligent multimode grounding mode. K1 is high voltage vacuum contactor.

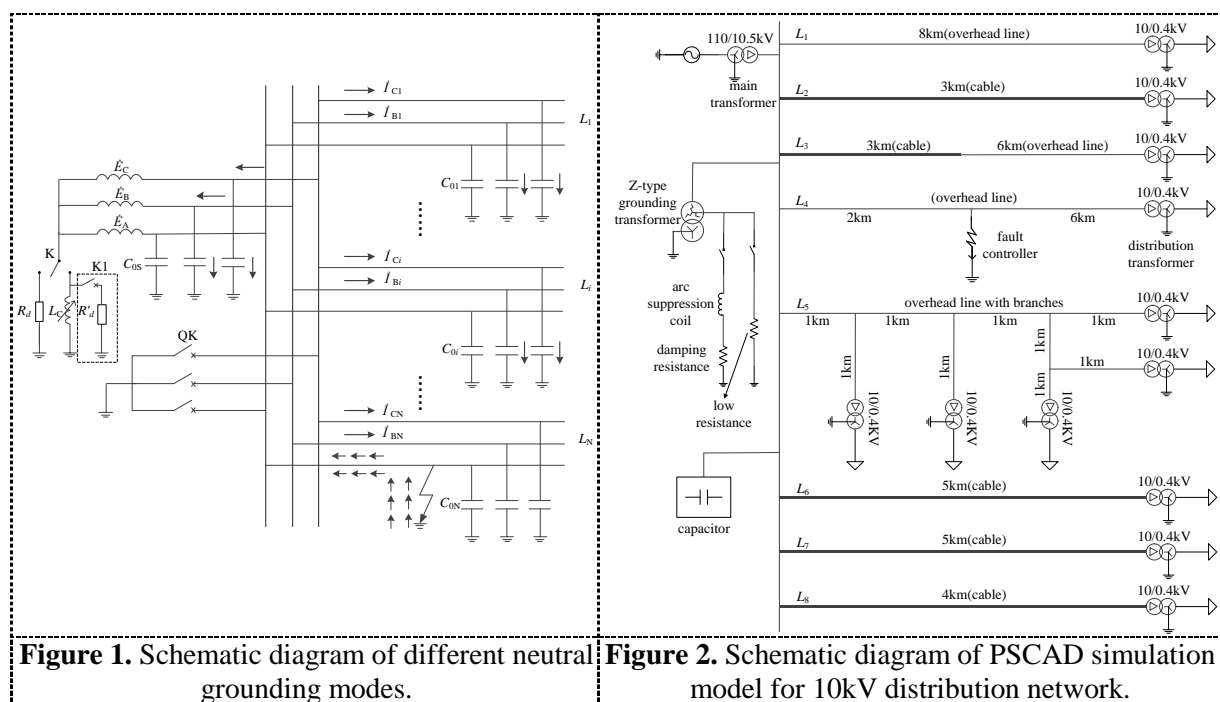


Figure 1. Schematic diagram of different neutral grounding modes.

Figure 2. Schematic diagram of PSCAD simulation model for 10kV distribution network.

For accurate fault analysis of composite grounding arc-suppression modes, great efforts are taken to establish a system simulation model for 10kV distribution network. We make a full investigation of the structure, feeder, distribution transformer and load configuration of 110kV substation. Besides, a large amount of design manuals and standard specifications related to the substation and distribution network are consulted. On the premise of a given load, equipment selection and parameter calculation is carried out according to the design standard and specification. Finally, we realize simulation modeling on the platform of PSCAD (Power Systems Computer Aided Design) as shown in figure 2. The simulation system includes main transformer, Z-type grounding transformer, neutral-point

grounding device, parallel compensation capacitor group and eight feeders. Distribution transformers are arranged on every feeder. The specific electrical parameters are as follows.

2.1. Transformer

The main transformer: the rated capacity is 20MVA, the change ratio is 110/10.5, the connection group is YNd11, the short-circuit loss is 88.4kW, and the no-load loss is 17.6kW. The distribution transformer: the rated capacity is 2MVA, the change ratio is 10/0.4, the connection group is Dyn11, the short-circuit loss is 13.1kW, and the no-load loss is 2.58kW. Z-type grounding transformer: the rated capacity is 250kVA, the connection group is ZNyn11, the short-circuit loss is 540W, the no-load loss is 580W, and zero sequence impedance is 22.8Ω.

2.2. Feeder

L_1 and L_4 are overhead line. L_2 , L_6 , L_7 and L_8 are cable line. L_3 is hybrid overhead cable line. L_5 is overhead line with branches. L_1 is 8km long. L_2 is 3km long. L_3 is the combination of 3km cable and 6km overhead line. L_4 is 6km long. The parameters of feeders refer to [10].

2.3. Neutral-point grounding device

The inductance of the arc suppression coil is 0.596H, and the series damping resistance is 18.7Ω. In order to make the over voltage less than twice the peak of the maximal phase voltage, the grounding resistance is set as 15Ω.

2.4. Parallel compensation capacitor group

The capacity of the parallel compensation capacitor is 30% that of the main transformer. So its rated capacity is 6Mvar and the capacitance of each phase is 173uF.

In reality, the majority of grounding fault is arc grounding [11]. In order to simulate real grounding arc, the two classical arc models of Mayr and Cassie are combined to construct our arc model. Inputting arc voltage and arc current into the model so as to output arc resistance, which regulates voltage and current in turn. The process is controlled in closed-loop. What's more, temporal logic is designed for intermittent arc.

3. Grounding fault transfer mode

3.1. Fault analysis

As for grounding fault transfer mode, fast switches used for grounding are arranged on three phases of bus. The switches are opening during normal running. When single-phase arc grounding fault happens to line, Whether single-phase ground fault happens and the grounding phase are judged according to the change of the angle between zero sequence voltage and line voltage. Then fault phase fast switch closes instantly. The unstable fault grounding point is turned into stable metallic grounding point. The voltage of fault point is close to 0 so that the grounding arc can't reignite. The overvoltage of non-fault-phase can be stabilized around 1.732 times phase voltage, which makes devices run safely. For fault through resistance or fault with arc extinguishing, the grounding current is the capacitive current to the ground. For metallic grounding fault, the fault point will have shunting current.

The figure 3 shows the schematic diagram of grounding fault transfer mode which has two arc-suppression schemes. Scheme one only installs fault phase fast grounding device. Fault phase fast switch closes for 14 to 20ms after single-phase grounding fault. Scheme two combines arc suppression coil with fault phase fast grounding device. When metallic grounding fault or fault through resistance happens, fault phase fast switch doesn't operate and arc suppression coil is switched on for following capacitive current compensation. When single-phase arc grounding fault happens, fault phase fast switch closes rapidly and arc is extinguished. After about 6ms, arc suppression coil is switched on to reduce the grounding current of fast switch of fault phase.

The above two arc-suppression schemes are simulated in a situation where stable arc grounding fault happens to C phase. When the voltage of C phase peak, the fault locates at L_2 the distance of 1.8km from bus. For scheme one, single-phase arc grounding fault occurs to C phase at 0.12s. Fast grounding switch of C phase is switched on at 0.135s. On one hand, the current of fault point changes to 0. On

the other hand, the voltage of non-fault phase reaches line voltage and the voltage of neutral point reaches phase voltage. Assuming that arc fault extinguishes, fast switch turns off at 0.195s. On the same time, the overvoltage of non-fault phase will rise in some degree. The voltage of fault phase recover from 0.2s at low speed due to the voltage of neutral point can't reduce to 0 instantly. The process is shown in figure 4.

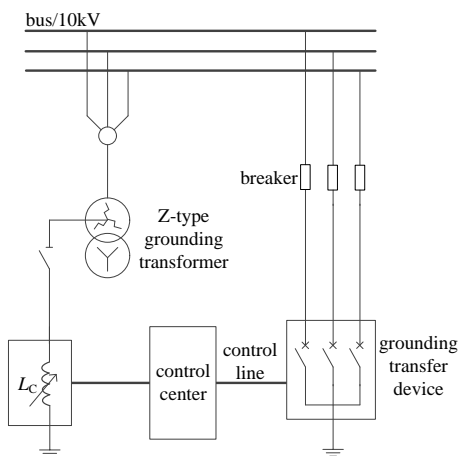


Figure 3. Wiring diagram of grounding fault transfer mode.

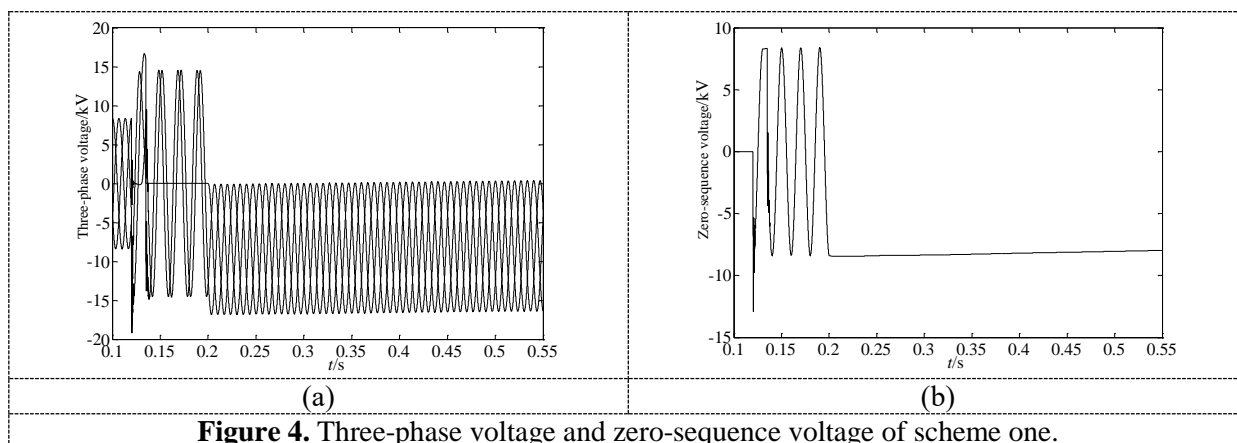


Figure 4. Three-phase voltage and zero-sequence voltage of scheme one.

For scheme two, the condition different from scheme one is that arc suppression coil will be put into at 0.141s. As shown in figure 5 and figure 6, the current of grounding point on bus is compensated. The voltage of neutral point is close to 0 after continuing damped oscillation. The voltage of fault phase rise to normal phase voltage. The voltage of non-fault phase decay to normal phase voltage. Therefore, scheme two has advantages of grounding current compensation and quick voltage recovery.

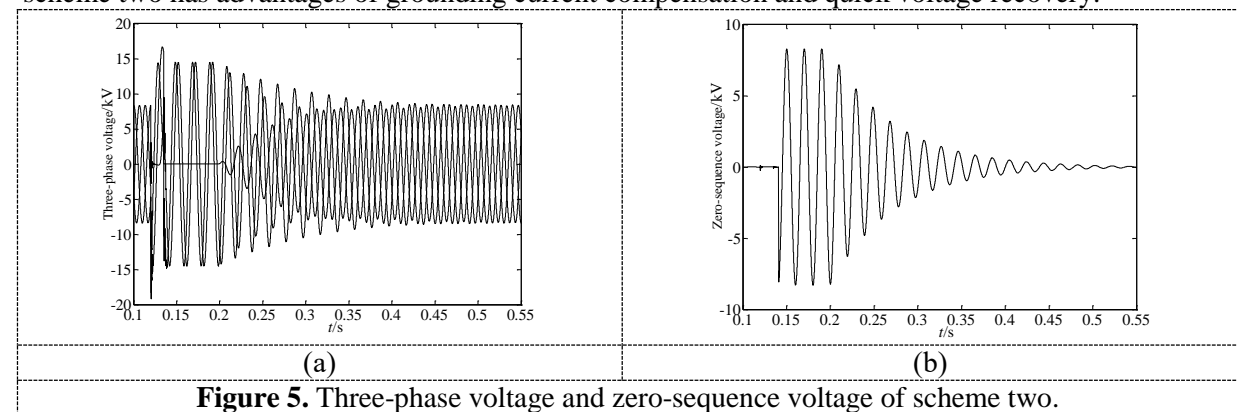
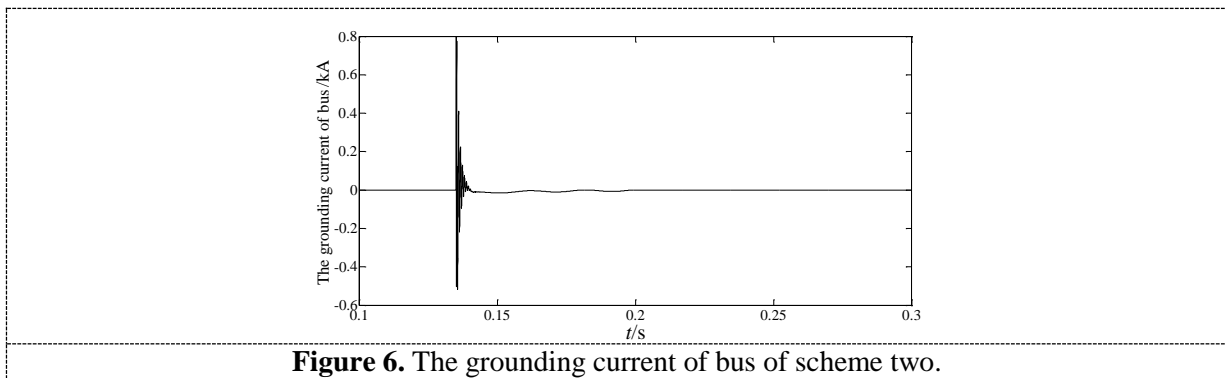


Figure 5. Three-phase voltage and zero-sequence voltage of scheme two.



3.2. Protection measures

Although grounding fault transfer mode extinguishes arc effectively, fault may happen again for the damaging insulation of fault line. Fault line need to be found quickly. Because fast switch will finish closing within one period after fault, transient process may be not over. It would be unreliable to use line selection method based on steady character of zero-sequence current.

Taking zero-sequence voltage as a reference, traditional line selection based on the first transient half wave judges fault line by comparing the polarity of the first transient half wave of zero-sequence current of all lines. It is a kind of group phase comparison method about transient zero-sequence current. It can be seen that there is few method using the characters of the development process of fault to select the fault line. Since there are two process of fault grounding and operation grounding, we can study fault line selection method by combining with the transient character of the two process.

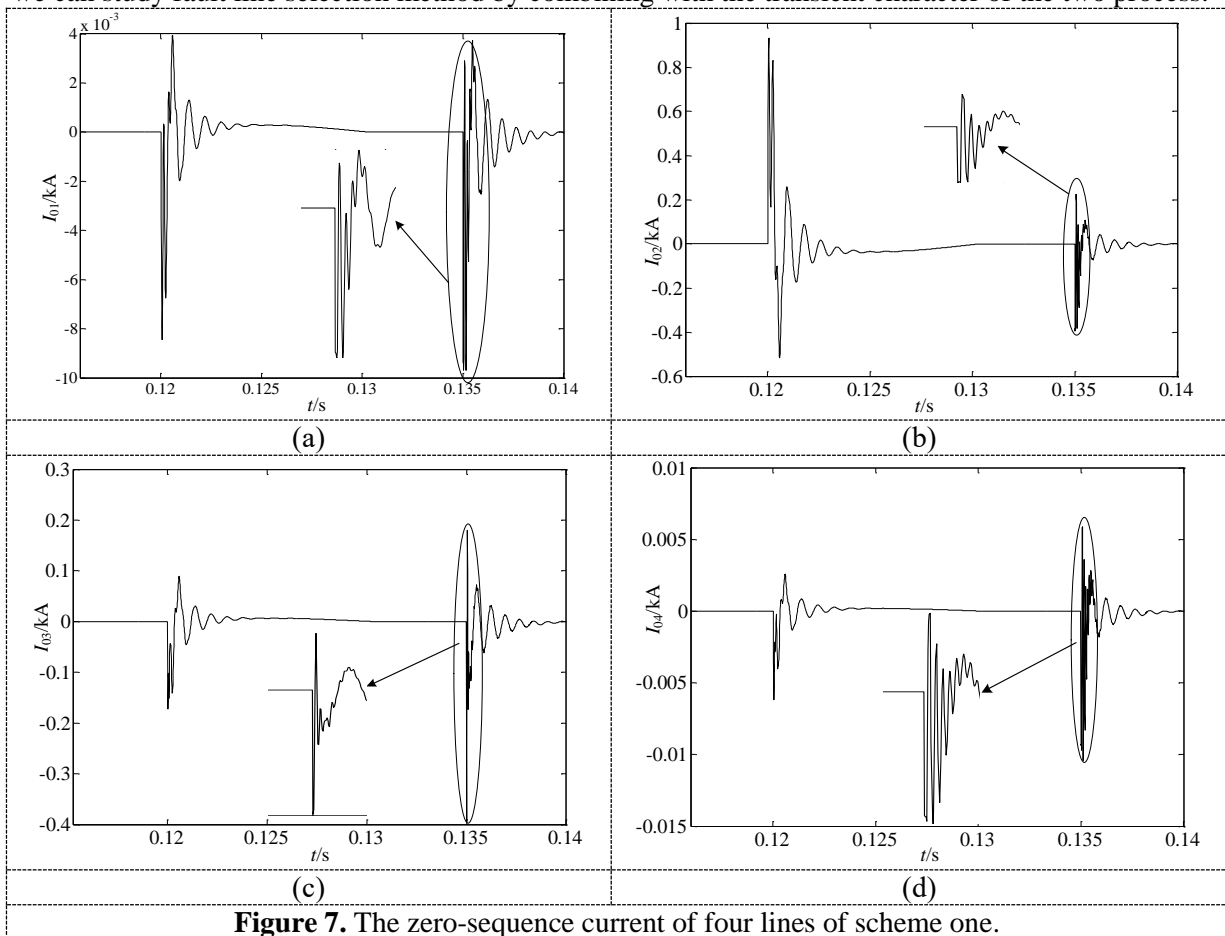


Figure 7 shows the zero-sequence current of L_1, L_2, L_3, L_4 in scheme one. It can be seen that the amplitude and phase of zero-sequence current for L_2 change obviously after grounding fault and the closure of fast switch, and that of normal lines change little. As for the fault line, the polarity of the first transient half wave of zero-sequence current after grounding fault is the opposite of that of zero-sequence current after the closure of fast switch. Besides the impact value of the former is bigger than that of the latter. But the case of normal lines is the exact opposite. In view of the above-mentioned facts, we construct the line selection criterion below.

$$\begin{cases} |I_f| > |I_t| \\ \text{sgn}(I_f) \neq \text{sgn}(I_t) \end{cases} \quad i \in [1, N] \quad (1)$$

Where I_f is the amplitude of the transient current travelling wave of the i th line after grounding fault; I_t is the amplitude of the transient current travelling wave of the i th line after grounding transfer. The method has the advantage that line selection only needs the character of the first transient half wave of fault grounding and operation grounding of this line.

4. Intelligent multimode grounding mode

4.1. Fault analysis

Intelligent multimode grounding mode develops on the base of resonant grounding mode and low resistance grounding mode. On one hand, it keeps the advantage of handling the transient fault quickly of resonant grounding mode. On the other hand, it inherits the merits of isolating grounding fault quickly and accurately from low resistance grounding mode.

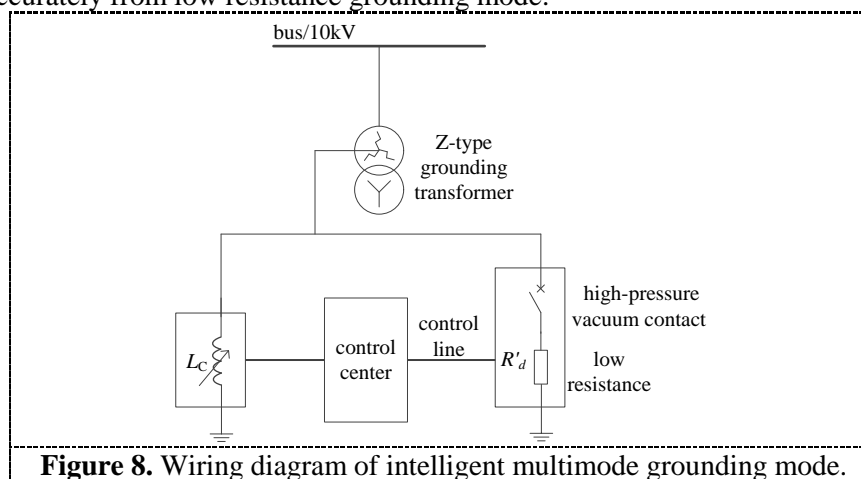


Figure 8. Wiring diagram of intelligent multimode grounding mode.

As shown in figure 8, intelligent multimode grounding mode can realize the integrated control of grounding fault of feeders. Different responding scheme will be adopted for different fault. The principle of intelligent multimode grounding mode can be described as: when grounding fault happens, short-time controllable reactor which has the advantages of quick compensation and continuing stepless regulation will compensate capacitive current accurately within around 5ms, then grounding arc can be extinguished. The transient single-phase grounding fault can be removed and related fault information will be recorded automatically. As for permanent single-phase grounding fault, if the time of grounding exceeds the set value (10s), low resistance will be put into system by high-pressure vacuum contact. Then line protection device makes the grounding line trip.

Simulating the above two situations in the simulation system. The function of short-time controllable reactor is simplified as that of arc suppression coil. Other simulation conditions are the same as the previous section.

Transient grounding fault is removed after compensating current is output by arc suppression coil. Residual current of grounding point, arc suppression coil compensation current, three-phase voltage and zero-sequence voltage for transient grounding fault are shown in figure 9 and figure 10.

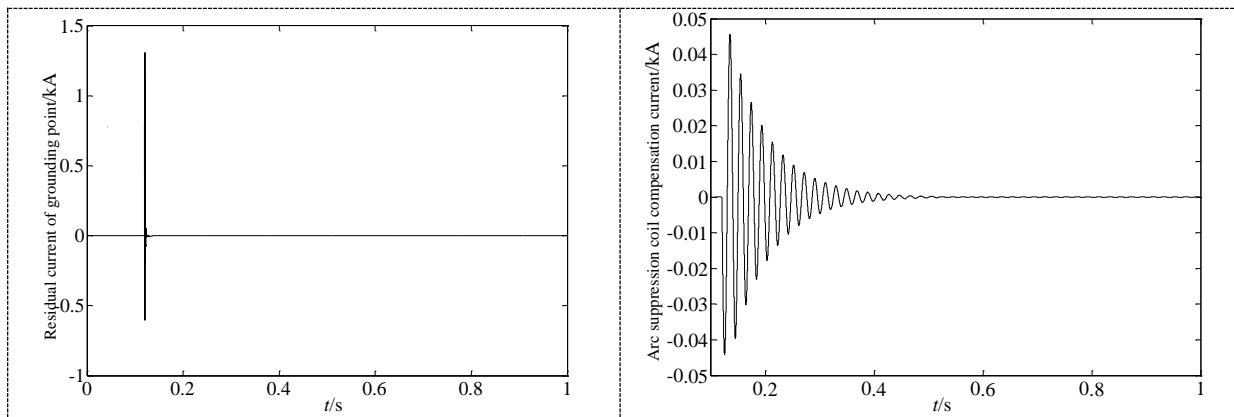


Figure 9. Residual current of grounding point and arc suppression coil compensation current for transient grounding fault.

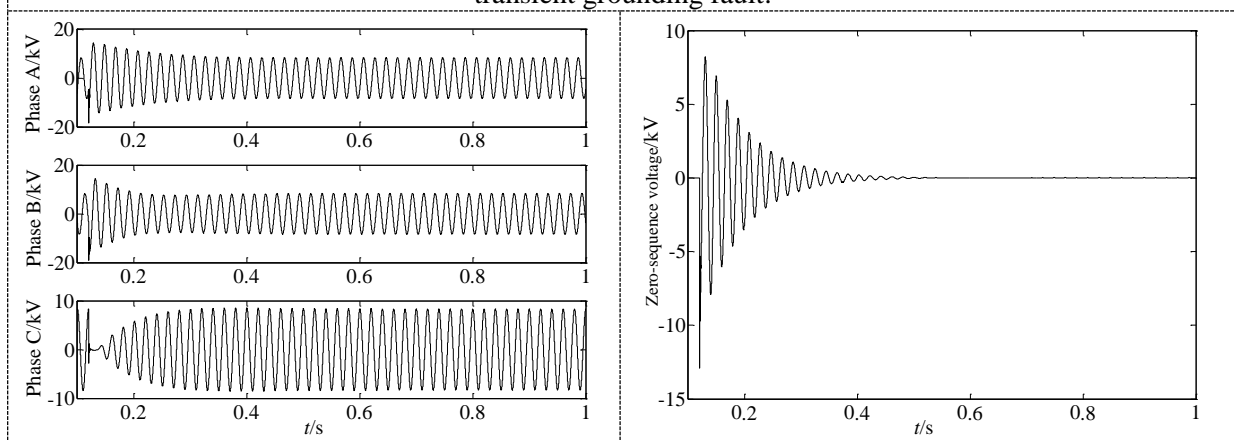


Figure 10. Three-phase voltage and zero-sequence voltage for transient grounding fault.

For permanent grounding fault, we set the same fault condition except the fault is metallic grounding fault. Arc suppression coil compensates the fault current of grounding point after fault. For the convenience of simulation, low resistance device will be put into after 3.12s, and arc suppression coil will drop out at the same time. Assuming that line protection device operating tripping at 3.32s, the system will go back to normal running. The waveform of electrical parameters in this process are shown in figure 11 and figure 12.

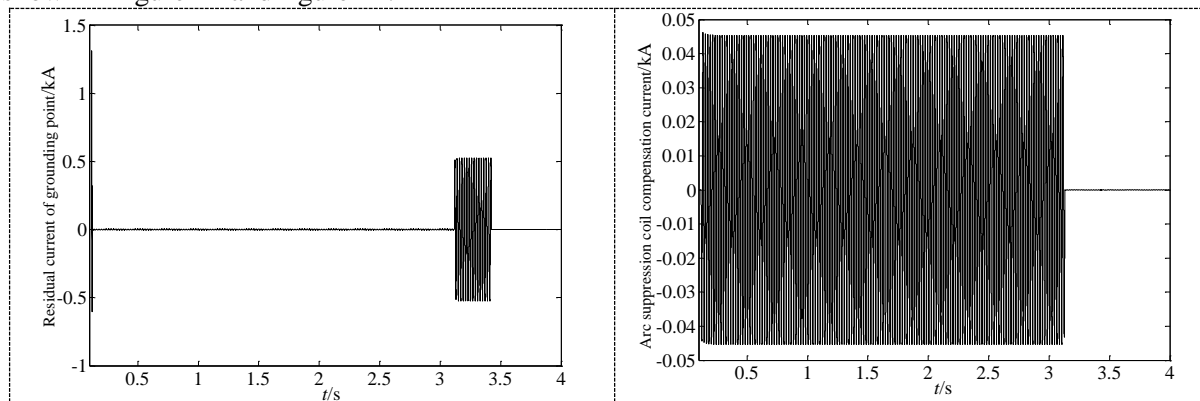


Figure 11. Residual current of grounding point and arc suppression coil compensation current for permanent grounding fault.

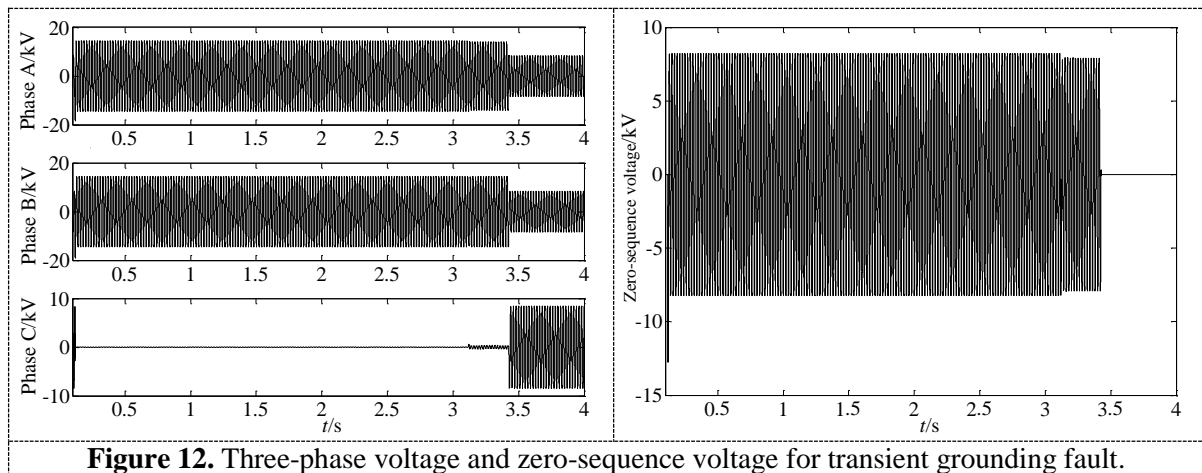


Figure 12. Three-phase voltage and zero-sequence voltage for transient grounding fault.

4.2. Protection measures

Intelligent multimode grounding mode can remove the transient grounding fault by quick and accurate compensation. For the permanent grounding fault, the fault line is removed by zero-sequence current protection after low resistance’s join. The single-phase grounding fault of feeders often grounds with transition resistance [12]. The resistance will reduce the fault current. And a high-resistance will cause reject-action of protection. This section will analyze the process that zero-sequence current protection removes the permanent grounding fault after adding low resistance and define the influence of transition resistance to the sensitivity of zero-sequence current protection.

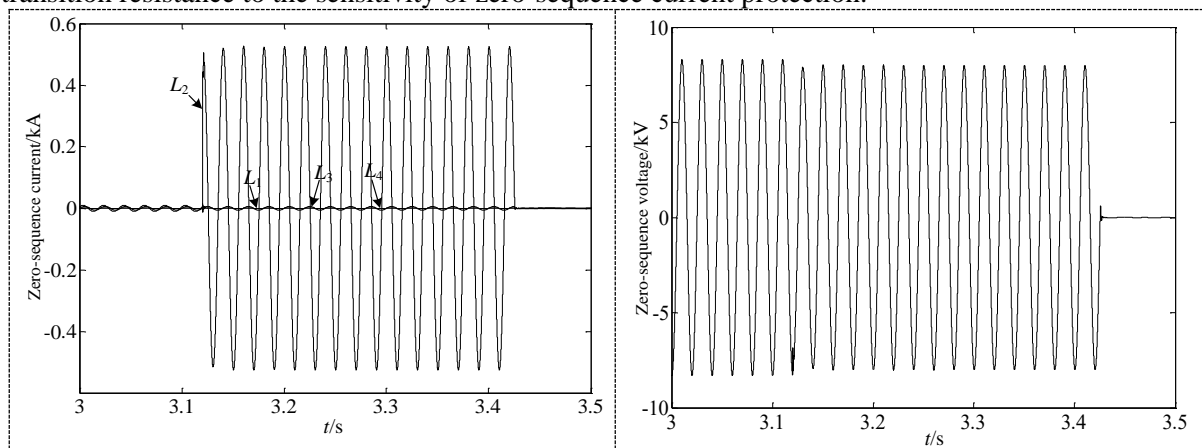


Figure 13. Zero-sequence current and zero-sequence voltage for metal grounding fault.

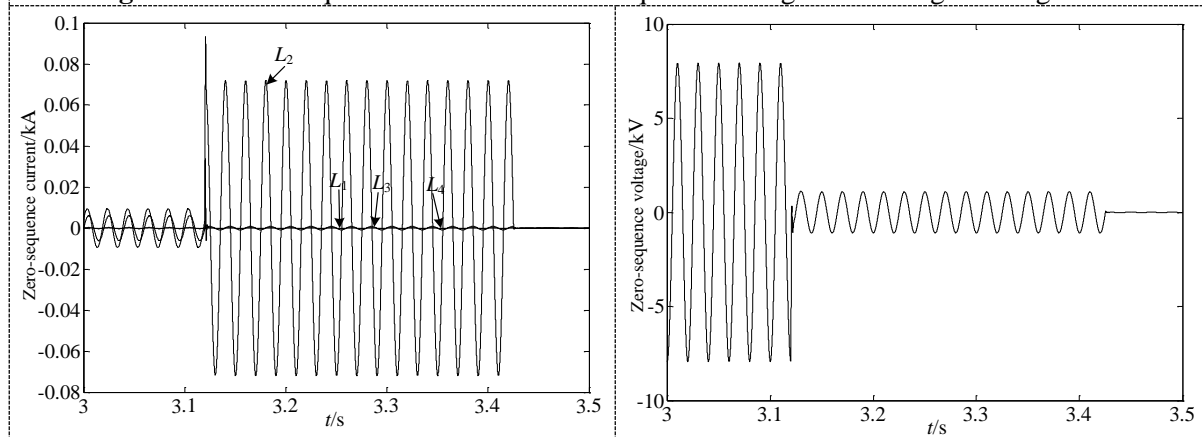


Figure 14. Zero-sequence current and zero-sequence voltage for grounding fault with 100Ω transition resistance.

Figure 13 and figure 14 shows the zero-sequence current of $L_1\sim L_4$ and system zero-sequence voltage in the case of metallic ground and ground with transition resistance after adding low resistance. As we can see from figure13, under metallic short-circuit fault, there is a short-time transient process after adding low resistance. The zero-sequence current peak of the fault line is about 526.5A, which is small for the impedance Z-type transformer and lines. But it's amplitude is greater than that of non-fault lines. In figure15, the zero-sequence current amplitude of L_2 is close to that of L_3 before adding low resistance, which may cause wrong line selection result. The enlargement of transition resistance will greatly reduce the amplitude of zero-sequence current and zero-sequence voltage of the fault line, which may cause reject-action of protection. So we should study the influence of transition resistance to zero-sequence current of feeders. According to the stipulations of DL/T 584-2007, the relay setting of the first section of zero-sequence current protection refers to the minimal single-phase grounding fault current.

$$I_{0I}^{(line)} = \frac{I_{Dmin}^{(1)}}{k_{LM}} \quad (2)$$

Where $I_{Dmin}^{(1)}$ is the minimal single-phase grounding fault current, k_{LM} is the sensitive coefficient which is equal or greater than 2. The relay setting of the second section of zero-sequence current protection should be bigger than capacitive current of lines and unbalanced current of phase-to-phase fault.

$$I_{0II}^{(line)} = K'_K I_C \quad (3)$$

Where I_C is the capacitive current of this line, K'_K is the reliable coefficient which is set as 1.5. The relay setting of the second section will increase with the length of cables increasing. Then the ability of zero-sequence current protection to reverse transition resistance will decline sharply.

The relay setting of the first section of zero-sequence current protection is set as 186A and that of the second section is set as 9A. The simulation results of different transition resistance are shown in figure 16. With the increase of transition resistance, zero-sequence current of the fault line will decrease. When transition resistance is low, zero-sequence current decrease rapidly with the increase of transition resistance. When transition resistance is bigger than 16Ω , zero-sequence current is smaller than 186A so that the first section can't trip and the second section trip with long time. When transition resistance is bigger than 640Ω , zero-sequence can't operate reliably.

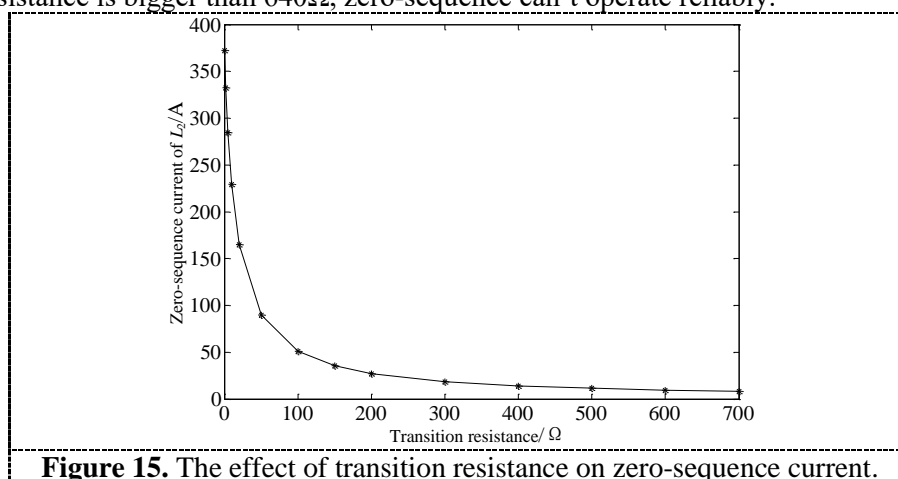


Figure 15. The effect of transition resistance on zero-sequence current.

5. Conclusion

With the large scale of construction and renewal of distribution network, the enlargement of cables leads to more complex grounding modes. This paper makes fault analysis and fault protection measures study for grounding fault transfer mode and intelligent multimode grounding mode based on the accurate simulation model. Research results help to enhance our recognition for the change of

electric parameters in composite grounding arc-suppression modes. It also lays the theoretical foundation for applying to practice and has important implications for improving reliability and security of distribution network.

6. References

- [1] Yao J G, Gao Z Y, and Yang S C 2015 Understanding and prospects of energy internet *J. Automation of Electric Power System*. AEPS20151101004
- [2] Fu Z X, Wang N, Huang L and Zhang R 2014 Study on neutral point grounding modes in medium-voltage distribution network *J. International Symposium on Computer, Consumer and Control*. IS3C.2014.51
- [3] Dong L, He L and Pu T 2013 Effect of neutral grounding mode on reliability of distribution network *J. Power System Protection and Control*. j.issn.1674-3415.2013.01.015
- [4] Tian S M, Luan W P, Zhang D S, Liang C H and Sun Y J 2015 Technical forms and key technologies on energy internet *J. Proceedings of the CSEE*. PCSEE2015.14.002
- [5] Zhang J H, Zeng B, Zhang Y Y, Liu D C, Yang X, Li C and Liu W X 2014 Key issues and research prospects of active distribution network planning *J. Transactions of China Electrotechnical Society*. TCES.2014.02.002
- [6] W X Chen, S P Xiao, H Y Liu, P Li and Z Feng 2018 Analysis of the abnormal treatment of the first end line failure test by using transferring-type arc-suppression device *J. Journal of Hunan University of Technology*. j.issn.1673-9833.2018.01.013
- [7] Yang J Z 2016 Design and implementation of intelligent multi-modes grounding system (Beijing: North China Electric Power University).
- [8] R Chen, F Zhou, H J Weng, X J Zeng and W Wang. 2015 Flexible grounding device with the dual-loop control method for arc suppression *J. Journal of Electric Power Science and Technology*. j.issn.1673-9140.2015.04.009
- [9] F Yan, Z J Liao, W P Liu, J G Zhou, B Yang and C Guo 2017 The test and analysis of automatic tracking arc suppression compensation device and fault transfer grounding device on-site fault treatment *J. Distribution & Utilization*. j.cnki.1006-6357.2017.11.017
- [10] Jiang B, Dong X Z and Shi S X 2014 A method of single phase to ground fault feeder selection based on single phase current traveling wave for distribution lines *J. Proceedings of the CSEE*. PCSEE.2014.34.025
- [11] J N Li, H Y Zhang, X H Wang and R M Gong 2016 Arc modeling and simulation of the ground faults of the middle voltage cable network *J. Power System Protection and Control*. 10.7667/PSPC152207
- [12] Liu B W and Ma S H 2015 Transition resistance measurement and fault phase selection under single-phase ground fault based on producing mechanism of zero-sequence voltage *J. Power System Technology*. PST.2015.05.041

Acknowledgments

This research is supported by the Science and Technology Project of State Grid Hunan Electric Power Company Limited (Grant No. 5216A516002Y). B Yu wishing to thank the research supervisor for the helpful guidance. I will remember you forever. Thanks for the meet with T Wang. You are always in my heart.

Research on Intelligent Diagnosis Strategy of Secondary Device Abnormity in Smart Substation

Meizi Hong¹, Peng Li¹, Di Wu², Bo Wen¹, Hengxuan Li¹

¹State Grid Hubei Electric Power Research Institute, Wuhan Hubei 430077, China

²State Grid Hubei Electric Power Company, Wuhan Hubei 430077, China

Abstract. With the high integration of smart substations, the traditional secondary cable in the conventional substation, which is unable to carry out online monitoring, has been replaced by the fiber-optic network with online monitoring function. The operation and maintenance personnel conduct the status of the secondary circuit through the communication messages in the network message analyzer. However, the rapid growth of information result in a series of issues, for example information is not intuitive and coverage of important information. As the consequence, it is difficult to quickly find the location and cause of fault. For the issue of abnormal diagnosis of secondary equipment of intelligent substation, this paper studies the operation and maintenance mode and physical modelling of the secondary system, visualization technology, on-line state evaluation technology and the fault location technology. On this basis, an intelligent diagnosis strategy for the secondary device of the smart substation is put forward. Furthermore, a fault diagnosis platform is developed to implement real time monitoring of secondary circuit and analyze abnormal situation to ensure the safe and reliable operation of smart substation.

1. Introduction

The smart substation adopts optical fiber instead of the traditional cables, and uses digital information to replace the analog information of the conventional substation resulting the traditional non on-line monitoring cables transferring into on-line monitoring network. The secondary system network and the new smart substation monitoring greatly improves the controllability of the secondary system in the smart substation, and provides powerful support for the fault diagnosis of the smart substation [1]. In the smart substation, the operation and maintenance personnel obtain the state of the secondary circuit by monitoring the communication message in the network message analyser instead of monitoring the analog quantity. Since the amount of information of the secondary system increases, the information is too much to be monitored and not intuitionistic leading to ignoring some important information. Therefore, it is difficult to find the fault location and the cause of the fault quickly [2]-[4]. Aiming at the needs and problems of the smart substation operation and maintenance, this paper studies the architecture of intelligent diagnosis system which includes the secondary system operation and maintenance mode, physical modeling of secondary system, visualization technology, online state assessment technology and fault location technology. Subsequently, the modelling specification of physical circuit is proposed, and the demonstration of the whole secondary circuit of the device is achieved. The “trend” and “loss” evaluation system based on the full message of the substation is then established. To evaluate the health status of the device, the multi-parameter information fusion analysis method is used. By introducing the method of fault location of the secondary circuit in the process layer, a data set of all possible fault points is obtained. Hence, the most likely fault point is obtained through demonstrating the state of the equipment related to the fault circuit.



This paper proposes an intelligent diagnosis strategy for secondary equipment of smart substation, and develops a diagnosis platform for the secondary device fault and abnormality of the smart substation. The proposed method can obtain the state of secondary circuit in real time and analyze the abnormal situation for safe and reliable operation of smart station.

2. The main problems of operation and maintenance of the secondary system of Smart substation

In the smart substation, the communication network has replaced the traditional secondary circuit, the digital signal takes the place of the traditional physical and electrical signals. Compared with the traditional substation, there are three problems in the smart substation.

secondary systems profession deep fusion, physical circuit complexity increased.

Relay protection sampling, calculation and outlet are Integrated in conventional substations, data information, protection objects and devices are bound together, and operation and maintenance are simple and convenient. The composition of the smart substation equipment has changed greatly, newly added the process layer, merging unit, intelligent terminal, network switch and so on, the amount of information has increased greatly, and the secondary systems are more complex [5]-[8].

It is not intuitive to replace the cable with the optical fiber in the secondary circuit.

The equipment in the conventional substation is connected by cables, and the secondary circuit is intuitively visible. The smart substation uses optical cable instead of cable, and the secondary circuit becomes virtual circuit. All the configuration of the case and communication parameters are included in the SCD file, and the SCD file can not directly reflect the secondary circuit, configuration information such as communication parameters, signal association and so on, which can cause great inconvenience to operation and maintenance [9]-[12].

The secondary circuit state assessment and fault diagnosis methods are lacking, fault points can not be found quickly.[13]

Compared with the traditional substation, the secondary system structure of the smart substation is more complex, the visibility of the secondary circuit is poor, the secondary circuit state evaluation and the fault diagnosis means are short. At present, when the smart substation has the fault, the operation and maintenance personnel dependence on the factory to deal with it, which seriously affects the progress of the fault treatment and affects the safety of the smart substation maintenance. Therefore, it is necessary to study the intelligent diagnosis of the secondary device abnormality in smart substations.

3. Research on intelligent diagnosis strategy of the secondary device abnormality in Smart substation

From the conventional substation to the smart substation, although the secondary circuit turns into a virtual circuit, it brings problems to operation and maintenance, but the information provided by the smart substation is more comprehensive, and the information between device and device can be fully interactive. Using appropriate technology and means, the operators can master the status of the device more accurately. The following four main problems are studied in depth: 1) physical circuit model expansion; 2) visual display; 3) online status assessment; 4) fault location.

3.1. Expansion modeling of physical secondary circuits in smart substations

Expansion modeling of physical secondary circuits in smart substations means the abstract modeling of the existing physical circuits and combination to the SCD file, then form the physical and logical panoramic model of the substation.

The main technical points of expansion modeling of physical secondary circuits in smart substations include: the decoupling design of the physical circuit and the logic circuit, the designers can design the logical circuit configuration file and the physical circuit configuration file in parallel to improve the design efficiency. When designing drawings or debugging, the two configuration files can be corresponded with virtual reality to realize the integrated design and application of virtual reality. Secondary circuit panoramic model design flow is shown in Figure 1.

The design process of the physical circuit includes: importing the IPCD files of different physical equipment of secondary systems into the SPCD file configuration module, completing the hierarchical construction and the real circuit configuration in the SPCD. The system software completes the cable

layout automatically according to the above information. After the information configuration is completed, the whole SPCD file is generated.

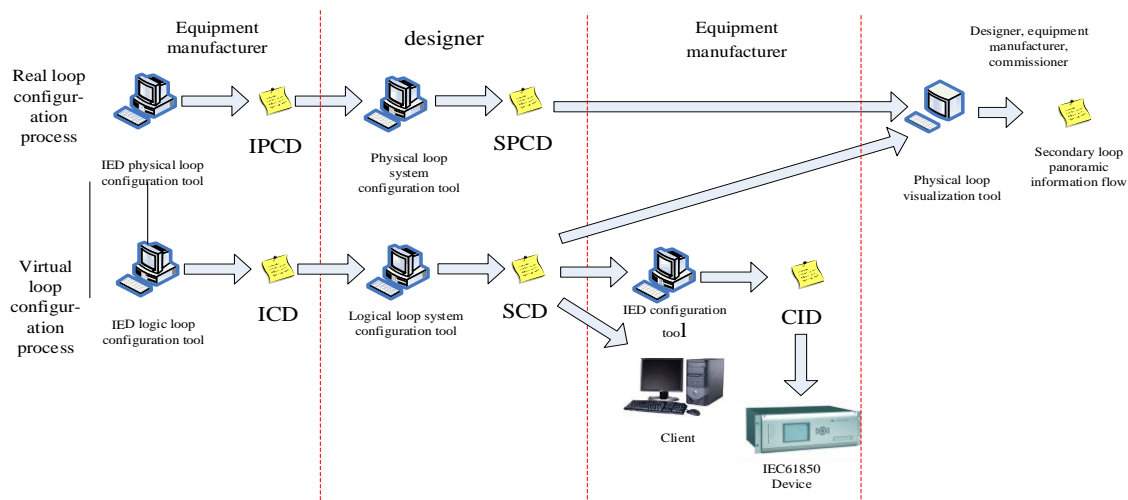


Figure 1. Secondary circuit panoramic model design flow

The design process of the logic circuit includes: the equipment manufacturer generate the intelligent electronic device capability description (ICD) file through the IED configuration tool. The design unit completes the SCD file design of the whole substation through the ICD file. The SCD file can show the communication parameters and the virtual connection of the secondary device in smart substations. The application of secondary physical circuit expansion modeling techniques can not only improve the efficiency of work, and also make operation and maintenance of the smart substation more conveniently, and because upgrade the traditional image management mode to the visualization mode, the operation and maintenance personnel will no longer rely on a large amount of drawings.

3.2. Visualization technology of smart substation secondary system

The visualization technology of smart substation secondary system means through analyzing the SCD file to match the SV, GOOSE and MMS messages which are obtained online, set up the mapping relationship between the physical connection of the optical cable and the logical link connection and the mapping relationship between the logical link and the secondary functional circuit, then through pattern mapping, the physical connection diagram, optical cable communication link diagram, relay protection principle and pressure plate diagram are automatically generated, achieve no "blind spot" online monitoring and self-diagnosis alarm, so as to realize the visual monitoring of the smart substation secondary system.

The innovation of the visualization technology is the use of core automatic search algorithm. In the analysis of the physical level, because the physical path is more complex and the fiber is more difficult to draw, the use of the core automatic search algorithm can solve this problem well. The core automatic search algorithm uses the Core element and the IntCore element in the SPCD file format as the entry point, extending the search on both sides, and finally searching for the devices on both sides. For example, when the A side is the device, how automatic search algorithm works is shown in Figure 2.

The secondary system visualization tool mainly realize the display of physical device hierarchical relationship, physical circuit display, "virtual and real correspondence" display of physical circuit and logic circuit. After the visualization tool import the SCD files and the SPCD files, at first, it enters the initialization, provides the analytical basis for the subsequent core automatic algorithm, and after the initialization, it enters the formal process of parsing, through three functional modules: the SPCD level parsing module, the SPCD display module and the SCD display module, analysis physical device

hierarchy, physical circuit, and logical circuit of IED device , and the "virtual reality correspondence" technology is adopted to complete the judgement of the information flow, to draw the panoramic information flow graph. The panoramic information flow graph can automatically switch between the virtual circuit and the real circuit. Through the real circuit connection, the virtual circuit line can be displayed, and the corresponding real circuit line can also be found through the virtual circuit line. The analysis flow of the SPCD file visualization tool is shown in the figure3:

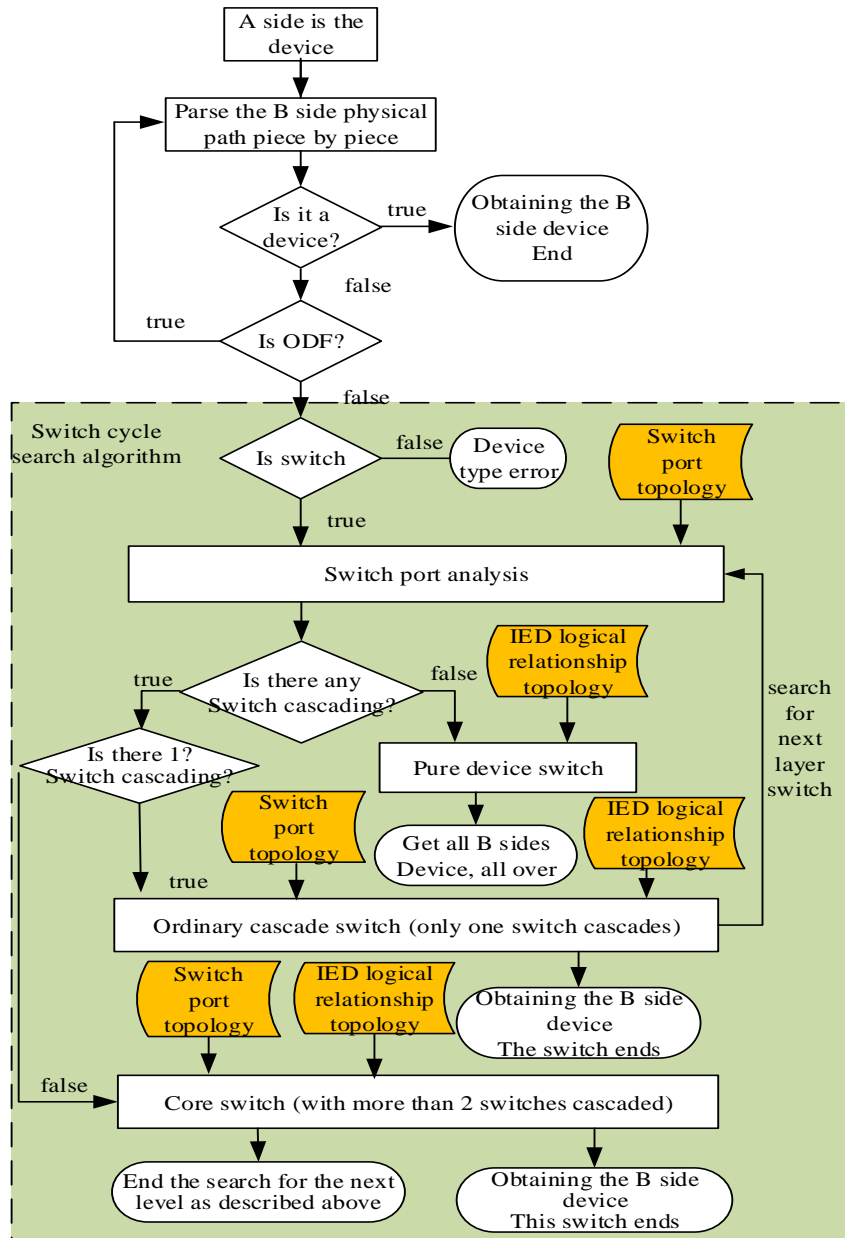


Figure 2. Core automatic search process

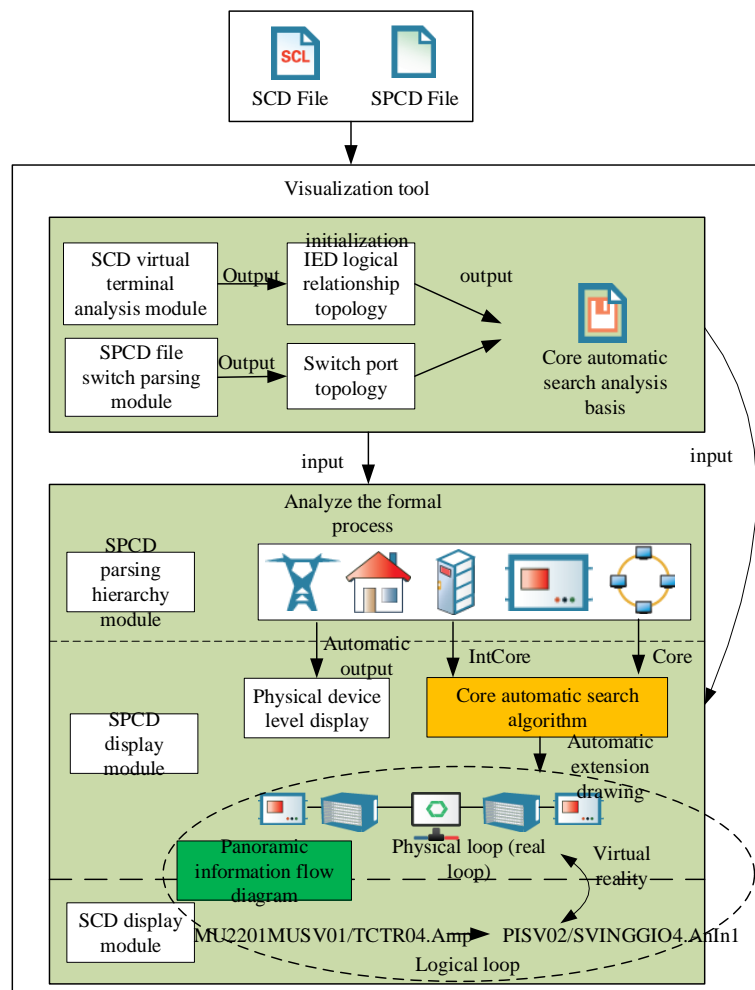


Figure 3. Parsing method of SPCD file visualization tool

3.3. Smart substation secondary system evaluation technology

The secondary system evaluation technology, based on the full data of the secondary system operation of smart substation, establishes the secondary device on-line monitoring and state evaluation system which are based on the multi parameter information fusion. The state evaluation system includes two evaluation methods based on "trend" and "loss".

The secondary device evaluation system of smart substation mainly includes evaluation objects, evaluation subitems and evaluation parameters. The relationship between each element is shown in Figure 4. In the evaluation system of figure 4, the evaluation object is the secondary physical device of the smart substation. Each evaluation object contains different evaluation subitems, and the state of each evaluation subitem is evaluated by multiple evaluation parameters. The state of the evaluation objects is calculated by the results of each subitem, and the operation state of the whole substation is obtained according to the state of all evaluation objects.

The health status of the relay protection device components can be divided into two cases, which are gradually changing with the running time and sudden variation. The former is known as trend assessment by monitoring data in a period of time, which is called trend assessment, and the latter determines the loss of function by reflecting the signal of the abnormal condition of the device, it is called a loss assessment.

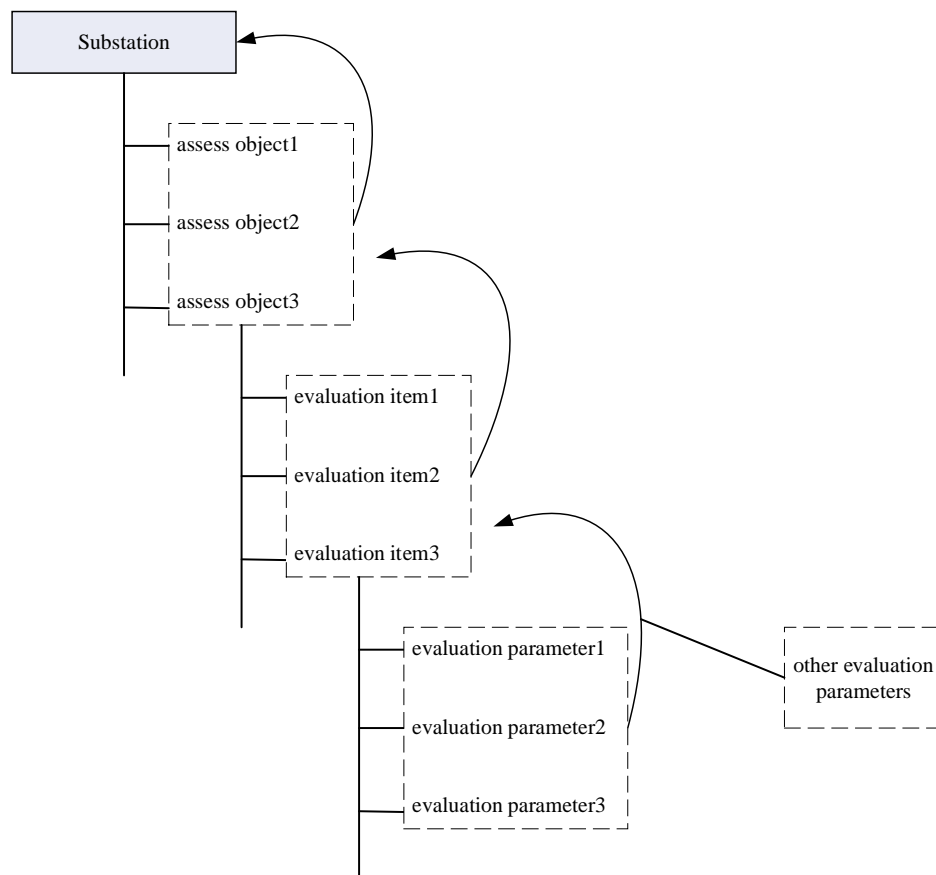


Figure 4. Smart substation Secondary Equipment Status Evaluation System

4. Trend assessment

The trend assessment method refers to the long-term monitoring and recording of the steady-state value of the device, reflecting the change trend of the component performance in a period of time, which include the accuracy of the sampling value, the consistency of the switch value, and the change of the other self inspection parameters of the device. This type of state is evaluated by the threshold value method, which is to alert the device component when the value of the monitored component exceeds a given threshold. Through the accumulation of long term operation data, the operation trend of smart device components is analyzed.

5. Loss assessment

The method of loss assessment means that when the device has abnormal alarm, the specific nature of the malfunction, such as the severity level, duration, range of influence and the most possible fault location, is inferred by analysis and statistics of the alarm information by type, that provides assistance for the defect handling.

Through the trend assessment and loss assessment, the smart substation secondary system can be comprehensively evaluated, and hidden hazards can be discovered in time, the alarm abnormality can be accurately judged, and the normal operation of the secondary equipment can be maintained.

5.1. Intelligent diagnosis technology for secondary system of smart substation

The intelligent diagnosis technology of the secondary system of smart substation is that when the fault or alarm occurs, which can be used to determine the fault source quickly and accurately.

The evaluation methods used in this technology include:

Secondary equipment fault diagnosis method based on fault characteristics, including sampling value anomaly evaluation of relay protection device, evaluation of synchronization anomaly between multiple MU and SV data of merging unit anomaly evaluation method

The secondary circuit fault diagnosis method based on the proof table, is to use the normal communication link and the abnormal communication link as the corresponding physical channel node failure probability "proof", and then according to the results of multiparty proof to determine the most likely fault channel node, and implements the process layer channel fault positioning.

The secondary system fault diagnosis method based on information association relationship refers to process the information that can characterize the working performance and condition of each part of the secondary system of the smart substation, and obtains the working condition and hardware state of each part of the relay protection, so as to determine the malfunction of secondary system.

Through the above methods, the state of the two equipment id evaluated and the fault is diagnosed, that provides the final result of the health assessment of all the secondary devices.

6. Design of online monitoring and intelligent diagnosis system for intelligent secondary equipment

6.1. Function design

The smart substation secondary equipment online monitoring and intelligent diagnosis system mainly has three functional modules:

1) Secondary equipment status assessment and fault diagnosis module

The module includes smart substation secondary equipment state method and maintenance strategy based on multi-parameter identification, forms a typical fault diagnosis method and processing strategy for secondary equipment, and establishes a secondary sub-equipment state assessment and fault diagnosis system for smart substation, implements "Effective evaluation before abnormality, rapid positioning after abnormality."

2) Secondary system network security detection module

Based on the IEC-61850 protocol of smart substation, the network information security detection rules are proposed. Through the information security detection system outside the physical isolation device, the abnormal or malicious behavior in the smart substation network is discovered, alerted and recorded in time to improve the network security of the smart substation.

3) Secondary equipment status monitoring and visualization module

This module implements the secondary system physical circuit modeling method, panoramic visualization display, the visual monitoring and analysis function of protection equipment and secondary circuit status, and lay the foundation for advanced application function modules, and provide functions for intelligent safety measures, fault diagnosis and network early warning. Visual display platform.

The specific display layout is shown in Figure 5.

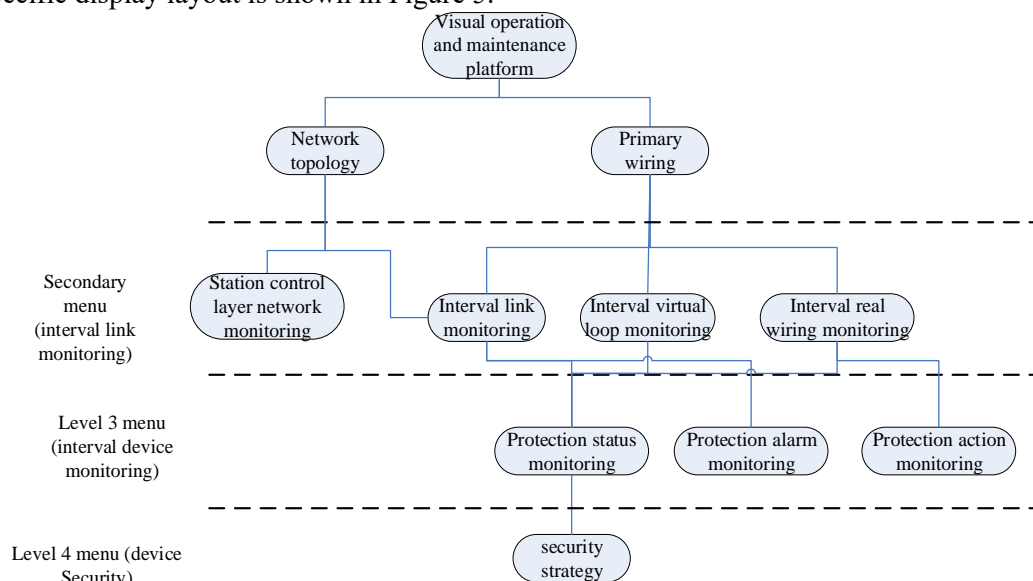


Figure 5. System platform architecture

Divided into four layers. The first layer includes: one main wiring diagram and network topology diagram; the second layer includes: interval real wiring monitoring, interval virtual circuit monitoring, interval link monitoring, station control layer network monitoring; the third layer includes: protection status monitoring, protection Alarm monitoring and protection action monitoring; the fourth layer includes: safety maintenance strategy generation, online calibration, and Anto offline simulation.

6.2. Overall architecture

The intelligent operation and maintenance system obtains information from the process layer network and the station control layer network, implements applications such as visual online monitoring and intelligent diagnosis, and supports the remote upload function. The smart substation visual operation and maintenance system is mainly composed of four levels of software shown in Figure 6.

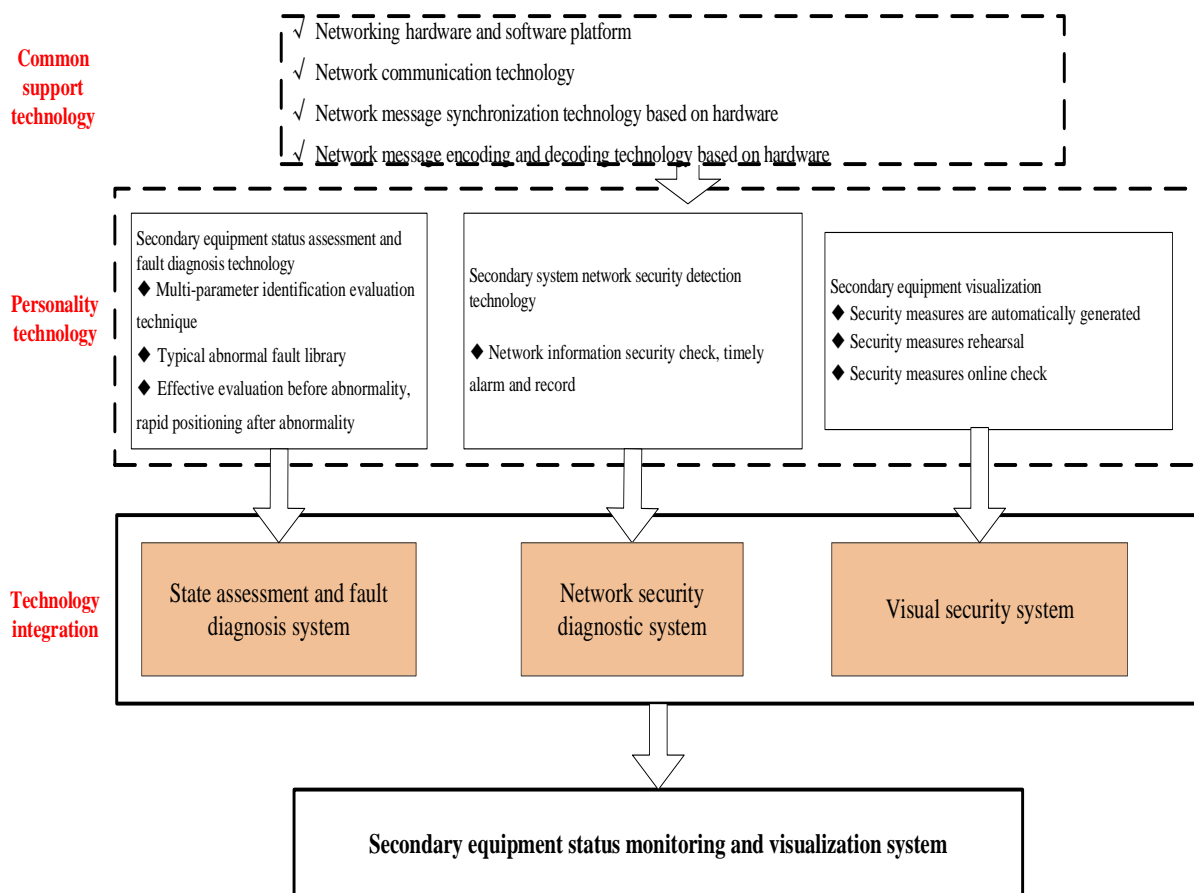


Figure 6. Software framework

The research on common protection technology mainly includes the following aspects: The development of software and hardware platforms based on the requirements of high-precision synchronous characteristic detection technology; The network communication technology based on Ethernet; The network message synchronization technology based on EPGA hardware which can measure the synchronization delay of network packets accurately, implements the delay characteristic test of the network communication of the smart device; The network message editing and decoding technology based on the EPGA hardware which improves the network packet throughput capability and the transmission delay accuracy of the test platform.

The hardware framework is shown in the figure 7.

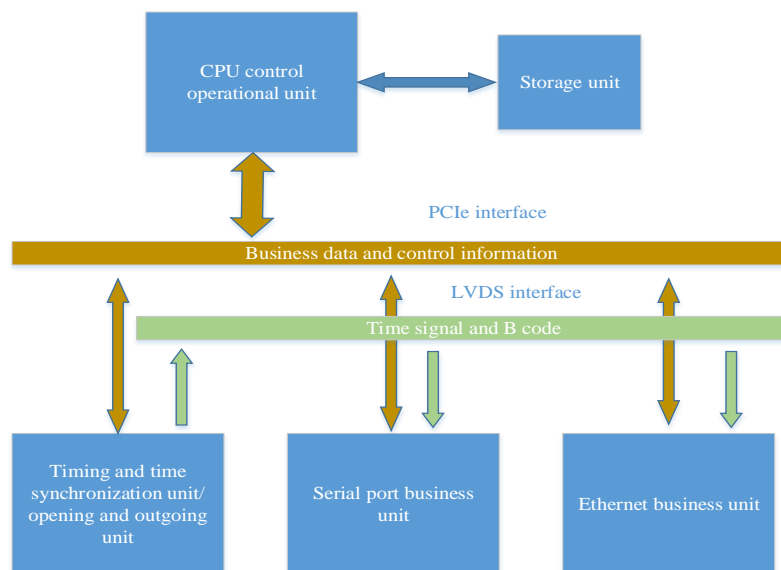


Figure 7. Hardware framework

7. Practical example of smart substation secondary equipment fault and abnormality intelligent diagnosis system

7.1. Application environment

Taking the minimum system of 220kV smart substation as an example, a simulation platform is built in the laboratory based on the typical structure of 220kV direct sampling and direct outlet network of smart substation. The simulation platform has passed the dynamic model test and can simulate the operation and fault condition of the smart substation secondary system. The 220kV line structure is as shown in Figure 8:

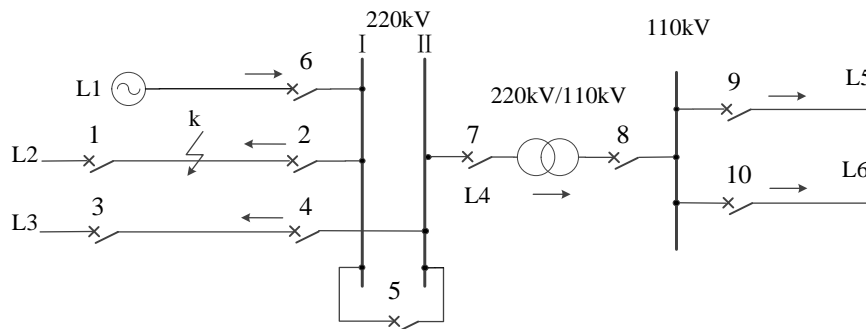


Figure 8. The minimum system of 220 kV smart substation

The minimum system contains a total of seven intervals, one transformer interval, five line intervals, and one bus-link circuit breaker interval. 220kV voltage level relay protection device, merging unit and smart terminal, and process layer network are dual configuration.

7.2. Application

When a fault occurs at point k, for protections 1 and 2 are internal faults, under normal conditions, protection 1, 2, 5, and 6 are started at time t_1 , and protection 1 and 2 are operated at time t_2 , and protection 5 and 6 are returned. If the protections 1 and 2 are rejected, the protections 5 and 6 act as backup protection actions.

Taking the protection 6 startup abnormality as an example, the state evaluation and fault diagnosis system can use the multi-parameter identification evaluation technology. Comparing the the startup

status of the protection 5 and 6 based on the protection of the state information of 1, 2. Due to the protection 1, 2 and protection 5, 6 start the relationship is chain relationship, when the protection 1, 2 start, protection 5 start, but the protection 6 does not start, you can determine the protection 6 startup exception.

Taking the SV channel fault of protection 6 as an example, through the state assessment and the associated fault diagnosis function of the fault diagnosis system, the main secondary system fault type of the substation and the key conditions of the fault occurrence are combined with the secondary equipment operating state and the secondary circuit state, topology model, networking mode, circuit breaker displacement and circuit breaker status, telemetry, timing, etc. for correlation analysis and comprehensive diagnosis. In a certain time window, the analog protection device samples the interrupt alarm, and at the same time, detects and detects the protection device light. The port receives the power alarm, but at the same time, it detects that the measurement and control device is sampling normally, the communication message is monitored normally, and the network is normal. At this time, we can infer the SV channel failure of the protection device according to the multi-event correlation model. The reasoning and prompt diagrams are shown in the figure 9.

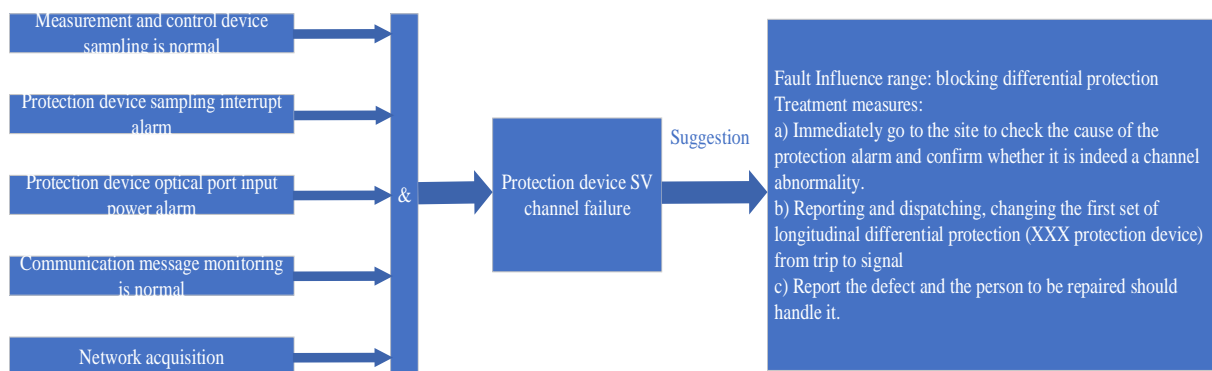


Figure 9. Comprehensive diagnosis of protection SV channel fault

Finally, taking the switching value collected by the first intelligent terminal of protection 2 is abnormal as an example. When a fault occurs at point k, the protection 2 is started (t_2) under normal circumstances, and the circuit breaker is in the breaking position (t_2+).

Since the protection 2 adopts a dual configuration, the state information between the two sets of intelligent terminals A and B has a redundant relationship. The state vectors of the intelligent terminal A and the intelligent terminal B are respectively $X_{1n \times 1}$ and $X_{2n \times 1}$. The elements in the state vector are the respective switch quantities collected by the intelligent terminal. $H_{n \times 1} = X_{1n \times 1} - X_{2n \times 1}$. Then, the system searches $H_{n \times 1}$. If finds there is a non-zero element, the position of the circuit breaker corresponding to the protection 2 is inconsistent, wherein the information of the first set is "1" and the second set is "0".

To further determine whether the abnormality is caused by the abnormal position of the circuit breaker itself or the information collected by the intelligent terminal is incorrect, the online monitoring method based on the physical law constraint relationship is used for judgment. Before the occurrence of short-circuit fault (t_1-), the sampled value satisfies $i_{L1} = i_{L2} + i_{L3} + i_{L4}$, $i_{L4} = i_{L5} + i_{L6}$. After fault removal (t_2+), the sampled value satisfies $i_{L1} = i_{L3} + i_{L4}$, $i_{L4} = i_{L5} + i_{L6}$. The above criteria can indirectly determine that protection 2 acts normally, the circuit breaker is in the breaking position, the status information is "0".

In summary, it can be determined that the switch quantity collected by the first set of intelligent terminal A of the protection 2 is abnormal.

7.3. Application effect

The simulation platform implements the establishment of the virtual reality correspondence

relationship of the smart substation secondary system and the display of the secondary loop visualization that solves the problem that the secondary circuit of the smart substation is not visually visible. The platform establishes an evaluation system based on “trend” and “loss”, and obtains operational data of all devices including merging unit, intelligent terminal, protection measurement and control, switch, etc., evaluates the health status of the device, and solves the problem of real-time online assessment of secondary device operating status. The fault diagnosis function of the platform implements the secondary circuit fault positioning, which solves the problem that the operation and maintenance personnel are difficult to find the fault point on the site.

The smart substation secondary equipment defect and abnormality intelligent diagnosis system solves the problems of physical circuit expansion model, visual display, secondary equipment status evaluation, fault diagnosis and so on, and provides guarantee for efficient and reliable operation of smart substation.

8. Research summary

Aiming at the needs and issues faced by smart substation in the operation and maintenance of secondary equipment in recent years, this paper uses physical modeling to visualize the congruent relationship between virtual and reality. And, it establishes an evaluation system and fault diagnosis system based on “trend” and “loss”. The systems effectively solve the issue that the secondary circuit of the smart substation is not intuitive, they can implement real time monitoring of secondary circuit and are helpful to clear the fault to ensure the safety of smart substation.

9. References

- [1] Xujiang Song; Ruihong Ma; Zhengxiang Ma; Min Zhang; Amin Gholamzadeh; Nadim Hossain and Shuping Dang. Multifunctional smart electricity use monitor design, programming and tests based on LabVIEW, 2014 International Conference on Information Technology Systems and Innovation (ICITSI), Bandung, 2014, pp. 299-305.
- [2] N. Enose and R. Analyst, A Unified management system for Smart Grid, ISGT2011-India, Kollam, Kerala, 2011, pp. 328-333.
- [3] X. Changfu, B. Bin and T. Fengbo, "Research of Substation Equipment Abnormity Identification Based on Image Processing," 2017 International Conference on Smart Grid and Electrical Automation (ICSGEA), Changsha, 2017, pp. 411-415.
- [4] Jae-Duck Lee, Seong-Joon Lee, Jeong-Hyo Bae and Dae-Yun Kwon, "The PMU interface using IEC 61850," 2013 International Conference on ICT Convergence (ICTC), Jeju, 2013, pp. 1125-1128
- [5] O. Siirto, J. Kuru and M. Lehtonen, "Fault location, isolation and restoration in a city distribution network," 2014 Electric Power Quality and Supply Reliability Conference (PQ), Rakvere, 2014, pp. 367-370.
- [6] I. Ali, M. S. Thomas and S. Gupta, "Integration of PSCAD based power system & IEC 61850 IEDs to test fully digital protection schemes," 2013 IEEE Innovative Smart Grid Technologies-Asia (ISGT Asia), Bangalore, 2013, pp. 1-6.
- [7] Bin Duan, Guojing Li, Chaowu Qiu, Jiaqi Pan and Yunqiang Tan, "Fault location and self-healing of distribution network based on function block and wireless sensor," 2012 IEEE PES Innovative Smart Grid Technologies (ISGT), Washington, DC, 2012, pp. 1-9.
- [8] P. Xi, P. Feilai, L. Yongchao, L. Zhiping and L. Long, "Fault Detection Algorithm for Power Distribution Network Based on Sparse Self-Encoding Neural Network," 2017 International Conference on Smart Grid and Electrical Automation (ICSGEA), Changsha, 2017, pp. 9-12.
- [9] N. Dorsch, B. Jablkowski, H. Georg, O. Spinczyk and C. Wietfeld, "Analysis of communication networks for smart substations using a virtualized execution platform," 2014 IEEE International Conference on Communications (ICC), Sydney, NSW, 2014, pp. 4239-4245
- [10] O. Naidu, R. Gore, N. George and Ashok S, "A new approach for fault location on modern distribution systems with integrated DER," 2016 Biennial International Conference on Power and Energy Systems: Towards Sustainable Energy (PESTSE), Bangalore, 2016, pp. 1-6
- [11] J. E. Bowen and N. Weber, "Future trends in electrical substations from the end-users perspective - Near future safety features," 2011 Record of Conference Papers Industry Applications Society 58th Annual IEEE Petroleum and Chemical Industry Conference (PCIC),

Toronto, ON, 2011, pp. 1-11.

- [12] H. Späck, B. Schüpferling, J. Riemenschneider and M. Schelte, "Intelligent transformer substations in modern medium voltage networks as part of "smart grid"," 7th Mediterranean Conference and Exhibition on Power Generation, Transmission, Distribution and Energy Conversion (MedPower 2010), Agia Napa, 2010, pp. 1-7.
- [13] T. Popovic and M. Kuhn, "Automated fault analysis: From requirements to implementation," 2009 IEEE Power & Energy Society General Meeting, Calgary, AB, 2009, pp. 1-6.

Research on Logic Optimization and Reliable Calculation Model of Satellite Based Wildfire Monitoring for Power Transmission Line

Zhenzhen Zhou¹ and Gang Chen²

¹ Senior Production Editor, Maintenance & Test Center, EHV, China Southern Power Grid, Guangzhou, China

² Production Assistant, Baise Bureau of EHV, China Southern Power Grid, Baise, China

E-mail: joebuuaa@163.com

Abstract. In order to improve the accuracy of wildfire monitoring for transmission line based on satellite sensing data, this paper proposed a new method that can be used to verify different data from synchronous satellite and polar orbiting satellite mutually. Also, this paper optimized the wildfire identification logic by considering surface elements, wide-area meteorology, cultural environment, and history records, and then proposed a corresponding calculating model to evaluate the reliability of wildfire detected. Relied on the improvements above, the accuracy of wildfire monitoring of EHV Power Transmission Company increased almost 30% in April to May 2018.

1. Introduction

At present, the application of meteorological satellites has gone far beyond the traditional meteorological scope. Detecting heat sources for forest fire monitoring is an important aspect of the application of meteorological satellites in non-meteorological fields. With the growth of China's power grid, large-capacity and long-distance transmission lines are increasing year by year. And many transmission lines pass through mountains and dense forest areas. The special topography and climatic conditions of these areas are very likely to initiate wildfires, which threaten the overall security and stability of the large regional power grid [1]. Traditional human or helicopter inspection methods for transmission line cannot meet the requirements of timeliness and accuracy for wildfire monitoring [2]. Therefore, it is necessary to build wildfire warning system which could analyze the heat detecting data acquired from meteorological satellites to find out the real fire that may threaten the stability of power transmission lines or power grids.

However, due to the limitations of satellite remote sensing technology, there are many problems in daily wildfire monitoring, low accuracy, for example [3]. During the long-term application and continuous modification for wildfire monitoring system based on satellite, this paper proposed a new method to optimize the logic of wildfire identification by considering multidimensional data including the data collection cycle from different satellites, surface morphology around fire point, recent meteorological data and so on. This method has significantly increased the accuracy of wildfire monitoring and been applied in the wildfire monitoring system of China Southern Power Grid EHV Power Transmission Company.

2. The principle of fire monitoring based on satellite



Content from this work may be used under the terms of the [Creative Commons Attribution 3.0 licence](https://creativecommons.org/licenses/by/3.0/). Any further distribution of this work must maintain attribution to the author(s) and the title of the work, journal citation and DOI.

Published under licence by IOP Publishing Ltd

2.1. Synchronous satellite and polar orbiting satellite

The synchronous satellites are located 36,000 kilometers above the equator, the orbital plane of which coincides with the equatorial plane, and the orbital velocity and direction are the same as the Earth's. Therefore, the synchronous satellite enables static observation as they are relatively stationary with the Earth. Although synchronous satellites are not as accurate as polar orbiting satellites, they can perform continuous observations on a given area.

The polar orbiting meteorological satellite, also called the sun-synchronous orbiting meteorological satellite, has an orbit of 800 to 1000 km above the Earth. The instantaneous orbital plane in which polar orbiting satellites are located is always in a stable orientation with the sun, so that the local time when the satellite passes the same area is the same [4]. Compared with synchronous satellites, polar orbit satellites have lower orbital heights, and can get better observation results. Also, because they keep in sync with the sun, the illumination in each observation is almost the same, which is conducive to the comparative analysis of the observed data [5]. However, polar orbiting satellites can only carry out observations twice a day for the same area, so it is impossible to achieve the goal of real-time monitoring.

In view of the respective characteristics of the satellites mentioned above, it is recommended to take use of both synchronous satellites and polar-orbiting satellites in practical applications, in order to get more reliable data. Take the wildfire monitoring system of EHV Power Transmission Company as an example, the satellite data of this system acquired from the Guangzhou Meteorological Satellite Ground Station, one of four major satellite ground stations in China, is mainly consisted by synchronous geostationary satellites and polar orbiting satellites as a supplement. The synchronous geostationary satellite, which mainly include Himawari-8 geostationary satellite of Japan, FengYun satellite of China, scans the earth surface every 10 minutes. And the polar orbiting satellites include TERRA, AQUA of US and other meteorological satellite data. All the satellites connected to the system collect a large amount of data including remote sensing data, vegetation index data, and meteorological cloud map, the resolution of which is 1×1 km.

2.2. The principle of remote sensing recognition

The normal temperature of earth surface is about 300K [6], and the flame temperature of wildfire can reach 1000K. According to Stephen Boltzmann's law and Wien's law of displacement, the total amount of radiation is in a quadratic relationship with temperature. A small change in the temperature of the black body will cause significant radiation changes. Therefore, the high temperature of heat source would cause a drastic change in the radiation, which makes the monitoring of wildfire possible. According to Planck's law of black body radiation [7], the wavelength of the hot spot radiation at normal temperature is close to that of the mid-infrared channel, while the one of the high-temperature heat source is close to that of the far-infrared channel. The feature can be used to make coarse judgments to high temperature heat sources. The radiation growth rates of the mid-infrared and far-infrared channels are quite different, which can be used for the identification of fire points on the ground.

2.2.1. Method for calculating channel brightness temperature. From the Planck black body radiation formula:

$$W_{\lambda} = \frac{2\pi hc^2}{\lambda^5} \cdot \frac{1}{e^{hc/k\lambda T} - 1} \quad (1)$$

The brightness of channel p as T_p can be drawn:

$$T_p = \frac{hc}{\lambda_p k} \ln^{-1} \left(\frac{2\pi hc^2}{\lambda_p^5 W_{\lambda}} + 1 \right) \quad (2)$$

Where: w_{λ} is the corresponding radiance of the channel with wavelength of λ , $W \text{ m}^{-2} \cdot \mu\text{m}^{-1} \text{ Sr}^{-1}$; T is the channel brightness temperature value, K ; T_p is the brightness temperature value of channel p, K ; h is the Planck constant, $h=6.63 \times 10^{-34} \text{ J s}$; c is the speed of light in vacuum,

$c=3.0 \times 10^8 \text{ m s}^{-1}$; λ is the channel data wavelength, μm ; λ_p is the data wavelength of channel p , μm ; k is the Boltzmann constant, $k=1.38 \times 10^{-23} \text{ J K}^{-1}$.

2.2.2. Hot spot discrimination. The identification of fire point is the key of fire monitoring system based on satellite for power transmission line. Set the brightness parameter T_h as the threshold to determine whether the pixel is fire point. After the picture taken by the satellite processed by noise reduction algorithm, the point will be considered to be a fire if the calculated bright temperature value of the corresponding bright spot is greater than the threshold value. That is, the judgment condition is:

$$T_C > T_h \quad (3)$$

As delivered to the wildfire monitoring system, the satellite data will be automatically processed with the threshold fire point identification method [8] to initially determine the existence of fire point.

3. Difficulties in satellite wildfire monitoring and early warning

Using satellite data to monitor wildfire for transmission lines can effectively improve the response speed for wildfires disposal and reduce the risk for power grid. However, the accuracy rate of wildfire monitoring based on satellite is far less than 100% because of interferences from complicated ground factors. After the fire point was found out by the system, the power transmission line operation department should organize personnel to check on site. As the high-voltage transmission lines often cross mountain or jungle, fire point review costs much human labor. Therefore, how to improve the accuracy has become the biggest difficulty in wildfire monitoring based on satellite.

According to the experience of power transmission line operation and maintenance, there are many factors that may affect the accuracy of the wildfire monitoring. It is necessary to analyze all those interferences comprehensively and use the computer to calculate the credibility of fire point.

4. Wildfire monitoring logic optimization

4.1. Monitoring frequency analysis

If a hot spot is considered to be fire (suspected fire spot) by calculating channel brightness temperature, the wildfire monitoring system will load this spot into a task queue, and then carry out periodic comparison with different logic according to the data acquisition satellites. The logic map is as shown in Figure 1:

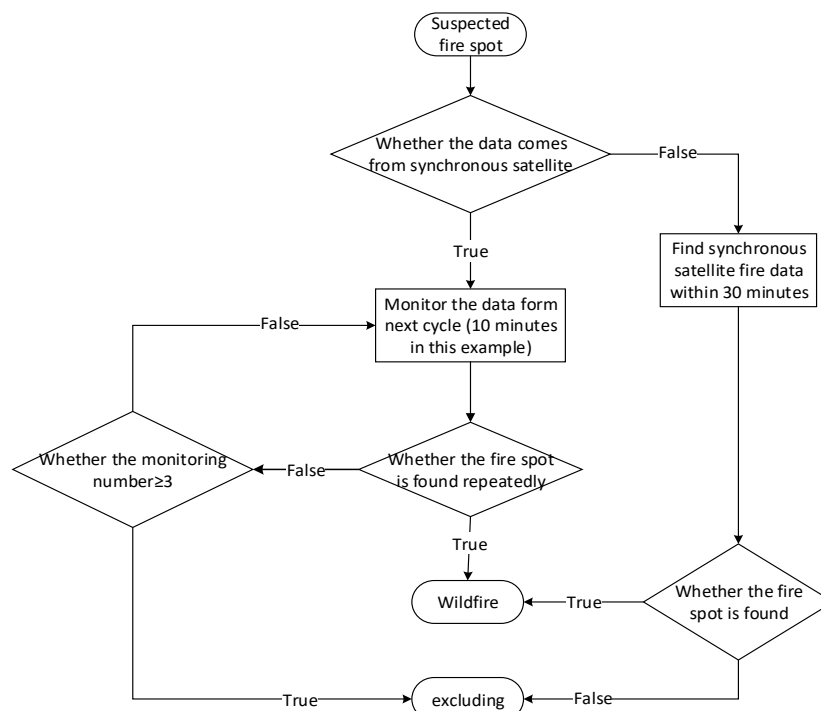


Figure 1. Multiple satellite monitoring data comparison logic

If this suspected fire spot is confirmed as a wildfire at the end of the procedure above, the system will take more influence factors as below into consider in order to make a more accurate judgement.

4.2. Earth surface element analysis

Check the earth surface around the fire based on the hot spot coordinates provided by the satellite data. There are usually two ways to acquire information about the surface: geographic image data, and lidar scan data especially for transmission line corridors. In real application, geographic image data can be viewed on GIS platform such as Google Earth (also, image data can be purchased separately and superimposed on GIS platform in monitoring system), and the resolution can satisfy the requirement for surface elements discrimination. Lidar scan data is much more precise, and can be also used to check the vegetation information around the hot spot. However, due to the high cost of lidar scanning, image data is more often used for element recognition in fire monitoring. The common earth surface elements [9] and their application in wildfire discrimination are shown in Tab 1 :

Table 1. Surface elements and their discriminating methods

Earth surface elements	Discriminant method
Natural vegetation	If the natural vegetation between the fire point and the nearby line corridor is dominated by low-lying plants, the fire will not have a large impact on the high-voltage transmission line. If natural vegetation is dominated by densely growing trees, the fire point should be focused on.
Bare rocks	If a rock is exposed to strong light for a long time, its surface temperature would rise and show a significant temperature difference from periphery. Therefore, if the hot spot is located in a large area filled with exposed rock, it is less likely to be a real fire.
Lakes and rivers	The water surface can reflect sunlight, and it may be identified as fire by satellite sometimes. Therefore, if located in lake or river, the hot spot is should be defined as a false alarm and recorded into database storing ignore areas. If there is a large river between the hot spot and transmission line corridor, the fire point would not affect the transmission line.
Farmlands	If the fire point is located in a large area of farmland, it is more likely transient fire caused by farmers burning straw and will not last long time. It would not have a major impact on the transmission line [10].
Industrial plants	If the fire point is located near the industrial plant area, it is more likely to be an industrial fire (such as chimneys). After several times detected as fire by satellite, this area can be moved into ignore areas of the system.

4.3. Wide-area meteorological analysis

The meteorological information of the area where the corridor is located is an important reference for judging the authenticity of the satellite fire. It can be acquired from the public network or the provincial meteorological department by information system connected to the internet. Among meteorological information, temperature, humidity, rainfall should be focused on:

- If there is strong precipitation before or at the same time the hot spot detected, the hot spot is made by the water ripple probably, which should be ignored.
- If the air humidity in the wildfire located area is relatively high, in which large-scale wildfires would not happen, the credibility of the fire point should be reduced.

- If the weather in the wildfire located area is hot and dry, which is conducive to make fire, the credibility of the fire point should be increased.

4.4. Cultural environment analysis

After above screening, if the fire point is not excluded, it still needs further analysis combined with cultural environment. The cultural environment includes two categories: residents' habits and seasons. Among them, residents' habits include burning habits, open fire worship, and other habits or customs that may cause wildfires. Generally, this information is entered into system by line operation and maintenance department or line guards based on experience. The season mainly contains the period before and after the Qingming, the harvest period of crops, the high temperature and dry season [11]. If the above-mentioned facts exist around suspected fire point, the probability of real fire is high.

4.5. Historical data analysis

Some areas are prone to wildfire due to complicated factors such as geographical environment and humanistic environment. The historical data of real wildfire has a high reference value for the current wildfire determination. After the wildfire is discovered by the satellite, the system will search historical wildfire records about the surrounding area of this fire point. If there is a real confirmed historical wildfire record, the credibility of the fire point should be increased.

4.6. Fire point distribution analysis

If the satellite monitoring data shows that there are multiple fire points in a area around the corridor, the probability that these are real fires is high, and also maybe it is a big fire that affects large areas, which needs to be focused on. When counting fire points, the ones within 5 km can be combined as a single point.

According to experience, the 6 steps mentioned above can intercept most of false wildfire alarms. However, some fire points are still confirmed as false alarms by the line guards. Therefore, it is necessary to introduce a kind of confidence algorithm for wildfire monitoring based on satellite, which could assist the wildfire monitoring personnel to carry out disposal measures according to the credibility and scale of wildfire.

5. Credibility calculation model for wildfire monitoring

The identification of wildfire monitoring based on satellite involves complex factors such as earth surface, meteorology and culture. It is useful to establish a reasonable credibility calculation model to minimize the false alarm rate and improve the practicability of the fire monitoring system. Generally, the same as influence factors, different ones plays different roles in the identification of wildfires. The traditional full probability model can not meet the requirement of calculating credibility for wildfire monitoring. Therefore, the concept of dynamic weighting factors will be introduced next. The weights of influence factors are assigned by event priority.

The wildfire credibility calculation model is established for the five aspects mentioned in (3.2-3.6) in wildfire identification logic, as follows :

$$P = \begin{bmatrix} P_A = P_{\max} \{P_{A1}, P_{A2} \dots P_{An}\} \\ P_B = P_{\max} \{P_{B1}, P_{B2} \dots P_{Bn}\} \\ P_C = P_{\max} (P_{C1} + P_{C2} + \dots + P_{Cn}) \\ P_D = P_{D1} \\ P_E = P_{E1} \end{bmatrix} \times \begin{bmatrix} H_A \times Q_A \\ H_B \times Q_B \\ H_C \times Q_C \\ H_D \times Q_D \end{bmatrix} \quad (4)$$

Among them, PA is the credible probability of the wildfire corresponding to the surface element, taking the maximum value of the sub-item, HA as the corresponding weight of the surface element, QA as the corresponding dynamic adjustment factor of HA; PB is the credible probability of the wildfire corresponding to the wide-area meteorology, taking the maximum value of the sub-item, HB is the weight of the wide-area meteorology, QB is the corresponding dynamic adjustment factor of HB;

PC is the credible probability of the wildfire corresponding to the human environment, taking the sum of the sub-items, HC is the corresponding weight of the human environment, QC is the corresponding dynamic adjustment factor of HC; PD is the credible probability of the wildfire corresponding to the historical data, HD is the historical data corresponding weight, QD is the dynamic adjustment factor corresponding to HD; PE is the credible probability of the wildfire corresponding to the historical data, HE is the historical data corresponding weight, QE is the dynamic adjustment factor corresponding to HE. The variables of Equation 4 are specified as shown in the following table:

Table 2. Credibility calculation model variables in Satellite wildfire monitoring

Identification element	Low-lying plants	Bare rocks	Lakes or rivers	Farmlands	Industrial plants
P_A	$P_{A1}=0$, True	$P_{A2}=0$, true	$P_{A3}=0$, true	$P_{A4}=0.4$, true	$P_{A5}=0$, true
	$P_{A1}=1$, Densely growing trees	$P_{A2}=0.5$, false	$P_{A3}=0.5$, false	$P_{A4}=0.5$, false	$P_{A5}=0.5$, false
	$P_{A1}=0.5$, Others				
Weights, $H_A=0.3$					
Wide-area meteorology	Temperature and humidity	Precipitation	cultural environment	Resident habit	Season
P_B	$P_{B1}=1$, High temperature and dry	$P_{B2}=0$, Heavy precipitation	P_C	$P_{C1}=0.4$, used to fire	$P_{C2}=0.6$, Ching Ming Festival
	$P_{B1}=0.2$, Large humidity	$P_{B2}=0.1$, normal precipitation		$P_{C1}=0.1$, others	$P_{C2}=0.5$, Crop harvesting period
	$P_{B1}=0.5$, others	$P_{B2}=0.5$, no precipitation			$P_{C2}=0.6$, others
Weights, $H_B=0.1$			Weights, $H_C=0.1$		
historical data	Historical fire point	Fire point distribution	Fire point aggregation		
P_D	$P_D=0.5$, no records	P_E	$P_E=1$, Fire spots gathered>3		
	$P_D=0.8$, Recorded but less than 3		$P_E=0.7$, 1< Fire spots gathered ≤3		
	$P_D=1$, Recorded and more than 3		$P_E=0.5$, Fire spots gathered = 1		
Weights, $H_D=0.2$			Weights, $H_E=0.3$		

The dynamic adjustment factor Q is used to adjust the corresponding weight according to the probability distribution of the influence factors. With Q, the system gets the ability of adjusting the proportion of other influencing factors according to the key factors (the factors about earth surface and strong precipitation that cannot produce fire). And the initial value is:

$$Q = [1 \ 1 \ 1 \ 1 \ 1]^T \tag{5}$$

The dynamic adjustment factor can be adjusted according to the operation experience. Take an example and use pseudo code to illustrate as follows:

If ($P_{Amin} = 0 \parallel P_{Bmin} = 0$) // P_{Amin}, P_{Bmin} are the minimum of the P_A and P_B sub-items.

$$Q = [0 \ 0 \ 0 \ 0 \ 0]^T \text{ // Exclude wildfire}$$

Else if ($P_{Amax} = 1 \ \&\& \ P_{Bmax} = 1$) // Surface vegetation and meteorology is prone to fire

$Q = [0.5 \ 0.5 \ 2 \ 1.5 \ 1]^T$ // Increase the weight of the cultural environment and historical data

Else if ($P_C = 1$) // Residents nearby and season are prone to fire

$$Q = [0.5 \ 1 \ 2 \ 2 \ 0.5]^T \text{ // Increasing the weight of historical data}$$

6. Conclusion

The wildfire identification logic and credibility calculation model proposed in this paper analyzes various satellite data sources, surrounding environment, and introduces historical monitoring records into consider. During the period of April to May 2018, 51 wildfires had been confirmed in 69 fire alarms issued by the satellite-based fire monitoring system in China Southern Power Grid EHV Power Transmission Company. The accuracy of fire alarm improved significantly, reaching almost 75%.

7. References

- [1] Zhu Shiyang, Deng Yurong . Research and application of wildfire monitoring technology in transmission line corridor [J]. *Guangxi Electric Power*, 2013, **36(3)**: 25-27 .
- [2] Chen Xiyang, Hu Changmeng, Xia Yunfeng, Xie Congzhen, Dai Dong. Study on the warning of wildfires on transmission lines based on laser radar technology [J]. *Electrical Applications*, 2015, **34(09)**: 58-61.
- [3] Ye Liping, Chen Xiyang. Application status of wildfire early warning technology in transmission lines [J]. *Power System Protection and Control*, 2014, **42(6)**: 145-153 .
- [4] Meng Zhizhong. China's polar orbiting meteorological satellite [J]. *Chinese Engineering Science*, 2004 (**10**): 1 – 5 .
- [5] Liang Yun, Li Zhe, Qu Yanyan, et al. Application of polar orbiting meteorological satellites in monitoring wildfires on transmission lines [J]. *Henan Science*, 2013, **31(10)**: 1664-67 .
- [6] Li Jiaguo, Gu Xingfa, Yu Tao . HJ satellite remote sensing monitoring of forest fires in southeastern Australia [J] . *Journal of Beijing Aerospace University*. 2010, **36(10)**: 1221-24 .
- [7] Yongyi Huang . Planck's process of establishing blackbody radiation law [J]. *Guangxi Physics*, 2011, **32(3)**: 32-37 .
- [8] Lu Jiazheng; Liu Yu; Wu Chuanping; Zhang Hongxian; Zeng Jun Research on Satellite Fire Monitoring and Alarming Algorithm for Transmission Lines [J]. *Chinese Society for Electrical Engineering, Proceedings of the CSEE*, 2015, 21
- [9] GUAN Ling, LI Hong-yun, CHEN Xiao-ming, WANG Yi, HUANG Jun-jie, WU Qiong, XIONG Yu. A Risk Analysis of Line wildfire Trip Based on Remote Sensing and Meteorological Data [J]. *Electric Power Information and Communication Technology*, 2016, **14(07)**: 42-45.
- [10] Fonseca J R, Tan A L, Silva R P, et al Effects of agricultural fires on the performance of overhead transmission lines [J]. *IEEE Transactions on Power Delivery*. 1990, **15(2)**: 687-694 .
- [11] Lu Jiazheng, Liu Wei, Yang Li, et al. Analysis of the occurrence law of wildfires on transmission lines [J]. *Fire Science and Technology*, 2014, **33(12)**: 1447-51.

The Research of Anomaly Detection Method for Transformer Oil Temperature Based on Hybrid Model of Non-Supervised Learning and Decision Forests

Fei Xiao¹, Xiwu Leng², Kang Ye¹, Youlin Hu¹, Xiongli Li³, Licheng Zhu³

¹ State Grid Shanghai Electric Power Company Power Dispatch Control Centre, Shanghai, P.R. China

² National Power Dispatch Communication Centre, Beijing, P.R. China

³ Tellhow Software Co. Ltd., Nanchang, P.R. China

E-mail: xiaofei@sh.sgcc.com.cn; xiwu-leng@sgcc.com.cn;
yekang_yk@sh.sgcc.com.cn; 3311481@qq.com; 66653752@qq.com;
zhulc@tellhow.com

Abstract. The anomaly detection of transformer's oil temperature is critical and valuable issue for the safe operation of transformers and power system. In terms of the defects of traditional anomaly detection approaches of transformer's oil temperature, such as high investment, poor generality, and non-real time, this paper proposed a hybrid model with non-supervised learning and decision forests method to detect anomaly of transformer's oil temperature. Based on non-supervised clustering algorithm, firstly, the clusters of transformers' working conditions are explored from big data sets of transformers. After that, the abnormal temperature threshold value of each cluster is deduced by hypothesis tests method and utilizes to tag anomaly in data sets of working conditions. Finally, the data sets with anomaly tags are inputted into random decision forests model to construct the classifier of abnormal oil temperature and generate the rules for anomaly detection. This method was validated by empirical data of main transformer in Shanghai, and the results represented its conspicuous competitive advantages to traditional oil temperature anomaly detection methods in the factors of real-time and accuracy.

1. Introduction

Transformer [1]-[3] is the core component of energy transmission in power system, which is expensive and technically complex, and the oil temperature of transformer is closely related to the service life of transformer [4]-[6]. Excessively high oil temperature will seriously shorten the service life of transformer. The main reasons for excessively high oil temperature involve the insulation damage of the metal parts of the transformer, winding inter-turn short-circuiting, overload of transformer, failure of transformer cooling system and so on. At present, the classical method for the calculation, prediction and abnormal analysis of transformer oil temperature are generally based on transformer modified heat path model technology, transformer oil chromatographic discrimination technology and top layer oil temperature anomaly detection technology.

The heat path model calculation technique is a traditional method for anomaly detection of transformer oil temperature. It is mainly based on the heat path model calculation of the main transformer equipment [7]-[9], which establish a heat path for the heat transfer process of the transformer and judge the abnormal oil temperature. Oil chromatographic anomaly detection technique, which analyse the content of measurable gas in transformer oil by chromatographic analyser to detect anomaly of oil



temperature, is widely used at present [12], [13]. The anomaly detection technology of oil temperature at the top layer is to identify the abnormal oil temperature based on the sampling data of the top oil temperature of transformer and the characteristic model of oil temperature. A semi-physical model for short-term prediction about the peak oil temperature of the top layer was constructed, and the oil temperature was forecasted with consideration on the influence of the operation of the cooler and the abnormal working condition of the transformer [10], [11].

Despite that these classic anomaly detection methods of oil temperature already have many outstanding achievements, which still has the problems involving high costs, difficulty of configuration, and non-real time, how to be more efficient in anomaly detection of transformer oil temperature is still an important research topic. In the era of big data, this paper proposes a non-supervised hybrid model method for oil temperature anomaly detection, which bases on clustering, hypothesis testing and decision forest algorithm [14], [15]. Compared with the classical temperature anomaly detection methods, this method has the advanced features of low investment, pervasive generalization, and real time.

2. Anomaly detection hybrid model of oil temperature based on non-supervised learning and decision forests

According to the practical experiences of oil temperature anomaly detection, which summarized by experts of State Grid Shanghai Electric Power Company, the expert rules was manifested as following: 1) When a transformer is in same working condition, the abnormal temperature is small probability event. 2) When a transformer is in the same temperature and with different working conditions, the temperature may be normal or abnormal.

Moreover, the relevant data set of anomaly detection of oil temperature can be considered as a five-element information system, which composed of the objects, the attributes of relevant working conditions, the anomaly tagging attributes of oil temperature, the domain of attributes' value and the relationship of value function. The oil temperature anomaly tagging information system can be formally described as $IS = \{U, C, D, V, f\}$. In this system, $U = \{S_1, S_2, \dots, S_m\}$ means the objects

collection for working condition records of m transformers. $C = \{C_1, C_2, \dots, C_n\}$ means the attributes collection for relevant n working condition records, in which oil temperature is also an attribute.

D represents a tagging attribute of oil temperature anomaly, V represents the value domain of relevant working conditions attributes and oil temperature anomaly tagging attribute. $f = U \times (C/D) \rightarrow V$ represents the functional relationship between the attributes of different objects

and their values, such as the attribute values of object S_i can be recorded as $C_{i1}, C_{i2}, \dots, C_{in}$ and D_i .

In terms of null original values of D attribute of all objects in oil temperature anomaly tagging information system IS , that is $D_i \equiv \phi, i \in m$, the main purpose of this paper is to determine how to obtain the value of the oil temperature anomaly tagging attribute D , according to the n working condition attribute sets $C = \{C_1, C_2, \dots, C_n\}$ of the transformer at a certain time.

Based on the expert rules and the oil temperature anomaly tagging information system, the anomaly detection method in this paper, firstly, was to cluster working conditional data set of transformers via non-supervised learning method. Secondly, abnormal oil temperature in each condition clustering with small probability is tagged, and the granular threshold value of anomaly detection was determined by hypothesis testing strategy. Finally, abnormal oil temperatures were tagged by decision forest algorithm model from big data set of relevant transformers' working conditions.

2.1. Machine learning strategy for anomaly detection hybrid model of oil temperature

In this paper, based on oil temperature anomaly tagging information system $IS = \{U, C, D, V, f\}$ and experience of industrial experts, anomaly detection of oil temperature is taken consideration as typical non-supervised learning problem, and a novel anomaly detection hybrid model with clustering,

hypothesis testing and decision forest algorithm is proposed. Figure 1 as following describes the work flow and steps of this hybrid model.

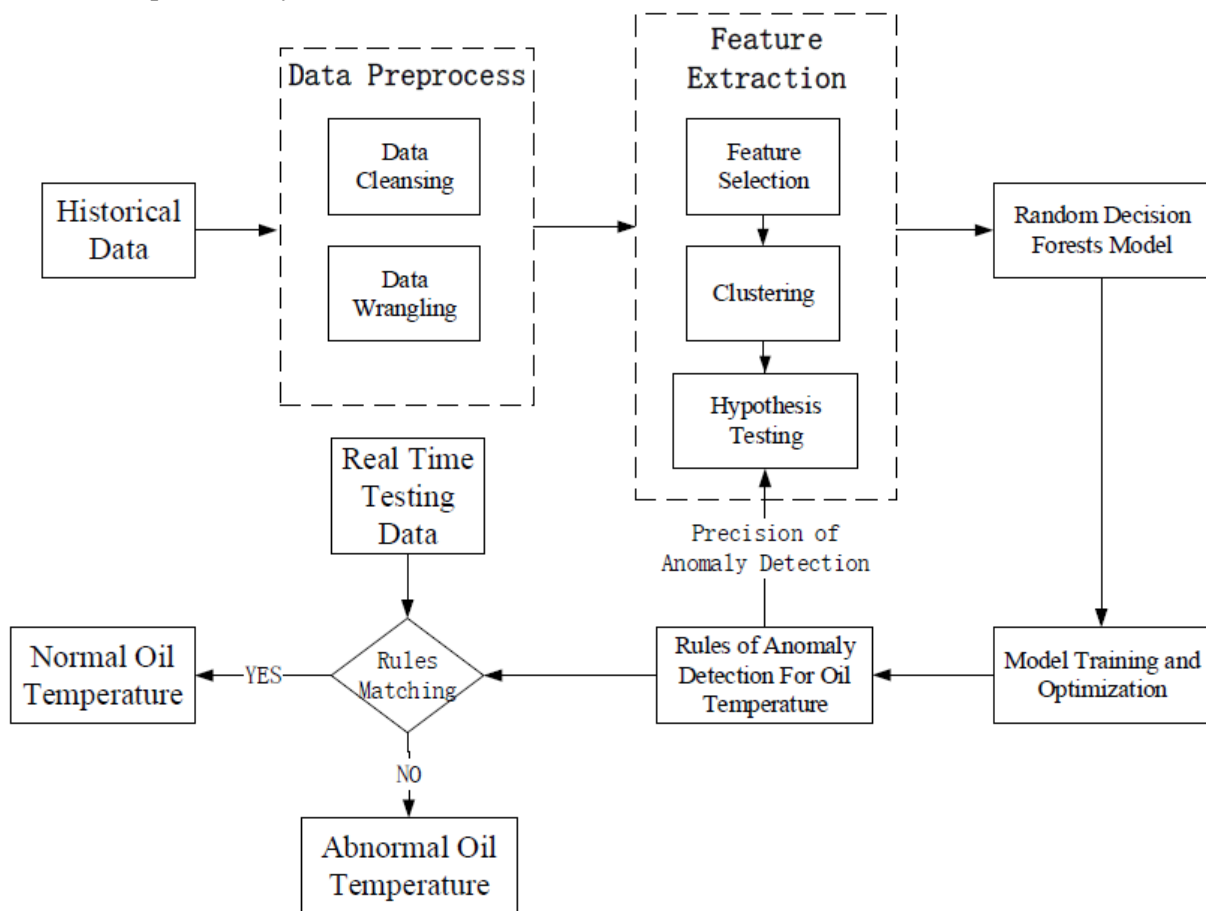


Figure 1. Flow chart of anomaly detection hybrid model of oil temperature

The stages of this hybrid model are as follows:

Stage 1: Data preprocess. Historical data of relevant working conditions, which include winding temperature, oil temperature, environmental temperature, active power, reactive power, current etc, were preprocessed. The preprocessing works included data cleansing, data wrangling and data discretization.

Stage 2: Feature Extraction. big data set of relevant working conditions were clustered via K-means algorithm [16], [17]. Different types of working conditions were explored, and the probability density distribution of oil temperature in each cluster of working condition were computed. Furthermore, the small probability samples of each cluster are tagged as anomaly of oil temperature by granular threshold value via hypothesis testing, and a two-dimensional decision information table for anomaly detection can be constructed.

Stage 3: Classifier Construction. The classifier of oil temperature was constructed to detect the abnormal oil temperature via decision forests model [18]-[20]. The decision forests model was trained firstly by the data in two-dimensional decision information table and utilized to detect anomaly of oil temperature after training stage from real-time data of transformers' working condition.

Stage 4: Classifier Evaluation. The classifier of oil temperature was evaluated, and the granular threshold value was updated if precision and recall test of model did not reach the preset. The gradient pattern adjustment of threshold value was repeated to execute from stage 2 to stage 3 until the preset was satisfied.

2.2. The methodology of anomaly detection hybrid model of oil temperature

The anomaly detection hybrid model of oil temperature involved clustering of transformers' working conditions, anomaly tagging of oil temperature, decision forests, and hypothesis testing. However, based on K-means clustering about transformers' working conditions, the final classifier was deduced from decision forests algorithm, which was evaluated and optimized via hypothesis testing. The critical algorithms and methods of model was illustrated in algorithm 1 as following:

Algorithm 1: anomaly detection hybrid model for oil temperature based on K-Means clustering and decision forests algorithm.

Algorithm input: historical data of relevant transformers' working condition, k values of K-means clustering, granular threshold value γ of anomaly.

Algorithm output: efficient classifier of abnormal oil temperature.

Step 1: according to historical data of relevant transformers' working condition, K-Means clustering algorithm is applied to obtain k types of data sets, and j cluster are described as $U_j, j \in [1, 2, \dots, k]$

Step 2: based on the clusters from Step 1, the conditional probability of oil temperature in each cluster is computed, and the conditional probability of j cluster is described as $|t_i^j|/|U_j|$.

Step 3: conditional probability value of every oil temperature in each cluster was compared with the granular threshold value γ . If $|t_i^j|/|U_j| \geq \gamma$, the oil temperature samples are tagged as normal in its cluster. Otherwise, when $|t_i^j|/|U_j| < \gamma$, the oil temperature samples are tagged as anomaly in its

cluster. Finally, two-dimensional decision information system $IS = \{U, C, D, V, f\}$ was established via anomaly tagging, which based on granular threshold value.

Step 4: the two-dimensional decision information system IS in Step 3 was input into decision forests as training data set to obtain a strong classifier of transformers' oil temperature. Thus, when online data of transformers' working conditions was input into this strong classifier, the normal or abnormal oil temperature can be tagged from the data set.

Step 5: the precision and recall rate of the strong classifier in Step 4 was evaluated to test its efficiency. If the precision and recall rate was fails to reach the preset value, the granular threshold value γ of anomaly was updated to $\gamma = \gamma + \alpha$ and α was adjusted as the greedy algorithm. The optimized process of the strong classifier was iterated from Step 1 to Step 4, until the preset value was satisfied.

3. Experiments and analysis

In the experiment, the data of no. 4 transformer of substation in Shanghai from December 2014 to January 2017 were utilized to validate the efficiency of anomaly detection hybrid model of transformers' oil temperature. There were 18 rational attributes of transformers' oil temperature to be input into model, which include temperature of environment, temperature of A winding, active power from high voltage side, active power from middle voltage side, active power from low voltage side, A phase current amplitude from high voltage side etc. The data from year 2015 to year 2016 were leveraged to train the anomaly detection hybrid model, and the final classifier of model was applied to explore abnormal oil temperature from data set of year 2017. A synthetic index with precision and recall rate was used to evaluate the efficiency of final classifier of anomaly.

Figures 2 and 3 demonstrate the experimental results of the anomaly detection hybrid model, which tag the abnormal oil temperature in March 2017 and July 2017 with red spot mark. Obviously, the abnormal oil temperature of the main transformer equipment had been tagged accurately in figure 2 and 3. In figure 2 and 3, the above subgraph represents the values of 3 main attributes in a month, including the temperature of environment (red line), the current amplitude of phase A from high voltage side (blue line), and the temperature of Phase A winding (green line). In figure 2 and 3, the below subgraph represents the value of oil temperature with anomaly tagging (red spot).

The experimental results were compared with the records in EMS and analyzed by the experts. The precision of oil temperature anomaly tagging is 90%, and the recall rate of oil temperature anomaly tagging is 89%. However, the precision of classical transformers' oil chromatographic anomaly

detection method has only 86%. The method proposed in this paper is better than the classical oil chromatographic anomaly detection method in the factor of precision and efficiency.

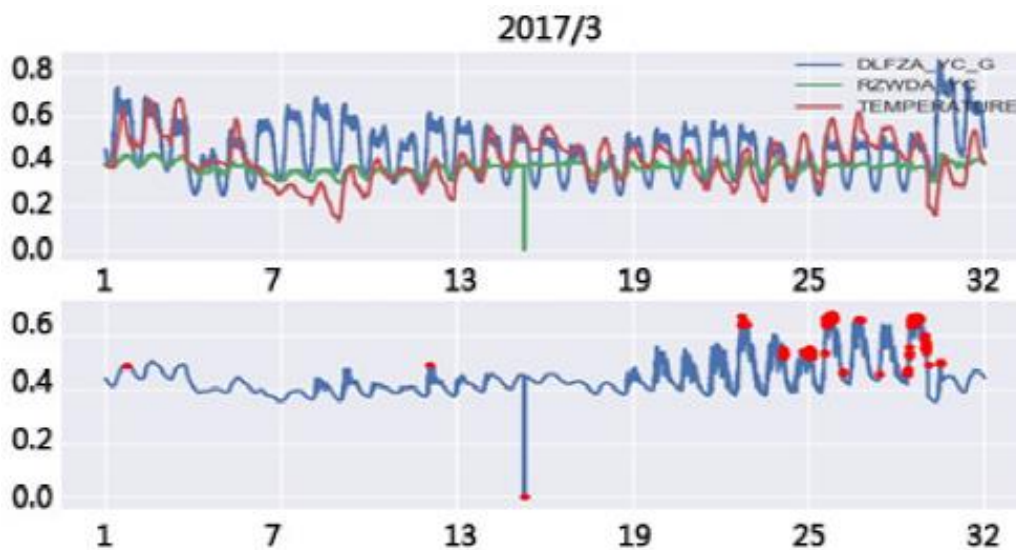


Figure 2. Anomaly tagging of oil temperature in March 2017

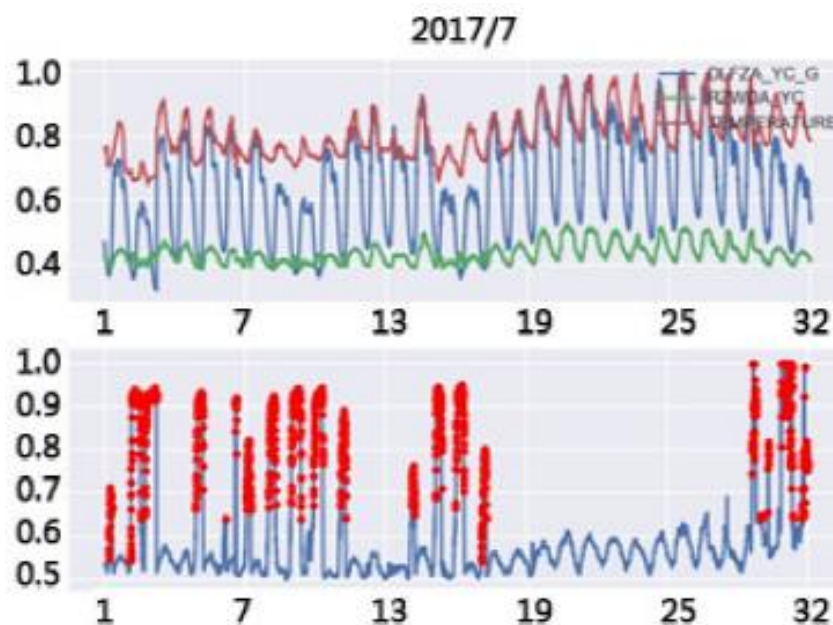


Figure 3. Anomaly tagging of oil temperature in July 2017

4. Conclusion

The anomaly detection of oil temperature can explore the abnormal state of working condition of transformer, and provide clues to support the prediction of transformers' defects. According to the research of classical anomaly detection technology of oil temperature, a novel anomaly detection hybrid model of transformers' oil temperature, which combined non-supervised learning strategy with decision forests algorithm, was established from the electrical big data of transformers' working conditions in this paper. The critical approach was to tag anomaly of oil temperature with non-supervised learning methods from the aspect of statistical meanings, and to adjust the threshold value of tagging anomaly via hypothesis testing method, which optimized the anomaly detection method of oil temperature adaptively. Furthermore, the results of experiment, in which the method was implemented to detect abnormal oil temperature of some real transformers in Shanghai, have validated

the efficiency and accuracy beyond classical methods mentioned before. In addition, this novel anomaly detection methods of oil temperature, did not need extra investment for specific equipment, and can be suitable for heterogeneous types of the transformers oil temperature alarm system. Thus, it is worth to promote for its sound commercial value and social value.

5. Acknowledgments

I really appreciate the support and assistant of every expert and colleague from State Grid Shanghai Company for this project. Their advices and knowledge made this method discussed in the paper to be feasible and implement. However, I also thank for the help of Dr. Yu, Dr. Xu and Dr. Zhao from Nanchang University and Tellhow Company.

6. References

- [1] Lu Z G, Zhao G, Yang D L, et al. 2016. Overview of Research on Power Electronic Transformer in Distribution Network. *Proceedings of the CSU-EPSCA*. 28(5). p48-54.
- [2] Anonymous. Future development trend of distribution transformer industry in China[J]. *Transformer*, 2012, 49(2). p51-51.
- [3] Han L, Wang M Y, Zhou Y X, et al. 2015. Effect of Oil Gap Spacing on Characteristics of Partial Discharge of Oil-Paper. *Transformer*. 52(8). p24-27.
- [4] Lai R H. 2017. Analysis of substation main transformer status maintenance technology status quo and development trend. *Science and Information Technology*. (2).
- [5] Wei Y B, Wang D H, Han L F, et al. 2015. A novel method for discharging fault diagnosis and location of oil-immersed power transformers based on MIA. *Power System Protection and Control*. 43(21). p41-47.
- [6] Li S G, Xue H, Li Z, et al. 2017, Fault diagnosis of mine-used transformer based on optimized fuzzy Petri net. *Industry and Mine Automation*. 43(5). p54-57.
- [7] Wei B G, Huang H, et al. 2012. Algorithm for Transformer Top-Oil Temperature and Winding Hot-Point Temperature Based on Modified Thermal Circuit Model. *East China Electric Power*. 40(3). p0404-0407.
- [8] Chen W G, Su X P, Chen X, et al. 2011. Influence Factor Analysis and Improvement of the Thermal Model for Prediction Transformer Top Oil temperature. *High Voltage Engineering*. 37(6). p1329-1335.
- [9] Wang Y Q, Yue G L, He J, et al. 2014. Study on Prediction of Top Oil Temperature for Power Transformer Based on Kalman Filter Algorithm. *High Voltage Apparatus*, (8). p74-79.
- [10] Chen J M, Wu Y, Zhu H B, et al. 2015. Research and Application of Transformer Top Oil Temperature Short - term Prediction Model. *Electrotechnical Application*. (22). p89-93.
- [11] Du S Y, Wang H B, Li F. 2015. Transformer oil temperature abnormal state identification method. *Electrotechnical Application*. (s2). p859-862.
- [12] Zhou D J. 2015. Analysis of Abnormal Chromatogram in Large Transformer Oil and its Technology Principle for Investigation. *Electric Power Science and Engineering*. 31(1). p31-37
- [13] Gao S G, Wang X L, Li Q M, et al. 2014. Outliers Detection and Distribution Characteristics of the Transformer DGA Data Based on MCD Robust Statistics. *High Voltage Engineering*. 40(11). p3477-3482.
- [14] Zhuang C J, Zhang B, Hu J, et al. 2016. Anomaly Detection for Power Consumption Patterns Based on Unsupervised Learning. *Proceeding of the CSEE*. 36(2). p379-387
- [15] Wang X, Liu X Q, Song S L, et al. 2014. Unsupervised Learning Algorithm for Abnormal Behavior Detection. *Opt-Electronic Engineering*. 41(3). p43-48
- [16] Naveen A, Velmurugan T. 2015. Identification of calcification in MRI brain images by k-means algorithm. *Medical Mycology*.
- [17] Bhowmik T K, Parui S K, Kar M, et al. 2016. Segmental K-Means Algorithm Based Hidden Markov Model for Shape Recognition and its Applications. *International Journal of Human - Computer Studies*. 88(38). p38-50.
- [18] Afanador N L, Smolinska A, Tran T N, et al. 2016. Unsupervised random forest: a tutorial with case studies. *Journal of Chemometrics*. 30(5).

- [19] Wu X Y, He J H, Zhang P, et al. 2015. Power System Short-term Load Forecasting Based on Improved Random Forest with Grey Relation Projection. *Automation of Electric Power Systems*. 39(12). p50-55.
- [20] Zhao T, Wang L T, Zhang Y, et al. 2016. Relation Factor Identification of Electricity Consumption Behavior of Users and Electricity Demand Forecasting Based on Mutual Information and Random Forests. *Proceeding of the CSEE*. 36(3). p604-614

Fault Ride through Strategy for Virtual Synchronous Control based Doubly-Fed Induction Generators

Xuekun Cheng^{1,2}, Hui Liu^{1,2}, Peng Song^{1,2} and Hao Jiang^{1,2}

¹ State Grid Jibei Electric Power Co. Ltd. Research Institute, Beijing, China

² Grid-connected Operation Technology for Wind-Solar-Storage Hybrid System State Grid Corporation Key Laboratory, Beijing, China.

E-mail: chengxk027@126.com

Abstract. Virtual Synchronous Control (VSynC) strategy for Doubly-Fed Induction Generator (DFIG) has attracted much attention because of its advantages in providing dynamic supports of frequency and voltage. In this way, most researches of VSynC strategy concentrate on analysis of its electromechanical behaviours, but pay little attention to its electromagnetic transient responses and fault characteristics, which may hinder its promotion in engineering application. This paper pays special attention to the electromagnetic transient behaviours of VSynC-based DFIG and proposes a voltage compensation VSynC strategy to implement fault ride through during symmetrical grid faults. The proposed strategy improves the transient response of existing VSynC strategy, capable of limiting the overcurrent in DFIG rotor circuits and suppressing the oscillations of electromagnetic torque. Simulation results validate the effectiveness of the proposed strategy.

1. Introduction

The scale of wind power integrated to the grid has been tremendously increasing, in this situation, Virtual Synchronous Control (VSynC) strategy [1]-[3] outweighs Vector Control (VC) strategy for providing expected inertial supports and enhancing the stability of system operation. However, existing VSynC strategy for Doubly-Fed Induction Generator (DFIG) concentrates mainly on its steady-state performances and electromechanical dynamic behaviours, paying little attention to electromagnetic transient process and fault characteristics [4], which are of equal importance due to the following two reasons. Firstly, DFIG is directly connected to the grid, making it vulnerable to grid faults [5]. Secondly plenty of researches have been carried out on the behaviours of VC-based DFIG during grid faults [6]-[9], indicating that grid faults will bring about severe fault currents and great possibility of damaging the converters. Therefore, it's quite necessary to study the fault characteristics of VSynC-based DFIG, verify the applicability of existing VSynC strategy during grid faults and improve its fault ride through capability.

Previous researches have studied the VSynC strategy for DFIG under asymmetrical grid faults [13]. Enlightening and innovative as paper [13] is, there is much to improve in aspects of depth of analysis. Considering that symmetrical grid faults are more frequent and more serious in practical operation, this paper pays special attention to VSynC strategy for DFIG during symmetrical grid faults, and the study goes further and deeper on the basis of researches in paper [13]. The paper is organized as follows. Section II analyses the principle of existing VSynC strategy and reveals the mechanism of DFIG synchronization. Then the fault characteristics of VSynC-based DFIG are carefully studied in Section III, which is followed by the discussion of the proposed voltage compensation VSynC strategy



in Section IV. Simulation results on a 1.5MW DFIG system are provided in Section V to validate the effectiveness of the proposed strategy. And finally, conclusions are drawn in Section VI.

2. Fault characteristics of VSynC-based DFIG during symmetrical grid faults

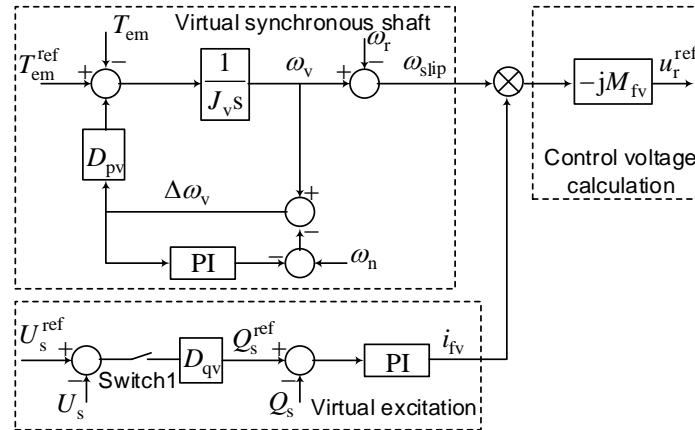


Figure 1. Existing VSynC strategy for DFIG.

Fig.1 shows a typical VSynC strategy for DFIG [10], where J_v and D_{pv} are virtual inertia and virtual damping coefficient, D_{qv} represents virtual droop coefficient. T_{em} and T_{emref} are electromagnetic torque and its reference value, ω_v is electrical angular velocity of virtual shaft, $\Delta\omega_v$ is the deviation of ω_v from grid frequency ω_n , i_{fv} is virtual excitation current, and M_{fv} is the mutual inductance between stator and virtual excitation windings.

Paper [13] has defined virtual stator electromagnetic force (EMF) e_{0v} by referring to the excitation characteristics of synchronous generator,

$$e_{0v} = \omega_v M_{fv} i_{fv} e^{-j\frac{\pi}{2}} - M_{fv} \frac{di_{fv}}{dt} e^{-j\frac{\pi}{2}} \quad (1)$$

And at the same time, DFIG stator EMF has also been defined as,

$$e_m = jL_m \omega_v \Psi_r / L_r \quad (2)$$

where Ψ_r is rotor flux, L_r is inductance of rotor windings, and L_m is mutual inductance between stator and rotor windings.

It has been illustrated that DFIG stator EMF can be controlled by adjusting the reference value of DFIG rotor voltage, once the equation (3) is satisfied, DFIG will successfully imitate the electromechanical and electromagnetic characteristics of synchronous generator.

$$e_m = e_{0v} \quad (3)$$

During symmetrical grid faults, the drop of DFIG stator voltage will exert impact on stator flux Ψ_s , and furthermore influence rotor electromotive force e_r , rotor current i_r and electromagnetic torque. The analysis of fault characteristics of VSynC based DFIG is conducted by analysing the fault characteristics of physical quantities above.

Assume that the amplitude of DFIG stator voltage before grid faults is V_s , and at the time $t=0$, the amplitude drops to λV_s because of grid faults, then the stator flux can be expressed as

$$\Psi_s = \frac{\lambda V_s}{\omega_s} e^{j\omega_s t} + \frac{(1-\lambda)V_s}{\omega_s} e^{-t/\tau_s} \quad (4)$$

where $\tau_s = L_s/R_s$ is the time constant of stator windings.

In equation (4), the first item is the steady state component of stator flux ψ_{sw} , corresponding to stator voltage during grid faults; the second item is the transient state component of stator flux ψ_{st} , functioning to maintain the continuity of stator flux at the instant of voltage drop.

The rotor voltage equation of DFIG can be expressed as [12]

$$\mathbf{u}_r = \frac{L_m}{L_s} \left(\frac{d}{dt} - j\omega_r \right) \boldsymbol{\psi}_s + (R_r + L_{r\sigma} \frac{d}{dt} - j\omega_r L_{r\sigma}) \mathbf{i}_r \quad (5)$$

where R_r and $L_{r\sigma}$ represent rotor resistance and leak inductance respectively.

DFIG rotor electromotive force can be obtained as:

$$\mathbf{e}_r = \frac{L_m}{L_s} \left(\frac{d}{dt} - j\omega_r \right) \boldsymbol{\psi}_s \quad (6)$$

During the transient process of symmetrical grid faults, the steady state component and the transient state component of stator flux will correspondingly induce rotor electromotive force \mathbf{e}_{rw} and \mathbf{e}_{rt} , which can be derived from equation (6) as

$$\mathbf{e}_{rw} = j\omega_{slip} \frac{L_m}{L_s} \boldsymbol{\psi}_{sw} \quad (7)$$

$$\mathbf{e}_{rt} = -j\omega_r \frac{L_m}{L_s} \boldsymbol{\psi}_{st} \quad (8)$$

The amplitude of rotor electromotive force is the superposition of its components, and its maximum value should be

$$|\mathbf{e}_r|_{\max} = |\mathbf{e}_{rw}| + |\mathbf{e}_{rt}| \quad (9)$$

Fig. 2 demonstrates the variation of $|\mathbf{e}_r|_{\max}$ with slip and the depth of voltage dip. It can be seen that with the increase of the absolute value of slip and the depth of voltage dip, grid faults exert greater impact on DFIG.

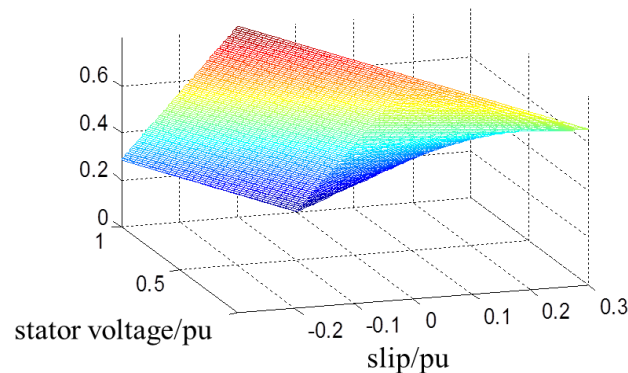


Figure 2. Variation of $|\mathbf{e}_r|_{\max}$ with slip and stator voltage.

Currents in DFIG rotor windings satisfy

$$-\mathbf{e}_{rw} + \mathbf{u}_{rw} = \mathbf{i}_{rw} (R_r + j\omega_{slip} L_{r\sigma}) \quad (10)$$

$$-\mathbf{e}_{rt} + \mathbf{u}_{rt} = \mathbf{i}_{rt} (R_r - j\omega_r L_{r\sigma}) \quad (11)$$

where the subscript w and t represent the steady state and transient state components of parameters. It has been figured out that existing VSynC strategy responds to grid faults in inertia time constant^[13]. Therefore, during symmetrical grid faults, existing strategy cannot generate corresponding

components of rotor voltage to counteract the fault components of rotor electromotive force, namely, $u_{rt} = 0$. This will induce overcurrent in rotor windings as well as oscillations of electromagnetic torque, making it difficult for DFIG to realize fault ride through.

3. Voltage compensation VSynC strategy for DFIG

It can be seen that it's necessary for VSynC strategy to take the fault characteristics of DFIG into consideration, in order to realize fault ride through during symmetrical grid faults. Analysis in part II indicates that the major supplementary should be the fault characteristics of virtual excitation current and virtual stator electromagnetic force, which will be studied in this part, and then an improved VSynC strategy for DFIG will be proposed.

During symmetrical grid faults, transient state component of DFIG stator flux will induce transient state component of flux in virtual excitation windings, i.e.

$$\psi_{fv} = \frac{M_{fv}\psi_{st}}{L_v} \tag{12}$$

Therefore, the transient state component of virtual stator electromotive force can be obtained as^[13],

$$e_{0vt} = -j\omega_v \frac{M_{fv}^2}{L_v L_{fv}} \psi_{st} \tag{13}$$

Based on analysis above, a voltage compensation VSynC strategy for DFIG is proposed as shown in Fig 3. Improvement is made by designing the voltage compensation part, which functions to accelerate the response to symmetrical grid faults and weaken the influence of the fault components of rotor electromotive force. In order to compensate the rotor voltage, the proposed strategy should satisfy,

$$u_{rt} = e_{0vt} = e_{rt} \tag{14}$$

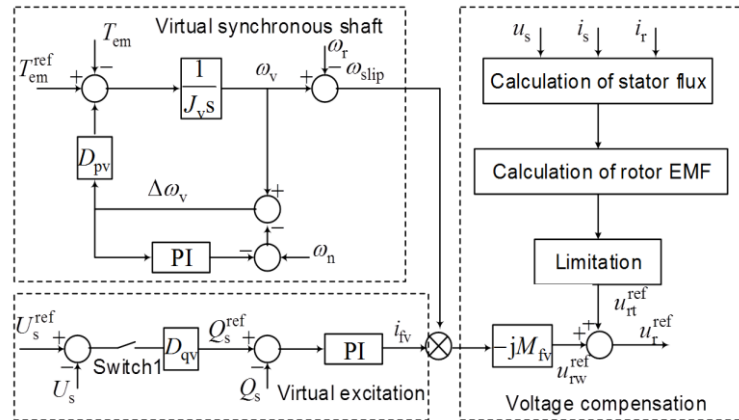


Figure 3. Voltage compensation VSynC strategy for DFIG.

The limitation of output voltage of rotor-side converter should be considered, referring to paper [13], the limitation of compensation voltage can be determined as

$$|u_{rc}|_{lim} = \frac{U_{dc_max}}{\sqrt{2} \cdot \sqrt{3} U_{rN}} - |e_{rw}| \tag{15}$$

where U_{rN} is the nominal phase voltage of DFIG rotor, and U_{dc_max} is the setting voltage of dc bus protection.

Once DFIG stator voltage drops deeply, the amplitude of e_{rt} may surpass $|u_{rc}|_{lim}$, thus the transient state component will be partially compensated. Figure 4 illustrates the range where the proposed strategy can implement full compensation.

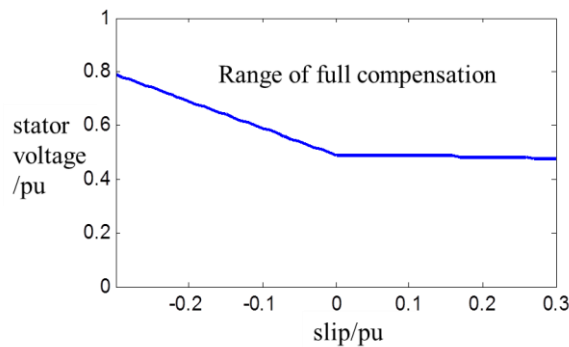


Figure 4. Range of full compensation with proposed strategy.

4. Simulation verification

In this part, simulation has been conducted in 1.5MW DFIG system to evaluate the control effect of proposed strategy. Parameters are given in Table I. Assume that under normal operation, DFIG stator voltage is nominal, the rotor speed $\omega_r=0.9$ pu, output active power $P_s=1.0$ pu, and output reactive power $Q_s=0$ pu.

Table 1. Parameters of DFIG system.

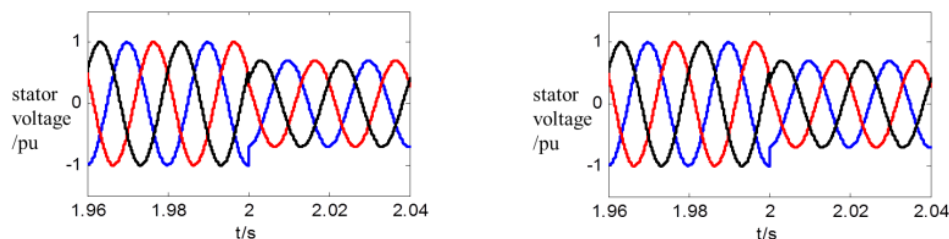
parameters	value	parameters	value
Rated power (MW)	1.5	L_m (pu)	2.9
Stator voltage (V)	690	R_r (pu)	0.016
Pole pairs	1	$L_{r\sigma}$ (pu)	0.16
R_s (pu)	0.023	Dc bus voltage (V)	1150
$L_{s\sigma}$ (pu)	0.18	Stator/rotor turns ratio	1/2.86

4.1. Mild symmetrical grid faults

At the first instance, mild symmetrical grid faults are simulated. At 2s, DFIG stator voltage drops to 0.7pu, corresponding to point (0.1, 0.7) in Fig 4, indicating that the transient state component of rotor electromotive force can be fully compensated. Fig. 5 compares the simulated results with existing VSynC strategy and voltage compensation VSynC strategy.

Fig. 5(a) clearly illustrates that with existing VSynC strategy, severe overshoot of fault currents and oscillations of electromagnetic torque are inevitable, which may cause severe damage to power electronic devices and wind turbine shafts. The sudden overshoot of rotor current reaches 2.0pu, and the amplitude of oscillations of electromagnetic torque is up to 1.5pu. Obviously, it's difficult for existing VSynC-based DFIG to implement symmetrical fault ride through.

Once DFIG rotor control voltage is fully compensated, the amplitude of DFIG currents hardly show any fluctuation before and after symmetrical grid faults. Moreover, the oscillations of electromagnetic torque are obviously limited, the amplitude of oscillations drops from 1.5pu to 0.55pu, decreasing by 63.3%, thus relieving the mechanical stress of DFIG shaft.



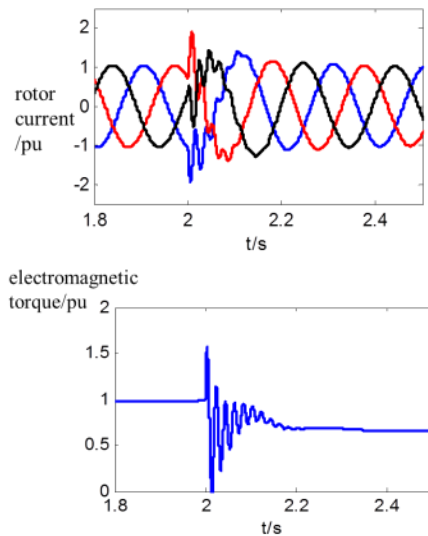


Figure 5(a). Simulation results of existing VSynC strategy under mild symmetrical grid faults.

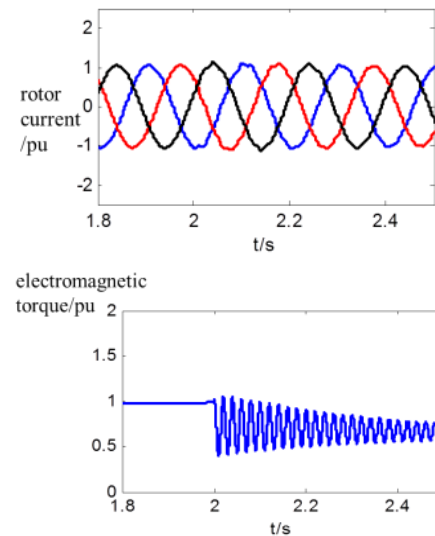


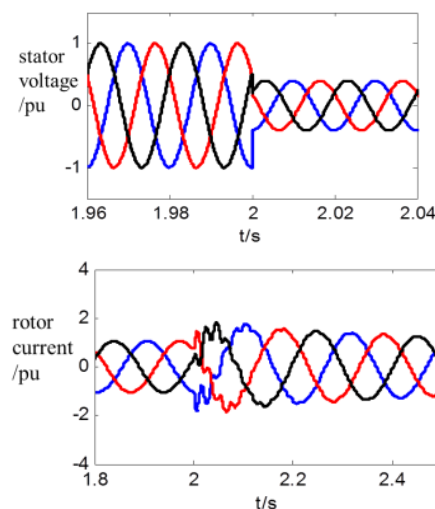
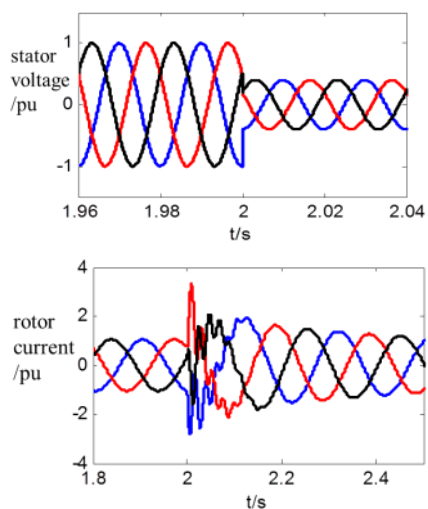
Figure 5(b). Simulation results of proposed VSynC strategy under mild symmetrical grid faults.

4.2. Severe symmetrical grid faults

This time, the proposed strategy is verified under severe symmetrical grid faults. At 2s, DFIG stator voltage drops to 0.4pu, corresponding to point (0.1, 0.4) in Fig 4, indicating that the transient state component of rotor electromotive force can only be partially compensated. Fig. 6 compares the simulated results with existing VSynC strategy and voltage compensation VSynC strategy.

It's obvious that the increase of severity of symmetrical grid faults will contribute to more violent electromagnetic transient characteristics, namely higher current overshoot and larger oscillations of electromagnetic torque. However rotor control voltage can only be partially compensated, overcurrents still exist but are significantly reduced. The amplitude of DFIG rotor current is decreased by 43% from 3.5pu to 2.0pu, and the overshoot of electromagnetic torque is suppressed from 3.0pu to 1.4pu.

The simulation results in Fig. 5 and Fig. 6 confirm the effectiveness of voltage compensation VSynC strategy, which is able to limit DFIG fault currents and suppress the oscillations of electromagnetic torque by making full use of the voltage output ability of rotor-side converter, therefore effectively enhancing DFIG symmetrical fault ride through capability.



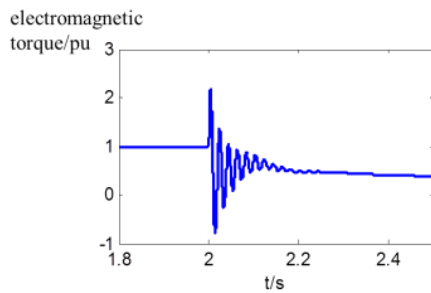


Figure 6(a). Simulation results of existing VSynC strategy under mild symmetrical grid faults.

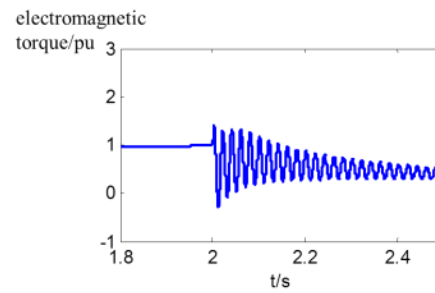


Figure 6(b). Simulation results of existing VSynC strategy under mild symmetrical grid faults.

5. Conclusions

This paper has carefully studied the symmetrical fault characteristics of DFIG based on existing VSynC mechanism, pointing out the incapability of existing strategy on implementing fault ride through during symmetrical grid faults. After investigating the defect of existing VSynC strategy and determining the main challenges in symmetrical fault ride through, a voltage compensation VSynC strategy is then proposed. The main principle is to compensate the transient state components of DFIG rotor voltage, and in this way, the overcurrent of DFIG can be completely diminished under mild symmetrical grid faults and significantly suppressed under severe symmetrical grid faults. Moreover, electromagnetic torque oscillations are effectively limited. Above all, the proposed strategy successfully enhances the fault ride through ability of VSynC-based DFIG.

6. References

- [1] Wang S, Hu J and Yuan X 2015 *IEEE J. Emerg Selec Top Pow Electr* **3** 932-44.
- [2] Zhong Q and Weiss G 2011 *IEEE Trans. Indus Electr* **58** 1259-67.
- [3] Wang K, Wang Z and Chai J 2015 *Autom Electric Pow Sys* **39** 152-8.
- [4] Lei S, Hu J and Yuan X 2017 *Proceedings of the CSEE* **37** 403-11.
- [5] Yang S and Chen Y 2015 *Autom Electric Pow Sys* **39** 12-8.
- [6] Zhang X, Xu D and Pan W 2010 *Autom Electric Pow Sys* **38** 13-9.
- [7] Yang S, Chen L and Sun D 2014 *Autom Electric Pow Sys* **38** 13-9.
- [8] Hu J, Sun D and He Y 2006 *Autom Electric Pow Sys* **30** 21-6.
- [9] Xiang D, Ran L, Tavner P J and Yang S 2006 *IEEE Trans Ener Convers* **21** 652-65.
- [10] Zhao Y, Chai J and Sun X 2015 *Proceedings of Applied Power Electronics Conference and Exposition, Charlotte (USA)* p 2980-3.
- [11] Hu S, Lin X, Kang Y and Zou X 2011 *IEEE Trans Pow Electr* **26** 3653-65.
- [12] Xu L 2008 *IEEE Trans Ener Convers* **23** 1073-81.
- [13] Cheng X, Sun X, Chai J and Zhao Y 2017 *Proceedings of Electrical Machines and Systems, Sydney (Australia)* p 2980-3.

Chapter 4:
High Voltage and Insulation Technology

Improved Control Strategy for AC-Filters Switching in UHVDC Converter Station

LI Hui, WANG Xiaofei, YU Bin, LIU Haifeng, XU Hao, GUO Siyuan

State Grid Hunan Electric Power Corporation Limited Research Institute, Changsha 410007, China

E-mail: lihui4219@sina.com.cn

Abstract. The AC-filter configuration, reactive power consumption, reactive power control function, switching and replacement strategy in SHANSHAN UHVDC converter station are introduced in detail. The various types of AC filters in the converter station are evenly configured in the large groups of filters based on their quantity. And the related types of filters within a large group are usually switched preferentially. The problem of this switching strategy that may cause large impact on the AC system and long reactive power recovery time during the large group of AC filter bus lines fault are analyzed. Then an improved strategy that the needed filters with same type are equally switched on the large AC-filter group is proposed. The proposed strategy can effectively reduce the influences of AC-filter bus fault to the AC system which will give some references for the design and operation of subsequent UHVDC projects.

1. Introduction

The AC-filter is an important part of the DC system in the converter station. It is mainly used to filter out the harmonics generated by the converter in the inverter process and provide reactive power compensation for the DC system, which directly affects the size of the transmission power and the power quality of the DC transmission system [1]-[9]. Take the example of the QISHAO (JIUHU) ± 800 kV UHVDC transmission project. This UHVDC transmission project starts from Jiuquan in Gansu Province to Xiangtan in Hunan Province, with a total length of 2361.5 kilometers. It carries the strategic mission of national clean energy delivery and air pollution prevention and control [1]-[2]. SHANSHAN Converter Station, as the receiving end converter station of the project, shoulders the heavy responsibility of converting DC to AC and feeding it into Hunan Power Grid. Due to the large transmission capacity, the reliability of the equipment in the station will directly affect the safe and stable operation of the entire DC system and even the Hunan power grid.

Compared with the UHVDC projects that have been put into operation, the receiving end of the QISHAO UHVDC transmission project—Hunan Power Grid, due to its unreasonable power supply layout, results in the AC system exhibiting weak reactive power support capabilities and low voltage stability margins. The system features make the significance of reactive power control strategies more prominent in this project.

In this paper, the AC-filter configuration, reactive power consumption and reactive power control functions in SHANSHAN converter station are introduced in detail, and the switching and replacement control strategies of the AC-filter in the station are emphatically analyzed. It is pointed out that the existing switching strategy may cause problems such as large impact on the AC system and long reactive power recovery time when the large group of AC filter bus lines in the station fails, which may further affect the safe and stable operation of the connected AC weak systems. On this basis, an improved input strategy is proposed that when the same type filter is put into operation, the



average input of the filters in each group is prioritized, which effectively reduces the impact and influence of AC bus fault on the AC system in the station. The research results can provide reference for optimization of UHVDC reactive control strategies.

2. SHANSHAN converter station AC-filter configuration

According to the Q/GDW 146-2006 《Technical guide for reactive power compensation and allocation of HVDC converter stations》, DL/T 5426-2009 《System design standard for ±800kv HVDC system》 and other standard specifications. The SHANSHAN converter station is equipped with a total of 4 groups and 19 sub-groups of AC filters, which can provide up to about 4940 MVar reactive power support: Among them, the HP-12/24 filter has 8 sub-groups, mostly used to filter 12th and 24th order harmonic; HP-3 filter has 2 sub-groups, mainly used to filter 3rd order harmonics; SC capacitor has 9 sub-groups, mainly used for reaction compensation. In addition, two low-voltage reactors are also deployed on the low-voltage side of the transformer used in the station to participate in reactive power control and adjustment. The specific configuration parameters, main circuit diagrams and grouping situations of various types of AC filters and reactors in the station are shown in Table 1, Figure 1 and Figure 2.

Table 1. Configuration of AC-filters and reactors at SHANSHAN converter station

Equipment type	Number of configuration groups	Single group capacity (MVar)
HP12/24	8	260
HP3	2	260
SC	9	260
Low resistance	2	60(Inductive Reactive Power)

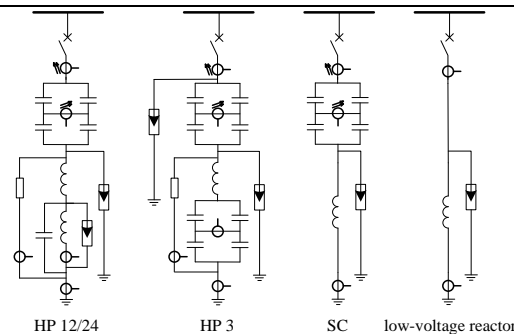


Figure 1. Circuit diagrams of AC-filters and reactors

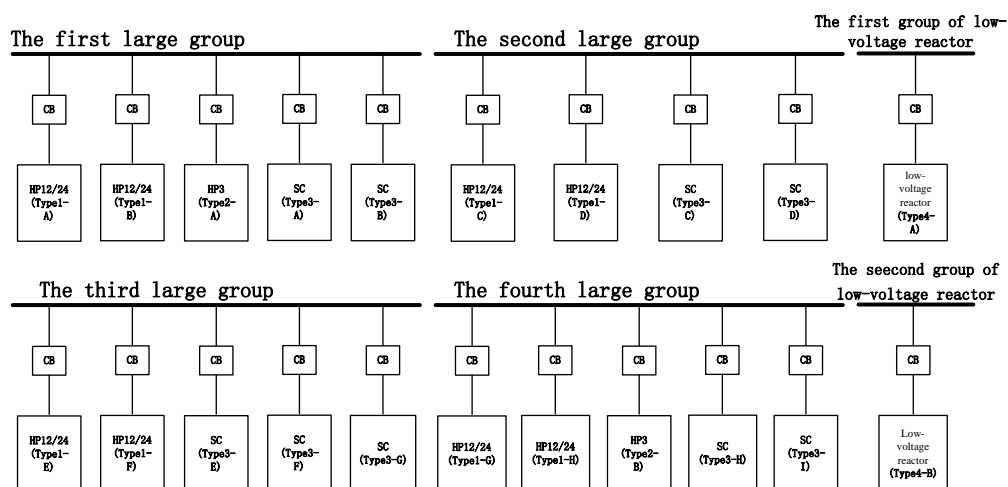


Figure 2. Grouping situations of AC-filters and reactors at SHANSHAN converter station

3. Reactive power control strategy at SHANSHAN station

The main control object of reactive power control is the AC filter (including low-voltage reactor) in the converter station. The main purpose of reactive power control is to guarantee the reactive power exchange between the converter station and the AC system within the allowable range or the AC bus voltage within the safe operation range, which is achieved by controlling the switching of the AC filter and the calculation of the reactive power consumption in the converter station according to the operating mode and working condition of the current DC system. In addition, the safety of AC filter equipment and the influence of harmonic on AC system should also be considered and realized in the reactive power control functions [10]-[15].

3.1. Calculation of reactive power consumption

The reactive power consumed by a 12 pulse converter can be expressed as:

$$Q_d = 2\chi I_d U_{di0} \quad (1)$$

Where χ is a function of the commutation overlap angle μ , for the inverting side:

$$\chi = \frac{1}{4} \frac{2 \frac{\pi}{180} \mu + \sin 2\gamma - \sin 2(\gamma + \mu)}{\cos \gamma - \cos(\gamma + \mu)} \quad (2)$$

The commutation overlap angle on the inverter side can be calculated according to formula (3):

$$\mu = \arccos(\cos \gamma - 2d_{xN} \frac{I_d}{I_{dN}} \frac{U_{di0N}}{U_{di0}}) - \gamma \quad (3)$$

Where: Q_d is reactive power, the unit is MVar; I_d is direct current, the unit is kA; U_{di0} is an ideal no-load DC voltage with a unit of kV; γ is the trigger angle of the inverter side (turn off angle), the unit is degree; μ is the phase overlap angle, the unit is degree; d_{xN} is the inductive DC voltage drop, per-unit value; the I_{dN} is the rated DC current, the unit is kA; the U_{di0N} is the rated ideal no-load DC voltage, the unit is kV.

According to equations (1)-(3), the relationship between I_d , γ and reactive power can be obtained as shown in Figure 3.

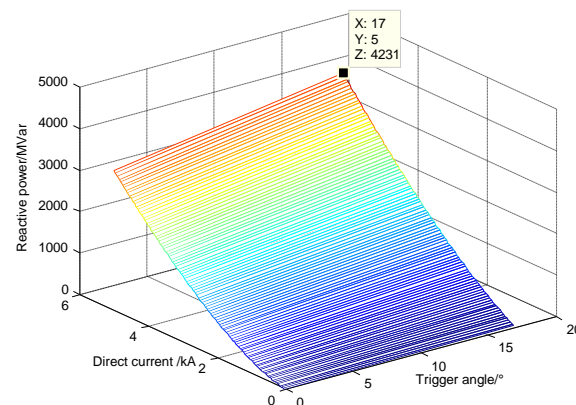


Figure 3. Relationship of reactive power, I_d and γ

As shown in Figure 3, reactive power consumption in converter station increases with the increase of DC current or γ . For SHANSHAN Converter Station, the reactive power consumption is 4231MVar under rated conditions (bipolar 4-valve bank, rated current 5kA, $\gamma=17^\circ$). Taking into account the certain overload capacity of the DC system, the total reactive power consumption will increase, but the AC filter bank configured in SHANSHAN converter station can still match the reactive power consumption requirements in the station.

3.2. Reactive power control function

The reactive power control function in the DC pole control host collects the operating parameters of the entire station, and switches the AC filter according to the power transmission level of the DC system and the reactive power consumption. The main control functions and the priority are shown in Table 2.

Through the six reactive power control sub functions described in Table 2, the reactive power exchange between the converter station and the AC system is within the allowable range or the AC bus voltage is within the safe operating range, whether in normal or fault conditions. On the other hand, it also effectively prevents the harmonic overload of the AC filter equipment in the converter station, protects the safe operation of the AC filter equipment and suppresses the influence of the station harmonics on the AC system.

Table 2. Functions and priorities of reactive power control

function name	Functional description	priority
Over voltage control	When the AC voltage reaches the reference value, quickly cut the AC filter to fulfil the absolute minimum filter requirement	1
Absolute minimum filter control (Abs Min Filter)	Filter bank required to prevent overloading of filter equipment (this condition must be satisfied during normal operation)	2
Highest/lowest voltage limit (U_{\max}/U_{\min})	Used to monitor and limit the steady state AC bus voltage of converter station	3
Maximum reactive switching limit (Q_{\max})	Limit the number of input filter banks and limit the steady state overvoltage according to the current operating conditions	4
Minimum filter capacity requirement (Min Filter)	Minimum filter bank required to meet the requirements of filtering out harmonics	5
Reactive power control/voltage control ($Q_{\text{control}}/U_{\text{control}}$)	Control the reactive power exchange (or AC bus voltage) in the station to match the set reference value	6

The priority of each sub-function in reactive power control is mainly used to coordinate the switching filter bank instructions issued by each sub-function. A switching instruction issued by a sub-function is valid only when it does not conflict with a higher-priority constraint. The priority of the above six reactive control sub-functions is from 1 to 6, and the priority levels are reduced in turn.

3.3. Filter bank switching strategy

3.4. Filter bank switching principle

During the rise and fall of DC power, input and excision of AC-filter banks must follow certain principles and sequence. In general, first of all, it is necessary to ensure the safe operation of the AC-filter device, that is, to prevent the AC-filter harmonic overload occurring, which is generally achieved by the absolute minimum filter control; Secondly, the influence of the harmonics in the station on the AC system should be considered. That is, the harmonics in the station should be suppressed within a certain level, which is generally controlled by the minimum filter capacity requirement. In addition, it is also necessary to ensure that the reactive power exchange between the converter station and the AC system is within the allowable range or the AC bus voltage is within the safe operation range, which is generally implemented by AC overvoltage control, maximum/minimum voltage limitation, maximum reactive power exchange limitation, reactive exchange control/voltage control, etc.

The switching points of the absolute minimum filter and the minimum filter are usually determined by the AC filter research report; Reactive power control (Q_{control}) is determined by calculating the reactive power exchange quantity ΔQ on both sides of AC and DC in real time. ΔQ can be calculated from equation (4):

$$\Delta Q = Q_d - \sum Q_{\text{filter}} \quad (4)$$

Where: Q_d is the total reactive power consumed by the converter in the station and can be calculated by formula (1)-formula (3). $\sum Q_{\text{filter}}$ is the reactive power provided by the filter/shunt capacitor bank and can be calculated by equation (5):

$$\sum Q_{\text{filter}} = \sum_{n=1}^N \left(\frac{U_{\text{ac}}}{U_{\text{acN}}} \right)^2 * \frac{f_{\text{ac}}}{f_{\text{acN}}} * Q_{\text{filterNn}} \quad (5)$$

Where: U_{ac} is the actual voltage of the AC system, the unit is kV; U_{acN} is the rated voltage of the AC system, the unit is kV; f_{ac} is the actual frequency of the AC system, the unit is Hz; f_{acN} is the The rated frequency of the AC system, the unit is Hz; Q_{filterN} is the rated working condition of the filter/shunt capacitor bank, that is, reactive power supplied under U_{acN} and f_{acN} . n is the number of filter/capacitor groups actually put into operation.

When the amount of reactive power exchange on both sides of AC and DC exceeds the limit value, the instruction is issued to control the switching of the filter/shunt capacitor bank, that is, when the equation (6) is satisfied, a command to excise AC-filter/shunt capacitor bank is issued. When the equation (7) is satisfied, a command to input the AC-filter/parallel capacitor bank is issued.

$$\Delta Q > Q_{\text{ref}} + Q_{\text{dband}} \quad (6)$$

$$\Delta Q < Q_{\text{ref}} - Q_{\text{dband}} \quad (7)$$

Where: Q_{ref} is the reference value set by the operator, the unit is MVar; $Q_{\text{dband}} (Q_{\text{dband}} > Q_{\text{filterN-max}}/2)$ is the dead zone of the action set by the operator, the unit is MVar. In addition, considering that when the DC system is running at low power and the absolute minimum filter is guaranteed, there will usually be an excess of reactive power compensation at the converter station. Generally, low-voltage reactors are added to absorb excess reactive power.

Table 3 shows the switching power point of the AC-filter determined by the absolute minimum filter and the minimum filter condition under the operating conditions of the bipolar 4 valve group in SHANSHAN converter station. As shown in Table 3, the power points required by the minimum filter are usually less than the power points required by the absolute minimum filter after the start of the pole. Therefore, the minimum filter is normally required to issue an input filter instruction prior to the absolute minimum filter requirement.

Table 3. Configurations of abs min filter and min filter at SHANSHAN converter station

Input filter bank number	HP 12/24	HP 3	Absolute minimum filter corresponding power point (MW)	Minimum filter corresponding power point (MW)
1	1	0	0	0
2	2	0	1582	1190
3	3	0	3128	2360
4	3	1	4265	3129
5	4	1	6115	4265
6	5	1	7197	5381
7	6	1	-	6478
8	6	2	-	7900

Figure 4 shows the switching sequence of filter/capacitor bank in SHANSHAN converter station from blocking to 1.0 p.u. power, then to blocking. As can be seen from Figure 4, each reactive control sub-function issues a switching command to control the switching of the filter/capacitor group according to its own requirements. When the power rises, the number of AC-filters/capacitors that are put into operation gradually increases, and the AC-filter input order is: HP12/24→HP12/24→HP12/24→HP3→HP12/24→HP12/24→HP12/24→HP3→HP12/24→HP12/24→SC→SC→SC→SC→SC→SC(→SC→SC→SC) (The last three groups of capacitors serve as backup).

During light load (the transmission power is less than 2000MW), the input of the filter is mainly issued by the minimum filter and the absolute minimum filter control function. It shows that the system is mainly restricted by the harmonic characteristics of the converter station access point and the performance of the AC-filter equipment, and a certain amount of AC-filter banks must be put into the system. However, due to the reasonable selection of AC-filter single-group capacity and the cooperation of low-voltage reactors, the reactive power exchange ΔQ on both sides of AC and DC does not exceed the Q_{control} limit. With the continuous rise of the power, more and more reactive power is consumed in the station. Q_{control} gradually seizes the control. When ΔQ exceeds the limit, a set of filters is input in order.

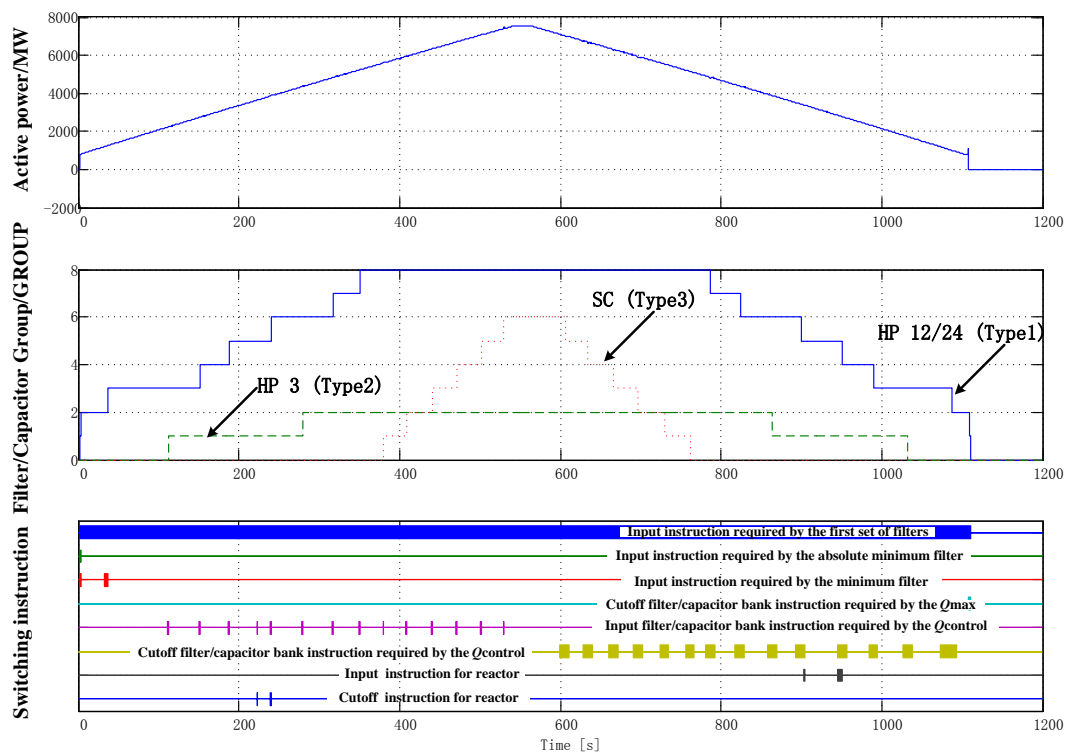


Figure 4. Switching of AC-filter during active power change

When the power of the DC system drops, the AC-filter is gradually removed, and the cut order is opposite to the power rises.

3.5. Filter bank replacement principle

As shown in Figure 5, when the AC filter is removed due to an unusual action such as a protection action or a switch sneak-off, the reactive power control sub-function of the AC filter will issue a filter input command to control the input of the filter, since the original reactive power balance is destroyed. As mentioned earlier, the Abs Min Filter is the least filter bank required to prevent harmonic overload of AC-filter. Therefore, when the Abs Min Filter is not satisfied, the resected filter will be replaced by the same type of filter. If there is no available same type filter at this time, the power return command

will be executed to meet the absolute minimum filter bank condition. If the power dropped to the last stage still fails to meet the absolute minimum filter bank requirement, the reactive power control will stop the DC system after the default time delay.

When the requirement of harmonic filtering is not satisfied, the Min Filter module is used to send the input instruction of AC-filter group, and the resected filter is replaced by the same type of filter. If there is no available same type filter at this time, an alarm signal is sent to the operator, and the operator decides whether or not to perform power back-off.

In the same way, when the voltage or reactive power exchange capacity does not meet the requirements, U_{\min} , U_{control} , Q_{control} and other functions will issue instructions to input the AC-filter for replacement.

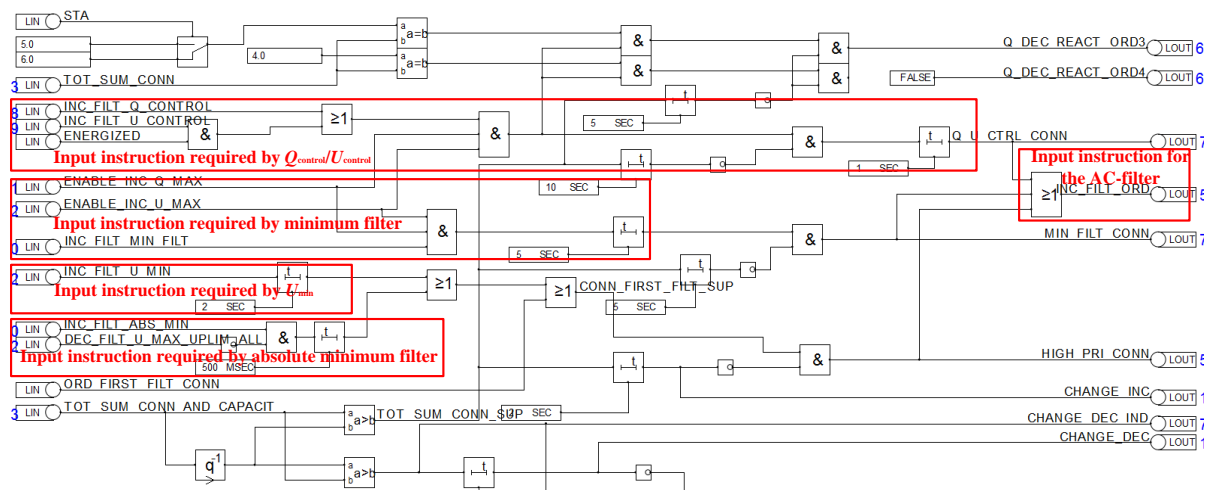


Figure 5. Replacement of AC-filter Optimization of Reactive Power Control Strategy in SHANSHAN Station

3.6. Requirement of transient voltage change rate

According to the Q/GDW 146-2006 《Technical guide for reactive power compensation and allocation of HVDC converter stations》, the voltage change rate caused by reactive group switching should generally not exceed 1.5%~2%; The change rate of the transient voltage of the bus bar at the converter station caused by the large group of reactive power removal is generally not more than 5%~6%.

The following relationship exists between the each group of AC filter reactive power capacity in the converter station and the transient voltage change rate of the AC bus:

$$\Delta U = \frac{\Delta Q_{\text{filter}}}{S_d - \sum Q_{\text{filter}}} \quad (8)$$

Where: ΔU is the transient voltage change rate of the AC bus of the converter station; ΔQ_{filter} is the each group of AC filter reactive power capacity in the converter station, and the unit is MVar; S_d is the short-circuit capacity of the AC bus of the converter station and the unit is MVA.

Taking SHANSHAN converter station as an example, according to formula (8), the voltage change rate caused by switching a group of filters is about 1.2%; the maximum voltage change rate caused by removing a large group of reactive power is about 5.9%, which meets the standard requirements. However, taking into account the relatively heavy load in the near area of SHANSHAN converter station, poor dynamic reactive power support capability, and the low voltage problem of the power grid, the removal of large groups of filters will result in large transient voltage fluctuations, which is obviously very unfavorable for the operation of the Hunan power grid. Therefore, how to reduce the influence of the removal of large group filters on the AC system and the AC-filter equipment in the station should be considered as much as possible on the basis of the existing filter configuration.

3.7. Problems with existing strategies

The various types of filters of the SHANSHAN converter station are usually evenly configured in the large groups of filters based on the quantity, as shown in Figure 2, and 8 groups of HP12/24 filters are evenly distributed to four large filter groups. 2 groups of HP3 filters are evenly distributed to two filter large groups. 9 groups of SC capacitors are evenly distributed to four filter large groups. During the DC system operate at high power level (in this situation, the AC filters except some capacitor bank are all put into use), this configuration can avoid the power fall back caused by the mismatch of the Abs Min Filter requirements when a large group of filters is cut off. The input of the filter is considered by a large group of filters. That is, according to the input sequence, the related types of filters within a large group are preferentially used. Then the input of the next large group of filters is considered. In actual operation, the two groups of HP12/24 filters in the first large group are preferentially put into operation according to the order, and then a group of HP12/24 filters in the second large group are put into operation. Next, a group of HP3 filters in first large group are put into operation, etc.

Assuming the current transmission power of the SHANSHAN converter station is 2000MW, as mentioned above, the function of reactive power control will put into two groups of HP12/24 filters in the first large group, and then put into a group of HP12/24 filters in the second large group. If the bus of the first group of filters fails at this time, the two sets of filters connected to this group of filters will be cut off. With reference to the replacement logic diagrams shown in figure 5 and figure 6, and the switching power points of Abs Min Filter and Min Filter shown in Table 3, both the Abs Min Filter and the Min Filter conditions are not satisfied. The Abs Min Filter has higher priority than the Min Filter. It will give priority to request input of filter instructions and replace the already-removed filter with the same type of filter. The first HP12/24 filter is put into operation at 0.5s, and the second HP12/24 filter is input after a delay of 2s, for a total of 2.5s to complete the replacement. During the replacement process, although DC system blocking and power back-off will not occur, it can be known from equation (8) that the maximum transient voltage disturbance of the AC bus will reach 2.447%. Meanwhile, the running filters will withstand the harmonic overload of 2.5s. Also, the power quality of the transmission power cannot meet the requirements (Min Filter is not satisfied). Taking into account the weak power supply characteristics of Hunan power grid, this result is extremely unfavorable for the safety and stability of Hunan power grid and AC filter equipment in the station.

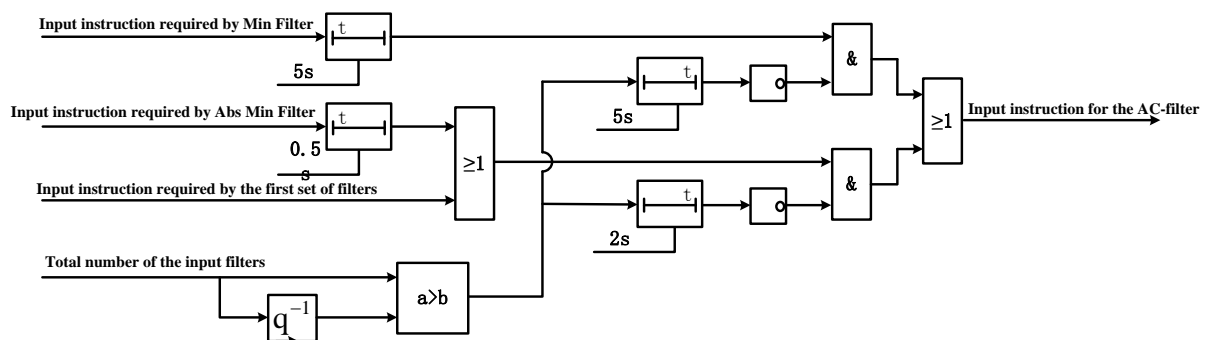


Figure 6. Automatic replacement logic of AC-filter with Abs Min Filter and Min Filter not fulfilled

3.8. Improve control strategy

If the input strategy of the same type filters is changed. The same type filters are evenly input among the large groups of filters preferentially instead of the related types of filters within a large group being preferentially used. It can effectively shorten the recovery time and reduce the harmonic and voltage disturbance. It is still assumed that 3 groups of HP12/24 filters are used in the SHANSHAN station, but unlike the existing strategies, the 3 groups of HP12/24 filters are evenly put into operation from the first large group to the third large group, that is, each large group has one small group. If the first large group of filter bus faults still occurs at this time, only one HP12/24 type filter will be removed. According to the calculation of (8), the maximum transient voltage disturbance of the AC bus will be reduced to 1.223%. Meanwhile, because the replacement time will be shortened to 0.5s, the running

filter withstands harmonic failure and transmission power quality failure time will also reduce synchronously to 0.5s, which will greatly reduce the impact on Hunan power grid.

Table 4 shows the comparative results of switching optimization strategy in SHANSHAN Converter Station. It can be seen that the performance with the proposed strategy has improved significantly compared to the existing strategies.

If only two sets of AC filters are put into use in SHANSHAN converter station. When the first large group of bus faults occurs, the recovery time is slightly different from that of the three groups filters used, because the existence of “first set of filters require input commands”, the recovery time is 2s. However, it is still longer than the optimized switching strategy, as shown in Table 4. The replacement time of other filter input groups and the influence on the grid can be analyzed in the same way.

Table 4. Comparative analysis of switching optimization strategy at SHANSHAN converter station

Input filter bank number		Before optimization	After optimization
3	Resection filter number (group)	2	1
	Maximum transient voltage change rate (%)	2.447	1.223
	Recovery time (s)	2.5	0.5
	Whether it will cause DC blocking	no	no
	Whether it will cause DC power back drop	no	no
2	Resection filter number (group)	2	1
	Maximum transient voltage change rate (%)	2.417	1.209
	Recovery time (s)	2	0.5
	Whether it will cause DC blocking or tripping	no	no
	Whether it will cause DC power back drop	no	no
Minimum short circuit capacity ^[1] (MVA)			21914

When the system is running at high power level with the AC filter fully input, the replacement is unavailable, so the reactive power shortage and voltage disturbance can only be reduced by the Q_{control} input capacitor bank. When using this method, the capacitor bank is also preferred to put into use evenly among the large groups of filters. When the single bus fault occurs, especially the previous groups of AC-filter bus faults, the number of excised filters will be less than the original strategy. Thus, with the proposed strategy, the recovery time is shorter and the impact on the system is smaller. Of course, the influence of voltage disturbances on AC system can be further suppressed and better control effects can be obtained through the adjustment of γ -kick (transition angle transient control), SVC, STATCOM and synchronous condenser [16], etc.

4. Conclusion

In this paper, the AC-filter configuration, reactive power consumption, reactive power control function, switching and replacement strategy in SHANSHAN UHVDC converter station are introduced in detail. An improved strategy that the needed filters with same type are equally switched on the large AC-filter group is proposed to reduce the influences of AC-filter bus fault to the AC system. Considering that the power grid in Hunan will not be able to operate under heavy load for a long period of time in the future. In this case, the filter will have a large amount of redundancy, Compared with the existing

strategy, the proposed strategy can effectively reduce the impact on the AC system, shorten the recovery time and reduce harmonics and voltage disturbances when the failure of the filter bus in the station, which has positive significance for the safe operation of Hunan power grid. The method proposed in this paper also has certain reference significance for the design and operation of subsequent HVDC transmission projects.

With the application of the synchronous condenser, SVC and STATCOM in UHVDC transmission project, the interrelationship and coordination control strategy of these equipments are the subjects for further investigations.

5. References

- [1] ZOU X, JIANG W Y, LI Y N. Reactive power configuration scheme of ± 800 kV Jiuquan-Hunan UHVDC project. *Electric Power Construction*, 2015, 36(9):43-49.
- [2] GUO H, DANG J, XI JH, et al. Analysis on Power Receiving Capability of Hunan Power Grid During the Initial Operation of UHVDC Project from Jiuquan to Hunan. *Electric Power*, 2017, 50(10):57-63.
- [3] WANG H N, ZHENG C, REN J, et al. Dynamic Reactive Power Trajectory of HVDC Inverter Station and Its Optimization Measures. *Power System Technology*, 2015, 39(5):1254-1260.
- [4] XIAO L L, LIN Q F, WANG C T. Analysis and Improvement on Abnormal Switching of AC Filter in Converter Station. *Power Capacitor & Reactive Power Compensation*, 2014, 35(3):73-78.
- [5] CHENG G H, KANG Y. Investigation on Size of AC Filters and Shunt Capacitors at DC Converter Station. *Electric Power*, 2016, 49(1):114-118.
- [6] YANG M, ZHAO S L, LI H Y, et al. Design of AC Filter Capacitor Bank for HVDC Transmission System. *Power Capacitor & Reactive Power Compensation*, 2017, 38(5):1-6.
- [7] YANG Y H, FENG Z W, DAI J S. Typical Failure Analysis of AC Filter at Converter Station. *Power Capacitor & Reactive Power Compensation*, 2014, 35(3): 69-72, 82.
- [8] ZHANG Q, LIANG D T, LIU N. Reactive Power Compensation Scheme and Configuration for ± 800 kV Pu'er Converter Station. *High Voltage Apparatus*, 2015, 51(3):117-121.
- [9] Tao Y. DC Transmission Control Protection System Analysis and Application. Beijing: *China Electric Power Press*, 2015.
- [10] ZHU K L, WEN B Y. Reactive Power Balance and Control Methods in HVDC Transmission System. *Electric Power Construction*, 2015, 36(9):35-42.
- [11] CHEN F, ZHAO W W. Optimization of Voltage Selection for UHVDC Reactive Power Control. *High Voltage Apparatus*, 2015, 51(3):29-33.
- [12] ZHENG C, TANG Y, MA S Y, et al. Study on the Dynamic Reactive Power Characteristic of HVDC Rectifier Stations and Optimization Measures. *Proceedings of the CSEE*, 2014, 34(28):4886-4896.
- [13] ZHAO J, XIONG H Q, CHEN Q, et al. Analysis and Model of Output Power Characteristics in UHVDC Inverter Stations. *Proceedings of the CSEE*, 2018, 38(6):1612-1621.
- [14] WANG J J, LIANG Z Y, LI Z L, et al. Reactive Power Control Strategy for Low Power Operation of HVDC Transmission System. *Automation of Electric Power System*, 2017, 41(6):154-158.
- [15] LI Z R, FA Y F, CHANG X Q. Study on the SVC and STATCOM to Improve the Performance of Islanded Operation DC System. *High Voltage Apparatus*, 2017, 53(7):67-72.
- [16] RUAN L, WANG Q, LING Z X. Study on the Performance Feature and Key Engineering Application of New Large Capacity Condenser. *Electric Power*, 2017, 50(12):57-61.

Acknowledgments

This research is supported by the Science and Technology Project of State Grid Hunan Electric Power Company (Grant No. 5216A5170013).

Researches on Two Kinds of Fault Restart Logic of Qishao \pm 800 kV UHVDC Project

Hao Xu¹, Lei Zhang², Haifeng LIU¹, Wenwu LIANG¹, Hui LI¹

¹ State Grid Hunan Electric Power Limited Corporation Research Institute, Hunan Changsha 410007;

² State Grid Hunan Electric Power Limited Corporation, Hunan Changsha 410004;

Abstract: In order to improve the availability and operating efficiency of the DC system, Qishao \pm 800kV UHVDC transmission project pole layer control system is equipped with two kinds of fault restart logic, namely the instantaneous fault restart and the valve group fault restart. In this paper, the triggering mechanism, timing and opening conditions of these two fault restart logic are analyzed in detail, and the relationship between the instantaneous fault restart logic and other protections reacting transient faults in pole and bipolar zone is studied emphatically, DC system debugging scene recorded wave diagram is referred to illustrate the two restart logic of the action process and effect, with a view to provide some guidance and reference significance to the field operation and research work.

1. Introduction

UHVDC transmission has the advantages of large transmission capacity, long transmission distance, relatively low loss, et al, and is an effective way to solve China's energy-load reverse distribution, achieve energy clean alternatives and optimization configuration, and prevent air pollution. It has entered an all-round development and construction stage for UHVDC transmission in China [1]-[4]. The Qilian-Shao \pm 800 kV UHVDC transmission project begins in the Jiuquan region of Gansu Province in the northwest, passes through four provinces including Gansu, Shaanxi, Chongqing, and Hubei, and finally locates in Xiangtan, Hunan Province. Its total length is 2385.6 km. The operation of the project will help to make full use of Gansu's abundant wind energy and coal resources, and guide the rational development of the Jiuquan energy base in an orderly manner, while relieving the tension of electricity consumption in Hunan power grid and restraining the increasingly serious haze situation in Central China [5]-[7].

In order to improve the availability and efficiency of the UHVDC system, two kinds of fault restart functions are configured, namely, instantaneous fault restart and valve group fault restart. Among them, transient faults include transient grounding faults on the UHVDC transmission line, metal return line, and grounding electrode and bipolar neutral bus under monopolar operation. Valve group fault refers to the grounding fault in a single converter area. Depending on the rich and complete control capability of UHVDC systems, both fault restart logics can achieve fast and effective fault isolation, deionization, and system restart without relying on arc extinguishing capability of DC circuit breaker, which avoids the unnecessary monopolar outage of the system and improves the operation level of UHVDC projects. In this paper, the logic of ABB technology-based instantaneous fault restart and valve group fault restart in DC control and protection systems is studied in detail, and the two fault restart operation sequences are elaborated in detail in conjunction with the debug field recording of Qilian-Shao UHVDC transmission project, In order to provide guidance and reference for field operation and scientific research work.

2. Research on instantaneous fault restart logic



Instantaneous faults can be caused by lightning, branch discharge, line touch due to wind deflection, et al. Such faults do not have the ability to self-retain the fault circuit. If the fault is isolated for a short time, the power supply side will have a higher probability to achieve arc extinction and fault isolation and the system operation restore. Due to the low arc breaking ability of DC breakers at present, the transient faults in UHVDC projects must be extinguished by short-term blocking of the corresponding DC pole system. In other words, the execution subject of extinguishing the fault arc is the control system rather than the protection system. When a transient fault occurs, the control system can quickly adjust the trigger angle of the converter valve, instantaneously transform the rectifier side into an inverter property, and at the same time of interrupting the power output of the rectifier side, simultaneously release the energy of the fault point from the two stations, and the arc extinguishing effect is faster than the AC line reclosing.

Table 1 Protection types and principles for triggering transient fault restart logic

Protection object	Protection type	Protection principle	Protection fault features
DC line	Travel wave protection	$\frac{dP}{dt} > \Delta_1 I \quad \Delta P > \Delta_2 I \quad G > \Delta_3$ $P = Z_{\alpha} I_{dl} - U_{dl}$ $G = Z_0 (I_{DEL} + I_{CN1} + I_{CN2}) \times 0.5 - (U_{dl1} + U_{dl2}) \times 0.5$	When a ground fault occurs on the DC line, fault waves travel to both ends of the line, causing rapid changes in pole and ground waves.
	Voltage sudden changing protection	$U_{dl} < \Delta_1, \quad dU_{dl}/dt > \Delta_2$	Detect bolted ground faults on the DC line. When the DC line has a ground fault, the DC voltage on both sides will drop rapidly.
	Low voltage protection	$U_{dl} < \Delta$	Detect bolted ground faults and high-resistance ground faults on the DC line.
	Longitudinal differential protection	$ I_{dl} - I_{dl_{os}} > B + K \times I_{dl}$	When there is a ground fault on the DC line, the DC currents of the two stations are inconsistent, resulting in a differential current.
Metal return line	metal return line ground protection	$ I_{DGND} + I_{DEL1} + I_{DEL2} > B + K \times I_{DNE}$	In normal operation, there is no DC current flow at the ground point on the inverter side; if there is a ground fault in the DC system, the fault current in the ground will flow through the ground electrode.
	metal return line longitudinal differential protection	$ I_{DME} + I_{DME_{OS}} > B + K \times I_{DME} - I_{DME_{OS}} $	If there is a ground fault in the metal return line, the fault point and the grounding pole on the inverter side form a loop. This loop is connected in parallel with the faulty point on the metal return line on the inverter side, which causes the differential current to appear.
Grounding electrode lead	Ground lead unbalance protection	$ I_{DEL1} - I_{DEL2} > I_{set}$	Ground fault detection grounding wire, disconnection will automatically block. The grounding lead is erected on the same rod with double return.
	Earthing pole differential	$ I_{DEL} - I_{DEE} > B + K \times I_{DEL}$	When a ground fault occurs in one of the grounding pole lines, the current

protection			at both ends of the grounding pole line will be inconsistent and a differential current will be formed.
Bipolar Neutral Bus	Bipolar Neutral Differential Protection	$I_{\text{diff}} > B + K \times I_{\text{DNE}} - I_{\text{DNE_OP}} $ $I_{\text{diff}} = \left \begin{array}{l} I_{\text{DNE}} - I_{\text{DNE_OP}} - I_{\text{DME}} \\ I_{\text{DGND}} - I_{\text{DEL1}} - I_{\text{DEL2}} \end{array} \right $	Detect ground fault on bipolar neutral bus. When the bipolar neutral bus is grounded, the grounding point diverts the grounded pole and forms a differential current.

Notes: Among the above formulates, P is a polar wave, G is ground wave; Z_{α} is the polar wave impedance; I_{dl} is the DC line current, Z_0 is ground wave impedance; U_{dl} is the DC line voltage, Subscripts 1 and 2 indicate pole 1 and pole 2; I_{DEL} is combined current of ground lead; I_{CN} is a very neutral bus capacitor current; Δ_i is fixed, $i=1,2,\dots$; $I_{\text{dl_os}}$ is the DC current of the other station, B is the starting current, K is the proportional coefficient. I_{DGND} is the grounding current in the station, I_{DNE} is the pole-neutral bus ground current. I_{DME} is the metal return line current, $I_{\text{DME_OS}}$ is metal return live current of the other station.

2.1. Triggering of instantaneous fault restart logic

The fault restart logic is triggered by the corresponding protection action signal, which is controlled by the master pole. The QiShao DC project is configured with instantaneous fault restarts for DC line, metal return line, grounding electrode circuit and bipolar neutral bus bar, as shown in Table 1.

2.2. Related issues description of Restart logic

Faults in different parts of the DC system may have similar fault characteristics. In order to ensure the selectivity and reliability of the restart logic, the coordination relationship between logic and related protection under similar fault characteristics must be carefully restarted.

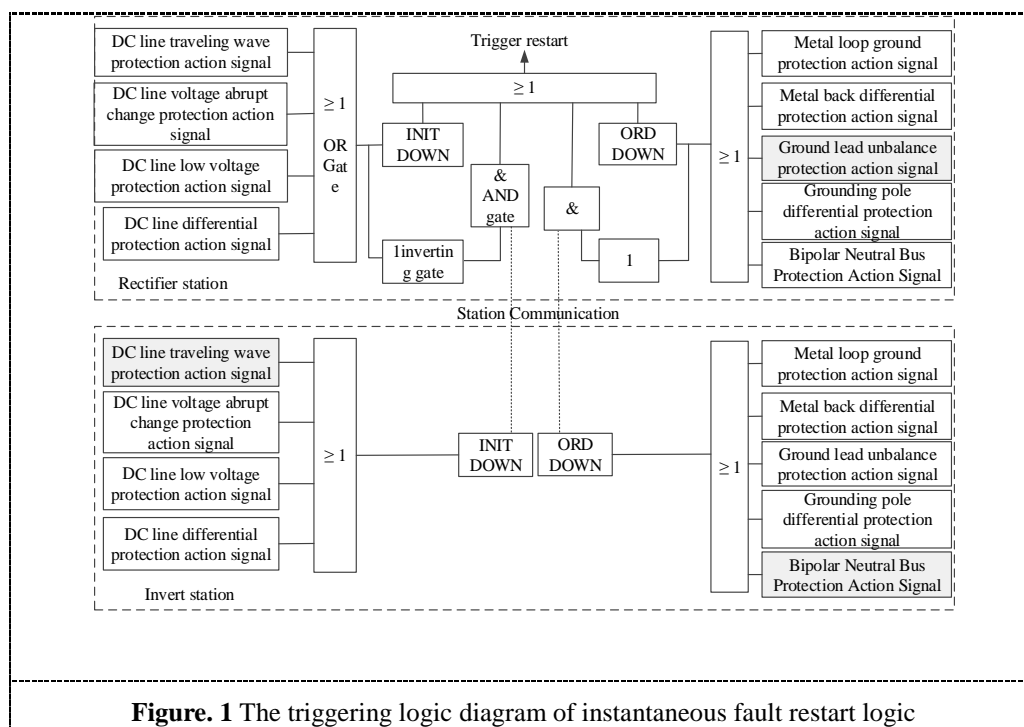
2.2.1. The distinction between pole bus grounding and DC line grounding fault. The characteristics of the pole bus grounding fault is that the DC voltage reduces, the DC current on the rectifier side increases, and the DC current on the inverter side reduces, which is similar to the DC line grounding. However, because the pole bus fault is more serious and generally permanent, the DC line protection should not be activated to avoid unnecessary secondary shocks on the DC system.

The traveling wave protection and the voltage abrupt change protection are based on the direction discrimination of the DC line current change rate dI_{dl}/dt , and when the pole bus ground fault occurs, the main line protection will not operate reliably. The longitudinal differential protection has natural selectivity and will not act on the outside fault. DC line low voltage protection has no directionality, and mismatch can occur if the protection is not compatible with other polar grounding protection.

2.2.2. Comparison of Grounding Fault between Bipolar Neutral Bus and Metal Loop. In the condition of metal return line operation, only the inverter-side grounding electrode is used to clamp the zero potential, so the grounding of the inverter-side bipolar neutral bus bar area will not have obvious fault characteristics. If the rectifier side bipolar neutral busbar is grounded, the connection place constitutes the temporary grounding electrode in the station, which is connected with the reverse side grounding pole, and the fault current can simultaneously promote the bipolar neutral bus differential protection and the reverse side metal return protection, which may lead to the situation that the metal loop ground protection acts first. However, under the condition of monopole metal loop operation, the bipolar neutral bus differential protection also triggers the restart logic, that is, the metal loop operation and the bipolar neutral bus differential protection have the same action effect, and the misoperation causes no additional adverse effects will be produced.

2.3. Instantaneous fault restart operation timing

Transient fault restart can only be performed by rectifier station, because rectifier station is the power side. The protection action signals listed in Table 1 are transmitted directly or indirectly to the station's pole control system, and then triggered by the logic diagram shown in Fig. 2. In the figure, INIT DOWN and ORD DOWN have the same definition, both are deionization signal and restart logic trigger signal, but the former is applicable to the DC line protection action signal, the latter is applicable to the metal return line, the grounding lead and the bipolar Neutral bus protection action signal. On the rectifier side, INIT DOWN and ORD DOWN directly trigger the restart logic via the OR gate; On the inverter side, the INIT DOWN and ORD DOWN signals are transmitted to the rectifier station via the inter-station communication, and are then triggered at the rectifier station via an OR gate. When the communication between the stations is interrupted, the above protection action signal on the inverter side cannot be transmitted to the rectifier side, and no restart will be triggered. The corresponding fault will be directly acted on the trip by other protection of the inverter station or the above-mentioned protection delay section. In addition, if the above protection of the rectifier station and the inverter station operates simultaneously, the rectifier station will shield the protection action signal sent from the inverter station.

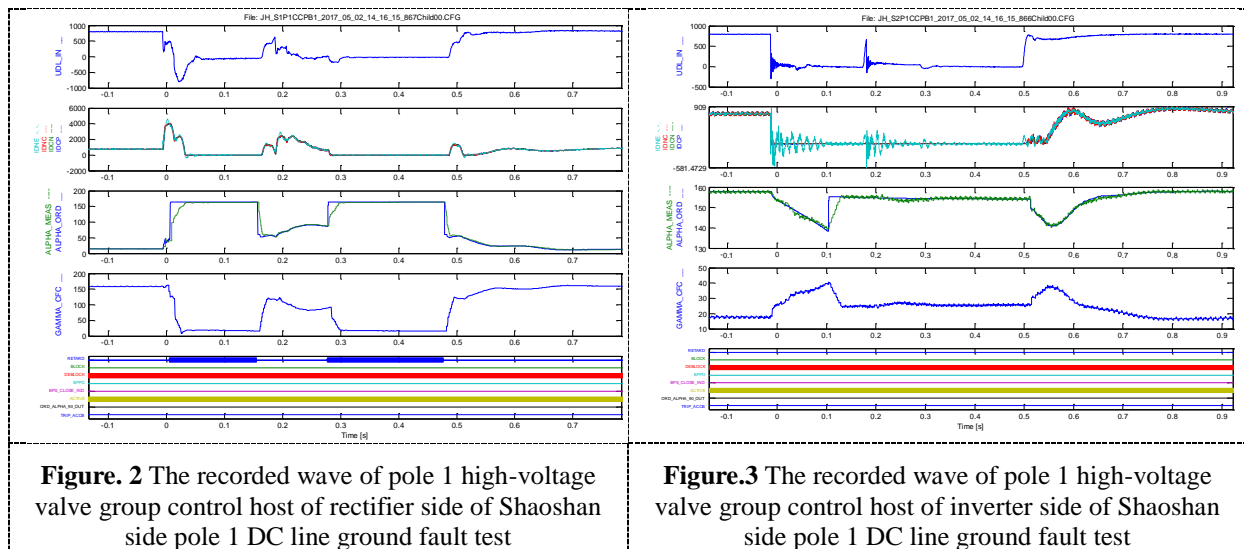


The time sequence of transient fault restart operation can be summarized as three phases: phase shifting, deionization and restart. Instantaneous fault restart in sequence includes the full voltage restart, the reduction voltage restart,. Among them, the full voltage restart is to restart the DC voltage to the level before the fault, the reduction voltage restart is to restart the DC voltage to the reduced operation level. The control system specifies the number of restarts under various operating conditions. For example, under bipolar full-voltage operation conditions, if the failure is more stubborn, the system will perform two full voltage restarts and one reduction voltage restart.

2.4. System debug record waveform analysis

Fig. 2 and Fig. 3 show the recorded waveforms of the high-side valve group control host of the rectifier side and the inverter side pole 1 during the test of the DC line ground faults on the side of the Shaoshan HVDC system. In the figure, UDL_IN is the pole I pole bus to ground voltage, the unit is kV; IDCP and IDCN are respectively the high-side current and the low-side current of the high-end valve group of pole I, and IDNC and IDNE are the currents of the pole-neutral bus near the valve side

and near the grounding pole, and the unit is A; ALPHA_MEAS and ALPHA_ORD are the measured value and the command value of the trigger angle, and GAMMA_CFC is the measured value of the extinguish angle. RETARD is the phase-shift signal, BLOCK is the valve block lock signal, DEBLOCK is the valve block unlock signal, BPPO is the input bypass signal, ACTIVE is the main signal of the valve bank control host, BPS_CLOSE_IND is the valve bypass switch co-position signal, ORD_ALPHA90_OUT is input the ALPHA90 signal, TRIP_ACCB is the AC switch signal.



From Fig. 2 and Fig. 3, it can be seen that there have been two restarts during the grounding test of the DC line on the Shaoshan side, that is, two RETARD signals have occurred. After the grounding fault, the DC voltage at the rectifier side drops and the DC current increases sharply. At the same time, the DC voltage and DC current at the inverter side disappear at the same time, causing the main protection action of the line. The first restart is triggered. The response is kept for the first RETARD signal for 150ms in the oscillogram. Then the system restarts trying to recover the DC voltage, that is, the RETARD signal disappears and the rectifier side falls back the firing angle, but because the fault is not eliminated, the rectifier side cannot establish a normal DC voltage after restart and is accompanied by a large fault DC current, but at this time the line main protection can't be operated due to the increase of the DC voltage change trend. The low-voltage protection delay is 80ms to trigger the second restart. The response is the second RETARD signal held in the oscillogram for 200ms. Then the system restarts again, that is, RETARD disappears for the second time. At this time, the grounding copper wire is still not fully burned, so the instantaneous rectifier side cannot still establish a normal DC voltage after the second restart, and the DC current increases sharply. The copper is grounded after about 20ms. The line is completely burned, the fault disappears, the fault point returns to normal voltage level, and the DC current also falls back. In the oscillogram, a small arch appears in the DC current waveform after the second RETARD signal disappears; after the fault disappears, the rectifier side rapidly establishes a normal voltage, and the low-voltage protection returns and the system restarts successfully.

3. Valve group fault restart logic research

3.1. Characteristics of grounding fault in converter area

The converter fault restart logic means that under the condition that the two poles are all operated in the bipolar power control mode and the communication between the stations is normal, the ground fault in the single inverter area of the station causes the differential protection of the inverter to act on blocking both poles. Then the control system automatically inputs non-fault valve groups to quickly restore bipolar balancing operation. Figure 4 shows the fault current path when Shaoshan station pole 1 low-voltage converter zone high-pressure wall bushing fault occurs. The C12 valve group was

short-circuited, that is, the DC voltage on the inverter side was reduced by about 400 kV, so the DC current will increase significantly when the fault occurs. At the same time, the fault current flows through the IDC2P without flowing through the IDC2N, so the differential protection of the low-side converter with IDC2P and IDC2N as differentials will operate. For ungrounded faults in the converter area, the control system after the relevant protection action can quickly isolate the fault by the by-pass function generated by the bypass switch; But for the grounding fault in the converter area, such as the fault point F, the bypass function fails after closing the BPS2, because the fault point can still form the loop through the earth and the rectifier station, and the circuit is less impedance because it does not pass through the smoothing reactor on the very neutral bus. Since the anode/cathode switch of the valve group does not have the capability of arc breaking, the ground fault in the single converter must be blocked by blocking the same-pole dual valve group, and short-term interruption of the DC current to achieve rapid arc extinction at the fault point.

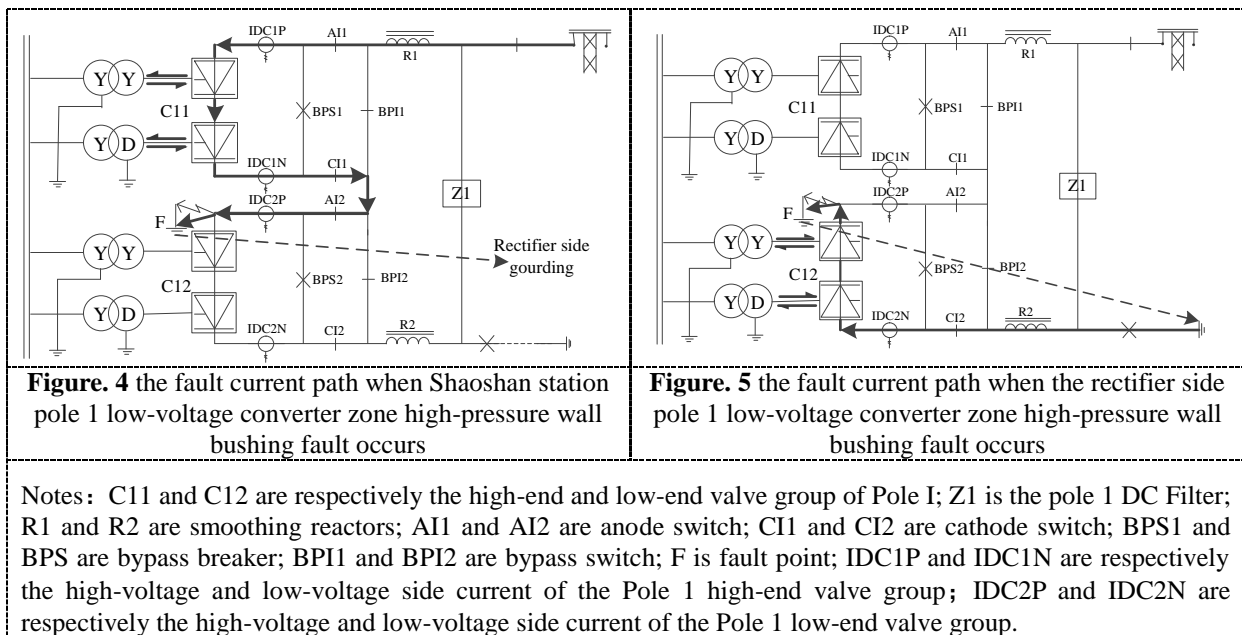


Figure 4 shows a relatively special grounding fault in the converter area. When the fault point moves down and approaches the common-cathode point of the low-voltage six-pulse bridge, the fault circuit is also present, but the fault current must flow through the valve side windings of the converter first, and the fault loop impedance will increase while the fault current reduce. It is worth noting that at this time, the low-end valve group has been blocked. Due to the semi-controllability of the converter valve, the bridge arm that is open before the lock-out will continue to conduct, and will not be re-commutated. The flow through the valve side windings of the converter transformer will be direct current instead of alternating current. So even if the low-side valve group is open-circuited on the network side of the converter, the fault current can still form a loop through its valve-side winding. When the high-end valve group faults, the situation is slightly different. If a ground fault occurs in the high-side converter area, the fault current flows directly from the fault point back to the ground pole of the Qilian station, causing the fault point to be short-circuited to the common cathode point of the low-voltage six-pulse bridge of the low-side converter. The DC voltage of the inverter side is larger and the fault current is larger. At this time, although the low-end valve group does not supply power to the fault point, it still needs to close the same-pole dual valve group to stop power supply to the fault point. In addition, the ground fault in the rectifier-side converter area is different from the inverter side, as shown in Figure 5. It can be seen from the figure that after a ground fault occurs at the high-voltage wall bushing in the low-side converter area of the rectifier side pole 1, the fault point and the ground electrode on the rectifier side constitute a loop, and the low-side converter forms a large forward

voltage drop to the fault point resulting in a larger fault current. At the same time, the low-end converter is short circuited by the fault point resulting in interruption of the DC line current.

3.2. Valve group fault restart action sequence

The timing sequence of the valve group failure restarts is as follows: ①the valve control host blocks the fault valve group and transmits the differential protection action signal to the pole control host by real time control LAN net after receiving the converter differential protection action signal; ②the pole control host sends a command to block the non-fault valve group and perform pole isolation and discriminates fault valve group and trigger valve group fault restart logic after receiving the converter differential protection action signal; ③After the valve group fault restart logic is triggered, the pole control host sends a valve group isolation instruction to the fault valve group and sends a non-fault valve group number and a restart command to the same-pole dual valve group; ④After the non-fault valve group receives the pole control command, if it is judged that its own number is consistent with the number issued, the restart command takes effect, and after receiving the fault valve group isolation indication (that is, the fault valve group BPI is closed, AI, and CI are in open), the logic of entering a valve group is automatically restarted, and the fault valve group is locked due to the inconsistency between its own number and the number issued by the pole control host.

3.3. System debug record waveform analysis

Fig. 6 and Fig. 7 are the recorded waveforms of group block process and valve group restart process of ShaoShan Railway Station non fault valve group (high-voltage valve group) automatic restart test. According to the time scale in the figure, the interval between the two is about 2 minutes. The variables in the figure are the same as in Figure 2. The test is done through the program configuration number. From Fig. 6 and Fig. 7, it can be seen that the high-end valve group and the low-end valve group performs blocking after the failure. Inverter side pole 2 dual valve group is bypassed and the the voltage drop to zero, resulting in a drastic increase in DC current. But after the rectifier side receives the protection action signal from the station, the blocking pole is closed so that the DC current is interrupted and the fault point is extinguished. After the pole isolation, low-end valve block isolation and pole connection automatic sequence operation, that is, after about 2 minutes, the low-end valve group automatically restarts and the DC current is successfully restored.

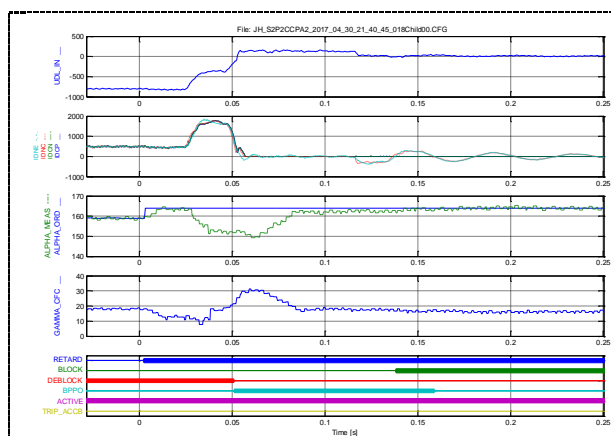


Figure. 6 valve group block process of ShaoShan Railway Station non fault valve group (high-voltage valve group) automatic restart test

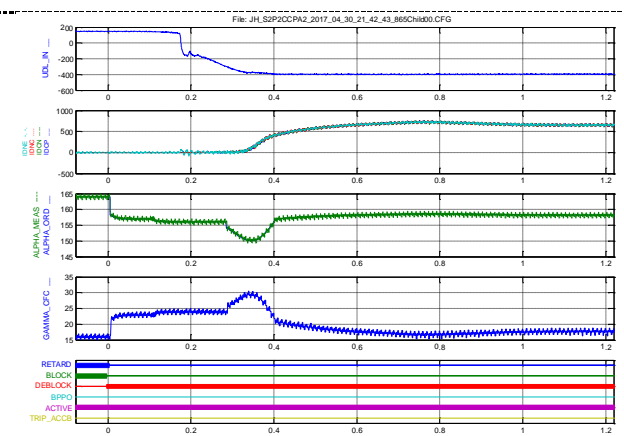


Figure.7 valve group restart process of ShaoShan Railway Station non fault valve group (high-voltage valve group) automatic restart test

4. Conclusion

UHVDC transmission has become a reality due to the existence of strict logic and perfect control system. In this paper, instantaneous fault restart logic and valve group fault restart logic in polar layer control system of Qi-Shao UHVDC project are thoroughly studied, and the trigger mechanism, action sequence and open conditions of the two restart logics is analyzed, the relationship between

instantaneous fault restart logic and other instantaneous fault protection is studied. According to the Qi-Shao UHVDC system debugging field oscillogram, the implementation of two restart logics was analyzed. Instantaneous fault restart can effectively improve the availability of the DC system, and in the meanwhile the valve group fault restart logic is beneficial to optimize the operation level of the DC system. Some other special and complex control logics of Qi-Shao UHVDC project will be studied in our future researches, and it is hoped that our studies can help on-site operation and abnormal analysis.

5. Reference

- [1] GUO Siyuan, LI Hui, XU Hao, et al. Modeling of ± 800 kV Jiuhu UHVDC Transmission System Based on RTDS. *Hunan ELECTRIC POWER*, 2017, 37(3):11-15.
- [2] ZHOU Guowei, GU Yongdi, ZHOU Jianping, et al. Analysis of non-characteristic harmonic in UHVDC system[J]. *Power System Protection and Control*, 2016, 44(3): 122-128.
- [3] Zhiqing Yao, Qun Zhang, Peng Chen, et al. Research on fault diagnosis for MMC-HVDC Systems. *Protection and Control of Modern Power Systems*, 2016, 1(1): 1-7.
- [4] GUO Hongguang, WU Qingfan, HUANG Jinhai, et al. Study on the influence of electromagnetic coupling of UHVDC power transmission lines on the voltage derivative protection [J]. *Power System Protection and Control*, 2015, 43(18):114-119.
- [5] ZHANG Yining, SHU Hongchun, TIAN Xincui, et al. Research on fault location algorithm for HVDC electrode line high impedance fault [J]. *Power System Protection and Control*, 2015, 43(24): 1-7.
- [6] ZOU Xin, JIANG Weiyong, LI Yanan. Reactive Power Configuration Scheme of ± 800 kV Jiuquan-Hunan UHVDC Project [J]. *Electric Power Construction*, 2015, 36(9): 43-49.
- [7] ZHENG Wei, ZHANG Nan, YANG Guangyuan. Comparative and improvement investigation on the DC transmission line traveling wave protections of Siemens and ABB [J]. *Power System Protection and Control*, 2015, 43(24): 149-154.

Study on the Electrochromic Label for High-voltage Equipment with $W\text{O}_3$

Linong Wang¹, Enwen Li¹, Bin Song¹ and Yaqi Fang¹

¹ School of electrical engineering, Wuhan University, Wuhan, China
E-mail: lienwen@whu.edu.cn

Abstract. Whether the equipment is charged or not is a working procedure that must be carried out to ensure the safety of personnel during the power failure maintenance work on the power transmission and transformation equipment. At present, UHV power transmission equipment mainly uses contact, non-contact electroscopes to check whether the equipment is electrified. However, this type of electroscopes needs a wide response range because the stray capacitance to ground is greatly affected by the actual working environment and operating position. At the same time, the contact type high voltage electroscopes generally need to be used with the insulated test pole. As the voltage level rises, the required safety distance increases. The length and deflection of the test pole cannot meet the requirements. The overall quality is larger and the operation is inconvenient. The use of material colour changes to indicate the charged state of the device is a promising technical means. Based on the electrochromic technology, this paper makes use of tungsten trioxide materials to prepare charged state indicator materials for UHV transmission equipment, and characterizes whether the equipment is charged by the colour change of materials. Experiments show the effectiveness of the material.

1. Introduction

Before carrying out related operations on some power outages, it is necessary to conduct the power test first to verify that there is no voltage on the electrical equipment or transmission lines, to prevent the occurrence of accidents such as charged ground wire or contacting with charged equipment. At present, UHV power transmission equipment mainly uses contact, non-contact electroscopes for charged state detection [1]-[2]. Contact electroscopes cannot effectively solve the problem of detecting the live state of DC equipment [3]-[4]. Non-contact electroscopes can detect the electric function by detecting the electric field or partial discharge in the vicinity of the charged equipment, but it has the advantages of accuracy, adaptability, cost performance, etc. insufficient. And, in the UHV substation, converter stations and other electromagnetic environment complex places, the reliability of non-contact electroscopes is poor [5]. It is of great practical significance to develop new technical means to detect the charged state of equipment.

Inorganic electrochromic materials have become an increasingly active research field, and gradually applied to new energy-saving windows, building glass curtain walls, large passenger aircraft and other fields [6]. In this paper, electrochromic materials are applied to the power system to indicate the charged state of the equipment through the change of material colour.

2. Electrochromic mechanisms

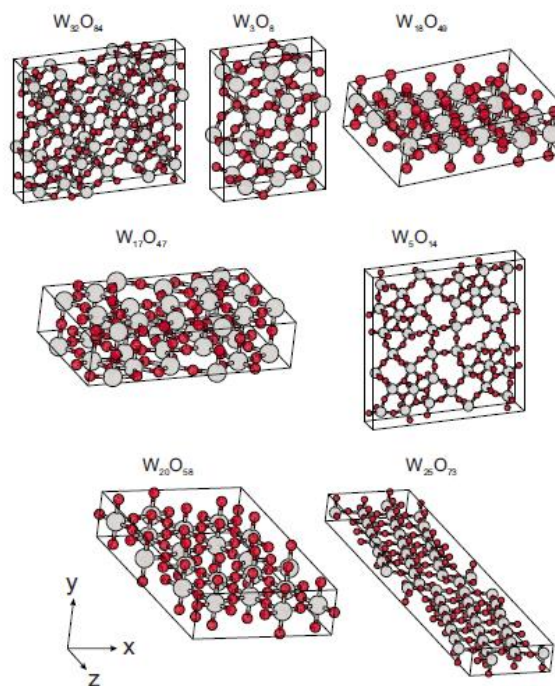
Electrochromism refers to the reversible change of the material between the colored state of low transmissivity or the decolorized state of high transmissivity by the injection or extraction of charges (ions or electrons) by the action of alternating electric fields [7]. Appearance performance is reflected in the reversible changes in colour and transparency. Depending on the internal characteristics of the



different electrochromic materials and their combination, they can produce a great deal of transmittance and reflectivity regulation in the visible and solar spectrum, even in the microwave range.

Since the discovery of the electrochromism of WO_3 thin films by Deb in 1969 [8], extensive research has been carried out on inorganic materials, and great progress has been made. Inorganic electrochromic materials are mostly transition metal oxides or hydroxides, such as WO_3 , MoO_3 , TiO_2 , V_2O_5 , $\text{Ni}(\text{OH})_2$ and the like. WO_3 has the characteristics of high colour contrast; good cycle stability and good thermal stability, making tungsten trioxide become the most studied and commercially available inorganic material in recent years [9].

Ideally, crystalline WO_3 can be considered as a deformed perovskite-type crystal structure. As shown in Fig 1(a), the chemical bond is an ionic bond between W^{6+} and O^{2-} , but also has obvious covalent components. This distorted perovskite structure consists of the $[\text{WO}_6]$ octahedron with octahedral stacking. Tungsten atoms are located in the center of the octahedron and each oxygen atom is shared by two $[\text{WO}_6]$ octahedrons as bridging oxygen. Among WO_3 crystal phases, the hexagonal WO_3 lattice has one-dimensional ion channels in the lattice, which is conducive to ion transport and diffusion. Crystal water in the hydrated WO_3 lattice also enhances ion transport efficiency. Therefore, its electrochromic properties are also relatively good. In addition, there are a variety of metallic non-stoichiometric phase in the tungsten oxide material system, as shown in Fig 1(b), often with excellent optoelectronic properties.



(a) tungsten oxide non-stoichiometric structure diagrams

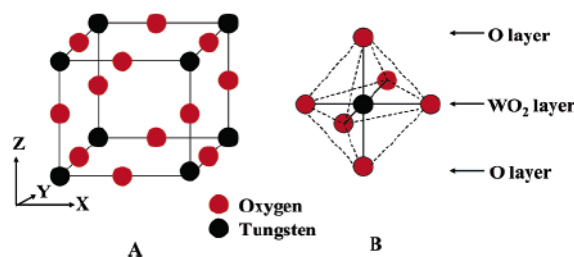


Figure 1 tungsten oxide structure (a) non-stoichiometric structure, (b) ideal tungsten oxide structure

Oxygen vacancies are often present in tungsten oxide and combine with the electrons injected into the cathode to form a colour center when voltage is applied, thereby inducing electrochromism [10]. The specific mechanism can be expressed by the following (1) and (2):



3. Preparation of electrochromic materials

The WO_3 sol and the MoO_3 sol are first prepared, and then the two are mixed and treated with a stabilizer. Table 1 shows the reagents and related drugs used in the experiment. The drugs used are of analytical grade, including tungsten powder and molybdenum powder are 200 mesh sizes.

Table 1. Raw materials and reagents

Name	Structural formula	Level and purity	Manufacturer or supplier
Metallic tungsten powder	W	A.R>99.8%	Tianjin Reagent Co.
Metallic molybdenum powder	Mo	A.R>99%	Shanghai Reagent Co.
Hydrogen peroxide	H_2O_2	A.R>30%	Tianjin Reagent Co.
Anhydrous ethanol	C_2H_5OH	A.R>99%	Hengyang Reagent Co.
Glacial acetic acid	HAc	A.R>99%	Changsha Reagent Co.

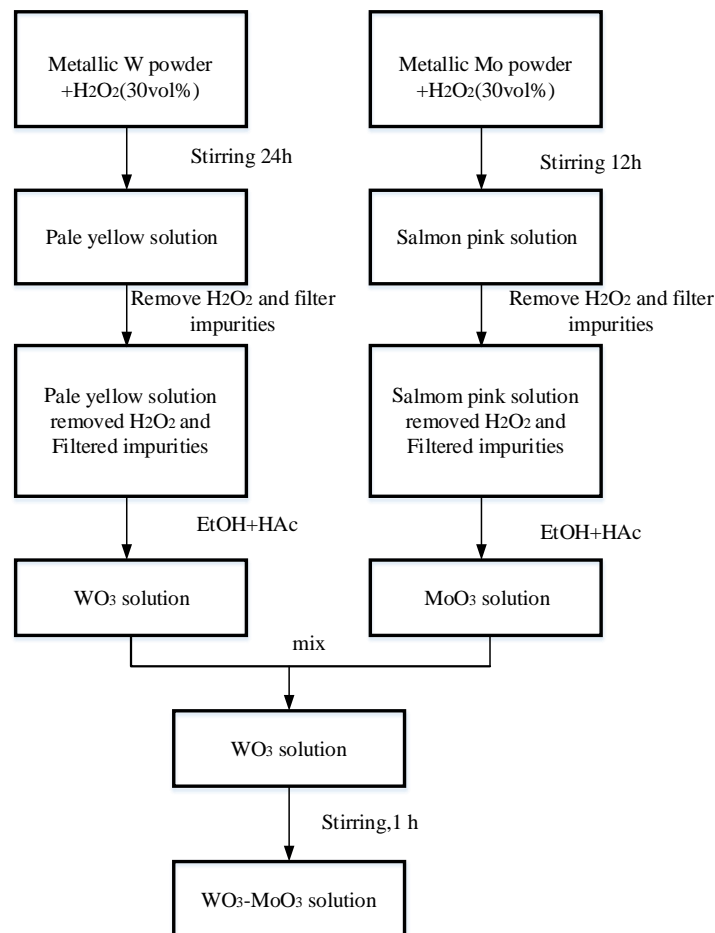


Figure 2. Preparation WO_3 - MoO_3 hybrid sol

The preparation of WO_3 sol process is briefly described as follows:

- A certain amount of W powder was weighed with an analytical balance into a round bottom flask, excess H_2O_2 (30 vol% concentration) was added dropwise and magnetically stirred in an ice-water bath for 24 hours;
- With platinum black mesh catalytic decomposition of excess H_2O_2 , filtered to give a light yellow transparent sol;
- Then, an appropriate amount of $\text{C}_2\text{H}_5\text{OH}$ and HAc were added to the sol as a stabilizer to prepare WO_3 sol.
- The preparation of MoO_3 sol is the same as WO_3 .

The prepared WO_3 sol and MoO_3 sol are mixed according to a certain proportion, and the magnetic stirring WO_3 - MoO_3 mixed sol is obtained after the magnetic stirring for 1 hour. The technological process is shown in Fig 2.

The prepared sol is shown in Fig 3. The low concentration of sol is a pale yellow clear solution, although it's clear but tending phenomenon can be observed, which indicates the presence of colloidal cluster particles. High concentrations of tungsten oxide pigment particle dispersion is completely opaque, showing a dark yellow sticky state, but still remain at room temperature for more than a month without significant precipitation, indicating sufficient stability of the pigment particle dispersion.



Figure 3. The prepared sol.



Figure 4. The WO_3 coating material

Sol gels usually require the addition of stabilizers, also known as dry-control chemicals (DCCA), which are a class of organic liquids with a low vapour pressure. They can stabilize the particle size of the gel network and the size of the network gap, allow uniform distribution of tension in the gel without cracking, and shorten of the drying cycle. Select glycerol as a drying control agent, and control the amount added about 2%. The prepared WO_3 coating material is shown in Fig 4.

4. Performance Testing

Wipe clean the hollow steel pipe, and then apply the WO_3 coating to the steel pipe, and apply a coating thickness of 1mm and 2mm on each steel pipe respectively. The length of each coating is about 10cm. The paint then dries naturally, as shown in Fig 5.

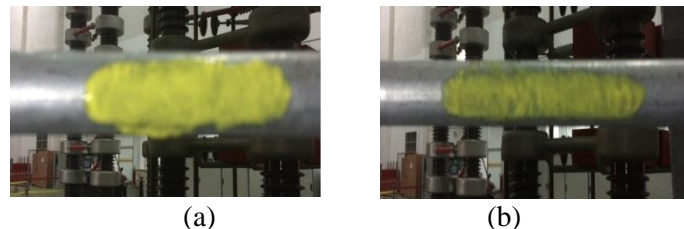


Figure 5. Steel pipes coated with WO_3 . (a) thick coating; (b) thin coating

Connected the hollow pipe to the regulator, and then applied 500mA current to the pipe for 30 minutes. Material remains yellow and no colour change appears. Then, we increased the current to 200A, and the material started to change colour slowly. Thirty minutes later, the colour of the material is as shown in Fig 6.

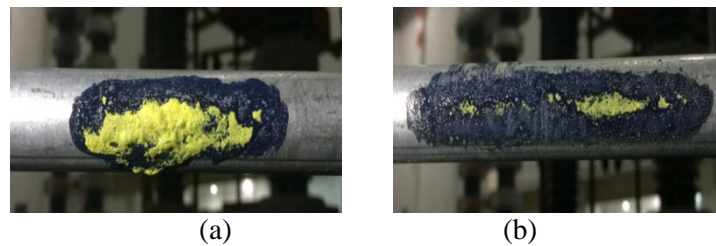


Figure 6. The material colour after applying 200A current. (a) thick coating; (b) thin coating

The experimental results show that when the current of 500mA passed to the steel pipes, no colour change occurred after half an hour of energization, regardless of the thickness of the material. When the hollow steel pipes were connected with a large current of 200A, the materials undergone obvious discoloration phenomenon after half an hour. Most of the paint changed from the original yellow to blue-violet, and the colour change of thinner areas was significantly larger than that of thicker area. After the power is off, the colour of the material gradually resumes within half an hour.

5. Conclusion

This paper attempts to use the colour change of materials to indicate the charging status of high-voltage power transmission equipment. A tungsten oxide-based pigment particle sol was prepared, a stabilizer was added to the dispersion, and a tungsten oxide coating was obtained after sufficiently stirring. Tests show that the paint can be discoloured under the action of high current for a long time, indicating the charged state of the equipment. Although the colour change of the material has a time delay and is not effective for small currents, it is still a meaningful exploration.

6. References

- [1] Zhou, Momo, and C. Li. 2016, Development of non-contact electroscopes. *IEEE International Conference on High Voltage Engineering and Application* IEEE, pp:1-4.
- [2] D. L. Millard, K. R. Umstadter, 1992. Noncontact testing of circuits via a laser-induced plasma electrical pathway. *IEEE Design & Test of Computers*, 9, pp: 55-63.
- [3] T. Koyama, T. Yoshida, I. Ideno. 2012. Development of a Non-contact Direct-voltage Detector. *Jr East Technical Review*, 22, pp: 23-26.
- [4] Weiwei Pan; Yuqun Fang; Tian Wu; Yujiao Zhang. 2017, Alarm threshold settings and field test of non-contact MEMS UHVDC electroscopes. *20th International Conference on Electrical Machines and Systems (ICEMS)*, pp:1-4.
- [5] Huayong Liu; Fan Yang; Tao Chen; Wei He; Jingang Wang. 2008, Application of Electric Field Measurement Method in electroscopes for ultra-high voltage appliances. *World Automation Congress*. pp: 1-4.
- [6] S. S. Kalagi, D. S. Dalavi. 2010, Polymer assisted deposition of electrochromic tungsten oxide thin films. *Journal of Alloys and Compounds*.493, PP: 335-339.
- [7] J. R Platt. 1961, Electrochromism, a Possible Change of Colour Producing in Dyes by an Electric Field. *Journal of Chemical Physics*. 34, pp: 862-863.
- [8] S. K. Deb. 1969, A novel electrophotographic system. *Applied Optics*. 8, pp: 192-195.
- [9] K. H. Krishna, O. M. Hussain. 2008, Growth, microstructure and electrochromic properties of activated reactive evaporated WO₃ thin films on flexible substrates. *Optoelectronics and Advanced Materials-Rapid Communications*. 2, pp: 242-246.
- [10] Ö. Tuna, et al. 2015, Electrochromic properties of tungsten trioxide (WO₃) layers grown on ITO/glass substrates by magnetron sputtering. *Vacuum* 120, pp: 28-31.

Study on Influence Factors of Lightning Impulse Test Waveform of UHV GIS Equipment

Jiadong Meng¹ Tianxiang Chen² Dajin Chen³ Rongquan Wang¹ and Lei Wang⁴

1 Xiamen University of Technology, Xiamen, China

2 Chengdu University of Technology, Chengdu, China

3 ABB (China) Co., Ltd, Xiamen, China

4 Xiamen University of Technology, Xiamen, China

E-mail:mjdxmlg@foxmail.com

Abstract. The lightning impulse withstand voltage test is a test item that must be carried out for type testing, factory test or even field test of electrical equipment such as gas insulated metal-enclosed switchgear (GIS). However, the factors affecting the lightning impulse test waveform are complex and diverse. In this paper, the discharge principle of the impulse voltage generator is studied. Combined with simulation, the influence of different factors on the waveform parameters of lightning impulse test of UHV GIS equipment is obtained. The common methods and improvement measures of waveform debugging are pointed out, and the main factors affecting the parameters of lightning waves are studied.

1. Introduction

The impulse test is a test that simulates the adverse effects of power systems and equipment on lightning strikes (direct lightning, inductive lightning or operating overvoltage) [1]. The purpose is to evaluate the insulation withstand strength of the equipment. Moreover, the GB/T 16927.1-2011 and IEC 60060-1 standards have strict requirements on the lightning impulse voltage waveform, that is, the wavefront time is $1.2\mu\text{s}\pm 30\%$, the half-peak time is $50\mu\text{s}\pm 20\%$ of the full-wave lightning, and the oscillation Overshoot must not exceed 10% [2]. Whether the waveform parameters meet the standard requirements determines the degree of qualification of the lightning impulse test of power equipment, so it is very important to study the influencing factors of the lightning impulse test waveform parameters [3].

At present, China's UHV engineering 1100kV switchgear is all using GIS. GIS is one of the important components in UHV power grids [4]. Compared with traditional air-insulated switchgear, GIS concentrates many devices such as bus bars, disconnectors, circuit breakers, arresters and transformers in a closed grounded metal casing [5]. The utility model has the advantages of small occupied area, small influence by the natural environment, safe and reliable operation, and so on. GIS has been widely used in domestic and international power systems. The insulation performance of UHV GIS equipment plays an important role in the reliable and stable operation of the power grid [6], [7]. The research content of this paper can provide an appropriate theoretical basis and important data support for the analysis of the influencing factors of the lightning impulse test waveform parameters and its overshoot coefficient suppression technology.

2. Lightning impulse test circuit

The lightning impulse voltage was generated by a impulse voltage generator and the test circuit was designed by Marx in 1923 [8]. In order to calculate the waveform or the various elements of the



impulse circuit, the Marx generator is simplified to the equivalent circuit showed in figure 1. C_1 is the charging capacitor; R_d is the wavefront resistance; R_e wave tail resistance; L is the test circuit inductance; S is the discharge gap; C_2 is the load capacitance. Among them, when C_1 is charged to U_0 , S is triggered, C_2 is charged through C_1 , and attenuated by R_f .

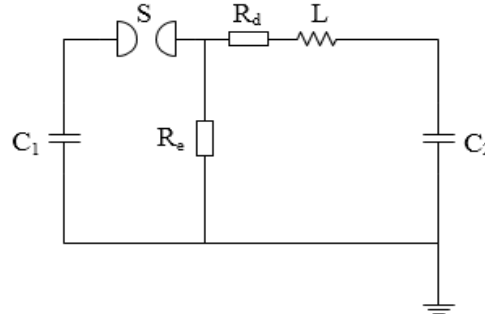


Figure1. Impulse voltage generator discharge equivalent circuit.

Since the maximum oscillation overshoot occurs near the peak of the lightning impulse, the wave tail resistance is large and has little effect on the waveform oscillation. The discharge equivalent circuit in the wavefront stage is shown in figure 2.

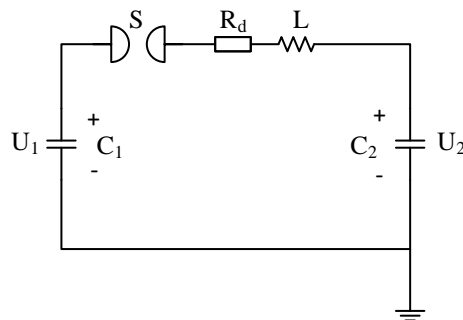


Figure2. Wavefront discharge equivalent circuit.

A inequation should be given as (1) if we want to obtain a non-oscillating wave

$$R_d \geq \left[\frac{4L(C_1 + C_2)}{C_1 C_2} \right]^{\frac{1}{2}} \tag{1}$$

Take the critical value

$$R_d = \left[\frac{4L}{C} \right]^{\frac{1}{2}} \tag{2}$$

In the equation (2), $C = \frac{C_1 C_2}{C_1 + C_2}$. The operational impedance under the Laplace transform for the entire circuit in figure 1 is

$$Z(s) = R_d + sL + \frac{1}{sC} \tag{3}$$

Finished up

$$U_2(s) = \frac{U_1}{sC_2L \left(s^2 + \frac{sR_d}{L} + \frac{1}{LC} \right)} \tag{4}$$

Performing Laplace inverse transformation under critical damping, we get

$$u_2(t) = \frac{C_1U_1 \left[1 - \left(1 + \frac{R_d t}{2L} \right) e^{-\frac{R_d t}{2L}} \right]}{C_1 + C_2} \tag{5}$$

According to standard wave definition, the wavefront time can be calculated

$$T_f = 2.33R_d C \tag{6}$$

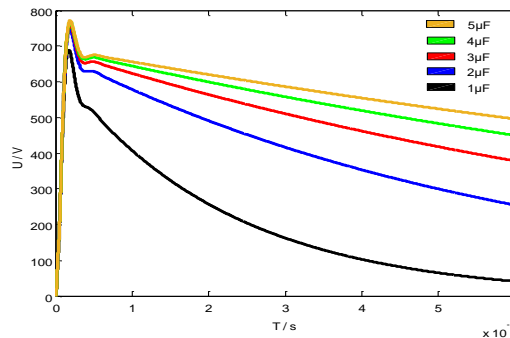
Put the critical damping condition $R_d = \left(\frac{4L}{C} \right)^{\frac{1}{2}}$ into equation (6)

$$T_f = 4.66(LC)^{\frac{1}{2}} \tag{7}$$

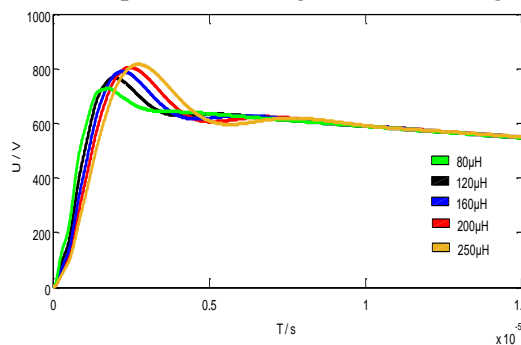
It can be seen from equations (7) and (8) that the wavefront time T_f is positively correlated with R and C . When T_f is constant, the load capacitance C_2 is also limited by the circuit inductance L .

3. Analysis on influencing factors of waveform parameters

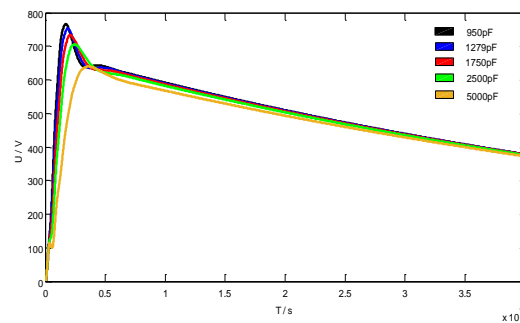
The waveform parameters of the lightning impulse test are mainly influenced by the following factors: the main capacitance of the impulse generator, the inductance of the impulse test circuit, and the capacitance of the sample. The effect of various factors on the waveform of the lightning impulse test is shown in figure 3.



(a) Main capacitance change waveform diagram



(b) Circuit inductance variation waveform diagram



(c) Sample capacitance change waveform diagram

Figure3. Relationship between lightning waveform and main capacitor, impact test circuit inductance, and sample capacitance

From figure 3(a), (b) and (c), we can see that keeping the other conditions constant, the smaller the main capacitor value of the generator is, the steeper the tail portion is, and the overshoot is larger. On the contrary, the tail portion is smoother and the overshoot is smaller. The circuit inductance is positively correlated with the wavefront time and the overshoot. The capacitance of the sample is positively correlated with the wavefront time and is negatively correlated with the overshoot. However, when the sample has a large capacitance, the waveform will oscillate at the beginning.

4. Waveform debugging method

In order to effectively solve the problem that oscillation overshoot near the peak of the lightning impulse voltage, many work has been done at home and abroad. There are two main measures: one is to reduce the circuit inductance, the other is to improve the circuit method, that is, a low-pass filter circuit with parallel resistance and capacitance is connected in series at the output end of the impulse voltage generator, and the oscillation overshoot of the lightning waveform is improved by the filter circuit.

4.1 Reduce circuit inductance

In the test, the following methods are used to reduce the inductance of the circuit: (1) The arrangement of the wavefront resistors should be paralleled by multiple resistors; (2) Reduce the number of generators while satisfying the test voltage; (3) Use a low-inductance connecting wire as the high-voltage connecting wire.

4.2 Series low-pass filter

The reason why the lightning wave output be overshoot is that the lightning wave contains high frequency harmonic components. Based on the above discussion, this paper proposes an overshoot suppression circuit that is consist of a compensation circuit, a passive low-pass filter composed of a capacitor C and a resistor R in parallel, as shown in figure 4 .

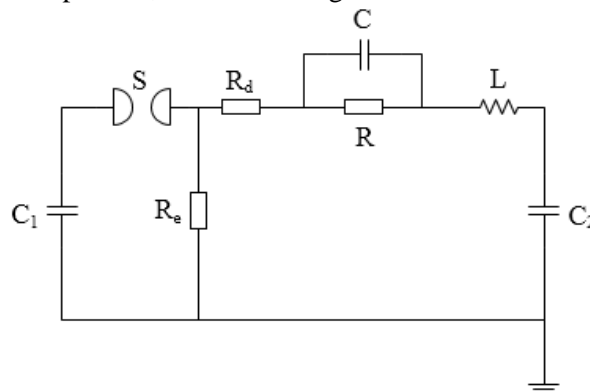


Figure 4. Circuit diagram of series low-pass filter device

By changing the values of the capacitance C and the resistance R of the damping device, the simulation can be concluded that the influence of the change of the capacitance C and the resistance R on the waveform is shown in figure 5 and figure 6.

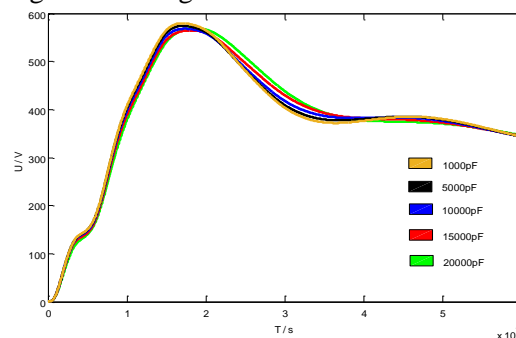


Figure 5. Filter device capacitance change waveform

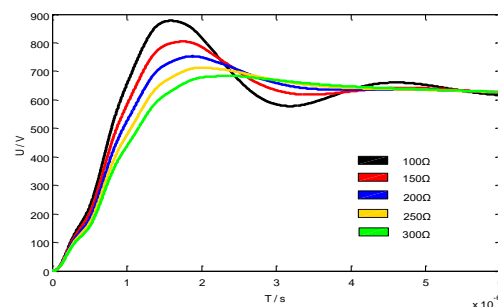


Figure 6. Filter device resistance change waveform

From the simulation results, it can be concluded that there is a contradiction between C and R . For products with large capacitance such as UHV switchgear, the larger the C is selected, the shorter the wavefront time can be effectively shortened, but the oscillation will be aggravated, and the capacitance will increase to a certain extent, which has no obvious effect on the wavefront time. At this time, once the wave head oscillation is intensified, it needs to be damped by R . As R increases, the oscillation can be attenuated, but the second peak after the oscillation is pulled high. If we simply increase R to reduce the overshoot oscillation, the second peak will exceed the first peak, and the calculated wavefront time will increase greatly, far exceeding the standard requirements. Therefore, in order to meet the requirements of the standard for waveforms, the selection of overshoot damping device parameters is particularly important. Due to the different capacitance of the UHV switch gear, the parameters of the device need to be adjustable within a certain range [9], [10].

5. Conclusion

- Increasing the main capacitor value of the surge voltage generator can significantly reduce the wavefront time.
- As much as possible to reduce the lightning impulse test circuit inductance to improve the test waveform is more effective.
- Adding a filtering device to the lightning impulse test circuit can significantly improve the waveform parameters, and there is an optimum value between the resistance value and the capacitance worth ratio in the resistance-capacitance device.

6. Reference

- [1] Filipović-Grčić B, Filipović-Grčić D and Gabrić P 2015 Estimation of load capacitance and stray inductance in lightning impulse voltage test circuits *Electric Power Systems Research* **119** 439-46
- [2] Okabe S, Ueta G and Tsuboi T *et al* 2012 Study on switching impulse test waveform for UHV-class electric power equipment *IEEE Transactions on Dielectrics & Electrical Insulation*

19 803-11

- [3] Ueta G, Tsuboi T and Okabe S 2012 Evaluation of overshoot rate of lightning impulse withstand voltage test waveform based on new base curve fitting methods - application to practical diverse waveforms *IEEE Transactions on Dielectrics & Electrical Insulation* **18** 1336-45
- [4] Cui D, Wang J S and Zhang X Y 2013 Discussion on test waveform Parameter and overshoot limit of lightning impulse voltage to UHV equipment *High voltage apparatus* **49** 77-81
- [5] Hu W, Cheng Y and Wan Q F *et al* 2011 Test on Lightning Impulse Withstand Voltage of the Three Gorges Right Bank 550 kV GIS Substation *High Voltage Engineering* **37** 883-7
- [6] Li G F, Liao W M and Li Q F *et al* 2008 Voltage output performance of 7200 kV/480 kJ impulse voltage generator *Proceedings of the CSEE* **28** 1-7
- [7] Shen M, Zhong L and Lu J T *et al* 2012 Test and simulation study on standard lightning impulse voltage overshoot inhibit loop. In: 2012 Symposium of Transmission and Transformation Annual Meeting 259-66
- [8] Wen T, Zhang Q G and Zhao J P *et al* 2016 On-site test technology of standard lightning impulse for power equipment with large capacitance *High Voltage Engineering* **42** 2968-73
- [9] Zhang R Y, Chen C Y and Wang C C 2009 *High voltage test techniques*: Beijing, China, Tsinghua University press
- [10] Zhong L, Shen M and Li H L *et al* 2014 Test circuit development for limit the lightning impulse overshoot for UHV switchgear *High voltage apparatus* **50** 20-4

Acknowledgments

This work was supported by the National Natural Science Foundation of China (51008262), the Science and Technology Plan Project of Xiamen City (3502Z20183041), and the scholarship for overseas study of Fujian Province, China.

Electric Field Analysis on Buffer Layer of HV XLPE Power Cable by Finite Element Method

Weiwei Zhang¹, Youxiang Yan², Weiling Lin¹, Shanshan Li¹ and Lei Wang³

¹ School of Electrical Engineering and Automation, Xiamen University of Technology, No.600, Ligong Road, Jimei District, Xiamen, P.R.China

² State Grid Xiamen Electric Power Supply Company, No.21, Hubinnan Road, Siming District, Xiamen, P.R.China

³ School of Environmental Science and Engineering, Xiamen University of Technology, No.600, Ligong Road, Jimei District, Xiamen, P.R.China

Abstract. In recent years, white defects in power cable buffer layer has been discovered many times around the world. It would be a hazard to electricity transmission if these defects are not detected and solved in time, finally resulting in a power outage. In this paper, the selection of a physics field and the building of a three-dimensional model on cable electric field simulation are mentioned and improved. The distribution of electric field was calculated with two factors: the gap between water-blocking tape and aluminum sheath, the conductivity of water-blocking tape. The results demonstrated that the existence of the gap increases the electric field intensity in the air layer. Increasing the conductivity of water-blocking tape is beneficial to reduce the electric field intensity. It was explained that white defects is closely related to the air discharge in buffer layer.

1. Introduction

The power cable gradually replaces the overhead line and becomes a main power transmission channel in the city. In Xiamen, the cable rate has reached 23% as the length of high-voltage (HV) cable has exceeded 400 kilometers. With a large number of cables being put into operation, some similar faults of 110 kV Cross Linded Polyethylene (XLPE) cables have been found these years, that is, many white defects appeared on insulating shielding, water-blocking tape and the inner wall of the aluminum sheath. The problem has been declared in Beijing, Shanghai, Zhejiang etc. and some foreign countries like Singapore, Australia. Continued deterioration of these defects may lead to complete penetration of insulating shield and main insulation, which would cause a serious power outage. Therefore, it is never a question that could be ignored.

Yang Juan et al. found that the longitudinal water-blocking structure would cause a typical partial discharge and it is very important to control the gap between the metal sheath and core [1]. Liu Xiaodong et al. found through experiments that alternating current resistance of the buffer layer in faulty cable are much larger than those in normal cable. It is assumed that there is a large potential difference between insulating shielding and metal sheath [2]. Li Chenying thought moisture is at the root of defects [3]. Sun Jin found the volume resistivity of water-blocking tape conforms to standard while the surface resistance is higher than what standard suggests [4]. She supposed the cable has been infiltrated by water and dried up later. Charles Q. Su [5], a researcher at Monash University in Australia, believed buffer layer is failed to withstand the charging current, and then the current caused local overheating and finally jeopardized insulating shield.



Cable manufacturers, cable operators, and scientific researchers have not determined the cause of this phenomenon. According to several fault cases of Xiamen's power cable, this paper analyzed the influence of different factors on the electric field distribution in buffer layer by using COMSOL, a finite element simulation software. The simulation results in this paper can provide a suitable theoretical basis and important data support for next study of the cause of buffer layer discharge and its design in high-voltage cable.

2. Model and method

2.1 Model building

110 kV XLPE cable generally consists of a copper conductor, a conductor shield, a main insulation (XLPE), an insulating shield, a buffer layer (water-blocking tape and air), a corrugated aluminum sheath and an outer sheath. The structure of 110 kV XLPE cable is shown in figure 1. The parameters of 110 kV XLPE cable from a reliable manufacturer are given in table 1.

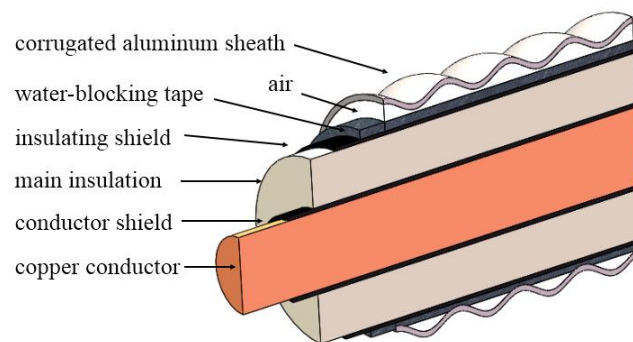


Figure 1. The structure of 110 kV XLPE cable.

Table 1. The parameters of 110 kV XLPE cable from a reliable manufacturer.

NO.	Structures	Outside radius / mm	Thickness / mm
1	Copper conductor	13	-
2	Conductor shield	14.7	1.4
3	Main insulation (XLPE)	31.7	16.5
4	Insulating shield	32.9	1
5	Water-blocking tape	35.1	2
6	Air	35.6	0.5
7	Corrugated aluminum sheath	42.6	2

The structure of aluminum sheath and buffer layer is relatively special:

- For a better bending property, aluminum sheath is usually made into a spiral structure. It is called a corrugated aluminum sheath for it is wavy with peaks and troughs in each waveform cycle when viewing from a longitudinal section. The gap between corrugated aluminum sheath and water-blocking tape is not a constant value.
- Buffer layer is located between insulating shield and corrugated aluminum sheath. It comprises of a water-blocking tape and air in order to meet a buffer requirement. When cable is running, its internal structures displaced downward due to gravity. It can be assumed that the underside of water-blocking tape is subjected to extrusion deformation because of its large flexibility, while other structures of cable are hardly deformed.
- Water-blocking tape would swell or shrink influenced by humidity and temperature. As a result, it also makes a variety of the gap between itself and corrugated aluminum sheath, as shown in figure 2.

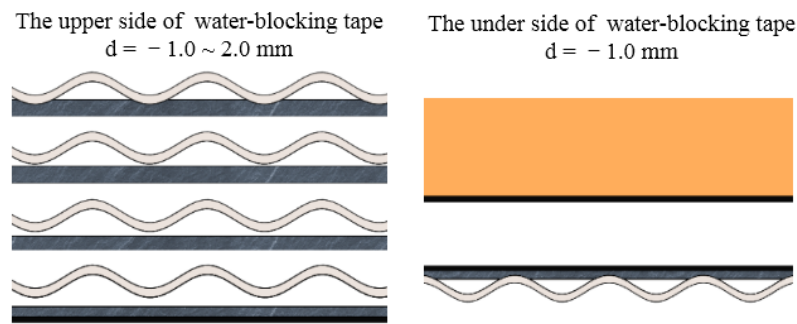


Figure 2. The variety of the gap between water-blocking tape and corrugated aluminum sheath.

With above factors, simply considering a radial section or a longitudinal section of the cable cannot accurately reflect the structure of corrugated aluminum sheath and buffer layer. In this paper, the cable was modeled in three dimensions. Since outer sheath has a zero potential after aluminum sheath being grounded, it can be ignored and need not to be constructed on this model.

2.2 Finite element method

For high-voltage power cables, its conductor shield, insulation shield and water-blocking tape are made of semi-conductive materials. Distribution of electric field influenced by current cannot be overlooked for the resistivity of semi-conductive materials is relatively small (i.e., conductivity is relatively large). Electric quasi-static (EQS) is selected because Both relative permittivity and conductivity would be taken into account when calculating. The differential form of EQS is [6]-[8]:

$$\begin{cases} \nabla \times H = J + \frac{\partial D}{\partial t} \\ \nabla \times B = 0 \\ \nabla \times E = 0 \\ \nabla \times D = \rho \end{cases} \quad (1)$$

The governing equation is :

$$(\gamma + j\omega\varepsilon)\nabla \cdot E = 0 \quad (2)$$

In this simulation, the outer side of copper conductor was applied to a phase voltage (64 kV), the outer surface of aluminum sheath was grounded and frequency was set to 50 Hz. The cable model was divided by free tetrahedral meshes and the meshes in small parts were refined specially. According to GB/T 11017.2-2014, material parameters of 110 kV XLPE cable are shown in table 2. The meshes of the cable model is shown in the figure 3.

Table 2. Material parameters of 110 kV XLPE cable.

NO.	Structures	Relative permittivity / ε_r	Conductivity / $S \cdot m^{-1}$
1	Copper conductor	1e7	5.998e7
2	Conductor shield	100	$\geq 1e-3$
3	Main insulation (XLPE)	2.3	1e-15
4	Insulating shield	100	$\geq 2e-3$
5	Water-blocking tape	500	$\geq 2e-3$
6	Air	1	1e-16
7	Corrugated aluminum sheath	1e7	2.746e7

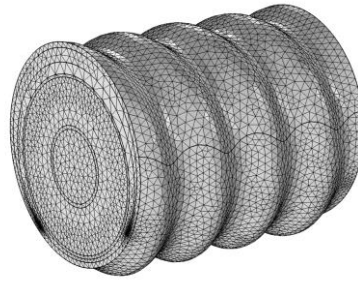


Figure 3. The meshes of the cable model.

3. Results and discussion

3.1 Gap variation

When cable is running, the upper side of water-blocking tape may be separated from aluminum sheath and then a continuous air layer is formed between aluminum sheath and water-blocking tape. As showed in figure 4, when the conductivity of water-blocking tape is 0.002 S m^{-1} , the maximum electric field intensity E_{max} in the air layer is substantially positively correlated with the gap between aluminum sheath and water-blocking tape.

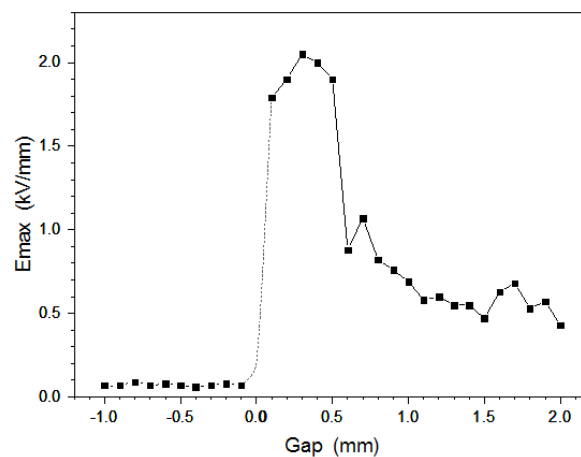


Figure 4. The relationship between E_{max} and gap.

When there is only a tiny gap, electric field intensity in the air is really large. As the gap is gradually increased, electric field intensity is reduced. It should be noted that electric field intensity in the upper air layer is very small and can be ignored. E_{max} is situated on the tangent surface between water-blocking tape and aluminum sheath (i.e., the junction of extrusion part and non-extrusion part). It proves that why discharge points on the inner wall of aluminum sheath contain sodium which from water-blocking tape. Electric field distribution when gap is 0.1mm is shown in figure 5.

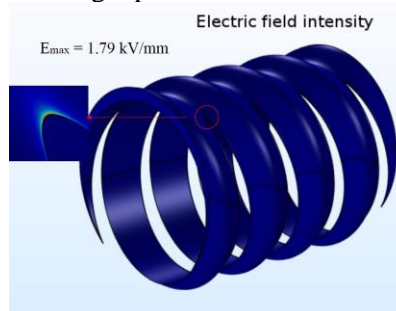


Figure 5. Electric field distribution when gap is 0.1mm.

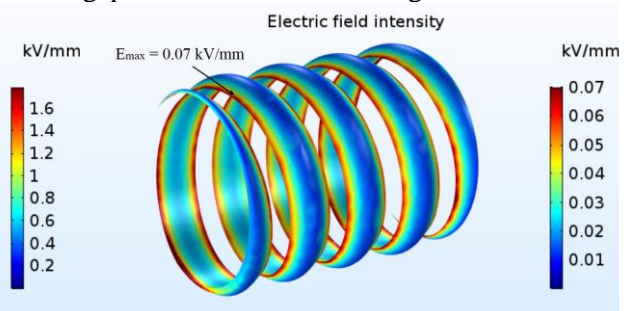


Figure 6. Electric field distribution when gap is -1mm.

When the upper side of water-blocking tape is in good contact with aluminum sheath (i.e., the gap is negative), the E_{\max} (0.07 kV mm^{-1}) is much smaller than E_{\max} when there is a gap present. In this situation, those points which easily discharge in the above case are no longer present and E_{\max} is located in both sides of water-blocking tape extrusion. Electric field distribution when gap is -1mm is shown in figure 6.

3.2 Conductivity variation

Water-blocking tapes from different manufacturers have different conductivities. For a certain water-blocking tape, its conductivity can vary between several orders of magnitude as it becomes wet or dry. If there is a gap, E_{\max} would increase sharply when conductivity drops below the order of 10^{-3} S m^{-1} . E_{\max} is less than 3 kV mm^{-1} as conductivity returns to the minimum recommended by the standard. When conductivity continues being improved, E_{\max} is infinitely close to zero. However, when there is not any gap, E_{\max} is almost zero regardless of how large conductivity is. The relationship between E_{\max} and conductivity is shown in figure 7.

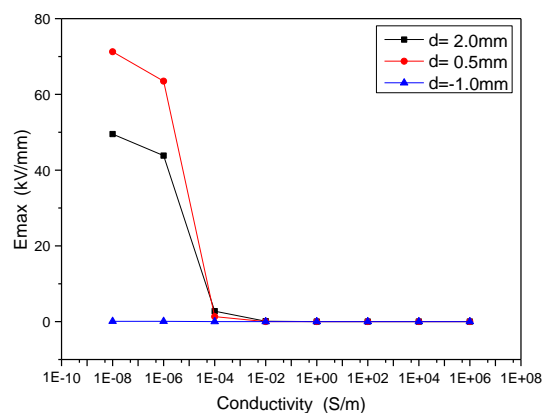


Figure 7. The relationship between E_{\max} and conductivity.

There are several points which the value is a lot more than 3 kV mm^{-1} when there is a low conductivity. When constructing this three-dimensional model, water-blocking tape was subtracted by the convex portion of the aluminum sheath to form a shape of extruded concave. The air sandwiched between aluminum sheath and water-blocking tape is extremely thin so that some large electric field intensity points can be caused by a very low potential difference. Although the points with a large electric field intensity cannot be avoided, they do not affect the conclusion that discharge would definitely occur here once the conductivity.

In fact, when objects come into contact, they are bridged by a certain film rather than in contact with a geometric face. For cable, when conductivity is low as water-blocking tape is getting wet, the tangent plane always adheres to water film so that extremely thin air there cannot be existed. The points with a large electric field are eliminated. Furthermore, the presence of water film makes water-blocking tape indirectly connected to aluminum sheath, it could be considered that current is flowing. Therefore, these points do not affect the judgment of final conclusion.

4. Conclusions

The cable should be built as a 3D model when studying the buffer layer discharge problem.

Electric quasi-static should be selected for several layers are made of semi-conductivity materials.

Ensure water-blocking tape is in full contact with aluminum sheath. In this case, even if the conductivity of water-blocking tape is extremely low, any discharge point is not existed in air layert.

Improving the conductivity of water-blocking tape can reduce electric field intensity. When the conductivity is large, the air layer does not discharge even if there is a large gap between water-blocking tape and aluminum sheath.

Large electric field intensity in tangent plane is unavoidable but would not abrupt the judgment of final discharge conclusion.

5. Reference

- [1] Yang J 2010 Study and Analysis of the Water-Blocking Construction in HV Power Cables *Electric Wire & Cable*
- [2] Liu X D, Liu P Z and Wang X G *et al* 2017 Study of Measurement of AC & DC Resistance of High Voltage Cable Related to Insulation Screen Burn **4** pp15-8
- [3] Li C Y, Li H Z, and Chen *et al* J 2018 Analysis of Buffer Discharge Problem of High Voltage XLPE Power Cable *Power Engineering Technology*
- [4] Sun J, Li D C, and Hu X L *et al* 2016 Analysis and Mechanism Study on Internal Discharge Failure of 110 kV Cable *Contemporary Chemical Industry* **45** 2014-6
- [5] Su C Q 2011 Failure analysis of three 230 kV XLPE cables. In: *Transmission and Distribution Conference and Exposition: Latin America*, pp 22-5
- [6] Liu Y, Su Y and Li W P *et al* 2016 Study on Electric Field Simulation Method of 10 kV XLPE Cable Joint *High Voltage Electrical Appliance* 30-5
- [7] Xu Z N, Lv F C and Li H M *et al* 2011 Effect of Drying Belt on Electric Field Distribution of Stained Post Insulator *High Voltage Technology* **37** 276-83
- [8] Zhang L, Zhang W, and Li R P *et al* 2014 Defect Simulation and Electric Field Analysis of 10 kV XLPE Cable Terminal *Insulating Materials* 83-8

Acknowledgements

This work was supported by the National Natural Science Foundation of China (51008262), the Science and Technology Plan Project of Xiamen City (3502Z20183041), the scholarship for overseas study of Fujian Province, China, and Science and Technology Research Foundation of State Grid Corporation of China.

Chapter 5:

Smart Grid Analysis and Optimization

Preferably Receiving End's Infeed Modes for UHVDC Power Transmission

Zhen Bi¹, Qiang Guo¹, Qinyong Zhou¹, Yilang Jiang¹, Xiaohui Qin¹

¹Power System Department, China Electric Power Research Institute, Haidian District, Beijing, China 100192

²State Grid Corporation of East Branch, Shanghai, China 200120

Abstract. With unceasing increase of traditional HVDC transmission capacity, it became more and more obvious that the voltage supporting ability of receiving end power system restricts the development of HVDC power transmission, which also blocks the application of HVDC. This paper according to nodal impedance matrix, short-circuit ratios of the receiving end system under hierarchical connection mode and multi-terminal feed mode are derived. Besides, the voltage support capabilities of different modes are analyzed. The simulation was carried out and verified the feasibility and rationality of multi-terminal feed mode, which proved the UHVDC multi-terminal feed mode is helpful to increase the voltage support capability and enable the reasonable power flow distribution between 1000kV layer and 500kV layer.

1. Introduction

China has a vast territory, with an inverse distribution of primary energy and load [1]. In order to ensure sufficient electricity supply in the central and eastern regions where China's economy is developing rapidly, measures must be taken to achieve ultra-long-distance, ultra-large-capacity power transmission. UHVDC transmission has the advantages of long distance, large capacity, low energy consumption, and high stability. It is an effective way to implement the "West-East Electricity Transmission" strategy [2]-[3]. However, the traditional two-terminal direct current can realize the point-to-point DC power transmission. When the UHVDC power transmission project provides a large amount of power for the AC power grid, it will inevitably interact with the AC power grid, which will have a certain impact on the AC system.

In recent years, UHVDC transmission has made breakthrough progress in China. In the next 10 to 20 years of planning, there will be dozens of UHVDC transmission projects completed and put into operation to supply power to the East Central Load Center. Traditional HVDC transmission technology which based on LCC requires the receiving end AC grid to provide sufficient commutation voltage, and absorbs a large amount of reactive power in the course of power recovery after commutation failure occurs [4]-[6]. The multi-infeed DC will supply the receiver AC grid and bring serious problems involving security and stability. The main problem of the multi-infeed DC system is whether the receiving end network can provide strong voltage support, the voltage supporting effect of the AC grid on the DC system depends on the relative size between the AC system and the DC transmission capacity. That is short-circuit ratio index [7]-[8]. Based on the discussion of multi-infeed system strength standards, the literature [9] innovatively proposed UHVDC access to the AC grid using a hierarchical access method and studied multi-feedback in a hierarchical access mode about the short circuit ratio study. According to the national grid plan, the newly-built ± 800 kV Ximeng-Taizhou and ± 1100 kV Inverter Stations of UHVDC power transmission lines in Inner Mongolia Hulunbeier-Anhui-Fujian two loops are proposed to use hierarchical access to 1000kV and 500kV AC grids.



Reference [10] proposed two methods of multi-terminal single-layer feeding and multi-level hierarchical feeding of receiving end of HVDC transmission. By comparing the short-circuit ratio and power transmission curve of the receiving end system under different feeding modes, the advantages of multi-end feeding were verified [11]. The single feed end and multiple distributed receiver HVDC multi-terminal feed connection methods can improve the line utilization rate and improve the problems of commutation failure in the traditional two-end HVDC transmission systems [12]. This article starts with the analysis of multi-terminal feed-in DC, discusses the advantages and disadvantages of the receiver's layered access and multi-feeds, and uses the $\pm 800\text{kV}$ Ximeng-Taizhou UHVDC power transmission project as a background to build a simulation model to verify the feasibility of multi-terminal feeding.

2. Mathematical model and analysis of HVDC hierarchical access scheme

2.1 UHVDC single-layer access and hierarchical access methods

The AC side of the UHVDC power transmission inverter station has only one voltage level for single-layer access, and two voltage levels for layered access. Take the 800kV Ximeng-Taizhou UHVDC transmission project as an example. The two access methods are shown in Figure 1 and Figure 2, respectively.

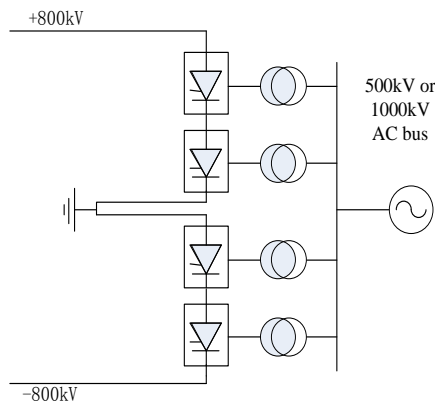


Figure 1. UHVDC single-layer connection mode to AC system

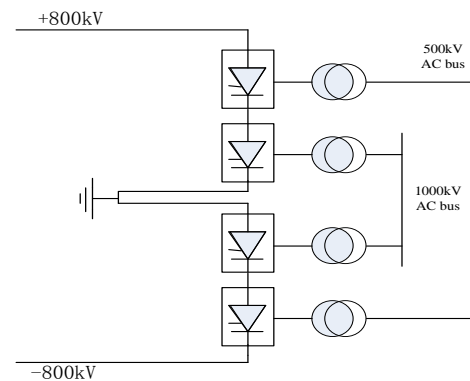


Figure 2. UHVDC hierarchical mode to AC system

2.2 Multi-infeed short circuit ratio analysis of UHVDC

The equivalent diagram of a multi-infeed DC system is shown in Fig.3. There is a link impedance z_{ij} between the DC system i and j , so when a disturbance causes a voltage change ΔU_i on the commutation bus i , the voltage change ΔU_j at the commutation bus j will also be caused. Multi-infeed short-circuit ratios are often used to calculate and analyze the AC system's voltage support capability for multi-infeed DC system.

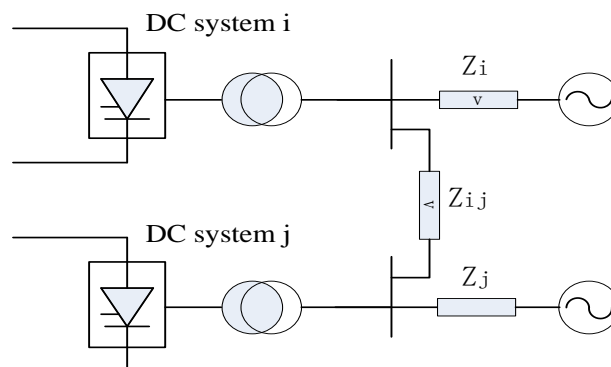


Figure 3. Multi-infeed HVDC equivalent system

The multi-infeed short-circuit ratio calculation formula proposed by CIGRE Multi-infeed DC Working Group in 2007 is as follows:

$$MISCR_i = \frac{S_{aci}}{P_{di} + \sum_{j=1, j \neq i}^n P_{dj} \frac{\Delta U_j}{\Delta U_i}} \quad (1)$$

$$MISCR_i = \frac{U_{iN}^2}{|Z_{eqii}| P_{di} + \sum_{j=1, j \neq i}^n P_{dj} |Z_{eqij}|} \quad (2)$$

If $U_{iN}=1$, then there is

$$MISCR_i = \frac{1}{|Z_{eqii}| P_{di} + \sum_{j=1, j \neq i}^n |Z_{eqij}| P_{dj}} \quad (3)$$

In the formula: each physical quantity is the standard value; $MISCR_i$ is the multi-infeed short-circuit ratio corresponding to the i -th DC system; S_{aci} is the short-circuit capacity of the AC side of the i -th commutation bus; U_{iN} is the i -th commutation bus. The rated voltage on Z_{eqii} is the self-impedance corresponding to the i -th commutation bus in the equivalent impedance matrix; Z_{eqij} is the mutual impedance between the i -th commutation bus and the j -th commutation bus; P_{di} is the rated power of i -th DC system; P_{dj} is the rated power of the j -th DC system.

2.3 Analysis of multi-infeed short circuit ratio under layered access of UHVDC

The ± 800 kV Ximeng-Taizhou UHVDC transmission project adopts a layered access method on the inverter side, which is equivalent to dividing a single-circuit DC transmission line into two DC lines with half capacity and connecting 500kV and 1000kV converter busbars respectively. Then formula (3) becomes:

$$MISCR_i = \frac{1}{\frac{1}{2} |Z_{eqii}| P_d + \sum_{j=1, j \neq i}^n \frac{1}{2} |Z_{eqij}| P_d} \quad (4)$$

Analysis method of HVDC multi-infeed can be referred to multi-infeed short-circuit ratio calculation of UHVDC with layered access. Points to note:

(1) Multiple feed-in short-circuit ratios are calculated for each busbar that is accessed hierarchically. The n hierarchically connected converter stations need to calculate the multi-infeed short-circuit ratio of $2n$ commutation buses.

(2) Retain the busbars of the converter stations that are layered into the AC grid, calculate the system-wide node admittance matrix, and form the Thevenin's equivalent network.

From the equivalent network in Figure 3, the node admittance matrix is

$$Y = \begin{pmatrix} \frac{1}{Z_i} + \frac{1}{Z_{ij}} & -\frac{1}{Z_{ij}} \\ -\frac{1}{Z_{ij}} & \frac{1}{Z_j} + \frac{1}{Z_{ij}} \end{pmatrix} \quad (5)$$

Then find the inverse node impedance matrix as

$$Z = \begin{pmatrix} \frac{z_i z_{ij} + z_i z_j}{z_i + z_{ij} + z_j} & \frac{z_i z_j}{z_i + z_{ij} + z_j} \\ \frac{z_i z_j}{z_i + z_{ij} + z_j} & \frac{z_j z_{ij} + z_i z_j}{z_i + z_{ij} + z_j} \end{pmatrix} \quad (6)$$

$$\begin{cases} Z_{eqii} = \frac{z_i z_{ij} + z_i z_j}{z_i + z_{ij} + z_j} \\ Z_{eqij} = Z_{eqji} = \frac{z_i z_j}{z_i + z_{ij} + z_j} \\ Z_{eqjj} = \frac{z_j z_{ij} + z_i z_j}{z_i + z_{ij} + z_j} \end{cases} \quad (7)$$

Where z_i and z_j are the 1000 kV and 500 kV plane equivalent impedances; z_{eqii} and z_{eqjj} are the self-impedances of the 1000 kV and 500 kV commutation buses respectively; z_{eqij} is the mutual impedance between the two commutation buses.

From formula (7), we know $Z_{eqii} > Z_{eqij}$. Therefore, the short-circuit ratios of the 1000kV and 500kV busbars in the layered access mode are all higher than those of the 1000kV and 500kV busbars in the single-layer access mode. After calculation, the short-circuit ratio of the direct access 1000kV program is 4.08; the short-circuit ratio of the direct access 500kV program is 3.62; the short-circuit ratio of the 1000/500kV scheme of hierarchical access is 5.42/5.43.

3. Stability analysis of multi-end feeding of UHVDC

HVDC transmission multi-feed refers to a UHVDC transmission line fed into the receiver power grid through a number of converter stations. It can be subdivided into multi-end single-layer feeding mode and multi-terminal hierarchical feeding mode. Multi-terminal single-layer feeding mode means that a tributary line is fed to the receiver voltage level through two or more converter stations at the same. Multi-tiered hierarchical feeding means that a branch line is fed to different voltage levels through two or more converter stations. As shown in Figure 4. Connect the transformer to the II-type equivalent. The simplified equivalent network is shown in Figure 5. The node number sequence is i, j, k .

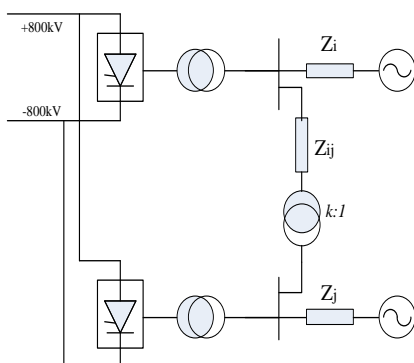


Figure 4. Multi-infeed hierarchical HVDC equivalent system

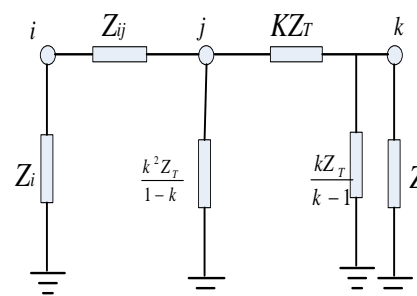


Figure 5. Multi-infeed hierarchical HVDC equivalent node network

From Figure 5, we can get the node admittance matrix:

$$Y_0 = \begin{pmatrix} \frac{1}{z_i} + \frac{1}{z_{ij}} & 0 & -\frac{1}{z_{ij}} \\ 0 & \frac{1}{z_j} + \frac{k-1}{kz_T} + \frac{1}{kz_T} & -\frac{1}{kz_T} \\ -\frac{1}{z_{ij}} & -\frac{1}{kz_T} & \frac{1}{z_{ij}} + \frac{k-1}{kz_T} + \frac{1}{kz_T} \end{pmatrix} \quad (8)$$

Block the matrix, use the node elimination formula, eliminate the extraneous node k , get the admittance matrix of node i, j , then get the impedance matrix of the node i, j .

$$Y = \begin{pmatrix} \frac{1}{z_i} + \frac{1}{k^2 z_T + z_{ij}} & -\frac{k}{k^2 z_T + z_{ij}} \\ -\frac{k}{k^2 z_T + z_{ij}} & \frac{1}{z_j} + \frac{1}{k^2 z_T + z_{ij}} \end{pmatrix} \quad (9)$$

$$Z = \begin{pmatrix} \frac{z_i(z_{ij} + k^2 z_j + k^2 z_T)}{z_i + z_{ij} + k^2(z_j + z_T)} & \frac{kz_i z_j}{z_i + z_{ij} + k^2(z_j + z_T)} \\ \frac{kz_i z_j}{z_i + z_{ij} + k^2(z_j + z_T)} & \frac{z_j(z_{ij} + z_i + k^2 z_T)}{z_i + z_{ij} + k^2(z_j + z_T)} \end{pmatrix} \quad (10)$$

We can calculate the short-circuit ratio in the multi-layered feeding mode when substituting the result into equation (2).

4. Simulation and result

The simulation model is based on the Ximeng-Taizhou UHVDC power transmission project. The rated operating voltage on the AC side of the rectifier station is 530kV, the rated operating voltage on the AC side of the inverter station is 520kV, and the rated operating voltage on the AC side of the inverter station is 1050kV. The rated voltage of the DC transmission line is ± 800 kV, the rated current is 6.25kA, and the rated transmission power is 10000MW.

Control strategy: The rectifier side maintains the reference value of the direct current by the direct current of the rectifier side by controlling the trigger angle α of the converter. With constant power control mode, the DC current reference value is determined as follows: $I_d = P_{ref}/U_d$. where U_d is the line side of the rectifier side smoothing reactor

By controlling the rectifier-side transformer taps such that α is maintained within the range of $\alpha_N \pm 2.5^\circ$, as long as the firing angle is within this range, the tap change tap will not act to bring the firing angle closer to the rated value. The side extinction angle γ of the inverter side is kept constant, and the DC voltage of the rectifier side is controlled by adjusting the inverter side commutation tap. When the inverter side tap is adjusted, the DC voltage changes, and the DC current on the rectifier side will change to make the DC power constant. For example, when the DC voltage U_d decreases by 0.625%, the DC current will increase by 0.625% to maintain the DC power unchanged.

The waveforms of AC voltage, DC voltage and current, active and reactive power, and trigger angle during steady-state operation of the rectifier station are shown in Figs. 6, 7, 8, and 9

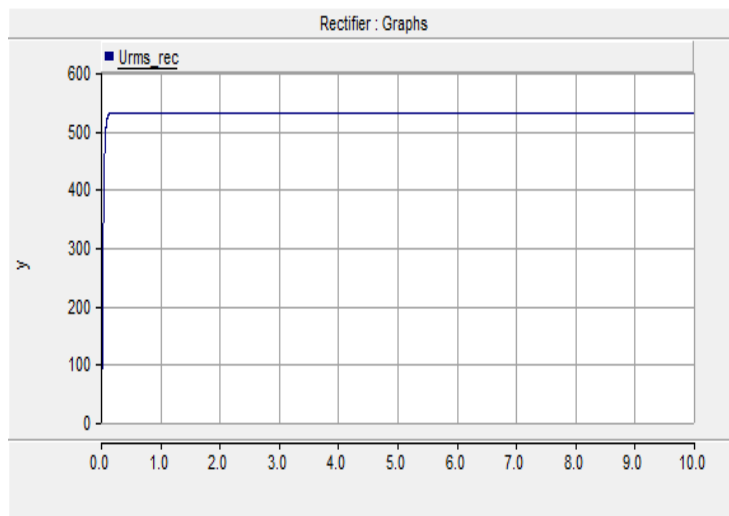


Figure 6. Rectifier steady-state operation AC voltage waveform

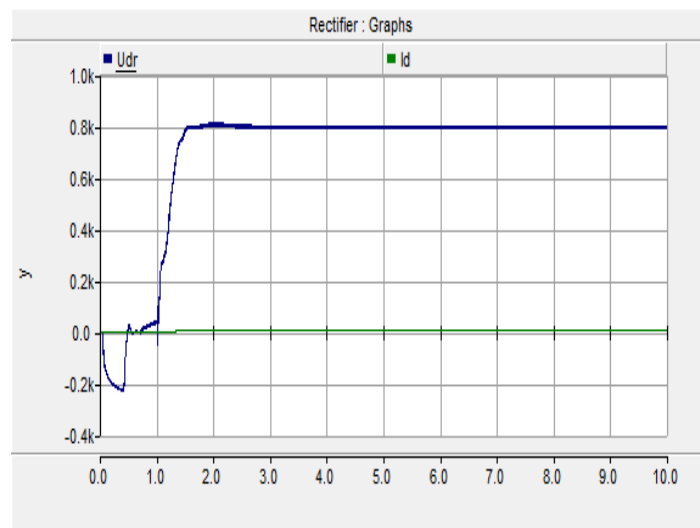


Figure 7. Rectifier steady-state operation DC voltage and current waveform

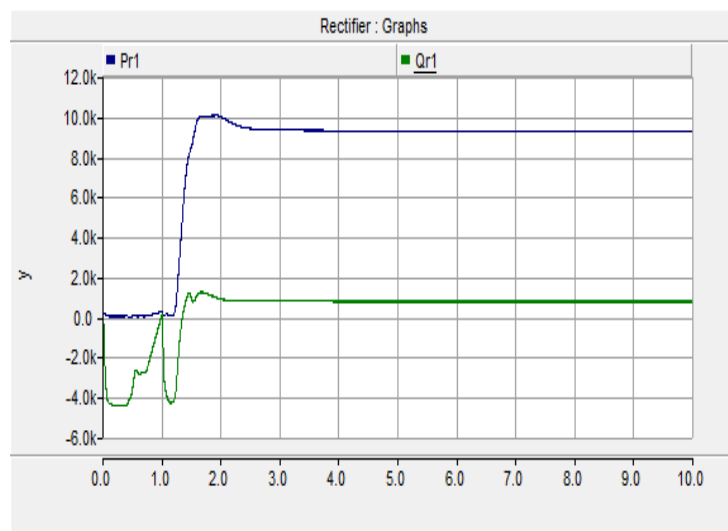


Figure 8. Rectifier steady-state operation active power and reactive power waveform.

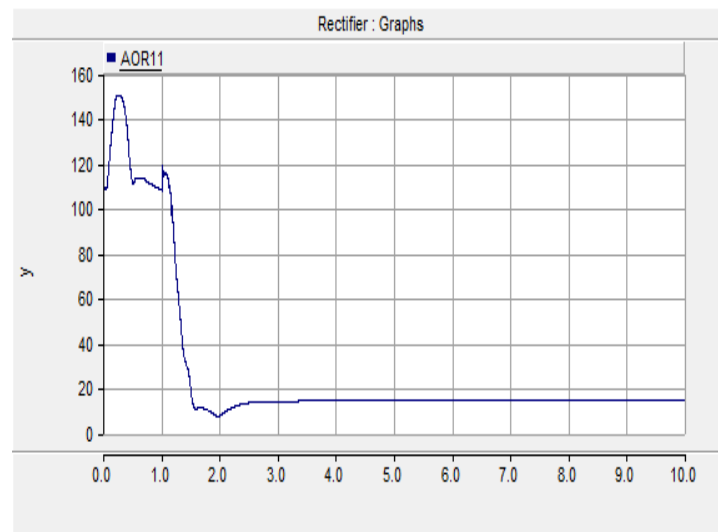


Figure 9. Rectifier steady-state operation firing angle waveform

It is calculated that the ratio of multiple feed-in short-circuits for the 1000kV commutation bus and the 500kV commutation bus under this feed-in mode is 5.18 and 4.65 respectively, compared to the short-circuit ratio of 4.08 and the direct access 500kV scheme for direct access to the 1000kV scheme. Short circuit is much higher than 3.62.

5. Conclusion

The multi-infeed short-circuit ratio calculation method proposed by CIGRE can deduce the short-circuit ratio of UHVDC layered access mode and UHVDC multi-terminal feeding mode. The short-circuit ratio of the 1000kV and 500kV busbars in the two methods of UHVDC layered access and UHVDC multi-terminal feeding is higher than that of the 1000kV and 500kV busbars in the single-layer access mode, which can cause the system to have a large short circuit as a whole. Ratio and voltage support capabilities. Hierarchical access and multi-terminal infeed can improve the system voltage support capability, reduce the risk of inverter station commutation failure, and have important significance for promoting the coordinated development of AC and DC power grids. It is also important for UHVDC development, DC networking, and power grid planning.

6. References

- [1] Shao Yao, Tang Yong. Research survey on multi-infeed AC /DC hybrid power systems [J]. *Power System Technology*, 2009, **33**(17):24-30.
- [2] Yuan Qingyun. Present state and application prospect of ultra HVDC transmission in China [J]. *Power system Technology*, 2005, **29**(14):1-3(in Chinese).
- [3] SU Hong-tian, QI Xu, WU Yun. Study on Market Demand of UHVDC Power Transmission in China [J]. *Power System Technology*, 2005, **24**:1-4+41.
- [4] Xiang Ling, Zheng Jianyong, Hu Minqiang. Study on commutation failure in MTDC and MIDC systems [J]. *Automation of Electric Power Systems*, 2005, **29**(11):29-33(in Chinese).
- [5] LI Mingjie. Characteristic Analysis and Operational Control of Large-Scale Hybrid UHV AC/DC Power Grids [J]. *Power System Technology*, 2016, (**04**):985-991.
- [6] Shao Yao, tang Yong, Guo Xiaojiang, et al. Analysis on commutation failures in multi-infeed HVDC transmission systems in North China and East China power grids planned for UHV power grids in 2015 [J], *Power System Technology*, 2011, **35**(10):9-15.
- [7] Xu Zheng. Characteristics of HVDC Connected to Weak AC System Part I: HVDC Transmission Capacity [J]. *Power System Technology*, 1997, **01**:12-16.
- [8] Xu Zheng. Characteristics of HVDC Connected to Weak AC System Part II: Control Modes and Voltage stability [J]. *Power System Technology*, 1997, **03**:1-4+9.

- [9] LIU Zhenya, QIN xiaohui, ZHAO Ling, ZHAO Qingbo. Study on the Application of UHVDC Hierarchical connection mode to Multi-infeed HVDC System [J]. *Power System Technology*, 2013, **10**:1-7+25.
- [10] Gao Yuan, Han Minxiao. Study State Characteristics of Multi-infeed UHVDC Power Transmission [J]. *Power System Technology*, 2014, **12**:3447-3552.
- [11] Liu Zhenya, Shu Yinbiao, Zhang Wenliang. Study on voltage class series for HVDC transmission system [J]. *Proceedings of CSEE*, 2008, **28**(10):1-8.
- [12] Wen J Y, Chen X, Yao M Q, Li N H, Sun S M, Li G L. Study on mixed multi-terminal DC transmission technology fit for connection of off-sea wind farms to grids [J]. *Electric System Protection and Control*, 2013, **41**(2): 55-61.

Acknowledgments

This research was financially supported by HQ sponsored S&T project of State Grid Corporation of China: Study on the development scale, bearing capability and evolutionary principle of balanced structure for power grids. (XT71-17-003)

Droop control Based Seamless Transfer Strategy for Three-phase Converter in Microgrid

ZHAO Guopeng^{1,2}, ZHOU Xinwei², YANG Hongwei², XU Feng³
and WANG Yanjie²

¹ State Key Laboratory of Alternate Electrical Power System with Renewable Energy Sources (North China Electric Power University), Beijing, China 102206

² School of Electrical and Electronic Engineering, North China Electric Power University, Beijing, China 102206

³ State Grid Zhejiang Electric Power Research Institute, Zhejiang, China 310000

E-mail: zhaoguopeng@ncepu.edu.cn

Abstract. This paper proposes a seamless transfer strategy based on the droop control strategy for three-phase converter in microgrid, which consists of the voltage limiter and the frequency limiter. In grid-connected mode, both the two limiters don't work, and the VSC is controlled by PQ control, transmitting constant power between micro-sources and power grid. When the unplanned islanding occurs, the PCC voltage and frequency may exceed the allowable range because the reference of active power and reactive power are not equal to the loads power. Then the voltage limiter and the frequency limiter begin to take effect, ensuring the power supply quality for loads. The difference between the input signal of these two limiter and the output signal will pass through the proportional regulator, and the new references of active power and reactive power can be obtained according to the droop curve. After the islanding detection detects the islanding condition, the control strategy will be changed to the droop control. All the converters can work in parallel and provide the voltage and frequency supply for loads. At last, the simulation results verified the proposed seamless transfer strategy.

1. Introduction

Microgrid is an integrated system which is composed of micro-sources, energy storage system and local loads. It's a new structure of power supply which can make full use of distributed generation (DG) and guarantee the reliable power supply for critical loads [1]. Thus, microgrid has aroused extensive concern for these years. The typical topology of microgrid is shown in Fig.1. DGs and energy storage equipment usually connected to the power grid by three-phase voltage source converter (VSC) [2].

Usually, microgrid has two operation mode, i.e., grid-connected mode and islanding mode. In grid-connected mode, the DGs and energy storage equipment usually work as current sources, and constant power is transmitted between the microgrid and the power grid [3]. In islanding mode, converters in the microgrid are usually controlled by V/f control or droop control, working as voltage sources and providing the voltage and frequency supply for the loads in microgrid [4].

Droop control is widely used to realize the automatic power sharing between different micro-sources without telecommunication lines, especially for parallel converters used in microgrid. The output characteristics of converters controlled by droop control are imitate as the synchronous generator. Several papers have studied droop control, such as [5]-[7].



When the unplanned islanding occurs, in order to realize uninterrupted power supply for critical and sensitive loads in microgrid, seamless transfer strategy for three-phase converter in microgrid is necessary and has also attracted lots of attention. In [8], a control scheme is presented, wherein the micro-source inverter works in voltage control mode amid stand-alone operation. And in current control mode amid grid-connected operation and switches over easily between these two modes during the transition phase. In [9], a soft-start virtual impedance and single loop current feedback control is proposed to transfer between the islanding mode and the grid-connected mode seamlessly. In [10], a transfer strategy based on output current of the three-phase converter with energy storage in the microgrid is proposed, which consists of an external inductor current loop, a grid voltage loop and an inner inductor current loop.

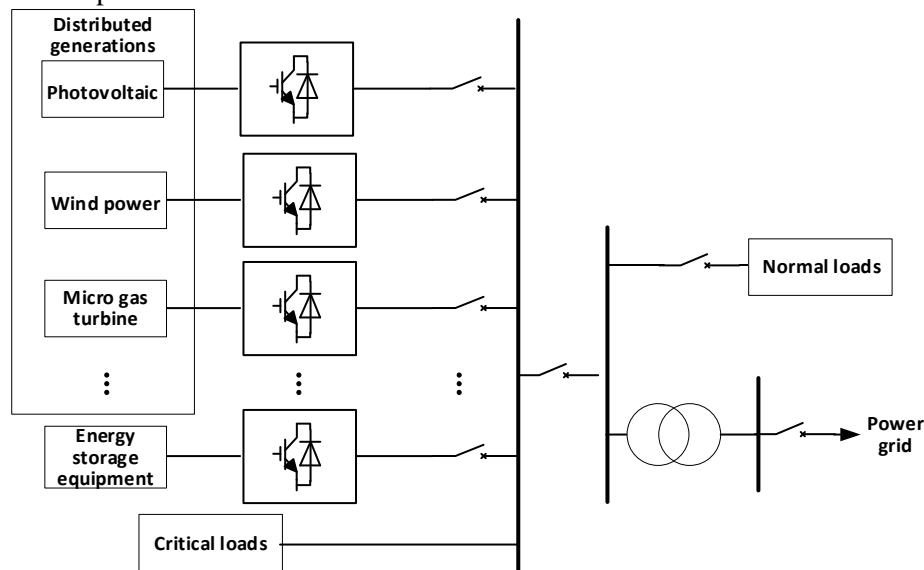


Figure 1. The schematic of typical microgrid

In this paper, a droop control based seamless transfer strategy for three-phase converter in microgrid is proposed. Starting with the typical topology of three-phase converter in microgrid, the principle of droop control method is introduced briefly. Then, according to the characteristics of droop control, the seamless transfer strategy is designed, which contains the voltage limiter and the frequency limiter. The limiters begin to take effect only under the circumstance that the voltage or frequency at the point of common coupling (PCC) exceeds the limit value when the unplanned islanding operation occurs. After the islanding condition is detected by islanding detection techniques, the control strategy can switch to the droop control. All the converters can work in parallel and provide the voltage and frequency supply for loads. At last the simulation verifies the proposed seamless transfer strategy.

2. Droop control strategy

2.1. The topology of three-phase converter in microgrid

The three-phase converter in microgrid is usually used for connecting micro-sources with grid. When the microgrid is operating in grid-connected mode, the converters are controlled by PQ control [11]. PCC voltage is supported by grid. The converters work as current sources, transmitting constant power into the grid. When in islanding mode, there are two kinds of control strategy, master-slave control and peer-to-peer control. The latter control strategy usually adopts droop control mode to control all the converters paralleled in microgrid [12]. The typical topology of converter is shown in Fig. 2.

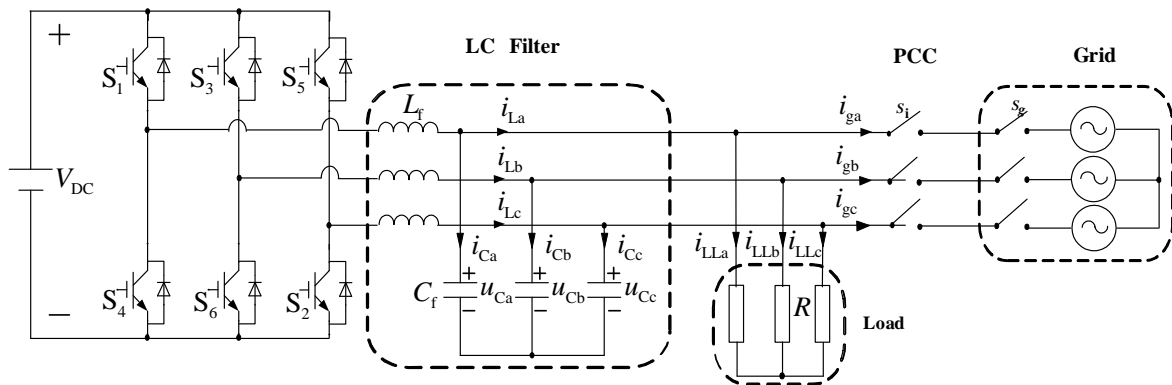


Figure 2. The topology of the typical three-phase converter in microgrid

The micro-source can be equivalent to a constant DC voltage source. V_{DC} is DC voltage. $S_1 \sim S_6$ are the insulated gate bipolar transistors (IGBT). L_f is AC filter inductance. C_f is AC filter. i_{La}, i_{Lb}, i_{Lc} are the output currents of VSC. $i_{LLa}, i_{LLb}, i_{LLc}$ are the currents in loads. i_{ga}, i_{gb}, i_{gc} are the currents flowing between the power grid and microgrid.

2.2. The relationship of paralleled converters

In Fig.3, the single-phase equivalent circuit of two converters in parallel is shown. Define i as the serial number of converters. E_i is output voltage of converter. R_i and L_i respectively are the resistance and inductance of equivalent line between converters and PCC. U is PCC voltage. R_L and L_L are the loads' resistance and inductance respectively.

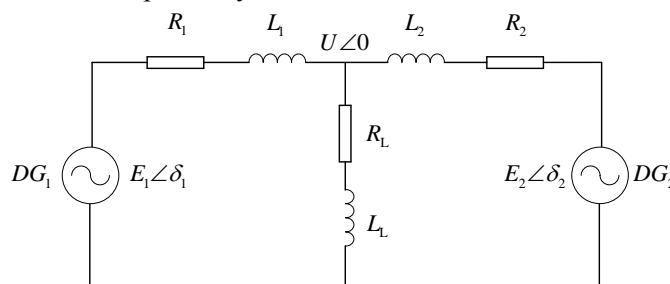


Figure 3. The single-phase equivalent circuit of two converters in parallel

According to Fig.3, the output power of converters can be calculated, as shown in equation (1).

$$\begin{cases} P_i = \frac{R_i(E_i U \cos \delta_i - U^2)}{X_i^2 + R_i^2} + \frac{X_i E_i U}{X_i^2 + R_i^2} \sin \delta_i \\ Q_i = \frac{X_i(E_i U \cos \delta_i - U^2)}{X_i^2 + R_i^2} - \frac{R_i E_i U}{X_i^2 + R_i^2} \sin \delta_i \end{cases} \quad (i=1,2) \quad (1)$$

Usually, $L_i \geq R_i$, and the δ_i is very small, so the $\sin \delta_i$ is approximately equal to δ_i . Thus, equation (1) can be simplified, as equation (2) shows.

$$\begin{cases} P_i = \frac{E_i U}{X_i} \delta_i \\ Q_i = \frac{U(E_i - U)}{X_i} \end{cases} \quad (i=1,2) \quad (2)$$

2.3. The principle of droop control

According to equation (2), the active power P_i is related to the phase angle δ_i , and the reactive power Q_i is related to the output voltage of converter. And the phase angle is dependent on the frequency, so the output active power can be controlled by changing the frequency of output voltage. Thus, the P-f droop characteristic and Q-V droop characteristic can be obtained, as shown in Fig.4.

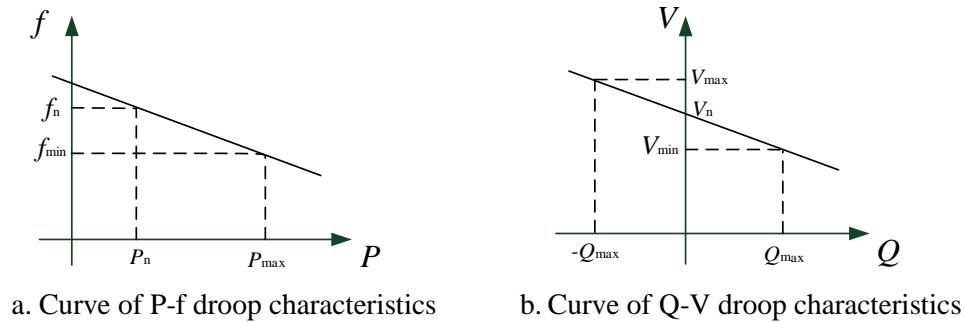


Figure 4. The frequency and voltage droop characteristics

Fig.4 can be expressed by equation (3). The output voltage and frequency of converters will be controlled according to the output power. Equation (3) corresponds to the droop control module in Fig.5, in which the control block diagram of droop control is shown.

$$\begin{cases} f = f_o + m(P - P_0) \\ E = E_o + n(Q - Q_0) \end{cases} \quad (3)$$

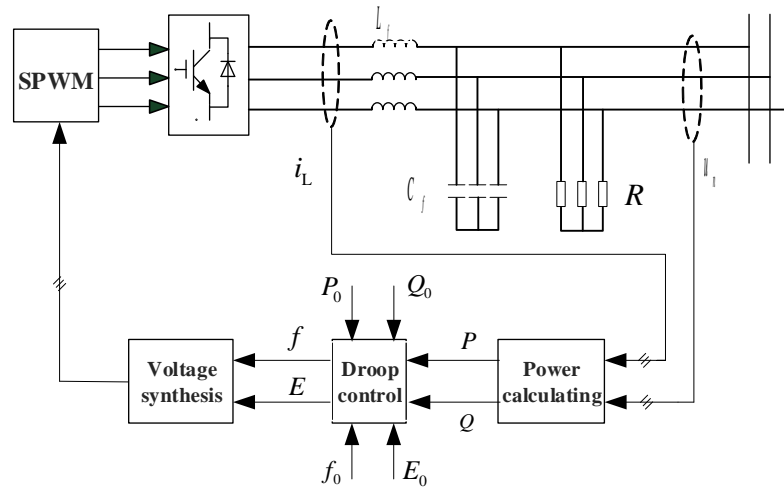


Figure 5. The control block diagram of droop control

3. Proposed seamless transfer strategy

3.1. Basic idea of proposed strategy

When the unplanned islanding operation occurs, because of the time delay of islanding detection technique, the converters in microgrid are still operating in grid-connected mode, controlled by PQ control. If the reference of power is not equal to the loads, the quality of PCC voltage may be damaged, and the critical loads may work improperly even breakdown. In order to prevent this case, the seamless transfer strategy proposed by this paper designs the frequency limiter and voltage limiter, as Fig.4 shows. The difference between the input signal of these two limiters and the output signal will pass through the proportional regulator, and the new reference of active power and reactive power can be obtained according to the droop curve.

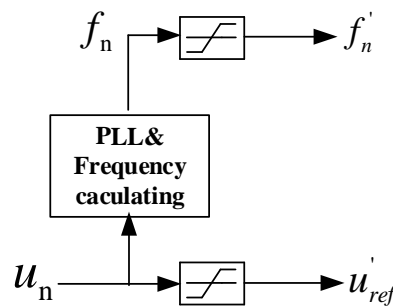


Figure 6. The frequency limiter and voltage limiter

It is necessary to consider the allowable range of frequency fluctuation when designing the limit value of the frequency limiter, as equation (4) shows. D_{f_max} and D_{f_min} are the upper limit and lower limit of the frequency limiter respectively. f_n is the acted frequency. Δf is the frequency deviation.

$$\begin{cases} D_{f_max} = f_n + \Delta f \\ D_{f_min} = f_n - \Delta f \end{cases} \quad (4)$$

The voltage limiter is the key to providing the voltage supply with good quality for loads during the transfer from grid-connected mode to islanding mode. According to IEEE Std_1547 2003 [13], the voltage fluctuation should be within 10% of rated voltage in the case that the rated capacity of converter is lower than 500kVA. So the voltage is designed according to equation (5).

$$\begin{cases} D_{V_max} = 110\%V_n \\ D_{V_min} = 90\%V_n \end{cases} \quad (5)$$

3.2. The control block diagram

The control block diagram is shown in Fig.5. The part which is in a dotted box is the droop control unit. And the outside part is PQ control unit. The switch between droop control and PQ control can be controlled by the single-pole double-throw (SPDT) switch. When the microgrid is operating in grid-connected mode, the frequency limiter and voltage limiter is ineffective because the PCC voltage and frequency is supported by the power grid. The SPDT selects the PQ control to control the converters. When the unplanned islanding occurs, if the PCC voltage and frequency exceeds the bounds of these two limiters, the reference of voltage and frequency would be the limit values. And the new reference of active power and reactive power can be obtained from the difference between the input signal of these two limiter and the output signal and the droop curve, which is shown in equation (4).

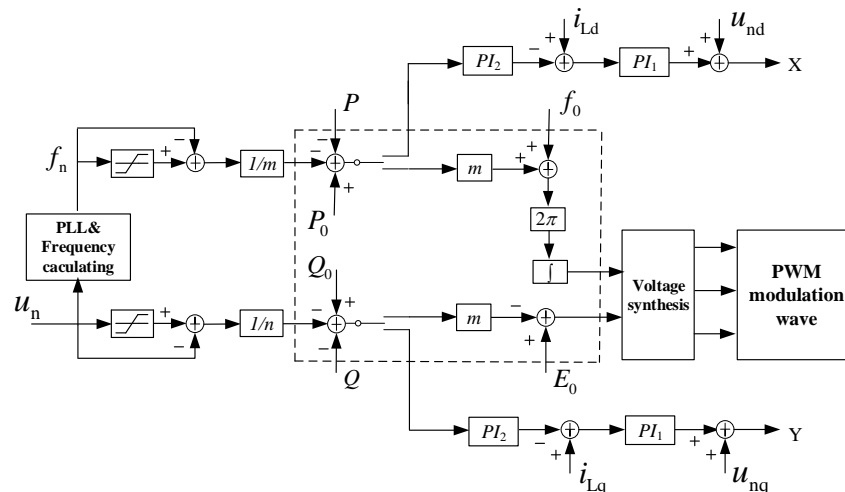


Figure 7. The frequency limiter and voltage limiter

$$\begin{cases} P^* = P_0 - \frac{1}{m}(f_{\text{lim}} - f_0) \\ Q^* = Q_0 - \frac{1}{n}(E_{\text{lim}} - E) \end{cases} \quad (6)$$

In equation (4), E_{lim} and f_{lim} are the limit values of the voltage limiter and frequency limiter respectively. P^* and Q^* are the references of active power and reactive power caused by the frequency and voltage fluctuation in unplanned islanding situation. Thus, the output power of converter can be equal to the loads. The PCC voltage and frequency can be guaranteed within the prescribed range.

After the islanding detection technique has detected the islanding condition, the SPDT selects the droop control to control the converters. Thus, the seamless transfer can be realized.

4. Simulation results

The simulation is presented to verify the droop control based seamless transfer strategy for three-phase converter in microgrid. The parameters of the simulation model are shown in Table 1.

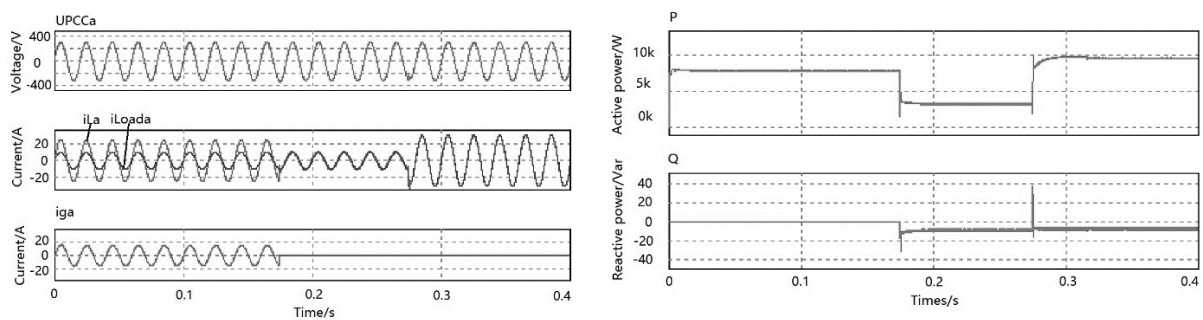
Table 1. The parameter of the main circuit in simulation

Parameter	Value
DC voltage V_{dc}	700V
Filter inductance L_f	3mH
Filter capacitor C_f	20 μ F
Slope of P-f droop curve m	0.005Hz/W
Slope of Q-V droop curve n	0.0038V/Var
The reference of active power in grid-connected mode P_{ref}	7.75kW
The reference of reactive power in grid-connected mode Q_{ref}	0kVar
loads	30 Ω

The unplanned islanding occurs at $t=0.175\text{s}$, and the loads are increased at $t=0.275\text{s}$. The results are shown in Fig.7. The PCC voltage, the output current of converter, the load current and the current flowing between power grid and microgrid are shown in Fig.7(a). The output active and reactive power of converter are shown in Fig.7(b).

Fig.7(a) shows that, after the unplanned islanding occurs, the PCC voltage and frequency are limited within the acceptable range via the seamless transfer strategy. The loads can work properly when the unplanned islanding is occurring. Fig.7(b) shows that the converter can provide the power supply for loads when the unplanned islanding is occurring. And after the islanding detection technology detects the islanding condition, the control strategy can switch over to the droop control. When the loads are increased, the output power of converter can fit the load power by changing the output frequency and voltage of converter in islanding mode.

The simulation results shows that, the droop control based seamless transfer strategy for three-phase converter is useful to realize the seamless transfer between PQ control and droop control. The frequency limiter and voltage limiter can ensure the PCC voltage within the allowable range. The critical loads can work normally in the transfer process. After the control strategy switches over to droop control, the converter can provide the frequency and voltage supply with good quality for loads.



(a) The PCC voltage, output current of converter, the load current and the current flowing between power grid and microgrid

(b) The output active and reactive power of converter

Figure 8. The simulation results

5. Conclusion

This paper proposes a seamless transfer strategy based on droop control for three-phase converter in microgrid, which contains frequency limiter and voltage limiter. When the unplanned islanding occurs, the limiters can ensure the PCC voltage and frequency are within the required range for proper operation of loads. After the islanding detection technique detects the islanding condition, the control strategy switches over to the droop control unit, controlling the converters work as voltage sources and provide the voltage and frequency supply for loads. At last, the seamless transfer strategy is verified by the simulation results.

6. Acknowledgments

This study was supported by the National Key R&D Program of China (2017YFB0903100), and the Project Supported by Science and Technology Foundation of SGCC (521104170043).

7. References

- [1] U. Akram, M. Khalid and S. Shafiq, "An Innovative Hybrid Wind-Solar and Battery-Supercapacitor Microgrid System—Development and Optimization," in *IEEE Access*, vol. 5, pp. 25897-25912, 2017.
- [2] C. Shah, M. Abolhassani and H. Malki, "Fuzzy controlled VSC of battery storage system for seamless transition of microgrid between grid-tied and islanded mode," 2017 International Joint Conference on Neural Networks (IJCNN), Anchorage, AK, 2017, pp. 3224-3227.
- [3] Y. Xiaodong, Z. Youbing, W. Guofeng, R. Shuaijie, S. Weiwei and L. Junjie, "Coordinate optimization for grid-connected microgrid considering uncertainties of renewable energy sources and electric vehicles," 2017 29th Chinese Control And Decision Conference (CCDC), Chongqing, 2017, pp. 3224-3231.
- [4] D. K. Jeong, H. J. Yun, H. J. Kim, H. S. Kim and J. W. Baek, "Distributed control strategy of DC microgrid for islanding mode operation," 2017 19th European Conference on Power Electronics and Applications (EPE'17 ECCE Europe), Warsaw, 2017, pp. P.1-P.5.
- [5] A. Trivedi and M. Singh, " L_1 Adaptive Droop Control for AC Microgrid with Small Mesh Network," in *IEEE Transactions on Industrial Electronics*, vol. PP, no. 99, pp. 1-1.
- [6] Z. Peng, J. Wang, D. Bi, Y. Dai and Y. Wen, "The Application of Microgrids Based on Droop Control with Coupling Compensation and Inertia," in *IEEE Transactions on Sustainable Energy*, vol. PP, no. 99, pp. 1-1.
- [7] Phuong Le Minh, Hoa Pham Thi Xuan, Duy Hoang Vo Duc and Huy Nguyen Minh, "Control of power in an island microgrid using adaptive droop control," 2017 International Conference on System Science and Engineering (ICSSE), Ho Chi Minh City, 2017, pp. 148-153.
- [8] A. H. Kadam, K. Unni and S. Thale, "Control scheme for seamless operating mode transfer of AC microgrid," 2017 IEEE International Conference on Smart Energy Grid Engineering (SEGE), Oshawa, ON, 2017, pp. 123-130.

- [9] Y. Chen et al., "Seamless transfer control strategy for three-phase inverter in microgrid," 2016 IEEE 8th International Power Electronics and Motion Control Conference (IPEMC-ECCE Asia), Hefei, 2016, pp. 1759-1763.
- [10] Y. Wang and G. Zhao, "An output current based seamless transfer control strategy for three-phase converter with energy storage in micro-grid," International Conference on Renewable Power Generation (RPG 2015), Beijing, 2015, pp. 1-6.
- [11] D. Zhang and E. Ambikairajah, "De-coupled PQ control for operation of islanded microgrid," 2015 Australasian Universities Power Engineering Conference (AUPEC), Wollongong, NSW, 2015, pp. 1-6.
- [12] Jie Feng Hu, Jian Guo Zhu and G. Platt, "A droop control strategy of parallel-inverter-based microgrid," 2011 International Conference on Applied Superconductivity and Electromagnetic Devices, Sydney, NSW, 2011, pp. 188-191.
- [13] IEEE Standard for Interconnecting Distributed Resources with Electric Power Systems," in IEEE Std 1547-2003, vol., no., pp.1-28, July 28 2003

Study on Coordinated Optimization of the Gird Voltage Control Strategy Considering Comprehensive Cost

Jingbo WU¹, Jianling ZHANG¹, Weijun ZHU¹, Dijun HU², Xinfan JIANG², and Wei ZHONG²

¹ State Grid Hunan Electric Power Co. Ltd. Power Research Institute, Changsha 410007, Hunan Province, China;

² State Grid Hunan Electric Power Co. Ltd., Changsha 410004, Hunan Province, China.

E-mail: jinbowul112@qq.com

Abstract: The spoilage of the discrete reactive power devices such as shunt capacitor or on-load tap changer by control are far greater than that of the continuous reactive power devices such as generator or SVG. To reduce the comprehensive cost including the gird loss and the device spoilage, This paper proposed a novel gird voltage control coordinated optimization strategy. The comprehensive cost including the gird loss and the device spoilage is used as an objective function. The corresponding calculation method based on improved genetic algorithm is presented. The proposed strategy would be combined with the three-level voltage control mode of existing AVC systems. The simulation contrast results in IEEE-14 system show that the proposed strategy is more reasonable than the traditional control strategy without consideration of the discrete reactive power devices spoilage. Especially in the case of network load periodic change, the repeated controls of the discrete devices are effectively avoided by using the proposed strategy.

1. Introduction

The system of automatic voltage control (AVC) [1] is used to control the grid voltage and reactive power. It could regulate the reactive power equipment automatically, improves the voltage quality, reduces the loss, and ensures the safe and high-quality operation of the grid [2]. The grid reactive power equipment includes various types of continuous devices and discrete devices. The former includes various types of generators, dynamic reactive power compensation equipment and other continuous equipment. The latter includes shunt capacitor/reactor, on-load tap-changer and other discrete equipment.

The AVC system only controls continuous or discrete devices in early period. With the development, the global coordinated control mode [3] of AVC system has replaced the distributed control mode. Both of continuous and discrete equipment would be coordinated controlled. The control principle is proposed [4]. That is priority adjustment by discrete device and fine adjustment by continuous devices. This principle has become the mainstream in existing AVC system [5].

The spoilage of the discrete reactive power devices by control are far greater than that of the continuous reactive power devices. The continuous devices are controlled by power electronic components such as thyristors. The control has less effect on the reduction of continuous device life [6]. The discrete devices are controlled by mechanical components. The number of controls directly determines the discrete device life.

To reduce the comprehensive cost including the gird loss and the device spoilage, a novel gird voltage control coordinated optimization strategy is proposed in this paper. The proposed strategy would be



combined with the three-level voltage control mode of existing AVC systems [7]. The calculation method is given. And the comparative simulation calculations are performed on the IEEE14-node system to verify the effectiveness of the proposed strategy.

2. Comprehensive cost analysis of power grid

2.1 Grid gird loss cost model

Power grid [8] loss P_{loss} is mainly the line loss of power transmission, the formula of P_{loss} is given as follows:

$$P_{\text{loss}} = \sum_{i,j} G_{ij} [V_i^2 + V_j^2 - 2V_i V_j \cos(\theta_i - \theta_j)] \quad (1)$$

where, i and j are the node numbers of the grid branch ij . G_{ij} is the branch conductance. V_i , V_j , θ_i , and θ_j are the voltage amplitudes and phase angles of nodes i and j , respectively.

The cost caused by the loss of the unit network assumed to be λ . The calculation formula of the grid loss cost F_1 is given in time T as follows:

$$F_1 = \lambda \int_T \left(\sum_{i,j} G_{ij} [V_i^2 + V_j^2 - 2V_i V_j \cos(\theta_i - \theta_j)] \right) dt \quad (2)$$

2.2 Equipment spoilage model

As far as discrete equipment is concerned, the controls number of the circuit breakers and taps is much greater than the electrical parts of the equipment. Therefore, the spoilage of the discrete equipment is mainly the spoilage of circuit breakers and taps.

The service life of circuit breakers and taps is related to a number of factors such as the number of movements of mechanical components and the running time of equipment. The number of movements of mechanical components is much greater than the other factors. Therefore, the service life of circuit breakers and taps can also be represented by the number of mechanical device design operations.

Within the time T , the cost of the equipment transportation inspection caused by the k -th parallel capacitor/reactor investment/cutting operation of node n is $F_{k,n}$.

$$F_{k,n} = \frac{C_{k,n}}{N_{k,n}} \int_T |y_{k,n,t} - y_{k,n,t-1}| dt \quad (3)$$

$$F_{ml} = \frac{C_{ml}}{N_{ml}} \int_T \frac{|z_{ml,t} - z_{ml,t-1}|}{\Delta z_{ml}} dt \quad (4)$$

where, C is the life cycle cost of the corresponding discrete device, N is the number of mechanical device design actions corresponding to the discrete device, that is, the service life of the device, and y is the shunt capacitor/reactor circuit breaker status ($y=0$, the breaker is open, $y=1$, is the circuit breaker is closed), z is the variable ratio of on-load adjustable transformer, Δz_{ml} is the variation ratio value of the gear ratio of the tap changer of the on-load tap changer transformer between nodes m and l , t and $t-1$ are the current control time and the previous time.

2.3 Comprehensive network cost model

From the perspective of full life economic operation of the power grid, the comprehensive cost of the grid should include the Grid Gird Loss costs and equipment transportation inspection costs. According to equations (2), (3) and (4), the total cost of the grid F within the time T is calculated as follows:

$$\begin{aligned}
F &= F_1 + \sum_n \sum_k F_{k,n} + \sum_m \sum_l F_{ml} = \\
&\lambda \left\{ \int_T \left(\sum_{i,j} G_{ij} [V_i^2 + V_j^2 - 2V_i V_j \cos(\theta_i - \theta_j)] \right) dt \right. \\
&+ \sum_n \sum_k \alpha_{k,n} \int_T |y_{k,n,t} - y_{k,n,t-1}| dt \\
&\left. + \sum_m \sum_l \beta_{ml} \int_T |z_{ml,t} - z_{ml,t-1}| dt \right\}
\end{aligned} \tag{5}$$

where, $\alpha_{k,n} = C_{k,n} / (N_{k,n} \times \lambda)$ is the ratio of cost to cost per unit of network loss for the k -th group of parallel-connected capacitor/reactor single-action at node n . $\beta_{ml} = C_{ml} / (N_{ml} \times \Delta z_{ml} \times \lambda)$ is the ratio of the cost to the cost per unit network loss for a single action of the on-load tap changer tap between nodes m and l .

The formula for calculating the unit time grid comprehensive cost f is given as follows:

$$\begin{aligned}
f &= \frac{\partial F}{\partial t} = \lambda \left\{ P_{loss,t} + \sum_n \sum_k \alpha_{k,n} |y_{k,n,t} - y_{k,n,t-1}| \right. \\
&\left. + \sum_m \sum_l \beta_{ml} |z_{ml,t} - z_{ml,t-1}| \right\}
\end{aligned} \tag{6}$$

3. Automatic voltage control coordination optimization strategy

3.1 Coordination optimization strategy mathematical model

This paper proposes a coordinated automatic voltage control coordination optimization strategy with the goal of reducing the overall cost of the grid. The total cost f of the grid per unit time given by equation (6) is used as an objective function. The mathematical model is given as follows:

$$\begin{cases} \min f(x, y, z) \\ g(x, y, z) = 0 \\ h^{\min} \leq h(x, y, z) \leq h^{\max} \end{cases} \tag{7}$$

where, x is the expected value of reactive power output of continuous equipment and shunt capacitor/reactor equipment, y is the shunt capacitor/reactor circuit breaker status, z is the ratio of on-load adjustable transformer, x , y , and z are the control variables of the optimized strategy; $g(x, y)$ is the boundary condition of the equation, and $h(x, y)$ is the boundary condition of the inequality.

The mathematical model of $g(x, y)$ is shown in Equation (8):

$$\begin{cases} P_i - V_i \sum_{j \in i} V_j (G_{ij} \cos \theta_{ij} + B_{ij} \sin \theta_{ij}) = 0 \\ \sum x_{k,i,t} - Q_i - V_i \sum_{j \in i} V_j (G_{ij} \sin \theta_{ij} - B_{ij} \cos \theta_{ij}) = 0 \\ x_{k,n,t} = y_{k,n,t} V_n^2 B_{kn} \\ V_m / V_l = z_{ml,t} \end{cases} \tag{8}$$

where, $x_{k,i,t}$ is the reactive power output expected value of the k -th continuous device or shunt capacitor/reactor device that is connected to node i , B_{kn} is the k -th group of node n shunt capacitor/reactor branch susceptance.

The mathematical model for $h(x, y)$ is shown in Equation (9):

$$\left\{ \begin{array}{l} x_{k,i}^{\min} < x_{k,i,t} < x_{k,i}^{\max} \\ |x_{k,i,t} - x_{k,i,t-1}| < \Delta x_{k,i} \\ z_{ml}^{\min} < z_{ml,t} < z_{ml}^{\max} \\ |z_{ml,t} - z_{ml,t-1}| < M * \Delta z_{ml} \\ V_i^{\min} < V_i < V_i^{\max} \end{array} \right. \quad (9)$$

where, x^{\max} and x^{\min} are the reactive output upper and lower limits of the continuous device or shunt capacitor/reactor device, respectively, and Δx is the reactive power adjustable step length per unit time;; z^{\max} and z^{\min} are the upper and lower limits of the on-load tap changer transformer, respectively. Δz is the change ratio of the gear ratio change of the load tap changer transformer between the nodes m and l . M is the adjustable number of taps of on-load tap changer transformer tap per unit time. V^{\max} , V^{\min} are the node voltage upper and lower limits, respectively.

By formulae (6)~(9), the automatic voltage control of the power grid is transformed into a problem of minimizing the overall cost of the grid per unit time, and the continuous and discrete variables with the boundary conditions are coordinated and optimized.

3.2 Coordination and optimization control system

The proposed strategy would be combined with the three-level voltage control mode of existing AVC systems, as shown in Figure 1.

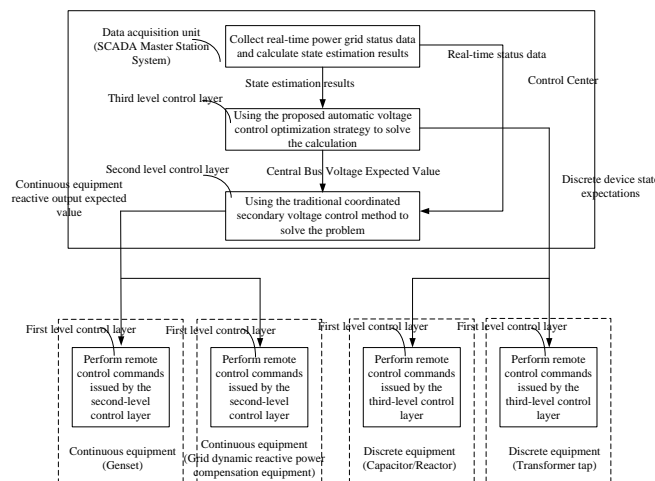


Figure 1. Schematic diagram of the coordinated optimization control system

The above optimization control system still follows the three-level voltage control mode of the existing AVC system. The third layer adopts the automatic voltage control optimization strategy of the power grid, namely formula (7). The optimized calculation determines the expected values of the discrete equipment state, namely y , z , and the expected value of the regional hub bus voltage. This set of optimization systems, based on the existing AVC system, does not require the addition of new systems and hardware, nor does it change the control mode of the existing AVC system, and is easy to implement.

4. Improved Genetic Algorithm Solving

To facilitate the calculation, the continuous variables in equation (7) are discretized. In this paper, an improved genetic algorithm is used to solve the problem and make appropriate improvements. The algorithm flow chart is shown in Figure 2.

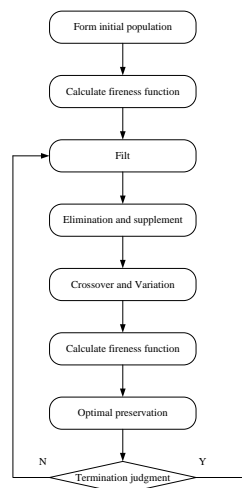


Figure 2. The process flow diagram of the improved genetic algorithm

5. Simulation Examples

This paper takes IEEE-14 node standard power grid model as an example to carry out simulation analysis. IEEE-14 node standard grid model, as shown in Figure 3, the grid model parameters see appendix A.

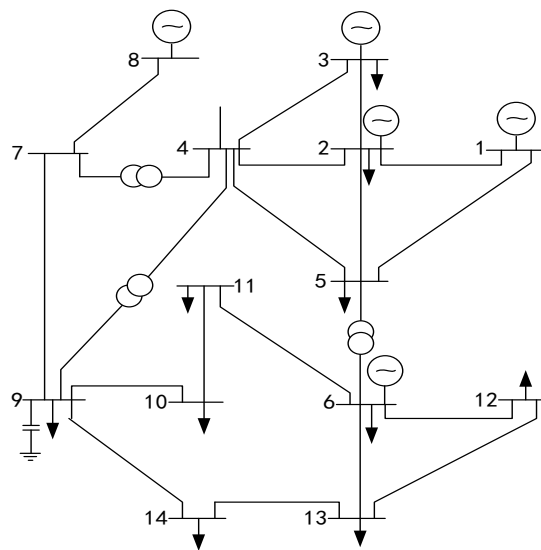


Figure 3. The model of IEEE-14 system

The No. 1 node is connected to the upper grid and is a balanced node. All nodes are P and Q nodes. The voltage amplitudes and the lower limits of the nodes are 1.1 and 0.9 respectively. No. 2 and No. 14 nodes have grid-connected generators. No. 5 nodes have dynamic reactive power compensation equipment, No. 3, No. 6 and No. 8 nodes have two parallel capacitor banks, and all transformers are no-load regulator transformers.

Node load and generator output will change over time. The AVC system controls the period of time as a unit. Please refer to appendix A for nodal load and generator output at time 0~4.

Set the ratio of the cost and unit network loss cost of the shunt capacitor bank in a single example to be 0.004, that is $\alpha_1, \alpha_3 = \alpha_2, \alpha_6 = \alpha_1, \alpha_8 = \alpha_2, \alpha_8 = 0.004$.

In the same initial state, the optimized control strategy based on comprehensive cost analysis and the traditional control strategy aiming at minimum network loss are adopted respectively, and automatic voltage control simulations are performed for the examples 1 to 4 respectively. The optimized control

strategy proposed in this paper is based on the improved genetic algorithm. The length of the continuous device gene block is 5, the number of population per generation is 20, P_c is 0.6, P_m is 0.2, and the optimal number of saved and replaced individuals is 1. The termination criterion is that the maximum value of the fitness function remains constant for five consecutive generations or reaches the maximum number of iterations of 200. The traditional control strategy adopts the control principle of "priority adjustment by discrete device and fine adjustment by continuous devices". Table 1 and Table 2 respectively show the results obtained by using two control strategies. The value at time 0 is the initial state. Figure 4 shows the number of discrete device actions when using two control strategies.

Table 1. Simulation results of the proposed strategy

	0 time	1 time	2 time	3 time	4 time
$x_{1,2}$	0.4	-0.0387	0.4	-0.1161	0.4
$x_{1,5}$	0.1	0.1	0.1	-0.0548	0.1
$x_{1,14}$	0.1	-0.0677	0.1	-0.1	0.1
$y_{1,3}$	1	1	1	1	1
$y_{2,3}$	1	1	1	1	1
$y_{1,6}$	1	1	1	0	1
$y_{2,6}$	0	0	1	1	1
$y_{1,8}$	1	0	1	0	1
$y_{2,8}$	0	0	1	0	1
P_{loss}	/	0.2061	0.2860	0.2114	0.2887
$f/\%$	/	0.2101	0.2980	0.2234	0.3007

Table 2. Simulation results of the traditional control strategy

	0 time	1 time	2 time	3 time	4 time
$x_{1,2}$	0.4	0.4	0.4	0.4	0.4
$x_{1,5}$	0.1	0.0935	0.1	0.0935	0.1
$x_{1,14}$	0.1	-0.0032	0.1	-0.1	0.1
$y_{1,3}$	1	0	1	0	1
$y_{2,3}$	1	0	1	0	1
$y_{1,6}$	1	0	1	0	1
$y_{2,6}$	0	0	1	0	1
$y_{1,8}$	1	0	1	0	1
$y_{2,8}$	0	0	1	0	1
P_{loss}	/	0.2038	0.2860	0.2077	0.2887
$f/\%$	/	0.2198	0.3100	0.2317	0.3127

From Figure 4, we can see that at each time of the example, the proposed optimal control strategy is used for simulation control, and the number of discrete device actions is far less than that of the traditional control strategy.

Comparing with Tables 1 and 2, we can see that at some moments (such as time 1 and 3), the optimized control strategy is used to perform simulation control, and the network loss is greater than when the traditional control strategy is used to control the simulation. However, considering the discrete device motion loss, the optimized control strategy is used to carry out the simulation control. The total cost f of the grid at each moment is obviously less than when the traditional control strategy is used to control the simulation. And the optimized control strategy proposed is not to reduce the number of discrete device actions and over-reliance on continuous devices.

6. Conclusion

This paper propose a novel gird voltage control coordinated optimization strategy to reduce the comprehensive cost. The comprehensive cost includes the gird loss and the device spoilage. The proposed optimization strategy is combined with the existing three-level voltage control mode of the AVC system. The corresponding calculation method based on improved genetic algorithm is presented. The IEEE-14 system is used as an example to carry out simulation and comparison calculation. The simulation contrast results show that the proposed strategy is more reasonable than the traditional control strategy without considering the discrete devices spoilage. Especially in the case of gird load periodic change, the repeated controls of the discrete devices are effectively avoided by using the

proposed strategy. In future, the proposed strategy would be used in actual power grid. And we hope that the paper can provide reference for optimization of AVC system.

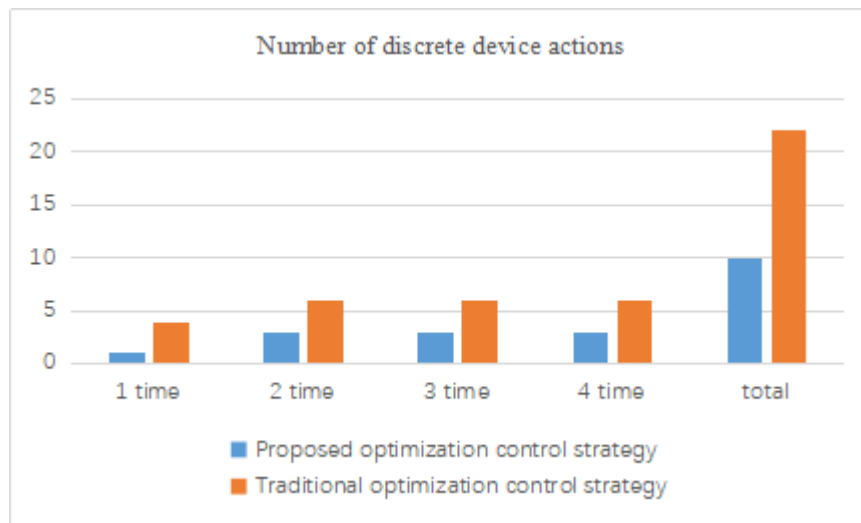


Figure 4. The comparison of the the proposed strategy and the traditional control strategy

7. Reference

- [1] Sun H B, Zhang Z G, Liu Y S, et al. Autonomous- synergic Voltage Control for Complicated Power Systems: Key Technologies and Prospects [J]. *Power System Technology*, 2017, 41(12): 3741-3749.
- [2] Sun L, Niu Q Y, Zhang Q, et al. Study on Entire Network Reactive Power Voltage Coordination Control Based on Smart AVC System [J]. *Power Capacitor & Reactive Power Compensation*, 2017, 38(3): 147-150.
- [3] Xu J, Yuan Z C, Wang L L, et al. Design and Simulation of Voltage Control Strategies for STATCOM Participating in AVC [J]. *Electric Power Automation Equipment*, 2015, 35(10): 115-120.
- [4] Wang B, Guo Q L, Zhou H F, et al. Applications of Coordinated Automatic Voltage Control Integrated for Regional, Provincial and Prefectural Control in China Southern Power Grid[J]. *Automation of Electric Power Systems*, 2014, 38(13): 208-215.
- [5] Wang B, Guo Q L, Sun H B, et al. Method of Coordination Among Strongly Coupled Power Plants for Automatic Voltage Control [J]. *Automation of Electric Power Systems*, 2015, 39(12): 165-171.
- [6] Yang Z C, Li X J, Lu W W, et al. Life cycle cost research of high voltage circuit breaker based on principal component analysis [J]. *Electrical Measurement & Instrumentation*, 2017, 54(1): 55-60.
- [7] Bao W, Zhu T, Zhao C, et al. A three-stage network partition method for secondary voltage control based on agglomerative analysis [J]. *Automation of Electric Power Systems*, 2016, 40(5):127-132.
- [8] Wu J B, Sheng Y, LI H. The Discussion on the Configuration of DC Control and Protection System [J]. *Hunan Electric Power*, 2013, 33(4): 38-40.

Acknowledgments

This work was supported by Science & Technology Project of State Grid Electric Power Corporation in China(5216A018000Q), and Science & Technology Project of State Grid Hunan Electric Power Corporation in China (5216A515002V).

Appendix A

Table A1. The node load and generator output in 0 moment

Node number	Active load	Reactive load	Generator output
2	-0.217	0.1	0.4
3	-0.942	0	/
4	-0.478	0.039	/
5	0.124	-0.016	/
6	-0.112	0	/
7	0	0	/
8	0	0.1	/
9	-0.295	-0.1	/
10	-0.09	-0.058	/
11	-0.035	-0.018	/
12	-0.061	-0.016	/
13	-0.135	-0.058	/
14	-0.149	-0.05	0.2

Table A2. The node load and generator output in 1st moment

Node number	Active load	Reactive load	Generator output
2	-0.217	0.1	0.4
3	-0.942	0	/
4	-0.478	0.039	/
5	0.124	-0.016	/
6	-0.112	0	/
7	0	0	/
8	0	0.1	/
9	-0.295	-0.1	/
10	-0.09	-0.058	/
11	-0.035	-0.018	/
12	-0.061	-0.016	/
13	-0.135	-0.058	/
14	-0.149	-0.05	0.2

Table A3. The node load and generator output in 2nd moment

Node number	Active load	Reactive load	Generator output
2	-0.217	-0.2	0
3	-0.942	-0.2	/
4	-0.478	0.039	/
5	-0.076	-0.016	/
6	-0.112	-0.1	/
7	0	0	/
8	0	-0.1	/
9	-0.295	-0.3	/
10	-0.09	-0.058	/
11	-0.035	-0.018	/
12	-0.061	-0.016	/
13	-0.135	-0.058	/
14	-0.149	-0.05	0

Table A4. The node load and generator output in 3rd moment

Node number	Active load	Reactive load	Generator output
2	-0.217	-0.0932	0.4
3	-0.942	-0.1392	/
4	-0.478	0.2	/
5	0.124	0	/
6	-0.112	-0.1477	/
7	0	0	/
8	0	-0.0238	/
9	-0.295	-0.166	/
10	-0.09	0.1	/
11	-0.035	0.1	/
12	-0.061	-0.016	/
13	-0.135	-0.058	/
14	-0.149	0.1	0.2

Table A5. The node load and generator output in 4th moment

Node number	Active load	Reactive load	Generator output
2	-0.217	-0.0932	0
3	-0.942	-0.1392	/

4	-0.478	0	/
5	-0.076	-0.2	/
6	-0.112	-0.1477	/
7	0	0	/
8	0	-0.0238	/
9	-0.295	-0.166	/
10	-0.09	-0.1	/
11	-0.035	-0.1	/
12	-0.061	-0.016	/
13	-0.135	-0.058	/
14	-0.149	-0.1	0

Research on Improved Droop Control Strategy Based on Virtual Impedance

X M Liu¹, B C Lu², Z P Ren³ and R X Zhang⁴

¹ Liaoning University of Technology, Liaoning Province, China

² Liaoning University of Technology, Liaoning Province, China

³ Liaoning University of Technology, Liaoning Province, China

⁴ Liaoning University of Technology, Liaoning Province, China

E-mail: 2284777389@qq.com

Abstract. Due to the property of line impedance and other factors in micro-grid, power supplied by distributed generation units could not be shared accurately based on their traditional droop coefficient. To improve the power sharing accuracy of distributed generation units, improved droop control of power sharing strategy which was based on virtual impedance is proposed in this paper. Simulations results show that improved droop controller can achieve good load active and reactive power sharing.

1. Introduction

In recent years, distributed generation (DG) technology has been widely studied by scholars both at home and abroad. In order to cope with the flexible nature of DG and solve the problem of its reliable access, micro-grid is proposed as an effective solution [1]. A micro-grid can operate in parallel to grid or in island. The control technology of micro-grid is a key part of the operation of the micro-grid. Mature control technologies can improve the flexibility of micro-grid operation and improve power quality [2]. Droop control adjusts amplitude of the output voltage and frequency according to DG's output. The system distributes load according to droop coefficient. However, traditional droop control is generally considered to be used only when it is satisfied $X \gg R$. Traditional droop control of the low-voltage micro-grid running in island will cause frequency and voltage to deviate from the rated values. Power supplied by DG units could not be shared accurately based on their traditional droop coefficient [3]. In order to solve this problem, [4] proposed a whole-cycle adaptive adjustment method, so that the system could obtain high dynamic performance under different loads. [5] considered the linear impedance effect, and ignored linear resistance according to the linear relationship between the system output reactive power and line voltage drop. [6] proposed a control strategy for automatically adjusting the droop coefficient.

Based on the analysis of the droop characteristic, this paper analyses the reasons for the deviation of reactive power distribution. In order to reduce the error of power distribution, virtual impedance control loop is added to the traditional droop control so that DG in micro-grid can complete the decoupling control of power. Simulation result shows that the proposed scheme can effectively improve the power distribution relationship between DG units.

2. Analysis of droop characteristic

In the analysis of power flow for micro-grid, equivalent circuit of its power transmission which is shown in figure 1.



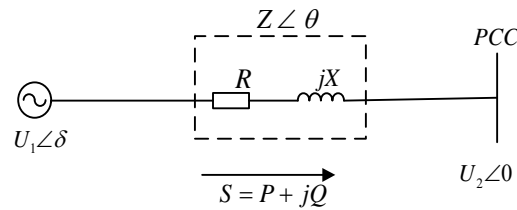


Figure 1. Power transmission equivalent model.

P and Q output from inverter are respectively shown in equations (2.1) and (2.2).

$$P = \left(\frac{U_1 U_2}{Z} \cos \delta - \frac{U_2^2}{Z} \right) \cos \theta + \frac{U_1 U_2}{Z} \sin \delta \sin \theta \quad (2.1)$$

$$Q = \left(\frac{U_1 U_2}{Z} \cos \delta - \frac{U_2^2}{Z} \right) \sin \theta - \frac{U_1 U_2}{Z} \sin \delta \cos \theta \quad (2.2)$$

Where, P and Q output by the inverter supply are related to the voltage amplitude, phase angle of inverter output and line impedance. There is a serious coupling.

(1) The impedance of the transmission line used by the high voltage micro-grid is much greater than resistance ($X \gg R$), so the effect of R can be ignored. Equations (2.1) and (2.2) can be written as:

$$P = \frac{U_1 U_2 \sin \delta}{X} \quad (2.3)$$

$$Q = \frac{U_1 (U_1 - U_2)}{X} \quad (2.4)$$

Since phase angle is small, P can be adjusted by the phase angle. Q can be adjusted by voltage amplitude. This method is the traditional droop control ($P - f / Q - V$). Droop control equations are shown in (2.5) and (2.6):

$$f - f_N = k_p (P_N - P) \quad (2.5)$$

$$U - U_N = k_q (Q_N - Q) \quad (2.6)$$

(2) The low voltage micro-grid exhibits pure resistance. Equations (2.1) and (2.2) can be written as:

$$P = \frac{U_1 (U_1 - U_2)}{R} \quad (2.7)$$

$$Q = \frac{U_1 U_2 \sin \delta}{R} \quad (2.8)$$

Droop control equations are shown in (2.9) and (2.10):

$$f - f_N = k_q (Q_N - Q) \quad (2.9)$$

$$U - U_N = k_p (P_N - P) \quad (2.10)$$

Figure 2 uses the same capacity inverter with the same droop coefficient as an example to analyse the causes of reactive power error. (E_1, Q_1) and (E_2, Q_2) are the actual operating points for two inverters operating in parallel. It can be seen that the output reactive power is unbalanced due to the different line impedances [7].

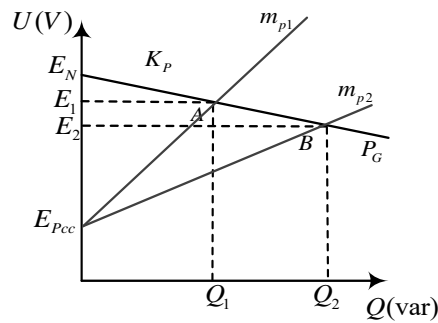


Figure 2. Traditional Q-V droop control.

From equations (2.4) and (2.6), it can be approximated as follows:

$$\Delta Q_{err} = \frac{Q_1 - Q_2}{Q_1} \approx \frac{R_2 - R_1}{R_2 + K_q E_{PCC}} \tag{2.11}$$

From equation (2.11), the distribution error is related to the line impedance, droop coefficient and inverter output voltage.

In summary, the transmission impedance components of lines are diverse and the use of two droop control is cumbersome. In order to solve this problem, this paper introduces a virtual impedance to cover the previous impedance, that is, the virtual impedance method.

3.Improved droop control strategy based on virtual impedance

3.1Power decoupling analysis of virtual impedance is introduced

The virtual impedance method firstly obtains the inductor current, I_0 , at the output side of the inverter through sampling. I_0 multiplied by Z_v to form a feedback loop. U_{ref} is obtained according to the traditional droop control. U_{ref} minus the voltage drop from the virtual impedance is the U_{ref}^* . Then passes the voltage outer loop PI control link and current inner ring P control link, finally obtain SPWM modulation signal control the inverter. Express it as equation (3.1):

$$U_{ref}^*(s) = U_{ref}(s) - Z_v(s)I_0(s) \tag{3.1}$$

Figure 3 shows an equivalent system diagram with virtual impedance added. The impedance between the DG and the bus in low voltage micro-grid $Z_L = R + jX$ is resistive without adding the virtual impedance. First is to remove the DG and add a virtual generator, VG, which is still connected to the N point through the virtual impedance $Z_v = R_v + jX_v$. When $|X_v| \gg |Z_L|$, the sum of Z_v and Z_L is perceptual. Droop control is applied to VG, so that P_0 and Q_0 can be decoupled [8].

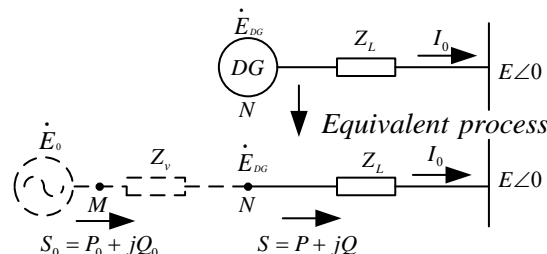


Figure 3. Equivalent system diagram after adding virtual impedance.

(1)Active power decoupling

The virtual impedance used here considers the inductance, since it does not lose active power on it. Therefore $P_0 = P$, and the decoupling control of M active power can be accomplished by changing the power angle, δ , of the virtual generator.

(2)Reactive power decoupling

Line impedance $Z_L = R + jX$, satisfy $\sin \theta = \frac{X}{Z}$ and $\cos \theta = \frac{R}{Z}$. Substitute it into equation (3.2):

$$Q = \frac{U_2}{|Z|} [(U_1 \cos \delta - V) \sin \theta - U_1 \sin \delta \cos \theta] \tag{3.2}$$

After finishing:
$$Q = \frac{U_2}{R^2 + X^2} [(U_1 \cos \delta - U_2)X - U_1 R \sin \delta] \tag{3.3}$$

At point M, $Z_M = R + j(X + X_v)$. According to equation (3.3):

$$Q_N \approx \frac{U_2 [(E_0 - U_2)(X_v + X) - X_v (E_0 - U_2)^2]}{R^2 + (X + X_v)^2} = \frac{(E_0 - U_2)(U_2 X - E_0 X_v + 2U_2 X_v)}{R^2 + (X + X_v)^2} \tag{3.4}$$

According to equation (3.4), Q decoupling control of N point can be realized by changing E_0 .

3.2 Improved droop control strategy by introducing virtual impedance

Figure 4 shows the structure of a dual-loop control system based on a virtual impedance feedback loop. The essence of the virtual impedance introduced in figure 4 is to multiply the collected current signal by the virtual impedance value and introduce it into the voltage regulator, which helps to increase the stability of the system and reduce the influence of the circulation [5].

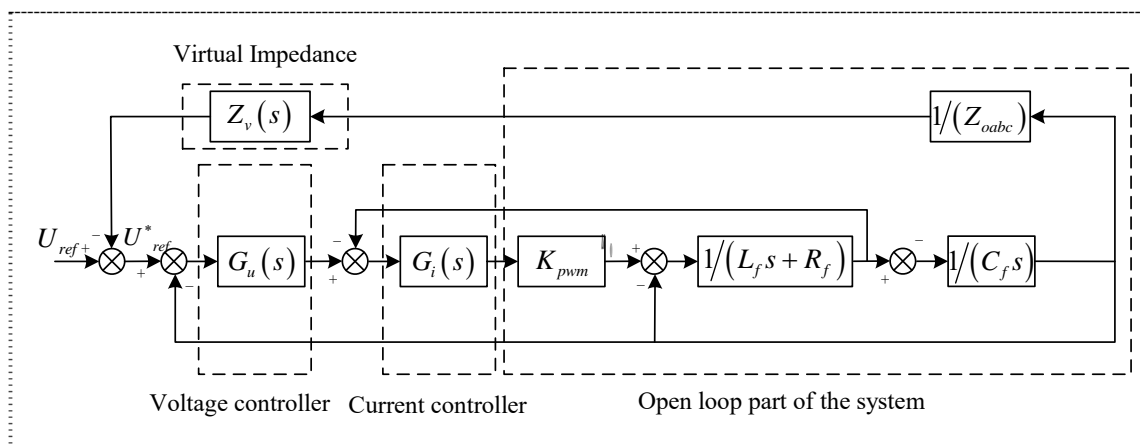


Figure 4. Structure diagram of double loop control system based on virtual impedance feedback link.

In order to make the system have good stability and dynamic response speed, voltage outer loop and current inner loop adopt PI control and P control respectively. $G_u(s)$ and $G_i(s)$ are shown as equations (3.5) and (3.6) respectively:

$$G_u(s) = K_{up} + K_{ui}/s \tag{3.5}$$

$$G_i(s) = K_{ip} \tag{3.6}$$

In the equations (3.5) and (3.6), K_{up} is proportional coefficient of the voltage outer loop PI controller.

K_{ui} is integral coefficient of the voltage outer loop PI controller. K_{ip} is proportional coefficient of the current inner loop P controller.

Different from traditional droop control, this article adds a control loop to the traditional droop control. After adding, the voltage reference can be expressed as equation (3.1). Substitute equation (3.1) into $U_0 = G_u(s)U_{ref}^* - Z_0(s)I_0(s)$. It can be expressed as equation (3.7):

$$U_0 = G(s)U_{ref} - [Z_0(s) + G(s)Z_v(s)]I_0 \quad (3.7)$$

$$G(s) = \frac{k_{ip}k_{up}k_{pwm}S + k_{ip}k_{ui}k_{pwm}}{LCS^3 + (k_{ip}k_{pwm} + r)CS^2 + (k_{ip}k_{up}k_{pwm} + 1)S + k_{ip}k_{ui}k_{pwm}} \quad (3.8)$$

$$Z_0(s) = \frac{(k_{ip}k_{up}k_{pwm}L_v + L)S^2 + (k_{ip}k_{ui}k_{pwm}L_v + k_{ip}k_{pwm} + r)S}{LCS^3 + (k_{ip}k_{pwm} + r)CS^2 + (k_{ip}k_{up}k_{pwm} + 1)S + k_{ip}k_{ui}k_{pwm}} \quad (3.9)$$

Where, $G(s)$ is the voltage gain transfer function. $Z_0(s)$ is the equivalent output impedance of the closed-loop system of the inverter.

After adding the new virtual impedance, the new equivalent output impedance is $Z_{ov}(s)$. The voltage proportional gain function is $G(s)$. R_v can be ignored. It can be expressed as equation (3.10):

$$Z_{ov}(s) = Z_0(s) + G(s)Z_v(s) \quad (3.10)$$

From equation (3.10), after introducing virtual impedance feedback link, the impedance characteristic of the inverter output can be flexibly changed, improving the droop characteristic [4].

4. Simulation analysis

In order to verify the improved droop control scheme proposed in this paper, the micro-grid system as shown in figure 5 is built in the Matlab/Simulink environment for simulation.

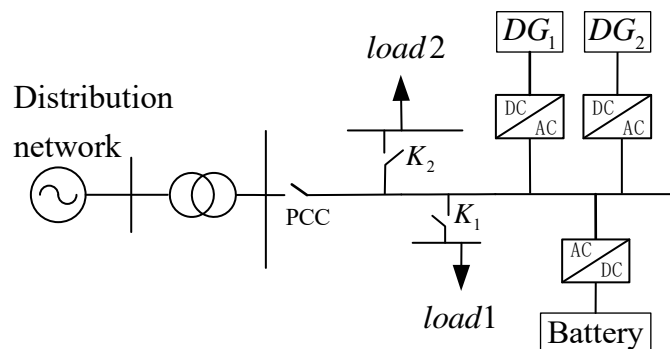


Figure 5. Micro-grid architecture.

Example 1 verifies the influence on the distribution of power before and after the virtual impedance is introduced under the condition that the droop coefficient is equal and the load changes. Example 2 verifies the influence of the distribution of power before and after the virtual impedance is introduced under the condition that the droop coefficient is not equal and the load changes. The simulation time is set to 10s. K_1 closed at 1s and disconnected at 7s. K_2 closed at 4s.

Example 1: When the droop coefficient of DG_1 and DG_2 is equal.

When no virtual impedance is added, the active power output from the two inverters which is shown in figure 6 and the reactive power in figure 7.

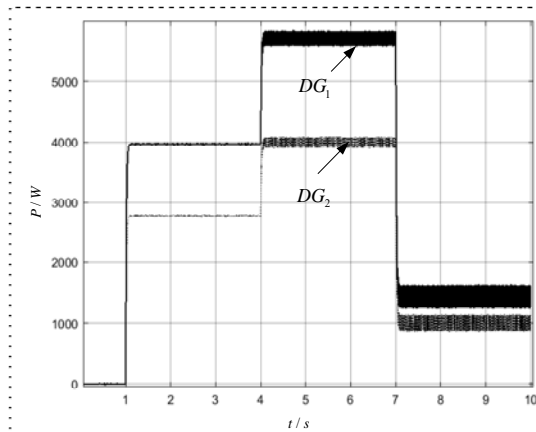


Figure 6. Active power of DG_1 and DG_2 without virtual impedance.

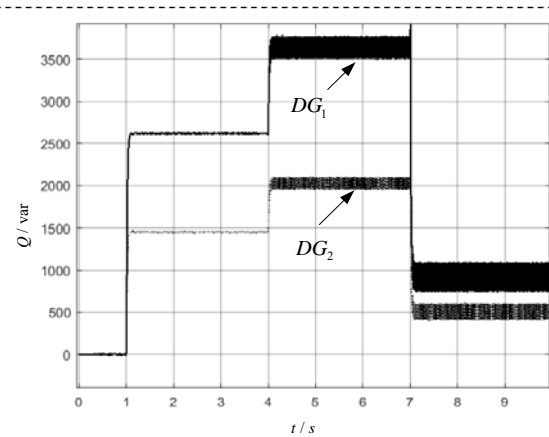


Figure 7. Reactive power of DG_1 and DG_2 without virtual impedance.

Due to the power coupling between active and reactive power, even if the droop coefficient is considered to be the same, the active and reactive power cannot be evenly distributed during the load switching process.

When virtual impedance is added, the active power output from the two inverters which is shown in figure 8 and the reactive power in figure 9.

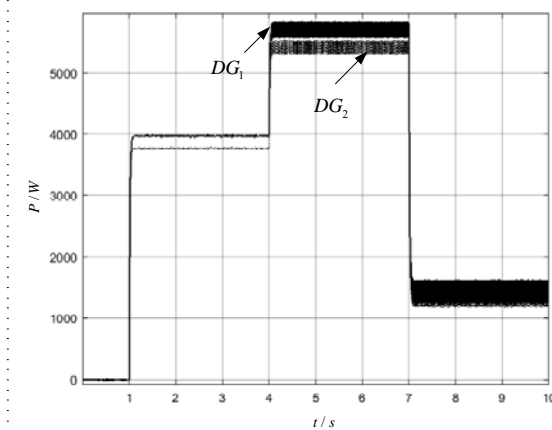


Figure 8. Active power of DG_1 and DG_2 with virtual impedance.

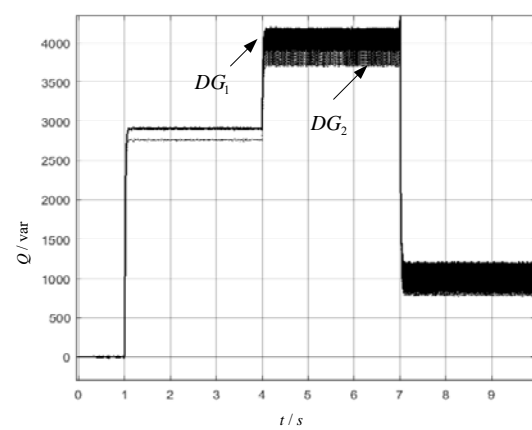


Figure 9. Reactive power of DG_1 and DG_2 with virtual impedance.

From Figure 8 and Figure 9, in the case of adding virtual impedance, the average distribution of active and reactive power is realized in the process of changing. The disturbance of the system is reduced, and the decoupling control of active and reactive power is realized.

Example 2: When droop coefficient of DG_1 and DG_2 is 1:2.

(1) When no virtual impedance is added, the active power output from the two inverters which is shown in figure 10 and the reactive power in figure 11.

Due to the existence of power coupling between active and reactive power, the active power and reactive power of the output cannot be allocated strictly in accordance with 2:1 in the switching load process.

(2) When virtual impedance is added, the active power output from the two inverters which is shown in figure 12 and the reactive power in figure 13.

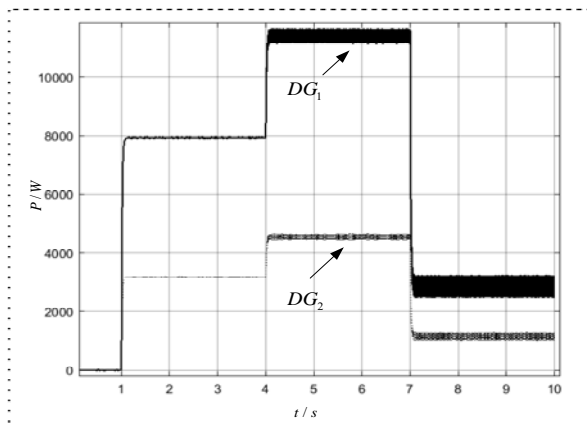


Figure 10. Active power of DG_1 and DG_2 without virtual impedance.

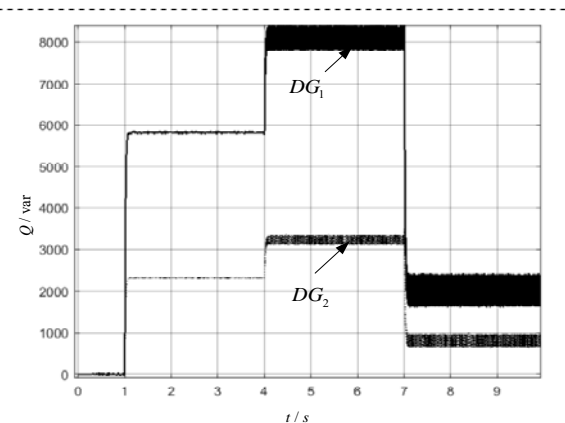


Figure 11. Reactive power of DG_1 and DG_2 without virtual impedance.

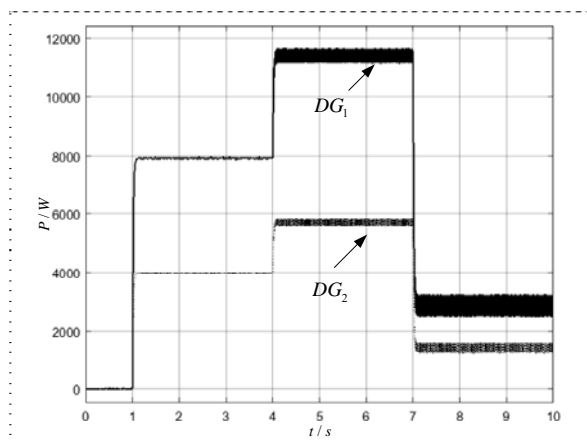


Figure 12. Active power of DG_1 and DG_2 with virtual impedance.

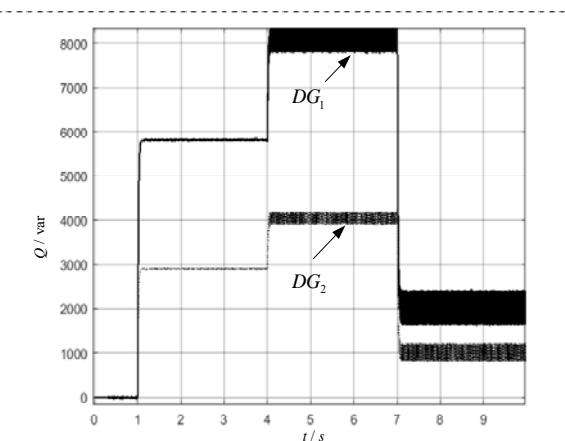


Figure 13. Reactive power of DG_1 and DG_2 with virtual impedance.

By adding a virtual impedance in the process of switching load, the active and reactive power output can basically be allocated according to the droop coefficient, which reduces the system disturbance and enables the decoupling control of active and reactive power.

5. Conclusion

Due to the influence of line impedance, the power of droop control unit running in parallel cannot be reasonably distributed. In this paper, the traditional P - f and Q - V droop control was improved. The virtual impedance control loop was added to traditional droop control, so that DG in micro-grid can complete the decoupling control of power. The improved droop control can effectively perfect the power distribution relationship between the DG units. The active and reactive power output can basically be allocated according to the droop coefficient.

Due to the time limit, there are still many deficiencies in this paper, which requires further research in the later stage, mainly including:

During the simulation, when the load power varies greatly, it is difficult to maintain the micro-grid's voltage and frequency at the rated value.

When the value of the virtual impedance is large, the inverter output voltage decreases.

6. References

- [1] Wu T, Liu Z and Liu J 2016 *IEEE Trans. Power Electron.* **31**(8) 5587-5603
- [2] Zhu S S, Wang F, Guo H, Wang Q F and Gao Y X 2018 *Proc. Chin. Soc. Electr. Eng.* **38**(01) 72-84 (in Chinese)

- [3] Wang C S, Li W, Wang Y F, Meng Z and Yang L 2017 *Proc. Chin. Soc. Electr. Eng.* **37(01)** 84-97 (in Chinese)
- [4] Zhu Y X, Fang Z, and Fang W 2015 *IEEE Trans. Power Electron.* **30(12)** 6706-19
- [5] Guo L, Feng Y B and Li X L 2016 *Proc. Chin. Soc. Electr. Eng.* **36(4)** 927-936 (in Chinese)
- [6] Mahmood H, Michaelson D and Jiang J 2015 *IEEE Trans. Power Electron.* **30(3)** 1605-17
- [7] Sun X F, Liu B J, Chen D, Wang B C and Wang D Y 2017 *Power Acta. Energi. Sin.* **38(02)** 309-316 (in Chinese)
- [8] Cheng Q M, Gao J, Cheng Y M, Zhang Y, Yu D Q and Tan F R 2018 *Power Sys. Techno.* **42(01)** 203-209 (in Chinese)

7.Acknowledgment

This work is supported by Education Committee Foundation of Liaoning province (JFL201715401).

Analysis of Hierarchical and Time-phased Model of Large-scale Power Grid Based on Fp-growth Algorithm

Tianyue Wang¹, Jinxiu Hou² and Zhihong Yu²

¹North China Electric Power University, Beijing, China

²China Electric Power Research Institute, Beijing, China

E-mail: weety_W@163.com

Abstract. The scale of UHV AC/DC hybrid power grids in China is continuously expanding, and the operational characteristics of power grids have undergone profound changes. With the advancement of measurement technology and communication technology, power data has grown rapidly. Therefore, data mining technology is required to provide safety warnings and risk prevention, and intelligently adjust control strategies to help dispatchers correct the operating status of the power grid. This paper adopts association rules analysis based on fp-growth to construct a hierarchical and time-phased analysis model of power grid, giving association rules for different security and stability levels of the power grid at different time phases. Based on actual historical data of the large-scale power grid and the application of hierarchical and time-phased analysis mode, the association rules of overload conditions of different time periods are extracted.

1. Introduction

At present, long-distance, high-power transmission, extensive access to new energy, and increased interaction between flexible loads and the grid have increased the difficulty of dispatch control. Faced with the complex and ever-changing power grid situation, it is difficult to meet the requirements of high-level security and stability of the power grid, relying on traditional power grid analysis and control technologies. The increasingly developed power grid technology, combined with big data mining analysis and artificial intelligence technology, has become the main trend of future power grid development [1].

Dispatching centres at various levels have accumulated a large amount of dispatching operation data. Based on the Synchronous Vector Measurement Unit (PMU), the sampling rate is 100 times per second, which provides uninterrupted power system synchronization operation data. On the dispatching table, an on-line security and stability analysis is performed every 15 minutes, and the data amount and the result data amount can reach about 1G, and the data amount exceeds 2T in a month, and the data volume is astonishing [2]. Therefore, data mining technology is required to mine knowledge related to the safety and stability of power grids from massive amounts of power data, enhancing the ability of dispatching departments to control the power grid.

The core of big data analysis is data mining algorithms, including decision trees, artificial neural networks, and support vector machines, etc. The analysis of the safety and stability of power systems is mainly through two methods: predicting the system's disturbed trajectory or giving safe and stable identification information [3]-[5].

The method of predicting the disturbed trajectory of the system is based entirely on numerical sequence analysis and data mining, and does not rely on prior knowledge of power system mathematical models and parameters. The literature [6] proposes a method for predicting wide-area



time and space big data, and discovers the time-space relationship and variation law of power grids from big data, so as to predict the future trajectory and weak links of the power grid, and effectively predict and prevent future stability of the power grid. This kind of method only uses response information, the principle is simple and easy to implement.

Another method is to discriminate the safety and stability of the power grid directly, find the mapping relationship between data characteristics and system security and stability from the power big data sample set, and construct a classifier to predict the safety and stability of the system online without human experience. The literature [7] applied cluster analysis to the operation state of the power grid to obtain finer rules in different forms. The literature [8] introduces the time series related association rule mining algorithm into the transient stability assessment. The obtained correlation result can provide decision-making basis for the staff. The literature [9] makes use of the characteristics of rapid learning stability of the extreme learning machine to quickly judge the transient stability results. The improved algorithm can continuously update the rolling data to adapt to the dynamic process of the power system.

2. Association rule analysis

2.1. Associative classification principle

Association rule is one of the important machine learning methods. It is mainly used to explore frequent patterns, association dependencies, or causal structures among project collections, and discover valuable association rules based on the frequency of occurrences among data item sets [10].

Let dataset D contain N samples and Y is a collection of categorical variables for the samples in D . Each sample d in D is represented by a set of characteristic variables x and a category variable y . Let I be the set of all the feature variables in data set D . A class association rule is as follows

$$x \Rightarrow y \quad (1)$$

In the formula, x represents a set of characteristic variables, $x \subseteq I$, $y \in Y$, x and y are disjoint item sets.

There are two important metrics for measuring an association rule - support and confidence. $\text{support}(X \Rightarrow Y)$ is the proportion of transaction item sets containing $|X \cup Y|$ item set in the transaction database D , defined as

$$\text{support}(X \Rightarrow Y) = \frac{|X \cup Y|}{|D|} \quad (2)$$

Support determines the frequency of occurrence of item set $|X \cup Y|$, $|X \cup Y|$ represents the number of transactions contained $|X \cup Y|$ in the data set, $|D|$ indicates the total number of transactions in the data set.

Confidence is the percentage of under the condition that data set D contains item set X , it also contains item set Y , defined as $\text{conf}(X \Rightarrow Y)$

$$\text{conf}(X \Rightarrow Y) = \frac{\text{support}(X \cup Y)}{\text{support}(X)} \times 100\% \quad (3)$$

The role of confidence is to describe the degree of trust of the rules, and support describes how often the rules appear. Mining association rules is to find the association rules that meet the user's minimum support and minimum confidence threshold from all transaction data sets. The basic process of association rule analysis is shown in Figure 1.

It is divided into the following two steps [11]:

Step one: Find the frequent item set in the data set D . That is, the support degree is calculated according to the formula (2) and according to the minsupport given by the user, the frequent item sets which support degree is not less than the minimum support degree are selected.

Step 2: Generate association rules using frequent item sets. That is, from the frequent item set obtained in step 1, the rule satisfying the minimum confidence is found according to the formula (3).

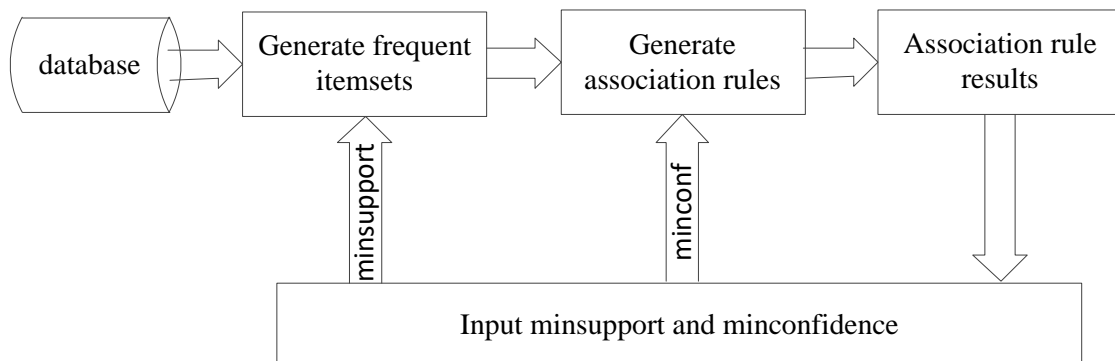


Figure 1. Basic model of association rules.

2.2. FP-Growth algorithm

Mining frequent item sets is an important and time-consuming step in the association analysis process [12]. As one of the most classic algorithms, fp-growth can avoid the generation of a large number of candidate sets and only need to scan the database twice to quickly find frequent item sets. To facilitate efficient processing, we use a new data structure called FP-tree. It can be divided into two steps: FP-tree construction and frequent pattern mining based on FP-tree. The process is shown in the figure 2.

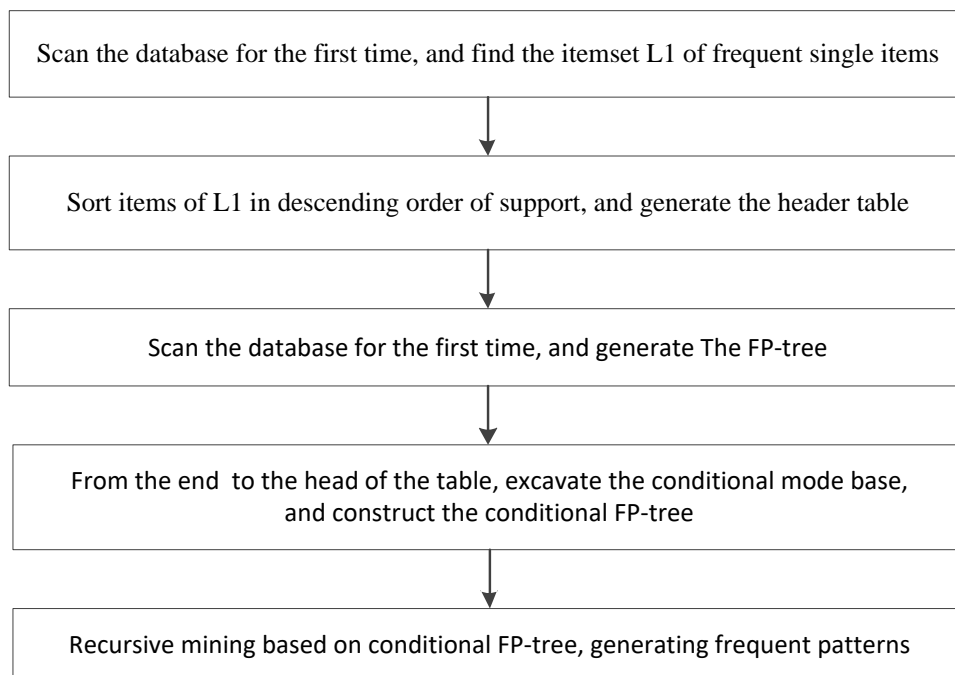


Figure 2. The process of FP-Growth algorithm.

The general idea is to find the frequent single items and then we partition the database based on each such item. Then we recursively grow frequent patterns by doing the above iteratively or recursively for each partitioned database, also called conditional database. The whole mining can be summarized as follows. We recursively construct and mine conditional FP-trees. Until the result FP-tree is empty or until it contains only one path, the single path will generate all the combinations of its sub-paths each

of which is a frequent pattern. Pseudo code of frequent pattern mining algorithm based on FP-tree such as Table 1,

Table 1. Pseudo code of extracting frequent item sets.

Input: constructed FP-tree
Output: Full set of frequent patterns
Let the set of items in the header table be I
for item α_i in I
FP-Growth(FP-tree, α_i)
End
FP-Growth(FP-tree, α_i)
if Tree contains a single Path then
for the combination of each node in Path (indicated as β)
generate the mode $\beta \cup \alpha$, support_count equals to
the minimum support value of each node in β
else for α_i in the header table of Tree
{
generate the mode $\beta = \alpha_i \cup \alpha$, support_count= α_i .support_count
construct the conditional pattern base of β , and conditional FP-Tree $_{\beta}$
if Tree $_{\beta} \neq \emptyset$ then
FP-Growth(FP-tree, α_i)
}

3. Association analysis model

The smart grid dispatching technical support system utilizes a global position system (GPS) and has synchronous timing capabilities, realizing a wide-range space-time unified measurement of large-scale power grids. Therefore, the accumulation of wide-area time-space measurement information in the smart grid scheduling technical support system can accumulate over a long period of time (days, months, and years), which can better reflect the spatial-temporal correlation characteristics of the power grid and have a very large value of excavation and utilization[13]. This paper makes use of the spatio-temporal characteristics of data to build a hierarchical and time--phased model for association analysis. It is aimed at a variety of grid security and stability issues and refines the association rules.

3.1. Hierarchical association analysis

At present, China has formed a hierarchical dispatching operation model of national dispatch, regional dispatch, provincial dispatch, city dispatch, and county dispatch. Due to the division of the management scope and responsibilities of the dispatch, generally according to the geographical location and voltage level, and according to the characteristics of the administrative region and the power system, the scheduling functions and priorities at different levels are different. National dispatch focuses on UHV AC/DC transmission power and emergency support capabilities. The regional dispatch focus on more concerned with the critical liaison sections of the regional power grid, and the provincial dispatch directly controls the output of key power plants in the region and controls the load [14].

At the same time, the security and stability of the power grid also presents typical regional characteristics and spatial correlation. According to different levels of grid security and stability issues, a hierarchical correlation analysis model is established as figure 3.

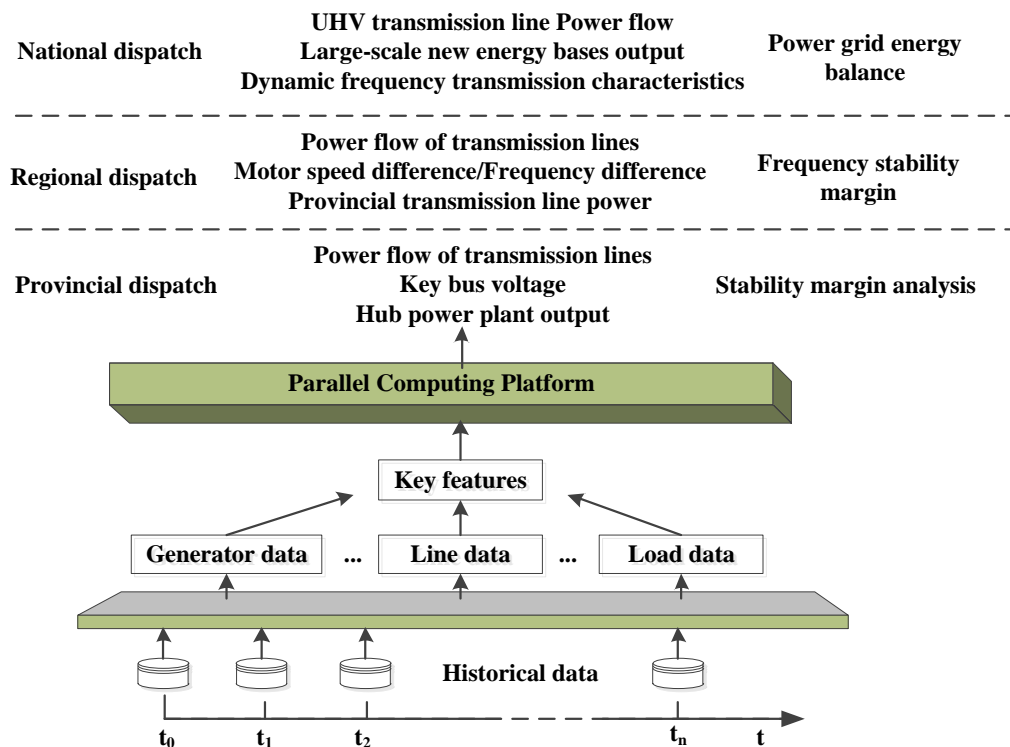


Figure 3. Hierarchical association analysis model.

The hierarchical association analysis model is established through experience and historical data, key factors affecting the stability of different levels of the power grid are obtained, and the combined input feature space is selectively optimized.

3.2. Time-phased association analysis

The power system is a continuous time-varying system, and the power operation data has time correlation, which is reflected in the following two aspects [15]-[17]:

- 1) The change of power grid operation mode is closely related to time, and the output curve and load curve all show some regularity with time. In the actual operation of the power system, the time-varying curves of a large amount of measurement and calculations contain the inherent operating characteristics of the power system.
- 2) The large amount of operational data collected by the dispatch centre, as well as the calculated data and the resulting data, all have time scales. These data are the response of various dynamic indicators of the power system at different times and have the characteristics of time series.

When using the association classification method to model the security and stability analysis, we should fully consider the characteristics of its time series. In general, it is difficult to analyse the entire time series in data mining. This paper proposes a time-phased association analysis model, which divides the system state data into local sub-segments, establishes multiple feature input spaces, and obtains association rules at different time periods.

4. Case study and analysis

Based on the online historical data accumulated by a provincial dispatching centre for 4 months, an association analysis model for the heavy load situation of the provincial power grid is established. A total of 6500 samples were collected and organized. The transmission power of important tie lines was extracted from the online data as input features of the model, including two 750kV sections, seven 330kV sections and six 220kV sections. The key sections are usually selected by experts through long-

term operating experience. They are high-voltage grade and large-capacity transmission lines or line sets, which are important security features of the power grid [18].

In this paper, according to the dispatching centre in the calculation of grid operation mode, the line stability limit value is given to evaluate the risk degree of the whole network section. The limit values of the critical sections are generally obtained based on off-line analysis and simulation calculations of the power grid to achieve ‘dimension reduction’ control of complex power systems [19]. According to the ratio of the section power to the stability limit value, determine the risk degree of the safe and stable operation of the grid, and set the evaluation indicators as shown in the Table 2.

Table 2. Evaluation indicators.

Section power/ limit value	Stable risk level
0~50%	0
50%~70%	1
70%~90%	2
90%~110%	3
110%~130%	4
>130%	5

Table 3. Partial association rules.

23:00~1:15	Rule 1. Support is 20.69% Confidence is 87.5%. Section CS [-1400, -1200) MW → Stable risk level [16,18]
	Rule 2. Support is 13.44% Confidence is 87.5%. Section DQ [500,600) MW and Section HQ [-400,-200) MW → Stable risk level [16,18]
	...
1:30~4:45	Rule 1. Support is 10.04% Confidence is 83.33%. Section HZ [-400,-200)MW → Stable risk level [16,18]
	Rule 2. Support is 10.04% Confidence is 83.33%. Section CS [-1400, -1200) MW → Stable risk level [16,18]
	...
5:00~8:30	Rule 1. Support is 17.83% Confidence is 87.5%. Section HZ [-100,200)MW → Stable risk level [16,18]
	Rule 2. Support is 18.38% Confidence is 90.63%. Section DQ [500,700) MW and Section HQ [-400,-300) MW → Stable risk level [16,18]
	...
8:45~18:15	Support is 15.16% Confidence is 92.8%. Section CS [-1700, -1400) MW → Stable risk level [16,18]
	Rule 2. Support is 13.14% Confidence is 81.06%. Section DQ [500,600) MW and Section HQ [-400,-200) MW → Stable risk level [16,18]
	...
18:30~22:45	Rule 1. Support is 16.60% Confidence is 85.71%. Section HZ [-300,300)MW → Stable risk level [16,18]
	Rule 2. Support is 19.37% Confidence is 97.6%. Section DQ [500,700) MW and Section HQ [-400,-200) MW → Stable risk level [16], [18]
	...

When the power flow is approaching or even beyond the limits of safe and stable operation, once the disconnection or other serious failure occurs, there may be grid safety and stability problems. According to the statistical analysis of the load situation of the power grid, the entire time series sample is divided into five time phases, and the association rules are mined separately.

In order to ensure the reliability of the extracted association rules, we consider setting the minimum confidence threshold to 80%. In the actual operation of the power grid, severe overload occurs less frequently. If the minimum support threshold is set too high, an effective overload rule cannot be obtained. Therefore, the minimum support threshold is set to 10%. According to the evaluation rules of the table, the overall degree of danger of the grid of each sample is calculated. The degree of danger [16]-[18] is a situation where the grid is overloaded and the safety risk is high. It needs the attention of the dispatcher. Mining partial association rules as shown in Table 3.

From the analysis of the grid structure and the distribution of the power grid in the province, it can be seen that the section CS is an important current collection channel. The new energy generated in the vicinity of this area is all sent through it and then sent through the DC line in a large scale. section CS has long been in heavy-duty operation. From the generated rules, we can also see that in the period of 8:45~18:15, when the new energy output is large, section CS [-1700, -1400) MW \rightarrow the degree of danger of the power grid [16], [18], confidence degree is 92.8%. Through the above rules, the dispatcher is informed of the sections that require special attention and the dangerous section of the section at different time periods.

It can be seen that the generated rules are in line with the operating rules of the power grid and the operational experience accumulated by the operating personnel for a long time. At the same time, it can also help the dispatching operators to find some unknown and potential operating laws of the power grid and provide auxiliary decision-making.

5. Conclusion

The rapid accumulation of power data and the rapid development of computer and big data technologies have provided new directions for the development of power grids. In this paper, the method of correlation analysis is applied to the analysis of power grid security and stability, and the hierarchical and time-phased correlation analysis model is established. Relying on the actual historical data of large-scale power grids, the correlation analysis between the operating status of key sections of the power grid and the heavy-load overload conditions of the power grid is conducted, and the association rules under different time phases are obtained to demonstrate the feasibility of the model. With the rapid development of the power grid in the future, this method can provide assistant decision-making for dispatchers, to accelerate understanding of the power grid, and increase operational experience.

6. References

- [1] LIN Weifang, TANG Yong, The “2·4” blackout in Brazil and its implications for the safe and stable operation of power grids [J]. Automation of Electric Power Systems, 2011, 35(09): 1- 5. [2017-09-12].
- [2] Yu Zhihong, Huang Yanhao, et al. Extraction method of stable operation rules based on time series correlation analysis [J/OL]. Proceedings of the Chinese Society of Electrical Engineering, 2015, 35(03):519-526.
- [3] Huang Ruoyan. On-Line Power System Transient Stability Online Identification and Algorithm Based on Energy Function Method [D]. Huazhong University of Science and Technology, 2013.
- [4] Wu Wei. Research on real-time discrimination and control technology of power system transient stability based on response [D]. China Electric Power Research Institute, 2014.
- [5] Zhang Chun, Research on Power System Transient Stability Assessment Method Based on Association Rules [D]. North China Electric Power University, 2017.
- [6] Liu Daowe, Zhang Dongxia. Quantitative assessment of the stability situation of large-scale power grids under the space-time big data environment and the construction of adaptive prevention and control system [J]. Chinese Journal of Electrical Engineering, 2015, (02): 268-276.
- [7] Jiang Weiyong, Research on online comprehensive security early warning and emergency dispatch decision of power grid [D]. Beijing: Tsinghua University, 2008
- [8] Kamwa, S. Samantaray and G. Joos, On the accuracy versus transparency trade-off of data-mining models for fast-response PMU-based catastrophe predictors, 2013 IEEE Power & Energy Society General Meeting, Vancouver, BC, 2013, pp. 1-1.

- [9] Huang Yanhao, Yu Zhihong. Fast determination strategy for large power grid based on massive online historical data [J]. Proceedings of the CSEE, 2016, 36(03): 596-603.
- [10] Huang Tianen, Sun Hongbin. Knowledge management and advanced security early warning based on power grid operation simulation big data [J]. Power System Technology, 2015, 11:3080-3087.
- [11] Huang Tianen, Sun Hongbin. Online distributed security feature selection based on power grid operation big data [J]. Automation of Electric Power System, 2016, 04:32-40.
- [12] Zhou Yanzhen, Power System Transient Stability Analysis and Preventive Control Based on Data Mining Technology [D]. Beijing: Beijing Jiaotong University, 2017
- [13] Yu Z H, Huang Y H, Xie C, et al. Operation rule extracting based on time series association analysis in transient stability study: International Conference on Power System Technology, 2014[C].
- [14] I. Kamwa, S. R. Samantaray and G. Joos, Catastrophe Predictors From Ensemble Decision-Tree Learning of Wide-Area Severity Indices, in IEEE Transactions on Smart Grid, vol. 1, no. 2, pp. 144-158, Sept. 2010.
- [15] Chi Lining. Classification algorithm mining algorithm based on FP-Growth and its application [D]. Qingdao University, 2012.
- [16] He M, Vittal V, Zhang J. Online dynamic security assessment with missing pmu measurements: A data mining approach [J]. IEEE Transactions on Power Systems, 2013, 28 (2):1969-1977.
- [17] Sun Hongbin, Wang Kang, Zhang Boming, et al. Transient Stability Rule Extraction Using Linear Decision Tree [J]. Proceedings of the CSEE, 2011(34): 61-67.
- [18] Wang B, Fang B, Wang Y, et al. Power System Transient Stability Assessment Based on Big Data and the Core Vector Machine [J]. IEEE Transactions on Smart Grid, 2016:1
- [19] Yan Jianfeng, Yu Zhihong, Tian Fang, et al. On-Line Dynamic Safety Assessment and Early Warning System of Power System [J]. Proceedings of the CSEE, 2008(34):87-93.

Deep Learning Algorithm for Preliminary Siting of Substations Considering Various Features in Distribution Network Planning

Liang Feng¹, Can Cui¹, Runze Ma^{2,3}, Jian Wu¹, Yang Yang¹, Xiaolei Zhang⁴, Shengyuan Liu²

¹ Economic & Technology Research Institute, State Grid Shandong Electric Power Company, Jinan, China

² College of Electrical Engineering, Zhejiang University, Hangzhou, China

³ Powerchina Huadong Engineering Corporation Limited, Hangzhou, China

⁴ State Grid Shandong Electric Power Company, Jinan, China

E-mail: eelsy@zju.edu.cn

Abstract. Substation siting and sizing planning is one of the important contents of distribution network planning, which directly affects the results of subsequent distribution network planning, and affects the quality of power supply and the economy of power grid operation. Given this background, a deep learning algorithm for preliminary siting of substations in distribution network planning is proposed in this work. Features related to the principle of siting of substations are extracted and multichannel data characterization are utilized. Then, the features are integrated into a convolutional neural network (CNN), which is one of deep learning algorithms, based on actual geographical relationships. Next, the preliminary siting of substations for the subsequent planning process is completed. Finally, the validity of the proposed algorithm considering different input features is demonstrated on a distribution network of one certain province in China by case studies and comparisons. The simulation results show that the proposed deep learning algorithm for preliminary siting of substations is more accurate with more input features, and is better than shallow learning algorithms, thus can be employed to preliminary siting of substations in distribution network planning.

1. Introduction

The planning of the substations and grids is one of complex issues of distribution network planning [1], [2]. Further, substation siting and sizing planning are important contents of distribution network planning, which directly affects the results of subsequent distribution network planning, and affects the quality of power supply and the economy of power grid operation.

The specificity of actual geographical conditions should be taken into consideration in substation siting. Thus, research on the siting of substations has been conducted by some experts and scholars. There are studies to plan the number, capacity, and power supply range of substations, and the substation load capacity is taken as the main constraints of the planning model [3], [4]. The more complex principle of substation siting selection has been considered in some studies, and the corresponding characteristic indexes are extracted. Then, an index system is established, and the candidate areas are evaluated according to the index system and the substation site is selected [5], [6]. In [7]-[9], the heuristic algorithm such as genetic algorithm and particle swarm algorithm are utilized to solve the siting optimization model, and the analytic hierarchy process (AHP) and other evaluation methods are used to modify the siting results. So far, there are mainly three type of planning methods



in the practical application and research: 1) Subjective determination based on the experience of power system planners; 2) Extract general principles of substation siting as characteristic indexes, establish the index system, and evaluate and screen the candidate sites; 3) Plan the substation siting with the number, capacity and power supply scope of the substations considered, and determine whether the substation siting results in the distribution network planning are feasible. If it is not feasible, further adjustments should be made for the substation siting.

In the planning process of substation siting, human judgment is required based on planners' experience in the aforementioned methods. Deep learning is a subfield of machine learning that has evolved from shallow learning. For shallow learning, when it comes to the representation of complex functional relationships, the learning volume is large, the generalization ability is weak, and it is easy to over fit. The data is abstracted by deep learning model through a series of multilayer nonlinear transformations and fewer learning units are used to realize the approximation of more complex functions [10]. The hidden layer increased by deep learning to form a deep network [11] to overcome the problem of gradient dispersion caused by network deepening. The common models [12]-[15] of deep learning include Auto Encoder (AE), Convolutional Neural Network (CNN), Recurrent Neural Networks (RNN), Restricted Boltzmann Machine (RBM), etc.

Given this background, a deep learning algorithm for preliminary siting of substations in distribution network planning is proposed in this paper. Features related to the principle of siting of substations are extracted and multichannel data characterization are utilized. Then, the features are integrated into a convolutional neural network (CNN), which is one of deep learning algorithms, based on actual geographical relationships. Next, the preliminary siting of substations for the subsequent planning process is completed. Finally, the validity of the proposed algorithm considering different input features is demonstrated on a distribution network of one certain province in China by case studies and comparisons.

2. Deep learning algorithm for preliminary siting of substation

Substation siting and sizing planning is one of the important contents of distribution network planning, which directly affects the results of subsequent distribution network planning, and affects the quality of power supply and the economy of power grid operation [16]. To determine the optimal siting of the substations, the principle to be followed includes the terrain and geology where the substations locates; the convenience of transportation, and urban and rural planning are also should be considered [17]. Some terrains (e.g. rivers and roads) do not have the conditions for the construction of substations, and areas with high population densities (e.g. commercial areas) are not suitable for the construction of substations. On the one hand, different properties of land use have different impacts on the preliminary siting and daily operation and maintenance of substations; on the other hand, substation construction has different effects on users of different land properties. Therefore, it is complex to choose the substation site.

In the planning process, the location of the substation is usually assessed by the planners based on the substation siting principle or the established index system, which has high requirements for the planners' experience and is time-consuming and laborious [18], [19]. If an appropriate algorithm is used for preliminary screening through the features related to the planning area and the planning principles, the workload of distribution network planners and their dependence on their experience can be reduced. Because the area involved in the substation siting is relatively large, there are many features related to siting. Therefore, data-intensive problems will be caused and it is difficult for the traditional mode of shallow learning of pattern recognition to handle such high-dimensional features. Therefore, deep learning method is adopted in this paper to extract and learn the characteristics related to the principle of substation siting, and determine whether or not the blocks in the planned area are suitable for substations, so as to perform preliminary siting of substations. Thus, the selection process is based on a large number of proven planning schemes, and the reliance on the planner's experience is reduced. Besides, preliminary siting results can be substituted into the distribution network planning model for further planning calculations.

The basic unit of the convolutional neural network includes a convolutional layer and a downsampling layer [20]. A convolution kernel is used for each feature to be learned in the convolution layer, and neurons are connected to the input of the layer to perform feature extraction using a convolution

operation. The downsampling layer is also called the Pooling Layer. By calculating the average and maximum of a feature in an area of an image, the summary features of the image are obtained and sent to the next convolutional layer. This operation can effectively reduce the dimension of the feature and reduce the probability of over fitting the model. After several convolution and downsampling layers, the extracted features are gradually transformed from low-level to high-level. Finally, all local features are integrated through a fully connected layer, and a classifier or a regression device is added at the top of the network to implement classification or prediction functions [21].

At the convolution layer, multiple features of the image can be learned using multiple convolution kernels, and each feature can be compared to each channel of the image. The network reduces the number of training parameters through sparse connection [22] and weight sharing [23]. The sparse connection means that each neuron is connected with only part of the feature map of the previous layer through the convolution kernel, so that only partial images are perceived. Weight sharing means different neurons learn the same feature using the same set of weight parameters. In addition, in order to prevent over fitting, the dropout technique can also be adopted by convolutional neural network so that some hidden neuron output values are zero, and thus do not participate in the forward and backward propagation process. The complexity of adaptation between neurons is reduced and the over fitting is prevented [24].

A typical convolutional neural network structure (i.e., LeNet5) [25] is shown in Figure 1. There are eight layers of LeNet5: input layer, convolutional layer C1, pooling layer S2, convolutional layer C3, pooling layer S4, convolutional layer C5, fully connected layer F6, and output layer; where sparse connections are applied only in layers C1 and C3 [25], and the number and size of feature maps for each layer are also indicated in Figure 1.

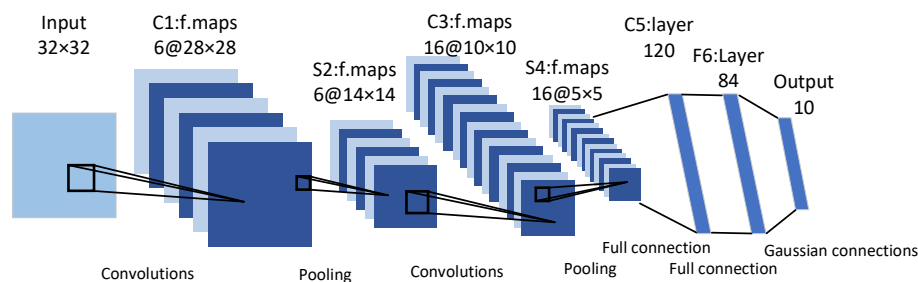


Figure 1. The network structure of LeNet5 [25]

The algorithm for preliminary siting of substations based on CNN is as follows.

(1) Extract the features of land type, terrain, neighbouring substations, etc. The type of land use is represented by the sketch map, and different types are denoted by different colors. Most of the land use planning maps are drawn according to the reference color standard. For the same land type, the land is represented by the same color, and the color of the schematic at a certain pixel can be used to represent the corresponding type of the site. Besides, the terrain can be derived from the GIS system elevation data. If there is no corresponding data, the data can be directly scaled according to the steepness of the terrain, such as 2, 1 and 0 for the definitions of mountains, hills and plains (i.e., plateau, flatland).

(2) Mark the non-image features of the training data and the data to be predicted on the geographic coordinates and align them with the pixels of the image. The training data and the data to be predicted are organized according to the geographic coordinates of the input data vector and the channels (3 to 4 channels for land use type, 1 channel for terrain, and 1 channel to the neighbouring substation), and represent the ground for the input vector in the training data. If substations are contained, the output of the training data is set to 1; otherwise, it is set to zero.

(3) Input the training data and the data to be predicted into the convolutional neural network and set the parameters for prediction.

The flowchart of the method of preliminary siting of the substations based on convolutional neural network (CNN) is shown in Figure 2.

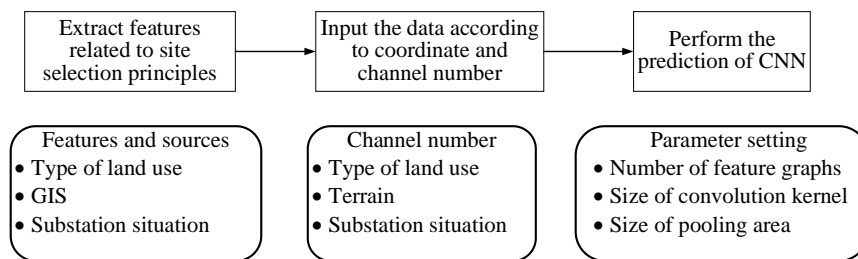


Figure 2. The flowchart of preliminary siting method based on deep learning algorithm

3. Case Studies

In order to demonstrate the effectiveness of the proposed algorithm, a distribution network of one certain province in China is taken as an example. The sketch map of the land use plan and the distribution of the substations in the area is extracted from the distribution network planning reports. Then, the topographic data from Google Earth is extracted to form 2,100 5-channel training data. The size of each training data is 10×10 , including land type (3 channels), terrain (1 channel), and distance from the nearest substation outside the supply area (1 channel). k -fold cross-validation is performed and the training data is randomly divided into 21 clusters (i.e., 21-fold cross-validation). One cluster is used as a test set at a time and the remaining 20 clusters are used as training set.

Take the training data size and characteristics into consideration, the structure of the established CNN network is as follows.

- (1) Input layer: the number of input data channels is 5;
- (2) Convolution layer: convolution kernel is with 5×5 , and the number of feature maps (number of channels) is 4;
- (3) Pooling layer: pooling area is with 1×1 , and the number of feature maps (channels) is 4;
- (4) Convolution layer: convolution kernel is with 5×5 , and the number of feature maps (number of channels) is 4;
- (5) Pooling layer: pooling area is with 2×2 , and the number of feature maps (channels) is 4;
- (6) Output layer: it is fully connected, the number of output data channels is 1, and the activation function is Sigmoid function.

3.1. Preliminary siting results based on deep learning algorithm

After inputting the above data into the CNN network, a total of 2043 data correctly judge whether there is a substation in the concerned area, and the accuracy rate is equal to 97.29%. The correctness of each cluster as a test set is shown in Figure 3, and the number of data clusters for each accuracy rate interval is shown in Figure 4. The results show that it has a high accuracy rate of the judgment that using the CNN of deep learning algorithm for the distribution of existing substations and regional characteristics of learning.

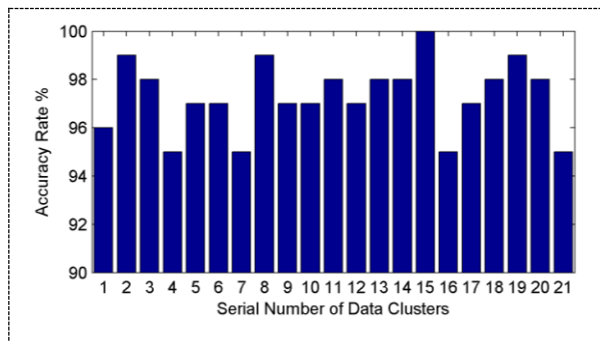


Figure 3. The accuracy rate of each cluster as a test set for deep learning algorithm

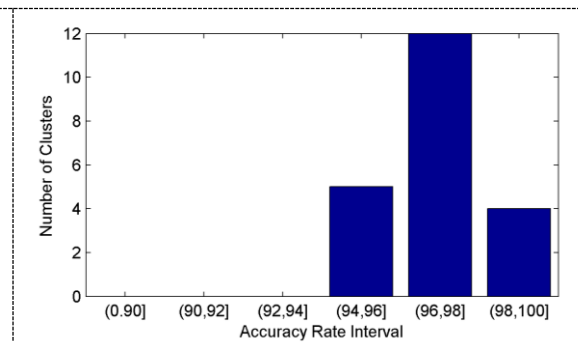


Figure 4. The number of data clusters for each accuracy rate interval for deep learning algorithm

In order to analyse the impact of input features on the accuracy rate of the judgment, the circumstances of lacking in terrain data, lacking in neighbouring substations, and features that contain only the type of land are input to the network, and the results are analysed.

(1) Judgment results in the absence of terrain data

A total of 2019 data correctly judge whether there is a substation in the area, and the accuracy rate is equal to 96.14%. The accuracy rate of judgment for each cluster as a test set is shown in Figure 5, and the number of data clusters for each accuracy rate interval is shown in Figure 6.

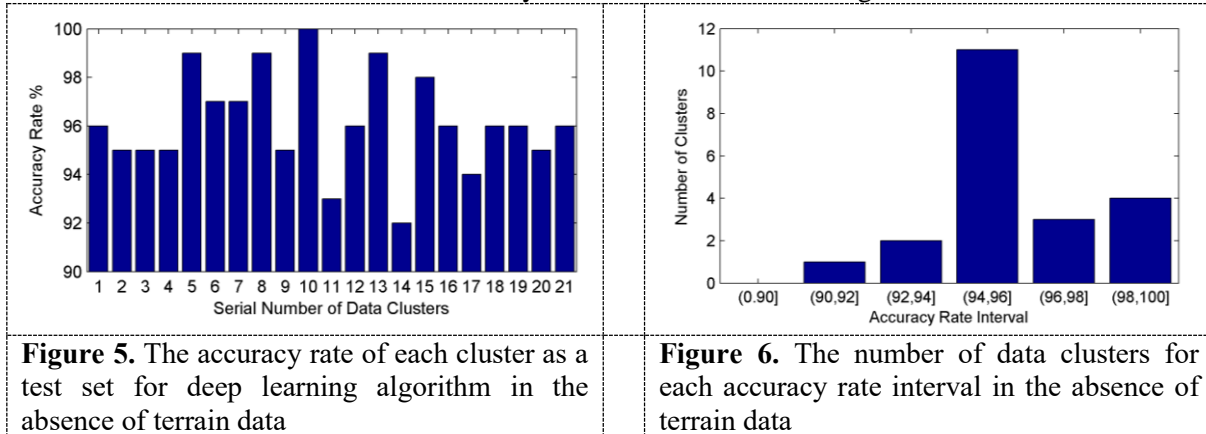


Figure 5. The accuracy rate of each cluster as a test set for deep learning algorithm in the absence of terrain data

Figure 6. The number of data clusters for each accuracy rate interval in the absence of terrain data

(2) Judgment results in the absence of neighboring substations information

A total of 1996 data correctly judge whether there is a substation in the area, and the accuracy rate is equal to 95.05%. The accuracy rate of judgment for each cluster as a test set is shown in Figure 7, and the number of data clusters for each accuracy rate interval is shown in Figure 8.

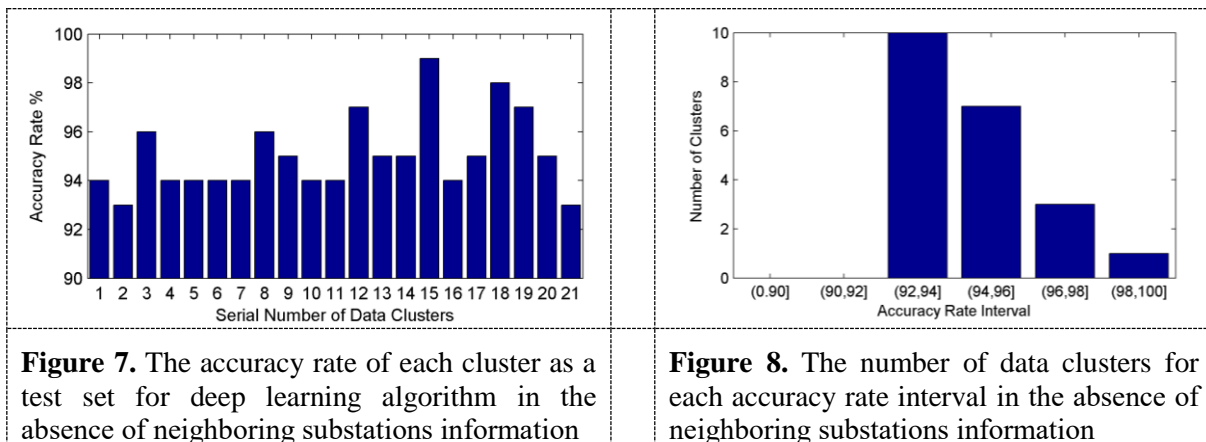


Figure 7. The accuracy rate of each cluster as a test set for deep learning algorithm in the absence of neighboring substations information

Figure 8. The number of data clusters for each accuracy rate interval in the absence of neighboring substations information

(3) Judgment result considering the land type only

A total of 1932 data correctly judge whether there is a substation in the area, and the accuracy rate is equal to 92.00%. The accuracy rate of judgment for each cluster as a test set is shown in Figure 9, and the number of data clusters for each accuracy rate interval is shown in Figure 10.

The results show that the accuracy rate is the lowest when input features only include the type of land (that is, the lack of terrain and neighbouring substation data). The accuracy of some clusters is lower than 90% or even 80%, and the stability is relatively low. When the terrain or neighbouring substation data are added, the accuracy rate of judgment will be improved. The accuracy rate of judgment of each cluster is above 90%, but both are lower than the input data including the terrain and neighbouring substation data simultaneously. It shows that adding terrain features and neighbouring substation features will help improve the accuracy rate of the CNN-based substation pre-siting model in preliminary siting of substations.

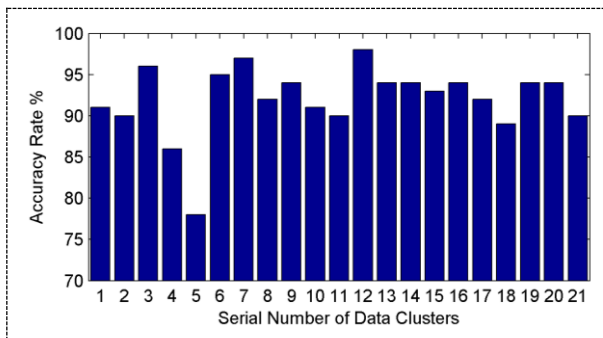


Figure 9. The accuracy rate of each cluster as a test set for deep learning algorithm considering the land type only

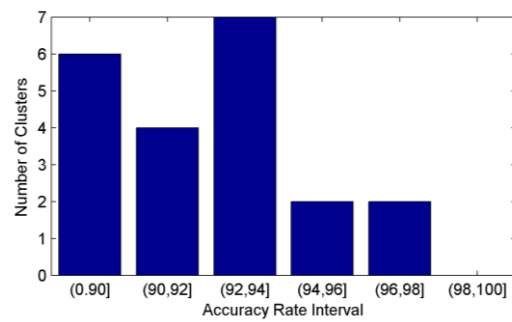


Figure 10. The number of data clusters for each accuracy rate interval considering the land type only

3.2. Comparisons of preliminary siting results with shallow learning algorithms

To demonstrate the superiority of the preliminary siting method based on the convolutional neural network, two commonly used shallow learning models, i.e., Back Propagation (BP) neural network and Radial Basis Function (RBF) neural network, are selected. The input features were input into the above model for preliminary siting of substations. The above 2100 training data are still used and the *k*-fold cross validation method is used. The training data is randomly divided into 21 clusters (i.e., 21-fold cross-validation). One cluster is used as a test set at a time and the remaining 20 clusters are used as training set. The results are as follows.

(1) Judgment results based on BP neural network

A total of 1625 data correctly judge whether there is a substation in the area, and the accuracy rate is equal to 77.38%. The accuracy rate of judgment for each cluster as a test set is shown in Figure 11, and the number of data clusters for each accuracy rate interval is shown in Figure 12.

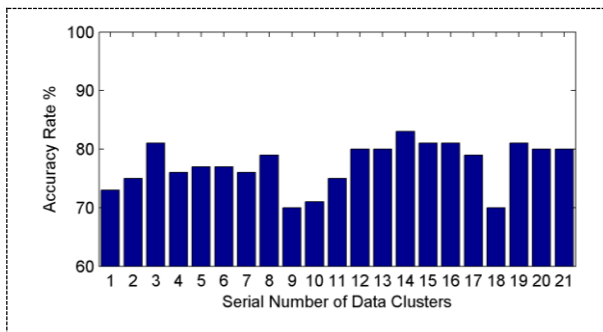


Figure 11. The accuracy rate of each cluster as a test set for BP algorithm

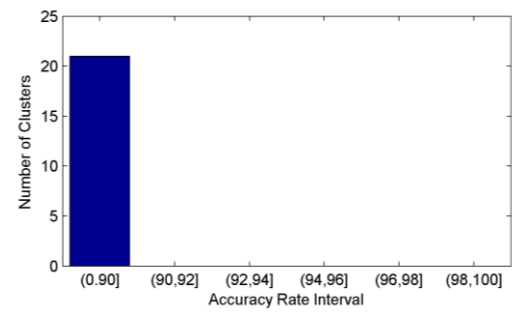


Figure 12. The number of data clusters for each accuracy rate interval for BP algorithm

(2) Judgment results based on RBF neural network

A total of 1719 data correctly judge whether there is a substation in the area, and the accuracy rate is equal to 81.86%. The accuracy rate of judgment for each cluster as a test set is shown in Figure 13, and the number of data clusters for each accuracy rate interval is shown in Figure 14.

The results show that the accuracy rate of the preliminary siting based on BP neural network and RBF neural network is significantly lower than that based on CNN. It indicates that the preliminary siting of the substation based on CNN is superior to the preliminary siting based on shallow learning algorithms such as BP neural network and RBF neural network.

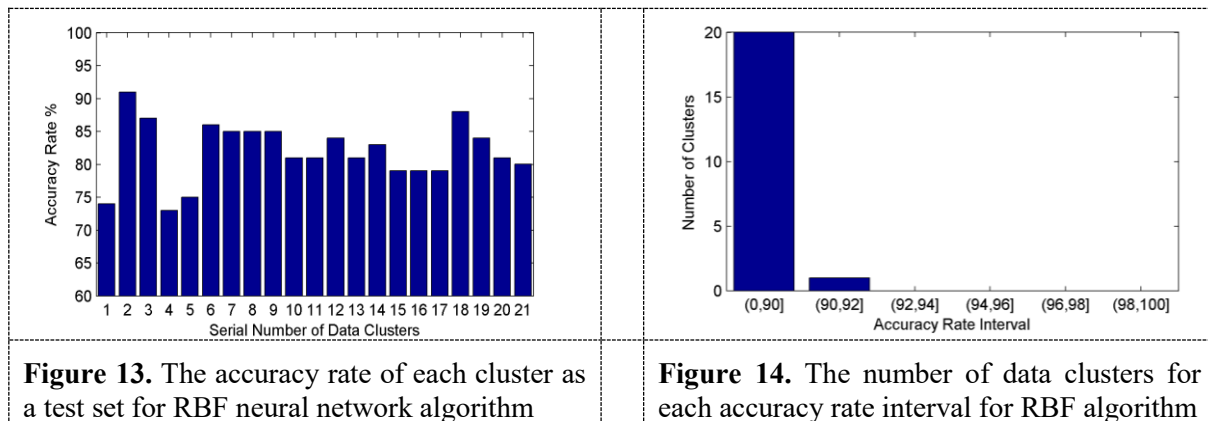


Figure 13. The accuracy rate of each cluster as a test set for RBF neural network algorithm

Figure 14. The number of data clusters for each accuracy rate interval for RBF algorithm

4. Conclusion

This paper proposes a deep learning algorithm for preliminary siting of substations in distribution network planning. By extracting features related to the principle of substations siting and using multichannel data characterization methods which are analogous to pictures, the features based on actual geographical relationships are integrated into a convolutional neural network for preliminary siting method of substations. The preliminary siting of substations for the subsequent planning process is completed. Finally, the validity of the proposed algorithm considering different input features is demonstrated on a distribution network of one certain province in China by case studies and comparisons. The simulation results show that the proposed deep learning algorithm for preliminary siting of substations is more accurate with more input features, and is better than shallow learning algorithms, thus can be employed to preliminary siting of substations in distribution network planning.

5. References

- [1] Kaabi S S A, Zeineldin H H and Khadkikar V 2014 Planning active distribution networks considering multi-DG configurations *IEEE Transactions on Power Systems* **29** 785
- [2] Mohtashami S, Pudjianto D and Strbac G 2017 Strategic distribution network planning with smart grid technologies *IEEE Transactions on Smart Grid* **8** 2656
- [3] Li Y, Xie Q, Wang L and LÜ F 2014 Application of cloud theory to optimal planning of substation locating and sizing *Proceedings of the CSEE* **34** 672
- [4] Guan H and Tang W 2010 Substation location method based on Voronoi diagram *Power System Protection and Control* **38** 196
- [5] Huang S and Xu S 2011 Substation locating based on GIS and grey clustering evaluation model *Power System Protection and Control* **39** 84
- [6] Yan L, Xu A, Ren S and Chen J 2007 New method of selecting location of transformer substation *High Voltage Engineering* **33** 75
- [7] He Y, Liu G, Xiao Y and Zhang Z 2017 Locating optimization for substation based on refined GA-PSO hybrid algorithm *Power System Protection and Control* **45** 143
- [8] Yan S, Yao J, LI F, Wang X and LIU J 2010 Two-phase optimal planning of substation locating based on refined PSO algorithm *Power System Protection and Control* **38** 34
- [9] Ghadiri A, Haghifam M and Larimi S M M 2017 A novel approach for hybrid AC/DC distribution network planning using genetic algorithm *IET Generation Transmission & Distribution* **16** 3892
- [10] Tang M, Gao H and Zhang Y 2018 Research on deep learning techniques in breaking text-based captchas and designing image-based captcha *IEEE Transaction on Information Forensics and Security* **13** 2522
- [11] Bengio Y, Lamblin P and Dan P 2006 Greedy layer-wise training of deep networks *International Conference on Neural Information Processing Systems* 153
- [12] Tong C, Li J, Lang C, Kong F, Niu J and Rodrigues, J 2018 An efficient deep model for day-ahead electricity load forecasting with stacked denoising auto-encoders *Journal of Parallel and Distributed Computing* **117** 267

- [13] Li J, Zhang, Z and He, H 2018 Hierarchical convolutional neural networks for EEG-based emotion recognition *Cognitive Computation* **10** 368
- [14] Alani A 2017 Arabic handwritten digit recognition based on restricted boltzmann machine and convolutional neural networks *Information* **8** 142
- [15] Wang Y, Liu F and Zhang K 2018 LFNNet: A novel bidirectional recurrent convolutional neural network for light-field image super-resolution *IEEE Transactions on Image Processing* **27**, 4274
- [16] Wang C, Liu T and Xie Y 2006 Substation locating and sizing based on hybrid genetic algorithm *Automation of Electric Power Systems* **30** 30
- [17] Li J, Zhang T and Luo W 2016 Sparseness analysis in the pretraining of deep neural networks *IEEE Trans Neural Networks and Learn Systems* **28** 1425
- [18] Li H, Lv M and Liu J 2014 Distribution substation site planning method summary and discussion *3rd International Conference on Industrial Design and Mechanics Power* **620** 158
- [19] Temraz H and Salama M 2002 A planning model for siting, sizing and timing of distribution substations and defining the associated service area *Electric Power Systems Research* **62** 145
- [20] Wang D T C, Ochoa L F and Harrison G P 2011 Modified GA and data envelopment analysis for multistage distribution network expansion planning under uncertainty *IEEE Transactions on Power Systems* **26** 897
- [21] Bayer B and Stamm M C 2018 Constrained convolutional neural networks: a new approach towards general purpose image manipulation detection *IEEE Transaction on Information Forensics and Security* **13** 2691
- [22] Zhou F, Jin L and Dong J 2017 Review of conventional neural work *Chinese journal of computers* **40** 1229
- [23] Lee S H, Chan S and Remagnino P 2018 Multi-organ plant classification based on convolutional and recurrent neural networks *IEEE Transaction on Image Processing* **27**, 4287
- [24] Cao F, Liu Y and Wang D 2018 Efficient saliency detection using convolutional neural networks with feature selection *Information Sciences* **456** 34
- [25] LeCun Y, Bottou L, Bengio Y and Haffner P 1998 Gradient-based learning applied to document recognition *Proceedings of The IEEE* **86** 2278

Study on Power Quality Impacts of Rural Distribution Network with Large-scale Heat Pumps

Zhenwei LI¹, Wenliang ZHU¹, Pengfei SUN², Siyao HU², Kaiyuan JIN³ and Jianhua YANG^{3*}

¹ State Grid Handan Electric Power Supply Company, Handan, China

² State Grid Hebei Economic Research Institute, Shijiazhuang, China

³ College of Information and Electrical Engineering, China Agricultural University, Beijing, China

*E-mail: yang.haag@163.com

Abstract. With the advance of the “*Coal-to-electricity*” program in northern China, heat pump units are used more and more widely for rural household heating at a high operating efficiency. When large-scale heat pump units are connected to rural distribution networks, the power quality problems should be considered because of the voltage sag, the current surge, and the harmonics caused by the units. The typical feature, the efficiency index, the operation process and the types of the domestic heat pump units are introduced. The starting characteristics of different heat pump units are compared. Impacts on distribution networks with heat pumps are discussed, including the additional load forecast method of heat pump units and the power quality problems. The startup current of the fixed-speed heat pump is too large to cause voltage sag. The variable-speed heat pump may inject the harmonic current into distribution system. A rural distribution network are simulated with the actual measurement data in order to analyse the voltage sags during the starting process of the heat pump units with different permeability of the units. The corresponding simulation results can be used as the reference for the further implementation of the “*Coal-to-electricity*” program.

1. Introduction

Heat pumps are designed to obtain low-grade thermal energy from the natural air, water or soil, to do work through electric power, and to provide people with high grade thermal energy. A heat pump unit uses a small amount of electric power to transfer energy from the source of low-grade thermal energy to the heat sink. Heat pump technology was available in its current form in the 1930s, experienced a real boom after the first oil crisis in the 1970s, tested in cold climates in the 1980s. The market for heat pumps did not revive until the mid - 1990s and is currently experiencing high annual growth rates [1]. The application of the heat pumps can drastically reduce greenhouse gases, in particular CO₂ emissions [2]. In recent years “*Coal-to-electricity*” programs have been applied in northern China [3], which directly consume electricity instead of coal in the energy consumption to heat home in the winter, and fundamentally solve the problems that restrict sustainable development of human society such as energy environment and climate change, especially the haze problem. Because the heat pump units offer energy efficient and environmentally-friendly heating in domestic applications, they are applied more and more in domestic electric heating radiators in the programs. The heat pumps include the air source heat pump (ASHP) and the ground source heat pump (GSHP). An ASHP unit absorbs heat from the outside air, which is different from a GSHP unit that absorbs heat from groundwater or ground with a ground heat exchanger/collector.



Content from this work may be used under the terms of the [Creative Commons Attribution 3.0 licence](https://creativecommons.org/licenses/by/3.0/). Any further distribution of this work must maintain attribution to the author(s) and the title of the work, journal citation and DOI.

Published under licence by IOP Publishing Ltd

The climate impacts of two heat pump units, ASHP and innovative GSHP, were compared for domestic heating, i.e. the energy consumption for space heating of a residential building [4]. To save energy consumed for spacing heating and enhance the indoor thermal environment, the performance improvement of the heat pumps has become one of the research foci in the relevant field, and some studies have been carried out on investigating the frosting, defrosting and low ambient heating performances of ASHP [5], [6]. The impacts of frosting evenness of outdoor coil were experimentally investigated on the heating performances of an ASHP unit [5]. A review of the advances in ASHP units was presented for the units to apply in cold climate, in which the related advanced units were divided into single-stage, dual-stage and multi-stage compression units [6]. A model of a GSHP unit with variable speed compressor, variable speed water pumps and variable speed fans is presented in order to evaluate the operation conditions of the maximum seasonal *COP* of the unit [7]. The development of a performance based model of a water-to-air variable capacity GSHP was presented, and the recommended control strategy is applied to vary the speed of the compressor for each mode of operation and to be able to switch from one mode to the other [8]. The performance problems of the heat pump units were considered in the above literatures, however the power quality impacts of the heat pump units on distribution networks were not involved.

The typical features of the heat pump units are introduced, and the power quality problems such as the air voltage sag and the harmonics caused by the units are discussed with the parameters of the units and the actual measurement data of the rural distribution networks in this paper. According to the information and data of the distribution network in an actual “Coal-to-electricity” program, the power quality problems are simulated with the large-scale the heat pump units which are connected to the rural distribution network.

2. Typical feature of heat pumps

2.1. Efficiency index of heat pump units

Measure of the relative efficiency of a heat pump unit can be expressed as the ratio of output to the energy consumed (both in kilowatts). The most commonly efficiency indexes of the heat pump units are coefficient of performance (*COP*) used for heating and energy efficiency ratio (*EER*) used for refrigeration.

COP of a heat pump unit is defined as follows:

$$COP = q_{HP} / P_{HP} \quad (1)$$

Where q_{HP} is the thermal power provided by the heat pump unit in kW, P_{HP} is the electric power input to the heat pump unit in kW. The power input P_{HP} and the refrigerating capacity q_{Source} of the low-temperature heat source together produce the heat flow q_{HP} :

$$q_{HP} = q_{Source} + P_{HP} \quad (2)$$

If, for example, a heat pump with electrically driven power $P_{HP} = 2$ kW produces heat flow of $q_{HP} = 6$ kW, $COP = 3$. The difference of $q_{Source} = 4$ kW derives from the low-temperature heat source.

COP only applies to transient values. The annual average is applied, too. This is called an annual coefficient of performance (*ACOP*). A high *ACOP* is essential for the ecological and economical operation of a heat pump. For example, a heat pump can cover a heating requirement of 10500 kWh per year using 3000 kWh of electric energy with an *ACOP* = 3.5. *ACOP* of very good units can reach about 4. The practical values of *ACOP* for different types of heat pumps are shown as Table 1, which are gotten from a field test [1].

Table 1. Typical *ACOP* for heat pumps

Heat pump	Heat source	<i>ACOP</i> with underfloor heating	<i>ACOP</i> with radiators
GSHP (Brine/water)	Ground	3.6	3.2
GSHP (Water/water)	Groundwater	3.4	3.0
ASHP (Air/water)	Air	3.0	2.3

During cooling mode the definition remain the same and follow to calculate *EER* by replacing the condenser heat flow rate with the evaporator cooling power.

2.2. Schematic systems of heat pumps

A heat pump is basically a machine in which an electrically driven pump generates heat from a low-temperature heat source. This heat is then used to provide heating or to produce hot water. Before a heat pump can even function, a low-temperature heat source must be available. The higher the temperature level of the heat source, the more efficiently the heat pump can work.

The heat from the heat source is absorbed at low temperature by a heat pump refrigerant in a cycle as it vaporizes and releases heat when it is condensed, as shown in Figure 1. The working fluid then passes through a compressor where its temperature is increased, and transfers its higher temperature heat to the hot water-filled radiators with the domestic heating pipelines. The vaporization and the condensation of the refrigerant are facilitated by applying an electric pump that forces the water or air through an evaporator and then into a condenser. In order to drive the pump, electric power is required.

2.3. Types of GSHP units

According to different heat sources which are available to houses, there are three main types of GSHP units, *ground water (water/water)*, *ground heat exchanger/collector (brine/water)* and *earth probing device (brine/water)*, as shown as Figure 2.

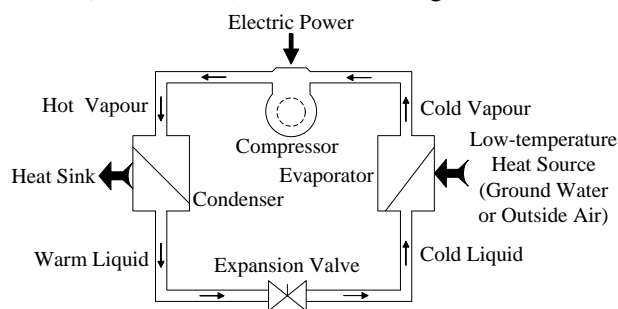


Figure 1. The schematic system of a heat pump

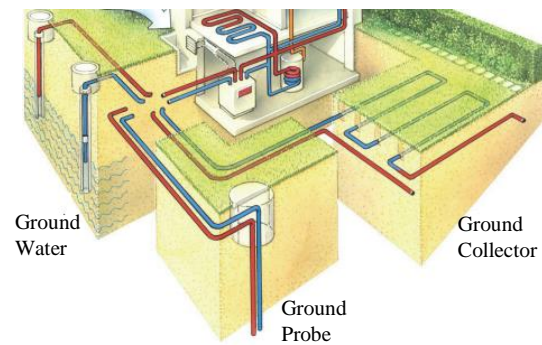


Figure 2. Heat sources for GSHP

According to different control form of the compressor speed in the GSHP unit, there are two types of GSHP units, *fixed-speed* and *variable -speed*.

Table 2. Specifications of a GSHP unit, Brand A

Operation State	Cold	Thermal at -7.6 °C	Thermal at -12.0 °C
Rated capacity /kW	12.0	13.5	11.4
Rated input power /kW	4.85	5.20	4.90
EER or COP /p.u.	2.47	2.59	2.32
Rated input current /A	29.0	30.0	29.3
Maximum input current /A			39.0
Maximum input power /kW			6.76
Rated voltage / V~			220
Maximum working pressure of water system /MPa			0.3
Maximum discharge pressure /MPa			2.8
Maximum inspiratory pressure /MPa			0.8
Pump capacity /(m ³ /h)			1.72
Refrigerant gas			R22 / 5.0 kg
Ambient temperature / °C			-25~45

Because the power supply frequency cannot be changed, the compressor speed of the fixed-speed GSHP unit is constant. Normally the GSHP unit operates intermittently in the on or off mode to adjust the heating capacity to the load required in the house with a fixed-speed. If the temperature reaches the set value, the compressor stops working. Otherwise, it starts working and adjusts the temperature by

constantly opening and stopping the compressor. A GSHP unit at a village in northern China is shown as Figure 3. The technical specifications provided by the manufacturer of a GSHP unit, Brand A, with the fixed-speed are shown in Table 2.

If a variable-speed compressor is used, the GSHP unit could simply follow the load, taking advantage at partial loads from the oversized heat exchangers and thus increasing its efficiency.

2.4. Types of ASHP units

ASHP has been widely applied to many parts of the world due to its simple structure and low initial cost. The ASHP units function at ambient temperatures as low as $-20\text{ }^{\circ}\text{C}$.

According to different heat exchange media indoors, there are two main types of ASHP units, *air-to-water* and *air-to-air*.



Figure 3. Outdoor part of a GSHP unit at a village in northern China



Figure 4. Outdoor part of an ASHP unit at a village in northern China

Table 3. Specifications of an ASHP unit, Brand B

Operation State	Cold	Thermal at $-7.6\text{ }^{\circ}\text{C}$	Thermal at $-12.0\text{ }^{\circ}\text{C}$
Rated capacity /kW	12.0	13.5	11.4
Rated input power /kW	4.85	5.20	4.90
EER or COP /p.u.	2.47	2.59	2.32
Rated input current /A	29.0	30.0	29.3
Maximum input current /A		39.0	
Maximum input power /kW		6.76	
Rated voltage / V~		220	
Maximum working pressure of water system /MPa		0.3	
Maximum discharge pressure /MPa		2.8	
Maximum inspiratory pressure /MPa		0.8	
Pump capacity /(m^3/h)		1.72	
Refrigerant gas		R22 / 5.0 kg	
Ambient temperature / $^{\circ}\text{C}$		$-25\sim 45$	

According to different installation position of ASHP components, there are three basic types of ASHP units, *split systems*, *packaged systems* and *ductless room heat pumps*.

Split ASHP units are the most common type of ASHP in the “Coal-to-electricity” programs. These units have one heat exchanger coil outdoors and one heat exchanger coil indoors. The compressor, located outdoors as shown as Figure 4, compresses the refrigerant and then forces it indoors where it releases heat into the supply ducts. Once in the duct, heat is moved through the house by a fan. The working fluid then moves through the expansion valve outdoors where it evaporates into a gas, absorbing heat, before being returned indoors. Cool air indoors is circulated back to the fan via return ducts.

Some ASHP units are packaged systems. Both the coils and the fan of the packaged systems are installed outdoors. Then heated air is delivered to the interior from a duct system.

Ductless room heat pumps are essentially another form of packaged system that does not use ductwork. These pumps can efficiently heat a room or small house with an open floor plan. They can be installed in a window or through a hole in the wall.

Similarly, there are two types of ASHP units, *fixed-speed* and *variable-speed*, according to different control form of the compressor speed in the ASHP unit. The specifications provided by the manufacturer of a 6 HP ASHP unit, Brand B, with the fixed-speed in the “Coal-to-electricity” programs are shown in Table 3.

3. Impacts on distribution networks with heat pumps

3.1. Additional load forecast of heat pump units

The additional load forecast formula is determined to the heat pump units for the “Coal-to-electricity” programs with difference load rate, simultaneity rate, and day conversion rate in different counties.

$$\Delta P = N \cdot P_{AV} \cdot \eta \cdot K_S \cdot k_d \quad (3)$$

where ΔP is additional load in kW, N is the number of additional households using the heat pump Units, P_{AV} is the additional average power per household in kW/ per household (It is approximately equal to 9kW, the expected load per household, minus the original average load per household), η is load rate in per unit, K_S is the load simultaneity rate of all households in per unit, k_d is the day conversion rate in per unit (according to the actual load situation in different counties, $k_d \approx 0.4 \sim 0.6$ in the summer, and $k_d \approx 1$ in the winter).

3.2. Power quality problems of heat pump units

The influence of the heat pump units on the power quality of the distribution network is mainly in two aspects, the voltage sag and the harmonic. The fixed-speed heat pump unit needs a lot of current during startup, and the startup current is usually 4~7 times of the maximum operation current, which is easy to cause obvious voltage sags in the distribution network. Although variable-speed conversion technology can properly reduce the starting current of a single heat pump, the variable-speed compressor may inject the harmonic current, and the total harmonic distortion rate of the distribution system is possibly larger than the permissible value of the distribution network.

The voltage sags and harmonic currents are measured to three heat pump units, Brand A, Brand B and Brand C, in several villages which have completed the “Coal-to-electricity” programs. Ambient temperature is about $-2 \sim -6$ °C. The operation voltages of the measurement nodes are near 220V when the heat pump units are switched off.

After the steady operation of the both Brand A and Brand B, the total harmonic distribution (THD) of the operation current is small. The measurement results are shown in Table 4.

Table 4. The starting data and THD of Brand A and Brand B

Type of the heat pumps	Brand A	Brand B
Maximum startup current / A	30.37	146.16
Maximum active power / kW	3.68	15.97
Minimum startup voltage / V	201.96	191.89
Duration of transient process / s	0.45	0.21
Ratio of maximum startup current to rated heat current / per unit	3.65	5.84
THD / %	10.2~10.8	10.5~10.9

Brand C is an ASHP unit with the variable-speed. In the process of starting, the soft start of the compressor speed conversion is applied, and the impact current is very small. The starting voltage is basically stable at about 220V. After the steady operation of the unit, its THD of the operation current is about 11.5~23.6%.

4. Simulation of rural distribution network with large scale heat pumps

4.1. Rural distribution network for simulation

The ratio of the maximum startup current to the rated heat current of Brand B is larger. Therefore Brand B is selected for the heat pump unit of the simulation. And the rural low voltage distribution network of the corresponding village is shown in Figure 5. The main line where the node number is from 1 to 15 and the line type is JKLYJ-120. The type of all the branch lines is JKLYJ-70. The parameters of the lines are shown in Table 5. The distribution network is connected to the distribution transformer in 315 kVA, the type being S11-315/10 and the voltage ratio being 10kV / 0.4kV. The line length between two nodes is assumed to be 400 m for the purpose of simplicity. The power load of node 5, 15, B1-1, B1-3, B1-4, B2-1, B2-6, B3-2, B4-2, B5-2 and B5-3 is assumed to be 3.1 kW, and the power load of node 10, B1-5, B2-4, B2-5, B3-1, B4-3 and B5-1 is 4.6 kW. All users are basically evenly distributed in each phase.

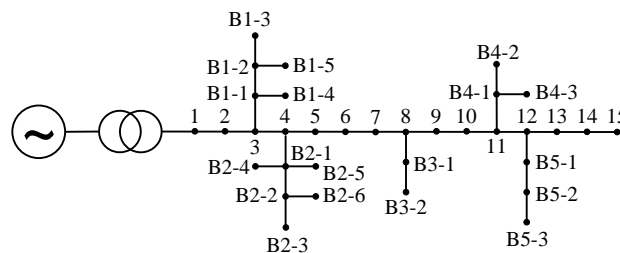


Figure 5. Rural distribution network diagram of a village

Table 5. Resistance and reactance of lines

Type of lines	JKLYJ-120	JKLYJ-70
Resistance of the one km length /(Ω /km)	0.27	0.297
Reactance of the one km length /(Ω /km)	0.46	0.315

4.2. Permeability of ASHP units

When the establishment of different simulation scenes is done, the permeability of the heat pump units, represented as r_{per} in per unit, is considered.

$$r_{per} = P_{HP} / P_{All} = P_{HP} / (P_{HP} + P_{LV}) \quad (4)$$

where P_{HP} is the total power of the steady operation of all the heat pump units in kW, P_{All} is the total power of the distribution network in kW, P_{LV} is the total power of the other ordinary load of the low voltage (LV) distribution network in kW.

4.3. Simulation of voltage sags

When the establishment of different simulation scenes is done, the permeability of the heat pump units, represented as r_{per} in per unit, is considered.

When the number of the heat pump units connected to the distribution network is changed, i.e. r_{per} being different, the startup influence of the units is simulated with the other constant LV loads. While $r_{per} = 0$ with the load of all users in the LV distribution network, the voltage of node 15 is 215.7 V.

If the heat pump units are only connected to the node 15 with $r_{per} = 0.18$, then the minimum residual voltage of node 15 is about 183.5V during the heat pump starting process, which is much lower than the threshold value of the voltage sags, 90% rated voltage, i.e. 198 V [3]. The sudden voltage drop must affect the operation of other electrical equipment.

If the heat pump units are only connected to the node 7 and node 15 with the same capacity and $r_{per} = 0.36$, then the minimum residual voltage of node 15 is about 165.7V during the heat pump starting process, which is far below the threshold value, 198 V.

5. Conclusion

The voltage sags in a rural distribution network are simulated during the starting process of the heat pump units with different permeability of the units in this paper. With the increase of permeability of the fixed-speed heat pump units, the larger voltage sag may be caused during the heat pump starting process in the rural distribution network. The length and the section area of the distribution line affect the allowable permeability ratio of the heat pump units and the starting number of the units at the same

time. When the heat pump units are installed in the rural area with the “coal-to-electricity” program, it is necessary to consider whether the new load demand of the heat pump units will be met according to the distribution transformer capacity and line parameters. With the increase of permeability of the variable-speed heat pump units, the current harmonic content will increase in the rural distribution network. It is necessary to take measures to suppress the harmonic content based on the actual situation of the distribution network.

Based on the typical feature and the types of the domestic heat pump units, the additional load forecast method of heat pump units is put forward. The power quality problems are analyzed by using the actual measurement data of the voltage sags and the harmonics of the heat pump units in the rural distribution network. The simulation results in the distribution network can be used as the reference for the further implementation of the “Coal-to-electricity” program.

6. Acknowledgments

This work is financially supported by Science and Technology Project of SGCC (SGHEJY00GHJS1700176).

7. References

- [1] Quaschnig V 2010 *Renewable Energy and Climate Change* (New York: Wiley-IEEE Press)
- [2] Mattinen M K, Nissinen A, Hyysalo S and Juntunen J K 2015 *J. Indus. Ecology* **19** 1 pp 61-70
- [3] Gao Z, Chen D M, Yang J H and Ji B 2015 *Electrotechnics Electric* **209** 5 pp 1-5
- [4] Zhang L, Jiang Y Q, Dong J K and Yao Y 2018 *Renewable and Sustainable Energy Reviews* **81** 1 pp 353–365
- [5] Song M J, Xia L, Mao N and Deng S M 2016 *Applied Energy* **164** pp 36-44
- [6] Col D D, Azzolin M, Benassi G and Mantovan M 2015 *Energy and Buildings* **91** pp 105-114
- [7] Bouheret S and Bernier M 2017 *J Building Performance Simulation* **5** pp 1-11
- [8] Vieira A S, Stewart R A and Beal C D 2015 *Buildings and Energy* **91** pp 148-162

Power Grid Partition Method for Black Start Based On Complex Network Theory

Xu Fubin¹ Zhang He² Li Run³ Cai Jian⁴

¹ State Grid Dalian Power Supply Company, Dalian, China

² State Grid Dalian Power Supply Company, Dalian, China

³ State Grid Dalian Power Supply Company, Dalian, China

⁴ State Grid Dalian Power Supply Company, Dalian, China

E-mail: 1009545047@qq.com

Abstract. The paper proposes one power grid partition method for black start based on complex network theory. The method is composed of splitting algorithm and agglomerative algorithm. The former algorithm divided grid to some temp zone according to the number of black-start unit, which determines the basic structure of the partition and reduces the number of iterations in agglomerative process. The latter algorithm redefines the line weight and weighted modularity based on flow distribution and network topology, then merges neighbouring temp zone to maximum weighted modularity. The method can reflect the close degree of the partition, accurately assess the partition quality and determine the optimal number of partitions. The simulation results on IEEE 39-bus test system illustrate the validity of this methodology.

1. Introduction

When power grid subjected to large-scale blackout after large disturbance or failure, system recovery can be realized by black-start scheme [1]-[3]. The units with self-start ability in grid can be used to bring others to start up and recover the system gradually. Finally, the whole power system can be restored to normal operation state. In order to speed up the recovery process, the network can be divided into several sub zones in which black start unit can recover corresponding load. When some sub zones run in a stable state, Quasi-synchronizing parallel devices can achieve the grid connection between two sub zones. There are two main types of power system partition methods: the fixed partition method based on the administrative division or jurisdiction scope, and the dynamic partition method based on the power failure information after the accident [4]. Due to the especially serious power outage, earthquake and typhoon, the communication system cannot receive sufficient information which lead s to the invalidation of dynamic partition method. So power grid should keep a watchful eye on predetermined fixed partition scheme. The traditional partition method makes a mechanical partition and cannot describe the tightness of inner zone [5].

Complex network theory studies the areal network in social, natural and engineering systems, aiming to reveal the connection between network function and structural features [6]-[9]. With the establishment of small world network and scale-free network model, this theory has been paid more attention in many fields of scientific research. A large number of researches show that, as one of the large scale and complex artificial networks, the power system also has the characteristics of small world network, community structure and other complex networks. Community structure is generally properties in complex network topology properties [10]-[13], it automatically divided network into several subnets. The structure has typical characteristic that there is a close connection within the community and relatively sparse connection between communities. The characteristic is highly similar



to the requirement of grid partition. This result provides a new way for the research of power system partition, which can help overcome lack of traditional partition method.

The paper proposes a novel power grid partition algorithm for black start based on complex network theory. The method redefines the line weight and weighted modularity based on flow distribution and network topology. The algorithm divided partitioning process into two phases. The first stage applies splitting algorithm to reasonably determine the maximum partition number in black start stage on the basis of the number of black start units. The second stage uses the agglomerative algorithm to combine the adjacent area according to the weighted modularity, ultimately determine the optimal partitioning scheme.

2. Community structure

Community structure is most important branch of the complex network theory, has been widely used in the social relations, the Internet and business conduct clustering [14]. It also has been gradually introduced into the complex behaviour study of power grid [15]. Some apexes constitute special set which has a close contact between vertices in set and relatively spars contact between vertices external set. so the network can be divided into some community structures consist of special set, it is shown as figure 1.

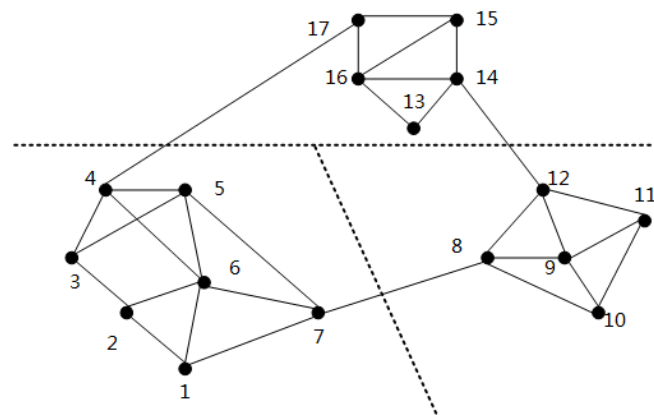


Figure 1. Community structure.

At present, the most commonly used description indicators of community structure is module degree defined by Girvan and Newman, it is usually called Q function. module degree is the fraction of the edges that fall within the given communities minus the expected fraction if edges were distributed at random [16]. For a given division of the network's vertices into some modules, modularity reflects the concentration of edges within modules compared with random distribution of links between all nodes regardless of modules [17], [18].

$$Q = \frac{1}{2m} \sum_{ij} \left(A_{ij} - \frac{k_i k_j}{2m} \right) \delta(c_i, c_j) \quad (1)$$

Where A_{ij} is the weight of line between node i and node j , $k_i = \sum_j A_{ij}$ is the sum weight of all line connected to node i ; $m = 0.5 \sum_j A_{ij}$ is the sum weight of all line. c_i is serial number of community structure within node i . If the node i and node j are in same community structure, then $c_i = c_j$ and $\delta(c_i, c_j) = 1$, otherwise $\delta(c_i, c_j) = 0$. If the k_i of all node keep unchanged and form the random network, $\frac{k_i k_j}{2m}$ is the weight expectation of line between node i and node j .

The range of module degree is from 0 to 1, if the sum weight in community structure is not greater than the expectation weight of the random network, $Q=0$ [19]. The closer to upper limit Q is, the more

obvious the community structure is. Generally, when Q is around 0.32 or greater than 0.32, it indicates that the partitioning method is a more appropriate approach. According to above characteristics of module degree, the maximum module degree of different networks can be compared to evaluate its structure separability. The local peak of Q is usually not more than 2, so it is easy to carry out the partition based on Q . In conclusion, according to the peak of module degree, the optimal partition number can be selected to determine the optimal partition mode.

3. Power grid partition method

3.1. Line weight

Complex network theory uses node set V , edge set S and edge weights w_{ij} to describe complex network. The model of complex power system usually considers generator and load as node, considers line as edge. The double or multiple circuits are usually merged into one edge. The traditional method uses the reciprocal of the line reactance as weight. Based on flow distribution and network topology, this paper defines weight of line (i, j) as:

$$w_{ij} = \sum_{m \in G, n \in L} \sqrt{W_m W_n} |I^{mn}(i, j)| \quad (2)$$

Where (m, n) is a plant-load pairs; $|I^{mn}(i, j)|$ is the current of line ij caused by the injection of per unit current in; W_m and W_n are weighted coefficients of generator m and load n , corresponding to the rated capacity or actual output of the generator and the actual or peak value of the load, respectively; G and L are sets of generators and loads, respectively. According to circuit equation, the proportion of power from each plant-load pair in line can be clearly described. The method quantifies the role of each line in entire grid power flow.

3.2. Weight module degree

The line weight can consider the connection between the nodes and the strength of the connection in community partition process, it is able to partition the grid more accurately. According to the line weight, this paper redefines the weight module degree as:

$$\begin{cases} Q = \sum_s (\alpha_s - \beta_s)^2 \\ \alpha_s = \frac{1}{2m} \sum_{ij} w_{ij} \delta(c_i, s) \delta(s, c_j) \\ \beta_s = \frac{1}{2m} \sum_i w_{ij} \delta(c_i, s) \end{cases} \quad (3)$$

Where α_s is ratio between sum line weight in community s and sum line weight in network; β_s is ratio between sum weight of line connected to node i in community s and sum line weight in network.

3.3. Partition method

Based on the similarity or intensity of connections between nodes, a certain algorithm can be used to divide the network into multiple sub-groups. The algorithm can be divided into splitting algorithm and agglomerative algorithm according to whether the process of partition is to add edge to network or remove edge from network. Single aggregation algorithm and splitting algorithm are not sufficient [20], because the two algorithms are used in this paper. The two algorithms all have certain advantages and shortcomings, so the paper combines two algorithms at different stage. At black start initial phase, the method uses splitting algorithm to set up the initial zones, then uses aggregation algorithm to

compete zone merging. The method calculates the weight module degree of initial zone which is written as Q^0 .

Further, the method assumes merge any two contiguous zone p and q as zone (p, q) , calculates the module degree of the zone (p, q) which is written as $Q_{temp}(p, q)$. If zone m and n are merged as zone (m, n) and zone (m, n) has maximal module degree $\max(Q_{temp})$, then the method merges zone m, n and defines $Q^r = \max(Q_{temp})$, where r is times of iteration. If the module degree Q^s after g times of iteration is equal to the maximum module degree in the iteration process, which corresponds to the optimal partition scheme. The specific process of power grid partition method is as follows:

(1) Initialize parameter, times of iteration $r = 0$, the initial partition number $N = ng$, where ng is number of black start unit,

(2) Calculate the module degree of initial partition Q_0

(3) Construct the edge weight matrix $W_{nl \times nl}$, nl is number of line.

$$w_{ij} = \sum_{m \in G, n \in L} \sqrt{W_m W_n} |I^{mn}(i, j)| \quad (4)$$

(4) Calculate module degree of any two zone p, q as Q_{temp}

$$Q_{temp}(p, q) = \begin{cases} 0 & p, q \text{ is not connected} \\ \frac{1}{2m} \sum_{ij} \left(A_{ij} - \frac{k_i k_j}{2m} \right) \delta(c_i, c_j) & p, q \text{ is connected} \end{cases} \quad (5)$$

$p = 1 : N, q = p + 1 : N$

(5) Merge two zone p, q

$$\begin{aligned} IF \quad Q_{temp}(p, q) &= \max(Q_{temp}) \\ \Rightarrow \begin{cases} Q_j^{r+1} = Q_j^r \cup Q_k^r \\ Q_k^{r+1} = \emptyset \end{cases}, \end{aligned} \quad (6)$$

(6) Update the variable

$$\begin{aligned} N &= N - 1 \\ r &= r + 1 \\ Q^r &= \max(Q_{temp}) \end{aligned} \quad (7)$$

(7) Return to step (4) until initial partition number $N = 1$

(8) Determine the optimal partition scheme. If $Q^t = \max_{r=0 \sim n-1} (Q^r)$, the partition scheme is final result.

3.4. Partition result evaluation

If any node i and community s satisfy $Q(i \in s) > Q(i \notin s)$, any node of s connection with all other nodes inside the community is closer than connection with all other nodes outside the community, the community s has strong community structure. The partition method should ensure all zones have strong community structure. The paper introduces the index such as A and B to evaluate the result of partition method. A is the ratio of number of edges in community and total number of edges in the rule

network with same nodes, it reflects the connection tightness inside community. B is the ratio of number of edges between communities and total number of edges in the network, it reflects the connection tightness between communities. If the A large value and B has little value, the partition method is more effective.

4. Study case

The paper applies IEEE 39-bus test system to validate the validity of the partition method, the parameters of test system can be found in reference [21]. The betweenness defined in paper and traditional impedance are used to describe weight of line respectively, the corresponding partition results are shown in figure 2 and figure 3. The Q , A and B are used to evaluate the result of two partition methods, the comparison is listed in Table 1.

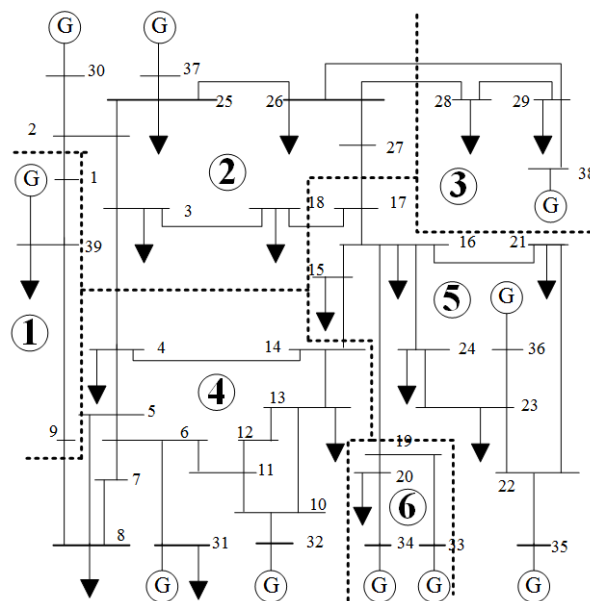


Figure 2. Partition result with impedance weight.

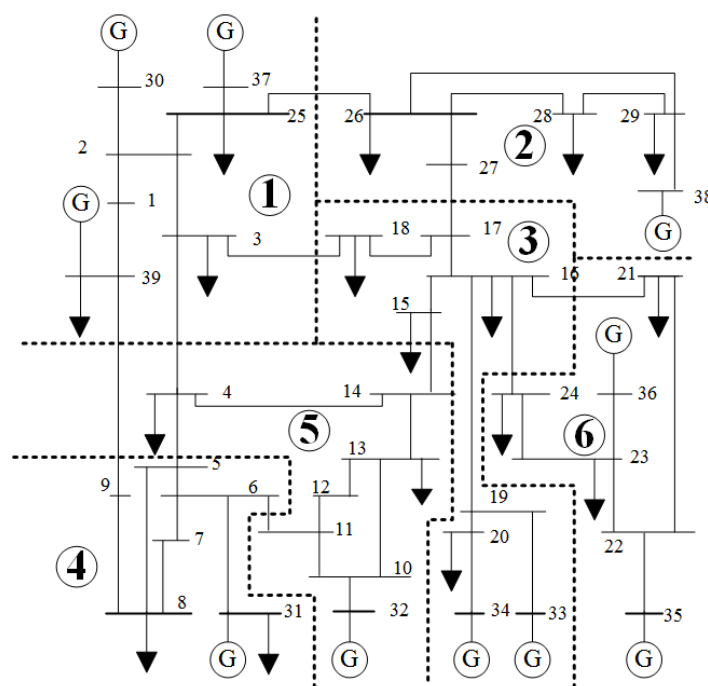


Figure 3. Partition result with betweenness weight.

Table 1. The comparison between two method

	Line Weight	A	B	Q
Method 1	Impedance	0.3545	0.0319	0.6235
Method 2	Betweenness	0.4713	0.0168	0.76545

With the same grid, the two methods divide test network into six zones. The figure 2 and figure 3 shows the two weight algorithm forms some similar areas, which shows that two models can reflect the local characteristics of the power grid and present the locally community structure. According to the above constraint condition of strong community structure, the six zones in figure 3 are all strong community structure, the zone 2 and zone 6 in figure 2 is weak community structure, it shows the method 1 has worse division effect, the betweenness weight can more effectively measure strength of connection between nodes.

The data in table 1 shows method 2 has larger A and Q than method 1, the nodes are more closely connected inside community. The less B of method 2 shows that the connection between communities is more spars, the flow coupling relationship between communities is weaker.

5. Conclusion

The paper proposes one power grid partition method for black start based on complex network theory. The method is composed of splitting algorithm and agglomerative algorithm. The former algorithm divided grid to some temp zone according to the number of black-start unit, which determines the basic structure of the partition and reduces the number of iterations in agglomerative process. The latter algorithm redefines the line weight and weighted modularity based on flow distribution and network topology, then merges neighbouring temp zone to maximum weighted modularity. The method can reflect the close degree of the partition, accurately assess the partition quality and determine the optimal number of partitions. The simulation results on IEEE 39-bus test system illustrate the validity of this methodology.

6. Acknowledgments

This work is supported by Science and Technology Project of Dalian Power Supply Company (Research on blackstart based on large capacity energy storage power station in Dalian, No. 522DL17000G).

7. References

- [1] Qiu F, Wang J, Chen C, Tong J 2016 *IEEE Transactions on Power Systems* **31** 2493.
- [2] Bahrman, M. and Bjorklund, P.E 2014 *IEEE Power and Energy Magazine*, **12** 44.
- [3] Di Giorgio A, Giuseppi A, Liberati F, Pietrabissa A 2017 *Mediterranean* **3** 781
- [4] Leng Y, Lu Q, Liang C 2018 *International Journal of Electrical Power & Energy Systems* **100**, 279.
- [5] Yuanwang G, Xueping G, Yan L, Desheng S, Shaofeng L, Lianwu D 2014 *Automation of Electric Power Systems* **13** 12.
- [6] Lin J, Li T, Zhao Z, Zheng W, Liu T 2012 *Power System Technology* **36** 115.
- [7] Zeng S, Lin Z, Wen F, Ledwich G 2012 *International Journal of Electrical Power & Energy Systems*. **34** 114.1
- [8] Liang H, Gu X, Zhao D 2010 *Power and Energy Engineering* **28** 1.
- [9] Zhou C, Ding L, Skibniewski MJ, Luo H, Jiang S 2017 *Safety science* **98** 145.
- [10] Yang Y, Liu Y, Zhou M, Li F, Sun C 2015 *Safety science* **79** 149.
- [11] Ji Q, Zhang HY, Fan Y 2014 *Energy Conversion and Management* **1** 856.
- [12] Halverson MJ, Fleming SW 2015 *Hydrology and Earth System Sciences* **9** 3301.
- [13] Cao YJ, Chen XG, Sun K 2006 *Electric power automation equipment* **12** 1.
- [14] Pagani GA, Aiello M 2013 *Physica A: Statistical Mechanics and its Applications* **392** 2688.
- [15] Arianos S, Bompard E, Carbone A, Xue F 2009 *Chaos: An Interdisciplinary Journal of Nonlinear Science* **19** 013119.

- [16] Sun K. 2005 *Transmission and Distribution Conference and Exhibition* **1** 61.
- [17] Girvan M, Newman ME 2002 *national academy of sciences*. **99** 7821.
- [18] Newman ME, Girvan M 2004 *Physical review E* **69** 026113.
- [19] Clauset A, Newman ME, Moore C 2004 *Physical review E* **70** 066111.
- [20] Leskovec J, Lang KJ, Dasgupta A, Mahoney MW 2008 *World Wide Web* **21** 695.
- [21] Demetriou P, Asprou M, Quiros-Tortos J, Kyriakides E 2007 *IEEE Systems Journal* **11** 2108.

The Power Grid Development with Distributed Wind Plant Growth Based on Coordination Analysis

Tan Yudong^a, Li Xianghua^b, Zhang Pengfei^c, Li Yong^d, Peng Dong^d

a: State Grid Hunan Electric Power Corporation Limited Economic & Technical Research Institute Changsha China

b: State Grid Loudi Power Supply Company, Loudi, China

c: The department of development planning State Grid Corporation of China

d: The center of transmission grid planning State Power Economic Research Institute Beijing China

E-mail: Yulongtan@126.com.

Abstract. the wind plant capacity developed continuously since 2009. However, the wind plant type changed quietly, those preformed in the unit capacity increased from 1MW to 5MW, the wind farm located from onshore wind power to offshore wind power, and the large-scale distributed wind plant transformed into small-scale distributed one. Recently, the distributed wind plant was growing rapidly for policy guidance, which has a great influence on the power grid operation because of the change of the power supply layout. How to analyze the influence is an important matter to power system development. The analyzed results will decide the trends of the distributed wind plant in future. Therefore, the coordination analysis of distribute wind plant growth is crucial to those developments. In this paper, the reasonable distributed generation scale arrangement was discussed based on the difference measures.

1. Introduction

Due to the global climate warming become more and more crucial, the worldwide eventually factored the carbon emission into ecological environment. The percentage of fossil-fired energy decreased for the 21st century due to renewable energy explosive growth [1]. As report by IEA, In 2016, total combustible fuel plants accounted for 60.8% of total OECD (Organization for Economic Co-operation and Development) gross electricity production (made up of 57.8% from fossil-fuel-fired plants and 3.2% from biofuels, waste, etc. plants), nuclear plants 18.0%, hydroelectric plants 12.9%, and geothermal, solar, wind, tide and other plants at 8.2%. One reason why production fell was lower demand of China in 2016. Those decreased around 320 million tons. The most important factor of why demand fell in China was lower consumption of electricity generation, though China still uses half the world's coal. Alongside the decrease of fossil-fired generation, 2016 also saw the continued increase of renewable generation across the OECD and in countries like China. In the OECD, renewables generation grew by 3.8% to account for 23.8% of all electricity generated, its highest share to date. The growth was largely driven by wind and solar WIND, which saw annual average growth rates of 21% and 43% between 2000 and 2016. The share of non-hydro renewable electricity in total OECD electricity production increased from 1.8% in 1990 to 10.9% in 2016. These technologies grew much faster than any other power source between 1990 and 2016. In 2017, the wind plant capacity was 539.5GW in the world. There was 188.4GW in China. In 2017, 19.7GW wind plant was installed. According to NEAC (National Energy Administration of China)'s distributed wind power planning, the distributed wind power was defined as the plant must access to grid below 35 kV, but the generated power is not allowed to boost into the higher voltage grid. And those would be supported significantly by simplifying review and approval procedures and allowing market transaction in local



power grid [2]. Moreover, several provinces had published their distributed wind power development planning, which is shown in Table.1. 20.6 GW wind plant has been arranged from 2018 to 2020.

Table 1. Planning capacity of distributed wind plant from 2018 to 2020

Province	Planning capacity (GW)
Hebei	4.3
Shanxi	1
Henan	2.1
Guangdong	0.45
Shanxi	1.25
Guangxi	5
Anhui	4.5
Guizhou	2
Total*	20.6

* Because other provinces haven't published the development planning, the whole capacity cannot census completely; the total in table represents the amount of 8 provinces.

The sharply development of distributed wind plant produced a profound influence to power grid, which is not same as the centralized wind generation. Since the centralized one construction and operation, the power interconnection systems for above 110kV grade had been design details, and the impact of power station to power system had been analyzed clearly. But the distributed wind plant was connected into 35kV or 10kV, the power interconnection system was oversimplified, the impact of distributed electricity generation does not discuss specialized, this question would be analyzed based on simulation calculation.

2. Power grid operation mode

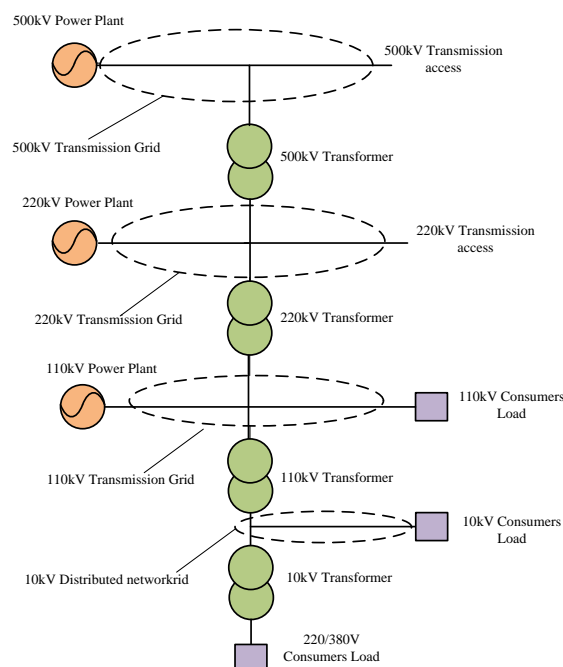


Figure 1. The hierarchical structure of 500/220/110/10/0.38 (0.22) kV series power grid.

To analyse the impact of the distributed wind plant, the normal operation mode should be analyzed firstly. The power transmission structure had been analysed to reflect the transferring characteristics from power plant to consumer [3]-[4]. In China, the 220kV power grid was the backbone network in 1981, and then, 500kV power grid were established as main network in following 30 years, 500 kV power grid covered provinces or regions. Nowadays, the 1000kV UHV power grid and ± 800 kV UHVDC project were successes, 7 UHV projects and 7 UHVDC projects were put into operation, and 2 UHV projects and 5 UHVDC projects were under construction. Synchronous UHV power grid will cover the East, North and Middle China in 2020 [5]-[6]. Therefore, the power grid is made up of different voltage grades. The hierarchical structure for 500/220/110/35/10 kV power grid was described as Figure.1.

2.1. Traditional power grid operation

The traditional electric energy was thermal power and hydropower in China. The installed capacity of each generation exceeds 20MW almost, which coupled with high voltage level. Generally, the interconnect grade was above 220kV. However, the loads were mostly connected to a low voltage grade, such as 35kV, 10kV or lower one. In the circumstances, the power flow usually transfers from high voltage to low voltage at the hierarchal structure. The large power plants generate electrical energy, which are transmitted to high voltage grade. A part of the electrical energy is transmitted to load center of power system, and then that is transferred to low voltage grade by transformers. Another part of electrical energy is transmitted to other power grid by transmission access. Correspondingly, the electrical energy might be transmitted into this power grid from other one. The power flow in hierarchical structure power grid is shown in Figure.2. The lower voltage grades accept the electricity purely throughout the year.

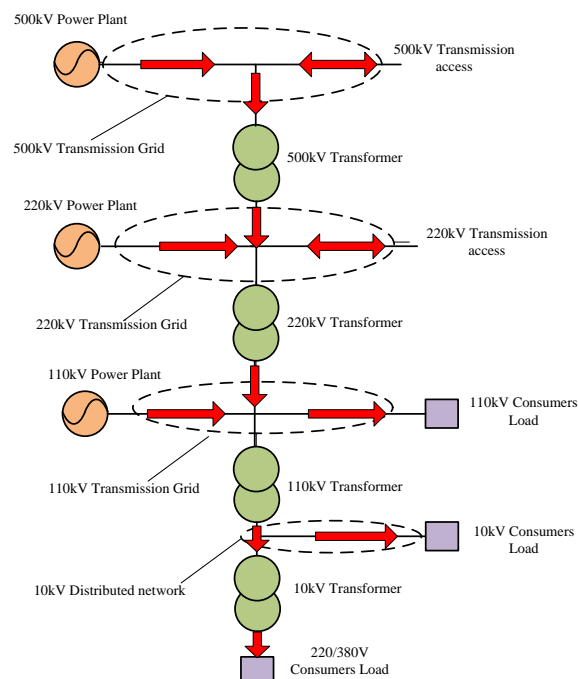


Figure 2. The traditional power flow in hierarchical structure power grid.

2.2. Power system load characteristics

The most of load was connected in lower voltage grade, such as 110kV, 10kV and 0.38 (0.22) kV. The daily load curve of the province A was collected on primary equipment, which is shown as Figure 3. The load curves of 110kV transformer substations have two load peaks in a day, one peak appears at 8:45, and another peak appears at 18:45. The peak load of province A was 20540 MW.

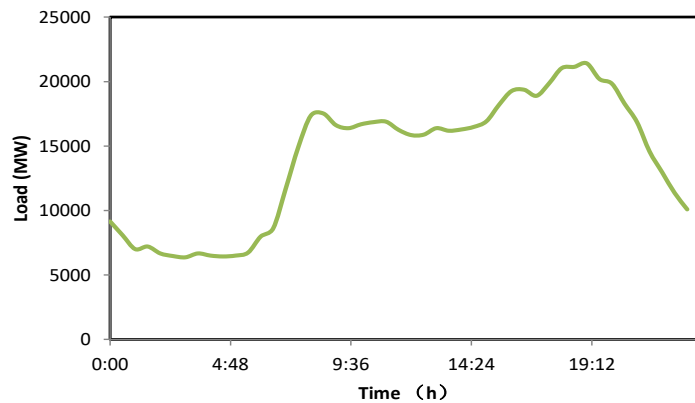


Figure 3. The load curves of Provincial A grid.

The typical daily load curve of different voltage grade is shown in Figure 4 – Figure 5, which collected on transformer or transmission line. From Figure 4, the load a curve of 110kV transformer substations is be similar to provincial grid one. From Figure 5, the load curve of 10kV transformer substations fluctuated persistently.

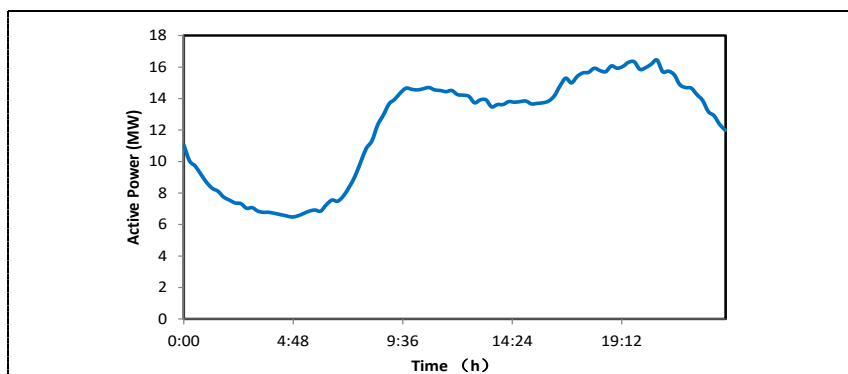


Figure 4. the load curves of 110kV transformer substations.

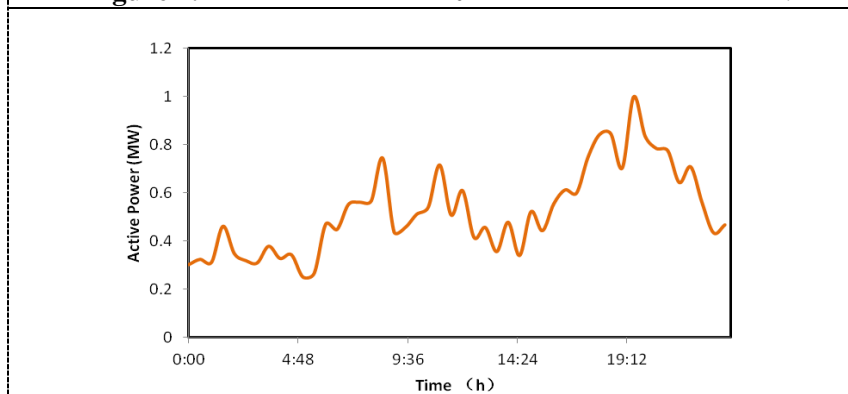
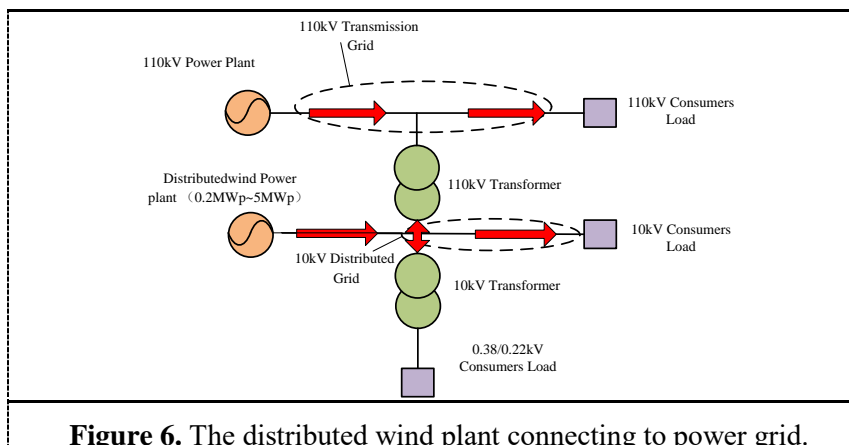


Figure 5. The load curve of 10kV transformer substations.

3. Distributed wind plant

3.1. Interconnection of the distributed wind power generation

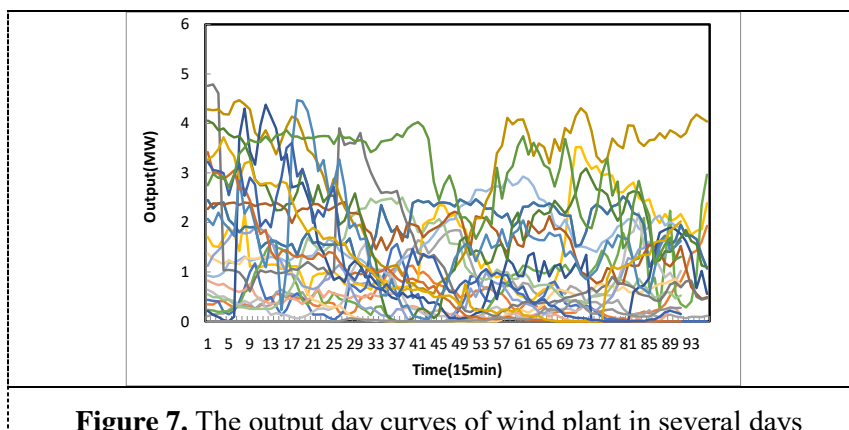
What level grid to which the distributed wind plant connected is depended on the scale of installed capacity and the native power grid structure.



Generally speaking, the power plant which installed capacity exceeded 0.2 MWp is proposed to connect into power grid with 10 kV. The power station whose installed capacity exceeded 5 MWp is proposed to connect into power grid with 110 kV. Therefore, there are three connection modes, and those are shown in Figure 6.

3.2. Output curves of wind plant generation

The output power of wind plant was affected by many influencing factors. The wind speed was the most critical factor to output power because it is the energy source of wind generation. The output day curves of a 5 MW plant station were shown in Figure 7, the generated power fluctuated greatly in a day. In order to describe the output character of wind power, the raw data of wind plant output should be deal with though statistical methods. In this way, the typical character of wind plant was shown in Figure.8, the max represented the maximum output value at 15 minutes in whole year; the mean represented the average output.in the year. The max output power was able to cover any condition in a year, although the output power curves at different wind speed condition had great variability. Therefore, the max output power characteristics were used to analyze the impact to power grid.



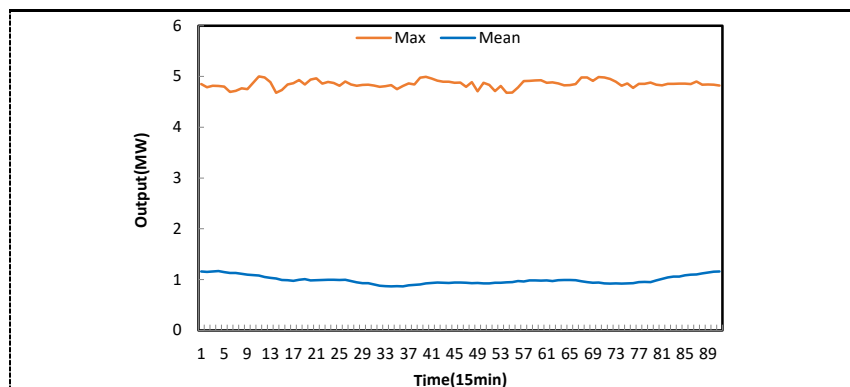


Figure 8. The output character of wind plant in one year.

4. Impact analysis

In Figure 6, the interconnect position of wind plant is described. With the distributed wind plant development, the output power from wind generation increase correspondingly, and the power flow in distributed power grid has changed for new power pumped into. At the same time, the load characteristics are variation for power generated at daytime. Furthermore, the coordination evaluation about the distribution grid is needed to be adjusted. In this section, the impact of distributed wind generation is analyzed as following.

4.1. Load flow analysis

With the wind electricity generation connected into power grid, the output power is absorbed by local grid firstly. Meanwhile, the electricity supplies from higher voltage grid decreased, which are counteracted local load by output power of wind plant. The load power of transformer which the lower voltage system contain distributed wind station is equal to actual load subtract the output, as in

$$L_T(t) = L_A(t) - P_s(t) \quad (1)$$

In which, L_T is load power of transformer which the lower voltage system contained distributed wind station, L_A is actual load of the system, P_s is the max output of the distributed wind plant, t is the time in a day.

For the power supply area connected with distributed wind plant, the power of wind plant is forbidden to up-step to high voltage since the definition proposed by NEAC, therefore, the coordination analysis have to obey those. Generally speaking, the distributed wind plant installed capacity should match to the local load level synchronously. For achieve the target, the distributed wind plant is required developing in order. So that, several ways can be adopted to arrange more capacity wind plant in some area. Frist, the storage equipment which installed in distributed voltage ranking is main measure to improve the capacity by move the electricity from peak to the valley, however, this ways request to build energy storage power stations and .need investment. Second, it is possible to raise the lowest load in a distributed grid by enlarging the supply district. Similarly, this measure requires constructing the new project to connect other grids. But there was spare line between two supply-areas in modern power grid commonly, and the cost will be declined distinctly.

4.2. Experimental analysis

A distributed wind farm was arranged to in Zhuzhou city in Hunan Province. The area of wind farm with average wind speed of 5.6m/s is about 30 km², and the wind energy content arrived 8.9MW, the whole distributed wind generation was planned to develop by 2020. However, the maximum and minimum load of the 110kV transformer which is used to access to power was 8.3MW and 4.4MW respectively in 2017. To 2020, those were forecasted to 9.3MW and 5.4MW according to a particular demand analysis. The acceptance of wind power was 5.4MW without any measures. Therefore, the 8MW wind generated power was impossible to develop for the distributed wind plant defined.

In order to accomplish the target of distributed wind capacity development, the cost of two measures mentioned in above section was analyzed through calculation; moreover, the combinatorial cost was optimized based on adopting two measures. The storage equipment adapt to battery technology that

the average price is 16 RMB/W, the cost of enlarging supply area depended on the peripheral network conditions, the connect principles included security, impedance matching and priority to construct project with lower cost. And the cost of the rest of wind power was shown in table. 2, which represented that additional investment would be 41million RMB to increase the wind capacity from 5.4MW to 8.9MW, the supererogatory project included 1MW capacity storage equipment and 2.5MW capacity from enlarging supply area.

Table 2. The cost of different arranged wind capacity with different measures by 2020

Capacity	Cost-optimized combination(million RMB)	Installing storage equipment(million RMB)	Enlarging supply area(million RMB)
0.5MW	1.5	8.0	1.5
1MW	5.40	16.0	5.4
1.5MW	14.0	24.0	12.0
2MW	18.0	32.0	18.0
2.5MW	25.0	40.0	25.0
3MW	33.0*	48.0	34.0
3.5MW	41.0*	56.0	48.0

5. Discussions

The operation and flow direction of distribution network was effect seriously by the distributed wind plant [7]. The network structure become complexity because of the control of communication facilities increased in some sense. The distribution network changes to active electric network with the distributed generation appearing [8]. The native load is supplied by local wind plant handy [9]-[10]. Those reduced the transmission demand from higher voltage grade to lower one. That will reduce the loss in power transmission. Moreover, the power flow in midday might change the direction top. As a result, the construction and investment of distribution network should take into account the transmission demand of network, which is not allowed power boosting. The traditional invest experience which is fully meet the demand of local might be not applicable. The investment about satisfy power supply should be cautious in distributed Wind plant fast-growing regions, the invest direction must pay close attention to absorption and delivery of the wind power.

The most important impact of distributed wind generation to power system is the load charities. A certain scale wind generation capacity will decrease that difference peak valley, which is good for power system operation. However, the capacity of wind generation keeps growing, the load character become worse, and the difference peak valley increase directly because of the randomly output character. The constructed scale of wind generation in a system should be planned based on valley load and some measures contained storage equipment and enlarging supply area, the cost can be adopted to meet the excess wind power capacity. It is noteworthy that the coordination among power grid. To reduce the transmission loss, the wind generations could not concentrate on a grid, which designed as distributed system. Those avoid the wind power transmits far away from wind generations concentration area to load area. The investment and planning of power station should arrange balanced in different area.

6. Conclusion

The power grid operation mode was proposed to analyze influence of the fast-grown distributed wind plant. The output character of wind electricity generation and load curve was investigated. The measures included the storage technology and enlarging supply area to increase installed wind capacity were studied, and the cost of those was analyzed based on project investment. The reasonable combination scheme was obtained according to the optimized model. Those could provide a reference to how much cost under different additional wind capacity.

7. References

- [1] Coal falls as gas rises: World energy balances in 2016
[<http://www.iea.org/newsroom/news/2017/august/coal-falls-as-gas-rises-world-energy-balances-in-2016.html>]
- [2] The editorial committee of China Electric Power Yearbook, China Electric Power Yearbook 2013, Beijing: China Electric Power Press, pp.20-34, 2013.
- [3] W. Long, F. Han, J. Xiao and X. Wang. "The Study of Adequacy Evaluation Method of Power Scale," *Electro. App.*, Vol.34, (5), p.20-23, 2015.
- [4] W. Long, X. Wang, D. Peng, P. Zhang and F. Han, "The Adequacy Discrete Analysis Based on Hierarchical Structure of Power Grid". *IEEE POWERCON*, p.1701, 2014.
- [5] Z. Liu. *The Ultra-high Voltage Grid*. Beijing: Economic Press of China, pp.57-69, 2005.
- [6] D. Ding, *the Development of Modern Power Grid and Security*, Tsinghua University Press, pp. 20–124, 2012.
- [7] George A. Orfanos, Pavlos S. Georgilakis, Nikos D. Hatziargyriou. "Transmission Expansion Planning of Systems with Increasing Wind Power Integration", *IEEE Transactions on Power Systems* 2013, 28(2), pp.1355-1362.
- [8] Weiping Wu, Zechun Hu, Yonghua Song, Giovanni Sansavini, Huimiao Chen, Xiaoshuang Chen, "Transmission Network Expansion Planning Based on Chronological Evaluation Considering Wind Power Uncertainties", *IEEE Transactions on Power Systems* 2018 4(1) pp.1-10.
- [9] J. Yu, F. Chi, K. Xu, S. Li, H. Liu, H. Li, D. Li. Analysis of the Impact of distributed generation on power grid, *Proceedings of the CSU-EPSA*. Vol.24, (1), p.138-142, 2012.
- [10] X. Shen, M. Cao. Research on the Influence of Distributed Power grid for Distribution Network. *Transactions of China Electrotechnical Society*, Vol. 30(1). p. 346-351, 2015.

Acknowledgment

This work was supported in part by the Technology Project of State Grid Corporation of China, Management Consulting Project of State Grid Corporation of China and the Technology Project of State Grid Corporation of China and State Grid Tianjin Electric Power Company.

Power Quality Monitoring and Energy Efficiency Management of Microgrid based on wind-PV-ES Hybrid System

Guanlu Yang, Minxu Wu, Yang Wang and Zehong Huang

College of Information and Science Engineering, Huaqiao University, Xiamen, China
E-mail:979576109@qq.com

Abstract. With the vigorous development of new energy power generation technology, the use of a large number of power electronic components and non-linear loads seriously threatens the power quality of microgrid systems. Therefore, it is necessary to monitor the power quality parameters. Therefore, it is necessary to monitor the power quality parameters during its operation in real time so as to maximize the use of energy resources. This article focuses on the overall design of the microgrid power quality monitoring system. In the hardware design part, this paper uses two chips of DSP and FPGA to collect, process and analyze the signals of the power grid. Mainly includes the system overall design idea, the signal conditioning module design, the digital signal processing circuit, the communication port circuit and so on. Based on this, combined with the virtual instrument technology, designed and completed a micro-grid power quality inspection platform based on Labview. This paper also establishes the reactive power compensation scheme of the microgrid TSC system by using Matlab/Simulink software, further improves the power quality and power factor of the operation, and verifies the power quality improvement scheme of the microgrid through simulation.

1. Introduction

At this stage, distributed generation can be divided into two main types: one is a photovoltaic power generation system; the other is a wind power generation system. Under the current state of energy demand and environmental protection in our country's current economic development, as a very effective supplement to the large power grid, the development of microgrids has great potential [1]. Today, although Distributed generation and microgrid technology have received increasing attention in many countries, they are mainly in the equipment development and control of microgrid systems, most of the research on core technologies related to energy efficiency management and grid-connected operation stability of microgrids is in its infancy. Therefore, the in-depth study of the microgrid system can lay a solid foundation for the development of China's micro-grid and has a very important engineering application value [2].

2. Design of power quality monitoring system based on FPGA and DSP

2.1. Overall system design

This article aims at the power system's requirements for the power quality analyzer, and designs a power quality monitoring and analysis system based on DSP and FPGA. The DSP chip, also known as the digital signal processor, is a microprocessor that is particularly suitable for digital signal processing operations. Its main application is to implement various digital signal processing algorithms in real time and quickly. FPGA is a product of further development based on programmable devices such as PAL, GAL, and CPLD. It emerged as a semi-custom circuit in the field



of application specific integrated circuits (ASIC), which not only solves the shortcomings of the custom circuit, but also overcomes the shortcomings of the limited number of original programmable device gates. The designed system is composed of a DSP28335 minimum system board and a FPGA-based data acquisition board, the data acquisition board can achieve 8 single-ended and 16-bit high-speed synchronous analog signal data acquisition. The system can be divided into three parts: signal conditioning module, data acquisition and processing module and human-machine interface module.

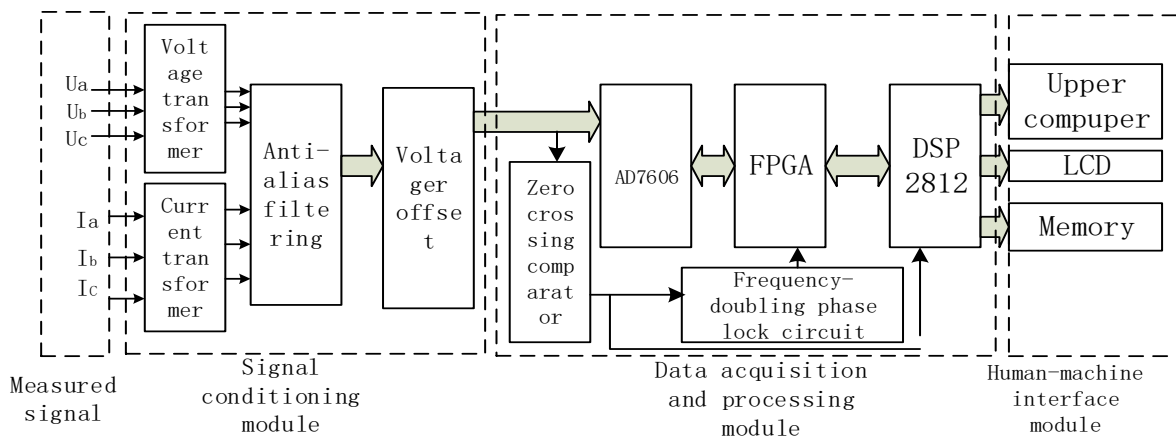


Figure 1. Overall system block diagram

2.2. Signal conditioning module design

In order to achieve high-quality data acquisition and prevent different frequency spectrums from interfering with each other, the design incorporates an anti-aliasing filter based on a second-order filter network. The harmonics required for this analysis are up to 64 times, that is, the highest frequency of harmonics is 3.2kHz. The number of sampling points in the AC voltage signal cycle is 128, so the frequency of the analog-digital sampling chip should be more than twice the maximum frequency of the harmonics, and the sampling frequency of 6.4 kHz is beneficial to prevent spectrum aliasing. Furthermore, in order to enhance the effect of signal recovery, a low-pass filter must be added to the sampling circuit. Considering the actual situation, we chose to set the cut-off frequency of the low-pass filter to 3.5 kHz. This paper designs an active anti-aliasing filter with low delay, low signal attenuation and high noise attenuation based on the OP07AH [3].

2.3. Data acquisition and processing module

2.3.1. AD module selection. This design chose the AD7606 chip instead of the sampling module that comes with the DSP to achieve high-precision, low-latency sampling. This design selects the parallel mode to read the AD7606's AD data and selects an input voltage range of $\pm 5V$. The AD7606 chip data port is connected to the IO port of the FPGA. Through FPGA's signal to CONVST, it can control 8 sampling channels at the same time in order to guarantee high precision. And the RD and CS ports of the AD7606 are connected to the FPGA so that the FPGA can better control the sampling chip. Send the RD and CS signals to the AD7606 to read the data on the DB [15:0] pins.

2.3.2. Zero-cross comparison circuit design. In order to provide the back-end circuit with a square-wave signal that is consistent with the grid frequency, a LM393 zero-cross comparison circuit was designed. This circuit provides a frequency reference for the back-end phase-locked loop and the measurement circuit. The working principle of the circuit is that when the input signal is greater than zero, the reverse voltage of the zero-crossing comparison circuit is greater than the voltage in the same direction, so the low-level signal is output, and the circuit can output the voltage signal on the AC side at a high level of 5 V. Convert to a square wave signal with the same frequency and phase.

2.3.3. Digital phase-locked loop circuit. The input side of the phase-locked loop CD4046 is the output square wave signal of the zero-crossing detection circuit, and the synchronous sampling circuit is composed of a CD4046 phase-locked loop chip and a CD4040 binary counter, and the output signal

thereof can be used after being multiplied by 128. The circuit guarantees the dynamic characteristics of the output signal. Even if the measured signal changes, it can acquire the corresponding frequency multiplication signal and achieve the function of synchronous sampling.

2.3.4. DSP and FPGA communication interface circuit. This design will configure the FPGA as an external expansion chip of the DSP, send the data collected by the DSP to the FPGA for calculation, and return the result to the DSP. Since the clock frequency of the DSP is about 150M, it will not interfere with the system and the transmission speed is fast, so this solution can be used as a communication solution for power quality monitoring. In order to facilitate the system's debugging and development, the system is configured with an extended RS-232 serial port to communicate and interact with the host computer. The port implements data output, and then the host computer performs image drawing.

3. Design and development of system software design

What this design wants to achieve is to control the AD chip through the FPGA to collect the data of the power system in real time, and then transmit the digital quantity after the AD conversion to the DSP. The data obtained by the analysis is analyzed and processed by the DSP.

3.1. Data acquisition module software design

The software design of the data acquisition module is mainly controlled by the FPGA, which completes the effective sampling and data storage of the data. This data acquisition system uses Verilog HDL language programming.

The system applies parallel sampling to the 6-channel signal. Before each sampling, the FPGA updates the sampling rate according to the command. The collected data is stored in the FIFO code. After the DSP receives the sampling command, it reads it and then uses the relevant electrical parameters. Do the operation. In order to ensure that the read conversion data pointer points to the first data to be converted, the AD7606 must be reset. As long as two CONVST pins (CONVSTA and CONVATB) are connected, the channels can all be set to sample at the same time. Therefore, we can start the rising edge of the shared CONVST signal and sample all the analog input channels at the same time.

3.2. Labview-based PC software building

The main functions of the labview PC set up this time are: the data obtained after DSP acquisition and processing are displayed on the monitoring panel in real time [4], and these data are saved in the Access database for reference and query. When the host computer displays the measurement results, the function module uses a pagination display, a total of six sub-pages, namely: the basic parameters of the power module, power module, three-phase unbalanced module, harmonic module, voltage fluctuation and flicker module and power supply Reliability rate module.

4. Research on microgrid energy efficiency management system

4.1. MATLAB modeling of micro-grid TSC reactive power compensation device

The main circuit of this modeling is composed of wind power and photovoltaic generation with energy storage microgrid system and a reactive power compensation device. The validity of this model can be verified by comparing the various states before and after the reactive power compensation of the microgrid. The device simulation mainly includes the following parts: wind power generation module, photovoltaic power generation module, load module, microgrid grid-connected controller module, TSC module, and reactive power compensation control module [5]. In this design, a model of wind power storage and microgrid grid-connected power generation is first built. Firstly, the voltage and current on the line are detected, and then the active power and reactive power on the line are calculated by a power detection module, and then the controller Calculate the reactive power to calculate the capacitor bank that needs to be switched, and then switch through the TSC system.

4.2. Simulation analysis

The main purpose of the reactive power compensator built in this paper is to compensate for the reactive power required for the operation of the microgrid. When the reactive power of the load changes, the system can compensate the reactive power in the system by switching the capacitor bank.

Power, so that the power generated by the microgrid can be maximized. In order to observe the effect of the reactive power compensation of this design, we established the three-phase controllable load and control the reactive power of the load. The simulation waveform is as follows:

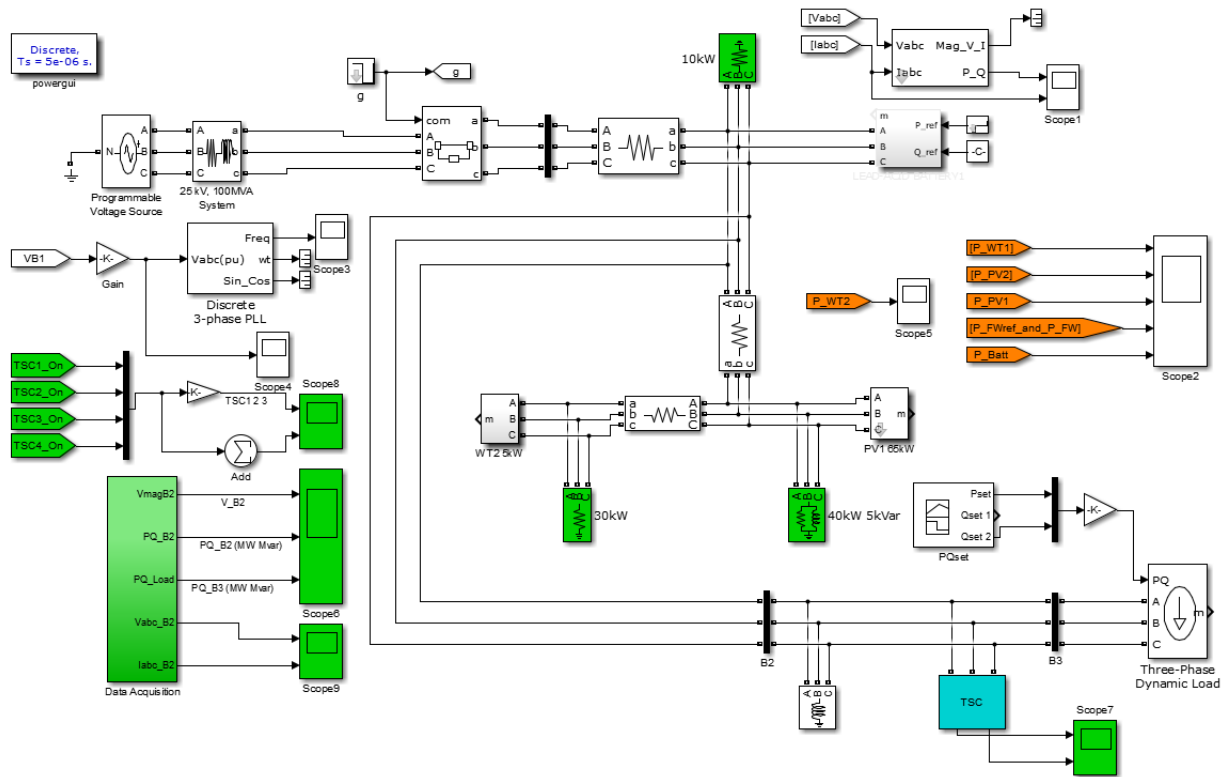


Figure 2. System Simulation



Figure 3. Reactive power curve of the load

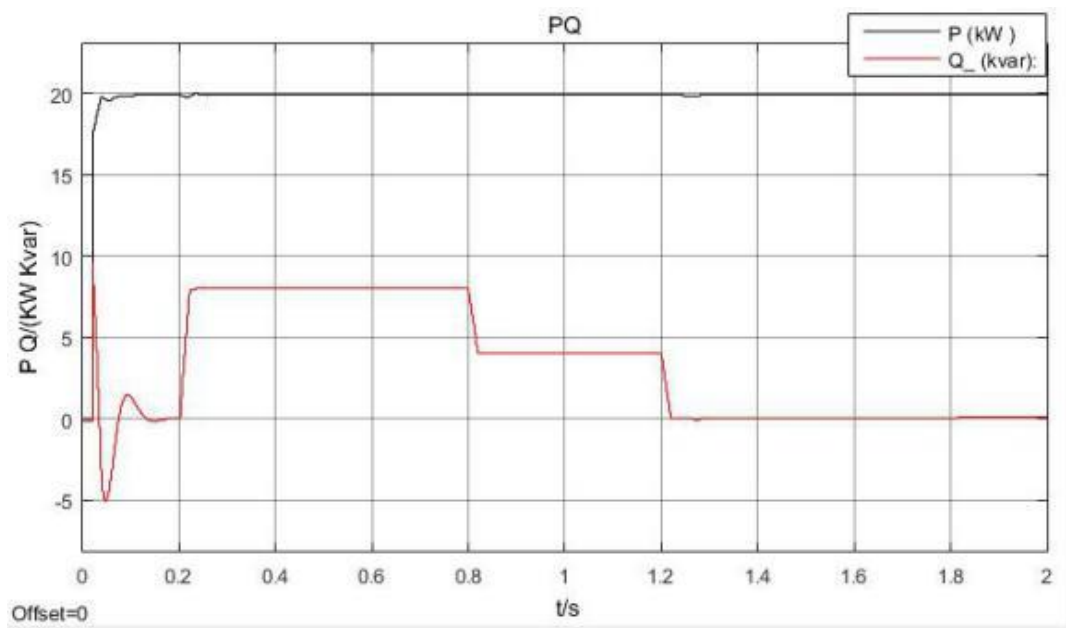


Figure 4. Waveforms of active and reactive power

When we change the reactive power of the load from 0 to 8 kvar at 0.2 s, after 0.02 seconds, the active and reactive power in the system fluctuate drastically. When the reactive power compensation device is input, the voltage lags after 0.02 seconds. For stability, the reactive power in the line is significantly increased and harmonics in the circuit are effectively suppressed. It proves that this device can effectively improve the microgrid power quality.

5. Experiments and analysis

In this design, a small stand-alone wind and light storage microgrid system was actually built on the building platform. The experimental system is mainly composed of a wind turbine (300W) and a photovoltaic panel (50W×4), battery, inverter equipment and other components. The load is 3 23W energy-saving lamps.

The microgrid power quality monitoring system designed this time is applied to the stand-alone wind and solar storage microgrid built above. The following is the microgrid operational data obtained through the monitoring system. Since there are many parameters for this monitoring, this data only lists the A-phase power quality parameters.

From the above, we can see that this system can accurately monitor the power quality of the microgrid system. Through the obtained data, it can be proved that the independently constructed wind and solar storage microgrids actually built this time meet the national standards and can be operated stably.

Table 1. A-phase frequency data table

Number of measurements	A-phase frequency (HZ)	Frequency deviation (HZ)
1	50.02	0.02
2	50.02	0.02
3	49.99	0.01
4	49.98	0.02
5	50.01	0.01

Table 2. Voltage and current rms data sheet

Number of measurements	A-phase voltage (V)	A-phase current (A)
1	221.5	0.574
2	221.3	0.569
3	221.4	0.584
4	221.7	0.604
5	221.9	0.583

Table 3. A-phase active power and reactive power data sheet

Number of measurements	Active power (W)	Reactive power (VA)	Power factor
1	57.75	113.31	0.454
2	58.57	126.15	0.464
3	58.97	115.39	0.455
4	55.91	119.05	0.592
5	58.82	115.47	0.453

Table 4. A-phase voltage and current distortion rates

Number of measurements	Voltage distortion rate (%)	Current distortion rate (%)
1	1.067	89.861
2	0.987	92.894
3	1.174	83.113
4	1.092	91.132
5	1.174	85.000

6. Conclusions

This article focuses on the hardware and software design ideas of this system. The overall design of the power quality detector is introduced in detail. The system is divided into multiple sub-modules and each module is elaborated. Then the specific flow chart of the sub-modules of the lower computer software system is introduced. The design of the upper computer based on LabVIEW is completed, real-time communication with the lower computer can be realized. The simulation diagram of the reactive power compensation device is constructed by Matlab, and the reactive power compensation device can be obtained through simulation, which can effectively improve the power quality of the micro grid.

7. References

- [1] Laasseter R H, Akhil A, Marnay C, et al. Integration of distributed energy resources: the CERTS microgrid concept. Berkeley, USA: *Consortium for Electric Reliability Technology Solutions*, 2002.

- [2] Atputharajah A, Ramach and aramurth V K, Pasupuleti J. Power Quality problems and solutions. IOP Conference Series: *Earth and Environment Science*, 2013, 16(1): 336-337
- [3] Seyyed Amir Gohari, Massoud Dousti, Khalil Mafinezhad. A Novel Analytical Technique to design a Tunable Bandpass Filter with Constant Bandwidth. *AEUE - International Journal of Electronics and Communications*, 2016, 70(10).
- [4] Meng Wusheng, Zhu Jianbo, Huang Hong, et al. Design of data acquisition system based on LabVIEW. *Electronic Measurement Technology*, 2008, 31 (11): 63-65.
- [5] Zhang X, Pei Wei, Deng W, et al. Energy management and coordinated control method for multi-source / multi-load DC microgrid. *Chinese Journal of Electrical Engineering*, 2014, 34 (31): 5553-5562.

Acknowledgments

This research was financially supported by the 12th Five-Year Plan for National Science and Technology Support (2015BA107b04) and Fujian Province Science and Technology Plan Project (2014H0031), People's Republic of China.

The Research on P2G Gas-Electric Hybrid Optimal Economic Dispatch Strategy

Zheng Zhang, Tianran Li, Quan Liu, Chao Yuan

Nanjing Normal University, Nanjing, China

E-mail: zzhengnju@163.com

Abstract. In many forms of the multi-energy complementary system, the regional multi-energy complementary distributed energy distribution system including distributed photovoltaic power generation (PV) and power-to-gas (P2G) equipment is a typical form. The P2G system uses non-peak excess power to produce hydrogen gas. Hydrogen can be stored directly for use as fuel, or it can be converted to natural gas for storage, enabling conversion of electrical energy to chemical energy. In this paper, the energy conversion and interconnection between electric energy and gas realizes the coordinated operation of distribution network and natural gas network, reduces the distribution pressure of distribution network, and improves the economic efficiency of energy utilization. First, the principle of P2G technology is introduced, and then the mathematical models of source device, conversion device and energy storage device are constructed separately. On this basis, an economic optimization-based micro-network system optimization scheduling model is established to investigate the economic benefits of gas-electric hybrid. Finally, the micro-grid system of the two scenarios is compared in the example, and the results prove that P2G has a good promotion effect on the economic benefits of the park.

1. Introduction

In the international background of the world's energy crisis and environmental pollution problems, innovative ideas such as energy Internet and integrated energy systems are constantly emerging. Transforming energy consumption patterns and achieving efficient and clean use of energy have become the common goal of people all over the world. The initial definition of the energy Internet [1] is based on the power system, based on the Internet and other cutting-edge information technologies, with distributed renewable energy as the primary primary energy source. It is a complex multi-network system formed by tight coupling with other systems such as natural gas networks and transportation networks. One of the structural characteristics of the energy Internet is that natural gas has the advantages of high efficiency, clean and environmental protection, which is compared with other primary energy sources. With the development of natural gas extraction technology, the cost of natural gas has declined, and the penetration rate in the power generation industry has tended to increase. On the other hand, the emergence of P2G technology can convert the surplus of renewable energy into methane and then inject it into the natural gas network for transportation or storage. Therefore, the degree of coupling between the power system and the natural gas system is deepened. It is forming a closed-loop system in which energy can flow in both directions. The planning method for power systems alone cannot meet the rules and operational requirements of the energy Internet. 'Gas-electric hybrid' in this paper refers to the coordinated operation of distribution network and natural gas network through energy conversion and interconnection between electric energy and natural gas [2]-[4].



In this paper, the combination of electro-gas technology and micro-grid system is used to study the regional multi-energy complementary distributed energy distribution system with distributed photovoltaic power generation (PV) and gas-electric hybrid (P2G). It helps to improve the economic benefits of energy Internet planning and helps to eliminate the intermittent and random renewable energy. Based on the microgrid energy hub model [5], the user-side microgrid system architecture in two different scenarios is established, and the pre-scheduling scheduling model is established on this basis. Comparing and demonstrating the power grid purchasing power and gas turbine output capacity of the microgrid system in two scenarios, the example shows that the P2G gas and electricity hybrid has positively promoted the economic benefits of the park.

2. Introduction to P2G technology

The emergence of P2G technology has deepened the gas-electric coupling and formed a closed-loop operation of the power system and the natural gas system. In other words, the P2G technology produces H₂ and O₂ by electrolysis of H₂O, and then catalyzes the production of CH₄ by H₂ and CO₂. CH₄ is the most important component of natural gas. P2G-converted CH₄ can be directly injected into the natural gas network for transportation and storage. In addition, P2G is also beneficial to enhance the system's ability to accept intermittent renewable energy generation. By January 2016, there are about 50 P2G demonstration stations in Europe, most of which are located in Germany. The installed capacity of P2G ranges from a few kW to several MW [6], [7]. Compared with the capacity of modern interconnected power systems, the installed capacity of P2G projects at this stage is still very limited. The design capacity of future P2G projects will gradually increase with the advancement of technology. It will have an increasingly obvious impact on the coordinated planning and operation of power systems and natural gas systems.

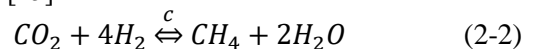
P2G technology refers to the process of converting H₂O and CO₂ into H₂ or CH₄ by using electric energy. It is mainly divided into two types: electric to H₂ and electric to CH₄ [8]. Considering that the natural gas network has very limited ability to absorb H₂ [9], the P2G referred to in this paper refers to the electric transfer CH₄ that can be directly connected to the natural gas network.

The realization process of P2G mainly consists of two steps of electrolyzing water and hydrogen methanation [10], [11].

Step 1: Electrolyzing water is to use electricity to electrolyze water to produce H₂ and O₂. The chemical equation [12] is shown as formula (2-1). At present, the energy conversion efficiency of this step can reach 75%-85% [13].



Step 2: Hydrogen methanation. It is also known as Sabatier catalytic reaction^[9]. The H₂ produced in the first step is chemically reacted with CO₂ which is under high temperature and pressurized environment to produce H₂O and CH₄. The chemical reaction equation [14] is shown as formula (2-2). At present, the energy conversion efficiency of this step can reach 75%-80% [15].



The P2G energy conversion efficiency can reach 49%~65% [9]. The P2G plant station contributes to the surplus power generation of intermittent renewable energy. On the one hand, it balances the power generation of renewable energy. On the other hand, it realizes the flow of energy from the power system to the natural gas system, and promotes the power system and the natural gas system positively.

3. Microgrid mathematical model with P2G energy storage

The purpose of energy optimization management of the campus microgrid system is to find the optimal electric and gas power distribution method from the online unit of the system to meet specific operational objectives while satisfying the system constraints. This paper focuses on the optimization effect of the current scheduling strategy in energy management. It analyzes the structure of the park system, clarifies the objective function, optimizes variables and constraints, establishes an energy optimization management model, and constructs a numerical example for verification. It's focused on the impact of the economic strategy on P2G energy storage.

This section first classifies the various units within the system to establish a reasonable and accurate mathematical model. Generally, it includes a variety of energy kinds (electricity, gas, cold, heat, etc.). From the structure, it can be divided into energy input, conversion, output and other links. From the

function, it can be divided into source equipment, conversion equipment and energy storage equipment. The microgrid system containing P2G energy storage studied in this paper can be represented by Figure 1.

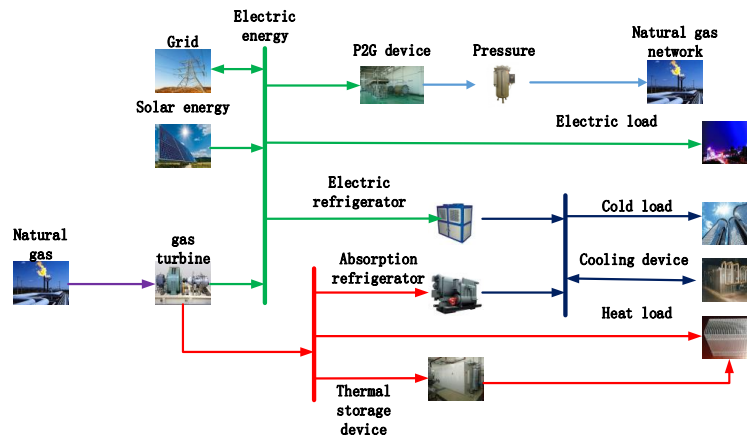


Fig.1. Typical structure of the park

As is shown in the figure 1, the source device refers to a device capable of generating heat, electricity, cold, and the like in the form of primary energy, and mainly includes a gas turbine, a power grid, a photovoltaic panel, and the like. A conversion device refers to a device capable of converting one form of energy generated by a source device or other device into another form of energy, mainly including a P2G conversion device, an electric refrigerant, an absorption refrigerating machine, and the like. The energy storage device refers to a device capable of storing energy, and mainly includes a gas storage device, a heat storage device, a cold storage device, and a power storage device.

3.1 Mathematical model of the source device

3.1.1 Gas turbine

$$\begin{cases} P_{GT} = V_{HG} \cdot q_{HG} \cdot \eta_{GT} \\ Q_{GT}^S + Q_{GT}^W = V_{HG} \cdot q_{HG} \cdot (1 - \eta_{GT} - \eta_{GT}^{loss}) \\ \eta_{GT}^S = Q_{GT}^S / P_{GT} \\ \eta_{GT}^W = Q_{GT}^W / P_{GT} \\ P_{GT}^{min} \leq P_{GT} \leq P_{GT}^{max} \end{cases} \quad (3-1)$$

Where P_{GT} , Q_{GT}^S and Q_{GT}^W represent the output of electric power, flue gas heat power and hot water heat power. V_{HG} and q_{HG} represent the consumption and calorific value of natural gas, respectively. η_{GT} , η_{GT}^{loss} , η_{GT}^S and η_{GT}^W represent power generation efficiency, energy loss rate, flue gas thermoelectric ratio, and hot water thermoelectric ratio. P_{GT}^{min} and P_{GT}^{max} represent the lower and upper limits of the output power.

3.1.2 Solar power generation equipment

Photovoltaic power generation equipment does not need to consider operational regulation, and the power generation can be used preferentially.

$$P_{PV}^{min} \leq P_{PV} \leq P_{PV}^{max} \quad (3-2)$$

P_{PV}^{min} and P_{PV}^{max} are the lower and upper limits of the power generated are respectively.

3.2 Mathematical model of the conversion device

3.2.1 P2G device

P2G device converts electrical energy into natural gas.

$$\begin{cases} P_{P2G}^g = \eta_{P2G} \cdot P_{P2G}^c \\ 0 \leq P_{P2G}^c \leq P_{P2G}^{rated} \end{cases} \quad (3-3)$$

P_{P2G}^c and P_{P2G}^g represent input and output power. η_{P2G} is the efficiency factor of P2G device. P_{P2G}^{rated} indicates the rated power of P2G device.

3.2.2 Electric refrigerator

Electric refrigerator is a device that converts electrical energy into cold energy.

$$\begin{cases} C_{EC} = P_{EC} \cdot COP_{EC} \\ C_{EC}^{min} \leq C_{EC} \leq C_{EC}^{max} \end{cases} \quad (3-4)$$

P_{EC} and C_{EC} are the input electrical power and the output cooling power. COP_{EC} is refrigeration coefficient. C_{EC}^{min} and C_{EC}^{max} are the lower and upper limits of the output cooling power respectively.

3.2.3 Absorption type heating and cooling machine

The machine is used as a cold and heat energy conversion device.

$$\begin{cases} Q_{CH/C}^{out} = Q_{CH/C}^{in} \cdot \eta_{CH/C} \\ Q_{CH/C}^{min} \leq Q_{CH/C}^{out} \leq Q_{CH/C}^{max} \\ C_{CH/C}^{out} = Q_{CH/C}^{in} \cdot COP_{CH/C} \\ C_{CH/C}^{min} \leq C_{CH/C}^{out} \leq C_{CH/C}^{max} \end{cases} \quad (3-5)$$

$Q_{CH/C}^{in}$, $Q_{CH/C}^{out}$ and $C_{CH/C}^{out}$ are the input thermal power, the output thermal power, and the output cooling power. $\eta_{CH/C}$ and $COP_{CH/C}$ represent heating efficiency and cooling coefficient. $Q_{CH/C}^{min}$ and $Q_{CH/C}^{max}$ represent the lower and upper limits of the output thermal power. $C_{CH/C}^{min}$ and $C_{CH/C}^{max}$ are the lower and upper limits of the output cooling power.

3.3 Mathematical model of energy storage equipment

3.3.1 Power storage device

A power storage device has the ability to store electrical energy for a long time and to release electrical energy.

$$\begin{cases} 0 \leq P_{ES,C} \leq \gamma_{ES,C} \cdot Cap_{ES} \\ 0 \leq P_{ES,D} \leq \gamma_{ES,D} \cdot Cap_{ES} \\ W_{ES}^{min} \leq W_{ES} \leq W_{ES}^{max} \\ W_{ES}^t = W_{ES}^{t-1}(1 - \sigma_{ES}) + (P_{ES,C} \cdot \eta_{ES,C} - \frac{P_{ES,D}}{\eta_{ES,D}})\Delta t \end{cases} \quad (3-6)$$

3.3.2 Heat storage device

A heat storage device has the ability to store thermal energy for a long time and to release thermal energy.

$$\begin{cases} 0 \leq Q_{HS,C} \leq \gamma_{HS,C} \cdot Cap_{HS} \\ 0 \leq Q_{ES,D} \leq \gamma_{ES,D} \cdot Cap_{HS} \\ W_{HS}^{min} \leq W_{HS} \leq W_{HS}^{max} \\ W_{HS}^t = W_{HS}^{t-1}(1 - \sigma_{HS}) + (Q_{HS,C} \cdot \eta_{HS,C} - \frac{Q_{HS,D}}{\eta_{HS,D}})\Delta t \end{cases} \quad (3-7)$$

3.3.3 Cool storage device

A cold storage device has the ability to store refrigeration for a long time and to release the amount of refrigeration.

$$\begin{cases} 0 \leq Q_{CS,C} \leq \gamma_{CS,C} \cdot Cap_{CS} \\ 0 \leq Q_{CS,D} \leq \gamma_{CS,D} \cdot Cap_{CS} \\ W_{CS}^{min} \leq W_{CS} \leq W_{CS}^{max} \\ W_{CS}^t = W_{CS}^{t-1}(1 - \sigma_{CS}) + (C_{CS,C} \cdot COP_{CS,C} - \frac{C_{CS,D}}{COP_{CS,D}})\Delta t \end{cases} \quad (3-8)$$

3.3.4 Gas storage device

The gas storage device can store natural gas and release natural gas for a long time.

$$\begin{cases} W_1 = W_0 + (Q_c \eta_c - Q_d / \eta_d)\Delta t \\ W_{min} \leq W \leq W_{max} \\ 0 \leq Q_c \leq Q_{c,max} \\ 0 \leq Q_d \leq Q_{d,max} \end{cases} \quad (3-9)$$

4. Energy optimization management of P2G multi-source energy storage microgrid

The daytime scheduling strategy of the campus system refers to the completion of the scheduling plan before the scheduling date, and then the scheduling plan is executed during the scheduling day without change.

4.1 Objective function

Considering the economics of the operation of the park system, the goal of daytime scheduling should minimize the cost of running the schedule. The operation scheduling cost does not consider the cost of purchasing, maintenance, overhaul, etc. of the equipment, and only includes the cost of purchasing electricity and gas. At the same time, regardless of whether the system sells electricity to the grid, the objective function is

$$\min C = C_e + C_g \quad (4-1)$$

C represents the total cost of the operation schedule. C_e and C_g represent the purchase cost of electricity and natural gas respectively. It can be calculated by the equation (4-2).

$$\begin{cases} C_e = \sum_{t=1}^n c_e^t P_G^t \Delta t \\ C_g = c_g^t \sum_{t=1}^n (P_{CU}^t + P_{CH/C}^t + P_{GB}^t) \Delta t \end{cases} \quad (4-2)$$

n indicates the number of points in the schedule. c_e^t and c_g^t are the price of electricity and natural gas at the t -th scheduling time point. P_G^t , P_{CU}^t , $P_{CH/C}^t$ and P_{GB}^t respectively indicate the purchase power of the grid during the t -th scheduling time, the gas power consumed by the cogeneration unit, the gas power consumed by the heating and cooling unit, and the gas power consumed by the gas boiler. Δt indicates the interval duration between two adjacent scheduling time points.

4.2 Restrictions

Each component of the system should meet its respective output power constraints:

$$\begin{cases} P_{imin} \leq P_i \leq P_{imax} \\ Q_{imin} \leq Q_i \leq Q_{imax} \\ C_{imin} \leq C_i \leq C_{imax} \end{cases} \quad (4-3)$$

P_i , Q_i and C_i respectively indicate the electric power, thermal power and cooling power output of a certain component. The subscript min indicates the lower limit of the output power, and the subscript max indicates the upper limit of the output power.

For energy storage equipment, the following constraints should also be met.

4.2.1 Charge/discharge power constraints

$$\begin{cases} P_{min}^C \leq P_{ES,C} \leq P_{max}^C \\ Q_{min}^C \leq Q_{HS,C} \leq Q_{max}^C \\ C_{min}^C \leq C_{CS,C} \leq C_{max}^C \end{cases}, \begin{cases} P_{min}^D \leq P_{ES,D} \leq P_{max}^D \\ Q_{min}^D \leq Q_{HS,D} \leq Q_{max}^D \\ C_{min}^D \leq C_{CS,D} \leq C_{max}^D \end{cases} \quad (4-4)$$

4.2.2 Energy storage constraints

$$W_{imin} \leq W_i \leq W_{imax} \quad (4-5)$$

4.2.3 Energy storage mechanism constraints

$$W(t+1) = (1 - \sigma)W(t) + (P_c \eta_c - P_D / \eta_D) \Delta t \quad (4-6)$$

$W(t)$ and $W(t+1)$ represent the energy storage at the current time and the next time respectively. σ is energy self-loss rate. P_c and P_D represent charge/discharge power. η_c and η_D indicate the efficiency at the time of charge/discharge.

4.2.4 Working state constraints

Let 0-1 variable $X(1, t)$ denote the energy storage state of the energy storage device at time t . $X(1, t)=1$ indicates that the device is in energy storage state, and $X(1, t)=0$ indicates the device is not in storage state. Similarly, let 0-1 variable $X(2, t)$ denote the discharging energy state at time t . As is known, the energy storage and discharge states cannot exist at the same time

$$X(1, t) + X(2, t) \leq 1 \quad (4-7)$$

5. Case analysis

The example system constructed in this paper is shown as Figure 2. The system source equipment includes a utility grid, a photovoltaic device, a gas turbine, and the conversion device includes an electric gas transfer device, an electric refrigerator, an absorption type warm and cold machine, a heat

pump, an energy storage device, a storage battery, and a storage battery, and the load includes an electric load, a heat load, and a cold load. In order to compare the differences in electric power of microgrid systems in different scenarios, this paper compares and analyzes the economic dispatch results of two different structures.

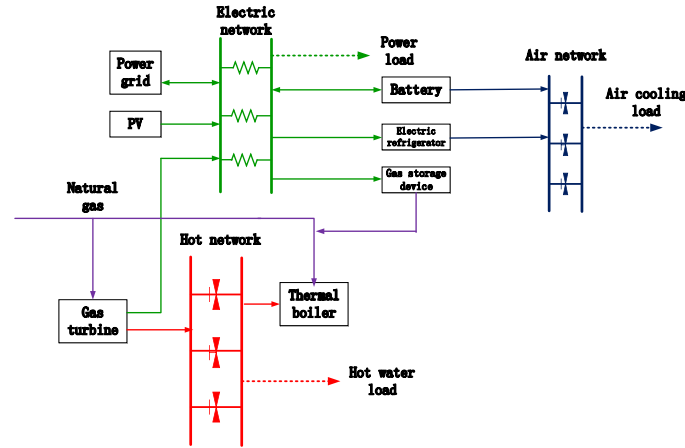


Fig.2. Study structure diagram

In the first scenario, the microgrid system does not contain energy storage equipment and P2G equipment, and only contains coupling elements between different energy sources. In the second scenario, the microgrid system adds P2G equipment and gas storage equipment to improve the coupling characteristics of the power network and the natural gas network. The model device types of the two microgrid systems are shown in Table 1.

Table.1. Components of two microgrid systems

Device	Scene 1	Scene 2
Gas Turbine	✓	✓
PV	✓	✓
Hot and cold machine	✓	✓
Electric refrigerator	✓	✓
P2G	✗	✓
Electric energy storage	✓	✓
Thermal energy storage	✓	✓
Cold energy storage	✓	✓
Gas storage	✗	✓

As is shown, it is the main calculation data used in this example. The daily scheduling period takes 1 hour. In the system, the daily load and PV output prediction curve are shown in Figure 3. The time-of-use price and natural gas price are shown in Figure 4.

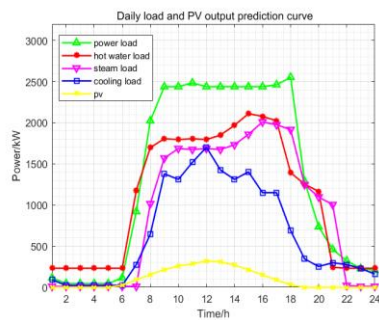


Fig.3. Daily load and PV output prediction curve

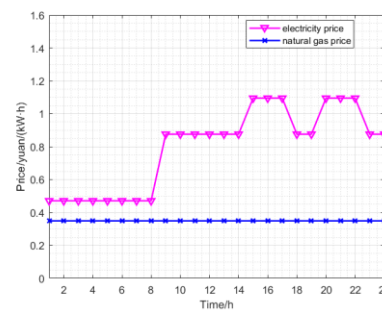
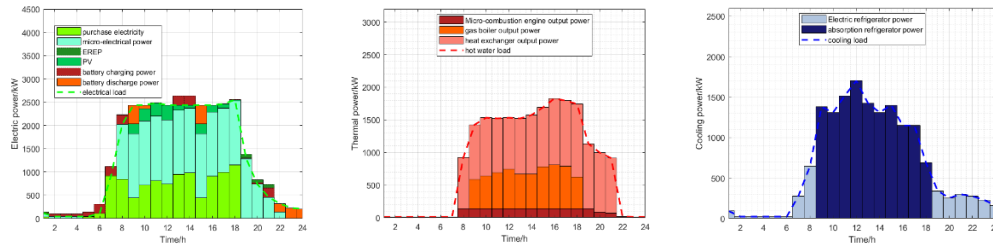


Fig.4. Time-sharing tariff

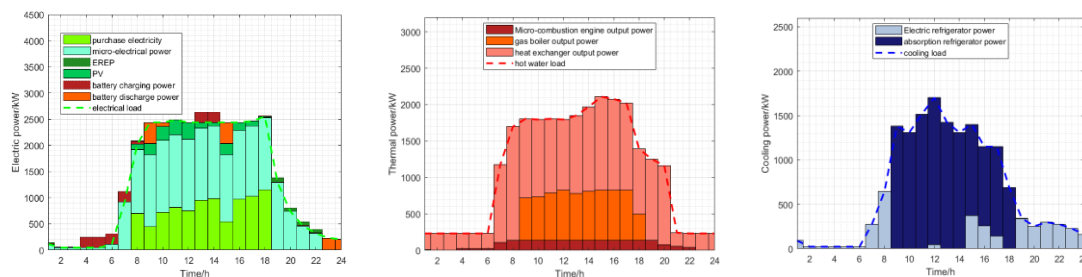
Don't consider the influence of the electrical gas conversion characteristics on the daily dispatching strategy. According to the system parameters, the MATLAB program is programmed, and the CPLEX solver in the YALMIP toolbox can be called to obtain the optimal scheduling results of cold, heat and electric power.



(a) Electric power optimization (b) Hot water power optimization (c) Cooling power optimization
Fig.5. Day-time optimization scheduling results without P2G

Without considering P2G equipment and energy storage equipment, the daily operating cost of the system is 40,156 yuan.

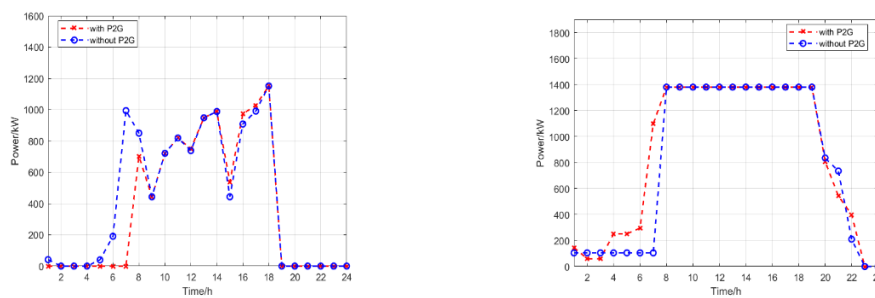
When considering the characteristics of electrical gas conversion, the optimal cooling, heat and electricity scheduling results of the system are shown in Figure 6.



(a) Electric power optimization (b) Hot water power optimization (c) Cooling power optimization
Fig.6. Day-time optimization scheduling results with P2G

In the case of considering P2G equipment and energy storage equipment, the daily operating cost of the system is 38,750 yuan.

Considering the electrical gas conversion characteristics, the power purchase power of the grid and the gas power of the gas turbine are compared as follows.



(a) Grid purchase power comparison chart (b) Gas turbine electric power output comparison chart
Fig.7. Consider the P2G characteristics output comparison chart

The running cost with P2G is lower than that without P2G. The reason is that when the P2G device is added, the cost of the microgrid system will be reduced without considering the cost of the device. It can be seen from Fig.7. The power purchase power of the grid changes significantly between the 4th and 8th scheduling moments; the output power of the gas turbine changes significantly before the 8th scheduling time point and after the 20th scheduling time point. Therefore, P2G equipment consumes residual solar energy, reduces power purchase power of the grid, and increases gas turbine output.

6. Conclusion

This paper combines P2G equipment and micro-grid system to construct a multi-source energy storage micro-network system model in two scenarios. On this basis, the goal of the P2G multi-source energy storage microgrid system is established. In both scenarios, the impact of P2G device access on system cost is analyzed. Finally, through the example verification, P2G can reduce the overall energy purchase cost of the system. In the follow-up work, on the one hand, the model of the microgrid system in this paper is relatively simple, and the equipment cost is not considered, and the system model construction will be further improved; On the other hand, the scheduling strategy is a relatively rough energy management method. In the future, the intraday scheduling strategy will be considered to improve the prediction accuracy.

7. Acknowledgements

I really appreciate the help from my tutor and classmates. With their help, I finished the paper.

8. References

- [1] Dong Chaoyang, Zhao Junhua, Wen Fushuan, et al. From Smart Grid to Energy Internet: Basic Concept and Research Framework [J]. Automation of Electric Power Systems, 2014, 38 (15) : 1-11.
- [2] Sun Guoqiang, Chen Shuang, Wei zhinong, et al. Probabilistic optional power flow of combined natural gas and electric system considering correlation [J]. Automation of Electric Power System, 2015, 39(21);11-17.
- [3] Qiu Jing, Dong Zhaoyang, Zhao Junhua, et al. Low carbon oriented expansion planning of integrated gas and power systems [J]. IEEE Transactions on Power Systems, 2015, 30(2):1035-1046.
- [4] Xu Xiandong, Jia Hongjie, Jin Xiaolong, et al. Study on hybrid heat-gas-power flow algorithm for integrated community energy system [J]. Proceedings of the CSEE, 2015, 35(14):3635-3642.
- [5] Schulze M, Friedrich L, Gautschi M. Modeling and optimization of renewables: applying the Energy Hub approach[C]// IEEE International Conference on Sustainable Energy Technologies. IEEE, 2009:83-88.
- [6] Grond L, Schulze P, Holstein J. Systems analyses power to gas: technology review[EB/OL].www.eu, ropean powertogas.com/fm/download/28
- [7] World's largest power-to-gas plant for generating methane enters operation[EB/OL].http://www.z, sw-bw. de
- [8] Bunger U, Landinger H, Pschorr-Schoberer E, et al. Power-to-gas(PtG)in transport status quo and perspectives for development[EB/OL].http://www.bmvi.de/SharedDocs/EN/Anl agen/UI-MKS/mks-studie-ptg-transport-status-quo-and-perspectives-for-development.pdf.
- [9] Jentsch M, Trost T, Sterner M. Optimal use of power-to-gas energy storage systems in an 85% renewable energy scenario [J]. Energy Procedia,2014,46:254-261.
- [10] Baumann C, Schuster R, Moser A. Economic potential of power-to-gas energy storages[C]// European Energy Market. IEEE, 2013:1-6.
- [11] Gahleitner G. Hydrogen from renewable electricity: An international review of power-to-gas pilot plants for stationary applications [J]. International Journal of Hydrogen Energy, 2013, 38(5):2039-2061.
- [12] Ni Meng, Leung M K H, Sumathy K. Progress of hydrogen production through water electrolysis[J]. Energy Environmental Protection, 2004, 18 (5):5-9.
- [13] Moskalenko N, Lombardi P, Komarnicki P. Multi-criteria optimization for deter-mining installation locations for the power-to-gas technologies [C]//2014 IEEE PES General Meeting, 27-31 July, 2014, National Harbor, MD, USA:1-5.
- [14] Hoekman S K, Broch A, Robbins C, et al.CO2 recycling by reaction with renewably-generated hydrogen [J].International Journal of Greenhouse Gas Control, 2010, 4(1):44-50.
- [15] Krause T, Andersson G, Frohlich K, et al. Multiple-energy carriers: modeling of production, delivery, and consumption [J]. Proceedings of the IEEE, 2011, 99(1):15-27.

Chapter 6:
Power System and Automation

Study on Data Selection Method of Historical Operation Data for Large Scale Power System

Hongyang Dai, Ying Lv, Zhihong Yu, Guangming Lu, Chang Xie and Jinxiu Hou

Power System Department, China Electric Power Research Institute, Beijing, China

Abstract. A data selection method based on similarity measurement and support vector machine (SVM) is proposed. At first, the critical clearing time (CCT) is used as the class label, and features which are strongly correlated with the class label will be extracted. Secondly, a SVM classifier is trained on the initial training instances with extracted features, and the instance which is misclassified will be removed. Thirdly, the concept of the most similar instance pair is proposed, which two instances with the minimum distance are selected, and then removes the eligible instances which is noisy and redundant instances. The proposed method which can simultaneously prune data in horizontal and vertical directions is tested by online historical data of an actual large scale power system. Experimental results demonstrate that more than 70% features and 30% instances are reduced, and the accuracy and storage reduction are also improved. This method can be well used with the good performance in large scale power system.

1. Introduction

With the rapid development of DC and AC hybrid grid, the power system becomes larger and more complicated, which brings profound influence to the operation stability of power grid [1]. It is necessary to continuously expand the performance of online security analysis, in order to meet the requirements of dispatching operation work adjusting to large scale power system. Recently, the big data technology has developed, which provides more means to solve the problems in many technical fields [2]-[4]. At present, a lot of dispatching operation data had been accumulated day by day in dispatching institutions. For example, the size of calculated data and result data which produced by the online security analysis can be amounted to 1GB in every 15 minutes. Such huge amount of data must be dealt with in learning process, which will cost massive computational resources and have long runtimes. Thus, data selection can be applied for reducing the data to a manageable size, leading to a reduction of the useless, erroneous or noisy data, before applying learning algorithms [5]-[8].

Data selection is one of the important pre-processing steps that can be applied in many data mining tasks [9]. This step aims at two aspects: (1) the data size can be reduced, leading to a reduction of the training time as long as the improvement of learning efficiency; (2) the noisy or erroneous data can be removed, leading to the improvement of the accuracy in classification problems. There are two common methods of data selection: feature selection and instance selection. Feature selection aims at reducing the number of power grid characteristics from longitudinal dimension of dataset; and instance selection aims at reducing the number of instances from latitudinal dimension of dataset, choosing a subset of the total available data to achieve the original purpose of the data mining application as if the whole data had been used.

In the last years, several approaches for data selection have been proposed in power system area. Most of methods are proposed to preserve the boundaries between different classes in the dataset, because of the relevant information provided by border instances for supporting discrimination between classes,



which destroy the structure of the data set and is bad for further analysis[10]-[11]. According to [12], [13], SVM (support vector machine) is usually used for classification with good performance. A segmentation method based on a two-level SVM is proposed [14], which reduce the negative effects of the mistaking instance. But the most useless and reductant instances are preserved with low reduction efficiency. Hybrid methods (e.g. RIPE) use ENN (Edited Nearest Neighbour) [15] to removing border points that are noisy aiming at smoothing the boundary, and use the concept of the nearest similar pair with the same class of datasets to removing redundant instances. The algorithm make better compromise in the classification accuracy and the storage compression ratio, but ignoring the problem of the nearest similar pair with the different class.

This paper is organized as follows: Section II presents the method of feature selection based on similarity measurement; Section III presents the method of instance selection combining the repetitive screening, SVM and similarity measurement; Section IV presents the experimental results, including the evaluation of the method and the comparison of three similarity measurement; finally, section V presents main conclusions of our work.

2. Feature selection base on correlative coefficient

When selecting the features to be processed, it is needed to select the features that are most related with the class label. In order to find the features having high relationship with the class label, the correlation coefficient between them is calculated. In the probability theory and statistics, the correlation coefficient reflects the strength and direction of the linear relationship between two variables, and the most commonly used is Pearson correlation coefficient. Pearson Correlation coefficient calculation formula is defined as follows.

$$\text{Cor}_{AB} = \frac{\sum_{i=1}^n (a_i - \bar{A})(b_i - \bar{B})}{(\sum_{i=1}^n (a_i - \bar{A})^2)^{1/2} (\sum_{i=1}^n (b_i - \bar{B})^2)^{1/2}} \quad (1)$$

Where A and B are two linear variables, N is the number of elements in A or B, a_i is the value in A, b_i is the value in B, \bar{A} is the average of A, \bar{B} is the average of B.

The range of the correlation coefficient is $[-1, +1]$, the correlation coefficient greater than “0” represents that two groups of variables are positive correlation, and more closer to “+1”, more stronger correlation degree; on the contrary, the correlation coefficient less than “0” represents that two groups of variables are negative correlation, and more closer to “-1”, more stronger correlation degree; “0” represents that two groups of variables are uncorrelated. The correlation degree is determined by following scope of correlation coefficient showed in Table 1.

Table 1. The relation between correlation coefficient and correlation degree.

Correlation coefficient	Correlation degree
0.8-1.0	Very strong correlation
0.6-0.8	Strong correlation
0.4-0.6	Middle degree correlation
0.2-0.4	Weak correlation
0.0-0.2	Zero correlation

3. Instance selection based on SVM and similarity measurement

One method of instance selection often has limitations, Combination of several methods can give play to complementary advantages and make up for the shortcomings each other. The method of instance selection proposed in this paper was the combination of the SVM and similarity measurement, which can remove the noisy and useless instances. This method was mainly divided into three steps: repetitive screening, selection based on SVM, selection based on similarity measurement

3.1. Repetitive screening

The operation of the power system is periodic. The periodicity is relatively stable in a short period of time, and with the growth of time scale, the difference of operation mode for power system will inevitably increase. Features are reduced greatly after feature selection used to the initial dataset, the difference between two instances will be disappear, that there will be two or more instances of the same characteristics. Thus, the repetitive instances need to be deal with at first, for choosing one of the same instances and deleting the remaining instances.

3.2. Instance selection based on SVM

The support vector machine (SVM) is a widely used tool in classification problems. It trains a classifier by finding an optimal separating hyperplane which maximizes the margin between two classes of data in the kernel induced feature space. In learning by SVM, SVM calculates an alignment discernment line which maximize margin. SVM is excellent in generalization capability and it can extend to nonlinear by a kernel trick [13]-[14].

The instance was trained by SVM algorithm with the kernelled decision function represented as:

$$f(\mathbf{x}) = \text{sgn}\{(\mathbf{w}^* \cdot \mathbf{x}) + b^*\} = \text{sgn}\left\{\sum_{i=1}^n \alpha_i^* y_i K(\mathbf{x}_i \cdot \mathbf{x}) + b^*\right\} \quad (2)$$

Where sgn is the sign function to determine the classification of the instance (for example, the calculation result is negative or positive which represent the different classification respectively), K is linear kernel, α and b are the parameters occurred in training process, \mathbf{x}_i is support vector, y_i is the class label, \mathbf{x} is instance to be discriminated.

The Gaussian kernel is commonly used.

$$K(\mathbf{x}_i, \mathbf{x}_j) = \exp\left(-\frac{\|\mathbf{x} - \mathbf{x}_i\|^2}{\sigma^2}\right) \quad (3)$$

Where the parameter $\sigma > 0$.

Except the parameters in kernel function, c called cost parameter need to be specified in the training process which is a positive constant. The cost parameter that denotes the penalty of slacks can enhance the generalization ability of SVM algorithm.

It need to be clear that, the parameters of decision function are default in the model training process if using the mature data analysis tools, such as R programming language or MATLAB. Generally, c is equal to reciprocal of characteristics, and c is equal to 1 in SVM decision function.

The step of instance selection base on SVM is described below.

- Step 1: Labelled training set S is trained by SVM, finding an optimal separating hyperplane and learning a classification model.
- Step 2: S as the test set is classified by classification model learned in step 1, obtaining the classification result R .
- Step 3: If the instance in test set classified by SVM differs from the class in the given training data, the instance need to be removed.
- Step 4: Step1 ~ Step3 is repeated until there is no incorrect discernment.
- The method is a process of removing instances iteratively, it can be used to remove noise instances, make the decision boundary more clearly.

3.3. Instance selection based on similarity measurement

The method in section B can effectively remove noise instances near the boundary, but also remain all of the internal instance, leading to unsatisfactory compression ratio of capacity. The instance selection method based on similarity measurement was described in this section.

First of all, a new concept was introduced: the most similar instances pair. For an instance A in dataset, computing the most similar instance B, if A is also the most similar instance to B, it can say that A and B are the most similar instances pair.

In this paper, three methods were used to calculating the most similar instance pair: Euclidean Distance, Hausdorff Distance [15] and Correlation distance.

There are two n-dimensional instances A $(a_1, a_2 \dots a_n)$ and B $(b_1, b_2 \dots b_n)$.

- The Euclidean Distance is defined as follows:

$$D_{AB} = \left(\sum_{i=1}^n (a_i - b_i)^2 \right)^{1/2} \quad (4)$$

- The Hausdorff Distance is defined as follows:

$$H_{AB} = \max(h(A,B), h(B,A)) \quad (5)$$

Where

$$h(A,B) = \max_{a \in A} \min_{b \in B} \|a-b\| \quad (6)$$

And $\|a-b\|$ is the Euclidean distance.

- The Correlation Distance is defined as follows:

$$D_{AB} = 1 - Cor_{AB} \quad (7)$$

Where, Cor_{AB} is the correlation coefficient defined in section 2.

The step of instance selection base on similarity measurement is described below.

- Step 1: the most similar instance x' of the instance x was calculate and marked, and repeat this step until all instance's most similar instance were calculate and marked in dataset S.
- Step 2: all the most similar instance pair were extracted after traversal of the instance x and its most similar instance x'.
- Step 3: the class of each instance in the most similar pair was compared. If the same class, anyone of two instances was deleted; if not the same class, the two instances were deleted at the same time.

The method is a process of removing instances either closed to the boundary or internal instance far away from the boundary, it can be used to remove either noise instances or reductant instances.

4. Experiments

4.1. Initial Dataset

State variables of power system were selected as the analysis of the attribute in dataset, including the electric variables of equipment in static state and statistics of area and power plants and stations. Selecting static variables under the static state can shorten the time of stability judgement. The speed of stability judgement was reduced if transient variables were selected, which needed a period of time in transient stability simulation process. There was no definite conclusion of the relation between static variables and power system stability, so that more static variables were choose as far as possible under the premise of computing resources. The static variables and statistics are shown in Table 2.

Critical clearing time (CCT) that represent the system boundary of stable and unstable was selected as class label to analysis the dataset. And it can characterize the stability degree when specified fault occurred in power system, the longer critical clearing time, the less impact to power system, and the system is more stable. System instability will be created by the specified fault if the critical clearing time is less than the normal protection operation time.

The historical data of online security and stability analysis in June was selected to be the instance of initial dataset in which 2484 instances and 9815 attributes existed at last. The information of initial dataset is shown in Table 3.

Table 2. The state variables and statistics.

	Equipment	Variables
State variables	AC line	Active power/PAC
	DC line	Power/ PDC
	Generator	Power/ PG、 Voltage/VG
	Load	Voltage/V _L
Statistics	Area	The sum of generators active output/ PAG
		The sum of loads / PAL
		The average of voltage/ VA
	Plants and stations	The sum of generators active output/ PTG
		The number of operated generators/ NTG
		The sum of loads/ PTL

Table 3. The Information Of Initial Dataset.

Dataset	Instances	Attributes	Class
Number	2484	9815	9

In order to verify the validity of this method, the data set was divided into training set and test set before using algorithm. So that, 80% instances were randomly selected in each class as the training set, and the remaining instances as test set. 10 kinds of random numbers were used to get the result after calculating the average as the final result of this method.

4.2. Results of Feature Selection

Features that beyond middle degree correlated to the CCT were selected for subsequent analysis by the method in section 2, and features that weak correlated and zero correlated to the CCT were removed. Then, the correlation coefficient that was equal to 0.4, 0.5, and 0.6 was selected to be threshold respectively, the number of features and accuracy after feature selection were compared in Figure 1.

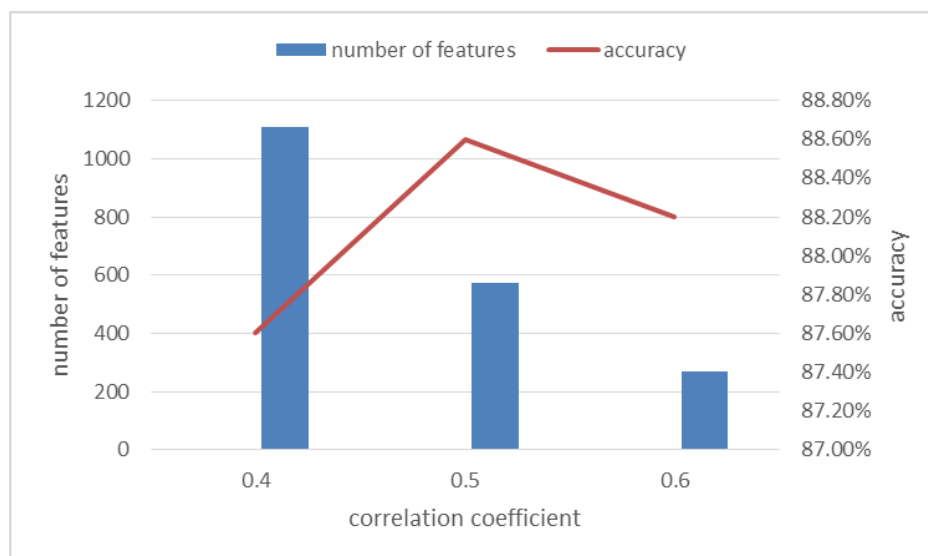


Figure 1. Comparison of different threshold.

Figure 1 shows that with the increase of the correlation coefficient threshold, the number of features reduced sharply, but the change of the classification accuracy was more complex. Thus, 0.5 has been used as threshold to select features, and 574 features were selected in the end for the further analysis.

4.3. Results of instance selection

The instance selection method proposed in this paper was applied, and Table 4 shows the results. Except *accuracy* and *reduction* to evaluate the performance of instance selection method, *effectiveness* was introduced in this paper which has a comprehensively assessment. Thus, we consider *effectiveness* equals *accuracy* multiple *reduction*. In Table 4, *No.* represents ten random numbers; *Accuracy* represents the classification result of dataset without instance selection; *Accuracy1* represents the classification result of dataset after using the instance selection based on SVM and *Reduction1* represents its selection effect; *Accuracy2* represents the classification result of dataset after using the combined instance selection based on SVM and similarity measurement and *Reduction2* represents its selection effect.

Table 4. The information of initial dataset.

No.	Accuracy	Accuracy1	Reduction1	Accuracy2	Reduction2
1	0.8864	0.8783	0.1070	0.8783	0.3842
2	0.8945	0.8986	0.1236	0.8945	0.4043
3	0.8945	0.9047	0.1135	0.8945	0.4018
4	0.8925	0.8884	0.1120	0.8864	0.3918
5	0.9006	0.8966	0.1226	0.9026	0.4028
6	0.8864	0.8844	0.1130	0.8864	0.3998
7	0.8864	0.8966	0.1215	0.8884	0.3988
8	0.9249	0.9229	0.1190	0.9128	0.4013
9	0.9067	0.9087	0.1175	0.9067	0.3968
10	0.9006	0.9026	0.1190	0.9047	0.3953
Average	0.8974	0.8982	0.1169	0.8955	0.3977
effectiveness	--	0.1050		0.3561	

Table 4 shows that instance selection based on SVM has a good performance in terms of accuracy and the instance selection based on SVM and similarity measurement has a good performance in terms of reduction. Through the comprehensive comparison of effectiveness between two methods, the second method is better than the first one which prove the validity and efficiency of the method proposed in this paper.

4.4. Comparison of three similarity measurement

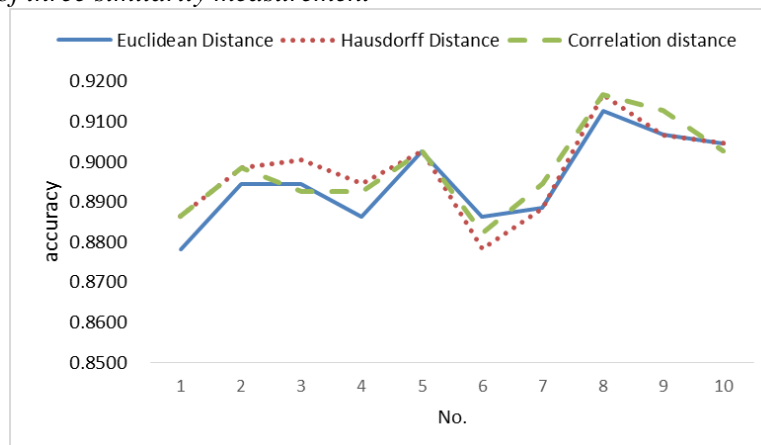


Figure 2. Comparison of accuracy.

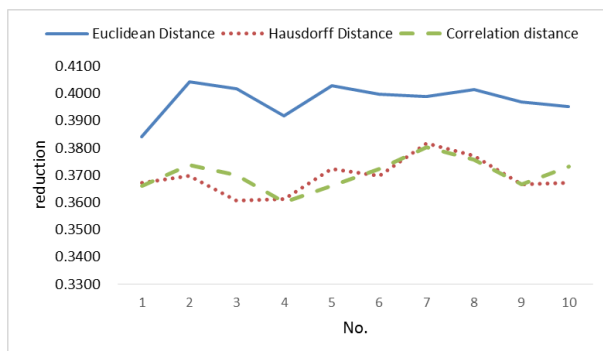


Figure 3. Comparison of reduction.

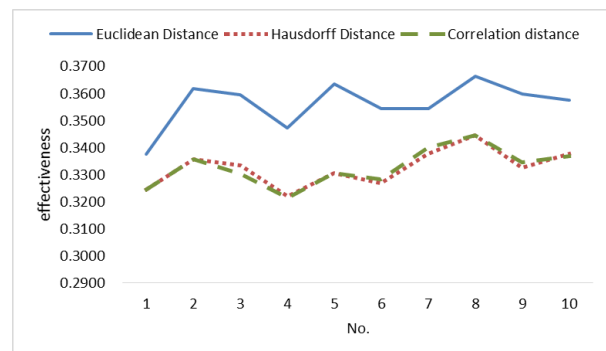


Figure 4. Comparison of effectiveness.

To find a better similarity measurement of instance selection, the performance of three methods including Euclidean Distance, Hausdorff Distance and Correlation distance were compared considering the indexes: accuracy, reduction and effectiveness. The Figure 2, 3 and 4 show, respectively, the resulting indexes of each method.

Considering the accuracy, although there is little difference between three methods, the performance of Hausdorff Distance and Correlation distance are little better than Euclidean Distance. Once considering the reduction, the reduction of Euclidean Distance is much better than others. Thus, Figure 4 shows that, after comprehensive comparison of effectiveness, Euclidean Distance can better applied to instance selection.

5. Conclusions

In this paper, we have presented a data selection method based on similarity measurement and SVM. This methodology efficiently deals with the feature selection and instance selection. The experiments have shown that the method can remove internal reductant instances and noisy instances, not only keep the distribution of dataset, but also meet the requirement of data selecting. The comparison of three similarity measurements shows that Euclidean Distance can well applied to instance selection. In conclusion, the data selection method proposed is valid and effective, with the additional advantage of being able to scale up to large datasets.

6. References

- [1] LI Mingjie, "Characteristic Analysis and Operational Control of Large-Scale Hybrid UHV AC/DC Power Grids," *Power System Technology*, vol. 40, pp. 985-991, Apr. 2016.
- [2] XUE Yusheng, LAI Yening, "Integration of Macro Energy Thinking and Big Data Thinking Part One-Big Data and Power Big Data," *Automation of Electric Power Systems*, vol. 40, pp. 1-8, Jan. 2016.
- [3] XUE Yusheng, LAI Yening, "Integration of Macro Energy Thinking and Big Data Thinking Part Two-Applications and Explorations," *Automation of Electric Power Systems*, vol. 40, pp. 1-13, Apr. 2016.
- [4] PENG Xiaosheng, DENG Diyuan, et al, "Key Technologies of Electric Power Big Data and Its Application Prospects in Smart Grid," *Proceedings of the CSEE*, vol. 35, pp. 503-511, Feb. 2015.
- [5] S. Garcia, J. Luengo, and F. Herrera, *Data preprocessing in data mining*. Springer, 2015.
- [6] Noor Izzri Abdul Wahab et al. "Transient Stability Assessment Of A Large Actual Power System Using Least Squares Support Vector Machine With Enhanced Feature Selection", *2008 Australasian Universities Power Engineering Conference*, pp. 1-6.
- [7] Rui Zhang, Yan Xu, Zhao Yang Dong, David J Hill. "Feature Selection for Intelligent Stability Assessment of Power Systems", *2012 IEEE Power and Energy Society General Meeting*, pp. 1-7.
- [8] Oveis Abedinia, et al. "A New Feature Selection Technique for Load and Price Forecast of Electrical Power Systems", *IEEE Transactions on Power Systems*, vol. 35, pp. 1-11, Apr. 2016.

- [9] E. Leyva et al. “Three New Instance Selection Methods Based on Local Sets: A Comparative Study with Several Approaches from A Bi-Objective Perspective”, *Pattern Recognition*, vol. 48, no. 4, pp. 1523-1537, 2015.
- [10] K. Nikolaidis, J.Y. Goulermas, and Q. Wu. “A Class Boundary Preserving Algorithm for Data Condensation”, *Pattern Recognition*, vol. 44, no. 3, pp. 704-715, 2011.
- [11] D.L. Wilson, “Asymptotic Properties of Nearest Neighbor Rules Using Edited Data”, *IEEE Trans. Systems, Man, and Cybernetics*, vol. 2, no. 3, pp. 408-421, July 1972.
- [12] D.R. Wilson, and T.R. Martinez, “Reduction Techniques for Instance-Based Learning Algorithms”, *Machine Learning*, vol. 38, no. 3, pp. 257-286, Mar 2000.
- [13] V.N. Vapnik, *Statistical Learning Theory*. John Wiley and Sons, 1998.
- [14] Nello Cristianini, John Taylor, *An Introduction to Support Vector Machines: And Other Kernel-Based Learning Methods*, Cambridge University Press, 2000.
- [15] Huttenlocher D P, Klanderman G A, Rucklidge W J. Comparing images using the Hausdorff distance. *IEEE Transactions on PAMI*, vol. 9, pp. 850-863, 1993.

7. Acknowledgments

Project supported by Science and Technology Projects of SGCC: Research on online early warning and fault disposal decision technology for multiple serious faults in large power grid.

Tuning Approach for Power System Stabilizer PSS4B using Hybrid PSO

Siyuan Guo¹, Shoushou Zhang², Junying Song³, Yongsheng Zhao¹, Weijun Zhu¹

¹State Grid Hunan Electric Power Company Limited Research Institute, Changsha 410007, China

²Bangor College, Central South University of Forestry and Technology, Changsha 410018, China

³State Grid Hunan Electric Power Company Limited, Changsha 410004, China

Email: siyuanguo2001@163.com

Abstract. As a multi-band PSS, PSS4B draws wide attention for its great potential in constraining the ultra-low frequency oscillations. In this paper, the crossbreed operation in genetic algorithm is introduced to particle swarm optimization (PSO) algorithm to form a hybrid PSO, so as to optimize PSS4B parameters. According to the single machine infinite system model, the phase frequency characteristic of excitation system without compensation is calculated by Heffron-Philips model. Based on phase frequency characteristic, the PSS4B parameters are tuned and excellent phase compensation effect is obtained. In Matlab/Simulink platform, the time domain dynamic response without PSS, adding PSS2B and PSS4B is compared and analyzed in detail. Simulation results show that the optimized PSS4B can provide effective damping in different frequency bands and have strong applicability.

1. Introduction

With the interconnection of China's large-scale power grids and high-gain excitation systems being put into operation, the level of system damping is continuously declining, which increases the dynamic stability risk of the power system [1].

Since the PSS2B power system stabilizer can't take into account both the high-band and low-band suppression effects on oscillations [2], a multi-band power system stabilizer is proposed by Hydro-Québec, which is included in the IEEE standard and named PSS4B [3]. The literature [4] proposed a phase and amplitude coordination tuning method for PSS4B parameters, but the phase compensation effect of the low frequency band still needs to be strengthened. In literature [5], one parameters tuning method for only the high-frequency band time constants is proposed, but the method is dependent on the experience of the engineering staff. To enhance the damping of the rotor oscillations and system stability, an efficient tuning approach known as harmony search algorithm is applied to PSS4B stabilizer [6]. Rimorov D *et al.* present a methodology for PSS4B parameters optimisation based on an improved modal performance index. By taking the proposed modal performance index as objective function, the properly selected constraints ensure stability of the closed-loop system and robustness of the proposed design [7]. In [8], the parameters to be optimized for PSS4B are divided into two kinds. Based on the particle swarm optimization (PSO) algorithm, a method of optimizing two types of parameters in turn is proposed. However, the method has a large amount of calculation and the process is relatively complex.

In this paper, a hybrid PSO is employed to optimize PSS4B parameters. Firstly, a single machine infinite system model is established, and the phase frequency characteristic of excitation system



without compensation is calculated based on the Heffron-Philips model [9]. Then, producing the largest positive damping torque by PSS is chosen as the goal, the hybrid PSO algorithm is used to convert the problem into a set of PSS4B parameters optimization process with inequality constraint. Finally, the dynamic response characteristics without PSS, adding typical PSS2B [3] and PSS4B are compared in detail. It shows that the optimized PSS4B has good low-frequency oscillation suppression effect over a wide frequency range.

2. PSS4B parameter optimization model

2.1. Optimization variables of PSS4B

According to the center frequency method [3], the PSS4B parameters setting are mainly reflected in the center frequency F_L, F_1, F_H and the corresponding band gains $K_L, K_I,$ and K_H . The two-stage lead-lag phase compensation time constants for three frequency bands are optimization variables to be tuned, as shown in Fig. 1.

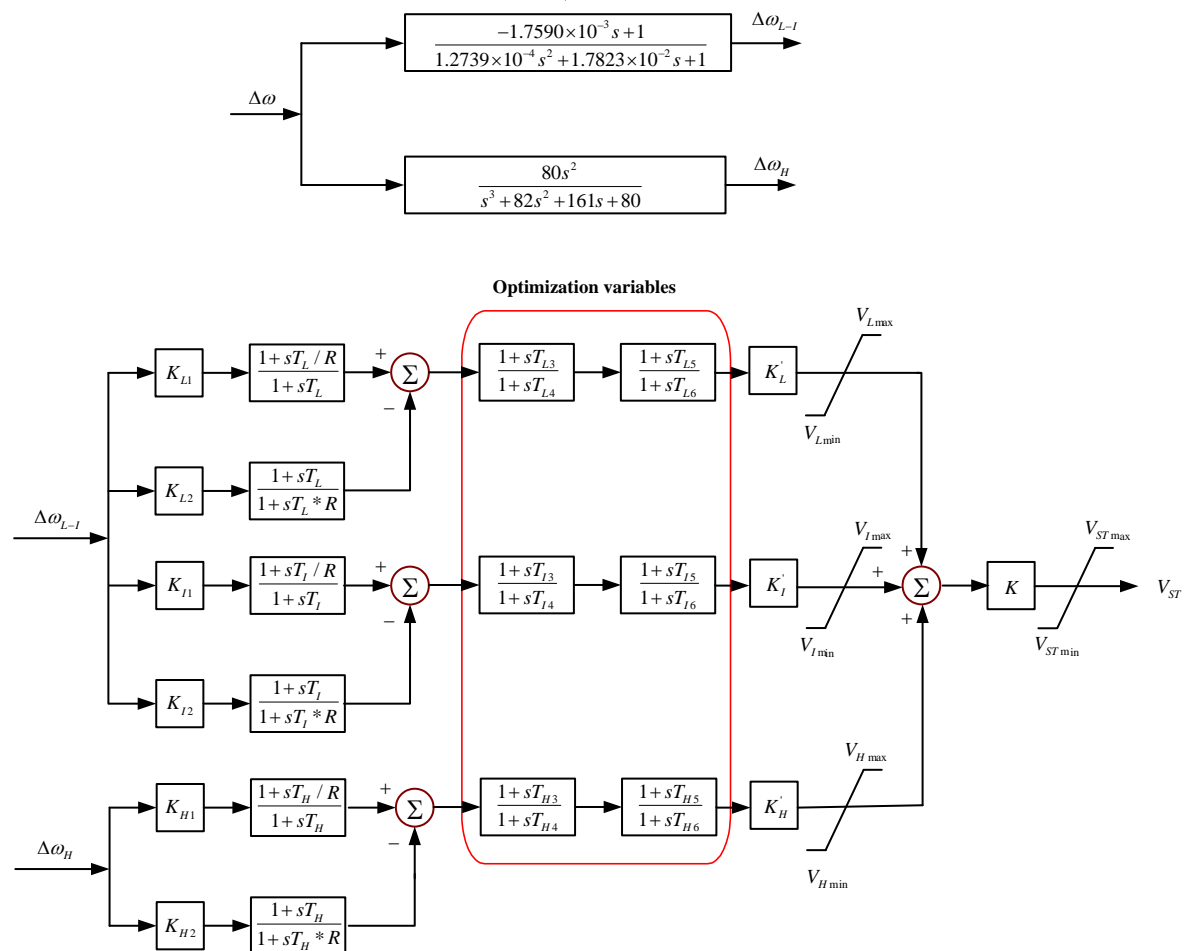


Figure 1. Optimization variables of PSS4B.

2.2. Hybrid PSO algorithm implementation process

According to the principle of phase compensation [9], the additional torque generated by PSS is in phase with the $\Delta\omega$ axis to generate the maximum positive damping torque. Assume the phase-frequency characteristic of the excitation system without compensation is φ_x , and the phase-frequency characteristic of PSS4B is φ_s . Then the phase setting relationship between the two phase-frequency characteristic is

$$\varphi_x + \varphi_s(\Delta\omega) = 0^\circ \tag{1}$$

And the objective function of the optimization model is as follows:

$$\min J = \sum_{n=1}^N |\varphi_x(f_n) + \varphi_s(f_n)| \quad (2)$$

with

$$\begin{cases} 0.04\text{Hz} < f_n < 2\text{Hz}, \varphi \in [-15^\circ, 15^\circ] \\ T_{L3}, T_{L4}, T_{L5}, T_{L6} \in [0.0001, 10] \\ T_{I3}, T_{I4}, T_{I5}, T_{I6} \in [0.0001, 10] \\ T_{H3}, T_{H4}, T_{H5}, T_{H6} \in [0.0001, 10] \end{cases} \quad (3)$$

Among them f_n is the frequency point within the low-frequency oscillation range of 0.1~2.0Hz, $T_{k3} \sim T_{k6}$ ($k=L, I, H$) are the two-stage lead-lag phase compensation time constants of PSS4B, namely the optimization variables.

The PSO initializes a group of random particles whose number of particles is N . All particle positions and velocities are vectors determined by the particle dimension D , and all particles have a fitness value determined by an optimized function, namely the fitness function. In each iteration process, all particles derive the individual optimal solution ***pbest*** and the population optimal solution ***gbest*** according to the fitness function, and update the velocity and position according to the following formula:

$$v_{i,j}(t+1) = wv_{i,j}(t) + c_1r_1[pbest(t) - x_{i,j}(t)] + c_2r_2[gbest(t) - x_{i,j}(t)] \quad (4)$$

$$x_{i,j}(t+1) = x_{i,j}(t) + v_{i,j}(t+1) \quad (5)$$

$$X_i = [x_{i,1}, x_{i,2}, \dots, x_{i,D}], i = 1, 2, \dots, N \quad (6)$$

$$V_i = [v_{i,1}, v_{i,2}, \dots, v_{i,D}], i = 1, 2, \dots, N \quad (7)$$

Where w is inertia weight, c_1 and c_2 are positive learning factor, r_1 and r_2 are uniformly distributed random numbers between 0 and 1.

In this paper, the crossbreed operation in the genetic algorithm is used to select a specified number of particles to be placed in the hybridization pool, according to the probability of crossbreed in each iteration process. The parent particles produce the same number of progeny particles, and the parent particles are replaced with the progeny particles to form a hybrid PSO algorithm. If the set number of iterations is satisfied, the search is stopped and the optimal solution ***gbest*** of the population is given.

In the PSS4B parameter optimization model, the time constants $T_{L3} \sim T_{L6}$, $T_{I3} \sim T_{I6}$, and $T_{H3} \sim T_{H6}$ for three bands are optimization variables, *i.e.*, a set of particles of the hybrid PSO algorithm, and the dimension is 12. The process of this optimization algorithm is shown in Fig. 2.

3. Simulation example and verification

3.1. Phase-frequency characteristic of excitation system without compensation

In order to test the low-frequency oscillation suppression effect of the PSS4B, a single machine infinite system model is built in Matlab/Simulink platform. The apparent power of the generator is 200MVA and rated voltage is 13.8kV.

The literature [9] pointed out that the theoretical phase-frequency characteristic of excitation system without compensation is the phase angle characteristic between the voltage superposition point and the torque ΔM_{e2} on the Heffron-Philips model, as shown in Fig. 3. According to the infinite system model, the operating conditions of the generator can be obtained. The Heffron-Philips model with open-loop power angle in Fig. 3 can be used to plot the phase-frequency characteristic of excitation system [9], as shown in Fig. 4.

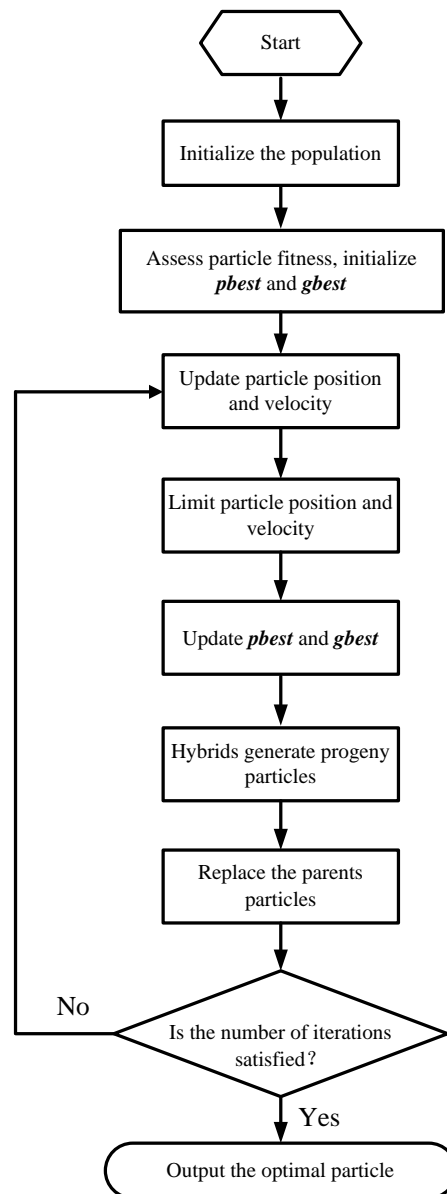


Figure 2. The flowchart of Hybrid PSO Algorithm.

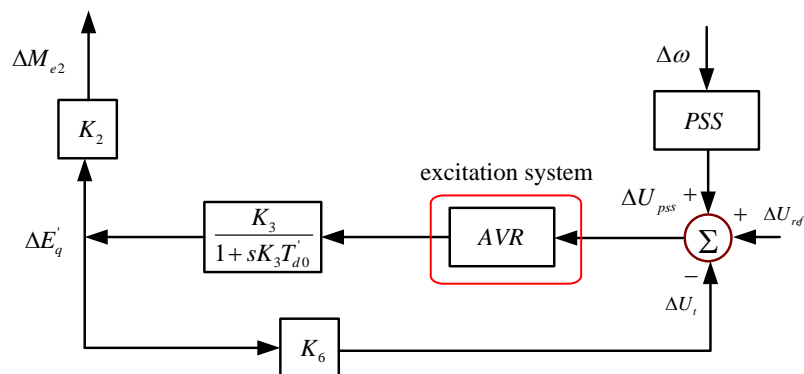


Figure 3. Heffron-Philips model with open-loop power angle.

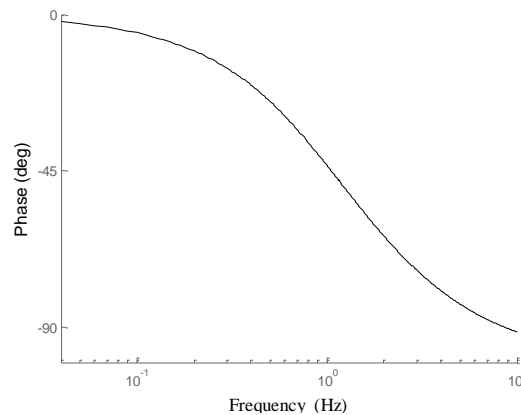


Figure 4. Phase-frequency characteristic of the excitation system without compensation.

Based on the phase-frequency characteristics in Fig. 4, the PSS4B parameters optimization model is used to obtain the optimized parameters. Select the centre frequency and band gain of PSS4B with $F_L = 0.04\text{Hz}$, $F_I = 0.6\text{Hz}$, $F_H = 6\text{Hz}$ and $K_L = 20$, $K_I = 40$ and $K_H = 80$. The optimization results for three bands are $T_{L3} = 1.4460$, $T_{L4} = 1.8800$, $T_{L5} = 1.6662$, $T_{L6} = 0.8213$; $T_{I3} = 0.7656$, $T_{I4} = 1.2222$, $T_{I5} = 1.3091$, $T_{I6} = 1.4657$; and $T_{H3} = 0.8442$, $T_{H4} = 0.0001$, $T_{H5} = 0.0628$, $T_{H6} = 0.6676$.

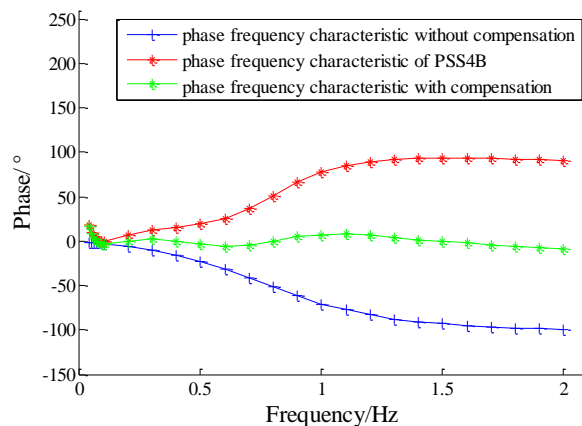


Figure 5. Phase-frequency characteristic of excitation system with compensation after PSS4B parameters optimization.

After optimizing the PSS4B parameters, the phase-frequency characteristics of excitation system with compensation in the frequency range of 0.04–2.0Hz is shown in Fig. 5. It can be seen that the phase-frequency characteristic of excitation system with compensation is close to zero, which means the phase compensation effect is very good.

3.2. Time domain dynamic response

In the Matlab/Simulink single machine infinite system model, the band gains K_L , K_I , and K_H are changed in the same proportion, and the final gain value of the PSS4B can be determined by the critical gain method. According to Heffron-Philips model, the natural oscillation frequency of the generator is determined by the mechanical inertia. Therefore, the oscillation mode at different local oscillation frequencies can be simulated by modifying the inertia moment of the generator. A 5% step test is conducted on the excitation voltage of the generator, and the damping effects without PSS, adding typical PSS2B [3] and optimized PSS4B are compared at four typical frequencies 1.6Hz, 0.77Hz, 0.34Hz and 0.1Hz. The simulation results are shown in Fig. 6.

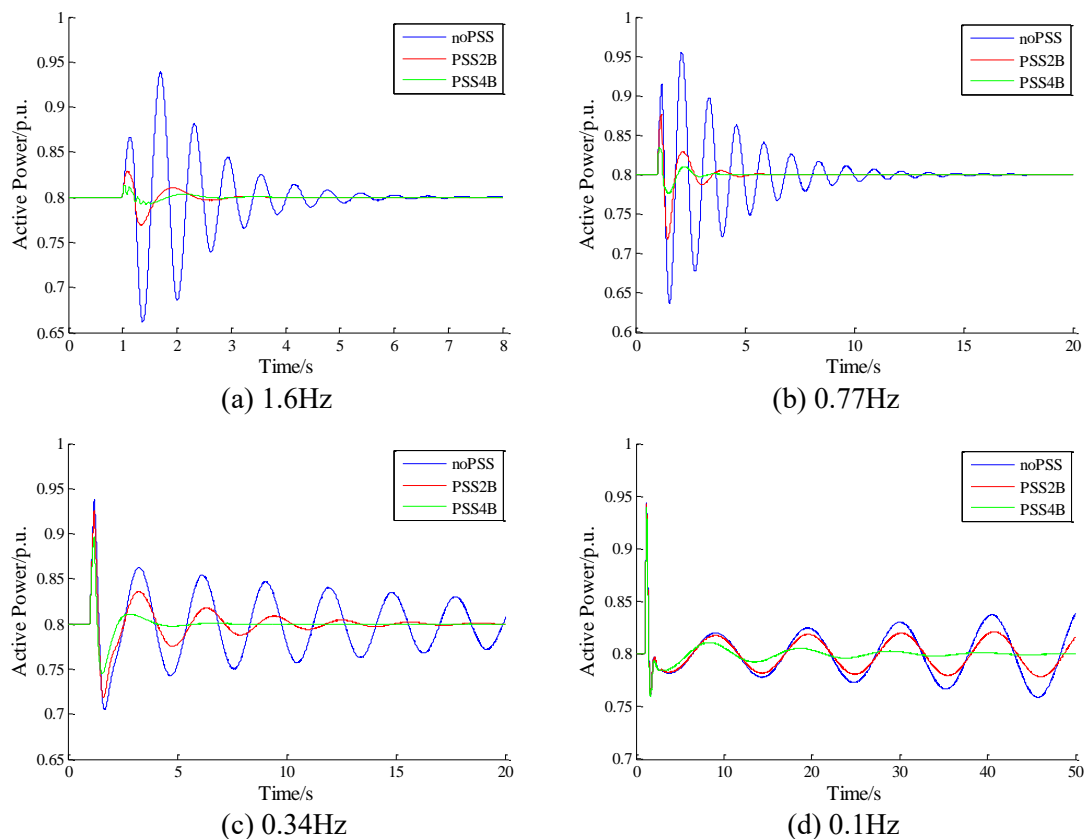


Figure 6. Dynamic response results comparison at different oscillation frequencies.

When the local oscillation frequency is 1.6Hz and 0.77Hz respectively, the excitation system can suppress the oscillations effectively with PSS2B and PSS4B, and the PSS4B has better effect.

As can be seen from Fig. 6(c), when a large inertia moment is set, the local oscillation frequency gradually decreases. Adding PSS2B requires longer time to suppress oscillations, while adding PSS4B can suppress the power oscillation within one and half cycle. When the local oscillation frequency is 0.1Hz, system without PSS has begun to oscillate, and PSS2B can't quell the power oscillation. At this time, the PSS4B can still calm oscillation down within three cycles. Dynamic response results comparison shows that optimized PSS4B can suppress low-frequency oscillations in a wider frequency range and improve the stability of the system.

4. Conclusions

In this paper, a hybrid PSO algorithm is applied to the parameters optimization process of PSS4B. The time domain simulation results without PSS, PSS2B and optimized PSS4B are compared in the single-machine infinite system simulation model. The results show that the PSS4B optimized by hybrid PSO algorithm has good low-frequency oscillation suppression effect over a wide frequency range. In the future, we will focus on the application of PSS4B in multi-machine systems.

5. References

- [1] Wang G, Yu Z, et al. Trouble Shooting and Analysis of Ultra-Low Frequency Oscillation Mode in Power System. *Power System Technology*, 2016, 40(8): 2324-2329.
- [2] Guo S, Li Z, et al. The Discussion on Performance of Power System Stabilizer PSS4B. *Hunan Electric Power*, 2016, 36(5): 15-20.
- [3] IEEE Power and Energy Society. IEEE Recommended Practice for Excitation System Models for Power System Stability Studies. *IEEE Std 421.5TM*, 2016: 64-65.
- [4] Yuan Y, Xu Q, et al. Effect Verification of Multiband Power System Stabilizer Based on RTDS. *Automation of Electric Power Systems*, 2013, 37(18): 126-131.
- [5] Zhao X, Xie H, et al. Parameter Setting and On-Site Test of Power System Stabilizer-PSS4B.

Power System Technology, 2016, 40(2): 508-513.

- [6] Krishan R and Verma A. An Efficient Approach to Tune Modern Power System Stabilizers using Harmony Search. *Annual IEEE India Conf.*, 2015, 1-6.
- [7] Rimorov D, Kamwa I, et al. Model-based Tuning Approach for Multi-band Power System Stabilisers PSS4B Using an Improved Modal Performance Index. *IET Generation, Transmission & Distribution*, 2015, 9(15): 2135-2143.
- [8] Zhu L, Li W, et al. Model Analysis and Parameter Coordination Optimization of New PSS. *Water Resources and Power*, 2014, 32(6): 171-175.
- [9] Huo C, Liu Z and Zhu F. Theory and Field Practice of Phase Compensation on Generator Excitation System by Utilizing Power System Stabilizer. *Proc. of the CSEE*, 2015, 35(12): 2989-2997.

Acknowledgments

This work was supported by State Grid Hunan Electric Power Company Limited Scientific Research Project (5216A5170017). I would like to show my deepest gratitude to the colleagues helping with the application for the scientific research project.

Short-term Electricity Load Forecasting in Thailand: an Analysis on Different Input Variables

Su Wutyi Hnin¹ and Chawalit Jeenanunta¹

¹School of Management Technology, Sirindhorn International Institute of Technology, Thammasat University, Pathum Thani, Thailand, 12120
E-mail:d6022300203@g.siit.tu.ac.th, chawalit@g.siit.tu.ac.th

Abstract. This paper suggests a support vector regression model to make short-term load forecasting in Thailand by different training inputs. The primary objective of this paper is to describe the importance of data pre-processing and the external factors for accurate forecasting. The Electricity Generating Authority of Thailand (EGAT) provides the half-hourly electricity load demand. For numerical analysis, a dataset of net peak load of Thailand for a period of weeks from January 2016 to December 2017 is selected. The historical load demand is filtered for each day by Local regression filtering technique. After filtering the data, the effectiveness of input variables is important for accurate performance. Mean absolute percentage error (MAPE) is used to evaluate the model performance. By comparing the three models, model which considerate the temperature and seasonal factors enhances the model performance.

1. Introduction

According to the economy growth, the improved life-style, and the usage of electricity demand is increasing year by year. As a consequence, load forecasting plays an important role in power energy management. There are three types of electricity load forecasting in order to time horizon. Short-term load forecasting is to forecast one hour to a week and forecasting a month up to a year is mid-term load forecasting as well as long-term is over a year. Basically, long-term load forecasting (LTLF) and mid-term load forecasting (MTLF) intend for planning new transmission line, and power station. Short-term load forecasting (STLF) plays a key factor in planning and maintenance, load flow analysis, and operating strategies in power system [1]. The main target in load forecasting has been on STLF because it is a vital thing for the day to day operation of the power utility system. There are three basic steps before forecasting: exploring the data, data pre-processing, and developing the forecasting model. The electricity load demand is non-linear and correlation with many exogenous variables, involving the weather conditions, seasonality, trend and calendar effect. The data must be accurate. However, the data collected from many resources is often noises, full of errors, outliers, and duplicates. Therefore, pre-processed and cleaned data is needed in order to the data structure [2]. In the past few decades, the bulk of research has concerned electricity load forecasting. The techniques applied in STLF can be classified into two groups, namely classical group and artificial intelligence based group. The classical methods are widely supported for forecasting areas, which include regression [3], exponential smoothing [4], ARIMA models [5] and gray forecasting model [6]. However, there are some limitations and difficult to solve the non-linear data. Since artificial intelligence based techniques are able to solve nonlinearity problem, it has been popular in these days. Some of those are neural network [7], fuzzy logic [8] and support vector regression [9]. By introducing structural risk minimizing principle, support vector regression (SVR) gives better generalization capability.



According to the ability of solving nonlinearity problems, SVR became an efficient model among machine learning algorithms [10].

The aim of this study is to improve the STLF models for net peak load demand in Thailand. The paper structures as follows. Section 2 reviews the analysis of the data. Methodology is described in section 3. Then, the preparation of the data is examined in section 4. In section 5, the forecasting results are discussed and the last session concludes the findings and presents the future research.

2. Data analysis

The first thing is to observe the behavior of the electricity load demand. There are some relations among load demand and other external factors, such as seasonality, temperature, and holidays. The following are the observations of the demand described in each section.

2.1. Behavior of load demand

The data are collected as half an hour per day. Figure 1 shows the net peak load of Thailand 2017 and November, 2017. By simple analysis, it is easy to discover that there are some properties of the electricity load. It has seasonality: high demand in the summer while low demand in the winter. In order to the load pattern, it has the relation between weather condition and electricity load in the seasons. Then, the daily load pattern of each day has different demand. The load in weekdays is higher than that of weekend (Saturday and Sunday). Further, the load on Saturday is slightly higher than that on Sunday. Moreover, there can be seen low load pattern especially the load demand in April and December due to the Songkran festival and end year holidays.

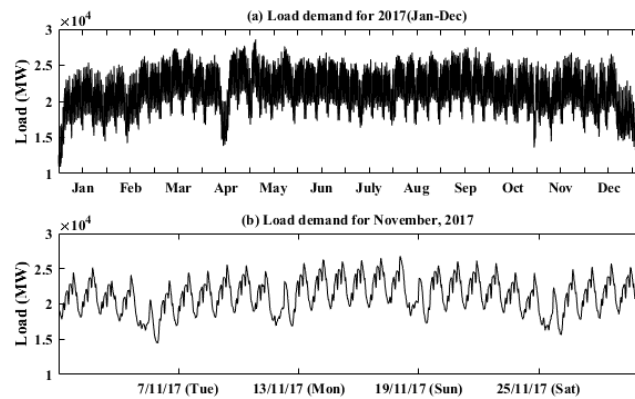


Figure 1: The load demand curve for 2017 and November, 2017

2.2. Weather influence

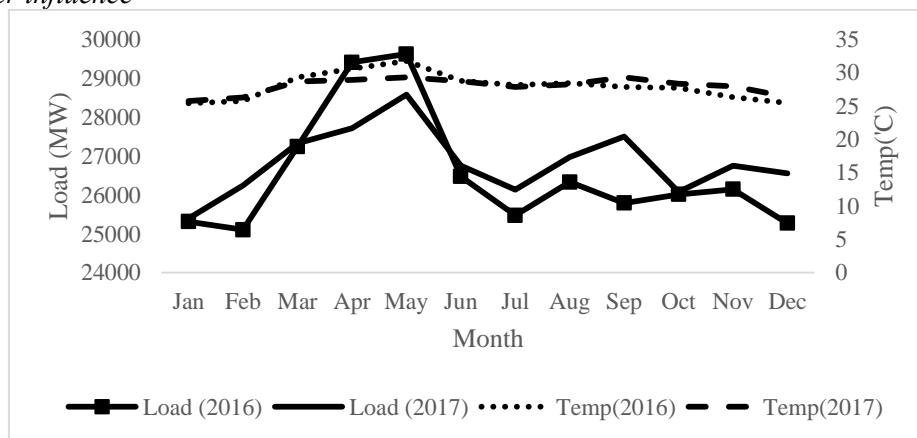


Figure 2: The yearly load demand and temperature for 2016 and 2017

Weather conditions always play an essential role in the electricity forecasting. Temperature, rainfall, humidity and some special condition like storms included as weather conditions for forecasting. However, these considerations are regarded on different situation in order to different location. Temperature has the higher effect than other weather conditions in Thailand. The correlation coefficient between the load and temperature is 0.5. It is clearly seen from figure 2 that the higher the temperature, the higher the electricity load demand. It is estimated that cities the size of Bangkok may need about 2 GWs of additional electricity for increasing of 1 degree Celsius according to the increased demand for air conditioning [11].

3. Methodology

3.1. Support vector regression (SVR)

Support vector machine (SVM) is a supervised learning technique which is originally approach from Vapnik's statistical learning theory [12]. It was first introduced for classification then extended for regression. The main idea of support vector regression (SVR) is to apply the non-linear mapping function $f(x)$ and to minimize the error, individualizing hyper plane which maximizes the margin. The training data $L = \{(x_i, y_i)\}_{i=1}^T$, where x_i is the input data and y_i is the associated output value of x_i , the non-linear problem can be defined by a regression function.

$$f(x) = w\phi(x) + b \quad (1)$$

Where, w represents the regression coefficients and b is the bias term. The empirical structural risk function can be described as:

$$R = \frac{1}{2} \|w\|^2 + C \left(\sum_{i=1}^l \xi_i + \xi_i^* \right) \quad (2)$$

Subjected to the constraints; $y_i - wx_i - b \leq \varepsilon + \xi$, $wx_i + b - y_i \leq \varepsilon + \xi_i^*$, $\xi_i^* \geq 0$, $\xi_i \geq 0$

Where, ε is the width of the loss function, C denotes the tuning parameter between the training data set and model complexity. ξ_i^* and ξ_i are the slack variables with non-negative values to ensure feasible constraints. There are three kinds of kernel function used in SVR. The radial based function (RBF) is widely used in SVR as it relies on only the parameter γ to be tuned upon the data. The RBF kernel function is regarded as $K(x, x_i)$.

$$K(x, x_i) = \exp \gamma \|x - x_i\|^2 \quad (3)$$

Where, x and x_i are the inputs in the respective dimensions and γ is the width of the RBF function.

3.2. R-loess

Loess is a special case for linear regression which is locally estimated scatter plot smoothing. It considered the neighboring points within a span to smooth the data. The span is calculated for each point by the regression weight function.

$$w_i = \left(1 - \left| \frac{x - x_i}{d(x)} \right|^3 \right)^3 \quad (4)$$

Where,

x = the predictor value associated with the responded value to be smooth

x_i = the nearest neighbors of x as defined by the span

$d(x)$ = the distance along the abscissa from x to the most distant predictor value within the span

The weighted value of the surrounded data points determines the smoothed value if there is no influence of the outside points of the span. The outliers of the dataset are along with the loess curve. So, the robust smoothing is modified to loess (r-loess). The idea is to eliminate the effect of the outliers on loess. R-loess can put zero weights on the outliers and non-influence on the data to be smoothed [13]. The bisquare function gives the weights of the r-loess.

$$w_i = \begin{cases} (1 - (r_i/6MAD)^2)^2, & |r_i| < 6MAD, \\ 0, & |r_i| \geq 6MAD, \end{cases} \quad (5)$$

Where,

r_i = the residual of the i^{th} data point produced by the regression smoothing procedure,

MAD = the median absolute deviation of the residuals,

MAD = median ($|r_i|$)

The spread out of the residual is measured by MAD . If the value of r_i is small in comparison with $6MAD$, the robust weight is zero and the related data point is not in the smooth calculation. The range of the span is between 0 and 1. The greater the value of the span, the smoother is the fitted curve.

4. Data preparation

4.1. Smoothing of the temperature and electricity load demand

First, the load and temperature data is separated into seven group according to the day such as Monday, Tuesday etc. Then, each group is organized by each time period: 00:00 a.m., 01:00 a.m., etc. The data between 2016 and 2017 is selected to train and test the model.

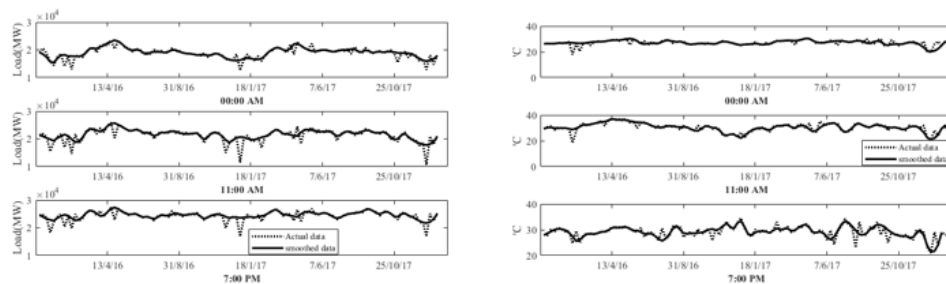


Figure 3: The load and temperature curve (2016-2017) before smoothing and after smoothing by r-loess

Therefore, the load data from 2015 December and 2018 January for data smoothing is taken because an r-loess span of seven is used to calculate the smooth data. The total data points of each period for each group are 112 data points. An r-loess span of seven defines the data which is smoothed by using a span of 6.25% of the total number of the data points. Figure 3 show the load demand curve and temperature curve for before and after smoothing at 00:00 a.m., 11:00 a.m., and 7:00 p.m. from December, 2015 to January, 2017.

4.2. Training and testing data of segmentation

The load data is organized into seven groups as Monday, Tuesday and so on. Forecasting for Monday is that the testing and training data includes only Monday load. Therefore, there are the total of seven groups for testing and training. The walk-forward testing routine [14] is used for testing and training the data. Testing 1 dataset is meant by training 52 datasets. For that reason, the data is sliding forward for the rest 51 dataset and implement the same process. The testing dataset slides 1 dataset forward (1-52 testing dataset), the SVR model is performed with the new sliding training dataset as shown in figure.

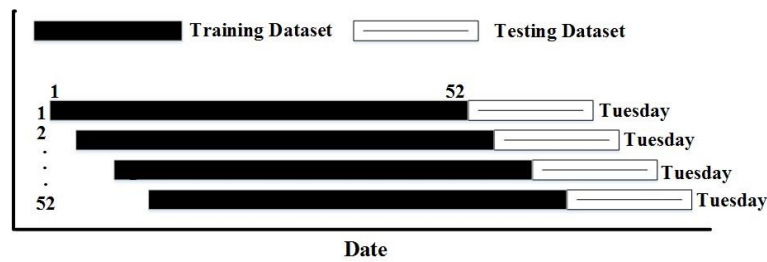


Figure 4: Walk-forward testing routine

4.3. Model specification

The testing data is from January 2017 to December 2017 by training 2016 the whole year. There are three models to forecast the load demand of 2017.

Model 1:

$$F_t^d = a_1L_t^{d-7} + a_2L_{t-1}^{d-1} + a_3L_{t-2}^{d-1} + a_4L_t^{d-1} \tag{6}$$

Model 2:

$$F_t^d = a_1L_t^{d-7} + a_2L_{t-1}^{d-1} + a_3L_{t-2}^{d-1} + a_4L_t^{d-1} + a_5T_t^{d-1} \tag{7}$$

Model 3:

$$F_t^d = a_1L_t^{d-7} + a_2L_{t-1}^{d-1} + a_3L_{t-2}^{d-1} + a_4L_t^{d-1} + a_5T_t^{d-1} + a_6SI^m + a_7Jan\ or\ not + \dots + a_{18}Dec\ or\ not \tag{8}$$

Where

F_t^d = Forecasted load of day d at period t ,

L_t^{d-7} = Previous week same day load of day d at period t ,

L_t^{d-1} = Yesterday load of day d at period t ,

T_t^{d-1} = Yesterday temperature of day d at period t ,

SI^m = Monthly seasonal index (monthly load divided by yearly load)

Jan or not = 0 or 1 {e.g if it is January-> only January is 1, others are 0}

5. Result and Discussion

The comparison analysis of the three models is described in this section. All the data of three models are filtered by r-loess and perform STL on different input training variables. The performance of the monthly and yearly MAPE for three models is shown in table 1. The average for each column is the MAPE performance for each month in 2017. The yearly MAPE is to select the best one among the three models. The yearly average of the model 3 is 2.57 while model 1 is 3.32 and model 2 is 2.87. So, considering the yearly MAPE, model 3 performs well in comparison with the other models. The minimum and the maximum monthly average of the model 3 is 1.84 (January) and 4.82 (December). Both model 1 and model 2 give the maximum monthly average MAPE in December which is 5.74 and 5.45 respectively. The minimum monthly average is 2.13 (July) for model 1 and that of the model 2 is 2.02 (November).

The forecasting performance in December, during which the lowest temperature of the year are examined, are usually the worst performance of the year due to the lowest temperature and lower load demand. Since there is a correlation between temperature and load demand, seasonality and load demand, model 3 performs better than other months which the training input variables are included the

seasonality and temperature. Seeing that Thailand is a tropical climate region, electricity load demand is sensitive to temperature and seasonality.

Table 1: Comparison of MAPE for the three models

	Model 1	Model 2	Model 3
JANUARY	3.71	2.29	1.84
FEBRUARY	4.55	2.83	3.16
MARCH	3.47	3.24	2.62
APRIL	4.53	4.11	3.06
MAY	3.49	3.12	2.96
JUNE	2.84	2.66	2.40
JULY	2.13	2.10	2.03
AUGUST	2.22	2.06	1.93
SEPTEMBER	2.73	2.39	2.05
OCTOBER	2.17	2.14	2.08
NOVEMBER	2.30	2.02	1.93
DECEMBER	5.74	5.45	4.82
Total Average	3.32	2.87	2.57

There are eight plots to show the average monthly MAPE for each day and total average for each day in 2017. The plots show the model 3 (solid line) compared with the other two models: model 1 (dotted line), model 2 (dashed line). The first plot is Monday monthly MAPE. Normally Monday MAPE is difficult to forecast because it is the first day of working day. The forecasting model includes yesterday load demand in input variables. So the influence of the difference of load demand between Monday and Sunday is large since the load demand on Sunday is significantly low compared to the other days. However, model 3 which includes the temperature and dummy variables is effective to overcome this problem. It can be seen that the MAPE of Monday of model 3 in April is considerably better than the other two models. On the other hand, monthly MAPE of Tuesday and Thursday are almost the same in all models except January and February. The three models go the same pattern for Wednesday in every month but go slightly difference for December. Nevertheless, the total average of Wednesday monthly MAPE in model 3 is slightly higher than other models as the December MAPE of Wednesday is 6.908. Thursday's monthly MAPE of model 3 performs well especially in December. However, the MAPE of Thursday and Friday in May is moderately high as the holidays of May are on Thursday and Friday. Load forecasting on holiday is not easy to handle. Weekend's load forecasting is normally insufficient compared to weekdays'. But, some companies and industries are still opened on Saturday in Thailand. Therefore, the load demand on Saturday is not too low like that of Sunday. The value of the monthly MAPE of Saturday on model 3 is not more than 3 except December. Due to many factors affecting on December, the performance of model 3 on Thursday and Saturday are poor compared to model 1 and model 2. Since the load demand trains on the separated day (training on the same day), it is strongly sufficient on Sunday.

February 14 (Tuesday) and April 23 (Sunday) are selected for illustration because the temperature values in these days are minimum and maximum temperature in 2017. It is like a hard case for load forecasting. Figure shows the actual electricity load demand compared with all three forecasting models. According to figure 6, all three models follow the actual demand. The MAPE of model 1 on February 14 is 7.74 while that of model 2 and model 3 are 3.01 and 2.37. As for April 23, model 1 is 7.39, model 2 is 6.54, and model 3 is 2.67. Considering temperature variables and seasonal variables gives accurate forecast.

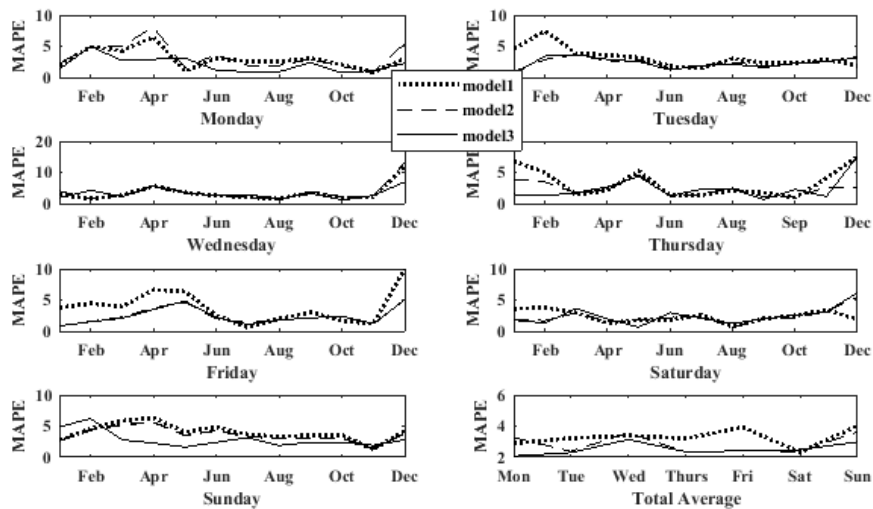


Figure 5: Average monthly MAPE for each day and total average of each day in 2017

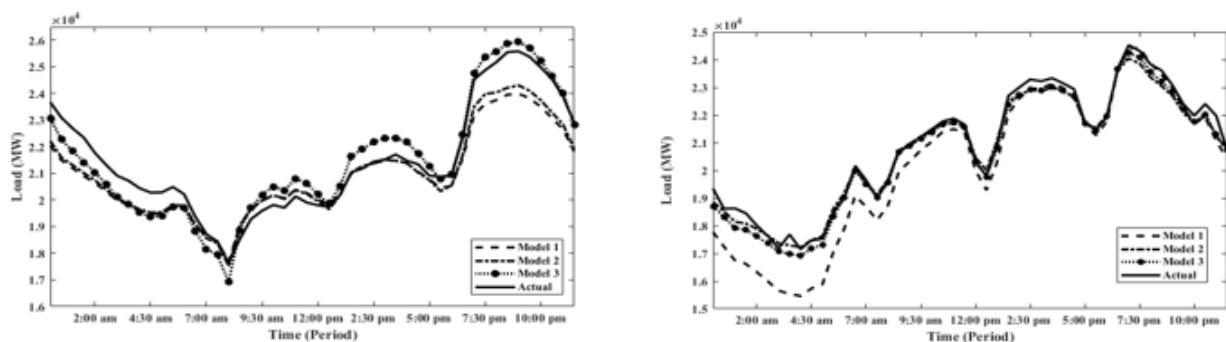


Figure 6: Actual demand and forecasted demand of three model on 23rd April and 14th February, 2017

6. Conclusion

The main contribution of the paper is to propose the importance of data preprocessing before forecasting and the effectiveness of selecting external variables. An SVR based model has been built for comparative study. There are three models which have been trained and tested on the dataset from EGAT (Electricity Generating Authority in Thailand). Among all three models, choosing the appropriate variables enhance the model performance. It can be seen that temperature and seasonality are strongly influenced on the load forecasting of Thailand. Model 3 can generate forecasting distributions incorporating the randomness from the model and exogenous variables. The study has found that the performance on December is still weak. The data are smoothed by r-loess for each period of the day. Furthermore, there are some outliers left which are long holidays as the window span is seven for the data point. Therefore, future research is to find a new way to get better performance on December.

7. Acknowledgement

This research is partially supported by the Logistics and Supply Chain Systems Engineering Research Unit (LogEn), Sirindhorn International Institute of Technology (SIIT), Thammasat University (TU), Thailand. Data used in this research is provided by EGAT. Therefore, we acknowledge their support for completing this research successfully.

8. References

- [1] E. A. Feinberg and D. Genethliou, "Load forecasting," in *Applied mathematics for restructured electric power systems*: Springer, 2005, pp. 269-285.
- [2] M. MathWorks, "the Mathworks," *Inc., Natick, MA*, 1992.
- [3] A. D. Papalexopoulos and T. C. Hesterberg, "A regression-based approach to short-term system load forecasting," *IEEE Transactions on Power Systems*, vol. 5, no. 4, pp. 1535-1547, 1990.
- [4] W. Christiaanse, "Short-term load forecasting using general exponential smoothing," *IEEE Transactions on Power Apparatus and Systems*, no. 2, pp. 900-911, 1971.
- [5] M. Cho, J. Hwang, and C. Chen, "Customer short term load forecasting by using ARIMA transfer function model," in *Energy Management and Power Delivery, 1995. Proceedings of EMPD'95., 1995 International Conference on*, 1995, vol. 1, pp. 317-322: IEEE.
- [6] J.-f. Zhang, Y.-a. Wu, and J.-j. Wu, "Application of gray system theory in load forecasting [J]," *Electric Power Automation Equipment*, vol. 5, p. 005, 2004.
- [7] C. Jeenanunta and K. D. Abeyrathna, "Combine Particle Swarm Optimization with Artificial Neural Networks for Short-Term Load Forecasting."
- [8] M. B. Mbarek and R. Feki, "Using fuzzy logic to renewable energy forecasting: a case study of France," *International Journal of Energy Technology and Policy*, vol. 12, no. 4, pp. 357-376, 2016.
- [9] A. J. Smola and B. Schölkopf, "A tutorial on support vector regression," *Statistics and computing*, vol. 14, no. 3, pp. 199-222, 2004.
- [10] M. Barman, N. D. Choudhury, and S. Sutradhar, "A regional hybrid GOA-SVM model based on similar day approach for short-term load forecasting in Assam, India," *Energy*, 2018.
- [11] C. Greacen and A. Palettu, "Electricity sector planning and hydropower in the Mekong Region," *Democratizing water governance in the Mekong region*, pp. 93-125, 2007.
- [12] S. R. Gunn, "Support vector machines for classification and regression," *ISIS technical report*, vol. 14, pp. 85-86, 1998.
- [13] W. Wettayaprasit, N. Laosen, and S. Chevakidagarn, "Data filtering technique for neural networks forecasting," in *Proceedings of the 7th WSEAS International Conference on Simulation, Modelling and Optimization*, 2007, pp. 225-230: World Scientific and Engineering Academy and Society (WSEAS).
- [14] L.-J. Cao and F. E. H. Tay, "Support vector machine with adaptive parameters in financial time series forecasting," *IEEE Transactions on neural networks*, vol. 14, no. 6, pp. 1506-1518, 2003.

Design of Rated Power Control Strategy of Wind Turbine Based on Particle Swarm Optimization

YC Yang^{1,2,3}, Y Liu^{2,3}, P Song^{2,3}, Y Cui^{2,3}, and Y Bai¹

¹Department of Control and Computer Engineering, North China Electric Power University, Beijing, 102206, China

²North China Electric Power Research Institute Co., Ltd., Smart Grid and New Energy Institute, Beijing, 100045, China

³Grid-connected Operation Technology for Wind-Solar-Storage Hybrid System State Grid Corporation Key Laboratory

E-mail: yyc941213@sina.com

Abstract. In view of the reduction of wind turbine operating efficiency caused by wind speed measurement errors, this paper proposes a rated power control strategy for wind turbines for practical applications; in order to solve the problem that the pitch PI controller parameters of wind turbines are not easy to calculate and tune in the process of design and optimization, this paper proposes a complete set of methods for parameter tuning of pitch control PI controllers for wind turbines. This paper establishes a Bladed-Matlab co-simulation platform, uses Bladed software to build a complete model of a 2MW wind turbine, and designs a rated power control strategy for wind turbines. After the wind turbine model is linearized at different wind speed points by applying Bladed software, the linearized model for PI parameter tuning is obtained, and then the optimal PI parameters for each wind speed point are set by using particle swarm algorithm. According to the variation law between the PI parameters and the pitch angle obtained before, the PI parameters are adjusted adaptively by variable gain PI control. The simulation results show the superiority of the control strategy and parameter tuning method used in this paper.

1. Introduction

Precise pitch control is essential to ensure a stable power rating of mechanical structures and electrical components when wind turbines operating above the rated wind speed. The current control strategy for wind turbines working on rated power stage is mostly variable pitch PI control. The "quickness, accuracy, and stability" of variable pitch control are directly related to the stability of the output power of wind turbines, which means, the rated power control of wind turbines directly affects the stability of power grid frequency under the trend of large-scale access to wind power. Although pitch control has many advantages, a corresponding pitch actuator is heavily required which structure and controlling are quite complex, requiring the blade pitch angle control system to be sufficiently responsive at different wind speeds [1]. The accuracy of pitch PI controller parameters is directly related to the reliability of the unit, and serious overshoot or delay will directly threaten the safety and stability of the unit.

Due to the characteristics of nonlinearity and time-varying parameters of the wind power generation system, the unit linear model is not easy to obtain and the linearized model parameters at each wind speed operating point vary greatly. The PI parameters based on a certain wind speed point model cannot achieve the optimal control effect in the whole working range. Meng designed the PI controller



to pitch the wind turbine, but its control was not good in real time and the system was unstable [2]. Cui designed the PID controller to pitch the wind turbine, which has fast response and good adjustment characteristics, but poor robustness [3]. Conventional PI control is a linear control method based on a certain operating point cannot automatically identify and adjust the parameters, which is not suitable for a wind power generation system with strong nonlinearity because of the difficulty to establish an accurate model. At the same time, the precision of wind speed measurement in actual production hardly meet the design requirements, so the wind turbine works in a non-optimal condition in most cases.

This paper proposes a strategy for rated power control of wind turbines based on practical requirements, and presents a complete method for parameter tuning of pitch PI controllers. This paper establishes a Bladed-Matlab co-simulation platform and uses Bladed software to build a complete machine model for a 2MW wind turbine. After the wind turbine model is linearized at different wind speed points by applying Bladed software, the linearized model for PI parameter tuning is obtained, and then the optimal PI parameters for each wind speed point are set by using particle swarm algorithm. According to the variation law between the PI parameters and the pitch angle obtained before, the PI parameters are adjusted adaptively by variable gain PI control. Based on this, the rated power control strategy for wind turbines is designed. The simulation results show the superiority of the control strategy and parameter tuning method used in this paper.

2. Wind turbine rated power control strategy

The wind energy utilization factor represents the ratio of the wind energy obtained by the wind turbine to the original wind energy applied to the wind turbine per unit of time, denoted by C_p , which represents the conversion efficiency of the wind turbine to convert wind energy into electrical energy [4].

$$C_p = \frac{P}{\frac{1}{2} \rho S v^3} \quad (1)$$

Where: P is the actual shaft power obtained by the wind turbine, ρ is the air density, S is the swept area of the rotor, and v is the actual wind speed.

The wind energy utilization factor C_p is simultaneously affected by the tip speed ratio λ and the pitch angle β . The tip speed ratio is an important parameter used to describe the characteristics of a wind turbine. It is equal to the line speed at the tip of the blade to wind speed, denoted by λ , which reflects the wind turbine rotor speed at a certain wind speed.

$$\lambda = \frac{\omega_0 R}{v} = \frac{\omega R}{Gv} \quad (2)$$

Where: ω_0 is the wind wheel rotation angular velocity, R is the wind wheel radius, v is the wind speed, ω is the generator rotation speed, and G is the generator box gear ratio.

The pitch angle is the angle between the rotation plane of the wind wheel and the chord line of the blade, denoted by β . Wind energy utilization curve under different pitch angles is shown in Figure 1.

The wind turbine needs to limit the power output when it reaches the rated power. And the mechanical power captured by the wind turbine from the wind is shown in formula (3):

$$P_w = \frac{1}{2} \rho S C_p v^3 \quad (3)$$

Where: P_w is the mechanical power captured by the wind turbine from the wind, ρ is the air density, S is the swept area of the wind wheel, C_p is the wind energy utilization factor, and v is the actual wind speed.

As shown in formula (3), for wind turbines operating below the rated wind speed, higher output power can be obtained at the same wind speed by selecting the larger possible wind energy utilization factor; and for wind turbines operating at rated wind speeds and above, the pitch angle can be controlled to change the wind energy utilization factor, as shown in Figure 1, in order to maintain the unit's mechanical power P_w stabilized at rated power. Variable pitch control means that when the unit reaches rated power and the wind speed continues to increase, the pitch angle is changed and the wind

energy utilization factor is reduced to maintain the constant power operation of the wind turbine. The specific control logic is shown in Figure 2.

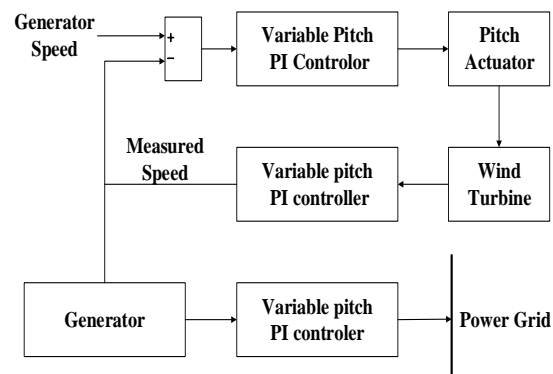
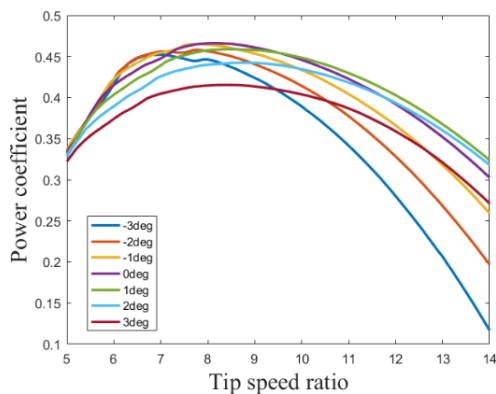


Figure 1. Curve of wind energy utilization at different pitch angles, **Figure 2.** Wind Turbine Control System Structure

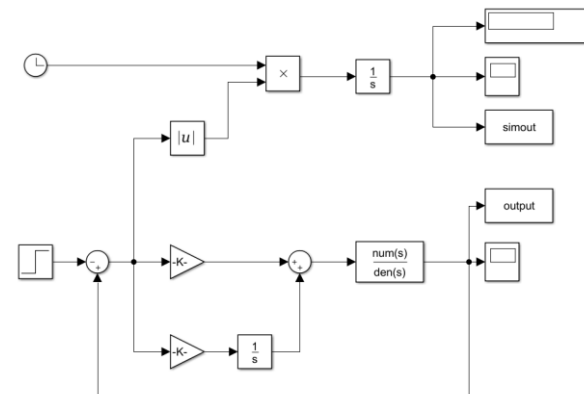
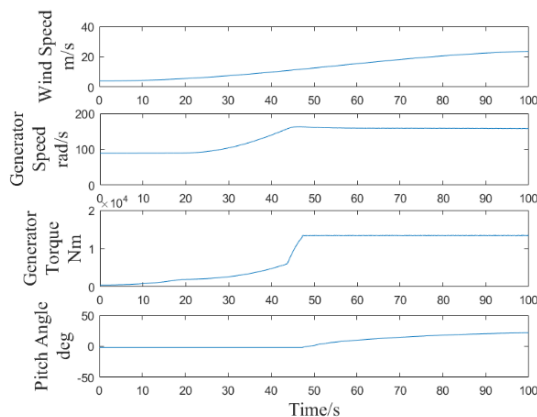


Figure 3. Generator speed, torque, and pitch angle with wind speed curve; **Figure 4.** Simulink model diagram

There is an upper limit of the generator speed called the rated speed; and the electromagnetic torque of the generator is limited by the inverter and electrical design, there is also an upper limit called rated torque. When the generator speed is increased to the upper limit and the torque reaches the rated torque (at this time, the unit is in: rated speed, rated torque, rated power), the wind speed continues to increase, variable pitch PI control can be adopted. Through the pitch actuator, the pitch angle is changed to reduce the wind energy utilization factor of the wind wheel to ensure that the unit will continue to work at rated speed, rated torque and rated power. Generator speed, torque and pitch angle with wind speed curve shown in Figure 3.

The existing control strategy usually uses the wind speed as input to judge the working status of the wind turbine, and based on this, control strategy designed will inevitably be affected by the wind speed measurement error. Therefore, this paper proposes a variable pitch PI control strategy for wind turbines for practical applications.

When the wind turbine is operating above the rated wind speed, the nonlinearity between the pitch angle and the generator speed is particularly obvious, then the PI parameters based on a working point model cannot achieve optimal control effects over the entire working range. Therefore, this paper obtains wind turbine models at different wind speeds by model linearization, and then sets corresponding PI controller parameters. At the same time, it determines the optimal pitch angle for the corresponding wind speed, and finds out the variation of PI parameters with the pitch angle. The

control strategy of adaptively adjusting the PI parameters based on the pitch angle is implemented to eliminate the influence of the wind speed measurement error on the pitch control to the greatest extent.

3. Model linearization and its processing

Wind turbine is a complex system with the characteristics of nonlinear and time-varying parameters. Taking into account the complex environmental factors, changing operating conditions, the application of nonlinear control and other advanced control algorithms is not ideal, so consider the model linearization.

3.1 Bladed model linearization

The authoritative wind turbine simulation software Bladed, developed by GH, can use a large number of detailed equipment parameters to create a mathematical unit simulation model. Due to the accurate simulation calculation of the software and the high precision of the model, it has become one of the recognized industry standards which has already been certified by German classification society and IEC. The Model Linearization function is used for the unit model established by Bladed, and then the Linear Model module is used for post-processing the result of the operation. The MIMO linearized model data file shaped as Equation (4) can be obtained [5].

$$\begin{cases} \dot{x} = Ax + Bu \\ y = Cx + Du \end{cases} \quad (4)$$

In the formula: The coefficient matrix A, B, C, D is a three-dimensional array based on wind speed. The input of the state space equation obtained by the linearization of Bladed model is wind speed, pitch angle demand and generator torque demand. In this paper, the generator speed is selected as the output.

3.2 Matlab data processing

The MIMO state space equation is imported into MATLAB and converted to a SISO transfer function model at any wind speed. At 16 m/s wind speed, the transfer function of the pitch angle-generator speed model is as follows:

$$G_{\beta}(s) = \frac{-137.63s(s+640.1)(s+3.333)^2(s^2-0.1216s+8.193)(s^2+0.08863s+8.76)(s^2+4.308s+48.81)(s^2+4.435s+49.7)(s^2-0.763s+51.15)(s^2+0.2918s+82.95)(s^2+0.3031s+85.27)(s^2+0.1575s+266.7)(s^2+9.724s+378.4)(s^2+0.371s+366.6)(s^2+5.798s+629.3)}{(s+3.333)^3(s+0.1287)(s+0.01822)(s^2+0.04482s+8.387)(s^2+0.3168s+8.6)(s^2+4.376s+48.74)(s^2+4.433s+49.6)(s^2+4.129s+50.9)(s^2+0.2919s+82.95)(s^2+0.3044s+85.26)(s^2+1.75s+204.4)(s^2+0.5883s+280.6)(s^2+0.3615s+366.5)(s^2+5.081s+408.8)(s^2+3.653s+661.2)} \quad (5)$$

4. PID parameter tuning based on particle swarm optimization

4.1 The basic concept of PSO algorithm

Suppose a group consists of M particles, each particle is in the D-dimensional search space, the velocity of the i-th particle can be represented as the vector $v_i = (v_{i1}, v_{i2}, \dots, v_{iD})$, and the position is represented as the vector $x_i = (x_{i1}, x_{i2}, \dots, x_{iD})$, the particles update their positions and velocities according to the fitness value [6]-[8], and the updated basis is based on two extreme values—the individual extremum and the global extremum. The individual extremum is the best position currently found by the i-th particle, denoted as $p_{best} = (p_{i1}, p_{i2}, \dots, p_{iD})$. The global extremum is the best position for all particles in the population, and is denoted as $g_{best} = (p_{g1}, p_{g2}, \dots, p_{gD})$. For the k-th iteration, the particle velocity and position update rules in the PSO are:

$$\begin{cases} v_{id}^{k+1} = \omega v_{id}^k + c_1 r_1 (p_{id} - x_{id}^k) + c_2 r_2 (p_{gd} - x_{id}^k) \\ x_{id}^{k+1} = x_{id}^k + v_{id}^{k+1} \end{cases} \quad (6)$$

Among them, d represents the current search space dimension; i represents particles; k represents evolutionary algebra; x_{id}^k is the d-dimensional component of the position vector of particle i in the k-th iteration; v_{id}^k is the d-dimensional component of the velocity vector of particle i in the k-th iteration; p_{gd} is the d-dimensional component of the global extreme g_{best} of the population; p_{id} is the d-dimensional component of the particle extremum p_{best} ; c_1 and c_2 are acceleration factors; ω is the inertia weight; r_1 and r_2 are random numbers between $[0,1]$.

4.2 PSO parameter optimization

The PI parameters of each transfer function obtained by linearizing the model are adjusted by using the particle swarm algorithm. The specific parameters of the PSO algorithm are set as follows: particle swarm size $M=100$, maximum iteration number $k=50$, dimension $D=2$, inertia factor $\omega=0.6$, acceleration constant $c_1=1, c_2=1$, and the fitness function is selected:

$$Q = \int |e(t)| dt \quad (7)$$

Build a Simulink model, as shown in Figure 4. Under the unit step input, the optimal PI parameters of the pitch angle-generator rotational speed transfer function under different operating points are obtained through operation optimization. Taking the transfer function of pitch angle-generator speed at 16m/s wind speed as an example, see equation (10). The PI parameters obtained by particle swarm optimization are: $K_p=0.0149$ and $K_i=0.0132$.

4.3 Variable gain PI controller parameter setting

The particle swarm optimization algorithm is used to optimize the PI parameters for linear models under different wind speeds at 12-24 m/s. The changes of the blade pitch angle β and controller parameters K_p and K_i are shown in Table 1:

Table 1. Partial controller parameters and pitch angle at 12-24m/s wind speed

Wind(m/s)	K_p	K_i	β (deg)
12	0.033	0.0117	-0.03477
14	0.0179	0.0112	0.162199
16	0.0105	0.0049	0.177321
18	0.0149	0.0132	0.198041
20	0.0078	0.0016	0.220163
22	0.0077	0.002	0.24962
24	0.0056	0.0018	0.299954

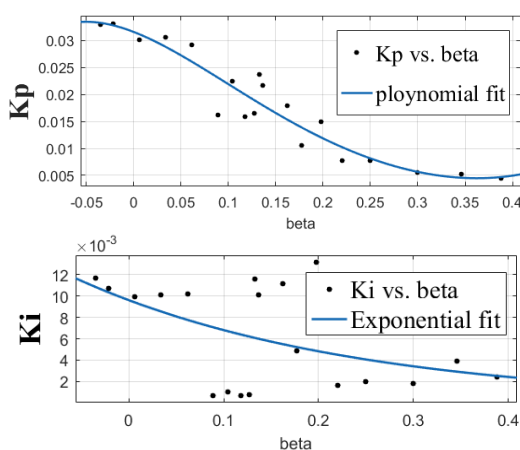


Figure 5. K_p and K_i fitting curves

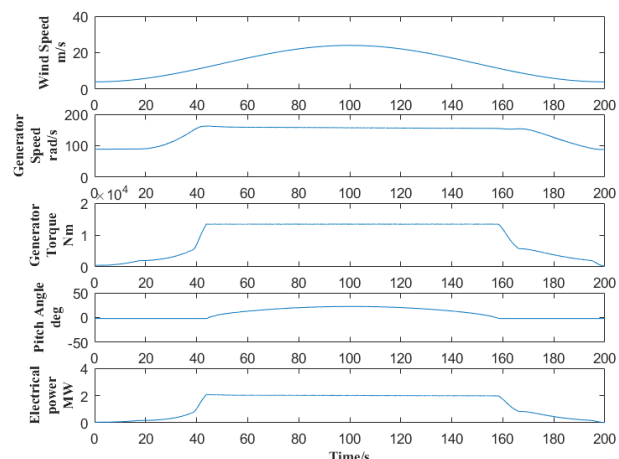


Figure 6. Generator speed, torque, pitch angle and electrical power

output power curve under 12-24m/s wind

Using the Matlab Curve Fitting Toolbox curve fitting, the obtained curve as follow, which shows the variation of controller parameters K_p , K_i with pitch angle β :

The rules of controller parameter K_p , K_i changing with pitch angle β are as follows:

$$K_p = -1.419\beta^4 + 1.619\beta^3 - 0.4155\beta^2 - 0.06288\beta + 0.03152 \quad (8)$$

$$K_i = 0.009622 \exp(-3.456\beta) \quad (9)$$

5. Example analysis

5.1 Wind turbine modeling and control strategy implementation

Model the blades, airfoils, rotor, towers, power train, nacelle and other components of a 2MW wind turbine unit based on Bladed. The key parameters are shown in Table 2.

Table 2. Key parameters of wind turbines

Blade length(m)	38.75
Number of blades	3
Rotor diameter(m)	80
Tower height(m)	60
Gearbox ratio	83.3
Generator rated speed (rpm)	1500
Rated torque(T)	13403

Bladed allows external controllers to be designed from the dynamic link library (DLL). Compile the control strategy into a DLL file, select the external controller and invoke the DLL in the Control function module of Bladed to complete the controller design and implementation.

5.2 Analysis of simulation results

The generator speed, torque, pitch angle and electrical power under a 12-24m/s time varying wind are shown in Figure 6. Under 15m/s wind with a turbulence of 4%, the generator speed, torque, pitch angle, and electrical power are shown in Figure 7.

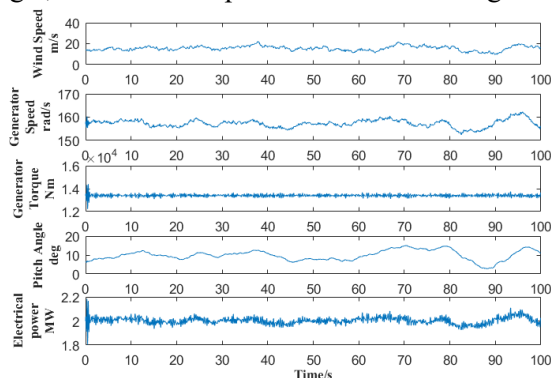


Figure 7. Generator speed, torque, pitch angle and electrical power under 15m/s turbulent wind

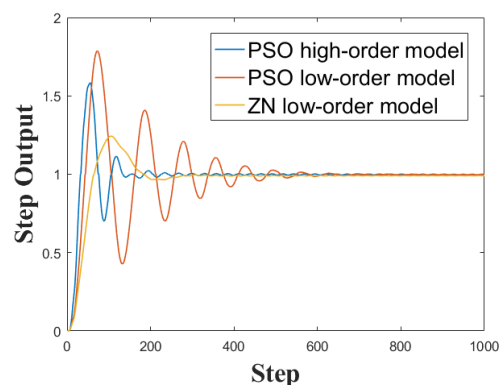


Figure 8. Unit step response under different PI parameters

As can be seen from the above figure, the rated power control strategy can effectively control the pitch angle to ensure the constant power operation of the unit.

The traditional PI controller parameter tuning is usually to use the least square method, Pade method or Routh method to reduce the order of high-order systems, and then through the Z-N, C-C and other empirical formulas or PSO and other intelligent algorithms for PI parameter tuning. The pitch angle-generator speed transfer function can be reduced to the first-order inertial delay link which in the form of formula (15) (FOLPD):

$$G(s) = \frac{K}{Ts+1} e^{-Ls} \quad (10)$$

Taking the wind speed of 16m/s as an example, the FOLPD model obtained by reducing the formula (10) is as follows:

$$G_{\beta}(s) = \frac{-112.2}{0.3548s+1} e^{-0.597s} \quad (11)$$

For formula (16), the PI parameters determined by the Z-N empirical formula are: $K_p=0.0046$, $K_i=0.0023$

For formula (16), the PI parameters set by the PSO algorithm are: $K_p=0.0045$, $K_i=0.0086$

For the pitch angle-generator speed model at 16m/s wind speed, as shown in equation (10), the corresponding unit step response for each group of PI parameters is shown in Figure 8.

As can be seen from the figure 8, the PI parameters obtained by optimizing the higher-order linearization model using the PSO algorithm have shorter rise time and shorter adjustment time, and have better control effect.

6. Conclusion

The main content of this article is:

A control strategy for rated power of wind turbines for practical production needs is proposed. Compared with traditional control strategies, the new strategy can minimize the impact of wind speed measurement errors on control strategies.

A method of parameter tuning of PI controller under full wind speed range is proposed. Compared with the traditional method of tuning the reduced-order model parameters, the new method has a better control effect. Relative to the enumeration method for a certain operating conditions for parameter tuning, the new method has a greater scope of application and faster setting speed.

7. Acknowledgement

This work is supported by the Science and Technology Project of State Grid Corporation of China.

8. References

- [1] Tian J J 2016 Conf. National Metallurgical Automation Information Network 2016 Annual Conference Proceedings.**40** 5
- [2] Xue J N and Ma P 2008 *J. Equipment Manufacturing Technology*.**02** 42-44
- [3] Cui Z Z, Wang S L, Shi L Q and Song L W 2013 *J. Transactions of China Electrotechnical Society*. **28** 80-86
- [4] Liu H 2009 *Wind Turbine System Dynamic Model and Optimization of Key Components* Chongqing University 138
- [5] Bladed User Manual (Version 4.2) 2011. Garrad Hassan & Partners Ltd. England
- [6] Khandani K, Jalali A A and Alipoor M 2009 *Conf. IEEE International Conference on Intelligent Computing and Intelligent Systems*. 862-866
- [7] Adel T and Abdelkader C 2013 *Conf. International Conference on Electrical Engineering and Software Applications*. 1-4
- [8] Jalilvand A, Kimiyaghalam A, Ashouri A, et al. Advanced Particle Swarm Optimization-Based PID Controller Parameters Tuning. 2008 *Conf. IEEE International Multitopic Conference*. 429~435

The Profit Influence of Additional Heat Sources on Combined Heat and Power System in Existing Peak Shaving Compensation Mechanism

Yang Bai¹, Jianxing Qin², Qi Guo³ and Zhongkai Yi³

¹Guangdong Power Grid Dispatching Control Center, Guangzhou 510600, China

²Guangzhou Yiyun Information Technology Co., Ltd, Guangzhou 510275, China

³School of Electrical Engineering and Automation, Harbin Institute of Technology, Harbin 150001, China

E-mail: Gqtiffany@163.com

Abstract. In combined heat and power system, configuring of electric boilers, heat storage and other additional heat sources (AHS) is an effective way to alleviate the problem of wind curtailment in northeast China. In this paper, according to the currently existing peak shaving compensation mechanism, a production simulation model with AHS has been established. Based on them, the impact of AHS on the profit of combined heat and power (CHP) units, conventional (CON) units and wind farms is analyzed. Simulation system derives from a city of Jilin province, northeast of China, simulation result shows that with AHS involved, wind farms benefit most, and CHP units face profit decline. Besides, this paper also gives some advice to promote the configuration and operation of AHS, which has a guiding significance for the improvement of peak shaving compensation mechanism.

1. Introduction

In northeast China, CHP units are the main heating sources in winter, and their proportion is considerable. The use of CHP units, electric boilers and heat pumps creates linkages between electricity and heat networks [1]. Because of the opposite peak-valley characteristics of power load and heat load and the constraint of thermal-electrical coupling of CHP units, the CHP units have to output more power in heating consuming peak time. Therefore other thermal power plants have to regulate depth peak load cycling, even shut down directly, which increase the difficulties of peak shaving.

Recent years, large-scale grid integration of wind power further exacerbates the difficulty of peak shaving. As a result, wind curtailment often occurs in northeast China and the maximum wind-removal rate is even above 20% [2]. Especially in northeast China, the areas which are rich of wind resource also badly need heating in winter, and the higher proportion of thermal power units adversely affects the wind power consumption.

There are mainly three methods to solve the problem of wind power curtailment: (1) Using the characteristics of district heating system such as heat storage characteristics and thermal inertia to consume the wind power [3]. (2) 'Wind power heating' [4]. (3) Allocating additional heat source (AHS) to reduce thermal-electric coupling [5]. Among them, the third way of allocating AHS is effective to promote wind power consumption. AHS include the electric boiler, heat storage and heat pumps and so on [6], [7]. In the literature [6], the optimal allocation method of AHS is studied. In the literature [7], the heat storage is used to reduce the thermal-electric coupling of CHP units. Ref [8]-[10]



show that the electric boiler can promote the wind power consumption and the heat storage can increase the economic efficiency of the whole system.

In this paper, a production simulation model of heating season with AHS is established. The power generation of CHP units, CON units and wind farms are obtained, both with and without AHS. And according to the existing power peak shaving compensation mechanism, the profit of each unit participated in the power market can be calculated. Based on them, this paper aims to analyze the profit influence of AHS on combined heat and power system and wind farms, then puts forward reasonable suggestions for the improvement of the power peak shaving compensation mechanism.

2. Mechanism of AHS to relieve wind curtailment

The policy of planning and operating CHP units based on ‘Ordering Electricity by Heat’ limits the lower heat output limit of CHP units during the heating season, which exacerbates the phenomenon of wind power curtailment. The AHS can improve the peak shaving capacity of CHP units. Arranging the heat storage and electric boiler inside the thermal power plant can provide extra heat source for the heat network and reduce the heat output demand of CHP units. And it is a good way to release the limited potential for regulation of CHP units, therefore the wind power curtailment during heating season could be relieved effectively.

3. Production simulation model with AHS

3.1. Objective function

In order to increase the utilization rate of new energy sources and relieve wind power curtailment, the cost of wind power generation is excluded in the scheduling model, and the objective function is to minimize the total system coal consumption:

$$\min F = \sum_{t=1}^T \left(\sum_{r=1}^R \sum_{n=1}^N F_{\text{CHP}}^{t,r,n} (P_e^{t,r,n}, P_h^{t,r,n}) + \sum_{s=1}^S F_{\text{CON}}^{t,s} (P_e^{t,s}) \right) \quad (1)$$

Where, F is the minimum system coal consumption; $F_{\text{CHP}}^{t,r,n}$ is the coal consumption of the n^{th} CHP unit at the r^{th} thermal power plant in period t ; $P_e^{t,r,n}$ and $P_h^{t,r,n}$ are respectively electric power and thermal power; $F_{\text{CON}}^{t,s}$ is the coal consumption of the s^{th} CON unit in period t ; T is the scheduling cycle.

3.2. Unit coal consumption characteristics

The coal consumption characteristics of CON unit is as:

$$F_{\text{CON}} = b_1 + b_2 P_h + b_3 P_h^2 \quad (2)$$

Where, F_{CON} is the coal consumption; P_h is the electric power; b_1 - b_3 are the fitting coefficients.

The coal consumption characteristics of CHP unit is as:

$$F_{\text{CHP}} = a_1 + a_2 P_e + a_3 P_e^2 + a_4 P_h^2 + a_5 P_e P_h + a_6 P_h \quad (3)$$

Where, F_{CHP} is the coal consumption; P_e and P_h , respectively, are the electrical power and thermal power; a_1 - a_6 are the fitting coefficients.

3.3. Constrains

Electric power balance. Electric power balance formula of CHP unit, CON unit and wind farm in the power grid is:

$$\sum_{r=1}^R \sum_{n=1}^N P_{\text{CHP}}^{t,r,n} + \sum_{s=1}^S P_{\text{CON}}^{t,s} + P_{\text{wind}}^t = P_{\text{load}}^t + \sum_{r=1}^R \sum_{l=1}^L P_e^{t,r,l} + \sum_{i=1}^I P_{\text{eb}}^{t,i} \quad (4)$$

Where, $P_{\text{CHP}}^{t,r,n}$ is the electric power of the n^{th} CHP unit at the r^{th} thermal power plant in period t ; $P_{\text{CON}}^{t,s}$ is the electric power of the s^{th} CON unit in period t ; P_{wind}^t is the total power of the wind farm in period t ; P_{load}^t is the electric load in period t ; $P_{\text{eb}}^{t,i}$ is the electric power of the i^{th} electric boiler in period t ; $P_e^{t,r,l}$ is the electric power consumed by the l^{th} heat exchanger station in the r^{th} thermal power plant in period t .

Thermal power balance. In each district heating area, heat load should also be balanced as following:

$$\sum_{n=1}^N Q_{\text{CHP}}^{t,r,n} + \sum_{n=1}^N Q_{\text{eb}}^{t,r,n} = Q_{\text{load}}^t, \quad r = 1, 2, \dots, N$$

$$Q_{\text{CHP}}^{t,r,n} = \frac{P_h^{t,r,n} \Delta H^{t,r,n}}{1000} \quad (5)$$

Where, $Q_{\text{CHP}}^{t,r,n}$ is the heat supply of the n^{th} CHP unit at the r^{th} thermal power plant in period t ; $Q_{\text{eb}}^{t,r,n}$ is the heat power of the n^{th} electric boiler at the r^{th} thermal power plant in period t ; Q_{load}^t is the heat load in period t ; $P_h^{t,r,n}$ is the extraction of the n^{th} heating unit at the r^{th} thermal power plant in period t ; $\Delta H^{t,r,n}$ is the steam enthalpy drop of the n^{th} heating unit at the r^{th} thermal power plant in period t .

3.4. Wind power balance.

$$P_{\text{wind}}^{t,m} + P_{\text{abandon}}^{t,m} = P_{\text{forecast}}^{t,m} \quad (6)$$

Where, $P_{\text{wind}}^{t,m}$ is the amount of wind power actually consumed by the m^{th} wind farm in period t ; $P_{\text{abandon}}^{t,m}$ is the amount of abandonment of the m^{th} wind farm in period t ; $P_{\text{forecast}}^{t,m}$ is the forecast power generated by the m^{th} wind farm in period t .

3.5. Unit output constrains.

$$H_{\text{CHP}}^{\min,r,n} \leq H_{\text{CHP}}^{t,r,n} \leq H_{\text{CHP}}^{\max,r,n}$$

$$P_{\text{CHP}}^{\min,r,n} \leq P_{\text{CHP}}^{t,r,n} \leq P_{\text{CHP}}^{\max,r,n}$$

$$P_{\text{CON}}^{\min,r,n} \leq P_{\text{CON}}^{t,r,n} \leq P_{\text{CON}}^{\max,r,n}$$

$$0 \leq P_{\text{wind}} \leq P_{\text{forecast}} \quad (7)$$

Where, $H_{\text{CHP}}^{\min,r,n}$ and $H_{\text{CHP}}^{\max,r,n}$ are respectively the lower limit and the upper limit of the steam extraction amount of the n^{th} CHP unit at the r^{th} thermal power plant in period t ; $P_{\text{CHP}}^{\min,r,n}$ and $P_{\text{CHP}}^{\max,r,n}$ are respectively the lower limit and the upper limit of the electric power of the n^{th} CHP unit at the r^{th} thermal power plant in period t ; $P_{\text{CON}}^{\min,r,n}$ and $P_{\text{CON}}^{\max,r,n}$ are respectively the lower limit and the upper limit of the electric power of the r^{th} CON unit in period t ; P_{forecast} is the forecast power of wind farm.

3.6. Ramping constrains.

$$\begin{aligned}
-r_{\text{CHP}}^{\text{down}} \Delta t &\leq P_{\text{CHP}}^t - P_{\text{CHP}}^{t-1} \leq r_{\text{CHP}}^{\text{up}} \Delta t \\
-r_{\text{CON}}^{\text{down}} \Delta t &\leq P_{\text{CON}}^t - P_{\text{CON}}^{t-1} \leq r_{\text{CON}}^{\text{up}} \Delta t
\end{aligned} \tag{8}$$

Where, $r_{\text{CHP}}^{\text{down}}$ and $r_{\text{CHP}}^{\text{up}}$ are respectively the ramping down and ramping up constraints of the CHP unit; $r_{\text{CON}}^{\text{down}}$ and $r_{\text{CON}}^{\text{up}}$ are respectively the ramping down and ramping up constraints of the CON unit.

3.7. Electric boiler constrains.

$$\begin{aligned}
P_{\text{eb}}^{\text{min}} &\leq P_{\text{eb}} \leq P_{\text{eb}}^{\text{max}} \\
Q_{\text{eb}} &= \beta_{\text{eb}} P_{\text{eb}}
\end{aligned} \tag{9}$$

Where, $P_{\text{eb}}^{\text{min}}$ and $P_{\text{eb}}^{\text{max}}$ are respectively the lower and upper electric power limits of electric boiler. Q_{eb} is the heat output of electric boiler. β_{eb} is the conversion efficiency of electric boiler.

3.8. Heat storage tank constrains.

$$\begin{aligned}
0 &\leq Q_{\text{tank}}^t \leq Q_{\text{tank}}^{\text{max}} \\
H_{\text{tank}}^t &= Q_{\text{tank}}^t - Q_{\text{tank}}^{t-1} \\
(1 - \eta_{\text{loss}}) Q_{\text{tank}}^{t-1} - Q_{\text{tank}}^t &\leq H_{\text{tank}}^{\text{max}} \\
Q_{\text{tank}}^t - (1 - \eta_{\text{loss}}) Q_{\text{tank}}^{t-1} &\leq H_{\text{tank}}^{\text{min}}
\end{aligned} \tag{10}$$

Where, Q_{tank}^t is the heat energy of heat storage tank in period t ; $Q_{\text{tank}}^{\text{max}}$ is the storage capacity of heat storage tank; $H_{\text{tank}}^{\text{max}}$ and $H_{\text{tank}}^{\text{min}}$ are the maximum and minimum output power of heat storage tank respectively; η_{loss} is the loss rate of heat storage tank.

4. Peak shaving compensation algorithm

In order to give full play to the role of economic levers, maximize the effectiveness of limited resources, substantially reduce wind curtailment, and increase the acceptance rate of clean energy, the northeast power peaking shaving compensation management has been established. The core rules of the management approach are divided into: basic peak-shaving ancillary services and paid peak shaving ancillary services, and the latter mainly includes three options: unit operation peaking, peak load operation, cross-provincial peaking. To analyze the impact of the heat source operation on the profit of various units of the power system, this paper considers the auxiliary service compensation mechanism, and the detailed algorithm flowchart is shown as Figure 1.

In Figure 1, P is the power generation of each unit; α is the coefficient of the fine; M_{final} is the total amount of fine; Limit_{up} is the upper limit of the fine; Ele_price is the compensation price; M_{sum} is the total amount of compensation.

The profit of each unit is that revenue from electricity sales minus coal consumption costs and minus M_{final} or add M_{sum} .

5. Case study

Simulation system derives from a city of Jilin province, northeast of China, which includes 6 CHP units, 4 CON units and a wind farm. To promote the wind power consumption of this regional power system, some AHS (electric boiler and heat storage) have been configured in each district heating areas. The structure of the system is shown as Figure 2, which also shows the installed capacity of all units.

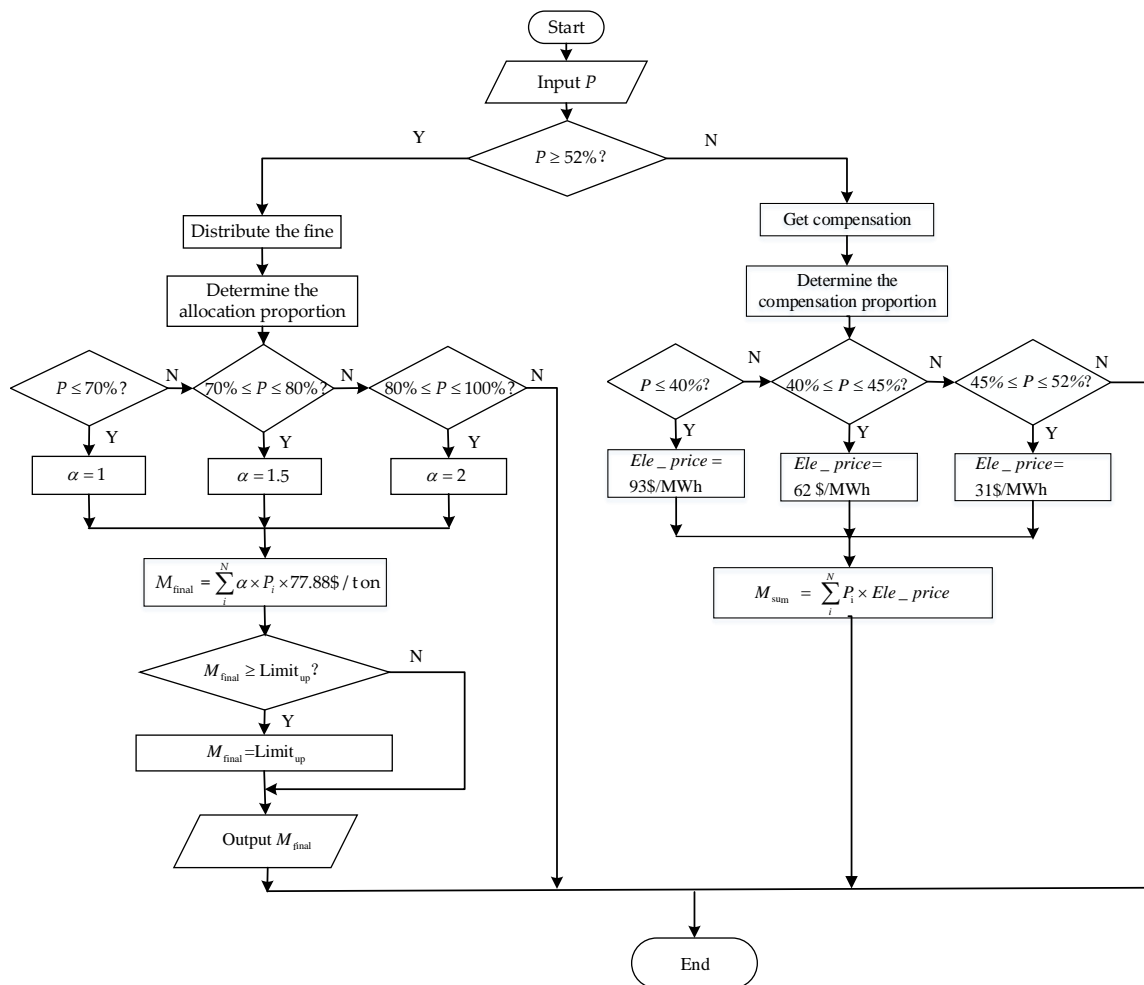


Figure 1. Flow chart for calculating the fine and compensation of each unit.

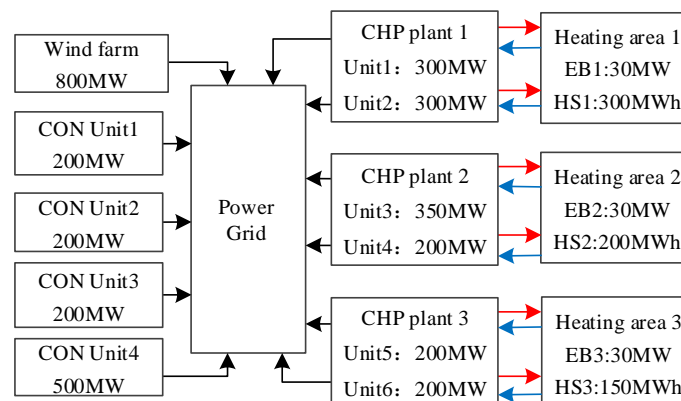


Figure 2. The sketch map of the simulation system.

Fitting parameters of coal consumption characteristic of CON units is shown as Table 1.

In this simulation system, the coal price is 77.88 \$/ton, generation price of the CHP units and CON units is 59.19 \$/MWh, and that of wind farm is 109.03 \$/MWh. As shown in Table 3, adding AHS to the system, the total profit of 6 CHP units and 4 CON units is \$ 1.7182×10⁸, while without AHS, the total profit is \$ 1.7347×10⁸. On the country, wind farm gains more with AHS.

Table 1. Coal consumption parameters of CON units.

CON	b_1	b_2	b_3
1,2,3	3.5	0.3	8.5×10^{-5}
4	4	0.3	6.5×10^{-5}

Fitting parameters of coal consumption characteristic of CHP units is shown as Table 2.

Table 2. Coal consumption parameters of CHP units.

CHP	a_1	a_2	a_3	a_4	a_5	a_6
1	0.75	0.27	7.6×10^{-5}	4.28×10^{-5}	1.14×10^{-4}	0.2037
2	0.75	0.27	7.6×10^{-5}	4.28×10^{-5}	1.14×10^{-4}	0.2037
3	0.75	0.27	7.6×10^{-5}	4.05×10^{-5}	1.14×10^{-4}	0.1719
4	0.75	0.27	7.1×10^{-5}	3.99×10^{-5}	1.08×10^{-4}	0.2029
5	0.75	0.27	7.1×10^{-5}	3.99×10^{-5}	1.06×10^{-4}	0.2029
6	0.75	0.27	7.1×10^{-5}	3.99×10^{-5}	1.06×10^{-4}	0.2029

Based on the simulation system, the profit of the whole heating season (145 days) of each unit both with and without AHS is obtained, as shown in Table 3.

Table 3. Profit of each unit.

Unit	With AHS/\$	Without AHS/\$
CHP 1	5.8858×10^6	5.7780×10^6
CHP 2	5.9674×10^6	5.8526×10^6
CHP 3	1.6687×10^7	1.6829×10^7
CHP 4	9.6481×10^6	9.8642×10^6
CHP 5	7.7650×10^6	7.9955×10^6
CHP 6	7.7358×10^6	7.6907×10^6
CON 1	3.2511×10^7	3.2958×10^7
CON 2	3.2441×10^7	3.2897×10^7
CON 3	3.9283×10^7	3.9790×10^7
CON 4	1.3898×10^7	1.3819×10^7
Wind farm	1.7671×10^8	1.5867×10^8

It can be concluded that if there is no compensation income, CHP units and CON units will face losses and wind farm will gain more profits. This will reduce the enthusiasm of thermal power plants to participate in the construction and operation of AHS. Therefore, after the AHS consuming wind power, it is necessary for the wind farm to compensate part of profits to the thermal power plants.

Figure 3 and Figure 4 show that adding AHS to the system can relieve the phenomenon of wind curtailment and promote wind farm to generate more power, however, CHP units and CON units face profit decline due to less power generation, especially in the evening.

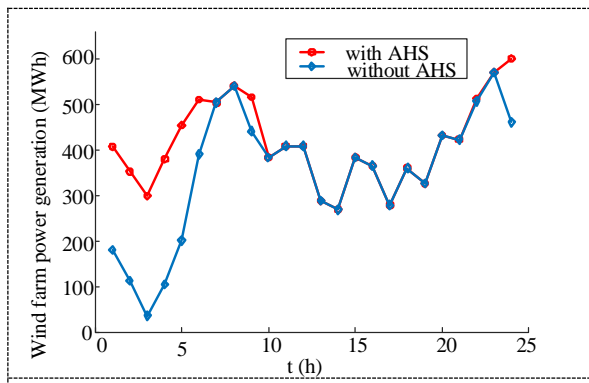


Figure 3. Wind farm power generation on a typical day.

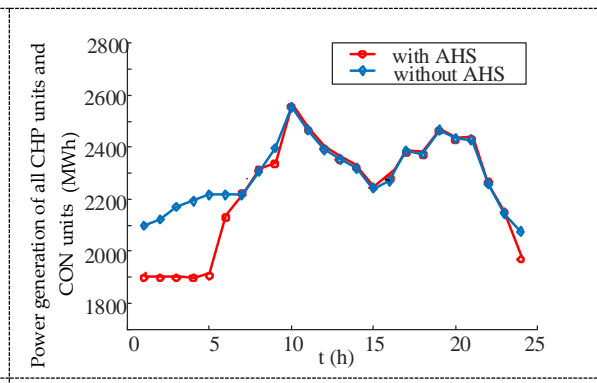


Figure 4. Power generation of CHP units and CON units on a typical day.

Figure 5 shows the profit difference of CHP1 after adding AHS and before adding AHS. The profit difference increase with the rise of coal price. Adding AHS indicates that the required heat output of CHP units has been reduced, the amount of coal consumption will also decline. Therefore, when the coal price is higher, CHP units will be more willing to participate in the operation with AHS. The critical point of coal price is about 62.3\$/ton.



Figure 5. Profit difference of CHP1.

At last, we get the marginal curves of CHP units and wind farm and the average compensation price feasible region, as shown in Figure 6.

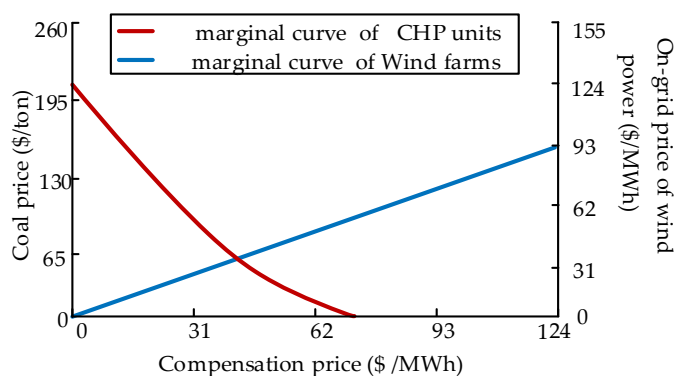


Figure 6. Feasible region analysis of the compensation price.

In Figure 6, the curve in red and blue color are the marginal curves of CHP units and wind farm. From this two marginal curves, we can conclude that with the increase of coal price, the expected minimum

compensation price of CHP units has decreased. And for wind farm, with the increase of on-grid price of wind power, the acceptable maximum compensation price also increases. The upper area between the two curves is the feasible region of the two parts.

6. Conclusions

In this paper, a production simulation model with AHS during heating season is established and the peak shaving compensation mechanism in northeast China is considered. Based on the model, the profits variation has been analyzed and we can get the following conclusions:

- (1) With AHS configured, wind farm generates more power, while CHP units have reduced their power generation. So the wind farm gains more profits, CHP units face profit decline.
- (2) When the coal price is higher, the CHP units will be more willing to participate in the operation with AHS and the critical point of coal price is nearly 62.3\$/ton.
- (3) Through the simulation study, the reasonable value of compensation price varies with wind power on-grid price and coal price. Besides, the feasible region of the compensation price is obtained, which have a guiding significance on the improvement of peak shaving compensation mechanism.

7. References

- [1] Cho H, Smith AD, Mago P 2014 Combined cooling, heating and power: a review of performance improvement and optimization *Applied Energy* **136** 168-185.
- [2] Wang J, Zhong H, Tan CW, et al. 2018 Economic Benefits of Integrating Solar-Powered Heat Pumps in a CHP System *IEEE Transactions on Sustainable Energy* **1**.
- [3] Wu C, Gu W, Jiang P, et al. 2017 Combined Economic Dispatch Considering the Time-Delay of a District Heating Network and Multi-Regional Indoor Temperature Control *IEEE Transactions on Sustainable Energy* **1**.
- [4] Fitzgerald N, Foley A M, Mckeogh E 2012 Integrating wind power using intelligent electric water heating *Energy* **48**(1) 135-43.
- [5] Nielsen M G, Morales J M, Zugno M, et al. 2016 Economic valuation of heat pumps and electric boilers in the Danish energy system *Applied Energy* **167** 189-200.
- [6] Rong S, Li Z, Li W 2015 Investigation of the Promotion of Wind Power Consumption Using the Thermal-Electric Decoupling Techniques *Energies* **8**(8) 8613-29.
- [7] Rong S, Li W, Li Z, et al. 2015 Optimal Allocation of Thermal-Electric Decoupling Systems Based on the National Economy by an Improved Conjugate Gradient Method *Energies* **9**(1) 17.
- [8] Chen X, Kang C, O'Malley M, et al. 2015 Increasing the Flexibility of Combined Heat and Power for Wind Power Integration in China: Modeling and Implications *IEEE Transactions on Power Systems* **30**(4) 1848-57.
- [9] Christidis A, Koch C, Pottel L, et al. 2012 The contribution of heat storage to the profitable operation of combined heat and power plants in liberalized electricity markets *Energy* **41**(1):75-82.
- [10] Liu D, Zhang G, Huang B, et al. 2016 Optimum Electric Boiler Capacity Configuration in a Regional Power Grid for a Wind Power Accommodation Scenario *Energies* **9**(3):144.

Suppression Methods for Low Frequency Oscillation of Wind Farm Considering SVG Minimum Output Dead Zone

Yangfan Zhang ^{1,2}, Xu Xie ³, Peng Song ^{1,2}, Hui Liu ^{1,2}, Tao He ³

¹ State Grid Jibei Electric Power Research Institute (North China Electric Power Research Institute Co. Ltd), Beijing, China

² Grid-connected Operation Technology For Wind-Solar-Storage Hybrid System State Grid Corporation Key Laboratory, Beijing, China

³ State Grid Zhangjiakou Power Supply Company, Zhangjiakou, China

E-mail: zhangyangfanhit@163.com

Abstract. At present, the research of Static Var Generator (SVG) mainly focuses on the main circuit topology, the optimization of control strategy, the method of selection, and lack of research on the low frequency oscillation of the wind farm caused by SVG minimum reactive output dead zone in practical engineering applications. For this reason, this paper first studies the mechanism of the low frequency oscillation of the wind electric field induced by the SVG minimum output dead zone of the wind farm, and discusses the conditions of this type of oscillation. On this basis, the automatic voltage control system (AVC) optimization model of wind farm is established with the minimum reactive variation of SVG output near the zero point as the optimization goal, and an optimization control strategy of wind farm with SVG minimum output reactive dead zone is proposed. Finally, the correctness of the result is verified by simulation. The results show that, due to the existence of the minimum output dead zone in the wind farm, the large reactive step may occur near the zero point of the SVG output, which causes the voltage low frequency oscillation of the wind farm. The optimization strategy proposed in this paper can significantly suppress the low frequency oscillation by coordinating and optimizing reactive power output near the zero point of multiple SVGs in wind farm.

1. Introduction

Wind power has the characteristics of random fluctuation and access to the end of power grid, which has an increasingly prominent impact on power quality and voltage stability of power system. SVG is an important measure to improve the power quality of the wind farm and improve the stability of the power system. It has been widely used in the wind farm. At present, the reactive power equipment such as SVG, wind turbine and capacitor in wind farms are generally controlled by the wind farm automatic voltage control system (AVC), in order to ensure the voltage stability of wind farm.

In the existing literature, the optimization of SVG control strategy [1]-[5], the influence of SVG on the voltage stability of the power system [6]-[7], and the reactive power coordination strategy of SVG and wind turbine [8]-[11] are studied in a large amount. In [3], a SVG optimization control strategy under unbalanced voltage is proposed. The effect of reactive power compensator's position to the synchronous oscillation is studied in [6], and a PID control based on phase compensation method is proposed to suppress subsynchronous oscillations. In [10], a set of two stage voltage control systems considering the fast dynamic reactive power compensator is proposed, which take advantage of SVG in steady voltage control and transient voltage stability. However, in the actual application, SVG usually sets the minimum output dead zone. If the wind farm AVC strategy does not consider the



influence of this factor, it may lead to the voltage low frequency oscillation near the zero point of SVG reactive power output, which has not yet been studied in the literature.

In this paper, the mechanism of the low frequency oscillation of the wind electric field induced by the SVG minimum output dead zone of the wind farm is studied first, and the conditions of this type of oscillation is discussed. On this basis, the automatic voltage control system (AVC) optimization model of wind farm is established with the minimum reactive variation of SVG output near the zero point as the optimization goal, and an optimization control strategy of wind farm with SVG minimum output reactive dead zone is proposed. Finally, the correctness of the result is verified by simulation

2. Mechanism of low frequency oscillation

An actual wind farm contains two 7.5Mvar SVG, and the reactive dead zone of each SVG is 0.85Mvar. AVC regulation period of the wind farm is 60s, the voltage dead zone is 0.3kV. The phenomenon of low voltage oscillation occurs during the operation of wind farm, as shown in the figure 1. The voltage and reactive power of the wind farm during the period of t_1 - t_2 are shown in Table 1.

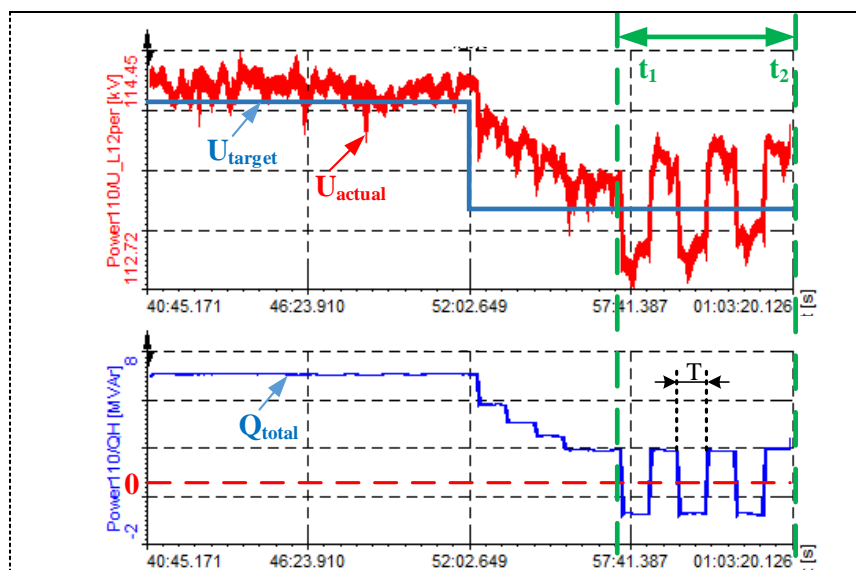


Figure 1. Low frequency oscillation of an actual wind farm.

Table 1. Wind farm values during t_1 and t_2

Time	Voltage		1#SVG		2#SVG	
	Instruction value (kV)	Actual value (kV)	Instruction value (Mvar)	Actual value (Mvar)	Instruction value (Mvar)	Actual value (Mvar)
t_1	113	113.38	0.33	0.85	0.33	0.85
t_1+T	113	112.60	-0.3	-0.85	-0.3	-0.85
t_1+2T	113	113.36	0.33	0.85	0.33	0.85
t_1+3T	113	112.68	0.41	0.85	0.41	0.85

It is known that when the AVC voltage instruction value of the wind farm is 113kV, the demand reactive power of the wind farm is calculated by the AVC strategy. The reactive power instructions issued to each SVG is 0.33Mvar at t_1 moment, but the actual output reactive power of each SVG is 0.85Mvar because of the existence of output dead zone. At this time, the actual voltage of the grid is

113.38kV, which beyond the upper limit of the AVC voltage dead zone, so the AVC continue to calculate and modulate. Similarly, the calculated reactive power instruction of each SVG is -0.3Mvar at t_1+T moment, but the actual output reactive power of each SVG is -0.85Mvar. The actual voltage of the node is 112.6kV at t_1+T moment, which beyond the low limit of the AVC voltage dead zone, so the AVC continue to calculate and modulate. The output reactive power of each SVG changes step by step between 0.85Mvar and -0.85Mvar, and the voltage of the wind farm oscillates between 112.6kV and 113.38kV.

It can be seen that when the voltage of the wind farm is adjusted to near the output zero point of SVG, due to the existence of the minimum output reactive dead zone of SVG in the wind farm, the output reactive power of the SVG may have great step change near zero point, resulting in the repeated regulation of the voltage because of exceeding the voltage dead zone of AVC. Besides, the oscillation period is two times that of the AVC regulation period.

3. Generating conditions of oscillation

The low frequency oscillation of this type of wind farm requires the following conditions:

- (1) There is reactive output minimum dead zone in SVG in wind farms.
- (2) The wind farm is connected to the weak power grid, that is, the short circuit capacity of the wind farm is small.
- (3) The voltage variation caused by the step of SVG dead time is greater than 2 times of the dead time of AVC voltage, that is

$$\Delta U > 2U_d \quad (1)$$

Where

$$\Delta U = \frac{\Delta Q}{S} \quad (2)$$

- (4) The AVC voltage instructions issued to SVG is near the zero point, and satisfy:

$$\begin{cases} U_{ref} - U_{min} > U_d \\ U_{max} - U_{ref} > U_d \end{cases} \quad (3)$$

4. Oscillation suppression method

This paper propose a method to suppress the low-frequency oscillation near zero point considering the dead zone of SVG, as follows:

- (1) Suppose the wind farm has a number of n SVG, each SVG output reactive power dead zone is from small to large: Q_{1d} 、 Q_{2d} ... Q_{nd} , that is

$$Q_{1d} \leq Q_{2d} \leq L \leq Q_{nd} \quad (4)$$

Define variables:

$$\begin{cases} Q_1 = Q_{1d} + Q_{2d} + L + Q_{nd} \\ Q_2 = -Q_{1d} + Q_{2d} + L + Q_{nd} \\ \quad \quad \quad L \\ Q_{n+1} = -Q_{1d} - Q_{2d} - L - Q_{nd} \end{cases} \quad (5)$$

- (2) Suppose that according to the AVC voltage command, the total reactive power of SVG needs to be Q_{svg} , and satisfied.

$$\frac{Q_i + Q_{i+1}}{2} < Q_{svg} < \frac{Q_i + Q_{i-1}}{2}, \quad (1 < i < n+1) \quad (6)$$

- (3) The optimal total reactive power for SVG is Q_i , that is, the reactive power instructions to SVGs are $[-Q_{1d}; -Q_{2d}; \dots; -Q_{(i-1)d}; Q_{id}; Q_{(i+1)d}; \dots; Q_{nd}]$, at this point, SVG has the smallest step of reactive power near zero point.

5. Simulation result

A wind farm model is built in Matlab, the wind farm contains three 6Mvar SVG, and the reactive dead zone of each SVG is 0.6Mvar. AVC regulation period of the wind farm is 30s, the voltage dead zone is 0.2kV. The simulation waveforms before and after the suppression method adopted are shown in Figure 2~ Figure 3, and the variable values during the time between 2.5min and 4min are shown in Table 2.

It can be seen from Figure 2 that before the optimization method adopted, when the AVC instruction voltage is leaped from 112kV to 113.15kV, the calculated SVG reactive instruction is near the zero point. Thus, the output reactive power of each SVG is simultaneously step changed between -0.6Mvar and 0.6Mvar, resulting in the grid voltage continue beyond the AVC voltage dead zone and oscillates in low frequency, the oscillation period is 1 min, as shown in Figure 2.

After the optimization method described in this paper adopted, the reactive power instructions of each SVG are -0.6Mvar, 0.6Mvar, 0.6Mvar, and the actual grid voltage is 113.24kV at this time. It can be seen that the low frequency oscillation of voltage is disappeared, as shown in Figure 3, which proves the correctness of the method described in this paper.

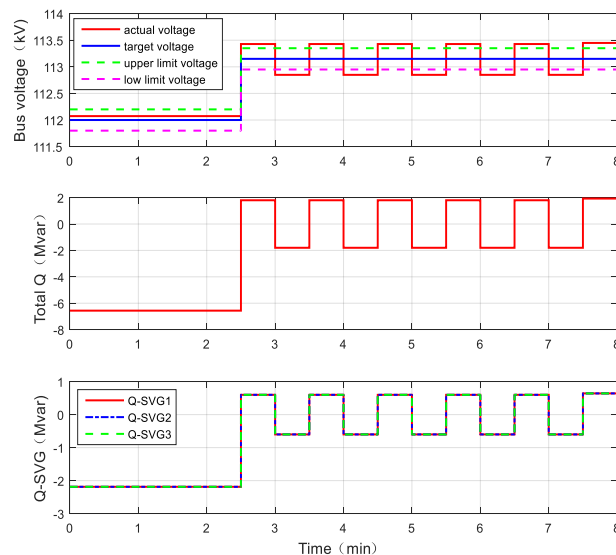


Figure 2. Voltage step waveform before optimization methods adopted.

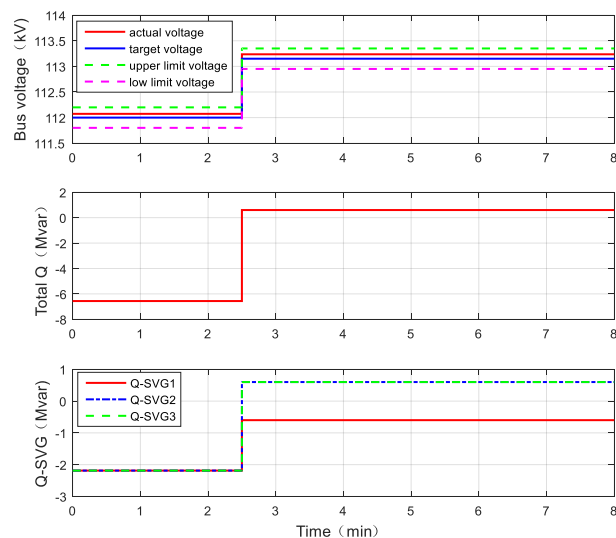


Figure 3. Voltage step waveform after optimization methods adopted.

Table 2. Wind farm values during 2.5~4min

	Time (min)	Voltage		1#SVG value (Mvar)	2#SVG value (Mvar)	3#SVG value (Mvar)	SVG total value (Mvar)	State
		Instruction value (kV)	actual value (kV)					
before optimization	2.5~3	113.15	113.43	0.6	0.6	0.6	1.8	low
	3~3.5	113.15	112.85	-0.6	-0.6	-0.6	-1.8	frequency oscillation
	3.5~4	113.15	113.43	0.6	0.6	0.6	1.8	
after optimization	2.5~3	113.15	113.24	-0.6	0.6	0.6	0.6	no oscillation
	3~3.5	113.15	113.24	-0.6	0.6	0.6	0.6	
	3.5~4	113.15	113.24	-0.6	0.6	0.6	0.6	

6. Conclusion

In this paper, the mechanism and production conditions of the low frequency oscillation of wind farm caused by the SVG minimum output dead zone are studied. On this basis, an optimization model for the minimum reactive variation near the zero point of SVG is established, and an optimization suppression strategy is put forward, and the simulation verification is carried out at the end of the simulation. The main conclusions are as follows:

- (1) Due to the existence of the minimum output reactive dead zone of SVG in the wind farm, the output reactive power of the SVG may have great step change near zero point, resulting in the repeated regulation of the voltage because of exceeding the voltage dead zone of AVC. Besides, the oscillation period is two times that of the AVC regulation period.
- (2) The proposed AVC optimization strategy, which considers the SVG minimum output reactive dead zone, can reduce the step reactive power variation by coordinating the reactive power output of SVGs near the zero points, and can significantly suppress this low frequency oscillation of the wind farm.

7. Acknowledgments

This work was supported by the Science and Technology Project of State Grid Corporation of China.

8. References

- [1] Lei Wang; Chi-Seng Lam; Man-Chung Wong. A Hybrid-STATCOM with wide compensation range and low DC-Link voltage [J]. IEEE Transactions on Industrial Electronics, 2016, 63(6): 3333–3343.
- [2] Tzung-Lin Lee; Shang-Hung Hu; Yu-Hung Chan. D-STATCOM with positive-sequence admittance and negative-sequence conductance to mitigate voltage fluctuations in high-level penetration of distributed-generation systems [J]. IEEE Transactions on Industrial Electronics, 2013, 60(4): 1417-1428.
- [3] Yueqiu Wang; Jie Tang; Xionger Qiu. Analysis and control of D-STATCOM under unbalanced voltage condition [C]. 2011 International Conference on Mechatronic Science, Electric Engineering and Computer (MEC), 2011, 1623-1625.
- [4] Cui Zhengpai, Wang Haojing, Ma Suoming, et al. Operation situation analysis and improvement measure study for dynamic reactive compensation equipment applied in large-scale wind power systems [J]. Power system technology, 2015, 39(7):1873-1878.
- [5] Yidan Li, Bin Wu. A novel DC voltage detection technique in the CHB inverter-based STATCOM [J]. IEEE Trans on Power Delivery, 2008, 23(3):1613-1619.
- [6] Zhao Xin, Gao Shan, Zhang Ningyu. Influence of SVC location on subsynchronous oscillation and SVC control strategy research[J]. Proceedings of the CSEE, 2013, 33(25): 107-114.

- [7] Rita Manuela Monteiro Pereira; Carlos Manuel Machado Ferreira; Fernando Maciel Barbosa. Comparative study of STATCOM and SVC performance on dynamic voltage collapse of an electric power system with wind generation [J]. IEEE Latin America Transactions, 2014, 12(2):138-145.
- [8] Yang Shuo, Wang Weisheng, Liu Chun, et al. Coordinative strategy for reactive power and voltage control of wind farms cluster considering wind power fluctuation [J]. Proceedings of the CSEE, 2014, 34(28): 4761-4769.
- [9] Wang Chengfu, Liang Jun, Sun Hongbin, et al. Hybrid reactive power compensation system and its control strategy for windfarm [J]. Machines and Control, 2013, 17(5): 38-44.
- [10] Wang Xuran, Guo Qinglai, Sun Hongbin, et al. Secondary voltage control considering rapid dynamic reactive power compensation [J]. Automation of Electric Power Systems, 2015, 39(2): 53-60.
- [11] Chen Huifen, Zhang Yiwei, Min Yong, et al. Graded voltage control strategy for clustering wind farms based on doubly fed induction generators [J]. Automation of Electric Power Systems, 2013, 37(4): 7-13.

RPT Runner Flow Structures Dependence on Guide Vane Opening Angle: A CFD Numerical Simulation

Maxime Binama¹, Wei-Hua Cai^{1,*}, Wen-Tao Su^{1, 2*}, Feng-Chen Li^{3,*}, Xian-Zhu Wei², Alexis Muhirwa¹

¹ Harbin Institute of Technology, 92 West Dazhi Street, Harbin, 150001, China.

²State Key Laboratory of Hydropower Equipment, Harbin 150040, China

³Sun Yat-Sen University, Zhuhai, 519082, China

E-mail: binamamaxime@hit.edu.cn

Abstract. Pumped storage power plants are now honored for different novelties mostly to do with large energy storage ability and electrical grid stabilization capacity. However the control of Reversible pump Turbines (RPT) operations within these plants is still an issue, where the so-called S-shape flow instabilities cause different problems especially when under low discharge operating conditions. Taking from the grounds that these instabilities have been found to mostly be based within the vaneless space between the guide vanes and the runner, this paper intends to investigate the effect of guide vanes opening (GVO) on runner flow characteristics. CFD-backed numerical simulations were carried out on a RPT complete flow passage under different GVOs; namely 17mm, 21mm and 25mm openings. Instabilities were found to take source from low flow conditions where resulting hydraulic losses maybe the trigger of s-shape characteristics appearance. The GVO however, showed the ability to tame the severity of these flow instabilities and associated pressure pulsations.

1. Introduction.

The energy sector has seen big changes in the last decades, where energy actors are now more than ever before, concerned with renewable sources. In line with this, owing to their different advantages; big and long term energy storage capacity, electrical grid stabilization, and operational flexibility among others; Pumped storage power plants have recently seen a very rapid development. In accordance with the electrical grid load-demand situation at hand, Reversible Pump Turbines (RPT) within these plants are subject to quick and frequent switches between the pumping and generating modes with prolonged periods under off design operating conditions, which in turn results into different flow instability occurrences. Trying to tackle the pump turbine generating mode-related instabilities; through many and varied attempts, different investigators have tried to get an understanding as to the cause as well as the onset and development mechanisms of these flow instabilities within RPT flow zones. Zhang et al. [1] noticed the flow unsteadiness increase as the flow decreased where flow vortex structures appeared and blocked some runner channels leading to flow reversal in the guide and stay vanes. Xia et Al. [2] blamed the flow losses within the runner channels to be the triggers of the s-shape characteristics occurrence. As for Histamuchi et Al. [3], the investigated flow blockage at runner flow channels take source from rotating flow separations at the same zones, which gives birth to rotating stall within the vaneless space and associated flow reversal within the inter-guide vane flow areas. Note that the so called “rotating stall” was defined by Frigne [4] as the flow unsteadiness that results into the occurrence of sub synchronous rotating velocity pulsations. In their studies, Widmer et al. [5] and Seidel et al. [6] found this rotating stall to rotate at



Content from this work may be used under the terms of the [Creative Commons Attribution 3.0 licence](https://creativecommons.org/licenses/by/3.0/). Any further distribution of this work must maintain attribution to the author(s) and the title of the work, journal citation and DOI.

Published under licence by IOP Publishing Ltd

speeds in the range of 50 to 70% of the runner rotational frequency. On the other hand, different studies have emphasized on parameters that influence the s-shape characteristics occurrence, where geometric design modifications such as variations of distributor pitch diameter [7], blade meridional section [8], blade leading edge profile [9] and runner blade number [10]; have made a great deal of change in terms of hydraulic losses occurrence mechanisms and the associated flow instabilities. Though the here mentioned studies and so others, have made a great contribution towards fundamental understanding of the flow unsteadiness onset and eventual development within RPTs, RPT flow instabilities have not yet been fully understood thus still requiring much more research efforts. In line with this, the present study seeks to investigate the influence of guide vane opening (GVO) on flow structures within the RPT runner flow zones for a pump turbine operating under off-design conditions. CFD-backed Numerical simulations are carried out on a high-head pump turbine's complete flow passage, where the guide vanes were successively set to three different openings namely 17mm, 21mm, and 25mm; under which the changes in terms of flow unsteadiness onset and development mechanisms within the runner channels are analyzed.

2. Research object and method.

2.1. RPT geometrical model

The investigated pump turbine model is a single stage centrifugal type with the specific speed N_s : 36.8m^{-1} . It's composed of five components namely volute casing, stay vanes, guide vanes, runner, and draft tube. More details on the investigated pump turbine model are given through table 1, while figure 1 displays its external view.

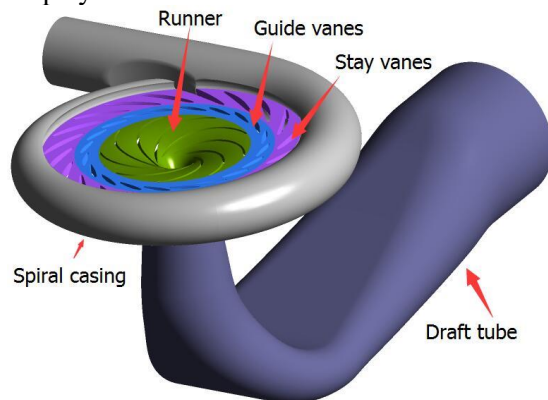


Figure1. RPT computational model.

Table1. RPT geometry details

Parameter	units	Symbol	Value
Runner Inlet Diameter	(mm)	D_2	560
Runner Outlet Diameter	(mm)	D_1	270
Runner Blade Number	(-)	Z_R	9
GV Distr. Diameter	(mm)	D_V	662
Guide Vane Height	(mm)	B_V	37.8
Guide Vane number	(-)	Z_V	20
Stay Vane Number	(-)	Z_S	20
Stay Vane Inlet Diameter.	(mm)	D_{SI}	966
Stay Vane Outlet Diameter.	(mm)	D_{SO}	763

2.2. Turbulence model

The RPT flow turbulence was modeled using Menter's SST turbulence model[11]. This model is known to combine the advantages of two other $k-\varepsilon$ and $k-\omega$ models to be able to adequately model wall-bounded as well as free stream flows. Its mathematical expressions are as follows:

$$\frac{\partial(\rho k)}{\partial t} + \frac{\partial(\rho u_j k)}{\partial x_j} = P - \beta^* \rho \omega k + \frac{\partial}{\partial x_j} \left[(\mu + \sigma_k \mu_t) \frac{\partial k}{\partial x_j} \right] \quad (1)$$

$$\frac{\partial(\rho \omega)}{\partial t} + \frac{\partial(\rho u_j \omega)}{\partial x_j} = \frac{\gamma}{v_t} P - \beta \rho \omega^2 + \frac{\partial}{\partial x_j} \left[(\mu + \sigma_\omega \mu_t) \frac{\partial \omega}{\partial x_j} \right] + 2(1 - F_1) \frac{\rho \sigma_{\omega 2}}{\omega} \frac{\partial k}{\partial x_j} \frac{\partial \omega}{\partial x_j} \quad (2)$$

2.3. Numerical scheme

Using CFD commercial code Ansys CFX 18.0, the 3D flow through the complete flow passage of the RPT model under different operating conditions was modeled. Ansys ICEM was used to generate structured hexahedral grid for most of the model components, at the exception of the volute tongue, where unstructured tetrahedral grid was adopted, due to its sharp shape. After a grid independence test, and in line with the available computational resources, a grid of 7.5 million grid nodes was chosen. Fine mesh was used at walls situated in critical flow zones like guide/stay vanes as well as the runner

blades. The Y^+ value globally varied between 20 and 300. Experimentally found inlet flow discharge and outlet pressure values were used as boundary conditions at the same boundaries.

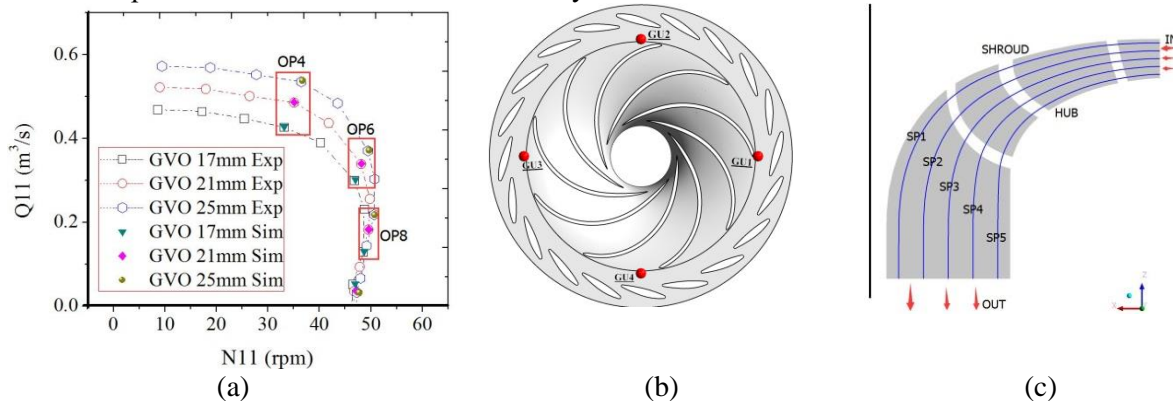


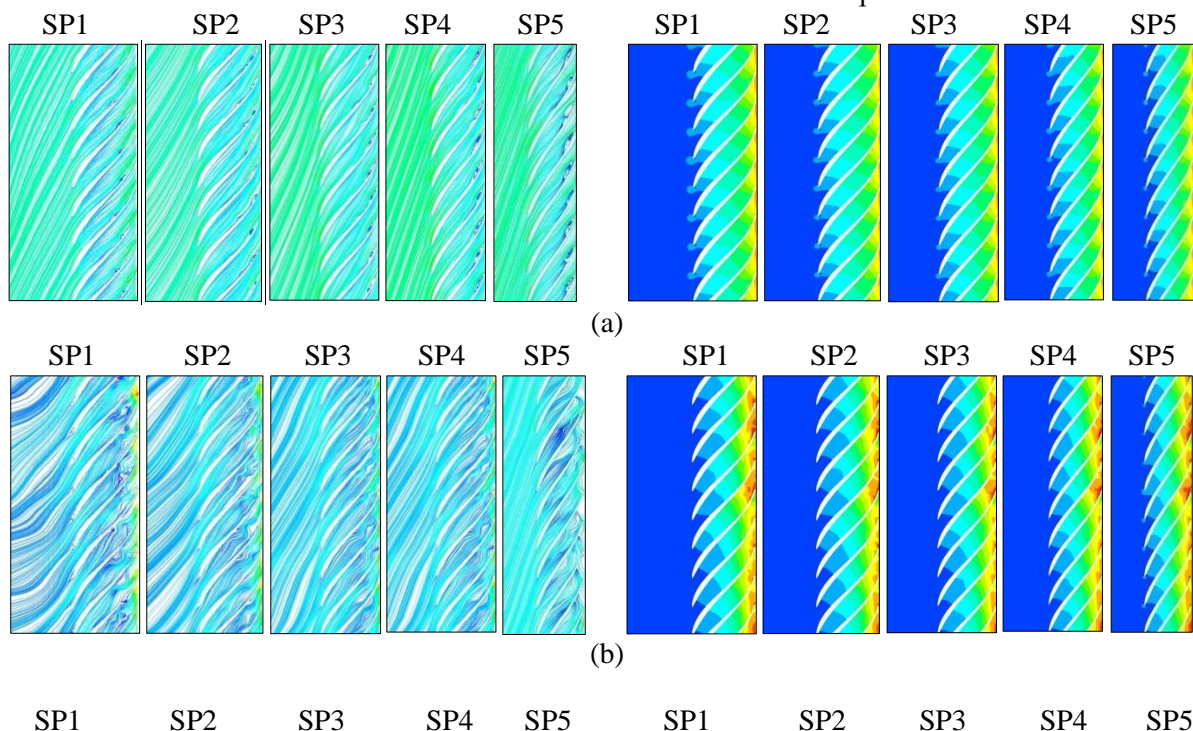
Figure 2. Numerical simulation details. (a) Investigated Operating conditions, (b) Pressure monitoring point locations, (c) investigated runner span positions.

The transient numerical simulations were run for 7 runner revolutions with 1° rotation as the length of 1 time step. Numerical results agreed well with experimental ones with a global error rate less than 3%. Three operating points (OP) expanding from normal turbine conditions to runaway vicinities were simulated for every GVO as shown in Figure 2 (a). Four Pressure monitoring points were also positioned at the runner inlet zone as shown in Figure 2 (b).

3. Results and discussion

3.1. Flow field characteristics

In order to have an understanding on the eventual flow behaviors, flow stream lines at 5 selected runner span positions (See figure 2(c)) are displayed through Figure3. The analysis is first carried out for three operating points as seen in Figure 2(a) under the GVO of 25mm. At OP4 the flow speed is high with quite ordered streams but also some vortices can be noticed at each blade’s suction side. The flow unsteadiness rises with the flow decrease where the runaway vicinities (OP8) are the most disturbed among the three investigated conditions. As the machine entered the unstable operating zone, the noticed inter-blade vortex flow shifted from the blade suction side to pressure side.



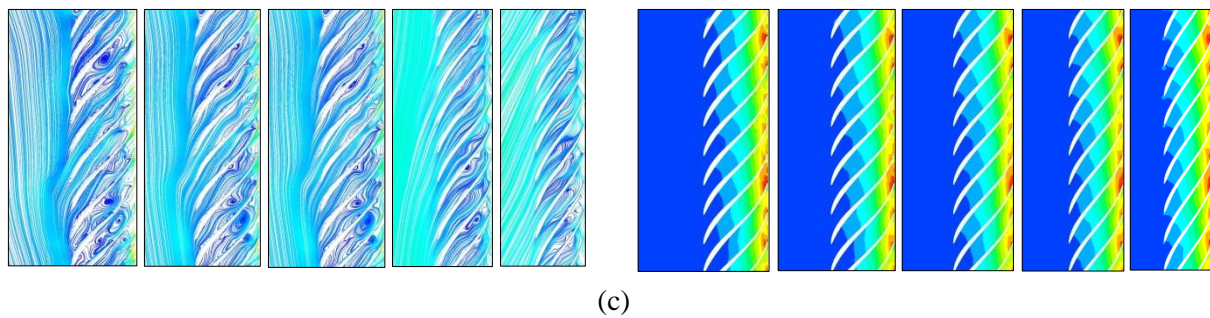


Figure 3. Flow streamlines and pressure contours for the 3 operating conditions under GVO25mm. (a) GVO25mm-OP4: normal turbine conditions, (b) GVO25mm-OP6: normal turbine conditions, and (c) GVO25mm-OP8: runaway vicinities.

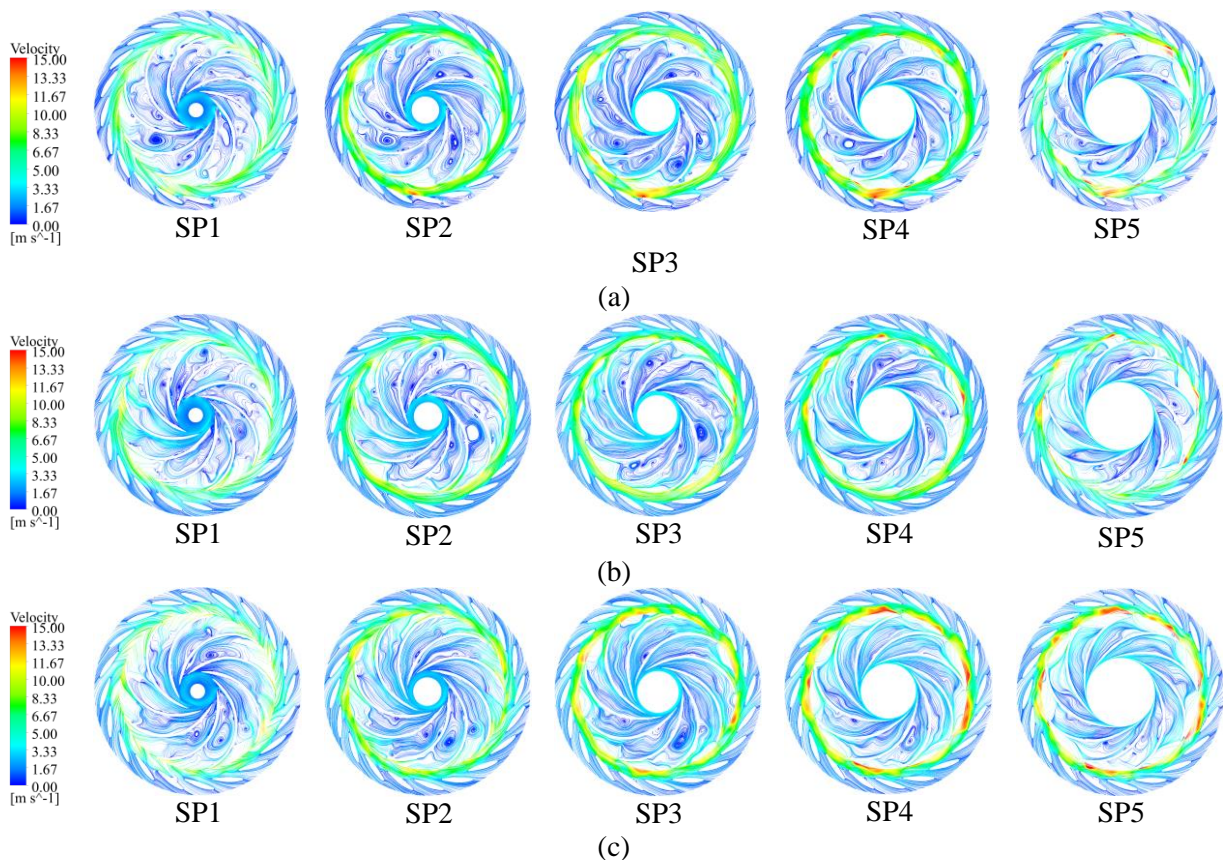


Figure 4. Velocity streamlines at five runner spans (SP) for three GVOs. (a) GVO17mm-OP8, (b) GVO21mm-OP8, and (c) GVO25mm-OP8

Moreover, the flow turbulence locus moves from the hub to the shroud vicinities. The low pressure zones at the blade trailing edge were also found to widen up with the flow decrease. The here shown OP8 characteristics mark the beginning of the S-shape characteristics zone. In figure 4, the flow under OP8 conditions, is analyzed for different GVOs. It can be seen that for all GVOs the flow unsteadiness remains within the flow zones in the vicinities of the runner shroud (SP1, SP2 and SP3). However the flow complexity within inter-blade channels get weaker as the GVO increases, leading to conditions with GVO17mm and GVO25mm being the most and least disturbed flow states respectively. This takes source from the guide vanes resistance to vaneless space back flows when under small GVO, which in turn strengthens the vaneless space water ring and the inter-blade vortices.

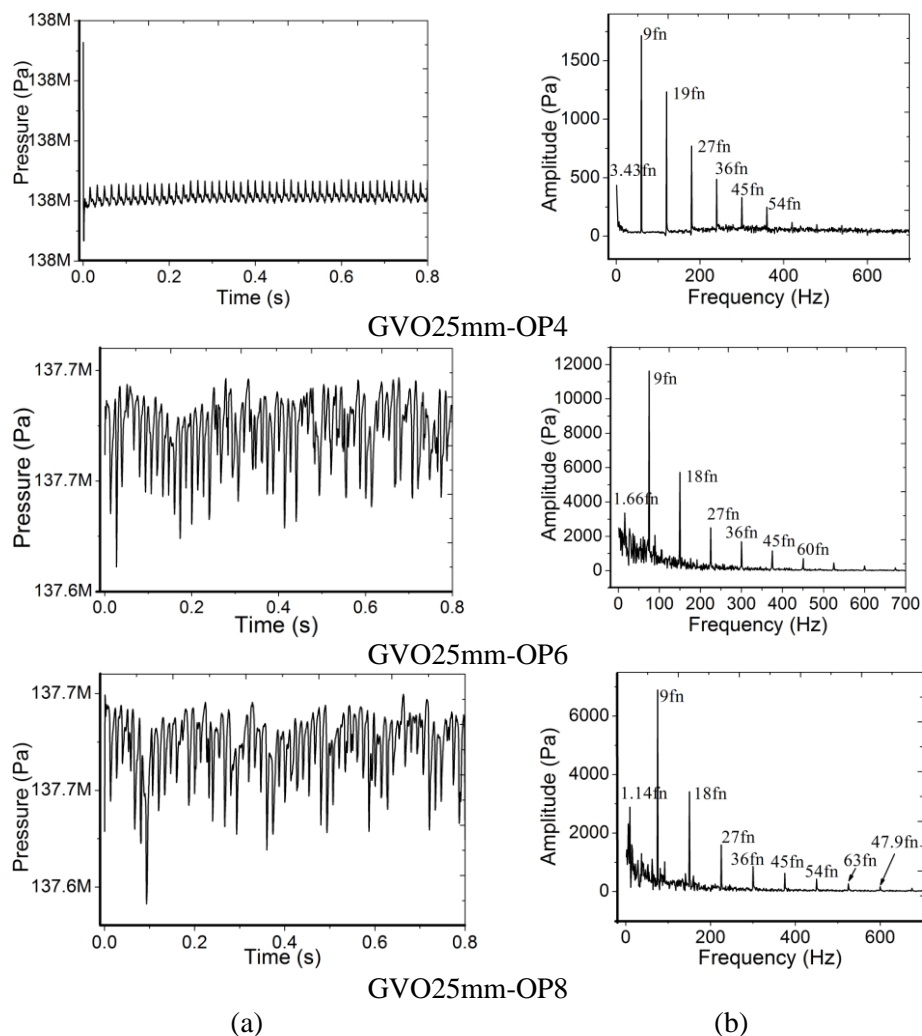


Figure 5. Pressure pulsations at GU1. (a) Time domain (b) Frequency domain

Therefore bigger GVOs weaken the vaneless space water ring as well as the inter-blade runner vortices, allowing for reverse flow occurrence in the upstream flow zones.

3.2. Pressure pulsation characteristics.

Four pressure monitoring points (GU1-GU4) were located at the vaneless space outlet (runner inlet) to investigate the combinational effect of runner channels back flow and guide vane opening on pressure pulsations at the runner inlet. Figure 5 shows the pressure pulsations under one guide vane opening (25mm), at one monitoring point (GU1), for three operating conditions (OP4, OP6, and OP8). The low discharge conditions (OP6 and OP8) are characterized by high amplitude pressure pulsations, which is the consequence of incurred severe flow separations under these conditions (See Figure 3). For all cases, the dominant frequencies are the blade passing frequency (BPF: $9fn$) and its harmonics (2 to 7 BPF), for which with a gradually decreasing flow, the amplitudes first rose from OP4 to OP6 and then decreased downwards to OP8. However, sub-synchronous frequencies can also be noticed at each OP. These may take source from different flow instabilities be it upstream (guide vanes) or downstream-based (draft tube). Figure 6 shows pressure spectrums at GU3 for the three investigated guide vane openings. The increase of the dominant frequency's amplitudes as the guide vane opening increases is obvious, which is in good agreement with Figure 4. The increase of GVO destroyed the vaneless space water ring, which caused the emergence of different flow separation zones and associated increased pressure pulsations.

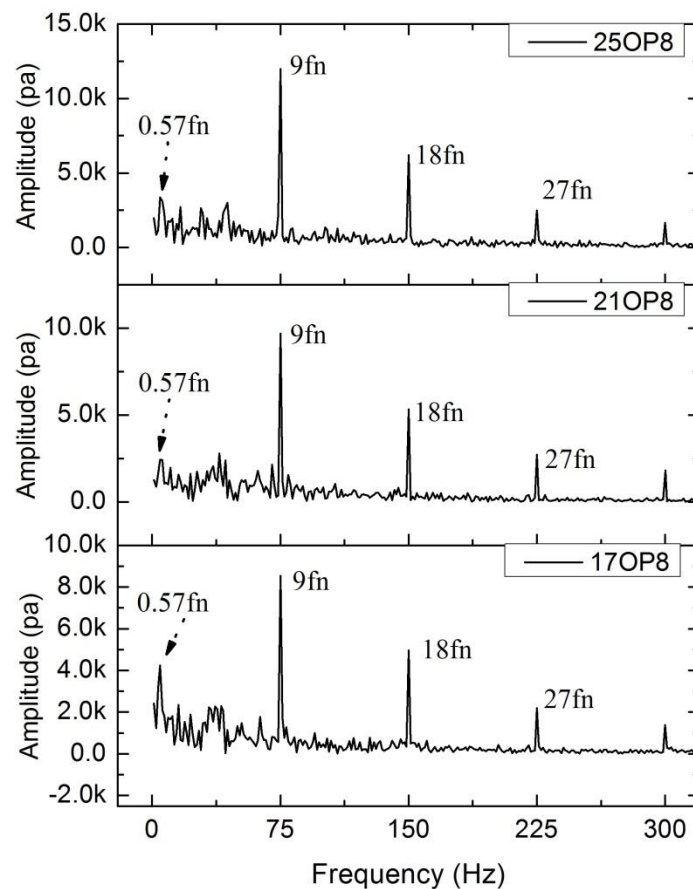


Figure 6. Frequency domain Pressure pulsations at GU3 for three GVOs: GVO17mm-OP8, GVO21mm-OP8 and GVO25mm-OP8.

There was no much change of the available pressure frequencies for the three openings, except the changing sub-synchronous frequencies ($0.57fn$) where their highest amplitudes were recorded under 17 mm guide vane opening. These maybe related to the draft tube vortex rope effect.

4. Conclusion

In this paper the 3D turbulent flow simulations are performed on an RPT model's complete flow passage to investigate the flow unsteadiness onset and development, where the effect of guide vane opening on runner flow characteristics is analyzed. A comparatively smooth flow was first noticed under normal turbine operating conditions, which deteriorated as the machine discharge decreased leading to tough flow separations accompanied with inter-blade channels obstruction by the developed vortex flow. The increase of the GVO destroyed the vaneless space water ring, which itself had been enhanced by the small GVO-caused resistance to vaneless space backflows. Therefore with the GVO increase, the inter-blade flow structures improved, whereas different flow separations emerged within the vaneless space. Pressure pulsations at runner inlet were also found very dependent on guide vane opening, where the dominant frequencies were the blade passing frequency and its harmonics. Low flow conditions were characterized by high amplitude pressure pulsations. These ones however, increased with the increasing guide vane opening. Therefore, the RPT flow unsteadiness mainly takes source from the frequently experienced low flow conditions, especially when shifting between operating modes. However, the guide vane opening when adequately controlled can considerably improve these operations thus contributing to the machine operational safety.

5. Acknowledgement

This work is supported by national Natural Science Foundation of China (51606050, 51506037), Chinese Postdoctoral Science Foundation (2016M591527), Heilongjiang Postdoctoral Fund (LBH-Z16057), and Natural Science Foundation of Heilongjiang Province (E2017038).

6. References

- [1] Zhang SQ, Shi QH, Zhang KW. Flow behaviour analysis of reversible pump-turbine in "S" characteristic operating zone. *IOP Conference Series: Earth and Environmental Science*. 2012; 15: 032045.
- [2] Xia L, Cheng Y, You J, Zhang X, Yang J, Qian Z. Mechanism of the S-Shaped Characteristics and the Runaway Instability of Pump-Turbines. *Journal of Fluids Engineering*. 2016; 139: 031101--14.
- [3] Hasmatuchi V, Farhat M, Maruzewski P, Avellan F. Experimental investigation of a pump-turbine at off-design operating conditions. In: Pavel R, editor. 3rd International Meeting of the Workgroup on Cavitation and Dynamic Problems in Hydraulic Machinery and Systems. Brno, Czech Republic: Brno University of Technology; 2009. p. 339-47.
- [4] Frigne P, Van Den Braembussche R. Distinction between different types of impeller and diffuser rotating stall in a centrifugal compressor with vaneless diffuser. *Journal of Engineering for Gas Turbines and Power*. 1984; 106: 468-74.
- [5] Widmer C, Staubli T, Ledergerber N. Unstable characteristics and rotating stall in turbine brake operation of pump-turbines. *Journal of Fluids Engineering*. 2011; 133: 041101.
- [6] Seidel U, Koutnik J, Martin G. S-curve characteristic of pump-turbines. *HYDRO 2012 Innovative Approaches to Global Challenges*. Bilbao, Spain 2012.
- [7] Sun Y, Zuo Z, Liu S, Wu Y, Liu J. Numerical simulation of the influence of distributor pitch diameter on performance and pressure fluctuations in a pump-turbine. *IOP conference series: earth and environmental science: IOP Publishing*; 2012. p. 072037.
- [8] Yin J-l, Wang D-z, Wei X-z, Wang L-q. Hydraulic improvement to eliminate S-shaped curve in pump turbine. *Journal of Fluids Engineering*. 2013; 135: 071105.
- [9] Olimstad G, Nielsen T, Børresen B. Dependency on runner geometry for reversible-pump turbine characteristics in turbine mode of operation. *Journal of Fluids Engineering*. 2012; 134: 121102.
- [10] Li D, Sun Y, Zuo Z, Liu S, Wang H, Li Z. Analysis of Pressure Fluctuations in a Prototype Pump-Turbine with Different Numbers of Runner Blades in Turbine Mode. *Energies*. 2018; 11: 1474.
- [11] Menter FR. Two-Equation Eddy-Viscosity Turbulence Models for Engineering Applications. *AIAA Journal*. 1994; 32:1598-605.

Research on Reduced Scene Sets Based on ARMA Model of Wind Farms Day-ahead Total Output Forecasting

Hui chao WANG¹, Lei LIU², Jin hui MA³, Jie DING¹ and Chang ZHOU¹

¹Renewable Energy Research Center, China Electric Power Research Institute, Nanjing, 210003, China

²Power Dispatch Department, State Grid Jiangxi Electric Power Company, Jiangxi, 330077, China

³Power Dispatch Department, State Grid Anhui Electric Power Company, Anhui, 230061, China

E-mail: 17600271330@163.com

Abstract: In this paper, the ARMA model is used to linearly fit the time series data of wind farms' prediction error with the software E-views. And then the error linear curve is sampled by four sampling methods, including random sampling, important sampling method, Latin hypercube sampling method and quasi-Monte Carlo method, to obtain some Ascending and disorderly samples respectively. Finally, the reduced scene sets are obtained by substituting the samples into the scene reduction model. Through analysing the reduced scenes output curve with the evaluation indicators of wind farms' forecast output curve, we find that the reduced scenarios are closer to the actual output curve than the traditional predicted. It also can be concluded that they have great effect on prediction correction and sampling methods have little effect on the output trend of reduced scenarios. Whereas, comparing the reduced scenes' output curve before and after sorting the sample data, the disorder and randomness of the sample data will lead to great volatility in the reduced scenes.

1. Introduction

With the continuous increase of installed capacity and output contribution of grid -connected wind farms, the uncertainty of wind farms' output prediction will pose a significant threat to safe and stable operation of power system. To deal with this problem, we often use the scene analysis technique that converts the uncertainty to some deterministic scenarios with unequal probability.

At present, the ARMA model is commonly used to analyze and model the forecasting data and combined with the sampling methods and the current prediction output to generate the basic scene sets. In order to reduce the calculation amount and time when optimizing the generation plan, we often use the scene reduction technology to reduce the number of basic scenes and get the reduced scene sets [1]. In this process, the commonly used sampling methods are the random sampling method [2]-[3], the important sampling method, the Latin hypercube sampling method, and the quasi-Monte Carlo method [4]-[6].

2. ARMA model

The ARMA model, also known as the Auto-Regressive and Moving Average model, is the most extensive time series model. It not only reveals the structure and regularity of dynamic data,

This work is supported by State Grid Anhui Electric Power Company Technology Project (Research on the evaluation method and construction plan of the short-term new energy consumption in Anhui).



Content from this work may be used under the terms of the [Creative Commons Attribution 3.0 licence](https://creativecommons.org/licenses/by/3.0/). Any further distribution of this work must maintain attribution to the author(s) and the title of the work, journal citation and DOI.

Published under licence by IOP Publishing Ltd

quantitatively understands the linear correlation of observed data and predicts its future value, but also can study the relevant characteristics of the system from various aspects. In this paper, the best ARMA model will be used to linearly fit the historical forecasting error data of wind farms with the E-views software. The model expression is:

$$\Delta p_g^t = \sum_{i=1}^p \alpha_i \times \Delta p_g^{t-i} - \sum_{j=1}^q \beta_j \times \varepsilon_{t-j} + \varepsilon_t \quad (\Delta p_g^t = 0, \varepsilon_t = 0, t \leq 0) \quad (1)$$

Where, p, q are the order of ARMA model, α_i, β_j are the model parameters, ε is a Gaussian distribution with mean 0 and variance σ^2 , Δp_g^t is the wind farm forecast error rate at time t .

3. Reduced scene set

3.1. Basic scene set

The reduced scene sets are derived from the base scene sets with the scene reduction technology. And the basic scenes are generated by ARMA model with various sampling methods. Sampling methods to sample ε , the sample is T data, namely $\varepsilon_1(s), \dots, \varepsilon_T(s)$, and then substituted into equation (1) to obtain the prediction error rate $\Delta p_g^t(s)$ at each time point. Substituting them into equation (2) to get the output forecast scene of wind farm.

$$p_g^t(s) = p_g^t - C \times \Delta p_g^t \quad (2)$$

Where, p_g^t is forecasting power of wind farm at time t , C is the installed capacity of the wind farm. The above steps are repeated to generate N forecasting output scenes with probability of $1/N$ to form a basic scene set.

3.2. Reduce scenes

In order to reduce the amount and time of calculation when using the scene analysis technique to optimize the generation schedule, the scene reduction technique will be used to reduce the number of basic scenes. The basic idea of the scene reduction method is to minimize the possible distance between the basic scene set and the subset of scenes that are ultimately reserved. That is, under the condition given by the number of deleted scenes J , the pursuit of formula (3) is the smallest.

$$\sum_{i \in J} p_j \times \min_{j \notin J} \| (p_g^{i(t)} - p_g^{j(t)}) \|_2 \quad (3)$$

Where, J is the set of elimination scenes in the scene reduction process. This paper uses the backward reduction method to reduce the basic scene set.

3.3. Sampling method

At present, the classical sampling methods are random sampling, important sampling, Latin hypercube sampling and quasi-Monte Carlo [7].

Random sampling aims to ensure that each value of the variable may have a known, non-zero probability to be sampled to ensure sample representativeness. Whereas, the important sampling method will modify the given probability distribution function before sampling to make the sample more subjective. The paper uses the kernel function method to modify the original probability distribution function.

The Latin hypercube method and the quasi-Monte Carlo method both improve the sample generation process and effectively reflect the overall distribution of variables, ensuring that all sample areas can be covered by sampling points. Differently, the Latin hypercube sampling method is an equal probability interval sampling while the quasi-Monte Carlo method is a low differential sequence sampling.

4. Wind farm forecast evaluation indicators

Wind farm forecasting and evaluation indicators can accurately measure wind farm forecasting errors, which mainly including maximum error rate, accuracy rate, qualification rate, correlation coefficient and comprehensive evaluation index [8].

The maximum error rate is used to describe the maximum error data in all time points. The expression is:

$$EV = \max\left(\frac{|P_{fi} - P_{ri}|}{C_i}\right) \times 100\% \quad (4)$$

Where, P_{fi} is the predicted power at time i , P_{ri} is the measured power at time i , and C_i is the startup capacity of wind farm at time i .

The accuracy rate is the overall error range describing the predicted curve and the actual output curve. The expression is:

$$CR = \left(1 - \sqrt{\frac{1}{n} \sum_{i=1}^n \left(\frac{P_{fi} - P_{ri}}{C_i}\right)^2}\right) \times 100\% \quad (5)$$

Where, n is the number of time points in the predicted and actual output curve.

The qualified rate is the ratio of the number of qualified points in the prediction curve. The expression is:

$$QR = \frac{1}{n} \sum_{i=1}^n B_i \times 100\% \quad (6)$$

Where, B_i is 1 when the prediction error is qualified at time i , and 0 otherwise.

The correlation coefficient is the degree of correlation between the forecasting output curve and the actual output curve of the wind farm. The expression is:

$$R = \frac{\sum_{i=1}^n (P_{fi} - \bar{P}_f)(P_{ri} - \bar{P}_r)}{\sqrt{\sum_{i=1}^n (P_{fi} - \bar{P}_f)^2} \sqrt{\sum_{i=1}^n (P_{ri} - \bar{P}_r)^2}} \times 100\% \quad (7)$$

Where, \bar{P}_f is the average of the predicted output curve, \bar{P}_r is the average of the actual output curve.

The comprehensive evaluation index is used to evaluate the overall accuracy of the forecasting curve and the combination of the above four indicators. The expression is:

$$CEI = k_1 \times (1 - EV) + k_2 \times CR + k_3 \times QR + k_4 \times R \quad (8)$$

$$k_1 + k_2 + k_3 + k_4 = 1 \quad (9)$$

Where, k_1, k_2, k_3, k_4 are weight coefficients corresponding to different error indicators and 0.25 in the paper.

5. Analysis of examples

The data of calculation example includes the predicted total output curve and actual total output curve of some wind farms on a certain day in the province (the total installed capacity of some wind farms is 1917.2MW) and the prediction error data of the day. The specific data is shown in Figure 1, the blue curve is the prediction error curve, the black curve is the predicted total output curve and the red curve is the actual total output curve. At the same time, the evaluation index data of the prediction scene is displayed in Table 1.

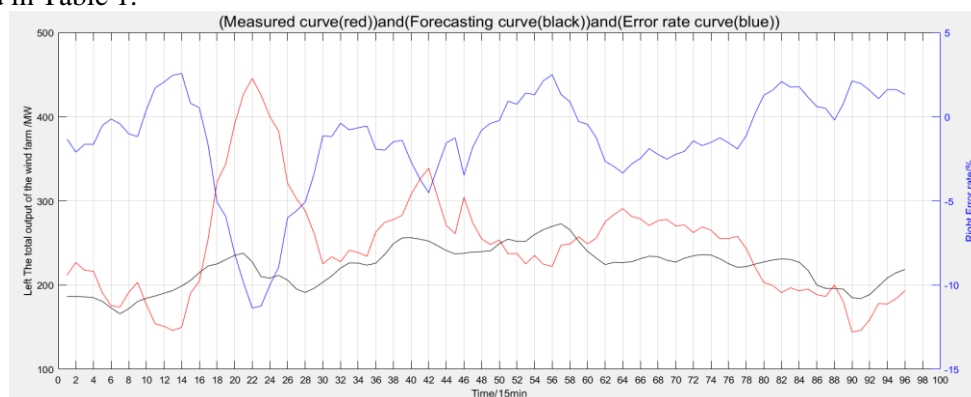


Figure 1. Forecast data of some wind farms in the province in one day

Table 1. The evaluation data of wind farm’s day-ahead forecast output curve

Evaluation index	Maximum error rate	accuracy rate	Qualified rate	Correlation coefficient	comprehensive evaluation index
Prediction scenario	0.1136	0.9673	1.0000	0.4242	0.819

The software E-views is used to calculate the ARMA model. The model parameters are used to solve the residual series, and then the approximate maximum likelihood estimation method is used to solve the white noise variance. The ARMA model of the prediction error data is ARMA (2,6), the formula is:

$$\Delta p_g' = 1.6 \times \Delta p_g^{t-1} - 0.8 \times \Delta p_g^{t-2} + 0.4 \times \varepsilon_{t-1} - 0.03 \times \varepsilon_{t-2} - 0.2 \times \varepsilon_{t-3} - 0.3 \times \varepsilon_{t-4} - 0.2 \times \varepsilon_{t-5} - 0.2 \times \varepsilon_{t-6} + \varepsilon_t \quad (10)$$

Combining with four sampling methods and backward reduction method, two reduced scene sets are generated to depict the uncertainty of the prediction. And one set is obtained before sorted sample data, the other is obtained after sorted sample data in ascending order.

5.1. Random sampling

(1) The sample data is not sorted

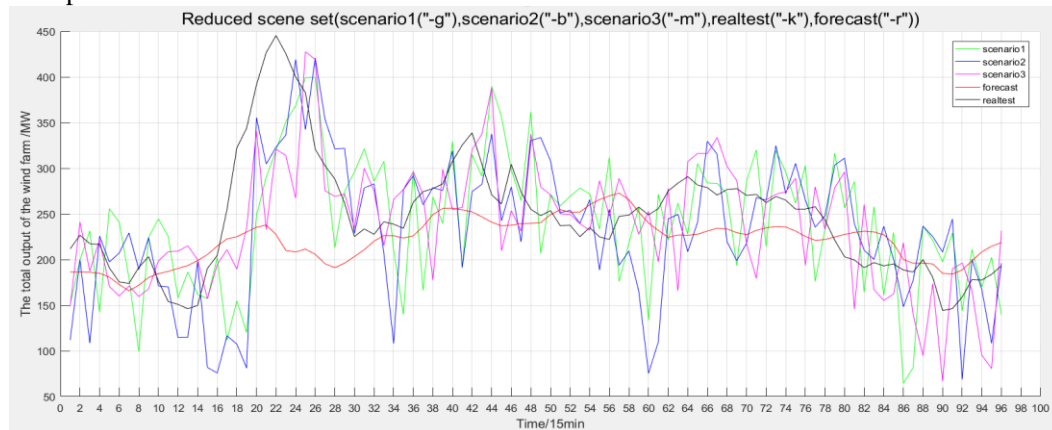


Figure 2. Reduced scenes of wind farms with random sampling

Table 2. Evaluation parameters of reduced scenes with random sampling

Reduce scenes	scenario 1	scenario 2	scenario 3	Expected value
Probability	0.225	0.297	0.478	1
Maximum error rate	0.131	0.113	0.090	0.106
accuracy rate	0.963	0.894	0.898	0.911
Qualified rate	1.000	1.000	1.000	1.000
Correlation coefficient	0.436	0.552	0.553	0.526
comprehensive evaluation index	0.817	0.804	0.811	0.833

(2) Ascending sorting of sample data

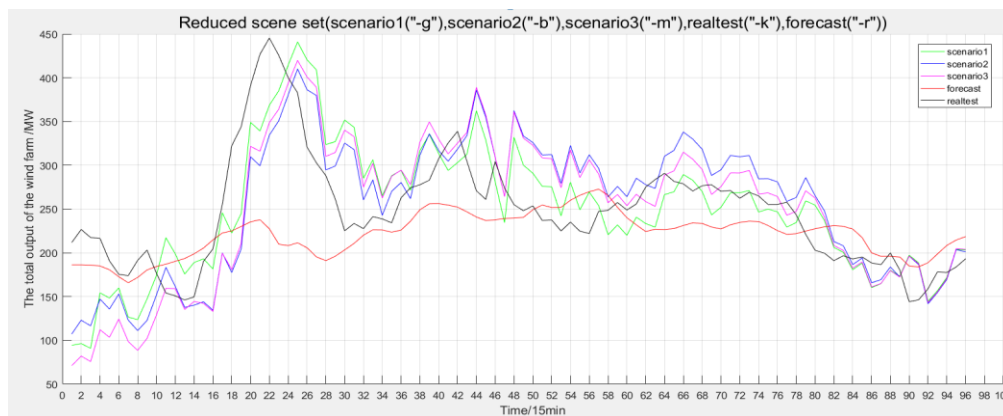


Figure 3. Reduced scenes of wind farms with random sampling

Table 3. Evaluation parameters of reduced scenes with random sampling

Reduce scenes	scenario 1	scenario 2	scenario 3	Expected value
Probability	0.650	0.008	0.342	1
Maximum error rate	0.089	0.090	0.066	0.081
accuracy rate	0.968	0.895	0.900	0.944
Qualified rate	1.000	1.000	1.000	1.000
Correlation coefficient	0.638	0.633	0.738	0.672
comprehensive evaluation index	0.879	0.861	0.868	0.884

Random sample data varies greatly. When the sample data is not sorted, the general trend of the forecasting reduced scenes is same with the actual output curve, but they all have strong volatility which make the overall evaluation slightly better than the predicted scene. After sorting the sample data in ascending order, the overall trend of the reduced scenarios is not changed, but the prediction curve is less volatile and the overall evaluation has be greatly improved.

5.2. *Important sampling method*

(1) The sample data is not sorted

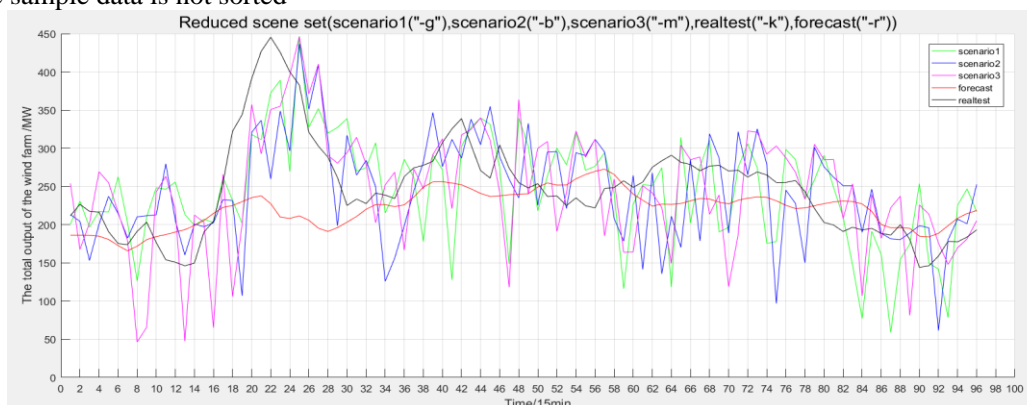


Figure 4. Reduced scenes of wind farms with the important sampling method

Table 4. Evaluation parameters of reduced scenes with the important sampling method

Reduce scenes	scenario 1	scenario 2	scenario 3	Expected value
Probability	0.122	0.273	0.605	1

Maximum error rate	0.128	0.133	0.087	0.105
accuracy rate	0.967	0.894	0.900	0.906
Qualified rate	1.000	1.000	1.000	1.000
Correlation coefficient	0.549	0.534	0.641	0.600
comprehensive evaluation index	0.847	0.828	0.840	0.850

(2) Ascending sorting of sample data

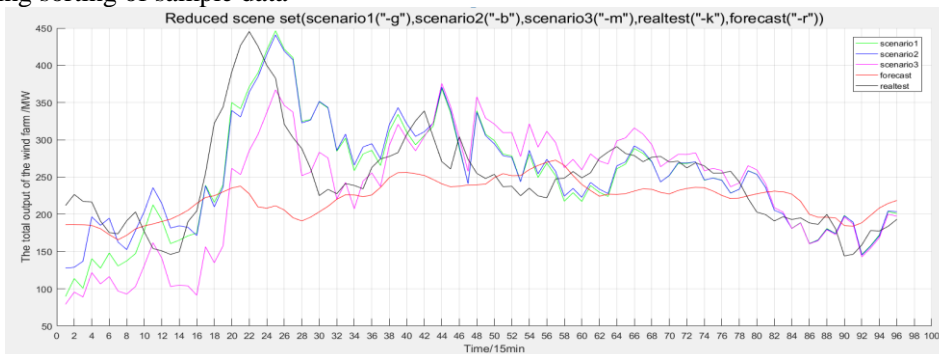


Figure 5. Reduced scenes of wind farms with the important sampling method

Table 5. Evaluation parameters of reduced scenes with the important sampling method

Reduce scenes	scenario 1	scenario 2	scenario 3	Expected value
Probability	0.562	0.370	0.068	1
Maximum error rate	0.066	0.097	0.063	0.077
accuracy rate	0.972	0.894	0.900	0.939
Qualified rate	1.000	1.000	1.000	1.000
Correlation coefficient	0.739	0.595	0.736	0.685
comprehensive evaluation index	0.911	0.884	0.894	0.887

The important sampling method modify the white noise probability distribution function using the kernel function method with a width of 1, so that the samples has some similarity with each other. Therefore, when the sample data is not sorted, the reduced scenarios have more similar volatility. Comparing the predicted output curve, the overall trend of the reduced scenes is closer to the actual output curve, but the curve fluctuates strongly. After sorting the sample data in ascending order, the fluctuation of the reduced scenarios is reduced, and the overall forecasting evaluation is more better.

5.3. Latin hypercube sampling

(1) The sample data is not sorted

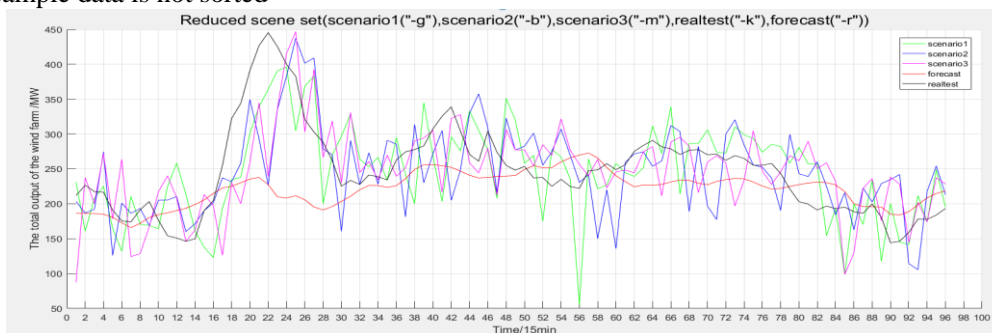
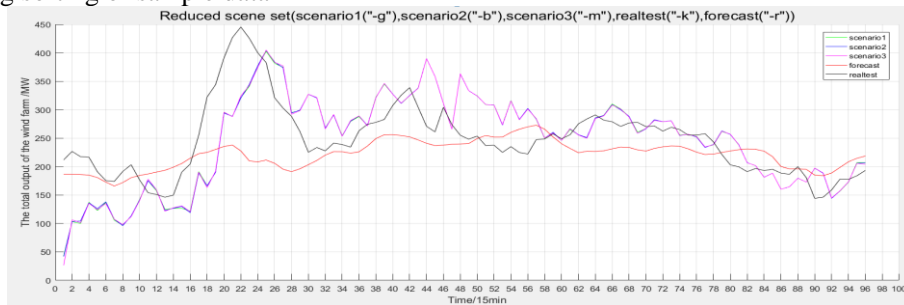


Figure 6. Reduced scenes of wind farms with Latin hypercube sampling

Table 6. Evaluation parameters of reduced scenes with Latin hypercube sampling

Reduce scenes	scenario 1	scenario 2	scenario 3	Expected value
Probability	0.387	0.377	0.236	1
Maximum error rate	0.086	0.081	0.108	0.090
accuracy rate	0.970	0.895	0.899	0.925
Qualified rate	1.000	1.000	1.000	1.000
Correlation coefficient	0.590103	0.569	0.592	0.583
comprehensive evaluation index	0.868	0.851	0.845	0.854

(2) Ascending sorting of sample data

**Figure 7.** Reduced scenes of wind farms with Latin hypercube sampling**Table 7.** Evaluation parameters of reduced scenes with Latin hypercube sampling

Reduce scenes	scenario 1	scenario 2	scenario 3	Expected value
Probability	0.007	0.991	0.002	1
Maximum error rate	0.084	0.0837	0.092	0.084
accuracy rate	0.969	0.895	0.898	0.895
Qualified rate	1.000	1.000	1.000	1.000
Correlation coefficient	0.666	0.667	0.663	0.667
comprehensive evaluation index	0.888	0.869	0.868	0.870

Latin hypercube sampling divides the white noise probability distribution function into equal probability intervals, and then sampling in each probability interval randomly. Sample values can effectively reflect the overall distribution of variables. When the sample is not sorted, the overall forecasting evaluation of the reduced scenarios is better than the predicted output scenario, but they have very strong volatility. After the samples are sorted in ascending order, there is strong similarity between the samples for the sampling space is same and small at the same time point, and the fluctuation of reduced scenes is reduced.

5.4. Monte Carlo sampling method

(1) The sample data is not sorted

Quasi-Monte Carlo sampling is a low differential sequence sampling, and the sample can effectively reflect the overall distribution of variables. When the sample is not sorted, the overall trend of reduced scenario is closer to the actual output than the predicted scenario, but they also have strong volatility. After sorting the sample data in ascending order, the output fluctuation of reduced scenes is greatly reduced, and the overall evaluation is more better.

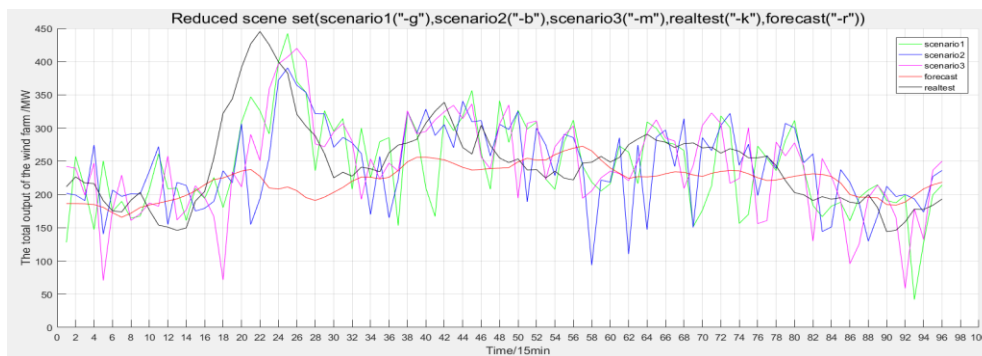


Figure 8. Reduced scenes of wind farms with Monte Carlo sampling method

Table 8. Evaluation parameters of reduced scenes with Monte Carlo sampling method

Reduce scenes	scenario 1	scenario 2	scenario 3	Expected value
Probability	0.300	0.430	0.270	1
Maximum error rate	0.095	0.095	0.075	0.090
accuracy rate	0.970	0.895	0.898	0.918
Qualified rate	1.000	1.000	1.000	1.000
Correlation coefficient	0.606	0.600	0.578	0.596
comprehensive evaluation index	0.870	0.852	0.857	0.856

(2) Ascending sorting of sample data

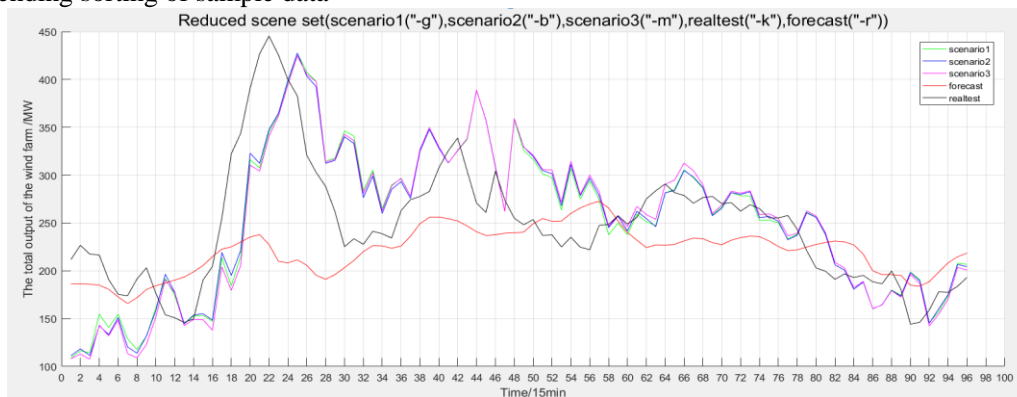


Figure 9. Reduced scenes of wind farms with Monte Carlo sampling method

Table 9. Evaluation parameters of reduced scenes with Monte Carlo sampling method

Reduce scenes	scenario 1	scenario 2	scenario 3	Expected value
Probability	0.497	0.060	0.443	1
Maximum error rate	0.097	0.091	0.092	0.095
accuracy rate	0.966	0.895	0.898	0.932
Qualified rate	1.000	1.000	1.000	1.000
Correlation coefficient	0.624	0.623	0.631	0.627
comprehensive evaluation index	0.873	0.857	0.858	0.866

6. Conclusion

Based on the ARMA model, this paper linearly fits the wind farms' day-ahead prediction error data and generates the reduced scene sets with four sampling methods. The following conclusions can be drawn from analysis, evaluation and comparison of these reduced scenes.

- 1) The reduced scenes are closer than the predicted output curve. It can be seen that wind farms predictive reduction scenes do have a great prediction correction.
- 2) The four sampling methods have little effect on the trend of the reduced scenes output curve, but the disorder and randomness of sample data will make the reduced scenes more volatile.
- 3) In order to get better prediction scenarios, it is necessary to sort sample data reasonably to reduce the fluctuation of reduced scenes.

7. References

- [1] LEI Yu, YANG Ming, HAN XUE Shan. A two-stage stochastic optimization of unit commitment considering wind power based on scenario analysis [J]. *Power System Protection and Control*, 2012, 40(23): 58-67.
- [2] DENG Wei, LI Xin-ran, XU Zhen Hua, et al. Calculation and impact analysis of probability of wind speed correlation [J]. *Power System Technology*, 2012, 36(04): 45-50.
- [3] DING Ming, WU Xing-long, LU Wei, et al. Three-phase random flow calculation of distribution network with multiple asymmetric photovoltaic grid-connected systems [J]. *Automation of Electric Power Systems*, 2012, 36(16):47-52.
- [4] B. Zou and Q. Xiao, "Solving Probabilistic Optimal Power Flow Problem Using Quasi Monte Carlo Method and Ninth-Order Polynomial Normal Transformation," in *IEEE Transactions on Power Systems*, vol. 29, no. 1, pp. 300-306, Jan. 2014.
- [5] HAJIAN M, ROSEHART W D, ZAREIPOUR H. Probabilistic power flow by Monte Carlo simulation with Latin super cube sampling [J]. *IEEE Trans on Power Systems*, 2013, 28(2):1550 - 59。
- [6] HUANG H Z, CHUNG C Y, CHAN K W, et al. Quasi -Monte Carlo based probabilistic small signal stability analysis for power system with plug-in electric vehicle and wind power integration [J]. *IEEE Trans on Power Systems*, 2013, 28(3): 3335 – 43.
- [7] LIU Yu, GAO Shan, YANG Sheng Chun, et al. Overview of probabilistic trend algorithms for power systems [J]. *Automation of Electric Power Systems*, 2014, 38(23):127-35.
- [8] THE National Energy Administration. NB/T 31046-2013 Function specification of wind power forecast system [S]. Beijing: Electric Power Press of China, 2014

Design and Energy Efficiency Management of Cascade Hydropower System

Guanlu Yang, Zehong Huang, Shuyang Wang and Minxu Wu

College of Information and Science Engineering, Huaqiao University, Xiamen, China
E-mail: 535830236@qq.com

Abstract. Under the background of energy shortage and environmental pollution, the development and utilization of building hydropower power generation and utilization of resources positively respond to the construction of national sponge city. In this paper, the concept of building cascade hydropower is put forward from the view of making full use of building water energy, and the upper computer of building cascade hydropower power management system is built by using LabVIEW software platform. The calculation and measurement error of hardware circuit is reduced, and the design of building cascade hydropower power management system is completed. The feasibility and advantage of building cascade hydroelectric power generation system are verified through field test.

1. Introduction

With the problem of one-off energy shortage becoming more and more prominent, it is a serious threat to the survival and development of human society. In recent years, a lot of hot topics have emerged in the research direction of smart grid and micro-grid. The demand for new energy generation technology is increasing, and the research on distributed energy and clean and renewable energy is becoming more and more in-depth [1]. Common clean and renewable sources of energy, including wind, solar and hydro, can be used to generate electricity. These small distributed sources generate less electricity and are installed on the proximity principle and in combination with buildings by adopting off-net working mode [2], [3].

With the continuous growth of population and the rapid development of society, the problems of water shortage, urban waterlogging and environmental deterioration are becoming more and more serious [4]. The development of urbanization and industrialization has increased the impermeable areas in urban areas, and caused a series of problems in urban areas. The deterioration of water quality, urban waterlogging, rain island effect and heat island effect make the infiltration and storage function of Rain Water decrease in urban areas [5]. The utilization of building water resources can not only produce good economic and social benefits, but also produce good ecological and environmental benefits. In this paper, the precipitation data of Xiamen from 2015 to 2016 and the water consumption of residents are analyzed, and the calculation of available building water resources is analyzed to evaluate the benefits of the utilization of building water energy resources.

It can be seen from the above Figure 1 that monthly precipitation in Xiamen is unevenly distributed, mainly in the spring rain season, rainy season and summer, accounting for 75% of the annual precipitation, which is due to the influence of typhoon weather in summer and Meiyu season in southern China. During this period, we can make full use of the peak load of hydraulic energy and accumulate water energy on the top of the building. When the peak wind and solar power supply is insufficient, as a backup power supply, it play the role of peak regulation. The collection and utilization of Rain Water and the filtration and classification of water in buildings can effectively



reduce the investment in urban flood control, drainage and sewage treatment, and can also reduce runoff pollution [6].

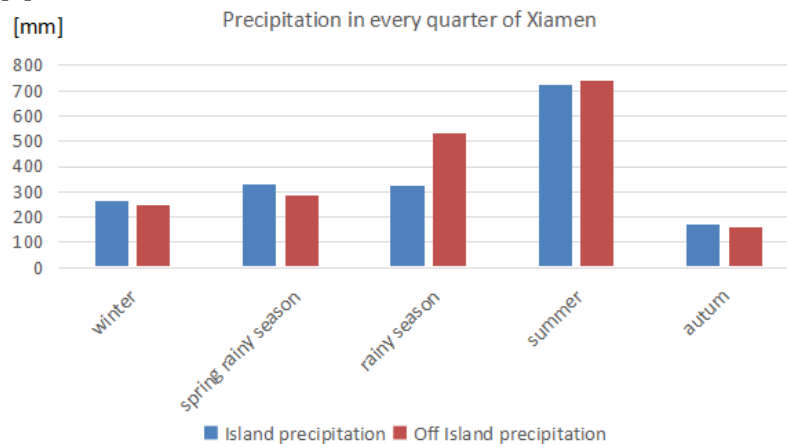


Figure 1. Precipitation in every quarter of Xiamen

2. Design of building cascade hydropower system

2.1. Design of building hydropower system

At the top of the building, the Rain Water is confluent in the upper reservoir, and the turbine is installed at the bottom of the building. The reservoir is connected with the turbine through pipes, and the blade of the turbine is driven to rotate by the potential energy of water, thus generating electric energy. Rain Water flows into the lower reservoir after passing through the turbine. It can be used as the living water for human being by electroflocculation treatment [7]. The purpose of building cascade hydropower system is to make full use of water energy and improve the utilization ratio of water energy under the premise of 220 V output voltage of hydrogenerator.

In the field test, the type of hydraulic generator is SLF series oblique strike permanent magnet synchronous generator. The parameters of the motor are shown in Table 1.

Table 1. Motor parameters

Type	SLF-4	Phase	Single phase
Power	500w	Volts	230v
Waterhead	6-15m	Q.Max	0.005-0.05m ³ /s
Rpm	1500r/min	INS.Cl	E level

In the case of satisfying the above two conditions, the working head of the turbine with 220 V output voltage is selected to install the turbine. There is no need to unload the turbine at this time, and the maximum utilization of electric energy can be achieved.

After continuous debugging, the output voltage of SLF-4 series turbine can reach 220 V when the working head is 10 meters. Taking the experimental building as an example, the height of the building is 27 meters, the water storage device is installed on the top of the experimental building, the No. 1 turbine is installed on the fourth floor platform, and the No. 2 turbine is installed on the second floor platform. The building water resources are collected in the water storage device after filtration device. In order to prevent the water from blocking the roof, the water storage device should be provided with overflow hole.

Inspired by cascade hydropower station, this paper designs a building cascade hydropower system. The turbine of each floor can be stabilized by 220 V output voltage after on-site debugging, and then connected to the same bus bar. The bus can be connected to AC load, or it can be reduced to 12 V by transformer, and the battery can be charged by AC/DC module.

2.2. Hydropower power management system based on LabVIEW

As a standard data acquisition and instrument control software, LabVIEW has been widely accepted by academics, industry, and research laboratories [8]. The user can set parameters on the front panel, use the block diagram to implement VI logic functions, and connect functions, constants, etc. [9]. The programming of LabVIEW is to create a new VI file and complete the module selection and related programming of the front panel, the module selection and design of the block diagram, and the connection between each module. Users can design their own desired interface format on the front panel according to their own needs, and add the necessary modules for each string element, numerical element, and Boolean element, and then find the corresponding module in the block diagram for connection and Compilation of related programs [10].

Use LabVIEW to first write the user login module interface and block diagram, and then write the serial port operation, including the serial port configuration, data receiving and sending, serial port close to achieve the communication between LabVIEW and the serial port. Recompile the various parameter measurement modules and calculation modules of the building cascade hydropower system, including the basic parameter measurement module, the power module, the voltage fluctuation and flicker module, the electricity monitoring module and the blackout recording module. The front panel of the voltage fluctuation and flicker module is shown in Figure 2.

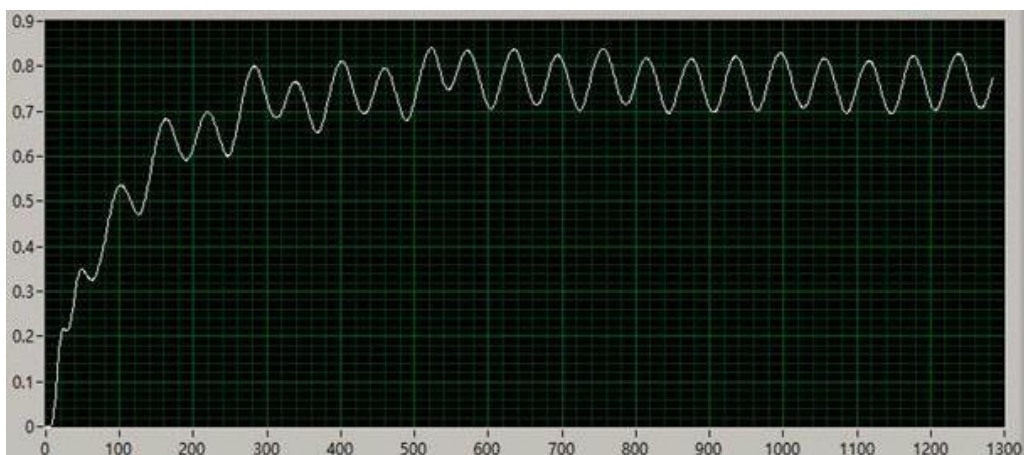


Figure 2. The front panel of the voltage fluctuation and flicker module

Finally, each sub-module is connected with the user login module to complete the design of the upper computer for the power management system of the cascade hydroelectric power generation system.

3. System hardware platform and field test

In order to further verify the advantages of building cascade hydropower system, this paper builds a hardware experimental platform to carry out related experiments. The hardware of building cascade hydroelectricity system includes hydraulic turbine and micro hydropower load regulator. The output of the hydroelectric generator does not need to pass through the distribution box, as long as it is loaded by the micro-hydroelectric load controller.

The field test is conducted in an experimental building. Firstly, a water storage device is installed on the top of the experimental building to store energy. The first turbine is installed on the fourth floor of the laboratory building. The second turbine is installed on the platform on the second floor of the experimental building, and the top water storage unit is connected directly to the first turbine through the water diversion pipeline. The outlet of the first turbine is connected to the second turbine through the diversion pipeline through the hemisphere-type water collection device to achieve two-stage power generation. The output current and output voltage of the two turbines were collected by the current transformer and the voltage transformer respectively and transmitted to the serial port via FPGA and AD7606. Finally, the data analysis and calculation of serial port are read by LabVIEW. The field experiment is shown in figure 3.



Figure 3. Field test diagram

The experiment is divided into two levels of power generation system, the first level of the working head is 10.1 meters, the second level of the working head is 10.4 meters. Because there is no need to unload the output of hydraulic generator in building graded power generation system, the system has improved the utilization of water energy and did not cause power loss due to unloading.

The wiring diagrams of the power supply system, protection system and acquisition system of the building cascade hydroelectric power generation system are shown in Figure 4.

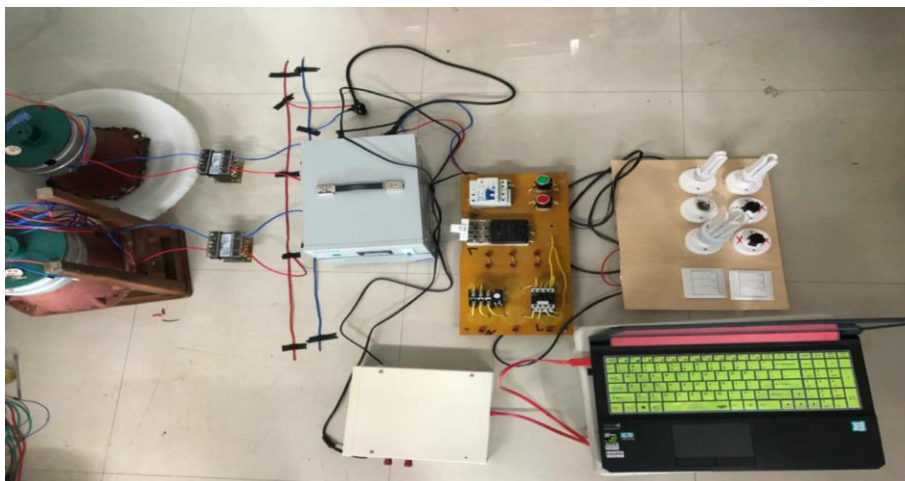


Figure 4. Wiring diagram of graded hydropower system

The experimental data is collected by the host computer LabVIEW. Reading the power module can obtain experimental power data. Table 2 shows the experimental data of a single-stage hydropower system. Table 3. shows the experimental data of a hierarchical hydropower system. The specific data are shown below.

In the field experiment, the data comparison of the hierarchical generation system to the single stage generation system is shown in Table 4.

Table 2. Data analysis of single-stage hydropower system

Number of measurements	Apparent power (VA)	Active power (W)
1	87.89	78.22
2	83.38	70.87
3	82.14	69.81
4	81.93	69.64
5	84.42	74.29
6	89.70	79.07

Table 3. Data analysis of graded hydropower system

Number of measurements	Apparent power (VA)	Active power (W)
1	54.67/57.74	47.02/49.66
2	51.69/53.21	44.61/45.80
3	55.96/58.61	48.19/50.89
4	54.11/56.79	46.21/48.56
5	51.92/54.03	44.45/46.06
6	52.06/56.84	44.75/48.69

Table 4. Comparative analysis of data

	Apparent power (VA)	Active power (W)
Single stage power generation	84.91	73.65
Graded generation stage I	53.40	45.87
Graded generation stage II	56.20	48.28

From Table 4, it can be seen that the active power of the single-stage hydropower system of the building is 73.65W, and the active power of the building's cascade hydropower system is 94.15W. At the same height of the water head, the multi-level hydraulic system emits 27.83% more power than the single-stage hydraulic system, which has obvious advantages, thus verifying the feasibility of the building's cascade hydropower system.

4. Conclusions

The LabVIEW software platform was used to compile the upper computer of the cascade hydroelectric power management system in the building. Functions such as the user's login authority, communication configuration of LabVIEW and serial port, measurement of basic parameters, monitoring of power, calculation and analysis of voltage fluctuation and flicker, power monitoring and blackout record were specifically implemented. Finally, through the combination of sub-VI and login interface, the user interface design is completed.

This paper introduces the hardware part of the building cascade hydropower system, and sets up the hardware experimental platform to carry on the field test. Finally, the experimental data were collected and analyzed to verify the advantages of building cascade hydropower system.

5. References

- [1] Kumars Rouzbehi, Arash Miranian, Jose Ignacio Candela, et al. A Generalized Voltage Droop Strategy for Control of Multiterminal DC Grids. *IEEE Transactions on Industry Applications*, 2015, 51(1): 607~618.
- [2] Zhou Fengquan, Huang Wei. Discussion on key Technologies of DC Distribution Network system. *Power system Protection and Control*, 2014 (22): 62-67.

- [3] Zhang X, Pei Wei, Deng W, et al. Energy management and coordinated control method for multi-source / multi-load DC microgrid. *Chinese Journal of Electrical Engineering*, 2014, 34 (31): 5553-5562.
- [4] SHADEED S, LANGE J. Rainwater harvesting to alleviate water scarcity in dry conditions: a case study in Faria Catchment, Palestine. *Water Science and Engineering*, 2010, 3(2): 132-143.
- [5] LYE D J. Rooftop runoff as a source of contamination: A review. *Science of the Total Environment*, 2009, 407(21): 5429-5434.
- [6] Zhang Kangnian. Study on Comprehensive Utilization Technology of Rain Water and Resource Utilization of Rain Water in Xi'an City. *Xi'an University of Architectural Science and Technology*, 2008.
- [7] Ling Xiao, Cai Bo. Automatic Control of Oil pressure device of Governor in medium and small Hydropower Plant. *Hydropower Automation and Dam Monitoring*, 2008, 34 (4): 31-33.
- [8] Elliott C, Vijayakumar V, Zink W, et al. National Instruments LabVIEW: A Programming Environment for Laboratory Automation and Measurement. *Journal of the Association for Laboratory Automation*, 2007, 12(1):17-24.
- [9] Meng Wusheng, Zhu Jianbo, Huang Hong, et al. Design of data acquisition system based on LabVIEW. *Electronic Measurement Technology*, 2008, 31 (11): 63-65.
- [10] Yao Juan, Zhang Zhijie, Li Lifang. Design and implementation of data acquisition system based on LabVIEW and TCP. *Application of Electronic Technology*, 2012 (7): 72-74.

Acknowledgements

This research was financially supported by the 12th Five-Year Plan for National Science and Technology Support (2015BA107b04) and Fujian Province Science and Technology Plan Project (2014H0031), People's Republic of China.

The Solar Power Plant Prediction A case Study in Phitsanulok, Thailand

W Srisuriyajan¹ and C Thongchaisuratkrul²

¹King Mongkut's University of Technology North Bangkok, Bangkok, Thailand

²King Mongkut's University of Technology North Bangkok, Bangkok, Thailand

E-mail: withawint@me.com

Abstract. This research aims to find ways to predict the generated solar energy of 800 kW solar power plants. The investigated factors affecting on the plant consisted of irradiance, humidity, wind speed, ambient temperature, module temperature and real power. The plant located in Phitsanulok province, Thailand. Simple Regression Analysis and Multiple Linear Regression were used to analyse correlation. From the results, it is clear that solar energy directly depended on irradiance. Moreover it was an inverse of the module temperature. It is investigated that humidity and wind speed had not effect on solar energy generation. Furthermore real power value had little effect. Finally, the four correlations between generated solar energy and variables were used to predict. Four correlations were classified by temperature.

1. Introduction

Presently, the energy is in the many forms; oil, coal, wind, thermal, light electricity and so on. The electricity is the most versatile form of energy because it can easily transforms to other energy. Therefore the electricity has been used more and more [1]. However, the electricity needs natural resources to be generated. Oil, natural gas and coal are commonly the sources. Although they are sufficient to produce electricity, the process emits CO₂. According statistics of CO₂ emissions [2], it tends higher up in the rate 2.3% per year. The gas affects greenhouse effect. It is the cause of global warming. However the electricity consumption still rising about 2.2% per year [3]. For Thailand, although, Energy Conservation Act has been declared [4], energy consumption still rising [5]. The renewable energy sources are interesting. In the future, power plant needs to reduce energy production from fossil resources. It is replaced by renewable energy [6]. Although the renewable energy is the best choice, it is not replaced completely. It is very much investment for performance. Therefore, the development of renewable energy technology is needed [7]. Solar energy is interesting as renewable energy. Luckily, Thailand is located in a uniquely suitable location to take advantage of solar energy [8].

The solar power plant is promoted by Thai government [9]. Especially the government declares policies of promotion for spreading solar power plants [10]. However the investment of solar power plant is still expensive. To the highest efficiently use, features, and phenomenal have been understood. If technicians know well about solar power plant, they will do maintenance effectively. Therefore the prediction of solar power plant behaviour is important. It tells us about system efficiencies. To predict phenomenal of solar power plant, effecting factors have been studied. The example of effecting factor is the angel of installation which 15° for Thailand location [11], [12]. Therefore the best direction solar tracking for generating at maximum energy was presented [13]. Furthermore, dusty or soiled surface are the factors effecting on electricity generation of solar power plant [14]-[16]. They affect lower



generation efficiencies. Hence modules have to be cleaned periodically. The prediction help technicians choose the time for cleaning effectively.

Therefore this paper presents solar power plant prediction. The prediction is gotten from effecting factors. The independent variable is generated energy. The dependent variables consist of irradiance, humidity, wind speed, ambient temperature, module temperature and power peak. Eventually the correlation of factors is gotten. It can predict the electricity from solar power plant.

2. Basic concept

2.1. Simple regression analysis

Linear simple regression analysis is used in this research to find correlation between the two variables. Simple regression analysis equation is show in equation (1).

$$Y_i = \alpha + \beta X_i + \varepsilon_i \quad (1)$$

Which; Y_i is dependent variable.

X_i is independent variable.

α is Y_i intercept (constant if $X_i = 0$).

β is slop or coefficient simple regression.

To estimate α and β are gotten by least squares method.

$$\hat{Y}_i = a + bX_i \quad (2)$$

Which; a is α estimation value.

b is β estimation value.

\hat{Y}_i is estimation of Y_i .

$$a = \frac{\sum Y_i}{n} - \frac{\sum X_i}{n} \quad (3)$$

Correlation level between parameters is obtained by coefficient of determination (R^2). It is calculated by (4).

$$R^2 = \frac{b \times S_{xy}}{S_{yy}} \quad (4)$$

Where;

$$b = \frac{S_{xy}}{S_{xx}} \quad (5)$$

$$S_{xx} = \sum X_i^2 - \frac{(\sum X_i)^2}{n} \quad (6)$$

$$S_{yy} = \sum Y_i^2 - \frac{(\sum Y_i)^2}{n} \quad (7)$$

$$S_{xy} = \sum X_i Y_i - \frac{\sum X_i Y_i}{n} \quad (8)$$

If the coefficient of determination (R^2) is high, it shows Y and X are high correlation level.

2.2. Multiple linear regression

This method is use for analysing more than two variables correlation. Multiple linear regression analysis equation is show in (9).

$$Y_i = a + b_1 X_1 + b_2 X_2 + \dots + b_k X_k \quad (9)$$

3. Experimental setup

3.1. The solar power plant

The 800kW solar power plant is located in Phitsanulok province, Thailand. There are 4000 solar modules. They are installed on the roof of building. Data had been collected by SCADA system a year ago. The energy, irradiance, humidity, wind speed, ambient temperature, module temperature and power were recorded. Normally this plant is cleaned 3 times a year.



Figure 1. Solar power plant in Phitsanulok province, Thailand.

3.2. The correlation analysis

All data were analysed by simple regression analysis and multiple linear regressions. Independent variable was electrical energy. Dependent variables were irradiance (kWh), humidity (%), wind speed (m/s), ambient temperature ($^{\circ}\text{C}$), module temperature ($^{\circ}\text{C}$) and real power (kW).

4. Experimental results

The data was recorded from Phitsanulok power plant. The data includes generated energy, irradiance, humidity, wind speed, ambient temperature, module temperature and real power. They were obtained by SCADA system. They were recorded for 1 year since January to December in 2015.

4.1. Simple regression analysis result

Simple regression analysis method was used for analysing. Six factors are plotted as figure 2 – figure 7. All data were obtained directly by SCADA system in real environment. The environment was not controlled. They were plotted without correction factors. The correlation is shown in table 1.

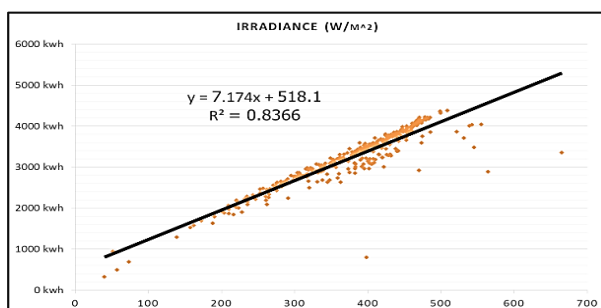


Figure 2. The plot of electrical energy and irradiance.

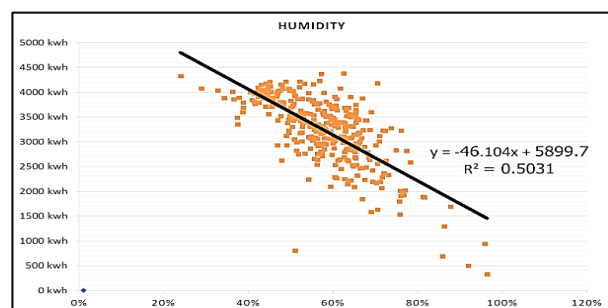


Figure 3. The plot of electrical energy and humidity.

The table 1 shows correlations obtained by two variables simple regression analysis method. The correlation and coefficient of determination (R^2) are computed by Matlab program. It is investigated that all correlations have less than 0.8507 coefficient of determination (R^2). Therefore, they cannot be use to predict the energy generation. However, simple regression analysis is not enough to summarize the correlation between investigated factors. Hence the multiple linear regression method is applied to

analyse the correlation. Multiple linear regression method is use for analysing more than two variables correlation.

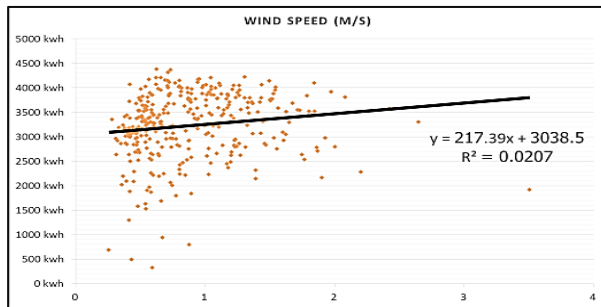


Figure 4. The plot of electrical energy and wind speed.

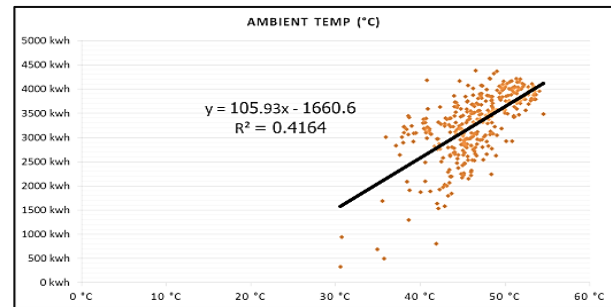


Figure 5. The plot of electrical energy and ambient temperature.

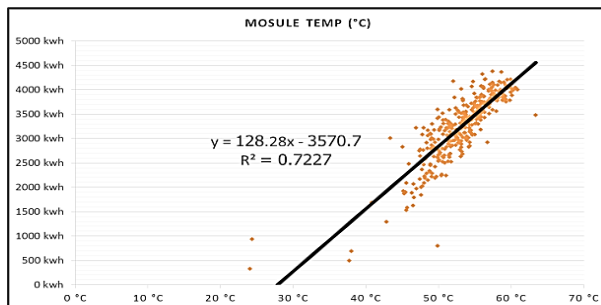


Figure 6. The plot of electrical energy and module temperature.

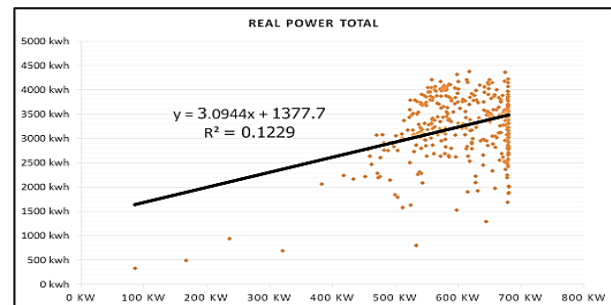


Figure 7. The plot of electrical energy and power peak.

Table 1. Two variables simple regression equation.

Factors	Equation	R ²
Irradiance (Ir)	kwh = 518.1 + 7.174Ir	0.8366
Humidity (H)	kwh = 5899.7 – 46.104H	0.5031
Wind speed (W)	kwh = 3038.5 + 217.39W	0.0207
Ambient temperature (AT)	kwh = -1660.6 + 105.93AT	0.4164
Module temperature (MT)	kwh = -3570.7 + 128.28MT	0.7227
Real power (P)	kwh = 1377.7 + 3.0944P	0.1229

4.2. Multiple linear regression results

The correlation between electrical energy and irradiance for each range of temperature is shown in figure 8. There are six ranges. The graphs show that the slopes slightly decrease, if the temperature increases. That means temperature has effect on electrical energy generation. Therefore all data can be analysed by multiple linear regressions analysis. The analysis is done for each range of temperature. The results of analysis are shown in table 2.

From table 2, coefficients of determination (R²) can be calculated at 40.0-50 °C. The correlation cannot be determined at 35.0-40.0 °C. The coefficients of determination are more than 0.8507. It means that correlation can be use for predicting using following equation as shown in table 2. These equations will be used to analyse competency of generation and opportunity throughout the year.

The figure 9 shows comparison between predicted and real energy value. For the range of 35.0-37.5 °C and 37.5-40.0 °C, the correlation equations were replaced by correlation of 40.0-42.5 °C in range. Because the temperature is the nearest and coefficients of determination is the highest. It is investigated that the predicted value and real values is almost the same as shown in figure 9.

The difference percent between real generated value and predicted value is shown in figure 10. It has shown that the highest error is about just -20%. Moreover the trend line of real generated energy is both higher and lower than predicted value. The line varies because solar cell modules are cleaned three times a year. The first time is on 21-23 February. The second time is on 12-14 July. The third time is on 12-14 November. Therefore generated electricity in mentioned duration trended higher than predicted value. Considering effect of irradiance as shown in figure 11, it is found that the irradiance for each seasons are not the same. The highest irradiance is in summer. The next is winter. And the lowest is rainy.

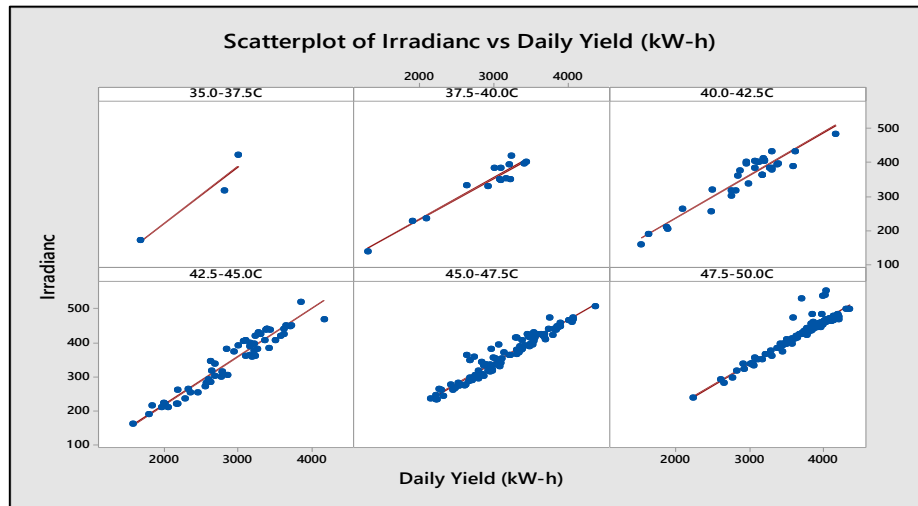


Figure 8. Scatter plot classified by module temperature.

Table 2. Multiple linear regression equation.

Temperature	Equation	R ²
35.0-37.5 °C	-	-
37.5-40.0 °C	-	-
40.0-42.5 °C	kWh = 6595 + 11.381Ir - 153.0MT	0.9634
42.5-45.0 °C	kWh = -247 + 8.622Ir + 87.9AT - 71.5MT	0.9524
45.0-47.5 °C	kWh = -1964 + 8.329Ir + 83.4AT - 41.1MT + 0.690P	0.9572
47.5-50.0 °C	kWh = -561 + 6.585Ir + 19.13AT + 0.811P	0.8969

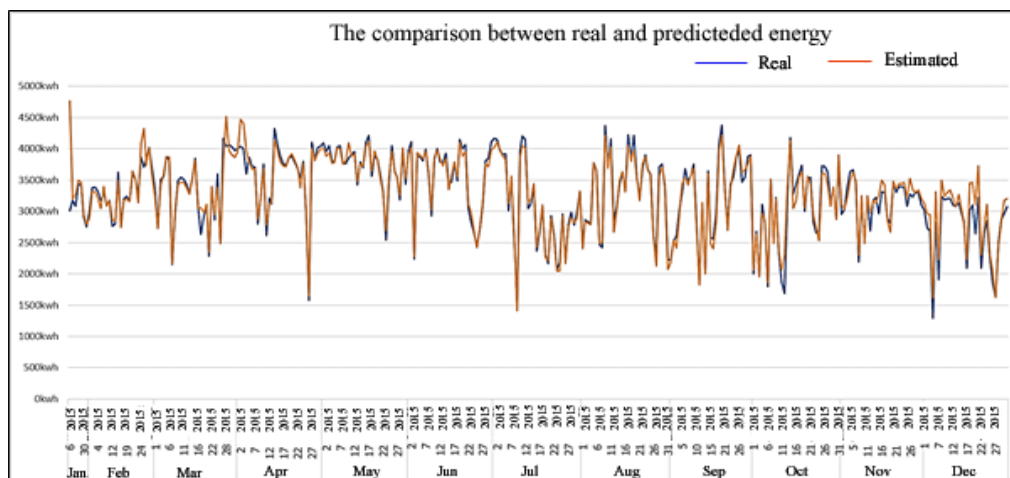


Figure 9. Comparison between real and predicted energy.

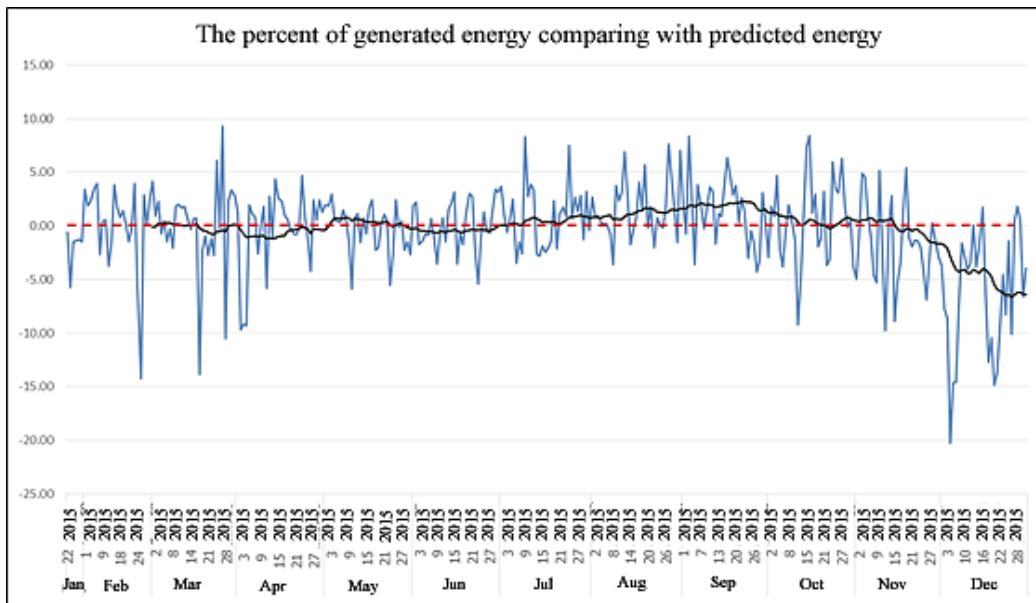


Figure 10. The percent of generated energy comparing with predicted energy.

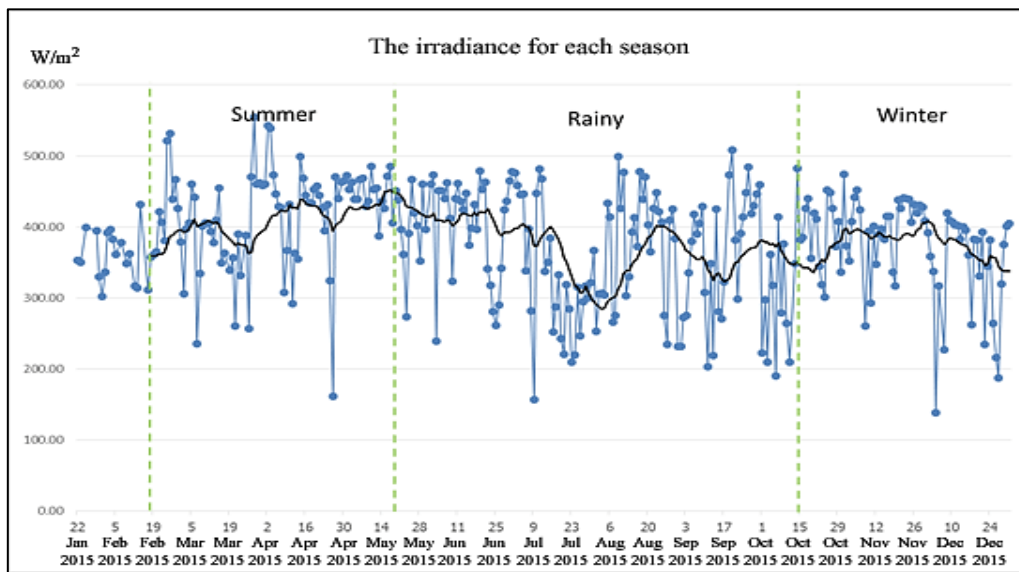


Figure 11. The irradiance for each season.

4.3. Effect of module temperature

From figure 12, it shows temperature influences on solar power plant. Five constant irradiances are recorded at different temperature. They consist of 350, 550, 750, 950 and 1150 W/m^2 . It is investigated clearly that the irradiances directly influence on real power. If the irradiance increases, the real power increases. It can be summarized that real power is a dependant of irradiance. On the other hand, generated real power inversely varies with the temperature. If temperature increases, real power decreases. Therefore if the temperature increases, the generated electrical energy also decreases.

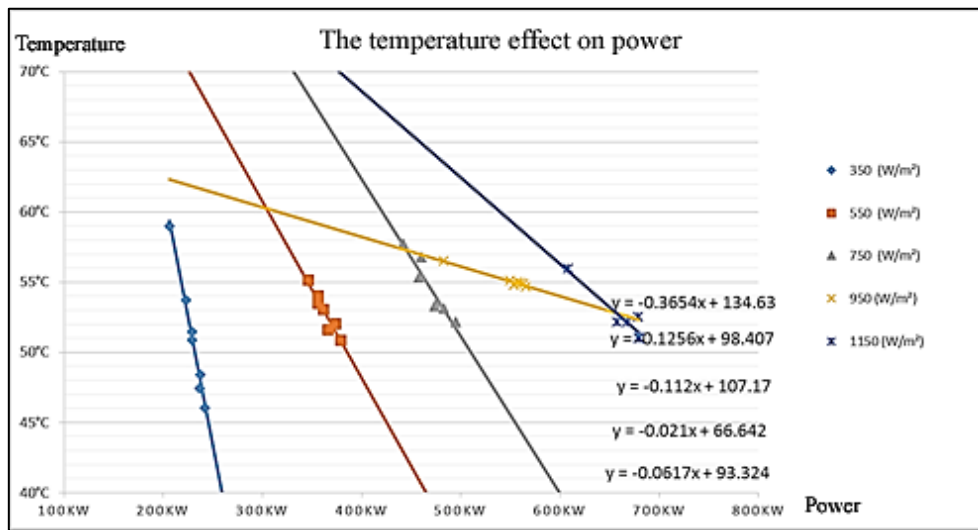


Figure 12. The temperature effect.

5. Discussion

From the results, it is investigated that the correlation equation in table 2 can predict generated electricity from solar energy. The highest error percent is about -20%. While generated energy is sometime higher than predicted value because the solar power plant are cleaned in that period. Therefore the automatic warning can be developed using prediction system. For example at error percent about -30% in the long time, the maintenance is scheduled. In the worst case, for example if the error percent about -70% or lower, the warning is alarm. Technicians have to check system immediately.

In the point of effecting factor, it can be summarized that irradiance directly influence on solar power plant. The ambient and module temperature are also effect factors. Moreover at the temperature is more than 45 °C, the real power is an effecting factor. On the other hand, humidity and wind speed had no effect on solar energy generation. The result of factors is shown in table 3.

Table 3. Effecting factors on solar power plant.

Temperature.(°C)	Effecting Factors					
	AT	MT	H	Ir	W	P
40.0-42.5	-	/	-	/	-	-
42.5-45.0	/	/	-	/	-	-
45.0-47.5	/	/	-	/	-	/
47.5-50.0	/	-	-	/	-	/

6. Conclusion

From the results, it can be concluded as follow;

1. The correlation equation can use to predict the generated value. The prediction is used following rang of temperature. There are four equations. Each equation depends on effecting factors as shown in table 3.
2. The solar module cleaning can improve efficiency of solar power plant. Cleaned solar cells can more generate energy.
3. The most effect occur from irradiance factor. It directly influences on solar power plant. If the irradiance increases, the energy generation increases.
4. The temperature effects on generated electrical energy. As the temperature increases, the generated electrical energy decreases.
5. Humidity and wind speed have no effect on energy generation in solar power plant.

7. References

- [1] Thongchaisuratkrul C 2011 *Energy management in buildings* (Bangkok: King Mongkut's University of Technology North Bangkok)
- [2] Enerdata. *Statistics of CO2 Emissions*. Accessed on July 15, 2017 from the World Wide Web: <http://yearbook.enerdata.net>.
- [3] Enerdata, *Statistics of World Electricity consumption*. Accessed on July 15, 2017 from the World Wide Web: <http://yearbook.enerdata.net>.
- [4] Ministry of Energy 2007 *Energy Conservation Act 1992 (amended 2007)*. (Bangkok: Ministry of Energy)
- [5] Energy Forecast and Information Technology Center 2015. *Thailand Energy Situation 2014* (Bangkok: Ministry of Energy)
- [6] Thomas G and P E Bellarmine 2000 Load Management Techniques *Proc. of the IEEE Southeast conf.* pp 139-145
- [7] J W Plasto 2011 Energy Services for an Electricity Industry Based on Renewable Energy. *Eng. Sci. and Edu. J.*: pp145-152.
- [8] Ministry of Energy 2011 *Development and Investment in Renewable Energy handbook* (Bangkok: Ministry of Energy)
- [9] Ministry of Energy 2012 *Renewable development plan* (Bangkok: Ministry of Energy)
- [10] Ministry of Energy 2017 *Energy policy 4.0* (Bangkok: Ministry of Energy)
- [11] L K David, E B William and A K Jay 2002 Analysis of Factors Influencing the Annual Energy Production of Photovoltaic Systems *IEEE*
- [12] Sunpower. *Key Factors for Solar Performance*, Accessed on July 5, 2017 from the World Wide Web: <https://global.sunpower.com/>
- [13] G Ericson, K Nashat and S Tyler 2015 Factors Affecting Solar Power Production Efficiency *New Mexico Supercomputing Challenge*
- [14] S R Dayal and K Sudhakar 2013 Effect of Dust on the Performance of Solar PV Panel *Int. J. of Chem. Tech. R.* pp 1083-1086
- [15] D Furkan and E M Mehmet 2010 Critical Factors that Affecting Efficiency of Solar Cells *Smart Grid and Renewable Energy* pp 47-50
- [16] M Kontges 2014 *Review of Failures of Photovoltaic Modules External final report IEA-PVPS* (Emmerthal: Institute for Solar Energy Research Hamelin)

Acknowledgments

Authors would like to thank staff of Faculty of Technical Education, King Mongkut's University of Technology North Bangkok.

Research on steady-state power distribution calculation technology of electrothermal coupled regional *energy system*

Jinning Shan ¹, Zhenyu Li ¹, Gang Chen ¹ and Xin Wang ¹

¹ State Grid Liaoning Electric Power Supply Co. Ltd, Fuxin Power Supply Company
Fuxin, China

E-mail: 13941840787@139.com

Thesis was funded by State Grid Liaoning Electric Power Co., Ltd.

Project number: 2018YF-24

Abstract. When large-scale power grids are connected to the power grid, it is conceivable that adverse effects on the operation and planning of power grids can be imagined. Therefore, wind power has characteristics such as intermittency, volatility, anti-peaking characteristics, and large prediction errors. At the same time, the ability to absorb wind power is also weakened by the contradiction between the peak load and the heating load. In addition, due to the thermo-electric coupling characteristics of the cogeneration unit, ie, "heating with electricity," this characteristic directly determines that its heat output severely limits the regulation of the electric output. The results of the study indicate that the co-production unit's electric power and thermal power are coupled. Strong nature, the peak load capacity of the unit is greatly affected by the heat load, and the electric power and thermal power distribution lacks a unified calculation and analysis method, which restricts the means of improving the peaking capacity of the unit by controlling the thermal power output of the unit, and through implementation, establishes the main power equipment, The steady-state power model of the thermal equipment, the steady-state power analysis and calculation method of the regional energy system of the power thermocouple, and the realization of adjusting the thermal load related parameters to improve the peak capacity of the thermal power unit.

1. Introduction

According to the planning goal, by the end of the "Thirteenth Five-Year Plan" period, the installed capacity of hydropower, wind power, and photovoltaic power generation in the State Grid Corporation will increase to 270 million kW, 220 million kW, and 110 million kW respectively, totaling 600 million kW, scenery, etc [1]-[2]. The issue of energy integration will be more prominent. The difficulties in the adoption of Fengpu Optoelectronics are, to a certain extent, hampered by the inconsistencies in the integration of this intermittent renewable energy source with traditional energy systems. Taking Northeast China as an example, the heating units account for a large proportion of the total installed capacity. In the winter heating season, due to the abundant wind energy resources at this time, its output tends to exhibit anti-peaking characteristics, and winds in the troughs and wind power. Under large-scale grid-connected conditions, there is a huge pressure on the peaking of the grid [3]. On the other hand, combined heat and power has obvious economic advantages over thermoelectric production, so the proportion of cogeneration units for further improvement in energy efficiency will increase further.[4]-[6]

In order to alleviate environmental pollution and improve the energy efficiency of the terminal, the integrated energy system has become an important direction for China's energy structure adjustment.



Content from this work may be used under the terms of the [Creative Commons Attribution 3.0 licence](https://creativecommons.org/licenses/by/3.0/). Any further distribution of this work must maintain attribution to the author(s) and the title of the work, journal citation and DOI.

Published under licence by IOP Publishing Ltd

The electricity network and the heating network form an electro-thermally coupled energy system through the cogeneration unit. In this energy system, fuel is transferred to boiler water by boiler combustion, heated to form superheated steam, a part of steam is used for heating, and another part is used for generator power generation. The heating part is sent to the end user's heating load through the heating pipe network; the power generation part is sent to various power loads through the power grid. Due to the differences in the energy forms of heat and power, there are also great differences in response time scales. The thermal response time is slow, and the power response time is very fast. In other words, if the same cogeneration unit suddenly goes out of service, the situation reflected to the end-user is that the power load is immediately stopped and the heating load takes a while to cool slowly.[7]-[9]

The cogeneration units participate in the power peak adjustment. The thermal power unit continuously adjusts as the power load changes, generating more power during the peak load period and generating less or even not generating power when the load level is low. Due to the limitation of the adjustment range of the heat-generating machine itself, the change in the power generation of the heat-generating unit will cause a change in the heat production, and it may not satisfy the heat supply quality.

The heating quality directly reflects the indoor temperature at the heating end. However, the change of the actual operation mode of the thermal power unit will not always immediately affect the indoor temperature of the heating end. This is the thermal hysteresis of the heating system. Therefore, by analyzing the relationship between the output of the thermal power unit and the indoor temperature, the thermal power unit participates in the system peaking method.[10]

The use of thermal hysteresis in the heating system essentially changes the continuous and stable operation of the heating system. When the heat generated by the thermal power unit changes, it causes temperature fluctuations in the heating network and the hot building to form a thermal dynamic change process of the heating system. This method requires the heating unit to participate in system peaking while ensuring the heating quality. purpose.

The factors affecting the indoor temperature change are influenced by factors such as solar radiation and outdoor temperature, in addition to the heating of the heat-generating unit. Even in the continuous and stable operation mode of the thermal power unit, the indoor temperature will periodically fluctuate within a certain range. And a certain range of different indoor temperatures can meet the human body's thermal comfort requirements. This is to change the way of the continuous stable operation of the traditional thermal power unit and make it possible to participate in system peaking.

For example, the heat output of a thermal power unit at different times of the day can be changed. When the load is at a peak, the thermal power unit increases its output. At this time, the heat output is large and the indoor temperature is increased. A certain amount of heat is stored in the heat grid and the thermal structure; when the load is low, the thermal power unit stops or reduces heat generation. Release heat from thermal grids and thermal buildings to meet heating needs. [11]

Therefore, to use the thermal hysteresis of the heating system to improve the peak shaving capacity of the cogeneration unit, it is necessary to clearly understand the power distribution of the electricity-heat coupled energy system. Set up steady-state power models for major power equipment and thermal power equipment, and grasp steady-state power analysis and calculation methods for thermal energy-coupled regional energy systems, and realize the coordinated control of heating networks and power networks to improve power grid utilization Unit capacity for peaking. [12]

Accurately calculating the steady-state power distribution of the thermodynamically coupled regional energy system helps to study the interaction between the power system and the thermal system, helps to analyze the various forms of energy distribution in the entire energy system, and can effectively study the total energy. The use of efficiency, thereby improving energy efficiency. [13] Take advantage of the comprehensive energy system, adjust the heat supply appropriately, effectively use the thermal inertial characteristics of the thermal network, improve the peaking capacity of the combined heat and power unit, thereby dissipating more clean electric energy, reducing grid peaking input, and improving cleanliness Energy efficiency, reduce the total capital investment, improve energy efficiency.

2. Study of the influence of thermal load parameters on peak shaving capacity of cogeneration units

The operating parameters of the boiler unit are mainly superheated steam pressure, superheated steam and reheated steam temperature, steam drum water level, boiler evaporation amount, and oxygen content of flue gas. For example, when the steam flow rate required by the unit turbine is changed, the boiler steam pressure, steam temperature, and water level all change with other conditions unchanged. At this time, it is necessary to make corresponding adjustments to the boiler's water supply volume, fuel volume, and air volume (ie, combustion) so that the boiler's evaporation capacity can be adapted to the turbine's load. The operating parameters are kept within the rated value or within the specified range.

The stability of the steam pressure during operation of the boiler depends on the balance between the boiler evaporation and the external load. If the boiler evaporation is greater than the amount of steam required by the external load, the vapor pressure rises; otherwise, it decreases. When the boiler evaporation is equal to the amount of steam required by the external load at each instant, the steam pressure remains stable.

The change in steam pressure reflects the imbalance between boiler evaporation and the amount of steam required for external loads. The amount of evaporation depends on the exothermic state of fuel combustion. Therefore, under normal circumstances, both external disturbances and internal disturbances cause changes in the vapor pressure, which can be adjusted by adjusting the combustion method: the vapor pressure is reduced and the combustion is enhanced; the vapor pressure is raised and the combustion is weakened. In an abnormal situation, when the steam pressure rises sharply and the combustion is too late to be adjusted, the superheater trap door can be opened or the steam can be vented to the empty exhaust valve to depressurize as quickly as possible.

Whether the steam temperature changes depends on how much steam (including desuperheated water) flows through the heat exchanger and how much heat the flue gas passes to it at the same time. If the balance of the above relation can be maintained at any time, the steam temperature will remain unchanged; and when the balance is destroyed, the steam temperature will change. The greater the degree of imbalance, the greater the change in steam temperature.

According to the principle of energy conversion of cogeneration units, the mathematical relationships between fuel, steam and electricity are established, a typical heat load model is established, the relationship between heat load temperature and heat consumption is studied, and heat supply is studied when the heat load temperature fluctuates within a certain range. The changes in the heat supply and power generation capacity of the unit were studied, and the methods for improving the peak shaving capacity of the cogeneration units by rationally adjusting the heat supply were studied.

3. Study the working mechanism of back pressure turbines and establish a steady-state model for back pressure steam turbines considering factors such as fuel, steam and electricity

Heated steam turbines include back-pressure turbines, steam turbines with regulated extraction, dual-use condenser heating, and condensed-gas turbines with low vacuum heating. This project mainly studies commonly used back pressure turbines. Back-pressure steam turbines use exhaust gas to heat outwards, and their exhaust pressure is usually higher than the exhaust pressure of condensing steam turbines. Although the unit mass of steam is reduced within the steam turbine, there is no loss of cold source, so the use of this unit has a high utilization of heat energy. When the back press operates, heat and electricity cannot be adjusted independently. Often, heat is used to set the electricity, and the electricity supplied by the grid is missing. Therefore, the size of the heat load has a greater impact on the economics of back pressure turbines. Figure. 1 is a schematic diagram of a back pressure steam turbine thermal system. After the steam enters the back pressure turbine expansion work, the exhaust steam is directly led out for use by external users.

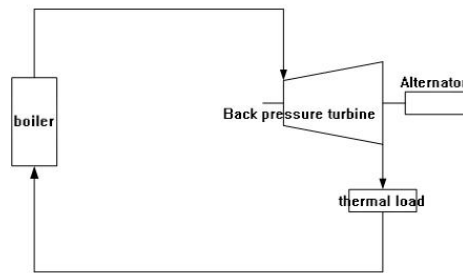


Figure 1. Schematic diagram of back pressure steam turbine thermal system.

As an important multi-energy coupling element, a combined heat and power unit (CHP) can generate both electrical energy and thermal energy. It can be divided into two types: constant thermal power ratio (such as back pressure type units) and variable thermal power ratio (such as pumping condensation type units). The thermoelectric ratio characteristics are shown in Figure. 2.

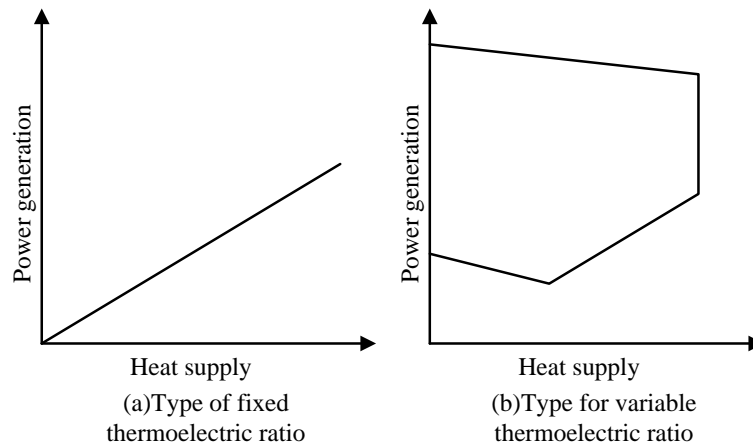


Figure 2. Type of thermoelectricity ratio of cogeneration unit.

The relationship between the thermal output ratio and the thermal output ratio is

$$c_m = \Phi_{CHP} / P_{CHP} \quad (1)$$

The thermoelectric ratio of the thermal power ratio is variable, which can be expressed as a certain operating mode.

$$Z = (\eta_e F_{in} - P_{CHP}) / \Phi_{CHP} \quad (2)$$

In the formula, it is the fuel input rate. However, in the actual operation of a certain period of time, remain unchanged.

4. Study the thermal process of long steam pipes and establish a thermal model under set conditions

The main difference between different energy flow networks is the difference in branch characteristics. The electricity-heat coupled integrated energy system, power network, and heat-reserved branch model are as follows.

The branch of the power network is mainly composed of resistors, reactances and capacitors. In the form of communication, it can be expressed as

$$\dot{U}_k = Z_k \dot{I}_k \quad (3)$$

Where: \dot{U}_k is a complex voltage; \dot{I}_k is a complex current; Z_k is equivalent impedance based on RLC parameters.

For the heating network, a hydraulic model considering the steady flow of the thermal medium and a thermal model considering the temperature drop along the way are established. In the calculation of the hydraulic thermal-mechanical coupling calculation model for the heat-transfer medium flow, the following simplifications are made: The heat medium in the tube is a one-dimensional stable flow, that is, the heat medium parameters only change along the length of the tube along the axial direction, and the cross-section thermal medium parameters do not change with time; All are placed horizontally, ignoring the influence of gravitational potential energy; thermal media is a single-phase material and phase change is not considered.

The model of the heating network branch is divided into two parts: the hydraulic model and the thermal model.

The static hydraulic model of a general pipeline is

$$h_f = Km|\dot{m}| \quad (4)$$

In the formula, \dot{m} is the branch flow; h_f is the branch pressure drop caused by the friction; K is the impedance coefficient. In addition, the branch pressure drop is also related to height, accessories, pumps, etc. In order to simplify the problem, it is considered that the heights of the nodes are equal, and the attachments have been converted into pipes. There are no pumps on the branches outside the heat source.

The static thermal model of the general pipeline is

$$\Phi = C_p \dot{m}_q (T_s - T_o) \quad (5)$$

$$T_{end} = (T_{start} - T_a) e^{\frac{\lambda L}{C_p \dot{m}}} + T_a \quad (6)$$

$$(\sum \dot{m}_{out}) T_{out} = \sum (\dot{m}_{in} T_{in}) \quad (7)$$

In the formula: Φ is the heat obtained by the load or the heat source; C_p is the specific heat capacity of the water; \dot{m}_q is the flow rate through the load or the heat source; T_s is the temperature at the water supply side of the corresponding node; T_o is the temperature at the water return side of the corresponding node; T_{start} is the beginning of a certain branch road The water temperature; T_{end} is the water temperature at the end of the branch; T_a is the ambient temperature; L is the length of the branch pipeline; λ is the heat transfer coefficient per unit length of the pipeline; T_{out} is the temperature of the water actually flowing out of a node; T_{in} is the temperature of the water actually flowing into the node. Equation (5) represents the relationship between heat and temperature; Equation (6) represents the temperature relationship of the water at the start and end of the branch, indicating the presence of heat loss; Equation (7) represents the hot water at the node Ideally, the temperature of the water flowing into the node is different, and the temperature of the water flowing out of the node is the same.

5. Research on Steady State Power Distribution Model and Its Solution Algorithm for Thermal Power Coupling Network

5.1. Thermal power coupling network steady-state power distribution model

Taking energy as the main line, comprehensive consideration is given to the steam pipe network and power grid, as well as energy production equipment and energy consumption equipment, to form a unified node branch network. The branch is the energy transmission link and the node is the energy conversion link. The ability of the branch to transmit energy is generally determined by the

performance parameters of the branch itself and does not change with time. Node state variables are parameters to be evaluated.

Based on the power flow equation of the electric network, the output power of the generator node is further expanded, represented by the amount of coal per unit time of the boiler, and the load power of the motor of the load node is represented by the amount of raw material of the chemical plant per unit time. Since the power generation and the electricity load are both steam-related expressions, a steam pipe transmission model is established to form an energy network equation including coal, heat, and power. As shown in Figure 3.

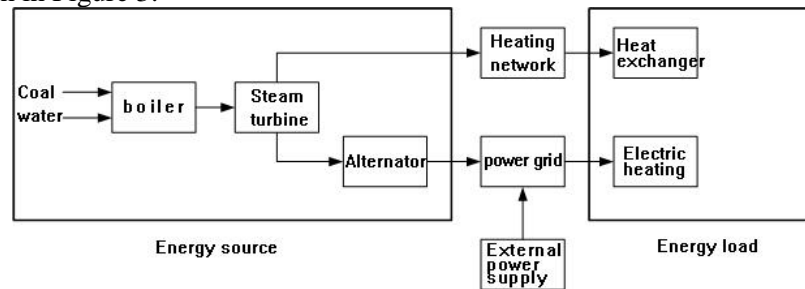


Figure 3. Electrothermal comprehensive energy system.

The solution of the energy network equation is essentially the solution of a set of nonlinear algebraic equations. The joint solution solves all the equations of different energy flows together as a whole, specifically

$$F(x) = \left. \begin{array}{l} f_1(x_1) \\ f_2(x_2) \\ \dots \\ f_n(x_n) \\ g(x_1, x_2, \dots, x_n) \end{array} \right\} = 0 \quad (8)$$

It is assumed that the multi-energy flow system is composed of energy flow subsystems, i is the subscripts represent different subsystems, x is the state variables, $f_i(x_i) = 0$ is the equations of the independent part of the energy flow system i , and $g(x_1, x_2, \dots, x_n) = 0$ is the equations of the coupling part.

5.2. Solution

The energy network equation solver solves other variables under certain conditions or variables. In different energy domains, a mature and widely used solution model and algorithm has been developed for a single energy flow network, such as node admittance matrix, power flow model and rapid decomposition method in power networks, solution loop solution method in hydraulic calculations, and solutions. The nodal equation method and the deducted section equation method. For the multi-energy flow system, there are no widely used solution models and algorithms. There are two commonly used joint solutions and decoupling solutions.

Equation (8) can be solved using the Newton-Raphson method. In the concrete solution, the known variables, state variables, reference nodes, etc. of different nodes need to be determined, and related problems related to numerical solution are involved. The benefits of the unified solution are intuitive and easy to understand. The problem is that the values and characteristics of different energy flow systems are very different. The Jacobian matrix may be irreversible.

The decoupling solution is solved $f_i(x_i) = 0$ separately for each energy flow subsystem i and then iterated through the coupling equations $g(x_1, x_2, \dots, x_n) = 0$ until the convergence criteria are met.

The advantage of the decoupling solution is that it can use the solution methods and procedures of existing networks. The disadvantages are that the number of iterations is relatively large, and it is difficult to ensure the convergence when the coupling is tight.

6. Summary

In this paper, calculate the power distribution of a power thermocoupled energy system, adjust the relevant parameters, such as: modify the terminal heat load temperature, pipe network insulation characteristics, observe the changes in power generation output of the cogeneration unit, analyze the interaction between the thermal system and the power system Investigate the conditions and methods for improving the peak shaving capacity of the combined heat and power unit by controlling the thermal system. Due to the strong coupling of electric power and thermal power of the combined heat and power unit, the peak load capacity of the unit is greatly affected by the heat load, and the electric power and thermal power distribution lacks a unified calculation and analysis method, which restricts the increase in peak load capacity of the unit by controlling the thermal power output of the unit. Through the implementation of this paper, a steady-state power model of major power equipment and thermal equipment is established, and a steady-state power analysis and calculation method for the regional energy system coupled with thermal power is grasped, and the peak load adjustment capability of the thermal power unit is improved by adjusting the relevant parameters of the heat load.

7. References

- [1] IEEE standard 738 —1993 IEEE standard for calculating the current-temperature relationship of bare overhead conductors.1993.
- [2] M. W. DAVIS. A new thermal rating approach: the real-time thermal rating system for strategic overhead conductor transmission lines: Part I general description and justification of the real-time thermal rating system. *IEEE Trans on Power Apparatus and Systems*, 1978, 96 (3): 803-809.
- [3] M. W. DAVIS. A new thermal rating approach: the real-time thermal rating system for strategic overhead conductort ransmission lines: Part II steady state thermal rating. *IEEE Trans on Power Apparatus and Systems*, 1978, 97 (3): 810-825.
- [4] D. Liu, G. Zhang, B. Huang, W. Liu. *Optimum Electric Boiler Capacity Configuration in a Regional Power Grid for a Wind Power Accommodation Scenario* [J]. *Energies*, 2016, 9(3):144-153.
- [5] S. Hiibner, M. Eck, C. Stiller, et al. *Techno-economic heat transfer optimization of large s`cale latent heat energy storage systems in solar thermal power plants* [J]. *Applied Thermal Engineering*, 201, 98(4):483-491.
- [6] D. A. DOU GLASS, A. A. EDRIS. Real-time monitoring and dynamic thermal rating of power transmission circuits. *IEEE Trans on Power Delivery*, 1996, 11 (3): 1407-1417.
- [7] M. G. Nielsen, J. M. Morales, M. Zugno, et al. *Economic valuation of heat pumps and electric boilers in the Danish energy system* [J]. *Applied Energy*, 2016, 167:189-200.
- [8] BANA KAR H, AL GUACIL N, GALIANA F D. Elect rot hermal coordination: Part I theory and implementation scheme. *IEEE Trans on Power Systems*, 2005, 20 (2): 798-805.
- [9] Lv Quan, Chen Tianyou, Wang Haixia, et al. *Analysis of peak regulating ability of thermoelectric unit after heat storage* [J].*Power system automation*, 2014, 38(11): 34-41.
- [10] D. Balic, D. Maljkovic. District h ZHANG Ming, WANG Wu, ZHAO Lili, et al. *The simulation analysis of power loss prediction model based on large data analysis* [J].*Shaanxi Electric Power*, 2016, 44(6):31-35.
- [11] Long Hongshu, Fu Lin, Xu Ruilin, et al. *Power grid dispatching using gas turbine and heat pump to reduce uncertainties* [J]. *Transactions of China Electrotechnical Society*,2015,30(20):219-226.
- [12] AL GUACIL N, BANA KAR H, GALIANA F D. Elect rot hermal coordination: Part II case studies. *IEEE Trans on Power Systems*, 2005, 20 (2): 173821745.
- [13] D. A. DOU GLASS, A. A. EDRIS. Field studies of dynamict hermal rating met hods for overhead lines/ / *Proceedings of IEEE Transmission and Dist ribution Conference: Vol 2*, April 11-16, 1999, New Orleans, LA, USA: 842-851.

Acknowledgments

First of all, I would like to thank everyone who helped me during the writing of this article. I am very grateful for the help of the remaining authors who provided me with valuable advice in academic research. In preparing this paper, everyone spent a lot of time reading each draft and provided me with inspiring suggestions. Without their patient guidance, profound criticism and expert guidance, the completion of this paper will not be possible.

Secondly, I am particularly grateful to professors in the field of electricity. They provided many useful teaching and inspirational lectures for my dissertation and made a lot of preparations for my study.

Finally, I finally want to thank my dear parents, who have been helping me out of difficulties and support without complaint.

Chapter 7:
Energy Development and Utilization

Optimal design of distributed energy systems in rural area of developing country: a case study of Guanzhong area, China

Y Zhu¹, X X Yan² and Q L Tong²

1 Associate Professor, Xi'an University of Architecture and Technology, Xi'an, 710055, China

2 Research assistant, Xi'an University of Architecture and Technology, Xi'an, 710055, China

E-mail: zhuying@xauat.edu.cn

Abstract: This paper optimized the design of renewable distributed energy systems (R-DES) based on interval linear programming. The total cost of this system is used as an objective function of system configuration problem. The optimal configuration of this system is obtained. In order to prove practicability of this system, this paper took the remote rural areas of Guanzhong as an example to optimize energy supply and operation mode. Through calculations, it can be seen that this system reduced power supply by 29.0%~63.6%, and carbon emission reduction rate is 4.0%~49.6%.

Keywords: optimal design; distributed energy systems; rural area; uncertainty

1. Introduction

In 2017, the Ministry of Housing report that China's rural residential area reached 32.32 billion m², which higher 23.3% than 2012. The building industry is considered to be a major contributor to the world's energy consumption. During construction and operation, the energy consumption of buildings accounts for 40%. Among construction energy consumption, rural residential buildings consume 60% in China[1]. However, with the rapid development of country's economy and the improvement of residents on living standards, comfortable quality of buildings in rural area is increasing, which leads to the increase of construction energy consumption rapidly.

In this study, the optimization of R-DES using interval linear programming (ILP) was researched to coordinate the relationship between energy supply, economic benefits and environmental protection. ILP is used to deal with uncertainties resulting from the range of admissible values in problem coefficients[2]. R-DES has some advantages: a) Ability to meet the needs of special areas for energy. For instance, rural, pastoral, mountainous and developing areas; b) Improve the reliability and stability of energy supply; c) Provide the potential for the use of cascade energy[3]; d) Realize the comprehensive utilization of various renewable energy sources[4].

2. Application

2.1. Overview of the study area

The research area is Guanzhong area. According to the "Development Plan of Guanzhong Plain Urban Agglomeration" published by National Development and Reform Commission Ministry of Housing and Urban-Rural Development in 2018, Guanzhong Plain Urban Agglomeration refers to the center of Xi'an (including Xianyang) and Baoji as sub-centers, including Weinan, Tongchuan, Shangluo and Yangling. Demonstration area city group, Pingliang, Qingyang, Linyi, Yuncheng[5]. In the urban area, the land area is 107,100 km². By the end of 2017, the permanent population was 38.65 million, and the regional



GDP was 216 billion RMB.

The Guanzhong Plain Urban Agglomeration locates in a cold temperate zone with an average elevation of about 500 m. The climate is characterized by four distinct seasons: hot summer, cold winter, great temperature difference. The rural areas in Guanzhong are underdeveloped and the living conditions of the residents are relatively backward. Especially, the indoor thermal environment is poor in winter. Residents use coal or electric heating, which not only consumes a lot of energy, but also causes pollution of atmospheric environment. The Guanzhong area is rich in renewable energy sources, such as biomass, geothermal energy, and solar energy, which can establish renewable distributed energy system (R-DES) in this study[6], [7].

With “*Development Plan of Guanzhong Plain Urban Agglomeration*”, the contradiction between backward power grid construction and economic development has become increasingly prominent. It sets new requirements for power grid construction. Considering the existing economic level and natural resources in this area, in order to ensure the safety and reliability of energy supply in Guanzhong area, R-DES was developed.

2.2. Modeling formulation

This paper will base on the interval linear programming, aiming at system economy, and considering the factors such as energy availability, devices matching and economics under the premise of satisfying the user load. Get the optimal configuration and optimal operating mode of the system. The goal of R-DES model is to minimize the total system cost. It depends on the following equation:

$$\min f = (C_{Capital} + C_{OM} + C_{Fuel} + C_{Elec} - C_{Sub}) \quad (1)$$

(1) Devices cost:

$$C_{Capital} = 4/365 \times \left[\sum_i \sum_u Maxcap_{iu}^{\pm} \times PN_i^{\pm} \times CapCost_{iu}^{\pm} \times IRate / \left(1 - 1 / (1 + IRate)^{Tlife_i} \right) + \sum_u MaxCapC_u^{\pm} \times PNC_u^{\pm} \times CapCostC_u^{\pm} \times IRate / \left(1 - 1 / (1 + IRate)^{TlifeC_u} \right) + \sum_u MaxEStor_u^{\pm} \times PNS_u^{\pm} \times CapCostS_u^{\pm} \times IRate / \left(1 - 1 / (1 + IRate)^{TlifeS_u} \right) \right] \quad (2)$$

IRate is 10%[8].

(2) Operating cost:

$$C_{OM} = \sum_s \sum_h \sum_i \sum_u OM_{iu}^{\pm} \times G_{shiu}^{\pm} + \sum_s \sum_h \sum_u OMC_u^{\pm} \times CT_{shu}^{\pm} + 4/365 \times \sum_u OMS_u^{\pm} \times MaxEStor_u^{\pm} \quad (3)$$

(3) Fuel cost:

$$C_{Fuel} = \sum_s \sum_h \sum_i \sum_u PFuel_{iu}^{\pm} \times G_{shiu}^{\pm} / \eta_{i,u} \quad (4)$$

(4) Power grid purchase cost:

$$C_{Elec} = \sum_s \sum_h PElec_h \times EP_{sh}^{\pm} \quad (5)$$

(5) Subsidy:

$$C_{Sub} = 4/365 \times \sum_i \sum_u PSub_{iu}^{\pm} \times MaxCap_{iu}^{\pm} / Tlife_i + \sum_s \sum_h \sum_i \sum_u PSubV_{iu}^{\pm} \times G_{shiu}^{\pm} \quad (6)$$

Subject to:

(1) Maximum power constraints for devices:

$$G_{shiu}^{\pm} \leq PN_i^{\pm} \times MaxCap_{iu}^{\pm} \quad (7)$$

$$CT_{shu}^{\pm} \leq PNC_u^{\pm} \times MaxCap_u^{\pm} \quad (8)$$

$$\lambda G_{shi=NG,u=heat}^{\pm} \leq G_{shi=NG,u=elec}^{\pm} \quad (9)$$

(2) Solar photovoltaic panel generation constraints:

$$G_{s,h,i=Pv,u=elec}^{\pm} \leq PN_{i=Pv}^{\pm} \times SA \times SI_{sh}^{\pm} \times \eta_{i=Pv,u} \quad (10)$$

(3) Energy conversion devices conversion constraints:

$$\omega_{u=cold} \sum_i G_{s=sum,h,i,u=heat}^{\pm} = CT_{s=sum,h,u=heat}^{\pm} \tag{11}$$

$$\omega_{u=elec} \sum_i G_{s=sum,h,i,u=elec}^{\pm} = CT_{s=sum,h,u=elec}^{\pm} \tag{12}$$

$$\omega_u \sum_i G_{s=spr/aut/win,h,i,u}^{\pm} = CT_{s=spr/aut/win,h,u}^{\pm} \tag{13}$$

(4) Storage devices constraints:

Energy storage device at $h = 1$, which are expressed as follows:

$$EStor_{s,h=1,u}^{\pm} = 0 \tag{14}$$

$$IStor_{s,h=1,u}^{\pm} \geq 0 \tag{15}$$

$$OStor_{s,h=1,u}^{\pm} = 0 \tag{16}$$

When energy storage device is at $h > 1$. Its operation can be represented by the following formula:

$$EStor_{shu}^{\pm} = EStor_{s,h=1,u}^{\pm} + \alpha_u \times IStor_{s,h=1,u}^{\pm} - OStor_{s,h=1,u}^{\pm} \tag{17}$$

$$0 \leq EStor_{shu}^{\pm} + \alpha_u \times IStor_{s,h=1,u}^{\pm} - OStor_{s,h=1,u}^{\pm} \leq MaxEStor_u^{\pm} \tag{18}$$

$$0 \leq EStor_{shu}^{\pm} \leq MaxEStor_u^{\pm} \tag{19}$$

(5) Energy balance constraints:

$$CT_{s,h,u=elec}^{\pm} + EP_{sh}^{\pm} + OStor_{s,h,u=elec}^{\pm} \geq IStor_{s,h,u=elec}^{\pm} + ED_{s,h,u=elec}^{\pm} + CT_{s,h,u=cold}^{\pm} \times \gamma \tag{20}$$

$$CT_{s,h,u=heat/cold}^{\pm} + OStor_{s,h,u=heat/cold}^{\pm} \geq IStor_{s,h,u=heat/cold}^{\pm} + ED_{s,h,u=heat}^{\pm} \tag{21}$$

2.3. Data acquisition

The total construction area of the study area is 5.0×10^4 m². The cold and heat loads of users was simulated by Energy Plus 8.6 software and electrical loads was obtained through a questionnaire survey. The electric energy, cold and heat loads in this area are shown in Figure 1 and Figure 2. According to the "Standard Meteorological Data Book for Buildings", solar energy resources data are available[9]. The price of natural gas is 0.206 RMB/kWh and the electricity purchased from grid is 0.4983 RMB/kWh.

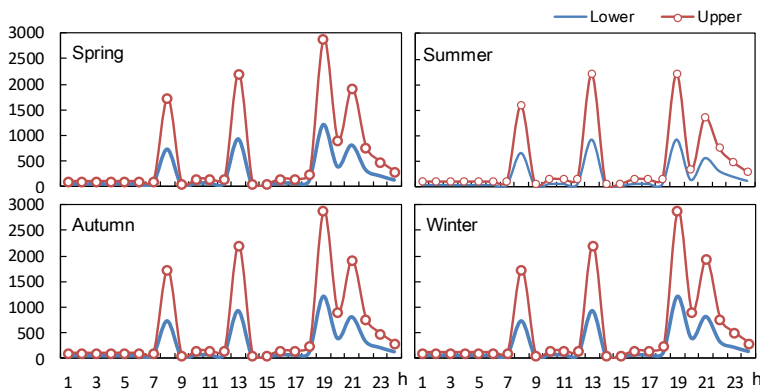


Figure 1. The electric energy loads (kWh)

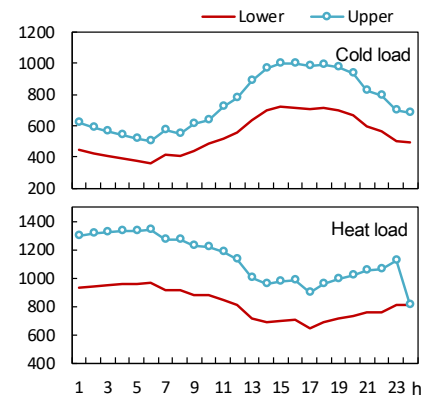


Figure 2. The cold/ heat load (kWh)

The main energy supply devices studied in this paper includes internal combustion engine generator set (NG), solar photovoltaic panel (PV), biomass boiler (BB), ground source heat pump (GP), absorption chiller (AC), heat exchanger (HE), ice-storage device (IS), heat storage tank (TS), battery (BA). Through the investigation of previous research literature and equipment products, the technical and financial characteristics of each equipment are summarized in Table 1[10].

Table 1. Technical and financial characteristics of equipment

Devices	Efficiency			Devices cost / RMB/kWh	Operating cost / RMB/kWh	Life / year
	Cold	Heat	Electric			
NG	0.35	0.50	—	[6625.6, 9234.4]	[0.06, 0.08]	30
PV	—	—	0.16	[6475.2, 9024.8]	[0.0084, 0.0012]	30
BB	—	0.85	—	[1158.9, 1615.1]	[0.07, 0.09]	20
GP	5.00	4.40	—	[8340.1, 11623.9]	[0.0087, 0.0113]	20
AC	1.20	—	—	[1230.7, 1715.3]	[0.007, 0.009]	20
HE	—	0.98	—	[167.9, 234.1]	[0.0018, 0.0026]	20
IS	0.65	—	—	[158.7, 221.3]	[0.17, 0.23]	20
TS	—	0.90	—	[75.2, 104.8]	[0.15, 0.21]	20
BA	—	0.75	—	[1488.9, 2075.1]	[6.93, 9.67]	13.5

3. Results Analysis

3.1. Energy consumption and carbon emissions analysis

In this paper, R-DES study is mainly based on natural gas and supplemented by renewable energy. Through municipal power grid construction to provide support and supplement to this system, to maximize the use of resources. Therefore, the amount of carbon discharged from this system is lower than that of a centralized energy system. R-DES reduces electric supply of the power grid construction by 29.0%~63.6%, which can reduce the loss of electric energy in transmission process. The carbon emission reduction rate of this system is 4.0%~49.6%, which is because system use renewable energy to reduce carbon emissions.

3.2. Optimal operation mode analysis

From Figure 3 we can see that internal combustion generator set does not work in the spring and autumn, so electrical loads are mainly provided by municipal power grid construction. This is due to that there is no requirement for cold and heat loads in the spring and autumn. The peak in electricity consumption shows in the morning, noon, and evening. Before these moments arrive, this system will store electricity to reduce the capacity of the power generation devices. The battery storage efficiency is 0.75. In Figure 3, electricity flowing into battery is higher than electricity flowing out of battery. When solar radiation intensity reaches photovoltaic panel power generation requirement, electric energy is generated for use by users. In Figure 3, solar photovoltaic panels generate relatively large amounts of electricity in spring and summer, and the amount of electricity generated in winter is relatively small.

From Figure 4 we can conclude that requirement for cold loads are mainly provided by lithium bromide chiller in summer. Cold loads do not fluctuate, and cold peak is usually concentrated in the time of period from 13:00 to 17:00.

From Figure 5 we can result that the heat production of primary heat generating devices includes biomass boiler and internal combustion generator set. After being converted to user through heat exchanger, since the conversion efficiency is 0.98. It can be seen from Figure 5 that there is no energy waste during heating process. In Figure 3, there is a serious overproduction of electricity in winter. With reference to Figure 5, this is because system generates heat while using internal combustion generating set to generate heat due to meet user's heat demand.

3.3. System cost analysis

Figure 6 is this system cost composition. The results show that devices cost accounting for approximately 50% of total cost in this system. Energy-generating devices consisting of internal combustion engine generator set and solar photovoltaic panels, resulting in higher system devices cost can be seen from Figure 6. In addition, the relevant policies of distributed energy system are imperfect, and subsidy is small. It is hoped that the state can increase subsidy so that renewable energy devices can be more widely used, which can promote the use and development of renewable energy.

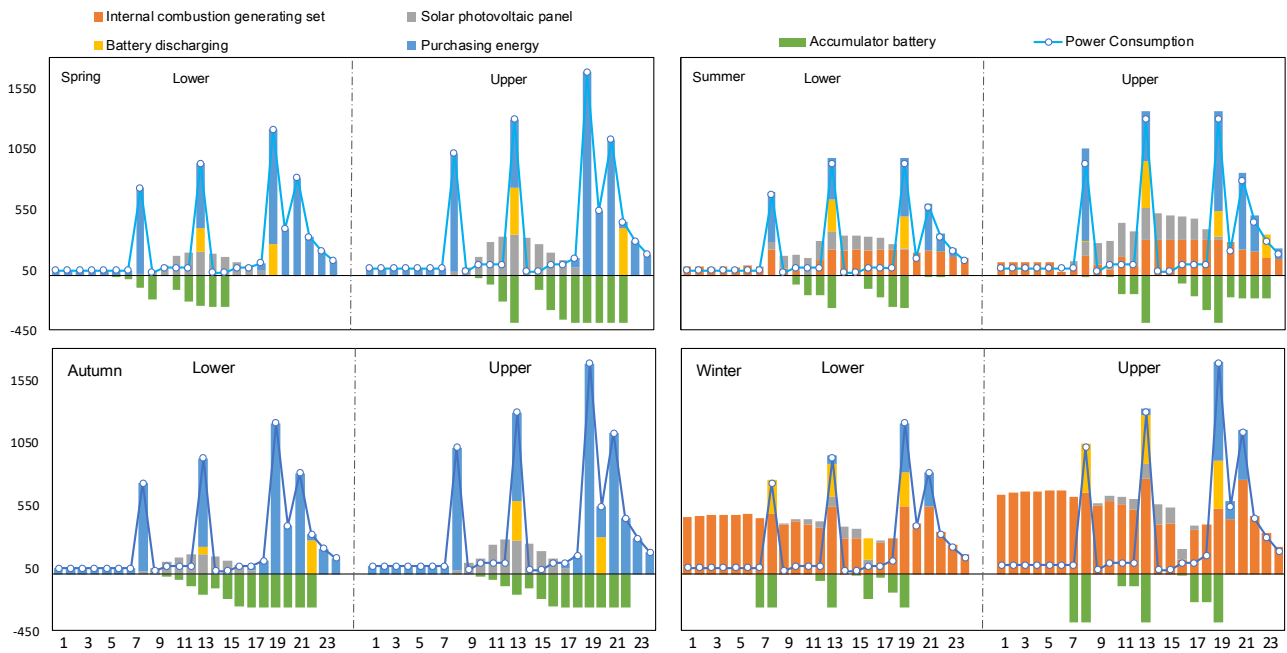


Figure 3. Power balance model for typical day (kWh)

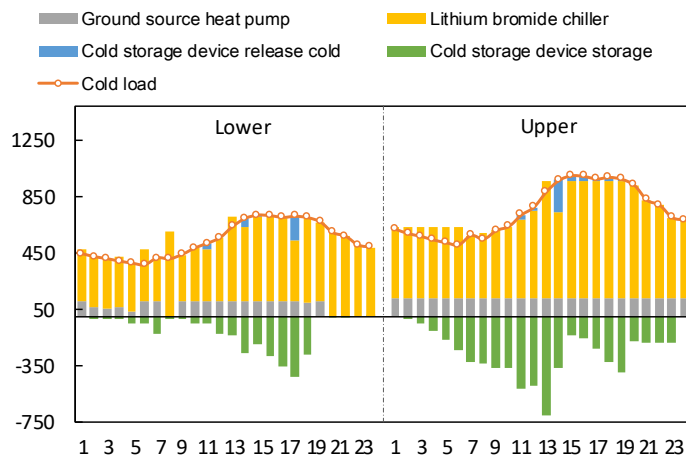


Figure 4. Cold balance model for typical summary day

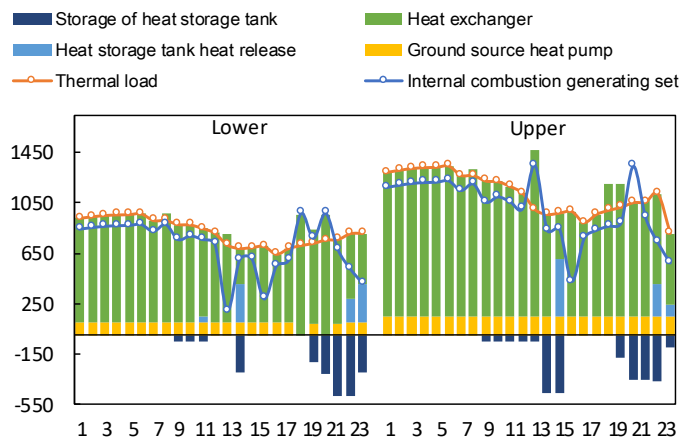


Figure 5. Heat balance model for typical winter day (kWh)

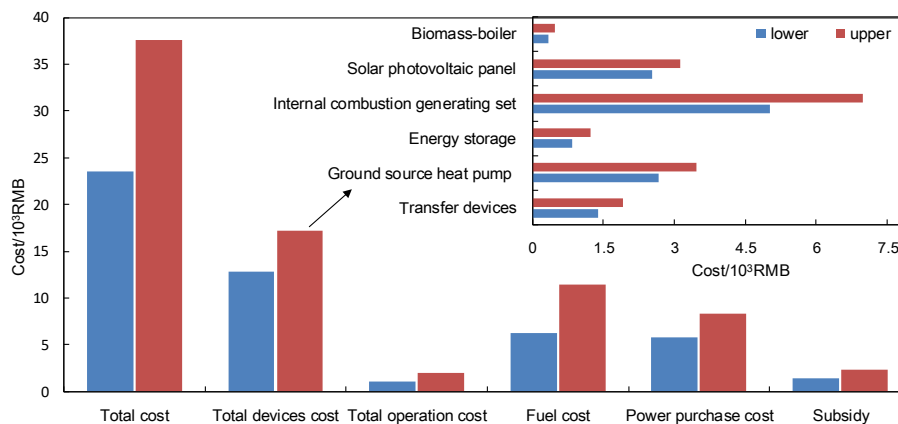


Figure 6. System cost composition

4. Conclusion

This paper establishes R-DES optimization model combined with renewable energy using the method of interval linear programming. Cold and heat loads are calculated by the software PlusPlus8.6 software simulation and questionnaire survey. Under premise of meeting needs of users, this system devices capacity, devices cost, devices efficiency and fuel price are comprehensively considered. Combined with abundant renewable energy in rural areas, the optimal configuration and optimal operation mode of Guanzhong rural area are calculated by LINGO11.0 software. This paper establishes R-DES model using the method of interval linear programming. Through analysis of results, the following conclusions can be drawn: a) The R-DES has obvious energy saving and emission reduction effects. The power supply of power grid construction reduced by 29.0%~63.6%, and carbon emission reduction rate is 4.0%~49.6%; b) R-DES can establish in renewable energy-rich rural areas and promote construction of new countryside; c) Due to the high price of devices using renewable energy, which will lead to increase system costs. It is recommended that the government should increase subsidies for renewable energy devices; d) It is recommended that R-DES should be connected to power grid construction to improve energy efficiency.

Acknowledgments

This research was supported by National Key Research and Development Program (2016YFC0207800), and National Natural Science Fund (51608422).

References

- [1] Liu Z, Wu D, Yu H, Ma W and Jin G 2018 Field measurement and numerical simulation of combined solar heating operation modes for domestic buildings based on the Qinghai-Tibetan plateau case. *Energy & Buildings*. **167**:312-21.
- [2] Allahdadi M, Nehi H M, Ashayerinasab H A and Javanmard M 2016 Improving the modified interval linear programming method by new techniques *Information Sciences*. **339**:224-36.
- [3] Yu F, Kikusato H, Yoshizawa S, Kawano S, Yoshida A, Shin-ichi T and Hayashi Y 2016. Distributed Energy Management for Comprehensive Utilization of Residential Photovoltaic Outputs *IEEE Transactions on Smart Grid*. (**99**): 1-1.
- [4] Mavromatidis G, Orehounig K and Carmeliet J 2018 A review of uncertainty characterisation approaches for the optimal design of distributed energy systems. *Renewable & Sustainable Energy Reviews*. **88**:258-77.
- [5] National Development and Reform Commission Ministry of Housing and Urban-Rural Development 2018 *Development Plan of Guanzhong Plain Urban Agglomeration*.

- [6] Liu Y F, Wang M, Wang D J and Zhou Y 2018. Feasibility analysis of solar energy and biomass energy combined heating resources in northwest China rural area. *Acta Energetica Solaris Sinica*. **39(4)**: 1045-51.
- [7] Shi Y X, Xu Y C and Wang P P 2018 Present situation of development and utilization of geothermal water resources in Guanzhong Basin and its impact on environment *Environment & Development*. **29(6)**:31-2.
- [8] Zhou Z, Liu P, Li Z and Ni W D 2013 An engineering approach to the optimal design of distributed energy systems in China *Applied Thermal Engineering*. **53(2)**:387-96.
- [9] Beijing: China Statistics Press 2017 *The Statistics Bureau of Shaanxi Province. Shaanxi Statistical Yearbook 2017*.
- [10] Zhang T, Zhu T, Gao NP and Wu Z 2015 Optimization Design and Multi-criteria Comprehensive Evaluation Method of Combined Cooling Heating and Power System *Proceedings of the Csee*. **35(14)**:3706-13.

Appendix: List of Symbols

Subscripts:

s season, s= spr/ sum/ aut/ win
 h hour, h=1, 2, ..., 24
 i device types, i=1, 2, 3. 1. energy production devices; 2. energy conversion devices; 3. energy storage devices.
 u energy types, u=cold/ heat/ electric

Decision variables:

$G_{s,h,i,u}$ production capacity devices produce energy, kWh
 $CT_{s,h,u}$ energy conversion devices produce energy, kWh
 $MaxEStor_u$ design capacity of energy storage devices, kWh
 $EStor_{s,h,u}$ energy in energy storage devices, kWh
 $IStor_{s,h,u}$ energy to enter the energy storage devices, kWh
 $OStor_{s,h,u}$ energy flowing out of the energy storage devices, kWh
 $EP_{s,h}$ power grid purchase, kWh

Parameters:

$C_{Capital}$ devices cost
 C_{OM} running cost
 C_{Elec} power grid purchase cost
 C_{Fuel} fuel cost
 C_{Sub} subsidy cost
 $MaxCap_{i,u}$ design capacity of production devices, kW
 $MaxCapC_u$ design capacity of energy conversion devices, kW
 PN_i number of production devices
 PNC_u number of energy conversion devices
 PNS_u number of energy storage devices
 $CapCost_{i,u}$ production devices unit capacity devices cost, RMB/kW
 $CapCostC_u$ energy conversion devices unit capacity devices cost, RMB/kW
 $CapCostS_u$ energy storage devices unit capacity

devices cost, RMB/kW
 $IRate$ depreciation rate
 $Tlife_i$ production devices life, year
 $TlifeC_u$ energy conversion devices life, year
 $TlifeS_u$ energy storage devices life, year
 $OM_{i,u}$ production devices operation cost, RMB/kWh
 OMC_u energy conversion devices operation cost, RMB/kWh
 OMS_u energy storage devices operation cost, RMB/kWh
 $PFuel_{i,u}$ fuel price, RMB/kWh
 $\eta_{i,u}$ production devices productivity efficiency
 $PElec_h$ hourly electricity price, RMB/kWh
 $PSub_{i,u}$ one-time investment subsidy for devices, RMB/kWh
 $PSubV_{i,u}$ devices operation subsidy, RMB/kWh
 λ ratio of power generation and surplus heat of gas combustion engine, 0.7
 SA monolithic PV plate area, m²
 $SI_{s,h}$ direct solar radiation, kW/m²
 ω_u efficiency of energy conversion devices
 α_u efficiency of energy storage devices
 $ED_{s,h,u}$ user loads, kWh
 γ power dissipation factor of absorption chillers

The Unit Commitment Model and Analysis for Promoting Clean Energy Consumption with Considering of Tie Line Plan Adjustment

Xu Zhang¹, Xinhong Shi¹, Bingquan Zhu², Ke Sun² and Yanwei Xiao²

¹Nanjing Research Division, China Electric Power Research Institute, Nanjing 210003, China

²Power Dispatch and Control Centre, Zhejiang Province Electric Power Company, Hangzhou 310007, China

E-mail: zhangxu@epri.sgcc.com.cn

Abstract. In recent years, China's clean energy has developed rapidly. The development level of clean energy does not match the local power consumption, resulting in a large number of abandoned winds and abandoned light. With the gradual completion of the UHV network, the transmission capacity between regions has been rapidly enhanced, providing a broad space for optimizing the allocation of resources across a wide range of areas and improving the level of clean energy consumption. In order to cope with the problem of difficult local consumption in clean energy delivery areas and current cross-regional power delivery methods, this paper considers the factors of the adjustment of the tie line plan and increases the consumption of new energy through more reasonable tie line planning based on the traditional unit commitment algorithm. A case study shows that the model proposed in this paper can promote cross-regional consumption of clean energy and improve the economics of the interconnected power grid.

1. Introduction

Clean energy is developing rapidly in China, showing a concentrated distribution and reverse distribution of load. The clean energy power plants are mainly concentrated in the northwest, north and northeast regions, and are transported to the east-central load centre through the ultra-high voltage transmission system [1]. At present, there are a series of problems in the development of clean energy, such as abandoning wind, abandoning light and abandoning water [2]. Promoting clean energy consumption through the optimal allocation of power generation resources has become a hot research topic.

Due to the uncertainty of wind power generation, many studies have included the uncertainty of wind power forecasting into the unit commitment (UC) [3] [4] [5]. In order to improve the level of clean energy consumption, unit commitment has been optimized by many scholars. Local consumption of clean energy is a top priority strategy. Based on grid peaking capacity and transmission constraints, clean energy units are arranged for generation as much as possible [6], [7]. If the local clean energy is surplus, it is necessary to optimize the regional power grid planning and realize the joint dispatch of the two-level power grid in the district and the province [8], [9]. Finally, according to the characteristics of inter-area load difference, peak-to-valley difference, and time difference, resource allocation can be realized in a larger range to maximize the consumption of clean energy [10]. Cross-regional long-distance transportation of clean energy becomes the main means of consumption



The construction of cross-provincial power transmission channels in China has made it possible to optimize the deployment of clean energy in China. This paper optimizes the generation and transmission resources and optimizes the tie-line power plan to improve the capacity of clean energy in inter-regional clean energy. First, the minimum operating mode of all thermal power units is constrained, and the maximum consumption of local clean energy in the sending area is calculated by the optimal unit commitment. Then, optimize the tie line power plan to explore the clean energy acceptance capability of the receiving area, and use the characteristics of load difference, peak-to-valley difference and time difference between the two areas to achieve the maximum consumption of clean energy at both ends.

The Section 2 of this paper establishes a UC model for promoting the clean energy consumption considering the adjustment of the tie line plan. Compared with the traditional UC model, the model considers the multiple constraints of the tie line plan adjustment. Section 3 calculates the optimal power curve of the cross-region tie line, and analyzes the expansion of the cross-region trading channel demand providing reference for promoting cross-regional consumption of clean energy.

2. UC model with considering the adjustment of the tie line plan

In the traditional optimization scheduling, the UC problem is to determine the resource allocation problem according to the load forecasting level in a certain period, and mainly optimize the unit opening and closing mode and the output level [11]. The goal is to minimize the total cost of the system under certain constraints (including unit operation, start-up and shutdown costs) [12].

In this paper, we hope to achieve the maximum consumption of clean energy by optimizing the generation and transmission resources. So the objective function expression is:

$$\max \text{CleanEnergy} = \text{sum}[i_{ce}, t), pi(i_{ce}, t, brch)] * PrdMin / 60 \quad (1)$$

Where i_{ce} represents clean energy unit, $pi(i_{ce}, t, brch)$ represents the power of i_{ce} at t point in the region $brch$, $PrdMin$ is constant parameter representing time interval of unit power generation plan.

2.1. System operation constraints

(1) Constraints of thermal unit minimum operation mode.

This constraint indicates that the online capacity and number of online units of unit group in the system cannot be less than a given value.

$$\text{sum}[i | \text{GroupUnitList}(grp, i) = 1, Ui(i, t)] \geq \text{MinOnUnitNum}(grp) \quad (2)$$

$$\text{sum}[i | \text{GroupUnitList}(grp, i) = 1, Pi(i, t)] \geq \text{MinOnUnitCap}(grp) \quad (3)$$

Where unit on-off flag $Pi(i, t)$ and unit power $Pi(i, t)$ are optimizable variables with other parameters. $\text{GroupUnitList}(grp, i)$ represents whether unit i belongs to unit group grp . $\text{MinOnUnitNum}(grp)$ represents the minimum number of on-line units and $\text{MinOnUnitCap}(grp)$ represents the minimum on-line capacity.

(2) Constraints of clean energy power forecast.

$$Pi(wd, t) \leq \text{SingleWindPlantPowerForecast}(wd, t) \quad (4)$$

$$pi(se, t) \leq \text{SingleSunPlantPowerForecast}(se, t) \quad (5)$$

Where $\text{SingleWindPlantPowerForecast}(wd, t)$ represents wind power generation forecast and $\text{SingleSunPlantPowerForecast}(se, t)$ represents photovoltaic power generation forecast.

(3) Constraints of Hydropower generation.

$$\text{sum}[(i,t) | \text{HydroPlantUnitList}(hdp,i), pi(i,t)] * \text{PrdMin}/60 \leq \text{HydroEnergyLimit}(hdp) \quad (6)$$

$$\text{sum}[(i,t) | \text{HydroPlantUnitList}(hdp,i), pi(i,t)] * \text{PrdMin}/60 \geq \text{HydroEnergyLimitDown}(hdp) \quad (7)$$

Where pi is optimizable variable. $\text{HydroPlantUnitList}(hdp,i)$, which is a boolean parameter, represents whether unit i belongs to hydropower unit group hdp . $\text{HydroEnergyLimit}(hdp)$ and $\text{HydroEnergyLimitDown}(hdp)$ respectively indicate the upper and lower limit values of the hydropower group generation.

(4) Constraints of system balance.

$$\sum_{i=1}^I p_i(t) = p_d(t) \quad (8)$$

Where the total power generation of the system is equal to the total power consumption.

(5) Constraints of spinning reserve.

$$\sum_{i=1}^I \bar{r}_i(t) \geq \bar{p}_r(t) \quad (9)$$

$$\sum_{i=1}^I \underline{r}_i(t) \geq \underline{p}_r(t) \quad (10)$$

Where $\bar{r}_i(t)$ and $\underline{r}_i(t)$ respectively represents the upper and lower spinning reserve which unit i can supply at time t . $\bar{p}_r(t)$ and $\underline{p}_r(t)$ respectively represents system demand of the upper and lower spinning reserve at time t .

2.2. Unit constraints

(1) Constraints of unit power.

$$\underline{p}_i u_i(t) \leq p_i(t) \leq \bar{p}_i u_i(t) \quad (11)$$

(2) Constraints of minimum running time and minimum outage time.

$$(V_{t,j}^{\text{on}} - T_j^{\text{min-on}}) \cdot f_1(U_i(t-1), U_i(t)) \geq 0 \quad (12)$$

$$(V_{t,j}^{\text{off}} - T_j^{\text{min-off}}) \cdot f_2(U_i(t), U_i(t-1)) \geq 0 \quad (13)$$

(3) The available state of unit.

$$u_i(t) = 0, t \in T_r \quad (14)$$

Where T_r is the time period of unit maintenance.

2.3. Analysis and modelling of tie line constraints

In this paper, all tie lines is high voltage direct current (DC) lines. All analysis and modelling are based on high voltage direct current (HVDC) lines.

(1) Constraints of tie line capacity

$$0 \leq \text{tie}P(\text{tie}, t) \leq \text{tie}P\text{Max}(\text{tie}) \quad (15)$$

Where $\text{tie}P\text{Max}(\text{tie})$ is the tie line capacity and $\text{tie}P(\text{tie}, t)$ is tie line power at time t .

(2) Constraints of tie line power change rate

$$\text{tie}P(\text{tie}, t) - \text{tie}P(\text{tie}, t-1) \leq \text{RampUp}(\text{tie}, t)\Delta t \quad (16)$$

$$\text{tie}P(\text{tie}, t-1) - \text{tie}P(\text{tie}, t) \leq \text{RampDown}(\text{tie}, t)\Delta t \quad (17)$$

Where $\text{RampUp}(\text{tie}, t)\Delta t$ and $\text{RampDown}(\text{tie}, t)\Delta t$ respectively represent upper and lower limits of power change rate. The tie line power change at adjacent time period cannot break the limits.

(3) Constraints of tie line continuous power adjustment direction

In order to protect the DC converter and ensure the smoothness of the DC plan, the increase and decrease of the adjacent time period cannot be adjusted in the opposite direction. Defining the boolean variables $x(\text{tie}, t)$, $x^+(\text{tie}, t)$, $x^-(\text{tie}, t)$ separately, where indicate whether the DC power is changed in each period, whether it changes in the forward direction (increased power), and whether it changes in the reverse direction (reduced power). The Related constraints are as follows:

$$x^+(\text{tie}, t) + x^-(\text{tie}, t) = x(\text{tie}, t) \leq 1 \quad (18)$$

The power of adjacent period cannot be adjusted. The constraints are as follows:

$$x^+(\text{tie}, t) + x^-(\text{tie}, t+1) \leq 1 \quad (19)$$

$$x^+(\text{tie}, t+1) + x^-(\text{tie}, t) \leq 1 \quad (20)$$

The value $x^+(\text{tie}, t)$ and $x^-(\text{tie}, t)$ can be obtained by constraining the change in DC power $\text{tie}P(\text{tie}, t)$ and by introducing auxiliary boolean variables $z_1(\text{tie}, t)$ and $z_2(\text{tie}, t)$.

$$\text{tie}P(\text{tie}, t) - \text{tie}P(\text{tie}, t-1) \leq M_1 z_1(\text{tie}, t) \quad (21)$$

$$x^+(\text{tie}, t) \geq z_1(\text{tie}, t) \quad (22)$$

$$\text{tie}P(\text{tie}, t-1) - \text{tie}P(\text{tie}, t) \leq M_2 z_2(\text{tie}, t) \quad (23)$$

(4) Constraints of the time interval of tie line power adjustment

After the DC power is adjusted once, at least a minimum time interval is run smoothly. In order to maintain the stability of the DC plan, after the DC power is adjusted once (single or multiple consecutive periods of rise or fall), at least a minimum interval is smoothly run. The following formula can be obtained with the values of boolean variables $IsTieUp(\text{tie}, t)$ and $IsTieDown(\text{tie}, t)$:

$$IsTieDown(\text{tie}, t) - \sum_{\tau=t+1}^{t+N_T} IsTieUp(\text{tie}, \tau) \leq 1 \quad (24)$$

Where N_T is the minimum number of intervals in which the DC line cannot be adjusted.

Constraints are obtained by introducing an additional boolean variable $y(\text{tie}, t)$:

$$IsTieUp(\text{tie}, t) \geq x(\text{tie}, t+1) - y(\text{tie}, t) \quad (25)$$

$$IsTieDown(\text{tie}, t) \geq x(\text{tie}, t) - y(\text{tie}, t) \quad (26)$$

$$y(\text{tie},t) \leq x(\text{tie},t) \quad (27)$$

$$y(\text{tie},t) \leq x(\text{tie},t+1) \quad (28)$$

$$y(\text{tie},t) \geq x(\text{tie},t)+x(\text{tie},t+1)-1 \quad (29)$$

(5) Constraints of interface power flow

$$P_{ij}(t) \leq \overline{P}_{ij} \quad (30)$$

Where P_{ij} and \overline{P}_{ij} represents interface power flow and its limit value.

3. Case study

3.1. Case setting

The actual two regions are selected as the research object. Region 1 is the delivery end with rich clean energy. Region 2 is the receiving end which is load center. The two regions are connected by 3 DC lines. The capacity of each tie line is shown in Table 1. Under the condition that the basic constraints of DC lines are satisfied, the tie line power curve can be freely optimized without increasing the cost of receiving region.

Table 1. The capacity of tie line

Tie Line	Capacity(MW)
Tie line 1	4000
Tie line 2	3500
Tie line 3	1200

3.2. Input data processing

In the model, each power plant is equivalent to one unit. If the capacity is too large, it will be divided into several equivalent units. The Region 1 has 74 million kW of new energy installed capacity, including 308 wind power plants and 506 photovoltaic power stations. 32 million new energy installed at Region 2, including 120 wind power plants and 329 photovoltaic power stations.

The minimum output of the heat supply unit in winter is 50% of its rated capacity. The minimum output of nuclear power unit is 80% of its rated capacity. The minimum output of hydropower unit is 20% of its rated capacity. The minimum output of photovoltaic unit and wind turbine is 0. The maximum output of all units is equal to the unit capacity.

The minimum operating time and minimum outage time of the thermal power unit is 36 hours. These time of nuclear power unit are 2,500 hours. For other types of units, the minimum operating time and minimum outage time are set as 0.

The system load is utilized for the actual load in 2017, and the system spinning reserve is set to 2% of the load.

Regional clean energy forecast electricity uses clean energy generation curve and the proportion of abandoned wind in 2017. The clean energy power of a single plant is predicted to be calculated from the region clean energy power forecast and the installed capacity of a single plant account for the proportion of all such clean energy installed in the region.

3.3. Results analysis

After optimization calculation, the proportion of abandoned wind in Region 1 is 1.62%. Compared with the actual transaction, the proportion of abandoned wind is reduced by 49.56% adding the use of 598 million kWh of wind power, and the maximum consumption of wind power is 5.27 billion kWh.

The proportion of abandoned light in Region 1 is 2.76%. Compared with the actual transaction, the proportion of abandoned photovoltaic is reduced by 39.8%, the power of abandoned wind is reduced by 120 million kWh, and the maximum consumption of photovoltaic is 2.38 billion kWh. Table 2 shows the power values before and after optimization of each tie line.

Table 2. The power values of each tie line before and after optimization

Periods	power before optimization (MW)			power after optimization (MW)		
	Tie line 1	Tie line 2	Tie line 3	Tie line 1	Tie line 2	Tie line 3
1	2400	980	777	3713.857	1800	550.10
2	2400	980	777	3713.857	1800	1105.10
3	2400	980	777	3713.857	1800	1110
4	2400	980	777	3713.857	1800	1110
5	2400	980	777	3713.857	1800	1110
6	2400	980	777	3713.857	1800	1110
7	2400	980	777	3713.857	1800	1110
8	2400	1190	777	3713.857	1800	1110
9	2400	1400	1110	3463.909	1800	1110
10	3000	1400	1110	3463.909	1800	1110
11	3000	1400	1110	3463.909	3000	1110
12	3000	1400	1110	3463.909	3000	1110
13	3000	1400	1110	3463.909	3000	1110
14	3000	1400	1110	3463.909	3000	1110
15	3000	1400	1110	3463.909	3000	1110
16	3000	1400	1110	3463.909	3000	1110
17	3000	1400	1110	3463.909	3000	1110
18	3000	1400	1110	2759.172	1556.25	1110
19	3000	1400	1110	2759.172	56.25	1110
20	3000	1400	1110	2759.172	56.25	1110
21	2400	1400	1110	2759.172	56.25	1110
22	2400	1190	1110	2759.172	56.25	1110
23	2400	980	1110	2759.172	1556.25	1105.10
24	2400	980	777	3713.857	1800	550.10
Electricity (MWh)	64200	29400	23643	81154.93	44137.5	25510.4
Total(MWh)	117243			150802.83		

Corresponding to Table 2, Figure 1 shows tie line power curve before and after optimization. Symbol b represents before optimization and Symbol a represents after optimization.

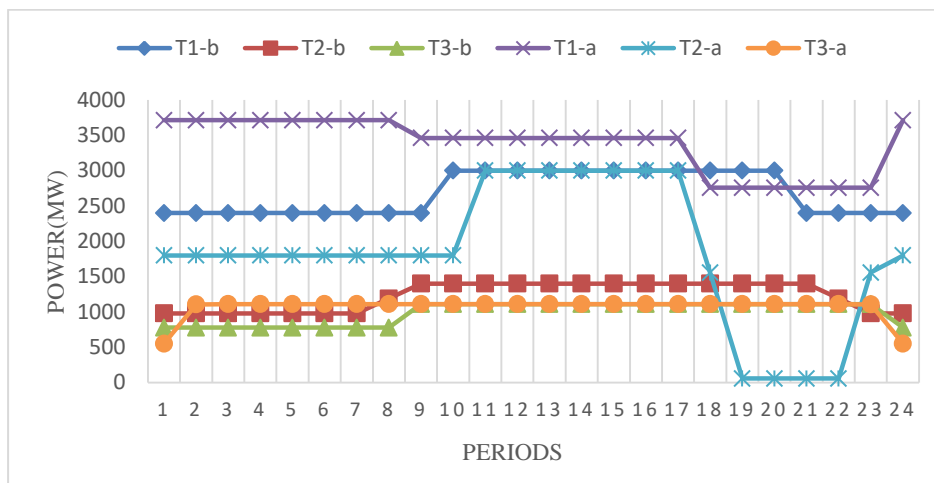


Figure 1. Power curves of tie lines.

According to Table 2 and Figure 1, the capacity of the regional transmission channel is more fully utilized, but the upper limit has not been reached. There is still a lot of room for clean energy consumption.

4. conclusion

In order to promote cross-regional consumption of clean energy, this paper analyzes and models the operational characteristics of tie line considering the DC line polarization adjustment direction constraint, the adjustment rate constraint and the adjustment interval constraint in the traditional unit commitment algorithm. Coordinating the output plans of traditional thermal power and new energy to promote the use of regional transmission channels and maximize the use of clean energy. The study shows that adjusting the tie line plan can maximize the consumption of clean energy according to the characteristics of inter-regional load difference, peak-to-valley difference and time difference.

5. References

- [1] Liu Zhengya, Zhang Qiping and Dong Cun, Efficient and security transmission of wind, photovoltaic and thermal power of large-scale energy resource bases through UHVDC projects, 2014 *Proceedings of the CSEE*. **34(16)** 2513-2522
- [2] Wang Jianhui, Botterud A and Miranda V, Impact of wind power forecasting on unit commitment and dispatch, 2009 *Proceedings of the 8th International Workshop on Large-scale Integration of Wind Power into Power Systems*
- [3] Wang Caixia, and Lu Zongxiang, Unit commitment based on wind power forecast, 2011 *Automation of Electric Power Systems*. **35(7)** 13-17
- [4] Tuiz P A, Philbrick C R and Sauer P W, Wind power day-ahead uncertainty management through stochastic unit commitment policies, 2009 *Proceedings of Power Systems Conference and Exhibition*. 1-9
- [5] Wang Caixia, Qiao Ying and Lu Zongxiang, Day-ahead dispatch mode for wind-thermal power system in low-carbon economy, 2011 *Automation of Electric Power Systems*. **35(22)** 111-117
- [6] Li Pengbo, Luo Rongjun and Mou Chunxiao, Digestion of wind power based on unit commitment, 2015 *Advanced Technology of Electrical Engineering and Energy*. **34(8)** 25-30
- [7] Liu Dewei, Huang Yuehui, Wang Weisheng and Guo Jianbo, Analysis on provincial system available capability of accommodating wind power considering peak load dispatch and transmission constraints, 2011 *Automation of Electric Power Systems*. **35(22)** 77-81
- [8] Yuan Tiejia, Peng Chaofeng and Mei Shengwei, A partitioning method to enhance accommodation capability of power network with balanced region of wind power, 2015 *Advanced Technology of Electrical Engineering and Energy*. **39(8)** 2129-2134

- [9] Wang Xiuli, Li Jun and Huang Bin, A two-stage optimal dispatching model for provincial and regional power grids connected with wind farms to promote accommodation of wind power, 2015 *Power System Technology*. **39(7)** 1833-1838
- [10] Xu Qian Yao, Kang Chongqing and Jiang Changming, Preliminary analysis on wind power accommodation system from multiple temporal and spatial scale perspective, 2013 *Power System Protection and Control*. **41(1)** 28-32
- [11] Baldick R, The generalized unit commitment problem, 1995 *IEEE Trans. Power Syst.* **10(1)** 465-475
- [12] Carrion M and Arroyo J M, A computationally efficient mixed-integer linear formulation for the thermal unit commitment problem, 2006 *IEEE Trans. Power Syst.* **21(3)** 1371-1378

Acknowledgments

This work was supported by the Science and Technology Foundation of Zhejiang Province Electric Power Company “Research on Key Technologies of Zhejiang Electricity Spot Market Technical Support System” and the Science and Technology Foundation of State Grid Corporation of China “Research and Development of Provincial Electricity Spot Market Operation Deduction Platform”.

Performance Analysis of the BIPV of an Industrial Park in Wuhan

BaJingkang¹, Huang Xiaoli², Yan Guogang³ and WangXiaojing^{1*}

¹ Wuhan Textile University Wuhan 430074, China

^{1*} Wuhan Textile University Wuhan 430074, China

² Hubei PV center of Engineering&Technology Wuhan 430074, China

³ Hubei PV center of Engineering&Technology Wuhan 430074, China

E-mail:584667356@qq.com¹,wxjisme@126.com^{1*},362468691@qq.com²,
19881090@qq.com³

Abstract: The performance of BIPV system is a crucial factor for its development. This paper chooses PV arrays installed on an industrial park buildings in Wuhan as a research object. The performance of PV array has been investigated at different tilt angles and orientations on the meteorological conditions of Wuhan. The performance of the amorphous silicon BIPV system and that of the polysilicon BIPV system are presented. The two BIPV systems are both 30 kW, with a tilt angle of 20 ° and facing south. The performance analysis shows that average monthly output energy of the polysilicon system and that of the amorphous silicon system are 2440.85kWh and 2209.14kWh respectively. The performance of amorphous silicon BIPV system is better in May, June, July and August. The maximum monthly output energy can be obtained in August (3768kWh and 3308kWh).For the amorphous silicon BIPV systems facing south and with different tilt angles of 20 ° and 10 °, more output energy can be obtained from the amorphous silicon BIPV system with a tilt angle of 20 °.The performance of the amorphous silicon BIPV systems oriented facing south with a tilt angle of 10 ° and that of the amorphous silicon BIPV systems oriented facing north with the same tilt angle are also analyzed respectively in this paper. These analyzes will provide a reference for the development of BIPV in Wuhan.

1. Introduction

With global environmental concerns and escalating demands for energy, renewable energy is becoming increasingly important. One of the biggest energy consumers is the buildings. According to the survey of International Energy Agency, building energy consumption accounts for 32% of the world's energy consumption [1]. So the concept of zero energy building (ZEB) is an attractive approach to reduce the energy requirement of buildings leading to a more sustainable society [2], [3]. To date, solar energy is the most abundant inexhaustible and clean of all the renewable energy resources. Among the ways to utilize the solar energy, BIPV is the most promising way [4].

In BIPV systems, some traditional building materials are replaced by photovoltaic materials, such as the roofs, skylights or facades [5]. The BIPV has the advantage of lower cost by reducing normal construction costs of building materials and labor for parts of the building replaced by BIPV modules [5]. The BIPV system is considered as a functional part of the building structure and is architecturally integrated into the building's design [6]. The most important part of the system is the photovoltaic modules, which can produce electricity [7], [8]. When in the absence of other energy generation



systems, the BIPV can balance the energy demand of the building [9].

Wuhan is a fast-growing city and the area of buildings is very large. The solar energy is abundant in Wuhan. All these provide good conditions for the development of BIPV. There are some investigations concerning the similar topics but few are conducted in Wuhan[10]. For this reason, an experimental study of the BIPV systems in Wuhan was presented. This paper studied the performances of different BIPV systems. The BIPV systems include systems with different tilt angles and orientations, an amorphous silicon BIPV system and a polysilicon BIPV system. Besides producing energy, all the PV arrays replace the traditional roof-tile as actual parts of the buildings.

2. The BIPV system

Wuhan is located at latitude 30°N and has a subtropical monsoon humid climate. The rainfall and sunshine in Wuhan is abundant. It has an annual average temperature of 15.8°C-17.5°C. The summer is hot and winter is cold. July and August is the hottest month with an average temperature of 28.7°C while January is the coldest with an average of 0.4°C. The summer is long for 135 days. The annual average sunshine time is up to 2000 hours and annual average frost-free period is up to 240 days. The solar elevation angle is up to 83°.

In this paper, three groups of BIPV systems are analyzed and are all nominal 30 kWp. The BIPV systems are composed of modules of 90 Wp. The modules are arranged in six strings. Fig.1 shows the electrical diagram of the modules of the BIPV systems. The BIPV systems run well and are in the same location, an industrial park in Wuhan. The first group are polysilicon BIPV system and amorphous silicon BIPV system oriented facing south with a tilt angle of 20°. The second group are the amorphous silicon BIPV systems oriented facing south with different tilt angles of 10° and 20°. The third group are the amorphous silicon BIPV systems with a tilt angle of 10° oriented facing south and north respectively. The three groups are showed to analyze the performance of the systems with different material, angles and orientations. All the systems are grid-connected by the same inverter. The monthly power output was measured and recorded in 2015 by data collection system automatically.

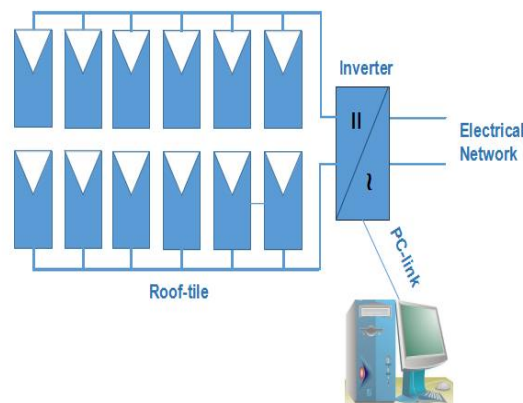


Figure 1. Electrical diagram of the modules of the BIPV systems.

3. Results and discussion

3.1 The performance of polysilicon BIPV system and amorphous silicon BIPV system

The monthly power output of the two BIPV systems is shown in Fig. 2. The maximum values of monthly output energy of the two BIPV systems can both be obtained in August (3308kWh and 3768kWh), in which the solar irradiance are the highest. The average monthly output energy of polysilicon BIPV system is 2440.85kWh, while that of the amorphous silicon BIPV system is 2209.14kWh, the latter is 90.5% of the former. The performance of the two BIPV systems is the best in summer. From May to August the performance of the amorphous silicon BIPV system is better than that of the polysilicon BIPV system. This is because that the temperature is high in the four months and that the temperature coefficient of polysilicon is larger than that of amorphous silicon. The energy conversion efficiency will become lower with the increase of the temperature. In other months, the temperature is not that high and the influence of temperature is reduced, so the performance of the

polysilicon BIPV system is better. In Spring, the performance of the systems becomes better and better with the increasing irradiance. In Autumn, the monthly output energy is reduced month by month with the decreasing of the irradiance. In Winter, because of the lower temperature, irradiance and snow, the output energy is the least of the four seasons. This will provide a reference for the design and investment of the BIPV systems.

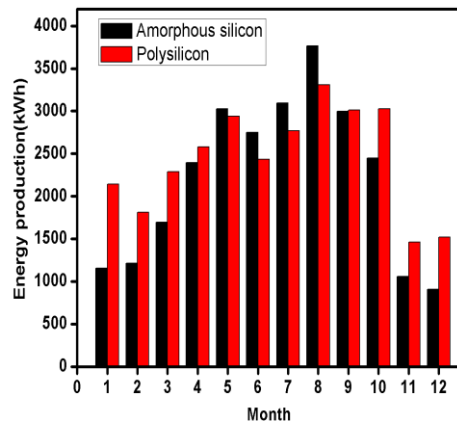


Figure 2. Monthly energy production from polysilicon BIPV system and amorphous silicon BIPV system

3.2. The performance of BIPV systems with different title angles

The performance of the BIPV systems with different title angles is showed in Fig.3. The maximum monthly energy production of the two BIPV systems both can be obtained in August, 3768kWh and 3540kWh respectively. It can be found that the performance of BIPV system with a tilt angle of 20° is better than that of BIPV system with a tilt angle of 10°. This is because that Wuhan is located at latitude 30° and the theoretical optimum tilt angle is about 30° [5]. The closer to the optimum tilt angle, the more the direct radiation on the

photovoltaic module is. On general sunny day, the direct radiation is the main factor to the energy output of the system. According to the weather forecast for Wuhan in 2015, many days are rainy, cloudy or snowy each month and in this climate, the irradiance is mostly of diffuse nature due to the scattering of sunlight by the predominantly overcast sky. Thus the impact of the tilt angles on the performance of the BIPV systems is reduced. The energy production of the two systems is similar and has little difference. In many cases, the design of BIPV should not only consider the amount of power generation, but also take the beauty, strength and lots of other factors into account. In general, the slope of the tile roof should not be less than 20%.

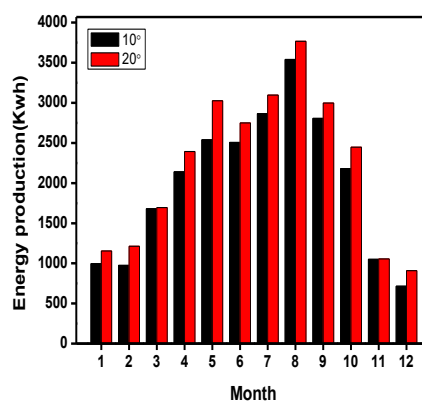


Figure 3. Monthly energy production from BIPV systems with different title angles

3.3. The performance of BIPV systems with different orientations

Fig. 4 shows the energy production of the BIPV systems with different orientations. The performance of the BIPV system facing south is better than that of the BIPV system facing north. In order to analyze the performance of the two BIPV systems with different orientations, the energy performance ratio defined as the ratio of the monthly output energy of the BIPV system oriented facing north to that of the BIPV system oriented facing south is shown in the Fig.5. The performance of the BIPV systems is the best in the August (4714kWh and 3743kWh) and the difference between the two BIPV systems is bigger in May, June, July and August than other months. This is because that the irradiance in August is the highest in the year of 2015 and that the direct irradiance in the four months is higher than that in other months.

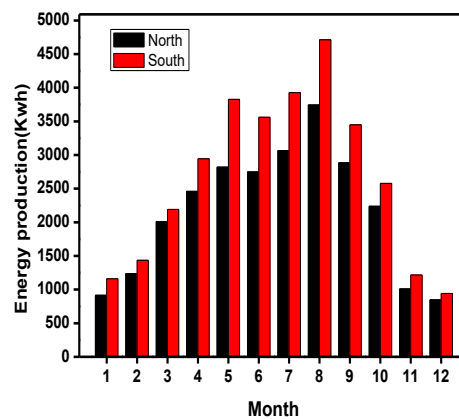


Figure 4. Monthly energy production from BIPV systems with different orientations

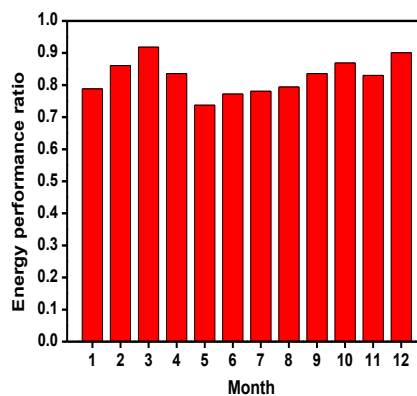


Figure 5. The ratio of the monthly output energy of the BIPV system oriented facing north to the that of the BIPV system oriented facing south

4. Conclusions

The presented performance of BIPV systems is a viable and reliable contributor in achieving the zero-energy target for the building in Wuhan. After analyzing the performance of the BIPV systems, the following conclusions can be drawn.

1. When the BIPV systems are both with a tilt angle of 20° and facing south, the monthly energy production of the amorphous silicon BIPV system is more than that of polysilicon BIPV system from May to August. In other months, the performance of the polysilicon BIPV system is better. In summer, the energy production of the two systems is the most and that is the least in winter.

2. The performance of amorphous silicon BIPV system with a tilt angle of 20° is better than that of amorphous silicon BIPV system with a tilt angle of 10° . The difference of the yearly energy production of the two BIPV systems is up to 2514kWh.

3. The performance of the BIPV system oriented facing south is better than that of the BIPV system oriented facing north. The performance of the BIPV systems is the best in the August and the difference between the two BIPV systems is bigger in May, June, July and August than other months. The difference of the yearly energy production of the two BIPV systems is up to 5958kWh.

5. Acknowledgments

This work was supported by the Schools and enterprises to build "basic data test platform for photovoltaic applications (Wuhan)" (Grant No. 14349).

6. References

- [1] T. Yang, A. K. Athienitis. A review of research and developments of building-integrated photovoltaic/thermal (BIPV/T) systems. *Renewable and Sustainable Energy Reviews*. 2016,66:886-912.
- [2] E. Sánchez, J. Izard. Performance of photovoltaics in non-optimal orientations: An experimental study. *Energy and Buildings*. 2015,87:211-9.
- [3] S. Wittkopf, S. Valliappan, L. Liu, K. S. Ang, S. C. J. Cheng. Analytical performance monitoring of a 142.5kWp grid-connected rooftop BIPV system in Singapore. *Renewable Energy*. 2012,47:9-20.
- [4] C. Peng, Y. Huang, Z. Wu. Building-integrated photovoltaics (BIPV) in architectural design in China. *Energy and Buildings*. 2011,43(12):3592-8.
- [5] M. Tripathy, S. Yadav, P. K. Sadhu, S. K. Panda. Determination of optimum tilt angle and accurate insolation of BIPV panel influenced by adverse effect of shadow. *Renewable Energy*. 2017,104:211-23.
- [6] N. Aste, C. Del Pero, F. Leonforte. The first Italian BIPV project: Case study and long-term performance analysis. *Solar Energy*. 2016,134:340-52.
- [7] S. V. Hudişteanu, C. G. Popovici, T. D. Mateescu, Cherecheş N-C. Efficiency Analysis of BIPV Systems for Different Locations in Romania. *Energy Procedia*. 2017,112:404-11.
- [8] G. P. Hammond, H. A. Harajli, C. I. Jones, A. B. Winnett. Whole systems appraisal of a UK Building Integrated Photovoltaic (BIPV) system: Energy, environmental, and economic evaluations. *Energy Policy*. 2012,40:219-30.
- [9] C. D. Zomer, M. R. Costa, A. Nobre, R. Rüther. Performance compromises of building-integrated and building-applied photovoltaics (BIPV and BAPV) in Brazilian airports. *Energy and Buildings*. 2013,66:607-15.
- [10] C. L. Cheng, C. S. Sanchez Jimenez, Lee M-C. Research of BIPV optimal tilted angle, use of latitude concept for south orientated plans. *Renewable Energy*. 2009,34(6):1644-50.

The Capacity Optimization of the Energy Storage System used for Peak Load Shaving

Kai Deng, Xiaobo Tang, Jie Lei, Zhenyao Qian and Bangcheng Wei

Nanjing Normal University, Nanjing, China
E-mail: dengkainjnu@163.com

Abstract. With the development of society, the demand for power increases sharply, and the peak valley difference of load curve will affect the power quality and the life of generator set. The energy storage system can be used for peak load shaving and smooth out the power of the grid because of the capacity of fast power supply. Because of the high energy storage cost, it restricts the wide use of energy storage system, so it is very important for optimizing the storage capacity allocation. This paper analyses the economic benefits of the battery energy storage system used for load shaving in the distribution network. Through genetic algorithm, and considering the investment costs and economic benefits of energy storage system, the optimal value of energy storage capacity allocation is obtained by maximizing annual income as the objective function which is based on time-sharing electricity price. Finally, a 17-node distribution network is tested with typical daily load curve to justify the effectiveness of this method, and the results show that this method can not only play the role of peak load shaving, but also obtain certain profits.

1. Introduction

As the load demand increases, the load fluctuation generated in the power grid becomes more and more obvious. The load fluctuation will affect the stability of the power grid, and even to the life of generator set, and in order to reduce the effects of load fluctuation, the grid company will invest a lot of manpower for peak load shaving and the main measures are: increasing generator installed capacity and the capacity for transmission lines. Both of these practices are not only large investment, but also inefficient. With the development of energy storage technology, it is an effective method to solve the load fluctuation by connecting the energy storage system to the distribution network. Because the energy storage system has the capacity of good power supply, it can transfer the user's power load and reduce the impact of peak load and valley load on the power grid. In addition, the energy storage system in taming scenery also plays an important role on renewable energy sources. In [1] establishes the user response decision model of benefit maximization as the goal for solar energy storage systems, to explore the capacity of energy storage device configuration, but it ignores the volatility of load demands and the intermittency of Photovoltaic (PV) power, so the conclusion remains to be further discussed. In [2] researches distributed energy storage optimization configuration method in distribution network with PV, with total capacity of energy storage configuration optimization as the target, the introduction of voltage fluctuation improves indicators to optimize the distribution of the energy storage capacity, and the simulation results show that adopting this method can reduce the energy storage capacity by 85% with strong practicability.

At present, the large-scale energy storage system has entered into the business model abroad. In 2016, Japan's new large-scale energy storage projects for almost all applications in the field of electric power distribution was established in 2020, and the Japanese manufacturers of energy storage battery



production occupies 50% market share of the global development goals. In order to achieve this goal, Japan fully implements the battery storage subsidy and incentive plan in the practical application of power generation, transmission, distribution and use of various links. But the domestic energy storage system application is still in the experimental stage and small-scale operations. Wuxi Singapore industrial park intelligent distribution network energy storage power station, the total power energy storage power station is 20 MW, the total capacity is 160 MWH, and it is currently the largest domestic commercial energy storage power station.

According to the technical requirements of energy storage system access distribution network: the energy storage system can be connected in the form of power or load. At present, in most parts of the country, the mode of time-sharing electricity price is adopted, and the time-sharing price mechanism is the charging method of electricity price charged in time-sharing section: when the load demand is high, the electricity price is relatively high. When the demand for load is low, the electricity price is low, which creates economic significance for cutting peak loads. Based on this charging mechanism, the energy storage system can charge at valley price and discharge when the load demand is large. The energy storage system can not only realize the smooth output of the power grid, but also realize the arbitrage. However, one of the key reasons for restricting the large range of energy storage batteries is the cost is too high, so experts and scholars are devoted to the optimization model of energy storage capacity. In [3] optimizes the different ways of storage capacity under the peak valley price in distribution network, thinking that the economic benefits of compressed air energy storage (CAES) is higher, but it ignores that CAES has relatively high topographic requirements, which does not take into account the actual engineering application scenario. In [4] the capacity optimization configuration is carried out in the system with the PV and wind power, and the double-level optimization model was established, the outer based on genetic algorithm optimization, inner optimal power flow optimization based on SQP. Finally, it draws energy storage capacity of the optimal value by an example. In [5] is based on economic dispatch to analyse the optimal allocation of energy storage, and to use the improved genetic algorithm to solve the optimal value of energy storage, which has certain improvement significance.

In summary, the commonly used energy storage capacity allocation method is mainly based on optimization algorithm [6]. The objective function is usually the minimum capacity of energy storage system, or the minimum system cost. Based on time-sharing price model, using MATLAB genetic algorithm(GA) toolbox, with annual revenue maximization as the objective function, to optimize the energy storage system capacity, and to the distribution network with 17 nodes object, using the typical daily load curve for example analysis. The results show that this method can optimize the capacity of energy storage system and has good economic value.

2. Analysis of the strategy of peak load shaving in energy storage system

Battery energy storage system has the advantages of fast response and high power supply, so it has a wide application in peak cutting [7]. The battery energy storage can participate in the peak shaving, and according to the daily load curve, different charging and discharging strategies are developed, such as "one charge and one discharge" in a single day, and "one charge and two discharge". There are two kinds of control methods: constant power control and power difference control in the figure 1.

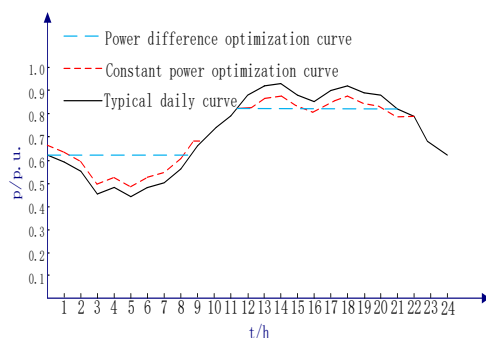


Figure 1. Load curve.

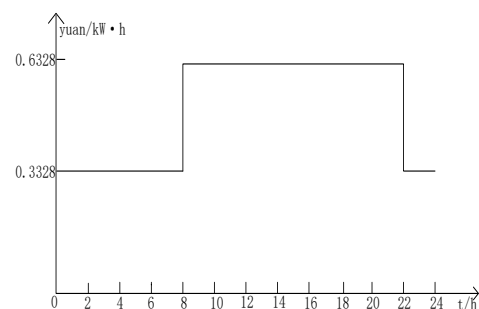


Figure 2. Time-sharing tariff.

The constant power charging and discharging control strategy is based on the energy storage battery charging and discharging energy, so it is necessary to ensure that the charge and discharge time is equal every day, and the control method is simple. Typical daily load curve as shown in a given area, adopt the strategy of "one charge and one discharge". The red curve is expected to peak sharpening effect, the actual load is shown in black and the charge and discharge time are 9 hours respectively. This method is relatively simple to control and reduce the peak value of load to a certain extent. But this kind of control strategy depends on the load curve forecasting, and as predicted by the load curve does not agree with the real load, this control method can not meet peak shaving goal, this is a kind of based on load curve is lesser known or load change control strategy. Because the constant power control strategy is simple and practical, it is widely used in practical engineering.

The power difference control mode can realize the smooth output power of the power grid. The blue curve shows the optimized curve of the power difference strategy, and the peak filling effect is better than the constant power control strategy. The power difference control strategy can effectively reduce the load pressure of the power grid and the huge investment. The power difference control method can respond to the real-time load condition, and the output power of the energy storage system can be configured according to the power difference at different moments. The advantage of dynamic adjustment is that the control precision is high, and the peak shaving is better. This paper is based on the power difference control method.

3. Economic analysis

3.1 economic benefits in distribution network

In the distribution network, the energy storage system can not only improve the stability of the system, but also generate certain economic benefits. Under the mechanism of time-sharing electricity price, energy storage batteries can be arbitrated through "low storage and high release". Factories such as commercial electricity peak valley price difference is close to 0.8 yuan/kWh, the residential electricity peak valley price difference of about 0.3 yuan/kWh. In the larger distribution network, with larger economic sense, also promote the energy storage system for peak cut a favorable factor. In addition, when the load fluctuation is large, the energy storage system can reduce the number of cutting, prolong the service life of the unit and reduce the cost of equipment input. At the same time, it can reduce the loss of the line and generate certain economic benefits [8].

3.1.1 economic benefit of time-sharing price

At present, the electricity market generally adopts the charging mode of time-sharing electricity price. In the case of a certain area, at the peak of the load, the electric charge was 0.6583 yuan/kWh, when the load was low, the electric charge was 0.3583 yuan/kWh. In the figure 2, the price difference of peak valley was about 0.3 yuan/kWh, and the peak valley price difference of industrial electricity consumption reached 0.8 yuan/kWh. With distributed energy storage, it can realize the arbitrage in time-sharing pricing mode. Assuming that the battery adopts the constant power charging and discharging mode and does not consider the peak valley price difference of industrial electricity consumption. The price difference of the peak valley is q , and t stands for discharging time, P_t representing the real-time output power of the energy storage system. Then, the annual economic

benefit in the distribution network is expressed as: $F1=0.1 \sum_{x=1}^{365} \sum_{t=8}^{22} qP_t$.

3.1.2 government subsidies

In 2016, the ministry of finance and the national development and reform commission promulgated *the interim measures on the administration of the central financial incentive fund management for the comprehensive pilot work on power demand side management*. The method is pilot in some areas, and it gives certain financial subsidy to the related enterprises. To improve the energy efficiency of power equipment, the reform project of saving power load permanently will be divided into three categories: 300 yuan/kW, 400 yuan/kW, 500 yuan/kW. Suppose the power capacity subsidy of the government is b , so the annual subsidy is: $F2=1000bP_{add}$.

3.2 cost analysis of distributed energy storage devices

The investment cost of distributed energy storage device mainly includes the cost of equipment purchase in the early stage and the maintenance cost of the later equipment. The cost of equipment purchase and energy storage capacity and power are all related. Maintenance costs are mainly related to power supply [9].

3.2.1 initial investment cost analysis

The initial investment cost of energy storage device mainly includes equipment cost and energy management system cost. The cost of equipment is related to the capacity of energy storage system, and the cost of energy management system is related to the power of energy storage system. The cost of the energy storage capacity is 1 million yuan /MWh, the total capacity of the battery energy storage system (BESS) is E_{add} , the cost of energy storage power is 20,000yuan/MW. The total investment cost can be expressed as: $f=f_1E_{add}+f_2P_{add}$, so the average annual investment cost can be expressed as: $F_3=(f_1E_{add}+f_2P_{add})/m$, m stands for the BESS whole life.

3.2.2 analysis of investment cost maintenance

After the energy storage device is put into use, the maintenance of the system and the maintenance of loss is required. The annual maintenance investment fee can be expressed as: $F_4=rP_{add}$, where r represents the annual maintenance cost of unit power.

According to the actual demand of peak shaving, the whole vanadium liquid battery energy storage system is selected, and the whole vanadium flow battery is compared to the lead-acid battery, which has higher energy density and higher discharge depth. Compared with lithium battery, it has less investment cost. Full - vanadium - flow battery charging and discharging depth, without affecting battery life. Therefore, it is the first choice and the technology is more mature. In 2016, Dalian Rongke company obtained the 200MW/800MWH full vanadium flow battery energy storage peak power station project, which is currently being implemented in an orderly way.

4. Optimized allocation model of energy storage capacity

Because of the high cost of energy storage system, it is difficult to get a large scale promotion. At present, it is popular to study the optimal allocation of energy storage capacity. The result of optimal configuration is to meet the demand of users and to achieve the optimal economic performance. Through the MATLAB GA toolbox, the objective function and constraints are set up to calculate the optimal allocation of energy storage capacity.

4.1 determine the objective function

According to the above analysis, from the perspective of investors, under the condition of considering power market, the objective function is to maximize annual income, which is expressed as:

$$T=\max (F_1+F_2-F_3-F_4) \quad (1)$$

4.2 establish constraints

Node power constraint: when the power system is in stable operation, it must meet the balance of power supply. In particular, at node i , the active power needs to be balanced, ignoring the line loss, and the power relationship of the energy storage system is as follows:

$$P_t+P_G=P_L \quad (2)$$

The P_L represents the load power of the distribution network, and P_G represents the load power of the power grid.

System operation constraint: in order to prevent the occurrence of the voltage limit of distribution network, the system needs to meet certain constraint conditions. In particular, at node i , the voltage and power of the node need to be within a range and cannot be limited [10].

$$U_i^{\min} \leq U_i \leq U_i^{\max} \quad (3)$$

$$P_i^{\min} \leq P_i \leq P_i^{\max} \quad (4)$$

The constraint condition of energy storage battery: in order to ensure the safe and stable operation of energy storage battery, it is necessary to meet the constraint of power and the constraint condition of battery charge state.

$$P_{\text{battery}}^{\min} \leq P_{\text{battery}} \leq P_{\text{battery}}^{\max} \quad (5)$$

$$\text{SOC}^{\min} \leq \text{SOC} \leq \text{SOC}^{\max} \quad (6)$$

The relationship between energy storage capacity and power: the capacity of the energy storage system is the power output at the unit time, and the relationship is as follows:

$$E_{\text{add}} = \int_{t_1}^{t_2} (P_L - P_G) dt \quad (7)$$

In the formula, t_1 and t_2 is the discharging start-stop time of energy storage battery.

4.3 GA is used to solve the problem

GA, also known as evolutionary Algorithm, is inspired by Darwin's theory of evolution and a heuristic search Algorithm proposed by the evolution of biology [11]. MATLAB comes with the genetic algorithm toolbox, the genetic algorithm is a method to search the global optimal solution, mainly used to solve the function optimization problem. The genetic algorithm is used to determine whether the first objective function is correct and the second constraint is reasonable.

The procedure for solving genetic algorithm is as follows:

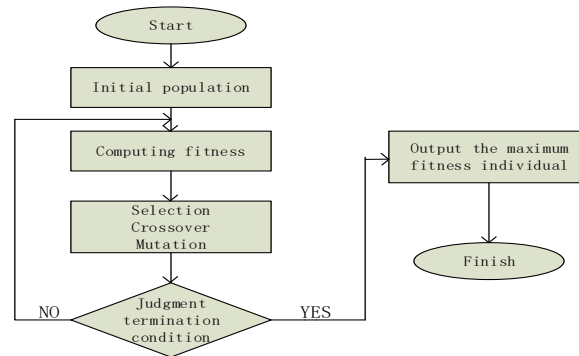


Figure 3. The GA flow chart.

5. Case analysis

5.1 calculation example overview

Distributed power access network technology regulation: distributed power supply access voltage level is appropriate: 200kW and the following distributed power supply connected to 380V voltage rating grid; More than 200kW distributed power supply to 10kV and above voltage rating grid. This paper selects the distribution network of 17 nodes, as shown in the figure 4. Node 1 is connected to the high voltage grid. In the distribution network, assuming the load demand is known, the typical daily load is used as the average load. The maximum power value in this example is 32.25MW and the minimum power value is 14.01MW [12]. Suppose that two sets of energy storage devices are installed in this distribution network, and two energy storage devices are installed on node 5 and node 14 respectively. The energy storage system is connected to the distribution network by the converter, which realizes the charge and discharge control and ignores the addressing problem of the energy storage system. According to the time price table above, the electricity price is the peak price at 8:00-22:00, and the distribution network load is supplied by the energy storage battery and the power grid, and the energy storage system is connected to the power supply. The other time load is relatively small, can be directly supplied by the power grid [13], [14]. During this period, the energy storage battery is connected to the power grid as a load, and the system is charged to ensure that when the next peak price arrives, it can supply the load in time.

5.2 calculation results

The optimal energy storage power configuration is 4MW through genetic algorithm, and the annual income is 0.630003 million yuan. Because the solution model adopts the ideal situation, the actual profits will have some error.

Further analysis of the relationship between benefits and power cost and peak valley electricity price is shown in the figure 5. As can be seen from the figure 5, when the peak valley price difference is 0.5 yuan/kWh, the annual income can reach 1.03 million; When the power cost goes down to 2.14 million yuan/MW, the annual revenue will reach about 1 million. The application of energy storage battery has a very broad prospect in the future.

Table 1. Parameter Settings.

parameter	Value
r	23
m	20
q	0.3
b	0.04
f1	105
f2	481

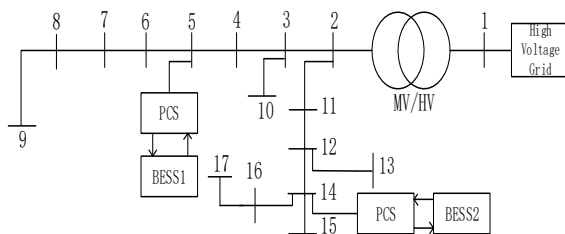


Figure 4. 17 node distribution network.

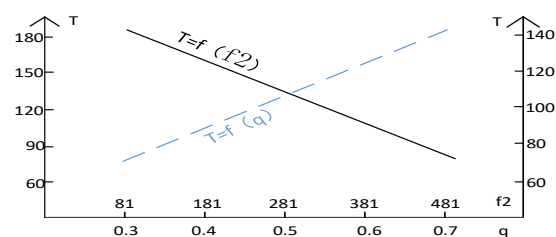


Figure 5. the relationship between benefits and power cost and peak valley electricity price.

6. Conclusions

1. The energy storage battery has good power supply capacity, and it has a good effect on cutting peak load. With the decrease of energy storage power cost, the application of energy storage battery for peak load shaving will be widely promoted.
2. When the peak valley electricity price difference is relatively high, the profit situation is obvious, so it will be more obvious to install the energy storage system in the industrial park.
3. Based on current storage costs, direct arbitrage condition is not very obvious, but the indirect benefits cannot be estimated. For the power grid, it has important application value, so the study of the energy storage technology will be a topic for a long time.

With the promotion of the energy Internet, the energy storage battery will be further developed, and the future energy storage technology will be widely used in the power system. The development of smart grid requires the continuous improvement of emerging technologies.

7. Acknowledgements

I really appreciate the help from my tutor and classmates. With their help, I finished the paper.

8. References

- [1] Cheng Yu, Zhao Pengfei. Demand response strategy and benefit analysis of residential load with PV and energy storage [J]. Acta Energiæ Solaris Sinica, 2017, 38(4):1055-1062.
- [2] Cui Yang, Liu Wen, et al. An optimal allocation method for energy storage batteries improving voltage level of distributed network with high penetration of distributed PV [J]. Acta Energiæ Solaris Sinica, 2017, 38(5):1157-1164.
- [3] Yan Zhimin, Wang Chengming, et al. Capacity plan of battery energy storage system in user side considering power outage cost [J]. Automation of Electric Power Systems, 2012, 36(11):50-53.
- [4] Wang Yanhong, Tai Nengling, Ji Kang. Optimal battery storage allocation in distributed network with large-scale of wind and PV generation [J]. Journal of Power Science and Technology, 2017, 32(2): 23-30.

- [5] Chen Xiu, Yang Jie, et al. Optimization allocation of energy storage for microgrid based on economic dispatch [J]. *Power System Protection and Control*, 2013, 41(1):53-60.
- [6] Li Jiaming, Zheng Xueyang, et al. Optimal design of capacity of distributed generation in island standalone microgrid [J]. *Transactions of China Electrotechnical Society*, 2016, 31(10):176-183.
- [7] Wang Chenming, Sun Weiqing, et al. Review on energy storage application planning and benefit evaluation methods in smart grid [J]. *Proceedings of the CSEE*, 2013, 33(7):33-41.
- [8] Luo Ni, Li Jianlin. Research progress of energy storage technology in power system [J]. *Power System and Clean Energy*, 2012, 28(2):71-79.
- [9] Guo Siqi, Yuan Yue, et al. Energy management strategy of isolated microgrid based on multi-time scale coordinated control [J]. *Transactions of China Electrotechnical Society*, 2014, 29(2):122-129.
- [10] Pei Wei, Sheng Kun, Kong Li, et al. Impact and improvement of distributed generation on distribution network voltage quality [J]. *Proceedings of the CSEE*, 2018, 28(13):152-157.
- [11] Wu Xiaogang, Liu Zongqi, Tian Liting, et al. Energy storage device locating and sizing for distribution network based on improved multi-objective particle swarm optimizer [J]. *Power System Technology*, 2014, 38(12):3405-3411.
- [12] Hu Guozhen, Duan Shanxu, et al. Sizing and cost analysis of PV generation system based on vanadium redox battery [J]. *Transactions of China Electrotechnical Society*, 2012, 27(5):260-267.
- [13] Xu Xiaoyan, Huang Yuehui et al. Influence of distributed photovoltaic generation on voltage in distribution network and solution of voltage beyond limits [J]. *Power System Technology*, 2010, 34(10):140-146.
- [14] Ding Wei, Wang Weisheng, et al. A review on the effect of large-scale PV generation on power system [J]. *Proceedings of the CSEE*, 2014, 34(1):1-14.

Review on Target Tracking of Wind Power and Energy Storage Combined Generation System

Xuwei Guo^{1,2}, Man Xu^{1,3}, Linlin Wu^{1,3}, Hui Liu^{1,3} and Siqing Sheng²

¹ State Grid Jibei Electric Power Co. Ltd. Research Institute, North China Electric Power Research Institute Co. Ltd., Beijing, China

² Department of Electrical and Electronic Engineering, North China Electric Power University, Baoding, China

³ Grid-connected Operation Technology for Wind-Solar-Storage Hybrid System State Grid Corporation Key Laboratory, Beijing, China

E-mail: gxw19940119@sina.com

Abstract. The utilization of large-scale renewable energy resources can effectively alleviate the shortage of traditional fossil fuel energy resources and the problem of environmental pollution. In order to realize the grid-friendly access of renewable energy power generation represented by wind power, it is necessary to involve energy storage, of which the battery energy storage is the most widely used type, and build a relatively controllable combined power generation system. Target tracking is one of the demand that wind power and energy storage combined generation system is supposed to meet. According to the discrepancies in tracking target, this paper firstly categorizes the target tracking issue into three parts, namely tracking wind power forecasting curve, tracking generation plan and tracking dynamic power generation index. Then based on the categories and considering their own research focuses, relevant literatures are summarized and compared. Conclusions and future research points are provided in the end. It is found that the issue of tracking dynamic power generation index worth more attention attributed to its novelty and complexity, where future work may be conducted from two aspects, the mathematical model dynamic power generation index and control strategy with overall management ability.

1. Introduction

The exploitation of renewable resources can effectively alleviate the shortage of traditional fossil fuel energy resources and the problem of environmental pollution. Power generation is a significant way of renewable resources utilization, represented by photovoltaic power generation and wind power generation, which has become a hot point in power and energy field.

China has a vast territory and abundant wind resources in the "Three-North Regions", providing the conditions to build large-scale wind power farms. The total grid-integrated capacity of China's wind power has reached 164 million kilowatts by 2017 [1]. However, the output characteristics of wind power differ from those of traditional power generation. The varying and stochastic nature of wind power can cause a series of problems when connected to the power grid, which hinders the full utilization and development of wind power to a certain extent, e.g. frequency problems, the frequent start-stop of the conventional unit and the increasing demand for the slope climbing ability of the regular units [2], [3]. Also, wind power is hard to be precisely forecasted, leading to difficulties in dispatch plan scheduling and executing.



One of the most widely discussed and adopted solutions to the grid-connected problems of wind power is to form a relatively controllable wind power and energy storage combined power generation system. There exist various types of energy storage system, e.g. pumped storage power plant, mechanical energy storage, battery energy storage, and electromagnetic storage. Although pumped storage power plant is one of the earliest used energy storage system, its high demands for topography and water resources limit its application under some circumstances. As for mechanical energy storage, some progress has been made in the theoretical research on the combined operation of wind power and mechanical energy storage, the typical representatives of which are flywheel energy storage and compressed-air energy storage [4], [5]. However, the use of mechanical energy storage mainly remains in the stage of theoretical research and the application technology is not mature enough. Battery energy storage mainly includes lead acid battery, sodium-sulphur battery, lithium iron phosphate battery, etc [6], [7]. Battery energy storage is less limited by geographical location and easy to expand. In recent years, it has been suggested theoretically that the use of multi-type energy storage can solve the problem of renewable energy access, but multi-type energy storage has not been widely used because complex coordination problems and consistency problems remain unsolved in engineering application [8], [9]. Above all, the battery energy storage become noticeable in the engineering application of facilitating the wind power to form relatively controllable wind power and energy storage combined power generation system.

Smoothing generation output, peak and valley shaving, control of target tracking, and frequency adjustment are the four major modes of wind power and energy storage combined system [10]-[12]. They are all crucial to the normal operation of the wind power and energy storage combined system, as well as to ensure the safety and economy of power system.

This paper focuses on the reviewing of wind power and battery energy storage combined system under target tracking mode. Firstly, literatures on target tracking issue are categorized into three parts, namely tracking wind power forecasting curve, tracking generation plan, tracking dynamic power generation index. Then the discrepancies of the three items are summarized. Section 2.1 reviews the literatures on tracking wind power forecasting curve and introduces the criteria of assessment. Section 2.2 reviews the literatures on generation plan tracking, with control strategies in these literatures summarized, categorized and compared. Section 2.3 introduces the connotation of dynamic power generation index, analyses the difficulties on tracking dynamic power generation index. Section 3 is about literatures exploring multi-mode coordinated optimization considering target tracking and mode switching, which try to furtherly make use of energy storage in the wind power and energy storage combined generation system. Finally, some conclusions and future work that is worthwhile to carry out are provided in Section 4.

2. Target tracking of wind power and energy storage combined generation system

Generally, the research contents of target tracking of wind power and energy storage combined generation system can be expressed as follows: determine the amount of active power released by energy storage based on the deviation between the wind power and the target that the combined system is supposed to follow, with the control strategy and the state of charge (SOC) being considered (see figure 1). At present, there is no uniform definition of the research content of target tracking. In the light of the discrepancies in tracking target, this paper firstly categorizes the target tracking issue into three parts, namely tracking wind power forecasting curve, tracking generation plan, tracking dynamic power generation index, which is summarized and compared in table 1. Review on the literatures on the three tracking target are given separately in the following subsections.

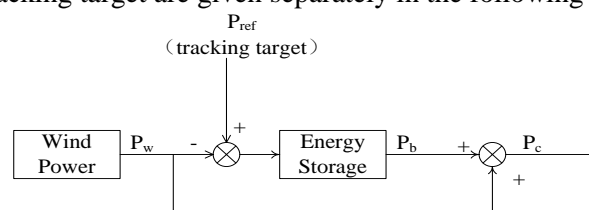


Figure 1. Target tracking of wind power and energy storage combined system

Table 1. Categories of target tracking of wind power and energy storage combined system

Tracking Target			Aims of tracking
Item	Source of data	Characteristic	
Wind power forecasting curve	Wind power forecasting system	A fixed curve	Reducing wind power forecast error Meeting the criteria of assessment
Generation plan	Power system dispatching organisation	A fixed curve	Ensuring the reliable execution of generation plan
Dynamic power generation index	Power system dispatching organisation	A set of curves	Ensuring the reliable execution of dynamic power generation index

2.1. Tracking wind power forecasting curve

Researches on tracking wind power forecasting curve aim to meet the criteria of assessment. Take China for example, the criteria of assessment is issued by National Energy Administration of China in July 2011, called The Interim Management Measures for the Power Forecast of Wind Power Farms (hereinafter referred to as The Interim Management Measures), where it is stipulated that the maximum error of the daily prediction curve provided by the power forecast system of wind farm is not more than 25%, the real-time prediction error is not more than 15%, and the root mean square error (RMSE) of the full day forecast results should be less than 20% [13], [14]. If a wind farm fails to meet the accuracy rate and qualified rate, it would be punished.

Researches prove that energy storage can facilitate the wind power to meet the criteria in The Interim Management Measures [14]. For example, in the calculating example of literature [15], with the participation of energy storage, the qualified rate rises from 43.8% to 100% and the RMSE is within the limit.

2.2. Tracking generation plan

The generation plan, provided by the power system dispatching organization, is the reference curve for power generation. In terms of tracking generation plan, wind power generation performs worse than the conventional unit due to the volatility and intermittency of its output. Thus, energy storage is required to facilitate the wind power in tracking generation plan [16].

Numerous literatures taking the generation plan as the tracking target of wind power and energy storage combined system are available, majority of which concentrate on the studies of control strategies. The commonly-used control strategies are summarized in figure 2, with their pros and cons listed and relationships among them presented.

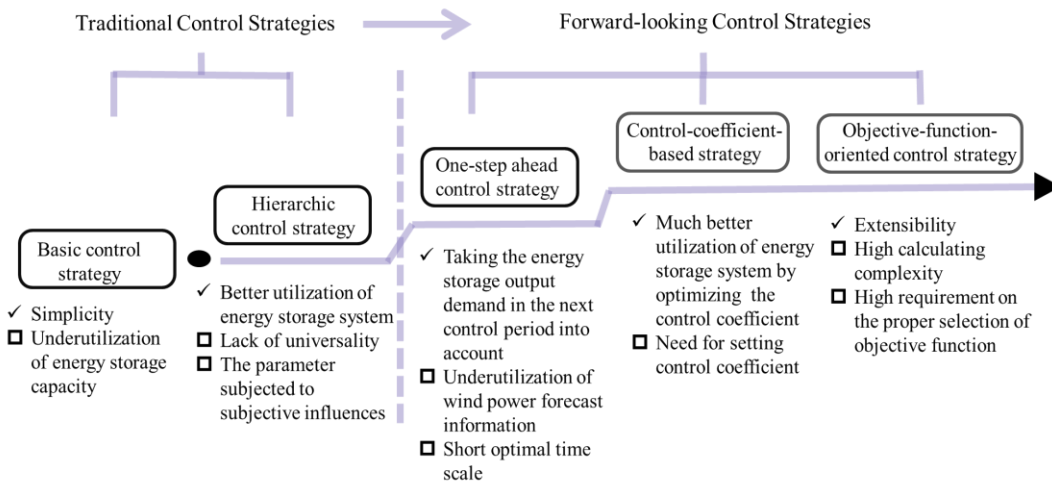


Figure 2. Four categories of control strategies commonly used in tracking generation

Traditional control strategies of wind power and energy storage combined system usually make decisions based on current operating conditions. Basic control strategy is one of the earliest adopted strategies in generation plan tracking of wind power and energy storage combined system. All the strategies to be introduced latter are improvements on the basis of the basic strategy. On the premise of satisfying the energy storage constraint, the strategy uses the bidirectional output ability of energy storage to compensate the deviation between the wind power and power generation plan in a control interval. To be more specific, the energy storage will be charged during the control intervals when wind power excess the generation plan, and be discharged in the opposite case. Otherwise, it does not participate in the tracking process. Basic control strategy is easy to implement. With this control strategy, the wind power and energy storage combined system performs well in tracking the generation plan. The simulation results in [16] showed that a satisfying performance in tracking the generation plan could be achieved if energy storage capacity is up to 15% to 25% of the wind farm capacity. Concerning the demand on prolonging service life of battery energy storage, basic control strategy sets a fixed limitation for the SOC (The upper limit varies from 0.8 to 1 while the lower limit varies from 0.1 to 0.2 in different literatures), and the battery energy storage can only operate in the case that its SOC is within the limitation interval. This way of SOC setting determines that in the case with basic control strategy, the deviation between the wind power and power generation plan is completely compensated or not a slightly compensated, which is not flexible and not conducive enough to make full use of the energy storage capacity. Therefore, some researches proposed hierarchic control strategy. Hierarchic control strategy improves the basic control strategy by refine the interval of SOC that the battery energy storage can operates, and gives more detailed rules. [17] is a typical literature that can be referred to, in which a sigmoid function is used to revise the degree of involvement of the energy storage. However, hierarchic control strategy is lack of universality and the performance varies in different cases.

Since traditional control strategies, represented by the basic strategy and hierarchic control strategy mentioned above, only consider current operating condition, and the combined generation system is not always equipped with sufficient capacity of energy storage, it is likely that the combined generation system is not able to tracking the generation plan curve continuously, and in some control intervals the deviation between the curve and the output of the combined generation system remains large [18]. Thus, it is necessary to design control strategies with overall management ability. On this background, efforts have been made by some researches and a series of forward-looking control strategies are put forward.

On the basis of short-term or ultra-short prediction values of wind power, the forward-looking control strategies arrange the timing and amount of energy storage charging or discharging in wind power and energy storage combined generation system in advance. The forward-looking control strategies can be categorized into one-step-ahead control strategy, control-coefficient-based strategy, and objective-function-oriented control strategy. One-step-ahead control strategy adjusts the current output of energy storage in the combined system by estimating the SOC at the end of next control interval and ensuring it is within the range of the limit interval. Literature [19] designed a series of adjustment rules, which is instructive for future studies. One-step-ahead control strategy is a primary forward-looking control strategy because it is short-sighted and does not make full use of the short-term or ultra-short prediction values of wind power. Control-coefficient-based strategy arrange the output of energy storage in advance of hours or a day by optimizing the energy storage charging or discharging power control coefficient indirectly. The key of the strategy lies in the setting of control coefficient. Literature [20] designed five control coefficients establishing the connections among the generation plan, the prediction value of wind power, the energy storage charge or discharge power and SOC of energy storage state. The five control coefficients are optimized by the particle swarm optimization algorithm in every rolling optimization period. Objective-function-oriented control strategy randomly select output of energy storage from the feasible interval to form a cluster of energy storage output sequence, and then under the guidance of the objective function, the optimized sequence of energy storage output is obtained by using the intelligent algorithm to solve the mathematical model. In the earlier researches, only the function that can reflect the tracking performance is used to construct a single-objective optimization model. In [21], maximum similarity between the total output curve of

hybrid wind/photovoltaic/energy storage system and the given scheduled output curve is taken as the objective function. In [22], the matching degree is presented by the credibility value of effective tracking, and maximum the mean value of the total credibility value within a day is taken as the objective function. Single-objective-function-oriented control strategy is lack of consideration on economic use and prolonging service life of battery energy storage. Thus, some multi-objective-functions-oriented control strategies are proposed to improve the model. In [23], the tracking effect was measured by the Manhattan distance of the combined generation system output curve and the generation plan curve, and three objectives were used to simultaneously achieve the effective tracking of power generation plan, the smoothness of output, and insurance of sustainable work ability of battery energy storage. In general, the objective-function-oriented control strategy is with flexibility and extensibility since the objective function can be adjusted according to the practical control demands. However, objective-function-oriented control strategy is confronted with the problem of complex calculating, which is usually needs to be solved by intelligent algorithm.

Except for the four categories of control strategies mentioned above, some innovative researches can be found, which are thought-provoking for future studies. For instance, [24] comprehensively considered tracking inaccuracy together with battery energy storage level, energy loss, and put forward a variable charge/discharge time-interval control strategy. Literature [25] proposed a coordinated optimal control strategy, which consists of online rolling optimization and active power real-time control, to realize precise tracking.

To sum up, traditional control strategies present basically satisfying performance for the wind power equipped with sufficient energy storage capacity. Otherwise, it is better to adopt forward-looking control strategies with overall management ability by considering the demand for energy storage strategy in certain period of future.

2.3. Tracking dynamic power generation index

Dynamic power generation index is a concept proposed under the background of universal existence of wind power curtailment phenomenon in large-scale wind power centralized area of China, which is caused by transmission path constraint or power system peak regulation constraint. Taking the transmission path constraint as an example, which is mainly caused by the mismatch between the development of grid construction and increasingly installation demand for wind power generation, the dynamic regulation characteristic of power generation index can be referred to in literature [26] and [27].

Few literatures take the dynamic regulation characteristic of power generation index into concern, which might be explained by two reasons. One is that the curve of dynamic power generation index is harder to be obtained than a generation plan curve because the dynamic regulation characteristic of power generation index is related to the tracking performance of the wind farms in a certain period of the passed time. Even though simplify dynamic regulation characteristic of power generation index as a fixed amount of augment in the case that the wind farm tracked the index well in the past hour, and a fixed amount of curtailment in the opposite case, the possible target to track presents as a cluster of curves, the amount of which is up to 2^{24} . It is unnecessary to take all the curves in the cluster as the tracking target and discussed one by one. Efforts might need to be made in how to select a reasonable number of curves from the curve cluster as the tracking targets to be studied. The other reason is that high demand on the control strategy of wind power and energy storage combined system is required with the dynamic regulation characteristic of power generation index being considered. As shown in figure 3, from 10:10 to 10:15, the participation of energy storage not only shortening the deviation between the power generation index and the wind power, but also contributes to obtain an augment of power generation index in the next control interval, which makes wind farm to be allowed to generate more power than that in the situation without energy storage. Thus, the overall management ability needs being attached more importance to when select the control strategy for tracking dynamic power generation index. The following ten minutes presents the similar situation.

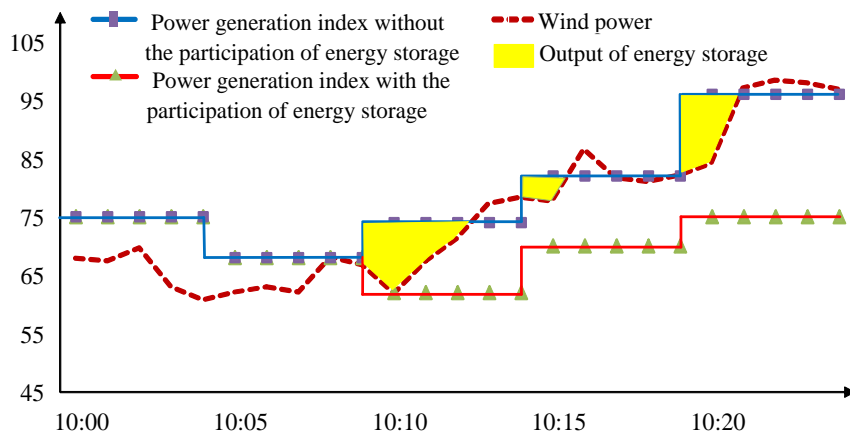


Figure 3. Tracking dynamic power generation index with or without the participation of energy storage

Above all, future studies on tracking dynamic power generation index might be conducted from two perspectives, the modelling of dynamic power generation index and the control strategy fitting the scenario.

3. Multi-mode coordinated optimization and mode switching considering target tracking

Smoothing generation output, peak shaving and valley filling, control of target tracking, and frequency adjustment are the four modes of wind power and energy storage combined system. Majority of the literatures only concentrate on the coordinated control of the combined generation system on a single mode. For example, literatures mentioned in Section 2 only focus on the target tracking mode, and literature [28] studies the optimizations on different modes separately.

To furtherly exploit the energy storage capacity, in recent years, some researches have explored the multi-mode coordinated operation and switching of wind power and energy storage system. By surveying the relevant literatures, it is found that a few literatures on multi-mode coordinated optimization and mode-switching considering target tracking are available. Literature [29] proposed a multi-mode coordinated optimization model for the wind power and energy storage combined system and realized highly efficient utilization of limited energy storage on both the peak shaving mode and target tracking mode. Literature [30] explored the integrated operation and switching technology of energy storage system of photovoltaic power station stabilizing fluctuation, tracking the generation plan, and shifting the power peak, and these real-time control strategies, which is thought-provoking.

4. Conclusions

In order to realize the grid-friendly access of renewable energy power generation represented by wind power, it is necessary to involve energy storage, of which the battery energy storage is the most widely used type, and build a relatively controllable combined power generation system. Target tracking is one of the operation modes of the wind power and energy storage combined system, which is crucial to study. This paper reviews relevant literatures on target tracking of wind power and battery energy storage combined system. Here are the conclusions:

- According to the discrepancies in tracking target, the target tracking issue could be categorized into three parts, namely tracking wind power forecasting curve, tracking generation plan, tracking dynamic power generation index.
- Researches taking wind power forecasting curve as tracking target aims to use energy storage to make wind power forecasting error within the allowable deviation so as to meet the criteria of assessment and avoid punishment. According to the literature surveyed, with the assistance of energy storage, wind farm can basically meet the criteria of assessment.
- Researches taking generation plan as tracking target mainly concentrate on the improvement and innovation of control strategies, which can be categorized as tradition strategies and forward-looking strategies. Traditional control strategies present basically satisfying

performance for the wind power equipped with sufficient energy storage capacity. Otherwise, it is necessary to adopt forward-looking control strategies though they are relatively complex.

- Dynamic power generation index is proposed for the full and fair utilization of the wind power in the large-scale wind power centralized areas with transmission path constraint problem. Few literatures on dynamic power generation index tracking are found, which may be explained by two reasons. One is the difficulty in obtaining the curve of dynamic power generation index. Another is high demand on the overall management ability of control strategy.
- Researches on multi-mode coordinated optimization considering target tracking and mode switching for wind power and energy storage combined generation system is still at a preliminary stage.

The improvement and innovation of control strategies in tracking generation plan still need further studies. More importantly, the issue of tracking dynamic power generation index and that of multi-mode coordinated optimization are worth exploring and should be paid more attention to in future work to furtherly make a full play of energy storage and promote the development of wind power.

5. References

- [1] Wind power grid operation in 2017 [EB/OL]. Retrieved from National Energy Administration of China Web site. 2018. www.nea.gov.cn/2018-02/01/c_136942234.htm.
- [2] S. Dutta, T. J. Overbye. Optimal Storage Coordination for Minimal Wind Generation Schedule Deviation [J]. North American Power Symposium, 2010:1-7.
- [3] Wu Qiong. Analysis on the impact of frequency regulation and peak load system when wind power connected to the power grid system [J]. Power Systems and Big Data, 2016(04):70-72.
- [4] WEI Kunpeng, WANG Yong and DAI Xingjian. Review of flywheel energy storage systems for wind power applications [J]. Energy Stor Sci Technol, 2015(02): 141-146.
- [5] YAN Fang, LI Wenbo and YIN Chengzhu. Necessity analysis of joint development of wind farm and compressed air energy storage power station[J]. China Electric Power Education, 2014(24): 115-116.
- [6] LI Xiangjun, WANG Shangxing, HUI Dong. Summary and Prospect of Operation Control and Application Method for Battery Energy Storage Systems [J]. Power System Technology, 2017(10):3315-3325.
- [7] Poullikkas A. A comparative overview of large-scale battery systems for electricity storage[J]. Renewable and Sustainable Energy Reviews, 2013, 27:778-788.
- [8] LOU Suhua, YANG Tianmeng, WU Yaowu, et al. Coordinated Optimal Operation of Hybrid Energy Storage in Power System Accommodated High Penetration of Wind Power [J]. Automation of Electric Power Systems, 2016(07): 30-35.
- [9] TIAN Chongyi, LI Ke, YAN Yi, et al. A multi-time scale control strategy of hybrid energy storage system in wind farm based on empirical mode decomposition [J]. Power System Technology, 2015(08): 2167-2172.
- [10] YAN Gangui, FENG Shuang, LI Junhui. Review on combined wind power generation and energy storage systems [J]. Energy Stor Sci Technol, 2014(04): 297-301.
- [11] GAO Mingjie, HUI Dong, GAO Zonghe, et al. Presentation of national wind /photovoltaic/ energy storage and transmission demonstration project and analysis of typical operation modes [J]. Automation of Electric Power Systems, 2013(01): 59-64.
- [12] REN Luoqing, BAI Zeyang, YU Changhai, et al. Research on active power control strategy for wind/photovoltaic/energy storage hybrid power system and its engineering application [J]. Automation of Electric Power Systems, 2014(7): 105-111.
- [13] XUE Yusheng, YU Chen, ZHAO Junhua, et al. A Review on Short-term and Ultra-short-term Wind Power Prediction [J]. Automation of Electric Power Systems, 2015(06):141-151.
- [14] Liu Yanfen, Bai Kai, Zhang Caiping, et al. Research on tracking power generation schedule strategy of wind power and battery energy storage combined system in real-time [J]. Renewable Energy Resources, 2015(03): 363-368.

- [15] JIN Wentao, LI Bei, XIE Zhijia. An analysis for the need of a battery energy storage system in tracking wind power schedule output [J]. *Energ Stor Sci Technol*, 2013(03): 294-299.
- [16] KOU Peng, GAO Feng, GUAN Xiaohong. Stochastic predictive control of battery energy storage for wind farm dispatching: Using probabilistic wind power forecasts [J]. *Renewable Energy*, 2015, 80: 286-300.
- [17] S Teleke, ME Baran, S Bhattacharay, et al. Rule-based control of battery energy storage for dispatching intermittent renewa.[J]. *IEEE Transactions on Sustainable Energy*, 2010, 1(3): 117-124
- [18] YAN Gangui, WANG Yue, LI Junhui, et al. Control strategy for regulatory requirements oriented energy storage system and evaluation on its economy [J]. *Guangdong Electric Power*, 2015(04): 12-18.
- [19] ZHAO Shuqiang, LIU Chenliang, WANG Mingyu, et al. Chance-Constrained Programming Based Day-Ahead Optimal Scheduling of Energy Storage [J]. *Power System Technology*, 2013(11): 3055-3059.
- [20] CHAI Wei, CAO Yunfeng, LI Zheng, et al. An optimal energy storage control scheme for wind power and energy storage system based on state forecast [J]. *Automation of Electric Power Systems*, 2015(02): 13-20.
- [21] YAN Heming, LI Xiangjun, MAXiufan, et al. Wind power output schedule tracking control method of energy storage system sased on ultra-short term wind power prediction prediction [J]. *Power System Technology*, 2015(02): 432-439.
- [22] HU Yongqiang, LIU Chenliang, ZHAO Shuqiang, et al. Optimal control of energy storage based on fuzzy correlated-chance programming[J]. *Automation of Electric Power Systems*, 2014(06): 20-25.
- [23] ZHAO Shuqiang, LIU Dazheng, XIE Yuqi, et al. Scheduling strategy of energy storage in wind-solar-battery hybrid power system based on dependent-chance goal programming [J]. *Automation of Electric Power Systems*, 2015(14): 30-36.
- [24] Chai W, Li Z, Cai X. Variable charge/discharge time-interval control strategy of BESS for wind power dispatch [J]. *Turkish Journal of Electrical Engineering & Computer Sciences*, 2015, 23: 1645-1659.
- [25] Qi Yongzhi, Liu Yutian. Output power rolling optimization and real-time control in wind-photovoltaic-storage hybrid system [J]. *Transactions of China Electrotechnical Society*, 2014(08): 265-273.
- [26] ZHUO Junfeng, JIN Xuezhu, DENG Bo, et al. An active power control method of large-scale wind farm considering security constraints of tie lines [J]. *Power System Technology*, 2015(04): 1014-1018.
- [27] WANG Jingran, WANG Yulin, YANG Zhigang, et al. An active power control strategy for large-scale cluster of wind power considering constraints on nested transmission sections [J]. *Automation of Electric Power Systems*, 2015(13): 16-21.
- [28] XU Hanchen, YUAN Zhichang, LU Chao, et al. Multi-mode optimization for hybrid wind and energy storage system based on modern interior-point method [J]. *Automation of Electric Power Systems*. 2013, 37(16): 1-6.
- [29] LU Qiuyu, HU Wei, MIN Yong. et al. A multi-pattern coordinated optimization strategy of wind power and energy storage system considering temporal dependence [J]. *Automation of Electric Power Systems*, 2015(02): 6-12.
- [30] XUE Yushi, XU Shaohua, LI Jianlin, et al. Research on cooperative operation and switching strategy of energy storage system in photovoltaic power plant [J]. *Electrical & Energy Management Technology*, 2017(13): 46-55.

Acknowledgments

This paper is partly supported by the national R&D project (A comprehensive demonstration project for smart grid supporting low-carbon winter Olympics, 2016YFB0900500) and State Grid Corporation of China Headquarter technology project.

Survey on the Operation of the District Energy Supply System in Japan According to Secular Change

Anna WON¹

¹School of Architecture, Kyungpook National University, Daehak-ro 80, Daegu, Republic of Korea

E-mail: woan749@hanmail.net

Abstract. Japan aimed for independent energy provision of large-scale energy consumers and energy efficient supply, so it actively introduced the District Energy System (DES) in the 1970s. A total of 133 sites (2 sites are unclear) are currently in operation, with 23 DESs established since 2000, and 110 sites consisting of superannuated facilities that are more than 20 years old. The purpose of this study is to compare and analyze the operational status of the DESs according to secular change, by identifying the supply area, the primary energy usage, and the utilization of renewable energy. As of 2003, 164 sites were in operation, and as of 2015, there were 133 sites. About 83% of the 133 sites were obsolete, being – more than 20 years old. About 87% areas showed lowered ratios of input primary energy in 2015 compared to that in 2003. The rate of operation of the main DES energy production system, cogeneration, has declined significantly, and the number of areas that use a current system rather than operate in cogeneration, has increased. This may have been due to the reduction of end use demand by the aging of the cities and the deterioration of the facilities. Therefore, it is necessary to suggest a new direction for the DES in preparation for the aging of their localities.

1. Introduction

To achieve independent energy supply of large-scale energy consumers, Japan has actively introduced district energy systems (DESs) [1]. The DES is responsible for cooling and heating, by piping cold water and hot water (or steam) from one or more plants to multiple buildings. This system independently produces and supplies electricity, using cogeneration. In regions where only heating and cooling are supplied, this system is known as district heating and cooling. Compared to individual heating and cooling, this system has attracted attention as an efficient means to reduce the peak load on the central power system, thanks to its intensive energy production and use [2]. According to Sadohara (1998) [3], it is appropriate to install district heating and cooling facilities in 1302 areas throughout Japan. Yamaguchi [4] suggested an optimal form of DES for building size and usage. Studies have been actively conducted on the introduction of DESs as a means to facilitate the efficient use of renewable energy [5]. Accordingly, many DESs were expected to be introduced, but as of 2016, they had only been introduced into 130 regions, and there have been no studies on the operating state of the existing DESs.

Now that more than 40 years have passed since the introduction of the DES, it is necessary to review their current operating state. Thus, we attempted to understand the changes of the DES due to various factors, such as the change of consumers and the deterioration of equipment, and to identify implications for the future DES direction. Therefore, this study aimed to investigate the secular changes of DES through data survey.

2. Overview of study subjects



The Japan Heat Service Business Association (JHSBA) publishes the “Heat Supply Business Concordance” which contains the basic information on heat service providers, facilities, fuel used, and energy sold every two years. In the 2004 and 2016 heat supply business agreement (“concordances”), information on new and existing DESs from 2003 to 2015, provided by the JHSBA, was used. Japan’s DES started at the Japan World Exposition, and peaked at 153 sites (including authorized zones and non-authorized zones) in 2005. A total of 136 sites were aggregated in 2016¹[6].

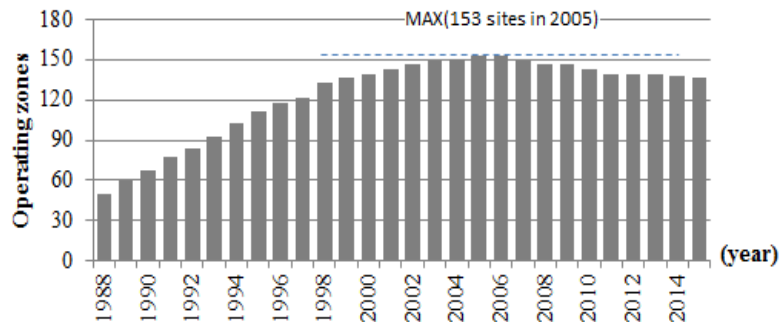


Figure 1. Number of areas that operated DES systems by year

3. Start year of energy supply under DES

There were 146 DESs in operation in 2003, and 12 new systems had been introduced by 2015. Of the total 158 areas, 25 sites (including two unspecified areas) were shut down between 2003 and 2015, leaving 133 DESs currently in operation.

Based on the start year of energy supply, 28 systems were introduced in the 1970s, 32 in the 1980s, and 76 were introduced the systems between 1990 and 1999—the highest number so far. Since 2000, systems were introduced in about 23 zones (Figure 2). The construction of DESs was mainly carried out between 1970 and 1999, when development of major urban areas took place in response to high economic growth.

The start year of DES energy supply in the various regions, by sites which have now ceased operation were as follows: 1970 to 1979 - 10 sites, 1980 to 1989 - four sites, and 1990 to 1999 - 10 sites, showing that many sites were more than 20 years old when their ceased being active. Eighteen regions are operating systems established in the 1970s, and 27 regions are operating systems constructed in the 1980s. Some of the heat source facilities are assumed to have been replaced because they are more than 40 years old, but we were not able to identify them and did not count them separately.

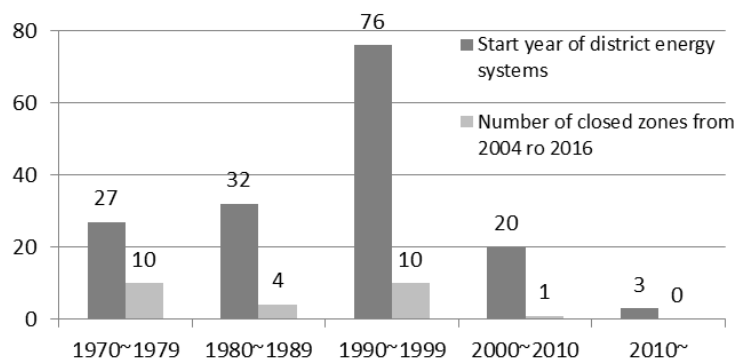


Figure 2. Start year of DESs and number of closed zones from 2004 to 2016 (information for two zones was unclear)

4. Results

¹ Japan’s Heat Supply Business Concordance is issued every two years, with 2016 being the latest version. According to its data, the 2016 edition is based on data for the year 2015, and the 2004 edition is based on data for the year 2003, and so forth.

4.1. Heat production rate of DESs

Figure 3 shows the amount of input primary energy for each plant in 2015 compared to that for 2003. The x-axis represents the start year of energy supply, and DES built since 2003 were excluded because there were no subjects for comparison. In addition, since the energy (calories) sold to the end use may vary depending on the efficiency of the plant, the amount of input primary energy in the plant was used for comparisons, rather than the output.

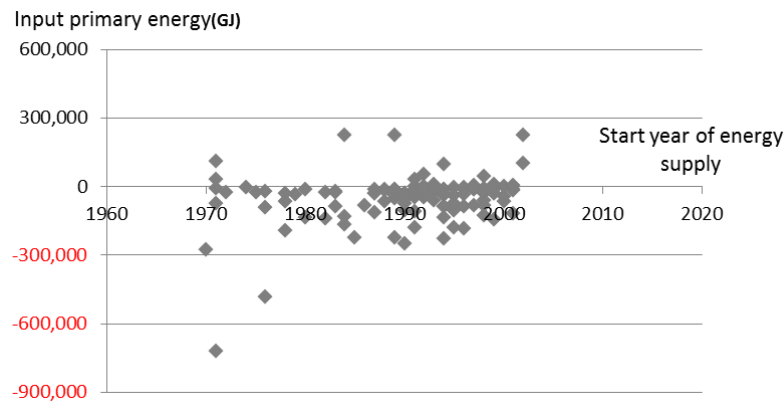


Figure 3. Increase or decrease in input primary energy in 2015, compared with 2003

The input primary energy was found to have decreased in about 87% of the areas, while it increased in about 13% of the areas (Figure 4). It is estimated that the operation rate of existing DESs decreased in line with the decline of districts over time.

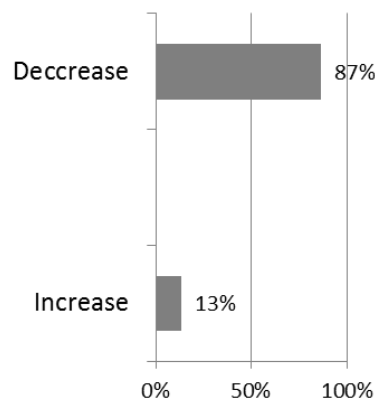


Figure 4. Ratio of Increase or decrease in input primary energy

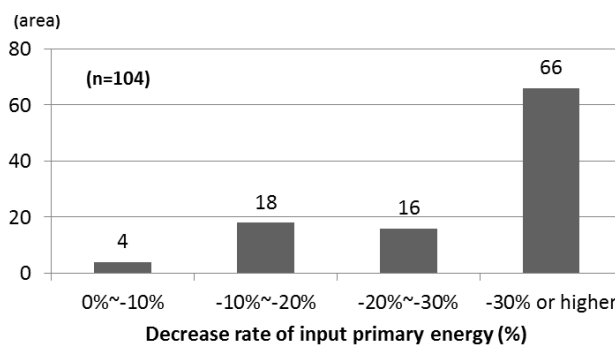


Figure 5. Numbers of districts with decreased amount of input primary energy

The decrease rates of the areas where the amount of the input primary energy decreased were higher (Figure 5). Eighteen areas showed 10–20% decrease, 16 areas showed 20–30% decrease, and 66 areas showed 30% or more. Thus, the input primary energy decreased in about 60% or more of the regions.

4.2. Cogeneration facility operating status

The decrease in energy consumption can also be seen in the main DES facility operations. In 2003, 39 districts operated cogeneration, of which four have since shut down, leaving the remaining 35 sites to be studied for cogeneration operation in 2015.

As of 2015, 23 districts operated cogeneration, showing a decrease since 2003 of 34% (Figure 6). In addition, 78% (18 sites) of the 23 sites in operation showed a decrease in energy production by cogeneration, and only 22% (five sites) showed an increased energy production. Since 2003, three sites added new cogeneration facilities.

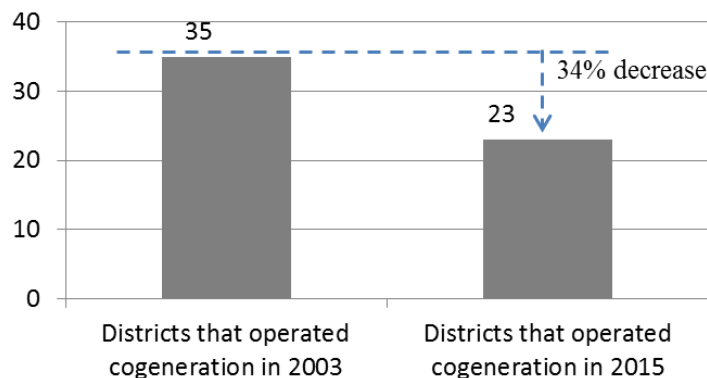


Figure 6. Numbers of cogeneration sites, and reduction between 2003 and 2015

As such, in many areas, the use of cogeneration declined, and instead the amount of power purchased locally from the main power supply system increased.

As shown above, the decrease in the input primary energy, and in the utilization of cogeneration (the main facility of the DES) seem to have been influenced by the decrease in the energy consumption by end users, possibly due to the decline of the region. Decreases in energy consumption lead to low-efficiency operation of the energy production facility, which is incompatible with the intrinsic purpose of the DESs (local energy self-sufficiency and energy conservation).

5. Conclusions

DESs are generally obsolete, and the amount of energy produced by DESs is decreasing. In Japan, metropolitan cities are already highly developed, with development at its limit. Therefore, the number of new development or redevelopment areas requiring high-density energy demand are limited. As a result, the increase in the introduction of DESs will be limited. However, the DES, which can provide high efficiency through intensive energy production and consumption, is a useful energy source for the cities, and in order for it to continue to fulfil its role, there should be studies on opportunities for refurbishment of DESs.

6. References

- [1] Japan *Heat Supply Business Association*, <<http://www.jdhc.or.jp/>> [accessed July 2018]
- [2] K. Watanabe 2006 Study on system COP used to evaluate heat source system efficiency *J. Environ. Eng., AIJ* No. 602 p53-60
- [3] S. Sadohara and K. Nagano and M. Miura and K. Murakami and M. Mriyama and Y. Shimoda and T. Kitayama 1998 Study on diffusion of district heating and cooling in Japan and its effects on global environment preservation *J. Environ. Eng., AIJ* No. 5 10 p61-67
- [4] Y. Yamaguchi and Y. Shimoda 2011 Estimation of appropriateness of areas for district heating and cooling system considering the distribution of building heat source system *J. Environ. Eng., AIJ* Vol. 76 No. 663 p509-515

- [5] K. Watanabe 2006 Study on energy saving effect at a district heating and cooling plant utilized with unused energy J. Environ. Eng., AIJ No. 607 p79-86
- [6] Japan Heat Supply Business Association (incorporated association) 2016 *Heat Supply Business Concordance*

Acknowledgement

This research was supported by Basic Science Research Program through the National Research Foundation of Korea (NRF) funded by the Ministry of Education, Science and Technology(NRF-2015R1C1A2A01053686)

Study on Modification of Phase Change Energy Storage Materials Suitable for Biogas Fermentation

Zhipeng Yang¹, Jinheng Li², Anxing Lai², Gang Li³ and Lei Wang⁴

¹ School of Electrical Engineering and Automation, Xiamen University of Technology, No.600, Ligong Road, Jimei District, Xiamen, P.R.China

² Xiamen University of Technology, No.600, Ligong Road, Jimei District, Xiamen, P.R.China

³ Gansu Rural Energy Office, No.106, Pingliang Road, Chengguan District, Lanzhou City, P.R.China

⁴ School of Environmental Science and Engineering, Xiamen University of Technology, No.600, Ligong Road, Jimei District, Xiamen, P.R.China

E-mail: yangzhipeng2016@outlook.com

Abstract. In this study, the problems of supercooling and phase separation of inorganic hydrated salts as phase change energy storage materials when applied to biogas generating devices were investigated. In the experiment, two common hydrated salts of zinc nitrate hexahydrate and disodium hydrogen phosphate dodecahydrate were selected as phase change materials, and tested at room temperature. Recording temperature and drawing the step cooling curve method, by adding different proportions of nucleating agent and dye to improve the supercooling and phase separation of the phase change materials, so that the reaction temperature of the biogas plant was always maintained at a suitable temperature (20- 30 °C) to ensure the activity of microorganisms. The experimental results showed that sodium tetraborate decahydrate can effectively reduce the subcooling degree of zinc nitrate hexahydrate, and the azo (-N=N-) dye not only improved the solar absorption rate but also weakened the phase separation of phase change materials to some extent. This study proposed a possible reaction mechanism and provided reference for the development and application of other solar energy storage materials for bioreactors.

1. Introduction

Phase Change Materials (PCMs) are characterized by their ability to absorb or release heat during storage changes [1], [2]. In recent years, PCMs have been widely used in the field of solar energy storage, industrial waste heat recovery and agricultural greenhouse insulation, etc. In order to solve the energy shortage in rural areas and reduce the pollution of burning straw to the atmosphere, Chinese government has widely promoted waste fermentation biogas projects [3].

As a common energy storage inorganic PCMs, crystalline hydrated salt has the advantages of low cost, large thermal conductivity, high latent heat of fusion and large unit heat storage density, but the supercooling of crystalline hydrated salt during phase transformation is an unavoidable problem [4]-[7]. That is, PCMs do not crystallize when they are cooled to the freezing point, and they need to be cooled to a temperature lower than the freezing point to cause crystallization. Furthermore, biogas fermentation requires the temperature of the reaction device to be strictly maintained within a certain interval (20-30 °C) to maintain the activity of microorganisms. The problem of supercooling seriously restricts the popularization and application of phase change energy storage materials in a series of



bioreactors such as biogas fermentation plants. In northern China, biogas fermentation plants often cannot produce biogas due to large temperature difference between day and night, which seriously affects the production and life of villagers. Therefore, how to improve or eliminate the problem of supercooling of crystalline hydrated salt has become an urgent practical application problem.

At present, experimental studies at home and abroad have shown that the addition of nucleating agents to PCMs can effectively suppress the problem of supercooling. However, there are few relatively studies on the application of composite PCMs in the field of bioreactors. Therefore, this paper selected the zinc nitrate hexahydrate and disodium hydrogen phosphate dodecahydrate to study the effect of the type and amount of nucleating agent on maintaining the temperature range and improved the problem of absorbing solar energy inefficiency and phase separation by adding dyes [8], [9].

2. Experimental

2.1 laboratory apparatus

In the experiment, the temperature of the PCMs were measured using a JM624 thermometer with an accuracy of ± 0.1 °C, and the time was recorded using a stopwatch. The tube containing the PCMs were heated by using a six-hole digital thermostat water bath. The absorption spectrum of the phase change material mixed with the dye was measured using a Shimadzu UV-2550 UV-Vis spectrophotometer. The experimental condensing unit is shown in figure 1.

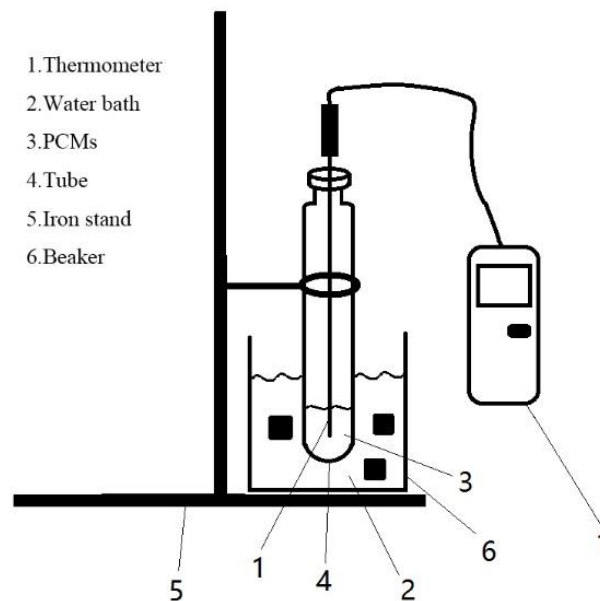


Figure 1. Experimental condensing device

2.2 Preparation of materials

According to the actual conditions required for the biogas plant, hydrated salt materials which are easy to chemical produce and are cheap are selected. Depending on the conditions in which the device is actually applied, hydrated salt materials with a phase transition temperature between 20 and 30 °C or slightly above this temperature range should be selected as much as possible. Therefore, the initially selected hydrated salt materials are disodium hydrogen phosphate dodecahydrate, zinc nitrate hexahydrate, and calcium chloride hexahydrate. At the same time, according to the reference, strontium chloride hexahydrate and borax (i.e. sodium tetraborate decahydrate $\text{Na}_2\text{B}_4\text{O}_7 \cdot 10\text{H}_2\text{O}$) were selected as nucleating agents, and the crystal parameters are shown in table 1. Considering that the simple PCMs absorb light energy inefficiently, it is proposed to add an azo (-N=N-) dye to the phase change material to enhance the light absorption performance.

Table 1. A slightly more complex table with a narrow caption.

	Crystal system	pH	Classification
Na ₂ HPO ₄ ·12H ₂ O	Monoclinic system	9.0	PCMs
Zn(NO ₃) ₂ ·6H ₂ O	Tetragonal system	4.0	PCMs
CaCl ₂ ·6H ₂ O	Rhombohedral system	7.0	PCMs
Na ₂ B ₄ O ₇ ·10H ₂ O	Monoclinic system	9.6	Nucleating agent
SrCl ₂ ·6H ₂ O	Hexagonal system	6.8	Nucleating agent

2.3 Experimental procedure

The phase change temperature was measured by the step-cooling curve method. The temperature value of the medium time interval was measured and the curve was drawn, and the phase transition temperature was determined according to the turning point on the curve and the parallel line segment (smooth or approximately parallel segment). In addition, physical blending was used to mix some materials, such as nucleating agents, light absorbing dyes, etc., to improve the properties of the phase change material.

Each PCM was separately mixed with the nucleating agent selected above according to different ratios, and the temperature was measured and the step cooling curve was drawn. The nucleating agent capable of reducing the supercooling phenomenon and the mixing ratio thereof can be selected by analysing the step cooling curve and observing the phase change effect. In addition, the phase change system with dye added was compared with the original system, and the step cooling curve was measured and plotted to analyse whether the dye would affect the crystallization and heat release effect of the PCMs.

3. Results and Discussions

3.1 Effect of Borax as a Nucleating Agent on PCMs

It can be seen from the Phase Rule that at normal pressure, during the solidification of pure crystals, the liquid-solid two phases coexist, and the degree of freedom is equal to zero, so the solidification temperature does not change. According to the second law of thermodynamics, under natural conditions, the direction in which the system spontaneously proceeds is the direction in which the free energy of the system decreases.

$$\Delta G_v = \frac{Q\Delta T}{T_m} \quad (1)$$

In the formula, ΔG_v is the unit molar free energy change from liquid phase to solid phase transition, $\text{kJ} \cdot \text{kmol}^{-1}$, Q is the heat of fusion. The heat absorption to the environment is defined as positive, $\text{kJ} \cdot \text{kmol}^{-1}$. $\Delta T = T_m - T$ is the difference between the melting point T_m and the actual solidification temperature T , defined as subcooling. During solidification, PCM radiates heat to the environment, Q is negative. In order to make $\Delta G_v < 0$, we have to make $\Delta T > 0$, ie $T < T_m$. Therefore, the freezing point of the crystal should be lower than the melting point T_m . The supercooling phenomenon for crystal solidification can be solved by adding a crystal nucleus, which is a nucleating agent to the material.

Figure 2, 3 are graphs of the step cooling curves of different proportions of sodium tetraborate decahydrate mixed with zinc nitrate hexahydrate and disodium hydrogen phosphate dodecahydrate. It can be seen from Fig. 2 that when 0.5 g of sodium tetraborate decahydrate is added, the degree of subcooling was reduced by about 4 °C compared with when no nucleating agent was added, and the phase transition temperature at this time was more suitable for the bioreactor and the heat preservation was more effective. The degree of subcooling when adding 1g of sodium tetraborate decahydrate was very close to the degree of subcooling when it was not added. Therefore, it can be considered that, within a certain ratio range, as the amount of nucleating agent increased, the degree of subcooling

gradually decreased. When the ratio exceeded a certain degree, the amount of nucleating agent continued to increase, which in turn caused the degree of subcooling to start to rise again. From the step cooling curve of the mixed sample in figure 3, it can be seen that the phase transition temperature of each group of disodium hydrogen phosphate dodecahydrate and sodium tetraborate decahydrate was below 25 °C, that is to say, the degree of subcooling was above 10 °C. The increase in the amount of sodium tetraborate decahydrate added has substantially no effect on the degree of subcooling of disodium hydrogen phosphate dodecahydrate. The possible reason may be that the crystal structure is too similar and the lattice parameters are proximity, and there is a similar compatibility, that is, the two materials dissolve each other so that sodium tetraborate decahydrate cannot perform nucleation.

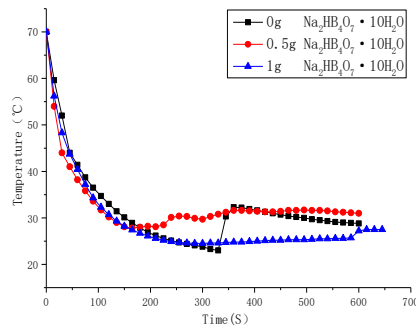


Figure 2. The cooling curve of zinc nitrate hexahydrate and sodium tetraborate decahydrate mixing.

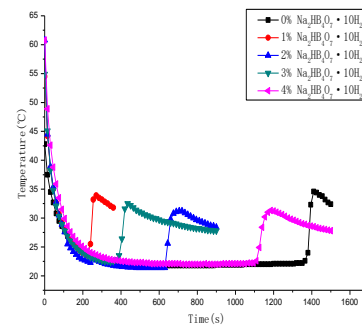


Figure 3. The cooling curve of Disodium hydrogen phosphate dodecahydrate and Sodium tetraborate decahydrate mixing.

3.2 Effect of Strontium Chloride Hexahydrate as a Nucleating agent on PCMs

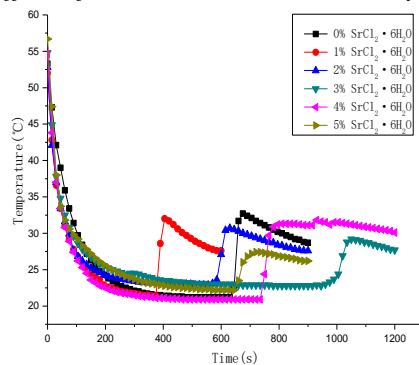


Figure 4. The cooling curve of zinc nitrate hexahydrate and Strontium chloride hexahydrate mixing.

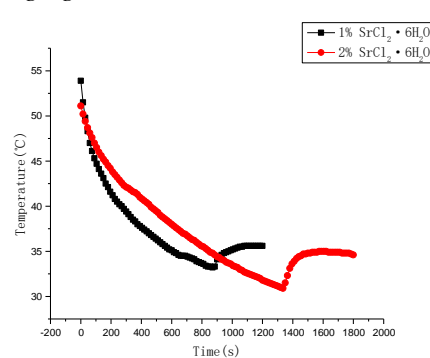


Figure 5. The cooling curve of Calcium chloride hexahydrate and Strontium chloride hexahydrate mixing.

Figure 4, 5 are graphs of the step cooling curves of different ratios of strontium chloride hexahydrate mixed with zinc nitrate hexahydrate and calcium chloride hexahydrate. According to the step cooling curve of the mixed sample in figure. 4, the phase transition temperature of the material was below 25 °C, that is, the degree of subcooling was above 10 °C. As the amount of strontium chloride hexahydrate added increases, the degree of subcooling of zinc nitrate hexahydrate decreases slightly. It can be considered that the addition of strontium chloride hexahydrate had little effect on improving the degree of subcooling of the material; when the amount of nucleating agent was different, the phase change rate was the fastest when adding 1% strontium chloride hexahydrate, and the subsequent phase transition speed was gradually slowed down. It can be seen from the step cooling curve of the mixed sample in figures 5 that the phase transition temperature was always above 30 °C. That is to say, the addition of strontium chloride hexahydrate may increase the instability of the material, it would start to

radiate heat when it had not fallen within a given temperature range, thereby causing overheating. From the perspective of crystal structure, zinc nitrate hexahydrate belongs to the tetragonal system, calcium chloride hexahydrate belongs to the trigonal system and strontium chloride hexahydrate belongs to the hexagonal system. There is a certain difference between the two hydrated salts, which may be one of the reasons for the abnormal phase transition temperature of the material.

3.3 Effect of adding dye

UV-visible absorption spectra of dyes and phase change materials were determined using an ultraviolet-visible spectrophotometer. The results are shown in figures 6. From bottom to top are the UV-visible absorption spectra of PCM, dyes and the mixture of PCM and dye. It can be seen that PCM has a greater absorbance than a single PCM and dye due to the addition of dye. It can be considered that the heat storage property of the phase change material is combined with the light absorbing property of the dye to improve the absorbance compared to the pure dye.

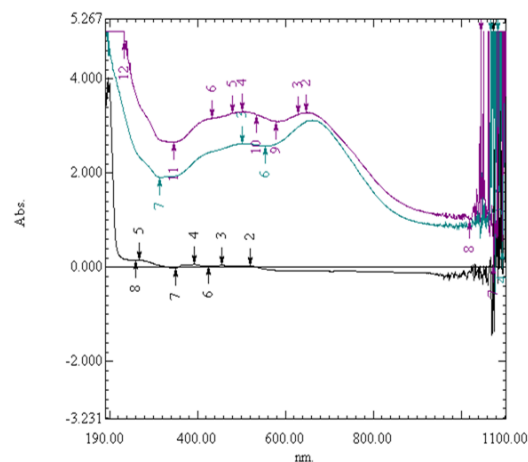


Figure 6. UV-visible absorption spectrum of phase change materials with dye.

In addition, figures 7 and 8 show the step cooling curves of disodium hydrogen phosphate dodecahydrate and zinc nitrate hexahydrate after dye addition. It can be seen that the dye has no effect on the degree of subcooling of disodium hydrogen phosphate dodecahydrate. The effect is that the zinc nitrate hexahydrate can slightly reduce the degree of subcooling, about 3-4 °C. At the same time, compared with the sample without added dye, the composite phase change material after dye addition has better crystallization condition and basically nucleation crystallization, indicating that the dye does alleviate the phase separation. Therefore, it can be concluded that the dye not only does not hinder the phase change of the phase change material, but rather helps the phase change material to crystallize better.

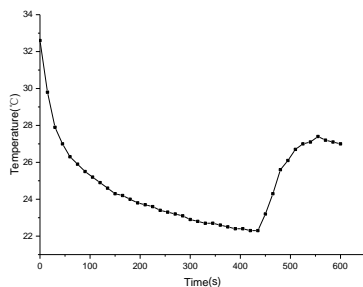


Figure 7. The cooling curve of disodium hydrogen phosphate dodecahydrate with dye after solarisation.

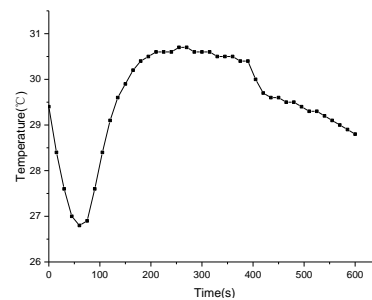


Figure 8. The cooling curve of zinc nitrate hexahydrate with dye after solarization

4. Conclusions

In this paper, the problem of supercooling in PCMs suitable for biogas plants was studied, a suitable nucleating agent and dye were selected to modify the system. The study explored the influence of the type and amount of nucleating agent on the degree of subcooling of phase change materials, and tried to add dyes to improve the light absorption properties of phase change materials. The main conclusions are as follows:

- With disodium hydrogen phosphate dodecahydrate as PCM, the composite phase change material with borax as nucleating agent is not very effective, and the phase transition temperature is basically below 25 °C, that is, the degree of subcooling is above 10 °C.
- Selecting zinc nitrate hexahydrate as the PCM, the phase transition temperature was 27.8 °C after adding 5% sodium tetraborate decahydrate, and the degree of subcooling was reduced by about 4 °C compared with that before the addition.
- The addition of dyes can improve the light absorption properties of phase change materials, make the materials make full use of solar energy, greatly improve the light absorption efficiency of the materials, and at the same time, the dyes have a certain viscosity, which can alleviate the phase separation to a certain extent and improve Crystallization effect.
- From the experimental results and analysis and calculation, 5% zinc nitrate hexahydrate added with sodium borate decahydrate was the best in the two materials tested; from the practical point of view, it is necessary to consider the energy source of the PCMs. Considering the efficiency of the PCMs in absorbing sunlight, zinc nitrate hexahydrate with 2% dye is more suitable.

5. Reference

- [1] Yan Y, Liu J and Zhang H 2009 Synthesis and Properties of Microcapsule Phase Change Materials by In-situ Polymerization *Journal of South China University of Technology (Natural Science Edition)* **37** 139-43
- [2] Jian S W, Ma B G and Li X G *et al* 2010 Fabrication and characterization of SiO₂/ stearic acid microencapsulated phase change materials prepared in different solvents *Journal of Chemical Engineering of Chinese Universities* **24** 280-5
- [3] Menanteau P, Finon D and Lamy M L 2003 Prices versus quantities: choosing policies for promoting the development of renewable energy *Energy Policy* **31** 799-812
- [4] Yang R, Xu H and Zhang Y 2003 Preparation, physical property and thermal physical property of phase change microcapsule slurry and phase change emulsion ☆ *Solar Energy Materials & Solar Cells* **80** 405-16
- [5] Wang F, Zheng M, Li Z and Lei B 2006 Application OF Phase Change Material in Solar Assisted Ground-Source Heat Pump System *Acta Energiæ Solaris Sinica* **27** 1231-4
- [6] Sharma R K, Ganesan P and Tyagi V V *et al* 2015 Developments in organic solid-liquid phase change materials and their applications in thermal energy storage *Energy Conversion & Management* **95** 193-228
- [7] Pause B 1995 Development of Heat and Cold Insulating Membrane Structures with Phase Change Material *Journal of Industrial Textiles* **25** 59-68
- [8] Marks S 1980 An investigation of the thermal energy storage capacity of Glauber's salt with respect to thermal cycling *Solar Energy* **25** 255-8
- [9] Lane G A 1981 Adding strontium chloride or calcium hydroxide to calcium chloride hexahydrate heat storage material ☆ *Solar Energy* **27** 73-5

Acknowledgments

This work was supported by the National Natural Science Foundation of China (51008262), the Science and Technology Plan Project of Xiamen City (3502Z20183041), the Xiamen University of Technology Graduate Science and Technology Innovation Program (YKJ CX2017015, YKJ CX2017018), and the Xiamen University of Technology College Student Innovation and Entrepreneurship Training Program (201811062048), China.

The Study of Banana Leaf Fiber Based Biomass Pellets Fuel

Xinwen Wang¹, Shimin Wu¹, Xin Rao¹, Jie Chi¹, Su Xu^{1*}

¹School of Environmental Sciences and Engineering, Xiamen University of Technology, Xiamen 361005, China

*Corresponding author e-mail:schnell19@qq.com

Abstract: The use of agricultural and forestry waste to produce energy-efficient biomass energy is one of the most energy-saving methods. Through the resource study and regional economic analyses, sawdust, hay and banana leaf fiber were selected as raw materials to study the main influencing factors of the palletization due to the substantial amount. Under the optimum condition: sawdust/ hay ratio of 1.49:1, fiber/particle ratio of 1:20 and the fiber length of 2.05cm, the crushing resistance increased by 12.12% and the calorific value of the mixed fuel is 17014kJ/kg. The results show that adding banana leaf fiber to hay and swadust can greatly improve the forming rate of biomass fuel, the heat value and ash content of biomass meet the national standard. There are a large number of agricultural and forestry waste can be well utilized.

1. Introduction

Biomass energy is the only renewable carbon source with carbon neutralization characteristics. The use of agricultural and forestry waste to produce energy-efficient biomass energy is one of the most energy-saving means. According to the related researches, the annual output of biomass pellets fuel abroad was more than 4.2 million tons [1] in recent years, of which the American region accounts for about 1.1 million tons [1] and the European region represents for about 3 million tons [1]. In the early 1980s, China began to attach importance to the utilization and development of biomass pellets fuel equipment. At first, the emphasis was placed on the screw extrusion molding machine. Due to a series of shortcomings such as large power consumption, short service life, the application of biomass pellets was limited. [2]-[4] With the technology improvement, at end of 2007, Chinese output of biomass pellets were about 20 tons [1] a year. But the problem of biomass pellets such as poor forming effect and bad economic application performance still unsolved. What's more, China has a land area and a large amount of biomass waste. There are a large number of agricultural and forestry waste not well utilized. For example, the annual output of bananas in the world is about 70 million to 80 million tons [5], of which 5 million to 6 million tons [5] are from China, and the by-products of banana phloem, banana leaves and banana pseudostems, which are almost equivalent amount to banana fruits, have not been exploited and utilized. They are often discarded as garbage. In the prophase treatment, incorporating the fibers can make the biomass particle structure more stable. In this study, banana leaf fibers were used as raw materials and added to sawdust and hay mixed particles to pressed as biomass pellets fuel, influence factors were determined by RSM [6], the crushing resistance was used as detector. With the addition of biomass fibers, the performance of pellets were improved and this technology could enhance the transport and utilize efficiency for other biomass resources, which might provide convenience for the transportation and popularization of biomass pellets fuel in the future. At the same time, the use of banana leaves has been developed, the effective utilization of resources would be realized.



2. Materials and methods

2.1. Materials

Sawdust: from a lumber mill in Xiamen. Hay: from the lawn in Xiamen. Banana leaves: from a banana plantation

2.2. Experimental design

In this experiment, banana leaf fibers were separated and collected to mixed with sawdust and hay in various ratio. The winding effect of fiber could make a stable "solid bridge" between sawdust and hay and improve the stability of the compressed biomass materials. The main factors affecting biomass internal briquetting were investigated, such as moisture content, fiber length, fiber to particle ratio and particle size.[7] The compressive resistance of biomass mixture fuel was determined by controlling variables strictly. The optimizations of processing were ascertained by using the RSM [6], and the test was carried out to assure the best forming effect. The combustion performance of the mixed biomass pellets fuel was determined by the calorific value and ash amount. The experiments were three repetitions.

2.3. Performance test

2.3.1. Determination of smash-resistance. Based on GB/t 21923-2008 general principles for solid biomass fuel inspection, the crushing degree of the molding compound was calculated after six free falls at a height of 1.5m.

2.3.2. Determination of calorific value. The verification experiment was conducted according to the industrial analysis method of biomass pellets fuel (GB/t 1.1-2009).

2.3.3. Determination of ash content. Based on the analysis method of solid biomass fuel industry (GB/t 1.1-2009), the ash content of banana leaf fiber blend biomass particles under the best conditions were determined.

3. Results and discussion

3.1. Experimental data analysis

Based on our previous research, the best molding effect can be seen from the addition of banana leaf fibers with different grain sizes of sawdust and hay (>0.45mm, 0.45-0.2mm, 0.2-0.125mm, <0.125mm), so the particle sizes of 0.45-0.2mm are adopted as experimental materials.

According to the analysis by response surface method, three factors that have the greatest influence on the pelletization and molding process of biomass materials were selected: (A) the ratio of sawdust to hay particles, (B) the length of fibers, (C) the ratio of fibers to particles. The three-factor three-level response surface experiment design was adopted and carried out by design-expert.v8.0.6. The results show in table 1.

The F value of the model is 4.05 and the P value is 0.0394, and the model is significant. The fitted value is greater than 0.05, which is not significant, indicating that the equation is well fitted and can be used for test data analysis. Among the three factors in the design, the ratio of sawdust to hay particles (F=11.18) had the greatest effect on the pelletization and molding of biomass. The other influencing factors are the ratio of fiber to particle and the length of fiber in order of significance. The three selected factors also intersect with each other, with the most significant cross effect between the ratio of sawdust to hay particles and the fiber length (F=1.36). The interaction of other factors is not obvious. The data shows that the accuracy and precision of the model are high, and the actual value has a good correlation with the predicted value. Therefore, the model can be used to predict and analyze the conditions of the optimization experiment during the pelletization and molding of biomass materials.

3.2. The effect of modification conditions

As shown in figure 1a, It can be seen that the surface map exhibits a "convex" shape. After the ratio of the fixed fiber to the particle, the degree of crushing increases first and then decreases with the growth of the fiber, and reaches a maximum at a rate close to 2 (1-3 cm). The ratio of sawdust to hay is similar

to the change of fiber length. The anti-fragmentation degree increases first with the increase of proportion, and then decreases slightly. The pelletization molding effect of biomass pellet fuel also changes. Because the P-value is greater than 0.05, the fiber length, there is no significant interaction between the ratio of sawdust and hay to the degree of fragmentation.

Table 1. Analysis of Variance Response surface

Source variance	Square Sum	Degrees of freedom	Mean square	Fvalue	P value F > Fa	Significance
Regression	174.89	9	19.43	4.05	0.0394	significant
A: The ratio of sawdust to hay particles	57.03	1	57.03	11.88	0.0107	significant
B: The length of fibers	2.38	1	2.38	0.49	0.5045	
C: The ratio of fibers to particles	23.26	1	23.26	4.84	0.0637	
AB	6.55	1	6.55	1.36	0.2809	
AC	0.94	1	0.94	0.2	0.6714	
BC	0.36	1	0.36	0.075	0.7921	
A^2	22.01	1	22.01	4.58	0.0695	
B^2	54.16	1	54.16	11.28	0.0121	significant
C^2	1.98	1	1.98	0.41	0.5408	
Stagger	33.61	7	4.8			
Lack of fit	25.41	3	8.47	4.13	0.1022	not significant
Pure Error	8.2	4	2.05			
Total Dispersion	208.5	16				
P < 0.05						

Figure 1b presented the results of the interaction between fiber to particle ratio and the ratio of sawdust to hay against fracture. When the fiber length is constant, the ratio of sawdust to hay is 0 (0:1), and the ratio of fiber to particle is 1 (1:60), the degree of crush resistance is the lowest. Then, the increase of fiber strengthens the forming effect, and the crushing resistance rises remarkably, mainly because the fiber can be connected with the particles to reinforce the molding, otherwise the pellet fuel is too loose, so that the crushing resistance is not good. The P value of AC is also greater than 0.05, and there is no significant interaction effect.

The interaction between fiber-to-particle ratio and fiber length shows in figure 1c. It can be seen that the fiber to particle ratio has a greater influence on the degree of breakage than the fiber length. After fixing the ratio of swadust to hay particles, the P value of BC is greater than 0.05, and there is no significant interaction effect. Both B and C variables have a slight arc effect, but the fiber length is about the median value. When the fiber weight is on the high side, the crush resistance is the highest.

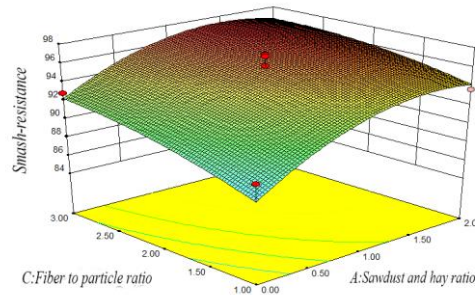


Figure 1-a. Response surface plots for A and C.

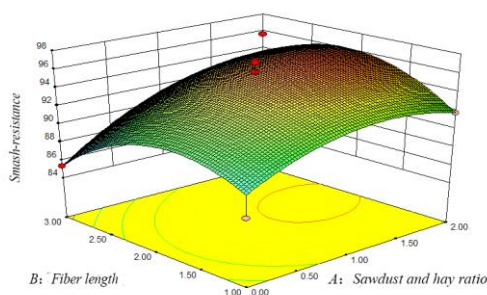


Figure 1-b. Response surface plots for A and B

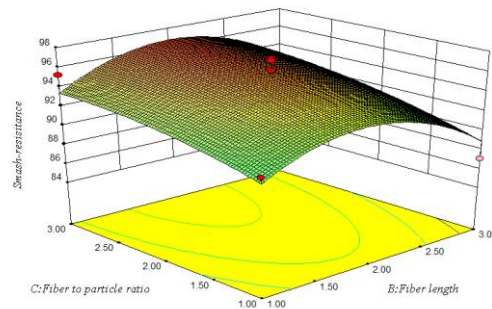


Figure 1-c. Response surface plots for B and C

3.3. Optimized study of biomass pelletization molding

Finally, according to the Design-Expert.V8.0.6 software, the best effect conditions for pelletization of biomass mixed materials. When the ratio of swadust to hay particles is 1.49:1, the fiber length is 2.05 cm, and the fiber to particle ratio is 20:1, the compression resistance of the tablet is the best.

The samples with 3 swadust and hay particles ratio of 1.49:1, fiber length of 2.05 cm and fiber to particle ratio of 1:20 were pressed to test whether it was the best condition. The results of 3 times of crushing resistance test show that the average degree of crushing resistance is 95.87%, so the results of pelletization molding of biomass materials under the condition were the best under the influence of certain error.

4. Conclusion

In this work, the results show that adding banana leaf fibers to hay and swadust can greatly improve the forming rate of biomass fuel and the heat value and ash content of biomass conform with the national standard. The optimum ratio is sawdust/ hay ratio of 1.49:1, fiber/particle ratio of 1:20 and the fiber length of 2.05cm, the crushing resistance increased by 12.12% and the calorific value of the mixed fuel is 17014kJ/kg. Biomass energy is one of the key renewable energy sources in China, especially the development of biomass fuel technology. Banana leaf fiber added with fiber winding around hay and sawdust greatly improved the anti-crushing performance, which can play a role in transportation. The potential cost saving form transportation will be practiced in future work. The fiber winding mechanism and effect of different forms of fiber will be verified by experiment in future. In addition, the sulfur content and chlorine content of biomass fuel are both less than 0.07%. Therefore, the content of harmful gases in biomass granule fuel combustion is extremely low, and the emission of less harmful gases is less.

5. Acknowledgments

The authors wish to thanks for the support of this study by research grants: Project of Education-Sciences Research of Fujian Province (JAT160352), Natural Science Foundation of Fujian (2018J01526) and Project of Key Laboratory for Ecological Industry and Green Technology of Fujian Province(WYKF2016-7), Innovative Training Program for College Students of Xiamen University of Technology(201711062227).

6. References

- [1] Tian YS 2009 Biomass solid formed fuel industry development present situation and prospect Agriculture Engineering Technology(New Energy Industry) (03) 20- 6
- [2] Wei W andZhang XK 2012Development status and prospect of solid biofuel-preparation inChina*Guangdong Agricultural Sciences***33**(05)135-8
- [3] Jian XK and Liu SC 2013 Research Status and Development Prospect of Densified Biofuel The chemical engineering of the biomass 47 (02) 54-8
- [4] Cui CL, Wang W Zhang N 2010 The Research on Construction in Energy-saving Industry Structure of Resource-based City Applied energy technology (06) 53-5
- [5] Xiong YL and Cui YH 2007 Research status of banana fiber and its prospect of development and application Journal of textile science (09) 122-4
- [6] Gao DD, Guo PH, Qi GZ and Wen HC 2015 Optimization of extraction technology of total flavonoids from *Mentha haplocalyx* by response surface methodology Food industry technology 36(02) 299-303+322
- [7] Hou PC, Wu P, Ma YH, Wang HY and Su H 2013 Analysis of influencing factors for pelletization of biomass solid fuel Agricultural technology and equipment (06) 4-6

Research on the Cellulase Hydrolysis of Colocasia Antiquorum in Producing Ethyl Alcohol

H Z Yan¹, H Y Fu^{1,2*}, G X Su³, D Zhao¹, Y C Wu^{1,2}, J F Liu^{1,2}, P F Gao^{1,2}, Y T Huang¹

¹School of Environmental Science and Engineering, Xiamen University of Technology, Xiamen 361024, China

²Key Laboratory of Environmental Biotechnology(XMUT), Fujian Province University

³Xiamen Ocean Vocational College, Xiamen 361100, China

*Corresponding Author. Phone: 0592-6291151, e-mail:fuhy@xmut.edu.cn

Abstract: The cellulase hydrolysis experiment in the process of the ethyl alcohol generated by colocasia antiquorum was studied in this paper. Adopting the single factor variable method, three influencing factors (the amount of cellulase, hydrolysis temperature and hydrolysis time) were selected to carry out enzymatic saccharification sugar production tests of pretreated colocasia antiquorums. The results demonstrate that the sugar yield amounts to the maximum (165mg/g) when the enzyme dosage is 0.04g/g, the enzymatic hydrolysis temperature is 45°C, and the reaction time is 48h.

1. Introduction

As one of the most abundant types of carbohydrates in nature, cellulose is also the most abundant biomass resource on the earth. The production of bioethanol is the most promising in terms of ethanol production. The use of modern biotechnology to develop bio-energy made up of fiber has become an important part of the energy strategies of developed countries in the world [1-4]. However, the main obstacle in the process of cellulose resource utilization is the low production efficiency and high cost of cellulase hydrolysis [5-7]. At present, only a small amount of cellulose in nature has been exploited, and most of the cellulose is wasted and even pollutes the environment [8-9]. There are plenty of cellulose and hemicellulose in the colocasia antiquorum, but little research has been carried out on the use of the cellulase hydrolysis of colocasia antiquorum to produce ethyl alcohol. Therefore, it is of great practical significance to study the factors affecting the cellulase hydrolysis of colocasia antiquorum to produce ethyl alcohol [10-11]. Taking advantage of the cellulase hydrolysis of pretreated colocasia antiquorum to obtain reducing sugar and its further fermentation to produce ethanol are of practical significance for the recycle of colocasia antiquorum and environmental protection [12-14].



2. Experiments

2.1 Experimental materials

Reagents: concentrated sulfuric acid (H_2SO_4) was purchased from Sinopharm Chemical Reagent Co., Ltd.; sodium hydroxide (NaOH) was purchased from Sinopharm Chemical Reagent Co., Ltd.; anhydrous calcium chloride ($CaCl_2$) was purchased from Sinopharm Chemical Reagent Co., Ltd.; The paste was purchased from Sinopharm Chemical Reagent Co., Ltd.

2.2 Experimental methods

(1) Pretreatment of colocasia antiquorum: A sample of colocasia antiquorum after comminution, concentrated sulfuric acid (H_2SO_4) concentration 0.50%, temperature $100^\circ C$, solid-liquid ratio 1:30, pretreatment for 60 min, then wash it with suction until the filtrate Neutral, then transfer the residue to the enzymatic system. The pretreated samples were washed to neutral and placed in 250mL stoppered conical flasks and numbered according to conditions. A hydrolyzed system (50mL) having a solid-liquid ratio of 1:50 was placed in an Erlenmeyer flask, sterilized at $121^\circ C$ for 20 min, pH was adjusted to 4.5, and 0.05g of $CaCl_2$ was added.

(2) Testing and determination of the optimal cellulase concentration: 0.01g, 0.02g, 0.03g, 0.04g, 0.05g according to the amount of enzyme added to the hydrolysis system, set the temperature to $45^\circ C$, the shaking tables speed to $120r \cdot min^{-1}$, Then, the stoppered conical flask was placed in a shaker and hydrolyzed, and the reducing sugar content of the sample solution in the conical flask was determined, and the optimal enzyme dosage of cellulase hydrolysis and saccharification was compared [15].

(3) Testing and determination of the optimal Enzymatic Saccharification Temperature: set the shaking table temperature to $30^\circ C$, $35^\circ C$, $40^\circ C$, $45^\circ C$, $50^\circ C$, $120 r \cdot min^{-1}$ after hydrolysis, then, The optimal temperature of cellulase hydrolysis glycosylation was obtained by measuring the content of reducing sugar in the sample solution in a tapered bottle.

(4) Testing and determination of the optimal enzymatic saccharification time: according to the optimal enzymatic hydrolysis temperature determined in (3), the temperature is set, $120r \cdot min^{-1}$, after hydrolysis for 12h, 24h, 36h, 48h, 60h, respectively. The sample solution in the stopper flask was used to determine the reducing sugar content, and the optimal enzymatic saccharification time of the enzymatic saccharification was determined.

3. Experimental results and discussion

3.1 Effects of the amount of enzyme on the cellulose hydrolysis

Figures 1 Show Effects Of The Amount Of Cellulase Enzyme On The Production Of Reducing Sugar During Diastatic Fermentation Of Zantedeschia. It can be seen that when 0.01g of cellulase is added, the yield of reducing sugar is the lowest, only 124mg/g, and as the cellulase content increases, the yield of reducing sugar also increases. When the content of cellulase was 0.04g, the yield of reducing sugar reached the maximum 165mg/g, and the amount of cellulase continued to increase. The yield of reducing sugar was basically unchanged and tended to be stable. Therefore, the optimum dosage of the enzyme is 0.04g/g substrate.

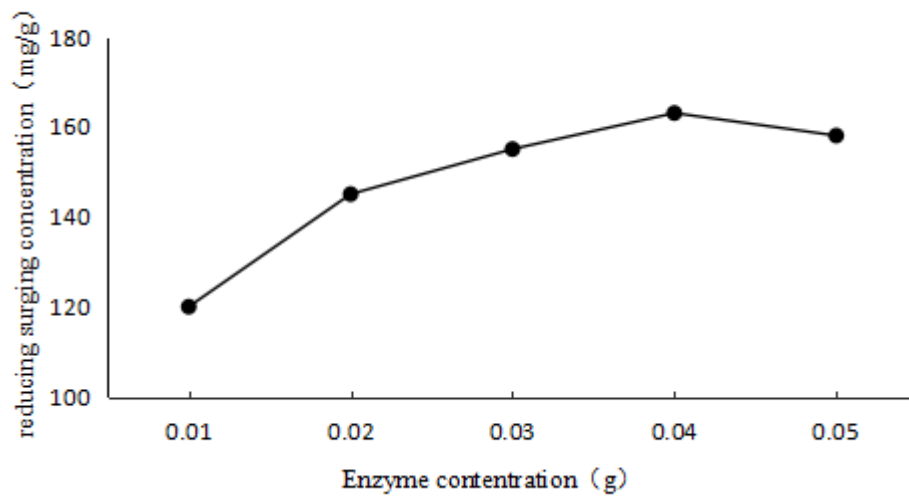


Figure 1. Effects of the amount of cellulose enzyme on the yield of reducing sugar

3.2 Effects of enzymatic saccharification temperature on enzymatic saccharification

As shown in Figure 2, when the temperature is 30°C, the yield of reducing sugar is the lowest. With the increase of temperature, the yield of reducing sugar also increases. When the temperature rises to 45°C, the yield of reducing sugar is up to 165mg/g. When the temperature is higher than 45°C, the yield of reducing sugar will no longer increase with the increase of temperature, but will decrease, instead, the yield of reducing sugar is not increased. It can be seen that when the temperature is 45°C, Cellulase has the largest activity and highest efficiency, which can make the vitamin substances into reducing sugars at the maximum layer. When the temperature reaches the optimal temperature, As the temperature increases, the structure of cellulase will be destroyed, the activity and efficiency of cellulase will be affected, and the yield of reducing sugars will begin to decline. Therefore, this experiment adopts saccharifying enzyme solution treatment temperature 45°C

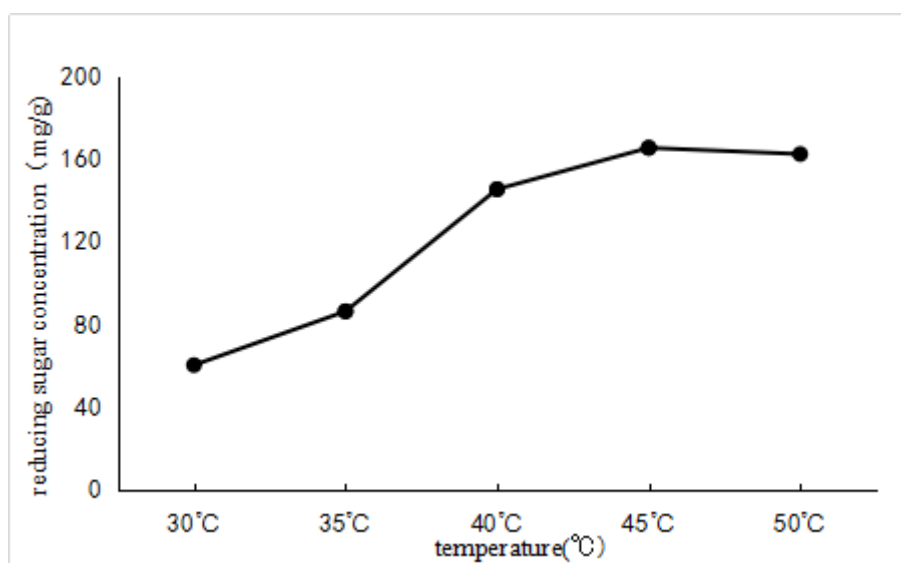
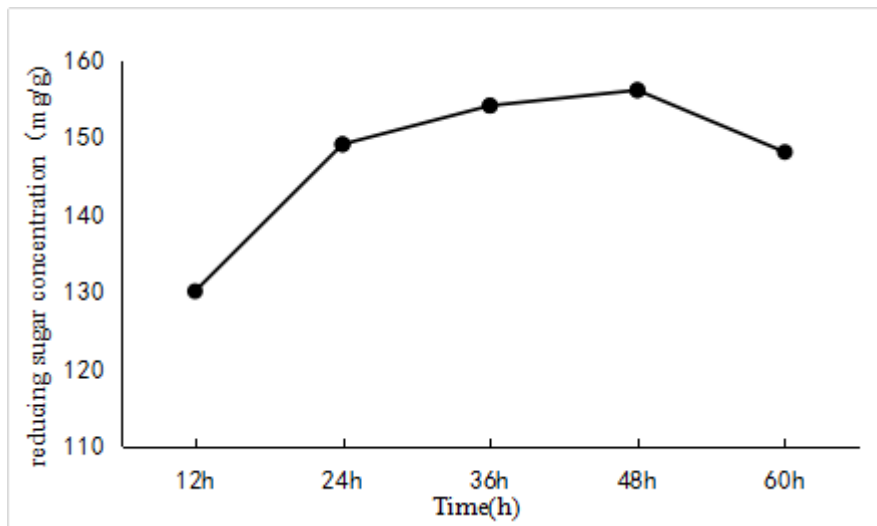


Figure 2. Effects of temperature on the concentration of reducing sugar

3.3 Effects of time on hydrolysis of cellulase enzyme

As shown in Figure 3, when the dosage of enzyme is 0.04mg/g, the temperature is 45°C, the time of enzymatic hydrolysis is 12h, the yield of reducing sugar is 130mg/g. With the increase of enzymatic hydrolysis time, the yield of reducing sugar is also increased. When the hydrolysis time is in 24-48h, the yield of reducing sugar increases faster in 14-36h with the increase of hydrolysis time, in 36-48h In the time period, the yield of reduction was also increasing, but the increase rate of reducing sugar began to slow down, and the maximum reducing sugar yield was 165mg/g at 48h. When the hydrolysis time continued to extend, the yield of reducing sugar began to decrease, which was too long with the enzymatic hydrolysis time, making partial reducing sugar unsteadily decomposed. Therefore, the optimum time for enzymatic saccharification is 48h.

**Figure 3.** Effects of enzymolysis time on the yield of reducing sugar

4. Conclusions

With the single factor controlled variable method, this research took the yield of reducing sugar as the standard and investigated the optimal conditions of the enzyme dosage, hydrolysis temperature and hydrolysis time during the cellulase hydrolysis of colocasia antiquorum. Results show that the sugar yield reaches its maximum (165mg/g) when the enzyme dosage was 0.04g/g, the enzymatic hydrolysis temperature was 45°C, and the reaction time was 48h.

Acknowledgements

This work was financially supported by Fujian Science and Technology Guiding Project (2018Y0079), National Natural Science Foundation of China(51109181), Natural Science Foundation Project of Fujian Province(2018J01527).

5. References

- [1] Ćilerdžić J, Galić M, Vukojević J, et al. Potential of selected fungal species to degrade wheat straw, the most abundant plant raw material in Europe [J]. *Bmc Plant Biology*, 2017, 17(2): 249.
- [2] Meng Z, Zheng X, Tang K, et al. Dissolution of natural polymers in ionic liquids: A Review[J]. *e-Polymers*, 2013, 12(1):317-345.
- [3] Sun Manbiao, Peng Taibing, He Shicheng, et al. Research progress in bio-ethanol production from combined bioprocessing of lignocellulose[J]. *Jiangsu Agricultural Sciences*, 2018, 46(8): 5-10.
- [4] Wang Duanchao. Study on Process Control and Optimization of Fuel Ethanol Production by Watermelon Fermentation[D]. East China Normal University, 2015.
- [5] C. Roger Mac Kenzie, Bilous D, Patel A G B. Studies on Cellulose Hydrolysis by *Acetivibrio cellulolyticus*. [J]. *Applied & Environmental Microbiology*, 1985, 50(2): 243-248.
- [6] SU Donghai, SUN Junshe. Improving Cellulase Hydrolysis Efficiency and Reducing Hydrolysis Cost[J]. *Chemical Progress*, 2007, 19(7): 1147-1152.
- [7] Liu Yuanyuan, Sun Junshe, Qi Haisheng, et al. Research progress in improving the hydrolysis efficiency of lignocellulosic enzymes[J]. *China Brewing*, 2011, 30(5): 16-20.
- [8] Liu Boshi. Screening of cellulase-producing bacteria and their utilization in the development of bacillary dysentery [D]. Tianjin University, 2008.
- [9] Liu Xiaojie, Guo Xiufeng, Ou Kai. Study on Degradation of Rice Straw by Cellulase[J]. *China Food Additive*, 2009(4):99-102.
- [10] Zhang Jian. Research on key technology of bio-transformation of lignocellulosic feedstock to produce cellulosic ethanol[D]. East China University of Science and Technology, 2011
- [11] JI Chunxue, DU Fengguang, SHI Jiping, et al. Research progress of cellulase for cellulosic ethanol[J]. *Journal of Brewing Science*, 2007(7): 118-121.
- [12] Yang Na. Study on the production of ethanol from water hyacinth and licorice residue [D]. Huazhong University of Science and Technology, 2009.
- [13] Sun Y, Cheng J. Hydrolysis of lignocellulosic materials for ethanol production: A review[J]. *Bioresource Technol*, 2002,83(1): 10-11.
- [14] Ni tianyu, tao ling, ren jun, et al. Advances in fuel ethanol pretreatment using lignocellulosic materials [J]. *Guangdong chemical industry*, 2010, 37(3):18-20.
- [15] Zheng Yuanjie, Hao Jianyu, Hou Hongping. Study on the Mixed Fermentation Conditions of Cellulase Produced by *Aspergillus niger*[J]. *China Brewing*, 2016, 35(12): 118-122.

Oil Price Factors: Forecasting on the Base of Modified ARIMA Model

Anthony Msafiri Nyangarika ^{1,2}, Bao-jun Tang ¹

¹School Management and Economy, Beijing Institute Technology, 5 South Zhongguancun Street, Beijing 100081, Peoples R China.

²Institute of Adult Education, P.O. Box 20679 Dar sea Salaam, Tanzania.

E-mail: nyangarikatz@gmail.com

Abstract. The paper proposes the modification of ARIMA model for finding the parameters of estimation and forecasts using exponential smoothing. The study use data Brent crude oil price and gas prices in the period from January 1991 to December 2016. The result of the study showed an improvement in the accuracy of the predicted values, while the emissions occurred near the end of the time series. It has minimal or no effect on other emissions of this data series. The study suggests that investors can predict prices by analyzing the possible risks in oil futures markets.

1. Introduction

Over the years, oil has remained one of the most important sources of energy. All countries, one way or another, are consumers of oil and oil products. There are already more than 100 countries in the oil-producing countries. Prices for oil and its derivatives are of concern to both producers and consumers. The dynamics of oil prices affect the level of costs in all production sectors. The economy of many countries is based on oil production and trade in oil and oil products, the forecasting of oil prices is an urgent task. Sectors of the economy are directly dependent on oil price forecasts. Oil prices influence the political and economic processes that determine the value of oil companies' shares, the level of inflation in the oil importing countries, and the speed of economic growth. It is important to note the impact of oil prices on the formation of prices for alternative energy sources.

The purpose of this work is to identify factors that affect the price of oil and to obtain a reliable forecast model of oil prices. To achieve this goal, it is necessary to perform a number of tasks:

- To study the factors influencing the price of oil;
- Consider the method of forecasting ARIMA data
- Collect and conduct descriptive data analysis;
- Build a regression model and identify significant factors;
- Get forecasts on the methods outlined above, choose the best one and build on it a forecast for the future.

The total volume of oil consumption in 2014 was approximately 4.2 billion tons, which is 54% more than in 1973. Thus, the average increase in oil consumption over the years since the oil shock was ~ 1% per year. At the same time, after the economic crisis of 1973-1983, oil consumption steadily grew until the beginning of the 2008 crisis. However, there is a widespread opinion that significant and unexpected fluctuations in oil prices have a negative impact on the welfare of both oil importers and oil-producing countries. Oil prices and oil price volatility both play important roles in affecting the global economy, although the effects are asymmetric depending on periods, regions, sectors, the



reason for oil shock, and others. Several studies found that higher oil prices have an adverse impact on the global economy [1]. Moreover, [2],[3] found an economic impact on oil importing countries such as South Korea. In order to make appropriate decisions about the direction of economic policy, therefore, it is important to accurately forecast future oil prices with effective models.

The price of oil is one of the key factors determining the country's budget in terms of its revenues. The practice of determining the forecast price of oil is based on the method of constructing consensus forecasts. This method is based on forecasts of the largest players in the oil market, investment banks, international economic and financial organizations. These include the International Energy Agency, the Organization of Petroleum Exporting Countries (OPEC), the World Bank, IHS Global Insight, Raiffeisen Bank, the International Monetary Fund [4].

The following shortcomings attributed to this approach.

1. The closed nature of forecasting techniques, based on the results of which consensus forecasts are built. Since almost every method of forecasting has certain drawbacks, the closed nature of the applied methods does not allow us to estimate the degree of possible forecast error. Using in the construction of a consensus forecast the results obtained from various sources, each of which used different forecasting techniques, can lead to an "inheritance" of the deficiencies inherent in the initial projections.

2. On the other hand, the initial estimates were based on specific assumptions and assumptions, methodological approaches that allow us to obtain an acceptable forecast, the use of the consensus forecast will actually level the result, distorting the results of qualitative initial projections and introducing a share of erroneous forecasts estimates obtained from other sources.

Analysis of the practice of constructing forecast estimates and forecasting methods applied by various scientific organizations, state bodies, and commercial companies has shown that today the most popular approaches used by various financial organizations and institutions are econometric forecasting methods. In this regard, as an alternative to the consensus forecast method, [14] proposed to use the prediction method.

In addition, some sectors of the economy directly depend on the forecast of oil prices. For example, airlines that rely on air ticket price forecasts, the automotive industry and simply homeowners who rely on oil price forecasts (and prices for secondary products such as gasoline or heating oil) in modeling the purchase of long-term goods use such as cars or home heating systems.

2. Literature review

Several studies found that the Organization of the Petroleum Exporting Countries (OPEC) decided to maintain oil production in 2014, the crude oil price dropped to less than \$50/Bbl. The price has stayed at mid-\$40/Bbl on continued sluggish oil demand and strong shale supply in 2015 and 2016.

[4],[5] proposed that consequently, oil price volatility and another oil crisis have been growing. In this context, knowing the long-term trend in crude oil prices is essential for ensuring future economic stability in many countries because significant changes in crude oil prices and unstable oil supplies may seriously affect their economies, which depend on crude oil imports and exports.

The Auto-Regressive Integrated Moving Average (ARIMA) methodology was used time-series data to reflect the wild volatility of time-series data. Besides ARIMA models forecast oil prices by using the interrelationship between the future price and the spot price of crude oil in short-term forecasting. [6], [7] explained a conditional variance that changes over time, to forecasting the Brent oil price. [11] estimated the oil price needed to maximize the producer's profit in a perfectly competitive and monopolistic market using dynamic optimization. In his results, oil prices followed a U- shape pattern in the case of a small initial reserve endowment but then showed a rise over time in the case of a large initial reserve endowment.

Since 2000, financial factors, including the penetration of speculative forces, a weakening dollar, and the financial crisis, have attracted attention as possible determinants of global oil prices. [15],[16] have also provided support for the role of speculation in the oil market, especially for its role in the rise of crude oil prices. For example, [17] found that financial shocks have considerably contributed to oil price increase since the early 2000s, and to a much larger extent since mid-2000s. Among several financial factors, the speculative expectation has been indicated as an important determinant of the price for a commodity.

Even though [18] explained the changing pattern in oil prices, his approach is difficult to apply to actual data and is limited in that it examines factors driving oil price fluctuations only from the supply side. Many research institutes have used EIA forecasts as credible data. Delphi approach, which repeatedly collects opinions to derive the joint subjective view of experts, can also be used to forecast oil prices. Using prices determined in the future oil market has been suggested as a forecasting methodology. [19],[20] analyzed if future prices from a certain time could be appropriately used to forecast spot prices by testing the Granger causality between WTI spot prices and future prices. While forecasting oil prices using future prices shows accurate performance in the short term. Such an approach tests if the future price is an unbiased predictor of the spot price at the maturity time [21],[22] evaluated forecasting accuracy by comparing future prices (1, 2, 3 and 4-month), future contracts with WTI spot prices from 1991 to 2016. [23] used WTI spot and future prices from July 2000 to June 2004 as sample data, selecting the forecasting period that yielded the most accurate forecasts by comparing quarterly forecasts based on future prices from the previous one to six months with the average of the quarterly WTI oil prices.

Previous research on oil price forecasting models has generally assumed that the current trend in oil prices will continue in the future and thus that factors influencing oil will have the same effects in the future. However, factors influencing oil prices have changed structurally over time. In the 1960s, supply-side factors determined the crude oil price, and this trend continued until the oil price collapse of the mid-1980s. Consequently, an oil pricing system linked to the oil market has existed since the late 1980s, and the crude oil price has been determined by demand as well as supply. In the 1990s, especially, emerging markets such as China and India led oil prices to rise.

However, the role of speculation in causing the significant changes in oil prices is still debatable. Several studies are not supportive of speculation being an important determinant of the real oil prices and. Even though the global oil market paradigm has been changing continuously, previous forecasting models have rarely reflected such structural changes. As such, this study can contribute to preparing quick and accurate oil market countermeasures by forecasting short-term oil prices. This study's model is highly applicable. The forecast oil prices reported here can thus be used to inform reasoned decision making by the government and the private sector.

3. Methodology

The auto-regressive integrated moving average (ARIMA) methodology was used time-series data, the wild volatility of time-series data. Besides time-series models such as ARIMA and GARCH models, ARIMA has also been employed to forecast oil prices by using the interrelationship between the future price and the spot price of crude oil, which explain a conditional variance that changes over time, to forecasting the Brent oil price which are used to prove the cointegration between the real (spot) oil prices and the prices of 1, 2, 3 and 4-month futures contracts. In this paper, we will consider the method of forecasting using the ARIMA model. Due to the constant changes occurring in the world, we found it prudent to build short-term and retro forecasts. In the framework of this work, we are primarily interested in such a method as ARIMA (Auto Regressive Integrated Moving Average). Despite the fact that this model belongs to the class of linear methods, it equally well describes stationary and non-stationary time series. In addition, independent variables are not used in this model, which means using only the information embedded in the data itself for forecasting. The autoregressive model (AR) of the order p has the following form:

$$Y_t = \varphi_0 + \varphi_1 Y_{t-1} + \varphi_2 Y_{t-2} + \dots + \varphi_p Y_{t-p} + \varepsilon_t \quad (1)$$

Where, Y_t - dependent variable at the time t ; $\varphi_0, \varphi_1, \varphi_2, \dots, \varphi_p$ - estimated coefficients; ε_t - an error describing the effects of variables that are not taken into account in the model. The moving average model (MA) of the order q is described as follows:

$$Y_t = \mu + \varepsilon_t - \omega_1 \varepsilon_{t-1} - \omega_2 \varepsilon_{t-2} - \dots - \omega_q \varepsilon_{t-q} \quad (2)$$

Where, Y_t - dependent variable at the time t ; μ - constant process average; ε_t - an error at time t ; $\omega_1, \omega_2, \dots, \omega_q$ - estimated coefficients. Some non-stationary time series can be reduced to stationary ones using the operator of a consecutive difference. Assume that there is a time series y_t , to which d times applied this operator, after which the series became stationary $\Delta^d y_t$ and satisfying the conditions of the model ARMA (p, q). The model of auto regression and moving average will have the form:

$$\Phi(L)y_t = \delta + \Theta(L)\varepsilon_t, \quad \varepsilon_t : \text{iid}(0, \sigma^2), \quad (3)$$

Where

$$\Phi(L) = 1 - \varphi_1 L - \varphi_2 L^2 - \dots - \varphi_p L^p \quad \text{and} \quad \Theta(L) = 1 - \theta_1 L - \theta_2 L^2 - \dots - \theta_q L^q$$

- polynomials from the shift

operator. In this case y_t will be called the integrated process of auto regression and moving average or ARIMA (p, d, q). This model allows you to build very accurate forecasts with a short forecasting range. It is also quite flexible and can be suitable for describing different time series. In addition, ARIMA models are simply checked for their adequacy. However, the disadvantages of this method include the need for a large number of initial data and the absence of a simple method of adjusting the parameters of the model.

4. Results and discussion

We use data on prices for Brent crude oil in the period from January 1991 to December 2016. We took this particular energy source as a substitute for oil because they are one of the most popular on the market today. The task was to see how much the price of oil depends on the price of alternative energy sources. The impact of armed clashes in the oil-producing countries is becoming less important in the formation of oil prices [8], [9] believe the opposite. Also, as a dummy variable, we included the global financial crisis - it was in 2008 that it had a significant impact on the price of oil, and caused one of the most significant falls. (Table.1) shows all the factors that we will include in the model - both in the form of time series (oil price, gold price, and gas price), and in the form of fictitious variables (World financial crisis, military conflicts of Iraq, Iran, Syria and Afghanistan, a terrorist attack in the United States). The right column of (Table.1) shows which designation for each variable we specify in the E-views program.

We use the econometric models to identify the dependence between the variables, we need to look at the descriptive statistics for our variables, as well as check the data for the presence of emissions. All this must be done to obtain the most accurate model. Descriptive statistics for a number of oil prices in (Fig. 1).

Therefore, from this histogram, shown in Figure 1, the mathematical expectation for the OIL variable is 48.93, which means that the average value of oil prices fluctuates around \$ 49 / bbl. The standard deviation of this variable is 34.93. Those the spread of individual values of OIL with respect to its mean value is 35. The following is the series for stationarity as shown below (Table. 2).

Table 1. Description of variables

Factor	Variable
Brent crude oil price, The price of gold Price gas	Oil, Gold, Gas
Dummy variables:	MFC
World financial crisis	Iraq
The Military company in Iraq	Iran
The Military company in Iran	Syria
The Military company in Syria	Afghanistan
The Military company in Afghanistan	Terror
The US Terror	

Source: Authors 'calculation

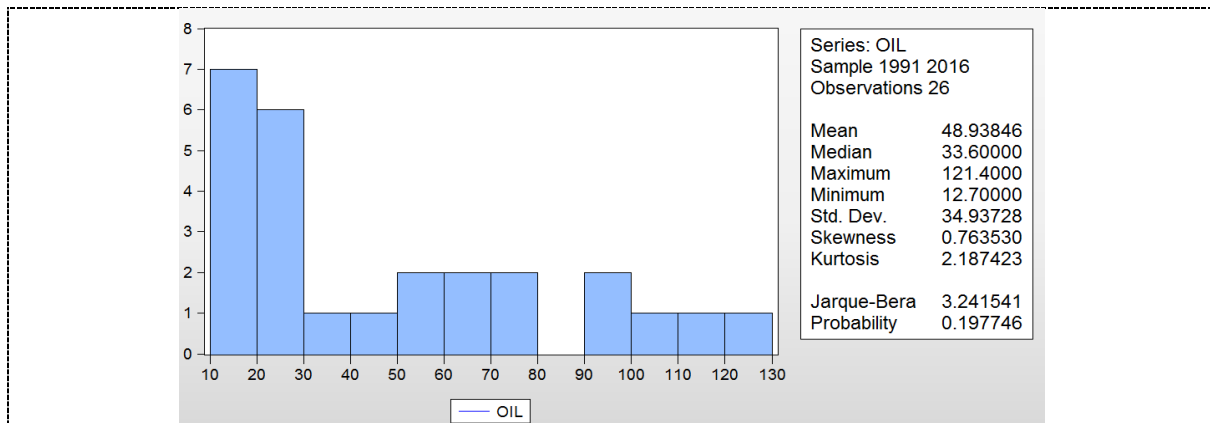


Figure 1. Histogram for oil prices

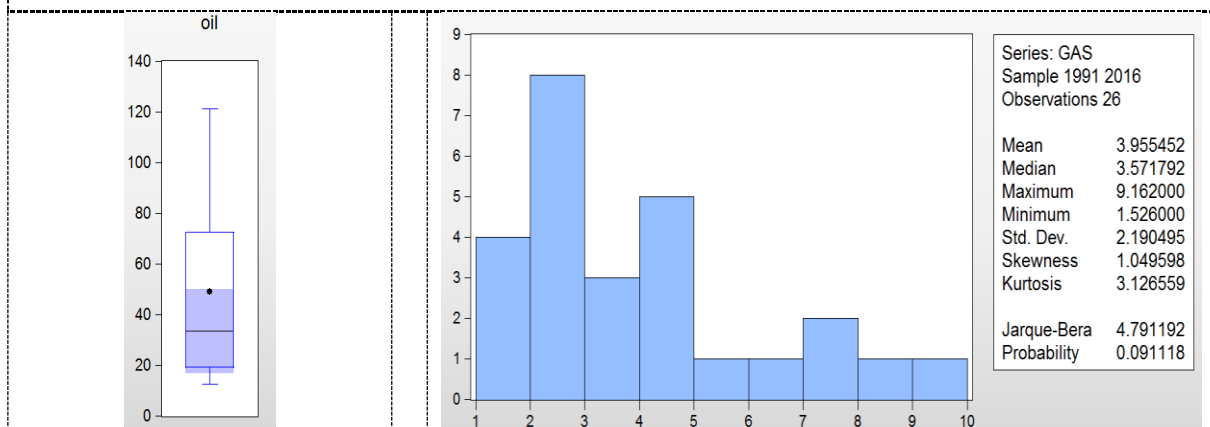


Figure 2. Schedule Boxplot for oil prices

Figure 3. Histogram for gas prices

Source: Authors ‘calculation

The series is not stationary (Table.2), the probability value Prob = 0.6137, we cannot reject the hypothesis of the presence of a unit root; therefore, the series is not stationary. In order to get rid of no stationarity, we check the series for the first difference

Table 2. Test for stationarity of a number of oil prices

Test	t-Statistic	Prob.
Augment Dickey-Fuller test statistic	-1.298902	0.6137

Source: Authors’ calculation

Table 3. Test for stationarity of a number of oil prices

Test	t-Statistic	Prob.
Augment Dickey-Fuller test statistic	-4,121776	0.0041

Source: Authors’ calculation

According to the results presented in (Table.3), the hypothesis of the presence of a unit root is rejected; we succeeded in bringing the series to a stationary form. In order to be convinced of the absence of emissions, a Boxplot graph should be constructed. Our graph for the OIL variable indicates no emissions (Fig. 2).

Boxplot graph carries out similar descriptive statistics for explanatory variables: gas and gold. We turn to a description of a number of gas prices.

From this histogram (Fig. 3) it can be seen that the mean for the GAS variable is 3.95, which indicates that the average value of coal prices fluctuates around 4. The standard deviation of this variable is 2.19. The spread of individual values of GAS with respect to its mean value is 2.2. By checking the series for stationarity, we again encountered the no stationarity of the data series (Table.4).

Table 4. Stationary test of a number of gas prices

Test	t-Statistic	Prob.
Augment Dickey-Fuller test statistic	-1,855319	0.3467

Source: Authors' calculation

The value $\text{Prob} > 0.05$, we cannot reject the null hypothesis about the presence of a unit root. Taking the first differences for a number of gas prices, the series to a stationary form (Table 5).

Table 5. Stationary test of a number of gas prices

Test	t-Statistic	Prob.
Augment Dickey-Fuller test statistic	-6,023421	0.0000

Source: Authors' calculation

The following test variable is the last of the series - gold prices.

From this histogram (Fig.4), it can be seen that the mathematical expectation for the variable GOLD is 685.25, which means that the average value of gold prices fluctuates around 685. The standard deviation of this variable is 457.02. The spread of individual values of GOLD with respect to its mean value is 457. A number of these gold prices were initially unsteady, so using the method of first differences already known to us; we bring the series to a stationary form.

The value of $\text{Prob} < 0.05$, therefore, we can reject the hypothesis of the presence of a unit root, thereby confirming the stationarity of the series (Table.7). Similarly, to complete the descriptive analysis, it is necessary to check the series for the presence of emissions. To do this, we built Boxplot graphics.

Table 6. Test for stationarity of a number of gold prices

Test	t-Statistic	Prob.
Augment Dickey-Fuller test statistic	-5,524744	0.0002

Source: Authors' calculation

According to the graphs (Fig. 5), we show that the gold variable GOLD has no emissions, which cannot be said about the variable that includes gas prices - GAS. Despite the presence of emissions from this variable, we will not get rid of them in order to get the most accurate and complete picture of the effect of gas prices on the price of oil. It will also be interesting to look at the correlograms for each of the series of data.

Analyzing the correlograms for each of the series of data (Fig.6), we can say that all our series are stationary - the correlograms decreases from the germ k after the first values. In addition, there is no periodic component in each of the series of data, which tells us that there is no seasonality. In order not to encounter the phenomenon of multi collinearity in the future when constructing the regression, we will check our variables for the presence of a correlation between them.

In order to construct an econometric model, we will use fictitious variables, which include military conflicts and the global financial crisis. We created variable with value 1, in case of conflict, and otherwise 0. For example, the variable world financial crisis in our regression model will take

the value 1 in the period from 2008 to 2010, when during 2008 (year of the financial crisis), the value of oil prices assumed the lowest values, in other cases it will be zero, similar data will be made for other fictitious parameters.

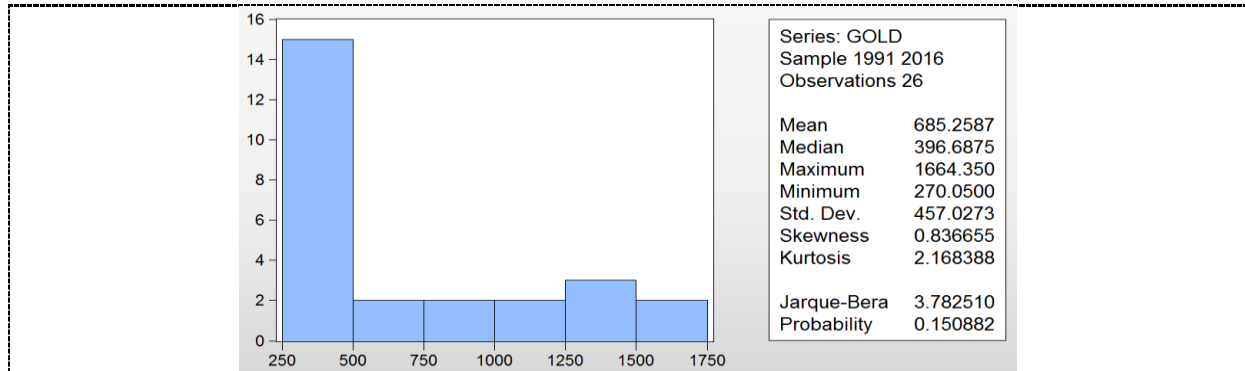


Figure 4. Histogram for gold prices

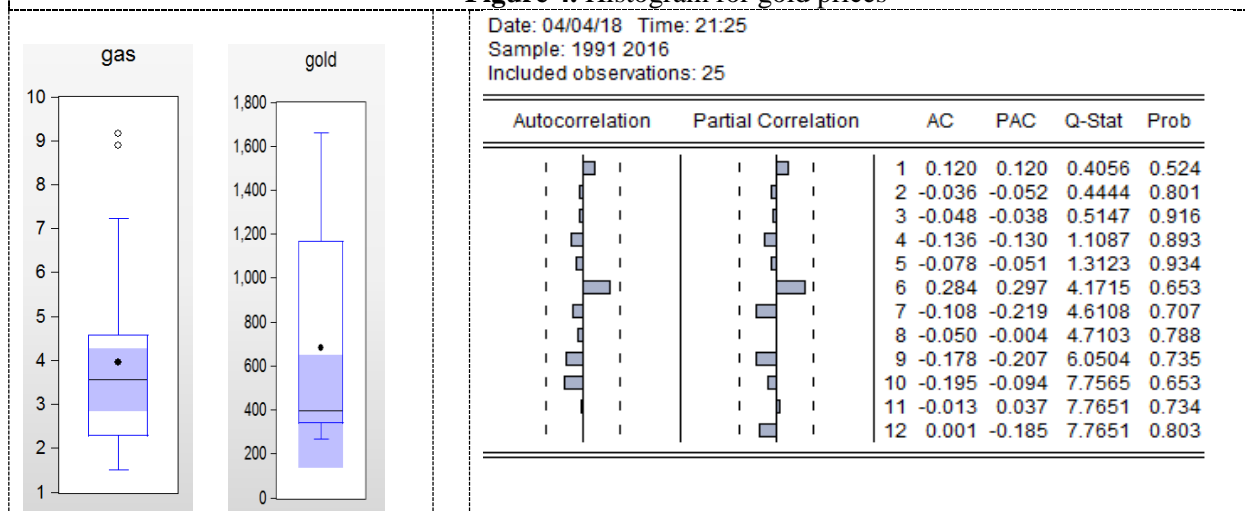


Figure 5. Pox Plot chart for gas and gold prices

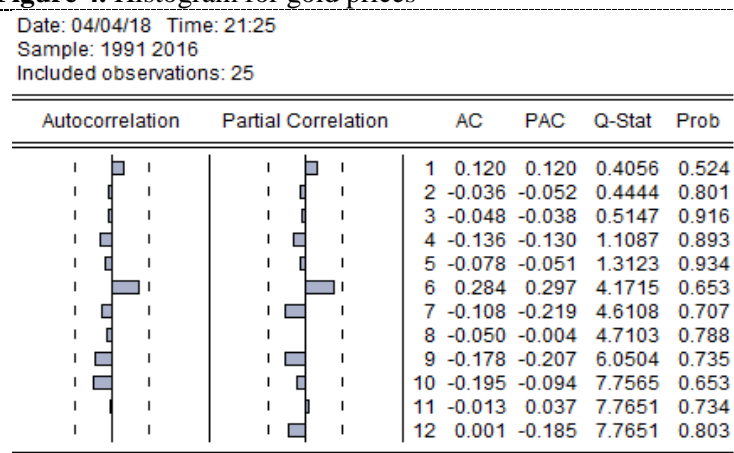


Figure 6. Correlograms of the price of oil

However, the construction of the regression model. As a dependent variable, we will use oil prices - OIL, as explanatory gas prices - GAS and gold - GOLD, as well as include dummy variables - CRISIS, IRAN, IRAQ, AFGHANISTAN, SYRIA, and TERROR. It is important to note that in order to construct the regression, we take all the data series in the differences. This is explained by the fact that initially, all our series were nonstationary, and we brought them to a stationary form by taking the first differences for each of the series of data. (Table.7) shows the values of the coefficients and probabilities for each of the variables included in the constructed model

Table 7. The value of the corresponding probabilities for the regression variables

Variable	Coefficient	Probability
D(GAS)	6,336001	0,0001
D(GOLD)	0,103214	0,0002
Iran	3,262685	0,6778
Iraq	-11,17840	0,0092
AFGHANISTAN	9,845998	0,2112
SYRIA	-7,859139	0,1227

Crisis	-9,544256	0,1353
TERROR	-7,998058	0,4246

Source: Authors' calculation

From the above (Table.7), we can conclude that the variables D (gas), D (gold) and Iraq are significant (Table.7)- show that they have an effect on the price of oil. While the probabilities of the rest are greater than 0.05, which indicates their insignificance. There is no correlation between these variables and the oil price variable - OIL. A more detailed table obtained in the construction of the model (Fig.7).

The results show the variable GAS was significant, i.e. rising or falling in gas prices leads to changes in oil prices. This can be explained by the fact that each of these types of energy resources is very widely used and the volumes of their production and consumption are quite large, which leads to the influence on each other. Another explanation can be the fact that gas in some industries is a substitute for oil, therefore, in the case of an increase in oil prices, the demand for it will decrease and the transition to other, cheaper energy resources, for example, gas will be implemented, which will increase the demand for it and subsequently the price.

Therefore, the gold, we cannot reveal the effect of the change in gold prices on the price of oil. This is explained by the fact that despite the apparent popularity of investing in precious metals, they do not stop investing in shares of oil companies. Of all the fictitious variables, only IRAQ was significant, a conflict that began in December 2004. It can be said that the significance of military conflicts in the oil-producing countries has an ever-smaller and insignificant effect on the price of oil. Thus, we perceive that over time, in fact, one factor increases in importance, while others decrease. In order to correctly estimate the model constructed, we carry out the Ramsey test (Table.8).

Table 8. Ramsey test

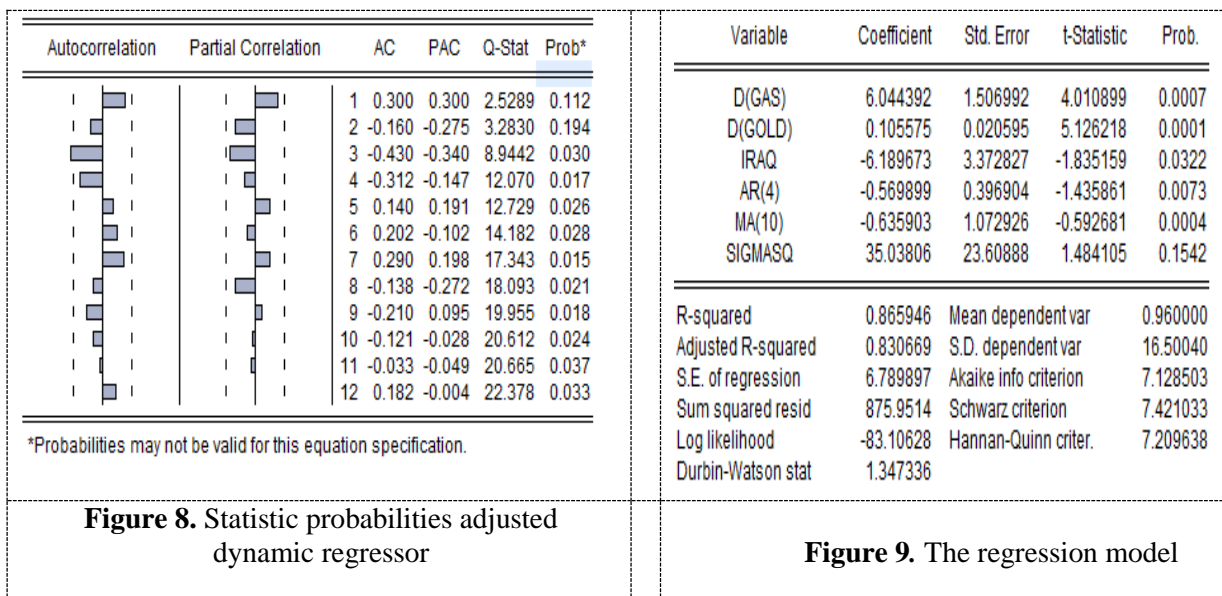
Test	F-Statistic	Prob. F(1, 15)
Ramsey RESET Test	2,123687	0.9697

Source: Authors' calculation

According to the values of F-Statistic and Prob. Presented in (Table.8), we can conclude that the hypothesis of the acceptability of the functional form is adopted, that is, this model is correctly specified. To get a more accurate model, we conducted a test for extra variables (Fig.8). This test confirmed that the insignificant variables of our regression model, namely, IRAN, AFGHANISTAN, SYRIA, TERROR, and CRISIS are superfluous and we can exclude them from the model. After analyzing the correlograms (Fig.8) and eliminating the extra variables, we constructed the following model (Fig. 9). From all variables are significant, low probabilities tell us this (Prob) in (Fig.9). The value of the criterion Akaike info criterion decreased, which again indicates that this model has become better. F-statistics has assumed a higher value. In addition, when constructing the regression, we included the processes AR and MA to get rid of the autocorrelation, which we found in the analysis of the correlograms.

Variable	Coefficient	Std. Error	t-Statistic	Prob.
C	-2.512660	2.574510	-0.975976	0.3436
D(GAS)	6.336001	1.250799	5.065564	0.0001
D(GOLD)	0.103214	0.021180	4.873226	0.0002
IRAN	3.262685	7.709218	0.423219	0.6778
IRAQ	-11.17840	6.589602	-1.696369	0.0092
AFGHANISTAN	9.845998	7.559718	1.302429	0.2112
CRISIS	-9.544256	6.067232	-1.573082	0.1353
TERRACT	-7.998058	9.760216	-0.819455	0.4246
SYRIA	-7.859139	4.823225	-1.629437	0.1227

Figure 7. Correlation between Oil Prices



Source: Authors' calculation

5. Conclusion

In this paper were considered: factors affecting the price of oil and ways to predict this price using different models. In the course of the analysis, it turned out that among all the factors we were considering, the value of oil prices is influenced by the price of gold (GOLD) and the armed conflict in Iraq that has occurred since 2004 (IRAQ). However, the factors that proved insignificant in this model: the financial crisis, the conflicts in Iran, Afghanistan, Syria, and the terrorist attacks that occurred in the Middle East and the United States. This can lead to increased demand for oil and, as a result, will lead to an increase in the price. In this paper, not all the problems that arise when forecasting oil prices were considered, therefore it would be advisable to continue to consider different forecasting methods in the future, so that the values obtained are as close as possible to the real ones. One of the directions for further research can be the application of a larger number of models of different types to obtain different forecasts of the series

Reference

- [1] Akpan, E. O. (2009), Oil price shocks and Nigeria's macro economy. A Paper Presented at the Annual Conference of CSAE Conference. Economic Development in Africa. Retrieved from <http://www.csae.ox.ac.uk/conferences/2009-EDIA/Papers/252-Akpan.Pdf>.
- [2] Amano, R. A. and Van Norden, S. (1998), Exchange Rates and Oil Prices. *Review of International Economics*, 6: 683–694. doi:10.1111/1467-9396.00136.
- [3] Baumeister, C., & Peersman, G. (2008), Time-varying effects of oil supply shocks on the US economy.
- [4] Backus, D. K. and M. J. Crucini (2000), Oil Prices and the Terms of Trade. *Journal of International Economics*, 50, 185-213.
- [5] Barsky, R.B.; Kilian, L. (2004), Oil and macro economy since the 1970s. *J. Econ. Perspect.* 18, 115– 134.
- [6] Buetzer, S., Habib, M. and L. Stracca (2012), Global Exchange Rate Configurations: Do Oil Shocks Matter? Working Paper, European Central Bank.
- [7] Farzanegan, M. R., & Markwardt, G. (2009), The effects of oil price shocks on the Iranian economy. *Energy Economics*, 31(1), 134-151. <http://10.1016/j.eneco.2008.09.003>.
- [8] Ferraro D., Rogoff K. and B. Rossi (2015), Can Oil Prices Forecast Exchange Rates? Available at: <http://www.econ.upf.edu/~brossi/OilAndExchangeRates.pdf>.
- [9] Huang, Y. and F. Guo (2007), The role of oil price shocks on China's real exchange rate. *China Economic Review*, 18: 403-416.

- [10] Hooker, M. (1996), Oil prices and the rise and fall of the US real exchange rate. *Journal of Monetary Economics*, 25, 195-213.
- [11] Hsu, T.-K.; Tsai, C.-C.; Cheng, K.-L. (2016), Forecast of 2013–2025 crude oil prices: Quadratic sine- curve trend model application. *Energy Sources Part B* 2016, 11, 205–211.
- [12] Kilian, L. (2009), Not all oil price shocks are alike: Disentangling demand and supply shocks in the crude oil market. *Am. Econ. Rev.* 99, 1053–1069.
- [13] Kilian, L.; Murphy, D.P. (2014), The role of inventories and speculative trading in the global market for crude oil. *J. Appl. Econ.*, 29, 454–478.
- [14] Mikhailov A. (2014), Faktory razvitiya ekonomiki Rossii v 2015 godu [Factors of development of the Russian economy in 2015]. *Voprosy regulirovaniya ekonomiki = Questions of economic regulation*, 4, pp. 62-69.
- [15] Mikhailov A. (2018), Pricing in Oil Market and Using Probit Model for Analysis of Stock Market Effects. *International Journal of Energy Economics and Policy*, 4, pp. 43–53.
- [16] Mikhaylov, A. (2018), Volatility Spillover Effect between Stock and Exchange Rate in Oil Exporting Countries. *International Journal of Energy Economics and Policy*, 2018, 8(3), 321-326.
- [17] Morana, C. A (2001), Semiparametric Approach to Short-term Oil Price Forecasting. *Energy Econ*, 23, 325– 338.
- [18] Li, H.; Wells, M.T.; Yu, C.L. (2008). Bayesian Analysis of Return Dynamics with Stochastic Volatility and Levy Jumps. *Rev. Financ. Stud*, 21, 2345–2378.
- [19] Olomola, P. A., & Adejumo, A. V. (2006), Oil price shock and macroeconomic activities in Nigeria. *International Research Journal of Finance and Economics*, 3(1), 28-34.
- [20] Sadorsky, P. (1999), Oil price shocks and stock market activity. *Energy Econ.* 21, 449-469.
- [21] Segal, P. (2011), Oil price shocks and the macro economy. *Oxf. Rev. Econ. Policy*, 27, 169–185.
- [22] Singer, E. (2007), Oil Price Volatility and the US Macroeconomy: 1983-2006. Working paper, Minnesota of USA: Carleton College.
- [23] Tuzova, Y., & Qayum, F. (2016), Global oil glut and sanctions: The impact on Putin’s Russia. *Energy Policy*, 90, 140–151. <https://doi.org/10.1016/j.enpol.2015.12.008>

DSGE Model of the Russian Economy: Economic Impact of Oil Price

Anthony Msafiri Nyangarika^{1,2*} and Bao Jun Tang¹

¹ Beijing Institute Technology, School Management & Economy, 5 South Zhongguancun Street, Beijing 100081, Peoples R China.

² Institute of Adult Education, P.O. Box 20679 Dar sea Salaam, Tanzania.
E-mail: nyangarikatz@gmail.com

Abstract: In the paper the DSGE model proposed on the base of the theory of adaptive expectations. The aim of this work is to describe the possibility of using DSGE models for forecasting the Russian economy. This paper examines how the methodology of dynamic stochastic general equilibrium models can be applied to predict the yields of government bonds in 2018-2020, the proposed modification of the Taylor rule and the components of the prediction rate of the Russian ruble, characteristic of resource economies, where there is a close relationship between the exchange rate and oil price. It proposed the forecast of main macroeconomic indicators in the period 2017-2020 years (economic growth, inflation, oil price, exchange rate, Bank of Russia key rate and effective yields of government bonds). The practical significance of this work lies in the structuring of existing knowledge on the applicability of DSGE models of the Russian economy. The article also outlines the macroeconomic trends and modeling the conditions of an unstable economic situation in Russia. The parameters of monetary policy are also significant for determining the government bond yields. In addition, this article sheds light on forecasting the term structure of interest rates based on macroeconomic indicators.

1. Introduction

Research on the role of oil price in the Russian economy has emphasized the importance of the market channel in RUBUSD fluctuations. In this paper, we develop a dynamic stochastic general equilibrium (DSGE) model to quantify the importance of the endogenous interaction between oil market, inflation and the bank capital position for the transmission of macroeconomic shocks. The model is estimated using Russian data over the period 2008Q1–2017Q4 from Thomson Reuters Datastream.

Dynamic stochastic general equilibrium (DSGE) model that is based on Neo-Keynesian economic theory. Traditionally, they are a modern means of analyzing the impact of monetary and fiscal policies. DSGE models can also be used to predict inflation, GDP, and interest rates. In addition, within the DSGE-models, it is possible to compare the effectiveness of the implementation of the economic policy of the authorities. Since the early nineties of the twenty-first century, they have been used by most Central banks, including the European Central Bank, the US Federal Reserve, the Bank of England, the Bank of Canada, the Bank of Russia and others.

The explanation of the key features of the time structure of interest rates is a problem for standard models. Macroeconomic models [1]-[10] have difficulties in rationalizing the average duration of the expectation hypothesis. At the same time, empirical data indicate a close relationship between bond yields and macroeconomic indicators [18], [19].



In addition, we prove the relationship between the slope of the curve zero-coupon bond yield and forecasts of economic growth [15]-[20].

2. Literature review

This research paper covers the gap in the finance literature on monetary DSGE models with credit market frictions and is related to several recent studies [5], [6]. Many researchers [13], [27], [35], [36] show that term structure of interest rates in a DSGE model with recursive preferences can depend on oil price.

[38] – [41] develop models with financial frictions, in which the real and financial sectors are linked through the spillover effect of financial markets.[37] assume that changes in the volatility of five central European stock markets arise from an exogenous stochastic loan default rate. Most closely related to our framework is a series of DSGE models that allow for an endogenous interaction between financial asset market pricing on the one hand and macroeconomic indicators on the other. In particular, [4] integrate new parameters into a DSGE model to investigate the potential of cyclical bank capital regulation for macroeconomic stabilization. [9] develop the financial parameter proposed in [11], [12] by considering financial contracts. In a similar framework, [34] discusses the effects of macro indicators for the propagation of technology and monetary shocks. [7], [8] develop the impact of money and wage contracts in an optimizing model of the business cycle, and discuss the cost channel of monetary transmission, capital depreciation, and bank riskiness shocks.

First, while [22]-[26] calibrate their models to the U.S. economy, we estimate a model with endogenous interactions between oil price and national currency rate. Second, we discuss the effects of the interaction between bond yield and inflation by explicitly considering a number of macroeconomic shocks.

3. Methods

The monetary policy transmission mechanism [31] describes a channel connecting changes in lending conditions and macroeconomic variables. The article proposes a mechanism based on the dynamic stochastic general equilibrium model (DSGE) for forecasting the time structure of OFZ rates, based on their conditions of monetary policy dynamics and macroeconomic variables.

In addition, it is assumed that the factor of endogenous growth of vertical innovations [16], [17] can also be included in the standard Neo-Keynesian DSGE model. This model has several distinctive features.

First, households are sensitive to uncertainty over the long-term prospects of economic growth [2].

Second, the Central Bank sets short-term nominal interest rates based on the Taylor rule.

Thirdly, the expected economic growth is associated with business solutions for the production of goods and services. Fourthly, the uncertainty factor of business activity changes over time.

When the time series are adjusted in accordance with macroeconomic variables such as consumption, production, investment, unemployment, inflation and wage dynamics. This model quantifies the return to the average, volatility and nominal yield of bonds. Bond yields can be predicted by spreads between forwarding contracts or by a linear combination of forwarding rates.

The following assumptions should be made for successful bond yield modeling. First, the channel of endogenous growth creates long-term risks due to innovative solutions of firms [3]. Second, the presence of nominal linkages helps to assess the relationship between expected economic growth and inflationary expectations. Third, changing the uncertainty of economic growth leads to a time-varying bond risk premium. The Taylor rule and asset price model has ceased to be effective after the transition to quantitative easing and keeping interest rates low for a long time. The modern model of the interrelation of dynamics of endogenous inflation and dynamics of growth of consumption [14] influences decisions of producers of goods and services.

The article contracts with asset price models within the framework of liquidity preference theory [21], which take into account long-term risks arising in the economy. Taking into account the positive results achieved before, it is possible to expand the existing paradigm to study the time structure of interest rates. The dynamic stochastic general equilibrium model, unlike the static models studied in the General Equilibrium Theory, shows the development of the economy based on the preferences of economic agents. For example, households optimize consumption and labor efforts. Firms usually

maximize profits. Technological restrictions on agent decisions may also include the cost of adjusting their stocks, labor relations, or the price of their products.

Agents must comply with the exogenous limitations of monetary and fiscal policy and may vary depending on the political process. Currently dominated by two competing scientific schools:

- The school of real business cycles is based on a neoclassical growth model. She studies how real shocks in the economy can cause business cycle fluctuations.
- Neo-Keynesian models suggest conditions of monopoly competition. They cannot react instantly to changes in macroeconomic variables.

The Bank of Russia uses a model of Smets–Wouters to analyze the Russian economy as a whole. Models contain three types of decision-making agents:

- Household ;Firms ;Central bank.

The parameters of the equations are estimated using Bayesian statistical methods in such a way that the model roughly describes the dynamics of GDP, consumption, investment, prices, wages, employment, and interest rates in the Russian economy (Fig. 1,2,3,4).

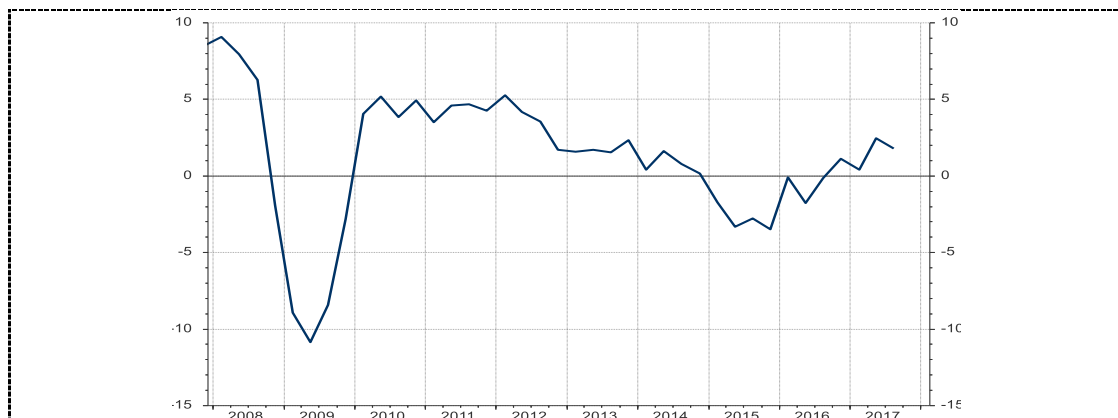


Figure 1. GDP Dynamics in the Russian Federation (2008-2017)
GDP (% YOY, Standardized): Russia Source Thomson Reuters Data Stream



Figure 2. CPI Dynamics in the Russian Federation (2008-2018)
CPI(YOY): Russia Source Thomson Reuters Data Stream



Figure 3: Crude oil price (1985-2018)
Crude Oil M1 Europe FOB\$ Bbl. Source Thomson Reuters Data Stream



Figure 4: Price dynamics of RUBUSD (2008-2018)
Russian Rouble To Us\$ Source Thomson Reuters Data Stream

To accurately reproduce the behavior of some variables, the model includes different types of frictions and shocks. The following formula is used to model GDP:

$$y_t = a_1 y_{t-1} - a_2 mci_t + a_3 y_t^* + \varepsilon_t^y \quad (1)$$

where y_t is the gap in the output of goods and services relative to the average level at time t ; the monetary policy index is calculated by the formula:

$$mci_t = a_4 r_t + (1 - a_4)(-z_t) \quad (2)$$

where y_t^* – the gap world output relative to the average level at time t ; ε_t^y – frictions of the demand in time t ; r_t deviation of the real interest rate relative to the equilibrium at time t ; z_t – deviation of the real exchange rate from the equilibrium at time t ; a_1 is the coefficient of inertia of the output gap; a_2 – coefficient of influence of monetary policy on the output of goods and services; a_3 – coefficient of influence of demand on the output of goods and services; a_4 – coefficient of influence of monetary policy on real interest rates.

The following formula is used to simulate inflation:

$$\pi_t = b_1 \pi_{t+1} + (1 - b_1) \pi_{t-1} + b_2 rmc_t + \varepsilon_t^\pi \quad (3)$$

where π_t - inflation; π_{t+1} – inflation expectations; rmc_t - real marginal costs are calculated by the formula:

$$rmc_t = b_a y_t + (1 - b_a) z_t \quad (4)$$

where ε_t^π – frictions of inflation at time t ; b_1 is the coefficient of inertia of inflation; b_2 – coefficient of influence of economic growth on inflation; b_a – the share of domestic goods and services consumption

Instead of the traditional Taylor rule for interest rate modeling, we use the following formula proposed by the First Deputy Chairman of the Bank of Russia Ksenya Yudaeva:

$$\dot{i}_t = f_1 \dot{i}_{t-1} + (1 - f_1) \dot{i}_t + f_2 (\pi_{t+1}^b - \pi_t^T) + f_a + f_4 + \varepsilon_t^i \quad (5)$$

where ε_t^i – is the friction of interest rates at the time t ; f_1 is the inertia degree of the nominal interest rate, f_2 is the elasticity of the interest rate of the real exchange rate, f_a is the elasticity of the interest rate of GDP, f_4 is the elasticity of the interest rate of the ruble.

The following formula is used to model the exchange rate of the national currency:

$$S_t = e_1 S_t^b + (1 - e_1) \left(S_{t+1}^B + \frac{\dot{i}_t^* - \dot{i}_t + prem_t}{4} \right) + \varepsilon_t^s \quad (6)$$

where

$$S_{t+1}^B = S_{t-1} + \left(\frac{-\pi_t^* + \pi_t + z_t}{4} \right) \quad (7)$$

where S_t – growth rate of nominal exchange rate of the ruble; S_{t+1}^B – is the expected growth rate of the nominal exchange rate; \dot{i}_t^* – the average nominal interest rate in the world; $prem_t$ – risk premium; ε_t^s – frictions of the ruble exchange rate at time t ; $-\pi_t^* + \pi_t$ – deviation of domestic inflation from global; z_t – the equilibrium level of the real exchange rate at time t ; e_1 – coefficient of inertia in the exchange rate. After calibration of the specified model, we obtained the optimal values of the model parameters (Table 1).

The complexity of DSGE modeling of the Russian economy is the high volatility of the dynamics of the exchange rate of the Russian ruble and the complexity of its forecasting, which, in fact, is the mathematical derivative of the price of oil. While forecasting oil prices on the basis of mathematical models is a futile exercise: the supply of oil depends on political arrangements and its accuracy, the demand for oil is largely regulated by reserve storages.

Table 1 : Parameters of the DSGE model of Russia

Parameter	Value
Impact of monetary conditions on the real economy	-0,2
The significance of interest rate in monetary policy	0,45
Impact of costs	0,18
Smoothing inflation expectations	0,37
Influence of the deviation of expected inflation from the target level	0,65
Effect of the exchange rate deviation from the stable	0,35
Smoothing of currency expectations	0,35
The inertia of interest rates	0,61
The influence of the deviation of expected inflation from the target level	0,65
Impact of the deviation of GDP from the steady state	0,34
Effect of the exchange rate deviation from the stable	0,35
The flexibility of the foreign exchange market	0,11
Smoothing of currency expectations	0,35

Source: compiled by the author.

4. Results

The price of bonds with n-period to maturity is expressed by the formula:

$$P_t^{(n)\$} = E_t \left[M_{t+1}^{\$} P_{t+1}^{(n-1)\$} \right] \quad (8)$$

where E_t is the yield on bond ownership during the period $[t; t+1]$, $P_t^{(n)\$}$ is the bond price at the time t , $P_{t+1}^{(n-1)\$}$ is the bond price at the time $t+1$, $M_{t+1}^{\$}$ is maturity at the time $t+1$

$M_{t+1}^{\$}$ has a conditionally normal distribution, the formula takes the form of:

$$P_t^{(n)\$} = E_t \left[\sum_{j=1}^n m_{t+j}^{\$} \right] + \frac{1}{2} \text{var}_t \left[\sum_{j=1}^n m_{t+j}^{\$} \right] \quad (9)$$

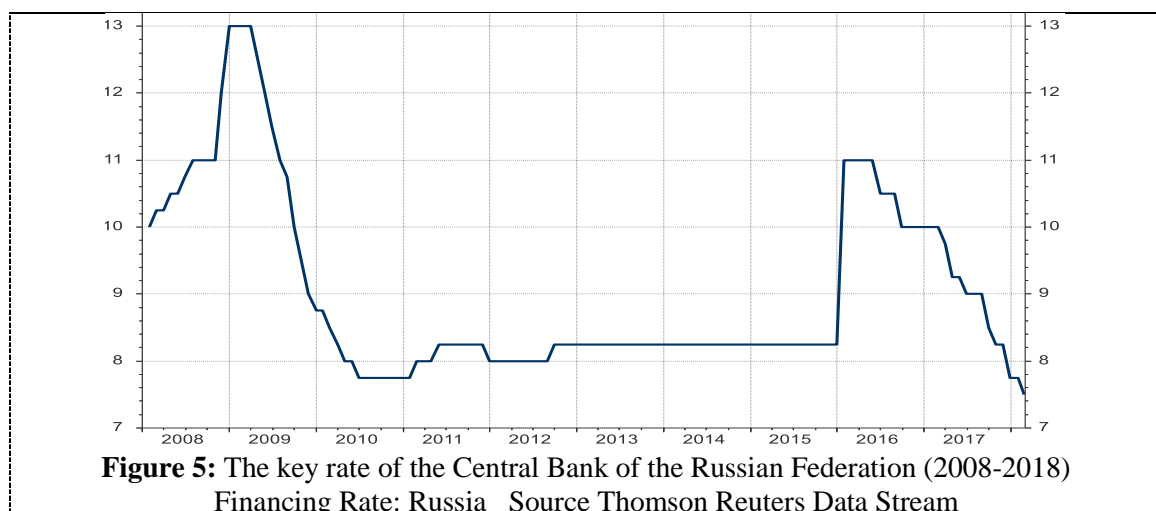
where var_t – variance at time t , n is the number of periods payments of the coupons.

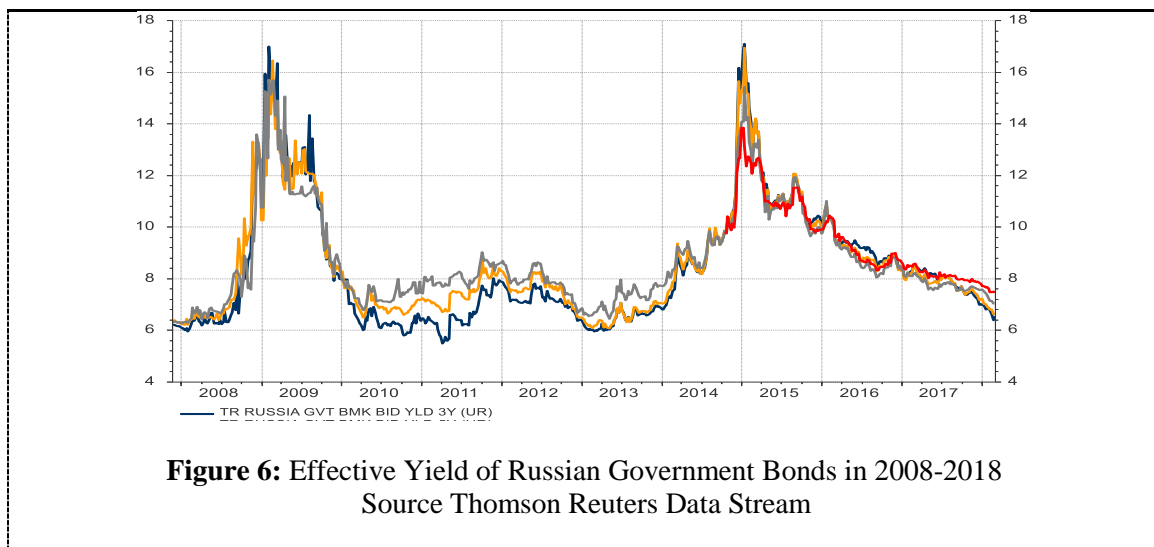
Then the yield of the bond to maturity ($y_t^{(n)\$}$) can be found by the formula:

$$y_t^{(n)\$} = -\frac{1}{n} E_t \left[\sum_{j=1}^n m_{t+j}^{\$} \right] - \frac{1}{2n} \text{var}_t \left[\sum_{j=1}^n m_{t+j}^{\$} \right] \quad (10)$$

The low frequency of economic growth and inflation, as well as the negative relationship between expected economic growth and inflationary expectations, have important implications for the temporary structure of rates. In the study period significantly increased correlation between the key rate of the Bank of Russia and interest rates on the bond market (Figure 5 and 6). In 2016 there is an alignment of the cordless yield curve. It acquires a positive slope inherent in a "healthy" economy. At the same time, the negative relationship between economic growth and inflationary expectations suggests that long-term bonds have lower yields when long-term growth is expected to be low. That is the zero-coupon yield curve of government bonds, acquires a negative slope [32]. To understand the negative long-term relationship between growth and inflation, It needs to consider a positive shock. A prolonged increase in productivity lowers real marginal costs over a long period of time and leads to lower inflation. The model of endogenous growth of consumption and inflation has been described in previous research in detail [28].

The slope of the nominal bond yield curve is a strong predictor of economic growth and inflation over a given business cycle. The growth channel plays an important role in explaining the average temporary spread while increasing the maturity of the bond. In addition to generating long-term growth risks, endogenous growth is also important for assessing the negative long-term relationship between inflation expectations and economic growth [29, 30]. The above model allows us to make a forecast of economic indicators.



**Table 2:** Forecast of the main economic indicators of Russia

Parameter	2017	2018	2019	2020
Growth rate of real GDP, %	1,02	0,64	0,46	1,14
Inflation expectations, %	4,20	3,54	5,31	6,27
Average exchange rate of RUBUSD, rubles	57,02	62,36	70,78	75,55
Average effective yield of OFZ 20Y, %	7,42	7,02	7,89	8,55

Source: compiled by the author.

Current trends in the strengthening of USD may presumably go until 2019-2020, based on the revealed in recent years, the long macroeconomic cycles characteristic of the world economy after the signing of the Bretton woods agreement [33]. Therefore, we believe that the proposed forecast values are fair and it has a maximum deviation error of $\pm 5\%$ (Table 2).

5. Conclusion

Thus, we adopt the DSGE model widely used in developed economies for the Russian one. The relationship between the parameters of monetary policy and the yield of the government bond market is studied. In addition, this article sheds light on the prediction of the yields of OFZ bonds on the base of macroeconomic indicators using a General stochastic equilibrium model of endogenous growth. As a result, a medium-term forecast of Russian macroeconomics is obtained: the current political and economic situation is maintained.

6. References

- [1] Ag énor, P.-R., Bratsiotis, G.J., Pfajfar, D. (2014), Credit frictions, collateral, and the cyclical behavior of the finance premium. *Macroecon. Dyn.* 18 (05), 985–997.
- [2] Albertazzi, U., Gambacorta, L. (2009), Bank profitability and the business cycle. *J. Financ. Stabil.* 5 (4), 393–409.
- [3] Aliaga-Daz, R., Olivero, M.P. (2010), Is there a financial accelerator in US banking? Evidence from the cyclical behavior of banks' price-cost margins. *Econ. Lett.* 108 (2), 167–171.
- [4] Angeloni, I., Faia, E. (2013), Capital regulation and monetary policy with fragile banks. *J. Monet. Econ.* 60 (3), 311–324.
- [5] Bansal, R., D. Kiku, A. Yaron (2012), An empirical evaluation of the long-run risks model for asset prices. *Critical Finance Review* 1(1), 183-221.
- [6] Bansal, R., I. Shaliastovich (2013), A long-run risks explanation of predictability puzzles in bond and currency markets. *Review of Financial Studies* 26(1), 1-33.
- [7] Barth, M.J.I., Ramey, V.A. (2002), The cost channel of monetary transmission. In: *NBER Macroeconomics Annual 2001*, Volume 16. National Bureau of Economic Research, Inc, pp. 199–256.

- [8] Benassy, J.-P. (1995), Money and wage contracts in an optimizing model of the business cycle. *J. Monet. Econ.* 35 (2), 303–315.
- [9] Benes, J., Kumhof, M. (2015), Risky bank lending and countercyclical capital buffers. *J. Econ. Dyn. Control* 58 (C), 58–80.
- [10] Beeler, J., J. Y. Campbell. (2012), The long-run risks model and aggregate asset prices: an empirical assessment. *Critical Finance Review* 1(1), 141-182.
- [11] Bernanke, B., Lown, C.S. (1991), The credit crunch. *Brookings Pap. Econ. Act.* 22 (2), 205–248.
- [12] Bernanke, B.S., Gertler, M., Gilchrist, S. (1999), The financial accelerator in a quantitative business cycle framework. In: Taylor, J.B., Woodford, M. (Eds.), *Handbook of Macroeconomics: Vol. I*. Elsevier Science B.V., pp. 1341–1392.
- [13] Binsbergen, J., J. Fernandez-Villaverde, R. Koijen, J. Rubio-Ramirez. (2012), The term structure of interest rates in a dsge model with recursive preferences. *Journal of Monetary Economics* 59(7), 634-648.
- [14] Bloom, N., M. Floetotto, N. Jaimovich, I. Saporta-Eksten, S. J. Terry. (2012), Really uncertain business cycles. Unpublished working paper. Stanford University.
- [15] Berrospide, J.M., Edge, R.M. (2010), The Effects of Bank Capital on Lending: What do We Know, and What does it Mean?. *Finance and Economics Discussion Series 44*. Federal Reserve Board.
- [16] Bikker, J.A., Hu, H. (2002), Cyclical patterns in profits, provisioning and lending of banks and procyclicality of the new Basel capital requirements. *BNL Q. Rev.* 55 (221), 143–175.
- [17] Bolt, W., de Haan, L., Hoeberichts, M., van Oordt, M.R., Swank, J. (2012), Bank profitability during recessions. *J. Bank. Finance* 36 (9), 2552–2564.
- [18] Borio, C., Zhu, H. (2012), Capital regulation, risk-taking and monetary policy: a missing link in the transmission mechanism? *J. Financ. Stabil.* 8 (4), 236–251.
- [19] Brooks, S.P., Gelman, A. (1998), General methods for monitoring convergence of iterative solutions. *J. Comput. Graph. Stat.* 7 (4), 434–455.
- [20] Buch, C.M., Eickmeier, S., Prieto, E. (2014), In search for yield? Survey-based evidence on bank risk taking. *J. Econ. Dyn. Control* 43, 12–30.
- [21] Carlstrom, C.T., Fuerst, T.S. (1997), Agency costs, net worth, and business fluctuations: a computable general equilibrium analysis. *Am. Econ. Rev.* 87 (5), 893–910.
- [22] Cecchetti, S.G., Li, L. (2008), Do capital adequacy requirements matter for monetary policy? *Econ. Inq.* 46 (4), 643–659.
- [23] Cho, J.-O., Cooley, T.F. (1995), The business cycle with nominal contracts. *Econ. Theory* 6 (1), 13–33.
- [24] Croce, M., H. Kung, T. Nguyen, L. Schmid. (2012), Fiscal policies and asset prices. *Review of Financial Studies*.
- [25] Croce, M., T. Nyugen, L. Schmid. (2012), Fiscal policies and the distribution of consumption risk. Unpublished working paper. Duke University 25(9), 2635-2672.
- [26] Haan, W. (1995), The term structure of interest rates in real and monetary economies. *Journal of Economic Dynamics and Control* 19(5-7), 909-940.
- [27] Mikhaylov A.Y. (2012), Ocenka ehffektivnosti funkcionirovaniya investicionnyh fondov v Rossii [Assessment of efficiency of functioning of investment funds in Russia]. *Vestnik Instituta Ekonomiki RAN = Bulletin of the Institute of Economics (RAS)*, no. 5, pp. 121–129.
- [28] Mikhaylov A.Y. (2013), Effektivnost ispol'zovaniya aktivov investicionnyh fondov na osnove GIPS [Efficiency of use of assets of investment funds on the basis of GIPS]. *Ekonomika i predprinimatelstvo = Economics and entrepreneurship*, no. 4, pp. 372–375.
- [29] Mikhaylov A. Y. (2014), Faktory razvitiya ekonomiki Rossii v 2015 godu [Factors of development of the Russian economy in 2015]. *Voprosy regulirovaniya ekonomiki = Questions of economic regulation*, no. 4, pp. 62-69.
- [30] Mikhaylov A.Y. (2018), Pricing In Oil Market And Using Probit Model For Analysis Of Stock Market Effects = *International Journal of Energy Economics and Policy*, 2, pp. 69–73.
- [31] Taylor, J. (1993), Discretion versus policy rules in practice. *Carnegie-Rochester Conference Series on Public Policy* (39), 195-214.

- [32] Mikosch, T. and Starica, C. (2004), Non-stationarities in financial time series, the long range dependence, and the IGARCH effects. *Review of Economics and Statistics*, 86, pp. 378-390.
- [33] Newey, W.K. and West, K.D. (1994), Automatic lag selection in covariance matrix estimation. *Review of Economic Studies*, 61, pp. 631-654.
- [34] Sanso, A., Arago, V. and Carrion-i-Silvestre, J. (2004), Testing for changes in the unconditional variance of financial time series. *Revista de Economia Financiera*, 4, pp. 32-53.
- [35] Wachter, J. (2006), A consumption-based model of the term structure of interest rates. *Journal of Financial Economics* 79(2), 365-399.
- [36] Walid, C., Chaker, A., Masood, O. and Fry, J. (2011), Stock market volatility and exchange rates in emerging countries: Markov-state switching approach. *Emerging Markets Review*, 12, pp. 272-292.
- [37] Wang, P. and Moore, T. (2009), Sudden changes in volatility: The case of five central European stock markets. *Journal of International Financial Markets, Institutions and Money*, 19, pp. 33-46.
- [38] Woodford, M. (2003), *Interest and Prices: Foundations of a Theory of Monetary Policy*. Princeton University Press, New Jersey.
- [39] Wright, J. H. (2011), Term premia and inflation uncertainty: Empirical evidence from an international panel dataset. *The American Economic Review* 101(4), 1514-1534.
- [40] Zhao, H. (2010), Dynamic relationship between exchange rate and stock price: Evidence from China. *Research in International Business and Finance*, 24, pp. 103-112.
- [41] Zivkov, D., Njegic, J. and Milenkovic, I. (2015), Bidirectional Volatility Spillover Effect between the Exchange Rate and Stocks in the Presence of Structural Breaks in Selected Eastern European Economies. *Finance a uver-Czech Journal of Economics and Finance*, 65, no. 6.

Chapter 8:
Environment and Economy

Study on Performance Optimization of SCR Denitrification of an Ultra-low Emission Coal-fired Power Unit

Li Bing¹, Song Yongqiang², Zhang Qilong¹, Zhou Can¹ and Duan Haoran¹

¹ Huadian Electric Power Research Institute Co.,LTD., Jinan, China

² Huadian Power International Corporation Limited Zouxian Power Plant, Jining, China

E-mail: 13869187893@163.com

Abstract. The distribution of NO_x concentration, flue gas flow field and temperature at the inlet and NO_x concentration at the outlet of SCR denitrification were measured in a 330MW ultra-low emission coal-fired power unit, and ammonia injection optimization was carried out to improve the performance of SCR denitrification. The test results show that the distribution of NO_x concentration and flue gas temperature at the inlet of SCR reactor is relatively uniform, and the distribution of flue gas flow field at the inlet of SCR reactor is nonuniform. The distribution uniformity of NO_x concentration at the outlet of SCR reactor is poor before optimization. The NO_x concentration distribution at the outlet of SCR reactor is improved by ammonia injection adjustment, and the relative standard deviation of NO_x concentration distribution at the outlet of SCR reactor A and B decrease from 48.7% and 33.8% to 12.1% and 14.7%, respectively.

1. Introduction

Coal-fired power plants are one of the main emission sources of nitrogen oxides (NO_x) in China. In 2014, with much attention paid to pollutant emission from coal-fired power plants, Chinese government has put forward the ultra-low emission (ULE) for coal-fired power units. The emissions of dust, sulfur dioxide (SO₂) and NO_x are below 10 milligrams per cubic meter, 35 milligrams per cubic meter and 50 milligrams per cubic meter, respectively [1]-[4].

Low nitrogen combustion technology (LNB) and selective catalytic reduction (SCR) flue gas denitrification technology are commonly used in coal-fired units to control NO_x emission. SCR technology uses ammonia as reducing agent, which can reach over 90% denitrification efficiency but also produce ammonia slip. The denitrification performance of SCR is not only related to catalyst activity, reaction temperature, molar ratio of ammonia to nitrogen oxide, but also related to the distribution of flue gas flow field and concentration field in the reactor [5]. With the retrofit of ultra-low emission SCR denitrification of coal-fired units, there exist nonuniform distribution of flue gas flow field and concentration field at the inlet of SCR reactor, which result in uneven distribution of NO_x concentration at the outlet of SCR reactor, high concentration of ammonia slip, air preheater clogging, catalyst blocking and wear. It seriously affects the safety and economic operation of the unit [6]-[8]. Under the ultra-low emission standard, the distribution uniformity of concentration field in SCR reactor is more and more strict, which affects SCR denitrification performance. The optimization of the distribution of molar ratio of ammonia to nitrogen oxide in SCR reactor should be carried out.

This paper has measured the distribution of NO_x concentration, flue gas flow field and temperature at the inlet of SCR reactor and the distribution of NO_x concentration at the outlet of SCR reactor in a 330MW ultra-low emission coal-fired power unit. The ammonia injection optimization was carried out



to optimization of the distribution of molar ratio of ammonia to nitrogen oxide in SCR reactor so as to improve SCR denitrification performance.

2. Experiment

2.1. Unit overview

The field measurements were conducted in a 330MW coal-fired power unit. This unit adopts LNB and SCR technology to control NO_x emission. The catalyst is arranged in three layers and the reducing agent is liquid ammonia. The liquid ammonia is first evaporated into gas ammonia, and then injected into flue gas before catalyst layers through the ammonia injection grid (AIG). NH₃ reacts with NO_x through catalyst into N₂ and H₂O. Each SCR reactor is equipped with eight groups of AIG, and each group of AIG is divided into two independent modules, which are arranged in different depth of flue gas duct respectively. A manual control valve is set on the pipe of each module to adjust ammonia flow so as to achieve uniform distribution of molar ratio of ammonia to nitrogen oxide on the whole flue gas duct section. NO_x concentration at the inlet of SCR reactor is 450 mg/m³, NO_x concentration at the outlet is less than 50 mg/m³, and therefore the denitrification efficiency is no less than 88.9% under the design condition.

2.2. Test method

According to DL/T 260-2012 (Performance checkup test code for flue gas denitration equipment of coal-fired power plants), NO_x concentration, flue gas temperature and flue gas dynamic pressure at the inlet of SCR reactor and NO_x concentration at the outlet were measured under 90% BMCR(boiler maximum continuous rating). The distribution of NO_x concentration, flue gas flow field and temperature at the inlet of SCR reactor and the distribution of NO_x concentration at the outlet were obtained. According to the distribution of inlet NO_x concentration, inlet flue gas flow field and outlet NO_x concentration, the manual control valve on the pipe of each module was adjusted to improve distribution uniformity of molar ratio of ammonia to nitrogen oxide before the first catalyst layer.

The distribution uniformity of physical quantity such as NO_x concentration and flue gas flow field is expressed by the relative standard deviation, which is defined by the following formula:

$$C_v = \frac{\sigma}{\bar{x}} \times 100\% \quad (1)$$

$$\sigma = \sqrt{\frac{1}{(n-1)} \sum_{i=1}^n (x_i - \bar{x})^2} \quad (2)$$

$$\bar{x} = \frac{1}{n} \sum_{i=1}^n x_i \quad (3)$$

Where C_v is the relative standard deviation, σ is standard deviation and \bar{x} is the mean value.

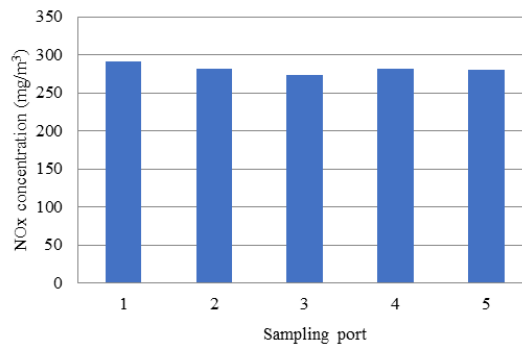
3. Results and discussion

3.1. The outlet NO_x concentration distribution before optimization

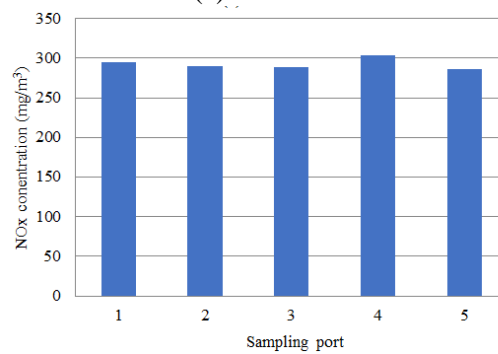
NO_x concentration distribution at the inlet of SCR reactor before optimization is shown in figure 1. NO_x concentration distribution at the inlet is uniform, and the relative standard deviation of inlet NO_x concentration distribution of reactor A and B is 2.4% and 2.3%, respectively.

The distribution of flue gas dynamic pressure and temperature at the inlet of SCR reactor are shown in figure 2 and figure 3, respectively. The temperature distribution at the inlet is uniform, and the relative standard deviation of temperature distribution of reactor A and B is 0.5% and 0.3%, respectively. The distribution of flue gas flow field at the inlet of SCR reactor is nonuniform, and the relative standard

deviation of flue gas dynamic pressure square root distribution of reactor A and B is 21.9% and 21.3%, respectively.

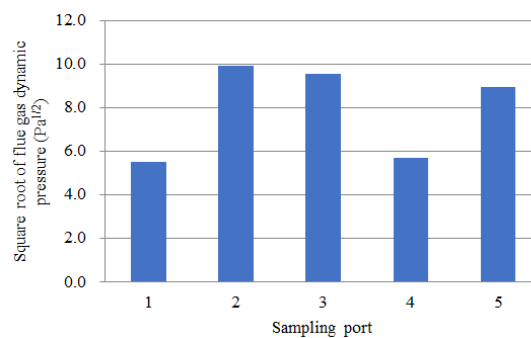


(a) Reactor A

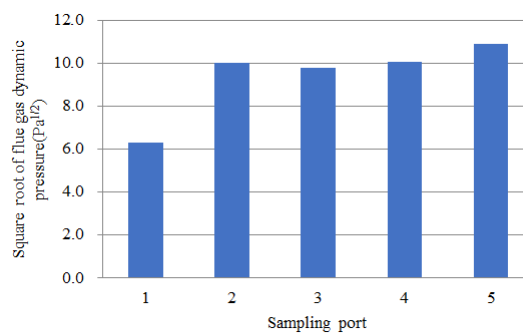


(b) Reactor B

Figure 1. NOx concentration distribution at the inlet.

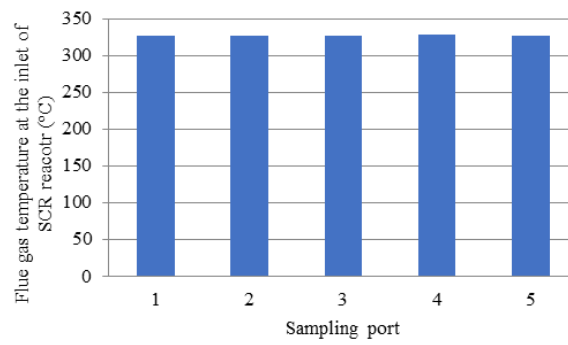


(a) Reactor A

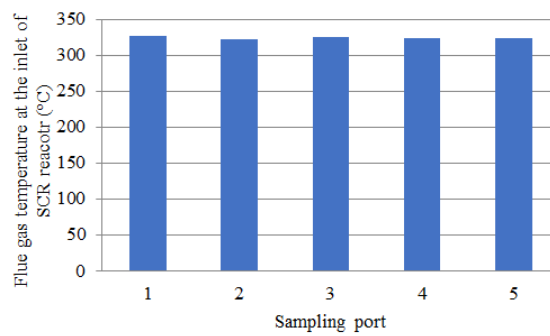


(b) Reactor B

Figure 2. Square root of flue gas dynamic pressure distribution at the inlet.

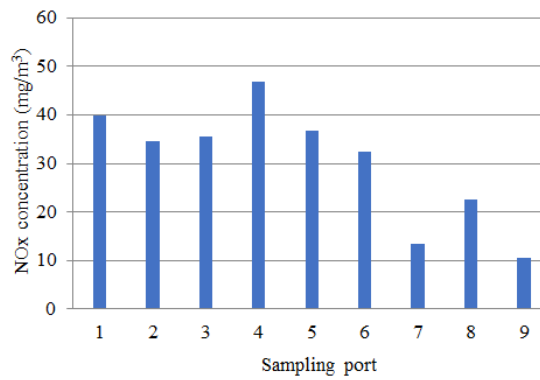


(a) Reactor A

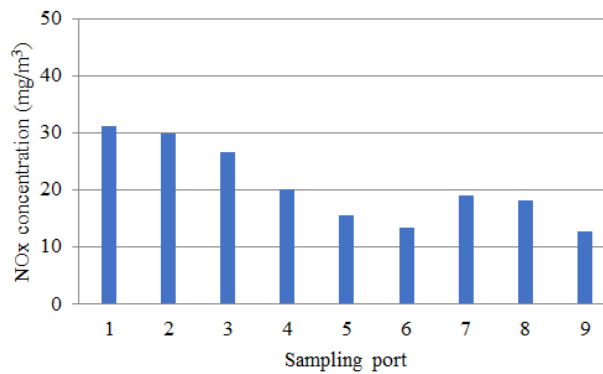


(b) Reactor B

Figure 3. Flue gas temperature distribution at the inlet.



(a) Reactor A



(b) Reactor B

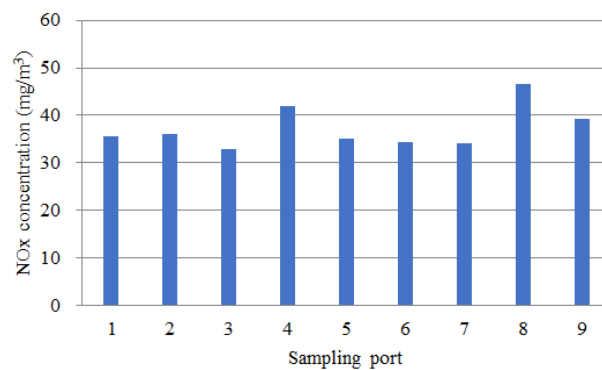
Figure 4. NOx concentration distribution at the outlet before optimization.

NO_x concentration distribution at the outlet of SCR reactor before optimization is shown in figure 4. NO_x concentration distribution at the outlet is nonuniform, and the relative standard deviation of outlet NO_x concentration distribution of reactor A and B is 48.7% and 33.8%, respectively. The result shows that the distribution of molar ratio of ammonia to nitrogen oxide before the first layer of catalyst is not uniform. The amount of ammonia injection is larger in some area, the corresponding NO_x concentration at the outlet is lower, and the concentration of ammonia slip at the outlet is higher. The escaping ammonia reacts with sulfur trioxide to form ammonium bisulfate, which will result in corrosion and blockage of air preheater.

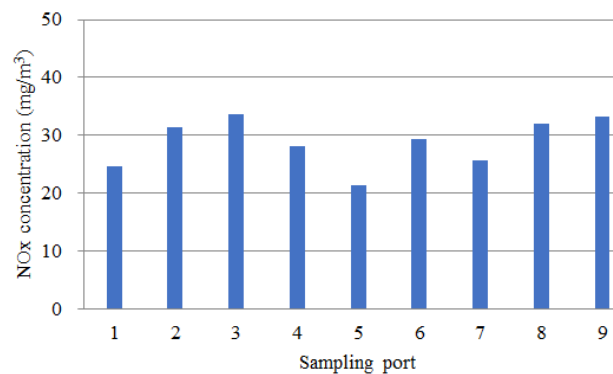
3.2. The outlet NO_x concentration distribution after optimization

The flue gas flow pattern in SCR reactor is close to plug flow [5]. The modules of AIG are independent, and then NO_x concentration at the outlet of reactor can approximately correspond to the opening size of the control valve of modules of AIG at the inlet of reactor. The opening of the manual control valve is larger in some area, the amount of ammonia injection is larger, and the corresponding NO_x concentration at the outlet is lower. The opening of the manual control valve is smaller in other area, the amount of ammonia injection is lower, and the corresponding NO_x concentration at the outlet is higher. Nonuniform distribution of molar ratio of ammonia to nitrogen oxide before the first catalyst layer affects denitrification performance. According to the distribution NO_x concentration at the outlet of reactor, the manual control valve on the pipe of each module is adjusted to improve distribution uniformity of molar ratio of ammonia to nitrogen oxide before the first catalyst layer.

NO_x concentration distribution at the outlet of SCR reactor after optimization is shown in figure 5. NO_x concentration distribution at the outlet is improved, and the relative standard deviation of the outlet NO_x concentration distribution of reactor A and B is 12.1% and 14.7%, respectively.



(a) Reactor A



(b) Reactor B

Figure 5. NO_x concentration distribution at the outlet after optimization.

4. Conclusion

The ammonia injection optimization was carried out to improve the performance of SCR denitrification in a 330MW ultra-low emission coal-fired power unit. The distribution of NO_x concentration, flue gas flow field and temperature at the inlet and NO_x concentration at the outlet of SCR reactor were measured. The distribution of NO_x concentration and flue gas temperature at the inlet of SCR reactor is relatively uniform. The distribution of flue gas flow field at the inlet of SCR reactor is nonuniform, and the relative standard deviation of inlet flue gas dynamic pressure square root distribution of reactor A and B is 21.9% and 21.3%, respectively. NO_x concentration distribution at the outlet of SCR reactor before optimization is nonuniform, and the relative standard deviation of NO_x concentration distribution of reactor A and B is 48.7% and 33.8%, respectively. NO_x concentration distribution at the outlet of SCR reactor is improved by ammonia injection optimization, and the relative standard deviation of NO_x concentration distribution of reactor A and B is 12.1% and 14.7%, respectively.

5. References

- [1] Zhu F H 2017 *Electric power* **50** 11
- [2] Zhao Y C, Ma S M, Yang J P, Zhang J Y and Zheng C G 2015 *J. Chin Coal. Soc.* **40** 2629
- [3] Zhang J, Zheng C H, Zhang Y X, Wu G C, Zhu S Q, Meng W, Gao X and Chen K F 2016 *Proc. Chin. Soc. Electrical. Eng.* **36** 1310
- [4] Li B, Song Y Q, Zhang Q L, Zhou C and Duan H R 2018 *IOP Conf. Ser.: Earth Environ. Sci.* **159** 012014
- [5] Li H T, Song Q and Yao Q 2017 *Proc. Chin. Soc. Electrical. Eng.* **37** 2599
- [6] Fang Z J, Lu C Z and Bai X L 2018 *Electric Power* **51** 143
- [7] Zhou L M. 2018 *Power Equipment* **32** 46
- [8] Ma D W, Zhang Q L, Huang Q S, Zha Z M and He J 2017 *Electric Power* **50** 168

6. Acknowledgments

This work has been supported by HUADIAN POWER INTERNATIONAL 2017 Science and Technology Project (HDPIKJ17-02-12).

Aquaculture Wastewater Treatment with Immobilized Microorganisms-aquatic Plants Strengthened Purification System

HY Cheng^{1,2}, JX Long^{1,2}, Z Liu^{1,2}

¹ School of environmental science and engineering, Xiamen University of Technology, 600 Ligong Road, Xiamen, 361024, China

² Key Laboratory of Environmental Biotechnology (XMUT), Fujian Province University, 600, Ligong Road, Xiamen, 361024, China

Abstract: Combined purification system of microorganism - aquatic plants were established by adding immobilized 3.0×10^{10} CFU/ m³ EM (Effective Microorganisms) to *Eichhornia crassipes* and *Pistia stratiotes*, to study the purification effect on prawn aquaculture water. The results showed that the purification effect of 2 groups of immobilized microorganism - aquatic plants (SEE and SEP) on ammonia nitrogen (NH₄⁺-N), total nitrogen (TN), total phosphorus (TP) and chemical oxygen consumption (COD) were significantly better than those of the immobilized microorganism SEM group (P<0. 05). The degradation efficiency of SEE and SEP system to ammonia nitrogen were 98.37% and 96.22%. The degradation rate of TP were 90.28% and 86.11% respectively. The removal efficiency of COD were both close to 86%. At the same time, *Eichhornia crassipes* was slightly better than *Pistia stratiotes* in microorganism - aquatic plants system.

1. Introduction

The zero discharge of ecological aquaculture and aquaculture water pollution is the direction and inevitable requirement of aquaculture development in China. Different experts and scholars adopt different methods to study the purification of aquaculture water. Effective microorganisms (EM) are composed of a variety of beneficial bacteria (Photosynthetic bacteria, Nitrobacteria, Lactobacilli, Actinomyces, Yeast and Bacillus cohn), which play an important role in purifying water quality, reducing the concentration of ammonia nitrogen (NH₄⁺-N) and nitrite nitrogen (NO₂⁻-N) and so on and realizing healthy culture [1], [2]. Wang added EM to source water in the ratio of 1 to 10000 into the experimental container, supplemented with low speed intermittent aeration treatment for 8 to 9 days, and the removal rates of TN, TP and COD in water samples were 45.25%, 55.48% and 82.37%, respectively [3]. Ma use the inoculation amount of 1 to 5 000 EM bacteria to treat nitrogen containing wastewater and this method has the characteristics of energy saving, sludge production less and deodorization [4]. Brasker and Han use immobilized algae bacteria to remove COD and ammonia nitrogen from aquaculture wastewater, and the effect is ideal [5], [6]. Mittler, Fraser, Badigannavar, Hunter and Hunter used aquatic plants to treat eutrophic aquaculture water, the results showed that aquatic plants such as shallot, Potamogeton crispus and other aquatic plants had better removal effect on N and P [7]-[10]. Tong used aquatic plants to control the eutrophic water body of the fish pond. The results show that 6 kinds of aquatic plants, such as golden fish and bitter grass, have good removal effect on total nitrogen and total phosphorus in water, but the effect on improving COD and DO is not obvious [11]. Therefore, under the indoor conditions, the immobilized effective bacteria group (EM) and the higher aquatic plant (*Pistia stratiotes*) and the water hyacinth (*Eichhornia crassipes*) were



combined to purify the circulating aquaculture wastewater, and the effects of the combined action of immobilized microorganism and two aquatic plants and the immobilized microorganism on the purification of the aquaculture wastewater were emphatically analyzed. The purpose of this study is to provide a basis for constructing an efficient and stable purification mode of aquaculture wastewater.

2. Materials and methods

2.1 Reagents and instruments

EM original solution is provided by Zhengzhou Nong Fukang Biotechnology Co., Ltd. The effective microorganism content is 3×10^{10} CFU/ml.

2.2 Experimental device

The experiment was carried out in the indoor aquarium (30 cm x 20 cm x 25 cm), and 2 treatment groups and 1 control group were set up. SEE was the strengthening group of the immobilized EM with *Eichhornia crassipes*, the SPE was the strengthening group of the immobilized EM with *Pistia stratiotes*, and the SEM was the control group of the immobilized effective bacteria group

2.3 Sampling and analysis method

The experiment time was from April 5 to April 30, 2018. During this period, the water temperature was maintained at about 28°C with the heating rod. The aeration for 12 h and the static for 12 h were used alternately, and the distilled water was supplemented every day to keep the water volume in the aquarium constant. Sampling 1 time every 4 days. The analysis indexes include COD_{Cr}, NH₄⁺-N, TN, TP.

2.3.1 Determination of water quality

Sampling time was 10:30 a.m. and water samples were collected at the same point. The collected water samples were immediately sent to the laboratory for testing. Determination method reference [12]: determination of COD with potassium dichromate method; determination of ammonia nitrogen (NH₄⁺-N) with Nessler Reagent Spectrophotometry; determination of total nitrogen (TN) with potassium persulfate oxidation UV spectrophotometry; determination of total phosphorus (TP) with Mo-Sb-Vc spectrophotometry method.

2.4 Data analysis

The experimental data were analyzed by SPSS16.0 software, and $P < 0.05$ was significant difference. Microsoft Excel 2007 is used for chart processing.

3. Results and discussion

3.1 Purification effect of immobilized EM and aquatic plants on ammonia nitrogen in water

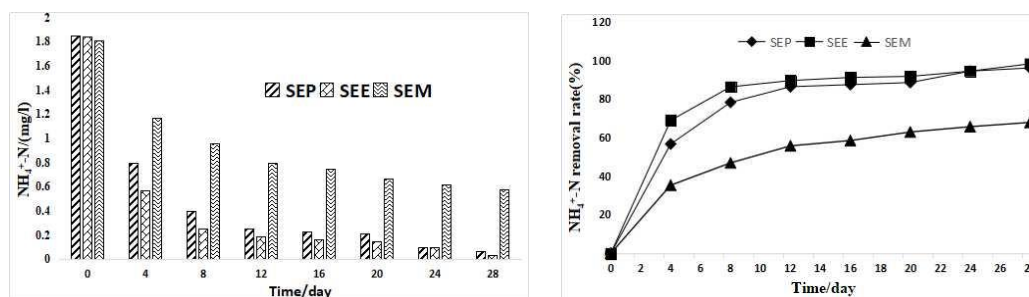


Figure 1. The changes of ammonia nitrogen (NH₄⁺-N) concentration and removal rate

From Figure 1, it can be seen that the fast removal of NH₄⁺-N in the aquaculture water body of SEE, SEP and SEM mainly appeared in the former 4 days. With the prolongation of the purification time, the removal rate of NH₄⁺-N was significantly decreased in three systems. After 4 days of degradation, the removal rates of NH₄⁺-N were 69.02%, 56.76% and 35.36% respectively by SEE, SEP and SEM. Then after 28 days purification, the NH₄⁺-N removal rates can be 98.37%, 96.22% and 67.96%, respectively. From the degradation effect of N NH₄⁺-N, the removal rates of the two kinds of composite strengthening systems were all above 90%, and the ranking of the removal rate (purification effect) was SEE > SEP > SEM in turn.

3.2 Purification effect of immobilized EM and aquatic plants on total nitrogen in water

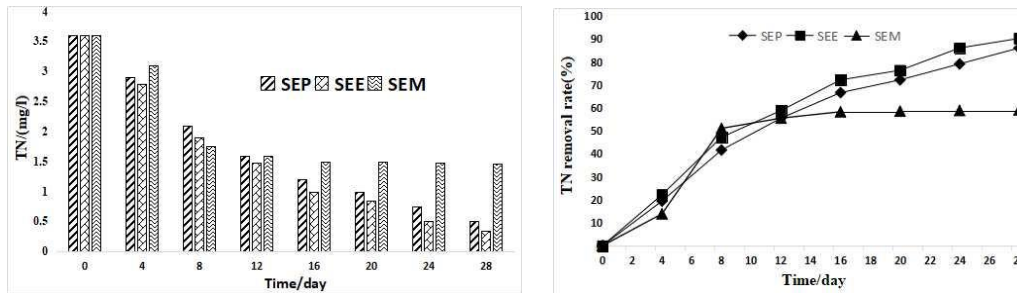


Figure 2. The changes of Total Nitrogen (TN) concentration and removal rate

The decrease of the total nitrogen mass concentration is faster in the first 16 days, and the decrease speed in the following 12 days is obviously slow down. It may be the soil matrix that adsorb and intercept part of the nitrogen. With the decrease of the mass concentration of TN in the water body, the nitrogen intercepted by the soil matrix may release back to the water body, making the TN mass concentration in the water body decreased slowly. The removal rates of SEE, SEP and SEM for shrimp aquaculture water TN were 90.27%, 86.11% and 59.17% respectively. The effect of combination of aquatic plants and immobilized EM to TN was better than that of Yuan, who using single aquatic plant *Acorus calamus* (TN removal rate was 77.77%) [13]. The microbiological enhancement effect of aquatic plant *Eichhornia crassipes* is close to that of Ma's experiment (TN removal rate of 90.4%), which is better than that of the *Pistia stratiotes* strengthening group [14].

Although the main degradation of organic nutrients in water is microorganism, the study of Gersberg [15] and Haberl [16] also showed that the main removal way of nitrogen is nitrification, denitrification and not plant absorption. However, the existence of aquatic plant community provides the substrate and habitat for microbes and microanimals. The microbe and aquatic plant form a good symbiotic relationship between microbes and aquatic plants by adapting to survival [17]. Microbes can degrade organic nitrogen and phosphorus and non soluble nitrogen and phosphorus in sewage into small soluble molecules, and continue to be absorbed and utilized by aquatic plants.

3.3 Purification effect of immobilized EM and aquatic plants on total phosphorous in water

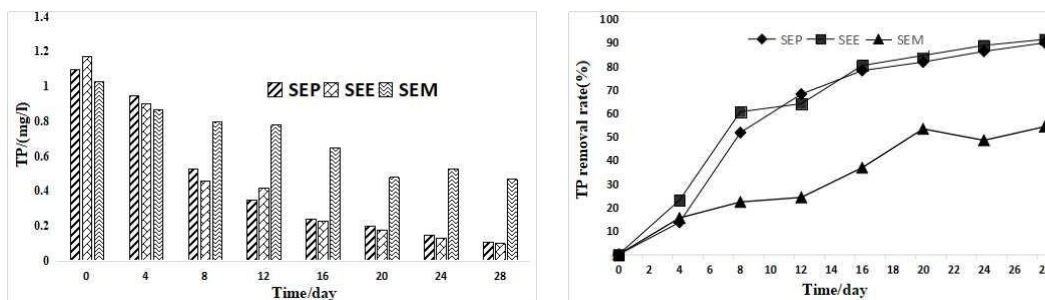


Figure 3. The changes of Total Phosphorus (TP) concentration and removal rate

Figure 3 showed the purification effect of immobilized EM and aquatic plants on total phosphorous in the aquaculture water. It can be seen that the removal rate of TP in the initial 4 days is lower, and the removal rate is 19.4%, 22.2% and 13.89%, which may be related to a short adaptation period of the aquatic plants which were initially implanted. In the following 5 to 16 days, the removal rate of TP was greatly accelerated, and the removal rate of TP reached 66.67%, 72.22% and 58.33% after 16 days. Although the TP removal rate in the final 12 days of the experimental design had a small increase, the effect was not very obvious, and the TP removal rates in 28th day were 86.11%, 90.28% and 59.17%, respectively. The significant difference may be due to the fact that aquatic plants are the main factors to remove TP. There was no significant difference between SEE and SEP during the

whole degradation process, the enhanced microbial aquatic plant combination was stronger than that of the enhanced microorganism SEM system for the removal of TP.

3.4 Purification effect of immobilized EM and aquatic plants on chemical oxygen demand

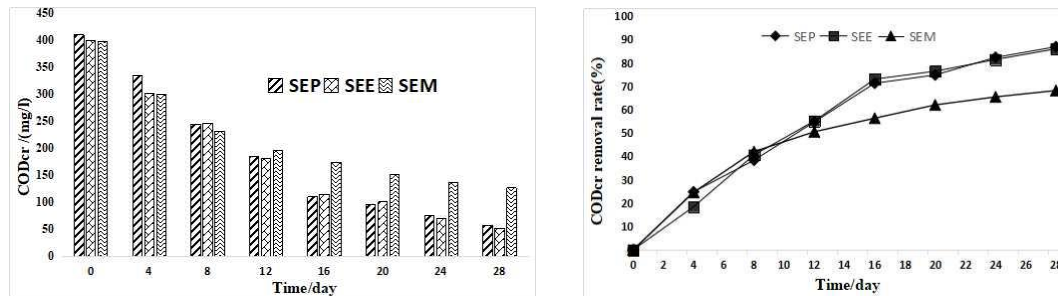


Figure 4. The changes of Chemical Oxygen Demand (COD) concentration and removal rate in System of SEE, SEP and SEM.

From Figure 4, it can be seen that in the first 8 days of purification, the content of COD in the immobilized microorganism system SEM is lower than the combined strengthening system of microbiological aquatic plants, indicating that the removal rate of aquatic plants to COD is obviously lower than that of the immobilized EM during this period, which may also be related to an adaptation period after the implantation of aquatic plants. From the tenth day, the removal rate of COD in the aquatic plant strengthening system was improved rapidly. The removal rate of COD by SEE and SEP aquatic plants was higher than that of SEM system containing EM. In the subsequent 20 days of purification process, the concentration of COD in each system decreased gradually, and the COD removal rates of 3 systems in 28th day were 86.92%, 86.03% and 68.2%, respectively.

4. Conclusion

(1) Both the immobilized microorganism SEM and the combined strengthening system of microorganism and aquatic plant (SEE and SEP) have better purification effect on the removal of $\text{NH}_4^+\text{-N}$, TN, TP and COD in the wastewater of shrimp culture. The removal of $\text{NH}_4^+\text{-N}$ by SEE and SEP is the best, the removal rate can reach 98.37% and 96.22%. The removal rate of SEE to TN is up to 90.27%, and the degradation rate of SEP to COD is higher than that of SEE.

(2) In most cases, the effect of the combined Strengthening System of microorganism and aquatic plants on the purification of shrimp culture wastewater is better than that of the immobilized effective bacteria group, and the addition of EM can greatly enhance the purification effect of combined purification system on aquaculture water.

(3) Considering the efficiency of comprehensive purification, two kinds of floating aquatic plants *Eichhornia crassipes* and *Pistia stratiotes*, *Eichhornia crassipes* are higher than those in the study.

5. References

- [1] Shao Q 2001, *China Water and Wastewater* **17** 74
- [2] Tian GT, Liu F, Duan DX, Du XH, Zhang JL, CHEN SJ, Zhang ML and Wang H 2012, *Journal of Shandong Agricultural University* **43** 381
- [3] Wang P, Wu XF and Li KL 2004 *Research of Environmental Sciences* **17** 39
- [4] Ma ZQ, Lou BF 2000 *Environmental Pollution and Control* **22** 6
- [5] Braskerud B 2002 *Ecological Engineering* **18** 351
- [6] Han SQ 2006 *Journal of Applied and Environmental Biology* **12** 251
- [7] Mittler R, Rizhsky L 2000 *Plant Molecular Biology* **44** 335
- [8] Fraser L, Carty S and Steer D 2004 *Bioresource Technology* 94 185
- [9] Badigannavar A, Kale D, Eapen S and Murty G 2002 *The journal of Heredity* **93** 50
- [10] Hunter R, Combs D and George D. 2001 *Archives of Environmental Contamination and, Toxicology* **41** 274
- [11] Tong CH, Yang X and Pu P 2005 *Journal of Applied Ecology* **15** 1447
- [12] Yu L 2002 *Manual of standards for water quality monitoring and analysis* China, Environmental Science Press Beijing 35

- [13] Yuan DH, Ren QJ and Gao SX 2004 *Journal of Applied Ecology* **15** 2337
- [14] Ma JQ, Zhou HD and Dong HR 2005 *Journal of China Institute of Water Resources and Hydropower Research* **3** 130
- [15] Gersberg R, Elkins B and Lyon S 1986 *Water Res* **20** 363
- [16] Haberl R, Perfler R 1991 *Water Sci Technol* **23** 729
- [17] Cheng W, Cheng D, Li Q 2005 *Industrial Safety and Environmental Protection* **31** 6

Acknowledgments

This research was supported by funding from XMUT with Grant 0900200611; Key Laboratory of Environmental Biotechnology, Fujian Province University.

Treatment of Candied Fruit Wastewater by Adsorption Oxidation Combined Process

Mengxiang Zeng

Xiamen University of Technology, Xiamen, 361024, China

E-mail: zengmx@xmut.edu.cn

Abstract. In this experiment, we applied a combined process of adsorption and oxidation for the treatment of candied fruit production wastewater. The influence of the pH value and dosage of the Fenton reagent on the treatment effect were investigated. The impact of regeneration temperature, power, and time on the efficacy of the regeneration of adsorbents were examined by ultrasonic wave. The results revealed that at pH 4, the removal rate of COD was 81.74% at a dosage of FeSO₄ 7H₂O of 7 g/L and 40 mL/L of H₂O₂. The maximum regeneration rate of the adsorbent 90.73%, reached at a temperature of 35 °C, ultrasonic power of 200 W, and 10 min.

1. Introduction

Over the recent years, the processing industry of candied fruits has been becoming increasingly more developed, and there are more and more kinds of preserves are produced. The processing technology of candied fruits production must be pickled. The pickling is a heavy pollution process. The high concentration of Cl⁻ discharged from the sauce makes it difficult to deal with the wastewater effectively. The pH value of candied fruit wastewater is low, salinity is high, the molecular weight of organic pollutants is large, and osmotic pressure is high, which seriously affects the treatment of sewage [1].

At present, the treatment of high-salt wastewater is performed mainly through the following methods: electrolysis, incineration, biological membrane purification, salt-adapted biological treatment technology and ozonation oxidation-biological method, etc.[2] Research work has made progress, but technical issues still . In this paper, we used activated carbon adsorption to pretreat preserved waste water. Meanwhile, the advanced oxidation technology of Fenton was introduced, and the ultrasonic method was employed to recycle the adsorbed activated carbon. Our findings provide a reference for solving the serious issues associated with the pollution of candied fruit wastewater.

2. Experimental part

2.1. Reagents and instruments

2.1.1 Experimental reagents

The experimental reagents were all analytically pure. The activated carbon particles were produced by Tianjin Guangfu Technology Co., Ltd., sodium hydroxide, concentrated sulfuric acid, potassium dichromate, and silver sulfate were produced from Xiqiao Chemical Industry Co., Ltd. and ferrous ammonium sulfate was produced from Guangdong Huaguang Chemical Factory Co., Ltd, phenanthroline, silver nitrate, hydrogen peroxide, ferrous sulfate heptahydrate was produced by Shanghai Sinopharm Group Chemical Reagent Co., Ltd.



2.1.2 Experimental instruments

Electronic balance produced in Fuzhou Hua Zhi Scientific Instrument Co., Ltd.(Fuzhou, Fujian, China).The pH-meter and the spectrophotometer produced in Shanghai Spectral Instrument Co.,Ltd. (Shanghai, China). COD digestion instrument, Super constant temperature water bath, Magnetic stirrer, ultrasonic cleaner, Suction filter and Oven were produced in Qingdao Hong Hai environmental protection equipment Co., Ltd. (Qingdao,Shandong, China)

2.1.3 Experimental water sample

The water sample was collected from a candied fruit processing plant in Quanzhou (Fujian, China). The water sample solution contained suspended fruit and vegetable matter. The water was acidic, with obvious pungent sourness and a pH value of 3.5. The COD value was 5,800 mg/L, the concentration of total phosphorus was 1.813 mg/L, and that of total nitrogen was 28.1 mg/L.

2.2 Experimental steps and methods

2.2.1 Experimental treatment of candied fruit wastewater by Fenton oxidation

The effects of the initial pH value, dosage of the Fenton reagent, and the reaction time on the influence of the treatment of candied fruit wastewater by oxidation were investigated.

2.2.2 Study on ultrasonic regeneration of activated carbon particles

The effects of regeneration temperature, regeneration power, regeneration time, and regeneration times on regeneration of activated carbon particles were examined.

3. Experimental results and discussion

3.1 Experiment on the treatment of candied fruit wastewater by Fenton oxidation

3.1.1 Effect of initial pH on Fenton oxidation treatment of candied fruit wastewater

The pH values of the wastewater were adjusted to 2, 3, 4, 5, and 6, respectively. The concentrations of the fixed $\text{FeSO}_4 \cdot 7\text{H}_2\text{O}$ solid amount was 6 g/L, and that of the 30% H_2O_2 solution was 30 mL/L. Further, the COD value was measured, and the COD was calculated as 5,800 mg/L. The COD removal rate by the Fenton oxidation treatment at different initial pH values is depicted in Figure 1.

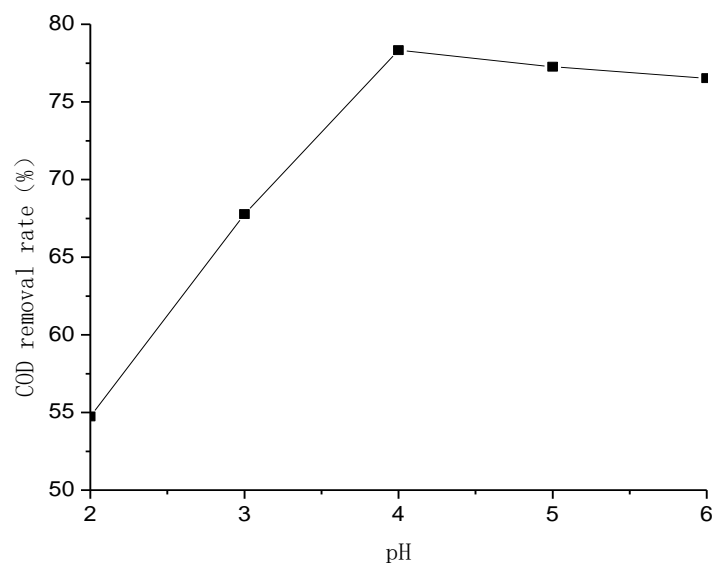


Figure 1. Effect of the pH value on the removal rate of COD.

As can be seen from Figure 1, with the increase of the pH value from 2 to 6, the removal rate of COD showed a trend of increasing first and then decreased. At a pH value 4, the COD removal rate of the solution reached its maximum (78.33%), because at low pH, the following reaction occurs: $\text{Fe}^{3+} + \text{H}_2\text{O}_2 \rightarrow \text{Fe}^{2+} + \text{H}^+ + \text{HO}_2\cdot$. As can be seen, the balance of the left side of the equation is not conducive to the production of the Fe^{2+} . When the pH increases, the same left movement according to the reaction of $\text{Fe}^{2+} + \text{H}_2\text{O}_2 \rightarrow \cdot\text{OH} + \text{Fe}^{3+} + \text{OH}^-$ is not conducive to the production of hydroxyl radicals, so the pH is high or low will reduce the removal of COD, so the optimum pH for this experiment is 4.

3.1.2 Effect of $\text{FeSO}_4 \cdot 7\text{H}_2\text{O}$ solid dosage on Fenton oxidation treatment of candied fruit wastewater

Fixed mass fraction of 30% H_2O_2 solution 30mL/L, Fixed pH is 4, and accurately weigh $\text{FeSO}_4 \cdot 7\text{H}_2\text{O}$ solid dosage 5.0 g/L, 6.0 g/L, 7.0 g/L, 8.0 g/L, 9.0 g/L, 10.0 g/L, and 11.0 g/L, the final determination of COD value, calculation of different $\text{FeSO}_4 \cdot 7\text{H}_2\text{O}$ solid dosage of Fenton oxidation COD removal rate, the results shown in Figure 2.

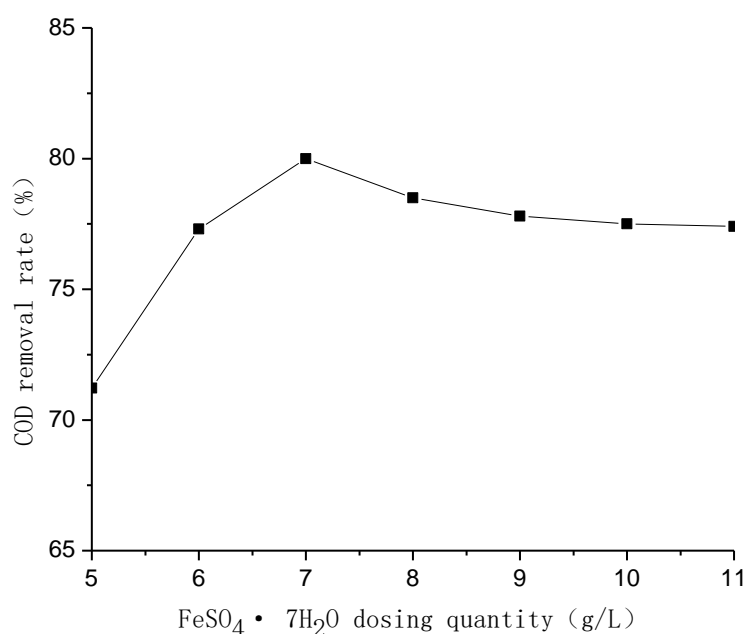


Figure 2. Effect of $\text{FeSO}_4 \cdot 7\text{H}_2\text{O}$ dosage on the removal rate of COD

As can be observed in Figure 2, at a dosage of $\text{FeSO}_4 \cdot 7\text{H}_2\text{O}$ of 7 g/L, the removal rate of COD was up to 80.63%. With the increase of the dosage of $\text{FeSO}_4 \cdot 7\text{H}_2\text{O}$, the removal rate of COD decreased slightly and then tended to stabilize. The reason for the analysis may be that when the Fe^{2+} is excessive, the H_2O_2 will be oxidized to Fe^{3+} while the H_2O_2 is consumed, and the removal rate of COD is slightly decreased. Therefore, according to the experimental data, the optimal $\text{FeSO}_4 \cdot 7\text{H}_2\text{O}$ dosage established in this experiment was 7 g/L.

3.1.3 Effect of H_2O_2 dosage on Fenton oxidation treatment of candied fruit wastewater

Fixed the dosage of $\text{FeSO}_4 \cdot 7\text{H}_2\text{O}$ is 7 g/L, adding 30% H_2O_2 solution 10 mL/L, 20 mL/L, 30 mL/L, 40 mL/L, 50 mL/L, 60 mL/L, and 70 mL/L respectively. At the beginning, a stirring time of 60 min was used, followed by measurements of the COD values was measured at the end of the reaction. According to the original water COD was 5,800 mg/L, the COD removal rate of Fenton oxidation treatment under different H_2O_2 dosage was calculated. The result shown in Figure 3.

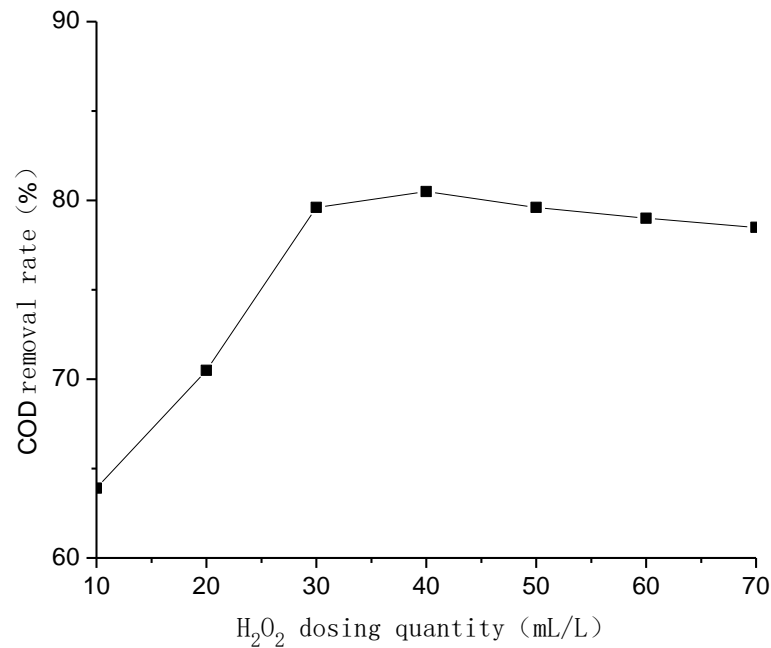


Figure 3. Effect of the amount of H₂O₂ added on the removal rate of COD.

H₂O₂ was utilized as an oxidant for the Fenton oxidation. We found that the removal rate of COD increased significantly with the rise of H₂O₂ dose, and the removal rate of 10 mol/L was 64.32%, whereas that of 40 mol/L was 81.25% (Figure 3). When 40 mol/L was reached, The excess of H₂O₂ can not decompose more hydroxyl radicals, instead of oxidizing Fe²⁺ to Fe³⁺ at the beginning of the reaction, which not only inhibits the generation of hydroxyl radicals, but also consumes the amount of H₂O₂. Therefore, the concentration of H₂O₂ of 40 mol/L in this experiment was the optimal dosage, resulting in the maximum removal rate of 81.85%.

3.1.4 Effect of the reaction time on Fenton oxidation treatment of candied fruit wastewater

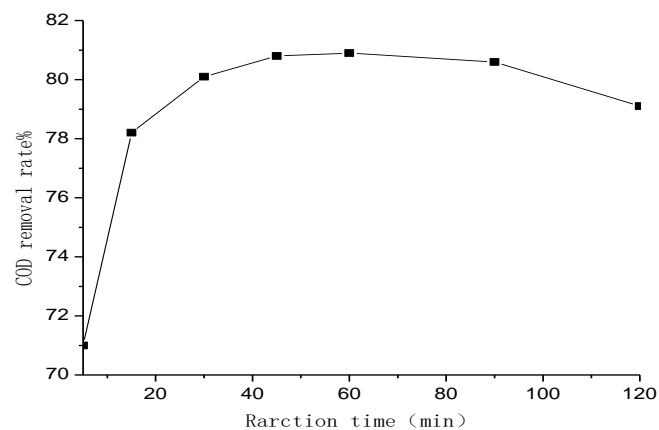


Figure 4. Effect of the reaction time on the removal rate of COD.

The fixed amount of solid $\text{FeSO}_4 \cdot 7\text{H}_2\text{O}$ was 7 g/L and 30% H_2O_2 solution 30 mL/L. The stirring time was 5min, 10min, 15min, 30min, 45min, 60min, 75min, 90min, 120min, respectively. The COD value was determined at the end of the reaction. According to the COD of the raw water (5,800 mg/L), the COD removal rates realized by the Fenton oxidation treatment at different reaction times were calculated (Figure 4).

In Figure 4, it can be seen that within the time interval 0–15 min, the reaction was rapid, and the removal rate of COD increased to 78.36%. Then, with the prolongation of the reaction time, the removal rate rose more slowly. The maximum removal rate at 45 min was 81.74%, and the reaction time is prolonged, and the COD removal rate is slightly decreased, but the amplitude is not significant. It is possible to analyze the cause of the high concentration of Fe^{2+} and H_2O_2 and the fastest rate of generating hydroxyl radicals, which may be due to the formation of a new possibility COD when the free radicals are more complex in the oxidizing water, increasing the COD value in the water and reducing the removal rate. Therefore, the best reaction time of this experiment was 45 min and the removal rate achieved 81.74%.

3.2 Study on ultrasonic regeneration of activated carbon particles

The regeneration of activated carbon plays an important role in industrial production. Therefore, it is necessary to explore the effects of temperature, power, and time on the regeneration of activated carbon particles [3].

3.2.1 Effect of temperature on the regeneration of activated carbon particles

In our experiment, the ultrasonic power was set at 200 W, and the ultrasonic time was 6 min. The activated carbon was regenerated at different temperatures, and the COD value was finally determined. The regeneration performance was determined by comparing the COD removal rate before and after regeneration. The results are illustrated in Figure 5.

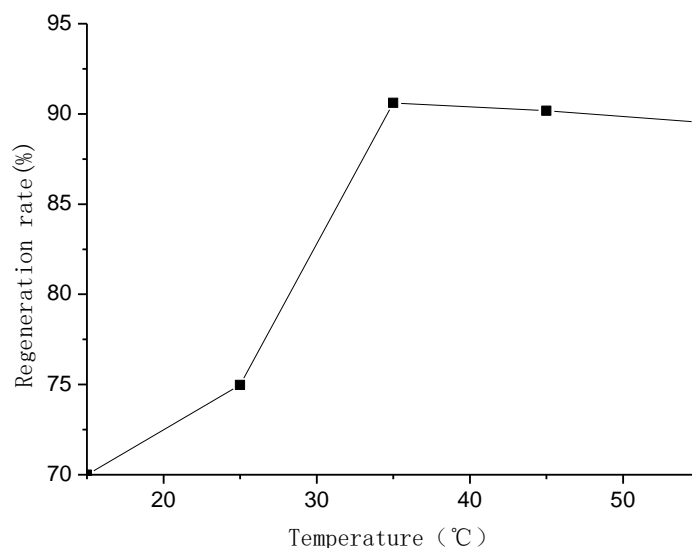


Figure 5. Influence of the temperature on the regeneration rate.

The results shown in Figure 5 reveal that the regeneration rate of activated carbon increased with the elevation of temperature, and the regeneration rate reached its maximum (90.61%) at 35 °C; then the temperature increased again, and the regeneration effect was not obvious. This was due to the increased energy conduction by the elevated temperature; cavitation effects were promoted, which helped the adsorbate to separate from the activated carbon. Nevertheless, after reaching a certain level,

the excessive temperature also increased the steam pressure of the bubbles in the water, thus affecting the regeneration effect. Therefore, the regeneration temperature of this experiment was set to 35 °C, leading to a maximum regeneration rate of 90.61%.

3.2.2 Effect of the power used on the regeneration of activated carbon particles

The ultrasonic temperature was set at 35 °C, and the ultrasonic time was 6 min. The activated carbons were regenerated under different power conditions, and the COD values were finally determined. The regeneration performance was determined by comparing the COD removal rate before and after regeneration. The results are presented in Figure 6.

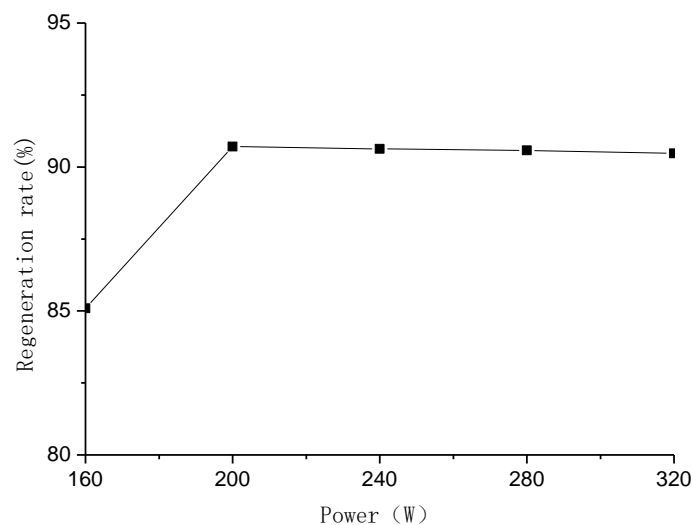


Figure 6. Influence of the power on the regeneration rate.

As illustrated in Figure 6, the regeneration rates at levels of the power of 160 W, 200 W, 240 W, 280 W, and 320 W were 85.09%, 90.71%, 90.63% and 90.58%, respectively. When the power reached 200 W its further increase exerted insignificant effects on the regeneration efficacy. The reason for this phenomenon may be that the power increased in a certain range, and the rise in the ultrasonic strength was beneficial to the desorption. Nonetheless, the excessive power may damage the structure of the activated carbon itself. The best activated carbon power was 200 W, and the regeneration rate was 90.71%.

3.2.3 Effect of time on the regeneration of activated carbon particles

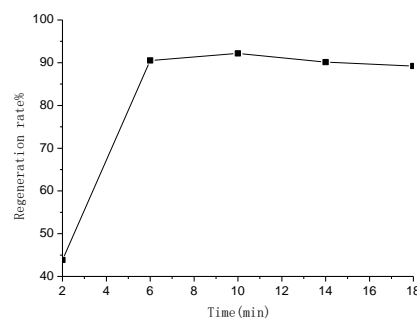


Figure 7. Effect of reaction time on regeneration rate

The ultrasonic temperature was set to 35 °C and the power to 200 W. The carbon was activated at different times, followed by determination of the COD value. The regeneration performance was determined by comparing the COD removal rates before and after regeneration (Figure 7).

The results in Figure 7, display regeneration rates of 43.86%, 90.51%, 92.18%, 90.13%, and 89.23% at 2 min, 6 min, 10 min, 14 min, and 18 min, respectively. When the reaction time was 10 min, the regeneration rate reached its maximum (92.18%). However, the further increase on the reaction time led to less obvious effects, and even to a slight decrease. Analyze the reason, It is may be that the long time of the ultrasonic wave causes the activated carbon to break, and the internal space structure of the activated carbon is broken to a certain extent, so that the adsorption performance is weakened. Therefore, the optimal regeneration time established in this experiment was 10 min, and the respective maximum removal rate was 92.18%.

3.2.4 Effect of the regeneration times on the regeneration efficacy of activated carbon particles

The effect of choosing the best regeneration conditions on the number of regenerations of activated charcoal was investigated. The temperature was 35 °C., the power was 200 W, and the time was 10 min. The regeneration adsorption effect is shown in Figure 8.

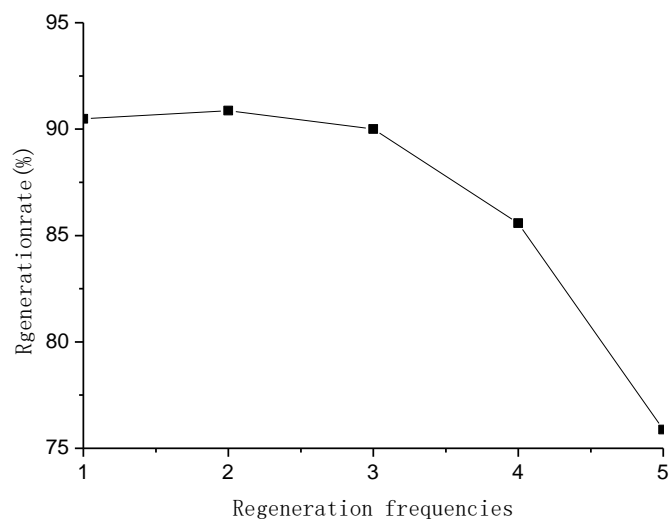


Figure 8. Effect of regeneration times on regeneration rate.

As shown in Figure 8, as the number of regeneration increases, the regenerative effect of the first three times is not changed, and there was a clear downward trend at the fourth time. From the 90% to 70%. The reason may be that the high pressure shock wave is produced with the increase of the number of regeneration times, which makes the surface of the activated carbon rise. High pressure increases and decomposes by heat, which changes the performance of activated carbon.

4. Conclusions

(1). The COD concentration of the candied fruit was reduced from 5,803.581 mg/L to 1,059.73mg/L, and the removal rate was 81.74% when pH = 4, FeSO₄ / 7H₂O was 7 g/L, 40 mol/L of H₂O₂, and a reaction time of Fenton oxidation of 45 min were used as reaction conditions.

(2). In the experiment of ultrasonic regeneration of activated carbon, the obtained temperature was 35°C, the power was 200W, the time was 10 minutes, and the regeneration frequency was more than 90% within three times.

5. References

[1] Liu Wenwei. Experimental study on treatment technology of high salinity cane processing

- wastewater [J].Journal of Fujian Teachers University(Natural Science), 2011, 27(4):87-91
- [2] Li Fengjuan, Xu Fei, Li Xiaolong et al. Research progress on high salinity wastewater treatment technology [J]. Environmental Science and Management, 2014, 39(2),72-75
- [3] Zhu Liping, Zheng Zhongbing, etc. progress in active regeneration technology of activated carbon [J] chemical intermediates, **2009, 02:1-4**

Fund Project: Fujian Provincial Department of Education JK Class: Study on treatment of high salinity preserved wastewater (Project No.: JAT160343)

Lead author: Mengxiang Zeng (1982.11-) male, Post-Graduate, the main research direction is environmental engineering and water pollution control. zengmx@xmut.edu.cn

Corresponding author: Mengxiang Zeng (1982.11-) male, Post-Graduate, the main research direction is environmental engineering and water pollution control. zengmx@xmut.edu.cn

Application of Deodorant in Odor Control of Municipal Solid Waste

Z N Dai¹, F S Zeng², J Liu¹, A L Yang and H Y Fu¹

¹ Key Laboratory of Environmental Biotechnology (Xiamen University of Technology) Fujian Province University, Xiamen, CN

² Yiyang Medical College, Yiyang, CN

E-mail: daizn@xmut.edu.cn

Abstract. More than 70% of China's municipal solid waste is disposed by landfill, which has caused lots of environmental problems, among which odor pollution is one of the most serious problems. The stench from landfills can seriously affect the daily life of nearby residents and cause a variety of diseases. Due to its wide spread and significant influence, it usually causes mass incident, and lead to bad social impact. An economical and efficient deodorant was developed in this paper. The results showed that the deodorant developed in this paper could remove 47% of ammonia gas, 40% of isobutylene and 20% of other gases with 20 min. The apparent deodorization rate in this paper is relatively low, which may be caused by the small experimental container and the continuous production of odor, the actual deodorization rate should be more than 50%. Moreover, the overall deodorization rate of the deodorant developed in this paper is higher than that of the commercial deodorant, but the cost is only 60% of that of the commercial deodorant.

1. Introduction

With the rapid development of China's economy and the increase of urban population, the generation of urban garbage is also increasing, and the pressure on the environment is also increasing. At present, more than 70% of China's garbage is buried in landfills, which not only occupied vast expanses of limited land resources, but also causes potential harm to the environment [1].

After the disposal of household garbage to the landfill site, it will ferment and produce more than 50 kinds of malodorous mixed gases with complex components, mainly including hydrogen sulphide, ammonia gas, methyl mercaptan, dimethyl sulphide, dimethyl sulfate and carbon disulphide [2]. These bad odors enter the human body through the respiratory system, which is harmful to human body. They could stimulate people's sense of smell and makes people feel unhappy. Hydrogen sulphide is an acute, highly toxic substance, and inhaling small amounts of high concentrations can be deadly in a short period of time [3]. Ammonia gas is a gas with irritating smell under normal temperature, which can absorb moisture tissue in the skin, make its protein degenerate, and make tissue fat saponify, damage skin cell membrane structure, and destroy human immune system. Most other malodorous gases can lead to asphyxiation and weak anesthesia, causing acute poisoning [4].

At the beginning of the 20th century, European countries began to study the deodorization of garbage odor, and accumulated much experience in prevention and treatment of odor. Among them, Germany, the United States, the Netherlands and Japan have developed relatively advanced technologies [5]-[7]. By contrast, research on China's odor pollution began in the late 1980s and has focused on investigations, tests and environmental standards [8], [9]. In addition, because of the difference of the dietary structure between foreign countries and China, the component of municipal solid waste is also



different from each other. So the source and category of the odor has significant difference, so as the treatment technology of the odor. So far, we can see that there are mainly physical, chemical, and biological methods for the removal of odor from garbage at home and abroad. These methods of deodorization are essentially aimed at removing the odor by changing the phase and material structure of the odor [10].

Deodorant is an end-of-pipe treatment technology that combines several deodorization principles. Deodorant available REDOX reaction, the decomposition reaction, neutralization reaction, etc., to produce the fetid stench into odourless gas or directly to eliminate odor, or change the adsorption odor molecules stereo configuration, weaken the molecular association bond, decrease the stability of odor molecules, or to make it easy to react with other molecules. For example, hydrogen sulphide reacts with deodorant to form sulfuric acid ions and water, while ammonia can form nitrogen and water [8], [11], [12].

According to the investigation, most deodorants sold in the market are ecological deodorant, and the active principle is so-called plant extracts, like enzyme. However, the exact composition of these deodorant were unknown, and the deodorization efficiency is also not good enough. A new deodorant was developed and compared with the commercial deodorant used in a landfill in Xiamen city. By optimizing the formula of deodorant, to make the deodorant with high deodorizing efficiency and low cost, and provides a possible solution to effectively alleviate the odor pollution in landfill sites.

2. Materials and methods

2.1 Materials and instruments

Mercury iodide, acrylic acid, maleic acid, ferrous sulphate, methenamine, and acetaldehyde were purchased from Tianjin fuchen chemical reagent factory. Peppermint essence, Holly essence from Guangzhou sipu essence and perfume co. LTD.

RAE 3000 VOC detector, PGM- 7340(ppb), RAE Systems, USA; Metrohm 883 Ion Chromatography, Swiss Metrohm co. LTD; 722 Visible spectrophotometer, Shanghai spectrophotometer co. LTD; 0.45 μ m, 0.22 μ m ultrafiltration membrane, Shanghai xinya purification device factory.

2.2 The preparation of deodorant

Based on literatures and the results of pre-experiment, the formula of the deodorant is as following: it contains 40ml wood vinegar, 20ml fungicide, 20ml mixed acids (3 ml of acrylic acid, maleic acid and boric acid combined with the ration of 1:1:1, neutralized by methenamine, and then diluted to 20ml), 10ml essence, 10ml ferrous sulfate (the ferrous sulfate solution was prepared in the concentration of 0.1mol/L and stored in a brown bottle), and 20ml ethylene glycol. This formula was named as Deodorant 1(DO1).To improve the possible deodorization efficiency, we increased the amount of wood vinegar to 50ml, fungicide to 30ml and mixed acids to 30 ml, and the others are keep the same amount. This formula was named as Deodorant 2 (DO2).A total of 50 ml、20 ml、10 ml DO1 were took and diluted to 1 L, and the diluted deodorants were named as DO11, DO12 and DO13. The DO2 was diluted as DO1, and then the DO21, DO22 was obtained.

2.3 Experiment methods

A total of 5kg of waste at a depth of 30cm was taken from the landfill site and placed in a transparent glass box. The waste in it was fully reacted in the natural state until the concentration of emitted odor gas is relatively steady, and then the lid was put on to make it a relatively sealed environment. The initial concentration of malodorous gas in the box was detected as the initial concentration. The deodorant developed by this project and the commercial deodorant was sparged respectively, and then the air sample was taken in 5, 10, 20, and 30 min. The concentration differences of odor gas were calculated before and after the deodorant spraying, and the deodorizing effect of deodorant was evaluated. In the parallel group and the control group, the odor was not treated to assess the concentration and composition changes of the odor in the experiment box. The results indicated that the concentration of odor gas slightly increased within 1h, but the increasing of the concentration is not significant.

Six gases were selected as the representative substances of odor, including ammonia gas, isobutylene, hydrogen sulphide, toluene, dimethyl sulfate and dimethyl sulphide. The determination of ammonia was carried out by the spectrophotometry of Nessler reagent. Other substances are determined using an atmospheric detector.

The odor produced was sampled by an anti-reverse suction device consisting of an atmospheric sampler, a beaker, a funnel, a glass tube and a rubber tube. The odor was absorbed for 4 minutes with 50ml, 0.5mol/L of H₂SO₄ as the absorbent. The colorimetric tube was rinsed with absorbent solution and 10ml was taken for test.

To verify the accuracy of RAE 3000, one sample was collected and detected by RAE 3000 and gas chromatograph. The results were listed in Table 1. The results of S1 and S2 were detected by RAE 3000, and the results of S3 were detected by gas chromatograph. The results showed that the differences between the two methods were not significant, and indicated that the odor concentrations determined by RAE 3000 were reliable.

Table 1 Concentrations of odor gas determined by RAE 3000 and gas chromatograph ($\mu\text{g/L}$)

Sample	isobutylene	hydrogen sulphide	dimethyl sulfate	dimethyl sulphide	toluene
S1	33.25	69.07	1372	14.37	26.30
S2	36.51	68.36	1478	13.61	25.94
S3	34.79	69.16	1450	14.00	25.55

2.4 QA and QC

Impurities such as ferric ion, organic matter and sulphide may be contained in the absorbed samples, which may interfere with the determination of the absorbance of samples. Interference can be removed by the following methods:

Adding 0.50ml sodium potassium tartrate solution to the absorption sample can eliminate the interference of ferric trivalent ions. When the sample produced heterochromic interference measurement, dilute hydrochloric acid can be added to remove the interference. When there are some interference caused by the formation and precipitation of certain organic substances in the sample, the absorbent sample can be acidified to a pH of no more than 2 with 0.1mol/l hydrochloric acid before colour comparison, and then boiled to remove the interference.

3. Results and discussion

3.1 The deodorization of deodorant DO1

As shown in Figure 1, the ammonia has the highest removal efficiency, followed by isobutylene, dimethyl sulphide, hydrogen sulphide, toluene and dimethyl sulfate. It is pointed out in the literature that wood acetic acid solution can significantly reduce ammonia in the air, and boric acid also can react with ammonia gas. When ammonia gas is dissolved in water, ammonia molecules and water molecules can combine to form ammonium hydroxide (NH₃·H₂O) which could be ionized into ammonium ion (NH₄⁺) and hydroxide ion (OH⁻) ions. Hydroxide ions then combine with hydrogen ions (H⁺) in boric acid to form water, allowing continuous inhalation of ammonia gas [13]. Ammonia gas could react with ferrous sulfate to form iron hydroxide and ammonium sulfate, and it also can effectively reducing the content of ammonium in odor gas. In addition, the deodorant contains abundant organic acid, which reacts with ferric hydroxide to improve the reaction speed. Relevant literatures have pointed out that methenamine plays an important role in the absorption of hydrogen sulphide [10], [14]. The relatively higher removal rate of hydrogen sulphide in this experiment may ascribe to the methenamine in deodorant.

It can be seen from the figure 2 that isobutene has the highest removal efficiency when compares to other substances, followed by hydrogen sulphide, dimethyl sulfate, dimethyl sulphide, toluene and ammonia. Hydrogen sulphide is easy to be reduced because of its low valence state. Compared with the DO11, the removal rate of ammonia gas dropped significantly. Isobutylene can reach up to 40%, hydrogen sulphide and dimethyl sulfate up to 20%. The optimal reaction time reduced to 10min, with rapid deodorization and consumption. After 30 minutes, the odor concentration goes up again.

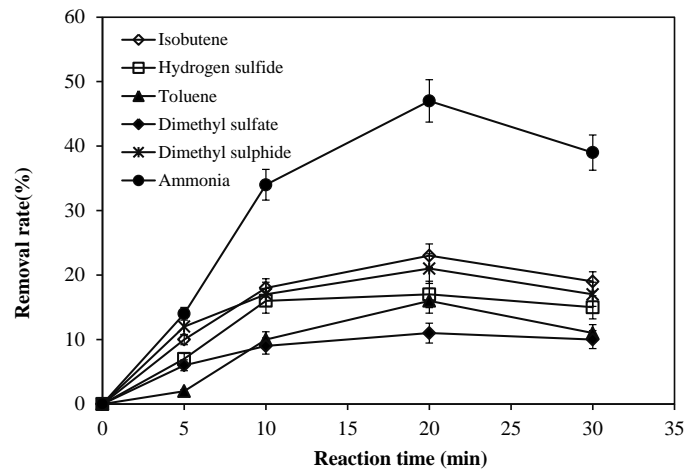


Figure 1. The removal rate of deodorant DO11 to isobutene, hydrogen sulphide, toluene, dimethyl sulfate, dimethyl sulphide and ammonia

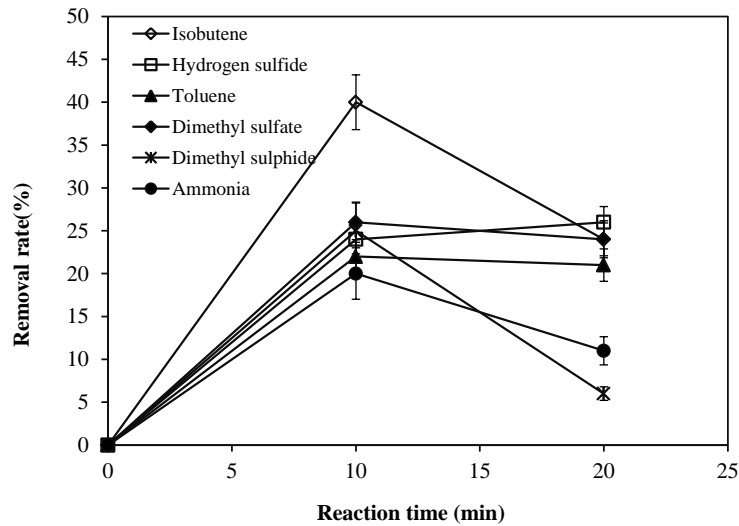


Figure 2. The removal rate of deodorant DO12 to isobutene, hydrogen sulphide, toluene, dimethyl sulfate, dimethyl sulphide and ammonia

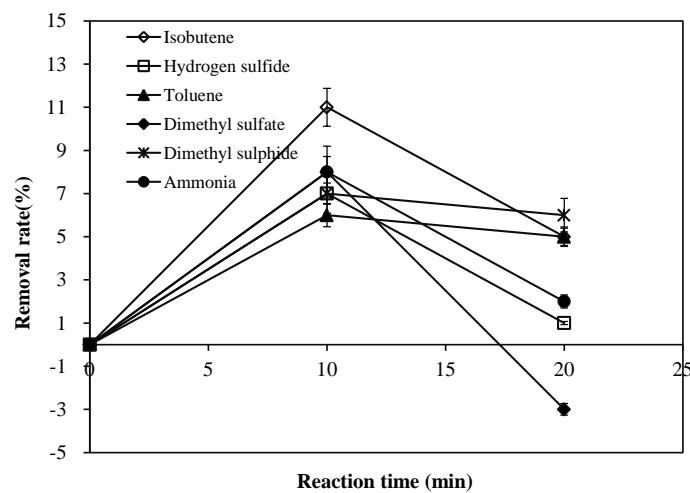


Figure 3. The removal rate of deodorant DO13 to isobutene, hydrogen sulphide, toluene, dimethyl sulfate, dimethyl sulphide and ammonia

It can be seen from the figure 3 that the biggest change of the deodorant is that the deodorizing time is shorter and the deodorizing efficiency is obviously decreased. The deodorization efficiency for several gases in odor tends to be the same. This is mainly because the concentration of the drug is lower and the reaction time is lower. After 10min, the odor concentration gradually increased, indicating that the deodorant had been consumed completely. In general, the deodorization effect is not good enough.

With the comparison of the deodorization rate of the different concentrations of deodorant 1, it's obvious that the deodorization effects have a positive correlation with the concentration of deodorant, and it decreased with the decreasing of deodorant concentration. In addition, the deodorant could react quickly with odor, and the maximum deodorization efficiency could be reached within 10 min.

Generally speaking, the deodorization rate is not good enough, for the removal rate of most odor composition is less than 50%. However, it works for some of the odor composition, such as isobutene, ammonia gas, and hydrogen sulphide.

The boric acid and wood vinegar in DO1 effectively reduced the concentration of ammonia, and methenamine reacted with hydrogen sulphide, but the removal efficiency was not ideally. After the spray, the odor concentration did not decrease significantly, but the effect of peppermint essence covered up parts of the odor, making the sensory deodorization effect seems better.

3.2 The deodorization of deodorant DO2

It can be seen from Figure 4, compared with DO1, DO2 has a high removal rate for toluene and dimethyl sulphide, but has a relatively lower removal rate for isobutene, hydrogen sulphide, and dimethyl sulfate. It is speculated that the increased concentration of fungicide in DO2 could kill the bacteria that will change the biochemical reaction in rubbish.

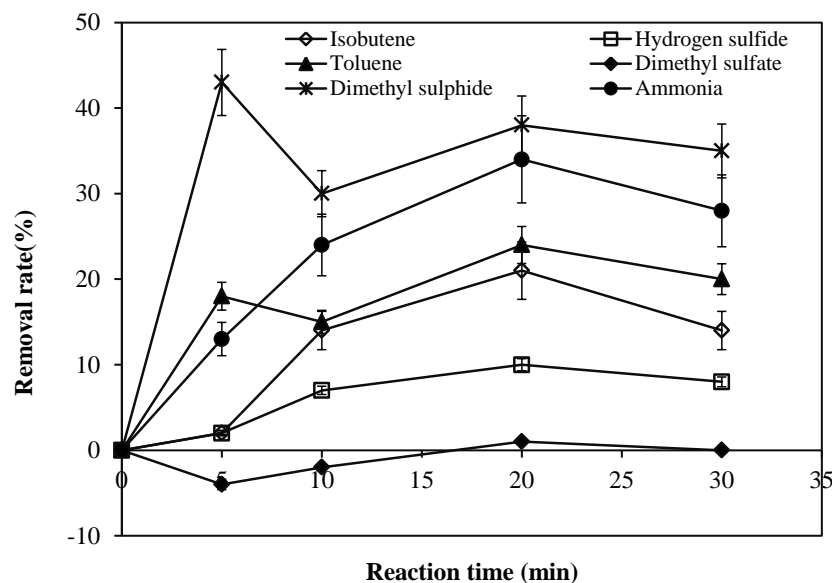


Figure 4. The removal rate of deodorant DO21 to isobutene, hydrogen sulphide, toluene, dimethyl sulfate, dimethyl sulphide and ammonia

The Figure 5 shows that the deodorization rate decreased significantly with decreasing of the deodorant concentration. The highest removal rate was only 18% (methyl sulphide), and the rest substances were about 10%. The results indicated that the increase of the concentration of wood vinegar, fungicide and mixed acids could not enhance the deodorization efficiency, and by contrast, the odor removal rate of DO1 is better than DO2. It indicated that the deodorization efficiency is not only related to the amount of each of the constituents of the deodorant, but the ratio of the constituents is also important. In addition, the deodorization efficiency is significantly related to the concentration, and it increase with the increasing of the deodorant concentration.

3.3 Comparison of the deodorization efficiency with commercial deodorant

In order to verify the commercial value and estimate the deodorization efficiency level when compares to other commercial deodorant, one kind of commercial deodorant (DO3) was chosen to compare the deodorization efficiency with the best performance deodorant DO11. The commercial deodorant DO3 was also diluted as DO11, and they were sparged in the same experiment box with the same condition. The results showed in Figure 6.

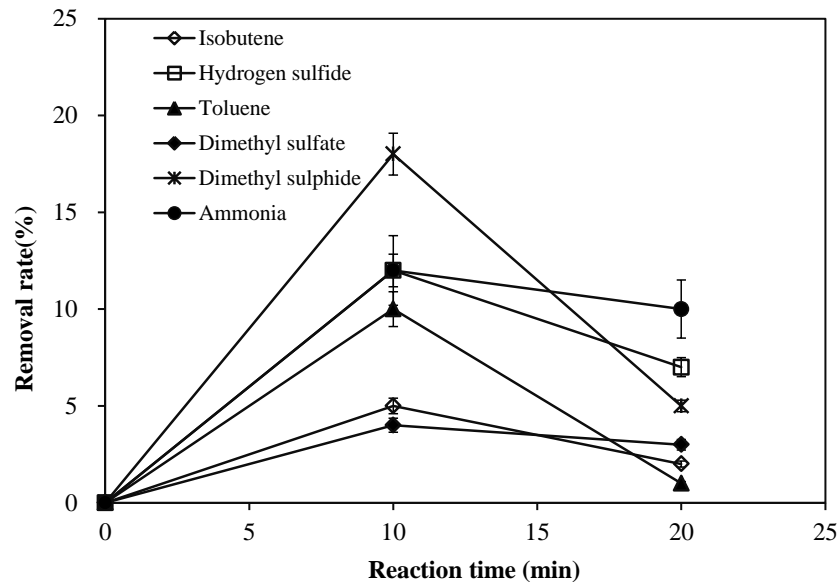


Figure 5. The removal rate of deodorant DO22 to isobutene, hydrogen sulphide, toluene, dimethyl sulfate, dimethyl sulphide and ammonia

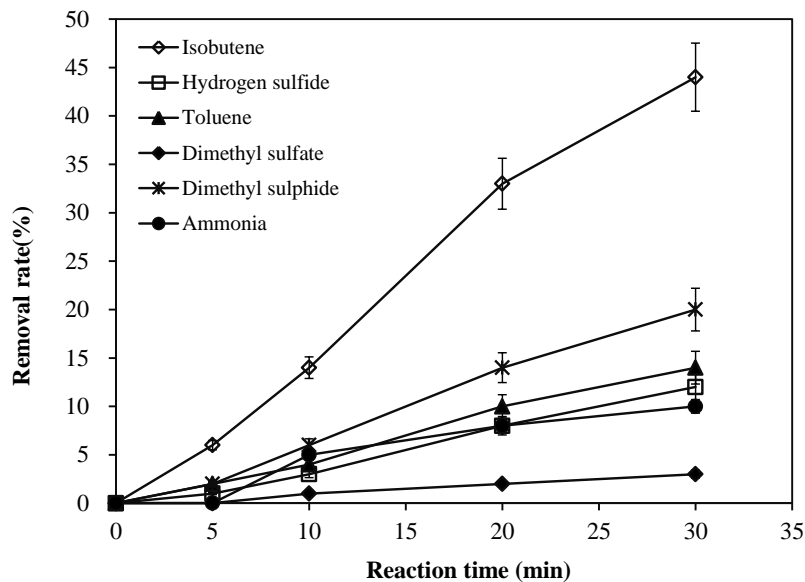


Figure 6. The removal rate of commercial deodorant (DO3) to isobutene, hydrogen sulphide, toluene, dimethyl sulfate, dimethyl sulphide and ammonia

With the comparison of Figure 1, the removal rates of DO11 for all the odor gas were higher than DO3 except isobutene. The odor gas could be decreased quickly within 10 to 20 min for DO11, and it is more than 30 min for DO3. It seems like that the deodorization efficiency of DO11 was better than DO3. And the cost of DO11 is only 60% of DO3.

One kind of ecological deodorant was applied by Lu et al to remove the NH₃ and H₂S, and the results indicated that, the removal rate of NH₃ and H₂S could up to 99% under optimal conditions [15], and the relatively high removal rate also reported in other literature [16]. However, the deodorization rate seems relatively low in this experiment, including the commercial deodorant. In fact, the declared deodorization rate is much better than its performance in this experiment. The possible reason may ascribe to the relative small volume of the experiment box. The odor gas could emit continuously in the small space, so the detected odor concentration include the new emitted part. By contrast, the high removal rate of odor reported in literatures were carried out in smaller space and use discontinuous odor source, so they can get the relatively higher removal rate. It means that, the real deodorization rate for our deodorant is possible higher than the results described above. And the results of the control group provide the evidence that the odor gas concentration increased when no deodorant was sparged.

4. Conclusion

The deodorant developed in this paper could effectively reduce the concentration of odor gas, and the deodorization efficiency is higher than the commercial deodorant. The deodorization efficiency is increased with the increasing of the deodorant concentration. However, the increase of the concentration of parts of the component of deodorant could not significantly increase the deodorization rate, and the ratio of the different component is plays an important role in the deodorization.

5. Acknowledgements

This study is supported by Xiamen science and technology plan project (3502Z20183064) and the Fujian Science and Technology Guiding Project (2018Y0079). We also thank the support of Key Laboratory of Environmental Biotechnology (XMUT), Fujian Province University.

6. References

- [1] Li X, Zhang C, Li Y, Zhi Q 2016 *J. Energy Procedia* **104** 498-503
- [2] Rappert S, Müller R 2005 *J. Waste Manag* **25** 887-907
- [3] Palmiotto M, Fattore E, Paiano V, Celeste G, Colombo A, and Davoli E, Palmiotto M, Fattore E, Paiano V, 2014 *J. Environ. International* **68** 16-24.
- [4] Veronika L, Štastná M, Magdalena V, Dana A, Jana K, and Štastná M 2015 *J. European Countryside* **7** 179-194
- [5] Durmusoglu E, Taspinar F, and Karademir A 2010 *J. Hazardous Materials* **176** 870-876
- [6] Laminack W, Baker C, and Gole J L 2016 *J. Air Quality Atmosphere and Health* **9** 231-239
- [7] Hudgins M, and Green L 2000 *J. Proc. Water Envi. Federation* **3** 914-936
- [8] Shi L, Bian B X, Zhao Y C, Niu D J 2005 *J.Tech. Equipment for Environ. Pollu. Control* **6** 6-9
- [9] Zhang Z, Wang Y, Xu H, Fang Y, and Wu D 2018 *J.Waste Manag. Res.* **36** 471-480
- [10] Hu B, Ding Y, Wu W X, Hu B G, and Chen Y X 2010 *Chinese. J. Applied Ecology* **21** 785-790
- [11] Gabaldón C, Martínez-Soria V, Martín M, Marzal P, Peña-Roja J M, and Alvarez-Hornos F J 2006 *J. Chemi. Tech. & Biotech* **81** 322-328
- [12] Chung Y C, Lin Y Y, and Tseng C P 2005 *J. Bioresour Technol* **96** 1812-1820
- [13] Chen S, Yu Z, Wang X, and Tai J 2017 *J. Environ. Sanitation Engin.* **25** 74-76
- [14] Huang H, Huang C, and Xie B 2010 *J. Environ. Sanitation Engin.* **18** 7-9
- [15] Lu G L, Guo G Z, Hou, L J, Zhang Y M, 2003 *J. Environ. Sci. and Tech.* **26** 4-6
- [16] Lu W L, Chen H Q, Xue H 2012 *J. Environ. Sanitation Engineering* **20** 30-31

Micro-weather Station System for Small Geographical Coverage in the Philippines

R C Muñoz, Jr.^{1,2}, X S Yumang¹, S J A Japitana¹, K R C Medina¹ and J E T Tibayan¹

¹Electronics Engineering Department, College of Engineering and Architecture, Bataan Peninsula State University, Philippines, 2100.

²Research and Development Office, Bataan Peninsula State University, Balanga City, Bataan, 2100 Philippines

E-mail: rhodjr@gmail.com, rhodjr@bpsu.edu.ph

Abstract. Drastic changes in the climate occur globally, and here in the Philippines, typhoons and storms are experienced all year round. According to the state weather bureau PAGASA, the Philippines visited by at least 8 to 9 tropical cyclones every year and more than million worth of crops and properties are being destroyed. To reduce the risk and danger due to extreme rainfall and strong winds caused by these disasters, early warning broadcast is necessary. In this article an Arduino-based weather data acquisition device was designed, tested, and installed. It measures temperature, relative humidity, and amount of rainfall to serve as a baseline data for studying the trend and its relationships on the occurrence of natural calamities to small geographical coverage in the Philippines. This also served as a warning system and source of information in the studies of weather patterns in the specific areas. It stored actual measurement of rainfall, temperature, and humidity to the database that can be printed or downloaded from the web page. The device alarmed the locals for incoming flood using GSM communications network. Test results revealed that the system gave an accuracy of 96.28%, with an efficiency of 97.06%, and effectiveness of 99.95%. The calculated Overall Equipment Effectiveness (OEE) of the whole device is 93.4%.

1. Introduction

Natural disaster such as earthquakes, flooding, volcanic eruption, landslide, hurricanes etc., are getting worst. Scientist from Intergovernmental Panel on Climate Change (IPCC) stated that global temperatures will continue to rise for decades to come, largely due to greenhouse gases produced by human activities. The IPCC also forecasts a temperature rise of 2.5 to 10 degrees Fahrenheit over the next century. This temperature rise will change the precipitation patterns, frequency of droughts and heat waves. The Hurricanes will become stronger and intense, and the sea level will rise 1-4 feet by 2100 [1]. The worst is that, this rising temperatures would cause some regions to experience more extreme heat while others may cool slightly. Due to this, flooding, drought, intense summer heat, violent storms and other extreme weather events would become stronger [2].

Due to stronger natural disasters, there is a need to study its relationship to the climate parameters which we can measure, gather, or monitor, and make the prediction. Today, meteorologist uses temperature, humidity, precipitation, atmospheric pressure, solar radiation and wind, in predicting the weather. If we can find a connection between these parameters and the increasing occurrences of the natural disasters, then we can make prediction of it. There are already studies that found a relation between these parameters and the occurrence of natural disasters like the preliminary study conducted



for the Northern areas of Pakistan by Muhammad Usman. That study shows a positive correlation between the temperature increase, due to global warming, and the earthquake frequencies. The study leads to a finding that an increase in earthquake frequency is connected to the temperature increase. The increase in temperature causes the glaciers to melt and thereby releasing pressure on the Earth. The earthquake is caused by the rebounding of the earth [3]. There are also a study that proves the relationship of humidity and temperature in the formation of storms [4].

The effects of climate change on the natural disaster are already felt in the world. On January 12, 2010, an earthquake with a magnitude of 7.0 and a depth of 8.1 miles hits Haiti [5]. This earthquake killed over 200,000, leave 2 million homeless and 3 million wounded. Another earthquake killed at least 225 people in Mexico City on September 19, 2017, and a week after another massive earthquake killed at least 96 people and 2.5 million people in need of aid [6]. 174 people were killed by a landslide in Democratic Republic of the Congo on August 2017. In Sierra Leone, Africa more than 500 people were dead and hundreds of people are still missing (Madison Park, 2017). Also on August 24, 2017, a landslide hits Switzerland causing a forced evacuation of over 100 people; according to the report, 8 people were missing after the landslide [7]. Severe rains and cyclones killed 117 people and thousand people were left homeless in Zimbabwe on October 2016 [6]. In Pakistan, sixteen people died from flash flooding caused by monsoons [8]. And on August 31, 2017, more than 1,200 people were dead, 40 Million was affected and 18,000 schools were shut down in India, Nepal and Bangladesh from the flood caused by Heavy monsoon rains [9]. An earthquake in Nepal, there was over 5 million people affected, over 8,000 people were dead and estimated \$85 billion damage [Infographic, 2016]. In India, Flood caused an estimated \$16 billion on 2014 [10]. In Japan, there were 19,846 deaths with estimated \$210 billion damage from Earthquakes and tsunami on 2011. In china, there were at least 114 people were killed by severe floods and destroyed 31,000 homes since January of 2017.

In the Philippines, Filipinos experience strong rainfalls in the past years. The monsoons are getting stronger especially the southwest monsoon that causes floods in some parts of the country. According to the Global Climate Risk Index 2015, the Philippines is the number one in the most affected country by climate change. Philippines is surrounded by bodies of water the reasons why it is more affected when the ocean's surface temperature increases. And this additional heat in the ocean and air can lead to stronger and more frequent storms [11]. Philippines has an average of 8 to 9 tropical cyclones each year [12]. But on the past years, the frequency of storms in the Philippines exceeds the average. On 2013 there were 13 destructive tropical cyclones recorded, 11 on 2014 and 10 on 2015 [13]. On part of the earthquake, there were 4 recorded earthquakes in 2017. One of this has a 6.5 magnitude in Leyte which killed 4 people and left 100 injured.

Bataan is located in the southwest of Luzon, the northern part of the Philippines. It experience mostly by floods and storms. On August 20, 2013, Bataan is placed under state of calamity due to the heavy rain from the southwest monsoon enhanced by Tropical Storm Maring. Figure 1 showed the year 2013 trend line data source from Weather Underground and Typhoon information form PAGASA that hit the province of Bataan.

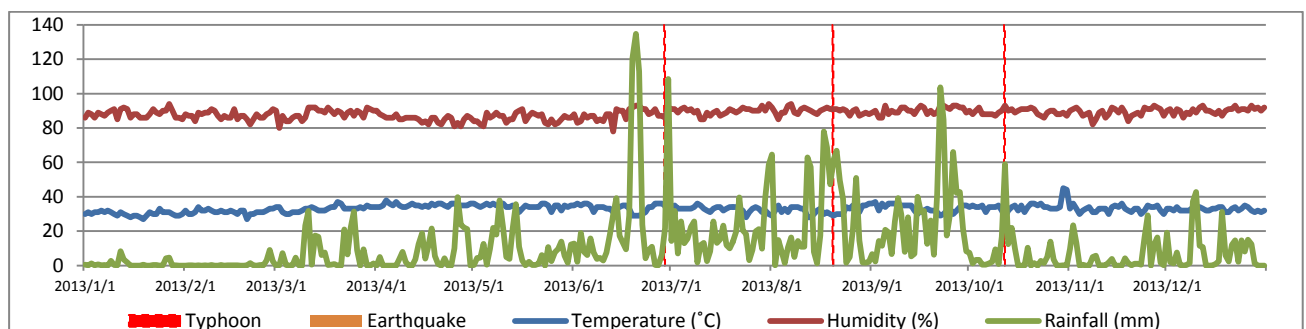


Figure 1. Year 2013 climate trend line with the occurrence of typhoon in Bataan

On August 13, 2016, Flash floods hit the 6 towns of Bataan; there were 3 villages in Dinalupihan, 8 in Hermosa, 4 in Orani, 3 in Samal, 2 in Abucay and 4 in Orion. Three Bataan towns were flooded due to

heavy rains on July 10, 2016. According to the report, there were 15 villages in the towns of Hermosa, Orani and Samal that are affected by the flood [14]. Figure 2 shows the year 2016 trend line data source from Weather Underground and Typhoon information form PAGASA that hit the province of Bataan.

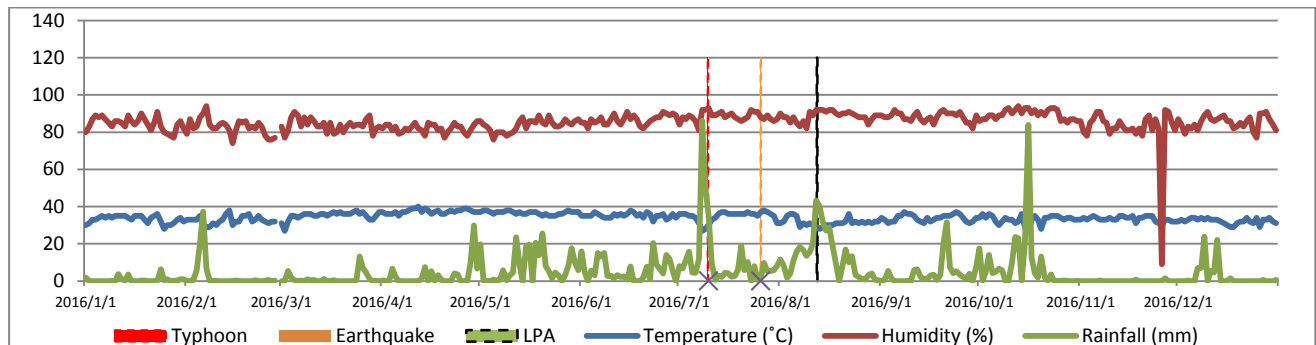


Figure 2. Year 2016 climate trend line with the occurrence of typhoon in Bataan

Climate change worsens the economic situation and food security among others of the Filipino people [15]. There is already a weather forecasting department in the Philippines which is called PAGASA (Philippines Atmospheric Geophysical and Astronomical Services Administration) which daily reports the condition of weather in the Philippines and there is also the Project NOAH which is the primary disaster risk reduction and management program of the Philippines. Though, PAGASA covers cities and regions in the Philippines but does not include the small municipalities and barangay. The Project NOAH is not enough to monitor a municipality. The government should also check the status of the municipalities since the conditions of its climate changed, where there are different rainfall, flood, etc., in a single district or municipality.

Looking to the figures 1 and 2, there is no much significant observations in the trend line of weather data and the occurrence of the calamities. One reason is the distant location of the actual sensors to the location of the concerned area. Based from the findings, the sensor is located in Subic Bay, Philippines which is approximately 33.77 kilometers from the City of Balanga. This study leads to create a system of localized micro-weather station system for small geographical coverage. It has data acquisition of three parameters, the temperature, rainfall, and humidity. The device has three possible outputs through the LCD, text messages, and the web. The transmission and display of outputs are shown every hour during stable weather, and a continuous reading depending on the weather in the vicinity when worse. The output is directed to the mobile phone of the locales and to the officer in charge from the municipality or barangay level. The web page is incorporated so the user can also monitor the weather in the vicinity when there is a presence of network access. Trend of historical data are saved and used for further study.

2. Significance of the study

Filipino local citizens mostly live near the sea or rivers have experience flooding and other natural calamities. A late dissemination of information may lead to fatal casualties and destruction of properties. Having a faster and precise weather condition reports on small municipalities can help the citizen to prepare for possible evacuations in case of occurrence of strong typhoons or other natural calamities. They can be aware about the status of the flood level especially when there is continuous heavy rainfall. The developed system is a self-monitoring device that tells whether to evacuate or not. In addition to this, the municipality will also be able to cancel or suspend classes ahead of time. Even those in agriculture sector can make necessary preparations. The data collected can be used in studying weather patterns in terms of humidity, rainfall and temperature.

One of the agencies that can benefit to this system is the Philippine Atmospheric Geophysical and Astronomical Services Administration (PAGASA). This project can help monitor the weather condition and forecast problems on smaller scale like barangays with accurate data. These data are supplemental information in their operational decision making. Agricultural agencies both public and private with concerns in weather related conditions can make good use of this device and all of its

features by implementing this technology in areas of their concern. They can conserve time, money and effort through this device.

3. Methodology

The major components of the system are divided into three stages. These are designing and building the system unit, gathering and analyzing the weather condition, and dissemination of analyzed data to the locales. Figure 3 shows the basic framework of the system which describes the interrelations of each subsystem. The parameters needed to assess the weather condition are the relative humidity, temperature and amount of rainfall. The input parameters will be transmitted to a computer database. Data is analyzed and provide an output to disseminate through text in the residence within the locality.

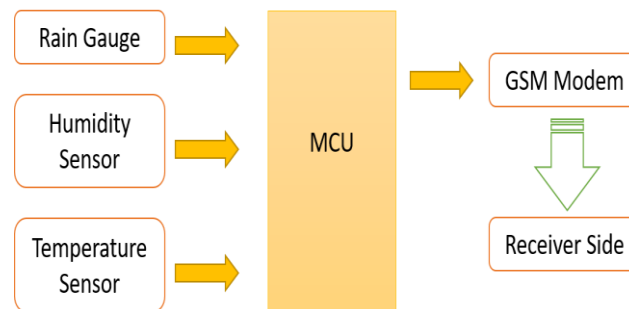


Figure 3. Framework of the micro weather station

3.1. Testing the accuracy of the device

Prior to the actual deployment of the device in the field to gather reliable data measurements, adjustment and calibrations were done under controlled environment which was setup in the laboratory.

3.1.1. Laboratory testing

During the laboratory testing, sensors' readings were compared and adjusted to make it almost similar with the accepted standard calibrated sensor. Mechanical adjustments and software numerical calibrations were implemented in this phase.

3.1.1.1. DHT22 temperature accuracy

Temperature sensor reading is compared with a calibrated room thermometer placed near the sensor. A thermoelectric cooler using peltier module is used in the controlled environment to test the temperature accuracy. There are at least 1095 sample trials ($n = 3$ samples/day \times 365days/year) for each temperature in the range of lowest to highest temperature recorded in the Philippines [16].

3.1.1.2. DHT22 humidity accuracy

Four plastic containers having dimension of 22.8cm \times 10.7cm \times 13.2cm with different salt solution contents is used as a replacement for a climatic chamber for economic reasons. For these set-ups, the following proportions were used [18]:

Table 1. Salt Solutions for Testing Humidity

Container	Salt	Salt Content (g)	Water Content (g)	Expected relative humidity
1	NaCl	53.33	27.28	75%
2	LiCl	53.33	43.64	11%
3	MgCl ₂	53.33	5.46	93%
4	K ₂ SO ₄	53.33	18.19	97%

The prepared salt solutions in each container are left undisturbed for 24 hours for the salt solution to stabilize. The calibrated hygrometer sensor and DHT22 sensor are placed in the container without affecting the internal environment, the hole or opening for passing the wiring has to be sealed. A waiting time of 2 hours is necessary to allow the sensors to stabilize and start taking the measurements. Measurements were conducted every hour for five days.

3.1.1.3. Accuracy of the debounce circuit (tipping bucket)

A tipping bucket rain gauge as shown in Figure 4 has several components that allow it to accurately measure rainfall. As rain falls, it lands in the funnel of a tipping bucket rain gauge. The rain travels down the funnel and drips into one of two very carefully calibrated buckets balanced on a pivot.



Figure 4. Tipping Bucket design for rain gauge measuring device

For the accuracy of the tipping bucket, three set ups were done which are based from PAGASA's category for rainfall. Light, Moderate, and Heavy rainfall simulations were done. Specific volume for each category was set. Light, Moderate, and Heavy rainfall are expected to be in the ranges of 30mL, 60mL, and 120mL respectively. The tips were counted when the volume of water has poured to the tipping bucket. Then the accuracy of the system was checked. The accuracy of each category was determined by identifying true values or false values. If the counted value is the same with the expected value, it will fall under true values, otherwise, false value.

$$Accuracy = \frac{Truevalue}{Truevalue+Falsevalue} \times 100\% \quad (1)$$

3.1.2 Field testing

The system was installed in an open field to measure the parameters. A comparison of the results in the laboratory test and the field test was done.

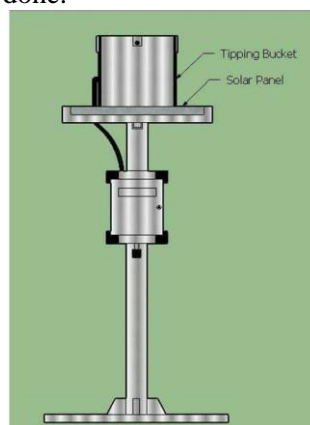


Figure 5. Front View with the Device Installed

Figure 5 shows the illustration of front view of the actual micro-weather data acquisition device. A tipping bucket was installed at the top most portion of the system with its base on the level of the solar panel. The solar panel serves as main source of power to the system. The circuit box which consists of the main board, battery, and sensor interconnection is located directly below the solar panel. The whole system is being framed in a round tubular tube with a solid metal plate.

3.2. Checking the device's efficiency

Efficiency is determined by the ratio of output over input. Mathematically, efficiency is defined as

$$\eta = \frac{\text{average measured value}}{\text{average actual value}} \times 100\% \quad (2)$$

3.3. Measuring device's effectiveness

For the effectiveness of the device, the time delay of SMS sending in each trial was measured. The time difference when the message was sent and the time received is measured. There are at least 1095 sample ($n=3\text{samples/day} \times 365\text{days/year}$) readings. The same procedure was done to compare the time sent by the GSM module and the time received by the web where outputs are saved into database. The effectiveness of the communication system is calculated with the use of the formula stated as:

$$\text{Effectiveness} = \left(\text{accepted time delay} - \frac{\text{total measure of time delay}}{\text{no.oftrials}} \right) \times 100\% \quad (3)$$

3.4. Calculating overall equipment effectiveness

Based from analysis earlier, the accuracy, efficiency, and effectiveness were identified. And to identify the overall equipment effectiveness for the reliability of the entire system is.

$$\text{OEE} = \text{Accuracy} \times \text{Efficiency} \times \text{Effectiveness} \times 100\% \quad (4)$$

4. Test results

4.1. Experimental setup

Three experiments were conducted for the calculation of accuracy, efficiency and effectiveness of the system. The standard used in this setup is according to the state weather bureau PAGASA in categorizing rainfall

Table 2 shows the data in simulation of light rain using a pressure sprayer done in a close environment that last up to 5 minutes.

Table 2. Tabulated data for Light Rain setup

No. of tips	Volume (mL)	Height (mm / 5min)	Height (mm / hr)
2	23	0.71	8.50
2	25	0.77	9.24
2	26	0.80	9.60
2	22	0.68	0.18
2	30	0.93	11.16
2	27	0.83	9.96
2	31	0.96	11.52
2	28	0.86	10.32
2	28	0.86	10.32
2	29	0.89	10.68

Average Volume: 26.9 mL

Average Flood Height per hour: 9.93mm/hr

Figure 6 is the graph that shows acceptable response of the tipping bucket of 2 tips for light rain in the range of 7~15 mm/hr of water rate.

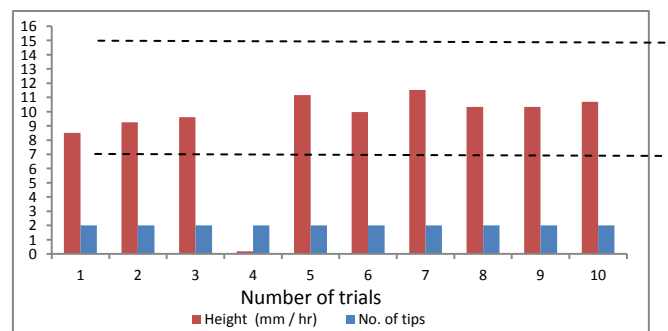


Figure 6. Comparison of number of tips and rain volume for light rain set up

Table 3 shows simulation of moderate rain using the same method in Table 2 but with increased water.

Table 3. Tabulated data for Moderate Rain setup

No. of tips	Volume (mL)	Height (mm / 5min)	Height (mm / hr)
3	45	1.39	16.65
3	43	1.33	15.91
3	43	1.33	15.91
3	51	1.57	18.87
4	56	1.73	20.72
3	42	1.30	15.54
5	66	2.04	24.42
5	71	2.19	26.27
5	73	2.25	27.01
6	81	2.50	29.97

Average Volume: 57.1 mL

Average Flood Height per hour: 21.13 mm/hr

Figure 7 is the graph that shows acceptable response of the tipping bucket of 4 tips for moderate rain in the range of 15~30 mm/hr of water rate.

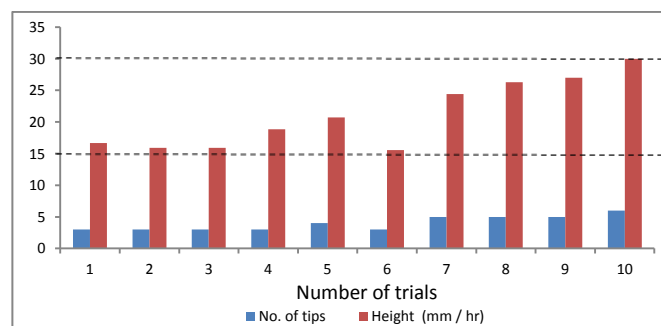
**Figure 7** Comparison of number of tips and rain volume for moderate rain set up

Table 4 shows the possible height for flood during heavy rain using the same method as the latter.

Table 4 Tabulated data for Heavy Rain setup

No. of tips	Volume (mL)	Height (mm / 5min)	Height (mm / hr)
7	100	3.0836	37.000
7	100	3.0836	37.000
9	115	3.5461	42.500
8	110	3.3920	40.704
7	110	3.3920	40.704
8	110	3.3920	40.704
9	120	3.7004	44.404
8	110	3.3920	40.704
7	100	3.0836	37.000
8	115	3.5461	42.500

Average Volume: 109 mL

Average Flood Height per hour: 40.33 mm/hr

Figure 8 is the graph that shows acceptable response of the tipping bucket of 7~8 tips for heavy rain in the range of 30 mm/hr and above of water rate.

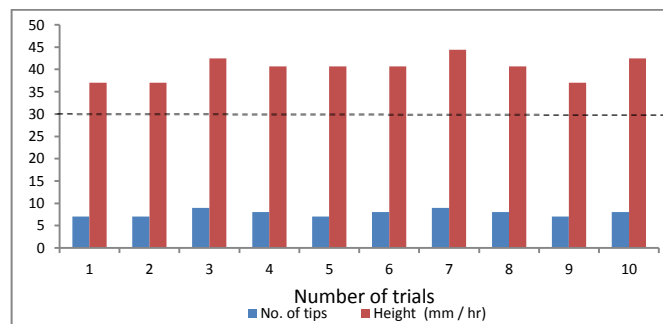


Figure 8 Comparison of number of tips and rain volume for heavy rain set up

DHT22 sensor was used in the system for the temperature and humidity measurement. It has 0~100% humidity range with an accuracy of $\pm 2-5\%$, and $-40\sim 80^{\circ}\text{C}$ temperature range with accuracy of $\pm 0.5^{\circ}\text{C}$. It is better over a slightly larger range, smaller, and cheaper. Sim800L has a dimension of 17.6x15.7x2.3mm which is used in the system considering the cheaper price.

4.1.1 Checking the DHT22 temperature accuracy

In a controlled environment, the sensor is tested from the range of $6^{\circ}\text{C}\sim 42^{\circ}\text{C}$. In each temperature, there are 1095 samples. The average difference between the two readings is 0.2°C and the calculated accuracy of the sensor for the laboratory testing is 99.32%. During the field testing, where the device is placed in an open field, the accuracy drops to 92.97%. The average difference of the two sensors is 0.4°C which coincide within the set accuracy for DHT22 temperature readings of $\pm 0.5^{\circ}\text{C}$.

4.1.2. Checking the DHT22 humidity accuracy

For DHT22 humidity readings, the sensors are tested in 11%, 33%, 75%, and 97% of relative humidity inside a controlled environment with 1095 sample of measurements. The average difference between the two readings is 0.8%. The accuracy for the DHT22 Humidity Sensor is 100% because all of its readings fall within the set accuracy of DHT22 for humidity of $\pm 5\%$. The results of field testing for the DHT22 humidity sensor were also tested for 1095 samples. The average difference drops to 2.5% and all of its reading still falls within $\pm 5\%$.

4.1.3. To observe sending time delay of the GSM shield (sim800L)

The optimum distances of transmission within 1km range are 300m and 800m for the specific location where the system was installed. There can be different results if the experiment will be done in different location because the speed of transmission depends on the strength of signal in every location. In locations where the signal strength is weak you will probably get a higher time delay. The delay for each designated distance falls within the accepted time delay which is 1 second. The average delay in the final testing is 0.549 seconds. This result is still within the acceptable time delay of 1 second. The average time delay for initial testing is 0.575 second while the average time delay for final testing is 0.557 second. Both results from two testing falls within the accepted time delay of 1 second.

4.1.4. Calculating device's overall equipment effectiveness

Accuracy:

$$\text{DHT22 Temperature Accuracy} = 92.97\%$$

$$\text{DHT22 Humidity Accuracy} = 100\%$$

$$\text{Average DHT22 Accuracy} = (\text{Temperature Accuracy} + \text{Humidity Accuracy})/2$$

$$\text{Average DHT22 Accuracy} = 96.49\%$$

Table 5. Tipping Bucket before Adjustment

Rain level	No. of True Values	No. of False Values
Light rain	934	161
Moderate rain	908	187
Heavy rain	902	193
Total	2744	541

Table 6 shows the results after adjusting the tipping bucket. The total number of true value became 3156 which is greater than 2744 that can be seen in Table 5. The accuracy of the tipping bucket got higher, from 83.53% to 96.07%. Computations can be seen below.

Table 6. Tipping Bucket after Adjustment

Rain level	No. of True Values	No. of False Values
Light rain	1057	38
Moderate rain	1053	42
Heavy rain	1046	49
Total	3156	129

The system accuracy is calculated using equation (1) and shown below.

$$Accuracy_{Initial\ test} = 83.53\%$$

$$Accuracy_{Final\ test} = 96.07\%$$

$$System\ Accuracy = \frac{(DHT\ Accuracy + Tipping\ Bucket\ Accuracy)}{2} = 96.28\%$$

Moreover, the efficiency of the tipping bucket is calculated using equation (2).

$$\eta_{light\ rain} = 98.52\%$$

$$\eta_{moderate\ rain} = 99.01\%$$

$$\eta_{heavy\ rain} = 99.50\%$$

$$\eta = \eta_L \times \eta_M \times \eta_H \times 100\% = 97.06\%$$

Both the effectiveness of the mobile phone and the modem is calculated using equation (3).

$$Effectiveness_{mobile\ phone} = \left(Accepted\ time\ Delay - \frac{Total\ Measure\ of\ Time\ Delay}{No.\ of\ Trials} \right) \times 100\% = 99.95\%$$

$$Effectiveness_{modem} = \left(Accepted\ time\ Delay - \frac{Total\ Measure\ of\ Time\ Delay}{No.\ of\ Trials} \right) \times 100\% = 99.95\%$$

$$System\ Effectiveness = \frac{Effectiveness_{mobile\ phone} + Effectiveness_{modem}}{2} = 99.95\%$$

The overall equipment effectiveness (OEE) is calculated using equation (4).

$$OEE = 93.04\%$$

4.2. Creation of a web page that display data.

The webpage where the data are stored can be seen by the public. Separate tables for temperature, humidity, and rainfall readings are provided and graphs for temperature, humidity, and rainfall readings are shown. These data can be used as baseline information in the study of its effect to natural calamities. For this purpose, the webpage created can also download or print the stored data.

Table 7 shows the stored information about the natural calamities that occurred in Bataan. These information can also be used as base line data for determining the relationship of temperature, humidity and rainfall in the occurrence of natural calamities.

Table 7. Sample data of Natural Calamities that hit Bataan stored on the system

Date	Temperature (°C)	Humidity (%)	Rainfall (mm)	Calamity
2009-05-06	29	88	48	Typhoon Emong
2009-06-25	26	82	7	Tropical Depression Feria
2009-09-23	28	79	38	Typhoon Ondoy
2009-10-30	27	74	44	Typhoon Santi

Table 8. Past 14 days data before the typhoon Ondoy hits Bataan

Date	Temperature (°C)	Humidity (%)	Rainfall (mm)
2009-09-09	26	87	38
2009-09-10	28	78	0
2009-09-11	26	82	13
2009-09-12	26	86	12
2009-09-13	27	81	5
2009-09-14	30	78	0
2009-09-15	32	71	0
2009-09-16	32	75	6
2009-09-17	31	76	27
2009-09-18	30	76	0
2009-09-19	30	75	0
2009-09-20	31	74	9
2009-09-21	32	46	15
2009-09-22	28	79	0

Table 8 shows the past 14 days sample data that can be seen in the database before the typhoon Ondoy hits Bataan. The user can choose the range of days to be viewed in the web page. It will show the temperature, humidity and rainfall of the past days picked by the user.

5. Conclusion

The microweather system station developed is significant for small geographical coverage areas. This collect more precise information of the conditions in the area of concerned for better decision making and early warning applications. It is a device that determined the calculated height of flood due to amount of rainfall measured by the tipping bucket. It sent real time rainfall data to the community via GSM network within the acceptable delay time of 1 second in less than 1km range then displayed data via LCD. With the use of a solar panel, the system can reliably operate in times of its intended purpose. The overall equipment effectiveness of the system reached up to 93.36%. An incorporated database connected via network is established in the system. And lastly, the information stored can be printed or downloaded for use as a baseline data to the study of its relationships on natural calamities.

6. Appendices

6.1. Actual installation of the micro weather system station



(a)



(b)

Figure 9. Testing Overall System with sensors for comparing the temperature, humidity and amount of rainfall (a) daytime and (b) night time

7. References

- [1] National Aeronautics and Space Administration 2017 “The consequences of Climate change”. IPCC 2007, Summary for Policymakers, in *Climate Change 2007: Impacts, Adaptation and Vulnerability. Contribution of Working Group II to the Fourth Assessment Report of the Intergovernmental Panel on Climate Change*, Cambridge University Press, Cambridge, UK. Retrieved from <https://climate.nasa.gov/effects/>
- [2] Suzuki D 2017 *Wins Annual Impact Report* 1-15
- [3] Usman M, Zafar M, Morata M, Amir N A, January 2010 *Effects of Temperature Increase on Earthquake Frequency and Depth in Northern Pakistan* **1**, 164-8
- [4] Hille K 2017 *Climate Change: How do we know?* Retrieved from <https://climate.nasa.gov/evidence/>
- [5] Josef 2017) *Massive earthquake strikes Haiti* Retrieved from <https://www.history.com/this-day-in-history/massive-earthquake-strikes-haiti>
- [6] Galvin G Sept. 20, 2017 *10 Deadliest Natural Disasters of 2017* Retrieved from <http://www.easybib.com/reference/guide/apa/website>
- [7] Oltermann P 2017 *Eight Missing After Landslide in Swiss Alps, Say police: The Guardian*. Retrieved from <https://www.theguardian.com/world/2017/aug/24/switzerland-landslide-in-swiss-alps-bondo>
- [8] Park M Sept. 01, 2017 *It's not just Harvey: August marked by deadly floods around world". Extreme Weather* Retrieved from <https://edition.cnn.com/2017/09/01/world/deadly-world-floods/index.html>
- [9] Siddique H 2017 *South Asia floods kill 1,200 and shut 1.8 million children out of school. The Guardian* Retrieved from <https://www.theguardian.com/world/2017/aug/30/mumbai-paralysed-by-floods-as-india-and-region-hit-by-worst-monsoon-rains-in-years>
- [10] The times of India April 19, 2016 *10 Worst Earthquake in 2016. Times of India*.
- [11] Climate Reality Project 2016 *How is Climate Change Affecting the Philippines". Climate Reality*. Retrieved from <https://www.climaterealityproject.org/blog/how-climate-change-affecting-philippines>
- [12] Whiteman H December 5, 2014 *Philippines gets more than its share of disasters. Cable News Network (CNN). Time Warner Center in New York City, CNN/ US*
- [13] Dela Cruz, G March 19, 2016 *In Numbers: Typhoons in the Philippines and the 2016 polls. Rappler*. Retrieved from <https://www.rappler.com/move-ph/issues/disasters/126001-typhoons-enter-philippines-fast-facts>
- [14] Roxas J July 10, 2016 *3 Bataan towns remain flooded amid intermittent heavy rains. GMA News Online*. Retrieved from <http://www.gmanetwork.com/news/news/regions/573088/3-bataan-towns-remain-flooded-amid-intermittent-heavy-rains/story/>
- [15] International Food Policy Research Institute 2015 *Addressing the impacts of climate change in the Philippine agriculture sector. National Economic and Development Authority*. Retrieved from <http://www.neda.gov.ph/addressing-impacts-climate-change-philippine-agriculture-sector/>
- [16] Liu T 2013 *Digital-output relative humidity & temperature sensor/module DHT22 (DHT22 also named as AM2302* Retrieved from <https://www.sparkfun.com/datasheets/Sensors/Temperature/DHT22.pdf>
- [17] Gonzalo Q, Azenha M, Barros J, Faria R, 2014 *Use of salt solutions for assuring constant relative humidity conditions in contained environments* Scholarly Journal 1-32

Acknowledgements

This work was supported by the Research and Development Office of the Bataan Peninsula State University grant funded by the university through General Appropriation Act (GAA).

The Effect of Silicon Fertilizer on The Growth of Chives

LONG Jiang-xue, CHENG Hui-yan, DAI Zhi-neng, LIU Jian-fu

College of environmental science and engineering, Xiamen University of Technology;
xiamen 361024

Abstract: Potted plants of chives to explore the growth effects of applying silicon fertilizer with 5 levels (0,180,360,540,720 mg/kg) for 3 weeks. Variables measured of plant development included fresh weight of whole plants, leaves, stalks; plant height; moisture and chlorophyll content in leaves. The results showed that the application of silicon fertilizer during 180-540 mg/kg concentration could improve the biomass weight and the growth height, increase chlorophyll and moisture content of chives leaves. The optimum effective silica concentration was 360 mg/kg, whereas the plants growth were decreased and even negatively affected with the increase of silica concentration to 720 mg/kg. This study provided a research foundation for the promotion of silicon fertilizer in the cultivation of chives and the further broadening of the application of silicon fertilizer. Funded by: Key Laboratory of Environmental Biotechnology (XMUT), Fujian Province University.

1. Introduction

Silicon fertilizer is a kind of mineral fertilizer and weakly alkaline, slightly soluble in water. Japanese scientists began to research systematically in the 1950s and have been widely used as a new type of fertilizer [1]. Then Korea, Philippines, Taiwan province and some countries in southeast Asia introduced the technology to promote and apply. Since then, silicon fertilizer has been recognized as the soil required nutrient to plant growth after nitrogen, phosphorus and potassium, and it has been listed as one of the four major elements for the yield increase of rice and other gramineous plants [2]-[5].

The started research on silicon fertilizer in China was in 1970s to 1980s, then the research was accelerated [6]. In 1996, the silicon fertilizer research center was set up in Henan province and responsible for the formulation of silicon fertilizer standards. The first "silicon and agriculture" research conference was held in the United States in 1999, which meanted that the world's agriculture and fertilizer industries began to pay attention to silicon fertilizer. In recent years, studies on the effects of application of silicon fertilizer on rice have been particularly outstanding in China [7]-[10] and it's also considered to be the second green revolution after hybrid rice.

The mechanism and effect of silicon fertilizer to plant was it could promote the formation silicide cells and thicken cell wall after absorbed silicon fertilizer [1], [4]-[6]. Therefore, it was beneficial for stems and leaves to straighten and increase leaf photosynthesis, enhance the capacity of crops resistant to pests [11]; Silicated cells could effectively regulate stomata and water transpiration of crops to improve drought resistance [12]. Supplement Silicon fertilizer could effectively prevent and control heavy metal pollution to crops and improve the ability to resist salt and alkali [13]-[15]. The application of



silicon fertilizer to rice could regulate the nutrient supply, increase roots oxidative power, promote the operation of carbohydrates and the growth of biomass [16]-[17].

Chive (*Allium schoenoprasum* L.) is a perennial herbaceous plant, belonging to the family Liliaceae. It is an important condiment, which has both edible and medicinal functions. However, because of the leaves' hollow tubular shape and high water content, they are fragile and easy to break down and cannot be stored for long time. At the same time, silicon is a quality element, which can improve the quality of agricultural products, so that the color, smell and taste become good, and beneficial to storage and transportation. But the application of silicon fertilizer in the cultivation of chives has not been reported. In this paper, the effect of appropriate silicon fertilizer on the growth of chives is investigated, which provides a reference for improving the quality of planted chives.

2. Materials and methods

2.1. Materials and equipments

Powdered silicon fertilizer was purchased in the market with an effective silicon content of 180 mg/g; The planting Soil was digged from local vegetable garden in Xiamen city, in which the effective Silicon was about 46-48 mg/kg.

Ultraviolet visible spectrophotometer (UV 3200), electronic balance (ML204T), and oven (dhg-9146a) would be used in tests.

2.2 Experimental methods

2.2.1 Applying silicon fertilizer to cultivate chives

Chive bulbs Evenly sized were potted in 20 cm diameter pot containing 2kg of garden soil, each potted 15. After the spring onion germinated 1-2cm, silicon fertilizer was dissolved in 200ml water and fertilized to the soil based on 4 groups of concentration as (180, 360, 540, 720 mg/kg), the control group no fertilization, 3 duplications per team of tests. All potted plants were cultured in greenhouse, watered at the right time, and the growth of plants were observed and recorded every day. After fertilization treated for 3 weeks, the plant biomass, height, water content and chlorophyll of chives were measured. The experiment was conducted three batches. The first batch was planted in autumn, the second in winter and the third in spring. Then the test statistics were carried out, and the average value of each batch of data was taken.

2.2.2 Measure plant height

The growth of chives was observed and recorded every day, and 5 chives were randomly selected to calculate the height of above ground growth after 3 weeks.

2.2.3 Measure plant biomass

After 3 weeks of treatment with different concentration of silicon fertilizer, the chives were removed gently from the basin. Five chives were randomly selected and the whole plant, the ground section (stems and leaves) and 10 leaves (8cm long) were weighed randomly, and the relative biomass was obtained separately.

2.2.4 Determine the moisture content in leaf

Ten leaves treated with different concentrations were harvested randomly, and then placed in oven at 105 °C for 2 h to dry weight, recorded its quality. The wet weight and dry weight was obtained by weighing 1/10000 electronic balance, and the moisture content of chives was calculated.

2.2.5 Determine chlorophyll content

Chopped leaves 0.2g were grounded into homogenate with 95% ethanol to extract the chlorophyll, and then filtered into 25ml volumetric flask. The absorbance of the extraction solution was determined and recorded at 665nm and 649nm by spectrophotometer with 95% ethanol as reference solution.

According to the formula, the content of chlorophyll a and chlorophyll b were calculated respectively, and the total content of chlorophyll was obtained.

3. Results

3.1. Measurement of growth height

Figure 1 showed the average height of growth of each batch of chives over 3 weeks. The average height of the control group was 8.83 cm, while the treatment groups height were increased by 21.74%、44.05%、24.58% and 12.34% respectively. The growth height showed a trend of first increasing and then decreasing with the increase of the amount of silicon fertilizer, among which 360mg/kg of silicon fertilizer was applied for the best growth, and the height was nearly 1.5 times higher than that of non-silicon fertilizer. It was also observed that the leaves were blown off by the wind with silicon fertilizer was lower than that of the control group, indicated that silicon fertilizer could promote the growth of chives and improve the ability of anti-fracture.

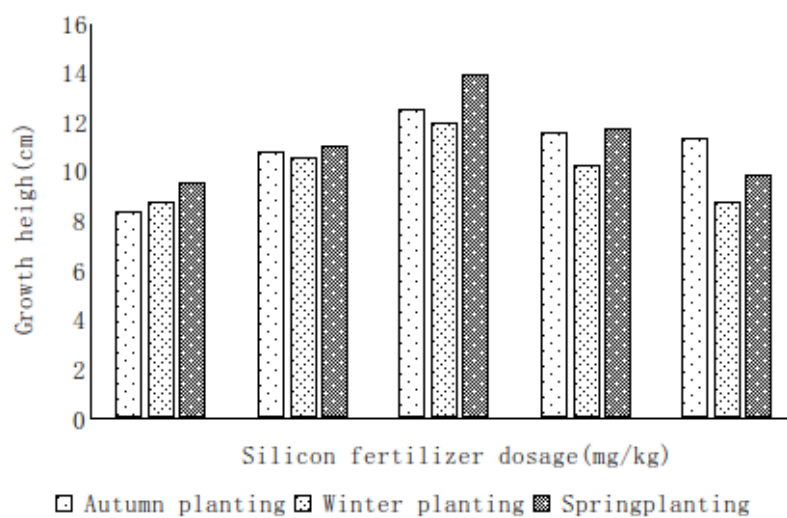


Figure. 1 The height of chievs

3.2. Measurement of biomass weight

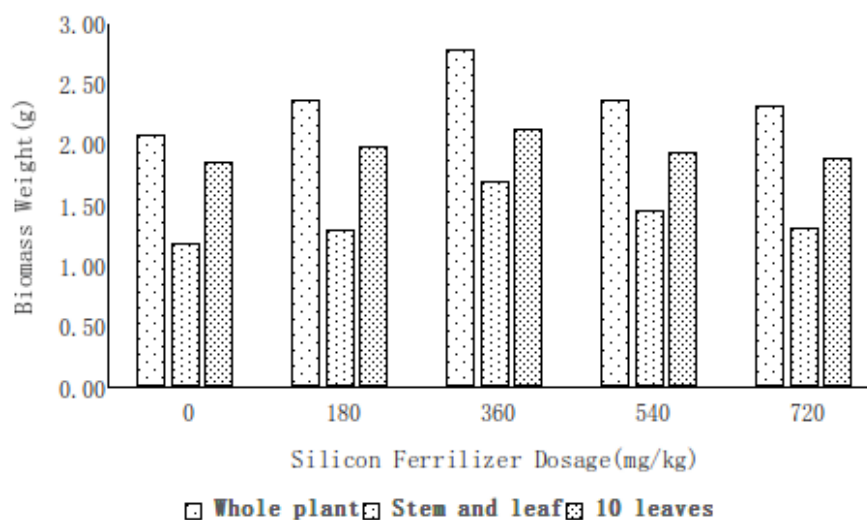


Figure 2. Biomass weight of chives

In order to explore the effect of silicon fertilizer on chives, the biomass of the whole plant, the aboveground part and the leaves were measured (grown in spring). As could be seen from FIG. 2, the same growth rules were observed in all three indexes of chives applied with different concentration of silicon fertilizer. The net biomass weight of the whole plant increased by 14.56%, 34.47%, 14.56% and 11.63% , the aboveground parts (stem and leaf) increased by 10.26%, 35.9%, 23.08% and 11.11% , and the leaves increased by 6.49%, 14.05%, 3.78% and 1.62% respectively. The relative increase in biomass which applied 360 mg/kg silicon fertilizer was the highest. In contrast, silicon fertilizer contributed more to allium roots than leaves.

When the amount of silicon fertilizer was greater or less than 360m g/kg, there was a certain decline in biomass. However, the biomass of the control group was the lowest, indicated that the effect of silicon fertilizer on the biomass of chives was relatively obvious.

3.3 Determination of water content in leaves

As could be seen from FIG. 3, the moisture content in control group leaves reached 87% - 90 % and its related to season, the highest water rate was in spring(89.02%) , followed by winter(88.25%) and the lowest in autumn(86.97%) .

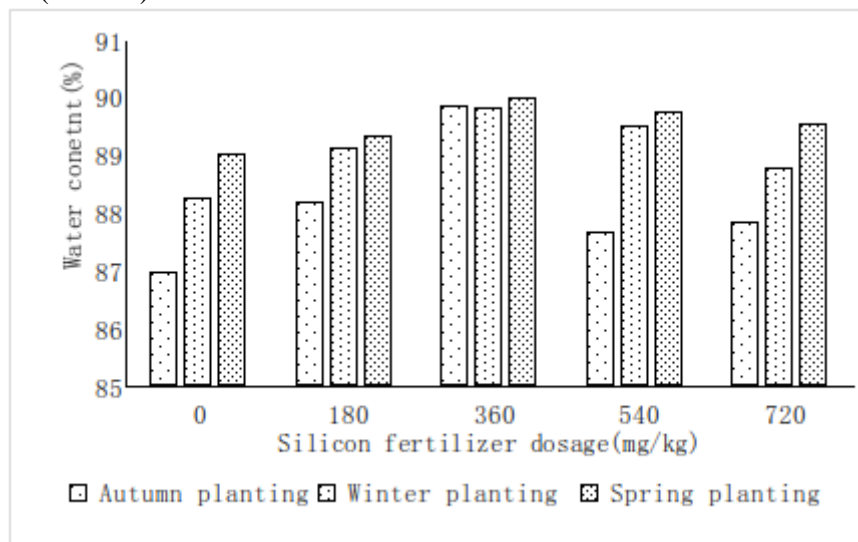


Figure 3. The water content in leaves

Appropriate supplementary silicon fertilizer could improve the leaf water content, and the plant treated with 360 mg/kg silicon fertilizer had the highest water content in leaves .When high concentration silicon fertilizer was applied (720 mg/kg), the water content decreased. In particular, during the drier autumn and winter, the water-retaining effect of application of silicon fertilizer was significantly higher than in spring. It was also found that when cutting the leaves treated 360m g/kg, the mucous material in tubular leaf was thicker than that of other chives significantly. It's probably the soluble sugar in the leaf, which was the ability to infiltrate a plant's cell and regulate it to protect the water. It also proved on the other hand that silicon fertilizer had the function of enhance the drought resistance of plants.

3.4 Determination of chlorophyll content in leaves

FIG. 4 showed the effect of silicon fertilizer on chlorophyll in the leaves of chives. After the application of 360 mg/kg silicon fertilizer, the content of chlorophyll increased by 28.75% compared with the control group, followed by 540mg/kg, up by 16.54%. When the application of silicon fertilizer was too high (720mg/kg), the increase was only 2.77%. At the same time, it could be observed that some leaves of chives turned yellow, which may be caused by too high concentration of silicon fertilizer applied to burn seedlings.

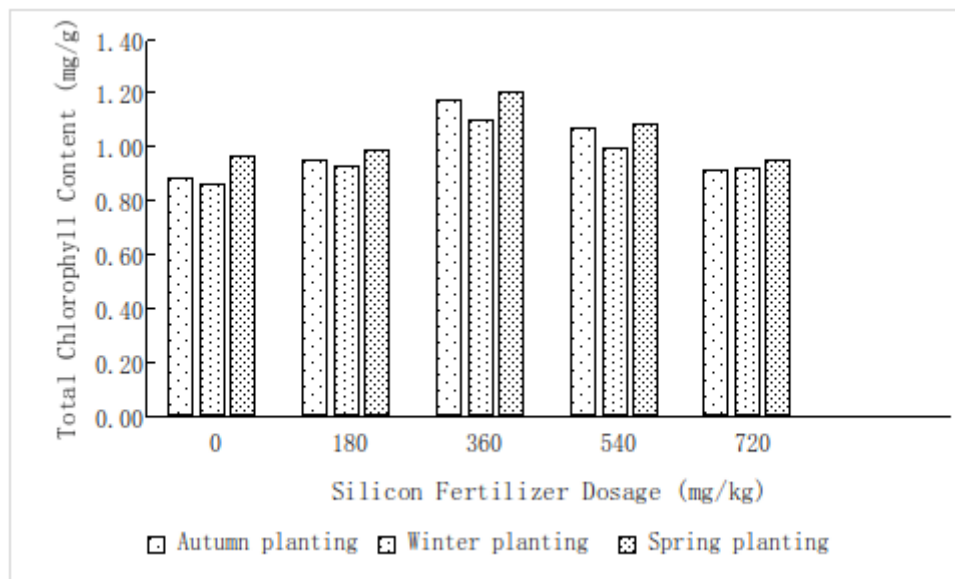


Figure 4. Total chlorophyll content in leaves

4. Conclusion

The study indicated that the application of a certain concentration of silicon fertilizer had a good effect on the growth of chives. The plant height, total biomass and chlorophyll content increased with the increase of silicon fertilizer application in the range of 180-540 mg/g silicon content. However, when the effective silicon content was 720mg/g, it would inhibit the growth of chives. The optimum dosage was 360 mg/kg, compared with the control group, the plant height increased by 44.05%, the total biomass weight increased by 35.9%, and chlorophyll content increased by 28.75%. In addition, applying silicon fertilizer could promote the capacity for water conservation of chives to improve the drought resistance and the anti-fracture ability.

5. References

- [1] R. B. Richard, Patricia A B, L. E. David, et al. Soluble silicon its role in crop and disease management of greenhouse crops [J]. *Plant Disease*, 1995, 4: 329-336.
- [2] L. E. Datnoff, C. W. Deren, G. H. Snyder. Silicon fertilization for disease management of rice in Florida [J]. *Crop Prot*, 1997, 16: 525-531.
- [3] XIA SH T, XIAO I T, PENG K Q. Physiological effects of silicon in higher plants and its application in agricultural production [J]. *Plant. Physiol. Commu*, 2001, 37(4):356-360.
- [4] J. F. Ma, Y. Miyake, E. Takahashi. Silicon as a beneficial element for crop plants [M]. Datnoff L, Korndorfer G, Snyder G. Silicon in agriculture. New York: Elsevier Science publishing, 2001: 17-39.
- [5] N. Mitani, J. F. Ma, T. Iwashita. Identification of the silicon form in xylem sap of rice (*Oryza sativa* L.) [J]. *Plant Cell Physiol*, 2005, 46(2): 279-283.
- [6] XING Xue-rang, ZHANG Lei. Review of the Studies on Silicon Nutrition of Plants [J]. *Chinese Bulletin of Botany*, 1998(2): 22-40.
- [7] A. Song, F. Fan, C. Yin, et al. The effects of silicon fertilizer on denitrification potential and associated genes abundance in paddy soil [J]. *Biology & Fertility of Soils*, 2017, 53 (6):1-12.
- [8] H. Peng, F. X. Tian, W. Wei, Y. J. Zhou, et al. Effects of silicon fertilizer application on the cadmium and silicon content of rice at different growth stages [J]. *Journal of Agro-Environment Science*, 2017, 6: 1027-1033.
- [9] X. Ji, S. Liu, J. Huang, E. A. Bocharnikova, VV Matichenkov. Effect of silicon fertilizers on cadmium in rice (*Oryza sativa*) tissue at tillering stage [J]. *Environmental Science & Pollution Research*, 2017, 24 (2):1-9.

- [10] LI Yuan-xing-lu , YE Chang-cheng, LIU Yu-ling, *et al.* Bioavailability of Silicon Fertilizer Coupled Water Management on Soil Bioavailability and Cumulative Control of Rice in Compound Contaminated Paddy Soils.[J].*Environmental Science* , 2018,39(2):944-953.
- [11] Cuidejie, Wangyuefu, Liuyanjan, *etc.* Study on Application Effect of Silicon Potash Fertilizer in Winter Wheat [J].*Soil notification*, 1999, 30 (3): 121 122.
- [12] Agari s SHU, Ag ta W, Kubo ta F, *et al.* effects of silicon on transpiration and leaf conductance in rice plants (*Oryzas atival*) [J]. *Plant p roducti on s ci*, 1998, 1(2): 89 95.
- [13] Liang Y, Wong J W C, Wei L. Silicon-mediated enhancement of cadmium tolerance in maize (*Zea mays L.*) grown in cadmium contaminated soil [J]. *Chemosphere*, 2005, 58(4):475-483.
- [14] Sun J, Cui J, Luo C, *et al.* Contribution of cell walls, nonprotein thiols, and organic acids to cadmium resistance in two cabbage varieties [J]. *Archives of Environmental Contamination and Toxicology*, 2013, 64 (2):243-252.
- [15] S. Wang, F. Wang, S. Gao. Foliar application with nano-silicon alleviates Cd toxicity in rice seedlings [J]. *Environmental Science and Pollution Research*, 2015, 22(4): 2837-2845.
- [16] Relationship between Nitrogen Absorption and Utilization and Silicone Nutrition in Rice [J]. *Chinese Agricultural Science*, 2004, 37(5): 648-655.
- [17] HUANG Hai-rong, BOKHTIARS M, XULin, *etc.* Effects of Silicon fertilization on yield and photosynthetic attributes in sugarcane. *Journal of Southern Agriculture [J]*, 2009, 40(12):1564-1569.

Influence Oil Price towards Economic Indicators in Russia

Anthony Msafiri Nyangarika^{1,2*}, Bao-jun Tang¹

¹School of Management and Economics, Beijing Institute of Technology, Beijing 100081, P. R. China.

²Institute of Adult Education, P.O. Box 20679 Dar sea Salaam, Tanzania.

*Email: nyangarikatz@gmail.com

Abstract. This paper examines the effect of oil price shocks on the Russian economic indicators using time series for the period 1991-2016 year to cover all of oil price shocks. We use the method of vector autoregressive (VAR) and the Dickey-Fuller test (ADF) were utilized to investigate the long-run and the short-run relationships between variables. From the results shows that one of the most important external impact factor is the world price of oil. This research work suggests a positive and significant long-term relationship between oil prices and Russian GDP dynamics. The study recommended a reducing the dependence of the Russian economy on energy resources, including oil, the transformation of the economy from industrial to innovative and improvement of the investment climate in the country for a foreign investor, the stabilization of foreign economic policy, which should lead to the abolition of anti-Russian sanctions. Apart from the fact that this will make the Russian economy more attractive for foreign investments, the opportunity will again become one of the main players in the oil market.

1. Introduction

Changing the price of crude oil, and especially the sharp fluctuations is definitely an important determinant that determines the world economic architecture. The supply and demand in the oil market, which is perhaps the key commodity nowadays, has a significant impact on world currencies in exporting countries. In 2014-2016 the oil market can be characterized by extreme volatility.

The aggregate of the fundamental factors that determined its business environment is almost comprehensive: macroeconomic conditions, market conjectures, transformation of the regulatory component, change in the structure of cost, geopolitical confrontation. In this paper, theoretical and empirical aspects of the mutual influence of oil prices and exchange rates are investigated.

Accordingly, if the prices for "black gold" in the world market tend to fall (in dollar terms), then the Russian economy begins to lose a certain part of the profit from the sale of oil, therefore it becomes necessary to devalue the national currency. It is oil and gas that are the main export products of Russia, half of the state budget revenues are their sale. In this regard, it is the size of foreign exchange earnings that depends on the price of oil.

In general, today there are three main marker grades of oil that correspond to three main exchanges: The New York Mercantile Exchange (NYMEX) is the major kind of West Light Oil (WTI); on the London Oil Exchange (IPE) - North Sea oil of Brent variety (Brent); at the Singapore International Commodity Exchange (SIMEX) - Middle Eastern oil of Dubai variety (Dubai) as found out [2]. Even earlier there was an OPEC basket, which included 12 grades of oil. In addition, each oil exporting country saves its own benchmarks of oil, which has certain stable parameters (Statfjord in Norway, Kirkuk in Iraq, two varieties in Iran - Iran Light and Iran Heavy).



The price of oil is fumigated by differentiation depending on the quality of oil and its location relative to consumers.

The fall in oil prices during 2014-2015 was so rapid that it became almost the most determinant of the economic and geopolitical architecture of the world. In December 2014, West Texas Intermediate (WTI) oil prices dropped from \$ 100 per barrel to 60; prices for Brent also headed for it. The fall continued in 2015, breaking the level of \$ 40 a barrel after a minor recovery.



Figure 1. WTI and Brent prices in 1991-2016

Source: Thomson Reuters DataStream.

The main reasons for such a fall are called: the transformation of the conjuncture on the oil market (the United States was the world's first oil producer due to the hydro-fraction of the reservoir, providing 95% of its own needs and ceasing to generate a lion's share of world imports; Saudi production growth; the start of supply of black gold from Libya and Iraq, exports from Iran at dumped prices, sluggish economic growth, increased efficiency and the transition from oil to other fuels reduce demand), a change in the regulatory environment and geopolitical factors.

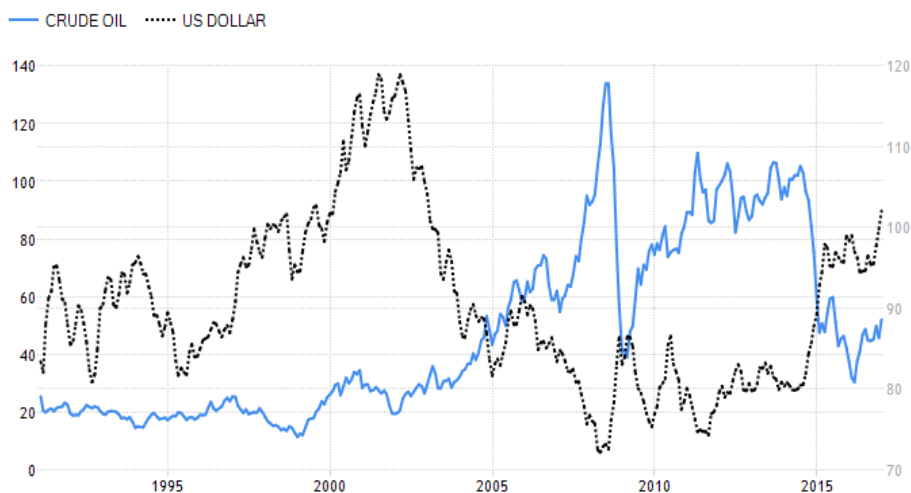


Figure 2. US dollar index and oil price

Source: Thomson Reuters DataStream.

The market for oil is largely reflected in the currency market. In particular, (Figure 2) shows the mirror correlation between the dynamics of the dollar index and changes in the price of oil. The strengthening of the US dollar as one of the stimulating factors in reducing oil prices did not attract

much attention. Since oil prices are determined in dollars, with the strengthening of the dollar - with all other equal conditions - oil prices for US consumers are reduced.

But the purchase of petroleum products by consumers in most countries are determined not in dollars, so they do not feel the decline in oil prices in dollars to the same extent as Americans. These disregarded factors may have global implications for the economic growth of countries, their national budgets, and geopolitics.

2. Literature review

Various research has been done examining the effect of oil price fluctuations on different economies driven by the importance of oil as a key player in the global economy. Specifically, a great deal of research has been written on the impact of oil prices on developed countries. [4] found evidence that oil price shocks resulted in a recession in the US economy. [3] assessed the impact of oil prices on the US's GDP and consumer price inflation. In addition, [17], [10] examined oil price shocks and found that the shock on 1973-74 was the most affecting for the US economy, whereas other shocks had fewer disturbances. [7] explored the impact of oil price shocks on the Iranian economy. He found a positive nexus between oil prices and both the Iranian's industrial output and the government expenditures. [1] found out that oil price shocks have no substantial effect on inflation and output on Nigeria, mitigated by tradable sector shrinking "Dutch Disease".

Moreover, [11] evaluated the impact of oil prices on the Nigerian's economy by using a VAR model. Results show evidence that the oil prices rise government expenditure, increase inflation and unexpectedly increase the industrial output growth. In addition, it has been investigated the effect of oil prices on Qatar's GDP, using the vector error correction model (VECM). They found that there is a substantial positive effect on Qatar's GDP but with expenses of higher inflation. [16] empirically investigated the impact of oil price shocks on Nigeria economy using the VAR models. With the existence of cointegration and causality, the findings suggest that the fiscal policy (i.e., government stimulant) is the most driver of the economy with the absence of monetary policy.

Finally, [6] tested the impact of oil on inflation in Kuwait and found that inflation is partly driven by high oil prices. [18] pointed to the key role of changing oil prices on the exchange rate, in particular, explicitly states that shock oil prices are the main source of the movement of the real exchange rate of the US dollar. The same conclusions came from the exchange rate of Russia.

But this only applies to countries that are heavily dependent on oil exports or imports, for example, the Chinese exchange rate is not responding to the sharp fluctuations in the price of crude oil, one of the main reasons is the binding of the rate to the basket of currencies as found out [9].

The problem of analyzing the dependencies between oil prices and exchange rates is the possibility of a bilateral reciprocal causation of indicators. The main channels of influence (they are distinguished by two), through which fluctuations in oil prices are transmitted to exchange rates, are widely covered by [13], [15].

The first channel is based on trading conditions. For oil importing countries, the latter price increase leads to a deterioration of the trade balance and subsequent depreciation of the national currency. In this context, [4], [13] demonstrated that variations in oil prices determine the lion's share of variations in terms of trade.

The second channel of influence finds its implementation through the effect of wealth (effects of wealth). [8] have shown that higher oil prices lead to a welfare shift from importers to exporters, which leads to a change in the exchange rate of the importing countries due to the current account deficit and the outflow of investments. On the other hand, a negative correlation may be due to the fact that changes in the dollar also have a significant impact on the price of oil. In particular, the exchange rate can transform oil prices through its impact on demand and supply of oil and through financial markets. [12] found out that exchange rates can also affect the price of oil directly through financial markets or indirectly through financial assets, the rebalancing of investment portfolios and, in particular, hedging practices. Since oil prices are denominated in dollars, oil futures may be a good hedging instrument against the expected depreciation of the dollar. The importance of this financial channel may only increase over time as the volume of oil futures at NYMEX has increased fivefold since the beginning of the 2000s. Unlike literary sources devoted to the causality of exchange rates from oil prices, the empirical evidence of reverse dependence is not so numerous. An empirical

confirmation of the influence of oil prices on the exchange rate can be demonstrated by the example of fluctuations in oil prices and the rate of the Russian ruble on (Fig. 3).

In general, the rate of the Russian ruble, to a large extent, is a determinant of oil prices. This is especially evident when the price of oil in rubles is displayed (Fig. 3). Due to this feature, a decision was made to study the influence of the price of crude oil on the exchange rate of the Russian Federation.

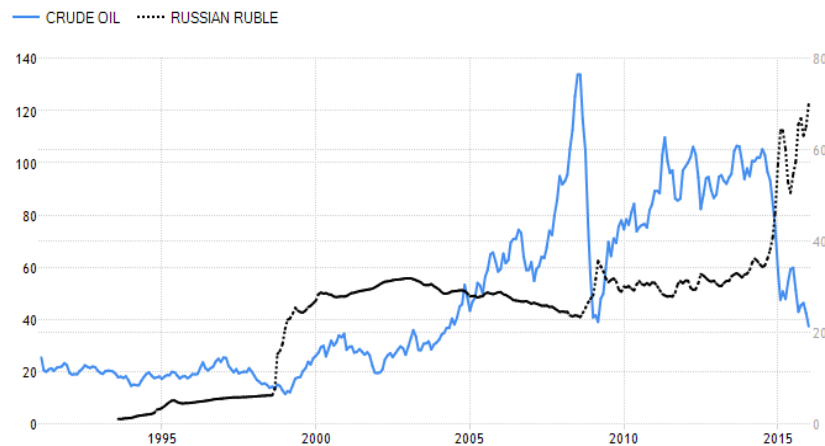


Figure 3. Crude oil price and USDRUB rate

Source: Thomson Reuters DataStream.

3. Methods

In this paper, the real exchange rate of Russia using the time series from 1991 till 2016, we used the vector model of autoregression (VAR-model), which is commonly used for prediction systems of related time series and for analyzing the dynamic effect of random perturbations on a system of variables. The approach to constructing VAR models is based on structural modeling, considering each endogenous variable in the system as a function of the lagged values of all endogenous variables. A real exchange rate model was constructed using five variables: consumer price index, gross domestic product, oil price, total country export, and a real effective exchange rate as a dependent variable. The real exchange rate model is specified as follows;

$$\text{LogEXCH}_t = \alpha + \beta_1 \log \text{CPI}_t + \beta_2 \log \text{OIL}_t + \beta_3 \log \text{GDP}_t + \beta_4 \log \text{EXPORT}_t + \varepsilon_t \quad (1)$$

Where, *EXCH* - real effective exchange rate national currency per US dollar (RUB/USD), *CPI* - consumer price index; *GDP* - gross domestic product measured in millions of US dollars, *OIL* - oil price US dollar per barrel ; *EXPORT* - total country export measured in millions of US dollars; β_1 , β_2 , β_3 , β_4 - coefficients of the model, α - intercept; ε_t - coefficients of error.

We use time series of gross domestic product, real effective exchange rate, consumer price index, total export oil price from Thomson Reuters DataStream.

4. Results and discussion

Since the VAR methodology is used only for stationary rows, the first step in identifying a process is to check the time series for stationary. The need for time series to be stationary in modeling is due to the fact that these models are used for forecasting, and to predict the behavior of only those processes whose main characteristics (average, variance, and coefficients of autocorrelation) are independent of time.

It is impossible to predict the behavior of the process, based on which the non-stationary time series (mathematical expectation, variance, and autocorrelation of it vary depending on time). In this case, it is difficult to find constant averages and variances, we should look for possible transformations of the series, which can reduce it to the stationary one. To determine stationary, we used the ADF test. The test procedure for the ADF test is the same as for the Dickey-Fuller test, but it is applied to the model.

We used E-views program to test the stationarity of variables to guarantee its non-stationarity in

order to examine the long-run equilibrium. Generally, the augmented Dickey- Fuller test was conducted to check whether a particular variable is stationary or not with relaxing the assumption that the error term is uncorrelated as follows:

$$\Delta y_t = \alpha + \beta t + \gamma y_{t-1} + \delta_1 \Delta y_{t-1} + L + \delta_{p-1} \Delta y_{t-p+1} + \varepsilon_t \quad (2)$$

where α - constant, β - coefficient of trend, p - lag order of the autoregressive process, y - data value. Imposing the constraints $\alpha = 0$ and $\beta = 0$ corresponds to modelling a random walk and using the constraint $\beta = 0$ to modeling a random walk with a drift.

Table 1. ADF unit root test results for exchange rate model

VARIABLE	5% level	t-Statistic	Probability
Log EXCH	-3,603202	-2,226360	0,4557
log CPI	-1,159153	-3,673616	0,8973
log OIL	-3,603202	-3,673616	0,8973
log GDP	-3,612199	-2,002570	0,5706
log EXPORT	-3,603202	-3,5889008	0,0514

Source: Authors' calculation

The result of the ADF (Table 1) indicates that all variables in the model are stationary because the value of the test statistic is rejected at the 5% significance level. Consequently, this series can be used to construct regression models. However, a positive long-run nexus between oil prices and economic growth exists referring to the error correction model's results. The real GDP is impacting the government spending. Absolutely, a country like Russia with huge output would require higher government spending to assure sustainability of growth.

The real exchange rate is affecting the output as expected, shown in (Table 2). The higher exchange rate would trigger economic activity through higher demand. Finally, real trade balance is found to be moving real investment at the Russian economy.

After founding variables non-stationary and the long run nexus between variables. This process is determined through two steps; the first one based on trace statistic and the second is based on the maximum eigenvalue statistic. Prior to the above, the optimal lag order for VAR model was determined. Based on the Akaike information criterion (AIC), shown in (Table 2 and Table 3). We examine the long-term relationship between the variables, we use cointegration analysis, the method proposed by Johansen (1991). Our VAR model generally can be re-written as follows:

$$\Delta y_t = \mu + \Pi y_{t-1} + \sum_{i=1}^{p-1} \Gamma_i \Delta y_{t-i} + \varepsilon_t \quad (3)$$

Where

$$\Pi = \sum_{i=1}^p A_i - I \text{ and } nxr \quad (4)$$

If the coefficient matrix Π has reduced rank $r < n$, then there exist $n \times r$ matrices α and β each with rank r such that $\Pi = \alpha\beta'$ and $t\beta'y$ is stationary. The r - number of cointegrating relationships, the elements of α are known as the adjustment parameters in the vector error correction model and each column of β is a cointegrating vector. It can be shown that for a given r , the maximum likelihood estimator of β defines the combination of $yt-1$.

Yields r largest canonical correlations of Δy_t with y_{t-1} after correcting for lagged differences and deterministic variables when present. Johansen (1991) proposes two different likelihood ratio tests of the significance of these canonical correlations and thereby the reduced rank of the Π matrix: the trace test and maximum eigenvalue test, shown in equations (5) and (6) respectively.

$$J_{trace} = -T \sum_{i=r+1}^n \ln(1 - \hat{\lambda}_i) \quad (5)$$

$$J_{max} = -T \ln(1 - \hat{\lambda}_{r+1}) \quad (6)$$

where T - sample size and λ_i - the largest canonical correlation. The trace tests the null hypothesis of r cointegrating vectors against the alternative hypothesis of n cointegrating vectors. The maximum eigenvalue test, on the other hand, tests the null hypothesis of r cointegrating vectors against the alternative hypothesis of $r + 1$ cointegrating vectors. Neither of these test statistics follows a chi square distribution in general.

Table 2. Unit Root Test Results for RUBUSD Rate and Output

Null Hypothesis: LGEXCHANGERATE has a unit root Exogenous: Constant, Linear Trend Lag Length: 0 (Automatic - based on SIC, maxlag=5)			Null Hypothesis: LGGDP has a unit root Exogenous: Constant, Linear Trend Lag Length: 1 (Automatic - based on SIC, maxlag=5)		
	t-Statistic	Prob.*		t-Statistic	Prob.*
Augmented Dickey-Fuller test statistic	-2.226360	0.4557	Augmented Dickey-Fuller test statistic	-2.002570	0.5706
Test critical values:			Test critical values:		
1% level	-4.374307		1% level	-4.394309	
5% level	-3.603202		5% level	-3.612199	
10% level	-3.238054		10% level	-3.243079	
Null Hypothesis: LGEXPORT has a unit root Exogenous: Constant, Linear Trend Lag Length: 0 (Automatic - based on SIC, maxlag=5)			Null Hypothesis: LGOILPRICE has a unit root Exogenous: Constant, Linear Trend Lag Length: 0 (Automatic - based on SIC, maxlag=5)		
	t-Statistic	Prob.*		t-Statistic	Prob.*
Augmented Dickey-Fuller test statistic	-3.588908	0.0514	Augmented Dickey-Fuller test statistic	-1.159153	0.8973
Test critical values:			Test critical values:		
1% level	-4.374307		1% level	-4.374307	
5% level	-3.603202		5% level	-3.603202	
10% level	-3.238054		10% level	-3.238054	
Null Hypothesis: D(LGCPI) has a unit root Exogenous: Constant, Linear Trend Lag Length: 5 (Automatic - based on SIC, maxlag=5)					
	t-Statistic	Prob.*			
Augmented Dickey-Fuller test statistic	-1.159153	0.8973			
Test critical values:					
1% level	-4.532598				
5% level	-3.673616				
10% level	-3.277364				

Source: Authors' calculation

Table 3: Cointegration Test result (trace)

Unrestricted Cointegration Rank Test (Trace)

Hypothesized		Trace	0.05	
No. of CE(s)	Eigenvalue	Statistic	Critical Value	Prob.**
None *	0.905738	129.8261	69.81889	0.0000
At most 1 *	0.811322	73.14586	47.85613	0.0000
At most 2 *	0.514332	33.12078	29.79707	0.0200
At most 3 *	0.368634	15.78724	15.49471	0.0452
At most 4 *	0.179575	4.750388	3.841466	0.0293

Trace test indicates 5 cointegrating eqn (s) at the 0.05 level

* denotes rejection of the hypothesis at the 0.05 level

**MacKinnon-Haug-Michelis (1999) p-values

We test here is that there are less than or equal to r cointegrating vectors and the alternative is the opposite, which is more or equal to as follows: $H_0: r \leq 1$ and $H_1: r \geq 2$. If the test statistic is greater than the critical value (i.e., probability is less than 5 %), then we reject H_0 and accept H_1 .

It is similar to the trace statistics but specifically tests whether r is equal to or not. We follow this procedure to determine how many cointegrating vectors are as follows: $H_0: r = 1$ and $H_1: r = 2$. If the test statistic is greater than the critical value (i.e., the probability is less than 5 %), then we reject H_0 and accept H_1 . We choose 5% level of significance. Hence, two cointegrating vectors are found based on the max eigenvalue statistic.

Johansen test indicate a long-term relationship between the variables consumer price index, gross domestic product, the oil price, total country export and real exchange rate (Table 3 and 4).

Table 4: Cointegration Test result (Maximum Eigenvalue)

Unrestricted Cointegration Rank Test (Maximum Eigenvalue)

Hypothesized No. of CE(s)	Eigenvalue	Max-Eigen Statistic	0.05 Critical Value	Prob.**
None *	0.905738	56.68022	33.87687	0.0000
At most 1 *	0.811322	40.02508	27.58434	0.0008
At most 2	0.514332	17.33354	21.13162	0.1568
At most 3	0.368634	11.03686	14.26460	0.1524
At most 4 *	0.179575	4.750388	3.841466	0.0293

Max-eigenvalue test indicates 2 cointegrating eqn(s) at the 0.05 level

* denotes rejection of the hypothesis at the 0.05 level

**MacKinnon-Haug-Michelis (1999) p-values

Table 5: Normalized cointegration vector

Normalized cointegrating coefficients (standard error in parentheses)

LGEXCHANG				
LGOILPRICE	LGEXPORT	ERATE	LGCPPI	LGGDP
1.000000	0.062451 (0.46237)	0.139571 (0.03252)	0.883733 (0.11063)	-0.758111 (0.39393)

In (Table 5) above shows the normalized cointegration vector. The long run equation for the real exchange rate model can be written as:

$$\text{Log EXCH} = 2.385934 + 2.385934 \log \text{CPI} - 1.466842 \log \text{GDP} - 1.666902 \log \text{OIL} + 0.084569 \log \text{EXPORT} \quad (7)$$

The equation above shows that: the consumer price index and export have a long-run positive relationship with the real exchange rate while the GDP and oil price have a long-run negative relationship with the real exchange rate. An increase in the consumer price index by 1% will lead to a 2.38% increase in the national currency against the US dollar. This is due to rising inflation that grows with the consumer price index, which reduces the exchange rate. The growth of GDP by 1% leads to the strengthening of the national currency by 1.47%, this fact can be explained by the growth of the country's economy as a whole with GDP growth.

The most fact is that with an increase of 1% of the price of oil - the national currency is strengthened by 1.66%, which again confirms the fact that the Russian economy depends on oil prices.

The increase in exports by 1% leads to ruble depreciation, as the flow of foreign currency, which leads to an increase in supply on the interbank market, increases.

From above (Table 5) explanation shows the long-term relationship between the variables namely consumer price index, gross domestic product, oil price, total country exports and real exchange rate, it's obligatory necessary to conduct a Granger Causality test.

The Granger approach to the question of whether x causes y is to see how much of the current y can be explained by past values of y and then to see whether adding lagged values of x can improve the explanation. y is said to be Granger-caused by x if x helps in the prediction of y , or equivalently if the coefficients on the lagged x 's are statistically significant.

Note that two-way causation is frequently the case; x Granger causes y and y Granger causes x .

It is important to note that the statement " x Granger causes y " does not imply that y is the effect or the result of x . Granger causality measures precedence and information content but does not by itself indicate causality in the more common use of the term (Table 6).

Table 6. Granger Causality Results

Variable	F-stats.
$\sum \log \text{CPI}$	0,951094
$\sum \log \text{GDP}$	1,795367
$\sum \log \text{EXPORT}$	0,632294
$\sum \log \text{OIL}$	2,406444

Source: Authors' calculation

The results of the F-statistics Granger Causality test for our model, from which it follows that the price of oil on a par with GDP has the greatest impact on the exchange rate in the short run see in appendix B (Figure 4). The results obtained as a result of Granger's cointegration and causality research show that world prices for crude oil directly affect the exchange rate of the Russian Federation, rising oil prices reduce the real exchange rate of the country. This, in its turn, positively affects the export opportunities of Russia, because the goods manufactured here "get cheaper" abroad. The reason for this dependence is likely to be the percentage of exports of petroleum products to total exports, and the floating exchange rate operating in the country. It can also be concluded that the Russian Federation is extremely dependent on world oil prices, and shocks in this market can become a real problem for the economy of this country.

5. Conclusion

The main goal of this work was to confirm the hypothesis of the impact of oil shocks on the exchange rate of the Russian Federation using time series with data from 1991 to the 2016 year. The methods proposed by Granger and Johansen in the VAR model were used, the statistical package E-views was used to obtain the results. The Johansen-Juselius cointegration result showed the relationship between changes in oil prices on the world market and the exchange rate of the Russian ruble. From the results of the study, it became known that one of the most important external factors that influences the ratio of the dollar to the ruble is the world price of oil. Russia is one of the world's largest suppliers of "black gold", its economy is mainly associated with oil production, the finding show that the slightest fluctuations in oil prices have the strongest impact on it. If oil prices on the world market grow, then, respectively, real exchange rate becomes stronger, but if prices fall, then there are problems. Thus, the result is the following: the higher the oil price, the lower the US dollar rate to the Russian ruble.

However, if the prices for "black gold" in the world market tend to fall (in dollar terms), then the Russian economy begins to lose a certain part of the profit from the sale of oil, therefore it becomes necessary to devalue the national currency. It is oil and gas that are the main export products of Russia, half of the state budget revenues are their sale. In this regard, it is the size of foreign exchange earnings that depends on the price of oil.

Proceeding from all of the above, as a recommendation, reducing the dependence of the Russian economy on energy resources, including oil. Translation of the economy from industrial to innovative. Improvement of the investment climate in the country for a foreign investor.

According to above conclusion several suggestions have be provided;

- 1) The stabilization of foreign economic policy, which should lead to the abolition of anti-Russian sanctions. Apart from the fact that this will make the Russian economy more attractive for foreign investments, the opportunity will again become one of the main players in the market.
- 2) The second step is the diversification of exports. The task is to turn this wealth from oil revenue into a tool that enhances the quality of the development of the Russian economy and the life of society as a whole.
- 3) The Russian oil brand the Urals must be recognized in the world as one of the world's oil brands.
- 4) The calculations for Russian oil and gas in rubles. The real convertibility of the Ruble largely depends on its attractiveness as a means used for settlements and savings. In particular, the ruble should become a more universal means for international settlements and should gradually expand its zone of influence. For the same purposes, it is necessary to organize exchange trade in oil, gas, and other goods on the territory of Russia.

6. References

- [1] Akpan, E. O. (2009), Oil price shocks and Nigeria's macro economy. A Paper Presented at the Annual Conference of CSAE Conference. Economic Development in Africa. Retrieved from <http://www.csaee.ac.uk/conferences/2009-EDIA/Papers/252-Akpan.Pdf>
- [2] Amano, R. A. and Van Norden, S. (1998), Exchange Rates and Oil Prices. *Review of International Economics*, 6: 683–694. doi:10.1111/14679396.00136
- [3] Baumeister, C., & Peersman, G. (2008), Time-varying effects of oil supply shocks on the US economy. <http://dx.doi.org/10.2139/ssrn.1093702>
- [4] Backus, D. K. and M. J. Crucini (2000), Oil Prices and the Terms of Trade. *Journal of International Economics*, 50, 185-213
- [5] Buetzer, S., Habib, M. and L. Stracca (2012), Global Exchange Rate Configurations: Do Oil Shocks Matter? Working Paper, European Central Bank.
- [6] Eltony, M. N., & Al-Awadi, M. (2001), Oil price fluctuations and their impact on the macroeconomic variables of Kuwait: A case study using a VAR model. *International Journal of Energy Research*, 25(11), 939-959.
- [7] Farzanegan, M. R., & Markwardt, G. (2009), The effects of oil price shocks on the Iranian economy. *Energy Economics*, 31(1), 134-151. <http://10.1016/j.eneco.2008.09.003>
- [8] Ferraro D., Rogoff K. and B. Rossi (2015), Can Oil Prices Forecast Exchange Rates? Available at: <http://www.econ.upf.edu/~brossi/OilAndExchangeRates.pdf>
- [9] Huang, Y. and F. Guo (2007), The role of oil price shocks on China's real exchange rate. *China Economic Review*, 18: 403-416.
- [10] Hooker, M. (1996), Oil prices and the rise and fall of the US real exchange rate. *Journal of Monetary Economics*, 25, 195-213.
- [11] Iwayemi, A., Fowowe, B., (2011). Impact of oil price shocks on selected macroeconomic variables in Nigeria. *Energy Policy* 39, 603–612. doi:10.1016/j.enpol.2010.10.033
- [12] Johansen, Søren (1991), Estimation and Hypothesis Testing of Cointegration Vectors in Gaussian Vector Autoregressive Models. *Econometrica* 59 (6), 1551–1580. JSTOR 2938278.
- [13] Mikhailov A. Y. (2014), Faktory razvitiya ekonomiki Rossii v 2015 godu [Factors of development of the Russian economy in 2015]. *Voprosy regulirovaniya ekonomiki = Questions of economic regulation*, 4, pp. 62-69.
- [14] Mikhailov A. (2018), Pricing in Oil Market and Using Probit Model for Analysis of Stock Market Effects. *International Journal of Energy Economics and Policy*, 4, pp. 43–53.
- [15] Mikhaylov, A. (2018), Volatility Spillover Effect between Stock and Exchange Rate in Oil Exporting Countries. *International Journal of Energy Economics and Policy*, 2018, 8(3), 321-326.
- [16] Olomola, P. A., & Adejumo, A. V. (2006), Oil price shock and macroeconomic activities in Nigeria. *International Research Journal of Finance and Economics*, 3(1), 28-34.
- [17] Singer, E. (2007), Oil Price Volatility and the US Macroeconomy: 1983-2006. Working paper, Minnesota of USA: Carleton College.
- [18] Tuzova, Y., & Qayum, F. (2016), Global oil glut and sanctions: The impact on Putin's Russia. *Energy Policy*, 90, 140–151. <https://doi.org/10.1016/j.enpol.2015.12.008>

Chapter 9:
Modern Information Science and
Technology

Routing Architecture of Software Defined Energy Internet

Dilin Mao¹, Xiu Cao¹, Xinyang Han², Chengzhi Zhu³ and Wei Geng¹

¹School of Computer Science, Fudan University, Shanghai, China

²State Grid Energy Research Institute Co., Ltd., Beijing, China

³State Grid Zhejiang Electric Power Co., Ltd, Hangzhou, China

E-mail: dlmao@fudan.edu.cn, xiucao@fudan.edu.cn, hanxinyang@sgeri.sgcc.com.cn, chengzhi_zhu@163.com, wgeng17@fudan.edu.cn

Abstract. Energy Internet is a new and constantly evolving technology, of which the most critical part is how the energy flows. The concept of software customization used in the field of information will decouple the control plane from the data plane. It adopts a logical centralized control model. The control part of the device is implemented by a centralized programmable controller. Referring to the basic concept of computer network, the energy internet can be divided into energy resource subnet and energy transmission subnet. Energy micro-network, wide area energy internet and global energy internet are introduced. The concept of software-defined is applied to the field of smart grid which is the foundation and critical part of energy internet. This paper describes a software defined wide area energy internet routing architecture and implementation approach, which not only takes into account the compatibility of power devices with smart grid standards such as IEC61850 but also provides flexible software defined innovative application deployment.

1. Introduction

With the development of smart grid, new energy technology, and information technology, energy internet combines the Internet and renewable energy technology. This technology makes people produce green renewable energy at factory, office and home, and the excess energy can be shared with others, just as we share information on the Internet now. Compared with other energy forms, electric energy has instantaneous generation and supply characteristics. In the future, energy internet will take electricity as the majority of the energy form. The future of energy internet is bound to integrate power grid, energy network, information network, traffic network and other types of network, so as to achieve comprehensive utilization of various energy forms.

Energy Internet is a new and constantly evolving technology, of which the most important part is energy flow. In traditional power grids, the power generated by large power plants is sent to users through transmission, transformation and distribution. With the development of distributed power, power electronic technology and information technology, electrical energy has evolved from the original one-way flow to two-way flow. That allows energy internet access to a controllable load. Distributed power supply and distributed energy storage are integrated into the energy internet anytime and anywhere.

IEC61850 was originally designed for substation automation systems. It allows the interconnection of Intelligent Electronics Device (IED) produced by different manufacturers and provides object-oriented modelling technology and communication service support. After that, the IEC61850 standard continues being extended for smart grid applications. The goal of IEC61850 is to solve the interoperability problems between different IED in the smart grid. IEC61850 can be used in the fields of renewable energy, equipment state monitoring, intelligent power use and distribution automation.



2. Significance

Software Defined Network (SDN) puts forward a new network structure. By decoupling the control plane and the data plane of network, the control ability of the network device is concentrated to the central controller. Network control and service configuration of the network operating system can be flexible and highly automated through software driven approach. Network structure adjustment, extension and upgrading can be easier. A large number of network equipment to be configured or replaced one by one is no longer needed when there is a new service to be deployed. Besides, it brings shorter deployment time and higher efficiency

3. Related work

At present, research on energy internet is mainly focused on the overall architecture of the energy internet and the prototype implementation of energy routers based on power electronic transformation. There are few studies on the routing of energy internet.

In [1], the authors design a software-defined approach for the IoT environment to dynamically achieve differentiated quality levels to different IoT tasks in very heterogeneous wireless networking scenarios. For this, they extend the Multinetwork INFORMATION Architecture (MINA), a reflective (self-observing and adapting via an embodied Observe-Analyze-Adapt loop) middleware with a layered IoT SDN controller.

In [2], the authors propose that energy routers are required which adjust dynamically the energy distribution in the grid, which is so called the Energy Internet in order to manage efficiently the energy supply and demand in the power grid. [2]'s work-in-progress on the design and implementation of energy router, a critical equipment to enable intelligent energy management in the smart grid.

In [3], the authors consider the objective of efficient transfer of electric energy between subsystems, where each 1 subsystem can generate, store, or consume energy. To ensure energy exchange, the interconnection of the storage and load devices is performed by using power converters.

Some key features of an energy internet compared with conventional energy grid such as openness and peer-to-peer are introduced in [4]. The definition of an energy internet call for a much greater degree of interactive flexibility for efficient energy management than the present system is designed to handle.

In [5], the authors present an architecture for a future electric power distribution system that is suitable for plug-and-play of distributed renewable energy and distributed energy storage devices.

In [6], the authors present the security, agility, robustness and survivability of a large-scale power delivery infrastructure. Similar as [6], the security and privacy issues in the Smart Grid are explored in [7], [8] discusses about integrating renewable energy sources into the smart power grid through industrial electronics

4. Architecture of energy internet

The computer network is composed of the resource subnet and the communication subnet, in which the resource subnet including end system provides resource service and the communication subnet provides the data transmission service for the end system. Referring to the basic concept of computer network, the energy internet can also be divided into energy resource subnet and energy transmission subnet. As shown in Figure 1, the smart grid is the main part of the energy Internet. Various types of energy networks at the end are fused together.

The resource subnet is composed of equipment for energy production and energy consumption. Of course, it also covers the equipment of power generation and power use in the smart grid, including the large-scale power plant station, power load, electric vehicle, energy storage devices, distributed power supply that can be directly connected to the distribution network. The energy transmission subnet is composed of transmission, distribution and substation equipment and power cable, which provides energy transmission services for power generation and electrical equipment in the energy resource subnet.

The energy micro-network is the basic unit of the energy internet. It connects the energy terminal equipment belonging to the resource subnet in a region. Generally speaking, energy micro-networks not only connect traditional loads, but also connect with elastic loads such as electric vehicles and smart appliances. At the same time, it may connect different types of distributed power generation such as photovoltaic and bio power generation, and may also connect some smart energy storage

devices. Energy micro-network is an autonomous system that can realize self-control, protection and management. It can realize power balance control, system operation optimization, fault detection and protection, power quality control and so on relying on its own control and management functions. The control function of the micro-network is done by the energy micro-network interconnection equipment called energy switch. These include the realization of distributed generation control, energy storage control, off grid switching control, real-time control of micro-network, energy management of micro-network, etc.

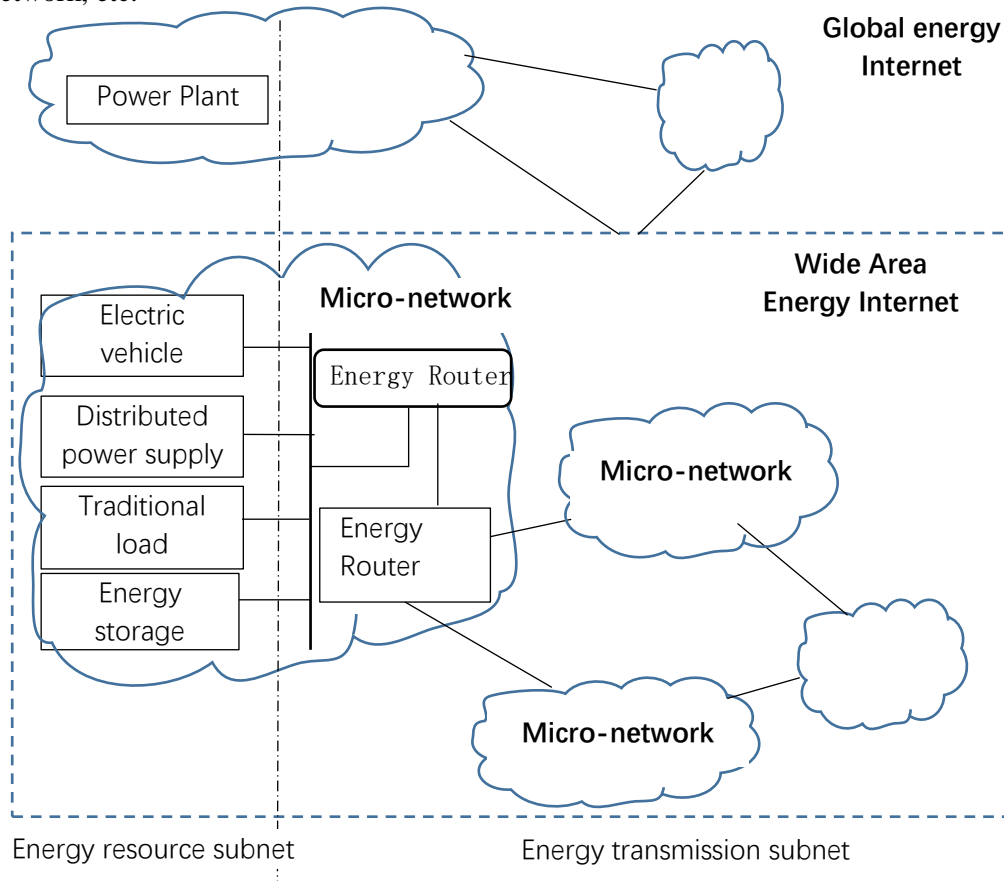


Figure 1. Energy Internet architecture.

The energy micro-network needs to connect to the main grid through the energy router which aims to ensure the efficient and safe transfer of energy. A wide range of energy network status monitoring, control, scheduling and transmission systems can ensure the energy balance between interconnected energy micro-networks. All energy micro-networks connected by energy routers form a wide area energy internet. Multiple wide area energy internet can be further connected through energy routers to form a wider range of wide area energy internet, so the wide area energy internet can also be considered as a network of networks.

The global energy internet connects and the large energy bases from the equator to the two poles. All States through intercontinental, transnational backbone and different voltage levels of the power grid (transmission network and distribution network) to meet the world's energy needs. This will achieve full utilization of renewable energy in the context of adequate and sustainable energy supply. National power grids (transmission networks and distribution networks) with different voltage levels are connected to meet the world's energy needs. In this way, the full use of renewable energy can be achieved in the context of adequate and sustainable energy supply.

5. Routing architecture

According to the overall structure of energy internet above, micro-networks are the terminals of the entire energy internet. Interconnection is carried out through internal energy switches, and the external interface is based on energy routers. The wide area energy internet is a network of networks that connect multiple micro-networks or lower levels of wide area energy internet through energy routers. For the global energy Internet, the issue of interconnection between the energy Internet managed by different management entities should be considered, but the regional energy Internet needs to consider about strategic issues.

In this paper, the method of software defined is applied to the field of smart grid as the main body of energy internet. A wide area energy internet routing architecture and implementation method based on software defined are described. This paper not only takes the compatibility between IEC61850 and other smart grid standards into account, but also provides flexible software-based innovative application deployment. The routing architecture and implementation method described in this paper can also be extended to the global energy internet. In the global energy Internet, the architecture defined by software is more likely to support policy based routing.

As shown in Figure 2, the substation automation system based on the IEC61850 standard introduces software defined switches for communication, energy routers for conversion and flow of energy flows and local controllers that control the information flow and energy flow. The control center is the brain of the entire energy internet. It detects the whole grid state by communicating with local controllers of each substation. The function of the control center is to control the flow of energy flow in the whole energy internet.

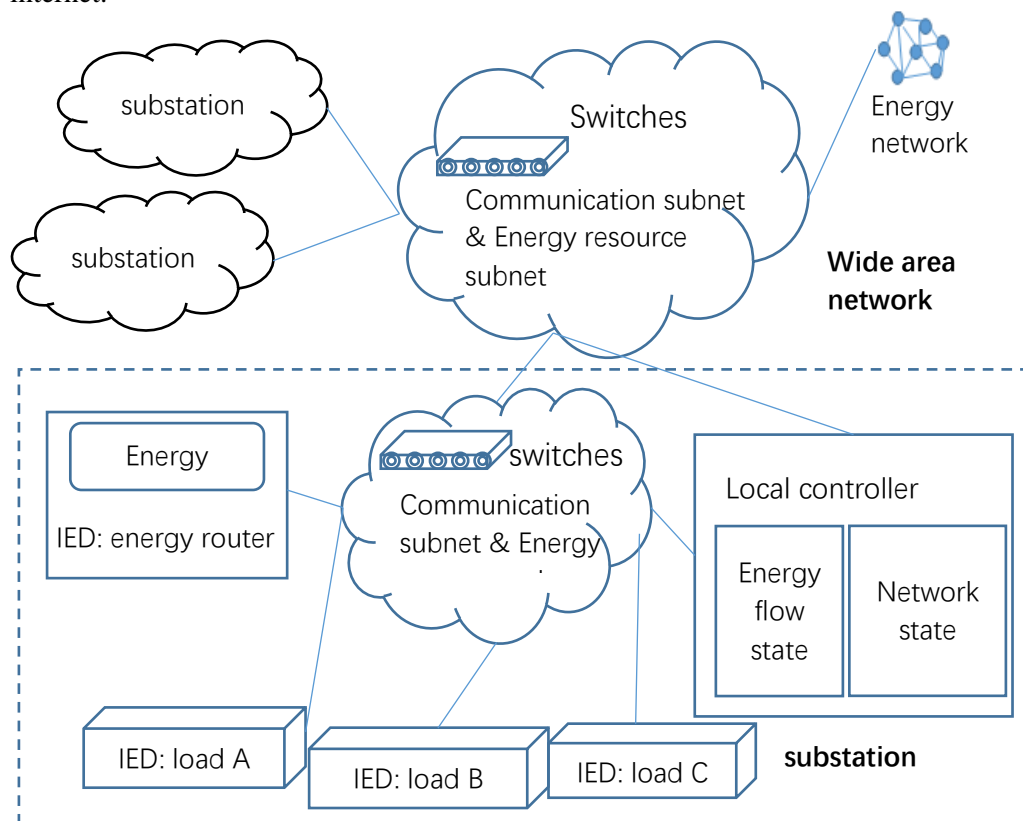


Figure 2. Software defined Energy Internet Routing Architecture.

In the substation based on IEC61850, the basic functions of information acquisition, measurement, control, protection, metering and monitoring are completed automatically through various IED devices. Substation can realize real-time automatic control, intelligent adjustment, online analysis and decision making, coordination and interaction when needed. The above functions require that IED devices exchange messages through the communication network inside the substation. The message exchange

between IED devices can take the Manufacturing Message Specification (MMS) above the point to point TCP connection and the universal object - oriented subsystem of the Ethernet multicast (Generic Object Oriented Substation Event, GOOSE) and sampling value protocol. Because these messages have different requirements of service quality, traditional Ethernet switches used to provide information exchange support for each IED device are replaced by software defined switches. The control plane of the software defined switch is stripped from the data plane. The actual control is carried out by the local controller. Software defined switches report the network topology and load by exchanging messages with local controllers. The local controller determines the switch path that these messages pass through and the scheduling and queue parameters of the switch according to the global topology information of the switch reports and the quality of service requirements for different types of 61850 messages. The local controller sends control instructions to the software defined switches. Considering the bidirectional energy flow between different nodes in the energy Internet, energy routers are introduced. One or more energy routers are responsible for connecting various types of loads, distributed energy storage, and distributed power sources in the smart grid. At the same time, these energy routers are connected with energy routers in other substations or main distribution networks through corresponding energy networks. We divestiture the control part of the energy routers from the actual execution part. The energy router is also an IED device inside the substation. In addition to the previous control of the communication network in the substation, the local controller is also responsible for obtaining the distributed energy and load in the substation based on the IEC61850 standard from each IED device. These are sent to the energy network control center. After receiving the dispatch instruction of the energy network control center, the local controller sends corresponding control instructions to the energy router managed by IEC61850. The executive part of the energy router actually controls the flow of energy according to the instructions received. In addition to the control of the communication network in the substation, the local controller is also responsible for obtaining the information of distributed energy and load in the substation from each IED device based on the IEC61850 standard. These are sent to the energy network control center. After receiving the dispatch instruction of the energy network control center, the local controller sends corresponding control instructions to the energy router based on IEC61850. The executive part of the energy router actually controls the energy flow according to the instructions received.

6. Information flow

The information flow inside the substation is controlled by software defined switches and local controllers. The Openflow protocol in [9] is used between switches and local controllers. As shown in Figure 3, the basic operation is as follows:

6.1 The local controller reads the Substation Configuration Description (SCD) created at the substation deployment at startup. The SCD file is described by Substation Configuration Language (SCL). A part of the configuration file describes the instance configuration, communication parameters of all IED and the contact information between IED.

6.2 The software defined switch regularly sends the link layer discovery protocol (Link Layer Discovery Protocol, LLDP) messages through all of its interfaces, and forward the LLDP messages received by each interface to the local controller. In this way, the topology of all software defined switches can be obtained by local controllers.

6.3 When the IED device sends a message, the software defined switches forward the message which is the first time received to the local controller. The local controller obtains the location of the switch, the IED.

6.4 When the IEC61850 message sent by IED arrives, it will be forwarded to the local controller if the message is the first packet. There are different requirements of service quality in the transmission of IED devices between substations. Based on the previous steps 1, 2 and 3, the local controller determines the forwarding path of the load flow, the scheduling and queue parameters of the various switches on the way according to the information about the topology of the communication network, the type of the load flow and the communication configuration between the IED devices. Finally, these control instructions are sent to the software defined switches.

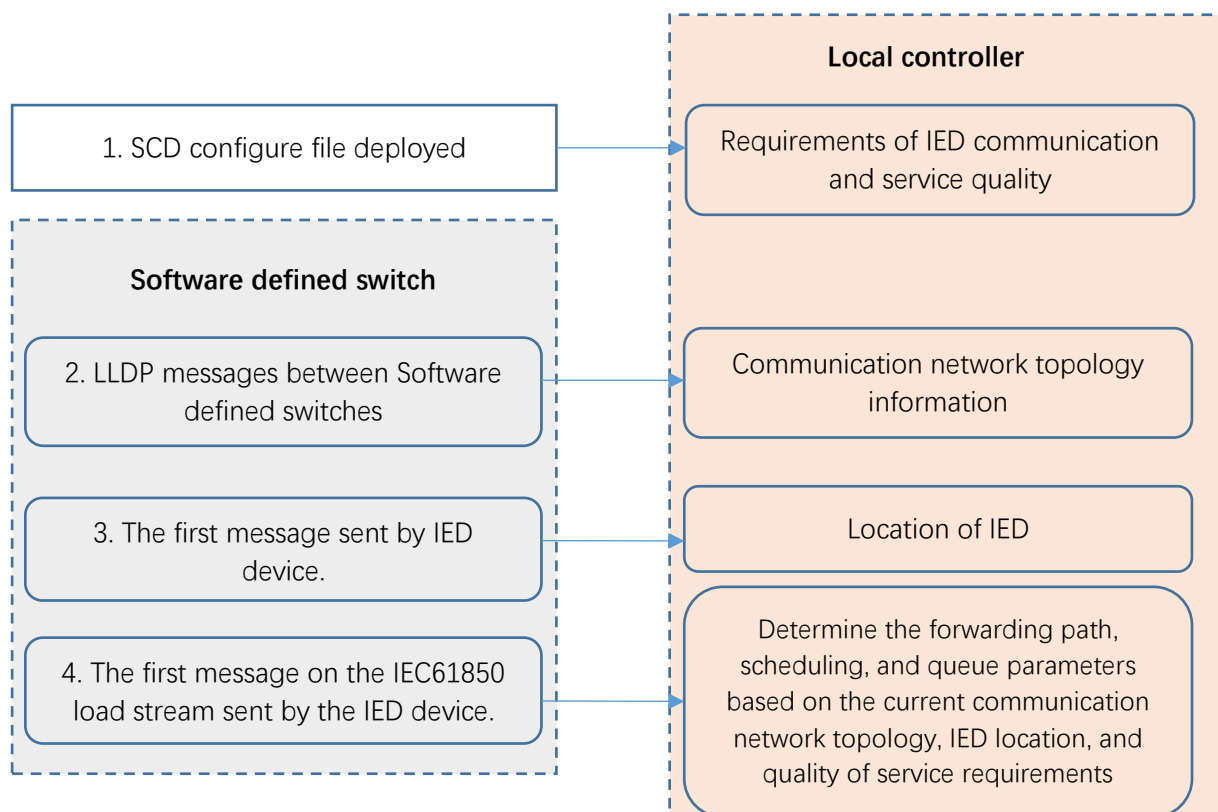


Figure 3. Information flow.

Each substation's local controller communicates with energy network control center through wide area communication network. Wide area communication network can adopt the existing technology in the power industry. Wide area network software defined switch can also be used in SDN. The local controller acts as an agent (Agent) in the wide area network as well as the controller of the software defined network inside the substation. The local controller can implement the function of the virtual switch. It summarizes the state information of the communication network in the substation and reports the state information to the energy network control center. The local controller and the wide area network software are defined as the agent. The actual routing, service quality and so on are determined by the control center of the energy network. The control instructions are given to the wide area network software defined switch and local controller, so as to ensure the service quality of the information flow transmission in the wide area network.

7. Energy flow

The energy flow is actually controlled by the information flow. The basic steps are as follows:

7.1 Firstly, the whole topology (primary system structure) of the energy network is described by SCL at deployment time. The local controller in the substation reads the SCL configuration file to obtain the topology of the energy network in the substation and the connection between the managed energy routers and other energy routers. The energy control center reads the SCL configuration files of the entire network to obtain the energy network topology of the entire network.

7.2 Each IED device, including load and energy routers, uses a IEC61850 based demand side response protocol to exchange demand and supply for energy, which are distributed through Ethernet multicast to the corresponding message group. Software defined switches in the substation forward the message of the corresponding message group to the local controller according to the configuration. In this way, the local controller's energy routing module can know the load situation inside the substation and report it to the energy network control center. The protocol used between the local controller and the energy network control center needs to be able to represent the energy flow status information, so the original Openflow protocol needs to be extended. It adds energy stream messages containing

multiple attributes of the current node ID, neighbour node ID, and the link to the neighbour node, which include the transmission overhead of the link itself, the load connection on the link, and so on.

7.3 After receiving the energy flow status report from the local controller, the energy network control center gets the load of each energy router and the state of the link between the energy routers. The energy network control center obtains the energy network state information of the whole network, reads the energy network system structure obtained by the SCL configuration file, executes the energy interconnection routing algorithm, determines the scheduling information of the energy flow, and finally sends it to the local controllers of all substations.

7.4 After receiving the scheduling instructions from the energy network control center, the substation local controller sends the control instructions to the corresponding energy routers through the IEC61850 protocol, which completes the actual energy flow control

8. Routing strategy

The topology information inside the substation is automatically detected and sent to the local controller by the internal software defined switch. Knowing the topology of the internal communication network, the local controller sends instructions to the software defined switch. The information of the energy flow inside the substation is aggregated to the local controller through two ways. One way is to load the internal energy network topology configuration file of the substation when the local controller starts, and the other is to get it through the demand side response protocol.

Because of the method of software defined, the local controller can make decisions based on the internal energy flow information and the interface information using traditional control algorithms or new control algorithms. Then the control instructions are sent to the internal IED devices through the IEC61850 interface to determine the internal energy flow. The local controller can also report the internal energy flow information to the upper energy control center. Energy control center uses the appropriate control algorithm to make decision according to the global information within the scope of its jurisdiction.

The local controller, the energy control center and the higher level energy control center can not only freely distribute the energy network topology and traffic information to a higher level according to the actual situation, but also put the internal information together and publish it to a higher level. Energy Internet routing architecture based on software defined uses a logical centralized control method, which can adopt the traditional power flow calculation method used in traditional power grid or some new method of power flow calculation.

9. Conclusion

In this paper, we discuss a software defined wide area energy internet routing architecture. The implementation approach is proposed. The compatibility of power devices with smart grid standards such as IEC61850 and flexible software defined innovative application deployment are both considered. In the future, the security of software defined wide area energy internet will be further researched.

10. References

- [1] Qin Z, Denker G, Giannelli C, et al. A Software Defined Networking Architecture for the Internet-of-things. Network Operations and Management Symp, 2014 IEEE. IEEE, 2014: 1-9.
- [2] Xu Y, Zhang J, Wang W, et al. Energy router: Architectures and Functionalities toward Energy Internet. Smart Grid Communications, 2011 IEEE Int. Conf. on. IEEE, 2011: 31-36.
- [3] Sanchez-Squella A, Ortega R, Grino R, et al. Dynamic Energy Router [J]. *IEEE Control Systems*, 2010, 30(6): 72-80.
- [4] Cao J, Yang M. Energy Internet--towards Smart Grid 2.0. Networking and Distributed Computing (ICNDC), 2013 4th Int. Conf. on. IEEE, 2013: 105-110.
- [5] Huang A Q, Crow M L, Heydt G T, et al. The Future Renewable Electric Energy Delivery and Management (FREEDM) System: The Energy Internet [J]. *Proc. of the IEEE*, 2011, 99(1): 133-148.
- [6] Amin S M, Wollenberg B F. Toward A Smart Grid: Power Delivery for the 21st Century [J]. *IEEE power and energy magazine*, 2005, 3(5): 34-41.

- [7] Fang X, Misra S, Xue G, et al. Smart Grid—The New and Improved Power Grid: A Survey [J]. *IEEE communications surveys & tutorials*, 2012, 14(4): 944-980.
- [8] Liserre M, Sauter T, Hung J Y. Future Energy Systems: Integrating Renewable Energy Sources into the Smart Power Grid through Industrial Electronics [J]. *IEEE industrial electronics magazine*, 2010, 4(1): 18-37.
- [9] McKeown N, Anderson T, Balakrishnan H, et al. OpenFlow: Enabling Innovation in Campus Networks [J]. *ACM SIGCOMM Computer Communication Review*, 2008, 38(2): 69-74.

Acknowledgment

The work was supported by Science and Technology Project of SGCC (Research on the Functional Framework of Global Energy Interconnection) . Xiu Cao is the corresponding author.

Optimizing Thermal Performance of Data Centers with Novel Local Partition Configurations

Hongjie Lu¹ and Zhongbin Zhang^{2*}

¹School of Energy and Mechanical Engineering, Nanjing Normal University, Nanjing, China

² Corresponding author, School of Energy and Mechanical Engineering, Nanjing Normal University, Nanjing, China

E-mail: zhangzhongbin@163.com

Abstract. The indoor environment of data center today has differed from the legacy data centers from the heat density to the air distribution. The energy consumption of cooling system has been taking up a large percent of the total energy of data centers. The reliability problem caused by local overheating and economic problem by undercooling attract the attention. novel local partition configurations are proposed in this paper to optimizing the air distribution and thermal performance of data centers. A basic model and 6 partition models have been simulated to analyze the effectiveness of the novel configurations. The result proves that the configurations with local enclosed partition at tile No.2 show great performance in eliminating the hot spots and undercooling problems.

1. Introduction

The energy consumption of data center is consisted of IT equipment energy consumption, cooling system energy consumption, power supply and lighting energy consumption. The consumption of cooling system has been taking up approximately 40% of the total energy consumption, which is one of the main sources of energy consumption in the data center [1]. Due to the high heat dissipation of IT equipment in the data center, the cooling system is requested to operate without stopping. The air conditioning system is facing severe challenges, not only in order to meet the reliability requirement of data center, but also to achieve the purpose of energy saving [2]. Air distribution have great influences on the thermal performance of data centers which has close relation with the energy consumption of cooling system [3]. Overheating and subcooling should be eliminated when a good air distribution solution is applied [4]. Optimizing the uniformity of airflow along the cold aisle is considered to be an effective solution to improve the air distribution and thermal performance [5]. In this paper, an novel local partition configuration is proposed. And a series of derived models have be simulated to prove the effectiveness for improving the thermal performance and to investigate the optimal configuration with local partitions.

2. Physical model and working condition

The basic physical model is a simulated data center computer room with a size of 10900mm (D)×7300mm(W)×3000mm(H) using underfloor air distribution(UFAD) system. There are 44 server racks arranged in the room divided into 4 rows equally. The rack rows are arrangement in the form of hot aisle/ cold aisle (HA/CA). The distance between each row is 1200mm. The computer room air conditioners (CRACs) are arranged at in the line of cold aisles against the wall.

Some parameters of the simulations are as follows in Table 1. There are numbers of investigations working on the geometry configurations of underfloor plenum [6], [7]. Perforated tiles with the



porosity of 20~30% are considered as the optimal for the thermal performance [8], [9]. And 600~800mm is thought to be the ideal height for underfloor plenum to obtain the most uniform airflow distribution [10], [11]. According to the previous investigations and reference, the plenum height is set to be 600mm and the porosity of perforated tiles is set to be 20% in this investigation.

Table 1. Parameters of the basic model

Parameter	Value
Room size	10900mm×7300mm×3000mm
Rack size	2000mm×1100mm×600mm
Tile size	600mm×600mm×10mm
Plenum height	600mm
Porosity of perforated tiles	20%
Porosity of rack outlet	60%
Supply air temperature	18°C
Volume of supply air	7.008 m ³ /s

The plan of models are shown in Figure 1. Model (a) is the basic model without any partition in the plenum. (b) and (c) use partitions to create two independent air distribution room in the underfloor plenum. With this configuration, one CRAC serves the corresponding one cold aisle. The novel partition configurations are meant to improve the uniformity of the airflow and to eliminate the hot spots that emerge at the racks close to the CRACs. Hence, local partitions are added to increase the pressure at the near tiles and to distribute the right amount of air to the far points [12]. The local partitions perpendicular to the cold aisle are perforated with the porosity of 0%, 20% and 80%. All the other partitions are enclosed and not perforated.

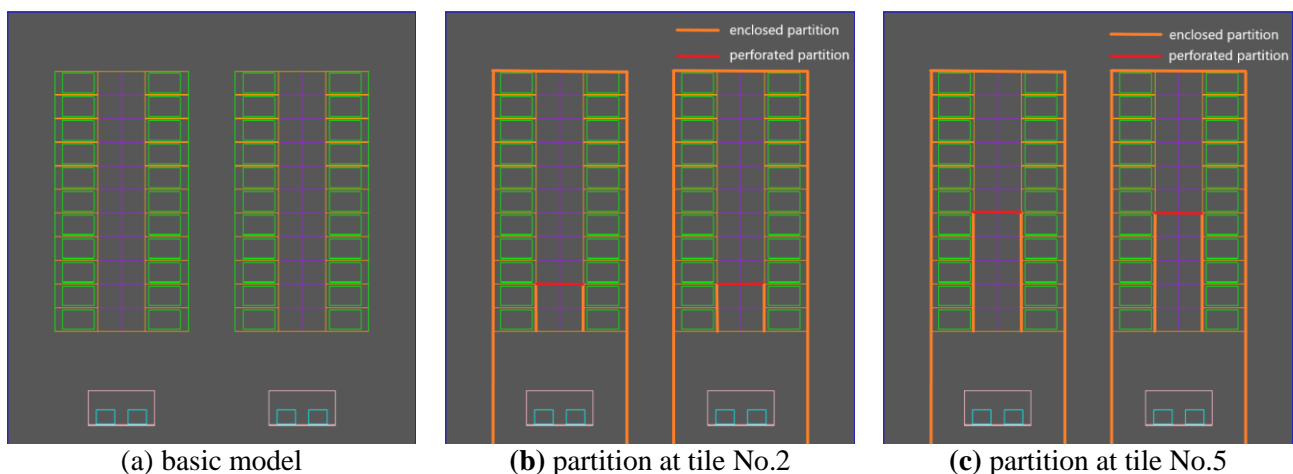
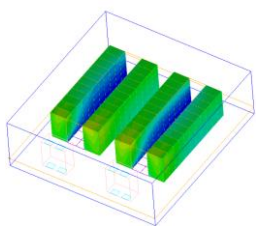
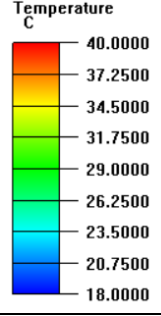
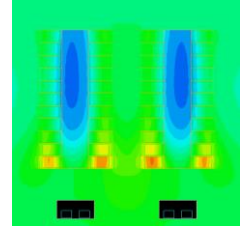
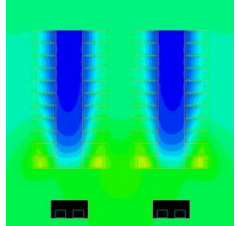
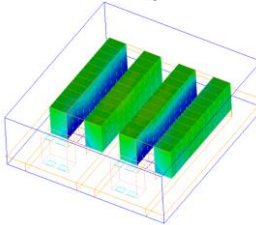
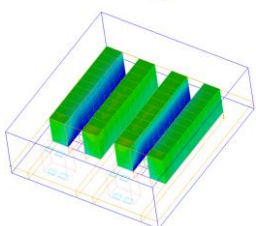
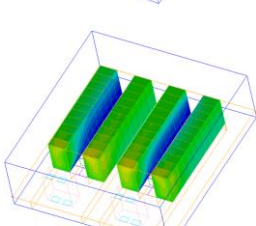
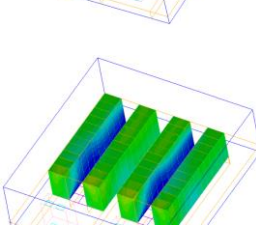
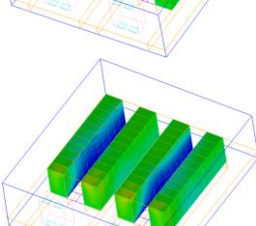


Figure 1. Plans of simulation models

3. Results

The rack surface temperature distribution and airflow temperature distribution results obtained from numerical simulations are shown in Table 2. The plate contours of airflow temperature distribution at the height of 1500mm and 500mm are selected to investigate the effects of different configurations have on the outflow distribution and the thermal performance.

Table 2. Numerical simulation results

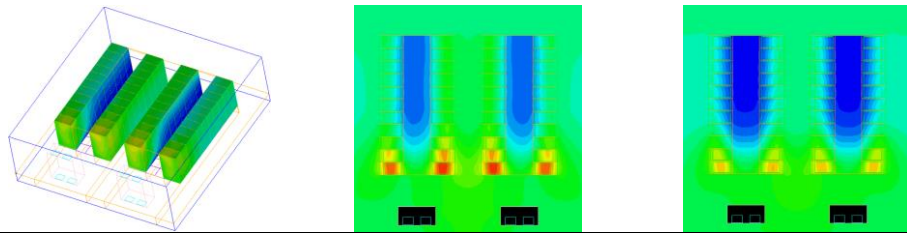
	Rack surface temperature distribution	Airflow temperature distribution Z=1500mm	Airflow temperature distribution Z=500mm
<p>01# Standard model No partitions</p> 			
<p>02# Enclosed partition at tile No.2</p> 			
<p>03# Perforated partition at tile No.2 Perforation rate 20%</p> 			
<p>04# Perforated partition at tile No.2 Perforation rate 80%</p> 			
<p>05# Enclosed partition at tile No.5</p> 			
<p>06# Perforated partition at tile No.5 Perforation rate 20%</p> 			

07#

Perforated partition

at tile No.5

Perforation rate 80%



4. Discussion

According to the rack surface temperature results, models 1#, 4#, 6#, 7# can obviously noticed that the hot spots emerge at the top parts of the racks close to the CRACs. This phenomenon is caused by the pressure distribution in the plenum. The flow rate of the outflow of perforated tile depends on the pressure drop between pressure of the room and the static pressure under the tile. When it gets closer to the CRAC, the flow rate will gets higher which leads to a high dynamic pressure and the corresponding lower static pressure. That makes the outflow rate of close tiles lower than others. At the mean time, the hot spots emerge at the close racks normally.

The rack surface temperature results also indicated that models 2#, 3#, 5# have eliminated the hot spots. From the temperature distribution at the cold aisle side surface of the rack rows, the airflow uniformity of model 2# shows the best thermal performance. However, comparing the airflow temperature at the height of 1500mm where the top part of racks are, the hot spots still exist except for model 2# and 3#. The model 4# & 7# with 80% perforated partitions even make the local overheating problem worse. The result shows that the maximum temperature has increase 2.1°C than that in the basic case. The model 5# & 6# shows great nonuniformity in air distribution. A large amount of chilled air was supplied to the 4th ~6th racks which also leads to the undercooling. Overall, the 20% perforated partition at tile No.2 and the enclosed partition at the tile No.2 are effective improving configurations to optimize the thermal performance and air distribution of the data centers.

The airflow temperature distribution at the height of 500mm is close to the tiles which makes it capable to reflect the air distribution of different models. The enclosed partition models 2# and 5# indicated that the enclosed partitions are able to increase the local static pressure to increase the airflow volume so that the local thermal environment can be improved. But it also need to be mentioned that an obvious temperature rise appears after the local enclosed partition. It is reckoned that the enclosed partition leads to a pressure drop behind it and create a low pressure area. So it is proposed that the perforation design is necessary for the local partition if the more uniform airflow is needed to be achieved. The local partitions at tile No.5 do show the influence on the air distribution, but it affects the racks in the middle part rather than those at the close part near the CRACs. The model 2# with enclosed partition at tile No.2 eliminates the hot spots completely, while the enclosed partition causes an obvious nonuniformity airflow which would increase the reliability of the system when the working condition is changed. The model 3# with 20% perforated partition at tile No.2 eliminates most of the hot spots and shows great uniformity. The partition configuration is also found to be capable to improve the thermal performance of airflow at the local tiles and the nearest two tiles. The influence of partition configuration on the airflow at the local tile is greater than that at the surrounding tiles. And the overheating problem is worst at the first rack at the tile No.1 closest to the CRACs. Therefore, it should be considered that arrange the partition configuration at tile No.1 to make the improvement match the racks with overheating problems of different severity.

5. Conclusions

This work proposed novel underfloor air distribution configurations with local partitions to improve the air distribution and the thermal performance of data centers. Simulations on different models with different partition configurations have been investigated and analyzed. The results are as follows:

- (1) This novel underfloor air distribution configuration with local partitions are proved to be effective in improving the air distribution and thermal performance of data centers.
- (2) The configuration with local enclosed partition at tile No.2 eliminates the hot spots completely; The configuration with 20% perforated partition at tile No.2 achieves the most uniformity airflow.

(3)The configurations with local partitions at tile No.2 shows better improvement than those at tile No.5. It does not improve the overheating problem at the racks closed to the CRACs obviously when the partitions are arranged at tile No.5.

(4)The local partition could be arranged at tile No.1 to match the improvement with the severity of overheating in the future works.

6. Acknowledgement

The project was supported by the Graduate Practical Innovation Projects of Jiangsu Province, China (SJCX18_0370) and the Higher Education Institutions of Jiangsu Province, China (15KJD470001).

7. References

- [1] Logic E. Reducing Data Center Energy Consumption by Creating Savings that Cascade Across Systems [J]. Emerson Network Power, 2007.
- [2] C. F. Gao, Z. Yu, J. L. Wu, Analysis of thermal environment and optimization of air distribution in typical data center [J]. Journal of HV&AC, 2013:101-106.
- [3] Makwana Y U, Calder A R, Shrivastava S K. Benefits of properly sealing a cold aisle containment system [C]// Thermal and Thermomechanical Phenomena in Electronic Systems. IEEE, 2014:793-797.
- [4] Fulpagare Y, Bhargav A. Advances in data center thermal management [J]. Renewable and Sustainable Energy Reviews, 2015, 43: 981-996.
- [5] Phan L, Bhusal S, Lin C X. Improving Cooling Efficiency by Using Mixed Tiles to Control Airflow Uniformity of Perforated Tiles in a Data Center Model[C]//ASME 2017 Heat Transfer Summer Conference. American Society of Mechanical Engineers, 2017: V001T08A005-V001T08A005.
- [6] Patankar S V. Airflow and cooling in a data center [J]. Journal of Heat transfer, 2010, 132(7): 073001.
- [7] Cho J, Yang J, Park W. Evaluation of air distribution system's airflow performance for cooling energy savings in high-density data centers [J]. Energy and buildings, 2014, 68: 270-279.
- [8] Fakhim B, Srinarayana N, Behnia M, et al. Effect of under-floor blockages and perforated tile openings on the performance of raised-floor data centres [J]. 2010.
- [9] Arghode V K, Joshi Y. Experimental Investigation of Air Flow Through a Perforated Tile in a Raised Floor Data Center [J]. Journal of Electronic Packaging, 2015, 137(1):011011.
- [10] Karki K C, Patankar S V. Airflow distribution through perforated tiles in raised-floor data centers [J]. Building & Environment, 2006, 41(6):734-744.
- [11] Zhang M, Zhang Z B, Hu Y et al. Effect of raised floor height on different arrangement of under-floor air distribution performance in data center [C].Procedia Engineering,2017, 205:556-564.
- [12] Kang S, Schmidt R R, Kelkar K M, et al. A methodology for the design of perforated tiles in raised floor data centers using computational flow analysis [J]. IEEE Transactions on Components & Packaging Technologies, 2000, 24(2):177-183.

Interpolation Estimation Method of Tropospheric Delay for Long Baseline Network RTK Based on Support Vector Machine

Jian Deng^{1,2}, Miaoqiang Xu^{3,*}, Xuexiang Yu³ and Aiguo Zhang^{1,2}

¹School of Computer and Information Engineering, Xia men University of Technology, Xia men 361024, China

²Big Data Institute of Digital Natural Disaster Monitoring in Fujian, Xia men University of Technology, Xia men 361024, China

³Surveying and Mapping Institute, Anhui University of Science and Technology, Huai nan 232000, China

*Correspondence: xmq2618@163.com

Abstract: In order to solve the problem of low precision of tropospheric delay interpolation under the long-distance sparse reference station, a method of tropospheric delay interpolation estimation based on support vector machine (SVM) theory was proposed. Firstly, the troposphere was assumed to be an infinitely thin single-layer membrane, and with the known information of reference stations, the puncture point coordinates and zenith tropospheric delay of each reference station on each visible satellite in the single-layer membrane were obtained. Then, the puncture point coordinates and zenith tropospheric delay were taken as training samples to optimize the appropriate core parameters of SVM and establish the SVM model of tropospheric delay. Finally, two sets of network RTK data with different lengths were selected to compare and analyze the effect of the interpolated tropospheric delay. The results showed that under the long-distance reference station, with the SVM tropospheric delay model established in this paper, the tropospheric delay accuracy of the interpolation estimation is better than 2cm, and the estimation error is generally stable, and the interpolation effect of satellite in different systems is basically the same.

1. Introduction

Network RTK is a high precision and real-time relative positioning technology based on global navigation satellite system (GNSS). This technology refers to establishing a plurality of GNSS reference stations more uniformly in an area, forming mesh coverage for the area, so as to establish a spatial error model based on the known coordinates of the reference stations and the satellite information observed in real time. With this model, GNSS users in the region can obtain error correction information such as tropospheric and ionospheric delay [1], thereby improving the real-time and accuracy of positioning. It can provide users with real-time centimetre positioning accuracy, which has been widely used in various fields such as power energy infrastructure construction, informatization, energy and environmental engineering.

At present, the distance between reference stations in network RTK is generally 30~70km. It is assumed that if the distance between reference stations can be extended, the number of reference stations will be reduced within the same area, which will greatly reduce the costs of system construction and maintenance. This is of great strategic significance for the establishment of a network RTK service system under the sparse reference stations for the underdeveloped western regions, poor



environmental conditions, and even the whole country. Therefore, the research on the key technology of network RTK under long-distance reference stations environment has important theoretical significance and practical value. For the network RTK technology, the ultimate goal is to use the spatial correlation errors (mainly ionospheric and tropospheric error) that the reference stations have solved, and combine the spatial position relationship between the mobile station and the surrounding reference stations to interpolate the differential correction information of mobile users in real time, so as to achieve centimetre-level high-precision positioning. Therefore, the accuracy of interpolation correction in tropospheric spatial error model is directly related to the validity and reliability of RTK positioning, which is one of the key technologies of network RTK.

The research on interpolation model for network RTK was relatively mature at home and abroad, and many improved theories and methods were put forward to solve the deficiency of traditional model, and good results had been achieved [2]-[5]. Li [6] established the multivariate linear regression model, combined estimation model, grey model and BP neural network model of tropospheric delay in short baseline network RKT, and proposed a weight coefficient determination method based on reliability of the combined model to eliminate the influence of tropospheric delay. With genetic algorithm and BP neural network technology, Chen [7] established a high-precision regional fusion model (GA-BPEGNOS model) based on EGNOS model, which improved the accuracy of tropospheric delay correction for short baseline network RTK. However, most of the existing researches were aimed at the study of spatial error correction within the network RTK coverage under medium and long baseline (<100km). When the distance between reference stations increases (150-200km), the spatial error correlation decreases, and the accuracy of tropospheric delay estimated by the conventional model also decreases. Therefore, this paper introduced the theory of support vector machine (SVM). The troposphere was assumed to be an infinite thin single-layer film, and the SVM model of regional tropospheric delay was established to realize the real-time estimation of tropospheric delay of user terminal.

2. Support vector machine

SVM [8], [9] is a two-class classification model, and also is a machine learning method based on the principle of structural risk minimization. Its essence is to transform the input space into a high-dimensional space by using a nonlinear transformation defined by the inner product function, and seek a nonlinear relationship between the input variable and the input variable in this high-dimensional space. Because the SVM algorithm has a rigorous mathematical theory foundation and good function approximation ability, it can solve practical problems such as finite samples, nonlinearity and high dimension, which makes it widely used in the field of regression.

The specific algorithm of the SVM method for nonlinear regression estimation is as follows [10]. Assuming that the data sample is $(x_i, y_i), i = 1, 2, \dots, n; x_i \in R^m$, which are input parameters; $y_i \in R$, which are the output parameters. n is the sample number. For linear regression, let the linear regression function $f(x) = \langle w, x \rangle + b$. w is the weight vector; b is the offset. If all the training data are fitted with linear function under the precision ε , then

$$\begin{cases} y_i - f(x_i) \leq \varepsilon + \xi_i, & \xi_i \geq 0 \\ f(x_i) - y_i \leq \varepsilon + \xi_i^*, & \xi_i^* \geq 0 \end{cases} \quad i = 1, 2, \dots, n \quad (1)$$

Among them, ξ_i and ξ_i^* are relaxation factors. Based on the principle of structural risk minimization, the problem can be transformed into the minimization optimization problem with constraint condition (1) seeking (2)

$$\frac{1}{2} w w + C \sum_{i=1}^n (\xi_i + \xi_i^*) \quad (2)$$

Where, C is the penalty factor.

According to the duality theory of nonlinear programming, the Lagrangian equation is established to convert the minimum value problem into the maximum value problem of the dual problem

$$f(x) = \sum_{i=1}^n (a_i + a_i^*) \langle x, x_i \rangle + b \quad (3)$$

Where, x_i is the support vector, a_i, a_i^* and b are the parameters obtained by the regression.

For the nonlinear regression estimation, a Kernel function $K(x_i, x_j)$ satisfying Mercer can be introduced instead of the inner product $\Phi(x_i)\Phi(x_j)$ of the mapping function, and the nonlinear regression function is obtained.

$$f(x) = \sum_{i=1}^n (a_i + a_i^*)K(x_i, x) + b \quad (4)$$

There are three main types of kernel functions in use:

Linear kernel $K(x_i, x_j) = \langle x_i, x_j \rangle$;

Polynomial kernel $K(x_i, x_j) = (\langle x_i, x_j \rangle + 1)^d$;

Gaussian radial basis kernel $K(x_i, x_j) = \exp(-\|x_i - x_j\|^2 / 2\sigma^2)$

Where, d is the degree of polynomials, and σ is the width of the Gaussian distribution.

3. Establishment of tropospheric model based on SVM

3.1 Overall process of model establishment

Figure 1 showed the process of SVM model establishment. The regional spatial troposphere was assumed to be an infinitely thin single-layer membrane [11]. Firstly, with the known information of reference stations, the puncture point coordinates of each reference station on each visible satellite in the single-layer membrane were obtained. Secondly, the tropospheric delay of each reference station corresponding to each satellite in the propagation path was transformed into the tropospheric delay in the zenith direction at the puncture point. Then, the puncture point coordinates and zenith tropospheric delay were taken as training samples to optimize the appropriate core parameters of SVM and establish the SVM model of tropospheric delay. Finally, for any receiver within the coverage of the network RTK, using the constructed model and taking the coordinates of the puncture point corresponding to the mobile user as input, the satellite tropospheric delay of the receiver can be estimated. In this way, the real-time and precision of RTK positioning were improved.

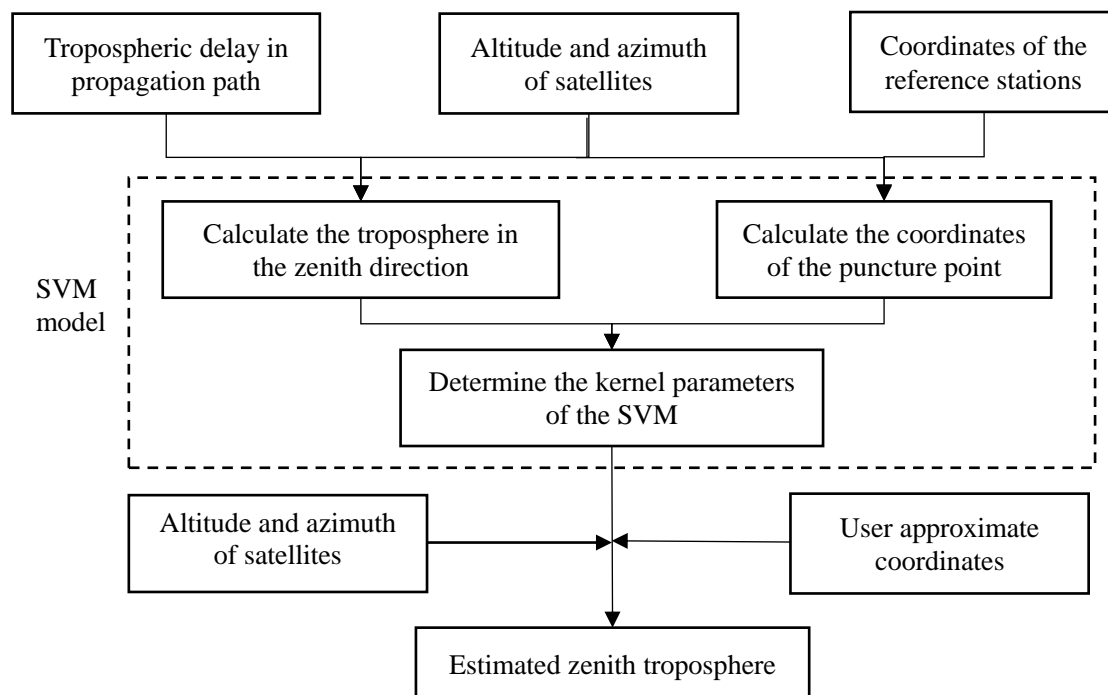


Figure 1. Process of SVM model establishment

3.2 Determination of the coordinates of the puncture point

First of all, the angle named α between the receiver station to the center of the earth and the satellite to the center of the earth is calculated [10].

$$\alpha = \frac{\pi}{2} - E - \arcsin\left(\frac{R}{R+H} \cos E\right) \tag{5}$$

Where E is the satellite elevation angle corresponding to the receiver; R is the radius of the earth, with a value of 6378.1363km; H is the height of the central troposphere, and the average height of the troposphere is different at different latitudes. The average troposphere height is 17-18 km in low latitudes, 10-12 km in the middle latitudes, and 8-9 km in the polar troposphere. Then the longitude λ_p and the latitude φ_p of the puncture point are:

$$\begin{cases} \lambda_p = \lambda_U + \arcsin\left(\frac{\sin \alpha \sin A}{\cos \varphi_p}\right) \\ \varphi_p = \arcsin(\sin \varphi_U \cos \alpha + \cos \varphi_U \sin \alpha \cos A) \end{cases} \tag{6}$$

In the formula, (λ_U, φ_U) is the latitude and longitude of the receiver station; A is the satellite azimuth corresponding to the receiver station.

3.3 Calculation of the zenith troposphere

At different times, the elevation angle of the satellite to the monitoring station is constantly changing, and the value of the troposphere is related to the length of the propagation path of the radio wave. Therefore, the larger the elevation angle of the satellite to the monitoring station, the smaller the tropospheric delay. Conversely, the greater the tropospheric delay. In order to calculate the tropospheric delay at different times more accurately, the tropospheric delay is converted from the propagation path direction to the zenith direction of the puncture point.

Combined with the propagation path of tropospheric delay DDT and satellite altitude angle E, the conversion formula for tropospheric delay calculation is as follows [12]:

$$VDDT = DDT \cdot \cos \beta \tag{7}$$

$$\beta = \arcsin\left(\frac{R}{R+H} \cos E\right) \tag{8}$$

Where β is the zenith distance of the satellite at the puncture point.

3.4 Model establishment and interpolation estimation

Based on the puncture point coordinates and zenith tropospheric delay, the Gaussian radial basis kernel function was selected from the Libsvm toolbox in matlab platform. Firstly, with a part of the sample data, the approximate values of C and σ were determined through the SVM based on the particle swarm optimization algorithm. Then, all the sample data were used to conduct multiple experiments in the rough range, and finally the values of kernel function parameters and penalty factors were determined, so as to establish the tropospheric delay model of SVM. For the RTK users in the area, as long as the current approximate location was uploaded to the data service centre, the established interpolation model can be used to estimate the tropospheric delay of each satellite corresponding to the station, in this way, the precision of RTK positioning was improved.

4. Experiments and Discussion

4.1 Case1: Estimation of tropospheric delay in network RTK under medium and long distance

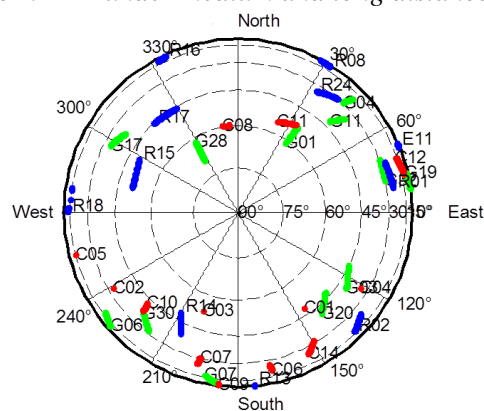
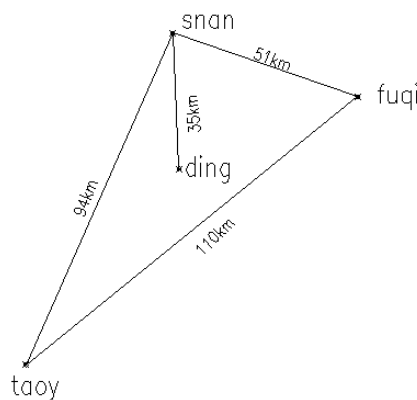


Figure 2.Distribution map of stations in suzhou network RTK **Figure 3.** Distribution map of satellites

Four reference stations were selected from Suzhou network RTK in China to verify the interpolating effect of the tropospheric model based on SVM in the medium and long distance. Figure 2 shows the approximate location distribution of the reference stations. Among them, snan, fuqi and taoy stations were set as reference stations, and the distance between each reference station is 51km, 94km and 110km, respectively, ding station as the user receiver station, about 35km away from the main reference station. The data of each station was selected from 21:20:01 to 21:40:00 on December 18, 2014 for 1200 seconds. Each second of the selected data includes GPS, GLONASS, and BDS satellite systems, figure 3 shows the distribution of all visible satellites during the observation period. After data pre-processing, the number of GPS, GLONASS and BDS satellites in the available satellites with elevation angles above 20 degrees is 6, 3 and 5 respectively. In practical applications, it is necessary to construct a SVM model and perform tropospheric delay estimation based on the reference stations and the observed satellite information every second.

In each second, firstly, according to the known coordinates of the three reference stations and the current altitude angle and azimuth of satellites, the coordinates of puncture point for each satellite corresponding to each station were calculated by formula (6). Then, using equation (7), the tropospheric delay of the three reference stations corresponding to each satellite were converted from the propagation path to the zenith direction at the puncture site. Due to the Suzhou network RTK belongs to the mid-latitude area, the average height H of the troposphere was determined to be 11 km; Finally, the coordinates of each puncture point were taken as input values, corresponding to the zenith tropospheric delay as output values, so as to determine the values of the kernel function parameter and the penalty factor. Thereby the tropospheric delay SVM model was established at the moment.

On the basis of the above, the latitude and longitude of puncture point for station ding were taken as the input values, and the zenith tropospheric delay at the puncture point of each satellite was estimated by using the SVM model established at the current time, and then the delay was converted from the zenith direction of the puncture point to the propagation path direction. Finally, compared with the actual value, the estimated effect of the model is checked. Figure 4 shows the difference between the estimated tropospheric delay and the actual value of each satellite in the three systems.

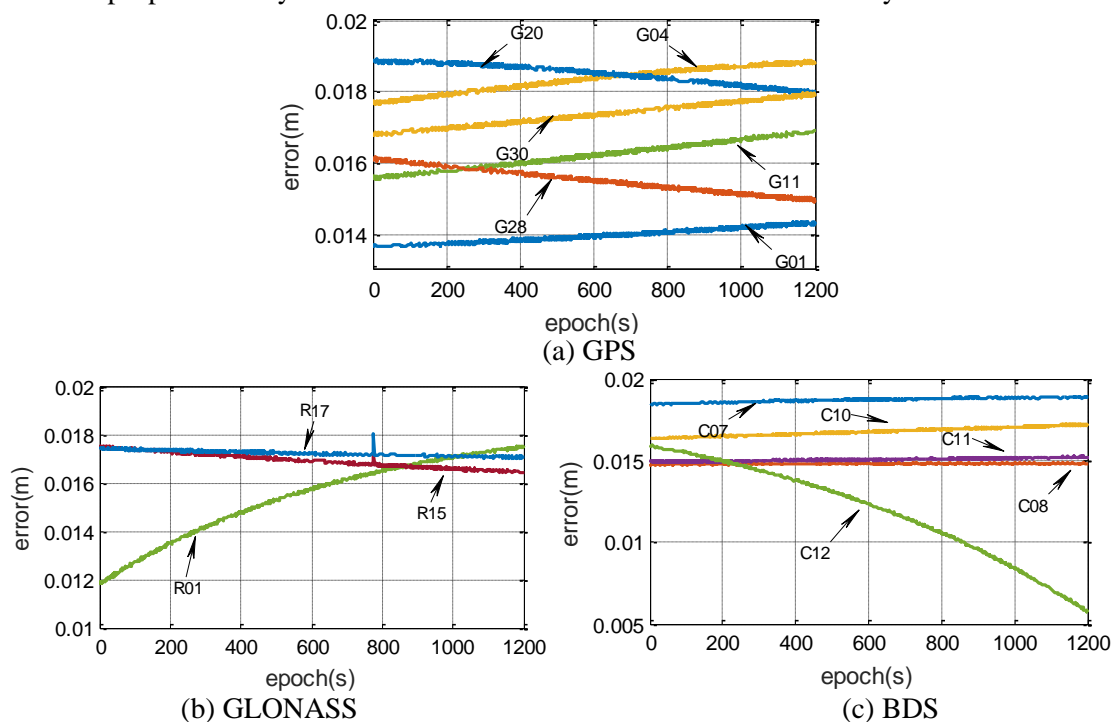


Figure 4. Comparison between tropospheric delay estimated by SVM and actual value

As can be seen from Fig.4, in this case, tropospheric delay estimation of GPS, GLONASS and BDS all achieve a good estimation effect. The estimated value is relatively close to the actual value, and the error fluctuation is small. Table 1 shows the maximum, median and average errors of each system in tropospheric delay estimation. Under the medium and long distance network RTK environment, the maximum deviation of tropospheric delay estimated for GPS, GLONASS and BDS are all less than 2cm, and the median error is between 0.01cm and 0.02 cm, with high estimation accuracy. Among them, the mean error of the tropospheric delay for BDS satellite is the smallest, followed by GPS system and GLONASS system, but in general, the mean errors of the three systems are relatively close, all of which are around 1.6cm.

Table 1 comparison between tropospheric delay estimated and actual value.

Serial number	Satellite number	Maximum error / m	Medium error / m	Serial number	Satellite number	Maximum error / m	Medium error / m
1	G01	0.0144	0.0140	8	R15	0.0175	0.0169
2	G04	0.0189	0.0183	9	R17	0.0181	0.0172
3	G11	0.0169	0.0162	10	C07	0.0189	0.0187
4	G20	0.0189	0.0185	11	C08	0.0149	0.0148
5	G28	0.0162	0.0155	12	C10	0.0172	0.0168
6	G30	0.0180	0.0174	13	C11	0.0152	0.0151
7	R01	0.0175	0.0155	14	C12	0.0159	0.0122
GPS Average error / m		0.0166	GLONASS Average error / m		0.0165	BDS Average error / m	
							0.0154

4.2 Case2: Estimation of tropospheric delay in network RTK under long distance

Four reference stations were selected from Henan network RTK in China to verify the interpolating effect of the tropospheric model based on SVM in long distance. Figure 5 shows the approximate location distribution of the reference stations.

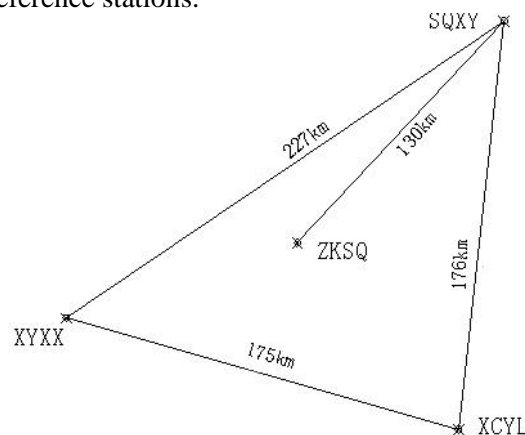


Figure 5. Distribution map of stations in Henan network RTK

Among them, SQXY, XYXX and XCYL stations were set as reference stations, and the distance between each reference station is 175km, 227km and 176km, respectively, ZKSQ station as the user

receiver station, about 130km away from the main reference station. The data of each station was selected from 19:30:00 to 19:49:59 on March 1, 2016 for 1200 seconds. Each second of the selected data includes GPS, GLONASS, and BDS satellite systems. After data pre-processing, the number of GPS, GLONASS and BDS satellites in the available satellites with elevation angles above 20 degrees is 6, 3 and 5 respectively.

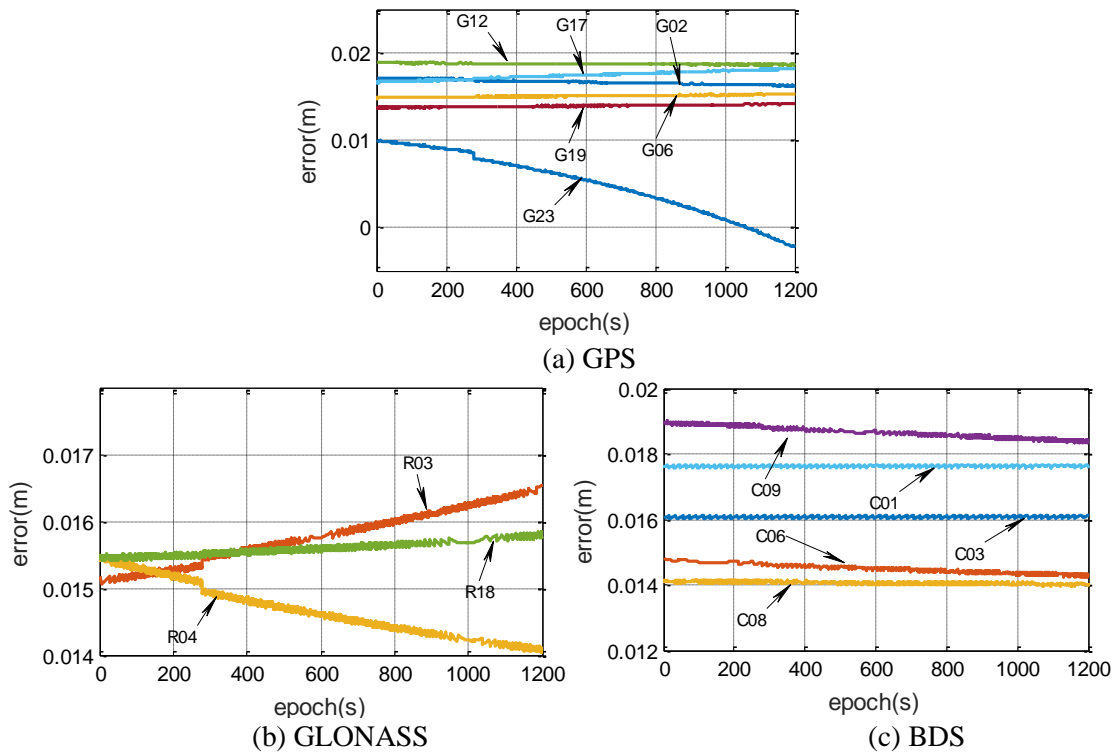


Figure 6. Comparison between tropospheric delay estimated by SVM and actual value

Table 2 comparison between tropospheric delay estimated and actual value.

Serial number	Satellite number	Maximum error / m	Medium error / m	Serial number	Satellite number	Maximum error / m	Medium error / m
1	G01	0.0144	0.0140	8	R15	0.0175	0.0169
2	G04	0.0189	0.0183	9	R17	0.0181	0.0172
3	G11	0.0169	0.0162	10	C07	0.0189	0.0187
4	G20	0.0189	0.0185	11	C08	0.0149	0.0148
5	G28	0.0162	0.0155	12	C10	0.0172	0.0168
6	G30	0.0180	0.0174	13	C11	0.0152	0.0151
7	R01	0.0175	0.0155	14	C12	0.0159	0.0122
GPS		GLONASS		BDS			
Average error / m		0.0166	Average error / m	0.0165	Average error / m	0.0154	

The method flow of establishing regional SVM tropospheric model and estimating tropospheric delay of user station in real time is the same as case 1. At last, the estimated tropospheric delay is compared with the actual value so as to check the estimated effect of the model. Figure 6 shows the difference between the estimated tropospheric delay and the actual value of each satellite in the three systems.

As can be seen from figure 6, tropospheric delay estimation of GPS, GLONASS and BDS also achieve a good estimation effect in this case. The estimated value is relatively close to the actual value, and the error fluctuation is small. Similarly, table 2 shows the maximum, median and average errors of each system in tropospheric delay estimation. Under the long distance network RTK environment, the maximum deviation of tropospheric delay estimated for GPS, GLONASS and BDS are all less than 2cm, and the median error is between 0.01cm and 0.02 cm, with high estimation accuracy. Among them, the mean error of the tropospheric delay for GPS satellite is the smallest, followed by GLONASS system and BDS system, but in general, the mean errors of the three systems are relatively close, all of which are around 1.5cm.

5. Conclusions

The validity and reliability of the spatial error model of regional tropospheric delay is one of the key technologies in network RTK. In this paper, the spatial troposphere was assumed to be an infinitely thin single-layer membrane, and the SVM theory was introduced to realize the real-time construction of regional tropospheric delay model. The comparative analysis of the above cases can lead to the following conclusions:

- (1) From single satellite, more than 90% of the satellites have a stable variation in the estimation error of the tropospheric delay, with fluctuations ranging from -3 mm to 3mm. The estimation error of individual satellites fluctuates greatly. The preliminary analysis is due to the low and high variation of satellite height angle during the observation process.
- (2) The estimation results of different system satellites are basically the same, that is, the SVM model established in this paper is independent of the type of satellite system.
- (3) Under different distances of network RTK, the tropospheric delay accuracy estimated by the SVM tropospheric delay model has little difference, and the accuracy is better than 2cm.

6. Acknowledgments

This work was partially supported by the National Natural Science Foundation of China (No.41204032, No. 41474026, No. 41704008), Fujian Natural Science Foundation of China (No.2015J01176). Educational Research Projects for Young and Middle-aged teachers of Fujian Province (No. JAT170419).

7. References

- [1] Snay R A and Soler T 2008 *Journal of Surveying Engineering* **134** 95-104
- [2] Huang D F, Li C G, Wu Y Q, Lv G P and Zhou L T 2007 *Chinese Journal of Surveying and Mapping* **36** 256-261
- [3] Tang W M, Liu J N, Liu H and Bai Q B 2007 *Journal of Wuhan University: Information Science Edition* **32** 1156-59
- [4] Wei E, Chai H, An Z and Liu J 2006 *Positioning* **5** 76-81
- [5] Gao X W, Guo J W, Mi J Z, Zhao C M and Zhu H Z 2009 *Journal of Surveying and Mapping* **34** 52-54
- [6] Li J F, Wang Y Q and Guo J Y 2015 *Journal of Surveying and Mapping Science and Technology* **32** 450-454
- [7] Chen Y and Hu W S 2018 *Surveying and Mapping Engineering* **27** 46-52
- [8] Li H 2012 *Statistical Learning Method* (Beijing: Tsinghua University Press)
- [9] Deng N Y and Tian Y J 2004 *A New Method in Data Mining* (Beijing: Science Press)
- [10] Li M L, Hu Y Z, Zhou C, Zhao Z Y and Zhang Y N 2015 *Journal of Xidian University* **42** 147-153
- [11] Schaer S 1999 *Mapping and Predicting the Earth's ionosphere Using the Global Positioning System* (Bern: The University of Bern)
- [12] Zhou P 2014 *Research on ionospheric delay model based on CORS data* (Xu Zhou: China University of Mining and Technology)

Application of Point Cloud Data in the Construction and Management of Interior Design

Minyong Li ¹ and Jianwen Liu ²

¹ College of art and architecture, Xiamen Xingcai Vocational & Technical College, Xiamen, China

² College of Landscape Architecture, Fujian Agriculture and Forestry University, Fuzhou, China

E-mail: 329094365@qq.com

Abstract. There are many defects in the construction and management of the previous interior design, which leads to the problems of inaccuracy, waste of materials, high labor cost and low efficiency in the actual construction and management. The application of three-dimensional scanning technology with high precision and high rate of point cloud data in construction and management of interior design is put forward. Through the three-dimensional laser scanning of the building body, the vector set of the building body in the set of three-dimensional coordinate system is obtained, and the data collected by the methods of multi frame data fusion and noise reduction are used to collect the data from the point cloud. Through processing, accurate indoor information data can be obtained and analyzed, and the foreseeable problems can be solved ahead of schedule. The extraction of indoor scene information by point cloud data improves the efficiency, accuracy and labor cost of the previous data collection, and improves the efficiency of construction and the ability to solve the problem.

1. Introduction

In recent years, the economic development of our country is in good condition, society enters a new economic era which is high integration of the knowledge economy and the information economy, and the interior design industry is further developed under the impetus of this new economic era. But this also puts forward higher requirements for the construction and management of the interior design engineering, and it has been applied in the past. The defects of construction and management in the past hindered the development of interior design. Point cloud data is a wide application of non-contact 3D scanning technology, which breaks through the traditional method of measurement, uses 3D laser scanner to obtain the point cloud data of target objects and processing into three-dimensional information. This makes this technology emerge in many fields, such as target recognition, ground mapping, building modeling and so on. In some complex and irregular building bodies and conditions which the traditional measurement methods can't measure accurately, three-dimensional laser scanning technology can still carry out rapid and accurate measurement and construct three-dimensional model, providing new technical support for the complex interior environment design. The technology optimizes the defects of traditional measurement methods, and it can obtain the required indoor scene information quickly and accurately. The point cloud data after splicing and noise reduction are very practical, speeding up the development of indoor information. After processing, the point cloud data can get the accurate three-dimensional data of the indoor scene, and the point cloud data model can be imported into the HD Modeling for CAD2013 software to drawing each two-dimensional plane, and extract the accurate and effective size and pipeline information. Therefore, according to the



characteristics of the 3D laser scanning technology, it can also make the interior design optimize and deal with the predictable problem in the process of construction and management in advance.

In this paper, commercial houses in new intercity plaza of xiamen city are taken as the research object, and a study on indoor scene 3D information based on high accuracy and high speed 3D laser point cloud data is proposed. Through 3D laser scanning, the collected point cloud data were preprocessed by splicing and denoising. Based on the point cloud data of algorithm, the brick and pipeline information can be extracted accurately to draw the interior plan and two-dimensional line drawing, and realize the effective acquisition and analysis of indoor information data. The application results show that the 3D laser scanning technology is efficient in the extraction of indoor 3D data, which greatly reduces the time cost and labor cost of data acquisition and improves the efficiency of generating practice.

2. The current situation of the construction and management in interior design

With the continuous development of interior design, the requirements for construction and management are getting higher and higher. The main work of construction and management of interior design is to design and decorate the indoor environment. In the process of construction, the required tool is various, construction technology is complex, and the construction link is repetitive, in some more complex engineering, there are many uncertain factors, so it will affect the construction and management of the interior design, construction quality will directly affect the quality of the buildings and the effect of the expected design. The importance of construction and management of interior design has been paid attention to, but there are still many problems in the process of construction and management, which need to be improved and solved. The following are the main problems of construction and management in interior design.

2.1. Low accuracy and efficiency

In interior design, it is necessary to measure the interior wall, ground, beam position, water and electricity road, which is called measuring room. There are three ways in the traditional measuring room: 1. Quantitative measurement: mainly measure the length, width and height of each space and calculate the area, and then put forward reasonable suggestions according to the daily needs of the owner. 2. Positioning measurement: in the positioning measurement, the position of the door, window and air conditioning hole is mainly marked, and the window requires scalar quantity. In the measurement of kitchen bathroom, the position of the downpipe, hole distance, toilet pit hole distance, distance from the wall, position of smoke pipe, position of gas pipe, distance under the pipe, and location of floor drain all need to make accurate measurement, so as to accurately locate in the future design. 3. Height measurement: generally, the height of the floor should be relatively fixed. However, because the construction of each building will be different, there may also be a certain drop. During the height measurement of the designer, the height of each area of the room should be carefully checked to ensure the accuracy in the future design drawings. The traditional manual measurement method has too many variables to accurately control the precision of complex building or space measurement, and the measuring efficiency will also follow the changes of the proficiency of the surveyor and the environment.

2.2. Waste materials and not environmental protection

In the construction process, because of the characteristics of the traditional measurement method, the measurement results will inevitably be error, and there may be data omission and loss. The deviation of the data can also be deviated in calculating the area of each space and the amount of material. In this case, the majority of construction personnel will choose to exceed the amount of billing documents for materials, and did not deal with returns, resulting in waste of materials. Inaccurate hydro-electric route positioning will also lead to material waste, not environmental protection. These situations have not been well solved due to technical problems. Most of the construction personnel only listed the materials needed in the construction based on their previous experience. In the current huge market of interior construction in China, the waste caused is conceivable. These problems of

excessive material consumption due to technical defects can be better solved through technical renewal.

2.3. Lack of safety awareness

In the process of construction, the awareness of construction safety should not only be reflected in the design of engineering drawings, but also permeate the whole construction process and the minds of the construction personnel. In the process of construction, it is more important to raise the safety awareness of the construction personnel while improving the construction efficiency. At present, in the design of interior design construction drawings, the interior designers lack of security considerations for the construction aspect. For example: in the early stage of the design drawings, there are some potential safety hazard in indoor fire protection, earthquake zone and secure channel design. In use process, if there was an accident, will threaten the life in the space. The safety awareness of the construction personnel is not high, for example: the construction process is not in accordance with the construction standards; The decorative materials are not orderly and piled up at will. Some construction techniques will produce open fire, which is easy to cause accidents, the safety of construction workers will be threatened. Due to inaccurate positioning, it is easy to lead to damage of hydropower pipes, water leakage and electricity leakage, and there are safety risks.

2.4. Lack of Standard Indoor Construction Work System

Without a standard indoor construction work system, it is difficult to guarantee the safety of construction. Most of the interior decoration construction teams in China lack a sound management system in the process of interior design construction and management. In the construction process, there is no unified management concept and practical experience, which leads to insufficient construction progress and quality assurance. In the review stage of the construction project, if there is no sound management system, the construction supervision work cannot be effectively connected. Without effective management system, the construction cost will increase. Therefore, it can be seen that a perfect standard construction system is great importance to construction and management. In traditional construction, most of the methods used by managers are based on feelings, experience and not strictly in accordance with the construction standards and norms, which leads to many avoidable problems in construction.

Most of the above construction status can be optimized by using point cloud data, such as: the traditional manual measurement method is not accurate and the budget is not accurate, which leads to the waste of materials, safety hazards and unnecessary economic losses caused by improper operation damage the pipeline equipment. This also reflects the advantages of the application of point cloud data in interior design construction and management from the side.

3. Comparison between traditional technology and new technology

3.1. Traditional construction methods

Although the traditional construction method has advantages in operation difficulty, price and other aspects, there are many defects and problems in the traditional construction method. First, it is difficult for traditional construction methods to accurately measure complex buildings or irregular Spaces when measuring buildings. Second, it will take a lot of time for the construction personnel. This is especially true for complex buildings and Spaces, where labor costs are high and efficiency is low. Most surveying and mapping tasks will have a certain time limit, and this measurement method will cost a lot of manpower and material resources. Third, the cost budget is not accurate. Fourth, there are safety hazards in the construction process. The failure to accurately measure the exact dimensions of complex buildings or irregular Spaces will lead to the deviation of material consumption in the later period. In the long run, many unnecessary wastes will be caused, which will increase many costs and reduce profit space. In indoor construction cost, labor costs account for a large proportion. Because inaccurate measurement in complex building or alien space cause the increased construction time, it will increase labor costs, it is unfavorable to control construction cost. When the construction is completed, the expenditure and the budget differ greatly, increasing the burden of the owner, bringing adverse impact on their own professionalism. At the same time, the safety hazards caused by

inaccurate measurement are fatal to the whole construction process, which will not only cause many unnecessary rework, but also threaten the physical and mental health of the owner. It can be seen that the improper traditional measurement method not only brings about the increase of construction cost, but also includes many problems that are closely related to safety. Therefore, the upgrading and updating of traditional technology can bring essential changes to the construction.

3.2. 3D Laser scanning technology

3D laser scanning technology is a non-contact measurement method with a wide range of applications, which can obtain the 3D information of objects without contact. This technology breaks through the traditional measurement method and has a far-reaching development prospect in many fields [1]. 3D laser scanning technology can realize rapid and accurate 3D model construction for various large irregular and complex buildings and environments with insufficient light, providing important technical support for complex interior environment design [2]. This technology enables the acquisition of indoor space information to get rid of the traditional bottleneck and accelerate the development of indoor informatization. The processed point cloud data has a strong practicability and a breakthrough in the acquisition of architectural information [3]. Based on this expression in the form of point cloud image, access to the indoor complete 3D data, reduce the amount of data registration, point cloud data model into HD Modeling for CAD 2013 software can draw two-dimensional Digital Line Graphic of each surface, and extract the effective information, pipe sizes, complete measurement and design of indoor scene information accurately [4]. The efficiency of 3D laser scanning technology is several times compare to traditional measurement, and the intuitiveness of point cloud data can greatly reduce the error rate of the internal and external industries, so as to avoid the external industry again, reduce labor cost, and the source data volume is more complete and rich.

From the above, it can be seen that the 3D laser scanning technology has a good performance in accuracy of measurement, safety degree before and after construction, material budget and other aspects. It has got rid of the bottleneck of traditional technology and made a breakthrough in the acquisition of information in various aspects of indoor environment.

4. Application of point cloud data in the construction and management of interior design

4.1. Drawing of the building survey plan

FARO Focus3D X130 3D laser scanning system was adopted to obtain high resolution 3D coordinate spatial point position information of the surface of the object under test in a large area through the measurement method of high precision, high speed and high density laser point cloud scanning [5]. Through the laser 3D scanner, the object is scanned in many dimensions, so as to obtain the point cloud data collection of the object. Using FAROScene software, the original point cloud data collected can be processed by splicing registration and de-noising. Only by splicing the points and data after pre-noise reduction can the complete indoor 3D model be obtained and the two-dimensional Digital Line Graphic information of the target object be obtained. Denoising process, the removal of the original point cloud data of useless information, will be left point cloud information of hole on the target object and it will affect the creation of a late model. Aiming at this problem, you can use the HD Modeling for CAD 2013 software layering slicing technology to carry on curve fitting for hollow point cloud information, thus completing the empty part of the point cloud data. Extract the required 3D data from the model, and draw the geometric contour lines of the interior facade and plane, such as walls, doors, Windows and balconies. The floor plan clearly shows the layout of the house and counts the total area of the house and calculates the area of each room [6]. According to the point cloud data, the two-dimensional Digital Line Graphic can be completed, and the dimensions can be measured in FAROScene software, and the accurate original plan can be obtained. The original plan is the first step of interior design, and whether it is accurate or not is vital importance, which affects the authenticity and validity of the whole interior design, and has a significant impact on the later construction. The following figure is the original plan obtained by the measurement of a commercial house in Xiamen city, the area size of each space can be accurately obtained. Using software layering, slicing point cloud data model, with HD Modeling for CAD 2013 area statistics to calculate house construction area is 90.4919 m². As shown in figure 1, the specific area of each room is the living room 36.4781 m², hall

3.7452 m², balcony 4.5021 m², master bedroom 13.0127 m², master bathroom 2.6321 m², guest bathroom 2.5378 m², daughter room 9.5802 m², study 8.1737 m². Compared with the data obtained by the traditional measurement method, the accuracy can be better guaranteed, and the accurate size of each indoor space can provide effective control of material budget, material use, carbon emission and construction period in each process of indoor construction. According to the building survey plan obtained by stratifying and slicing the point cloud data model, we can clearly and intuitively understand the indoor layout. If the layout of building survey plan is not reasonable, we can rearrange it directly according to point cloud data model. Drawing accurate building survey plan is the basis of design and construction.



Figure 1. Building survey plan

4.2. Positioning of pipeline equipment

The point cloud data is imported into FAROScene software for scanning to locate the precise location of pipeline equipment. Because after the completion of hydropower positioning and wiring, the pipeline equipment is usually buried in the wall, and when other ancillary facilities are installed, the pipeline equipment may be damaged due to inaccurate positioning. Using the scanned point cloud data to accurately locate the pipeline equipment can effectively avoid the problem of damaging the pipeline equipment. Using software to stratify and slice the point cloud data, the area information, the location of the pipeline equipment, the location and size of the door, window and all kinds of communication facilities can be extracted, it can effectively avoid the damage to pipeline equipment and communications facilities caused by the wrong operation in the construction process, ensure the construction safety and avoid unnecessary loss. As shown in figure 2 that the extraction of window and pipeline information can accurately show the distance between the top and the bottom of the pipe to the wall and the height above the ground, which brings convenience to the installation of socket and electrical equipment. At the same time, the non-contact 3D scanning technology of point cloud data is used to facilitate us to extract and analyze information from all aspects of the interior accurately and efficiently, providing new technical support for the construction, management and maintenance of interior design.

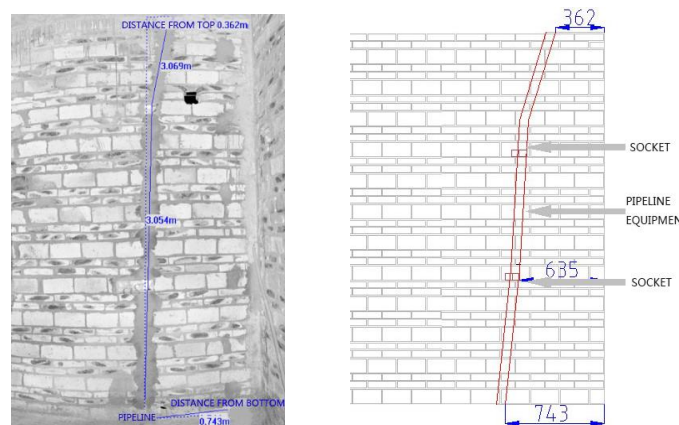


Figure 2. Extraction of information from pipeline equipment

4.3. Measurement of space dimensions

In interior design, the design is mainly aimed at a closed space formed by three surround surfaces, whose shape and size are determined by the ground, top surface and wall [7]. Interior design mainly covers wall design, ground design and ceiling decoration, and the basis of these designs is the measurement of space size. It is difficult to meet the requirement of complex building house measurement by manual measurement. With the high precision 3d scanning technology, the collection point cloud data of the device can be collected without arriving at the site, and then a two-dimensional Digital Line Graphic can be drawn according to the collection of point cloud data, which can be imported into FAROscene software for measurement after completion. Figure 3 shows some of the living room dimensions accurately measured by a three-dimensional laser. They are 1.953 m in height, 0.856 m in width, 2.837 m in height and 0.654 m in distance from the door to the post. Through the processing of point cloud data collection, the detailed space dimension information, doors and Windows, ground, wall and roof specific shape and size can be extracted. Every progress of interior design is measured by point cloud data technology, which can greatly reduce labor and time cost and improve work efficiency. For construction and management, these can not only reduce the budget and improve the profit space, but also substantially improve the quality of construction, so that construction can be carried out more effectively. This is incomparable to the traditional measurement.



Figure 3. Precise measurement of part size in the living room



Figure 4. Positioning of bricks

4.4. Positioning of bricks and cracks

After painting the indoor walls, it is easy to encounter obstacles of bricks when installing equipment such as electrical appliances. FAROscene software can be used to process the point cloud data obtained by scanning, extract the location information of bricks and cracks, and quickly find concrete cracks to facilitate the installation of the equipment. The extracted 2D line drawing can provide reliable information source for later information management. Setting the origin coordinates (0, 0), it

can be accurately extracted from point cloud data: brick boundary point A (0.509, 0.181); brick boundary point B (0.747, 0.234). As shown in figure 4 is the precise positioning of the brick and seam of the original point cloud. After importing the scanned point cloud data into the HD Modeling for CAD2013 drawing software, the point cloud data of the wall surface are extracted for fine drawing of two-dimensional line drawing. After the house walls are painted, they can be precisely lofted by locating the cracks and bricks that have already been positioned in the software. If the position of the brick and brick joints cannot be accurately located, the electrical equipment installed on the wall is likely to be a safety hazard, and it may take many attempts to install the equipment in place. To the walls which have been painted, it will bring adverse effect to the integrity and beauty, and increase cost, reduce efficiency either. This technology can avoid such problems.

4.5. Construction cost budget

The interior design is mainly designed for the interior floor, wall and roof, and the construction is also decorated for the three surrounding surfaces. Before the construction, 3D laser is used to scan the interior space, and registering and removing noise points from the point cloud data set are achieved. If the point cloud data volume is still large after the unified registration and denoising of the software, the data need to be filtered and simplified [8]. After the software is used for stratified sections and the accurate area of each room is calculated, the required materials can be calculated accurately according to the requirements of decoration. For example, Bricks, white latex, cement, etc. Traditional manual measurement methods not only have low efficiency, low time cost and high labor cost, there are also problems of data loss, omission and inaccuracy, which will increase the difficulty of on-site construction and require on-site coordination between designers and construction managers, so as to affect the effect of decoration construction period and design [9]. Compared to traditional manual measuring way, the point cloud data is a kind of non-contact 3D scanning technology, Scanning with a 3D laser, the point cloud data collected only need a single scan, which can accurately calculated the information needed for space by the relevant software, and not need to be back for measuring again, it can reduce time costs, labor costs, labor costs, reduce the waste of materials, increase the speed of construction decoration.

The standard sizes of brick used in house decoration are 300*300 mm, 500*500 mm, 600*600 mm and 800*800, which are mainly used to decorate the floor and wall of living room, kitchen, toilet and other rooms. Through three-dimensional laser measurement and using layered slicing technology calculate each elevation area of the house and according to the size of decoration needs, as well as the calculation of the house plan, elevation, design decoration drawings, accurate calculation of the size and quantity of bricks to be purchased. Part of the building decoration materials statistics as shown in Figure 5.

	AREA	SPECIFICATION	AMOUNT
LIVING ROOM	36.5m ²	GEOSTROPHY 500*500	146
HALL	3.8m ²	GEOSTROPHY 500*500	16
MASTER BEDROOM	13.1 m ²	GEOSTROPHY 500*500	53
MASTER BATHROOM	2.7 m ²	GEOSTROPHY 500*500	7
BALCONY	4.5m ²	GEOSTROPHY 500*500	18
DAUGHTER ROOM	9.6 m ²	GEOSTROPHY 500*500	39

Figure 5. Material data statistics

5. Conclusions

In view of the existing problems in the construction, management of interior design in China, the application of point cloud data in the construction, management of interior design is discussed and its feasibility is proved [10]. The breakthrough of point cloud data in the construction, management of interior design lies in the fact that the point cloud data collected is comprehensive three-dimensional spatial data. In addition to its advantages of high precision and high efficiency, it can help us to better

complete interior design and optimize some problems in the previous construction process. The application of new technology enables us to better control the construction progress and cost, improve the safety factor of construction, and reduce the difficulty of early measurement and late maintenance. Further development and application of 3D laser scanning technology, away from the bottleneck of traditional construction, management of interior design, and accelerate the development of indoor informatization [11].

6. Acknowledgment

Fund program: this paper is the research result of "the application of tilt photography technology in the protection and management of ancient buildings" for the science and technology project of the Fujian provincial education department. The project number: JAT171185.

7. References

- [1] Liu Jia. 3D modeling of indoor scene laser point cloud data [A]. Mapping press. Bulletin of surveying and mapping, BBS abstract set of frontier technology of surveying and mapping science [C]. Mapping publishing house: 2008:7.
- [2] Chen Ping. Research on 3D laser scanning in mobile interior based on SLAM [D]. China University of Geosciences (Beijing), 2016.
- [3] He Yuanrong, Zheng Yuanmao, Pan Huoping, Chen Jianzhi. True 3D modeling and application of complex architecture based on point cloud data [J]. Remote Sensing Technology and Application, 2016, 31(06):1091-1099.
- [4] Zhang Weiqiang. 3D laser scanning technology on the ground and its application in the mapping of ancient buildings [D]. Chang'an University, 2014.
- [5] Chen Yunbo, Feng Yafei, Ji Xiaobo. Research and practice of using 3ds Max and 3D laser scanning technology to generate 3D building models [J]. Survey Report, 2016(12):77-80.
- [6] Chen Huwei. Three-dimensional model construction and application research of open-pit coal mining [D]. Liaoning University of Engineering and Technology, 2012.
- [7] Zheng Peijun. Interior decoration design and construction management [D]. Shanghai Construction Engineering Design Research Institute co. LTD, 2018.
- [8] Huang Chengliang. Research on the application of indoor mobile measurement technology in completion measurement [J]. Urban Survey, 2017(05):133-135.
- [9] Li Lin. 3D reconstruction system of indoor environment based on laser scanning [D]. Harbin Institute of Technology, 2016.
- [10] Chen Huwei. Three-dimensional model construction and application research of open-pit coal mining [D]. Liaoning University of Engineering and Technology, 2012.
- [11] Yang Lin. Application research of 3D laser scanning technology in deformation monitoring of construction engineering [D]. Tianjin University, 2016.

The Application Research of Oblique Photogrammetry Technology in Road Planning

Zhihuang Zheng^{1,2}

¹ Managing Director, Fujian jingwei surveying and mapping information company, Fuzhou, China

² Vice Director, Big Data Institute of Digital Natural Disaster Monitoring in Fujian, Xiamen, China

E-mail: 273011974@qq.com

Abstract. This paper takes the planning and application of Ann Nine Railway as the demand, and adopting the multi-angle data information of the roads acquired by the oblique photogrammetry technology of UAV to realize the model reconstruction based on the Context Capture software. Then outputting data in kinds of formats to analyze. And based on Acute3D and LocaSpace to perform the viewing and measurement of the real 3D model, the model is repaired based on the Geomagic. The measurement and spatial analysis application of the 3D model based on LocaSpace. The application results show that the real 3D model was built could be applied to the railway planing based on the oblique photogrammetric data. And the measurement results can be used for various types of measurement and spatial analysis, which can provide the reference value of important data support for railway planning and design management, decision-making and construction operations and so on.

1. Introduction

With the development of the smart cities, the traditional two-dimensional road has been difficult to meet the demands of the road planning management and construction. The development and the application of oblique 3D modeling technology has brought about the major revolution to the project's planing design, management, examination and approval, construction and decision-making. In recent years, the rapid acquisition of ground information by low-altitude remote sensing technology has became more and more popular, so the UAV surveying and mapping technology has emerged as the times require. And the surveying and mapping personnel who use the oblique UAV to rapidly and efficiently perform the acquisition of surveying and mapping data are favored. Road is the skeleton of a city and it's also an important part of showing a city's style. The road planning develops with the development of social productivity. The road planning design is directly related to the living environment of human being, it's a comprehensive and complicated work [1]. With the development of science and technology, GIS technology is widely applied to the urban 3D modeling, which could greatly improves the efficiency and accuracy of road planning. However, the traditional orthophotography can only obtain the top information of the road, it could not obtain the side texture information of the buildings next to the road, but the oblique photogrammetry can break through the limitations of orthophotos.

As a new technical method, oblique photogrammetry has been widely used in 3D modeling, smart city construction and so forth [2]. For example, in foreign countries, San Jiang [3] et al. proposed the outdoor data acquisition based on UAV and an oblique photogrammetry measurement based on the off-line visual detection, and conducted an accuracy assessment test to explore the potential use of the



non-site inspection of the model construction based on the transmission lines. Kristian Svennevig [4] et al. proposed the 3D geological model construction of the opencast mine oblique photogrammetry measurement and applied it to the northern Greenland to better understand the evolution of structure. Grenzdörffer [5] et al. proposed that the oblique photogrammetry measurement is an effective tool of cadastral surveying, it could accurately draw the mapping of the cadastral activities in rural areas in three-dimensional space. In China, Hao Zeng [6] discussed the application of the oblique photogrammetry measurement technology in smart cities from the perspective of smart city. Yang Yanmei [7] et al. proposed to build 3D model based on acquiring oblique photographic image data, and based on the 3D models to realize the UAV digitalized large-scale mapping, as well as the result is good.

Three-dimensional modeling of oblique photogrammetry technology, smart city and other fields have been applied in some extent, but it is rarely used in engineering measurement. The three-dimensional model of oblique photogrammetry technology in road planning is mainly manifested in dynamic roaming effect display of 3D model, objects tagging, making thematic map, 3D model measurement and spatial analysis etc. [8] Among them, the oblique photogrammetric data in road planning design can assist the road planning design, construction measurement, Three-dimensional effect evaluation, assist in the completion and acceptance of roads, draw the thematic maps and assist in the old roads reconstruction, etc. The oblique photogrammetry has greatly improved the efficiency and accuracy of the road planning, and it could obtain the real 3D texture information of the ground objects. At the same time, UAV as a new low altitude remote sensing ground observation method, which has the characteristics of easy manipulation, short image acquisition period and strong maneuverability and so on [9]. It has the advantages of high performance-price ratio, limited monitoring area, fast acquisition of ground data and 3D modeling, and it is suitable for road design and measurement. Therefore, this research adopts the UAV oblique photogrammetry technology to obtain the road 3D model, which not only effectively avoids the low precision of traditional surveying and mapping industry, due to the large error to repeat round trip measurement, long acquisition cycle and high labor cost and so on. But also it provides the more abundant and intuitive data information for the road planning, design and completion acceptance in order to assist the road construction decision-making and administrative examination and approval department management decision.

2. Data acquisition

2.1. The oblique photogrammetry technology

The oblique photogrammetry, namely the oblique UAV measurement system. The oblique UAV measurement is performed by the aircraft carrying many oblique aerial cameras with rotating a certain oblique angle to obtain the image by taking photos from the air to the ground. In this research, the oblique image's data acquisition was carried out by Taiyi fixed wing oblique photogrammetry UAV and Dajiang Elf's four-rotor UAV. And the UAV aerial measurement of Taiyi PROPHET has the characteristics of easy to use, stable and reliable, high working efficiency, and it is suitable for the 1:1000 or 1:2000 aerial survey project in the area of 300 square kilometers. The Dajiang PHANTOM 4 UAV camera is equipped with a 1-inch 20 million pixel image sensor that could take the 4K/60fps video and take the static photos at a speed of 14/second. The Dajiang PHANTOM 4 has the five-eye machine vision and forward obstacle avoidance capabilities, which making it safer and more intelligent. The titanium material makes the machine body lighter and stronger, with 1 inch 20 million pixel sensor, 30 minutes battery's life, forward vision obstacle avoidance and intelligent manipulation, which can improve the efficiency value of data acquisition.

2.2. Acquisition of the oblique photogrammetry technology

The oblique photogrammetry data acquisition of this research mainly includes the flight route planning, the ground station preparation and the data acquisition. Taking the Dajiang Elf 4 flight route planning as the example, using the APP what is aimed for the Dajiang UAV planning route Altizure, the collected images could be uploaded to Altizure website to automatically generate the 3D models. Altizure APP could control the aircraft in real time on the flight path according to the pre-planned route, and set up the timing photo to take photos. The camera carried by the aircraft can automatically

collect the images of five angles downwards, after processing by the post-processing system, the 3D model of the real scene oblique could be generated. Meanwhile, the plane can be set up to take a positive photography downwards the plane in a vertical direction. The Altizure software planning route has the advantages of automatic route planning, intelligent continuous flight, full automation of data acquisition and intelligent task management. As shown in Fig.1 is the flight route planning interface of Altizure software.

Dajiang Elf 4 UAV collects data is based on the DJI GS PRO ground station, DJI GS Pro (Ground Station Pro) is an iPad application that can control the DJI aircraft to achieve the autonomous route planning and flight. The GS Pro has a simple and intuitive interactive design, and the application could manipulate the aircraft to achieve the automatic route flight and timing auto-photographing. Using the GS Pro to assist the field aircraft to collect data and apply it to all major fields where requiring aerial photography data collection, it will greatly improve the efficiency of the work. Before the UAV performs the mission, open the DJI GS PRO ground station and establish a connection with the aircraft.



Figure 1. Altizure flight route planning.

Before Altizure collects the data, at first we should install the DJIGO firmware and make sure the network is smooth before starting up the APP. After starting up, the software will connect to the DJI's background server for activation. After the first activation is completed, when it is reused after the first activation, it can be used offline directly. Next, making sure that a high speed SD card with sufficient capacity was inserted into the aircraft before taking off. Finally, making sure that the operators will correctly manipulate the Dajiang UAV to avoid the plane blasting. At the same time performing the preparation before taking off, firstly we should open the UAV and remote control power and set the UAV remote control to F level. Setting up the camera's parameters, such as the white balance, ISO sensitivity and exposure compensation and so on.

3. Data processing

3.1 Data preprocessing

After obtaining the field data of the oblique photographic images in this research area, the field data were preprocessed. The preprocessing work of the oblique data in this research area includes the classification and renaming of the oblique images and the processing of POS data. After the data acquisition of the Hubei province Huanggang section on the Ann Nine Railway was completed, the oblique images obtained by the oblique UAV were stored in the two cameras carried by the Taiyi fixed-wing UAV and the Dajiang Elf 4 UAV, respectively. The images in the two cameras were renamed and classified, so as to avoid the recognition errors what caused by the same image names in two cameras, that is, exporting the images from the two cameras respectively and stored them in the two folders respectively and named them respectively. And we should pay attention to the corresponding photos in two folders shouldn't name unanimously, at the same time we should check the photos and the corresponding POS data, check whether the photos in two folders correspond to the POS information, and delete the POS points without the corresponding photos. Among them, the POS data is copied from the aircraft, then the text files were exported, and check to see whether the photos correspond one-to-one. The POS data could provide the accurate external elements for the oblique

images by the error correction of the aircraft aerial photography system, and get the three-dimensional information of the DEM grid points by the condition of three points collinear. It could improve the efficiency of the post-processing software. After the data preprocessing finished, we can carry out the production of Ann Nine railway oblique three dimensional model.

3.2 The production of 3D model

3.2.1 The aerial triangulation.

This research design adopts the Context Capture image post-processing software to perform the model production of the oblique photogrammetric data for the Ann Nine Railway in the research area. The main processes of the oblique model are as follows: ①Photo modeling the pre-processed images in the Context Capture Center Master. ②Creating a new block and importing the information of the POS files, the POS file has been made into a text file in the preprocessing process. In order to obtain the optimal performance, the image must be divided into one or more image groups. The image group is a collection of the similar images, all of these images are from the same physical camera what has totally same internal orientation (image size, sensor size, focal length, etc.).After the images are classified and renamed in the process of preprocessing, the software can automatically determine the different image groups in the relevant file directory when importing. ③Checking whether the image attributes added in the information column of the imported photos are complete, if not complete, the software needs to be did the Empty Three encryption solution. And checking the information on the right side attribute column is mainly to compare the coordinates and the elevation information of the images whether is corresponding to each other. ④Submitting the aerial triangulation, the Context Capture software carries out a large number of the feature points extraction and matching of the same name for the oblique images. And calculating the three-dimensional coordinates of each image and the attitude angle of the photos so that determining the relationship between the images, the function of the aerial triangulation is to calculate the spatial three-dimensional coordinates of the images. ⑤Checking whether the processed image information is complete. If it is not complete, we need to match the image feature points and resubmit the Empty Three operations. ⑥After the end of the Empty Three, it could be view the results of the aerial triangulation by the 3D view view window. Clicking on the each waypoint at the top of the view to look over the relative position information of each image.

3.2.2 The reconstruction of 3D model.

After the aerial triangulation processing of the oblique photogrammetric data is completed, the construction of the three-dimensional model in the research area can be performed. There are mainly the following processes:

①The reconstruction of the oblique models is started after the success of the Empty Three solutions. The model reconstruction needs to reset the relevant parameters of the reconstruction models and define the output model spatial reference system. This research changed the coordinate system to the WGS84 coordinate system. In general, the data amount of the whole model is so large that the ordinary computers' performance could not reach the requirement of the model reconstruction operation. Therefore, the whole model is cut into blocks, this experiment defines the block mode as the regular stereoscopic block. extracting the tiles of the interest region to perform the model reconstruction, the setting of the tile size is referred to the computer's performance. The smaller the tile is, the more the number of tiles is, and the smaller the computer memory used in the reconstruction process is, and the higher the processing efficiency is.

②Setting the relevant parameters of the reconstruction model and defining the output model spatial reference system. This research sets the coordinate system to the WGS84 coordinate system. Taking the part of the section of Ann Nine Railway as the reference case, the spatial frame of the block area view was edited according to the interests and set as: the spatial reference system selection WGS84/UTM ZONE 50N, the mode is the regular stereoscopic cutting, the tile size is set as 100 meters, the expected maximum RAM usage of a task is 2GB.

③When the setting of the spatial frame is completed, submitting the new production project, in the guide of model reconstruction, it could perform the achievement output format and the selection of the achievement output quality .And it could define and output the 3MX,S3S,OSGB etc. and kinds of

format data. In this research, the corresponding WGS84/UTM ZONE 50N coordinate is selected in the option of the research experiment spatial reference system.

④The oblique model reconstruction is carried out by software automation. The operation efficiency of the image processing is related to the computer graphics processor, the high or low of the model reconstruction efficiency depends on the computer's performance. The higher the graphics card performance is, the higher the processing efficiency is. It could be viewed the production process of the three-dimensional models in the 3D view window, and it also could check the completion progress of each tile. After the reconstruction model is successful, the interface will display that all the tiles are processed, and the model effect is viewed in the 3D view window, as shown in Fig.2



Figure 2. Viewing Model effects in 3D View.

4. Achievement application

Viewing the results of Ann Nine Railway oblique 3D model in Acute3D.Acute3D Viewer is a lightweight visual module of Context Capture, which has been optimized for 3MX and S3C formats of Context Capture, it could deal with detail levels, paging and streaming transmission, as well as allow for the fluent frame rate to visualize 3D data locally or online. The 3MX format files produced after the model reconstruction in Acute3D can view the effect of the oblique 3D mode, and after the measurement analysis data processing of the model could obtain the kinds of formats oblique photogrammetry 3D model productions of Ann Nine Railway Hubei province Huanggang section. As shown in Fig.3 is the view effect of Ann Nine Railway Hubei province Huanggang section oblique 3D model in Acute3D.



Figure 3. The view of the 3D model.

4.1. The auxiliary planning and design

4.1.1 Auxiliary view of the filed planing picture.

The planning map is an important basis for the work of government planing departments and the planning design departments [10]. There are many deficiencies in the traditional way of viewing. First of all, the planning map are often made up of color blocks and lines, such plane planning maps are too abstract to correspond the corresponding areas and drawings for those unfamiliar with this area. The oblique photogrammetry could effectively solve the shortcomings. On basis of the 3D model results and the remote sensing images we could make the planning maps to connect the real scene with the planning maps, which could help users to intuitively and vividly understand the planning areas. It is

easier to obtain the image information by superposing the different types of planning maps such as the oblique 3D model, the remote images and the general planning maps, which could bring a great convenience to the planners.

4.1.2 Assisting the railway to choose lines.

The towards design of the preset line of Ann Nine Railway in this research area should not only pay attention to the geological situation of the location, but also should pay attention to the land use and development of this area such as the agriculture land, the construction land and the unused land. On the one hand, the state strictly restricts the conversion of agricultural land to construction land, and strictly controls the total amount of the land used for construction, and strictly controls the conversion of cultivated land to non-cultivated land, the urban land use planning can not be easily changed, the lines should be less occupied by the cultivated land. On the other hand, the railway will attract a large number of passengers after the construction and the operation, which makes the population in the city center will spread around the city. So that causing the change of land use natures around the railway station, and the two should be coordinated and jointly plan for development [11]. It is difficult to discriminate the land use situation in the present location at the preset lines in the ordinary town planning, however the oblique photogrammetry measurement technology could solve this problem. As shown in Fig.4, making use of the oblique photogrammetry measurement technology could superimpose the oblique 3D model of the planning area to the remote images by the LocaSpace software. It is easier to obtain the effective information of the land use situation by linking the planning area and the real geographical location of the provinces and counties in the area scope to help the planners more intuitively and vividly understand.

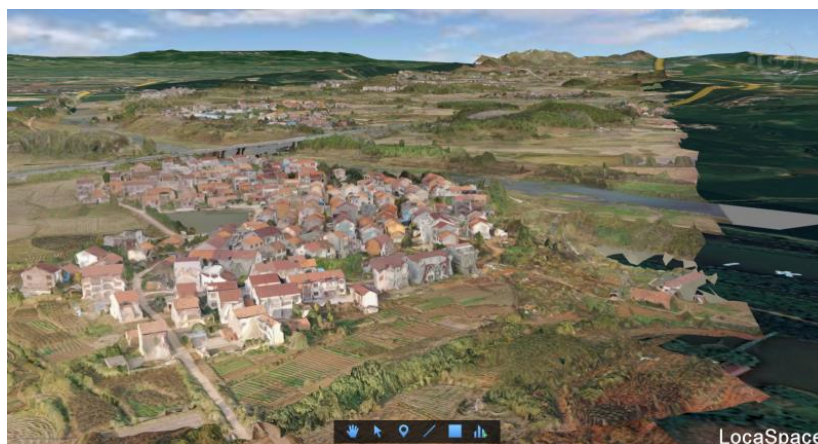


Figure 4. The view of land use status.

It is of great significance for the engineering decision-making to use the complete three-dimensional model of Ann Nine Railway which was acquired by the oblique photogrammetry measurement technology. For example, the preset lines should reduce the partition of the cultivated land and choose the scheme of the near the mountain. The interpretation of the key ground objects such as the electric towers what was near the mountain passed, and graves and so on, the scope area statistics of the villages the preset lines passed where needed to be demolished, the two periods quick construction of the planning before and after, the comparison of the non-conforming buildings, the compensation estimated for the auxiliary demolition. All of these brought the revolutionary change for the engineering planning and approval, management and decision-making. As shown in Fig.5, auxiliary line selection for the clear oblique photography 3D model of Railway, the key ground objects such as the electric towers and the graves can be interpreted.

The compensation estimation work of the single house demolition is carried out in Acute3D, Aute3D can not only view the three-dimensional effect of the house, but also the operation is simple. The area measurement of the single house is the surface measurement, the bottom area of the house is measured by 360 degrees surrounding finding the four corners of the house. And then performing the total areas estimate work of the house demolition by observing the number of house layer, the story height and so

on. The area measurement of the single house can also be carried out in Acute3D, so as to assist the compensation estimation of demolition.



Figure 5. The oblique model to assist the key ground objects to interpret.

4.1.3 Making the classification diagram of the house building.

Due to the design of the Hubei province Huanggang section of Ann Nine Railway through the rural towns, it took many problems to the urban construction of Ann Nine Railway and Hubei province Huanggang Huangmei town, etc. Such as the planning adjustment, the design change, the investment increase and the delay of the construction period. Especially the problem of house demolition work through the Ann Nine Railway Hubei province Huanggang section, the rural demolition work involves many aspects interests, the improper adjustment of demolition work will lead to various contradictions and disputes. Ann Nine Railway construction must take into account the many-sided interests such as the rural urban policies, the interests of the masses, the economic development and the social benefit [12]. Therefore, this research put forward that take the oblique photogrammetry measurement technology as the guidance, based on the Ann Nine Railway oblique three-dimensional model to make the house building structure and quality classification diagram of the rural urban in the research area. As shown in Fig.6, as well as the classification summary chart of the house structure and quality, this data has important reference value for the demolition compensation of Ann Nine Railway construction.

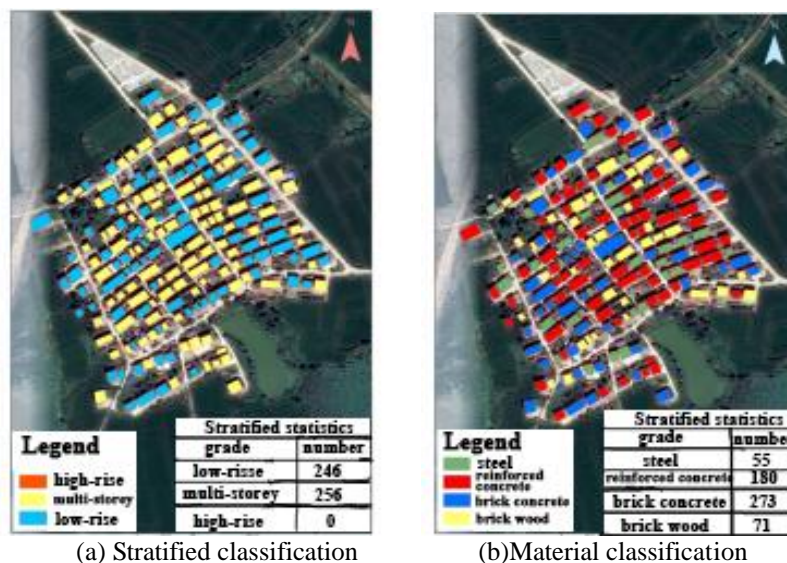


Figure 6. Classification of houses in Zhang Puxing village.

This research classifying and summarizing the building quality of Hubei province Huanggang section rural towns where was passed by Ann Nine Railway. This data will serve as an important reference basis for planning and design and assist the demolition compensation work. According to the principles of “suit one’s measurement to local conditions, take into consideration both needs of the state and the interests of the collectives, orderly propulsion, classification guidance and comprehensive improvement”, and it has the important value and significance to apply the oblique photogrammetry measurement technology into the road planning and design.

4.2. The auxiliary construction survey

In LocaSpace software, it is of great significance to carry out other measurement work and spatial analysis to the 3D model of Ann Nine Railway oblique photogrammetry for the engineering planning and examining and approving, management and decision-making, which could assist Ann Nine Railway construction work.

4.2.1 The generation and application of contour line.

Extracting the elevation points of a mountain section of the Ann Nine Railway, and extracting the elevation points of the sampling points in the range area according to the required draw rectangle and the selected area, which could extract the latitude and longitude and elevation information of the sampling points. At the same time, exporting these information in the format of grd data and importing them in LocaSpace to generate the contour terrain map. These contour data could provide the topographic reference such as judging the topographic slope is steep or smooth of the preset lines, recognition of the terrain types, drawing the river direction and the topographic profile and so on. The planning of Ann Nine Railway can be selected as far as possible on the smooth slopes to avoid the steep cliffs and the areas with poor geological conditions. At the same time, the contour terrain map is of great significance for the railway auxiliary lines selection. The railway lines are generally constructed along the contour lines, and in the construction of railway within the terrain of the hill should refer to the contour terrain map of this region. As shown in Fig.7, it is the topographic position of hills where is passed by Ann Nine Railway preset lines. On the right of the figure, it is the suitable route was built along the contour lines of hill terrain. Constructing the railway between E and F could effectively reduce the construction difficulty and reduce the amount of the road engineering, and it is not easy to cause the phenomenon such as the soil and water loss, which could facilitate the construction of railway tunnels and vehicles driving.

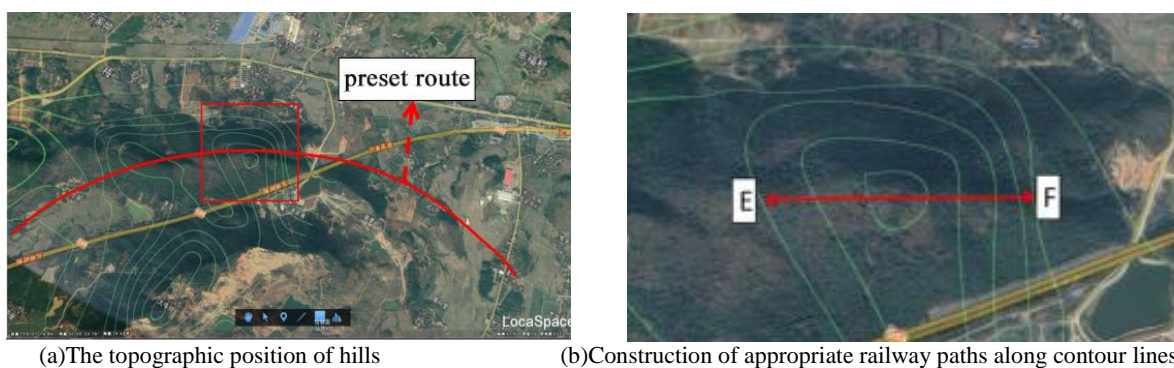


Figure 7. Choosing the appropriate path for railway Construction.

4.2.2 The spatial analysis.

Taking advantage of the LocaSpace software to perform the spatial analysis of Ann Nine Railway Hubei province Huanggang section for assisting the construction decision-making, such as the visibility analysis, the visible range analysis, the fill and excavation analysis and the profile analysis and so on. The general analysis operation steps is click the left mouse button on the two points that need to perform the visibility analysis. LocaSpace will automatically draw the visual view situation from the start point to the end point. The visible regions are in green, and the invisible regions are in red. This function could judge whether are visible or shelters between the two points. As shown in Fig.9, taking a point as the observation starting point to research the terrain of a certain area’s visible

situation. And the spatial distance is 916.39 meters between the start point and the end point, the vertical distance is 57.35 meters, the horizontal distance is 914.60 meters and the altitude is 92.98 from the start point, the visual condition between two points is invisible.

The visual area analysis operation steps is clicking the start point on the left mouse button on the map, as the start visual point, moving the mouse to click the above corresponding end point again, and taking the distance between the two points as the radius of the visual area analysis. It could be automatically generate the 360 degree visual status from the point of view to the surrounding range. The visible regions are in green, the invisible regions are in red. The visible region analysis realizes the circumferential effect of simulating the human's eyes, it could look around the visual situations of the surrounding regions, and it could adjust the height of the viewpoint by setting the view height. As shown in Fig.10, the start point height is 3 meters, the radius of the visible region is 981.77 meters, the longitude is 115.997685 °, and the latitude is 30.088544 °.



Fig 8. Visibility analysis of partial section of Ann Nine Railway

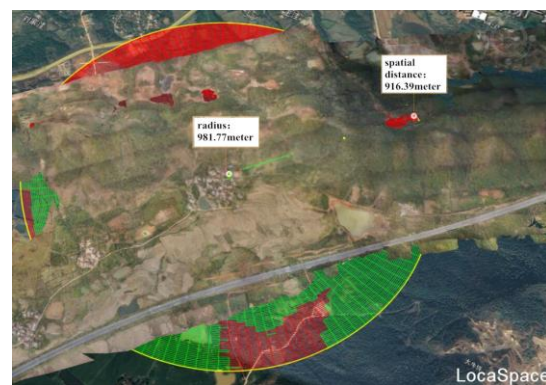
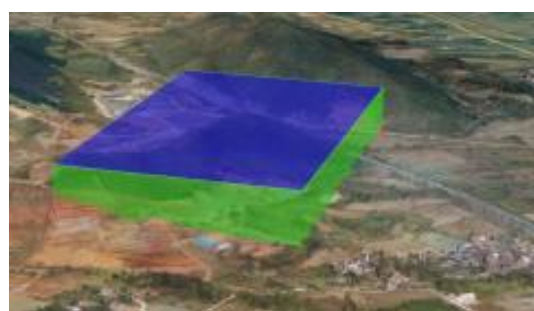


Fig 9. Visual analysis of the corresponding sections of Ann Nine Railway

The filling and excavating analysis can draw a polygon on the map to automatically enter the analysis results display interface and adjust the elevation values of the base level. Anew performing the filling and excavating analysis, it could be also directly select the surface by clicking the selection surface as the range of the filling and excavating analysis. When the preset route of Ann Nine Railway passes through the small hill terrain, it can analyze the various information of the filling and excavating according to the selected range and the defined elevation of the basis level. The information are include: the highest point, the lowest point, the filling amount, the excavation quality, the total amount of the excavation, the area of the filling region, the area of the excavation and filling region, as well as the total area of the region, etc. As shown in Fig.10 is the filling and excavation analysis of the Ann Nine Railway oblique images passed by a small hill. According to the calculation result, the elevation of the basis level in the research area is 158 meters, the highest point is 105.13 meters, the total amount of the filling and excavation is $3.44 \times 10^8 \text{m}^3$, and the total area of the filling and excavation is 416452.49m^2 . Combined with the project's reality, analyzing the calculation of the roadbed filling and excavation can effectively assist the construction decision-making of Ann Nine Railway.



(a)Excavation area required for Ann Nine Railway preset route



(b)Calculation of fill and excavation in small hills area

Figure 10. The area and calculation of filling region in small hills area.

The profile analysis could directly select points on the map, drawing a line on the place where needs to perform the profile analysis, it could automatically analyze the elevation change situation of this line and draw it in the format of graph. As shown in Fig.11 is the profile analysis between the two points, A and B of a section of Ann Nine Railway. The calculation results show that the start point A's longitude is 115.990623°, A's latitude is 30.086982°, and its elevation is 163.34 meters, the end point B's longitude is 115.994316°, B's latitude is 30.086613°, and its elevation is 76.40 meters. The projection distance is 402.85 meters, and the number of the sampling points is 100. These 100 sampling points give the longitude and latitude and the elevation information, and the textual data in the csv format can be exported, these data provide the important reference for the construction decision of Ann Nine Railway. In a word, it is of great significance for the Ann Nine Railway construction decision-making to use the oblique photogrammetry to generate the three-dimensional data with OSGB format so as to carry out all kinds of spatial analysis work by LocaSpace.

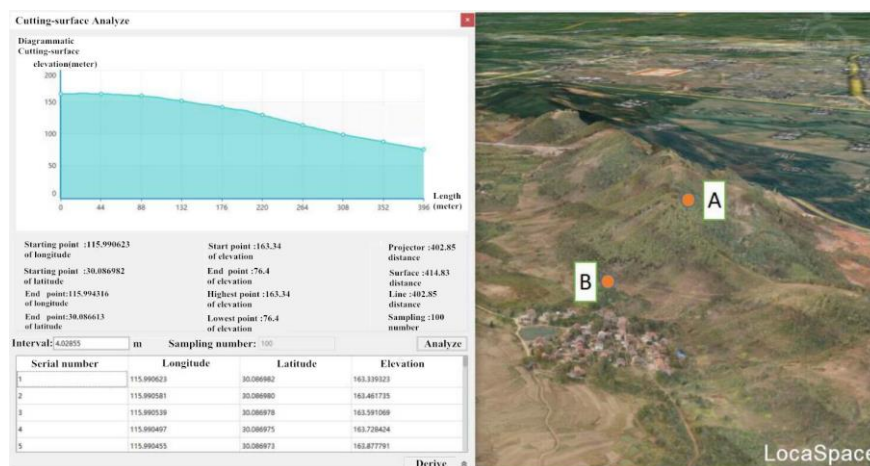


Figure 11. The profile analysis of a section of Ann Nine Railway

5. Conclusion

This research applied the oblique photogrammetry measurement technology to the planning and design of Ann Nine Railway, assisting the planning, design, management and decision-making of Ann Nine Railway, which reflects the application values of this technology in the engineering projects. Taking the planning of Ann Nine Railway as the research object, this research introduces the model reconstruction of oblique photogrammetry measurement data by using the Context Capture software, and introduces the model restoration based on the Geomagic repairing model software, as well as the measurement and the spatial analysis of Acute3D and LocaSpace. The application results show that the establishment of the real 3D model based on the oblique photogrammetry data could be applied in the planning and design of Ann Nine Railway. Such as assisting the line selection of Ann Nine Railway planning, assisting the estimate of the demolition compensation, making the thematic maps and assisting the decision-making of construction and so on. It provide the reference value of the important data support for the planning and design, management, examining and approving, construction decision-making of the Ann Nine Railway engineering projects.

6. References

- [1] Zuo Chuanyi. Exploring the Importance of Urban Road Design and Planning [J]. *Urban Construction Theory Research*, 2011, (14): 1.
- [2] Chen Xin. *Application of UAV Oblique Photogrammetry in Completion Surveying of Architectural Planning* [J]. *Urban Survey*, 2017, (1):82-90.
- [3] S. Jiang, & W. S. Jiang. *UAV-Based Oblique Photogrammetry for Outdoor Data Acquisition and Offsite Visual Inspection of Transmission Line* [J]. *Remote Sensing*, 2017, (3):1-25.
- [4] S. Kristian, G. Pierpaolo, S. Lars, *from oblique photogrammetry to a 3D model - Structural modeling of Kilen, eastern North Greenland* [J]. *Computers & Geosciences*, 1983, 2015(10):120-126.

- [5] G. J. Grenzdörffer, M. Guretzki., I. Friedlander, 2008, *Photogrammetric Image Acquisition and Image Analysis of Oblique Images- A New Challenge for the Digital Airborne System PFIFF* [J]. Photogrammetric Record, 2008,(12):372-386.
- [6] Hao Zeng. *Application of oblique photogrammetry in smart cities* [J]. Intelligent Construction and Smart City, 2017, 56-57.
- [7] Yang Yanmei, Shi Lei. *Experimental research on 3D digital mapping based on oblique photogrammetry* [C]. Proceedings of 2016 Academic Annual Meeting of Yunnan Institute of Surveying and Mapping Geographic Information, 2016, 25-27.
- [8] Liu Qiang. *Application of oblique photogrammetry in urban planning* [J]. Shanxi Architecture, 2017, 43(22): 203-205.
- [9] He Yuanrong, Zheng Yuanmao. *Application of UAV aerial photography technology combined with remote sensing for coastal zone planning* [J]. Modern Electronic Technique, 2015, 38(23):24-27.
- [10] Zhang Rubin, Bao Wan long. *Comprehensive renovation plan for old city renewal and pilot area in central Chifeng urban area* [J]. Urban architecture, 2018 (15): 60-67.
- [11] Yu Lingkun. *Research on the overall planning and design of railway crossing cities* [J]. Railway Standard Design, 2015, (3): 9.
- [12] SUN Xuejun. *Research on House Demolition and Compensation under Rural Urbanization—Taking Longhai City as an Example* [J]. Shanxi Agricultural Journal, 2016, (7): 2-45.

Fund project: The key technology and the system integration of special geographic national conditions monitoring in mining areas (Fujian Province Natural Science Foundation Project 2016J01199)

Research on LED Advertising Display Wireless Control System Based on MT6589

Yizhou Mao¹, Yingchao Xu^{1,2*}, Subin Wang³, Wenwei Zhu³

¹School of Opto-electronics and Communication Engineering, Xiamen University of Technology, Xiamen, CHN

²Fujian Provincial Key Laboratory of Optoelectronic Technology and Devices, Xiamen, CHN

³Xiamen Qiangli Jucai Opto-electronic Technology Co, Xiamen, CHN

Corresponding author Email: ycxu@xmut.edu.cn (Yingchao Xu)

Abstract. Aiming at the problems of wired control and database updating in LED display applications, a wireless advertising control system for LED advertising machines with low-cost, easy-to-update database and remote control is given. The system is based on the Cortex-A7 MT6589 chip of the ARM microprocessor and uses Wi-Fi communication technology to build the wireless transmission peripheral circuit module and the IEEE802.11b protocol. It uses the RP-SAM interface that comes with the development board to match the Wi-Fi function of the connected mobile client, which realizes wireless control and high quality display of LED advertising display. The mobile client's design of software is realized by Phone-Gap technology. The system is reliable in structure, low in hardware cost, convenient in software control, and satisfies the basic requirements for users to conveniently use it

1. Introduction

LED displays have many advantages, such as high brightness, bright color, large contrast, low power consumption, and easily being assembled in the display field. Today, LED dot matrix advertising displays are used in all walks of life, but it inevitably would be found some obvious problems. Especially in the way of controlling and transferring information, the cable transmission control systems need much investment that the high maintenance costs and its inconvenience by users have been unable to meet the needs of various industries. It can be seen everywhere that LED advertising displays in large shopping malls and public institutions are too low in pixels to display high-definition. There are thick cables and optical fibers, which not only increase the weight and cost, but also easily cause obstacles in communication [1]. Conventionally, LED displays usually use a single-chip microcomputer as a micro-controller. When the amount of display data is large, it is limited by the size of the clock frequency. Owing to the low frequency during the scanning process, the display effect is unstable obviously. There are many limitations on single-chip wired transmission control systems. So the high-density wireless transmission control system of the MT6589 chip with Cortex-A7 architecture has its outstanding advantages [2]-[5].

In order to meet the remote control of the LED advertising machine, a part of the GMS module is installed in the LED advertising machine control system. The wireless control of the LED advertising machine control system is realized by the wireless data transmission of the 3G/4G network card. Another parts use ZigBee, Bluetooth and other wireless communication technologies that are connected to the host computer [1]. Because the data transmission based on the CMCC's GPRS/GSM communication network, in addition to charging communication costs. It will bring additional costs.



ZigBee communication technology data transmission rate is low, which can not meet the transmission rate of LED advertising machine with high pixel density; Bluetooth technology's problems are that the power consumption is large and the transmission distance is short, and the network size is small [2], [5]. Taking into account the ubiquitous mobile phone being using everywhere, and coming with WIFI wireless connection function, LED advertising machine system uses Wi-Fi wireless communication technology. It can be better adapt to the market environment.

2. Overall system design

This system uses the Cortex-A7 architecture MT6589 as the core chip. Through the Phone-Gap technology, the designed mobile phone operating system platform is used to find the hardware ID number or IP address of the MT6589 chip for establishing a connection. After the connection is established, the signal is sent to the Wi-Fi on the development board. Then, the signal is received by the Wi-Fi module. It is transmitted to the MT6589 chip control terminal via the internal transmission control serial port, and then drives the LED display module. Considering the resource utilization of the development board, the PC can be directly implemented connection with the LED display module through the Ethernet when necessary. The overall design of the system is shown in Figure 1.

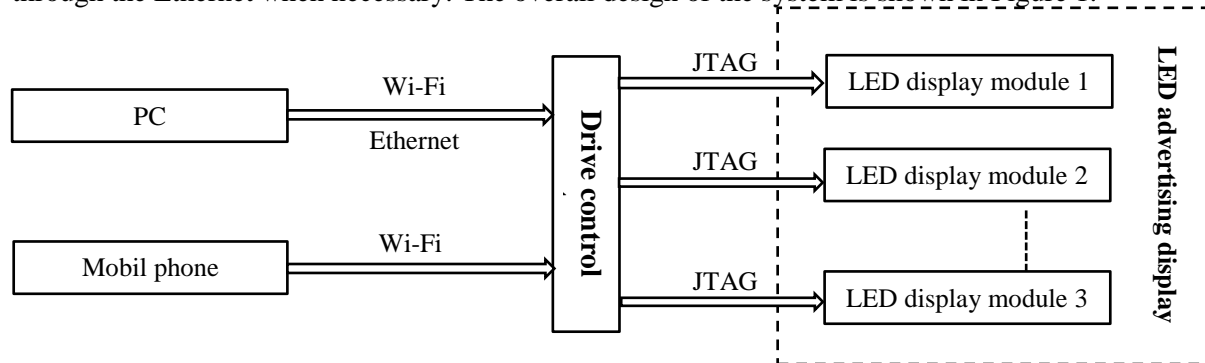


Figure1. The overall design of the system

3. Hardware design

The LED advertising machine wireless control system is implemented by Media Tek's MT6589, which uses the quad-core ultra-low-power processor Cortex-A7 and Imagination Technologies' Power VR Series 5XT graphics processor (GPU). The Cortex-A7 processor has a main frequency of 1.2GHz, which supports 1080P video decoding, and HDMI. The hardware circuit can be basically realized by building related peripheral circuits on the development board [7]. Compared with the current control system's heat dissipation, low power consumption and cost budget, the platform is the current price/performance ratio. The hardware structure of the control system is shown in Figure 2.

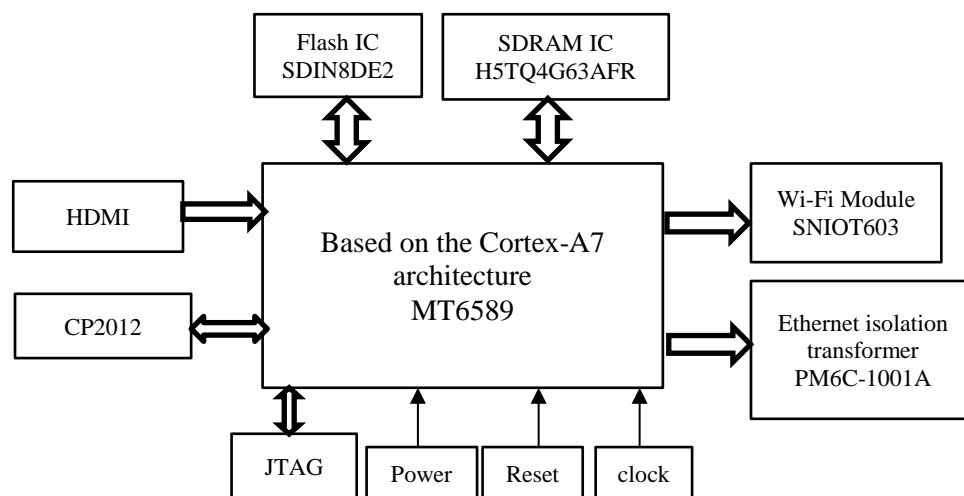


Figure2. Control system hardware structure diagram

3.1. Wi-Fi module

The title is Wi-Fi, also known as IEEE 802.11b. It is a short-range wireless transmission technology that supports wireless signals connected to the Internet in hundreds of feet [4], [6]. This system adopts Sinan Union SNIOT603 Wi-Fi module, which integrates micro-controller and 802.11b/g/n, 2.4GHz wireless RF transceiver chip, including RP-SAM, UART, 2C, PIO, DIO, CM, etc. The interface can be simulated and programmed with the emulator. The mobile client platform opens the Wi-Fi setting for searching, and the connection with the Wi-Fi module is established. The related data is transmitted and fed back. Then, the MT6589 internal data register receives the data transmitted by the serial port and buffers the data transmission in the SDRAM. Figure 3 shows the interface between the Wi-Fi module and the MT6589. The communication between the Wi-Fi module and the MT6589 can be completed with only four wires.

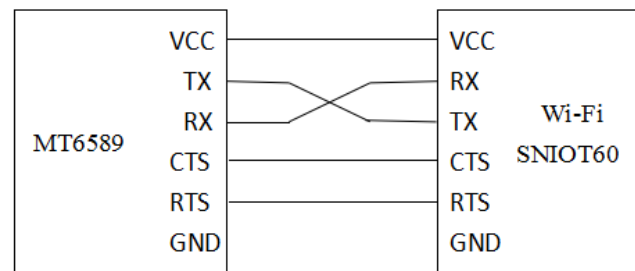


Figure 3. Interface diagram of Wi-Fi module and MT6589

3.2. SDRAM memory module

With the rapid development of the information age, the traditional small-capacity, slow-processing static memory has been unable to solve the problem in today's multimedia networks. The problem of large amount of data transmission and high bandwidth consumption must be solved. In the process of processing high-speed signals and large-capacity data storage, Synchronous Dynamic Random Access Memory (SDRAM) is the first choice for cached data, due to its low cost, high density, and high read/write data rate. For storing the device, this system uses SK Hynix's H5TQ4G63AFR chip. The chip has 8 zones inside. A single zone can store 64M*8bit data. Its total storage capacity can reach 512M*8bit, which the clock frequency can reach up to 1600MHz, and the working voltage of the system is 3.3V. Two SDRAM are used in the design, and data can be stored and read by ping-pong operation, which can process data at high speed [8]. In this control system, SDRAM is used to store various texts, pictures, audio and video data, which provides enough space to save and run temporary files. It is convenient for the program to call at any time.

3.3. Flash configuration module

The MT6589 not only supports the common serial and parallel standard configuration modes, but also supports the Serial Peripheral Interface (SPI) configuration mode. Because the flash memory is much lower than the cost of the master MT6589 controller of this design, in traditional flash memory, flash does not need UV light to erase memory. The control chip design software can eliminate data by using it. It can be used repeatedly. Therefore, SanDisk SDIN8DE2 is used as the flash memory configuration chip of MT6589 in this system, which has high capacity and small volume. It has many advantages, such as low power consumption, simple interface, 8G of the memory, 1.2GHz of the clock frequency, 3.3V of the working voltage. Its synchronous serial bus can communicate with data at any time, with its own SPI interface [6]. The flash memory is divided into two parts for data storage, one for storing the software program design of the MT6589, and the other for storing the relevant parameters in the control card.

3.4. JTAG interface module

Joint Test Action Group (JTAG) is an IEEE standard test protocol for testing the integrity of signal communication between chips on a PCB and for fault detection of hardware circuits, as well as debugging simulations of the system. The main controllers on the market today, such as DSP, ARM,

FPGA. Those controlling chip manufacturers will reserve JTAG test ports, which is convenient for developers to simulate and debug online. The JTAG interface typically has four output lines: Test Data Input (TDI), Test Mode Select (TMS), Test Clock (TCK), and Test Data Output (TDO) [1]. In the program programming design function, the flash configuration module can be programmed through the JTAG interface.

3.5. Power circuit

In this system, MT6589 requires 3.3V DC (Direct Current), Wi-Fi module requires 5.0V DC, and other modules are 3.3V DC. According to design requirements, the system adopts input voltage of 5.0V DC, which can be directly supplied to wireless module. use. The AXP209 chip is selected as the DC-DC converter for DC conversion from 5.0V to 3.3V. The system power supply circuit shown in Figure 4 has the advantages of high reliability, good stability, and high output voltage accuracy. In order to make the LED advertising machine power off, the system time will not disappear. The power supply of each system of 3.3V CR2032 battery is separately set to ensure the stability of the system.

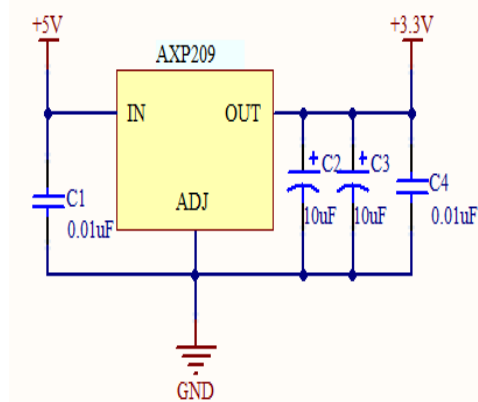


Figure4. Power circuit

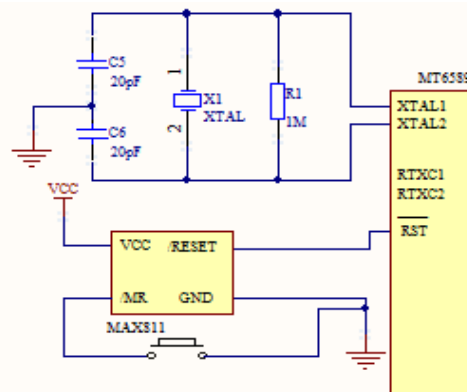


Figure5. Reset circuit and clock circuit

3.6. Clock and reset module

In the clock circuit of this system, 8MHz XTAL is adopted. After the frequency of the internal phase-locked loop circuit is doubled, the maximum frequency can reach 60MHz. At the same time, the PLL circuit has high frequency noise reduction, which can achieve the purification effect of the signal. It is sufficient to realize the basic requirements of scanning the advertisement screen.

The reset circuit uses the MAX811 chip, which is a power monitor device with a manual reset input pin and greatly enhances the stability of the system. As shown in Figure 5, the reset circuit normally resets the pin output level. When the reset button is pressed, the pin outputs a low level to reset the system.

4. Software design

Today's mainstream mobile platforms mainly include IOS, Android and Windows Phone. They are not compatible with each other. There is no unified method and interface to realize cross-platform application development. If enterprises develop unified software for different platforms, it will not only cause time. And the waste of human resources will also lead to the difficulty of developing customization [10]. In order to reduce the cost of the enterprise and make it more convenient for users to use, the mobile phone client software design of this system adopts Phone-Gap technology. It can realize full platform support in various smart phone systems such as Android, IOS and Windows Phone. Through the JavaScript code of Phone-Gap technology for network programming, the mobile client performs Wi-Fi setting to connect the Wi-Fi module in the same LAN. Then, It can drive the LED control chip through software control to realize the control of the mobile client to the control system. The overall program design flow As shown in Figure 6.

4.1. Phone-Gap cross-platform framework design

Phone-Gap is a free, open source, cross-platform mobile application framework. It is based on HTML, JavaScript and CSS and supports a variety of mobile operating system development frameworks such as IOS, Android and Windows Phone. As shown in Figure 7, Phone-Gap's Web view for different platforms becomes a powerful browser that can access the local API, and the Native APIs are encapsulated in the Plugin mode to implement the web-side call to the mobile client. Each mobile operating system platform has a mobile client component, which can realize the following functions: at any time, the module is called to parse the received data, construct user excuses data, present and operate the service system on the terminal [9].

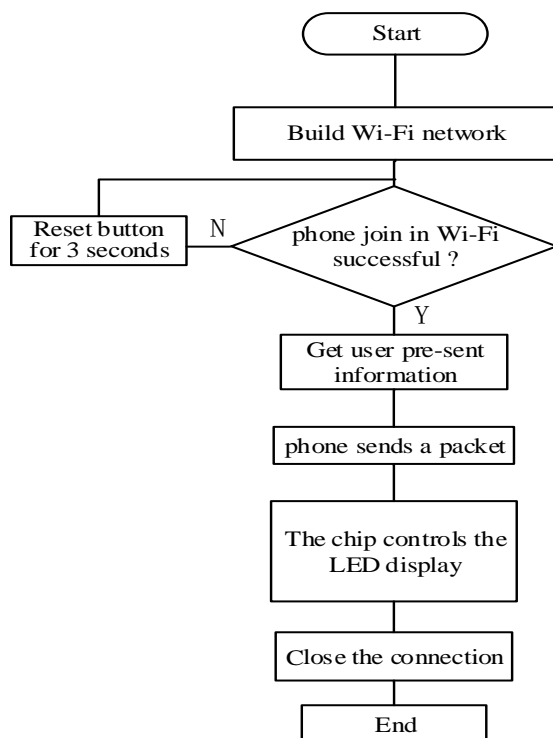


Figure 6. Overall programming process

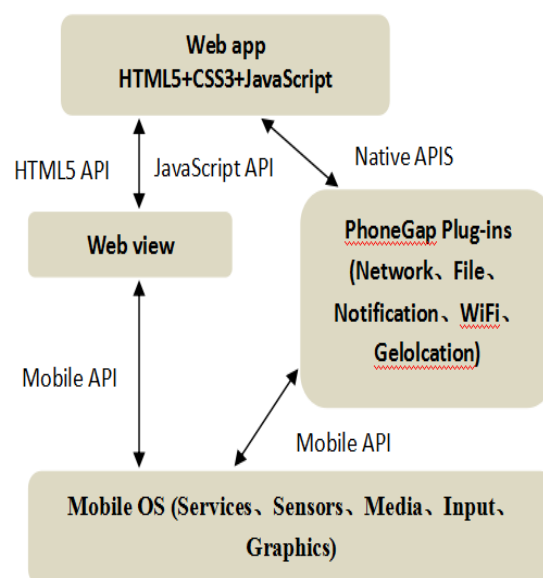


Figure7. Application framework design

4.2. Software playback function structure design

Phone-Gap The general function of the LED advertising machine playback control software is to control and edit the information displayed on the LED advertising machine. At first, various programs are created on the mobile client, and the required content is dragged to the reduced-scale placement box displayed on the software, and transmitted to the LED advertising machine through the Wi-Fi module, and the program display preview effect can be called at any time on the mobile client. For comparison treatment [8]. The display on the advertising machine is rich in content, and can basically cover all the playing content, such as text, forms, pictures, videos, and so on. The playing software is generally composed of the following parts: content editing, program playing, and corresponding simple daily application functions. The functional structure is divided into user interface, editing, playing, and hard and software setting mode function blocks. The overall software functional structure is shown in Figure 8.

4.3. Implementation of text and picture playback functions

In the LED advertising machine playback control software, in order to enhance the dynamic effect of the information displayed on the advertisement screen and attract the attention of the public, special effects such as telescopic, gradual, moving, rotating, etc. can be applied when playing pictures and texts. Phone-Gap technology provides very convenient CSS3 animation code, such as skew-1, rotate, shadow, etc., which can display the dynamic effect of text images. When implementing dynamic

playback effects, some obvious problems are often exposed. For example, when switching pictures or preparing the next video, the playback screen will flash a large area, and sometimes the screen will appear. Therefore, the system software is designed with double Buffering technology [10], the specific operation is to vacate an area in the system's memory for use as a background canvas, allowing related programs to be modified and drawn on the canvas. After the update is completed, the canvas directly covers the background of the display screen to achieve one display.

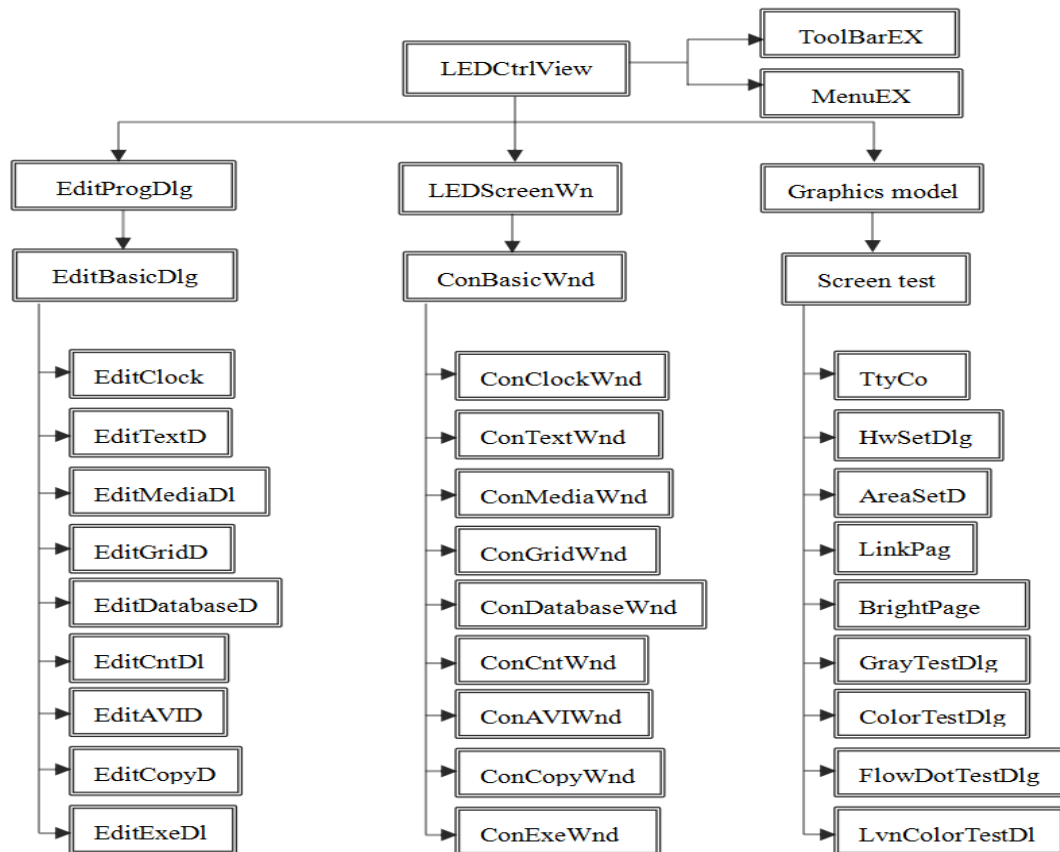


Figure8. Software overall functional structure

4.4. Audio and video playback functions

The audio and video program is mainly based on the Phone-Gap platform, which provides a series of APIs such as Media, File, and Network to process media files in various formats, audio and video collection, and can process various common media formats on the market, including ASF, AVI, DV, MPEG, MOV, etc. According to the actual application, implement a complete Media playback function.

5. System test

This paper has initially completed the hardware and software design part of the LED advertising machine wireless control system, including the hardware module circuit design and software-related playback functions. In order to verify whether the LED advertising machine can be used safely and smoothly at the playing site, the wireless control system testing experiment is a key link in the design process. The system test needs to complete the control of the LED advertising machine by the software on the mobile client, and check whether the related functions such as the playing of the advertising machine and the editing of the software are normal, including the following aspects, including the Wi-Fi connection test, the software interface effect test, and the program. Experiments were carried out on images and so on.

5.1. Wi-Fi connection test

The test process is as follows: the mobile client is set to set the Wi-Fi connection interface, so that the Wi-Fi module and the mobile client of the wireless control system are in the same local area network, and the Wi-Fi scanning module can generally scan multiple Wi-Fi access points, and the control system is connected. A network called XMUT-WiFi is used as an example for a mobile client Wi-Fi connection, as is shown in Figure 9. If the mobile client cannot search the Wi-Fi module network, press and hold the reset button for 3 seconds to reset the system Wi-Fi module.



Figure9. Phone’s Wi-Fi connection interface



Figure10. Software interface function display

5.2. Software interface effect test

The interface generated by CSS3 in Phone-Gap technology has the characteristics of beautiful display effect and high user experience. The control of the two makes the layout and color matching of the application page reach the level of the native application UI [10]. As is shown in Figure 10, the function interface implements basic functions such as system occupancy system resource, volume and brightness control, program management, and screen white balance.

5.3. Program play test

In the field application, an 800*320 full-color indoor LED advertising machine was tested, and the software program playback management interface was opened. As is shown in Figure 11, the rectangular screen of the interface is also the scaled version of the LED advertising machine large screen. The mobile client reads the picture or video and places it in the rectangular screen of the software interface to adjust the size of the picture or video playing area. The effect is shown in Figure 12.



Figure11. Software program play management interface



Figure12. Current test chart

6. Conclusion

- Based on the MT6589 chip structure of Cortex-A7 architecture, the hardware design of LED advertising machine wireless control system is carried out.
- The cross-platform software design of mobile client is realized by Phone-Gap technology. Diversified text, picture and video playback, network automatic update Time and other versatile implementations to meet the needs of the majority of users.
- The final test shows that the control system runs stably and has high reliability. The display effect of the LED advertising screen is clear. The software interface is intuitive to understand, and the user operation is easy to use, which greatly meets the market demand.

7. Acknowledgments

This work was supported by the Science and Technology Plan Project of Xiamen City (3502Z20183060), Fujian Provincial Department of Education JK Science and Technology Plan Project(JK2017036).

8. References

- [1] Jiang X, Chen M and Li Z *et al* 2012 Wireless real-time LED display control system based on single chip microcontroller *IEEE International Conference on Computer Science & Education* **951-952**
- [2] Song Y, Feng Y and Ma J *et al* 2011 Design of led display control system based on AT89C52 single chip microcomputer *Journal of Computers* **6** 718-724
- [3] Yang F, Qin X F, and Zhai L B 2015. Control system and control method for automatic adjustment of outdoor led display brightness *Lecture Notes in Electrical Engineering* **331** 613-619
- [4] Chen M C, Ciou J Y and Jhang G S *et al* 2016 Led image display system with mobile app control *Computers & Electrical Engineering* **52** 1-11
- [5] Liu S M and Chou Y C 2014 Color calibration for a surrounding true-color led display system by pwm controls *IEEE Transactions on Industrial Electronics* **61** 6244-6252
- [6] Cui T W, Chen H and Gao Y *et al* 2014 Design of LED control based on Android *Electronic Measurement Technology* **37** 102-124
- [7] Zhang S K and Peng P 2015 LED display word stock update wireless research based on LPC2103 *Video Engineering* **39** 107-110
- [8] Yi P, Iwayemi A and Zhou C 2011 Developing zigbee deployment guideline under wifi interference for smart grid applications *IEEE Transactions on Smart Grid* **2** 110-120
- [9] Friedman R, Kogan A and Krivolapov Y *et al* 2013 On power and throughput tradeoffs of wifi and bluetooth in smartphones *IEEE Transactions on Mobile Computing* **12** 1363-1376
- [10] Bo C, Shuai Z and Tang H 2015 Wireless machine to machine monitoring using cross-platform smart phone for district heating *Wireless Personal Communications* **83** 1229-1250

Author Index

A		Feng-Chen Li	351
A L Yang	488	Fubin Xu	275
Aiguo Zhang	536	G	
Alexis Muhirwa	351	G X Su	442
Anna Won	426	Gang Chen	381,157
Anthony Msafiri Nyangarika	457,512,447	Gang Li	431
Anxing Lai	241,431	Gentao Dong	72
B		Guangming Lu	307
B C Lu	244	Guanlu Yang	290,367
B Tang	33	Guibo Ma	11
B Yu	135	Guiping Zhu	59
Bangcheng Wei	411	Guo Qiang	219
Bao-jun Tang	457,447,512	Guogang Yan	406
Bi Zhen	219	Guopeng Zhao	227
Bin Song	199	H	
Bin Yu	181	H F Liu	135
Bing Li	469	H F Wang	27
Bo Wen	145	H Li	135
C		H Liu	3,96
C Thongchaisuratkrul	370	H X Pan	27
Can Cui	260	H Y Fu	442,488
Can Zhou	469	H Z Yan	442
Cao Wei	72	Haifeng Liu	79,181,191
Chang Xie	307	Hao Xu	181,191
Chang Zhou	358	Haoran Duan	469
Chao Yuan	297	Hao Jiang	171
Chengzhi Zhu	523	Hengxuan Li	145
Cunbing Gui	66	Hongjie Lu	531
Coordination Analysis	282	Hongming Wang	40
D		Hongwei Yang	227
D W Sun	96	Hongyang Dai	307
D Zhao	442	Hui chao Wang	358
Dajin Chen	204	Hui Li	181,191
Di Wu	145	Hui Liu	88,171,418,345
Dijun Hu	235	Hui-yan Cheng	506
Dilin Mao	523	Hulin Huang	59
Dong Peng	279	HY Cheng	475
Dong Zhao	11	He Zhang	275
E		J	
Enwen Li	199	J E T Tibayan	495
F		J F Liu	439
F S Zeng	488	J Liu	488
Fei Xiao	128,164	Jeenanunta Chawalit	322
Feng Xu	227	Jiadong Meng	204
		Jian Cai	275

Jian Deng	536	Pengfei Zhang	279
Jian Wu	260		
Jianfei Yang	72	Q	
Jian-fu Liu	506	Q H Shanggua	33
Jiang Yilang	219	Q L Tong	391
Jiang-xue Long	506	Qi Guo	337
Jianhua Yang	268	Qian Cheng	49
Jianling Zhang	235	Qilong Zhang	469
Jianwen Liu	544	Qin Xiaohui	219
Jianxing Qin	337	Qing Ye	11
Jie Chi	437	Quan Hong	79
Jie Ding	358	Quan Liu	297
Jie Lei	411		
Jin hui Ma	358	R	
Jingbo Wu	235	R C Muñoz Jr	495
Jingkang Ba	406	R Liu	105
Jinheng Li	431	R X Zhang	244
Jinning Shan	381	Rongquan Wang	204
Jinxiu Hou	252,307	Run Li	275
Junying Song	315	Runze Ma	260
JX Long	475		
		S	
K		S J A Japitana	495
K R C Medina	495	S Y Guo	135
Kai Deng	411	S Zhu	96
Kaiyuan Jin	268	Shanshan Li	210
Kang Ye	128,164	Shengyuan Liu	260
		Shi Xinhong	398
L		Shimin Wu	437
Lai Li	59	Shoushou Zhang	315
Lei Liu	358	Shuyang Wang	367
Lei Wang	210,204,431	Siqing Sheng	88,418
Lei Zhang	191	Siyao Hu	268
Li Li	79	Siyuan Guo	181,315
Liang Feng	260	Su Xu	437
Licheng Zhu	127,164	Subin Wang	563
Linlin Wu	88,418	Sun Ke	398
Linong Wang	199		
		T	
M		Tao He	345
M X Yin	3	Tianran Li	297
Man Xu	418	Tianxiang Chen	204
Maxime Binama	351	Tianyue Wang	252
Meizi Hong	145	Thongchaisuratkrul	373
Mengxiang Zeng	480		
Miaoqiang Xu	536	W	
Minxu Wu	290,367	W J Zhu	135
Minyong Li	544	W Song	3
		W Srisuriyajan	373
P		W W Liang	135
P F Gao	442	Wei Geng	523
P Song	96,105,330	Wei Zhong	235
Peng Li	145	Wei-Hua Cai	351
Peng Song	171,345	Weijun Zhu	315,235
Pengfei Sun	268	Weiling Lin	210

Weiwei Zhang	210	Y H Li	3
Wenhao Jiang	40	Y Liu	330,33
Wenjun Lu	79	Y T Huang	442
Wenliang Zhu	268	Y Zhu	391
Wenqi Mao	79	Yalan Ye	40
Wen-Tao Su	351	Yang Bai	337
Wenwei Zhu	563	Yang Wang	290
Wenwu Liang	191	Yang Yang	260
Wutyi Hnin Su	322	Yangfan Zhang	345
		Yanjie Wang	227
X		Yaqi Fang	199
X M Liu	244	YC Yang	330
X S Wang	105	Ying Lv	307
X S Yumang	495	Yingchao Xu	563
X X Yan	391	Yizhou Mao	563
X Zhang	27	Yong Li	279
Xi Lu	59	Yongqiang Song	469
Xiang An	40	Yongsheng Zhao	315
Xianghua Li	279	Youlin Hu	128,164
Xian-Zhu Wei	351	Youxiang Yan	210
Xiao Wang	88	Yuan Gao	18
Xiaobo Tang	411	Yudong Tan	279
Xiaofei Wang	181	Yu-liang Qian	117
Xiaoli Huang	406	Yun Zhang	117
Xidong Zhang	59	Y Bai	330
Xin Hu	18	Y C Wu	442
Xin Qiu	72		
Xin Rao	437	Z	
Xin Wang	381	Z D Zhang	135
Xinfan Jiang	235	Z F Xu	27
Xinwei Zhou	227	Z Liu	475
Xinwen Wang	437	Z N Dai	488
Xinyang Han	523	Z P Ren	244
Xinyu Wang	18	Z W Lin	105
Xiongli Li	164,128	Z Wei	96
Xiu Cao	523	Zehong Huang	290,367
Xiwu Leng	128,164	Zhang Xu	398
Xiaofei Wang	179	Zhangbao Chen	66
Xiaojing Wang	406	Zheng Qiu	116
Xiaolei Zhang	260	Zheng Zhang	297
Xuehui Luo	66	Zhenwei Li	268
Xuekun Cheng	171	Zhenyao Qian	411
Xuwei Guo	418	Zhenyu Li	11,381
Yanwei Xiao	395	Zhenzhen Zhou	157
Xiao Zhang	117	Zhihong Yu	252,304
Xiaobao Hu	88	Zhihuang Zheng	552
Xuexiang Yu	536	Zhi-neng Dai	506
Xun Liu	72	Zhipeng Yang	431
Xu Xie	345	Zhiwei Zhao	18
Xiao Yanwei	398	Zhongbin Zhang	531
		Zhongkai Yi	337
Y		Zhou Qinyong	219
Y Cui	330	Zhu Bingquan	398